

Geometry-based density functional theory: Construction and applications to soft matter

Matthias Schmidt

Institut für Theoretische Physik II
Heinrich-Heine-Universität Düsseldorf
Universitätsstraße 1
D-40225 Düsseldorf
Germany

E-mail: mschmidt@thphy.uni-duesseldorf.de

October 2004

Habilitationsschrift
vorgelegt der Mathematisch-Naturwissenschaftlichen Fakultät
der Heinrich-Heine Universität Düsseldorf

Abstract

The construction of density functionals for various model systems is summarized and applications to homogeneous and inhomogeneous situations are presented. The geometry-based method used relies on Rosenfeld's fundamental measures approach. Among the models treated are penetrable spheres, the Widom-Rowlinson model, non-additive hard sphere mixtures, the Asakura-Oosawa-Vrij (AOV) model of colloid-polymer mixtures, as well as extensions of the AOV model that treat the influence of polymer non-ideality, colloid-induced polymer compression, the influence of poor solvent quality, and polymer penetrability. For the AOV model studies of inhomogeneous situations are presented, like the free fluid-fluid interface and wetting properties, wall tension and contact angle of the liquid-gas interface and a hard wall, as well as response to external fields, like standing laser fields, confining hard or penetrable walls, and gravity. Further model systems include colloidal rod-sphere mixtures, hard body amphiphilic mixtures, and fluid adsorbate in random porous media, where bulk demixing and interfacial properties were investigated. This thesis includes all corresponding original publications as well as an overview in German.

Contents

Übersicht in deutscher Sprache	9
1 Introduction	11
2 Overview of density functional construction and applications	12
2.1 Basic model fluids	12
2.2 Colloid-polymer mixtures	13
2.2.1 Construction of a density functional	13
2.2.2 Interfacial properties	14
2.2.3 Response to external fields	15
2.2.4 Beyond Asakura-Oosawa-Vrij	16
2.3 Rod-sphere mixtures	17
2.4 Hard body amphiphiles	18
2.5 Fluids in random porous media	18
2.6 Soft interactions	20
2.7 Miscellaneous	21
3 Conclusions	22
Acknowledgments	23
List of coauthors	24
References	25
ORIGINAL PUBLICATIONS	29
Review	29
<i>Geometry-based density-functional theory: An overview</i> M. Schmidt, J. Phys.: Cond. Matt. 15 , S101 (2003)	29
Basic model fluids	35
<i>Ab-initio density-functional theory for penetrable spheres</i> M. Schmidt, J. Phys.: Cond. Matt. 11 , 10163 (1999)	35
<i>Fluid of penetrable spheres: Testing the universality of the bridge functional</i> Y. Rosenfeld, M. Schmidt, M. Watzlawek, H. Löwen, Phys. Rev. E 62 , 5006 (2000)	42
<i>Density functional for the Widom-Rowlinson model</i> M. Schmidt, Phys. Rev. E 63 , 010101(R) (2001)	47
<i>Rosenfeld functional for non-additive hard spheres</i> M. Schmidt, J. Phys.: Cond. Matt. 16 , L351 (2004)	51
Colloid-polymer mixtures: Construction of a density functional	58
<i>A density functional for a model colloid-polymer mixture</i> M. Schmidt, H. Löwen, J. M. Brader, R. Evans, Phys. Rev. Lett. 85 , 1934 (2000)	58
<i>Density functional theory for a model colloid-polymer mixture: bulk fluid phases</i> M. Schmidt, H. Löwen, J. M. Brader, R. Evans, J. Phys.: Cond. Matt. 14 , 9353 (2002)	62

Colloid-polymer mixtures: Interfacial properties	92
<i>Interfacial Properties of Model Colloid-Polymer Mixtures</i>	
R. Evans, J. M. Brader, R. Roth, M. Dijkstra, M. Schmidt, H. Löwen, Phil. Trans. Roy. Soc. Lond. A 359 , 961 (2001)	92
<i>Entropic wetting and the fluid-fluid interface of a model colloid-polymer mixture</i>	
J. M. Brader, R. Evans, M. Schmidt, H. Löwen, J. Phys.: Cond. Matt. 14 , L1 (2002)	107
<i>Statistical mechanics of inhomogeneous model colloid-polymer mixtures</i>	
J. M. Brader, R. Evans, M. Schmidt, Mol. Phys. 101 , 3349 (2003)	115
<i>Wall tensions of model colloid-polymer mixtures</i>	
P. P. F. Wessels, M. Schmidt, H. Löwen, J. Phys.: Cond. Matt. 16 , L1 (2004)	151
<i>Contact angle of the colloidal liquid-gas interface and a hard wall</i>	
P. P. F. Wessels, M. Schmidt, H. Löwen, J. Phys.: Cond. Matt. 16 , S4169 (2004)	159
<i>Direct visual observation of thermal capillary waves</i>	
D. G. A. L. Aarts, M. Schmidt, H. N. W. Lekkerkerker, Science 304 , 847 (2004)	175
 Colloid-polymer mixtures: Response to external fields	 179
<i>Laser-induced condensation in colloid-polymer mixtures</i>	
I. O. Götze, J. M. Brader, M. Schmidt, H. Löwen, Mol. Phys. 101 , 1651 (2003)	179
<i>Capillary condensation of colloid-polymer mixtures confined between parallel plates</i>	
M. Schmidt, A. Fortini, M. Dijkstra, J. Phys.: Cond. Matt. 48 , S3411 (2003)	187
<i>Capillary evaporation in colloid-polymer mixtures selectively confined to a planar slit</i>	
M. Schmidt, A. Fortini, M. Dijkstra, J. Phys.: Cond. Matt. 16 , S4159 (2004)	197
<i>Competition between sedimentation and phase coexistence of colloidal dispersions under gravity</i>	
M. Schmidt, M. Dijkstra, J. P. Hansen, J. Phys.: Cond. Matt. 16 , S4194 (2004)	207
<i>Floating liquid phase in sedimenting colloid-polymer mixtures</i>	
M. Schmidt, M. Dijkstra, J. P. Hansen, Phys. Rev. Lett. 93 , 088303 (2004)	217
 Colloid-polymer mixtures: Beyond Asakura-Oosawa-Vrij	 221
<i>Fluid demixing in colloid-polymer mixtures: Influence of polymer interactions</i>	
M. Schmidt, A. R. Denton, J. M. Brader, J. Chem. Phys. 118 , 1541 (2003)	221
<i>Colloid-induced polymer compression</i>	
A. R. Denton, M. Schmidt, J. Phys.: Cond. Matt. 14 , 12051 (2002)	230
<i>Demixing of colloid-polymer mixtures in poor solvents</i>	
M. Schmidt, A. R. Denton, Phys. Rev. E 65 , 061410 (2002)	242
<i>Penetrability in model colloid-polymer mixtures</i>	
M. Schmidt, M. Fuchs, J. Chem. Phys. 117 , 6308 (2002)	248
 Rod-sphere mixtures	 253

<i>Density functional theory for colloidal rod-sphere mixtures</i>	
M. Schmidt, Phys. Rev. E 63 , 050201(R) (2001)	253
<i>Colloidal rod-sphere mixtures: Fluid-fluid interfaces and Onsager limit</i>	
J. M. Brader, A. Esztermann, M. Schmidt, Phys. Rev. E 66 , 031401 (2002)	257
<i>Simulation and theory of fluid-fluid interfaces in binary mixtures of hard spheres and hard rods</i>	
P. G. Bolhuis, J. M. Brader, M. Schmidt, J. Phys.: Cond. Matt. 48 , S3421 (2003)	270
<i>Entropic wetting of a colloidal rod-sphere mixture</i>	
R. Roth, J. M. Brader, M. Schmidt, Europhys. Lett. 63 , 549 (2003)	278
<i>Density functional theory for sphere-needle mixtures: Toward finite rod thickness</i>	
A. Esztermann, M. Schmidt, Phys. Rev. E 70 , 022501 (2004)	285
<i>Colloids, polymers, and needles: Demixing phase behavior</i>	
M. Schmidt, A. R. Denton, Phys. Rev. E 65 , 021508 (2002)	289
Hard body amphiphiles	297
<i>Amphiphilic hard body mixtures</i>	
M. Schmidt, C. von Ferber, Phys. Rev. E 64 , 051115 (2001)	297
<i>Hard body amphiphiles at a hard wall</i>	
J. M. Brader, C. von Ferber, M. Schmidt, Mol. Phys. 101 , 2225 (2003)	307
Fluids in random porous media	314
<i>Density functional theory for fluids in porous media</i>	
M. Schmidt, Phys. Rev. E 66 , 041108 (2002)	314
<i>Replica density functional study of one-dimensional hard core fluids in porous media</i>	
H. Reich, M. Schmidt, J. Stat. Phys. 116 , 1683 (2004)	321
<i>Hard sphere fluids at surfaces of porous media</i>	
M. Schmidt, Phys. Rev. E 68 , 021106 (2003)	341
<i>Hard sphere fluids in random fiber networks</i>	
M. Schmidt, J. M. Brader, J. Chem. Phys. 119 , 3495 (2003)	347
<i>Model colloid-polymer mixtures in porous matrices: density functional versus integral equations</i>	
M. Schmidt, E. Schöll-Paschinger, J. Köfinger, G. Kahl, J. Phys.: Cond. Matt. 14 , 12099 (2002)	353
<i>Capillary condensation and interface structure of a model colloid-polymer mixture in a porous medium</i>	
P. P. F. Wessels, M. Schmidt, H. Löwen, Phys. Rev. E 68 , 061404 (2003)	372
<i>Freezing in the presence of disorder: A lattice study</i>	
M. Schmidt, L. Lafuente, J. A. Cuesta, J. Phys.: Cond. Matt. 15 , 4695 (2003)	384
Soft interaction potentials	398
<i>Density-functional theory for soft potentials by dimensional crossover</i>	
M. Schmidt, Phys. Rev. E 60 , R6291 (1999)	398
<i>A density functional for additive mixtures</i>	
M. Schmidt, Phys. Rev. E 62 , 3799 (2000)	402
<i>Fluid structure from density functional theory</i>	
M. Schmidt, Phys. Rev. E 62 , 4976 (2000)	406

<i>Density functional theory for structure and freezing of star polymer solutions</i>	
B. Groh, M. Schmidt, J. Chem. Phys. 114 , 5450 (2001)	412

Miscellaneous	419
----------------------	------------

<i>Density functional theory for random sequential adsorption</i>	
M. Schmidt, J. Phys.: Cond. Matt. 14 , 12119 (2002)	419
<i>Freezing transition of hard hyperspheres</i>	
R. Finken, M. Schmidt, H. Löwen, Phys. Rev. E 65 , 016108 (2002)	428
<i>Colloids confined to a flexible container</i>	
L. Maibaum, M. Schmidt, H. Löwen, Phys. Rev. E 63 , 051401 (2001)	437
<i>Topological defects in nematic droplets of hard spherocylinders</i>	
J. Dzubiella, M. Schmidt, H. Löwen, Phys. Rev. E 62 , 5081 (2000)	446
<i>Colloidal particles in emulsions</i>	
F. L. Roman, M. Schmidt, H. Löwen, Phys. Rev. E 61 , 5445 (2000)	457
<i>Do effective interactions depend on the choice of coordinates?</i>	
M. Schmidt, Phys. Rev. E 65 , 022801 (2002)	464
<i>Decoration lattices of colloids adsorbed on stripe-patterned substrates</i>	
H. M. Harreis, M. Schmidt, H. Löwen, Phys. Rev. E 65 , 041602 (2002)	468

Übersicht in deutscher Sprache

Die Entwicklung leistungsfähiger Dichtefunktionale [1, 2] ermöglicht das Studium relevanter inhomogener Situationen in Systemen der weichen Materie. Für eine Reihe von Modellsystemen werden in der vorliegenden Arbeit explizite Näherungen vorgestellt für die Helmholtzsche freie Energie, ausgedrückt als Funktional der Einteilchendichte. Ein solches Dichtefunktional ist spezifisch für gegebene Wechselwirkungen zwischen den Teilchen und ermöglicht die Behandlung von beliebigem externen Einfluss, sofern dieser durch ein externes (statisches) Potential modelliert werden kann, wie ein Substrat oder die Gravitation. Die Konstruktion der hier vorgestellten Dichtefunktionale basiert einerseits auf der geometrischen Form der Teilchen, andererseits auf der statistischen Mechanik des betrachteten Modells in stark einschränkender Geometrie. In diesem sogenannten nulldimensionalen Grenzfall des Modells kann man die Zustandssumme und damit die freie Energie exakt berechnen. Ein vermöge der geometrie-basierten Methode konstruiertes Dichtefunktional interpoliert dann zwischen dem nulldimensionalen Grenzfall und der für kleine Dichten gültigen Virialentwicklung. Die Anwendungen zeigen, dass die so erhaltene (approximative) Theorie für beliebig inhomogene Dichteverteilungen vernünftige Resultate liefert. Das Verfahren basiert auf Rosenfeld's *fundamental measure theory* für harte Kugeln [3], und deren moderner Formulierung [4–7]. Eine kurze Übersicht über behandelte Modelle und Fragestellungen findet sich in dem Konferenzband der *5th Liquid Matter Conference 2002* [12].

Zu der Reihe grundlegender Modelle, die erfolgreich behandelt wurden, gehören durchdringbare Kugeln, deren Paarpotential durch eine repulsive Stufenfunktion gegeben ist [13, 14], das Widom-Rowlinson-Modell [15] für eine Flüssigkeitsmischung in der nur Teilchen verschiedener Komponenten miteinander (wie harte Kugeln) wechselwirken [16], sowie nicht-additive harte Kugelmischungen [17]. Das jeweilige Dichtefunktional beschreibt die Korrelationsfunktionen in fluiden Zuständen sowie das Phasenverhalten sehr zufriedenstellend im Vergleich zu Simulationsdaten und eröffnet so die Möglichkeit des detaillierten Studiums inhomogener Situationen.

Mischungen von kolloidalen harten Kugeln und nichtabsorbierenden Polymeren sind nützliche Modellsysteme auf mesoskopischer Skala [21, 22], da das Phasenverhalten ähnlich dem von einfachen Substanzen ist, also Gas, Flüssigkeit und Kristall umfasst. Das Asakura-Oosawa-Vrij-Modell (AOV-Modell) [23, 24] ist wohl das einfachste theoretische Modell zur Beschreibung: Die Kolloidteilchen werden durch harte Kugeln mit Radius R_c beschrieben, die Polymere durch ideale (nicht-wechselwirkende) effektive Kugeln deren Radius R_p gleich dem Gyrationradius gesetzt ist, und die mit einer Hartkugel-Abstoßung mit Reichweite $R_p + R_c$ mit den Kolloiden wechselwirken. Das für das AOV-Modell hergeleitete Dichtefunktional [25] beschreibt Phasenverhalten und Korrelationsfunktionen sehr gut [27] und wurde für das Studium verschiedenster inhomogener Situationen verwandt: Benetzung von Wänden und freie Grenzflächen [28–30], die Grenzflächenspannung an Wänden [32], sowie der Kontaktwinkel der Flüssig-Gas-Grenzfläche mit einer harten Wand [33]. Vink, Horbach und Binder haben dieses Modell kürzlich detailliert mit Computersimulationen untersucht [35–37]. Dass es nützlich ist, solche mesoskopischen Systeme zu betrachten zeigt eine experimentelle Arbeit, in der es gelungen ist, thermische Kapillarwellen an einer flüssigen Oberfläche [38, 39] erstmals direkt (mit konfokaler Mikroskopie) sichtbar zu machen [40] (siehe auch die Referenzen [41, 42]).

Weiterhin wurde die DFT für das AOV-Modell [25] angewendet zum Studium von laserinduzierter Kondensation der flüssigen Phase [43], der Kapillarkondensation zwischen zwei parallelen Platten [44], der Kapillarevaporation zwischen zwei semipermeablen Platten (die als durchdringbar für die Polymere angenommen werden) [45], des Wettstreits zwischen Sedimentation und Phasentrennung [46] und der Vorhersage einer "schwebenden

Flüssigkeit” bei Einfluss von der Gravitation auf Kolloide *und* Polymere [47].

Die leistungsfähige geometrie-basierte Methode hat es ermöglicht, Modelle zu behandeln, die über das AOV-Modell hinausgehen: Jeweils der Einfluss auf das Phasenverhalten wurde untersucht von Polymererepulsion [48], durch Kolloidteilchen induzierte Kompression der Polymere [49], der Lösungsmittelqualität [50], sowie dem Eindringen von Kolloidteilchen in Polymere [51].

Mischungen von kolloidalen Kugeln und Stäbchen sind interessante Modelle um das Ordnen von Orientierungsfreiheitsgraden zu studieren [52]. Rosenfeld’s ursprüngliches Dichtefunktional für allgemeine konvexe Körper [53, 54] liefert nicht die richtige Virialentwicklung und einige Verbesserungen wurden vorgeschlagen [55–57]. Für eine Mischung von harten Kugeln und unendlich dünnen Stäbchen [52] wurde eine DFT hergeleitet, die die richtige Virialentwicklung bis zur zweiten Ordnung hat [58], und damit die Eigenschaften von flüssigen Grenzflächen studiert [59]. Bemerkenswert genau im Vergleich zu Simulationsdaten sind die vorhergesagten Dichteprofile über die Grenzfläche hinweg [60]. An einer harten Wand zeigt dieses Modell Benetzung durch die kugelige flüssige Phase [61]. Weitere Terme, die die Wechselwirkung zwischen Stäbchen beschreiben, konnten gefunden werden [62]. Als sehr reichhaltig hat sich das Phasenverhalten bei Zugabe von Polymeren erwiesen [63].

Der Frage ob sich amphiphiles Verhalten finden lässt in Modellen, die nur von sterischer Abstoßung bestimmt sind, wurde in Ref. [64] mit Hilfe einer ternären Mischung von Kugeln, Stäbchen und einem Hybrid aus beiden nachgegangen. Sowohl das Phasenverhalten als auch die Adsorption an einer harten Wand [65] lassen schließen, dass in der Tat amphiphile Eigenschaften durch die Teilchenform alleine entstehen können.

Um Flüssigkeiten, die in ungeordneten porösen Medien adsorbiert sind, zu beschreiben wurde ein *quenched-annealed* DFT hergeleitet [69]. Dabei wird das poröse Medium durch die gequenchten Komponenten einer Flüssigkeitsmischung beschrieben. Der Ansatz kann durch den Replica-Trick begründet werden [70], beschreibt zuverlässig die Adsorption an Oberflächen des porösen Mediums [72] und wurde verallgemeinert auf Netzwerke aus Stäbchen [74]. Mit dieser Theorie wurde gezeigt dass für Kolloid-Polymer-Mischungen in poröse Medien Kapillarkondensation auftritt [75] und die resultierende Grenzfläche wurde untersucht [77]. In einem Gittermodell wurde das Einfrieren in der Gegenwart von Unordnung studiert [78].

Für weiche Paarwechselwirkungen wurde eine DFT vorgeschlagen [79], für Mischungen verallgemeinert [80], und auf die Paarkorrelationen in der flüssigen Phase einiger Modellfluide angewendet [81]. Im Detail wurde ein Modell für Sternpolymere untersucht [82].

Weitere Studien enthalten eine DFT für den Wachstumsprozess *random sequential adsorption* [83], sowie eine Untersuchung des Einfrierens von harten Hyperkugeln in Raumdimensionen $D > 3$ [84]. Probleme, die mit anderen Methoden, wie Computersimulation, angegangen worden sind und die in der Zukunft mit DFT behandelt werden könnten, sind kolloidale Teilchen, die in einem flexiblen Container eingeschlossen sind [85], topologische Defekt in nematischen Tröpfchen [86], kolloidale Teilchen, die in einer Emulsion suspendiert sind [87], die Abhängigkeit von effektiven Wechselwirkungen von der Wahl der Koordinaten [88], sowie Dekorationsgitter von Kolloiden, die an streifenförmig gemusterten Substraten adsorbiert sind [89].

Zusammenfassend ist damit gezeigt worden, dass zuverlässige Dichtefunktionale im Rosenfeldschen Sinn für eine Reihe von Modellsystemen konstruiert werden können. Solch eine Theorie ermöglicht (und stimuliert) dann das Studium inhomogener Situationen wie man sie an Grenzflächen oder in äußeren Feldern findet.

1 Introduction

Inhomogeneous systems provide formidable challenges for both quantitative and qualitative description. Inhomogeneities in spatial properties, i.e. distribution functions, may arise intrinsically like in a crystal or at a free fluid interface or may be generated in response to an external field, like gravity or confining walls. Soft matter systems are excellent model systems to study such structuring due to the well-accessible time and length scales. The present thesis presents applications to models such as colloidal dispersions of spherical and elongated particles, mixtures of (hard sphere) colloids and non-adsorbing polymers. Interesting questions range from the bulk phase behavior to interfacial properties, behavior at walls or in narrow capillaries.

Density functional theory (DFT) for inhomogeneous classical fluids is a reformulation of classical Statistical Mechanics, such that the one-body density distribution $\rho(\mathbf{r})$, where \mathbf{r} is the space coordinate, represents the microscopic degrees of freedom. It can be shown [1, 2] that the grand potential Ω at fixed temperature T , volume V , and chemical potential μ can be expressed as a functional of $\rho(\mathbf{r})$. The existence of a minimization principle, $\delta\Omega/\delta\rho(\mathbf{r}) = 0$, enables one to obtain $\rho(\mathbf{r})$, and via reinserting the solution into the functional one obtains the equilibrium grand potential, $\Omega_0 = \Omega([\rho], T, V)$. This formulation becomes useful via the exact splitting

$$\Omega([\rho], T, V, \mu) = F_{\text{id}}([\rho], T, V) + F_{\text{exc}}([\rho], T, V) + \int d\mathbf{r} \rho(\mathbf{r})(V_{\text{ext}}(\mathbf{r}) - \mu), \quad (1)$$

where $F_{\text{id}}([\rho], T, V) = \int d\mathbf{r} \rho(\mathbf{r})[\ln(\Lambda^3 \rho(\mathbf{r})) - 1]$ is the (exact) Helmholtz free energy of the ideal gas, Λ is the thermal wavelength (being irrelevant in this context), $V_{\text{ext}}(\mathbf{r})$ is an external potential, and $F_{\text{exc}}[\rho]$ is the excess (over ideal) contribution to the Helmholtz free energy that is due to non-vanishing interparticle interactions. As $F_{\text{exc}}[\rho]$ is independent of $V_{\text{ext}}(\mathbf{r})$, a reliable approximation of the former will enable one to treat arbitrary realizations of $V_{\text{ext}}(\mathbf{r})$. The present work presents both, approximations of $F_{\text{exc}}[\rho]$ (also in the context of mixtures and non-spherical interactions, where obvious generalizations of the above one-component formulation hold), as well as applications to relevant situations that can be modeled via an external potential. In most investigations computer simulations are used to assess the accuracy and reliability of the DFT approximation or to back up DFT predictions.

A particular successful DFT is Rosenfeld's fundamental measures theory (FMT) for (additive) mixtures of hard spheres, as initially formulated in a remarkable letter in 1989 [3]. In contrast to its present (rather) widespread use, the community did not immediately embrace the approach. Possible reasons are its inherently very different structure as opposed to all other available DFT approximations, and the initial failure to describe the freezing transition, that was cured via imposing the correct dimensional crossover to reduced dimensionality [4, 5]. Tarazona and Rosenfeld showed later [6] that one can systematically construct a DFT for the three-dimensional system via systematically analyzing zero-dimensional density distributions. The present overview will not do justice to the exciting developments for the hard sphere functional, ranging from tensorial weight functions [7] necessary for describing freezing, improved equation of state [8], and, in particular, the illuminating Lafuente-Cuesta lattice DFT [9–11].

The present work is concerned with the application of the concept to generate a functional for a 3d system via systematically considering its behavior in the 0d situation. Sec. 2.1 present successful treatments of the penetrable sphere model, the Widom-Rowlinson model, and the general non-additive hard sphere mixture. Sec. 2.2 is concerned with model colloid-polymer mixtures like the Asakura-Oosawa-Vrij (AOV) model applied to adsorption at a hard wall, and external fields like gravity, as well as to various simple

extensions of the basic AOV model. An experimental investigation of thermal capillary waves using confocal microscopy demonstrates the usefulness of the colloid-polymer mixtures as model systems. Sec. 2.3 presents the treatment of colloid rod-sphere mixtures and investigations of the properties of free fluid interfaces and wetting of a hard wall. Sec. 2.4 is concerned with a ternary hard body mixture where one component possesses an amphiphilic character solely due to its geometric shape. In Sec. 2.5 the systematic extension of DFT to quenched-annealed fluid mixtures is presented. Such models are used to model adsorbates (annealed components) inside random porous media (represented by the quenched components). Sec. 2.6 reviews progress to formulate a fundamental-measure theory for general soft pair interactions. Sec. 2.7 summarizes various further studies, like the proposal of a DFT for the non-equilibrium process of random sequential adsorption, freezing of hyperspheres, colloids confined to a flexible container, topological defects in nematics, colloidal particles immersed in an emulsified host fluid, the dependence of effective interactions (obtained by integrating out microscopic degrees of freedom) on the choice of coordinates and the properties of decoration lattices adsorbed on stripe-patterned substrates.

A brief overview of the state of research in 2002 was published in the proceedings of the 5th Liquid Matter Conference [12] (*p.29*)¹.

2 Overview of density functional construction and applications

2.1 Basic model fluids

The treatment of three basic model fluids exemplifies the recent progress: Those are penetrable spheres [13, 14] that interact with a repulsive step-function pair potential, the Widom-Rowlinson model [15], where the like species possess ideal (vanishing) interactions, but the unlike species repel like hard cores [16], and the general non-additive hard sphere mixture [17]. A fourth, and particularly relevant system, that of model colloid-polymer mixtures, will be described later (Sec. 2.2).

Penetrable spheres that interact with a constant pair potential energy if their separation distance is smaller than their diameter are a prototype for intermicellar interactions in a solvent, and are a representative of a class of bounded potentials that allows complete interpenetrability of the particles. In order to treat this model with DFT, as sufficient input the geometrical properties of the particles and the exactly known statistical behavior of the system under strong confinement was needed [13] (*p.35*). The theory predicts bulk fluid properties in good agreement with computer simulations, as well as the freezing transition to a multiply occupied face-centered-cubic lattice. It was shown to become exact in the limits of strong confinement and high temperature, and reduces to Rosenfeld's functional for hard spheres in the limit of zero temperature.

Subsequently DFT and simulation results for the pair correlation functions in a bulk fluid of penetrable spheres were compared, as a stringent test for the “universality” of the bridge functional [14] (*p.42*). Considering either the fundamental-measure functional for penetrable spheres [13] or a perturbative treatment using a fundamental-measure hard-sphere functional [3], we concluded that hard-sphere-type bridge functionals are applicable for bounded potentials with high penetrability.

The Widom-Rowlinson model [15] is a symmetric mixture, where the like species possess ideal (vanishing) interactions, but the unlike species repel like hard cores. For the m -component version of this model a DFT was constructed [16] (*p.47*), that is exact for small densities and in the zero-dimensional limit. It predicts bulk fluid structure in

¹Page numbers in italics refer to the location of reprints below.

good agreement with simulations and yields a continuous demixing phase transition for $m = 2$. In the limit of large m the Widom-Rowlinson model reduces to effective hard spheres in the mixed phase and the AOV colloid-ideal polymer model in the demixed phase. Within the approximation of Ref. [16], both cases are captured correctly. For intermediate m we found a first order demixing phase transition, with a rapidly broadening density discontinuity upon increasing m .

Rosenfeld's functional [3] applies to additive hard sphere mixtures, i.e. for mixtures where the hard core distance between two unlike components is given by the mean of the diameters of both components. The DFT of Ref. [17] (*p.51*) describes non-additive hard spheres of arbitrary positive and moderate negative non-additivity between unlike components. In bulk it predicts fluid-fluid phase separation into phases with different chemical compositions. The location of the accompanying critical point agrees well with results from simulations [18–20] over a broad range of non-additivities and both for symmetric and highly asymmetric size ratios. Results for bulk partial pair correlation functions indicate good agreement with simulation data.

2.2 Colloid-polymer mixtures

Colloid-polymer mixtures are useful model systems to study many basic phenomena in condensed matter [21, 22]. In particular their bulk phase behavior resembles closely that of simple substances involving gas, liquid and crystalline phases. The simplest theoretical model to describe real colloid-polymer mixtures is that by Asakura and Oosawa [23] and Vrij [24] (AOV). In their prescription the colloids are assumed to be hard spheres and the polymers to be freely interpenetrating spheres that experience hard core interactions with colloids at a distance given by the sum of colloid and polymer radii, the latter taken to be the polymer radius of gyration.

2.2.1 Construction of a density functional

For the AOV model a DFT was obtained by employing a fundamental measures approach to construct a functional which incorporates the correct dimensional crossover and the exact low density limit [25] (*p.58*). In bulk fluid mixtures the functional yields the same free energy and, therefore, the same gas-liquid (demixing) transition as given by free-volume theory [26]. It generates consistent pair correlation functions; the partial structure factors $S_{ij}(k)$ diverge, as $k \rightarrow 0$, at the critical point obtained from the free energy. Our results for the structure agree well with those from simulation and Percus-Yevick theory.

Further details about this DFT are given in Ref. [27] (*p.62*), where dimensional crossover was discussed in detail. Emphasis was placed on the properties of homogeneous (bulk) fluid phases. We showed explicitly that the functional yields the same free energy and, therefore, the same fluid-fluid demixing transition as that given by a different approach, namely the free-volume theory. The pair direct correlation functions $c_{ij}(r)$ of the bulk mixture are given analytically. We investigate the partial structure factors $S_{ij}(k)$ and the asymptotic decay, $r \rightarrow \infty$, of the total pair correlation functions $h_{ij}(r)$ obtained from the Ornstein-Zernike route. The locus in the phase diagram of the crossover from monotonic to oscillatory decay of correlations was calculated for several size ratios $q = R_p/R_c$, where R_p is the radius of the polymer sphere and R_c that of the colloid. Furthermore we determined the (mean-field) behavior of the partial structure factors on approaching the fluid-fluid critical (consolute) point.

2.2.2 Interfacial properties

The DFT of Ref. [25] was used to investigate the free interface between demixed fluid phases of the AOV model [28] (*p.107*); many further details are given in Ref [29] (*p.115*) and a preliminary account of the results and discussion of other approaches can be found in Ref. [30] (*p.92*). We found that both the colloid and polymer density profiles oscillate on the colloid-rich side of the interface, provided the polymer reservoir packing fraction $\eta_{p,r}$ is sufficiently high. Results for the surface tension are in reasonable agreement with experiment [31]. When the mixture is adsorbed against a hard wall, entropic depletion effects give rise to a wetting transition whereby the colloid-rich phase wets completely. Prior to complete wetting we found three layering transitions, the first of which extends far into the single-phase region.

Subsequently, an analytic formula for the interfacial free energy of the fluid mixture in contact with a hard wall was obtained within a scaled-particle treatment [32] (*p.151*). The results were found to compare well with explicit DFT for the binary mixture. Expressions were given for the wall tension of the mixture when polymers interact via a simple stepfunction pair potential, and for the case of contact with a polymer-coated wall, which was taken to be hard for the colloids but penetrable for the polymers. On the gas side of the fluid-fluid demixing binodal the wetting transition at the hard wall was confirmed and complete drying of the polymer-coated wall on the liquid side of the binodal was predicted.

Inserting DFT results for the liquid-gas, wall-liquid and wall-gas interfacial free energies [33] (*p.159*) into Young’s equation we obtained the contact angle between the gas-liquid interface and the wall. As a function of polymer fugacity this angle exhibits discontinuities of slope (“kinks”) upon crossing first-order surface phase transitions located on the gas branch of the bulk binodal. Each kink corresponds to a transition from $n - 1$ to n colloid layers adsorbed at the wall, referred to as the n ’th layering transition. The corresponding adsorption spinodal points from $n - 1$ to n layers upon reducing the polymer fugacity along the bulk binodal were identified in Refs. [28, 29]. Remarkably, we found desorption spinodal points from n to $n - 1$ layers to be absent upon increasing polymer fugacity at bulk coexistence, and many branches (containing up to 7 colloid layers) to remain metastable. Results for the first layering binodal and both spinodal branches off-bulk coexistence hint at a topology of the surface phase diagram consistent with these findings. Both the order of the transition to complete wetting and whether it is preceded by a finite or an infinite number of layering transitions remained open questions. We compared the locations of the first layering binodal line and of the second layering binodal point at bulk coexistence with recent computer simulation results by Dijkstra and van Roij [34]. Vink and Horbach [35, 36] studied the free gas-liquid interface using grand canonical Monte Carlo simulation, and Vink, Horbach and Binder investigated in detail the critical behavior [37].

In an experimental collaboration with D. G. A. L. Aarts and H. N. W. Lekkerkerker, we studied the free fluid-fluid interface in a phase-separated colloid-polymer dispersion with laser scanning confocal microscopy and directly observed thermally induced capillary waves [38, 39] at the interface in real space [40] (*p.175*) (see also [41, 42]). Experimental results for static and dynamic correlation functions validated the capillary wave model down to almost the particle level. The ultralow interfacial tension, the capillary length, and the capillary time were found to be in agreement with independent measurements. Furthermore, capillary waves were observed to induce the spontaneous breakup of thin liquid films and thus were concluded to be of key importance in the process of droplet coalescence.

2.2.3 Response to external fields

Various further external influence on colloid-polymer mixtures has been studied: Laser-induced condensation [43], capillary condensation induced by confinement between smooth parallel hard walls [44], capillary evaporation induced by two parallel semi-permeable walls [45], the competition between sedimentation and demixing [46], and the occurrence of a “floating liquid phase” in sedimentation profiles [47].

The AOV model was studied when exposed to a plane wave external potential representing a three-dimensional standing laser field [43] (*p.179*). With computer simulations and DFT we investigated the resulting structure and phase behavior. For varying laser wavelength λ we monitored the emergence of structure in response to the external field, as measured by the amplitude of the oscillations in the one-body density distribution. Between the ideal gas limit for small λ and the bulk limit of large λ we found non-monotonic crossover that is governed by commensurability of λ and the colloid diameter. Furthermore, the effect of the periodic field on the liquid-vapor transition was studied, a situation that we referred to as laser-induced condensation. Above a threshold value for λ the theoretical phase diagram indicates the stability of a stacked fluid phase, which is a periodic succession (in the laser beam direction) of liquid and vapor slabs. This partially condensed phase causes a splitting of the liquid-vapor binodal leading to two critical points and one triple point. We argued that all these predictions should be experimentally observable for colloid-polymer mixtures in an optical resonator.

We investigated the fluid-fluid demixing phase transition of the AOV model confined between two smooth parallel hard walls [44] (*p.187*). Comparing fluid density profiles, obtained using DFT and computer simulations, for statepoints away from colloidal gas-liquid coexistence showed good agreement of the theoretical results with simulation data. Theoretical and simulation results predict consistently a shift of the demixing binodal and the critical point towards higher polymer reservoir packing fraction and towards higher colloid fugacities upon decreasing the plate separation distance. This implies capillary condensation of the colloid liquid phase.

We also investigated the AOV mixture under selective confinement of the colloids to a planar slab geometry [45] (*p.197*). This is a model for confinement of colloid-polymer mixtures by either two parallel walls with a semi-permeable polymer coating or through the use of laser tweezers. We found that such a model pore favors the colloidal gas over the colloidal liquid phase and hence induces capillary evaporation. A treatment based on the Kelvin equation gives a good account of the location of the capillary binodal for large slit widths. The colloid density profile was found to exhibit a minimum (maximum) at contact with the wall for large (small) slit widths.

Furthermore we have investigated the effects of gravity on the equilibrium behavior of colloid-polymer mixtures. Taking the polymers to possess vanishing buoyancy mass, the density profiles of the two components were calculated within DFT and using Monte Carlo simulations [46] (*p.207*). Under appropriate conditions the profiles were found to exhibit discontinuities or steeply varying regions associated with the interface separating colloid-rich and colloid-poor phases. The position of the interface could be shown to be very sensitive to the strength of the gravitational field and, more surprisingly, to the total height L of the suspension. Phase coexistence in the absence of gravity was shown to be entirely suppressed beyond a critical ratio of the height L over the gravitational length of the colloids.

Even more dramatic effects were found in the case where polymers are assumed to have nonzero buoyancy mass. Again DFT and computer simulation were used to investigate sedimentation equilibria of colloid-polymer mixtures within the AOV model of hard sphere colloids and ideal polymers [47] (*p.217*). If the ratio of buoyant masses of the two species

is comparable to the ratio of differences in density of the coexisting bulk (colloid) gas and liquid phases, a floating liquid stable phase was found, i.e., a thin layer of liquid sandwiched between upper and lower gas phases. The full phase diagram of the mixture under gravity shows coexistence of this floating liquid phase with a single gas phase or a phase involving liquid-gas equilibrium; the phase coexistence lines meet at a triple point. We argued that this scenario remains valid for general asymmetric binary mixtures undergoing bulk phase separation.

2.2.4 Beyond Asakura-Oosawa-Vrij

Several investigations have been undertaken to render the AOV model more realistic at small increase of complexity, i.e. by retaining most of the simplistic appeal. Those include a simplified description of polymer-polymer interactions [48], polymer-induced colloid-compression [49], the influence of poor solvent quality on the bulk demixing phase behavior [50], and taking into account that colloidal particles can penetrate inside polymer coils if polymer-to-colloid size ratios are sufficiently large [51].

In order to investigate colloid-induced polymer compression a mixture was considered where the polymer component is modeled as a polydisperse mixture of effective spheres, mutually noninteracting but excluded from the colloids, with radii that are free to adjust to allow for colloid-induced compression [49] (*p.230*). The bulk fluid demixing behavior of this model system was obtained from a DFT treatment that includes the polymer size polydispersity and configurational free energy, obtained from the exact radius-of-gyration distribution for an ideal (random-walk) chain. Free energies were computed by minimizing the free energy functional with respect to the polymer size distribution. With increasing colloid concentration and polymer-to-colloid size ratio, colloidal confinement was found to increasingly compress the polymers. Correspondingly, the demixing fluid binodal shifts, compared to the incompressible-polymer binodal, to higher polymer densities on the colloid-rich branch, stabilizing the mixed phase.

The influence of poor solvent quality on fluid demixing of a model mixture of colloids and nonadsorbing polymers was investigated [50] (*p.242*) using the AOV model with an addition of modeling the solvent as a two-component mixture of a primary solvent, regarded as a background theta solvent for the polymer, and a cosolvent of point particles that are excluded from both colloids and polymers. Cosolvent exclusion favors overlap of polymers, mimicking the effect of a poor solvent by inducing an effective attraction between polymers. For this model, a geometry-based DFT was derived and applied to bulk fluid phase behavior. With increasing cosolvent concentration (worsening solvent quality), the predicted colloid-polymer demixing binodal shifts to lower colloid concentrations, promoting demixing. For sufficiently poor solvent, a reentrant demixing transition is predicted at low colloid concentrations.

In order to treat polymer non-ideality the polymers were regarded as effective spheres that interact with one another via a repulsive step-function pair potential and with colloids solely via excluded volume [48] (*p.221*). The system was treated with a geometry-based DFT based on the exact zero-dimensional limit of the model. For bulk fluid phases, the calculated demixing binodals demonstrate that with increasing strength of polymer-polymer interaction the coexisting colloidal liquid (vapor) phase becomes more concentrated (dilute) in polymer. In contrast to a simple mean-field-like perturbative density functional, our approach yields good agreement with an experimental demixing phase diagram.

In order to study the effects of penetrability in mixtures of dissimilar particles hard colloidal spheres and penetrable spheres were considered [51] (*p.248*). The latter may be taken to represent ideal, noninteracting polymer coils. Polymers and colloids interact by means of a repulsive step-function pair potential, which allows for insertion of colloids

into the polymer coil. The potential strength was obtained from scaling arguments for the cross virial coefficient of true colloid-polymer systems. For this model the geometry-based density functional applied to bulk fluid demixing demonstrates that taking into account penetrability leads to a significant stabilization of the mixed phase for large polymer-to-colloid size ratio.

2.3 Rod-sphere mixtures

Mixtures of colloidal spheres and rods are excellent model systems to study a rich variety of ordering phenomena, including those of orientational degrees of freedom. A simple model, very much in the spirit of AOV, is that proposed by Bolhuis and Frenkel [52] of hard spheres and hard rods that are taken to be of vanishing thickness. Due to an excluded-volume argument, the interactions between rods vanish, but rods do interact with spheres in a hard core fashion. Recall that Rosenfeld's original DFT for general convex bodies [53, 54] does not feature the correct virial expansion (and improvements have been proposed [55–57]). For the above rod-sphere mixture a DFT was constructed [58] that is correct on the second virial level, subsequently extended to account for residual Onsager-like rod-rod interactions [59], and applied to the free fluid-fluid interface [59, 60], and to adsorption at a hard wall [61]. An improved DFT was formulated that uses new weight functions [62]. Furthermore the influence of polymer addition to the binary sphere-needle mixture was considered [63].

The DFT presented in Ref. [58] (*p.253*) applies to the model colloidal mixture of hard spheres and infinitely thin hard rods. For these freely rotating particles the fundamental measures approach was used to obtain a functional that features the correct dimensional crossover and the exact low density limit. For isotropic bulk fluid mixtures, the free energy, and hence the demixing phase diagram, were found to be identical to that obtained from free volume theory [52]. Results for the partial pair correlation functions of the bulk mixture were shown to be in good agreement with those of computer simulations.

The theory of [58] was used to investigate the free interface between demixed bulk fluid phases in the rod-sphere mixture [59] (*p.257*). Results were presented for the spatial and orientational density distributions of the particles, as well as for the interface tension. Density profiles display oscillations on the sphere-rich side of the interface provided the sphere-rich liquid phase is on the oscillatory side of the Fisher-Widom line in the bulk phase diagram. Needles tend to align parallel (perpendicular) to the interface on the needle-rich (sphere-rich) side. Furthermore, the DFT was generalized to the Onsager limit for interacting rods, and explicit expressions for the functional in simple geometries were given.

Carrying out Monte Carlo simulations for the free interface revealed that the agreement between theoretical and simulation results for density and orientation order profiles across the interface is remarkable, even for states not far from the critical point [60] (*p.270*). The simulation results confirmed the previously predicted preferred vertical (parallel) alignment of rod orientation to the interface plane at the sphere-rich (sphere-poor) side, and it was argued that this ordering should be experimentally observable in phase-separated colloidal rod-sphere mixtures.

Subsequently the DFT was extended to incorporate effects due to nonvanishing rod thickness. This was accomplished by introducing several new geometric weight functions into the framework, which were demonstrated explicitly to recover the sphere-rod Mayer bond [62] (*p.285*).

When exposed to a hard wall, for small size ratios of rod length and sphere diameter it was found that the colloidal liquid phase wets the wall completely upon approaching the fluid demixing binodal from the colloidal gas side, provided the density of the rods

lies below the wetting point [61] (*p.278*). Using an effective one-component description based on the pairwise depletion potential for higher density of rods, a finite sequence of layering phase transitions was found. For large rod-to-sphere size ratios, using a binary treatment, thick films are obtained even close to the triple point.

In order to investigate the effect of added polymers on the phase behavior of rod-sphere mixtures a ternary mixture of hard colloidal spheres, ideal polymer spheres, and rigid vanishingly thin needles, which model stretched polymers or colloidal rods was introduced [63] (*p.289*). For this model, a geometry-based DFT was developed and applied to bulk fluid phases to predict demixing phase behavior. In the case of no polymer-needle interactions, two-phase coexistence between colloid-rich and colloid-poor phases is found. For hard needle-polymer interactions, rich phase diagrams were predicted, exhibiting three-phase coexistence, and reentrant demixing behavior.

2.4 Hard body amphiphiles

In order to study ternary amphiphilic mixtures, a simplistic model featuring only hard body interactions was considered. In this mixture hard spheres correspond to water, hard needles correspond to oil, and amphiphilic hybrids consist of the hydrophilic head modeled as a hard sphere and the hydrophobic tail modeled as an infinitely thin needle attached radially to the sphere (hence resulting in a lollipop shape). The equation of state derived from the DFT [64] (*p.297*) was found to be in remarkable agreement with Monte Carlo simulation results. The trends in the theoretical demixing phase diagram were found to support the amphiphilic character of the model.

Focusing on the pure amphiphile system exposed to a hard planar wall results for the positional and orientational order profiles obtained from the DFT were found to agree well to those of computer simulations. For low densities the structure at the wall is ruled by the loss of orientational free volume due to direct fluid-wall interactions, while for higher densities packing of the spherical heads dominates. The wall sum rule was tested explicitly for this model fluid and rich structure of the contact distribution was found which was interpreted in terms of typical particle configurations [65] (*p.307*).

2.5 Fluids in random porous media

In order to study the behavior of fluids adsorbed inside random porous media, one often disregards microscopic details of the confinement and relies on equilibrium fluid configurations of model systems. The advantages are that the statistics of such model matrices are well studied and understood and a direct link to the statistical mechanics of equilibrated fluids is provided. The primary tool in the description of adsorbates in such matrices are quenched-annealed (QA) averages [66–68].

As simple models for substances adsorbed in amorphous solid matrices, mixtures of spheres with either hard or ideal interactions where several matrix components are quenched and the remaining adsorbate components are equilibrated. The proposed DFT, based on the exact zero-dimensional limit, treats both matrix and adsorbate components on the level of the respective one-body density profiles. As a test, pair correlation functions for hard spheres adsorbed in either a hard sphere or an ideal sphere matrix, were found to agree well with computer simulation results [69] (*p.314*).

A systematic derivation of the underlying replica DFT was given in Ref. [70] (*p.321*), where a binary quenched-annealed hard core mixture was considered in one dimension in order to model fluid adsorbates in narrow channels filled with a random matrix. As the model is one-dimensional, two different density functional approaches could be employed to calculate adsorbate bulk properties and interface structure at matrix surfaces. The first

approach uses Percus' exact functional [71] for the annealed component and an explicit averaging over matrix configurations; this yields numerically exact results for the bulk partition coefficient and for inhomogeneous density profiles. The second approach is based on the above quenched-annealed density functional whose results were found to approximate very well those of the former over the full range of possible densities.

Returning to three dimensions, in order to assess further the accuracy of the novel theory, an inhomogeneous test case was considered, by bringing an adsorbate fluid of hard spheres into contact with a semi-infinite porous matrix modeled by immobilized configurations of freely overlapping spheres with a sharp kink one-body density distribution [72] (*p.341*). Comparison of results from the DFT to those of computer simulations yields good agreement for the adsorbate density profile across the matrix surface. Furthermore it was argued that the matrix can be replaced by a fictitious external potential that only depends on the distance from the interface, and that leads to the same adsorbate density profile. This potential was found to be a smooth function of distance, although the matrix one-body distribution features a sharp kink. For high matrix densities, the porous medium becomes practically impenetrable, and its surface behaves like a rough hard wall whose roughness decreases with increasing matrix density.

One particular example of porous matrices in the colloidal domain are assemblies of thin rods that are immobilized due to coagulation or sedimentation [73]. The hard sphere fluids was considered in such a random fiber network modeled by quenched, vanishingly thin hard needles. The quenched-annealed DFT presented in Ref. [74] (*p.347*) treats arbitrary spatially inhomogeneous situations, in particular anisotropic and spatially varying needle distributions. As a test case the structure of the hard sphere fluid at the surface of an isotropic fiber network was considered and found to agree well with computer simulation results. For high needle densities the surface acts like a rough impenetrable wall. In the limit of infinite needle density the behavior near a smooth hard wall is recovered.

In order to allow for the possibility of fluid-fluid demixing, colloid-polymer mixtures served once more as an excellent model system. Hence a model mixture was considered in Ref. [75] (*p.353*) where colloids and matrix particles are represented by hard spheres and polymers by ideal spheres. Integrating out the degrees of freedom of the polymers leads to a binary colloid-matrix system with effective AOV pair potentials, which was treated with an integral equation theory using the (exact) replica Ornstein-Zernike relations and the optimized random phase approximation as a closure. DFT results for the structure were obtained through the direct correlation functions obtained through differentiation of the excess free energy. Inverting the replica OZ relations then yields (partial) pair distribution functions. Results from both theories were found to be in good agreement with computer simulation results. The theoretical results for the demixing binodals compare well, provided the polymer-to-colloid size ratio, and hence the effect of many body interactions neglected in the effective model, is not too large. Consistently, we found that hard (ideal) matrix polymer interactions induce capillary condensation (evaporation) of the colloidal liquid phase.

Especially desorption phenomena are believed to be strongly influenced by the presence of a planar fluid-fluid (gas-liquid) interface *inside* the porous medium [76]. For the present model density profiles normal to the interface and surface tensions were calculated and compared to the case without matrix [77] (*p.372*). Two kinds of matrices were considered: i) colloid-sized matrix particles at low packing fractions and ii) large matrix particles at high packing fractions. These two cases were found to show fundamentally different behavior and it was argued that both could be experimentally realizable. We find that in case ii), even at high packing fractions, the main effect of the matrix is to exclude volume and, to high accuracy, the results can be mapped onto those of a bulk system (without matrix) via a simple rescaling.

In the above studies the freezing transition was disregarded as this presents a formidable challenge for a continuum treatment. Progress, however, has been made by employing a lattice model where the space coordinates are discretized. The freezing transition was investigated in a two-dimensional lattice model of annealed hard squares that are subject to the influence of randomly placed quenched particles of the same size [78] (*p.384*). Hence the hard core interactions are such that nearest and next-nearest neighbors on the square lattice are excluded. The randomly placed particles serve to model a random porous medium. By combining two QA DFT with the lattice fundamental measure theory of Lafuente and Cuesta [9–11] a theory for quenched-annealed lattice fluids that treats the quenched particles on the level of their one-body density distribution was formulated. This approach was shown to yield thermodynamics that compare well with results from treating matrix realizations explicitly and performing subsequent averaging over the disorder. The freezing transition from a fluid to a columnar phase was found to be continuous and upon increasing matrix density to shift towards close packing vanishing beyond a threshold matrix density.

2.6 Soft interactions

An ultimate goal is to be able to construct a reliable density functional given any interaction potential. Some progress has been made resulting in a theory that inherits most of its features from the Rosenfeld functional [79], is applicable to mixtures, albeit with an additivity constraint [80], and predicts reasonable pair correlation functions for short-ranged models and moderated densities [81]. A detailed study has been carried out for a model of star polymers in solution [82].

The derivation of this DFT is solely based on limits, where the behavior is exactly known, namely, a zero-dimensional cavity and the low-density virial expansion [79] (*p.398*). The approach yields the structure and thermodynamics of the homogeneous fluid as an output. We applied the theory to an ultrasoft logarithmic potential that mimics star polymers in a good solvent. The theory, when supplemented by a rescaling procedure, reproduces the peculiar features of the pair correlations in this system that we also found in computer simulations

For various common fluid models, like those given through the inverse-power, Asakura-Oosawa, and Lennard-Jones potential, the pair correlations in the fluid phase at moderate densities were found to be reliably predicted as compared to computer simulation results. Explicit expressions for the weight functions and the fundamental measures were given which permit to carry out practical calculations for a large class of inhomogeneous systems [81] (*p.406*).

The generalization to mixtures is suitable for systems with soft or hard interactions between like species, but the cross interactions between unlike species are restricted to obey an additivity constraint [80] (*p.402*). The density functional respects both, the zero-dimensional limit and the virial expansion. For the pair distribution functions of a model mixture of colloidal hard spheres and star polymers, good agreement with computer simulation results was found.

For the model of pure star polymers in solution further liquid and solid structural properties, as well as freezing, solid-to-solid, and remelting phase transitions were investigated [82] (*p.412*). Even subtle physical effects, like deviations from Gaussian crystal peaks and an anomalous peak broadening upon increasing density as well as a reasonable vacancy concentration are captured correctly by the theory. Good overall quantitative agreement with simulation data is found, however, with a tendency to overestimate the structural correlations.

2.7 Miscellaneous

We summarize several further studies that either use DFT directly, like for random sequential adsorption [83] or the freezing of hard hyperspheres [84], or have been carried out using other means, like computer simulations. Interesting physical situations that could be treated in the future with DFT, like colloids confined to a flexible container [85], nematic crystals in spatial confinement [86], mixtures of colloidal particles and penetrable emulsion droplets [87], the dependence of effective interactions on the choice of coordinates [88], and freezing on stripe-patterned substrates [89],

The process of random sequential adsorption of hard particles onto a solid substrate represents a non-equilibrium growth process [90, 91]. Its statistical properties are closely related to quenched-annealed mixtures, albeit in a special limit of large numbers of components each with vanishing concentration in the sense of a differentially quenched system. A generalization of the approach of [69] allows to treat random sequential adsorption within a DFT framework [83] (*p.419*). As applications the influence of a hard boundary of the adsorption region in the one-dimensional car parking problem and for colloidal deposition on a two-dimensional solid substrate was studied and good agreement with computer simulation results for the oscillatory density profiles near the boundary was found. The amplitudes of the density oscillations are considerably smaller than in the corresponding equilibrium models.

In a system of D -dimensional hard spheres in D -dimensional space, where $D > 3$, we have generalized scaled particle theory and furthermore used the virial expansion and the Percus-Yevick integral equation to describe the fluid state [84] (*p.428*). For the crystalline phase of these hyperspheres, we adopted a cell theory based on elementary geometrical assumptions about close-packed lattices. Regardless of the approximation applied, and for dimensions as high as $D = 50$, we found a first order freezing transition preempting the Kirkwood second-order instability of the fluid. The relative density jump increases with D , and a generalized Lindemann rule of melting holds. We have also used ideas from fundamental-measure theory to obtain a free energy density functional for hard hyperspheres. We have also calculated the surface tension of a hypersphere fluid near a hard smooth (hyper-)wall within scaled particle theory.

For colloids confined to a flexible container a model of hard spheres trapped inside a container of fluctuating shape was proposed to describe colloidal particles in a vesicle or in an emulsion droplet [85] (*p.437*). In this model the container is assumed to be the convex hull of the particles and is described by an integral geometric approach including volume and surface terms. In the limit of large volume coupling, the model reduces to the well-known geometric problem of natural bin packing. Using computer simulations and cell theory, we calculated equilibrium properties for various finite numbers of confined particles in conformations ranging from clusters to planar and linear structures and identified transitions between these different conformations.

Using computer simulations we investigated the microscopic structure of the singular director field within a nematic droplet [86] (*p.446*) using the model of hard spherocylinders. To induce an overall topological charge, the particles were either confined to a two-dimensional circular cavity with homeotropic boundary or to the surface of a three-dimensional sphere. Both systems exhibit half-integer topological point defects. The isotropic defect core was found to possess a radius of the order of one particle length and to be surrounded by free-standing density oscillations. The effective interaction between two defects was investigated.

In a model for a mixture of colloidal particles and penetrable emulsion droplets [87] (*p.457*) we modeled the particles as hard spheres, the interaction between droplets also as hard, but the particles to be able to penetrate the droplets. A swelling of droplets is

taken into account to ensure mass conservation of the droplet liquid. Hence the presence of the colloids generates droplet polydispersity. Using computer simulation and liquid state theory, we found that the relative polydispersity exhibits non-monotonic behavior as a function of the particle packing fraction, and relate this phenomenon to hard sphere bulk density fluctuations.

A common approach to complex systems like colloidal suspensions or polymer solutions describes the mesoscopic behavior using effective interactions. These potentials act between the macromolecular entities and can be derived by integrating out the microscopic degrees of freedom. The remaining macroparticle coordinates need to be chosen a priori. Two obvious choices are (i) the centers of mass and (ii) distinct microscopic entities, like special “tagged” monomers. To assess whether effective interactions depend on the choice of coordinates we compared both choices in the framework of the AOV colloidal polymer mixture. Using computer simulations, we found that although the effective pair interaction between colloid and polymer differ markedly, correlation functions are in fair agreement [88] (*p.464*).

Harreis et al. [89] (*p.468*) calculated the equilibrium structure of decoration lattices composed of colloidal particles adsorbed on periodic stripe-patterned substrates as a function of the stripe width and separation and for different interparticle interactions. Due to a competition of length scales, a wealth of different decoration lattices occurs such as triangular, quadratic, rhombic, kite-like and sheared honeycomb lattices, triangular slices as well as triangle superlattices. This was argued to be of relevance for constructing templates that enforce crystal growth of unusual solid structures.

3 Conclusions

We have established that density-functionals in the Rosenfeld spirit can be constructed for quite a range of model systems including penetrable spheres, the Widom-Rowlinson model, the AOV model and variants thereof, as well as certain mixtures of non-spherical particles. The respective approximations share many desirable features with Rosenfeld’s theory for hard spheres, namely the correct expansion on the second virial level, and well-controlled dimensional crossover; the properties of fluid states are an output of the theory rather than an input as is frequent in other DFTs [2]. The construction of these functionals relies heavily on the concept of so-called zero-dimensional density distributions, given as (sums of) delta-distribution(s). Such density distributions correspond to external potentials modeling confinement in small cavities. Possibly somewhat contrary to intuition, the analysis of the Statistical Mechanics in that situation retains some of the essentials of the physics of the three-dimensional (and possibly inhomogeneous) system. This allowed to broaden the scope of an essentially equilibrium theory (see however e.g. [92, 93]) to non-equilibrium systems like quenched-annealed mixtures as models for adsorbates in porous media and to describe the process of random sequential adsorption.

Besides thorough investigations of the predicted bulk fluid structure, numerous applications to inhomogeneous systems have been presented, including free interfaces between demixed fluid phases, adsorption and wetting behavior of solid substrates, and unusual sedimentation phenomena. One can easily envisage many further applications of the derived DFTs.

Acknowledgments

I am grateful for the significant input of my coauthors who contributed essentially to the work summarized in this thesis. In particular I thank Hartmut Löwen for scientific exchange and continuous support and Bob Evans for ongoing scientific stimulation. I owe Marjolein Dijkstra both a pleasurable and productive time in Utrecht, and am grateful to Henk N. W. Lekkerkerker, Jean-Pierre Hansen, and Alfons von Blaaderen. I have greatly enjoyed very fruitful collaborations with Joe M. Brader, Alan R. Denton, Dirk G. A. L. Aarts, and Paul P. F. Wessels. I thank Joachim Dzubiella, Lutz Maibaum, Ingo O. Götze, Reimar Finken, and Hendrik Reich for working with me. I have enjoyed collaborations with Andrea Fortini, Ansgar Esztermann, Holger M. Harreis, Christian von Ferber, C. Paddy Royall, José A. Cuesta, Luis Lafuente, Matthias Fuchs, Roland Roth, Gerhard Kahl, Elisabeth Schöll-Paschinger, Jürgen Köfinger, Francisco L. Román, Benito Groh, Martin Watzlawek. I benefited from discussions with René van Roij, Kostya Shundyak, Antti-Pekka Hynninen, René Messina, Ronald Blaak, Klaus R. Mecke, Remco Tuinier, Pawel Bryk, David W. Oxtoby, Martin-Luc Rosinberg, Gilles Tarjus, Alfred Hüller, Richard L. C. Vink, Jürgen Horbach and Kurt Binder. Much of the work presented here is based on my personal (and limited) understanding of the work of Yasha Rosenfeld.

List of coauthors

Name	[reference] <i>starting page of reprint.</i>
Aarts, D. G. A. L.	[40] 175.
Bolhuis, P. G.	[60] 270.
Brader, J. M.	[25] 58, [27] 62, [30] 92, [28] 107, [29] 115, [48] 221 [43] 179, [59] 257, [60] 270, [61] 278, [65] 307, [74] 347.
Cuesta, J. A.	[78] 384.
Denton, A. R.	[48] 221, [49] 230, [50] 242, [63] 289.
Dijkstra, M.	[30] 92, [44] 187, [45] 197, [47] 217, [46] 207.
Dzubiella, J.	[86] 446.
Esztermann, A.	[59] 257, [62] 285.
Evans, R.	[25] 58, [27] 62, [30] 92, [28] 107, [29] 115.
von Ferber, C.	[64] 297, [65] 307.
Fortini, A.	[44] 187, [45] 197.
Finken, R.	[84] 428.
Fuchs, M.	[51] 248.
Götze, I. O.	[43] 179.
Groh, B.	[82] 412.
Hansen, J.-P.	[47] 217, [46] 207.
Harreis, H. M.	[89] 468.
Kahl, G.	[75] 353.
Köfinger, J.	[75] 353.
Lafuente, L.	[78] 384.
Lekkerkerker, H. N. W.	[40] 175.
Löwen, H.	[14] 42, [25] 58, [27] 62, [30] 92, [28] 107, [32] 151, [33] 159, [43] 179, [77] 372, [84] 428, [86] 446, [87] 457, [85] 437, [89] 468.
Maibaum, L.	[85] 437.
Reich, H.	[70] 321.
Roman, F. L.	[87] 457.
Rosenfeld, Y.	[14] 42.
Roth, R.	[30] 92, [61] 278.
Schöll-Paschinger, E.	[75] 353.
Watzlawek, M.	[14] 42.
Wessels, P. P. F.	[32] 151, [33] 159, [77] 372.

References

- [1] R. Evans, *Adv. Phys.* **28**, 143 (1979).
- [2] R. Evans, in *Fundamentals of Inhomogeneous Fluids*, edited by D. Henderson (Dekker, New York, 1992), Chap. 3, p. 85.
- [3] Y. Rosenfeld, *Phys. Rev. Lett.* **63**, 980 (1989).
- [4] Y. Rosenfeld, M. Schmidt, H. Löwen, and P. Tarazona, *J. Phys. Cond. Matter* **8**, L577 (1996).
- [5] Y. Rosenfeld, M. Schmidt, H. Löwen, and P. Tarazona, *Phys. Rev. E* **55**, 4245 (1997).
- [6] P. Tarazona and Y. Rosenfeld, *Phys. Rev. E* **55**, R4873 (1997).
- [7] P. Tarazona, *Phys. Rev. Lett.* **84**, 694 (2000).
- [8] R. Roth, R. Evans, A. Lang, and G. Kahl, *J. Phys.: Condensed Matter* **14**, 12063 (2002).
- [9] L. Lafuente and J. A. Cuesta, *Phys. Rev. Lett.* **89**, 145701 (2002).
- [10] L. Lafuente and J. A. Cuesta, *J. Phys.: Condensed Matter* **14**, 12079 (2002).
- [11] L. Lafuente and J. A. Cuesta, *Phys. Rev. Lett.* **93**, 130603 (2004).
- [12] M. Schmidt, *J. Phys.: Condensed Matter* **15**, S101 (2003). (*Reprinted on p. 29 ff.*)
- [13] M. Schmidt, *J. Phys.: Condensed Matter* **11**, 10163 (1999). (*Reprinted on p. 35 ff.*)
- [14] Y. Rosenfeld, M. Schmidt, M. Watzlawek, and H. Löwen, *Phys. Rev. E* **62**, 5006 (2000). (*Reprinted on p. 42 ff.*)
- [15] B. Widom and J. S. Rowlinson, *J. Chem. Phys.* **52**, 1670 (1970).
- [16] M. Schmidt, *Phys. Rev. E* **63**, 010101(R) (2001). (*Reprinted on p. 47 ff.*)
- [17] M. Schmidt, *J. Phys.: Condensed Matter* **16**, L351 (2004). (*Reprinted on p. 51 ff.*)
- [18] M. Dijkstra, R. van Roij, and R. Evans, *Phys. Rev. Lett.* **81**, 2268 (1998).
- [19] K. Jagannathan and A. Yethiraj, *J. Chem. Phys.* **118**, 7907 (2003).
- [20] W. T. Gózdź, *J. Chem. Phys.* **119**, 3309 (2003).
- [21] W. C. K. Poon, *J. Phys.: Condensed Matter* **14**, R859 (2002).
- [22] R. Tuinier, J. Rieger, and C. G. de Kruif, *Adv. Colloid Interface Sci.* **103**, 1 (2003).
- [23] S. Asakura and F. Oosawa, *J. Chem. Phys.* **22**, 1255 (1954).
- [24] A. Vrij, *Pure and Appl. Chem.* **48**, 471 (1976).
- [25] M. Schmidt, H. Löwen, J. M. Brader, and R. Evans, *Phys. Rev. Lett.* **85**, 1934 (2000). (*Reprinted on p. 58 ff.*)
- [26] H. N. W. Lekkerkerker, W. C. K. Poon, P. N. Pusey, A. Stroobants, and P. B. Warren, *Europhys. Lett.* **20**, 559 (1992).
- [27] M. Schmidt, H. Löwen, J. M. Brader, and R. Evans, *J. Phys.: Condensed Matter* **14**, 9353 (2002). (*Reprinted on p. 62 ff.*)
- [28] J. M. Brader, R. Evans, M. Schmidt, and H. Löwen, *J. Phys.: Condensed Matter* **14**, L1 (2002). (*Reprinted on p. 107 ff.*)
- [29] J. M. Brader, R. Evans, and M. Schmidt, *Mol. Phys.* **101**, 3349 (2003). (*Reprinted on p. 115 ff.*)
- [30] R. Evans, J. M. Brader, R. Roth, M. Dijkstra, M. Schmidt, and H. Löwen, *Phil. Trans. Roy. Soc. Lond. A* **359**, 961 (2001). (*Reprinted on p. 92 ff.*)
- [31] E. H. A. de Hoog and H. N. W. Lekkerkerker, *J. Phys. Chem. B* **103**, 5274 (1999).
- [32] P. P. F. Wessels, M. Schmidt, and H. Löwen, *J. Phys.: Condensed Matter* **16**, L1

- (2004). (*Reprinted on p. 151 ff.*)
- [33] P. P. F. Wessels, M. Schmidt, and H. Löwen, J. Phys.: Condensed Matter **16**, S4169 (2004). (*Reprinted on p. 159 ff.*)
- [34] M. Dijkstra and R. van Roij, Phys. Rev. Lett. **89**, 208303 (2002).
- [35] R. L. C. Vink and J. Horbach, J. Chem. Phys. **121**, 3253 (2004).
- [36] R. L. C. Vink and J. Horbach, J. Phys.: Condensed Matter **16**, S3807 (2004).
- [37] R. L. C. Vink, J. Horbach, and K. Binder (unpublished).
- [38] F. P. Buff, R. A. Lovett, and F. H. Stillinger, Phys. Rev. Lett. **15**, 621 (1965).
- [39] K. R. Mecke and S. Dietrich, Phys. Rev. E **59**, 6766 (1999).
- [40] D. G. A. L. Aarts, M. Schmidt, and H. N. W. Lekkerkerker, Science **304**, 847 (2004). (*Reprinted on p. 175 ff.*)
- [41] W. C. K. Poon, Science **304**, 830 (2004).
- [42] K. R. Mecke, Physik Journal **3(8)**, 19 (2004).
- [43] I. O. Götze, J. M. Brader, M. Schmidt, and H. Löwen, Mol. Phys. **101**, 1651 (2003). (*Reprinted on p. 179 ff.*)
- [44] M. Schmidt, A. Fortini, and M. Dijkstra, J. Phys.: Condensed Matter **48**, S3411 (2003). (*Reprinted on p. 187 ff.*)
- [45] M. Schmidt, A. Fortini, and M. Dijkstra, J. Phys.: Condensed Matter **16**, S4159 (2004). (*Reprinted on p. 197 ff.*)
- [46] M. Schmidt, M. Dijkstra, and J. P. Hansen, J. Phys.: Condensed Matter **16**, S4194 (2004). (*Reprinted on p. 207 ff.*)
- [47] M. Schmidt, M. Dijkstra, and J. P. Hansen, Phys. Rev. Lett. **93**, 088303 (2004). (*Reprinted on p. 217 ff.*)
- [48] M. Schmidt, A. R. Denton, and J. M. Brader, J. Chem. Phys. **118**, 1541 (2003). (*Reprinted on p. 221 ff.*)
- [49] A. R. Denton and M. Schmidt, J. Phys.: Condensed Matter **14**, 12051 (2002). (*Reprinted on p. 230 ff.*)
- [50] M. Schmidt and A. R. Denton, Phys. Rev. E **65**, 061410 (2002). (*Reprinted on p. 242 ff.*)
- [51] M. Schmidt and M. Fuchs, J. Chem. Phys. **117**, 6308 (2002). (*Reprinted on p. 248 ff.*)
- [52] P. Bolhuis and D. Frenkel, J. Chem. Phys. **101**, 9869 (1994).
- [53] Y. Rosenfeld, Phys. Rev. E **50**, R3318 (1994).
- [54] Y. Rosenfeld, Mol. Phys. **86**, 637 (1995).
- [55] K. R. Mecke (unpublished).
- [56] R. Roth, R. van Roij, D. Andrienko, K. R. Mecke, and S. Dietrich, Phys. Rev. Lett. **89**, 088301 (2002).
- [57] G. Cinacchi and F. Schmid, J. Phys.: Condensed Matter **14**, 12223 (2002).
- [58] M. Schmidt, Phys. Rev. E **63**, 050201(R) (2001). (*Reprinted on p. 253 ff.*)
- [59] J. M. Brader, A. Esztermann, and M. Schmidt, Phys. Rev. E **66**, 031401 (2002). (*Reprinted on p. 257 ff.*)
- [60] P. G. Bolhuis, J. M. Brader, and M. Schmidt, J. Phys.: Condensed Matter **48**, S3421 (2003). (*Reprinted on p. 270 ff.*)
- [61] R. Roth, J. M. Brader, and M. Schmidt, Europhys. Lett. **63**, 549 (2003). (*Reprinted on p. 278 ff.*)

- [62] A. Esztermann and M. Schmidt, Phys. Rev. E **70**, 022501 (2004). (*Reprinted on p. 285 ff.*)
- [63] M. Schmidt and A. R. Denton, Phys. Rev. E **65**, 021508 (2002). (*Reprinted on p. 289 ff.*)
- [64] M. Schmidt and C. von Ferber, Phys. Rev. E **64**, 051115 (2001). (*Reprinted on p. 297 ff.*)
- [65] J. M. Brader, C. von Ferber, and M. Schmidt, Mol. Phys. **101**, 2225 (2003). (*Reprinted on p. 307 ff.*)
- [66] L. D. Gelb, K. E. Gubbins, R. Radhakrishnan, and M. Sliwinska-Bartkowiak, Rep. Prog. Phys. **62**, 1573 (1999).
- [67] W. G. Madden and E. D. Glandt, J. Stat. Phys. **51**, 537 (1988).
- [68] J. A. Given and G. Stell, J. Chem. Phys. **97**, 4573 (1992).
- [69] M. Schmidt, Phys. Rev. E **66**, 041108 (2002). (*Reprinted on p. 314 ff.*)
- [70] H. Reich and M. Schmidt, J. Stat. Phys. **116**, 1683 (2004). (*Reprinted on p. 321 ff.*)
- [71] J. K. Percus, J. Stat. Phys. **15**, 505 (1976).
- [72] M. Schmidt, Phys. Rev. E **68**, 021106 (2003). (*Reprinted on p. 341 ff.*)
- [73] A. P. Philipse and A. M. Wierenga, Langmuir **14**, 49 (1998).
- [74] M. Schmidt and J. M. Brader, J. Chem. Phys. **119**, 3495 (2003). (*Reprinted on p. 347 ff.*)
- [75] M. Schmidt, E. Schöll-Paschinger, J. Köfinger, and G. Kahl, J. Phys.: Condensed Matter **14**, 12099 (2002). (*Reprinted on p. 353 ff.*)
- [76] M. L. Rosinberg, E. Kierlik, and G. Tarjus, Europhys. Lett. **62**, 377 (2003).
- [77] P. P. F. Wessels, M. Schmidt, and H. Löwen, Phys. Rev. E **68**, 061404 (2003). (*Reprinted on p. 372 ff.*)
- [78] M. Schmidt, L. Lafuente, and J. A. Cuesta, J. Phys.: Condensed Matter **15**, 4695 (2003). (*Reprinted on p. 384 ff.*)
- [79] M. Schmidt, Phys. Rev. E **60**, R6291 (1999). (*Reprinted on p. 398 ff.*)
- [80] M. Schmidt, Phys. Rev. E **62**, 3799 (2000). (*Reprinted on p. 402 ff.*)
- [81] M. Schmidt, Phys. Rev. E **62**, 4976 (2000). (*Reprinted on p. 406 ff.*)
- [82] B. Groh and M. Schmidt, J. Chem. Phys. **114**, 5450 (2001). (*Reprinted on p. 412 ff.*)
- [83] M. Schmidt, J. Phys.: Condensed Matter **14**, 12119 (2002). (*Reprinted on p. 419 ff.*)
- [84] R. Finken, M. Schmidt, and H. Löwen, Phys. Rev. E **65**, 016108 (2002). (*Reprinted on p. 428 ff.*)
- [85] L. Maibaum, M. Schmidt, and H. Löwen, Phys. Rev. E **63**, 051401 (2001). (*Reprinted on p. 437 ff.*)
- [86] J. Dzubiella, M. Schmidt, and H. Löwen, Phys. Rev. E **62**, 5081 (2000). (*Reprinted on p. 446 ff.*)
- [87] F. L. Roman, M. Schmidt, and H. Löwen, Phys. Rev. E **61**, 5445 (2000). (*Reprinted on p. 457 ff.*)
- [88] M. Schmidt, Phys. Rev. E **65**, 022801 (2002). (*Reprinted on p. 464 ff.*)
- [89] H. M. Harreis, M. Schmidt, and H. Löwen, Phys. Rev. E **65**, 041602 (2002). (*Reprinted on p. 468 ff.*)
- [90] J. W. Evans, Rev. Mod. Phys. **65**, 1281 (1993).
- [91] P. Schaaf, J. Voegel, and B. Senger, J. Phys. Chem. B **104**, 2204 (2000).

- [92] U. Marini Bettolo Marconi and P. Tarazona, *J. Chem. Phys.* **110**, 8032 (1999).
- [93] F. Penna and P. Tarazona, *J. Chem. Phys.* **119**, 1766 (2003).

Geometry-based density functional theory: an overview

Matthias Schmidt

Institut für Theoretische Physik II, Heinrich-Heine-Universität Düsseldorf, Universitätsstraße 1,
D-40225 Düsseldorf, Germany

E-mail: mschmidt@thphy.uni-duesseldorf.de

Received 28 October 2002

Published 16 December 2002

Online at stacks.iop.org/JPhysCM/15/S101

Abstract

An overview of recent developments and applications of a specific density functional approach that originates from Rosenfeld's fundamental measure theory for hard spheres is given. Model systems that were treated include penetrable spheres that interact with a step function pair potential, the Widom–Rowlinson model, the Asakura–Oosawa colloid–polymer mixture, ternary mixtures of spheres, needles, and globular polymers, hard-body amphiphilic mixtures, fluids in porous media, and random sequential adsorption that describes non-equilibrium processes such as colloidal deposition and random car parking. In these systems various physical phenomena were studied, such as correlations in liquids, freezing and demixing phase behaviour, the properties of fluid interfaces with and without orientational order, and wetting and layering phenomena at walls.

1. Introduction

Density functional theory (DFT) [1] is a powerful tool for studying many phenomena in condensed matter including freezing, and surface and interface behaviour. For most systems of interest the central quantity of DFT, the excess free energy functional that arises from interactions between particles, is unknown and one uses approximations to it. Hence having reliable approximative functionals is the essential prerequisite for studying any of the above phenomena.

For the generic model in the field, hard spheres (HS) and their mixtures, the Rosenfeld functional [2] plays a central role, due to its intrinsic structure that unifies earlier theories (Percus–Yevick and scaled-particle theory) and, more importantly, due to the high quality of the results when compared to those of computer simulations. A brief summary of some of the relevant work [2–9] that led to the present-day formulation of the Rosenfeld functional is given below. One essential step was the observation that by imposing the correct dimensional crossover, the HS functional can be constructively obtained [5]. Subsequently, it was realized

that this is not restricted to the HS case. Provided that the model features well-defined single-particle shapes, from its zero-dimensional (0D) free energy one can construct systematically a genuine DFT for the specific model. In the following an overview of such recent developments is given.

The paper is organized as follows. In section 2 the general structure of the theory is briefly outlined. The models for which such functionals were constructed are summarized in section 3 along with physical applications. We finish with concluding remarks in section 4.

2. Structure of the theory

2.1. Input

The first substantial building block of the theory is a geometrical representation of the particle shapes using four characteristic measures, namely the volume, surface, integral mean curvature, and Euler characteristic of the particles. As an example, the volume measure is a function that is unity inside and zero outside the particle shape. These functions are used to obtain weighted densities by convolutions with the actual density profile. In particular, the weight functions are constructed to obtain the Mayer bonds, $\exp(V_{ij}) - 1$, where V_{ij} is the pair potential between species i and j , by convoluting weight functions.

The second building block is the so-called 0D limit, a situation where all particles present in the system are forced to sit on top of each other. This is a well-defined limiting case that allows for an exact (in many cases analytic) solution of the many-body problem. The 0D limit can be viewed as a small cavity of particle size. As all particles present in the cavity overlap, the configurational integral becomes trivial and one can obtain the exact excess free energy F_{0D} . One then imposes that the functional, when applied to a corresponding situation, recovers this solution, i.e. $F_{\text{exc}}[\{\eta_i \delta(\mathbf{r})\}] = F_{0D}(\{\eta_i\})$, where η_i is the average particle number of species i .

2.2. Output

Applying the functional to constant-density profiles, the properties of the homogeneous bulk fluid are an output of the theory. This in contrast to many other approximations that require information about the fluid as an input. This implies that e.g. the fluid demixing phase diagram is an output of the theory. Pair correlation functions can be obtained via two routes. One is via the Ornstein–Zernike relation and obtaining the direct correlation functions from the second functional derivative of the excess free energy (evaluated for constant density distributions). This provides a severe test of the theory, as taking the derivatives will in general enhance any inaccuracies on the level of the free energy. The other, more powerful, approach is via the so-called test-particle route where one minimizes the grand potential in the presence of an external potential that is generated by a test particle fixed at the origin. Furthermore, as the 0D limit is described correctly, which is crucial for freezing [3, 4], one believes fluid–solid coexistence to be described correctly, although this has not been investigated in detail for systems other than pure HS yet.

3. Models and applications

3.1. Hard spheres

Rosenfeld’s original work [2] was already formulated for HS mixtures. Subsequently this was empirically modified for improved dimensional crossover [3, 4], and a good account of

the HS freezing transition obtained. Reversing the line of thought, Tarazona and Rosenfeld demonstrated that a HS density functional can be systematically *generated* from the 0D limit by considering multi-cavity distributions [5], and following this principle improved versions were obtained [6, 7]. Current work is devoted to the study of the dimensional crossover in HS mixtures. It turns out that a rank-three weight function is required to fulfil the 1D limit for mixtures [8]. Further progress is the implementation of the Carnahan–Starling equation of state for pure HS [7] and for mixtures [9]. High spatial dimensionalities have also been considered [10].

3.2. Penetrable spheres

Particles that interact with a step function pair potential share geometrical properties with HS, but feature an additional non-trivial energy scale $\epsilon/k_B T$, where ϵ is the step height, k_B is the Boltzmann constant, and T is the temperature. Due to the close relationship of the geometrical properties of this system with those of pure HS, the solution for the 0D free energy was the essential requirement for constructing a DFT for this system [11]. Fluid pair correlation functions (obtained by test-particle calculations) were shown to be in good agreement with simulation results, and the freezing phase diagram was obtained, indicating stabilization of the fluid upon decreasing $\epsilon/k_B T$. Subsequently, the penetrable sphere system was used to study the degree of universality of the bridge functional [12].

3.3. Colloid–polymer mixtures

The DFT for the Asakura–Oosawa (AO) colloid–polymer mixture (where colloids are HS and polymers are ideal spheres) was shown to recover free volume theory in bulk [13]; many details and an investigation of the bulk fluid phases can be found in [14]. This theory was applied to the free interface between demixed fluid phases and to the behaviour induced by a hard wall [15, 16] where entropic wetting (by colloidal liquid) and a novel scenario of a finite sequence of layering phase transitions was found.

Subsequent work was devoted to a more realistic description of colloid–polymer mixtures than that provided by the AO model. The influence of poor solvent quality [17] was modelled by assuming a two-component solvent: one component, the primary solvent, provides a homogeneous background and is (as usual) not explicitly treated. A further cosolvent component is a poor solvent for the polymer, and by tuning its density the overall solvent quality can be modified. In this simple model the cosolvent is assumed to be an ideal gas of point particles that cannot penetrate the polymers, hence generating an effective depletion attraction between the polymer spheres that was shown to stabilize fluid–fluid coexistence.

Actual polymers possess a flexible shape, and this will be influenced by the presence of colloidal particles. To account for such size fluctuations, a polydisperse (in polymer radii) AO model was proposed and treated within DFT [18], finding colloid-induced polymer compression. As a simple model for investigating the effects caused by polymer non-ideality, the polymer–polymer interaction was assumed to be a step function (like in the penetrable sphere model above) [19]. By matching the step height with estimates for the strength of the polymer–polymer repulsion, improved agreement with experimental results was obtained. In particular the liquid branch of the fluid demixing binodal moves toward higher polymer concentrations compared to the case for ideal polymer.

For large polymers the hard-core interaction between polymer and colloids in the AO model is no longer justified, as a small (compared to the radius of gyration of the polymer) colloidal particle may penetrate the open coil structure of a polymer. Assuming a finite interaction between colloid and polymer, whose strength is determined from known field theoretical

results, a penetrable AO model [20] was proposed. For polymer-to-colloid size ratios as large as 10, this greatly enhances the mixed region in the phase diagram.

Recently, in colloid–polymer mixtures exposed to a plane-wave external potential that models the influence of a standing laser field, so-called laser-induced condensation was found [21].

3.4. Spheres, needles, lollipops

Remedying a deficiency of Rosenfeld's original DFT for non-spherical hard bodies [22, 23] a mixture of HS and hard, vanishingly thin needles that may represent stretched polymers or colloidal rods was treated [24]. The interface between demixed fluid phases in this model was studied [25] by investigating density and orientational order parameter profiles as well as the surface tension. In particular, interesting orientational order of the needles was found: on the needle-rich side of the interface the needles preferentially lie parallel to the interface plane, similar to the behaviour near a wall. On the sphere-rich side the needles align perpendicular to the wall; the particles stick through the voids in the first sphere layer. The DFT was also extended to the case of interacting rods (in the Onsager limit) [25] by introducing orientational convolutions into the framework. For vanishing sphere density, this functional is a reformulation of the Onsager functional for rods in terms of single-particle geometries. Reference [25] also gives many explicit expressions for weight functions in simple geometries relevant for wall and test-particle calculations. With a similar approach, Roth and co-workers [26] calculated the entropic torque exerted on a spherocylinder (with finite width) in a sea of HS near a hard wall.

A further study was devoted to the phase behaviour of a colloidal suspension upon adding globular polymers *and* needles as depletion agents. In this ternary mixture, interesting fluid demixing phase behaviour with various critical points and a triple point was calculated for different needle–polymer interactions [27]. Particularly interesting is the case of hard-core repulsion between polymers and needles, where these two species *compete* to generate depletion interaction between the spheres.

Using the sphere–needle mixture as a generic model to study demixing that is solely driven by the particle shapes, a third component with an amphiphilic character was added. A hybrid shape of sphere and needle where the needle is attached rigidly to the sphere constitutes a minimal model for an amphiphilic molecule [28]. The equation of state derived within the DFT framework was found to be in good agreement with computer simulation results over a wide range of densities and compositions of the three species.

3.5. Fluids in porous media

To study the adsorption of fluids in porous media, i.e. disordered, amorphous solids, commonly one uses a model description for the matrix, assuming 'frozen' liquid configurations where the particles are immobilized. Such a random matrix is then brought into contact with a fluid that is allowed to equilibrate. Such systems are usually referred to as being quenched–annealed, where the quenched component constitutes the matrix and the annealed component constitutes the fluid. For such systems a new density functional approach that treats the matrix on the level of its density profile(s) was proposed [29]. As an application, the AO colloid–polymer mixture adsorbed in matrices of different kinds was considered [30]. Comparing to phase diagrams obtained from the optimized random phase approximation and replica OZ equations, quantitative agreement was found.

3.6. Miscellaneous

Further applications include the Widom–Rowlinson model which is a mixture where particles of the same species are assumed to be non-interacting, but particles from different species experience HS repulsion. Again this model features well-defined particle shapes and non-trivial 0D statistical properties that were used to obtain a DFT [31]. The predictions of the partial pair correlation functions compare well with simulation results, and the result for the phase diagram possess comparable quality to those from other theories, but also fails to give the precise location of the critical point.

Furthermore, the non-equilibrium process of random sequential adsorption of hard bodies onto a d -dimensional substrate was treated [32]. In 1D one usually refers to the random car-parking problem, and in 2D to (irreversible) colloid deposition. The DFT approach allows one to treat an adsorption probability that is non-uniform in space according to the Boltzmann factor of a prescribed external potential. For the simple test case of a hard boundary of the adsorption region, good agreement with simulation results was found. In particular, it was shown that considerably less structure is built up as compared to the case for the corresponding equilibrium model. This behaviour could be traced back to the smaller (by about a factor of 1/2) contribution of the excess free energy to the total grand potential.

4. Conclusions

Summarizing, geometry-based DFT has been shown to predict phase behaviour, structural correlations, and surface and interface behaviour for a (restricted) range of model systems. Comparison with computer simulation results and to those from other theories indicate the good quality of the results. Moreover, numerous predictions of interesting physical phenomena have been made.

Despite attempts to treat arbitrary soft interactions [33–38], from the existing studies one can conclude that the principal method for obtaining a geometry-based DFT works reliably if (at least) two conditions are fulfilled. First, the model under consideration needs to feature well-defined particle *shapes* that allow one to express the (pair) interactions naturally—the Lennard-Jones model may serve as a counter-example, where the two-particle interaction is clearly defined but the notion of the shape of a single particle is at least not immediate. Second, the 0D statistics (i.e. the stacking of particles on top of each other) needs to retain some of the essential physics of the model under consideration.

Acknowledgments

Inspiring discussions with J M Brader, R Evans, H Löwen, A R Denton, C von Ferber, M Fuchs, A Esztermann, R Finken, I O Götze, G Kahl, A Lang, E Schöll-Paschinger, J Köfinger, B Groh, P Wessels, M Sweatman, R Roth, K R Mecke, D W Oxtoby, L L Rassmussen, J A Cuesta, L Lafuente, M-L Rosinberg, G Tarjus, and P Viot are gratefully acknowledged.

References

- [1] Evans R 1992 *Fundamentals of Inhomogeneous Fluids* ed D Henderson (New York: Dekker) p 85
- [2] Rosenfeld Y 1989 *Phys. Rev. Lett.* **63** 980
- [3] Rosenfeld Y, Schmidt M, Löwen H and Tarazona P 1996 *J. Phys.: Condens. Matter* **8** L577
- [4] Rosenfeld Y, Schmidt M, Löwen H and Tarazona P 1997 *Phys. Rev. E* **55** 4245
- [5] Tarazona P and Rosenfeld Y 1997 *Phys. Rev. E* **55** R4873
- [6] Tarazona P 2000 *Phys. Rev. Lett.* **84** 694

-
- [7] Tarazona P 2002 *Physica A* **306** 243
 - [8] Cuesta J A, Martínez-Raton Y and Tarazona P 2002 *J. Phys.: Condens. Matter* **14** 11965
 - [9] Roth R, Evans R, Lang A and Kahl G 2002 *J. Phys.: Condens. Matter* **14** 12063
 - [10] Finken R, Schmidt M and Löwen H 2002 *Phys. Rev. E* **65** 016108
 - [11] Schmidt M 1999 *J. Phys.: Condens. Matter* **11** 10163
 - [12] Rosenfeld Y, Schmidt M, Watzlawek M and Löwen H 2000 *Phys. Rev. E* **62** 5006
 - [13] Schmidt M, Löwen H, Brader J M and Evans R 2000 *Phys. Rev. Lett.* **85** 1934
 - [14] Schmidt M, Löwen H, Brader J M and Evans R 2002 *J. Phys.: Condens. Matter* **14** 9353
 - [15] Brader J M, Evans R, Schmidt M and Löwen H 2002 *J. Phys.: Condens. Matter* **14** L1
 - [16] Evans R, Brader J M, Roth R, Dijkstra M, Schmidt M and Löwen H 2001 *Phil. Trans. R. Soc. A* **359** 961
 - [17] Schmidt M and Denton A R 2002 *Phys. Rev. E* **65** 061410
 - [18] Denton A R and Schmidt M 2002 *J. Phys.: Condens. Matter* **14** 12051
 - [19] Schmidt M, Denton A R and Brader J M 2003 *J. Chem. Phys.* at press
 - [20] Schmidt M and Fuchs M 2002 *J. Chem. Phys.* **117** 6308
 - [21] Götze I O, Brader J M, Schmidt M and Löwen H *Mol. Phys.* submitted
 - [22] Rosenfeld Y 1994 *Phys. Rev. E* **50** R3318
 - [23] Rosenfeld Y 1995 *Mol. Phys.* **86** 637
 - [24] Schmidt M 2001 *Phys. Rev. E* **63** 050201(R)
 - [25] Brader J M, Esztermann A and Schmidt M 2002 *Phys. Rev. E* **66** 031401
 - [26] Roth R, van Roij R, Andrienko D, Mecke K R and Dietrich S 2002 *Phys. Rev. Lett.* **89** 088301
 - [27] Schmidt M and Denton A R 2002 *Phys. Rev. E* **65** 021508
 - [28] Schmidt M and von Ferber C 2001 *Phys. Rev. E* **64** 051115
 - [29] Schmidt M 2002 *Phys. Rev. E* **66** 041108
 - [30] Schmidt M, Schöll-Paschinger E, Köfinger J and Kahl G 2002 *J. Phys.: Condens. Matter* **14** 12099
 - [31] Schmidt M 2001 *Phys. Rev. E* **63** 010101(R)
 - [32] Schmidt M 2002 *J. Phys.: Condens. Matter* **14** 12119
 - [33] Sweatman M B 1995 *PhD Thesis* University of Bristol
 - [34] Schmidt M 1999 *Phys. Rev. E* **60** R6291
 - [35] Schmidt M 2000 *Phys. Rev. E* **62** 4976
 - [36] Schmidt M 2000 *Phys. Rev. E* **62** 3799
 - [37] Groh B and Schmidt M 2001 *J. Chem. Phys.* **114** 5450
 - [38] Sweatman M 2002 *J. Phys.: Condens. Matter* **14** 11291

An *ab initio* density functional for penetrable spheres

Matthias Schmidt

Institut für Theoretische Physik II, Heinrich-Heine-Universität Düsseldorf, Universitätsstraße 1,
D-40225 Düsseldorf, Germany

Received 2 August 1999

Abstract. We develop a density functional theory for a system of penetrable spheres that interact with a constant pair potential energy if their separation distance is smaller than their diameter. As sufficient input, just the geometrical properties of the particles and the exactly known statistical behaviour of the system under strong confinement are needed. The theory predicts the bulk fluid properties in good agreement with computer simulations and better than liquid integral theories, as well as the freezing transition to a multiply occupied face-centred-cubic lattice. It becomes exact in the limits of strong confinement and high temperature, and coincides with a successful hard-sphere theory for zero temperature.

Classical density functional theory (DFT) is one important theoretical tool for the study of the microscopic structure of liquids [1] and solids [2, 3]. Its power lies in its ability to deal with inhomogeneous situations on a microscopic length scale. There are a large variety of physical situations where a liquid exhibits a spatial structure, ranging over the behaviours near confining walls, in gravitational fields, at interfaces and in capillaries [4]. But DFT can go beyond the description of fluids in contact with their surroundings. It also accounts for self-sustained inhomogeneities that are not being caused by external potentials. This phenomenon can occur if a system ‘decides’ to freeze and to build up a crystal with an intrinsic broken translational symmetry. As DFT is able to treat solid and fluid phases on an equal footing, it is considered as a major theoretical advance in statistical physics from a fundamental point of view. It is also of great practical importance, as explicit calculations can be done for toy models as well as for realistic systems.

The central quantity of DFT is the Helmholtz excess free energy expressed as a functional of the single-particle density. There are few systems for which this functional is known exactly; one example is a system of one-dimensional hard rods. Through the years, various approximations, like the one given by Ramakrishnan and Yussouff, the weighted-density approximation (WDA) and the modified WDA (see, e.g., reference [3]) have been developed. One common feature of these approaches is the requirement of having information about the homogeneous fluid phase in order to obtain results for inhomogeneous situations. The information about homogeneous fluids, like the equation of state and the pair distribution function, may be taken from the solution of liquid integral equations. The DFT then acts as a container for the knowledge about the homogeneous bulk phase. So it is of great interest to find approximations to the density functional of specific systems that ‘stand on their own feet’ and do not require input from other theoretical approaches involving further approximations.

There is one class of systems for which one has been able to derive powerful density functionals, namely those exhibiting hard-core interactions such as hard spheres [5–7] and

10164 *M Schmidt*

cubes [8,9]. One important property of these fundamental-measure functionals (FMF) is their correct dimensional crossover: the three-dimensional (3D) functional yields a reasonable 2D hard-disc functional, the exact 1D hard-rod functional and the exact statistical properties of the 0D limit represented by a cavity that can hold a single particle. Reversing this line of thought, one has been able to derive the 3D functional by imposing the correct behaviour for 0D [10]. So far, these approaches have been restricted to hard-core interactions, where the temperature scales out of the Boltzmann factor. In this article a systematic extension of the FMF to soft cores is proposed.

Therefore we study a system of penetrable particles. We call particles ‘penetrable’ if there is no divergence of the pair potential energy if two particles have zero separation. So far, these bounded potentials have attracted less interest than potentials with a divergence at the origin. One example of a penetrable potential is the Gaussian core model introduced by Stillinger *et al* [11, 12]. Graf and Löwen [13] have shown that Gaussian cores arise between the centres of star polymers if the polymeric arms are treated in a harmonic approximation. Although diverging at the origin, an ultra-soft pair potential between star polymers has been proposed [14] and validated [15] with computer simulations.

As the, in a sense, simplest model for a penetrable interaction, we assume a step function:

$$V(r) = \begin{cases} 0 & \text{if } r > \sigma \\ \epsilon & \text{if } r \leq \sigma. \end{cases}$$

This was recently studied by Likos *et al* [16] using liquid integral equations for the fluid phase and a cell model for the solid phase as well as computer simulation. Virial coefficients were studied in reference [17]. The model has two thermodynamic parameters, namely the packing fraction $\eta = (\pi/6)N/V_\infty$, where N is the number of particles inside a (large) volume V_∞ , and the reduced temperature $k_B T/\epsilon$, where k_B is Boltzmann’s constant.

In this work, we derive a functional for a thermal system of penetrable spheres on the same solid footing as was previously only possible for hard-core interactions. We would like to stress that the new functional is not built as a theory of perturbations around some reference hard-sphere system, but has the penetrability of the particles genuinely built in. It incorporates the geometrical shape of the particles and the statistical mechanics of clusters of two or more overlapping particles.

Let us sketch the derivation of the new functional. We first discuss a generic free-energy density functional. Then, the exact solution for the 0D limit for penetrable spheres is presented. This is needed as a situation of extreme confinement for which we require the functional to give the exact result. Then, the freedom in the generic functional is fixed by requiring that this solution comes out from the functional. Explicit expressions for the DF are given.

We start with a generic density functional possessing the Rosenfeld form [5]: it is assumed that the Helmholtz excess free energy in an inhomogeneous situation can be expressed as an integral over all space:

$$F^{\text{exc}}(T, [\rho(r)]) = k_B T \int dx \Phi(T, \{n_\alpha(T, x)\})$$

where T is the temperature and k_B is Boltzmann’s constant. The integrand is a reduced free-energy density Φ depending on T and on a set of weighted densities $\{n_\alpha\}$ indexed by α . Each weighted density is given by a convolution of its temperature-dependent weight function w_α with the density profile:

$$n_\alpha(T, x) = \int dr \rho(r) w_\alpha(T, x - r).$$

This DF is generic in the sense that the dependence on the interaction potential V between the particles is hidden in the as-yet unspecified functions Φ and w_α . Although it is generic,

it is of course not the most general form of a density functional. The severe approximation is that Φ is not a functional but only a *function* of the weighted densities n_α . One convenient property is that the weight functions do not depend implicitly on the density profile. However, they may depend on the thermodynamic state point, given by the temperature T . For hard-core interactions the only temperature dependence of the free energy is a trivial linear scaling with T . Hence, in the original work focusing on hard spheres [5], Φ and w_α are temperature independent. In the current work we are interested in soft cores; so we have included the temperature dependence in this way, which we believe is the most general one within the current framework.

Let us now solve for the 0D limit of penetrable spheres. Consider a cavity with volume V_{0D} , small enough that any two particles that are inside overlap. The system will be coupled to a heat bath and to a particle bath. If there are N particles present, the potential energy is proportional to the number of pairs of particles and is given by $\epsilon N(N-1)/2$. The grand partition sum is

$$\Xi(N_{\max}) = \sum_{N=0}^{N_{\max}} b^{N(N-1)/2} z^N / N!$$

with the Boltzmann factor $b = \exp(-\epsilon/k_B T)$ and the scaled fugacity $z = V_{0D} \exp(\mu/k_B T)$, where μ is the chemical potential, and V_{0D} is the volume accessible to one particle. In principle, we have to perform the limit $N_{\max} \rightarrow \infty$; it is, however convenient to keep this dependence, as no closed form for the free energy for arbitrary N_{\max} is obtainable. The grand potential is $\Omega = -k_B T \ln \Xi$. The mean number of particles is $\bar{N} = z(\partial/\partial z)\Omega$. Inversion of this relation yields the fugacity as a function of \bar{N} . Technically, this inversion is not possible analytically for arbitrary N_{\max} , as one has to find the roots of a polynomial of degree N_{\max} . From the fugacity we obtain the excess chemical potential as a function of the particle number through $\mu_{0D}(\bar{N}) = \ln(z(\bar{N})/\bar{N})$. (The excess free energy can be obtained by integrating $\phi_{\text{exc}} = \int_0^{\bar{N}} d\bar{N} \mu_{0D}(\bar{N})$.) It is not possible to find a general solution in the limit $N_{\max} \rightarrow \infty$. This is not a serious drawback for our current investigation: one can find general solutions for $N_{\max} \leq 4$ that provide excellent approximations for cases of small particle numbers, $N \lesssim N_{\max}/2$, or use numerical methods. For the case of $N_{\max} = 1$ we recover the hard-sphere solution $\mu_{0D}(T \rightarrow 0, N) = -\ln(1-N)$; for $N_{\max} = 2$ we have

$$\begin{aligned} \mu_{0D}(T, N) &= \epsilon - \ln(2-N) - \ln(N) \\ &+ \ln \left(\sqrt{(1-N)^2 + 2N(2-N) \exp(-\epsilon/k_B T)} - (1-N) \right) \end{aligned}$$

which contains the essential contributions for low temperatures.

The idea is to consider a multi-cavity limit [10]. There the confining potential is given by a small set of cavities. Physically, the cavities are hollow and have the shape of one particle. The particles are forced to be inside one of the cavities, so their density distribution vanishes outside. For an integer number C of cavities located at positions c_i we have

$$\rho(r) = \sum_{i=1}^C N_i \delta(r - c_i).$$

If the distance between two cavities is larger than the particle diameter, they are decoupled. If the distance is smaller than the diameter all particles overlap and the statistical behaviour is the same as for a single cavity. By considering consecutively the one-, two- and three-cavity cases, $C = 1, 2, 3$, one is able to fix the form of the generic functional. The geometrical analysis follows the hard-sphere case [10], where the strategy leads to the Rosenfeld hard-sphere functional [6, 7].

10166 *M Schmidt*

For penetrable spheres the FMT excess free-energy functional derived in this way is given by $\Phi = \Phi_1 + \Phi_2 + \Phi_3$. The individual contributions are

$$\begin{aligned}\Phi_1 &= n_0 \mu_{0D}(T, n_3) \\ \Phi_2 &= (n_1 n_2 - \mathbf{n}_{v1} \cdot \mathbf{n}_{v2}) \mu'_{0D}(T, n_3) \\ \Phi_3 &= n_2^3 (1 - (\mathbf{n}_{v2}/n_2)^2)^3 \mu''_{0D}(T, n_3) / (24\pi)\end{aligned}$$

where the prime denotes differentiation with respect to the argument n_3 (in the OD case, with respect to N) and the index v is a reminder that \mathbf{n}_{v1} and \mathbf{n}_{v2} are vectors. The linearly independent weight functions are given by

$$w_3(T, \mathbf{r}) = \Theta(R - r) \quad w_2(T, \mathbf{r}) = \delta(R - r) \quad w_{v2}(T, \mathbf{r}) = \delta(R - r) \mathbf{r}/r$$

where $r = |\mathbf{r}|$, and $R = \sigma/2$ is the particle radius. Dependent on the above are the further weights

$$w_1 = w_2 / (4\pi R) \quad w_0 = w_2 / (4\pi R^2) \quad w_{v1} = w_{v2} / (4\pi R)$$

where the arguments have been omitted. We find that the free-energy density carries a temperature dependence through μ_{0D} , but the weight functions remain independent of temperature.

Let us investigate the properties of the functional. For low densities one can expand the free-energy density to find $\mu_{0D} = (1 - \exp(-\epsilon/k_B T))n_3$; hence the total free-energy density becomes

$$\Phi = (1 - \exp(-\epsilon/k_B T))(n_0 n_3 + n_1 n_2 - \mathbf{n}_{v1} \cdot \mathbf{n}_{v2})$$

which is the deconvolution of the Mayer function for the penetrable-sphere interaction, and hence the low-density expansion of the true density functional. The deconvolution is also valid in the limit of high temperature, where we get the mean-field free-energy density $\mu_{0D} = \epsilon N(N - 1)/2$. The low-temperature limit $k_B T/\epsilon \rightarrow \infty$ yields $\mu_{0D} = -\ln(1 - \eta)$, which gives the well-known Rosenfeld hard-sphere functional including the Percus–Yevick direct correlation function [5], the cell model as the high-density limit of the crystal near close packing [18] and excellent values for the coexisting-liquid-and-solid packing fractions at the freezing transition [6, 7]. We repeat the fact that the functional is, by construction, exact in the zero-dimensional limit.

Having demonstrated the correct behaviour in limiting cases, we are confident in investigating the predictions of the current DFT for physically more interesting regions, namely intermediate temperatures and densities. First, we investigate the liquid structure predicted by the functional. To get the pair correlation function $g(r)$ we impose Percus’s test particle limit by minimizing the functional in the presence of an external potential that coincides with the pair potential. The results are shown for packing fraction $\eta = 0.5$ as solid lines in figure 1. The agreement with Monte Carlo simulation data (symbols) is very good outside the core, $r > \sigma$. For $r < \sigma$ and intermediate temperatures, the rise near the origin is overestimated by the DFT. Any thermodynamic integrals over $g(r)$ are robust against this error, because of multiplication with a volume element $4\pi r^2$ which vanishes for $r \rightarrow 0$. Recently, $g(0)$ has been used successfully within the framework of liquid integral equations to fulfil a zero-separation theorem [19]. The small wiggles in figure 1, e.g. for $k_B T/\epsilon = 0.2$ near $r/\sigma = 1.5$, are artifacts due to the numerical representation of the functions as cubic splines.

In general, our results are superior to those obtained from standard liquid integral equations, as there is ‘an inadequacy of the traditional liquid-state integral theories to describe in a satisfactory way the high-density fluid phase of the system’ [16] (see figure 3 therein for the result of the Percus–Yevick closure). We have also used a simpler way to get $g(r)$ via the second functional derivative of the free energy with respect to density together with the Ornstein–Zernicke relation. This result agrees fairly well at low density but the agreement becomes

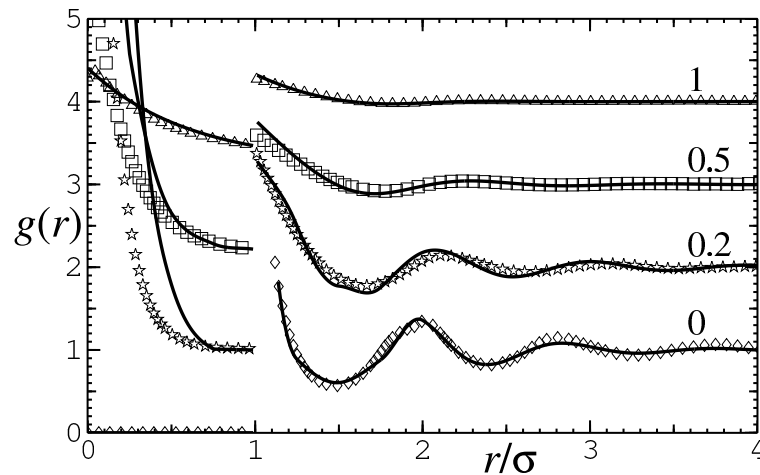


Figure 1. The pair correlation function for penetrable spheres with packing fraction $\eta = 0.5$ at different temperatures such that $k_B T/\epsilon = 0, 0.2, 0.5, 1$. Lines denote theoretical results; symbols indicate simulation data. (For the sake of clarity, the curves are shifted upwards by one unit and the $T = 0$ curve is not drawn near contact, $r/\sigma < 1.14$.)

worse upon increasing the density beyond $\eta > 0.3$. One encounters negative values inside the core, which are of course unphysical. For the fluid free energy, we take a linear combination of the compressibility and virial expressions with weights $1/3$ and $2/3$, respectively; this is similar to the Carnahan–Starling procedure [3]. The details will be presented elsewhere [20].

To investigate the solid phase, the density distribution is parametrized with a Gaussian *ansatz*:

$$\rho(\mathbf{r}) = \eta_0 (\alpha^3 / \pi^{3/2}) \sum_{\{\mathbf{R}_i\}} \exp(-\alpha^2 (\mathbf{r} - \mathbf{R}_i)^2)$$

where the summation runs over the lattice sites $\{\mathbf{R}_i\}$ of a face-centred-cubic (fcc) lattice. This *ansatz* allows for multiply occupied lattice sites through the occupancy number η_0 , which may be larger than unity. Upon minimizing the functional with respect to α and η_0 , we find the solid phase to be stable. The occupation number grows for increasing density and increasing temperature.

By imposing thermal, mechanical and chemical equilibrium between the fluid and solid phase, we calculate the phase diagram shown in figure 2. There appears a first-order freezing transition into an fcc structure with multiply occupied lattice sites. As expected physically, the solid phase becomes destabilized upon increasing the temperature. The solid–fluid coexistence is shifted towards lower packing fractions compared to those given by the combined integral–equation–cell-model approach of Likos *et al* [16] (e.g., $\eta = 0.8–1.0$ at temperature 0.2). The claimed clustering transitions [16] are not thermodynamic phase transitions, but merely sharp increases in the occupation numbers [21]. In accordance with this result from the cell model, the present DFT yields a single-crystalline phase.

To illustrate the physics of the penetrable-sphere model, we finally show snapshots taken from computer simulation in figure 3. In the fluid phase (figure 3(a)), there are large clusters of overlapping particles. In the solid phase (figure 3(b)), each lattice site can be occupied by more than one particle. Both configurations have the space-filling packing fraction $\eta = 1$, with temperatures such that $k_B T/\epsilon = 1, 0.1$.

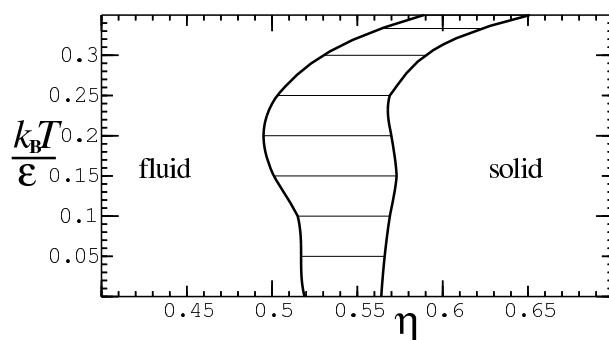
10168 *M Schmidt*

Figure 2. The phase diagram for penetrable spheres depending on the packing fraction and temperature. Coexistence is denoted by thin horizontal tie lines. The simulation results for $T = 0$ are $\eta = 0.494$ – 0.545 [3].

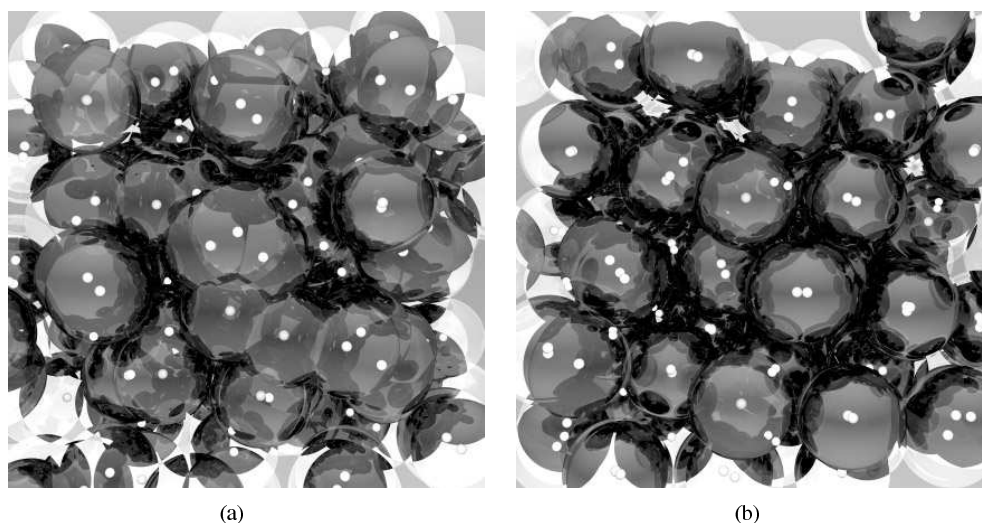


Figure 3. Snapshots from computer simulation of the fluid phase (a) and the solid phase (b) at packing fraction $\eta = 1$. The particles are rendered as transparent bubbles with small white balls indicating their centres.

In this work we have demonstrated that a very successful theory of hard-body fluids and solids, the so-called fundamental-measure density functional theory, can be generalized to penetrable particles, while retaining its simplicity and accuracy. The major advance is the systematic introduction of an internal energy scale into a hitherto purely entropic theory. We have considered a model of penetrable spheres, interacting with a step-function potential which is ϵ inside the core and zero outside. The functional is derived by considering both the geometric properties of the spherical particles and the so-called zero-dimensional limit, consisting of a hard cavity of the size of a single particle. To our knowledge, it is the first non-perturbative functional of the Rosenfeld type derived for a thermal system. We have considered the fluid structure derived using the functional, finding good agreement with simulations. Describing the solid as a superposition of Gaussian peaks, the theory predicts a freezing transition into a multiply occupied fcc lattice. Finally, we note that it is highly desirable to apply the current approach to more general pair potentials. Work along these lines is in progress.

Acknowledgments

I would like to thank Hartmut Löwen, Yasha Rosenfeld, Bob Evans, Jean-Pierre Hansen, Luc Belloni, José Cuesta, Maria José Fernaud and Martin Watzlawek.

References

- [1] Evans R 1992 *Fundamentals of Inhomogeneous Fluids* ed D Henderson (New York: Wiley) p 85
- [2] Oxtoby D W 1991 *Liquids, Freezing and Glass Transition* ed J-P Hansen, D Levesque and J Zinn-Justin (Amsterdam: Elsevier Science) p 147
- [3] Löwen H 1994 *Phys. Rep.* **237** 249
- [4] González A, White J A, Román F L, Velasco S and Evans R 1997 *Phys. Rev. Lett.* **79** 2466
- [5] Rosenfeld Y 1989 *Phys. Rev. Lett.* **63** 980
- [6] Rosenfeld Y, Schmidt M, Löwen H and Tarazona P 1996 *J. Phys.: Condens. Matter* **8** L577
- [7] Rosenfeld Y, Schmidt M, Löwen H and Tarazona P 1997 *Phys. Rev. E* **55** 4245
- [8] Cuesta J A 1996 *Phys. Rev. Lett.* **76** 3742
- [9] Cuesta J A and Martínez-Raton Y 1997 *Phys. Rev. Lett.* **78** 3681
- [10] Tarazona P and Rosenfeld Y 1997 *Phys. Rev. E* **55** R4873
- [11] Stillinger F H and Weber T A 1978 *J. Chem. Phys.* **68** 3837
- [12] Stillinger F H and Stillinger D K 1997 *Physica A* **244** 358
- [13] Graf H and Löwen H 1998 *Phys. Rev. E* **57** 5744
- [14] Likos C N, Löwen H, Watzlawek M, Abbas B, Jucknischke O, Allgaier J and Richter D 1998 *Phys. Rev. Lett.* **80** 4450
- [15] Jusufi A, Watzlawek M and Löwen H 1999 *Macromolecules* **32** 4470
- [16] Likos C N, Watzlawek M and Löwen H 1998 *Phys. Rev. E* **58** 3135
- [17] Katsura S and Abe Y 1963 *J. Chem. Phys.* **39** 2068
- [18] Rosenfeld Y 1996 *J. Phys.: Condens. Matter* **8** L795
- [19] Fernaud M J, Lombda E and Lee L L 1999 to be published
- [20] Schmidt M 1999 in preparation
- [21] Likos C N and Löwen H 1999 private communication

Fluid of penetrable spheres: Testing the universality of the bridge functional

Yaakov Rosenfeld

Nuclear Research Center Negev, P.O. Box 9001, Beer-Sheva 84190, Israel

Matthias Schmidt, Martin Watzlawek,* and Hartmut Löwen

Institut für Theoretische Physik II, Heinrich-Heine Universität Düsseldorf, Universitätsstrasse 1, 40225 Düsseldorf, Germany

(Received 23 May 2000)

Penetrable spheres have been the object of recent extensive investigations as a prototype for intermolecular interactions in a solvent, and as representing a class of bounded potentials allowing complete interpenetrability of the particles. Here we compare density-functional and simulation results for the pair-correlation functions in a bulk fluid of penetrable spheres, as a stringent test for the approximation of “universality” of the bridge functional. Considering either a fundamental-measure functional for penetrable spheres or a perturbative treatment using a fundamental-measure hard-sphere functional, we conclude that hard-sphere-type bridge functionals are applicable also for bounded potentials with high penetrability.

PACS number(s): 61.20.Gy, 05.70.Ce, 82.70.Dd, 61.25.Hq

I. INTRODUCTION

There has been continuous progress in the theory of non-uniform classical fluids in recent years, bringing new approximations and models within density-functional theory [1,2]. The central quantity is the Helmholtz free-energy functional, $F[\rho(\mathbf{r})]$, of the inhomogeneous density distribution, $\rho(\mathbf{r})$. The geometrical character of the hard-sphere interactions, which has been a major reason for their long-standing central role in the microscopic theory of classical fluids, also simplifies the construction of model functionals, and eventually led to the geometrically based so-called fundamental-measure theory (FMT) [3]. Several very recent analyses [4–6] revealed the important role played by the dimensional crossover properties of the fundamental-measure functionals, and in particular their zero-dimensional (0D) limit corresponding to a cavity with at most one particle. Recent studies showed [5,6] that the correct 0D crossover can be systematically imposed, and the exact 0D limit plays the role of a generating functional for D -dimensional hard-sphere FMT functionals. The original FMT [3] together with its extensions and modifications [4–6] proved very successful for describing the inhomogeneous hard-sphere fluid, and sophisticated algorithms for implementing the hard-sphere FMT in complex geometries have been developed recently [7]. FMT has also been applied successfully to parallel hard cubes [8], and a possible extension of FMT to general hard convex bodies was offered [9]. Very recently, the FMT was generalized to penetrable spheres [10] and to soft interactions [11], with particular extensions to star polymer solutions [12] and colloid-polymer mixtures [13].

It should be noted, however, that the Ornstein-Zernike equations using the second functional derivatives (i.e., the direct correlation functions) of the generally accurate FMT free-energy functionals do not always yield positive definite and physically acceptable bulk pair correlations. The Percus-

Yeovick pair correlations as obtained with the FMT for hard spheres are an exception which proves the case. The reason for such failures is that even generally accurate free-energy functionals will develop certain errors when functionally differentiated, especially to second and higher orders. Nevertheless, any approximate excess free-energy functional can be self-consistently corrected up to second order by employing the corresponding bridge functional in the test-particle limit [14–16]. Moreover, the approximation of “universality of the bridge functional” [14–19] enables us to use the accurate FMT hard-sphere functionals (with optimized hard-sphere radii when applicable) in order to obtain free-energy functionals for arbitrary pair interactions. Of particular importance is the possibility to solve accurately the inverse scattering problem (i.e., obtain the pair potential from a known structure factor) [17,18]. However, we should not forget the geometrical nature of the hard-sphere interaction, which means that, e.g., systems with a tendency to form pairs and higher-order clusters due to their attractions or peculiar repulsion are not expected to be well treated with the hard spheres as reference. In particular, the pairing in electrolytes [22] cannot be addressed by invoking the hard-sphere bridge functional. In this paper we focus attention on the system of penetrable spheres, i.e., particles that can sit on top of each other with a finite energy cost [20]. We employ both the hard-sphere and the penetrable-sphere FMT functionals in order to obtain a stringent test of the approximation of universality of the bridge functional.

The system under consideration is a fluid of penetrable spheres (PS) interacting via the following pair potential:

$$\begin{aligned}\phi(r) &= 0 \quad \text{if } r > 2R, \\ \phi(r) &= \epsilon \quad \text{if } r \leq 2R,\end{aligned}\tag{1}$$

and characterized by the reduced temperature, $T^* = k_B T / \epsilon$, and reduced density, $\eta = 4\pi\rho R^3/3$. For $\epsilon = \infty$ (i.e., for $T^* = 0$), this system corresponds to the hard spheres (HS), and then η is the standard hard-sphere packing fraction. This system is of interest as a prototype for the interaction be-

*Present address: Central Research, Building E 41, Bayer AG, D-51368 Leverkusen, Germany.

tween micelles in a solvent [23], and was investigated recently by several methods [20]. It is the simplest of the class of bounded interactions which allow penetrability, another example being the Gaussian core model [24,21] which was recently shown to arise between the centers of star polymers if the polymeric arms are treated in the harmonic approximation [25]. Although diverging at the origin, an ultrasoft pair potential between star polymers [26] was validated by simulations [27]. The glass transition for the penetrable spheres was investigated by simulations [28]. Standard integral-equation theories for the bulk pair structure employ closures which are biased towards the concept of a hard core in the pair correlation, and thus are less accurate for penetrable spheres [20]. A very recent work [29] demonstrated a successful approximate closure relation for penetrable spheres which employs, however, three free parameters which are determined from thermodynamic self-consistency requirements, in particular the zero-separation theorem. As will be shown below, comparable accuracy can be obtained from the penetrable-sphere FMT bridge functional without any free parameters, or from the hard-sphere FMT functional by optimizing the effective radius.

II. FREE-ENERGY FUNCTIONALS, BRIDGE FUNCTIONALS, AND THE TEST-PARTICLE LIMIT

The starting point for the application of the density-functional method for both uniform and nonuniform fluids is the density-profile equation, i.e., the Euler-Lagrange equation for minimizing the grand potential [1]. The equations determining the density profile $\rho(\vec{r})$ for the fluid subject to an external potential $u(\vec{r})$ can be written in the modified hypernetted-chain (MHNC) form [30,14–16] involving the *bridge functional*, which is related to the sum of all terms beyond second order in the functional Taylor expansion of the excess free energy $F_{\text{ex}}[\rho(\vec{r})]$ around some reference density. For a fluid in contact with a reservoir bulk fluid, of average density ρ_0 , the density profile equations can be written in the following form:

$$\ln g(\vec{r}) = -\frac{u(\vec{r})}{k_B T} - B[\rho_0; \rho(\vec{r}); \vec{r}] + \rho_0 \int d\vec{r}' c^{(2,FD)}(\rho_0; |\vec{r} - \vec{r}'|) [g(\vec{r}') - 1]. \quad (2)$$

Here $g(\vec{r}) = \rho(\vec{r})/\rho_0$, is the bulk limit of the direct correlation function given by the second functional derivative $c^{(2,FD)}(\vec{r}_1, \vec{r}_2) = -\delta^2 F_{\text{ex}}[\rho(\vec{r})]/k_B T \delta\rho(\vec{r}_1) \delta\rho(\vec{r}_2)$, and the ‘‘Bridge’’ functional is given by [14–16]

$$B[\rho_0; \rho(\vec{r}); \vec{r}] = \frac{\mu_{\text{ex}}[\rho(\vec{r}); \vec{r}]}{k_B T} - \frac{\mu_{\text{ex}}[\rho_0]}{k_B T} + \rho_0 \int d\vec{r}' c^{(2,FD)}(\rho_0; |\vec{r} - \vec{r}'|) [g(\vec{r}') - 1], \quad (3)$$

where $\mu_{\text{ex}}[\rho(\vec{r}); \vec{r}] = -\delta F_{\text{ex}}[\rho(\vec{r})]/\delta\rho(\vec{r})$. By truncating the expansion of the excess free energy after second order, the

bridge functional vanishes, and the density profile equation (2) then has the hypernetted-chain-approximation (HNC) form.

An elementary test of the accuracy of a model free-energy functional for a given pair potential $\phi(r)$, and of the corresponding bridge functional, is performed by considering the density profile equation for the same potential in the special case when the external potential is generated by a *test particle* at the origin of coordinates, $u(\vec{r}) = \phi(r)$. The resulting density profiles correspond to the bulk pair-correlation functions, $g(r) = \rho(r)/\rho_0$. The test-particle limit of the density profile equations takes the form [14–16]

$$g(r) = \exp\left(-\frac{\phi(r)}{k_B T} - b(r) + \rho_0 \int d\vec{r}' c^{(2,FD)}(\rho_0; |\vec{r} - \vec{r}'|) h(r')\right), \quad (4)$$

where $h(r) = g(r) - 1$, and the bridge function, $b(r)$, is derived from the *bridge functional* $B[\rho_0; \rho(\vec{r}); \vec{r}]$ by using $\rho(\vec{r}) = \rho_0 g(r)$,

$$b(r) = B[\rho_0; \rho_0 g(r); r]. \quad (5)$$

The *exact* free-energy functional must obey the ‘‘test-particle self-consistency’’: the exact $g(r)$ as obtained from the solution of the exact coupled density profile equations (4) and (5) is identical to that obtained from the Ornstein-Zernike relation using the direct correlation function from the second functional derivative of the functional

$$h(r) = c^{(2,FD)}(\rho_0; r) + \rho_0 \int d\vec{r}' c^{(2,FD)}(\rho_0; |\vec{r} - \vec{r}'|) h(r'). \quad (6)$$

Given a model free energy based on an approximate bridge functional, it can be *optimized up to second order* by imposing the test-particle *self-consistency* (SC) [14–16] which is achieved by *coupling* the density-profile equations (4) and (5) with the Ornstein-Zernike relation (6). A measure of the accuracy of an approximate excess free-energy functional for the potential $\phi(r)$ is given by the degree of test-particle self-consistency obtained by comparison $c^{(2,FD)}(\rho_0; r)$ with the self-consistent result $c^{(2,SC)}(\rho_0; r)$.

This method can be used also for potentials for which the free-energy functional is not available. The assumption one makes leading to the ‘‘universality’’ hypothesis is that the bridge functional is (approximately) independent of the precise form of the pair interaction, hence it is regarded as being a universal quantity that can be obtained from any appropriate given *reference* potential. When the potential and the reference potential are different, then it is possible to *optimize the reference-system parameters* by free-energy minimization that leads to an equation of the form [14–16]

$$\int d\vec{r} [g(\vec{r}) - g^{\text{reference}}(\vec{r})] \delta b(\vec{r}) = 0. \quad (7)$$

As the hard-sphere FMT is an especially successful theory, it is expected that it gives a reasonable approximation for the bridge functional, and the method is, in principle, applicable to any pair potential. The penetrable-sphere system, however, is a stringent test case, as it is *a priori* unclear whether the universality extends to systems without hard core. The

hard-sphere FMT functional realizes the nonoverlap criterion, whereas the penetrable-sphere FMT takes into account the effect of potential energy of overlapping particles.

III. RESULTS AND DISCUSSION

In this paper we compare simulation results for the pair-correlation functions in the bulk fluid of penetrable spheres, with the following four approximations. (i) The hypernetted-chain approximation (obtained by ignoring the bridge functions altogether), denoted HNC. (ii) The bulk pair correlations as obtained via the Ornstein-Zernike relation from the direct correlation functions as given by the second functional derivatives of the penetrable-spheres FMT free-energy functional, denoted by OZ-PS. (iii) The bulk pair correlations as obtained from the solution of the test-particle self-consistency equations using the penetrable-spheres FMT functional, denoted SC-PS. This is equivalent to using the bridge function in Eq. (4) as obtained from the penetrable-spheres FMT bridge functional through Eq. (5), without any adjustment of parameters. (iv) The bulk pair correlations as obtained from the hard-spheres FMT bridge functional, with an optimal value for the reference hard-sphere packing fraction, denoted SC-HS. The comparison of OZ-PS and SC-PS and both with the simulations reveals the accuracy of the penetrable-sphere FMT and its level of self-consistency. The comparison of SC-PS and SC-HS and both with the simulations enables us to test the ‘‘universality’’ hypothesis.

We compared an extensive set of Monte Carlo (MC) simulation results with many solutions of density-profile equations, for bulk pair correlations, of which we display graphically only two extreme representative cases: (a) substantial but relatively low penetrability (on average less than two particles with interpenetrating cores): $T^*=0.2$, $\eta=0.35$; and (b) high penetrability, mean field [31] cases: $4 \leq T^* = \eta \leq 12$. In the context of this paper, we must first consider the behavior of the HNC approximation, which ignores the bridge functions altogether. Recall that for hard spheres the HNC overestimates the first peak of $g(r)$ just outside the core. With increasing penetrability, the HNC results outside the core become almost indistinguishable from the simulations. For relatively small penetrability, the main drawback of the HNC approximation is the substantial overestimation of the penetrability, namely of $g(r)$ close to zero separation [Fig. 1(a)]. With increasing penetrability, the HNC results represent the simulations increasingly better, both inside and outside the core. In the high penetrability region, the simulations are reproduced very well [31] by the mean field (mean spherical approximation, denoted MSA) for the direct correlation function, i.e., $c(r) = -\phi(r)/k_B T$, and even better results are obtained with the HNC.

For cases of type (a), both SC-PS and SC-HS significantly improve on the HNC [Fig. 1(a)], and the overall picture is better seen in Fig. 1(b) for the structure factor. With respect to SC-HS, it should be emphasized that according to the standard criterion usually applied for optimizing the reference hard-sphere radius, an integral of a weighted difference between the reference hard-sphere and the penetrable-sphere pair correlations has to vanish. However, when the penetrability is non-negligible, and the pair correlations manifestly belong to different classes, this criterion is no longer appli-

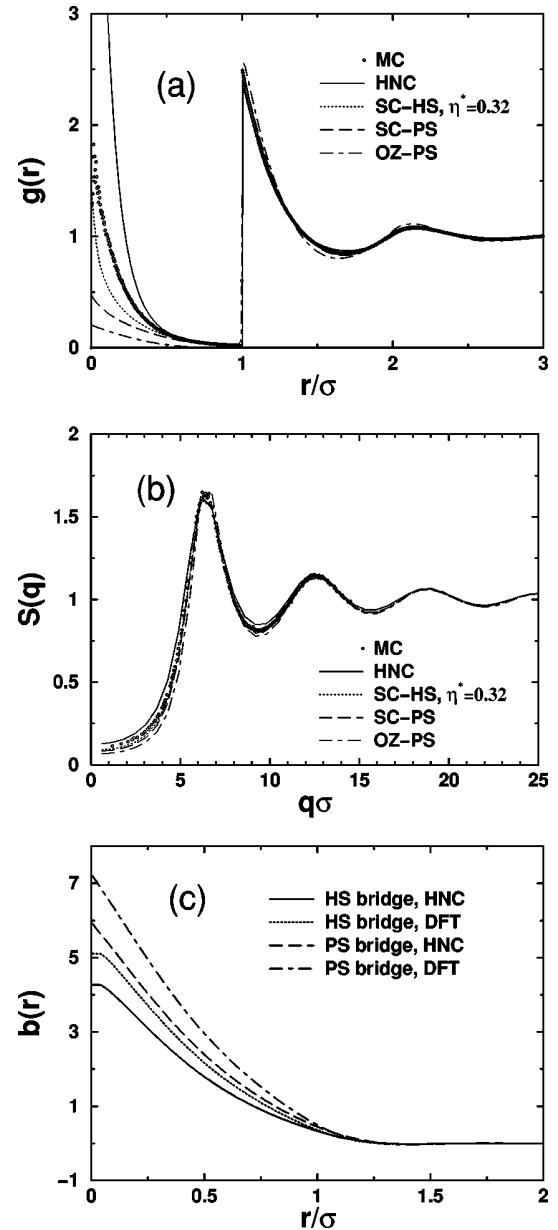


FIG. 1. (a) Pair-correlation function $g(r)$ for penetrable spheres for $T^*=0.2$, $\eta=0.35$. The lines and symbols represent the MC simulations (open circles), HNC (full line), method OZ-PS (short-dash-long-dash line), method SC-PS (dashed line), and method SC-HS (dotted line), with the value of the reference packing fraction $\eta^*=0.32$. (b) Structure factors $S(k)$ corresponding to (a). (c) Bridge functions, $b(r)$, as calculated by the bridge functionals: Penetrable-sphere functional with the HNC (long dash line), and the method SC-PS (short-dash-long-dash line) $g(r)$ results as input; hard-sphere functional, with indicated reference packing fraction $\eta=0.32$, with the HNC (full line), and the method SC-HS (dotted line) $g(r)$ results as input.

cable. Instead, in order to see to what extent the approximation of ‘‘universality’’ holds even when the hard-sphere reference is no longer expected *a priori* to be good, we have varied the value of the reference packing fraction in the hard-sphere bridge functional in order to see how it affects the bridge functions. The comparison with simulations shows that the reference parameter can be chosen by imposing any

single thermodynamic consistency criterion. Indeed, with an appropriately chosen value of the packing fraction for the reference hard-sphere system, η^* , the bridge functions from method SC-HS are comparable to those from method SC-PS [Fig. 1(c)]. The accuracy of OZ-PS for penetrable spheres is comparable to that of the same method, namely the Percus-Yevick result, when applied via the FMT functional for the case of hard spheres. As for hard spheres, the test-particle limit results for the penetrable-sphere functional improve on the corresponding Ornstein-Zernike results, i.e., SC-PS is more accurate than OZ-PS. However, the difference between the SC-PS and OZ-PS results is relatively small, demonstrating that the new penetrable-sphere functional obeys quite well (to about the same extent as the corresponding FMT theory for hard spheres) the “test-particle self-consistency” between the density-profile and the Ornstein-Zernike equations. Thus, by comparison with the simulations, both density-functional treatments are quite successful. We furthermore conclude that the hard-sphere bridge functional is applicable even for bounded potentials with substantial penetrability.

With increasing penetrability and the increase of the accuracy of the HNC, then the method SC-HS based on the hard-sphere bridge functional with a judicious choice of η^* will automatically work well since thermodynamic consistency will naturally impose $\eta^* \ll 1$ (i.e., the HNC). This, however, represents a favorable feature of the method which automatically resorts to the HNC when the HNC becomes thermodynamically consistent [30], but it does not mean that the bridge functional itself is accurate. In turn, the penetrable-sphere bridge functional does not contain any free parameters when applied to penetrable spheres, so that its performance in the test-particle limit checks its intrinsic accuracy. Considering cases of type (b), the pair-correlation function $g(r)$ in the regime of high penetrability, $T^* = \eta = 4, 6, 8, 10, 12$, is shown in Fig. 2. We see that OZ-PS describes the behavior quite well, while SC-PS essentially coincides with the HNC and the simulations.

In summary, by investigating the bulk fluid of penetrable

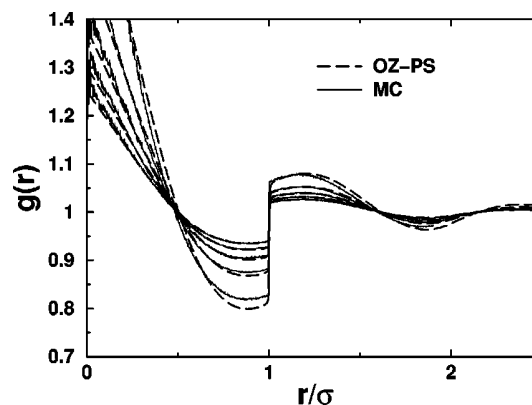


FIG. 2. Pair-correlation function $g(r)$ for penetrable spheres for $T^* = \eta = 4, 6, 8, 10, 12$. Method OZ-PS (dashed line) compared with the MC simulation results (thin line). On the scale of the figure, the HNC and MSA results are almost indistinguishable from the simulations, and therefore are not shown.

spheres, considering either a fundamental-measure functional for penetrable spheres or a perturbative treatment using a fundamental-measure hard-sphere functional in comparison with simulations, we conclude that hard-sphere-type bridge functionals are applicable also for bounded potentials with high penetrability. In particular, the penetrable-sphere bridge functional, as a generalization of the hard-sphere FMT functional, is applicable without any adjustable parameters for arbitrary penetrability including the special case of hard spheres. Moreover, the PS bridge functional can be employed for the treatment of bounded potentials other than PS themselves. Then the penetrable spheres act as a reference system with adjustable parameters ϵ and R , and the same theoretical framework can be used as in the case of diverging interactions and the hard-sphere bridge functional with adjustable R .

ACKNOWLEDGMENT

Y.R. thanks the Humboldt Foundation for generous support.

-
- [1] R. Evans in, *Fundamentals of Inhomogeneous Fluids*, edited by D. Henderson (Dekker, New York, 1992); H. Löwen, Phys. Rep. **237**, 249 (1994).
- [2] *New Approaches to Old and New Problems in Liquid State Theory*, edited by C. Caccamo, J.P. Hansen, and G. Stell (Kluwer, Dordrecht, 1999).
- [3] Y. Rosenfeld, Phys. Rev. Lett. **63**, 980 (1989); see also the short review Y. Rosenfeld, J. Phys.: Condens. Matter **8**, 9289 (1996).
- [4] Y. Rosenfeld, M. Schmidt, H. Löwen, and P. Tarazona, J. Phys.: Condens. Matter **8**, L577 (1996); Phys. Rev. E **55**, 4245 (1997).
- [5] P. Tarazona and Y. Rosenfeld, Phys. Rev. E **55**, R4873 (1997).
- [6] P. Tarazona, Phys. Rev. Lett. **84**, 694 (2000).
- [7] L.J.D. Frink and A.G. Salinger, J. Comput. Phys. **159**, 407 (2000); **159**, 425 (2000).
- [8] J.A. Cuesta, Phys. Rev. Lett. **76**, 3742 (1996); J.A. Cuesta and Y. Martinez-Raton, *ibid.* **78**, 3681 (1997); J. Chem. Phys. **107**, 6379 (1997).
- [9] Y. Rosenfeld, Phys. Rev. E **50**, R3318 (1994); Mol. Phys. **86**, 637 (1995).
- [10] M. Schmidt, J. Phys.: Condens. Matter **11**, 10 163 (1999).
- [11] M. Schmidt, Phys. Rev. E **60**, R6291 (1999); **62**, 3799 (2000); **62**, 4976 (2000).
- [12] B. Groh and M. Schmidt (unpublished).
- [13] M. Schmidt, H. Löwen, J.M. Brader, and R. Evans, Phys. Rev. Lett. **85**, 1934 (2000).
- [14] Y. Rosenfeld, J. Chem. Phys. **98**, 8126 (1993).
- [15] Y. Rosenfeld, Phys. Rev. Lett. **72**, 3831 (1994); J. Chem. Phys. **99**, 2857 (1995).
- [16] Y. Rosenfeld, Phys. Rev. E **54**, 2827 (1996).
- [17] G. Kahl, B. Bildstein, and Y. Rosenfeld, Phys. Rev. E **54**, 5391 (1996).
- [18] Y. Rosenfeld and G. Kahl, J. Phys.: Condens. Matter **9**, L89 (1997).
- [19] Y. Rosenfeld, Mol. Phys. **94**, 929 (1998).
- [20] C.N. Likos, M. Watzlawek, and H. Löwen, Phys. Rev. E **58**, 3135 (1998).

- [21] A. Lang, C.N. Likos, M. Watzlawek, and H. Löwen, *J. Phys.: Condens. Matter* **12**, 5087 (2000).
- [22] D.M. Zuckerman, M.E. Fisher, and B.P. Lee, *Phys. Rev. E* **56**, 6569 (1997).
- [23] C. Marquest and T.A. Witten, *J. Phys. (France)* **50**, 1267 (1989).
- [24] F.H. Stillinger and T.A. Weber, *J. Chem. Phys.* **68**, 3837 (1978); F.H. Stillinger and D.K. Stillinger, *Physica A* **244**, 358 (1997).
- [25] H. Graf and H. Löwen, *Phys. Rev. E* **57**, 5744 (1998).
- [26] C.N. Likos *et al.*, *Phys. Rev. Lett.* **80**, 4450 (1998).
- [27] A. Jusufi, M. Watzlawek, and H. Löwen, *Macromolecules* **32**, 4470 (1999).
- [28] W. Klein *et al.*, *Physica A* **205**, 738 (1994).
- [29] M.J. Fernaund, E. Lomba, and L.L. Lee, *J. Chem. Phys.* **12**, 810 (2000).
- [30] Y. Rosenfeld and N.W. Ashcroft, *Phys. Rev. A* **20**, 1208 (1979).
- [31] C. N. Likos, A. Lang, M. Watzlawek, and H. Löwen (unpublished).

Density functional for the Widom-Rowlinson model

Matthias Schmidt

Institut für Theoretische Physik II, Heinrich-Heine-Universität Düsseldorf, Universitätsstraße 1, D-40225 Düsseldorf, Germany
(Received 8 August 2000; published 19 December 2000)

We present a density functional theory for the m -component Widom-Rowlinson model, for a mixture of spherical particles where the unlike species interact with a hard-core potential and the interactions between like species vanish. The functional is exact for small densities and in the zero-dimensional limit. It predicts the fluid structure in good agreement with simulations and yields a continuous demixing phase transition for $m=2$. In the limit of large m the Widom-Rowlinson model reduces to effective hard spheres in the mixed phase and the Asakura-Oosawa (colloid-ideal polymer) model in the demixed phase. Within the present theory, both cases are captured correctly. For intermediate m we find a first order demixing phase transition, with a rapidly broadening density discontinuity upon increasing m .

DOI: 10.1103/PhysRevE.63.010101

PACS number(s): 64.10.+h, 64.70.Ja, 61.20.Gy, 64.60.Fr

Whether two or more fluids are miscible is often an important question, e.g., in engineering, physical chemistry, or food science. From a physical point of view, many multi-component fluids will be in a single phase because of a gain in mixing entropy. Changing the thermodynamical variables then may lead to demixing. There are (at least) two basic mechanisms that explain the phase separation. One is the depletion interaction, where the presence of one of the components generates an effective attraction between particles of the other component(s). The effective attraction accounts for the phase separation via the common entropy-versus-energy mechanism as is present in the gas-liquid transition of simple liquids, say the Lennard-Jones system. The second mechanism for demixing lies in the relative strengths of repulsion between like and unlike particles. If the unlike particles experience a stronger repulsion than the like ones, demixed phases are favored, at least at high density. The prototype for this behavior is the Widom-Rowlinson (WR) model [1–4]. There the interaction between m species is such that particles of the same species do not interact; that is, are assumed to be ideal, whereas the unlike species interact with a hard core potential. It is clear that for high densities a mixed phase will suffer from strong packing effects, which are greatly reduced in a demixed phase with a single majority component. At low density the system reaches ideal gas behavior, which, of course, will cause a mixed phase. The intervening phase transition has been studied with a range of approaches, including mean-field theory (MFT) [4], Percus-Yevick (PY) integral equation theory [3,5], scaled-particle theory (SPT) [6], as well as computer simulations [5,7,8].

Essentially all theories give a demixing phase diagram for $m=2$ with a lower critical point (as a function of total density) and a rapidly broadening coexistence region upon increasing density. The precise location of the critical point was a matter of discussion since the introduction of the model, and it is remarkable that only recently two independent simulations located it about 50% higher than previously thought [5,7].

Obviously, the WR model does not possess a solid phase for $m=2$, as any possible solid is preempted by demixing. It has been found, however, that for large number of components $m>31$, a crystal becomes stable for parallel hyper-

cubes [9]. This is a *mixed* phase, as only repulsion is present, which is the essential ingredient for freezing. Apart from this and the study of the free interface between demixed fluid phases [4,10], little is known about inhomogeneous situations. To study those, density-functional theory (DFT) [11] can be an important tool. It accounts for spatially varying density profiles, and, in its sophisticated versions, for the structure at the two- and higher-body level. To our knowledge the WR model has so far resisted any DFT treatment that goes beyond the MFT of Ref. [4].

In this work, we propose an approximation for the density functional of the m -component WR model. It is a fundamental-measure theory (FMT), an approximation scheme pioneered by Rosenfeld for hard spheres [12–14], and also applied to hard parallel cubes [15,16], penetrable spheres [17,18], as well as to the Asakura-Oosawa (AO) model [19].

The pair correlations *derived* from the functional are found to be in good agreement with simulation results. The $m=2$ phase diagram is comparable in quality to other theories. For $m\geq 3$, we find a first-order fluid demixing phase transition, with an increasingly large coexistence interval (in density) upon increasing m . We expect for $m\rightarrow\infty$ hard sphere behavior in the mixed phase and AO [20] behavior in the demixed phase (with the majority component identified as ideal polymer). Indeed we find that the functional reduces to the corresponding DFTs (Refs. [12,14], and [19], respectively) for these systems.

Let us define the WR model as an m -component mixture of spherical particles with radii R_i , and particle numbers N_i in a volume V . The interaction pair potentials $\phi_{ij}(r)$ between particles of species $i=1, \dots, N_i$ and $j=1, \dots, N_j$ are $\phi_{ii}(r)=0$; and $\phi_{ij}(r)=\infty$, if $r<R_i+R_j$, $i\neq j$, and zero else [21]. As reduced densities we use the packing fractions of each species i , given as $\eta_i=4\pi N_i R_i^3/(3V)$, and define the total packing fraction as $\eta=\sum_{i=1}^m \eta_i$.

Let us give an overview of our DFT. It is a weighted density approximation. This means that in order to smooth the possibly highly inhomogeneous density fields, convolutions with weight functions are performed. Here, the weight functions describe the shape and geometrical properties of

MATTHIAS SCHMIDT

PHYSICAL REVIEW E **63** 010101(R)

the particles and are explicitly given. In particular, there is a set of weight functions (and correspondingly weighted densities) for each of the species. The transcription of the weighted densities to the excess (over ideal gas) free energy is done, as usual, via a free energy *density*. Here this is an ordinary function (not a functional) of the weighted densities and is, again, explicitly known (up to a simple numerical root finding problem). Finally the total excess free energy of the inhomogeneous system is obtained as a spatial integral over the free energy density.

In detail, we express the excess Helmholtz free energy as

$$F_{\text{exc}}[\rho_i(\mathbf{r})] = k_B T \int d^3x \Phi(\{n_\alpha^{(i)}(\mathbf{x})\}), \quad (1)$$

where T is the absolute temperature, and k_B is Boltzmann's constant. The reduced free energy density Φ is a yet to be determined function of a set of weighted densities $\{n_\alpha^{(i)}(\mathbf{x})\}$, where i labels the species and α the type of weighted density. The weighted densities are obtained by convolutions

$$n_\alpha^{(i)}(\mathbf{x}) = \int d^3r \rho_i(\mathbf{r}) w_\alpha^{(i)}(\mathbf{x} - \mathbf{r}). \quad (2)$$

As all nonvanishing interactions are hard-core, it is sufficient to take the usual FMT weight functions [12,14]

$$w_3^{(i)}(\mathbf{r}) = \theta(R_i - r), \quad w_2^{(i)}(\mathbf{r}) = \delta(R_i - r), \quad (3)$$

$$\mathbf{w}_{v2}^{(i)}(\mathbf{r}) = w_2^{(i)}(\mathbf{r}) \mathbf{r}/r, \quad \hat{\mathbf{w}}_{m2}^{(i)}(\mathbf{r}) = w_2^{(i)}(\mathbf{r}) \left[\frac{\mathbf{r}\mathbf{r}}{r^2} - \hat{\mathbf{1}}/3 \right], \quad (4)$$

where $r = |\mathbf{r}|$, $\theta(r)$ is the Heaviside step function, $\delta(r)$ is the Dirac distribution, and $\hat{\mathbf{1}}$ is the identity matrix. Further, linearly dependent, weights are $w_1^{(i)}(\mathbf{r}) = w_2^{(i)}(\mathbf{r})/(4\pi R_i)$, $\mathbf{w}_{v1}^{(i)}(\mathbf{r}) = \mathbf{w}_{v2}^{(i)}(\mathbf{r})/(4\pi R_i)$, $w_0^{(i)}(\mathbf{r}) = w_1^{(i)}(\mathbf{r})/R_i$. The weight functions $w_\alpha^{(i)}$ are quantities with dimension of length $^{3-\alpha}$. They differ in their tensorial rank: $w_0^{(i)}, w_1^{(i)}, w_2^{(i)}, w_3^{(i)}$ are scalars; $\mathbf{w}_{v1}^{(i)}, \mathbf{w}_{v2}^{(i)}$ are vectors; $\hat{\mathbf{w}}_{m2}^{(i)}$ is a (traceless) matrix. The subscript letters help identifying the rank.

We determine the functional dependence of Φ on the weighted densities by imposing the exact crossover to zero dimensions (0D). This situation is modeled by $\rho_i(\mathbf{r}) = \eta_i \delta(\mathbf{r})$, where the packing fractions η_i describe the average occupation numbers of particles i in a cavity of radius R_i [13]. The exact grand partition sum for the WR model in this situation is

$$\Xi = 1 - m + \sum_{i=1}^m \exp(z_i), \quad (5)$$

where z_i is the fugacity of species i . Inverting the thermodynamical relation $\eta_i = z_i \partial \ln \Xi / \partial z_i$, we obtain the excess chemical potentials $\mu_{0d,i} = k_B T \ln(z_i/\eta_i)$ as a function of the set of η_i . Integrating with respect to density yields the 0D excess free energy $F_{0D}(\{\eta_i\})$. We follow recent treatments of FMT [14] by considering multicavity limits to obtain $\Phi = \Phi_1 + \Phi_2 + \Phi_3$, with the contributions

$$\Phi_1 = \sum_{i=1}^m n_0^{(i)} \varphi_i(\{n_3^{(i)}\}), \quad (6)$$

$$\Phi_2 = \sum_{i,j=1}^m (n_1^{(i)} n_2^{(j)} - \mathbf{n}_{v1}^{(i)} \cdot \mathbf{n}_{v2}^{(j)}) \varphi_{ij}(\{n_3^{(i)}\}), \quad (7)$$

$$\begin{aligned} \Phi_3 = & \frac{1}{8\pi} \sum_{i,j,k=1}^m (n_2^{(i)} n_2^{(j)} n_2^{(k)} / 3 - n_2^{(i)} \mathbf{n}_{v2}^{(j)} \cdot \mathbf{n}_{v2}^{(k)} \\ & + 3[\mathbf{n}_{v2}^{(i)} \hat{\mathbf{m}}_{m2}^{(j)} \mathbf{n}_{v2}^{(k)} - \text{tr}(\hat{\mathbf{n}}_{m2}^{(i)} \hat{\mathbf{n}}_{m2}^{(j)} \hat{\mathbf{n}}_{m2}^{(k)}) / 2] \varphi_{ijk}(\{n_3^{(i)}\}), \end{aligned} \quad (8)$$

where tr denotes the trace. Derivatives of the 0D free energy are $\varphi_{i,\dots,k}(\{\eta_l\}) \equiv \partial^m \beta F_{0d}(\{\eta_l\}) / \partial \eta_i \dots \partial \eta_k$, where $\beta = 1/k_B T$. This completes the prescription for the functional. Note that the weight functions $w_\alpha^{(i)}$ are constructed to recover the Mayer bond for low densities as well as to gain control over the 0D limit. The thermodynamical input into the DFT solely stems from the 0D statistics, Eq. (5).

Let us investigate some of the properties of the functional. First, the thermodynamics and structural correlations of homogeneous phases, $\rho_i = \text{const}$, are an output of the theory. In this case the weighted densities, Eq. (2), are obtained as $n_3^{(i)} = \eta_i$, $n_2^{(i)} = 3 \eta_i / R_i$, $n_1^{(i)} = 3 \eta_i / (4\pi R_i^2)$, $n_0^{(i)} = 3 \eta_i / (4\pi R_i^3)$. The nonscalar contributions vanish, $\mathbf{n}_{v1}^{(i)} = \mathbf{n}_{v2}^{(i)} = \hat{\mathbf{n}}_{m2}^{(i)} = 0$. Inserting this into Eqs. (6)–(8) gives the bulk free energy. Furthermore, the (bulk) direct correlation functions can be obtained as $c_{ij}(r) = \sum_{\alpha,\gamma} \partial^2 \Phi / (\partial n_\alpha^{(i)} \partial n_\gamma^{(j)}) w_\alpha^{(i)*} w_\gamma^{(j)}$, where $*$ denotes the convolution.

Second, the excess free energy density Φ can be calculated analytically in the case of equal (inhomogeneous) density profiles, $\rho_i(\mathbf{r}) = \rho_j(\mathbf{r})$. This is valid for equal sizes, $R_i = R_j$, equal chemical potentials, $\mu_i = \mu_j$, and equal external potentials acting on species i and j . Furthermore the system is assumed to be in a mixed phase. Then an effective one-component functional of the total density $\rho(\mathbf{r}) = m \rho_i(\mathbf{r})$ is obtained. The weighted densities are $n_\alpha^{(\text{total})} = m n_\alpha^{(i)}$, and the expressions for the free energy density are $\partial \beta F_{0D} / \partial \eta = \ln[m - (m w / \eta)]$, $\partial^2 \beta F_{0D} / \partial \eta^2 = w / (\eta - w \eta)$, $\partial^3 \beta F_{0D} / \partial \eta^3 = w [(w - 2) w + \eta] / [(w - 1)^3 \eta^2]$, with $w = W[\eta e^{-\eta} (1 - m^{-1})]$, where $W(z)$ is product log function, i.e., the solution of $z = W \exp(W)$. In general, however, the above assumptions do not hold, and $\rho_i(\mathbf{r}) \neq \rho_j(\mathbf{r})$. Then the $\mu_{0D,i}$ (and F_{0D}) need to be found numerically.

Third, for large number of components, $m \rightarrow \infty$, and fixed total density η , we consider two cases where the WR model reduces to (simpler) effective one- or two-component systems, if the partial densities (or chemical potentials) are chosen appropriately. For equal partial densities $\eta_i = \eta_j$, we expect hard sphere behavior, because each component is at vanishing concentration, so that the ideality between like species is negligible, and only the hard cores between unlike species remain. The 0D statistics [Eq. (5)] takes care of this fact and we recover $\beta F_{0d} = (1 - \eta) \ln(1 - \eta) + \eta$, which is characteristic of a cavity that can hold at most a single particle [13] (of any species i). Hence, the hard sphere FMT

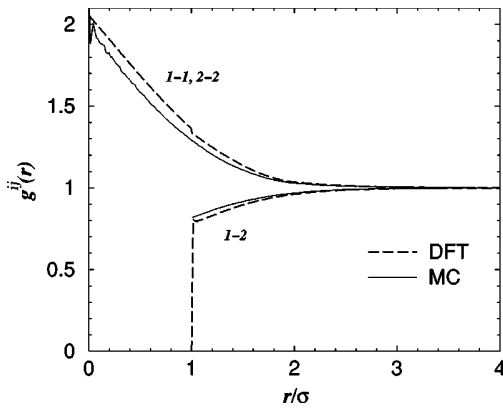


FIG. 1. Pair distribution functions $g_{ij}(r)$ for the $m=2$ component WR model as obtained by density-functional theory (DFT) compared to Monte Carlo simulation (MC) for $\eta_1 = \eta_2 = 0.1$. The symmetric, $i=j$, and asymmetric cases, $i \neq j$, are shown.

[12,14] is obtained. Next we consider the case that one of the components has a large density $\eta_1 \gg \eta_j, j > 1$, and the others are at vanishing density $\eta_j \rightarrow 0$, so that $\eta^* = \sum_{i=2}^m \eta_i = \text{const}$. Then we expect ideal particles ($i=1$) with density η_1 mixed with effective one component hard spheres (all $i > 1$) at density η^* . This is precisely the behavior of the AO colloid ideal-polymer mixture [20]. Indeed, the WR 0D free energy reduces to $\beta F_{0D} = (1 - \eta^* - \eta_1) \ln(1 - \eta^*) + \eta^*$, which describes AO behavior, and the recently found DFT [19] for this model is recovered. The correct reduction of the WR functional in both limits demonstrates the internal consistency of constructing DFTs from the 0D limit of the underlying model [22].

Let us turn to the results. As a first test for the ability of the DFT to describe the WR model, we investigate the structural correlations in the bulk fluid with $m=2$ components. To that end, we calculate the pair correlation functions $g_{ij}(r)$ from the direct correlation functions $c_{ij}(r)$ using the Ornstein-Zernike relation. In order to compare these results, we have carried out a canonical Monte Carlo simulation with 512 particles and 10^5 moves per particle. In Fig. 1 we compare both results. One observes that the clustering of like species, as well as the depletion zone of unlike species near contact are reproduced nicely by the DFT. The DFT, however, generally overestimates the correlations and a tiny artificial jump in $g_{ii}(r=\sigma)$ appears, as well as negative values of about -0.2 in the core region, $r < \sigma$. The overall agreement is fair, given that following the OZ route is a severe test for the functional. In accordance with integral equations [5] the pair correlation functions do not exhibit oscillations, not at short nor at long range. The latter behavior may be examined by an analysis of the poles of the structure factor in the complex plane [23]. Here this is technically simple, as the dependence on wave vector is analytically given. It turns out that the leading contribution always comes from the pole with vanishing real part, hence purely monotonic asymptotic decay results.

The phase diagram for $m=2$ is depicted in Fig. 2 as a function of the total density η and the relative concentration $\xi = \eta_1/\eta$. For small η a mixed fluid is stable. Above the

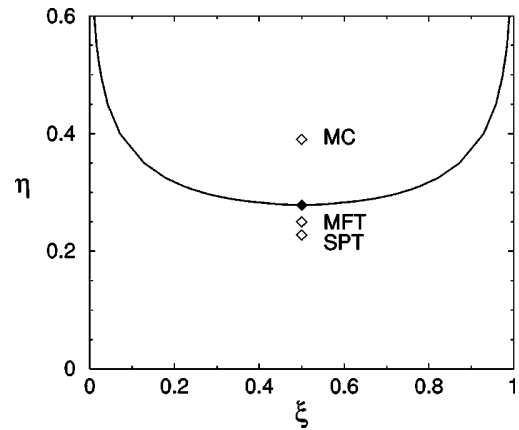


FIG. 2. Phase diagram of the $m=2$ component WR model as a function of relative concentration ξ and total density η as obtained by DFT. The critical points from various approaches are indicated by symbols: Monte Carlo (MC), mean-field theory (MFT), and scaled-particle theory (SPT).

critical point at $\eta_{\text{crit}} = 0.278$ (and $\xi = 1/2$ due to symmetry [3]) demixing happens. Upon increasing the density the coexistence interval rapidly broadens. The critical density is slightly higher than the results from mean-field ($\eta_{\text{crit}} = 0.25$) and scaled-particle ($\eta_{\text{crit}} = 0.228$) theories. However, the simulation values of Ref. [5] is $\eta_{\text{crit}} = 0.3990$, and of Ref. [7] $\eta_{\text{crit}} = 0.3919$ (obtained from a linear fit to the data from finite systems) are still significantly higher, and to the best of our knowledge, no theory can account for this value. As concerns integral equations [5], Percus-Yevick (PY) theory gives $\eta_{\text{crit}} = 0.30$ (see Fig. 4 in Ref. [5]) from the virial route. This is slightly better than the current approach. The compressibility route, however, gives a value of about 0.55. It was found that self-consistent closures, like Rogers-Young, do not improve much over this result [5]. We note that as the present approach performs the approximation on the level of the free energy functional, thermodynamics and structure are consistent, i.e., the structure factors $S_{ij}(k)$ diverge for $k \rightarrow 0$ at the critical point obtained from the free energy.

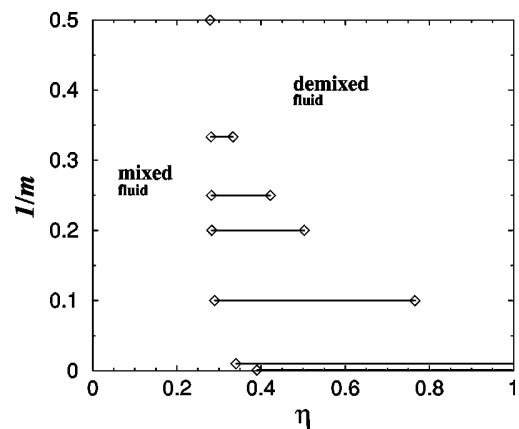


FIG. 3. Phase diagram of the WR model at equal concentrations $\eta_i = \eta_j$ as a function of total density η and inverse number of components $1/m$.

MATTHIAS SCHMIDT

PHYSICAL REVIEW E **63** 010101(R)

For larger number of components [9], $m > 2$, a rich variety of phase transitions is expected, e.g., for $m = 3$ tricritical points were found from a mean-field treatment [2]. Here we restrict ourself to the equimolar case, and calculate the phase transition between the mixed phase and m demixed phases; see Fig. 3. In accordance with previous findings the transitions are first order. The coexistence interval in density rapidly broadens upon increasing η . Numerically, the mean-field result [2] for $m = 3$ is $\eta = 0.3146 - 0.4789$, whereas the current theory gives lower values of $\eta = 0.2815 - 0.3333$, and the simulation value of a density within the coexistence region [7] is 0.4162.

In view of the successful treatment of the bulk properties, especially the internal consistency, we are confident for future applications to inhomogeneous situations. A preliminary investigation has shown that the DFT accounts for a crystalline phase for large m , with multiply occupied lattice sites.

Future investigations may treat the interface between demixed phases, and compare to the MFT results for $m = 2$ [4] and $m = 3$ [10], as well as adsorption at walls or in pores. Furthermore, whether the current approach can be extended to treat the morphological model [24] constitutes an interesting aspect.

On more general grounds, we conclude that fundamental measures can be used successfully to construct DFTs. The first such theory was Rosenfeld's hard sphere functional [12,14], which is by now well established and has been used for over one decade. Only recently, other models could be treated in a similar manner, namely, penetrable spheres [17] and the Asakura-Oosawa model [19]. The present study adds another member to the family. How large this family can actually become, still is an open question.

I thank Bob Evans, Joe M. Brader, and Roland Roth for many useful discussions and comments.

-
- [1] B. Widom and J. S. Rowlinson, *J. Chem. Phys.* **52**, 1670 (1970).
- [2] M. I. Guerrero, J. S. Rowlinson, and G. Morrison, *J. Chem. Soc., Faraday Trans. 2* **72**, 1970 (1976).
- [3] J. S. Rowlinson, *Adv. Chem. Phys.* **41**, 1 (1980).
- [4] J. S. Rowlinson and B. Widom, *Molecular theory of capillarity* (Clarendon Press, Oxford 1982).
- [5] C. Y. Shew and A. Yethiraj, *J. Chem. Phys.* **104**, 7665 (1996).
- [6] E. Bergmann, *Mol. Mater.* **32**, 237 (1976).
- [7] G. Johnson, H. Gould, J. Machta, and L. K. Chayes, *Phys. Rev. Lett.* **79**, 2612 (1997).
- [8] P. Borgelt, C. Hoheisel, and G. Stell, *J. Chem. Phys.* **92**, 6161 (1990).
- [9] R. P. Sear, *J. Chem. Phys.* **104**, 9948 (1996).
- [10] S. J. Bibb, J. S. Rowlinson, and C. Xiao, *Mol. Mater.* **84**, 1099 (1995).
- [11] R. Evans, in *Fundamentals of Inhomogeneous Fluids*, edited by D. Henderson (Wiley, New York, 1992), p. 85.
- [12] Y. Rosenfeld, *Phys. Rev. Lett.* **63**, 980 (1989).
- [13] Y. Rosenfeld, M. Schmidt, H. Löwen, and P. Tarazona, *J. Phys.: Condens. Matter* **8**, L577 (1996); *Phys. Rev. E* **55**, 4245 (1997).
- [14] P. Tarazona, *Phys. Rev. Lett.* **84**, 694 (2000).
- [15] J. A. Cuesta, *Phys. Rev. Lett.* **76**, 3742 (1996).
- [16] J. A. Cuesta and Y. Martinez-Raton, *Phys. Rev. Lett.* **78**, 3681 (1997); *J. Chem. Phys.* **107**, 6379 (1997).
- [17] M. Schmidt, *J. Phys.: Condens. Matter* **11**, 10 163 (1999).
- [18] Y. Rosenfeld, M. Schmidt, M. Watzlawek, and H. Löwen, *Phys. Rev. E* **62**, 5006 (2000).
- [19] M. Schmidt, H. Löwen, J. M. Brader, and R. Evans, *Phys. Rev. Lett.* **85**, 1934 (2000).
- [20] S. Asakura and F. Oosawa, *J. Chem. Phys.* **22**, 1255 (1954).
- [21] We restrict ourselves to an "additive" case. More generally, the hard core lengths between all pairs i and j are prescribed independently.
- [22] The present functional cannot be obtained from the hard spheres FMT by the same linearization in density as in the case of the AO model [19].
- [23] R. Evans, J. R. Henderson, D. C. Hoyle, A. O. Parry, and Z. A. Sabeur, *Mol. Mater.* **80**, 755 (1993).
- [24] K. R. Mecke, *Int. J. Mod. Phys. B* **12**, 861 (1998).

LETTER TO THE EDITOR

Rosenfeld functional for non-additive hard spheres**Matthias Schmidt**¹Soft Condensed Matter Group, Debye Institute, Utrecht University, Princetonplein 5,
3584 CC Utrecht, The Netherlands

Received 18 June 2004

Published 16 July 2004

Online at stacks.iop.org/JPhysCM/16/L351

doi:10.1088/0953-8984/16/30/L01

Abstract

The fundamental measure density functional theory for hard spheres is generalized to binary mixtures of arbitrary positive and moderate negative non-additivity between unlike components. In bulk the theory predicts fluid–fluid phase separation into phases with different chemical compositions. The location of the accompanying critical point agrees well with previous results from simulations over a broad range of non-additivities and both for symmetric and highly asymmetric size ratios. Results for partial pair correlation functions show good agreement with simulation data.

Density-functional theory (DFT) is a powerful approach to study equilibrium properties of inhomogeneous systems, including dense liquids and solids of single- and multi-component substances [1]. Its practical applicability depends on the quality of the approximation to the central object, the (Helmholtz) excess free energy functional arising from the interparticle interactions. The specific model of additive hard sphere mixtures constitutes the reference system *par excellence* to describe mixtures governed by steric repulsion, and Rosenfeld's fundamental-measure theory (FMT) [2–5] is arguably the best available approximation to tackle inhomogeneous situations. A rapidly increasing number of applications to interesting physical problems can be witnessed [6].

The more general non-additive hard sphere mixture is defined through pair potentials between particles of species i and j , given as $V_{ij}(r) = \infty$ for $r < \sigma_{ij}$ and 0 otherwise, where r is the centre–centre distance between the two particles, and σ_{ij} is the distance of minimal approach between particles of species i and j . In a binary mixture non-additivity is measured conventionally through the parameter $\Delta = 2\sigma_{12}/(\sigma_{11} + \sigma_{22}) - 1$. The physics of non-additive hard sphere mixtures is considerably richer than that of the additive case. In particular the case of $\Delta > 0$ is striking, as small values of Δ are known to be already sufficient to induce stable fluid–fluid demixing into phases with different chemical compositions (for recent studies see e.g. [7–10]).

¹ On leave from: Institut für Theoretische Physik II, Heinrich-Heine-Universität Düsseldorf, Universitätsstraße 1, D-40225 Düsseldorf, Germany.

The treatment of general non-additivity is elusive in the FMT framework. The author is aware of successful studies only in four special cases. First, for the Asakura–Oosawa–Vrij (AOV) model [11, 12], where species 1 represents colloidal hard spheres and species 2 (with $\sigma_{22} = 0$) represents non-interacting polymer coils with radius of gyration equal to $\sigma_{12} - (\sigma_{11}/2)$, an excess free energy functional was given [13]. Second, a free energy functional for the Widom–Rowlinson (WR) model, where $\sigma_{11} = \sigma_{22} = 0$, was obtained [14]. Third, the depletion potential between two big spheres immersed in a sea of smaller spheres was obtained through ‘Roth’s trick’ of working on the level of the one-body direct correlation functional [15–17]. In this case the functional for the additive case is sufficient to obtain results, but the approach is limited to small concentration of big spheres. Fourth, in the FMT of Lafuente and Cuesta for lattice hard core models, due to an odd–even effect of the particle sizes (measured in units of lattice constants), non-additivity of the size of one lattice spacing arises [18]. This effect, however, is specific to lattice models and vanishes in the continuum limit.

The aim of the present letter is to generalize FMT for hard spheres to the case of general positive and moderate negative non-additivity and arbitrary size asymmetry. The proposed extended framework accommodates, in the respective limits, the Rosenfeld functional for additive hard sphere mixtures [2], the DFT for the extreme non-additive AOV model [13], and the exact virial expansion up to second order in densities. The structure of the theory, however, goes qualitatively beyond that of either limit.

The excess (over ideal) Helmholtz free energy functional is expressed as

$$\mathcal{F}_{\text{exc}}[\rho_1, \rho_2] = k_B T \int d\mathbf{x} d\mathbf{x}' \sum_{\alpha, \beta=0}^3 K_{\alpha\beta}^{(12)}(|\mathbf{x} - \mathbf{x}'|) \Phi_{\alpha\beta}(\{n_v^{(1)}(\mathbf{x})\}, \{n_\tau^{(2)}(\mathbf{x}')\}), \quad (1)$$

where $\rho_i(\mathbf{r})$ is the one-body density distributions of species $i = 1, 2$ dependent on position \mathbf{r} , $k_B T$ is the thermal energy, $\Phi_{\alpha\beta}$ for $\alpha, \beta = 0, 1, 2, 3$ is the free energy density depending on the sets of weighted densities $\{n_v^{(i)}\}$ for $i = 1, 2$, and the kernels $K_{\alpha\beta}^{(12)}(r)$ are a means to control the range of non-locality between unlike components and depend solely on distance r . The weighted densities are built in the usual way [2] through convolution of the respective bare density profile with appropriate weight functions:

$$n_v^{(i)}(\mathbf{x}) = \int d\mathbf{r} \rho_i(\mathbf{r}) w_v(|\mathbf{x} - \mathbf{r}|, R_i), \quad i = 1, 2, \quad (2)$$

where $v = 0, 1, 2, 3$ labels the type of weight function, and $R_i = \sigma_{ii}/2$ is the particle radius of species $i = 1, 2$. The (fully scalar) Kierlik–Rosinberg form [19, 20] of the $w_v(r, R)$ is used in the following, as this renders the determination of the $K_{\alpha\beta}^{(12)}(r)$ more straightforward. The $w_v(r, R)$ are

$$\begin{aligned} w_0 &= -\delta''(R - r)/(8\pi) + \delta'(R - r)/(2\pi r), \\ w_1 &= \delta'(R - r)/(8\pi), \\ w_2 &= \delta(R - r), \\ w_3 &= \Theta(R - r), \end{aligned} \quad (3)$$

where $R = R_i$, the prime denotes the derivative w.r.t. the argument, $\delta(\cdot)$ is the Dirac distribution, and $\Theta(\cdot)$ is the step function. Alternatively, in Fourier space the weight functions are $\tilde{w}_\alpha(k, R) = 4\pi \int_0^\infty dr w_\alpha(r, R) \sin(kr)r/k$ and are given as

$$\begin{aligned} \tilde{w}_0 &= c + (kRs/2), \\ \tilde{w}_1 &= (kRc + s)/(2k), \\ \tilde{w}_2 &= 4\pi Rs/k, \\ \tilde{w}_3 &= 4\pi(s - kRc)/k^3, \end{aligned} \quad (4)$$

with the abbreviations $s = \sin(kR)$ and $c = \cos(kR)$. The kernels $K_{\alpha\beta}^{(12)}(r)$ in (1) can be viewed as $\alpha\beta$ -components of a second-rank tensor

$$\hat{\mathbf{K}}^{(12)}(r) = \begin{pmatrix} w_3 & w_2 & w_1 & w_0 \\ w_2 & w_1^\dagger & w_0^\dagger & w_{-1} \\ w_1 & w_0^\dagger & w_{-1}^\dagger & w_{-2} \\ w_0 & w_{-1} & w_{-2} & w_{-3} \end{pmatrix}, \tag{5}$$

where indexing is such that the top row contains $K_{00}^{(12)}, \dots, K_{03}^{(12)}$, etc, and \dagger distinguishes different elements. All $K_{\alpha\beta}^{(12)}(r)$ possess a range of $R_{12} = \sigma_{12} - (\sigma_{11} + \sigma_{22})/2$, i.e. vanish for values of r beyond that distance (see figure 1 for an illustration of the length scales). The dimension of $K_{\alpha\beta}^{(12)}$ is $(\text{length})^{-\alpha-\beta}$, and hence the dimension of w_γ is $(\text{length})^{\gamma-3}$. The elements of $\hat{\mathbf{K}}^{(12)}$ are defined, with $R = R_{12} > 0$, through (3), and furthermore

$$\begin{aligned} w_1^\dagger &= \delta'(R-r), \\ w_0^\dagger &= \delta''(R-r)/(8\pi), \\ w_{-1}^\dagger &= \delta^{(3)}(R-r)/(64\pi^2), \\ w_{-1} &= \delta''(R-r)/(2\pi r) - \delta^{(3)}(R-r)/(8\pi), \\ w_{-2} &= \delta^{(3)}(R-r)/(16\pi^2 r) - \delta^{(4)}(R-r)/(64\pi^2), \\ w_{-3} &= -\delta^{(4)}(R-r)/(8\pi^2 r) + \delta^{(5)}(R-r)/(64\pi^2), \end{aligned} \tag{6}$$

with the derivatives $\delta^{(\gamma)}(x) = d^\gamma \delta(x)/dx^\gamma$ for $\gamma = 3, 4, 5$. Again, we also give the Fourier space representation (being together with (4) also valid for $R = R_{12} < 0$), which reads

$$\begin{aligned} \tilde{w}_1^\dagger &= 4\pi(kRc + s)/k, \\ \tilde{w}_0^\dagger &= c - (kRs/2), \\ \tilde{w}_{-1}^\dagger &= -(k^2Rc + 3ks)/(16\pi), \\ \tilde{w}_{-1} &= (k^2Rc - ks)/2, \\ \tilde{w}_{-2} &= -k^3Rs/(16\pi), \\ \tilde{w}_{-3} &= (k^4Rc - 3k^3s)/(16\pi). \end{aligned} \tag{7}$$

In order to express the dependence of the free energy density, $\Phi_{\alpha\beta}$ in equation (1), on the weighted densities (2) we introduce ansatz functions $A_{\alpha\gamma}^{(i)}$ for species $i = 1, 2$ that possess the dimension of $(\text{length})^{\alpha-3}$ and the order γ in density (i.e. contain γ factors $n_\tau^{(i)}$). Explicit expressions for the non-vanishing terms are

$$A_{01}^{(i)} = n_0^{(i)}, \quad A_{02}^{(i)} = n_1^{(i)} n_2^{(i)}, \quad A_{03}^{(i)} = (n_2^{(i)})^3/(24\pi), \tag{8}$$

$$A_{11}^{(i)} = n_1^{(i)}, \quad A_{12}^{(i)} = (n_2^{(i)})^2/(8\pi), \quad A_{21}^{(i)} = n_2^{(i)}, \quad A_{30}^{(i)} = 1. \tag{9}$$

The excess free energy density is then constructed as

$$\Phi_{\alpha\beta} = \sum_{\gamma=0}^6 \sum_{\gamma'=0}^3 A_{\alpha\gamma'}^{(1)} A_{\beta(\gamma-\gamma')}^{(2)} \varphi_{0d}^{(\gamma)}(n_3^{(1)} + n_3^{(2)}), \tag{10}$$

where $\varphi_{0d}^{(\gamma)}(\eta) \equiv d^\gamma \varphi_{0d}(\eta)/d\eta^\gamma$ is the γ th derivative of the zero-dimensional excess free energy as a function of the average occupation number η [3], $\varphi_{0d}(\eta) = (1-\eta) \ln(1-\eta) + \eta$, and $\varphi_{0d}^{(0)}(\eta) \equiv \varphi_{0d}(\eta)$ for $\gamma = 0$. The specific form (10) ensures both that the terms in the sum in (1) possesses the correct dimension of $(\text{length})^{-6}$ and that the prefactor of $\varphi_{0d}^{(\gamma)}$ in (10) is of the total order γ in densities, as is common in FMT. This completes the prescription for

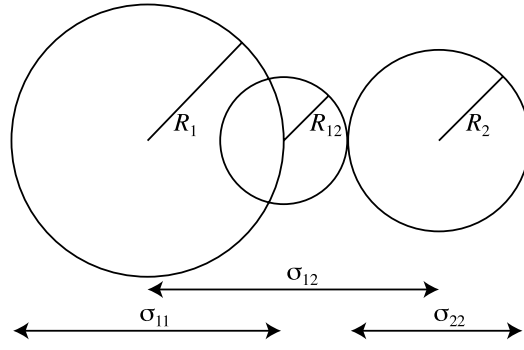


Figure 1. Illustration of the relevant length scales. The hard core interaction distances σ_{ij} between pairs of particles of species $ij = 11, 12,$ and 22 are related to radii through $\sigma_{11} = 2R_1$, $\sigma_{12} = R_1 + R_{12} + R_2$, and $\sigma_{22} = 2R_2$, respectively. The spheres of radii R_1 and R_2 represent the weight functions $w_\alpha^{(1)}$ and $w_\beta^{(2)}$, respectively, and can be viewed as ‘true’ particle shapes. The sphere of radius R_{12} represents the kernel $K_{\alpha\beta}^{(12)}$ being a mere construct to generate the correct hard core distance σ_{12} between species 1 and 2.

the functional; a full account of all details, also for multi-component mixtures and for lower spatial dimensionality, will be given elsewhere.

Here we discuss some of the properties of the theory. For small densities it is straightforward to show that the correct virial expansion up to second order in densities is obtained, $F_{\text{exc}} \rightarrow -\sum_{ij} \int d^3r d^3r' f_{ij}(|\mathbf{r} - \mathbf{r}'|) \rho_i(\mathbf{r}) \rho_j(\mathbf{r}')/2$, where the Mayer functions, $f_{ij}(r) = \exp(-V_{ij}(r)/(k_B T)) - 1$, are recovered through

$$f_{12} = -\sum_{\alpha\beta=0}^3 w_\alpha^{(1)} * K_{\alpha\beta}^{(12)} * w_\beta^{(2)}, \quad f_{ii} = -\sum_{\alpha=0}^3 w_\alpha^{(i)} * w_{3-\alpha}^{(i)}, \quad i = 1, 2, \quad (11)$$

where $*$ denotes the convolution, $g(\mathbf{r}) * h(\mathbf{r}) = \int d^3r' g(\mathbf{r}') h(\mathbf{r} - \mathbf{r}')$. In the limit of an additive mixture, $\Delta \rightarrow 0$ and hence $R_{12} \rightarrow 0$, one finds that $K_{\alpha\beta}(x) \rightarrow 0$ if $\beta \neq 3 - \alpha$ and $K_{\alpha(\alpha-3)}(x) \rightarrow \delta(x)$ otherwise. This leads to a cancellation of one spatial integration in (1) and yields the Rosenfeld functional for a binary additive hard sphere mixture [2] with radii R_1 and R_2 . In the AOV limit, $R_2 \rightarrow 0$, one finds that $n_\alpha^{(2)} \rightarrow 0$ if $\alpha \neq 0$, and $n_0^{(2)} \rightarrow \rho_2$ otherwise. The integration over \mathbf{x}' in (1) together with the kernel $K_{\alpha\beta}(|\mathbf{x} - \mathbf{x}'|)$ and the fact that the density $n_0^{(2)}(\mathbf{x}') = \rho_2(\mathbf{x}')$ appears linearly in $\Phi_{\alpha\beta}$, see $A_{01}^{(2)}$ in (8), plays the same role that building weighted densities for the polymer species in the AOV case does. The resulting functional is equal to that for the AOV model [13]. However, in the WR limit, in contrast to [14], terms higher than on the second virial level vanish. For $\Delta = -1$ the two species decouple, and $\mathcal{F}_{\text{exc}}[\rho_1, \rho_2] = \mathcal{F}_{\text{exc}}[\rho_1] + \mathcal{F}_{\text{exc}}[\rho_2]$ which is *not* obeyed by the present approximation, limiting its applicability to small values of Δ if $\Delta < 0$.

We next turn to an investigation of bulk properties of the theory. To assess structure, direct correlation functions can be obtained via

$$c_{ij}^{(2)}(|\mathbf{r} - \mathbf{r}'|) = -\left. \frac{\delta^2 \beta \mathcal{F}_{\text{exc}}}{\delta \rho_i(\mathbf{r}) \delta \rho_j(\mathbf{r}')} \right|_{\rho_1, \rho_2 = \text{const}}, \quad (12)$$

which can be shown to feature Percus–Yevick- (PY-) like behaviour: $c_{ij}^{(2)}(r > \sigma_{ij}) = 0$. Inverting the Ornstein–Zernike (OZ) relations permits us to calculate partial structure factors, $S_{ij}(k)$, and partial pair correlation functions, $g_{ij}(r)$. We have carried out Monte Carlo (MC) computer simulations in the canonical ensemble with 1024 particles and 10^5 MC moves per

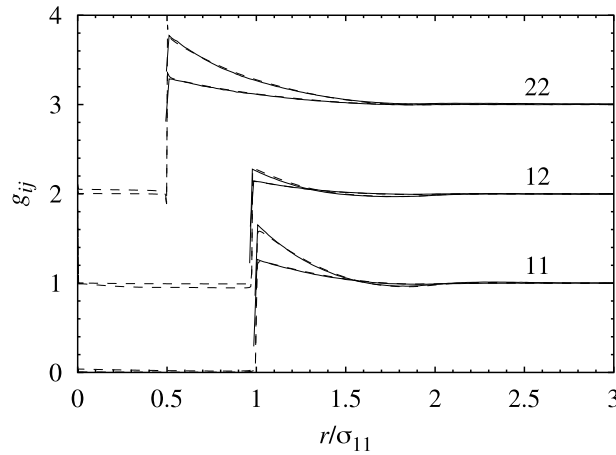


Figure 2. Partial pair correlation functions, $g_{ij}(r)$, between species $ij = 11, 12$ and 22 (as indicated), as a function of the scaled distance r/σ_{11} , as obtained from the present DFT using the OZ route (dashed curves) and from MC simulation (solid curves). Results for g_{12} (g_{22}) are shifted upwards by one (two) units for clarity. Parameters are $\sigma_{22}/\sigma_{11} = 0.5$, $\Delta = 0.3$, $\eta_2 = \eta_1/8$ and $\eta_1 = 0.05$ (lower), 0.1 (upper). For comparison, the theoretical critical point is located at $\eta_1 = 0.118$, $\eta_2 = 0.0321$.

particle; histograms of all distances between particles yield benchmark results for $g_{ij}(r)$. We have chosen an intermediate size ratio of $\sigma_{22}/\sigma_{11} = 0.5$ and have considered various values of Δ from -0.3 to 0.5 and a range of statepoints characterized by packing fractions, $\eta_i = \pi\rho_i\sigma_{ii}^3/6$ for $i = 1, 2$. For $\Delta = 0$, the current DFT reproduces the solution of the PY integral equation, as the functional reduces to the Rosenfeld case (which is known to yield the same $c_{ij}^{(2)}(r)$ as the PY approximation). Results for the representative case $\Delta = 0.2$ at two different statepoints are shown in figure 2. The core condition, $g_{ij}(r < \sigma_{ij}) = 0$, is only approximately fulfilled, but the overall agreement between results from theory and simulation is quite remarkable.

In principle, one could envisage that this approach permits us to study the depletion potential, $V_{\text{depl}}^{(1)}(r)$, between particles of species 1 being generated by the immersion into a ‘sea’ of particles 2 through $V_{\text{depl}}^{(1)}(r) = -k_B T \ln g_{11}(r)$ for $\rho_1 \rightarrow 0$, and $\rho_2 = \text{const}$. However, for the (relevant) case of small size ratios (e.g. $\sigma_{22}/\sigma_{11} \sim 0.1$, see [15, 16]) already in both limits of additive hard spheres and the AOV model the results are only of rather moderate accuracy, underestimating the strength of the depletion attraction [13], similar to results from the PY approximation. However, results from the present theory obtained through the OZ route (not shown) cross over smoothly between the additive hard sphere case and the AOV case, similar to the correct behaviour [15, 16]. Hence one can conclude that the pair structure predicted by the current DFT is similar to that of the PY approximation. This is a remarkable property, and one can anticipate test-particle calculations to yield superior results.

Evaluating (1) at constant density fields yields an analytic expression for the bulk excess free energy for fluid states, $F_{\text{exc}} = \mathcal{F}_{\text{exc}}[\rho_1 = \text{const}, \rho_2 = \text{const}]$. The total Helmholtz free energy is then $F = F_{\text{exc}} + k_B T V \sum_{i=1,2} \rho_i [\ln(\rho_i \Lambda_i^3) - 1]$, where Λ_i is the (irrelevant) de Broglie wavelength of species i , and V is the system volume. Via Taylor expanding F_{exc} in both densities one can show that it features the exact second virial coefficients (consistent with the correct incorporation of $f_{ij}(r)$ on the second virial level) and also the exact third virial coefficients (see e.g. [7]) provided $2\sigma_{12} > \max(\sigma_{11}, \sigma_{22})$.

The fluid–fluid demixing spinodal can be obtained from (numerical) solution of $|\partial^2(F/V)/\partial\rho_i\partial\rho_j| = 0$, and the location of the critical point can be determined from

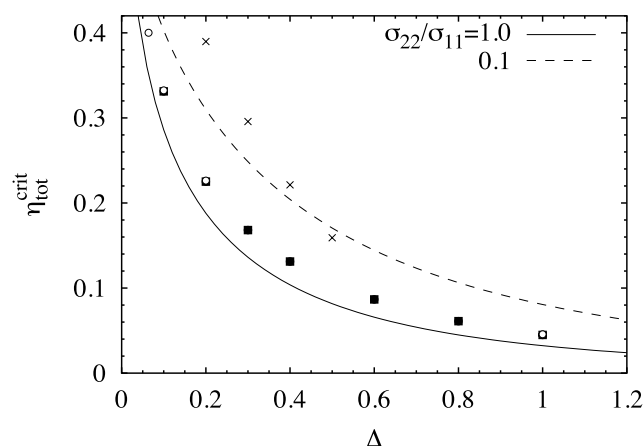


Figure 3. The total packing fraction at the critical point, $\eta_{\text{tot}}^{\text{crit}}$, where $\eta_{\text{tot}} = \eta_1 + \eta_2$, for a non-additive binary hard sphere mixture as a function of the non-additivity parameter Δ . Shown are results from the present DFT (curves) and from simulations (symbols) for the symmetric case, $\sigma_{22}/\sigma_{11} = 1$, by Gózdź [9] (filled squares) and by Jagannathan and Yethiraj [10] (open circles), as well as for the highly asymmetric case of $\sigma_{22}/\sigma_{11} = 0.1$ by Dijkstra [7] (crosses).

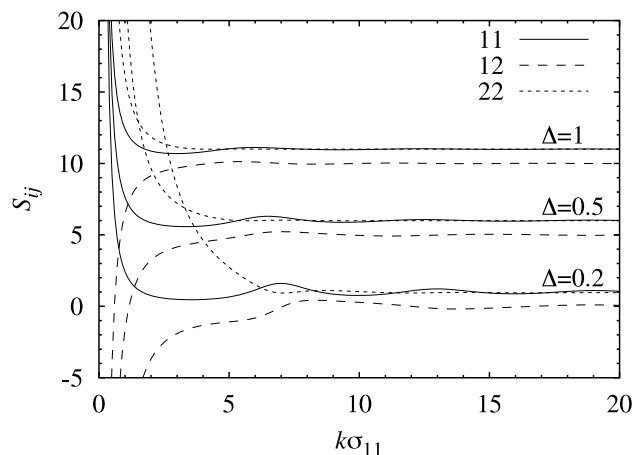


Figure 4. Partial structure factors, $S_{ij}(k)$ for $ij = 11, 12, 22$ (as indicated), as a function of $k\sigma_{11}$ at the fluid–fluid critical point for size ratio $\sigma_{22}/\sigma_{11} = 0.1$ and non-additivity $\Delta = 0.2, 0.5, 1$. The results for $\Delta = 0.5$ (1) are shifted upwards by 5 (10) units for clarity.

minimizing one of the chemical potentials, μ_1 or μ_2 , along the spinodal. Such results are compared in figure 3 to those from simulations for $\sigma_{11} = \sigma_{22}$, performed in the semi-grand ensemble by Jagannathan and Yethiraj [10] and by Gózdź [9], the latter study including a finite size analysis, for a variety of non-additivities ranging from $\Delta = 0.1$ –1. For the highly asymmetric case of $\sigma_{22} = 0.1\sigma_{11}$ results from Gibbs ensemble simulations were obtained by Dijkstra [7]. For both size ratios the strong decrease of the total critical packing fraction with increasing values of Δ , as well as the overall functional dependence, are very well described by the theory. However, the precise value at given Δ is underestimated. This behaviour is not uncommon for mean-field-like theories and is also present in the AOV case. A benefit of working on the level of the density functional is that the structure is consistent with the free

energy. In figure 4 partial structure factors are shown for a range of values of Δ evaluated at the fluid–fluid critical point obtained from the free energy, and indeed $|S_{ij}(k \rightarrow \infty)| \rightarrow \infty$.

In conclusion, having demonstrated the good accuracy of the predictions of the current theory for bulk fluid properties of the non-additive hard sphere mixture, we are confident that it is well suited to study interesting and relevant interfacial situations, such as the structure and tension of interfaces between demixed phases, wetting at substrates [21], and more. Note that any colloidal mixture interacting with soft repulsive forces, as e.g. present in charge-stabilized dispersions, can be mapped (e.g. by the Barker–Henderson procedure) onto an effective non-additive hard sphere system. Hence one can anticipate experimental consequences of the structure and phase separation predicted by the present theory. The treatment of freezing [8] requires additional contributions to the free energy functional [3, 4].

H Löwen, R Evans, R Blaak, K Jagannathan and J A Cuesta are thanked for useful comments. Support by the SFB TR6 of the DFG is acknowledged. This work is part of the research programme of FOM, that is financially supported by the NWO.

References

- [1] Evans R 1992 *Fundamentals of Inhomogeneous Fluids* ed D Henderson (New York: Dekker) chapter 3, p 85
- [2] Rosenfeld Y 1989 *Phys. Rev. Lett.* **63** 980
- [3] Rosenfeld Y, Schmidt M, Löwen H and Tarazona P 1997 *Phys. Rev. E* **55** 4245
- [4] Tarazona P 2000 *Phys. Rev. Lett.* **84** 694
- [5] Cuesta J A, Martínez-Raton Y and Tarazona P 2002 *J. Phys.: Condens. Matter* **14** 11965
- [6] See e.g. the special issue on DFT of liquids, 2002 *J. Phys.: Condens. Matter* **14**
- [7] Dijkstra M 1998 *Phys. Rev. E* **58** 7523
- [8] Louis A A, Finken R and Hansen J P 2000 *Phys. Rev. E* **61** R1028
- [9] Gózdź W T 2003 *J. Chem. Phys.* **119** 3309
- [10] Jagannathan K and Yethiraj A 2003 *J. Chem. Phys.* **118** 7907
- [11] Asakura S and Oosawa F 1954 *J. Chem. Phys.* **22** 1255
- [12] Vrij A 1976 *Pure Appl. Chem.* **48** 471
- [13] Schmidt M, Löwen H, Brader J M and Evans R 2000 *Phys. Rev. Lett.* **85** 1934
- [14] Schmidt M 2001 *Phys. Rev. E* **63** 010101(R)
- [15] Roth R and Evans R 2001 *Europhys. Lett.* **53** 271
- [16] Roth R, Evans R and Louis A A 2001 *Phys. Rev. E* **64** 051202
- [17] Louis A A and Roth R 2001 *J. Phys.: Condens. Matter* **13** L777
- [18] Lafuente L and Cuesta J A 2002 *J. Phys.: Condens. Matter* **14** 12079
- [19] Kierlik E and Rosinberg M L 1990 *Phys. Rev. A* **42** 3382
- [20] Phan S, Kierlik E, Rosinberg M L, Bildstein B and Kahl G 1993 *Phys. Rev. E* **48** 618
- [21] Brader J M, Evans R, Schmidt M and Löwen H 2002 *J. Phys.: Condens. Matter* **14** L1
- Brader J M, Evans R and Schmidt M 2003 *Mol. Phys.* **101** 3349
- Wessels P P F, Schmidt M and Löwen H 2004 *J. Phys.: Condens. Matter* at press

Density Functional for a Model Colloid-Polymer Mixture

Matthias Schmidt and Hartmut Löwen

Institut für Theoretische Physik II, Heinrich-Heine-Universität Düsseldorf, Universitätsstraße 1, D-40225 Düsseldorf, Germany

Joseph M. Brader and Robert Evans

H. H. Wills Physics Laboratory, University of Bristol, Royal Fort, Tyndall Avenue, Bristol BS8 1TL, United Kingdom

(Received 17 April 2000)

We present a density functional theory for mixtures of (hard sphere) colloidal particles and ideal polymers. For this extreme nonadditive system we employ a fundamental measures approach to construct a functional which incorporates the correct dimensional crossover and the exact low density limit. In bulk fluid mixtures the functional yields the same free energy and, therefore, the same gas-liquid (demixing) transition as given by free-volume theory. It generates consistent pair correlation functions; the partial structure factors $S^{ij}(k)$ diverge, as $k \rightarrow 0$, at the critical point obtained from the free energy. Our results for the structure agree well with those from simulation and Percus-Yevick theory.

PACS numbers: 82.70.Dd, 61.20.Gy, 64.10.+h, 64.60.Fr

Much of soft condensed matter science is concerned with simplifying a complex, multicomponent system to its bare bones so that a tractable theoretical model can be devised which will incorporate the essential physical mechanisms determining the properties of the system. Colloidal suspensions provide an excellent example of this strategy. A monodisperse suspension of colloidal particles can often be treated as a one-component fluid since the details of the solvent and colloid-solvent interactions are not of great importance in determining the equilibrium colloid-colloid structure or the phase behavior. In favorable circumstances, these properties are close to those of the hard sphere fluid.

Moving up one degree in complexity, one knows that the addition of nonadsorbing polymer significantly enriches the phase behavior of the colloidal system. For sufficiently large values of the size ratio R^g/R^c , where R^g is the radius of gyration of the polymer and R^c is the radius of the colloid, theory predicts stable colloidal gas, liquid, and solid phases with the fugacity of the polymer reservoir playing a role similar to that of inverse temperature for a simple substance. The theoretical [1–3] and simulation studies [3] are based on an idealized model introduced by Asakura and Oosawa (AO) [4] and independently by Vrij [5], which treats the colloids as hard spheres with radius R^c and the polymer coils as interpenetrating, noninteracting particles as regards their mutual interactions. The polymer particles are excluded from the colloids to a center of mass distance $R^c + R^p$, where the polymer radius $R^p = R^g$. This AO model thus describes an extreme nonadditive binary hard sphere mixture. The assumption of ideal polymer is, of course, a gross oversimplification which can be valid only near the theta point. Nevertheless, the main features of the bulk phase behavior arising from this simple model are found in experimental studies [6,7] which confirm the predicted trends of the phase behavior with increasing size ratio $q = R^p/R^c$.

Given the richness of the bulk phase behavior exhibited by the binary AO model it is somewhat surprising that very little attention has been paid to the equilibrium properties of *inhomogeneous* colloid-polymer mixtures described by this model. One might expect the same entropic depletion mechanism [4,5] that leads to an effective attraction between two colloidal particles and that is responsible for bulk gas-liquid separation [1–3] to yield a wide variety of interfacial and adsorption phenomena. However, we are aware of only one systematic treatment of the inhomogeneous AO mixture, that of Ref. [8], where it was shown that for $q < 2/\sqrt{3} - 1 = 0.1547$ one could derive an explicit effective Hamiltonian for the colloids by integrating out the degrees of freedom of the polymer.

The aim of the present Letter is to introduce a density functional theory (DFT) designed specifically for the binary AO model that will treat arbitrary inhomogeneities and size ratios. We are motivated by DFT studies of simple fluids and their mixtures which have provided much insight into a wide range of interfacial phenomena such as surface phase transitions, wetting, and confined fluids [9]. Our approach has its origins in the fundamental measures theory (FMT) of Rosenfeld [10] which has proved, together with its recent extensions and modifications [11–13], very successful for describing the inhomogeneous hard sphere fluid and additive hard sphere mixtures. FMT has also been applied successfully to hard cubes [14], penetrable spheres [15], and has been generalized to soft interactions [16]. The functional we propose here is exact for zero-dimensional situations of extreme confinement and reduces to the functional for pure hard spheres (no polymer) introduced recently by Tarazona [13] in his treatment of freezing. The bulk fluid equation of state which emerges from the theory is the same as that which results from the free-volume approach of Ref. [2]. Thus, our functional yields the same gas-liquid coexistence curve. Moreover, it provides a means of determining the correlation functions of

bulk mixtures as well as the density profiles and thermodynamic properties of inhomogeneous systems. Here we outline the theory and focus on its application to the structure of the bulk colloid-polymer mixture. Applications to interfaces and adsorption problems will be given elsewhere. We present results for the partial pair correlation functions $g^{ij}(r)$ from the Ornstein-Zernike (OZ) route and show that these agree well with the results of simulation and the Percus-Yevick (PY) integral equation theory. Our theory provides a consistent treatment of the fluid-fluid transition in that it predicts that all three partial structure factors diverge, as $k \rightarrow 0$, at the critical point and on the spinodal given by the bulk mixture equation of state. To the best of our knowledge this is the first nonperturbative DFT (other than that for the somewhat artificial parallel hard cube system [14]) based on purely repulsive interparticle forces which describes directly fluid-fluid separation.

We first define the AO colloid-polymer model. There are N^c colloids with radii R^c and N^p polymers with radii R^p within a volume V . The interaction potential between colloids is hard, i.e., $V^{cc}(r) = \infty$, if $r \leq 2R^c$, and is zero otherwise. The interaction between colloids and polymers is also hard: $V^{cp}(r) = \infty$, if $r \leq R^c + R^p$, and is zero otherwise, while the interaction between polymers vanishes: $V^{pp}(r) = 0$. The state of the system is governed by the packing fractions of colloids, $\eta^c = 4\pi N^c (R^c)^3 / (3V)$, and of polymers $\eta^p = 4\pi N^p (R^p)^3 / (3V)$, and the size ratio $q = R^p / R^c$. The diameters are denoted by $\sigma^c = 2R^c$ and $\sigma^p = 2R^p$.

In order to derive a density functional for this system, we follow [10] and express the excess (over ideal) Helmholtz free energy as a spatial integral

$$\beta F_{\text{exc}}[\rho^c(\mathbf{r}), \rho^p(\mathbf{r}')] = \int d^3x \Phi(\{n_\nu^c(\mathbf{x})\}, \{n_\lambda^p(\mathbf{x})\}), \quad (1)$$

where $\beta = 1/k_B T$. We assume that the (reduced) free energy density Φ is some *function* of a set of weighted densities n_ν^i , where index $i = c, p$ labels the species, and ν is an index corresponding to the type of weighted density. The weighted densities are obtained by convolutions of the actual colloid and polymer densities, $\rho^c(\mathbf{r})$ and $\rho^p(\mathbf{r})$: $n_\nu^i(\mathbf{x}) = \int d^3r \rho^i(\mathbf{r}) w_\nu^i(\mathbf{x} - \mathbf{r})$. The weight functions $w_\nu^i(\mathbf{r})$ are independent of the density profiles and are given by

$$w_3^i(\mathbf{r}) = \theta(R^i - r), \quad w_2^i(\mathbf{r}) = \delta(R^i - r), \quad (2)$$

$$\mathbf{w}_{v_2}^i(\mathbf{r}) = w_2^i(\mathbf{r}) \mathbf{r} / r, \quad \hat{\mathbf{w}}_{m_2}^i(\mathbf{r}) = w_2^i(\mathbf{r}) [\mathbf{r}\mathbf{r} / r^2 - \hat{\mathbf{1}} / 3], \quad (3)$$

where $r = |\mathbf{r}|$, $\theta(r)$ is the step function, $\delta(r)$ is the Dirac distribution, and $\hat{\mathbf{1}}$ is the identity matrix. Further, linearly dependent weights are $w_1^i(\mathbf{r}) = w_2^i(\mathbf{r}) / (4\pi R^i)$, $\mathbf{w}_{v_1}^i(\mathbf{r}) = \mathbf{w}_{v_2}^i(\mathbf{r}) / (4\pi R^i)$, $w_0^i(\mathbf{r}) = w_1^i(\mathbf{r}) / R^i$. The weight functions are quantities with dimension of $\text{length}^{3-\nu}$. They differ in their tensorial rank: $w_0^i, w_1^i, w_2^i, w_3^i$ are scalars; $\mathbf{w}_{v_1}^i, \mathbf{w}_{v_2}^i$ are vectors; $\hat{\mathbf{w}}_{m_2}^i$ is a traceless matrix.

It remains to determine the free-energy density Φ . To this end, we consider the zero-dimensional limit, which we define as $\rho^i(\mathbf{r}) = \eta^i \delta(\mathbf{r})$, where η^i are the average occupation numbers. These are also the zero-dimensional packing fractions [11,12]. For the present model this limit corresponds to a cavity that can hold at most one colloid but can hold an arbitrary number of polymers if no colloid is present. The grand partition sum reduces to $\Xi = z^c + \exp(z^p)$, where z^i is the fugacity of species i . Following Ref. [11] we obtain the excess free energy $\beta F_{0D}(\eta^c, \eta^p) = (1 - \eta^c - \eta^p) \ln(1 - \eta^c) + \eta^c$. We now follow recent treatments [12,13] of FMT which consider multicavity limits and express the excess free-energy density as $\Phi = \Phi_1 + \Phi_2 + \Phi_3$, with contributions

$$\Phi_1 = \sum_{i=c,p} n_0^i \varphi^i(n_3^c, n_3^p), \quad (4)$$

$$\Phi_2 = \sum_{i,j=c,p} (n_1^i n_2^j - \mathbf{n}_{v_1}^i \cdot \mathbf{n}_{v_2}^j) \varphi^{ij}(n_3^c, n_3^p), \quad (5)$$

$$\begin{aligned} \Phi_3 = \frac{1}{8\pi} \sum_{i,j,k=c,p} (n_2^i n_2^j n_2^k / 3 - n_2^i \mathbf{n}_{v_2}^j \cdot \mathbf{n}_{v_2}^k \\ + 3[\mathbf{n}_{v_2}^i \hat{\mathbf{n}}_{m_2}^j \mathbf{n}_{v_2}^k - \text{tr}(\hat{\mathbf{n}}_{m_2}^i \hat{\mathbf{n}}_{m_2}^j \hat{\mathbf{n}}_{m_2}^k)] / 2) \\ \times \varphi^{ijk}(n_3^c, n_3^p), \end{aligned} \quad (6)$$

where tr denotes the trace. Derivatives of the 0D free energy are $\varphi^{i \dots k}(\eta^c, \eta^p) \equiv \partial^m \beta F_{0D}(\eta^c, \eta^p) / \partial \eta^i \dots \partial \eta^k$. This completes the prescription for the functional. Further details will be given elsewhere.

We summarize some of the properties of the functional. Note first that $F_{\text{exc}}[\rho^c, \rho^p]$ reduces to the exact low-density limit [10]. This feature results from the properties of the weight functions, Eqs. (2) and (3), which are constructed to restore the correct Mayer functions for the mixture. The next observation is that the functional is *linear* in the polymer density profile. This originates from the linearity of F_{0D} and is preserved by the construction of Φ , Eqs. (4)–(6), as an equal number of multiplications and differentiations are applied. Three important consequences arise. First, an alternative way of obtaining the functional can be found. We begin by noting that the free-energy functional for a binary hard sphere mixture is constructed by the same procedure as that above (the weight functions w_ν^i are unchanged) but with F_{0D} replaced by F_{0D}^{bhs} , the 0D excess free energy appropriate to a cavity which can contain one particle of species 1 or species 2, but not more particles [17]. If F_{0D}^{bhs} is expanded in powers of the occupation of one of the species (which becomes η^p) and the expansion is truncated at first order in η^p , F_{0D}^{bhs} reduces to F_{0D} . It follows that the present functional can be recovered by an appropriate linearization of the hard sphere mixture functional. This suggests that a colloid-ideal polymer functional can be derived from any (FMT) hard sphere mixture functional, including the original Rosenfeld functional [10], i.e., $\hat{\mathbf{w}}_{m_2}^i = 0$. Further justification for the linearization comes from considering the

pair direct correlation functions of the bulk mixture, given by $c_2^{ij}(|\mathbf{r}_1 - \mathbf{r}_2|) = -\beta \delta^2 F_{\text{exc}}[\rho^c, \rho^p] / \delta \rho^i(\mathbf{r}_1) \delta \rho^j(\mathbf{r}_2)$. The c_2^{ij} generated by the functional are consistent with the first two terms in the known low density (diagrammatic) expansion of these functions. Second, by observing that the one-body direct correlation function of the polymers $c_1^p(\mathbf{r}) = -\beta \delta F_{\text{exc}}[\rho^c, \rho^p] / \delta \rho^p(\mathbf{r})$ depends only on the weighted densities of the colloid density profile $\rho^c(\mathbf{r})$, it follows from the Euler-Lagrange equation that the inhomogeneous polymer density profile $\rho^p(\mathbf{r})$ is an explicit functional of $\rho^c(\mathbf{r})$ (and of the external potential coupling to the polymers). This feature of the theory constitutes an important simplification for calculations of the equilibrium properties as only $\rho^c(\mathbf{r})$ needs to be determined by numerical minimization. The third consequence of the linearity in $\rho^p(\mathbf{r})$ is that the pair direct correlation function for the polymers vanishes, i.e., $c_2^{pp} = 0$, as in the PY approximation. As a further remark, we note that our functional generates the correct AO depletion potential between two colloids in a sea of ideal polymer at arbitrary density [18].

We now apply the functional to the determination of some properties of the homogeneous (bulk) mixture. The excess Helmholtz free-energy density is given by $\beta F_{\text{exc}}(\rho^c, \rho^p) / V = \beta f_{\text{hs}}(\rho^c) - \rho^p \ln \alpha(\rho^c)$, where $f_{\text{hs}}(\rho^c)$ is the excess free-energy density of pure hard spheres in the scaled-particle (PY compressibility) approximation and $\alpha = (1 - \eta^c) \exp(-A\gamma - B\gamma^2 - C\gamma^3)$, with $\gamma = \eta^c / (1 - \eta^c)$, $A = q^3 + 3q^2 + 3q$, $B = 3q^3 + 9q^2/2$, and $C = 3q^3$. This result is *identical* to that of free-volume theory for the AO model [2], which is known to yield stable gas-liquid coexistence for size ratios $q \gtrsim 0.32$. For smaller q this fluid-fluid transition becomes metastable with respect to a broad, in η^c , fluid-solid transition [2,3]. Within DFT there are two routes to the pair correlation functions g^{ij} of the homogeneous fluid. One is the test-particle route whereby a particle of a given species is fixed at the origin and the one-body density profiles of the resulting inhomogeneous fluid determine the $g^{ij}(r)$.

The other route, which we pursue here, is based on the OZ relations. The pair direct correlation functions obtained by differentiating the functional are given analytically by $c_2^{ij} = \sum_{\nu, \lambda} \psi_{\nu\lambda}^{ij} w_{\nu}^i w_{\lambda}^j$, where $\psi_{\nu\lambda}^{ij}$ denotes the convolution and $\psi_{\nu\lambda}^{ij} = \partial^2 \Phi / \partial n_{\nu}^i \partial n_{\lambda}^j$ [19]. The OZ relation then yields the partial structure factors $S^{ij}(k)$ and a numerical Fourier transform gives the $g^{ij}(r)$.

In Fig. 1 we compare our results with those from the PY approximation for a given state point. The structure factors almost coincide, except for $S^{pp}(k)$ at small k . Note that the PY results were obtained numerically [20], as there are no analytical solutions for the AO model. The $g^{ij}(r)$ are also very close to PY. In the case of $g^{cc}(r)$ the DFT result violates the core condition, i.e., $g^{cc}(r) \neq 0$ at small r , but this is numerically small.

Performing simulations for highly asymmetric mixtures is beset by problems of slow equilibration, as huge num-

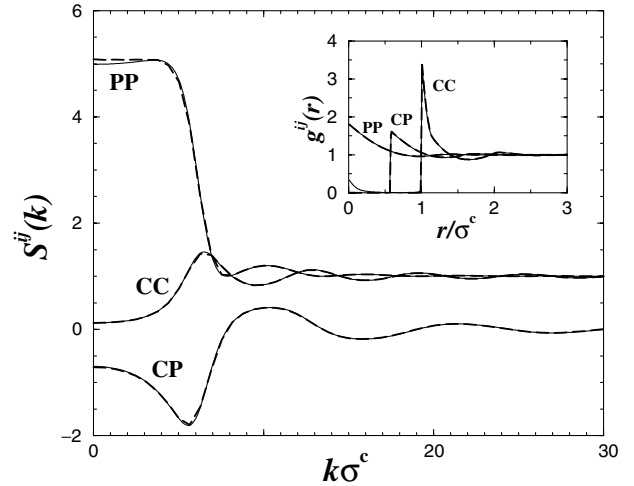


FIG. 1. Partial structure factors $S^{ij}(k)$ at $q = 0.15$, $\eta^c = 0.3$, $\eta^p = 0.05$, for colloid-colloid (CC), colloid-polymer (CP), and polymer-polymer (PP) pairs. Solid lines are DFT; dashed lines are PY results [20]. The inset shows the corresponding partial pair correlation functions $g^{ij}(r)$.

bers of polymers are required per colloidal particle. However, one can map the binary AO model onto an effective one-component system, in which the colloids interact via the AO pairwise depletion potential and for $q < 0.1547$ the mapping is exact [3,20]. This enables $g^{cc}(r)$ to be obtained by simulation of the one-component system and in Fig. 2 we compare such results [3] with those of our DFT. Although the structure factor $S^{cc}(k)$ is a little out of phase with the simulation result and the DFT underestimates the very high contact value $g^{cc}(\sigma^c)$, the overall performance is reasonable, given that the effective AO depletion potential is very deep and short ranged for this size ratio. Indeed we expect the binary mixture PY, and other integral equation closures, to exhibit similar failings for such state points

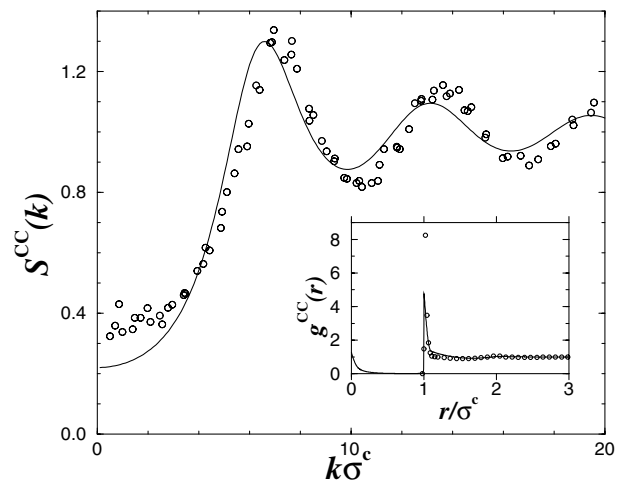


FIG. 2. Colloidal structure factor $S^{cc}(k)$ for $q = 0.1$, $\eta^c = 0.25$, and $\eta^p = 0.107$. The solid line is the DFT result; symbols are simulation data [3]. The inset shows the corresponding pair correlation function $g^{cc}(r)$.

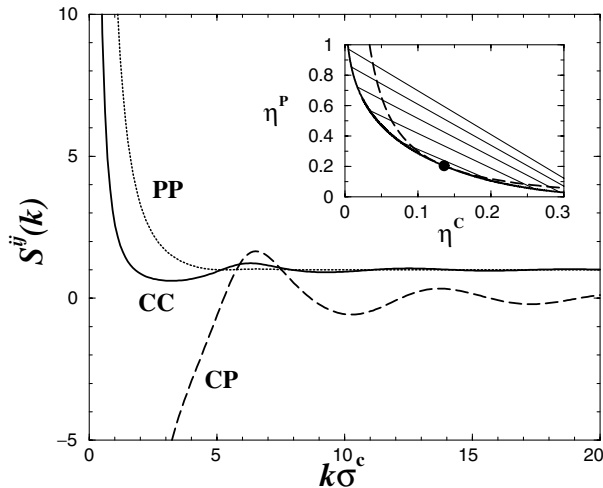


FIG. 3. Partial structure factors $S^{ij}(k)$ at the critical point for $q = 0.8$. The inset is the gas-liquid portion of the phase diagram obtained from DFT plotted in terms of packing fractions η^c, η^p . The binodal (thick line), spinodal (dashed line), tielines between coexisting gas and liquid phases (thin lines) and the critical point (dot) are shown.

[21]. It is likely that the test-particle route will improve the accuracy of the $g^{ij}(r)$, albeit at the expense of more numerical work.

The main advantage of the present route to structure is that the free energy of the homogeneous mixture is equivalent to that one would obtain from the compressibility route, i.e., by integrating the $S^{ij}(k=0)$, calculated as above, with respect to density. For example, this ensures that the thermodynamic and structural routes to the spinodal and critical point are consistent. We illustrate this in Fig. 3 for $q = 0.8$, where gas-liquid coexistence is stable. The inset shows the gas-liquid portion of the phase diagram in the η^c - η^p plane, while the main plot shows the three partial structure factors calculated at the critical point; all three diverge as $k \rightarrow 0$ (in particular, $S^{cp} \rightarrow -\infty$). For states slightly removed from criticality we expect OZ behavior: $S^{ij}(k) = S^{ij}(0)[1 - \xi^2 k^2 + O(k^4)]$, where ξ is the common correlation length. As our $S^{ij}(k)$ are given analytically we can confirm explicitly the OZ behavior. The common correlation length diverges with the mean-field exponent $\nu = 1/2$ and on a path at fixed $\eta^c = \eta_{\text{crit}}^c$ we define the amplitude ξ_0 via $\xi = \xi_0/(\eta_{\text{crit}}^p - \eta^p)^{1/2}$. ξ_0/σ^c depends only on the size ratio q . It is roughly proportional to the mean diameter and is conveniently expressed as $\xi_0 = \frac{1}{2}(\sigma^c + \sigma^p)/K(q)$, where typical values are $K(q) = 3.00, 2.36, \sqrt{5}$, for $q = 0.4, 0.8, \infty$, respectively.

That our DFT generates very satisfactory pair correlation functions in the bulk mixture provides an excellent indication [9] that it will yield accurate one-body correlation functions for an inhomogeneous AO mixture, e.g., for density profiles at walls or in model pores. Its roots in

fundamental measure theory ensure that short-ranged correlations, arising from packing of colloids, are properly incorporated. Since the DFT describes the bulk gas-liquid transition we can employ it for investigations of the “free” interface between the coexisting fluid phases and of depletion induced wetting phenomena at substrates. Moreover, the DFT is well suited for studies of bulk freezing and of “local” freezing of colloid layers at walls [22].

We thank M. Dijkstra, R. van Roij, R. Roth, A. Lang, and P. Tarazona for helpful discussions. This research was supported by the British-German ARC Programme (Project104b) and by the EPSRC Liquid Matter Network.

- [1] A. P. Gast, C. K. Hall, and W. B. Russell, *J. Colloid Interface Sci.* **96**, 251 (1983).
- [2] H. N. W. Lekkerkerker *et al.*, *Europhys. Lett.* **20**, 559 (1992).
- [3] M. Dijkstra, J. M. Brader, and R. Evans, *J. Phys. Condens. Matter* **11**, 10079 (1999).
- [4] S. Asakura and F. Oosawa, *J. Chem. Phys.* **22**, 1255 (1954).
- [5] A. Vrij, *Pure Appl. Chem.* **48**, 471 (1976).
- [6] F. Leal Calderon, J. Bibette, and J. Biasis, *Europhys. Lett.* **23**, 653 (1993).
- [7] S. M. Ilett, A. Orrock, W. C. K. Poon, and P. N. Pusey, *Phys. Rev. E* **51**, 1344 (1995).
- [8] J. M. Brader and R. Evans, *Europhys. Lett.* **49**, 678 (2000); J. M. Brader, M. Dijkstra, and R. Evans (to be published).
- [9] R. Evans, in *Fundamentals of Inhomogeneous Fluids*, edited by D. Henderson (Dekker, New York, 1992), p. 85.
- [10] Y. Rosenfeld, *Phys. Rev. Lett.* **63**, 980 (1989).
- [11] Y. Rosenfeld, M. Schmidt, H. Löwen, and P. Tarazona, *Phys. Rev. E* **55**, 4245 (1997).
- [12] P. Tarazona and Y. Rosenfeld, *Phys. Rev. E* **55**, R4873 (1997).
- [13] P. Tarazona, *Phys. Rev. Lett.* **84**, 694 (2000).
- [14] J. A. Cuesta, *Phys. Rev. Lett.* **76**, 3742 (1996); J. A. Cuesta and Y. Martinez-Raton, *Phys. Rev. Lett.* **78**, 3681 (1997).
- [15] M. Schmidt, *J. Phys. Condens. Matter* **11**, 10163 (1999).
- [16] M. Schmidt, *Phys. Rev. E* **60**, R6291 (1999).
- [17] Following the treatment in Appendix D of Ref. [11] one finds $\beta F_{\text{OD}}^{\text{hhs}}[\eta^1, \eta^2] = \eta^1 + \eta^2 + (1 - \eta^1 - \eta^2) \ln(1 - \eta^1 - \eta^2)$.
- [18] See the procedure in B. Götzelmann *et al.*, *Europhys. Lett.* **47**, 398 (1999).
- [19] Note that the colloid-polymer functional we obtain from the original Rosenfeld functional (i.e., $\hat{\mathbf{w}}_{m2}^i = 0$) generates identical bulk $c_2^{ij}(r)$ and free-energy density.
- [20] M. Dijkstra, R. van Roij, and R. Evans (to be published).
- [21] For small densities of colloids we expect that $g^{cc}(r) \propto \exp[-\beta \phi_{\text{eff}}(r)]$, where $\phi_{\text{eff}}(r)$ is the effective AO pair potential (see Ref. [3]). This is *not* found in our DFT, nor in the PY treatment of the binary AO model. Rather one finds that $g^{cc}(r) \propto -\beta \phi_{\text{eff}}(r)$.
- [22] A. D. Dinsmore, P. B. Warren, W. C. K. Poon, and A. G. Yodh, *Europhys. Lett.* **40**, 337 (1997).

Density functional theory for a model colloid–polymer mixture: bulk fluid phases

Matthias Schmidt¹, Hartmut Löwen¹, Joseph M Brader^{2,3} and Robert Evans²

¹ Institut für Theoretische Physik II, Heinrich-Heine-Universität Düsseldorf, Universitätsstraße 1, D-40225 Düsseldorf, Germany

² H H Wills Physics Laboratory, University of Bristol, Royal Fort, Tyndall Avenue, Bristol BS8 1TL, UK

Received 10 April 2002, in final form 18 June 2002

Published 27 September 2002

Online at stacks.iop.org/JPhysCM/14/9353

Abstract

We describe a density functional theory for mixtures of hard sphere (HS) colloids and ideal polymers, the Asakura–Oosawa model. The geometry-based fundamental measures approach which is used to construct the functional ensures the correct behaviour in the limit of low density of both species and in the zero-dimensional limit of a cavity which can contain at most one HS. Dimensional crossover is discussed in detail. Emphasis is placed on the properties of homogeneous (bulk) fluid phases. We show that the present functional yields the same free energy and, therefore, the same fluid–fluid demixing transition as that given by a different approach, namely the free-volume theory. The pair direct correlation functions $c_{ij}^{(2)}(r)$ of the bulk mixture are given analytically. We investigate the partial structure factors $S_{ij}(k)$ and the asymptotic decay, $r \rightarrow \infty$, of the total pair correlation functions $h_{ij}(r)$ obtained from the Ornstein–Zernike route. The locus in the phase diagram of the crossover from monotonic to oscillatory decay of correlations is calculated for several size ratios $q = R_p/R_c$, where R_p is the radius of the polymer sphere and R_c that of the colloid. We determine the (mean-field) behaviour of the partial structure factors on approaching the fluid–fluid critical (consolute) point.

1. Introduction

This paper describes a density functional theory (DFT) for determining the equilibrium properties of the so-called Asakura–Oosawa (AO) model of colloid–polymer mixtures [1, 2]. The model, which was first written down by Vrij [2], treats the colloids as hard spheres (HS) and the globular polymer coils as interpenetrating spheres, as regards their mutual interactions,

³ Present address: James Franck Institute, University of Chicago, South Ellis Ave. 5640, Chicago, IL 60637, USA.

but polymers experience an excluded volume (hard) interaction with the colloids. It can be regarded as the simplest, zeroth-order, model of a mixture of colloidal particles and non-adsorbing polymers. Much attention has been paid to the bulk properties of the AO model since this affords an important example of pure entropy-driven fluid–fluid phase separation. When q , the size ratio of the radius of the polymer sphere to that of the colloid sphere, is sufficiently large, the mixture separates into colloid-rich (liquid) and colloid-poor (gas) phases. The earliest detailed theoretical treatment of the model was that by Gast *et al* [3] based on liquid state perturbation theory for the (approximate) one-component version where colloids are assumed to interact via the AO pair potential. An alternative approach was introduced by Lekkerkerker *et al* [4] based on a free-volume theory for the free energy of the mixture—see section 3.1. These approximate theories, along with some simulation studies of simplified versions of the AO model [5, 6], indicate that when the size ratio q is larger than about 0.35 fluid–fluid separation is stable with respect to the fluid–solid transition. Other studies have investigated the equilibrium pair correlation functions in the AO model [5, 7–9] and the formal status of the mapping to a one-component fluid [8]. Although the AO model is highly idealized the variation of bulk phase behaviour with q predicted by studies of the model is in keeping with the experimental results [10, 11]. More recently attention has shifted towards inhomogeneous mixtures. An effective Hamiltonian for the colloids was obtained by integrating out the degrees of freedom of the polymer with both species subject to external fields [12, 13]. When the size ratio $q < (2/\sqrt{3} - 1) = 0.1547 \dots$ the effective Hamiltonian contains only one- and two-body (pairwise) contributions and for such mixtures it is straightforward to apply this to problems of adsorption at a hard wall [13]. For larger size ratios many-body terms are present in the effective Hamiltonian for both bulk and inhomogeneous mixtures [5, 8, 13] and incorporating such terms is rather complicated. Thus treating fluid–fluid interfaces and adsorption phenomena which occur for larger values of q is difficult within the effective Hamiltonian perspective and *ad hoc* prescriptions have been made [12] in order to calculate the density profile of colloids and the surface tension of the free fluid–fluid interface and compare with experimental data [14, 15].

The approach we adopt here for the AO model does not exploit the formal mapping to an effective one-component system of colloids. Rather we treat colloid and polymer on equal footing and develop a DFT specifically tailored for the AO mixture. DFT is recognized as powerful tool for describing the equilibrium properties of inhomogeneous fluids [16, 17]. Most effort has been expended on HS fluids, and the fundamental measure theory (FMT) introduced by Rosenfeld [18] and subsequently refined [19–22] has proved particularly versatile and reliable in a wide variety of applications to both pure HS and to mixtures. The FMT approach has also been applied to parallel hard cubes [23, 24]. Other recent advances in geometry-based DFT include

- (i) penetrable spheres [25], where the interatomic potential is a finite constant when the separation is smaller than the sphere diameter,
- (ii) the Widom–Rowlinson model [26], where the unlike species interact via a hard core potential and the like–like interactions are ideal,
- (iii) a model proposed by Bolhuis and Frenkel [27] that describes a mixture of HS and infinitely thin needles [28],
- (iv) a model of an amphiphilic hard body mixture [29] and
- (v) a ternary mixture of colloids, polymers and needles [30].

Our DFT for the AO model is also based on FMT ideas. An earlier letter [31] gave a brief outline of the theory and some results for bulk properties while a second letter described applications to fluid–fluid interfaces and wetting behaviour for the mixture adsorbed at a hard wall [32]. In this paper we provide a comprehensive description of the functional and its bulk properties

(thermodynamic functions and pair correlation functions) which explains the status of the DFT and which lists explicit expressions for all the relevant quantities required to implement the formalism. Detailed results for interfacial properties obtained from the DFT are given in [9].

Our paper is organized as follows: section 2 is devoted to the theory. We begin in 2.1 with an overview of DFT and describe the strategy for constructing functionals based on the FMT approach. The AO model is specified in 2.2 and in 2.3 we examine two exact limiting cases, namely the low density expansion and the zero-dimensional limit which corresponds to a small cavity that can hold at most one colloidal sphere. The free energy of the latter case constitutes a generating function for the three-dimensional functional and this is described in 2.4 where the functional for the AO model is presented explicitly. Section 2.5 focuses on the properties of the functional in various limiting cases and, in particular, how it accounts for zero-, one- and two-dimensional density distributions. An alternative derivation of the functional is presented in section 2.6. This is based on the original binary HS functional of Rosenfeld [18] and some observations on the diagrammatic expansions of the pair direct correlation functions for HS and for the AO model. We comment on the procedure of integrating out polymer degrees of freedom in the context of DFT and the nature of an effective one-component functional in 2.7. Section 3 is concerned with the predictions of the DFT for the properties of homogeneous (bulk) fluid phases. In 3.1 we focus on thermodynamic functions and show that the bulk free energy of the mixture is *precisely* the same as that obtained from the free-volume theory of Lekkerkerker *et al* [4]. Fluid-fluid demixing is described in 3.2 where it is shown that the spinodal in the η_p, η_c plane can be obtained analytically. η_p, η_c refer to the packing fractions of polymer and colloid, respectively. Section 3.3 describes the pair direct correlation functions $c_{ij}^{(2)}(r)$ obtained by functional differentiation of our AO functional; these are given analytically and their behaviour with η_p and η_c is discussed. In 3.4 we focus on the partial structure factors $S_{ij}(k)$ of the AO mixture and their behaviour when the mixture is close to the consolute (critical) point. Since the $S_{ij}(k)$ are given analytically the correlation length of the bulk fluid can be extracted straightforwardly. Section 3.5 is concerned with the nature of the asymptotic decay of pair correlations in the bulk AO mixture. We present results for the so-called Fisher-Widom (FW) line, which denotes the line in the phase diagram where the ultimate decay of the total pair correlation functions $h_{ij}(r)$ crosses over from monotonic to oscillatory. Section 3.6 discusses the predictions of the present DFT for the effective interaction (depletion potential) between colloidal particles, contrasting the Ornstein-Zernike (OZ) route with the alternative test-particle route. We conclude in section 4 with a summary and a discussion of some of the advantages and some shortcomings of our approach.

2. Theory

2.1. Overview and strategy

Within DFT the basic variables that describe the microscopic degrees of freedom of a many-body system are the one-body densities $\rho_i(\mathbf{r})$ of each species i : $\rho_i(\mathbf{r}) dV$ is the average number of particles (of species i) in an infinitesimal volume element dV located at position \mathbf{r} . Clearly $\rho_i(\mathbf{r})$ can resolve inhomogeneities (spatial deviations from a uniform value) on small length scales. Such inhomogeneous structuring is present in liquids under external influence and is manifestly present in crystalline solids. Introducing the particle positions $\mathbf{r}_i^{(j)}$, where $j = 1, \dots, N_i$, and N_i is the total number of particles of species i , one defines

$$\rho_i(\mathbf{r}) = \left\langle \sum_{j=1}^{N_i} \delta(\mathbf{r} - \mathbf{r}_i^{(j)}) \right\rangle, \quad (1)$$

where the angular brackets denote an appropriate ensemble average over many configurations. Evidently the $\rho_i(\mathbf{r})$ for a given statepoint (e.g. temperature and chemical potentials μ_i) contain considerable knowledge about the system. More significant is the fact that the thermodynamic potential of the system is determined solely by the one-body densities. The *existence of a functional* that converts the functions $\rho_i(\mathbf{r})$ to the grand potential Ω (which is a number) is one of the building blocks of DFT. Within this description, the $\rho_i(\mathbf{r})$ are basically the system's *only* degrees of freedom. At first glance this may seem to be a limitation: how can the important structural information contained in higher-body correlations such as the pair distribution functions be obtained, if the theory operates on the one-body level? The answer lies in the second building block of DFT: the variational principle states that upon varying the $\rho_i(\mathbf{r})$, the grand potential functional is a minimum at the true equilibrium densities and its value at the minimum is the true grand potential Ω . The grand potential functional has the form

$$\Omega[\rho_i(\mathbf{r})] = F_{\text{exc}}[\{\rho_i(\mathbf{r})\}] + \sum_i F_{\text{id}}[\rho_i(\mathbf{r})] + \int d^3r \rho_i(\mathbf{r}) [V_{i,\text{ext}}(\mathbf{r}) - \mu_i], \quad (2)$$

where $F_{\text{id}}[\rho_i(\mathbf{r})] = k_{\text{B}}T \int d^3r \rho_i(\mathbf{r}) [\ln(\Lambda_i^3 \rho_i(\mathbf{r})) - 1]$ is the (Helmholtz) free energy of the ideal gas, k_{B} is Boltzmann's constant, T is temperature, Λ_i is the thermal wavelength of species i and $V_{i,\text{ext}}$ is an external potential acting on species i . F_{exc} is the excess Helmholtz free energy arising from interactions between the particles. As this formalism is an exact reformulation of equilibrium statistical mechanics, the hierarchy of higher-body direct correlation functions can be obtained by functional differentiation of F_{exc} with respect to the density fields and the equilibrium distribution functions from the OZ equation. The main benefit of DFT is that powerful approximate theories can be obtained, provided the (generally unknown) excess part F_{exc} is prescribed. The effects caused by different classes of (time-independent) external potentials can all be treated within the *same* theory, as F_{exc} is independent of $V_{i,\text{ext}}$; it is a unique functional of $\{\rho_i(\mathbf{r})\}$ for a given choice of interparticle potential functions [16, 17]. Of course, the difficult part of any approximate DFT is finding a suitable prescription or recipe for F_{exc} that will incorporate the essential physics of short-range correlations (arising from the packing of the particles) and of attractive forces (if these are present) between the particles. However, in all cases, F_{exc} contains non-local contributions: when varying the density at a given point in space, the system is affected on the length scale of the inter-particle potentials (and beyond that through mediated correlations).

Our present DFT recipe to convert colloid and polymer density profiles to an (approximate) excess free energy for the AO model has the following key features. The non-local character is taken care of by convoluting the actual density fields $\rho_i(\mathbf{r})$ with various weight functions. The results of this procedure are *weighted densities*, and only these are subsequently used to obtain the excess free-energy functional, not the bare density fields. This type of weighted-density approximation (WDA) is now the most common tool to deal with very pronounced inhomogeneities: bare density profiles may change by orders of magnitude over distances as small as a particle diameter [33] and convolutions are a suitable means of treating this behaviour as they exhibit the property of smoothing out. Extensivity of the free energy is incorporated by expressing F_{exc} as a spatial integral over an excess free-energy *density* Φ . This ensures that, over length scales which are large compared with the system's correlation lengths, distinct regions of space give *additive* contributions to the free energy. In order to connect the free-energy density with the weighted densities, our crucial approximation is to regard Φ as a simple function (not a functional) of the weighted densities. This feature of the theory is identical to that of Rosenfeld's HS functional [18], and to various recent DFTs mentioned in the introduction. The three main differences between this approach and most other weighted-density [16, 17] DFTs are the following.

- (i) Rather than a single weight function, we use a *set* of weight functions w_ν^i (labelled by ν) for each species i . Consequently, we have a set of weighted densities n_ν^i for each species i .
- (ii) The range of the weight functions (defined as the distance beyond which a weight function vanishes) is determined not by the range of interactions, but by the radii of the particles.
- (iii) The free-energy density Φ is not modelled as a product of a bare density times a free energy per particle, but as a function only of the weighted densities n_ν^i .

Our DFT is constructed specifically to describe the AO model, i.e. the forms of the w_ν^i and of Φ are specific to this model. These are obtained by imposing the correct behaviour of the functional in several different cases, where the *exact* behaviour of the AO model is known. The low density (virial) expansion enables us to obtain the explicit form of the weight functions. As we shall see below, these are the same as for HS [18]. The other case is a situation of extreme confinement, where the particles of the system are only allowed to access a single location in space. This zero-dimensional limit is reminiscent of confining a particle to a crystal lattice site and corresponds to imposing the density distribution for a particle in a small cavity whose dimensions are of the same size as the particle. For HS the importance of this limit was demonstrated by Rosenfeld *et al* [19, 20]. Later it was shown that the original Rosenfeld functional [18], as well as improved versions, can be obtained from a systematic treatment of superpositions of (up to three) such density peaks [21, 22].

2.2. Specification of the Asakura-Oosawa model

The AO model describes colloids as hard impenetrable spheres and polymers as effective particles with spherical shape. These polymeric spheres are ideal (non-interacting) amongst themselves, but experience a hard core repulsion with the colloids. Clearly, the model is idealized, but it captures the essential physics of real colloid-polymer mixtures. In particular, the AO model describes polymer coils at the theta point, where repulsion is balanced by attraction, such that the effective interaction between polymers (as expressed by their second virial coefficient) vanishes. The AO model should also be regarded as a useful zeroth-order reference system for a wide variety of complex fluids where soft penetrable particles move in the space between hard bodies.

Thus, we consider a mixture of N_c colloids with radii R_c , and N_p polymers, with radii R_p , interacting via pair potentials V_{ij} , with $i, j = c, p$, contained inside a (large) volume V . The Hamiltonian consists of (trivial) kinetic energy terms and a sum of interaction terms:

$$H(\{\mathbf{R}_i, \mathbf{r}_j\}) = \sum_{i < j}^{N_c} V_{cc}(|\mathbf{R}_i - \mathbf{R}_j|) + \sum_i^{N_c} \sum_j^{N_p} V_{cp}(|\mathbf{R}_i - \mathbf{r}_j|) + \sum_{i < j}^{N_p} V_{pp}(|\mathbf{r}_i - \mathbf{r}_j|), \quad (3)$$

where $\{\mathbf{R}_i\} = \{\mathbf{r}_i^{(c)}\}$ denotes colloid and $\{\mathbf{r}_i\} = \{\mathbf{r}_i^{(p)}\}$ polymer coordinates.

The interaction potential between colloids is hard: $V_{cc}(r) = \infty$ if $r \leq 2R_c$, and zero otherwise. The interaction between colloids and polymers is also hard: $V_{cp}(r) = \infty$, if $r \leq R_c + R_p$, and zero otherwise. The interaction between polymers vanishes for all distances [2]: $V_{pp}(r) = 0$. Since all the interactions between particles are either hard or ideal, temperature T plays no role in determining phase behaviour or structure and the thermodynamic state of the bulk system is governed by the packing fractions of colloids, $\eta_c = 4\pi N_c R_c^3 / (3V)$, and of polymers, $\eta_p = 4\pi N_p R_p^3 / (3V)$. The properties of the system are governed by the size ratio $q = R_p / R_c$, which is the only adjustable parameter in the model. Unlike other theoretical treatments which are based on some integrating out of polymer degrees of freedom [3–5, 12, 13] the present DFT of the AO model treats colloid and polymer on equal footing.

2.3. Two exact limiting cases

2.3.1. Low density expansion. For small densities of all species, $\rho_i \rightarrow 0$, the probability that particles interact is small and for uniform fluids this enables one to make the systematic virial expansion of thermodynamic functions in powers of the (bulk) densities. The lowest order term governs the low density behaviour and for the excess free energy this is simply $\beta F_{\text{exc}}/V = -\sum_{ij} \rho_i \rho_j \int d^3r f_{ij}(\mathbf{r})/2$, where $f_{ij}(\mathbf{r}) = \exp(-\beta V_{ij}(\mathbf{r})) - 1$ are the Mayer functions, with $\beta = 1/k_B T$, and the summations run over all species. A similar expansion can be performed for inhomogeneous systems [16–18]. For a mixture the lowest-order term is

$$\beta F_{\text{exc}}[\{\rho_i(\mathbf{r})\}] = -\frac{1}{2} \sum_{ij} \int d^3r d^3r' \rho_i(\mathbf{r}) f_{ij}(|\mathbf{r} - \mathbf{r}'|) \rho_j(\mathbf{r}'). \quad (4)$$

Note that as the AO model exhibits only hard core interactions, the f_{ij} take on the values -1 and 0 only: $f_{cc}, f_{cp} = -1$ if the particle pair overlaps, and are zero otherwise. $f_{pp} = 0$ for all separations r . Equation (4) sums double convolutions of the density profiles, where the Mayer function is the convolution kernel. Although the functional is only second order in densities, an important feature is already present: the range of non-locality is the range of interactions.

2.3.2. Zero-dimensional limit. In statistical physics it is a common simplification to consider models in reduced spatial dimensionality d . Often two-dimensional systems are simpler to tackle than three-dimensional systems, and one-dimensional systems are usually simpler than two-dimensional systems. Reduced dimensionalities not only simplify theoretical treatments, but are also realized in nature, e.g. in films (two dimensions) or inside channels (one dimension) or cavities (zero dimensions). A versatile DFT should be able to describe accurately all situations of reduced dimensionality. In order to model the ultimate dimensional crossover to zero dimensions a special limit was introduced [19, 20]. In this so-called zero-dimensional limit the system is confined in all three spatial dimensions, such that only a single *point* in three-dimensional space is accessible for the particles. Physically, the zero-dimensional limit may be realized by a small cavity with rigid walls, that is of particle size. The zero-dimensional limit is also similar to that of a particle at a crystal lattice site, where each particle is confined within the cage of its nearest neighbours. Any theoretical description for structure and thermodynamics in highly inhomogeneous three-dimensional situations should be able to reproduce dimensional crossover, even to the extreme limit of a zero-dimensional situation. Clearly, this is a demanding requirement. It has been found, in the case of HS, that one can start with a point and by considering zero-dimensional cavities of increasingly complex shape build up a theory for higher dimensions. A strong guide for the general structure of the functional is provided by Percus's exact one-dimensional functional for hard rods [34]. In the case of HS knowledge of the exact zero-dimensional free energy was sufficient to derive a working theory [21], and was subsequently exploited to derive improved versions [22]. The same methodology was used to tackle other systems including penetrable spheres, which interact with a constant pair potential if they overlap [25], the Widom–Rowlinson model [26] and a needle–sphere mixture [28], as well as models for an amphiphilic [29] and a ternary mixture [30]. Here we follow the same route for the AO model.

To be explicit, we introduce an external potential $V_{\text{ext}}(\mathbf{r}) = 0$ if $|\mathbf{r}| < \epsilon$, and ∞ otherwise. Each particle's centre is then allowed to move inside a sphere of volume $4\pi\epsilon^3/3$. We consider the limit $\epsilon \rightarrow 0$, so that any particles present in the cavity overlap. In order to derive the zero-dimensional Helmholtz (excess) free energy, we consider the grand partition sum Ξ . The only states that are allowed are the following:

- (i) the empty state without any particle,

- (ii) the state with exactly one colloidal particle and
- (iii) all states without colloids but with an arbitrary number of polymers.

Hence, in that order,

$$\Xi = 1 + z_c + [\exp(z_p) - 1] = z_c + \exp(z_p), \quad (5)$$

where the (dimensionless) fugacities are defined here as $z_i = \exp(\beta\mu_i)\Lambda_i^{-3}4\pi\epsilon^3/3$. The mean occupation numbers of particles, η_i , which are the packing fractions in zero dimension, are obtained from

$$\eta_i = z_i \frac{\partial}{\partial z_i} \ln \Xi. \quad (6)$$

More explicitly,

$$\eta_c = \frac{z_c}{z_c + \exp(z_p)}, \quad (7)$$

$$\eta_p = \frac{z_p \exp(z_p)}{z_c + \exp(z_p)}, \quad (8)$$

which can be inverted to obtain the fugacities

$$z_c = \frac{\eta_c}{1 - \eta_c} \exp\left(\frac{\eta_p}{1 - \eta_c}\right), \quad (9)$$

$$z_p = \frac{\eta_p}{1 - \eta_c}. \quad (10)$$

The dimensionless excess chemical potentials, $\tilde{\mu}_i \equiv \ln(z_i) - \ln(\eta_i)$, given by

$$\tilde{\mu}_c(\eta_c, \eta_p) = -\ln(1 - \eta_c) + \frac{\eta_p}{1 - \eta_c}, \quad (11)$$

$$\tilde{\mu}_p(\eta_c) = -\ln(1 - \eta_c), \quad (12)$$

can then be used to integrate along a suitably chosen path in the (η_c, η_p) plane in order to obtain the excess free energy

$$\beta F_{\text{Od}}(\eta_c, \eta_p) = \int_0^{\eta_c} d\eta'_c \tilde{\mu}_c(\eta'_c, 0) + \int_0^{\eta_p} d\eta \tilde{\mu}_p(\eta_c). \quad (13)$$

(Alternatively, one could use $\beta F_{\text{Od}} = -\ln \Xi + \tilde{\mu}_c \partial \ln \Xi / \partial \tilde{\mu}_c + \tilde{\mu}_p \partial \ln \Xi / \partial \tilde{\mu}_p$.) The result is

$$\beta F_{\text{Od}}(\eta_c, \eta_p) = (1 - \eta_c - \eta_p) \ln(1 - \eta_c) + \eta_c. \quad (14)$$

This zero-dimensional free energy exhibits a number of physically realistic properties, that are generic to the model itself, independent of the precise situation under consideration, and which remain valid for other reduced dimensionalities and confining geometries:

- (i) The colloid packing fraction is restricted to $\eta_c < 1$. In three dimensions, $\eta_c \rightarrow 1$ corresponds to space-filling spheres. Although it is impossible to pack HS more densely than the close-packing fcc value of 0.7405, the limit $\eta_c \rightarrow 1$ does arise in many liquid state approximations such as scaled-particle and Percus–Yevick (PY) theories which commonly produce expressions containing factors of $1/(1 - \eta_c)$.
- (ii) Polymer packing fractions can be arbitrarily large, as no upper bound exists for η_p ; the ideality of the polymers means that there are no packing constraints for this species.
- (iii) The free energy depends linearly on η_p . As we shall show in section 2.6, this is not necessarily the case in three-dimensional bulk where terms of $O(\eta_p^4)$ and higher, but not $O(\eta_p^2)$ or $O(\eta_p^3)$, can arise. However, this simple linear dependence is a feature of the well known (approximate) free-volume theory [4, 5].

Additionally, it is interesting to compare the present result for the AO model with the result for HS mixtures. For a binary HS mixture of species 1 and 2, one obtains $\beta F_{0d}^{\text{bhs}} = (1 - \eta_1 - \eta_2) \ln(1 - \eta_1 - \eta_2) + \eta_1 + \eta_2$, where η_1, η_2 are the packing fractions of species 1 and 2. Guided by (iii), we observe that linearization in η_2 yields F_{0d} of equation (14) upon identifying $\eta_1 = \eta_c$ and $\eta_2 = \eta_p$. This linearization property will be exploited further in section 2.6 in an alternative derivation of the DFT.

These two exact limiting cases provide the key building blocks for constructing the free-energy functional.

2.4. Density functional for the AO model

Following previous work on HS mixtures [18–20], we express the excess Helmholtz free energy in terms of a functional of colloid and polymer density fields as a spatial integral over a free-energy density Φ that is a function of the weighted densities:

$$\beta F_{\text{exc}}[\rho_c(\mathbf{r}), \rho_p(\mathbf{r}')] = \int d^3x \Phi(\{n_v^c(\mathbf{x})\}, \{n_v^p(\mathbf{x})\}), \quad (15)$$

where the weighted densities for each species $i = c, p$ are obtained by convolutions with the actual density profiles

$$n_v^i(\mathbf{x}) = \int d^3r \rho_i(\mathbf{r}) w_v^i(\mathbf{x} - \mathbf{r}). \quad (16)$$

In previous work on HS, Φ was taken to be a function of species-independent weighted densities [18]. Here we must generalize and allow Φ to depend on species-dependent weighted densities. This is necessary in order to capture the intrinsically different nature of colloids and polymers. The weight functions w_v^i are independent of the density profiles and are given by

$$w_3^i(\mathbf{r}) = \Theta(R_i - r), \quad (17)$$

$$w_2^i(\mathbf{r}) = \delta(R_i - r), \quad (18)$$

$$w_1^i(\mathbf{r}) = \delta(R_i - r)/(4\pi r), \quad (19)$$

$$w_0^i(\mathbf{r}) = \delta(R_i - r)/(4\pi r^2), \quad (20)$$

$$\mathbf{w}_{v2}^i(\mathbf{r}) = \delta(R_i - r)\mathbf{r}/r, \quad (21)$$

$$\mathbf{w}_{v1}^i(\mathbf{r}) = \delta(R_i - r)\mathbf{r}/(4\pi r^2), \quad (22)$$

$$\hat{\mathbf{w}}_{m2}^i(\mathbf{r}) = \delta(R_i - r)(\mathbf{r}\mathbf{r}/r^2 - \hat{\mathbf{1}}/3), \quad (23)$$

where $r = |\mathbf{r}|$, $\Theta(r)$ is the step function, $\delta(r)$ is the Dirac distribution and $\hat{\mathbf{1}}$ is the identity matrix. The weight functions are quantities with dimension length $^{3-\nu}$. They differ in their tensorial rank: $w_0^i, w_1^i, w_2^i, w_3^i$ are scalars; $\mathbf{w}_{v1}^i, \mathbf{w}_{v2}^i$ are vectors; $\hat{\mathbf{w}}_{m2}^i$ is a (traceless) second-rank tensor. Equations (17)–(22) are the weights given in [18], whereas equation (23) is equivalent to the tensor formulation in [22]. The Fourier transforms of the weight functions are given in appendix A.

The free-energy density is composed of three parts

$$\Phi = \Phi_1 + \Phi_2 + \Phi_3, \quad (24)$$

which are defined as

$$\Phi_1 = \sum_{i=c,p} n_0^i \varphi_i(n_3^c, n_3^p), \quad (25)$$

$$\Phi_2 = \sum_{i,j=c,p} (n_1^i n_2^j - \mathbf{n}_{v1}^i \cdot \mathbf{n}_{v2}^j) \varphi_{ij}(n_3^c, n_3^p), \quad (26)$$

$$\Phi_3 = \frac{1}{8\pi} \sum_{i,j,k=c,p} \left(\frac{1}{3} n_2^i n_2^j n_2^k - n_2^i n_{v2}^j \cdot n_{v2}^k + \frac{3}{2} [n_{v2}^i \hat{\mathbf{n}}_{m2}^j n_{v2}^k - \text{tr}(\hat{\mathbf{n}}_{m2}^i \hat{\mathbf{n}}_{m2}^j \hat{\mathbf{n}}_{m2}^k)] \right) \varphi_{ijk}(n_3^c, n_3^p), \quad (27)$$

where tr denotes the trace, and derivatives of the zero-dimensional excess free energy (given by equation (14)) are

$$\varphi_{i\dots k}(\eta_c, \eta_p) \equiv \frac{\partial^m}{\partial \eta_i \dots \partial \eta_k} \beta F_{0d}(\eta_c, \eta_p). \quad (28)$$

In the absence of polymer, Φ_1 and Φ_2 are equivalent to the free-energy densities for HS introduced in [18], and Φ_3 is equivalent to the tensor treatment for pure HS in [22]. Equations (25)–(27) are direct generalizations of these earlier treatments to include summation over species. All the derivatives $\varphi_{i\dots j}$ that carry more than one polymer index vanish due to the functional form of F_{0d} , and we obtain

$$\Phi_1 = n_0^c \left[-\ln(1 - n_3^c) + \frac{n_3^p}{1 - n_3^c} \right] - n_0^p \ln(1 - n_3^c), \quad (29)$$

$$\Phi_2 = (n_1^c n_2^c - n_{v1}^c \cdot n_{v2}^c) \left[\frac{1}{1 - n_3^c} + \frac{n_3^p}{(1 - n_3^c)^2} \right] + \frac{n_1^p n_2^c - n_{v1}^p \cdot n_{v2}^c + n_1^c n_2^p - n_{v1}^c \cdot n_{v2}^p}{1 - n_3^c}, \quad (30)$$

$$\Phi_3 = \frac{\frac{1}{3} (n_2^c)^3 - n_2^c (n_{v2}^c)^2 + \frac{3}{2} (n_{v2}^c \hat{\mathbf{n}}_{m2}^c n_{v2}^c - 3 \det \hat{\mathbf{n}}_{m2}^c) \left[\frac{1}{(1 - n_3^c)^2} + \frac{2n_3^p}{(1 - n_3^c)^3} \right]}{8\pi} + \frac{(n_2^c)^2 n_2^p - n_2^p (n_{v2}^c)^2 - 2n_2^c n_{v2}^c \cdot n_{v2}^p + \frac{3}{2} \{2n_{v2}^p \hat{\mathbf{n}}_{m2}^c n_{v2}^c + n_{v2}^c \hat{\mathbf{n}}_{m2}^p n_{v2}^c - 3\text{tr}[(\hat{\mathbf{n}}_{m2}^c)^2 \hat{\mathbf{n}}_{m2}^p]\}}{8\pi (1 - n_3^c)^2}. \quad (31)$$

For brevity we have omitted the r dependence, e.g. $n_3^c = n_3^c(r)$. The DFT for the AO model is now fully specified. In the next subsection we examine several limiting cases in order to ascertain better the nature of the approximation we have introduced.

2.5. Examining limiting cases of the functional

2.5.1. Low density expansion. For low densities, $\rho_i \rightarrow 0$, the weighted densities also become small, $n_v^i \rightarrow 0$, since the latter are given by a convolution of the density with a density-independent weight function w_v^i , equation (16). In order to obtain the behaviour of the DF, we Taylor expand the free-energy density Φ in powers of weighted densities. The straightforward calculation yields to lowest order

$$\Phi = n_0^c n_3^c + n_1^c n_2^c - n_{v1}^c \cdot n_{v2}^c + n_0^c n_3^p + n_1^c n_2^p - n_{v1}^c \cdot n_{v2}^p + n_0^p n_3^c + n_1^p n_2^c - n_{v1}^p \cdot n_{v2}^c. \quad (32)$$

Each of the terms in the sum is a bilinear combination of weighted densities, $n_v^i n_\lambda^j$. We rewrite this formally as

$$\Phi \equiv \sum_{ij=cp} \sum_{v\lambda} C_{v\lambda}^{ij} n_v^i n_\lambda^j \quad (33)$$

where the coefficients take on values $C_{v\lambda}^{ij} = -1, 0, 1$. (Note that the coefficients $C_{v\lambda}^{pp}$ of terms $n_v^p n_\lambda^p$, with p representing species 2, which are non-zero in the corresponding expansion for the binary HS functional vanish in the AO model.) Next we rearrange the order of integrations in the density functional

$$\beta F_{\text{exc}} = \int d^3x \sum_{ij=cp} C_{v\lambda}^{ij} \int d^3r \rho_i(\mathbf{r}) w_v^i(\mathbf{r} - \mathbf{x}) \int d^3r' \rho_j(\mathbf{r}') w_\lambda^j(\mathbf{r}' - \mathbf{x}) \quad (34)$$

$$= \sum_{ij} \int d^3r \rho_i(\mathbf{r}) \int d^3r' \rho_j(\mathbf{r}') \sum_{\nu\lambda} \int d^3x C_{\nu\lambda}^{ij} w_\nu^i(\mathbf{r} - \mathbf{x}) w_\lambda^j(\mathbf{r}' - \mathbf{x}) \quad (35)$$

$$= \sum_{ij} \int d^3r \rho_i(\mathbf{r}) \int d^3r' \rho_j(\mathbf{r}') f_{ij}(|\mathbf{r} - \mathbf{r}'|)/2, \quad (36)$$

where in the last step we exploited the property of the weight functions to obtain the HS Mayer bond. This is the same argument as in Rosenfeld's HS mixture case [18]; the vanishing of the polymer–polymer Mayer bond is due solely to the functional form of Φ , which does not contain terms quadratic in polymer weighted densities. Thus the present functional does reduce to the correct low density limit when all densities $\rho_i \rightarrow 0$.

2.5.2. Zero-dimensional limit. For density distributions $\rho_i = \eta_i \delta(\mathbf{r})$ each weighted density becomes proportional to its weight function

$$n_\nu^i(\mathbf{x}) = \int d^3r \eta_i \delta(\mathbf{r}) w_\nu^i(\mathbf{r} - \mathbf{x}) = \eta_i w_\nu^i(\mathbf{x}). \quad (37)$$

We show that the contribution from Φ_1 yields the exact result. Consider

$$\beta F_{\text{exc}} = \int d^3r \Phi_1 \quad (38)$$

$$= \int_0^\infty dr 4\pi r^2 \sum_i \eta_i w_0^i(r) \varphi_i(\eta_c w_3^c(r), \eta_p w_3^p(r)) \quad (39)$$

$$= \int_0^\infty dr \sum_i \eta_i \delta(R_i - r) \varphi_i(\eta_c \Theta(R_c - r), \eta_p \Theta(R_p - r)) \quad (40)$$

$$= \int_0^\infty dr \sum_i \eta_i \frac{-d\Theta(R_i - r)}{dr} \varphi_i(\eta_c \Theta(R_c - r), \eta_p \Theta(R_p - r)) \quad (41)$$

$$= \int_0^1 dt [\eta_p \varphi_p(\eta_c, \eta_p t) + \eta_c \varphi_c(\eta_c t, 0)], \quad (42)$$

$$= \beta F_{0d}(\eta_c, \eta_p) \quad (43)$$

where we have assumed, without loss of generality, in equation (42) that $R_c > R_p$ and have used the definition of φ_i , equation (28), in the last step.

The contributions from Φ_2 and Φ_3 both vanish. This follows from symmetry considerations. From equation (37), and the fact that $w_{\nu\nu}^i = w_\nu^i r/r$ for $\nu = 1, 2$, it follows that $n_1^i n_2^j = n_{\nu 1}^i \cdot n_{\nu 2}^j$. Hence, from equation (30), $\Phi_2 = 0$. A similar argument holds for Φ_3 .

2.5.3. One-dimensional limit. Following [21] we can obtain an effective one-dimensional functional by imposing on the general three-dimensional functional density distributions $\rho_i(\mathbf{r}) = \rho_i(x) \delta(y) \delta(z)$. We omit the tedious details and show the final result:

$$\beta F_{\text{exc}}[\rho_c(x), \rho_p(x')] = \int dx \Phi(\{n_\nu^c(x)\}, \{n_\nu^p(x)\}), \quad (44)$$

where the weighted densities are obtained by one-dimensional convolutions

$$n_\nu^i(x) = \int dx' \rho_i(x') w_\nu^i(x - x'), \quad (45)$$

of the two one-dimensional weight functions

$$w_d^i(x) = \theta(R_i - |x|), \quad (46)$$

$$w_0^i(x) = [\delta(R_i + x) + \delta(R_i - x)]/2. \quad (47)$$

appears and gives a contribution of order ρ_p^2 to $c_{pp}^{(2)}(r)$. It should be noted that the Percus–Yevick theory for the binary AO model also gives $c_{pp}^{(2)} = 0$. A theory capable of going beyond the approximation $c_{pp}^{(2)} = 0$ would have to be accurate to at least the fourth virial level. As even sophisticated integral equation theories are usually exact to only third virial level this is clearly a difficult task. Equations (50)–(52) give no information about how to extract the colloid–polymer functional from the binary HS functional as information about the polymer–polymer interaction does not enter until higher terms in the expansion. However, the facts that

- (i) $c_{cp}^{(2)}$ is independent of the polymer density field and
- (ii) $c_{pp}^{(2)} = 0$ suggest that the simplest way to obtain a functional for the AO model is to linearize the binary HS functional with respect to $\rho_p(\mathbf{r})$.

This ensures that the bulk pair correlations are correct to the third virial level, i.e. $c_{pp}^{(2)} = -\delta^2 \beta F_{\text{exc}} / \delta \rho_p(\mathbf{r}) \delta \rho_p(\mathbf{r}') = 0$ and $c_{cp}^{(2)} = -\delta^2 \beta F_{\text{exc}} / \delta \rho_c(\mathbf{r}) \delta \rho_p(\mathbf{r}')$ is independent of the polymer density.

The exact AO free-energy functional contains terms linear in $\rho_p(\mathbf{r})$ but not terms in ρ_p^2 or ρ_p^3 , as these would lead to inconsistency with the low order diagrams. However, when expanding the binary HS functional in $\rho_p(\mathbf{r})$ we could have chosen to omit the ρ_p^2 and ρ_p^3 terms, but retain all higher orders; the low order diagrams exercise no constraint over these higher order contributions. In linearizing the functional we have chosen to set all higher order terms to zero. The justification for this can be found by looking at the exact diagrammatic expansion for a binary mixture to fourth virial level:

$$c_{ij}^{(2)}(r) = \circlearrowleft_{ij} + \sum_k \rho_k \circlearrowleft_{ij}^k + \sum_{k,l} \rho_k \rho_l \left(\circlearrowleft_{ij}^{k,l} + \circlearrowleft_{ij}^{l,k} + \circlearrowleft_{ij}^{k,l} + \circlearrowleft_{ij}^{l,k} + \circlearrowleft_{ij}^{k,l} + \circlearrowleft_{ij}^{l,k} + \circlearrowleft_{ij}^{k,l} + \circlearrowleft_{ij}^{l,k} \right) + \mathcal{O}(\rho^3). \quad (54)$$

The Rosenfeld binary HS functional generates bulk $c_{ij}^{(2)}$ identical to those from Percus–Yevick theory. The latter is not exact to fourth virial level as it contains only a subset of the required diagrams:

$$c_{ij}^{(2)}(r) = \circlearrowleft_{ij} + \sum_k \rho_k \circlearrowleft_{ij}^k + \sum_{k,l} \rho_k \rho_l \left(\circlearrowleft_{ij}^{k,l} + \circlearrowleft_{ij}^{l,k} + \circlearrowleft_{ij}^{k,l} + \circlearrowleft_{ij}^{l,k} \right) + \mathcal{O}(\rho^3). \quad (55)$$

All diagrams in PY theory, equation (55), have a Mayer bond connecting ij . We henceforth refer to diagrams of this category as A class and diagrams with no ij Mayer bond as B class and focus our attention on $c_{pp}^{(2)}$. Retaining quartic and higher order terms when expanding the Rosenfeld HS functional, only HS A-class diagrams would be included. For the AO model all A-class diagrams are identically zero in the expansion of $c_{pp}^{(2)}$ and only B-class diagrams contribute. Inclusion of quartic or higher order terms in the ρ_p expansion of the functional would incorporate only unphysical diagrams. The A-class diagrams required for the AO model are not contained within the original binary HS functional. We conclude that by linearizing the original Rosenfeld HS functional in the polymer density we should obtain a functional which describes the AO model. Indeed when such a linearization is performed we recover equations (24)–(31) for the free-energy density but with the tensor weighted densities $\hat{\mathbf{n}}_{m2}^i = 0$, since the original Rosenfeld functional does not have tensor weights.

2.7. Effective one-component functional

When investigating the statistical mechanics of soft matter systems it is frequently advantageous to integrate out some degrees of freedom in order to obtain effective interactions between the particles of the remaining species. This has proved particularly fruitful for the AO

model of colloid-polymer mixtures where the polymer degrees of freedom could be explicitly integrated out for certain size ratios [5, 8, 9, 13]. However, it is not obvious that an analogous procedure can generally be performed within the context of DFT. In order to minimize a functional Ω of two independent density fields it is necessary to solve simultaneously the coupled equations

$$\frac{\delta\Omega[\rho_c, \rho_p]}{\delta\rho_c(\mathbf{r})} = 0, \quad \frac{\delta\Omega[\rho_c, \rho_p]}{\delta\rho_p(\mathbf{r})} = 0. \quad (56)$$

The corresponding Euler-Lagrange equations are given by

$$\rho_c(\mathbf{r}) = z_c \exp(c_c^{(1)}(\mathbf{r}; [\rho_c, \rho_p]) - \beta V_c^{\text{ext}}(\mathbf{r})) \quad (57)$$

$$\rho_p(\mathbf{r}) = z_p \exp(c_p^{(1)}(\mathbf{r}; [\rho_c, \rho_p]) - \beta V_p^{\text{ext}}(\mathbf{r})), \quad (58)$$

where z_c and z_p are the fugacities and the functional dependence of the one-body direct correlation function $c_i^{(1)}$ is made explicit. While species have been labelled c, p, equations (57) and (58) apply to an arbitrary binary mixture. The Euler-Lagrange equations are usually coupled in a complicated way and must be solved using numerical methods.

Within the context of DFT the term 'integrating out' can be somewhat misleading because at no stage in the calculation have integrals been performed over the polymer degrees of freedom. The usual procedure of integrating out is performed directly on the partition function and the effective potentials which result are then input to a one-component theory or simulation to calculate the density distribution of the species of (main) interest [5, 8]. While an effective potential never appears explicitly within the DFT formulation, it is contained implicitly in the Euler-Lagrange equation of the species of interest. It is the variational minimization of Ω which takes the place of an explicit integrating out. The analogue of integrating out within DFT is expressing the free-energy functional as a functional of a reduced set of density fields

$$F_{\text{exc}}[\rho_c(\mathbf{r})] \equiv F_{\text{exc}}[\rho_c(\mathbf{r}), \rho_p[\rho_c(\mathbf{r})]]. \quad (59)$$

These considerations can be made explicit for the AO functional. The one-body direct correlation function of species i is given by

$$c_i^{(1)}(\mathbf{r}) = -\beta \frac{\delta F_{\text{exc}}[\{\rho_i\}]}{\delta\rho_i(\mathbf{r})} = -\sum_v \frac{\partial\Phi}{\partial n_v^i} \otimes \omega_v^i, \quad (60)$$

where \otimes denotes a convolution. $c_i^{(1)}(\mathbf{r})$ is independent of the polymer density as only colloid weighted densities appear on the RHS of equation (60). It follows that $c_p^{(1)}(\mathbf{r})$ is a functional of the colloid profile alone: $c_p^{(1)}(\mathbf{r}) \equiv c_p^{(1)}(\mathbf{r}; [\rho_c])$. Combining (60) with (58) thus provides an explicit expression for the polymer profile $\rho_p(\mathbf{r})$ as a functional of the colloid profile $\rho_c(\mathbf{r})$ [9]. If we constrain the colloid density field $\rho_c(\mathbf{r})$ to be fixed at some non-equilibrium value, then the polymer profile which minimizes the free energy subject to the constraint is automatically given. The AO functional, although a genuine two-component theory, can thus be regarded as an effective one-component free-energy functional of a single density field. For more general model fluids the Euler-Lagrange equations will not decouple and will not be as simple but the concept remains the same. Although the equations may be coupled in a complicated way, for given external potentials, $\rho_1 \equiv \rho_1([\rho_2]; z_1)$ and $\rho_2 \equiv \rho_2([\rho_1]; z_2)$ so one of the density profiles can, in principle, be eliminated to obtain the effective functional [37]. In order to obtain explicit forms for the effective potentials one must resort to alternative methods such as those described by Roth *et al* [38] for additive and non-additive [39] HS mixtures.

3. Application to bulk fluid phases

In this section we apply the theory developed in section 2 to the calculation of the thermodynamic and structural properties of the bulk AO mixture.

3.1. Thermodynamic functions

Homogeneous fluid phases are characterized by spatially constant density fields: $\rho_c(\mathbf{r}) \equiv \rho_c$, and $\rho_p(\mathbf{r}) \equiv \rho_p$. In order to determine the free energy, and hence all thermodynamic quantities, we evaluate the density functional $F_{\text{exc}}[\rho_c = \text{const}, \rho_p = \text{const}]$. First we need to calculate the weighted densities, equation (16). The integration over the weight functions (17–23) can be carried out explicitly, and yields the so-called fundamental measures

$$\xi_v^i \equiv \int d^3x w_v^i(\mathbf{x}), \quad (61)$$

which describe the volume $\xi_3^i = 4\pi R_i^3/3$, surface area $\xi_2^i = 4\pi R_i^2$, integral mean curvature $\xi_1^i = R_i$ and Euler characteristic $\xi_0^i = 1$ of the spherical particles. The resulting weighted densities are

$$n_3^i = \eta_i, \quad (62)$$

$$n_2^i = 3\eta_i/R_i, \quad (63)$$

$$n_1^i = 3\eta_i/(4\pi R_i^2), \quad (64)$$

$$n_0^i = 3\eta_i/(4\pi R_i^3), \quad (65)$$

$$\mathbf{n}_{v1}^i = \mathbf{n}_{v2}^i = \hat{\mathbf{n}}_{m2}^i = 0, \quad (66)$$

with, once again, $i = c, p$. Inserting these expressions into equations (29)–(31), we obtain the excess free-energy density Φ , equation (24), which is constant in space, so the integration in equation (15) is trivial. We find that the excess Helmholtz free-energy density is given by

$$\beta F_{\text{exc}}/V = \beta f_{\text{hs}}(\rho_c) - \rho_p \ln \alpha(\rho_c), \quad (67)$$

where $f_{\text{hs}}(\rho_c)$ is the *excess* free-energy density of pure HS in the scaled-particle (PY compressibility) approximation, given as

$$\beta f_{\text{hs}}(\rho_c) = \frac{3\eta_c[3\eta_c(2 - \eta_c) - 2(1 - \eta_c)^2 \ln(1 - \eta_c)]}{8\pi R_c^3(1 - \eta_c)^2}, \quad (68)$$

and

$$\alpha(\rho_c) = (1 - \eta_c) \exp(-A\gamma - B\gamma^2 - C\gamma^3), \quad (69)$$

where $\gamma = \eta_c/(1 - \eta_c)$, $A = q^3 + 3q^2 + 3q$, $B = 3q^3 + 9q^2/2$ and $C = 3q^3$. This result can be shown to be *identical* to that of free-volume theory for the AO model [4], where the quantity α is interpreted as the ratio of the free volume accessible to a test polymer sphere and the system volume. In order to demonstrate the equivalence we perform a Legendre transform on the total (canonical) Helmholtz free energy $F(N_c, N_p, V) = F_{\text{exc}}(N_c, N_p, V) + \beta^{-1}V \sum_{i=c,p} \rho_i [\ln(\Lambda_i^3 \rho_i) - 1]$ to obtain the semigrand potential

$$\tilde{\Omega}(N_c, z_p, V) = F(N_c, N_p, V) - \mu_p N_p. \quad (70)$$

The polymer chemical potential $\mu_p = (\partial F/\partial N_p)_{N_c, V} = \beta^{-1} \ln(\Lambda_p^3 \rho_p/\alpha)$ and equation (70) reduces to

$$\frac{\beta \tilde{\Omega}(N_c, z_p, V)}{V} = \rho_c [\ln(\Lambda_c^3 \rho_c) - 1] + \beta f_{\text{hs}}(\rho_c) - \rho_p(\rho_c, z_p), \quad (71)$$

where the polymer density in the system, ρ_p , depends on the colloid density ρ_c and on the polymer fugacity $z_p = \exp(\beta\mu_p)/\Lambda_p^3$. For ideal polymers $z_p = \rho_{p,r}$, the density of polymer in the reservoir is in chemical equilibrium with the system. Equating the two expressions for μ_p yields

$$\rho_p(\rho_c, z_p) = \alpha(\rho_c) \rho_{p,r} = \alpha(\rho_c) z_p, \quad (72)$$

with α given by equation (69). Inserting equation (72) into (71) leads to the standard free-volume result for the semi-grand potential density [4]. Note that $-V^{-1}\partial\tilde{\Omega}/\partial\mu_p = \rho_p$, consistent with the thermodynamic definition of $\tilde{\Omega}$.

At first sight it seems surprising that our DFT approach is equivalent to free-volume theory. Recall that the latter treats the semi-grand potential as the sum of a HS (colloid) part plus a contribution from an ideal gas of polymers in the free volume left by the colloids. The connections between the two approaches become clearer when we recognize the following.

- (i) The treatment of HSs is equivalent; α in free-volume theory is obtained from scaled-particle theory, while the DFT gives rise to the scaled particle equation of state for pure and binary HS mixtures.
- (ii) Free-volume theory can be regarded as an expansion of $\tilde{\Omega}$ in the fugacity z_p , about an HS reference system, that is truncated at the term linear in z_p [5, 13]. The linearity in z_p , or equivalently in η_p , is a key feature of our DFT which we imposed at the outset via the zero-dimensional route and in the alternative derivation of section 2.6. Note that once one has identified α as the ratio of polymer density in the system to that in the reservoir, see equation (72), its interpretation as the free-volume fraction for a single ideal polymer is immediate. That the DFT should yield the same formula for α as that of scaled-particle theory is then not so surprising. Nevertheless, it is pleasing that the two approaches, which appear to have rather distinct roots, do yield the same bulk free energy and hence the same (fluid) equation of state⁴. In particular they yield the same attractive contribution, $-\alpha(\rho_c)z_p$, to the grand potential density. It is this term which leads to the possibility of fluid-fluid demixing.

3.2. Fluid-fluid demixing

Phase behaviour in the AO model is a well studied problem [2–5]. It is striking that this simple model gives rise to stable, entropically driven fluid-fluid phase separation for sufficiently large size ratios q . Given that the free energy from our approach is identical to that from free-volume theory, it immediately follows that it gives rise to the same (fluid state) phase diagrams. We do not consider solid states in the present study. The phase separation into colloid-rich (polymer-poor) and colloid-poor (polymer-rich) fluid phases is analogous to liquid-gas separation with the polymer reservoir fraction $\eta_{p,r}$, or z_p , playing the role of inverse temperature. Free-volume theory for the AO model predicts stable liquid-gas coexistence for $q > 0.32$. For smaller values of q this transition becomes metastable with respect to a broad, in η_c , fluid-solid transition [4, 5]. Here we focus on demixing for size ratios in the range $0.4 \leq q \leq 1$, where we expect stable liquid-gas coexistence.

In order to calculate the binodal we perform a common-tangent construction on the semi-grand potential $\tilde{\Omega}$, equation (71), at fixed z_p (or $\eta_{p,r}$). This is equivalent to equating the total pressure and chemical potentials of each species in the two coexisting phases. It should be noted that the canonical free energy F does not display any obvious double-minimum structure as a function of η_c , η_p . The spinodal is the locus of statepoints where the curvature of the semi-grand potential changes its sign at fixed $\eta_{p,r}$. In practice, a canonical calculation can be performed more easily. The boundary of stability is obtained by solving $\det[\partial^2(F/V)/\partial\rho_i\partial\rho_j] = 0$, $i, j = c, p$. This can be done analytically, and we obtain the spinodal from the following equation:

⁴ We note that in calculations, e.g. [5], based on free-volume theory the Carnahan-Starling approximation is often used for f_{hs} whereas in the DFT approach the PY compressibility approximation (68) must be employed.

9368

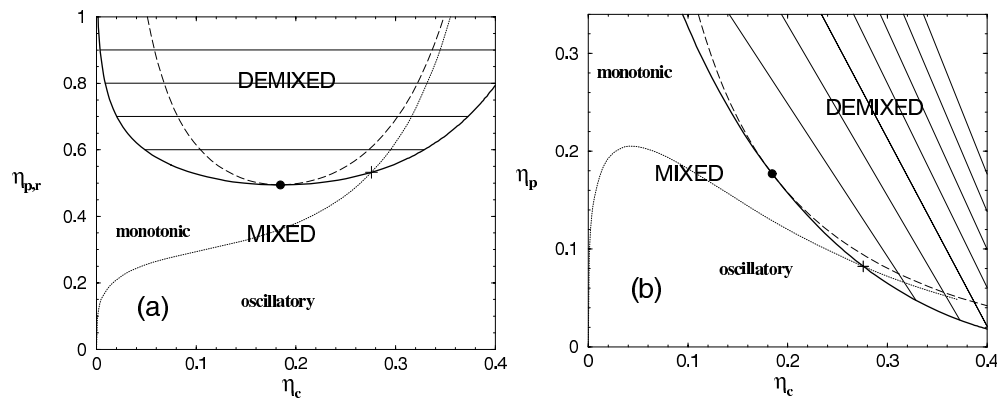
M Schmidt *et al*

Figure 1. Demixing phase diagram of the AO model for size ratio $q = 0.6$. The binodal (thick curve), spinodal (dashed curve), tie lines (thin curves), FW line (dotted curve), critical point (dot) and intersection of the binodal and the FW line (cross) are shown for (a) the reservoir representation using the colloid packing fraction η_c and polymer reservoir fraction $\eta_{p,r}$ as variables and (b) the system representation using η_c and the actual polymer fraction η_p as variables. The FW line denotes the line where the asymptotic decay of pair correlations crosses over from monotonic to oscillatory. Note that these phase diagrams display only the fluid portion of the phase diagram; a fluid–solid transition occurs for higher values of η_c .

$$\eta_p = \frac{\theta_1^4 \theta_2 / \eta_c}{12\theta_1^3 + 15q\theta_1^2\theta_2 + 6q^2\theta_1\theta_2^2 + q^3\theta_2^3}, \quad (73)$$

where $\theta_1 = 1 - \eta_c$, and $\theta_2 = 1 + 2\eta_c$. Results obtained in one representation are easily converted to the other using equation (72).

In figure 1 we display the demixing phase diagram for size ratio $q = 0.6$. In the reservoir representation (figure 1(a)), we see that the form of the phase diagram does resemble the gas–liquid portion of the phase diagram of a simple substance provided the polymer reservoir density $\eta_{p,r}$ is replaced by inverse temperature. Upon increasing $\eta_{p,r}$ the system separates into phases with different compositions and the tie lines connecting coexisting phases are horizontal in this representation. The binodal and spinodal coincide at the (lower) critical point. Also shown in figure 1 is the FW line, which divides the phase diagram into regions where the asymptotic decay of pair correlations is either monotonic or oscillatory. We shall discuss this in detail in section 3.5.

The actual polymer density in the system may be considerably different from that in the reservoir, because insertion of polymers into the system is hindered by the presence of the colloids, i.e. $\eta_p < \eta_{p,r}$. The phase diagram in the system representation (figure 1(b)) shows the mixed one-phase region in the lower left part and the demixed two-phase region in the upper right part of the η_c, η_p plane. The tie lines between coexisting phases now have a negative slope. Changing the size ratio q has a pronounced effect on the location of the binodal. We display results for $q = 0.4, 0.6, 0.8, 1$ in figure 2. As q increases, the binodals move to higher $\eta_{p,r}$, and the critical point shifts to lower colloid fractions η_c (see figure 2(a)). The actual polymer density η_p at the critical point increases slowly with q (figure 2(b)).

3.3. Direct correlation functions

We now shift our attention to the structural properties of the bulk AO mixture, focusing first on the pair direct correlation functions $c_{ij}^{(2)}(r)$. Recall that for binary HS mixtures the

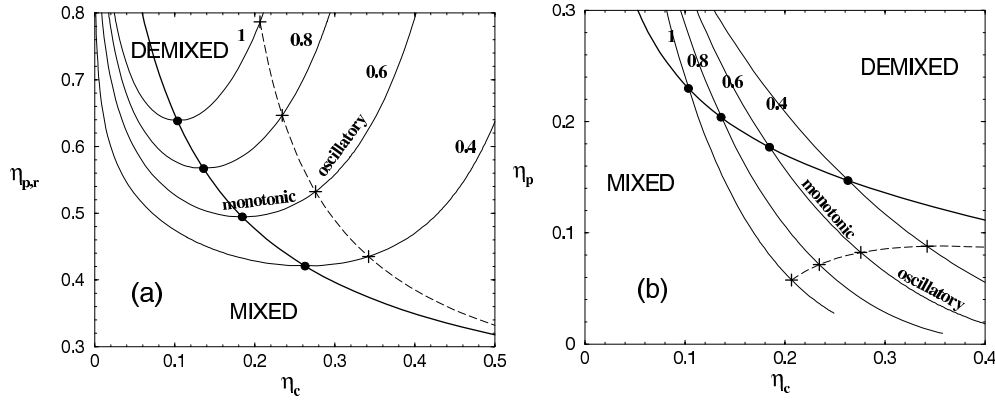


Figure 2. Phase diagram of the AO model for size ratios $q = 0.4, 0.6, 0.8, 1$. The binodals (thin curves), critical points (dots joined by a thick curve) and intersections of the FW line and the binodals (crosses joined by a dashed curve) are shown for (a) the reservoir representation with η_c and $\eta_{p,r}$ and (b) the system representation with η_c and η_p .

$c_{ij}^{(2)}(r)$ obtained from solving the PY closure are surprisingly simple (polynomial) expressions. Considerable insight into the structure of HS fluids was gained by introducing a new geometrical interpretation of the direct correlation functions [40]. This insight eventually led to the development of the FMT density functional for HS. In the present work the opposite route is followed. Here, starting from the functional we developed in section 2, the $c_{ij}^{(2)}(r)$ are obtained as second functional derivatives with respect to the density fields. This yields an (approximate) geometrical representation of the pair direct correlation functions of the AO model. Explicit analytic expressions are given below. It is important to note from the outset that the $c_{ij}^{(2)}(r)$ derived from the present DFT are not (except for special cases) equivalent to those obtained by solving the PY closure for the AO model. In particular, the core condition on the pair correlation functions, $g_{ij}(r < R_i + R_j) = 0$, is violated in the present approximation, if pair and direct correlation functions are related via the OZ relation. Nevertheless, in the light of the discussion of section 2.6, we do expect $c_{ij}^{(2)}$ to be similar to those from PY. Recall that the latter can only be obtained numerically for the AO model. The direct correlation functions are given by

$$c_{ij}^{(2)}(r, r') = -\frac{\delta^2 \beta F_{\text{exc}}}{\delta \rho_i(r) \delta \rho_j(r')} = -\sum_{v, \gamma} \psi_{v\gamma}^{ij} w_v^i \otimes w_\gamma^j, \quad (74)$$

where the \otimes denotes the convolution and $\psi_{v\gamma}^{ij} = \partial^2 \Phi / (\partial n_v^i \partial n_\gamma^j)$, and as usual $i, j = c, p$. Φ is the free-energy density given by equations (24)–(31). Carrying out this analysis reveals that the bulk direct correlation functions possess the following structure:

$$c_{cc}^{(2)}(\eta_c, \eta_p; r) = c_{\text{hs}}^{(2)}(\eta_c; r) + \eta_p c_*^{(2)}(\eta_c; r), \quad (75)$$

$$c_{cp}^{(2)}(\eta_c, \eta_p; r) = c_{\text{cp}}^{(2)}(\eta_c; r), \quad (76)$$

$$c_{pp}^{(2)}(\eta_c, \eta_p; r) = 0, \quad (77)$$

where $c_{\text{hs}}^{(2)}$ is the solution of the PY closure for one-component HS. The simple dependence on η_p originates from the linearity of F_{exc} in the polymer density profile. This dependence allows $c_{cc}^{(2)}$ to be split into two parts: $c_{\text{hs}}^{(2)}$ is the residual contribution, present even if polymers are absent, while $c_*^{(2)}$ is the contribution from introducing the polymers, i.e. the function $c_*^{(2)}$

describes the part of the direct correlations between pairs of colloid due to the presence of the polymers. The spatial dependence of $c_*^{(2)}$ is similar to that of $c_{\text{hs}}^{(2)}$, and will be discussed below. Linearity of the functional in $\rho_{\text{p}}(r)$ implies that $c_{\text{cp}}^{(2)}$ is independent of the polymer density. The size ratio q determines the shape of $c_{\text{cp}}^{(2)}$. Finally, the linearity ensures that the polymer–polymer direct correlation function vanishes, as in the PY closure for the AO model. These observations are, of course, consistent with the low density expansion of $c_{ij}^{(2)}$ used in the alternative derivation of the functional given in section 2.6.

The range of the $c_{ij}^{(2)}$ is determined by the geometric nature of the weight functions w_v^i . As these are characteristic of single-particle geometries, it is clear that the $c_{ij}^{(2)}$ must vanish beyond a separation which is the sum of both particle radii involved, i.e. $c_{ij}^{(2)}(r > R_i + R_j) = 0$, as is found in the PY treatment. Clearly, this property reflects the *approximate* nature of the functional. In an exact treatment we would expect contributions beyond the range $R_i + R_j$.

We now give explicit expressions for $c_{ij}^{(2)}$ entering equations (75)–(77). Recall that the PY solution [41] for HS with packing fraction η_{c} and diameter $\sigma_{\text{c}} (\equiv 2R_{\text{c}})$ is

$$c_{\text{hs}}^{(2)}(\eta_{\text{c}}; x) = -\frac{\Theta(\sigma_{\text{c}} - r)}{(1 - \eta_{\text{c}})^4} \sum_i \tau_i^{\text{hs}} x^i, \quad (78)$$

where τ_i^{hs} are functions of the colloid packing fraction η_{c} and $x = r/\sigma_{\text{c}}$. The only non-vanishing coefficients are

$$\begin{aligned} \tau_0^{\text{hs}} &= (1 + 2\eta_{\text{c}})^2, \\ \tau_1^{\text{hs}} &= -\frac{3\eta_{\text{c}}}{2}(2 + \eta_{\text{c}})^2, \\ \tau_3^{\text{hs}} &= \frac{\eta_{\text{c}}}{2}(1 + 2\eta_{\text{c}})^2. \end{aligned} \quad (79)$$

The polymer contribution to $c_{\text{cc}}^{(2)}$ is given by

$$c_*^{(2)}(\eta_{\text{c}}; r) = -\frac{\Theta(\sigma_{\text{c}} - r)}{2q^3} \sum_i \tau_i^* x^i, \quad (80)$$

where the only non-vanishing coefficients are

$$\begin{aligned} \tau_0^* &= 2[1 + A + 2A\gamma + 4B\gamma + 6B\gamma^2 + 3C\gamma^2(3 + 4\gamma)], \\ \tau_1^* &= -3 - 2A + (2B)/3 - 6A\gamma - 8B\gamma - 18B\gamma^2 - 2C\gamma[-1 + 9\gamma(1 + 2\gamma)], \\ \tau_3^* &= 1 + 2A\gamma + 6B\gamma^2 + 12C\gamma^3, \end{aligned} \quad (81)$$

where A, B, C and γ are defined below equation (69). The limiting form at small colloid density is

$$c_*^{(2)}(\eta_{\text{c}} \rightarrow 0; r) = \begin{cases} -2(1 + q)^3 + 3(1 + q)^2 x - x^3, & r < \sigma_{\text{c}}, \\ 0, & \text{otherwise.} \end{cases} \quad (82)$$

The colloid–polymer direct correlation function is given by

$$c_{\text{cp}}^{(2)}(\eta_{\text{c}}, r) = \begin{cases} -(1 + \gamma)(1 + A\gamma + 2B\gamma^2 + 3C\gamma^3), & r < |R_{\text{c}} - R_{\text{p}}| \\ -(1 + \gamma) \sum_i \tau_{\text{cp},i} x^i, & |R_{\text{c}} - R_{\text{p}}| \leq r \leq |R_{\text{c}} + R_{\text{p}}| \\ 0, & \text{otherwise,} \end{cases} \quad (83)$$

where the only non-vanishing coefficients are

$$\begin{aligned}\tau_{\text{cp},-1} &= -\frac{3\gamma}{32}(1-q)^2[3+q+3\gamma(1+q)]^2, \\ \tau_{\text{cp},0} &= \frac{1}{2}\{2+\gamma[7+3\gamma(5+3\gamma)+9\gamma q^2+(1+3\gamma)^2q^3+3q(1+q)]\}, \\ \tau_{\text{cp},1} &= -\frac{3\gamma}{4}[5+3\gamma(4+3\gamma)+2q+6\gamma q+(q+3\gamma q)^2], \\ \tau_{\text{cp},3} &= \frac{\gamma}{2}(1+3\gamma)^2.\end{aligned}\quad (84)$$

In the limit $\eta_c \rightarrow 0$ the colloid-polymer direct correlation function reduces to the colloid-polymer Mayer function $f_{\text{cp}}(r)$, i.e.

$$c_{\text{cp}}^{(2)}(\eta_c \rightarrow 0; r) = \begin{cases} -1, & r < R_c + R_p \\ 0, & \text{otherwise.} \end{cases}\quad (85)$$

Simpler expressions are obtained in the special case $q = 1$, where only a single length scale is present, and one can use $c_*^{(2)} = \frac{\partial}{\partial \eta_c} c_{\text{hs}}^{(2)}(\eta_c; r)$ and $c_{\text{cp}}^{(2)} = c_{\text{hs}}^{(2)}(\eta_c; r)$. It follows that

$$c_*^{(2)}(\eta_c; r) = -\frac{\Theta(\sigma_c - r)}{(1 - \eta_c)^5} \sum_i \tau_i^* x^i, \quad (86)$$

where the only non-vanishing coefficients are

$$\begin{aligned}\tau_0^* &= 4(2 + \eta_c)(1 + 2\eta_c), \\ \tau_1^* &= -\frac{3}{2}(2 + \eta_c)[2 + \eta_c(9 + \eta_c)], \\ \tau_3^* &= \frac{1}{2}(1 + 2\eta_c)[1 + \eta_c(9 + 2\eta_c)].\end{aligned}\quad (87)$$

In order to illustrate the variation with r and η_c , we plot the various functions, for $q = 0.6$, in figure 3. $c_{\text{hs}}^{(2)}(r)$ is shown in figure 3(a) with η_c in the range 0–0.4. This is the contribution to $c_{\text{cc}}^{(2)}$ arising solely from the ‘bare’ colloids. The polymers generate an (additive) contribution $\eta_p c_*^{(2)}(r)$, where the function $c_*^{(2)}(r)$, plotted in figure 3(b), has a similar form to $c_{\text{hs}}^{(2)}(r)$. Changing the size ratio q does not dramatically alter the shape; it merely changes the vertical scale of the plot. Finally, figure 3(c) shows $c_{\text{cp}}^{(2)}(r)$ for the same values of η_c . This function is constant for $r < |R_c - R_p| = 0.2\sigma_c$ and vanishes for $r > |R_c + R_p| = 0.8\sigma_c$, for the present size ratio. All three functions become more negative in the core region as η_c is increased. Note that the polymer density η_p only enters $c_{\text{cc}}^{(2)}$ through the linear dependence in equation (75).

Summarizing, we find it remarkable that the direct correlation functions for the AO model, which is characterized by two thermodynamic variables η_c and η_p , can be described by relatively simple analytic expressions and that all relevant information, for a given size ratio q , can be condensed into as few as three plots.

3.4. Structure factors and criticality

The total pair correlation functions $h_{ij}(r) = g_{ij}(r) - 1$, where $g_{ij}(r)$ are pair correlation functions, are related to the direct correlation functions $c_{ij}^{(2)}(r)$ via the mixture OZ relations [41]. These simplify in Fourier space:

$$h_{\text{cc}}(k) = \frac{c_{\text{cc}}^{(2)}(k) + \rho_p[(c_{\text{cp}}^{(2)}(k))^2 - c_{\text{cc}}^{(2)}(k)c_{\text{pp}}^{(2)}(k)]}{D(k)} \quad (88)$$

$$h_{\text{pp}}(k) = \frac{c_{\text{pp}}^{(2)}(k) + \rho_c[(c_{\text{cp}}^{(2)}(k))^2 - c_{\text{cc}}^{(2)}(k)c_{\text{pp}}^{(2)}(k)]}{D(k)} \quad (89)$$

$$h_{\text{cp}}(k) = \frac{c_{\text{cp}}^{(2)}(k)}{D(k)}, \quad (90)$$

9372

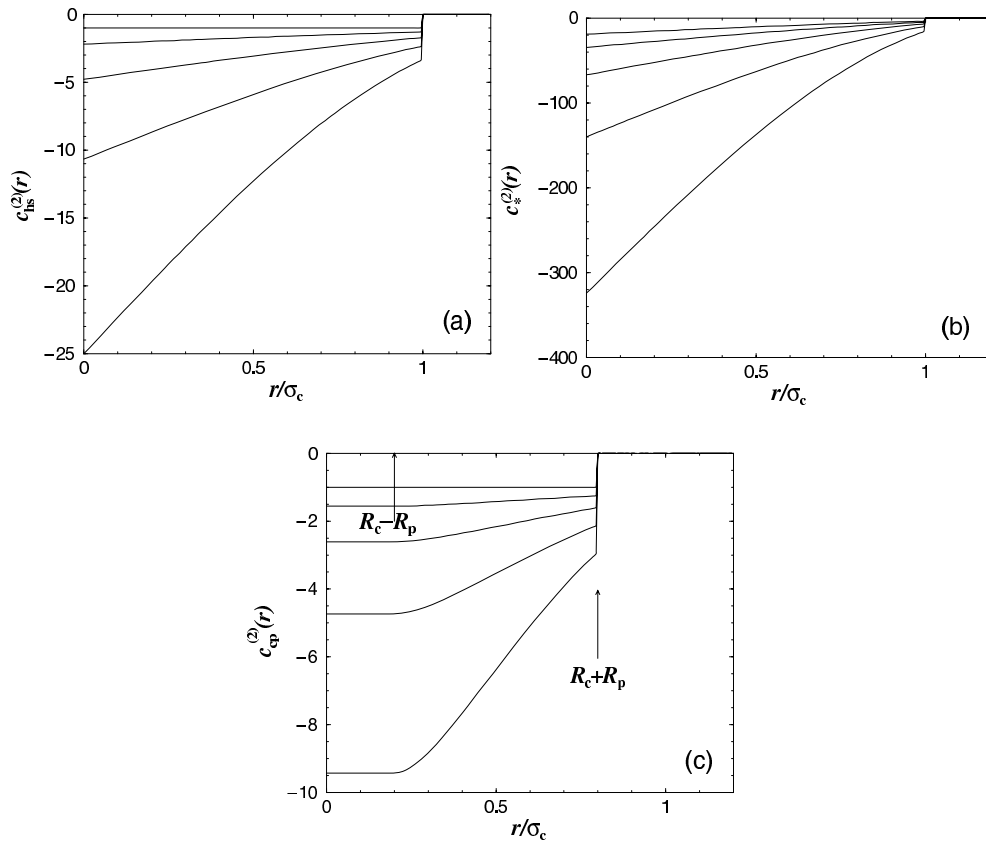
M Schmidt *et al*

Figure 3. Pair direct correlation functions for $\eta_c = 0, 0.1, 0.2, 0.3, 0.4$ (from top to bottom) obtained for the AO model with size ratio $q = 0.6$: (a) colloid contribution $c_{hs}^{(2)}(r)$ to $c_{cc}^{(2)}(r)$; (b) polymer contribution $c_p^{(2)}(r)$ to $c_{cc}^{(2)}(r)$; (c) full colloid–polymer direct correlation function $c_{cp}^{(2)}(r)$. These results are obtained from equations (78), (80), (83).

where $h_{ij}(k)$ is the three-dimensional Fourier transform of $h_{ij}(r)$ and the common denominator is given by

$$D(k) = [1 - \rho_c c_{cc}^{(2)}(k)][1 - \rho_p c_{pp}^{(2)}(k)] - \rho_c \rho_p [c_{cp}^{(2)}(k)]^2. \quad (91)$$

The corresponding partial structure factors $S_{ij}(k)$ then can be obtained via [41]

$$S_{ij}(k) = \delta_{ij} + (\rho_i \rho_j)^{1/2} h_{ij}(k). \quad (92)$$

It is sometimes useful to describe the like–like structure factors by means of the OZ relation

$$S_{ii}(k) = 1/(1 - \rho_i c_{ii}^{(2),\text{eff}}(k)), \quad (93)$$

that has the same formal structure as the OZ relation for a one-component system, and that employs an effective direct correlation function given by

$$c_{ii}^{(2),\text{eff}}(k) = c_{ii}^{(2)}(k) + \frac{\rho_j c_{ij}^{(2)}(k)^2}{1 - \rho_j c_{jj}^{(2)}(k)}. \quad (94)$$

It is straightforward to show that equations (93) and (94) are completely equivalent to the standard mixture formulation of equations (88)–(92). So far all is general but now we note

that in the present approximation $c_{pp}^{(2)} = 0$, see equation (77). This leads to rather simple expressions for the effective direct correlation functions:

$$c_{cc}^{(2),\text{eff}}(k) = c_{cc}^{(2)}(k) + \rho_p c_{cp}^{(2)}(k)^2, \quad (95)$$

$$c_{pp}^{(2),\text{eff}}(k) = \frac{\rho_c c_{cp}^{(2)}(k)^2}{1 - \rho_c c_{cc}^{(2)}(k)}. \quad (96)$$

In particular, equation (96) with (93) allows us to understand why S_{pp} can be significantly different from unity, the ideal gas result, even though $c_{pp}^{(2)} = 0$. Results for $S_{ij}(k)$ and $g_{ij}(r)$ were presented in an earlier letter [31]. We found that for $q = 0.15$, $\eta_c = 0.3$ and $\eta_p = 0.05$ all three partial pair correlation functions were close to the corresponding PY results. The latter were obtained numerically [8]. For $q = 0.1$, $\eta_c = 0.25$, $\eta_p = 0.107$ we compared our results for $S_{cc}(k)$ and $g_{cc}(r)$ with those of simulation (for this small size ratio there is an exact mapping to an effective one-component colloid system for which simulations are easily performed [5]). The overall agreement was reasonable, although the structure factor was a little out of phase and the results of the DFT strongly underestimated the very high contact value $g_{cc}(\sigma_c)$ and violated (weakly) the core condition $g_{cc}(r) = 0$, $r < \sigma_c$.

In the present study, we are concerned with less extreme size ratios where the effective (depletion) potential between colloids is longer ranged and less deep near contact than the cases investigated earlier and we expect the DFT to fare somewhat better. An important advantage of the present DFT approach (over most integral equation theories) is that the thermodynamic and structural routes to the spinodal, binodal and, therefore, the critical point are consistent. In particular, the spinodal line, equation (73), can equally well be found by considering the locus of divergence of $S_{ij}(k)$, i.e. the vanishing of $D(k)$ in equation (91). This consistency is especially important in the vicinity of the critical point.

The location of the critical point in the $\eta_c, \eta_{p,r}$ plane can be obtained by tracing the coexistence densities towards small $\eta_{p,r}$, but careful numerical work is needed to obtain accurate results. In the present case, the critical point can be obtained in a simpler way: starting from the spinodal in the system representation, equation (73), we switch to the reservoir representation using equations (72), (69), and obtain the spinodal polymer reservoir density as a function of colloid density, $\eta_{p,r}^{\text{spin}}(\eta_c)$. As the critical point is at the minimum of this function, finding the minimum is a stable and numerically trivial operation. For states slightly removed from criticality we expect OZ behaviour: $S_{ij}(k) = S_{ij}(0)/[1 + \xi^2 k^2 + O(k^4)]$, where the correlation length ξ is the *same* for all pairs ij . This general result is a direct consequence of the OZ relations for a mixture (88)–(90) and follows from the fact that $D(k)$ is the common denominator for all pairs, equation (91). As the $S_{ij}(k)$ are given analytically in the present theory, we can confirm explicitly the OZ behaviour. We find that the common correlation length diverges with the mean-field exponent $\nu = 1/2$ and on a path at fixed $\eta_c = \eta_c^{\text{crit}}$ we define the amplitude ξ_0 via $\xi = \xi_0/(\eta_{p,r}^{\text{crit}} - \eta_p)^{1/2}$. ξ_0/σ_c depends only on the size ratio q . It is roughly proportional to the mean of the colloid and polymer diameters and is conveniently expressed as $\xi_0 = \frac{1}{2}(\sigma_c + \sigma_p)/K(q)$, where typical values are $K(q) = 3.00, 2.36, \sqrt{5}$, for $q = 0.4, 0.8, \infty$, respectively. Note that $\sigma_p = 2R_p$. Figure 4 displays the partial structure factors calculated for $q = 0.6$ and a fixed value of η_c , equal to the critical point value $\eta_c^{\text{crit}} = 0.1843$. Results are presented for four values of $\eta_{p,r}$, corresponding to the critical ‘isochore’ in figure 1(a). For $\eta_{p,r} = 0$ (no polymer) $S_{cc}(k)$ is simply the (PY) HS structure factor for $\eta_c = 0.1843$. Upon increasing $\eta_{p,r}$, $S_{cc}(k)$ develops a maximum at $k = 0$, OZ behaviour ensues and then, at the critical value $\eta_{p,r}^{\text{crit}} = 0.4943$, $S_{cc}(0) \rightarrow +\infty$. $S_{pp}(k)$ has a somewhat different variation. This function develops its leading maximum at $k = 0$ for very small polymer fractions and $S_{pp}(0)$ is very large even for $\eta_{p,r} = 0.36$, well away from the critical point. As $\eta_{p,r} \rightarrow \eta_{p,r}^{\text{crit}}$, $S_{pp}(0)$

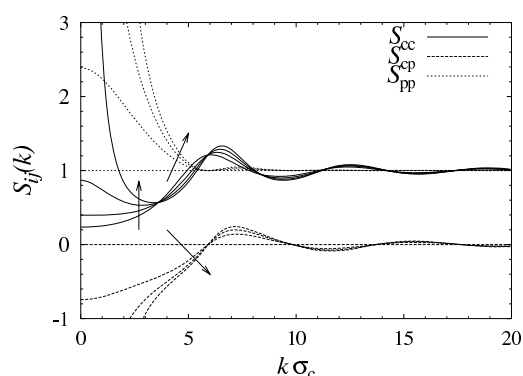


Figure 4. Partial structure factors S_{cc} , S_{cp} , S_{pp} for size ratio $q = 0.6$ at fixed colloid fraction $\eta_c = \eta_c^{\text{crit}} = 0.1843$, and increasing (indicated by arrows) polymer reservoir density $\eta_{p,r} = 0, 0.2, 0.36, \eta_{p,r}^{\text{crit}} = 0.4943$. On approaching the critical point, along a vertical path in the phase diagram of figure 1(a), $S_{cc}(k)$ and $S_{pp}(k)$ become increasingly positive and $S_{cp}(k)$ increasingly negative at small wavenumbers k . Note that for $\eta_{p,r} = 0$, $S_{cc}(k)$ corresponds to the pure HS structure factor.

diverges in the same fashion as $S_{cc}(0)$. By contrast, $S_{cp}(0)$ becomes increasingly negative and diverges to $-\infty$ on approaching the critical point. Similar features are found for other size ratios.

The form of $S_{pp}(k)$ is particularly striking and has repercussions for the distribution of polymer in the mixture. Note that similar shapes of $S_{pp}(k)$ were found in PY calculations [7, 8] for the AO mixture.

3.5. Asymptotic decay of correlations: Fisher–Widom line

The pair correlation functions $g_{ij}(r)$ should exhibit qualitatively different asymptotic decay at different points in the phase diagram. In the neighbourhood of the critical point $g_{ij}(r)$ will decay monotonically, as befits OZ behaviour, whereas for small values of $\eta_{p,r}$ the mixture is HS-like and the $g_{ij}(r)$ should exhibit damped oscillatory decay as $r \rightarrow \infty$. Thus upon varying the thermodynamic parameters $\eta_{p,r}$ and η_c the ultimate decay of $g_{ij}(r)$ should change from being oscillatory to purely monotonic [42–45]. The line in the phase diagram separating the two types of decay is termed the FW line [42] after the authors who introduced the concept. This is not a line of thermodynamic singularity. Rather it indicates crossover to different structural regimes. Although the FW line is defined by considering the decay of *bulk* pair correlation functions, it plays a key role in inhomogeneous situations since the asymptotic decay into bulk of one-body density profiles is determined by the same physical considerations. Thus it is relevant for several interfacial phenomena [32, 43, 44, 46].

In order to calculate the FW line, we again exploit the fact that our partial structure factors are given analytically. Since the asymptotic decay of $g_{ij}(r)$ is determined by the singularities of the $S_{ij}(k)$ in the *complex* plane our strategy is to trace the locations of these. We denote these singularities $k = a_1 + ia_0$. Oscillatory behaviour, $h_{ij}(r \rightarrow \infty) \propto \cos(a_1 r) \exp(-a_0 r)/r$, stems from poles with non-zero real part a_1 , whereas monotonic behaviour, $h(r \rightarrow \infty) \propto \exp(-a_0 r)/r$, stems from poles residing on the imaginary axis, $a_1 = 0$. The ultimate decay is governed by the pole with the *smallest* imaginary part a_0 [44]. We obtain the location of the singularities by finding the roots of $1/|S_{ij}(k)| = 0$ numerically, taking appropriate starting values. This is equivalent to finding the zeros of $D(k)$, equation (91), in the complex plane.

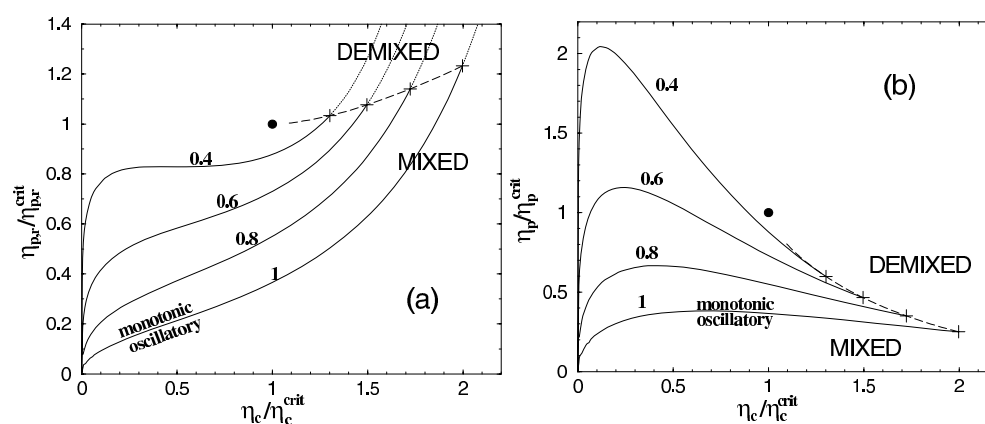


Figure 5. FW lines for size ratios $q = 0.4, 0.6, 0.8, 1$ plotted in scaled variables. The FW lines are denoted by solid curves; the dotted extensions are metastable, i.e. they lie inside the binodal. The intersections of the FW lines and the binodal are crosses joined by a dashed curve. (a) Scaled reservoir representation with $\eta_c/\eta_c^{\text{crit}}$ and $\eta_{p,r}/\eta_{p,r}^{\text{crit}}$; (b) scaled system representation with $\eta_c/\eta_c^{\text{crit}}$ and $\eta_p/\eta_p^{\text{crit}}$. For each q , increasing $\eta_{p,r}$ or η_p at fixed η_c leads to crossover from monotonic to oscillatory decay at the FW line.

Note that all partial structure factors possess the same singularities, because of the common denominator $D(k)$. That is why all the $h_{ij}(r)$ exhibit the same exponential decay length a_0^{-1} and, when oscillatory, the same wavelength $2\pi/a_1$, and why there is a *single* FW line that characterizes the crossover in a mixture. In practice we chose $S_{cc}(k)$ and calculated the pole with the smallest a_0 residing on the imaginary axis and also the pole with the smallest a_0 but with $a_1 > 0$. At fixed η_c , we varied η_p until the imaginary parts a_0 of both poles were identical, giving a point on the FW line. Following this procedure for all η_c maps out the complete FW line for a given size ratio. In figure 1 we plot the FW line for $q = 0.6$ in both the reservoir and system representations. The FW line intersects the binodal on the colloid-rich side (liquid) and is bounded at high $\eta_{p,r}$ by the liquid spinodal. For this size ratio the overall shape and location of the FW line appears similar to that found [43, 45] for simple fluids, whose interatomic pair potential is of finite range and which exhibit liquid-gas phase separation, once we recall that $\eta_{p,r}$ is equivalent to inverse temperature. Figure 2 displays the intersection of the FW line with the binodal for several values of size ratio q . As q increases the intersection occurs further from the critical point, exposing a larger range of monotonic decay along the liquid side of the binodal. In figure 5 we plot the FW lines in terms of the scaled variables $\eta_c/\eta_c^{\text{crit}}$ and $\eta_{p,r}/\eta_{p,r}^{\text{crit}}$ (or $\eta_p/\eta_p^{\text{crit}}$) for four values of q . As q increases we observe that a larger portion of the scaled phase diagram lies on the monotonic side of the FW line. For $q = 0.4$ the FW line lies just below the critical point and most of the single-phase portion of the scaled phase diagram now falls on the oscillatory side. This might reflect the fact that for $q = 0.4$ (and smaller values of q) the FW line exhibits a minimum when plotted in the reservoir representation, figure 5(a). The presence of the minimum implies that on increasing η_c at an appropriate fixed $\eta_{p,r}$ the decay of correlation functions should change from monotonic to oscillatory to monotonic and, finally, to oscillatory. Whether such behaviour reflects the fact that the fluid-fluid phase separation should be close to becoming metastable (w.r.t. fluid-solid) for these small values of q can only be ascertained by more sophisticated treatments. What is probably more relevant for a real colloid-polymer mixture is figure 5(b) which shows that in the system representation there is a maximum in the FW line for all four values of q . Thus increasing η_c at a sufficiently

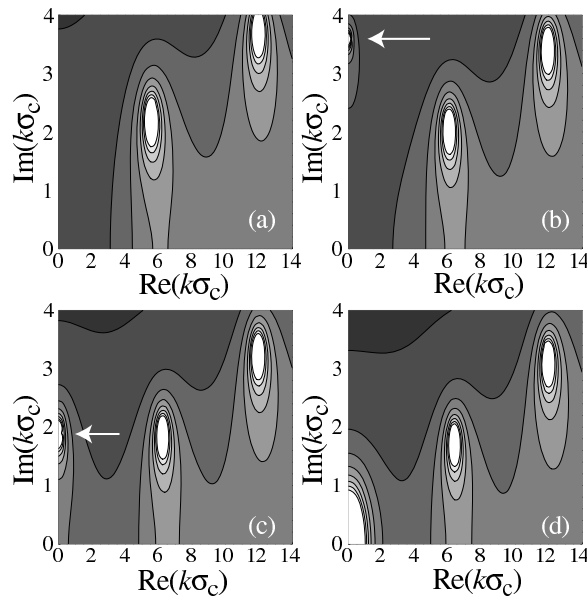


Figure 6. Absolute value of the colloid–colloid structure factor $|S_{cc}|$ in the complex plane for size ratio $q = 0.6$ at fixed colloid fraction $\eta_c = \eta_c^{\text{crit}} = 0.1843$, and four values of polymer reservoir density $\eta_{p,r}$: (a) pure HS, $\eta_{p,r} = 0$ ($\eta_p = 0$); (b) $\eta_{p,r} = 0.2$ ($\eta_p = 0.07161$) in the oscillatory regime; (c) on the FW line, $\eta_{p,r} = 0.36$ ($\eta_p = 0.1290$); (d) at the critical point, $\eta_{p,r} = 0.4943$ ($\eta_p = 0.1770$). Arrows indicate the (smallest) purely imaginary pole. This pole lies at the origin in (d). Bright (dark) colour indicates large (small) values. Note that these statepoints are the same as in figure 4.

small fixed polymer fraction η_p should lead to crossover from monotonic to oscillatory back to monotonic decay of correlations (see also figure 1(b)). Finally, we remark that in the limit $\eta_{p,r} \rightarrow 0$, the FW line smoothly approaches the origin, $\eta_c = 0$. This is to be expected, since for pure HS $g(r)$ exhibits oscillatory decay for all non-zero values of the packing fraction. Such behaviour is equivalent to that found for simple fluids in the limit $T \rightarrow \infty$ [45]. We can summarize and visualize much of what is described in this subsection by analysing the behaviour of the structure factors in the complex plane, and in figure 6 we report results for $|S_{cc}(k)|$ with $q = 0.6$, taken along the same critical ‘isochore’, $\eta_c = \eta_c^{\text{crit}}$, as in figure 4.

Pure HS (figure 6(a)) do not possess a pole on the imaginary axis so the two maxima correspond to complex poles; the dominant one corresponds to $a_1\sigma_c \sim 2\pi$. Upon increasing the polymer reservoir density to $\eta_{p,r} = 0.2$ (figure 6(b)), a pole appears on the imaginary axis and this moves downwards with $\eta_{p,r}$, until its value equals that of the imaginary part of the neighbouring complex pole (figure 6(c)) defining a point on the FW line. At the critical point, the pole on the imaginary axis reaches the origin (figure 6(d)). This pole leads to the divergence of the physical structure factors, $S_{ij}(k \rightarrow 0)$, at the critical point. Figure 4 displays the physical structure factors at the same statepoints.

3.6. Effective interaction between colloids: depletion potential

In their original study Asakura and Oosawa [1] determined the effective potential, $V_{AO}(r; z_p)$, between two HS colloids (or macroparticles) in a sea of ideal polymer of fugacity z_p . Their celebrated potential is attractive in the range $2R_c < r < 2(R_c + R_p)$ and vanishes for larger

separations r . The attraction arises from the depletion effect whereby polymer is excluded or depleted from the region between the colloids when the separation of their surfaces is $< 2R_p$. More formally, V_{AO} describes the two-body contribution to the effective one-component Hamiltonian, H^{eff} , obtained by integrating out the polymer degrees of freedom in the binary AO mixture. For a homogeneous system H^{eff} is given by [5]

$$\beta H^{\text{eff}}(\{\mathbf{R}_i\}; z_p) = V z_p (-1 + \eta_c (1 + q)^3) + \beta \sum_{i < j} V_{AO}(|\mathbf{R}_i - \mathbf{R}_j|; z_p) + \text{higher body terms}, \quad (97)$$

where the first term is independent of the colloid coordinates $\{\mathbf{R}_i\}$. The pair potential is

$$\beta V_{AO}(\{\mathbf{R}_i\}; z_p) = \beta V_{cc}(|\mathbf{R}_i - \mathbf{R}_j|) - z_p \int d^3r f_{cp}(\mathbf{R}_i - \mathbf{r}) f_{cp}(\mathbf{R}_j - \mathbf{r}), \quad (98)$$

where V_{cc} is the direct colloid-colloid (HS) interaction and f_{cp} is the colloid-polymer Mayer function. The second term in equation (98) is called the depletion potential. Another interpretation of V_{AO} comes from considering the pair correlation functions $g_{ij}(r)$ in a dilute (in colloid) binary AO mixture. In the limit $\eta_c \rightarrow 0$, $g_{cc}(r) \approx \exp(-\beta V_{AO}(r; z_p))$.

Clearly, any exact treatment of the mixture should yield this exact result. Note that this is equivalent to requiring the effective colloid-colloid direct correlation function, see equation (94), to reduce to

$$c_{cc}^{(2),\text{eff}}(r) \approx \exp(-\beta V_{AO}(r; z_p)) - 1 \quad (99)$$

for $\eta_c \rightarrow 0$. It is well known that the PY closure for the AO mixture (and, indeed, for highly asymmetric HS mixtures where V_{AO} should be replaced by the HS depletion potential) does not yield the correct limiting behaviour. Rather one finds that for low colloid fractions $g_{cc}(r) \sim 1 - \beta V_{AO}(r; z_p)$ for $r > 2R_c$, which implies the PY results for the contact value $g_{cc}(2R_c^+)$ are too small [8, 47, 48]. Given that our present DFT bears a close resemblance to the PY approximation we might expect to observe similar failings [31]. The advantage here is that we have explicit, analytic results for $c_{ij}^{(2)}$ so it is straightforward to analyse the behaviour of correlations in the low η_c limit. From equations (75), (78), (80), (82) we can ascertain the limiting behaviour of $c_{cc}^{(2),\text{eff}}(r)$ given by the Fourier transform of equation (95). Since $c_{cc}^{(2)}(\eta_p; r) = 0$ for $r > 2R_c$ and $c_{cp}^{(2)}(\eta_c \rightarrow 0; r) = f_{cp}(r)$ it follows that DFT predicts, for $\eta_c \rightarrow 0$,

$$c_{cc}^{(2),\text{eff}}(r) = -\beta V_{AO}(r; z_p), \quad r > 2R_c, \quad (100)$$

where we used the fact that $z_p = \rho_{p,r} = \rho_p$ in the limit $\eta_c \rightarrow 0$. Thus our DFT does not yield the exact limiting result (99); the latter only reduces to (100) in the limit $z_p \rightarrow 0$. The present approach, via the OZ route to the pair correlation functions, suffers from the same failing as the PY approximation. Clearly both approximation schemes fail to incorporate the physical ingredients which are required to exponentiate $-\beta V_{AO}$.

However, we must not infer that the present DFT fails to incorporate the depletion effect which is, after all, the crucial feature of colloid-polymer mixtures. We have already seen in section 3.1 that the bulk free energy of the mixture acquires an *attractive* contribution; this contribution can only arise from the depletion effect. Moreover, the theory does generate an attractive contribution in $c_{cc}^{(2),\text{eff}}$, equation (100), albeit one that is too weak.

Within DFT the OZ route is not the only one to pair correlation functions. The alternative is the test particle route, whereby one fixes a particle of species i at the origin and determines the inhomogeneous one-body density profile $\rho_j(r)$ arising from the external potential $V_{ij}(r)$ exerted by the fixed particle. It follows that $g_{ij}(r) = \rho_j(r)/\rho_j(\infty)$. In applying the test particle prescription one solves the Euler-Lagrange equations for the one-body densities so all

that is required are the one-body direct correlation functions $c_i^{(1)}(r)$; these involve only a first derivative of F_{exc} , see equation (60). One can show that in the limit $\eta_c \rightarrow 0$, the test particle route for the present DFT yields the exact result $g_{\text{cc}}(r) \approx \exp(-\beta V_{\text{AO}}(r; z_p))$. An instructive way of obtaining this result is to implement the procedure developed by Roth *et al* [38] for calculating the depletion potential. The latter is given by

$$-\beta V_{\text{dep}}(r; z_p) = \lim_{z_c \rightarrow 0} [c_c^{(1)}(r) - c_c^{(1)}(\infty)], \quad (101)$$

where $c_c^{(1)}(r)$ refers to the situation where a colloid, fixed at the origin, exerts its field on the polymer and on a (test) colloid inserted at r [38]. $c_c^{(1)}(r)$ is easily calculated for the present DFT (the calculation mimics that for the binary HS functional given in [38]) and in the limit where the colloid density vanishes we find that βV_{dep} is proportional to the convolution of two Mayer functions, i.e. it reduces precisely to the second term in equation (98). That the analysis can be performed analytically and the result is much simpler than that for HS mixtures simply reflects the fact that $f_{\text{pp}}(r) = 0$ in the AO model.

With hindsight it is, perhaps, not too surprising that geometrically based DFT should describe correctly the depletion potential; the latter is merely a manifestation of excluded volume effects. Nevertheless, this exercise does indicate that the test particle route to $g_{\text{cc}}(r)$ is likely to be much more accurate than the OZ route, especially for situations where η_c is low and $\eta_{\text{p,r}}$ is high so that the depletion potential is strongly attractive and contact values $g_{\text{cc}}(2R_c^+)$ are very large. The test particle route also has the advantage that it guarantees that $g_{\text{cc}}(r) = 0$ for $r < 2R_c$ and $g_{\text{cp}}(r) = 0$ for $r < R_c + R_p$.

4. Discussion

We have derived a DFT for the binary AO mixture based on geometrical information about the hard and ideal spheres which constitute the AO model. Our FMT approach follows the strategy which was employed successfully for other model systems. Imposing the correct dimensional crossover on the functional, section 2, appears to provide a systematic procedure for deriving approximate DFTs. Whether the procedure can be implemented explicitly depends on the particular model. In the present case, as for penetrable spheres [25], the Widom–Rowlinson model [26], a needle–sphere model [28], a model amphiphilic mixture [29] and a ternary mixture of colloids, polymers and needles [30], the procedure is tractable and leads to a relatively simple functional. An alternative derivation, section 2.6, which corresponds to linearizing the Rosenfeld functional for a binary HS system w.r.t. the density of one of the species, yielded the *identical* functional. Multi-component mixtures can also be treated by our procedures. For example, if a three-component mixture of HS of two different sizes plus polymer were required one would take the Rosenfeld HS functional for a ternary mixture of HS and linearize in one of the densities which is then identified as (ideal) polymer. Similarly, if a three-component mixture of HS plus two polymer species were required one would simply linearize the ternary HS functional w.r.t. two densities. The corresponding functionals are again identical to those obtained from application of the recipe outlined in section 2.4, where the generating zero-dimensional free energy $F_{0\text{d}}$ is replaced by that for the corresponding ternary mixture. In fact the free energy for the ternary system is simply equation (14) with colloid (polymer) packing fraction replaced by the sum of packing fractions of colloid (polymer) species. In section 2.7 we described the concept of integrating out degrees of freedom within the context of DFT. The present functional affords a valuable example because the Euler–Lagrange equations decouple in this case and $c_p^{(1)}(r)$ is a functional of the colloid profile alone. It is important to emphasize, however, that the mapping to an effective one-component

fluid of colloids that is implicit within the approximate DFT treatment is not equivalent to that which is obtained by an explicit and exact integrating out of polymer coordinates in the partition function. Recall that this latter route yields an effective Hamiltonian containing only one- and two-body contributions when $q < 0.1547$. This particular size ratio has no special significance within our approximate DFT.

Our present paper focuses on the properties of bulk fluid phases. We found that the bulk free energy of the AO mixture is identical to that derived from the free-volume theory of Lekkerkerker *et al* [4] and we pointed out some of the connections between the two approaches (see section 3.1), emphasizing that both impose linearity of the free energy in the polymer density. Since the two theories yield the same free energy, they predict identical fluid–fluid phase separation, i.e. the same binodal and spinodal. The latter can be determined analytically from equation (73), which is particularly useful for critical point studies. How accurate is the free-volume theory for the phase separation curve? When we completed our paper there were no systematic studies of the full binary AO model for the range of size ratios q where fluid–fluid phase separation occurs. Published studies consider either the effective one-component Hamiltonian (97) keeping only pair potential [5], which is strictly valid for $q < 0.1547$, or a lattice polymer version [6]. It is well known that treating highly asymmetric mixtures by brute force simulation is beset by ergodicity problems and slow equilibration when the packing fraction of the smaller species is large. A new study by Dijkstra [47] indicates that for $q = 1$ the fluid–fluid binodal does lie rather close to the free-volume result. This also seems to be the case for other values of q [50] and the current indications are that free-volume theory (and, therefore, our present DFT) does provide a reasonable account of the location of the fluid–fluid binodal in the $\eta_c, \eta_{p,r}$ plane for those values of $q (> 0.35)$ where fluid–fluid phase separation is stable w.r.t. fluid–solid. We have not considered solid phases in the present study. These could be investigated within the framework of the present DFT which would enable us to calculate the full phase diagram. Existing studies [4, 5] based on free-volume ideas employ the expression of Hall [49] for the Helmholtz free-energy density of the HS solid entering equation (71) and the same expression for the free-volume fraction $\alpha(\rho_c)$ as used for fluid phases. It would be interesting to compare DFT predictions for the (rich) fluid–solid phase equilibria in this model with those from other approximate theories and with simulation. Note that the tensor contribution, which depends on the weight function $\hat{w}_{m2}^i(r)$, entering Φ_3 in equation (31) is crucially important for the inhomogeneous solid phase [21, 22] but makes no contribution to the free energy of a homogeneous fluid phase.

An important feature of our present DFT is that pair correlation functions of the bulk fluid can be obtained very easily via the OZ route (sections 3.3 and 3.4). Thus the theory is much easier to implement than the PY integral equation theory for the AO mixture which can only be solved numerically [7, 8]. The pair direct correlation functions and the partial structure factors $S_{ij}(k)$ are given analytically, as is the case in the PY approximation for HS mixtures. What is remarkable here is that the AO mixture exhibits pure entropically driven fluid–fluid phase separation so that the $S_{ij}(k)$ display a divergence at a spinodal line which is identical to that obtained from the bulk free energy. This type of consistency is, of course, a direct consequence of the DFT approach. Having analytical results for the $S_{ij}(k)$ also enabled us to obtain directly the FW line (section 3.5), describing the line of crossover from monotonic to oscillatory asymptotic decay of the total pair correlation functions $h_{ij}(r)$. To the best of our knowledge this is the first time the FW line has been investigated in detail for this type of system. One intriguing feature, which warrants further attention, is the nature and location of the FW line as q becomes smaller and the fluid–fluid critical point shifts to lower η_p and higher η_c (figure 2). For $q = 0.4$ the monotonic regime, where $h_{ij}(r)$ exhibit OZ-like decay at large r , is restricted to a narrow portion of the phase diagram near the critical point—see

figure 5. This might be a structural indicator that the fluid–fluid phase separation is becoming metastable w.r.t. fluid–solid.

We expect the accuracy of the $h_{ij}(r)$ and $S_{ij}(k)$ obtained from the OZ route to be comparable with that of the PY approximation for the AO mixture. As remarked in section 3.6, both approximations fail to reproduce the correct limiting behaviour of $g_{cc}(r)$ as $\eta_c \rightarrow 0$. This is particularly significant for small size ratios at states with low η_c and high values of $\eta_{p,r}$ where the depletion potential is very deep and very short ranged. Neither PY nor the present theory can be expected to yield accurate pair correlation functions in this regime. The DFT has the additional drawback of not enforcing the core conditions $g_{cc}(r < 2R_c) = 0$ and $g_{cp}(r < R_c + R_p) = 0$. These core conditions constitute implicit (hidden) constraints when viewed from the perspective of taking functional derivatives to obtain $c_{ij}^{(2)}(r)$ and then inverting to obtain $g_{ij}(r)$. In principle, one might exploit the core conditions in order to derive (more sophisticated) approximations for the free-energy functional. In practice, such a procedure would be extremely difficult to implement. (In this context it appears remarkable that Rosenfeld's HS functional does yield $g_{ij}(r)$ that fulfill the core conditions. Of course, it is by virtue of the fact that the $c_{ij}^{(2)}$ generated from the Rosenfeld functional are those of PY that the resulting $g_{ij}(r)$ do satisfy the core condition.) DFT provides an alternative route to $g_{ij}(r)$, namely the test-particle procedure, and we have argued that this is likely to yield significantly better results than the OZ route, especially for situations where the depletion attraction is very strong. Once again systematic comparisons with simulation results are required in order to assess further the degree of consistency and, therefore, the reliability of the DFT. Note that the OZ and test particle routes do yield identical results for the decay length a_0^{-1} and wavelength $2\pi/a_1$, characterizing the asymptotic decay of the pair correlation functions. It follows that the FW lines calculated from both routes are identical.

The experience gleaned from the present study of bulk properties gives us confidence in applying our DFT to inhomogeneous fluids where the spatial variation of the density profiles arises from the imposition of external fields. Since the DFT incorporates fluid–fluid phase separation it has been applied [9, 32] to

- (i) the planar interface between coexisting colloid-rich and colloid-poor phases—the density profiles of both colloid and polymer exhibit oscillations on the colloid-rich (liquid) side of the interface provided the bulk liquid lies on the oscillatory side of the FW line—and
- (ii) the study of wetting phenomena for the mixture adsorbed at a hard wall. The interface between the wall and the colloid-poor phase is partially wetted by the colloid-rich phase at high $\eta_{p,r}$ but is completely wet at low $\eta_{p,r}$ ($> \eta_{p,r}^{\text{crit}}$).

A novel sequence of layering transitions accompanies the transition to complete wetting. It was argued [32] that the surface phase behaviour reflects the presence of many-body contributions to the effective one-component Hamiltonian for the colloids. Such contributions are included implicitly in the DFT. Other adsorption problems which can be tackled by our DFT include possible wall-induced crystallization (depletion at a hard wall leads to a very high contact density for colloids [13]) and wetting of the wall–fluid interface by the crystalline phase. Mixtures confined by planar walls or in other geometries are readily tackled which means that phenomena such as capillary condensation can be investigated in detail. Sedimentation in a gravitational field, behaviour in laser fields and the properties of solid–fluid interfaces are also topics ripe for investigation.

Acknowledgments

We thank M Dijkstra, R van Roij, R Roth, A Lang, P Tarazona, M Fuchs and I Götze for many helpful discussions. This research was supported by the British-German ARC Programme (project104b).

Appendix A. Weight functions in Fourier space

For completeness we list the (three-dimensional) Fourier transforms of the first six weight functions listed in equations (17)–(22):

$$w_3^i(\mathbf{k}) = -\frac{4\pi}{k^3}[kR_i \cos(kR_i) - \sin(kR_i)], \quad (\text{A.1})$$

$$w_2^i(\mathbf{k}) = \frac{4\pi R_i}{k} \sin(kR_i), \quad (\text{A.2})$$

$$w_1^i(\mathbf{k}) = \frac{\sin(kR_i)}{k}, \quad (\text{A.3})$$

$$w_0^i(\mathbf{k}) = \frac{\sin(kR_i)}{R_i k}, \quad (\text{A.4})$$

$$w_{v2}^i(\mathbf{k}) = \frac{4\pi}{k^2}[kR_i \cos(kR_i) - \sin(kR_i)]\frac{\mathbf{k}}{k}, \quad (\text{A.5})$$

$$w_{v1}^i(\mathbf{k}) = \frac{kR_i \cos(kR_i) - \sin(kR_i)}{k^2 R_i} \frac{\mathbf{k}}{k}, \quad (\text{A.6})$$

where $k = |\mathbf{k}|$.

Appendix B. Density functional in two dimensions

In the following we present the DF for the two-dimensional AO model obtained from the route described in section 2.6 starting from the two-dimensional Rosenfeld hard disc functional (see e.g. [20]). The excess free energy F_{exc} has the general structure, equation (15) of a two-dimensional integral over a free-energy density. The weighted densities are obtained by two-dimensional convolutions

$$n_v^i(x) = \int d^2r \rho_i(\mathbf{r}) w_v^i(\mathbf{x} - \mathbf{r}), \quad (\text{B.1})$$

of the four two-dimensional weight functions

$$w_d^i(\mathbf{r}) = \Theta(R_i - r), \quad (\text{B.2})$$

$$w_1^i(\mathbf{r}) = \delta(R_i - r), \quad (\text{B.3})$$

$$w_{v1}^i(\mathbf{r}) = \delta(R_i - r) \mathbf{r}/r, \quad (\text{B.4})$$

$$w_0^i(\mathbf{r}) = \delta(R_i - r)/(2\pi r), \quad (\text{B.5})$$

where \mathbf{r} in equations (B.2)–(B.5) denotes the two-dimensional position vector. The free-energy density is

$$\begin{aligned} \Phi = & -(n_0^c + n_0^p) \ln(1 - n_d^c) + \frac{n_0^c n_d^p}{1 - n_d^c} + \frac{n_1^c n_1^c - \mathbf{n}_{v1}^c \cdot \mathbf{n}_{v1}^c}{4\pi} \left[\frac{1}{1 - n_d^c} + \frac{n_d^p}{(1 - n_d^c)^2} \right] \\ & + \frac{n_1^p n_1^c - \mathbf{n}_{v1}^p \cdot \mathbf{n}_{v1}^c}{2\pi(1 - n_d^c)}. \end{aligned} \quad (\text{B.6})$$

References

- [1] Asakura S and Oosawa F 1954 *J. Chem. Phys.* **22** 1255
- [2] Vrij A 1976 *Pure Appl. Chem.* **48** 471
- [3] Gast A P, Hall C K and Russell W B 1983 *J. Colloid Interface Sci.* **96** 251
- [4] Lekkerkerker H N W, Poon W C K, Pusey P N, Stroobants A and Warren P B 1992 *Europhys. Lett.* **20** 559
- [5] Dijkstra M, Brader J M and Evans R 1999 *J. Phys.: Condens. Matter* **11** 10 079
- [6] Meijer E J and Frenkel D 1994 *J. Chem. Phys.* **100** 6873
- [7] Louis A A, Finken R and Hansen J 1999 *Europhys. Lett.* **46** 741
- [8] Dijkstra M, van Roij R and Evans R 2000 *J. Chem. Phys.* **113** 4799
- [9] Brader J M 2001 *PhD Thesis* University of Bristol
- [10] Leal Calderon F, Bibette J and Biasis J 1993 *Europhys. Lett.* **23** 653
- [11] Ilett S M, Orrock A, Poon W C K and Pusey P N 1995 *Phys. Rev. E* **51** 1344
- [12] Brader J M and Evans R 2000 *Europhys. Lett.* **49** 678
- [13] Brader J M, Dijkstra M and Evans R 2001 *Phys. Rev. E* **63** 041405
- [14] de Hoog E H A and Lekkerkerker H N W 1999 *J. Phys. Chem. B* **103** 5274
- [15] de Hoog E H A, Lekkerkerker H N W, Schulz J and Findenegg G H 1999 *J. Phys. Chem. B* **103** 10657
- [16] Evans R 1979 *Adv. Phys.* **28** 143
- [17] Evans R 1992 *Fundamentals of Inhomogeneous Fluids* ed D Henderson (New York: Dekker) p 85
- [18] Rosenfeld Y 1989 *Phys. Rev. Lett.* **63** 980
- [19] Rosenfeld Y, Schmidt M, Löwen H and Tarazona P 1996 *J. Phys.: Condens. Matter* **8** L577
- [20] Rosenfeld Y, Schmidt M, Löwen H and Tarazona P 1997 *Phys. Rev. E* **55** 4245
- [21] Tarazona P and Rosenfeld Y 1997 *Phys. Rev. E* **55** R4873
- [22] Tarazona P 2000 *Phys. Rev. Lett.* **84** 694
- [23] Cuesta J A 1996 *Phys. Rev. Lett.* **76** 3742
- [24] Cuesta J A and Martínez-Raton Y 1997 *Phys. Rev. Lett.* **78** 3681
- [25] Schmidt M 1999 *J. Phys.: Condens. Matter* **11** 10 163
- [26] Schmidt M 2001 *Phys. Rev. E* **63** 010101(R)
- [27] Bolhuis P and Frenkel D 1994 *J. Chem. Phys.* **101** 9869
- [28] Schmidt M 2001 *Phys. Rev. E* **63** 050201(R)
- [29] Schmidt M and von Ferber C 2001 *Phys. Rev. E* **64** 051115
- [30] Schmidt M and Denton A R 2002 *Phys. Rev. E* **65** 021508
- [31] Schmidt M, Löwen H, Brader J M and Evans R 2000 *Phys. Rev. Lett.* **85** 1934
- [32] Brader J M, Evans R, Schmidt M and Löwen H 2002 *J. Phys.: Condens. Matter* **14** L1
- [33] Groh B and Mulder B 2000 *Phys. Rev. E* **61** 3811
- [34] Percus J K 1976 *J. Stat. Phys.* **15** 505
- [35] Cuesta J A, Martínez-Raton Y and Tarazona P *J. Phys.: Condens. Matter* (special issue on density functional theory)
Cuesta J A, Martínez-Raton Y and Tarazona P 2002 *Preprint* cond-mat/0205256
- [36] Brader J M and Evans R 2002 *Physica A* **306** 287
- [37] A closely related, general scheme for constructing a free-energy functional for the effective one-component fluid and the corresponding hierarchy of effective direct correlation functions is given by
Cuesta J A and Martínez-Raton Y 1999 *J. Phys.: Condens. Matter* **11** 10 107
- [38] Roth R, Evans R and Dietrich S 2000 *Phys. Rev. E* **62** 5360
- [39] Roth R, Evans R and Louis A A 2001 *Phys. Rev. E* **64** 051202
- [40] Rosenfeld Y 1988 *J. Chem. Phys.* **89** 4272
- [41] Hansen J P and McDonald I R 1986 *Theory of Simple Liquids* 2nd edn (London: Academic)
- [42] Fisher M E and Widom B 1969 *J. Chem. Phys.* **50** 3756
- [43] Evans R, Henderson J R, Hoyle D C, Parry A O and Sabeur Z A 1993 *Mol. Phys.* **80** 755
- [44] Evans R, Leote de Carvalho R J F, Henderson J R and Hoyle D C 1994 *J. Chem. Phys.* **100** 591
- [45] Dijkstra M and Evans R 2000 *J. Chem. Phys.* **112** 1449
- [46] Archer A J and Evans R 2001 *Phys. Rev. E* **64** 041501
- [47] Dijkstra M, private communication
Dijkstra M and van Roij R 2002 *Preprint*
- [48] Louis A A 2001 *Phil. Trans. R. Soc. A* **359** 939 see appendix A
- [49] Hall K R 1972 *J. Chem. Phys.* **57** 2252
- [50] Bolhuis P G, Louis A A and Hansen J-P 2002 *Preprint* and cond-mat/020606

Interfacial properties of model colloid–polymer mixtures

BY R. EVANS¹, J. M. BRADER¹, R. ROTH¹, M. DIJKSTRA²,
M. SCHMIDT³ AND H. LÖWEN³

¹*H. H. Wills Physics Laboratory, University of Bristol, Bristol BS8 1TL, UK*

²*Debye Institute, Soft Condensed Matter Physics, Utrecht University,
Princetonplein 5, 3584 CC Utrecht, The Netherlands*

³*Institut für Theoretische Physik II, Universität Düsseldorf, Universitätsstrasse 1,
D-40225 Düsseldorf, Germany*

We summarize the main results of our recent investigations of the interfacial properties of the simplest model of a colloid–polymer mixture, namely that introduced by Asakura & Oosawa and by Vrij, in which colloid–colloid and colloid–polymer interactions are treated as hard sphere-like, while the polymer–polymer interaction is ideal (perfectly interpenetrating coils). In spite of its simplicity, we find that the model exhibits rich interfacial behaviour which depends on the size ratio $q \equiv \sigma_p/\sigma_c$, where σ_p and σ_c denote the diameters of polymer and colloid, respectively. For highly asymmetric mixtures, $q < 0.1547$, an explicit and exact mapping of the binary mixture to an effective one-component Hamiltonian for the colloids allows one to perform computer simulations for inhomogeneous mixtures. We investigate a mixture with $q = 0.1$ and find that small amounts of polymer give rise to strong depletion effects at a hard wall. The colloid density at contact with the wall is several times greater than that for pure hard spheres at a hard wall. However, for states removed from the bulk fluid–solid coexistence curve we find no evidence of wall-induced crystallization. In order to treat less asymmetric cases, where stable fluid–fluid demixing occurs in bulk, we have designed a density functional theory specifically for this model mixture. For $q = 0.6$ we find a first order wetting transition from partial to complete wetting by the colloid-rich phase at the hard-wall–colloid-poor interface as the packing fraction η_p^f of polymer in the reservoir is decreased. At a slightly higher value of η_p^f , there is a novel *single* layering transition, characterized by a jump in the densities in the first two adsorbed layers, as the bulk colloid packing fraction η_c is increased. The same density functional has been used to investigate the surface tension and colloid and polymer density profiles at the free interface between the demixed fluid phases.

Keywords: colloid–polymer mixtures; depletion forces; effective Hamiltonians; wetting and layering transitions; surface tension; adsorption

1. Introduction

It is well known that the addition of non-adsorbing polymers to a colloidal suspension gives rise to an attractive interaction between the colloidal particles. The physical mechanism for this phenomenon is the depletion effect, i.e. an effective attractive interaction is induced by the exclusion of polymer from a depletion zone

between colloids; the range of the interaction is set by the diameter of the polymer coils and the strength of the attraction is determined by the chemical potential of the polymer reservoir (Asakura & Oosawa 1954). The simplest model of the binary colloid–polymer mixture treats the colloids as hard spheres, with diameter σ_c , and the polymers as ideal interpenetrating coils, as regards their mutual interactions. It requires the polymers to be excluded by a centre of mass distance $(\sigma_c + \sigma_p)/2$ from the colloids (Asakura & Oosawa 1954; Vrij 1976). The parameter σ_p is usually taken to be $2R_g$, where R_g is the radius of gyration of the polymer. Assuming that the polymer is ideal is a drastic oversimplification. It is a situation achieved (approximately) for dilute solutions of polymer in a theta solvent. Nevertheless, this binary Asakura–Oosawa (AO) model does capture the main features of the observed variation of the bulk phase behaviour of real colloid–polymer mixtures with increasing size ratio $q = \sigma_p/\sigma_c$ (Gast *et al.* 1983; Lekkerkerker *et al.* 1992; Ilett *et al.* 1995). Surprisingly, little attention has been paid to *inhomogeneous* colloid–polymer mixtures where the average density profiles of both species are spatially varying. Such situations arise in adsorption at a solid substrate, in mixtures confined in narrow pores, at the planar interface between two coexisting (colloid-rich and polymer-rich) fluid phases and in colloidal crystals. Given the usefulness of the AO model for bulk phase behaviour, where it predicts stable solid, liquid and gas colloid phases for sufficiently large q , it is natural to investigate its properties for interfaces. Such a strategy is common in statistical physics. The Ising or lattice gas model provides only a crude description of a real liquid–gas (bulk condensation) phase transition but yields a wealth of predictions for surface transitions, with the substrate modelled as a simple external field, most of which have been found in adsorption experiments. Here we show that the interfacial properties of the AO model should be richer than those of the bulk and argue that adsorption-type experiments on real colloid–polymer mixtures could reveal striking phenomena. The results which emerge from the AO model are interesting from a fundamental statistical mechanics viewpoint since the *bare* interactions between the constituent particles are either hard or ideal; surface and bulk transitions are purely entropically driven. *Depletion* effects give rise to effective attractive interactions between colloidal particles or between colloids and a hard wall.

This paper describes the two different strategies we have employed in tackling the statistical mechanics of the AO model. The first involves integrating out the polymer degrees of freedom to obtain an effective one-component Hamiltonian for the colloids, while the second is based on a new density functional theory specifically designed for the binary AO mixture.

2. Bare and effective Hamiltonians

We consider an extreme non-additive binary hard sphere mixture consisting of N_c hard spheres, representing colloid, and N_p interpenetrable, non-interacting particles, representing ideal polymer, in a volume V at temperature T . This is a reasonable model of a colloid–polymer mixture, as the interaction between sterically stabilized colloidal particles can be made close to that of hard spheres, and dilute solutions of polymer in a theta solvent are very weakly interacting. We implicitly assume that any solvent molecules which are present in a real suspension can be treated as an inert continuum, and thus have no effect on bulk or interfacial properties. The colloids interact via the hard sphere potential, with diameter σ_c , and the polymers

Interfacial properties of model colloid-polymer mixtures

963

are excluded from the colloids to a centre of mass distance $(\sigma_c + \sigma_p)/2$. This simple model of an idealized colloid-polymer mixture is often called the Asakura-Oosawa (AO) model although it was first defined explicitly by Vrij (1976). It is specified by the bare pair potentials:

$$\left. \begin{aligned} \phi_{cc}(R_{ij}) &= \begin{cases} \infty & \text{for } R_{ij} < \sigma_c, \\ 0 & \text{otherwise,} \end{cases} \\ \phi_{cp}(|\mathbf{R}_i - \mathbf{r}_j|) &= \begin{cases} \infty & \text{for } |\mathbf{R}_i - \mathbf{r}_j| < \frac{1}{2}(\sigma_c + \sigma_p), \\ 0 & \text{otherwise,} \end{cases} \\ \phi_{pp}(r_{ij}) &= 0, \end{aligned} \right\} \quad (2.1)$$

where \mathbf{R} and \mathbf{r} denote colloid and polymer centre of mass coordinates, respectively, with $R_{ij} = |\mathbf{R}_i - \mathbf{R}_j|$ and $r_{ij} = |\mathbf{r}_i - \mathbf{r}_j|$. The Hamiltonian thus consists of (trivial) kinetic energy contributions and a sum of interaction terms: $H = H_{cc} + H_{cp} + H_{pp}$, where

$$\left. \begin{aligned} H_{cc} &= \sum_{i < j}^{N_c} \phi_{cc}(R_{ij}), \\ H_{cp} &= \sum_i^{N_c} \sum_j^{N_p} \phi_{cp}(|\mathbf{R}_i - \mathbf{r}_j|), \\ H_{pp} &= \sum_{i < j}^{N_p} \phi_{pp}(R_{ij}) = 0. \end{aligned} \right\} \quad (2.2)$$

Following the treatment of the bulk (Dijkstra *et al.* 1999*a, b*), we work in a semi-grand-canonical, (N_c, z_p, V, T) , ensemble in which the fugacity of the polymers, $z_p = \Lambda_p^{-3} \exp(\beta\mu_p)$, is fixed. μ_p denotes the chemical potential of the reservoir of polymer and $\beta = 1/k_B T$. In addition to the pairwise interactions, we add two, in general different, external fields which couple independently to the colloid and polymer degrees of freedom:

$$V_c^{\text{ext}} = \sum_{i=1}^{N_c} v_c^{\text{ext}}(\mathbf{R}_i), \quad V_p^{\text{ext}} = \sum_{i=1}^{N_p} v_p^{\text{ext}}(\mathbf{r}_i). \quad (2.3)$$

These potentials create inhomogeneous density profiles $\rho_c(\mathbf{r})$ and $\rho_p(\mathbf{r})$. The quantity of interest is the Helmholtz free energy, $F(N_c, V, z_p)$. Formally,

$$\exp[-\beta F] = \frac{1}{N_c! \Lambda_c^{3N_c}} \int d\mathbf{R}^{N_c} \exp[-\beta(H_{cc} + \Omega + V_c^{\text{ext}})], \quad (2.4)$$

where

$$\exp[-\beta \Omega] \equiv \sum_{N_p=0}^{\infty} \frac{z_p^{N_p}}{N_p!} \int d\mathbf{r}^{N_p} \exp[-\beta(H_{cp} + V_p^{\text{ext}})] \quad (2.5)$$

and Λ_i is the thermal de Broglie wavelength of species i ($i = c, p$). Ω is the grand potential of the ideal polymer coils in the presence of the applied external field V_p^{ext} and the external field that is generated by a fixed configuration of N_c colloids. If one can determine Ω explicitly, one has reduced the difficult problem of treating the

binary system to a much simpler one-component problem: equation (2.4) describes the statistical mechanics of a colloidal system interacting through an effective one-component Hamiltonian $H^{\text{eff}} = H_{\text{cc}} + \Omega + V_{\text{c}}^{\text{ext}}$.

For a general binary mixture, Ω consists of an infinite series of terms, representing zero-, one-, two-, ..., many-body contributions (Dijkstra *et al.* 1999a). In the particular case of the AO model, each contribution simplifies because $\phi_{\text{pp}} = 0$. For a homogeneous (bulk) fluid mixture with $V_{\text{c}}^{\text{ext}} = V_{\text{p}}^{\text{ext}} = 0$, $\rho_{\text{c}}(\mathbf{r})$ and $\rho_{\text{p}}(\mathbf{r})$ are constant and the series truncates after the two-body term, provided that $q < 2/\sqrt{3} - 1 = 0.1547$ (Gast *et al.* 1983; Dijkstra *et al.* 1999b). In this regime of high asymmetry there is no triple overlap of excluded volume regions, even when three colloids are contacting each other. We showed (Brader *et al.* 2001a) that similar geometrical considerations apply for the AO mixture in contact with a hard wall defined by

$$v_{\text{c}}^{\text{ext}}(z) = \begin{cases} \infty, & z < \sigma_{\text{c}}/2, \\ 0, & z > \sigma_{\text{c}}/2, \end{cases} \quad v_{\text{p}}^{\text{ext}}(z) = \begin{cases} \infty & z < \sigma_{\text{p}}/2, \\ 0 & z > \sigma_{\text{p}}/2, \end{cases} \quad (2.6)$$

where z is the coordinate of the centre of the particle measured normal to the wall. More precisely, we found that for $q < 0.1547$ the effective Hamiltonian for the inhomogeneous system reduces to

$$H^{\text{eff}} = H_{\text{cc}} + \sum_{i=1}^{N_{\text{c}}} v_{\text{c}}^{\text{ext}}(z_i) + \sum_{i=1}^{N_{\text{c}}} \phi_{\text{AO}}^{\text{wall}}(z_i) + \Omega_0^{\text{bulk}} + \Omega_1^{\text{bulk}} + \sum_{i < j} \phi_{\text{AO}}(R_{ij}), \quad (2.7)$$

where $\phi_{\text{AO}}^{\text{wall}}$ represents the attractive AO depletion potential between a colloid and the planar hard wall. The depth of this potential is proportional to z_{p} and its range is σ_{p} . The last three terms of equation (2.7) are those which define Ω for the bulk fluid,

$$-\beta\Omega_0^{\text{bulk}} = z_{\text{p}}V, \quad -\beta\Omega_1^{\text{bulk}} = -z_{\text{p}}N_{\text{c}}\pi(\sigma_{\text{c}} + \sigma_{\text{p}})^3/6 = -z_{\text{p}}\eta_{\text{c}}(1 + q)^3V,$$

where $\eta_{\text{c}} = (\pi/6)\sigma_{\text{c}}^3N_{\text{c}}/V$ is the colloid packing fraction. $\phi_{\text{AO}}(R)$ is the well-known AO pair potential between two colloids in a sea of ideal polymer. This attractive potential also has range σ_{p} , is proportional to z_{p} , has a similar shape to that of $\phi_{\text{AO}}^{\text{wall}}$, but is less deep.

It is important to recognize that in the regime $q < 0.1547$ the mapping of the binary mixture to an effective one-component fluid with the Hamiltonian specified by equation (2.7) is *exact* within the AO model. This observation is very significant when we recall that direct simulation of the model binary mixture, which constitutes a very asymmetric system, is prohibited by slow equilibration since huge numbers of polymer are required per colloid particle at state points of interest. It is much easier to perform computer simulations or develop a reliable integral equation theory for the effective Hamiltonian than for the bare binary mixture.

In a bulk fluid the equilibrium structure, i.e. the colloid correlation functions (Dijkstra *et al.* 2000), is determined solely by the effective pair potential,

$$\phi^{\text{eff}}(R) = \phi_{\text{cc}}(R) + \phi_{\text{AO}}(R). \quad (2.8)$$

Moreover since Ω_0^{bulk} and Ω_1^{bulk} are linear in N_{c} and V , respectively, they have no effect on the bulk phase equilibria (Dijkstra *et al.* 1999a, b). These terms do

contribute to the total pressure and total compressibility χ_T of the mixture, making the latter very different from the osmotic compressibility $\chi_{T,\text{eff}}$. More specifically, we find that $\chi_{T,\text{eff}}^{-1}$ makes only a small contribution to the total bulk modulus χ_T^{-1} . It is a term $-k_B T V (\partial z_p / \partial V)_{N_c, N_p}$ determined by the thermodynamics of the reservoir which provides the dominant contribution (Dijkstra *et al.* 2000).

Spontaneously generated inhomogeneities where the density profiles of colloid and polymer are spatially varying in the absence of external fields warrant special attention. Examples are the planar interface between demixed fluid phases, colloidal crystals where the densities vary periodically and the crystal-fluid interface. In such cases H^{eff} reduces to the effective Hamiltonian of the bulk system; there are no additional contributions associated with the inhomogeneity. At first sight this may seem somewhat surprising, as the distribution of polymer in a colloidal crystal, or in the region of the fluid-fluid interface, is clearly very different from that in a bulk fluid and one might imagine that different effective interactions might arise. However, because we work exclusively with a reservoir of polymer, it is the fugacity z_p of this reservoir which controls the interactions in the system. As z_p is constant throughout the inhomogeneous fluid, then so too is the effective interaction between the colloids, regardless of the local polymer density. This serves to reinforce the fact that the species which is integrated out is treated grand-canonically.

We emphasize that for less asymmetric mixtures, with larger size ratios q , the effective Hamiltonian becomes very complex. For $q > 0.25$, the effective pair potential depends on the distance of each colloid centre from the hard wall, not just on their separation R_{ij} , and higher-body potentials are present (Brader *et al.* 2001a).

As a final remark on the formal procedure of integrating out the polymer degrees of freedom we note that it is possible, in principle, to recover information about the polymer distribution by performing functional differentiation of the free energy F with respect to $v_p^{\text{ext}}(\mathbf{r})$. The polymer density profile $\rho_p(\mathbf{r})$ can be expressed in terms of the n -body correlation functions of the colloids as determined from the effective Hamiltonian. In practice, the applicability of this procedure is probably restricted to bulk mixtures with $q < 0.1547$, where one can derive (i) an exact and tractable formula for the free-volume fraction $\alpha(\rho_c; z_p) \equiv \rho_p / \rho_p^f$ of polymer in the fluid mixture and (ii) an approximation for the inhomogeneous polymer density associated with a crystalline array of colloids (Brader *et al.* 2001a).

3. Adsorption at a hard wall for size ratio $q = 0.1$

In this section we illustrate the use of the effective Hamiltonian for a mixture with $q = 0.1$. As remarked earlier, the bulk structure is determined solely by $\phi^{\text{eff}}(R)$ the effective pair potential of equation (2.8), and Monte Carlo results for the radial distribution function $g_{cc}(R)$ and structure factor $S_{cc}(k)$ of the colloids at various colloid packing fractions η_c are given by Dijkstra *et al.* (1999b). The complete phase diagram of the bulk mixture was also determined by simulation. In the ρ_p^f versus η_c representation there is a very broad, in η_c , fluid-solid coexistence curve which lies well below a metastable fluid-fluid coexistence. Note that the polymer density in the reservoir, ρ_p^f ($\equiv z_p$ for ideal polymer) is equivalent to inverse temperature in simple fluids; each term in the effective Hamiltonian is proportional to z_p . There is also an isostructural (FCC) solid-solid transition which is slightly metastable with respect to the fluid-solid transition (Dijkstra *et al.* 1999b). These simulation results provide a

benchmark against which approximate theories can be tested. For example, Percus–Yevick theory, applied with the same $\phi^{\text{eff}}(R)$, yields very accurate colloid radial distribution functions and structure factors while a perturbation theory, based on a hard-sphere reference system, yields a reasonable fluid–solid coexistence curve but the metastable fluid–fluid coexistence is at unphysically high values of η_c (Dijkstra *et al.* 1999b).

In figure 1 we show Monte Carlo results for the colloid density profile $\rho_c(z)$ in the same mixture adsorbed at a hard wall. These were obtained using the effective Hamiltonian (2.7) and refer to a fixed bulk colloid packing $\eta_c \equiv \pi\sigma_c^3\rho_c(\infty)/6 = 0.4$ and three values of the polymer reservoir packing fraction $\eta_p^r \equiv \pi\sigma_p^3\rho_p^r/6$. In the absence of polymer (figure 1a), the system reduces to pure hard spheres at a hard wall and the profile exhibits the usual pronounced oscillations arising from packing effects. On adding a small amount of polymer, $\eta_p^r = 0.05$ (figure 1b), the depletion attraction at the wall leads to a much higher contact density $\rho_c(\sigma_c/2)$ than for pure hard spheres at a hard wall. The effect is larger for $\eta_p^r = 0.10$ (figure 1c), where the reduced contact density is greater than 20. Plotted alongside the Monte Carlo results are the density profiles obtained from a simple one-component density functional theory (DFT), which treats the hard sphere contribution by the Rosenfeld (1989) fundamental measures theory and the attractive contribution, arising from $\phi_{\text{AO}}(R)$, in mean-field fashion. The overall agreement is quite good although differences do show up on the expanded scale of the insets. A similar trend in the profiles is obtained for $\eta_c = 0.3$ (Brader *et al.* 2001a).

While the addition of polymer gives rise to extremely high contact densities the colloid density profiles decay very rapidly to bulk-like values over the small range, $\sigma_p = 0.1\sigma_c$, of the wall depletion potential $\phi_{\text{AO}}^{\text{wall}}$. Crudely speaking, the colloid is behaving as an ideal gas in the deep effective wall potential, with some small enhancement of the local density due to packing effects. The Gibbs adsorption,

$$\Gamma = \sigma_c^2 \int_0^\infty dz (\rho_c(z) - \rho_c(\infty)),$$

does not increase rapidly with increasing η_p^r and there is no evidence for any wall-induced local crystallization for the states we have investigated, i.e. up to $\eta_p^r = 0.1$. However, this state point is still substantially removed from the bulk fluid–solid phase boundary. Whether wall induced crystallization sets in at slightly higher polymer packings or whether one must approach very close to the bulk phase boundary in order to observe such a phenomenon remains to be ascertained. One might certainly expect depletion effects to favour the development of crystalline layers prior to bulk crystallization. The main issues are (i) how close to the bulk transition must one be before the first adsorbed layer becomes crystalline and (ii) how do subsequent crystalline layers develop at the hard wall–fluid interface as η_p^r is increased (for a fixed η_c) towards its value at bulk fluid–solid coexistence? Various scenarios are possible. There could be an infinite sequence of layering transitions culminating in complete wetting of the wall–fluid interface by a nearly close-packed crystal. Alternatively, the interface could remain incompletely wetted by crystal.

We expect similar depletion phenomena for additive binary mixtures of hard spheres near a hard wall, provided the size ratio q is small enough. DFT calculations based on the Rosenfeld (1989) functional for such a binary mixture with $q = 0.1$ yield big sphere (colloid) density profiles which are very similar to those shown here.

Interfacial properties of model colloid-polymer mixtures

967

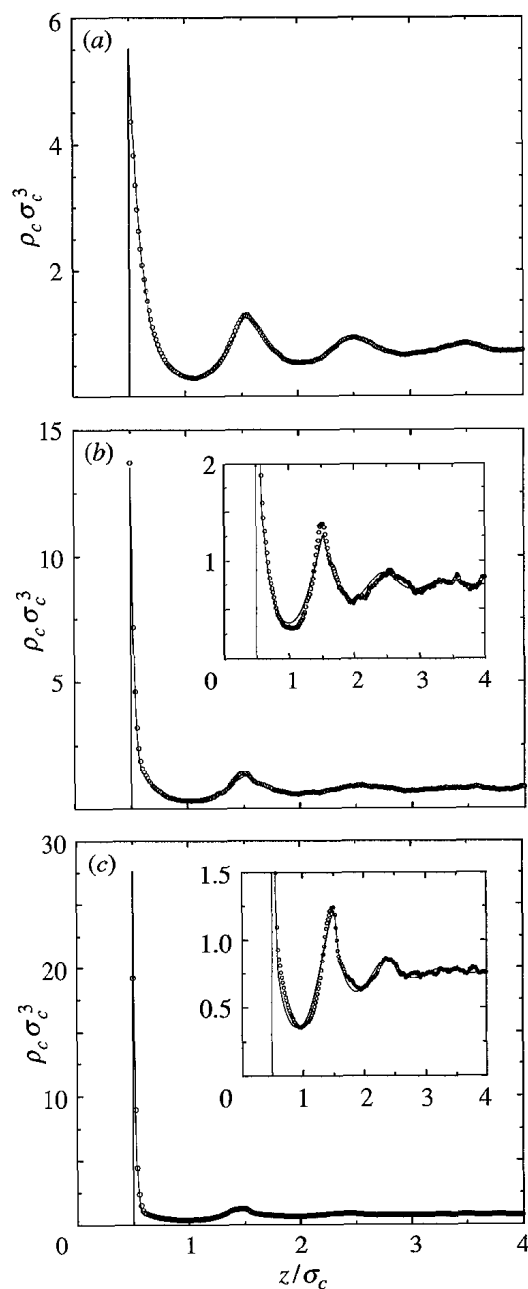


Figure 1. Colloid density profiles near a hard wall: the open circles are the Monte Carlo results while the solid lines denote the one-component DFT results. In each case the bulk colloid packing fraction $\eta_c = 0.4$ and the size ratio $q = 0.1$. The packing fraction of ideal polymer in the reservoir increases from (a) $\eta_p^r = 0$ (pure hard spheres) to (b) $\eta_p^r = 0.05$ and (c) $\eta_p^r = 0.10$. The insets show the results on an expanded vertical scale. Note the rapid increase in contact value $\rho_c(\sigma_c/2)$ as η_p^r is increased.

Once again there is no sign of crystallization at the wall for the state points which were investigated. Detailed comparisons of results for additive hard sphere mixtures with those from the AO model will be presented elsewhere when we shall compare

our findings with those from Poon & Warren (1994), who developed an empirical approach for the calculation of the onset of wall crystallization in additive binary hard sphere mixtures. These authors find hard wall induced crystallization at small sphere packing fractions which are far below the bulk fluid–solid transition. Our results show no evidence of wall induced crystallization at state points where Poon & Warren predict such a transition.

These findings have relevance for real colloidal mixtures in the presence of walls. Several authors have reported evidence for wall induced crystallization well below the bulk fluid–solid phase boundary in mixtures of hard sphere-like colloids at a planar wall. There are also earlier observations of wall induced crystallization in colloid–polymer mixtures (see, for example, Kose & Hachisu 1976; Gast *et al.* 1986). If, as now seems likely, the idealized AO model of a binary colloid–polymer mixture at a planar hard wall predicts that the onset of wall-induced crystallization occurs very close to the bulk transition, this means that factors other than depletion must be important in the experiments. These may include polydispersity, which could play a different role in wall crystallization from that in bulk crystallization, and the fact that the actual wall–colloid potential could be different from that of a hard wall. Any residual attractive dispersion forces between the substrate and the colloid could favour the onset of wall-induced crystallization. The theoretical framework which we have developed allows us to obtain reliable results for the well-defined AO model, which although simple, does incorporate the key features of depletion-induced colloid–colloid and wall–colloid attraction. As such it provides a valuable means of studying the effects of depletion on interfacial properties. The drawback is that the procedure is, for most practical purposes, restricted to $q < 0.1547$.

4. Density functional theory for the binary AO model

As emphasized in § 2, formally integrating out the polymer degrees of freedom yields very complicated effective Hamiltonians for the colloids when $q > 0.1547$. In order to tackle less asymmetric mixtures, an alternative strategy is required. Since direct simulation of the binary system is not practicable because of the large numbers of polymer coils required, we have designed a DFT specifically for the binary AO mixture (Schmidt *et al.* 2000). Here we describe the functional and report some results of its application to adsorption at a hard wall and to the properties of the free fluid–fluid interface.

(a) Description of the density functional

The procedure for constructing the DFT is based on the successful fundamental measures theory developed by Rosenfeld (1989) for additive hard sphere mixtures and the excess, over ideal, Helmholtz free energy functional is given by an equivalent form:

$$\beta F_{\text{exc}}[\rho_{\text{c}}(\mathbf{r}), \rho_{\text{p}}(\mathbf{r})] = \int d^3x \Phi(\{n_{\nu}^{\text{c}}(x)\}, \{n_{\lambda}^{\text{p}}(x)\}). \quad (4.1)$$

The weighted densities are

$$n_{\nu}^i(\mathbf{x}) = \int d^3r \rho_i(\mathbf{r}) \omega_{\nu}^i(\mathbf{x} - \mathbf{r}),$$

where the weight functions are $\omega_3^i(\mathbf{r}) = \theta(R^i - r)$, $\omega_2^i(\mathbf{r}) = \delta(R^i - r)$, $\mathbf{w}_{v2}^i(\mathbf{r}) = \omega_2^i(\mathbf{r})\mathbf{r}/r$, and where $r = |\mathbf{r}|$, $\theta(r)$ is the step function and $\delta(r)$ is the Dirac distribution. Further weights are $\omega_1^i(\mathbf{r}) = \omega_2^i(\mathbf{r})/(4\pi R^i)$, $\mathbf{w}_{v1}^i(\mathbf{r}) = \mathbf{w}_{v2}^i(\mathbf{r})/(4\pi R^i)$, $\omega_0^i(\mathbf{r}) = \omega_1^i(\mathbf{r})/R^i$. There are four scalar and two vector (\mathbf{w}_{v1} and \mathbf{w}_{v2}) weight functions. R^i denotes the radius of species i , with $i = c, p$, so that $R^c = \sigma_c/2$ and $R^p = \sigma_p/2$. In order to obtain the free energy density Φ appropriate to the AO model, Schmidt *et al.* (2000) considered the zero-dimensional limit which corresponds to a cavity that can hold at most one colloid but can hold an arbitrary number of ideal polymer coils if no colloid is present. We found

$$\begin{aligned} \Phi = n_0^i \varphi^i(n_3^c, n_3^p) + (n_1^i n_2^j - \mathbf{n}_{v1}^i \cdot \mathbf{n}_{v2}^j) \varphi^{ij}(n_3^c, n_3^p) \\ + \frac{1}{8\pi} (n_1^i n_2^j n_2^k / 3 - n_2^i \mathbf{n}_{v2}^j \cdot \mathbf{n}_{v2}^k) \varphi^{ijk}(n_3^c, n_3^p), \quad (4.2) \end{aligned}$$

where the Einstein summation convention is used, and

$$\varphi^{i\dots k}(\eta_c, \eta_p) \equiv \frac{\partial^m \beta F_{0d}(\eta_c, \eta_p)}{\partial \eta_i \dots \partial \eta_k}.$$

Here

$$\beta F_{0d}(\eta_c, \eta_p) = (1 - \eta_c - \eta_p) \ln(1 - \eta_c) + \eta_c$$

is the excess free energy appropriate to this particular cavity, and η_c and η_p are the packing fractions of the two species. In the original paper, Schmidt *et al.* included a tensor weight function; this is omitted here. The functional can also be regarded as a linearization, in the polymer density, of the original Rosenfeld functional.

For a homogeneous (bulk) fluid mixture our functional yields the excess Helmholtz free-energy density $\beta F_{\text{exc}}(\rho_c, \rho_p)/V = \beta f_{\text{hs}}(\rho_c) - \rho_p \ln \alpha(\rho_c)$, where $f_{\text{hs}}(\rho_c)$ is the excess free-energy density of pure hard spheres in the scaled-particle (Percus–Yevick compressibility) approximation and $\alpha = (1 - \eta_c) \exp(-A\gamma - B\gamma^2 - C\gamma^3)$, with $\gamma = \eta_c/(1 - \eta_c)$, $A = q^3 + 3q^2 + 3q$, $B = 3q^3 + 9q^2/2$, and $C = 3q^3$. This result is *identical* to that of the free-volume theory of Lekkerkerker *et al.* (1992) for the AO model, which is known to yield stable colloidal gas–liquid coexistence for size ratios $q \geq 0.32$. For smaller q this fluid–fluid transition becomes metastable with respect to a broad, in η_c , fluid–solid transition.

The bulk pair direct correlation functions $c_{ij}^{(2)}$ obtained by differentiating $F_{\text{exc}}[\rho_c, \rho_p]$ are given analytically. The Ornstein–Zernike relations then provide the bulk partial structure factors $S_{ij}(k)$. As a consequence of linearization in the polymer density, $c_{pp}^{(2)} = 0$, as in Percus–Yevick approximation for this model. The other two functions $c_{cc}^{(2)}$ and $c_{cp}^{(2)}$ are not the same as those from Percus–Yevick theory. Nevertheless, the resulting analytical $S_{ij}(k)$ are of a similar quality to those obtained from numerical solutions of the binary mixture Percus–Yevick integral equations (Schmidt *et al.* 2000). An important advantage of the present DFT over integral equation theories is that the structure factors and radial distribution functions, obtained from the Ornstein–Zernike route, are consistent with the bulk free energy, i.e. thermodynamic and structural routes to the fluid–fluid spinodal and critical point are equivalent. This property is particularly advantageous when one investigates interfaces at or near two-phase coexistence.

The functional treats colloid and polymer on equal footing. For inhomogeneous situations the colloid and polymer density profiles are obtained by minimizing the

970

R. Evans and others

grand potential functional,

$$\Omega[\rho_c, \rho_p] = F_{\text{id}}[\rho_c, \rho_p] + F_{\text{exc}}[\rho_c, \rho_p] + \sum_{i=c,p} \int d^3r (V_i^{\text{ext}}(\mathbf{r}) - \mu_i) \rho_i(\mathbf{r}), \quad (4.3)$$

where $F_{\text{id}}[\rho_c, \rho_p]$ is the ideal gas free energy functional and μ_i is the chemical potential of species i . Solving the resulting Euler–Lagrange equations is somewhat simpler than for a general binary mixture since $\rho_p(\mathbf{r})$ is an explicit functional of $\rho_c(\mathbf{r})$ and $V_p^{\text{ext}}(\mathbf{r})$; only $\rho_c(\mathbf{r})$ needs to be determined by numerical minimization.

(b) *Wetting and layering transitions at a hard wall*

Since our DFT incorporates bulk fluid–fluid phase separation it can be used to investigate fluid wetting phenomena at solid substrates. We choose to consider a planar hard wall defined by equation (2.6). For such a model we expect entropic depletion effects to favour the adsorption of colloid-rich phase at the wall so we might expect to observe complete wetting by this phase at the hard wall–colloid-poor interface.

In order to test the DFT we first calculated density profiles for $q = 0.1$, the mixture considered in §3, for which Monte Carlo results are available for the colloid profile; recall that the mapping to the effective Hamiltonian (2.7) is exact in this case. Our functional provides a very good description of the Monte Carlo results; the agreement is of similar quality to that between the simulation and one-component DFT results shown in figure 1. Explicit comparisons of theory and simulation results will be presented elsewhere, but we confirmed that the functional does account for the depletion attraction between the hard wall and the colloids.

We focus now on larger size ratios where a stable fluid–fluid transition occurs. Figure 2 shows the bulk phase diagram obtained from the present theory for a size ratio $q = 0.6$ for which the fluid–fluid demixing transition has a critical point at $\eta_{\text{p,crit}}^r \sim 0.495$. It should be emphasized that the fluid–fluid and solid–fluid phase boundaries presented here are those of the original free-volume theory of Lekkerkerker *et al.* (1992). A full investigation of the freezing properties of the present functional is outside the scope of the current study which is restricted to fluid states. Also shown in figure 2 is the Fisher–Widom (FW) line which divides the phase diagram into regions where the asymptotic decay of bulk pairwise correlations, $g_{ij}(r)$, is either monotonic or exponentially damped oscillatory (Evans *et al.* 1994). The FW line was determined by calculating the poles of the partial structure factors $S_{ij}(k)$. Note that in a binary mixture the three $g_{ij}(r)$ change simultaneously their asymptotic decay as the FW line is crossed.

In determining the adsorption characteristics, we choose to fix η_{p}^r and approach the bulk phase boundary from the colloid-poor side. This is analogous to performing a gas adsorption *isotherm* measurement for a simple fluid. Recall that η_{p}^r plays a role equivalent to inverse temperature. Depending on the value of η_{p}^r chosen, the adsorption behaviour changes dramatically. We consider size ratio $q = 0.6$ and describe some of the phenomena encountered. We first choose a path just above the critical point, with $\eta_{\text{p}}^r = 0.55$; see path I in figure 2. On approaching the phase boundary we find that the wall is completely wet by the colloid-rich phase. Figure 3 shows the colloid profiles signalling the growth of a thick layer of colloidal liquid against the wall. The corresponding polymer profiles are shown in the inset and indicate how

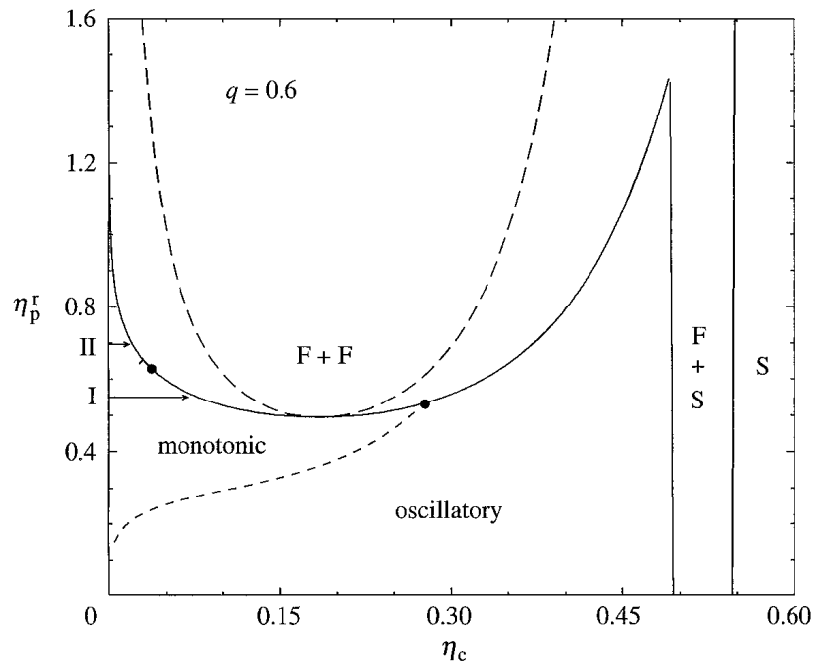


Figure 2. The bulk phase diagram calculated from free volume theory for $q = 0.6$. η_c is the packing fraction of the colloid and η_p^r that of polymer in the reservoir. F denotes fluid and S solid. The long-dashed line shows the fluid–fluid spinodal and the short-dashed line shows the Fisher–Widom line obtained from DFT. The latter intersects the binodal at $\eta_{p,FW}^r = 0.53$. Horizontal arrows indicate the paths I and II by which the phase boundary is approached for the adsorption studies. The point on the binodal at $\eta_{p,w}^r \approx 0.63$ indicates the location of the wetting transition.

polymer becomes more depleted as the colloid-rich layer grows. Strictly speaking, *macroscopically* thick wetting films can only occur on the monotonic side of the FW line, i.e. for $\eta_p^r < \eta_{p,FW}^r$, the point of intersection of the FW line and the binodal, since oscillatory binding potentials will stabilize very thick but finite films which would otherwise be infinite (Henderson 1994). For $\eta_p^r = 0.55$ (path I) we can easily obtain films of thickness 20 or $30\sigma_c$ and in the flat portion of the profiles the densities of colloid and polymer are equal to their values in the coexisting colloid-rich phase. At large values of η_p^r (> 0.75), we find that the wall is incompletely wetted by colloid; the layer thickness increases continuously remaining finite at the phase boundary. At lower values ($0.6 < \eta_p^r < 0.75$), we find a single, first order layering transition. This is illustrated in figure 4, where the colloid profiles are plotted for $\eta_p^r = 0.7$, following path II in figure 2, along with the Gibbs adsorption Γ . At the transition the densities $\rho_c(z)$ in the first (contact) layer and in the second layer increase substantially and Γ jumps discontinuously. Γ remains finite at bulk coexistence, i.e. there is still partial wetting. The layering transition line ends in a critical point at $\eta_p^r \approx 0.62$; the jump in the adsorption disappears for smaller η_p^r . It would appear that the layering represents a quasi-two-dimensional gas–liquid condensation transition. The layering transition line is quite separate from the prewetting line which emerges tangentially from the bulk coexistence curve at $\eta_{p,w}^r \approx 0.63$ (the wetting transition ‘temperature’) and ends in the prewetting critical point at $\eta_p^r \approx 0.60$. This pattern of surface transitions appears to be quite different from what is usually found for

972

R. Evans and others

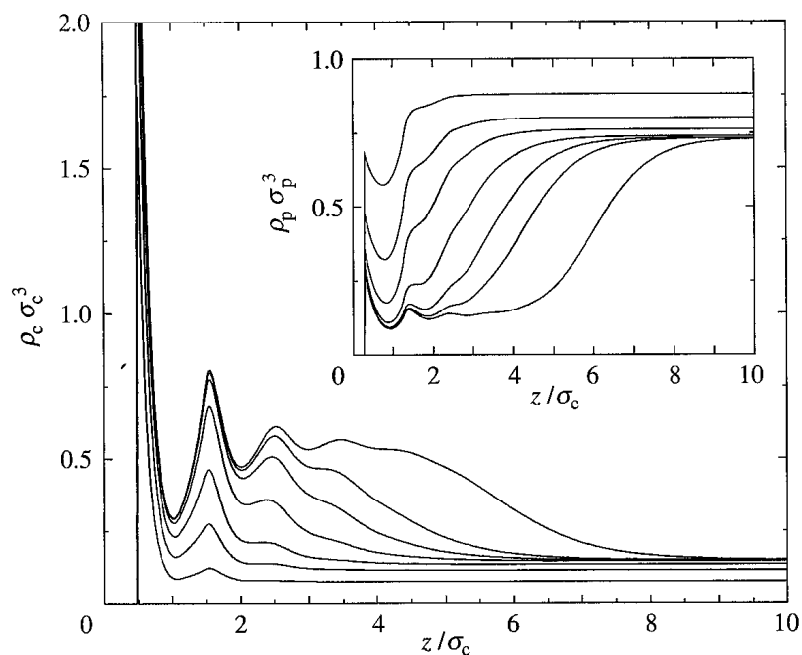


Figure 3. Colloid density profiles for $q = 0.6$ showing the complete wetting of a hard wall by the colloid-rich phase at $\eta_p^r = 0.55$ as the bulk phase boundary is approached along path I in figure 2. Bulk colloid fractions are $\eta_c = 0.04, 0.06, 0.07, 0.076, 0.0775, 0.0778$ and 0.0779 (from bottom to top). The inset shows the polymer profiles for the same η_c (from top to bottom).

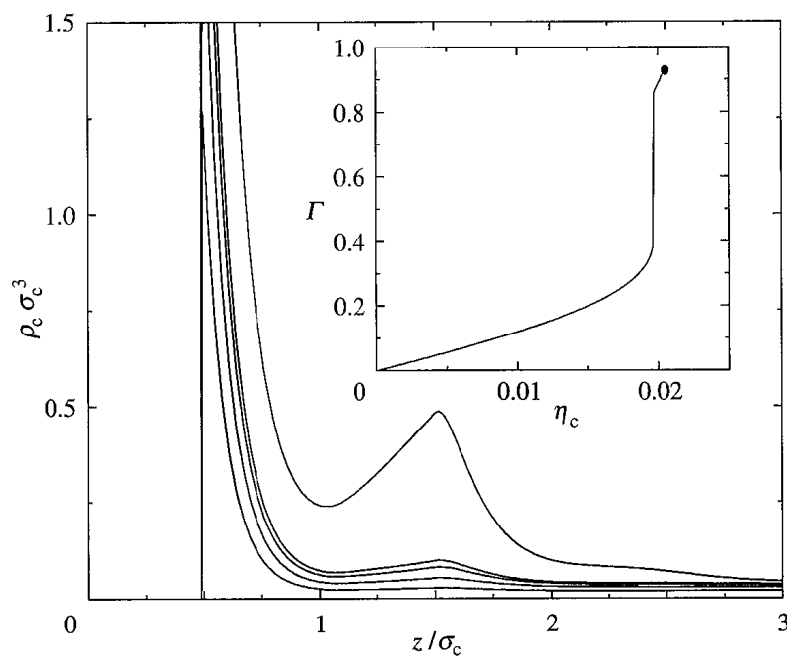


Figure 4. Colloid density profiles for $q = 0.6$ showing the layering transition at $\eta_p^r = 0.7$ corresponding to path II in figure 2. Bulk colloid fractions are $\eta_c = 0.010, 0.015, 0.018, 0.019$ and 0.020 (from bottom to top); the transition occurs between 0.019 and 0.020 . The inset shows the corresponding Gibbs adsorption Γ ; this remains finite at bulk coexistence $\eta_c = 0.0203$.

simple fluids adsorbed at strongly attractive substrates where, for temperatures not too far from the triple point, complete wetting often proceeds via a sequence (possibly infinite) of layering transitions (see, for example, Ball & Evans 1988). Here we have a *single* transition, distinct from prewetting, which occurs well away from the triple point; the latter is at $\eta_p^r \approx 1.43$ in the free-volume theory. It is very likely that the occurrence of the layering transition reflects the underlying difference between a one-component fluid, described by a simple pairwise fluid–fluid potential and a simple one-body wall–fluid potential representing interactions with a substrate, and the present binary AO mixture. As we have seen in § 2, the effective one-component Hamiltonian involves pairwise potentials which depend on the distance of the colloids from the wall as well as complex higher-body interactions for these (large) size ratios.

Although we have yet to determine how the pattern of surface transitions depends on the size ratio q , and there might well be surprises in store, we believe our present predictions of entropically driven wetting and layering transitions might encourage experimental investigations of adsorption in colloid–polymer mixtures. Real space techniques, such as confocal microscopy, may provide a useful tool for observing wetting in colloidal suspensions. Measurements of the contact angle θ formed at the contact line between the colloid-rich–colloid-poor (liquid–gas) interface and a suitable substrate modelling a hard wall could also be revealing. We are predicting that the colloidal liquid phase should incompletely wet the substrate ($\theta > 0$) for $\eta_p^r > \eta_{p,w}^r$, the wetting transition value, and wet completely ($\theta = 0$) for $\eta_p^r < \eta_{p,w}^r$.

(c) *The structure and tension of the fluid–fluid interface*

We have also calculated the properties of the free liquid–gas interface between demixed fluid phases using our new DFT approach. Detailed results are given in Brader *et al.* (2001b); here we merely state the main findings. For $q = 0.6$ and 1.0 , the two cases investigated in most detail, we find that the width of the interface is about one colloid diameter for states near the bulk triple point. This width is similar to estimates inferred from recent ellipsometric measurement on a real colloid–polymer mixture (de Hoog *et al.* 1999). The surface tension we calculate agrees reasonably well with data obtained from spinning-drop and breaking-thread measurements for mixtures of a silica colloid, coated with 1-octadecanol, and polydimethylsiloxane (PDMS) in cyclohexane at $T = 293$ K (de Hoog & Lekkerkerker 1999). The size ratio for this mixture is approximately 1.0. In order to compare our DFT results with experiment we choose $\sigma_c = 26$ nm, the mean diameter of the particles investigated in the experiment; there are no other adjustable parameters in the theory. The measured and calculated tensions are 3–4 $\mu\text{N m}^{-1}$, values which are about 1000 times smaller than tensions of simple fluids. Such small tensions result from the fact that colloids are much larger than atoms or simple molecules; the tension scales roughly as $k_B T \eta_p^r / \sigma_c^2$ for states well removed from the critical point (Brader & Evans 2000). The most striking results which emerge from the DFT are those for the form of the density profiles $\rho_c(z)$ and $\rho_p(z)$. We find that when η_p^r is sufficiently high, i.e. well removed from the critical point, both $\rho_c(z)$ and $\rho_p(z)$ exhibit oscillations on the colloid-rich (liquid) side of the free interface. The period, which is about σ_c , and the decay length of the oscillations are identical for both species, in keeping with general arguments concerning asymptotic decay of correlation functions in mixtures (Evans *et al.* 1994). For states with $\eta_p^r < \eta_{p,FW}$ (see figure 2), both $\rho_c(z)$ and

$\rho_p(z)$ decay monotonically into the bulk liquid. Although similar oscillations with a period of about one atomic diameter, are seen in DFT studies of the free liquid–gas interface for simple fluids near their triple points (Evans *et al.* 1993) here the amplitude of the oscillations in the colloid profile appears to be larger. Of course DFT treatments are mean-field-like in that they ignore the effects of capillary-wave fluctuations of the interface. We are presently investigating whether including these fluctuation effects will completely erode the oscillations or whether some oscillatory structure will remain in the ‘dressed’ colloid profile. From an experimental viewpoint it should be more favourable to investigate such structuring in colloidal fluids, where the period is of colloidal size, than in simple, atomic fluids.

5. Concluding remarks

Two different but complementary strategies for tackling the statistical mechanics of the AO model have been adopted. In the first we performed a formal integrating out of the polymer degrees of freedom to obtain an effective Hamiltonian for the colloids. Such a strategy is especially valuable for size ratio $q < 0.1547$, where the resultant effective Hamiltonian is exact and is sufficiently simple, even for inhomogeneous mixtures, to be investigated using computer simulation methods. The mapping makes tractable a difficult binary mixture problem which would not be tractable by direct simulation methods. This strategy has also proved valuable for determining the bulk phase behaviour of highly asymmetric binary mixtures of additive hard spheres (Dijkstra *et al.* 1999a). In this case the mapping to an effective one-component system of big spheres involves an infinite sum of terms for *any* value of q . However, if one truncates the series after the two-body (depletion potential) contribution, simulation results for the effective Hamiltonian capture accurately all the key features of the bulk phase equilibria as determined by direct simulation of the binary hard-sphere mixture—at least for size ratios up to $q = 0.2$ (Dijkstra *et al.* 1999a). How far in q one can trust an *approximate* effective Hamiltonian for studies of adsorption remains to be ascertained.

In the second strategy we did not perform any integrating out of the polymer degrees of freedom, rather we developed an approximate DFT for the binary AO mixture. Since there is no explicit integrating out, the DFT is applicable for all size ratios. This permits us to investigate mixtures for which stable fluid–fluid phase separation occurs, and allows us to tackle wetting and related adsorption phenomena as well as the free fluid–fluid interface. The same DFT could, in principle, be used to tackle bulk fluid–solid (freezing) transitions and the corresponding solid–fluid interface. It could also be used to investigate wall-induced crystallization, although this is a very demanding problem in DFT or in simulation. Confined mixtures constitute another class of problem which is well suited to investigation by DFT and we have observed capillary condensation phenomena when the mixture is confined between two parallel planar hard walls. Since the walls prefer the colloid-rich (liquid) phase, condensation occurs on the low η_c side of the coexistence curve (J. M. Brader 2000, unpublished work). We should emphasize that unlike DFT treatments of interfacial phenomena in simple fluids, where there is an explicit attractive fluid–fluid potential which is usually treated in a perturbative (mean-field) fashion (see, for example, Evans 1992), here the effective attractive interactions emerge from the theory and they are not treated perturbatively.

Interfacial properties of model colloid-polymer mixtures

975

In summary we have shown that interfacial properties of the simplest model colloid-polymer mixture can be extremely rich. That such a diversity of phenomena should arise in a system where the bare interactions are either hard or ideal is remarkable and points to the importance of entropic depletion forces in determining surface as well as bulk phase behaviour.

We thank E. H. A. de Hoog, A. Gonzalez, H. N. W. Lekkerkerker, A. A. Louis, R. P. Sear, M. M. Telo da Gama and P. B. Warren for helpful discussions. R. van Roij provided valuable insight into matters concerned with integrating out degrees of freedom and understanding the status of the resulting effective Hamiltonians. This research was supported by the British-German ARC Programme (Project 104b) and by DFG Lo 418/5.

References

- Asakura, S. & Oosawa, F. 1954 *J. Chem. Phys.* **22**, 1255.
 Ball, P. C. & Evans, R. 1988 *J. Chem. Phys.* **89**, 4412.
 Brader, J. M. & Evans, R. 2000 *Europhys. Lett.* **49**, 678.
 Brader, J. M., Dijkstra, M. & Evans, R. 2001a *Phys. Rev. E*. (In the press.)
 Brader, J. M., Evans, R., Schmidt, M. & Löwen, H. 2001b (Submitted.)
 de Hoog, E. H. A. & Lekkerkerker, H. N. W. 1999 *J. Phys. Chem. B* **103**, 5274.
 de Hoog, E. H. A., Lekkerkerker, H. N. W., Schulz, J. & Findenegg, G. H. 1999 *J. Phys. Chem. B* **103**, 10657.
 Dijkstra, M., van Roij, R. & Evans, R. 1999a *Phys. Rev. E* **59**, 5744.
 Dijkstra, M., Brader, J. M. & Evans, R. 1999b *J. Phys. Cond. Matt.* **11**, 10079.
 Dijkstra, M., van Roij, R. & Evans, R. 2000 *J. Chem. Phys.* **113**, 4799.
 Evans, R. 1992 In *Fundamentals of inhomogeneous fluids* (ed. D. Henderson), ch. 3, p. 85. Dekker.
 Evans, R., Henderson, J. R., Hoyle, D. C., Parry, A. O. & Sabeur, Z. A. 1993 *Molec. Phys.* **80**, 755.
 Evans, R., Leote de Carvalho, R. J. F., Henderson, J. R. & Hoyle, D. C. 1994 *J. Chem. Phys.* **100**, 591.
 Gast, A. P., Hall, C. K. & Russel, W. B. 1983 *J. Colloid Interface Sci.* **96**, 251.
 Gast, A. P., Russel, W. B. & Hall, C. K. 1986 *J. Colloid Interface Sci.* **109**, 161.
 Henderson, J. R. 1994 *Phys. Rev. E* **50**, 4836.
 Ilett, S. M., Orrock, A., Poon, W. C. K. & Pusey, P. N. 1995 *Phys. Rev. E* **51**, 1344.
 Kose, A. & Hachisu, S. 1976 *J. Colloid Interface Sci.* **55**, 487.
 Lekkerkerker, H. N. W., Poon, W. C. K., Pusey, P. N., Stroobants, A. & Warren, P. B. 1992 *Europhys. Lett.* **20**, 559.
 Poon, W. C. K. & Warren, P. B. 1994 *Europhys. Lett.* **28**, 513.
 Rosenfeld, Y. 1989 *Phys. Rev. Lett.* **63**, 980.
 Schmidt, M., Löwen, H., Brader, J. M. & Evans, R. 2000 *Phys. Rev. Lett.* **85**, 1934.
 Vrij, A. 1976 *Pure. Appl. Chem.* **48**, 471.

LETTER TO THE EDITOR

Entropic wetting and the fluid–fluid interface of a model colloid–polymer mixture

J M Brader¹, R Evans¹, M Schmidt² and H Löwen²

¹ H H Wills Physics Laboratory, University of Bristol, Bristol BS8 1TL, UK

² Institut für Theoretische Physik II, Heinrich-Heine-Universität Düsseldorf, Universitätsstraße 1, D-40225 Düsseldorf, Germany

Received 19 September 2001, in final form 22 November 2001

Published 7 December 2001

Online at stacks.iop.org/JPhysCM/14/L1

Abstract

A recent density functional theory is used to investigate the free interface between demixed fluid phases in a model colloid–polymer mixture. Both the colloid and polymer density profiles oscillate on the colloid-rich side of the interface, provided the polymer reservoir packing fraction η_p^* is sufficiently high. Results for the surface tension are in reasonable agreement with experiment. When the mixture is adsorbed against a hard wall, entropic depletion effects give rise to a wetting transition whereby the colloid-rich phase wets completely. Prior to complete wetting we find three layering transitions, the first of which extends far into the single-phase region. This pattern of surface phase transitions is very different from that observed for simple one-component fluids at planar substrates.

Adding non-adsorbing polymer to a colloidal suspension can considerably enrich the bulk phase behaviour. In particular, for sufficiently large size ratios R_g/R_c , where R_g is the radius of gyration of the polymer and R_c is the radius of the colloid, a colloid–polymer mixture can exhibit stable colloidal gas, liquid and solid phases, with the packing fraction of the polymer reservoir η_p^* playing a role equivalent to that of inverse temperature for a simple substance [1]. Colloidal gas–liquid phase separation is induced by the depletion effect, i.e. an effective attraction between the colloids arises from the exclusion of polymer from the depletion zone between colloids [2]. Although much attention has been paid to the bulk phase behaviour and structure, relatively few experimental [3, 4] or theoretical [5–7] studies have been carried out on the *interfacial* properties of such mixtures. One might expect the entropic depletion mechanism to lead to interesting adsorption phenomena and to rich surface phase behaviour. Here we investigate the free interface between the demixed colloid-poor (gas) and colloid-rich (liquid) fluid phases and the adsorption of the mixture at a hard wall using the simple model introduced by Asakura and Oosawa (AO) [2] and Vrij [8], which treats the colloids as hard spheres with radius R_c and the polymer coils as interpenetrating and non-interacting as regards their mutual interactions. The polymer particles are excluded from the

colloids to a centre-of-mass distance $R_c + R_p$, where the polymer ‘radius’ $R_p = R_g$. Assuming that the polymer is ideal constitutes a drastic oversimplification. Nevertheless the binary AO model does capture the observed variation of the bulk phase behaviour with increasing size ratio $q = R_p/R_c$ [1] and thus it is a natural choice for a first study of inhomogeneous colloid–polymer mixtures. Whilst some progress has been made in calculating the interfacial properties of the AO model, all work to date relies upon a mapping to an effective one-component system of colloids interacting via the AO pairwise potential [5–7]. This approach is useful for certain adsorption situations [6] but does have serious limitations as it is strictly valid only for highly asymmetric mixtures, with $q < 0.1547$, where many-body effective interactions between the colloids are absent [6, 9]. We have recently developed an alternative density functional theory (DFT) for the binary AO model using the techniques of fundamental measure theory (FMT) [10]. Our new functional treats arbitrary size ratios q and is thus able to incorporate the effects of many-body interactions which arise at larger values of q , and which represent an important feature of the model. In bulk a stable (w.r.t. the fluid–solid transition) fluid–fluid demixing transition occurs for $q \geq 0.3$ [9]. Our functional accounts for this transition as the bulk free energy is identical to that from the free-volume theory of Lekkerkerker *et al* [11]. The functional yields analytical partial structure factors via the Ornstein–Zernike (OZ) route of a similar quality to those obtained from Percus–Yevick (PY) theory but with the advantage that they are consistent with the bulk free energy, i.e. the thermodynamic and structural routes to the fluid–fluid spinodal are equivalent [10], a property which is especially advantageous for our present studies of interfaces at or near two-phase coexistence. We emphasize that, unlike DFT treatments of interfacial phenomena in simple fluids, where an explicit attractive fluid–fluid potential is treated in a perturbative (mean-field) fashion, here the effective interactions emerge naturally from the DFT and are treated non-perturbatively.

Applying the DFT to the free fluid–fluid interface we find oscillatory behaviour of both the colloid and polymer density profiles on the colloid-rich side for states removed from the bulk critical point. The calculated surface tensions are similar to those measured in real colloid–polymer mixtures [3]. At the hard wall we find novel depletion-induced wetting and layering transitions as the bulk fluid–fluid phase boundary is approached from the colloid-poor side by increasing the colloid packing fraction η_c at fixed η'_p . At first glance one might expect there to be little difference, in terms of the physical phenomena displayed, between the interfacial properties of this model complex fluid and those of a simple (atomic or molecular) fluid; the colloids behave as an effective one-component fluid where the strength of the attractive interaction is determined by η'_p . Since for an ideal polymer, and a hard wall, each term in the effective Hamiltonian is proportional to η'_p [6] one might expect equivalent Boltzmann weights in the two types of fluids. The crucial difference is that the functional now incorporates the effects of two- and higher-body interactions which depend on the distance of the colloids from the wall and which would be present in the effective Hamiltonian for the colloids. Studies of one-component fluids are usually based on a simple pairwise additive potential function for the fluid–fluid interaction and a simple one-body wall–fluid potential representing interactions with a substrate.

Details of the functional are given in [10]. We simply recall that this is constructed using the well-tried recipes of FMT developed for additive hard-sphere mixtures [12]. The full functional is designed to satisfy the zero-dimensional situation of extreme confinement and involves tensor weight functions [10]. Here we employ the simpler version which omits the tensor contribution to the free energy density and which can be regarded as a linearization, in the polymer density, of the original Rosenfeld FMT functional³. Density

³ In equation (6) of [10] we set $\hat{n}_{m2}^i \equiv 0$.

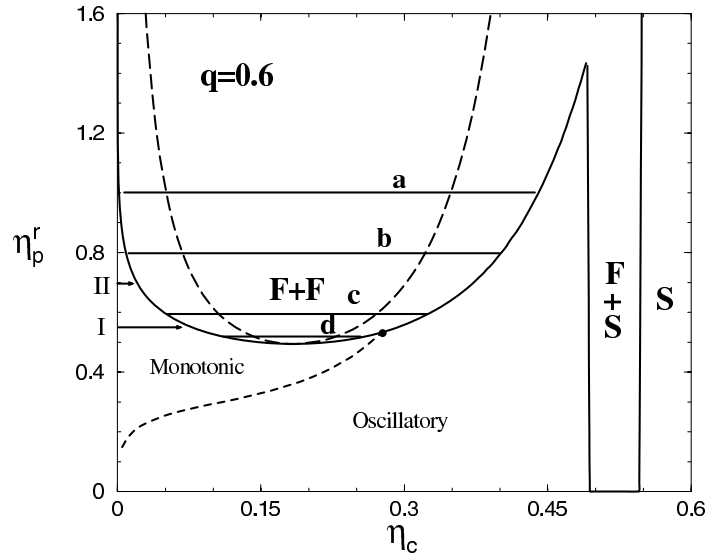


Figure 1. The bulk phase diagram calculated from free-volume theory [9, 11] for $q = 0.6$. η_c is the packing fraction of the colloid and η_p^r that of the polymer in the reservoir. F denotes the fluid and S the solid. The long broken curve shows the fluid–fluid spinodal and the short broken curve shows the (FW) line obtained from DFT (see footnote 4). The latter intersects the binodal at $\eta_{p,FW}^r = 0.53$. The horizontal tie lines a, b, c, d connect coexisting fluid states. Horizontal arrows indicate paths I and II by which the phase boundary is approached for the adsorption studies of figures 3 and 4.

profiles for colloid (c) and polymer (p) are obtained by minimizing the grand potential functional $\Omega[\rho_c(\mathbf{r}), \rho_p(\mathbf{r})] = \mathcal{F}[\rho_c(\mathbf{r}), \rho_p(\mathbf{r})] + \sum_{i=c,p} \int d^3r (V_i(\mathbf{r}) - \mu_i) \rho_i(\mathbf{r})$ where \mathcal{F} denotes the intrinsic Helmholtz free energy functional of the AO mixture, μ_i is the chemical potential (fixed by the reservoir) and $V_i(\mathbf{r})$ is the external potential coupling to species i with $i = c, p$. In the case of the free interface $V \equiv 0$; for a hard wall $V_c = \infty$ for $z < R_c$ and 0 otherwise, while $V_p = \infty$ for $z < R_p$ and 0 otherwise. z is the coordinate perpendicular to the wall. The thermodynamic state point is specified by the packing fraction of colloids: $\eta_c = 4\pi(R_c)^3 \rho_c / 3$ and of polymer in the reservoir: $\eta_p^r = 4\pi(R_p)^3 \rho_p^r / 3$, where ρ_c and ρ_p^r refer to the number densities. Diameters are denoted by $\sigma_c = 2R_c$ and $\sigma_p = 2R_p$.

We consider first the free interface between demixed fluid phases. Figure 1 shows the bulk phase diagram obtained from the present theory for a size ratio $q = 0.6$ for which there is a stable fluid–fluid demixing transition with a critical point at $\eta_{p,crit}^r \sim 0.495$. It should be emphasized that the fluid–fluid and solid–fluid phase boundaries presented here are those of the original free-volume theory [9, 11]. A full investigation of the freezing properties of the present functional is outside the scope of the present study, which is restricted to fluid states. The colloid density profiles are shown in figure 2. For states approaching the triple point the interfacial width is $\sim \sigma_c$, similar to values inferred from ellipsometric measurements [4]. Striking oscillations develop on the colloid-rich side. The general theory of asymptotic decay of correlations in mixtures with short-range forces predicts that the period and decay length of oscillations in the density profiles of both species should be identical [13]. We confirmed that, for states where the colloid profile oscillates, the corresponding polymer profiles exhibit oscillations, on the same, colloid-rich, side of the interface, with identical period and decay length as those of the colloid.

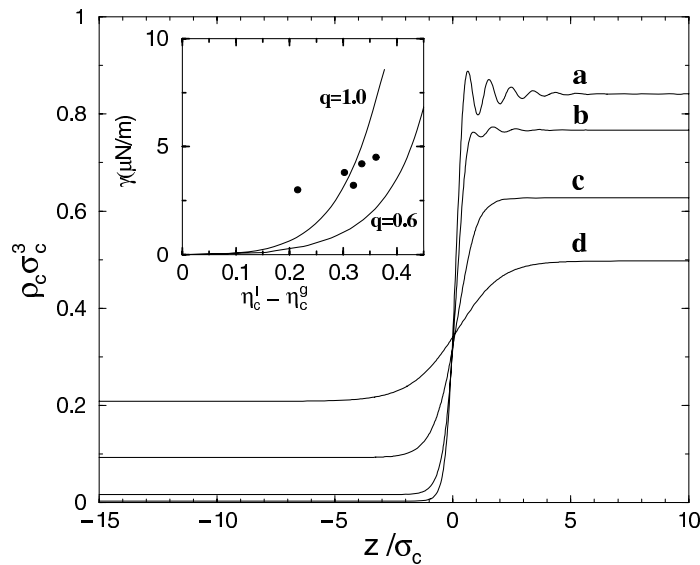


Figure 2. Colloid density profiles for the free interface between demixed fluid phases for a size ratio $q = 0.6$. The polymer reservoir packing fractions correspond to the tie lines in figure 1, i.e. $\eta_p^r = 1.0$ (a), 0.8 (b), 0.6 (c) and 0.52 (d) (near critical point). States a, b and c lie on the oscillatory side of the FW line. The inset shows the surface tension γ versus the difference in the colloidal packing fraction in coexisting liquid (l) and gas (g) phases for $q = 0.6$ and 1.0. The colloid diameter is taken to be 26 nm to compare with experimental data of [3] (points) where $q = 1.0$.

In simple fluids the presence of oscillations in one-body density profiles is intimately connected to the existence of the Fisher–Widom (FW) line which divides the bulk (density–temperature) phase diagram into regions where the asymptotic decay of bulk pairwise correlations is either monotonic or exponentially damped oscillatory [13, 14]. There is an analogous FW line for the present model (see figure 1), where the three partial pair correlation functions change their asymptotic decay simultaneously⁴.

For the present mixture oscillatory profiles arise at the free interface when the colloid density in the coexisting liquid is greater than the colloid density where the FW line intersects the binodal, i.e. for all states with $\eta_p^r > \eta_{p,\text{FW}}^r = 0.53$ for $q = 0.6$. However, the amplitude of oscillations can become very small for states just above the FW intersection point and this is why profile (c) does not show oscillations on the scale of figure 2. For state (a) with $\eta_p^r = 1.0$ the amplitude of the oscillations is substantial and appears to be larger than the corresponding amplitude for a square well fluid near its triple point [14]. Thermally induced capillary-wave fluctuations of the interface will act to erode the oscillations in the ‘bare’ (mean-field) density profiles obtained from DFT. Because of the extremely low surface tensions γ which occur in colloidal systems one might expect the oscillations to be completely washed out by fluctuation effects. However, it is the dimensionless parameter $\omega = k_B T / 4\pi \gamma \xi^2$ which determines the strength of these fluctuation effects and we find that ω takes values of a similar size as those for simple fluids. Further details will be given elsewhere [15]. This is due to the fact that the bulk correlation length ξ scales roughly as σ_c [10] and γ as $1/\sigma_c^2$ [5]. From our explicit calculations of γ and ξ we find that $\omega \approx 0.04$ for states such as (a) in figure 2. This implies

⁴ The FW line was determined by calculating the poles of the partial structure factors $S_{ij}(k)$, following [13].

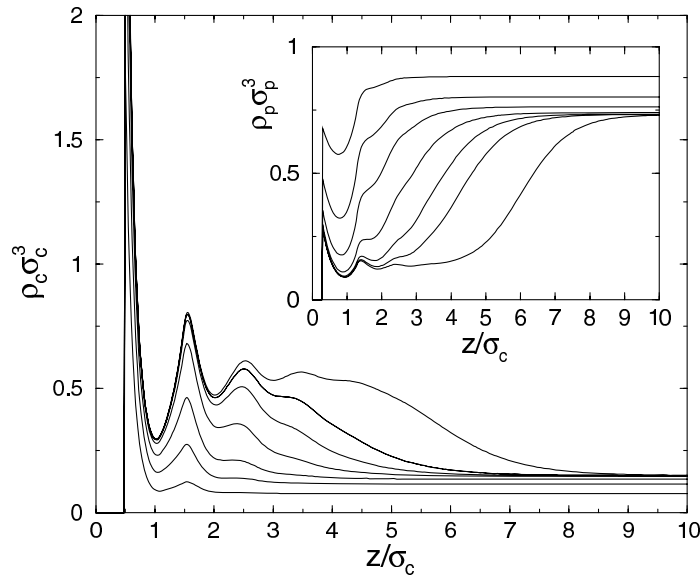


Figure 3. Colloid density profiles showing the complete wetting of a hard wall by the colloid-rich phase at $\eta_p^l = 0.55$ as the bulk phase boundary is approached along path I in figure 1. Bulk colloid fractions are $\eta_c = 0.04, 0.06, 0.07, 0.076, 0.0775, 0.0778$ and 0.0779 (from bottom to top). The inset shows the polymer profiles for the same η_c (from top to bottom).

that detecting oscillations of the colloid profile should be no more difficult than for simple fluids. Indeed, it could be more favourable to investigate such structuring in colloidal systems, where the period is of colloidal size, than in atomic fluids where the period is about one atomic diameter. The inset in figure 2 shows the tension, γ , for size ratios $q = 0.6$ and 1.0 . We find that the tension calculated using the present functional is consistently larger than that calculated using the effective one-component Hamiltonian treated by square gradient DFT [5] and agrees better with the experimentally measured tension for mixtures of a silica colloid, coated with 1-octadecanol, and polydimethylsiloxane (PDMS) in cyclohexane at $T = 293$ K [3]. The size ratio for this mixture is approximately 1.0 . In order to compare our DFT results with experiment we choose $\sigma_c = 26$ nm, the mean diameter of the particles investigated in [3]; there are no other adjustable parameters in the theory. The measured tensions are $3\text{--}4 \mu\text{N m}^{-1}$, values which are about 1000 times smaller than tensions of simple fluids. Theory predicts a rapid decrease of the tension as the critical point is approached, i.e. $\gamma \sim (\eta_c^l - \eta_c^g)^3$ in this mean-field treatment. The decrease should be even more rapid for proper Ising-like criticality where the exponent is replaced by $2\nu/\beta \approx 3.9$. That the experimental data do not indicate such a decrease probably reflects the difficulty in working close to the critical point⁵.

Next we consider the AO mixture adsorbed at a hard wall. As a test we first calculated profiles for $q = 0.1$ where simulation results are available for the colloid profiles since, for such a small size ratio, the mapping to an effective Hamiltonian with only a pairwise additive fluid–fluid potential and an explicit wall–fluid depletion potential is exact [6]. We find that the present functional provides a very good description of the colloid profiles, in particular the dramatic increase in the wall contact value as polymer is added [15]; the functional accounts

⁵ In a very recent study of a similar mixture of silica particles and PDMS in cyclohexane the density difference and surface tension between coexisting phases were determined closer to the critical point than in [3]. Chen *et al* [16] report tensions $< 1 \mu\text{N m}^{-1}$ and a good fit to Ising-like scaling.

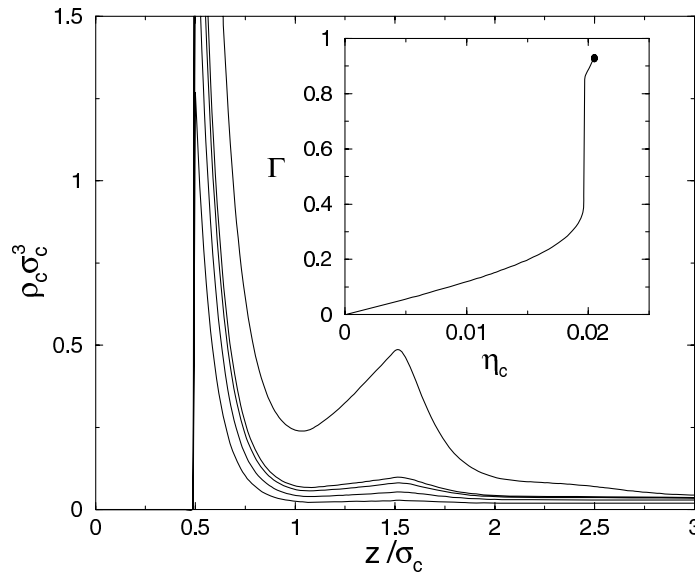


Figure 4. Colloid density profiles showing the layering transition at $\eta_p^r = 0.7$ corresponding to path II in figure 1. Bulk colloid fractions are $\eta_c = 0.010, 0.015, 0.018, 0.019$ and 0.020 (from bottom to top); the transition occurs between 0.019 and 0.020 . The inset shows the Gibbs adsorption Γ which jumps at the transition and remains finite at bulk coexistence $\eta_c = 0.0203$.

for the depletion attraction between the wall and the colloids. Here we focus on larger size ratios where fluid–fluid demixing occurs. We fix η_p^r and approach the bulk phase boundary from the colloid-poor side.

Depending on the value of η_p^r chosen, the adsorption behaviour changes dramatically. As an example we consider the size ratio $q = 0.6$ and describe the phenomena encountered. We first choose a path just above the critical point, $\eta_p^r = 0.55$, see path I in figure 1. On approaching the phase boundary we find that the wall is completely wet by the colloid-rich phase. Figure 3 shows the colloid profiles signalling the growth of a thick layer of colloidal liquid against the wall⁶. The corresponding polymer profiles are shown in the inset and indicate how polymer becomes more depleted as the colloid-rich layer grows. At large values of η_p^r (>0.72) we find that the wall is only partially wet by colloid; the layer thickness increases continuously, remaining finite at bulk coexistence. At lower values ($0.62 < \eta_p^r < 0.72$) we find a first-order layering transition. This is illustrated in figure 4 where the colloid profiles are plotted for $\eta_p^r = 0.7$, following path II in figure 1 along with the Gibbs adsorption $\Gamma = \sigma_c^2 \int_0^\infty (\rho_c(z) - \rho_c(\infty)) dz$. At the transition the densities $\rho_c(z)$ in the first (contact) layer and in the second layer increase substantially and Γ jumps discontinuously. Γ remains finite at bulk coexistence, i.e. there is still partial wetting. The layering transition line ends in a critical point at $\eta_p^r \approx 0.62$ (see figure 5), below which the adsorption increases continuously as η_c increases towards its value at bulk coexistence. Further layering transitions can be located by calculating the density profiles *along* the coexistence curve. These are shown in figure 5. At the second transition a third adsorbed layer of colloid develops and the local density in the second layer increases significantly so that Γ jumps discontinuously. Similarly, at the

⁶ Strictly speaking *macroscopically* thick wetting films can only occur on the monotonic side of the FW line, i.e. for $\eta_p^r < \eta_{p,FW}^r$, since oscillatory binding potentials will stabilize very thick but finite films which would otherwise be infinite [17]. For $\eta_p^r = 0.55$ (path I) we can easily obtain films of thickness 20 or $30\sigma_c$.

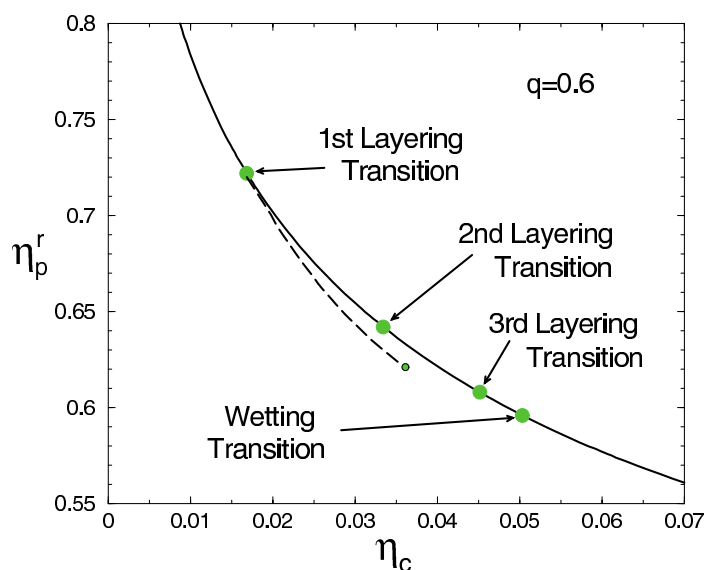


Figure 5. Surface phase diagram for the mixture at a hard wall. The full curve is a portion of the bulk coexistence curve of figure 1 and the circles denote the onset of three layering transitions. The first layering transition line (broken curve) extends deep into the single- (gas-) phase region, ending in a critical point near $\eta_p^r = 0.62$, whereas the second and third transition lines are extremely short. The transition from partial to complete wetting is denoted by the lowest circle and the accompanying pre-wetting line is also extremely short.

(This figure is in colour only in the electronic version)

third transition the fourth adsorbed layer develops with an accompanying increase in density of layer three, giving another jump in Γ . Unlike at the first transition the second and third transition lines are extremely short in η_p^r and as it is very difficult to determine these accurately we have simply represented the transitions as circles in figure 5. Below the third transition Γ remains finite at bulk coexistence until $\eta_p^r \sim 0.595$ where the transition to complete wetting occurs. This appears to be first order, i.e. Γ appears to diverge discontinuously. However, it is difficult to determine the prewetting line, which should emerge tangentially from the coexistence curve at the wetting transition. All we can say with certainty is that any prewetting line is extremely short⁷.

This pattern of surface transitions is quite different from what is usually found for simple fluids adsorbed at strongly attractive substrates where, for temperatures not too far from the triple point, complete wetting often proceeds via a sequence (possibly infinite) of layering transitions [19] extending away from bulk coexistence. Here we have three layering transitions, only the first of which extends far into the single (gas) phase, occurring far from the triple point which is at $\eta_p^r \sim 1.43$ in the free-volume theory. Although there may be a fourth, fifth, etc, layering transition we are unable to detect these. The occurrence of such a pattern of transitions reflects the underlying difference between a one-component fluid, described by a simple pairwise fluid–fluid potential, and the present binary AO mixture, for which the effective one-component Hamiltonian [6] involves pairwise potentials which depend on the distance of the colloids from

⁷ In a preliminary conference report of our results [18] we correctly identified the first layering transition line but failed to identify the second and third transitions and to determine accurately the wetting transition.

the wall as well as complex higher-body interactions⁸. How the pattern of surface transitions depends on the size ratio q will be described elsewhere [15] but we believe our present predictions of entropically driven wetting and layering transitions might encourage experimental investigations of adsorption in colloid-polymer mixtures. Real space techniques, such as confocal microscopy, should provide a useful tool for observing wetting in colloidal suspensions.

In summary we have shown that interfacial properties of the simplest model colloid-polymer mixture can be extremely rich. That such a diversity of phenomena should arise in a system where the bare interactions are either hard or ideal is remarkable and points to the importance of entropic depletion forces in determining surface as well as bulk phase behaviour.

We thank A J Archer, M Dijkstra, E H A de Hoog, A Gonzalez, J R Henderson, H N W Lekkerkerker, A O Parry and M M Telo da Gama for helpful discussions. We are particularly grateful to R Roth for valuable advice on numerical matters and for carrying out an independent check of the surface phase diagram. This research was supported by the British-German ARC programme and by DFG Lo 418/5.

References

- [1] See, e.g., Gast A P, Hall C K and Russel W B 1983 *J. Colloid. Interface. Sci.* **96** 251
Ilett S M *et al* 1995 *Phys. Rev. E* **51** 1344
Poon W C K, Pusey P N and Lekkerkerker H N W 1996 *Phys. World* **9** 27
- [2] Asakura S and Oosawa F 1954 *J. Chem. Phys.* **22** 1255
- [3] de Hoog E H A and Lekkerkerker H N W 1999 *J. Phys. Chem. B* **103** 5274
- [4] de Hoog E H A *et al* 1999 *J. Phys. Chem. B* **103** 10657
- [5] Brader J M and Evans R 2000 *Europhys. Lett.* **49** 678
- [6] Brader J M, Dijkstra M and Evans R 2001 *Phys. Rev. E* **63** 041405
- [7] Vrij A 1997 *Physica A* **235** 120
- [8] Vrij A 1976 *Pure Appl. Chem.* **48** 471
- [9] Dijkstra M, Brader J M and Evans R 1999 *J. Phys.: Condens. Matter* **11** 10079 and references therein
- [10] Schmidt M, Löwen H, Brader J M and Evans R 2000 *Phys. Rev. Lett.* **85** 1934
- [11] Lekkerkerker H N W *et al* 1992 *Europhys. Lett.* **20** 559
- [12] Rosenfeld Y 1989 *Phys. Rev. Lett.* **63** 980
Tarazona P and Rosenfeld Y 1997 *Phys. Rev. E* **55** R4873
Rosenfeld Y *et al* 1997 *Phys. Rev. E* **55** 4245
- [13] Evans R *et al* 1994 *J. Chem. Phys.* **100** 591
- [14] Evans R *et al* 1993 *Molec. Phys.* **80** 755
- [15] Brader J M 2001 *PhD Thesis* University of Bristol
- [16] Chen B-H, Payandeh B and Robert M 2000 *Phys. Rev. E* **62** 2369
- [17] Henderson J R 1994 *Phys. Rev. E* **50** 4836
- [18] Evans R *et al* 2001 *Phil. Trans. R. Soc. A* **359** 961
- [19] See, e.g., Ball P C and Evans R 1988 *J. Chem. Phys.* **89** 4412 and references therein

⁸ We have confirmed this assertion by investigating adsorption at a hard wall for $q = 0.6$, using the DFT described in [6], for a one-component fluid given by the AO pair potential at a wall which exerts the AO wall-fluid depletion potential. No layering transitions are found.

Invited article

Statistical mechanics of inhomogeneous model colloid–polymer mixturesJOSEPH M. BRADER¹, ROBERT EVANS^{2,3*†} and MATTHIAS SCHMIDT^{4‡}¹Institute of Physiology, University of Bern, Bülhplatz 5, 3012 Bern, Switzerland²H. H. Wills Physics Laboratory, University of Bristol, Royal Fort, Tyndall Avenue, Bristol BS8 1TL, UK³MPI für Metallforschung, Heisenbergstraße 3, D-70569 Stuttgart, Germany⁴Soft Condensed Matter, Debye Institut, Utrecht University, Princetonplein 5, 3584 CC Utrecht, The Netherlands*(Received 22 September 2003; revised version accepted 10 November 2003)*

We describe two strategies for tackling the equilibrium statistical mechanics of inhomogeneous colloid–polymer mixtures treated in terms of the simple Asakura–Oosawa–Vrij (AO) model, in which colloid–colloid and colloid–polymer interactions are hard-sphere like, whereas the polymer–polymer interaction is zero (perfectly interpenetrating polymer spheres). The first strategy is based upon integrating out the degrees of freedom of the polymer spheres to obtain an effective one-component Hamiltonian for the colloids. This is particularly effective for small size ratios $q = \sigma_p/\sigma_c < 0.1547$, where σ_p and σ_c are the diameters of colloid and polymer spheres, respectively, since in this regime three and higher body contributions to the effective Hamiltonian vanish. In the second strategy we employ a geometry based density functional theory (DFT), specifically designed for the AO model but based on Rosenfeld's fundamental measure DFT for additive mixtures of hard-spheres, that treats colloid and polymer on an equal footing and which accounts for the fluid–fluid phase separation occurring for larger values of q . Using the DFT we investigate the properties of the 'free' interface between colloid-rich (liquid) and colloid-poor (gas) fluid phases and adsorption phenomena at the interface between the AO mixture and a hard-wall, for a wide range of size ratios. In particular, for $q = 0.6$ to 1.0 , we find rich interfacial phenomena, including oscillatory density profiles at the free interface and novel wetting and layering phase transitions at the hard-wall–colloid gas interface. Where appropriate we compare our DFT results with those from computer simulations and experiment. We outline several very recent extensions of the basic AO model for which geometry based DFTs have also been developed. These include a model in which the effective polymer sphere–polymer sphere interaction is treated as a repulsive step function rather than ideal and one in which the depletant is a fluid of infinitely thin rods (needles) with orientational degrees of freedom rather than (non-interacting) polymer spheres. We comment on the differences between results obtained from these extensions and those of the basic AO model. Whilst the interfacial properties of the AO model share features in common with the those of simple (atomic) fluids, with the polymer reservoir density replacing the inverse temperature, we emphasize that there are important differences which are related to the many-body character of the effective one-component Hamiltonian.

1. Introduction

It is well established that certain colloidal suspensions behave as hard-sphere systems. Pioneering studies by

*Author for correspondence. e-mail: bob.evans@bristol.ac.uk

†Molecular Physics Lecture, Liblice Conference, Czech Republic, June 2002. Invited paper for journal.

‡On leave from Institut für Theoretische Physik II, Heinrich-Heine-Universität Düsseldorf, Universitätsstraße 1, D-40225 Düsseldorf, Germany.

Pusey, van Megen and co-workers in the 1980s established that polymethylmethacrylate (PMMA) particles, sterically stabilized by chemically grafted poly-12-hydroxystearic acid (PHSA), dispersed in a solvent whose refractive index matches that of the particles, exhibit phase behaviour which mimics closely that of pure hard spheres [1]. In particular, coexistence of colloidal fluid and crystal phases was found for colloid packing (volume) fractions, η_c , in the range $0.494 < \eta_c < 0.545$, values consistent with computer simulations

of hard spheres. For $\eta_c < 0.494$ there is a single fluid phase in which the diffusive dynamics of the colloidal particles, as measured by dynamic light scattering, is consistent with hard-sphere behaviour [1]. Other colloidal systems also behave as hard spheres. For example, the equation of state, obtained from X-ray measurements of the colloid density profile in a gravitational field, for charged polystyrene spheres suspended in water (with HCl) is in excellent agreement with the hard-sphere equation of state, on both the fluid and crystal branches [2]. Of course, the effective pair potential between colloids cannot be perfectly hard; this cannot jump discontinuously to infinite repulsion at some precise diameter. However, as the particles approach each other the effective potential rises by many $k_B T$ over a separation of one or two nanometres or so—a distance which is very small compared with the particle diameter (typically 6–700 nm, in the experiments mentioned above). Entropically driven freezing is the *only* phase transition that can occur in a system of ‘hard-sphere’ colloids.

Suppose now that non-adsorbing polymer is added to the suspension of colloids. The interactions are, in general, complicated but one can consider the case of flexible polymer chains under athermal ‘good’-solvent conditions, where the interactions between all the species are hard-core repulsive, i.e. polymer chains are mutually self-avoiding and are excluded from the hard-sphere colloids. From a statistical mechanics point of view, only packing constraints are relevant and the properties of the system, in particular any phase transitions, are determined by purely entropic effects. It then comes as something of a surprise to learn that the phase behaviour of colloid–polymer mixtures can be very rich. A series of experiments, performed mainly by groups in Utrecht, Bristol and Edinburgh in the 1980s and early 1990s, confirmed that adding sufficient non-adsorbing polymers can cause phase separation into two fluid phases, one rich in colloid and the other poor; references to the original papers can be found in [1, 3–5]. In order for fluid–fluid phase separation to occur there must be a mechanism that generates an effective attractive interaction between the colloidal particles. Moreover, this mechanism must be entropic in origin since all ‘bare’ interactions between species are hard-core repulsive. An appropriate mechanism was described as early as 1954 by Asakura and Oosawa [6] and this is now termed the depletion effect or depletion attraction. Asakura and Oosawa considered two big spherical colloidal particles in a ‘sea’ of rigid macromolecules. The latter were treated as hard spheres as regards their interaction with the colloids whereas macromolecule–macromolecule were set to zero, so that the solution of macromolecules was treated as an

ideal gas. Such an assumption should be appropriate for a dilute solution or for theta solvents where the second virial coefficient for macromolecule–macromolecule interactions vanishes. The centre of a macromolecule sphere is excluded from the surface of a colloid by a distance equal to $\sigma_p/2$, so there is a depletion zone (or excluded volume region) in which there are no macromolecule centres of mass. If two colloids approach each other, so that the depletion zones overlap, then there is an increase in free volume for the macromolecule spheres, i.e. an increase in their translational entropy, leading to an effective attractive (depletion) interaction between the two colloids. One can also view the attraction as arising from an unbalanced osmotic pressure pushing the colloids together as the macromolecules are expelled from the gap between the two colloids. By calculating the volume of the overlap between the two depletion zones, Asakura and Oosawa [6] obtained an explicit expression for the depletion force between two colloids whose centres are separated by a distance R , immersed in an ideal solution of macromolecules of fugacity z_p . The depletion potential $\phi_{AO}(R; z_p)$ vanishes when the depletion zones no longer overlap; the attractive potential has a finite range equal to σ_p . Increasing the concentration of the macromolecule sea increases z_p and the depth of the potential well, whereas increasing σ_p extends the range and, hence, the integrated strength of the attraction. It is clear that depletion attraction is a possible mechanism for driving phase separation. In a second paper, Asakura and Oosawa [7] focused on the depletion potential and discussed the possible aggregation of suspended colloidal particles. By assuming the polymers can be treated as spherical macromolecules, internal conformational degrees of freedom are ignored. Independently, in 1976 Vrij [8] proposed the same depletion mechanism, deduced the depletion potential between a pair of colloidal spheres and the associated second virial coefficient and went an important step further by writing down an explicit model Hamiltonian for the binary *mixture* of hard-sphere colloids and ideal polymer (macromolecule) spheres; this is the Asakura–Oosawa–Vrij or AO model—see section 2. Vrij’s paper provides the basis for a full statistical mechanical treatment for an (idealized) model of a colloid–polymer mixture. Vrij pointed out that his interparticle potentials define a ‘non-additive’ hard-sphere model in the theory of liquids. We return to this aspect in section 2. He also suggested that the colloid–polymer hard-sphere diameter should be $(\sigma_c + \sigma_p)/2$ with $\sigma_p/2 \sim R_g$, the radius of gyration of the polymer. The next important development in the theory was made by Gast *et al.* [9] who calculated the phase behaviour of the AO model using thermodynamic perturbation theories for an

approximation that assumes an effective colloid–colloid pair potential, $\phi^{\text{eff}}(R; z_p)$, consisting of the bare hard-sphere potential plus the attractive depletion potential $\phi_{\text{AO}}(R; z_p)$. Gast *et al.* predicted that the effect of adding polymer depends sensitively on the polymer to colloid size ratio $q = \sigma_p/\sigma_c$. For $q \lesssim 0.3$, adding polymer merely augments, in η_c , the colloidal fluid–crystal coexistence region above the range found for pure hard spheres, whereas for larger values of q a stable colloidal *liquid* phase can exist. In the (η_c, z_p) plane there is a triple point where gas, liquid and crystalline colloidal phases coexist [9] and for $q \gtrsim 0.6$ the phase diagrams resemble those of simple atomic fluids, with z_p playing the same role as inverse temperature, $1/T$. Thus, entropically driven depletion attraction can become sufficiently strong and sufficiently long-ranged to generate a van der Waals-like scenario for the gas–liquid transition.

As noted by Gast *et al.*, one significant drawback to their approach is that for size ratios $q > 0.1547$, the effective one-component Hamiltonian should contain three- and higher-body effective interactions between the colloidal particles—see section 2.1; these interactions are tedious to evaluate and cumbersome to incorporate into perturbation theories or computer simulations of the liquid and crystalline phases and are therefore usually ignored. However, the effects of many-body effective interactions are not necessarily small and we shall argue below that these can play a crucial role for both bulk and interfacial phase behaviour.

An alternative approach to determining the phase behaviour of the AO model, which does not rely upon mapping to an effective one-component Hamiltonian and which *does* capture some of the effects of many-body terms, is the so-called free-volume theory of Lekkerkerker *et al.* [4]. Some details of this approach will be given in section 2.2 but the approximation consists of replacing the exact (average) free volume available to the ideal polymers by the corresponding quantity evaluated in the low-density limit, $z_p \rightarrow 0$, for which an analytical approximation is available. Having an explicit expression for the free volume fraction, $\alpha(\eta_c)$, allows one to transform readily from the reservoir representation, where z_p or, equivalently, η_p^r , the packing fraction of ideal polymer is specified, to the system representation where η_p , the packing fraction in the actual system is specified: $\eta_p = \alpha\eta_p^r$. Experimental phase diagrams are plotted in the (η_c, η_p) plane. The free-volume theory predicts a stable colloidal gas–liquid transition for $q \gtrsim 0.32$ and the phase diagrams exhibit similar trends to those from the approach of Gast *et al.*, although there are some significant differences—see [10] for detailed comparisons and [11] for a discussion of the connections and distinctions between the two approaches. Subsequently Meijer and Frenkel [3]

performed pioneering Monte Carlo simulations for two separate models of colloids dispersed in a dilute polymer solution. The first was a lattice–polymer model in which polymers are represented by *ideal* (non-self-avoiding) chains confined to a cubic lattice. However, lattice sites occupied by colloidal hard-spheres are inaccessible to polymer. The second was the AO model, but with the polymer spheres restricted to a cubic lattice. Phase diagrams, calculated in the (η_c, z_p) plane, for the two models were rather close to each other and for the size ratios $q = 0.5$ and 0.7 considered the simulation results corresponding to the (lattice–polymer) AO model were in fair agreement with those from free-volume theory.

To summarize, by 1994 various theoretical and simulation studies of idealized models had shown that for small polymer–colloid size ratios the phase diagram is of the fluid–solid type, whereas for larger size ratios, where the depletion potential becomes longer ranged *and* many-body interactions become important, stable colloidal gas–liquid phase separation occurs. This trend in the phase behaviour was consistent with earlier experimental observations. Subsequent experiments [5, 12] provided convincing support for the scenario suggested by theory. In particular, three-phase coexistence was reported at certain size ratios for charged colloidal polystyrene particles mixed with hydroxyethyl cellulose [12] and for sterically stabilized PMMA particles mixed with random coil polystyrene (PS) in a *cis*-decalin solvent [5]. An admirable account of the work of the Edinburgh group on the latter system, which the author describes as a ‘model colloid–polymer mixture’, is given in the recent topical review by Poon [13]. We direct readers wishing to learn more about phase behaviour, equilibrium structure, phase transition kinetics, gels and glasses in *real* mixtures to this illuminating article. Another well-characterized system, much studied by the Utrecht group, consists of sterically stabilized silica particles and polydimethylsiloxane (PDMS) in cyclohexane. Silica has the advantage over PMMA that small particles are available (diameters as small as 20 nm) which is important in studies of interfaces—see section 3.

The thrust of the present article is quite different from that of Poon. Having established that the simple AO model captures the main features of the experimental bulk phase diagrams, here we enquire what are the properties of *inhomogeneous* colloid–polymer mixtures, as described by the same AO model. Inhomogeneous situations, where the average density profiles of both species are spatially varying, occur in the context of adsorption at a solid substrate, at the planar interface between two coexisting (colloid-rich and colloid-poor) phases, for mixtures confined in capillaries or porous

media or, indeed, in a colloidal crystal. Nucleation phenomena also require a description of the inhomogeneous fluid. Our strategy is not to attempt any realistic modelling of a colloid–polymer mixture which is, of course, a highly complex system involving multiple length and time scales, rather we seek to understand the basic adsorption and interfacial properties that arise in the context of the simple model fluids. Moreover, we restrict consideration to equilibrium aspects. Whether the predictions from the model are relevant to real mixtures is a separate issue. In defence of our strategy we remark (as humble theorists!) that without detailed theoretical and simulation studies of the Lennard-Jones and other model fluids, we would have little fundamental understanding of the properties of simple, atomic liquids at interfaces or under confinement—the experimentalists are certainly catching up but experiments on fluid interfaces are notoriously difficult. One might go further and argue that studies of the Ising or lattice gas model, with the substrate treated as an external field, led to a wealth of predictions for surface phase transitions most of which were found in adsorption experiments. Let us be clear, however. We are not suggesting that the AO model has the same significance in statistical physics as the Ising model! Nevertheless, the AO model has much appeal to the theorist. There is only one parameter, the size ratio q , and by varying q different types of bulk phase behaviour emerge. Moreover, we find that the same model predicts striking interfacial phenomena, some of which are very different from those found for simple fluids and which reflect the special character of the effective interactions in the AO model.

Those readers who are interested in recent developments in the theory of more realistic models of colloid–polymer mixtures are referred to the topical review by Fuchs and Schweizer [14] who describe liquid-state integral equation theories for tackling structural correlations starting at the polymer segment level. The polymers are treated as connected chains of segments which experience excluded-volume forces among themselves and with the hard-sphere colloids. Although the integral equation approaches provide much insight into the nature of correlations for a wide range of size ratios (including $q \gg 1$) and for a variety of polymer concentrations, they appear to be restricted to homogeneous (bulk) fluids and it is difficult to envisage extensions to inhomogeneous systems or to crystalline phases, i.e. to the full phase diagram. Very recently, Bolhuis and co-workers [15] have performed Monte Carlo simulations of the bulk phase diagram of a model in which the colloids are treated as hard spheres and the polymers as self-avoiding walks that are mapped to an effective pair potential. We shall make reference to their work in section 5.2, but for more details of

this powerful ‘polymers as soft colloids’ computational approach readers should consult the original paper and references therein.

The present article is organized as follows. In section 2 we describe the AO model Hamiltonian and two different strategies for tackling its statistical mechanics. The first is to integrate out the degrees of freedom of the polymer spheres, thereby obtaining an effective one-component Hamiltonian for the colloidal hard spheres. As mentioned above, this approach is particularly effective for small size ratios, $q < 0.1547$, where the one-component Hamiltonian consists of zero, one and two-body contributions only; there are no higher-body effective interactions. The second strategy is to tackle the binary AO mixture directly; the two components are treated on equal footing by means of a geometry-based density functional theory that is specifically designed for the inhomogeneous AO mixture [16, 17]. The procedure for constructing the DFT is based on the fundamental measure theory developed by Rosenfeld [18] for additive hard-sphere mixtures. For uniform (bulk) fluids the free energy obtained from the DFT is identical to that given by the free-volume theory of Lekkerkerker *et al.* [4] alluded to above. Section 3 describes an application of the DFT to the planar interface between demixed fluid phases, one rich in colloid, the other poor. We find that for coexisting states well away from the critical point, at high polymer fugacity, both the colloid and polymer density profiles exhibit oscillations on the colloid-rich (liquid) side of the interface. We also discuss the behaviour of the surface tension comparing with experimental results. In section 4 we consider adsorption of the AO mixture at a planar hard wall. When a colloidal particle is sufficiently close to a hard wall, such that the two depletion zones overlap, there is an effective attractive potential between the two which is similar to the potential, ϕ_{AO} , between two colloidal particles, i.e. expulsion of polymer induces an attractive wall–colloid depletion potential ϕ_{AO}^{wall} whose range is equal to σ_p . For small size ratios q , very large contact densities are found for the colloid profile $\rho_c(z)$, reflecting the form of $\phi_{AO}^{\text{wall}}(z; z_p)$. For larger q fluid–fluid phase separation can occur and we find novel entropic wetting and layering transitions using the DFT—see section 4.2. Results of recent computer simulations of the AO mixture, with $q = 1$, adsorbed at a hard wall are described in section 4.3; these also predict wetting and layering transitions [19]. Section 5 describes a recent extension of the DFT approach that incorporates, albeit in a simple way, polymer–polymer interactions [20]. In the ‘soft colloid’ picture [21] of polymers, segment–segment repulsion, averaged over conformations of the chains, leads to an effective

interaction, ϕ_{pp} , between the polymer centres of mass that is repulsive, soft and penetrable. By making the crude approximation that $\phi_{pp}(r)$ is a step-function pair potential of height ϵ , it is possible to construct a geometry-based DFT for a model that has as its limiting cases: (i) the AO model ($\epsilon = 0$, non-interacting polymer) and (ii) the binary hard-sphere mixture ($\epsilon \rightarrow \infty$). We present results for fluid–fluid phase separation, comparing with those for the AO model and with computer simulations. In section 6 we summarize briefly some other recent applications and extensions of the DFT for the AO model. Several of these are concerned with bulk properties only but we also describe recent work on mixtures of hard-sphere colloids and hard needles, modelling experimentally realizable stiff colloidal rods, where interfacial properties were considered [22–24]. This model system shares many features in common with the AO model—the needles act as the depletant. It has the additional feature of orientational degrees of freedom for the needles which can introduce orientational ordering at an interface, even though the bulk fluid is isotropic (the infinitely thin rods cannot interact). We conclude in section 7 with some remarks and an outlook on future work.

What follows is not intended to be a review of what is a large and rapidly developing literature on the experimental, theoretical and simulation aspects of colloid–polymer mixtures; we make no attempt to give a comprehensive overview or an exhaustive list of references. For example, we concentrate on the so-called ‘colloid limit’, $q \lesssim 1$, rather than the equally important ‘protein or nanoparticle limit’, $q \gg 1$, where the physics is, arguably, less understood. The choice of material reflects the personal viewpoints of the authors on the subject area and the presentation is based, in part, on the Molecular Physics Lecture given by R. Evans at the Liblice Conference in June 2002. Although much of the theoretical background has been published elsewhere, almost all the results presented in sections 3 and 4 appear for the first time: they are from the unpublished thesis of Brader [25]. Section 5.2 also contains new results. A brief summary of some of the earlier work can be found in a conference article [26].

2. The Asakura–Oosawa–Vrij model

We consider a suspension of sterically stabilized colloidal particles immersed together with non-adsorbing polymers in an organic solvent. The interaction between two sterically stabilized colloidal particles in an organic solvent is close to that between hard spheres, whereas dilute solutions of polymers in a theta-solvent can be represented by non-interacting or ideal polymers.

A simple idealized model for such a colloid–polymer mixture is the so-called Asakura–Oosawa–Vrij (AO) model [6–8]. This is an extreme non-additive binary hard-sphere model in which the colloids are treated as hard spheres with diameter σ_c and the interpenetrable, non-interacting polymer coils are treated as point particles but which are excluded from the colloids to a centre-of-mass distance of $(\sigma_c + \sigma_p)/2$. The diameter of the polymer sphere is $\sigma_p = 2R_g$ with R_g the radius of gyration of the polymer. The pairwise potentials in this simple model are given by

$$\begin{aligned} \phi_{cc}(R_{ij}) &= \begin{cases} \infty, & \text{for } R_{ij} < \sigma_c, \\ 0, & \text{otherwise,} \end{cases} \\ \phi_{cp}(|\mathbf{R}_i - \mathbf{r}_j|) &= \begin{cases} \infty, & \text{for } |\mathbf{R}_i - \mathbf{r}_j| < \frac{1}{2}(\sigma_c + \sigma_p), \\ 0, & \text{otherwise,} \end{cases} \\ \phi_{pp}(r_{ij}) &= 0, \end{aligned} \quad (1)$$

where \mathbf{R} and \mathbf{r} denote colloid and polymer centre-of-mass coordinates, respectively, with $R_{ij} = |\mathbf{R}_i - \mathbf{R}_j|$ and $r_{ij} = |\mathbf{r}_i - \mathbf{r}_j|$. Note that a general non-additive binary hard-sphere mixture is described by the ‘diameters’ σ_{11} , σ_{22} and σ_{12} , where subscripts 1 and 2 denote species 1 and 2. The cross-term is given by $\sigma_{12} = (\sigma_{11} + \sigma_{22}) \times (1 + \Delta)/2$, where the non-additivity parameter Δ is zero for additive mixtures. The AO model corresponds to $\sigma_{22} = 0$ and $\Delta = q$, the fixed size ratio σ_p/σ_c . The Hamiltonian of the AO model consists of (trivial) kinetic contributions and a sum of interaction terms: $H = H_{cc} + H_{cp} + H_{pp}$, where

$$\begin{aligned} H_{cc} &= \sum_{i < j}^{N_c} \phi_{cc}(R_{ij}), \\ H_{cp} &= \sum_i^{N_c} \sum_j^{N_p} \phi_{cp}(|\mathbf{R}_i - \mathbf{r}_j|), \\ H_{pp} &= \sum_{i < j}^{N_p} \phi_{pp}(R_{ij}) = 0 \end{aligned} \quad (2)$$

and we consider N_c colloids and N_p ideal polymers in a volume V at temperature T . The solvent is regarded as an inert continuum. See figure 1(a) for an illustration of the model.

There are several ways of tackling the statistical mechanics of the AO model. Brute force, direct computer simulations of this model mixture are not straightforward since problems of slow equilibration and non-ergodicity can arise for large size asymmetries, where huge numbers of polymers are required per colloid particle. Recently, however, simulation studies have been carried out for several values of the size ratio $q = \sigma_p/\sigma_c$

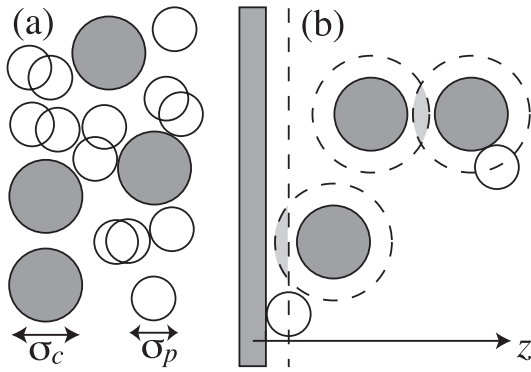


Figure 1. (a) Sketch of the Asakura–Oosawa–Vrij model of hard spheres (grey circles) with diameter σ_c and ideal polymers (white circles) with diameter σ_p . (b) Depletion zones (dashed lines) that are inaccessible to polymer centres. Overlapping depletion zones (light grey shapes) are indicated in two cases, that between two colloids and that between a colloid and a hard wall.

and we shall report on these in section 4.3. Here we describe two alternative approaches which have been successfully employed. The first is most appropriate for mixtures where the size ratio $q \ll 1$; it depends upon integrating out the degrees of freedom of the ideal polymer to obtain an effective one-component Hamiltonian for the colloids. The second approach employs a density-functional theory designed specifically for the AO mixture; this treats both species on an equal footing.

2.1. *The effective one-component Hamiltonian*

For a general binary mixture it is possible to construct an effective one-component Hamiltonian for one of the components—usually the larger species—by integrating out the degrees of freedom of the other—usually the smaller species [27]. As usual it is convenient to work in the semi-grand ensemble where (N_c, z_p, V, T) are fixed variables, i.e. the fugacity $z_p = A_p^{-3} \exp(\beta\mu_p)$ of a reservoir of polymer is fixed. μ_p is the chemical potential, $\beta = 1/k_B T$ and A_p is the thermal de Broglie wavelength of the polymer. In order to treat inhomogeneous fluids it is also convenient to allow the colloids and polymer to couple independently to two external fields. Thus one adds to the Hamiltonian H contributions

$$V_c^{\text{ext}} = \sum_{i=1}^{N_c} V_c^{\text{ext}}(\mathbf{R}_i), \quad V_p^{\text{ext}} = \sum_{i=1}^{N_p} V_p^{\text{ext}}(\mathbf{r}_i), \quad (3)$$

which can produce inhomogeneous density profiles. It is straightforward to show that the semi-grand free energy $F(N_c, V, z_p)$ is given by

$$\exp(-\beta F) = \frac{1}{N_c! A_c^{3N_c}} \int d\mathbf{R}^{N_c} \exp(-\beta(H_{cc} + \Omega + V_c^{\text{ext}})), \quad (4)$$

where A_c is the thermal de Broglie wavelength of the colloid and

$$\exp(-\beta\Omega) = \sum_{N_p=0}^{\infty} \frac{z_p^{N_p}}{N_p!} \int d\mathbf{r}^{N_p} \exp(-\beta(H_{cp} + V_p^{\text{ext}})). \quad (5)$$

Ω is simply the grand potential of the (ideal) polymer in the presence of the external field arising from (a) a fixed configuration $\{\mathbf{R}^{N_c}\}$ of N_c colloids and (b) any applied field V_p^{ext} . Provided one can determine Ω explicitly, or at least a good approximation to Ω , the binary mixture problem is reduced to a simpler one-component problem: equation (4) describes a system of colloids interacting through an effective Hamiltonian: $H^{\text{eff}} = H_{cc} + \Omega + V_c^{\text{ext}}$.

In a general mixture Ω consists of zero, one, two, ..., many-body contributions [28] and the resulting H^{eff} is unwieldy. However, for the particular case of the AO model the contributions simplify [10, 11] because the polymer is ideal, i.e. $\phi_{pp} = 0$. Moreover, for a homogeneous fluid, with no external potentials, the series truncates after the two-body term, provided that $q < 2/3^{1/2} - 1 = 0.1547$ [9, 10]. For such high asymmetry there is no triple overlap of excluded volume regions, even when three colloids are in simultaneous contact. Thus, for $q < 0.1547$, geometrical considerations ensure that there is an *exact* mapping from the bulk binary mixture to an effective Hamiltonian that contains only two-body interactions plus structure (configuration) independent contributions. The effective pair potential is given by [9, 10]

$$\phi^{\text{eff}}(R; z_p) = \phi_{cc}(R) + \phi_{AO}(R; z_p), \quad (6)$$

where $\phi_{AO}(R; z_p)$ is the well-known AO pair (depletion) potential between two hard-sphere colloids in a sea of ideal polymer [6, 7], see figure 1 (b) for an illustration. $\phi_{AO}(R; z_p)$ is attractive and has a finite range equal to σ_p . Its strength is proportional to z_p and it can be expressed as a polynomial in $s = R/\sigma_c$:

$$\beta\phi_{AO}(R; z_p) = \begin{cases} -\frac{\pi}{6} \sigma_p^3 z_p (1+q^{-1})^3 \left[1 - \frac{3s}{2(1+q)} + \frac{s^3}{2(1+q)^3} \right], & 1 < s < 1+q, \\ 0, & s > 1+q. \end{cases} \quad (7)$$

Perhaps more remarkably, Brader *et al.* [11] showed that for the AO mixture in contact with a hard wall defined by the external potentials

$$\begin{aligned} V_c^{\text{ext}}(z) &= \begin{cases} \infty, & z < \sigma_c/2, \\ 0, & z \geq \sigma_c/2, \end{cases} \\ V_p^{\text{ext}}(z) &= \begin{cases} \infty, & z < \sigma_p/2, \\ 0, & z \geq \sigma_p/2, \end{cases} \end{aligned} \quad (8)$$

where z is the centre of the particle measured normal to the wall, there is also an exact mapping of the binary mixture to a simple effective Hamiltonian. Using geometrical considerations (see figure 2 of [11]) they showed that for $q < 0.25$ all many-body terms Ω_n , with $n \geq 2$, are unaltered from their form in the bulk (homogeneous) fluid by the presence of the hard wall. For larger values of q the two-body potential becomes a complicated function of \mathbf{R}_1 and \mathbf{R}_2 and is not simply a function of the separation $|\mathbf{R}_1 - \mathbf{R}_2|$. Specifically, for $q < 0.1547$, the effective Hamiltonian for the inhomogeneous fluid at the hard wall reduces to

$$\begin{aligned} H^{\text{eff}} &= H_{\text{cc}} + \sum_{i=1}^{N_c} V_c^{\text{ext}}(z_i) + \sum_{i=1}^{N_c} \phi_{\text{AO}}^{\text{wall}}(z_i; z_p) \\ &+ \Omega_0^{\text{bulk}} + \Omega_1^{\text{bulk}} + \sum_{i < j} \phi_{\text{AO}}(R_{ij}; z_p). \end{aligned} \quad (9)$$

The additional one-body term $\phi_{\text{AO}}^{\text{wall}}$ represents the attractive AO depletion potential between the colloid and the planar hard wall. This potential has the same range, σ_p , as ϕ_{AO} and it has similar form [11]. In the absence of the wall equation (9) reduces to the effective Hamiltonian of the homogeneous system. The structure-independent terms are given by

$$\begin{aligned} -\beta\Omega_0^{\text{bulk}} &= z_p V, \\ -\beta\Omega_1^{\text{bulk}} &= -z_p N_c \pi (\sigma_c + \sigma_p)^3 / 6 = -z_p \eta_c (1 + q)^3 V, \end{aligned} \quad (10)$$

where $\eta_c = (\pi/6)\sigma_c^3 N_c/V$ is the colloid packing fraction.

Having such a simple effective Hamiltonian for the homogeneous fluid means that it is straightforward to perform computer simulations or to implement standard one-component integral equation closures. Recall that integral equation approaches for highly asymmetric mixtures are especially problematical whereas Percus–Yevick (PY) and similar closures provide a reliable description of the pair correlation function for a one-component fluid whose pair potential consists of a hard core plus an attractive tail. Of course, the usual issues of thermodynamic inconsistency remain.

Dijkstra *et al.* [10] carried out extensive investigations of the properties of the bulk mixture with $q = 0.1$ using

the effective Hamiltonian. The equilibrium structure, i.e. the colloid–colloid radial distribution function $g_{\text{cc}}(R)$ and the structure factor $S_{\text{cc}}(k)$, is determined solely by $\phi^{\text{eff}}(R; z_p)$, equation (6), for this size ratio and Monte Carlo and PY results at various colloid packing fractions are presented in [10]. Note that since the terms Ω_0^{bulk} and Ω_1^{bulk} depend linearly on N_c or V they have no effect on bulk phase equilibria and the latter is, once again, determined solely by the pair potential $\phi^{\text{eff}}(R; z_p)$ [10, 28]. (These terms do contribute to the total pressure and total compressibility of the mixture, however [29].) The complete equilibrium phase diagram of the mixture was determined by simulation of the effective one-component system for $q = 0.1$. It is extremely rich, displaying a very broad, in η_c , fluid–solid coexistence curve which lies at lower polymer densities than a (metastable) fluid–fluid coexistence region. There is also an isostructural (fcc) solid–solid transition which is very slightly metastable with respect to the fluid–solid transition [10, 11]. Note that as each term in the effective Hamiltonian is proportional to z_p (\equiv polymer density in the reservoir, ρ_p^* , for ideal polymer) this variable plays the same role as inverse temperature in simple atomic fluids. Thus, phase diagrams plotted in the (η_c, z_p) plane often display features similar to those plotted in the $(\text{density}, 1/T)$ plane for simple fluids. The simulation results for the bulk system provide a valuable benchmark against which approximate theories, e.g. integral equation, density functional or perturbation theory approaches, can be tested [10].

Similar remarks apply to the Monte Carlo simulation results obtained using the effective Hamiltonian (9) for the mixture at a planar hard wall. Brader *et al.* [11] considered the AO mixture, with $q = 0.1$, for two fixed values of the colloid packing fraction, $\eta_c = 0.3$ and 0.4 , and increasing amounts of polymer. Adding polymer (increasing z_p) leads to increased depletion attraction for the colloids at the hard wall which leads, in turn, to pronounced effects on the density profile near the wall. We shall comment further on this phenomenon in section 4.1 where we compare results from density functional theory with those of the simulations.

We conclude this subsection by making some remarks about the form of the effective Hamiltonian to be used for other types of inhomogeneity. If the wall–fluid potentials are soft or exhibit attractive portions then the integrating out of the polymer can lead to more complex contributions, even for small size ratios q . On the other hand, for *spontaneously* generated inhomogeneities, where the density profiles of colloid and of polymer are spatially varying in vanishing external fields, the appropriate effective Hamiltonian is that of the bulk, homogeneous system [11]. Relevant examples

are the planar interface between demixed fluid phases, colloidal crystals where the densities vary periodically, and the fluid–crystal interface. Although the distribution of polymer in a colloidal crystal or in the region of any interface is very different from that in a bulk fluid this does *not* give rise to different effective interactions, in the sense that the effective Hamiltonian needs to be modified. Since we work in the semi-grand ensemble, with a reservoir of polymer, it is solely the fugacity z_p that determines all the effective interactions in the system. As z_p is constant throughout the inhomogeneous system then so too are the effective interactions between colloids; these do not depend on the local polymer distribution. Also we note that although the polymer degrees of freedom have been integrated out it is still possible, at least in principle, to recover information about the polymer distribution from properties that are determined by the effective Hamiltonian. For example, the polymer density $\rho_p(\mathbf{r})$ can be obtained by functional differentiation of the free energy F with respect to $V_p^{\text{ext}}(\mathbf{r})$ and expressed in terms of n -body correlation functions of the colloids, which can be determined using the effective Hamiltonian [11]. When $q < 0.1547$ this procedure yields an exact and tractable formula for the free-volume fraction $\alpha(\rho_c; z_p) \equiv \rho_p/\rho_p^r$ (the ratio of polymer density in the mixture to that in the reservoir) of a bulk fluid mixture [11].

Finally, we should remark that the one-dimensional version of the AO model, in which the colloids are modelled by hard rods and the polymer by ideal particles that are excluded from the colloids by a certain distance, can be solved *exactly* by mapping the binary mixture to an effective one-component Hamiltonian [30]. The construction of the effective Hamiltonian proceeds as in three dimensions and the effective pair potential $\phi^{\text{eff}}(X; z_p) = \phi_{\text{cc}}(X) + \phi_{\text{AO}}^{\text{1D}}(X; z_p)$, where the depletion potential $\phi_{\text{AO}}^{\text{1D}}$ is now the difference in accessible length for the polymers when the colloids are separated by a distance $|X|$ and when their separation is infinite. This potential is linear in $|X|$, proportional to z_p and vanishes for separations beyond the length of the polymer. Since the mapping reduces the binary mixture problem to that of a one-component fluid in one dimension, in which the particles interact via a nearest-neighbour potential, the statistical mechanics can be solved using the standard Laplace transform techniques. Results for the (osmotic) equation of state and free-volume fraction $\alpha(\rho_c; z_p)$ are given in [30], where they are compared with the corresponding results from the approximate free-volume theory.

2.2. Density functional approach

We have recently developed a density functional theory (DFT) for the binary AO model using the

techniques of fundamental measure theory (FMT). Our new functional [16, 17] treats arbitrary size ratios q and is thus able to incorporate the effects of many body interactions which arise in the effective one-component description at larger values of q , and which represent an important feature of the model. Unlike DFT treatments of interfacial phenomena in simple fluids, where the attractive portion of the fluid–fluid pair potential is treated separately from the repulsive part in a perturbative fashion that is equivalent to a mean-field treatment (correlations are ignored) [31], here the effective attractive interactions emerge naturally from the DFT and are treated non-perturbatively. Of course, the present DFT is still mean-field like in that bulk critical fluctuations or, indeed, interfacial fluctuations are not incorporated. The excess, over ideal, Helmholtz free energy functional is given by a spatial integral over a reduced free energy density Φ which is a function of a set of species-dependent weighted densities

$$\beta\mathcal{F}_{\text{ex}}^{\text{AO}}[\rho_c(\mathbf{r}), \rho_p(\mathbf{r})] = \int d\mathbf{r} \Phi(\{n_v^c\}, \{n_v^p\}), \quad (11)$$

where the function $\Phi = \Phi_1 + \Phi_2 + \Phi_3$ consists of three terms given by

$$\begin{aligned} \Phi_1 &= n_0^c \left[-\ln(1 - n_3^c) + \frac{n_3^p}{1 - n_3^c} \right] - n_0^p \ln(1 - n_3^c), \\ \Phi_2 &= (n_1^c n_2^c - \mathbf{n}_1^c \cdot \mathbf{n}_2^c) \left[\frac{1}{1 - n_3^c} + \frac{n_3^p}{(1 - n_3^c)^2} \right] \\ &\quad + \frac{n_1^p n_2^c - \mathbf{n}_1^p \cdot \mathbf{n}_2^c + n_1^c n_2^p - \mathbf{n}_1^c \cdot \mathbf{n}_2^p}{1 - n_3^c}, \\ \Phi_3 &= \frac{(n_2^c)^3 - 3n_2^c(\mathbf{n}_2^c \cdot \mathbf{n}_2^c)}{24\pi} \left[\frac{1}{(1 - n_3^c)^2} + \frac{2n_3^p}{(1 - n_3^c)^3} \right] \\ &\quad + \frac{(n_2^c)^2 n_2^p - n_2^p(\mathbf{n}_2^c \cdot \mathbf{n}_2^c) - 2n_2^c \mathbf{n}_2^c \cdot \mathbf{n}_2^p}{8\pi(1 - n_3^c)^2}. \end{aligned} \quad (12)$$

The species-dependent weighted densities are given by convolutions of the density profiles $\rho_i(\mathbf{r})$, $i = c, p$, with weight functions $w_v^i(\mathbf{r})$

$$n_v^i(\mathbf{r}) = \int d\mathbf{r}' \rho_i(\mathbf{r}') w_v^i(\mathbf{r} - \mathbf{r}'). \quad (13)$$

The four scalar and two vector weight functions are functions characteristic of the geometry of the hard particles

$$\begin{aligned} w_3^i(\mathbf{r}) &= \Theta(R_i - r), \\ w_2^i(\mathbf{r}) &= \delta(r - R_i), \\ w_1^i(\mathbf{r}) &= \frac{\delta(r - R_i)}{4\pi R_i}, \end{aligned}$$

$$\begin{aligned}
w_0^i(\mathbf{r}) &= \frac{\delta(r - R_i)}{4\pi R_i^2}, \\
w_{v2}^i(\mathbf{r}) &= \frac{\mathbf{r}}{r} \delta(r - R_i), \\
w_{v1}^i(\mathbf{r}) &= \frac{\mathbf{r}}{r} \frac{\delta(r - R_i)}{4\pi R_i}, \quad (14)
\end{aligned}$$

where R_i denotes the radius of species i so that $R_c = \sigma_c/2$ and $R_p = \sigma_p/2$. $\Theta(r)$ is the Heaviside step function and $\delta(r)$ is the Dirac distribution.

The procedure for constructing the DFT is based on the successful FMT developed by Rosenfeld [18] for additive hard-sphere mixtures. In order to obtain the reduced free energy density Φ appropriate to the AO model, Schmidt *et al.* [16, 17] considered the zero-dimensional limit which corresponds to a cavity that can hold at most one hard-sphere colloid but can hold an arbitrary number of ideal polymers if no colloid is present. Full details of the derivation of the DFT and its applications to the determination of bulk fluid thermodynamics and structure are given in [17]. A summary is provided in section 5.1 of the present article where we consider an extension of the AO model. Here it suffices to make some remarks about the status of the theory. Note that in the original papers [16, 17] a tensor weight function was included; this contribution is omitted in the above formulation and in the calculations to be described later. Inclusion of the tensor (see equation (33) below), while essential for calculating crystalline properties, makes negligible difference for inhomogeneous fluid states and so would only serve to complicate matters without altering the basic phenomena. It is important to recognize that the functional can also be regarded as a linearization, in the polymer density $\rho_p(\mathbf{r})$, of the original Rosenfeld hard-sphere functional.

For a homogeneous fluid mixture the functional yields a reduced excess bulk free energy density

$$\beta F_{\text{ex}}^{\text{AO}}/V = \beta f_{\text{ex}}^{\text{AO}}(\rho_c, \rho_p; q) = \beta f_{\text{ex}}^{\text{HS}}(\rho_c) - \rho_p \ln \alpha(\rho_c), \quad (15)$$

where

$$\alpha(\rho_c) = (1 - \eta_c) \exp(-A\gamma - B\gamma^2 - C\gamma^3), \quad (16)$$

with $\gamma = \eta_c/(1 - \eta_c)$, $A = 3q + 3q^2 + q^3$, $B = 9q^2/2 + 3q^3$ and $C = 3q^3$. $f_{\text{ex}}^{\text{HS}}$ is the excess free energy density of pure hard spheres in the scaled particle (PY compressibility) approximation; an explicit expression is given later in equation (36). This result can be shown to be identical to the free-volume theory of Lekkerkerker *et al.* [4, 10], where $\alpha(\rho_c)$ is interpreted as the ratio of the free volume accessible to a single test polymer sphere and the system volume. It is not immediately obvious that the DFT

approach should be equivalent to free-volume theory. The starting points for the two theories are quite different and it is usually the semi-grand free energy that is considered in free-volume theory; connections between the two approaches are discussed in [17]. Free-volume theory treats the semi-grand free energy as the sum of a hard-sphere (colloid) part plus a contribution from an ideal gas of polymers in the free volume left by the colloids, which is treated as an expansion in the fugacity z_p truncated at the term linear in z_p [4, 10]. This linearity in z_p , or equivalently in ρ_p , is built into the DFT.

The bulk pair direct correlation functions $c_{ij}^{(2)}$, obtained by taking two functional derivatives of $\mathcal{F}_{\text{ex}}^{\text{AO}}[\rho_c, \rho_p]$, are given analytically [17]. The Ornstein–Zernike relations then provide the partial structure factors $S_{ij}(k)$. Linearization in the polymer density has the consequence that $c_{pp}^{(2)} = 0$, as in the PY approximation for this AO model. However, the other direct correlation functions $c_{cc}^{(2)}$ and $c_{cp}^{(2)}$ are *not* the same as those from PY approximation, even though $c_{ij}^{(2)}(r)$ vanishes for $r > R_i + R_j$ in both the DFT and the PY treatments. In an exact treatment we would expect contributions to $c_{ij}^{(2)}(r)$ beyond $R_i + R_j$. An important advantage of the DFT over integral equation theories is that the partial structure factors and radial distribution functions $g_{ij}(r)$ obtained from the Ornstein–Zernike equations yield a spinodal consistent with that from the bulk free energy (15), i.e. the free-energy and structural routes to the fluid–fluid spinodal are consistent. (Note that the spinodal can be obtained *analytically* from the canonical free energy (15)—see [17].) Such a property is especially advantageous when considering interfacial properties at or near two-phase coexistence. Schmidt *et al.* [17] also investigate the asymptotic decay, $r \rightarrow \infty$, of $g_{ij}(r)$ in different regions of the bulk phase diagram. Since the partial structure factors $S_{ij}(k)$ are given analytically it is straightforward to determine the poles of these functions in the complex plane and hence locate the so-called Fisher–Widom line [32–35] where the ultimate decay of $rg_{ij}(r)$ crosses over from oscillatory to purely monotonic, exponential decay. Examples of the cross-over lines and of (mean-field) critical point behaviour of $S_{ij}(k)$ for various size ratios q are given in [17].

It is important to emphasize that, within the framework of DFT, the Ornstein–Zernike route is not the only one to the pair correlation functions. The alternative is the test particle route, whereby one fixes a particle of species i at the origin and determines (by solving the appropriate Euler–Lagrange equations, obtained by minimizing the functional) the inhomogeneous one-body density profile $\rho_j(r)$ arising from the external potential exerted by the fixed particle i ; then $g_{ij}(r) = \rho_j(r)/\rho_j(\infty)$. All that is required to solve the

relevant equations are the one-body direct correlation functions $c_i^{(1)}(r)$, which involve only a first derivative of $\mathcal{F}_{\text{ex}}^{\text{AO}}$. One can show that in the limit $\eta_c \rightarrow 0$, the test particle route for the DFT yields the exact result $g_{cc}(r) \approx \exp(-\beta\phi^{\text{eff}}(r; z_p))$, where ϕ^{eff} is the effective depletion potential defined in equation (6) [16, 17]. In other words, the geometrically based DFT describes correctly the depletion effect between two hard-sphere colloids when implemented within the test-particle procedure. There are other good reasons to believe that the test-particle route to $g_{ij}(r)$ should be more accurate than the Ornstein–Zernike route [17].

3. The fluid–fluid interface

Phase separation in the AO model is a well-studied problem [4, 8–10]. As remarked earlier, for small size ratios q , fluid–fluid phase separation is pre-empted by a fluid–solid transition so the former is, at best, metastable. For larger values of q , however, there is stable, entropically driven, fluid–fluid phase separation. Free-volume theory for the AO model predicts stable liquid (colloid-rich)–gas (colloid-poor) phase coexistence for $q > 0.32$. It follows that our present DFT predicts the same behaviour. Figure 2 shows the bulk phase diagram obtained from the present theory for a size ratio $q = 0.6$ for which there is a stable fluid–fluid demixing transition with a critical point at $\eta_{p,\text{crit}}^r \sim 0.495$. The polymer reservoir packing fraction is defined as $\eta_p^r = (\pi/6)\sigma_p^3\rho_p^r$,

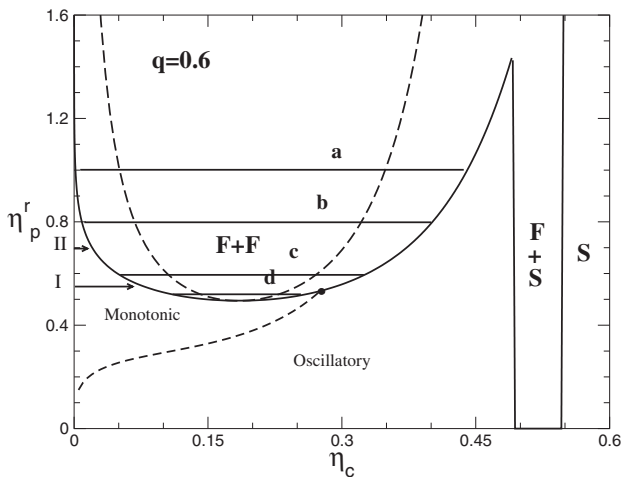


Figure 2. The bulk phase diagram calculated from the functional for $q = 0.6$. η_c is the packing fraction of the colloid and η_p^r that of polymer in the reservoir. F denotes fluid and S solid. The long dashed line shows the fluid–fluid spinodal and the short dashed line shows the Fisher–Widom line. The latter intersects the binodal at $\eta_{p,\text{FW}}^r = 0.53$. The horizontal tie lines (a), (b), (c) and (d) connect coexisting fluid states. Horizontal arrows indicate the paths I and II by which the phase boundary is approached for the adsorption studies in section 4.2.

with $\rho_p^r = z_p$ for ideal polymer. Note that the tie lines connecting coexisting states are horizontal in this (reservoir) representation. It should be emphasized that the fluid–fluid and fluid–solid phase boundaries presented here are those of the original free-volume theory [4, 10]†. While the fluid–fluid phase boundary shown is precisely that given by the functional, the true solid–fluid boundary from DFT would require a full minimization of the functional for a solid-like distribution. This is outside the scope of the present study. Also shown in figure 2 is the Fisher–Widom (FW) line which divides the phase diagram into regions where the asymptotic decay of the three bulk pairwise correlation functions, $rg_{ij}(r)$, is either monotonic or exponentially damped oscillatory. The FW line has important consequences both for our study of the free fluid–fluid interface and for adsorption at a wall as the asymptotic behaviour predicted for the bulk pair correlations applies also to the one-body density profiles [33, 34].

We turn now to the free interface between demixed fluid phases. The density profiles for colloid and polymer are obtained by minimizing the grand potential functional

$$\Omega[\rho_c(\mathbf{r}), \rho_p(\mathbf{r})] = \mathcal{F}_{\text{id}}[\rho_c(\mathbf{r}), \rho_p(\mathbf{r})] + \mathcal{F}_{\text{ex}}^{\text{AO}}[\rho_c(\mathbf{r}), \rho_p(\mathbf{r})] + \sum_{i=c,p} \int d\mathbf{r} (V_i^{\text{ext}}(\mathbf{r}) - \mu_i) \rho_i(\mathbf{r}), \quad (17)$$

where $\mathcal{F}_{\text{ex}}^{\text{AO}}$ is the excess Helmholtz free energy functional of the AO mixture given in equation (11), \mathcal{F}_{id} denotes the functional for the ideal mixture, μ_i is the chemical potential (fixed by the reservoir) and $V_i^{\text{ext}}(\mathbf{r})$ is the external potential coupling to species i with $i = c, p$. In the case of the free interface $V_i^{\text{ext}} \equiv 0$. The fact that the functional is linear in the polymer density makes solution of the AO Euler–Lagrange equations considerably simpler than for the more familiar binary hard-sphere Rosenfeld functional [18]. In the latter case, the two minimization conditions $\delta\Omega/\delta\rho_1 = 0$ and $\delta\Omega/\delta\rho_2 = 0$ give rise to two coupled equations for ρ_1 and ρ_2 which must be solved self-consistently. The AO functional can be minimized explicitly with respect to the polymer density and the level of computational complexity reduced to that of minimizing a functional with respect to a single density field [17].

The colloid density profiles and corresponding surface tensions are shown in figure 3. The surface tension is plotted here in μNm^{-1} to facilitate comparison with the experimental results of [36, 37] which we shall

†Note that in calculations, e.g. [10], based on free volume theory the Carnahan–Starling approximation is often used for $f_{\text{ex}}^{\text{HS}}$ whereas in DFT the PY compressibility approximation must be employed.

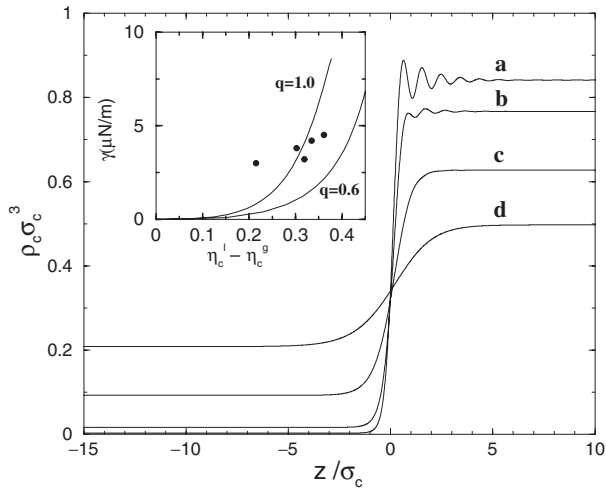


Figure 3. Colloid density profiles at the free interface between demixed fluid phases for a size ratio $q = 0.6$. The polymer reservoir packing fractions correspond to the tie lines in figure 2, i.e. $\eta_p^r = 1.0$ (a), 0.8 (b), 0.6 (c) and 0.52 (d) (near critical point). States (a), (b) and (c) lie on the oscillatory side of the FW line. The inset shows the surface tension γ versus the difference in the colloidal packing fraction in coexisting liquid (l) and gas (g) phases for $q = 0.6$ and 1.0. The colloid diameter is taken to be 26 nm to compare with experimental data of [36] (points) where $q = 1.0$.

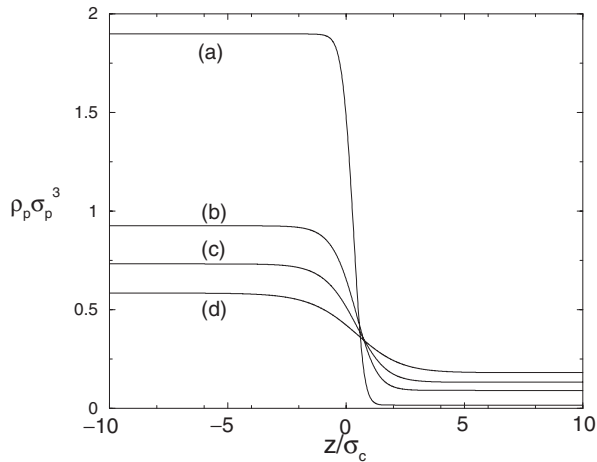


Figure 4. Polymer density profiles for $q = 0.6$ corresponding to the colloid profiles shown in figure 3. The polymer reservoir packing fractions correspond to the tie lines in figure 3, i.e. $\eta_p^r = 1.0$ (a), 0.8 (b), 0.6 (c) and 0.52 (d) (near critical point). States (a), (b) and (c) lie on the oscillatory side of the FW line.

return to later but which correspond to size ratio $q \sim 1$, i.e. we take the colloid diameter to be 26 nm in accordance with the experiments. The polymer profiles are given in figure 4 and demonstrate the polymer partitioning between the two phases. We show four profiles for states between the critical and triple points.

The labels (a)–(d) in figure 3 correspond to the tie lines in figure 2; (d) corresponds to the free interfacial profiles between coexisting densities near to the critical point and (a) to a near triple point state. For state (d) the colloid profile is smooth and reminiscent of the profiles of [38] calculated using an effective one-component Hamiltonian and employing a square gradient functional. For states approaching the triple point the interfacial width is found to be approximately σ_c , similar to values inferred from ellipsometric measurements on a colloid–polymer mixture [39] where a tan h function was fitted to the refractive index profile through the interface.

While the profiles near the critical point are smooth and rather unsurprising, for states nearer to the triple point striking oscillations develop on the colloid-rich ‘liquid’ side of the profiles. Such oscillations have been found previously in theoretical studies [33] of the free liquid–vapour interface of the square-well fluid and in simulation studies of the liquid–liquid interface [40] in a simple model of a liquid mixture. The presence of oscillations in one-body density profiles at interfaces is intimately connected to the asymptotic decay of bulk pairwise correlations [33, 34]. For the present mixture oscillatory profiles arise at the free interface when the colloid density in the coexisting liquid is greater than the colloid density where the FW (Fisher–Widom) line intersects the binodal, i.e. for all states with $\eta_p^r > \eta_{p,FW}^r = 0.53$ for $q = 0.6$ —see figure 2. The general theory of asymptotic decay of correlations in mixtures with short-range forces predicts [33, 34] that the longest-range decay of the density profiles should be

$$\rho_i(z) - \rho_i \sim \rho_i A_i \exp(-\alpha_0 z), \quad z \rightarrow \infty, \quad (18)$$

on the monotonic side of the FW line and

$$\rho_i(z) - \rho_i \sim \rho_i \tilde{A}_i \exp(-\tilde{\alpha}_0 z) \cos(\alpha_1 z - \theta_i), \quad z \rightarrow \infty, \quad (19)$$

on the oscillatory side; ρ_i is the bulk density of species i . Equivalent definitions exist for $z \rightarrow -\infty$, with appropriate bulk densities ρ_i . On the FW line, $\alpha_0 = \tilde{\alpha}_0$. The decay lengths α_0^{-1} and $\tilde{\alpha}_0^{-1}$ and the wavelength of oscillatory decay $2\pi/\alpha_1$ are common to both species and are properties of the bulk fluid. These are determined by the (common) poles of the structure factors $S_{ij}(k)$ [34]. The amplitudes A_i , \tilde{A}_i and the phase θ_i are species dependent and although there is knowledge about the amplitude ratios in binary mixtures [34], there is no theory for the absolute amplitude of the oscillations. We have confirmed that for states where the colloid profile oscillates, the corresponding polymer profiles also exhibit oscillations on the same, colloid-rich side

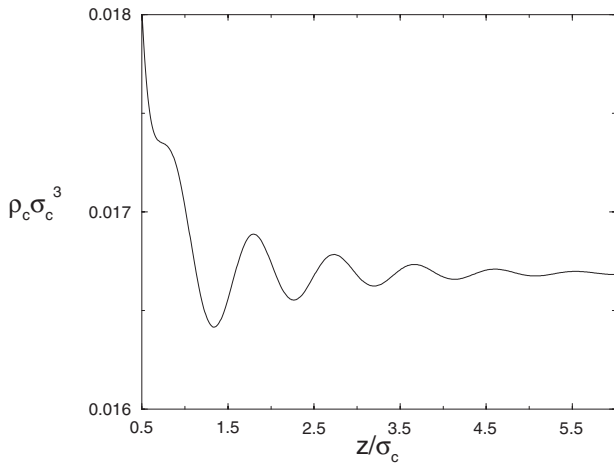


Figure 5. An enlargement of the polymer profile for $q = 0.6$ and $\eta_p^r = 1.0$, i.e. state (a) shown in figure 4. The oscillations, although not visible on the scale of figure 4, are present in the polymer profiles and display the same period and decay length as the corresponding colloid profiles (figure 3).

of the interface, with identical wavelength and decay length to those of the colloid. As the bulk density of the polymer is low in the colloid-rich ‘liquid’ phase, the amplitude of the polymer oscillations is very small; figure 5 shows an enlargement of the oscillations in the polymer profile for state (a). For states just above the FW intersection point, $\eta_{p,FW}^r$, the amplitude of the colloid oscillations can also become extremely small and this is why the profile (c) does not show oscillations on the scale of figure 3. For state (a), with $\eta_p^r = 1$, which is not especially close to the estimated triple point, the amplitude of the oscillations is substantial and appears to be larger than the corresponding amplitude for a square-well fluid very near its triple point where the oscillations have a wavelength of about one atomic diameter [33]. Our present results resemble closely those of a recent DFT treatment of binary mixtures of repulsive Gaussian core particles which exhibit fluid–fluid phase separation [41], although in that case there are states for which oscillations occur on both sides of the interface.

We note that all DFT treatments are mean-field-like in that they ignore fluctuation effects, both of the bulk liquid (critical fluctuations) and of the interface. Thermally induced capillary wave fluctuations of the interface will act to erode the oscillations in the ‘bare’ (mean-field) density profiles but it is argued that at least some of the oscillatory structure will remain in the ‘dressed’ colloid profiles. The standard method of incorporating capillary wave fluctuations is to assume that DFT calculations yield a ‘bare’ or ‘intrinsic’ profile and that interfacial fluctuations can be ‘unfrozen’ by an

appropriate renormalization of the mean-field profile [31, 33, 34, 42]. Because of the extremely low surface tensions γ which occur in colloidal systems one might expect the oscillations to be completely washed out by inclusion of these fluctuation effects but we will argue that this is not necessarily the case. In the simplest treatment of capillary wave fluctuations the intrinsic interface is smeared by a Gaussian convolution over the interfacial thermal roughness ξ_\perp . For oscillatory profiles which decay as equation (19) the wavelength and decay length are unaltered by this convolution but the amplitude is reduced by a factor $\exp[-(\alpha_1^2 - \tilde{\alpha}_0^2)\xi_\perp^2/2]$ [33, 34, 42]. The roughness ξ_\perp depends upon both the interfacial area L^2 and the external potential, i.e. the Earth’s gravitational field. For zero gravitational field, $\xi_\perp^2 = (2\pi\beta\gamma)^{-1} \ln(A_{\max}/A_{\min})$, where A_{\max} and A_{\min} are upper and lower cut-off wavenumbers for the capillary wave fluctuations. If we choose $A_{\max} = 2\pi/\xi$ and $A_{\min} = 2\pi/L$, where $\xi = \tilde{\alpha}_0^{-1}$ is the correlation length of the bulk coexisting ‘liquid’ phase, it follows that the amplitude of the oscillations in the density profile will be reduced by a factor

$$\tau = (L/\xi)^{-\omega[(\alpha_1/\tilde{\alpha}_0)^2 - 1]}, \quad (20)$$

where we have introduced the dimensionless parameter

$$\omega = \frac{k_B T}{4\pi\gamma\xi^2}, \quad (21)$$

which measures the strength of the capillary wave fluctuations. Smaller surface tensions give rise to larger values of ω and, as a result, the amplitude of the oscillations is damped more severely. Molecular dynamics simulations of a liquid–liquid interface have been performed by Toxvaerd and Stecki [40]. These authors (see also Chacón and co-workers [43, 44] who performed Monte Carlo simulations of the liquid–gas interface of a model of a metal) found a decrease in the amplitude of oscillation with increasing L , consistent with a Gaussian renormalization of the oscillatory intrinsic interface. We find for the present model that ω takes values of a similar order of magnitude as those for simple fluids [38]. This is due to the fact that the bulk correlation length ξ scales roughly as σ_c [16, 17] and the tension γ as $k_B T/\sigma_c^2$ [38, 45]. From our explicit calculations of γ and ξ we find that at state point (a), for which the profile has pronounced oscillations, see figure 3, $\tilde{\alpha}_0\sigma_c = 0.77$, $\alpha_1\sigma_c = 6.74$ and the reduced surface tension $\gamma^* = \beta\gamma\sigma_c^2 = 1.13$ which implies that $\omega = 0.042$ and $(\alpha_1/\tilde{\alpha}_0)^2 - 1 = 75.12$. We thus find that $\tau = (L/\xi)^{-3.23}$ which suggests that detecting oscillations of the colloid profile should be no more difficult than for simple fluids where the exponent is expected to take

a similar value. Indeed, from an experimental viewpoint such oscillations in a colloidal system offer an interesting opportunity for experimental study as it should be more favourable to investigate such structuring in systems where the period is of colloidal size than in atomic fluids, where the period is on the Angström scale.

We conclude this section by returning to the results for the surface tension. The inset in figure 3 shows the tension γ for size ratios $q = 0.6$ and 1.0 . We find that the tension calculated using the present DFT is consistently larger than that calculated [38] using the effective one-component Hamiltonian treated by square gradient DFT. The level of agreement with the experimentally measured tension for mixtures of a silica colloid, coated with 1-octadecanol, and polydimethylsiloxane (PDMS) in cyclohexane at $T = 293$ K [36] is somewhat better than in [38]. The size ratio for this mixture is approximately 1.0. As mentioned earlier, in order to compare our DFT results with experiment we choose $\sigma_c = 26$ nm, the mean diameter of the particles investigated in [36]; there are no adjustable parameters in the model [25, 26, 46].

Note that the measured tensions are typically $3\text{--}4\ \mu\text{N m}^{-1}$, values which are about 1000 times smaller than the tensions measured for simple atomic fluids near their triple points. Such small values of the tension are not so surprising when one recalls (i) that the tension scales roughly as $k_B T / \sigma_c^2$, provided the state is well removed from the critical point and (ii) that $\sigma_c \sim 100$ atomic diameters [38, 45]. In figure 3 the tension is plotted against the difference between η_c in the coexisting liquid (l) and gas (g) phases. Within the present mean-field treatment γ vanishes as $(\eta_c^l - \eta_c^g)^3$ on approaching the critical point. Incorporating critical fluctuations should lead to even faster decay; for Ising-like criticality the exponent 3 should be replaced by $2\nu/\beta \approx 3.9$. The experiments of [36] were not performed sufficiently close to the critical point to examine scaling behaviour. However, Chen *et al.* [47] do report results for the density difference and surface tension, in a similar mixture of silica particles and PDMS in cyclohexane, taken near the critical point. They report values for $\gamma < 1\ \mu\text{N m}^{-1}$ and a good fit to Ising-like scaling.

4. Adsorption at a hard wall

In this section we consider the AO mixture adsorbed at a planar hard wall described by the external potentials (8). Such a model constitutes the simplest framework in which one can address the statistical mechanics of colloidal adsorption or, more specifically, the effects of entropic depletion forces on the distribution of both colloids and polymer near a (repulsive) substrate. Of course, other more complex wall–fluid potentials can be considered which include soft repulsion and/or

attractive interactions. The advantages of the hard-wall model are (i) it encompasses the key feature of depletion-induced wall–colloid attraction and (ii) as emphasized in section 2.1, it can be mapped exactly to a very simple effective Hamiltonian (9), for $q < 0.1547$, that can be used efficiently in simulation studies.

We focus first on the case $q = 0.1$, for which there are Monte Carlo results [11] for the colloid density profile against which we can test the reliability of our DFT. Afterwards we consider larger size ratios where bulk fluid–fluid phase separation occurs. This enables us to investigate entropic wetting phenomena at the hard wall using the DFT approach.

4.1. Test case: $q = 0.1$

In order to test the performance of the DFT for adsorption studies we first calculate density profiles against a hard wall for $q = 0.1$. For this small size ratio, simulation results are available [11] for the colloid profiles. These make use of the exact mapping to the effective Hamiltonian (9); only a pairwise additive fluid–fluid potential (ϕ_{AO}) and an explicit one-body wall–fluid depletion potential (ϕ_{AO}^{wall}) are involved. As previously, we minimize the functional (17) but now for a hard wall with external potentials (8). The results obtained from the present DFT (figure 6) should be compared and contrasted with those of [11] where the effective one-component Hamiltonian was treated by means of a one-component mean-field DFT which treats the hard-sphere contribution by Rosenfeld’s FMT and the attractive contribution, arising from $\phi_{AO}(R)$, in mean-field fashion. We find that the present mixture functional provides an equally good description of the colloid profiles, in particular the dramatic increase in the wall contact value, $\rho_c(\sigma_c^+/2) \equiv \rho_{wc}$, as polymer is added; the present functional clearly incorporates the depletion attraction between the wall and the colloids. It should be noted that the binary mixture AO functional generates internally all depletion effects between the colloids and between the colloids and the hard wall, whereas in the previous one-component treatment these are essentially put in by hand. We choose polymer reservoir packing fractions $\eta_p^r = 0.05$ and $\eta_p^r = 0.1$ and a fixed bulk colloid packing of $\eta_c = 0.3$, as Monte Carlo simulation results exist for these state points. We intentionally stay away from the vicinity of the solid–fluid phase boundary which is at about $\eta_p^r = 0.16$ [10].

The present functional tends to give significantly more structured colloid profiles than does the effective one-component DFT of [11]. In fact it appears that the binary mixture AO DFT consistently overestimates the degree of structuring (more pronounced maxima and minima than in simulation) whereas the one-component DFT gives an underestimate. When there is no polymer

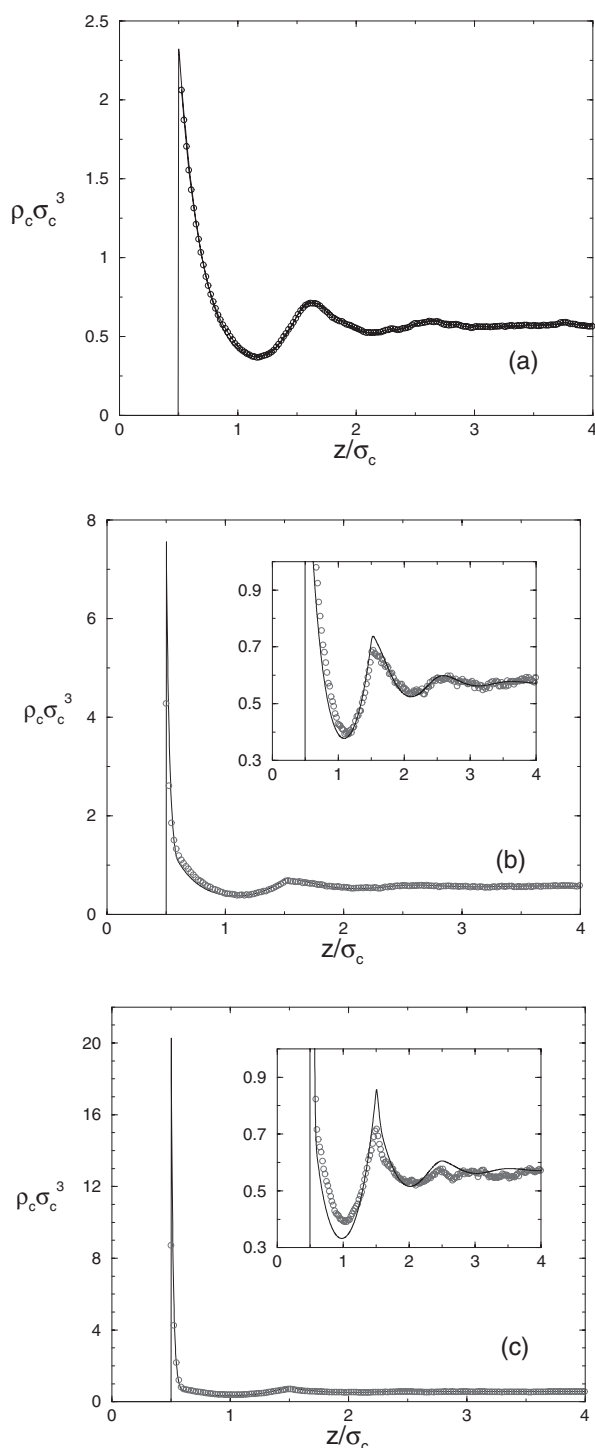


Figure 6. The colloid density profiles calculated from the binary mixture DFT compared with simulation results for a size ratio $q = 0.1$ and bulk colloid packing fraction $\eta_c = 0.3$. The packing fractions of the polymer reservoir are (a) $\eta_p^r = 0$ (hard spheres), (b) 0.05 and (c) 0.10, respectively. The circles are the Monte Carlo results [11] and the solid lines are the DFT results. The insets show the results on an expanded scale. Note the rapid increase in the density near contact as η_p^r is increased.

in the system, $\eta_p^r = 0$, see figure 6(a), both functionals reduce to the Rosenfeld functional for pure hard spheres and, as is well known, this performs very well for the full range of bulk packing fractions. The oscillations arise from packing effects at the hard wall.

On adding a small amount of polymer, $\eta_p^r = 0.05$, there is a pronounced increase in the contact value, figure 6(b), as a result of the wall-induced depletion which is now implicitly incorporated into the mixture DFT. We obtain a contact value of $\rho_{wc}\sigma_c^3 \sim 7.56$ which is slightly higher than the value 6.41 obtained from the effective one-component DFT [11]. For such small size ratios the wall–colloid depletion potential is strongly attractive and of short range ($0.1\sigma_c$) and it thus becomes difficult to achieve good simulation statistics close to the wall [11]. The simulation results have been extrapolated to contact and yield a value $\rho_{wc}\sigma_c^3 \sim 4.28$. For $\eta_p^r = 0.1$, see figure 6(c), the wall–colloid depletion attraction becomes even stronger and the present DFT gives a contact value $\rho_{wc}\sigma_c^3 \sim 20.29$; again this is larger than the corresponding result from the one-component functional, which is 15.52. Note that these very high values of the local density decay to roughly unity over the range of the wall–colloid depletion potential, i.e. $0.1\sigma_c$. The insets in figures 6(b) and 6(c) show that the DFT captures correctly the non-trivial ‘triangular’ structure of the second peak in the profile but for both $\eta_p^r = 0.05$ and 0.1 the first minimum is deeper than the simulation result and the height of the second maximum is overestimated. As η_p^r is increased the oscillations become damped more rapidly and $\rho_c(z)$ is close to the bulk value after a distance of approximately $4\sigma_c$. Numerical results were checked using the hard wall sum rule, $\beta P = \rho_c(\sigma_c^+/2) + \rho_p(\sigma_p^+/2)$, where P is the total pressure [11]. Recall that for each colloid profile we present here we also have the corresponding polymer profile. The sum rule was satisfied to better than 0.1% in all cases. It should be noted that comparing the DFT results with those of simulation for such a highly asymmetric mixture constitutes a severe test. The fact that the AO mixture DFT performs well under such difficult conditions is thus most encouraging. In addition, the free-volume theory, which gives a bulk free energy (15) identical to that of the AO functional, becomes increasingly accurate for larger q values. We might reasonably expect the performance of the functional to improve accordingly. Although the bulk free energy obtained from the functional improves with increasing q , this does not guarantee that one-body profiles will be any better. Nevertheless, since the profiles obey the hard wall sum rule, the contact values should become closer to those of simulation as q increases, in accordance with the increasing accuracy of the free-volume bulk pressure. These considerations are relevant

when we focus on larger size ratios ($q > 0.32$) where stable fluid–fluid demixing occurs and investigate interfacial phase transitions at the hard wall–fluid interface.

The physical significance of the simulation results for $q = 0.1$ were discussed in [11] and we do not dwell upon this here. Rather we simply emphasize that since the colloid density profiles decay so rapidly from their very high contact densities over the short range of the wall–fluid depletion potential, $\phi_{\text{AO}}^{\text{wall}}$, the amount of colloid adsorbed in the contact ‘layer’ is rather small (fraction of a monolayer). Indeed the Gibbs adsorption of colloid does not increase rapidly with increasing η_p^r [11]. From examination of the one-body profiles and simulation snapshots there was no evidence of wall-induced local crystallization at the polymer concentrations we examined. However, the state points we considered were still well removed from the bulk fluid–solid phase boundary. The issue of when and how wall-induced crystallization occurs is an important one, both conceptually and because there are several experimental papers reporting evidence for the phenomenon (in colloid–colloid as well as in colloid–polymer mixtures) occurring for state points well below the bulk phase boundary—see [11] for a summary.

4.2. Entropic wetting and layering: $q \geq 0.6$

For these larger size ratios the bulk phase diagram exhibits three stable phases, as in figure 2. In determining the adsorption characteristics, we choose to fix η_p^r and approach the bulk fluid–fluid phase boundary from the colloid poor side. This is analogous to performing a gas adsorption isotherm measurement for a simple atomic fluid, recalling that η_p^r plays a role equivalent to inverse temperature in the AO model. Depending on the value of η_p^r chosen, we find the adsorption behaviour changes dramatically. For the present AO model one might expect to observe similar behaviour as that pertaining to simple fluids adsorbed at attractive substrates; we have a system of colloids interacting via an effective Hamiltonian which gives rise to fluid–fluid phase separation in bulk and a depletion induced attraction acting between the colloids and the wall. However, in the present case we have effective many-body colloid–colloid and many-body wall–colloid potentials for the size ratios of interest, i.e. values of q large enough to give rise to a stable bulk fluid–fluid transition. For large size ratios the effective wall–colloid potential ceases to be a simple one-body potential acting on individual colloids and becomes a complicated function of multiple colloid coordinates. We find that these complex wall potentials do indeed give rise to new phenomena which are quite distinct from those seen in simple fluids. As an example we consider size ratio

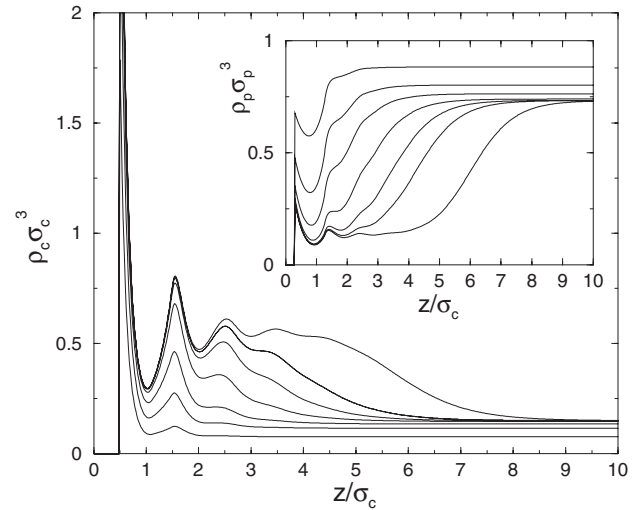


Figure 7. Colloid density profiles for $q = 0.6$ showing the onset of complete wetting of a hard wall by the colloid-rich phase at $\eta_p^r = 0.55$ as the bulk phase boundary is approached along path I in figure 2. Bulk colloid fractions are $\eta_c = 0.04, 0.06, 0.07, 0.076, 0.0775, 0.0778$ and 0.0779 (from bottom to top). The coexisting gas density is $\eta_c = 0.07812$. The inset shows the polymer profiles for the same values of η_c (from top to bottom). Note that the polymer distribution becomes progressively more depleted as the colloid-rich layer grows in thickness.

$q = 0.6$ and describe some of the phenomena encountered as we increase η_c , for fixed η_p^r , towards the bulk phase boundary. We consider, in turn, paths I and II shown in figure 2.

We first choose a path just above the critical point, $\eta_p^r = 0.55$, i.e. follow path I in figure 2. The layer of liquid-like colloid density grows continuously against the wall and becomes macroscopically thick as the phase boundary is approached. The colloid density profiles in figure 7 show the onset of complete wetting by the colloid-rich phase. We have confirmed that for states with smaller values of η_p^r (but above the critical value $\eta_{p,crit}^r$) the equilibrium film thickness, t_{eq} , or, equivalently, Γ_c , the adsorption of colloid, grows logarithmically with the deviation from the bulk phase boundary. Although a detailed investigation of the amplitude was not performed this should be the bulk correlation length of the wetting (colloid-rich) phase, as is appropriate to a system where all the interactions are of finite range—see e.g. [48]. The corresponding polymer profiles are shown in the inset and indicate how polymer becomes more depleted as the colloid-rich layer grows; the polymer can be effectively regarded as a ‘slave’ species with profiles determined by the distribution of colloid [17]. Strictly speaking, *macroscopically* thick wetting films can only occur when the density of coexisting liquid lies on the monotonic side of the

FW line in figure 2, i.e. for $\eta_p^r < \eta_{p,FW}^r$, the point of intersection of the FW line and the binodal. One can envisage a coarse grained description of wetting phenomena whereby the surface excess free energy can be regarded as an effective wall or binding potential, $\Phi_{\text{wall}}(t)$, acting on a single degree of freedom, the film thickness t [49]. For $\eta_{p,crit}^r < \eta_p^r < \eta_{p,wet}^r$ and $\eta_p^r < \eta_{p,FW}^r$ the potential $\Phi_{\text{wall}}(t)$ exhibits a single minimum at a finite equilibrium film thickness t_{eq} provided the state is off bulk coexistence. $\eta_{p,wet}^r$ denotes the polymer reservoir packing fraction at the wetting transition. As the value of η_c is increased towards coexistence the position of this minimum, and hence t_{eq} , increases continuously to infinity. If we are in the region where $\eta_{p,crit}^r < \eta_p^r < \eta_{p,wet}^r$ and $\eta_p^r > \eta_{p,FW}^r$ the decay of the density profiles is oscillatory. It can be shown [50] that in this region the effective binding potential $\Phi_{\text{wall}}(t)$ possesses a corresponding oscillatory decay. As a result the minimum, t_{eq} , of the binding potential will always lie at a finite value. Such oscillatory binding potentials will stabilize very thick but finite films, which would otherwise be infinite, even at bulk coexistence. This is because the global minimum lies at the trough of one of the oscillations and not at infinity. Such situations can easily lead to numerical difficulties when using iterative methods because of the presence of a large number of metastable minima and care must be taken to ensure that the global minimum of the excess (over bulk) free energy is reached. By choosing $\eta_p^r = 0.55$ we avoid many of these complications and can easily obtain films of thickness 20 or $30\sigma_c$. We confirmed that in the flat portion of the profiles the densities of colloid and polymer are equal to their values in the coexisting colloid-rich phase. In order to investigate such thick wetting films it is necessary to work very close to bulk coexistence and solving the Euler–Lagrange equations resulting from minimizing the functional can be very slow.

Very different scenarios arise for other paths approaching bulk coexistence. As η_c is increased along path II, see figure 2, at fixed $\eta_p^r = 0.7$ the colloids behave essentially as an ideal gas in the presence of the wall–colloid depletion potential but with some enhancement of the contact value due to packing effects. A selection of profiles calculated along this path is shown in figure 8. The profiles remain largely unstructured until $\eta_c = 0.0198$ where a first-order phase transition occurs and a second liquid-like layer is adsorbed against the wall. The inset to figure 8 shows the discontinuous jump in the (reduced) Gibbs adsorption of the colloids, Γ_c , at the transition. The Gibbs adsorption is defined as

$$\Gamma_c = \sigma_c^2 \int_0^\infty dz (\rho_c(z) - \rho_c(\infty)), \quad (22)$$

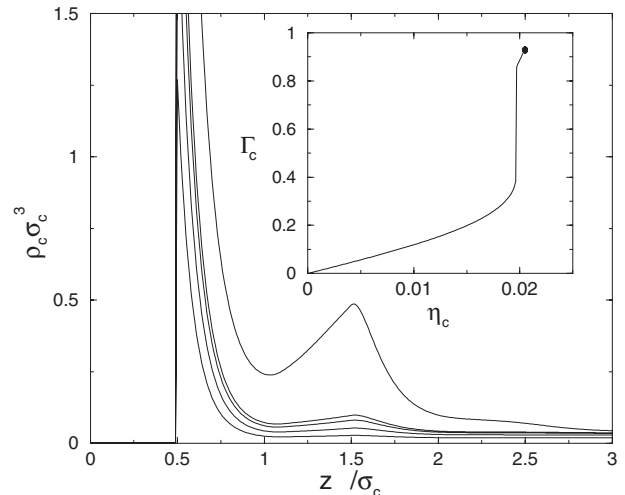


Figure 8. Colloid density profiles for size ratio $q = 0.6$ showing the first layering transition at $\eta_p^r = 0.7$ corresponding to path II in figure 2. Bulk colloid fractions are $\eta_c = 0.010, 0.015, 0.018, 0.019$ and 0.020 (from bottom to top); the transition occurs between 0.019 and 0.020 . The inset shows the corresponding jump in the Gibbs adsorption Γ_c . Γ_c remains finite at bulk coexistence $\eta_c = 0.0203$, i.e. the interface is partially wet by the colloid-rich phase.

where $\rho_c(\infty)$ is the density of colloid in the bulk. This layering transition is most unusual and is quite different from the transitions between layered liquid-like films found in DFT studies of simple fluids at attractive substrates—see e.g. [51] which considers a Yukawa fluid against an attractive Yukawa wall. The transitions found in [51] are for temperatures very close to the triple point and the sequence always leads to complete wetting at coexistence. In the present case we are far away from the free volume triple point at $\eta_p^r \sim 1.43$ (although its location within a full DFT treatment of the solid is not known). Moreover the transition is to only a single extra layer; the adsorption remains finite all the way to coexistence. Thus the wall is partially wet for this value of η_p^r . Since for $\eta_p^r = 0.7$ the wall is partially wet, whereas for $\eta_p^r = 0.55$ the wall is completely wet, we can infer that there exists an analogue of the wetting transition temperature, i.e. there is a wetting polymer reservoir packing fraction $\eta_{p,wet}^r$ at which along coexistence there is a transition from partial wetting to complete wetting. It should be noted that when the second layer is adsorbed its density is not that of the coexisting liquid, rather it is at some lower liquid-like density. For values of η_c away from the layering transition, numerical solution of the Euler–Lagrange equations is extremely rapid due to the very low bulk density of colloid. As the transition is approached convergence slows considerably and large numbers of iterations are required to overcome the free energy barrier separating layered

and unlayered profiles. In the sequence of layering transitions calculated in [51] the appearance of layer n is accompanied by a jump of density in the preceding layers, primarily effecting the $(n - 1)$ th layer. The jump in adsorption which occurs at the transition thus receives a contribution from all layers, not only layer n . A similar effect can be seen at the present layering transition where the first contact peak in the colloid profile jumps as a second layer is adsorbed.

The layering transition which we find from the AO functional, distinct from the wetting transition, appears to result from effective many-body wall-fluid and fluid-fluid potentials acting on the colloids. It does not appear to have a direct counterpart in the adsorption of simple fluids—see section 7. In order to test this assertion we have calculated colloid density profiles using the mean-field DFT employed in [11]. As described in the previous subsection, we treat the AO pair potential as a mean-field perturbation to a hard sphere reference system and apply an external potential consisting of a hard wall plus the one-body AO wall-colloid potential, see equation (9). We find that whilst a wetting transition does exist, there is no sign of the layering which we obtain from the AO mixture DFT. The phase boundary was approached for different fixed values of η_p^r above $\eta_{p,\text{wet}}^r$. In each case the adsorption was found to increase *smoothly* to a finite value at bulk coexistence.

In order to map out the full interfacial diagram and locate further layering transitions we calculate density profiles *along* the coexistence curve starting at large values of η_p^r working down towards the critical point, $\eta_{p,\text{crit}}^r$. Using the transition points (jumps) on the phase boundary as a guide we then take slices across the phase diagram, increasing η_c for a fixed value of η_p^r , so we can locate any lines of first-order transitions which may extend into the single phase (dilute in colloid) region. We have determined interfacial phase diagrams for size ratios $q = 0.6, 0.7$ and $q = 1.0$ in order to identify any variation of the topology with size ratio. Figure 9 shows the interfacial phase diagram for $q = 0.6$; it is very rich and features not only the wetting and first layering transitions discussed above but also two further layering transitions. Figure 10 shows the colloid density profiles calculated along the bulk coexistence curve for a number of values of η_p^r and the corresponding adsorption Γ_c is shown in figure 11. Since these layering transitions are rather unusual we give a brief description of how they are located.

We begin mapping out the phase diagram by calculating the profiles at coexistence for large η_p^r , region (a) in figure 9. In this region the profiles have little structure outside the contact region and the numerical iteration scheme used to solve the Euler-Lagrange equations converges rapidly. Decreasing η_p^r we encounter the point

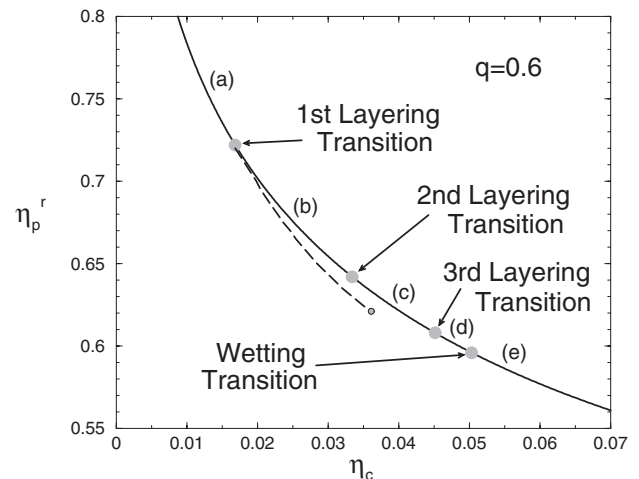


Figure 9. The interfacial phase diagram for a colloid-polymer mixture adsorbed at a hard wall for size ratio $q = 0.6$. The full curve is a portion of the bulk fluid-fluid coexistence curve shown in figure 2. We find a wetting transition at $\eta_{p,\text{wet}}^r = 0.596$ and three separate layering transitions at higher values of η_p^r . The first layering transition line extends from coexistence to deep into the single phase region (dashed line) and, when crossed, gives rise to a jump in the adsorption as shown in figure 8 for $\eta_p^r = 0.7$; it ends in a surface critical point near $\eta_p^r = 0.62$. The second and third layering transition lines and any prewetting line lie very close to the coexistence curve so the transition lines are simply denoted by circles.

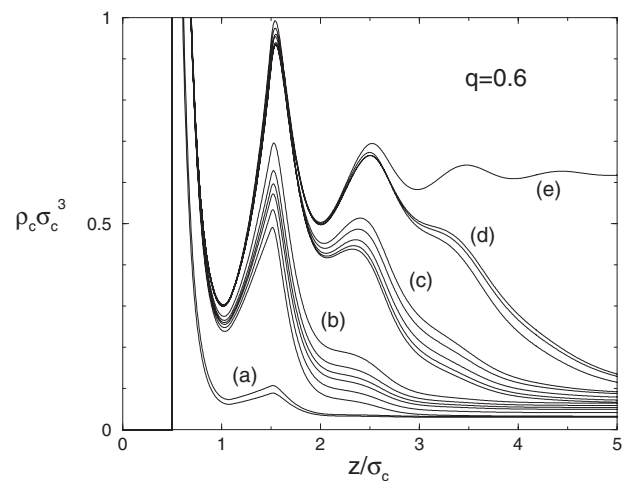


Figure 10. The colloid density profiles calculated at bulk coexistence on decreasing η_p^r (bottom to top) for a size ratio $q = 0.6$. The labels (a)–(e) indicate groups of profiles calculated on the different sections of the coexistence curve, see figure 9, and show clearly the four different transitions, e.g. the higher profile of (a) jumps to the lower profile of (b) at the first layering transition. The first three jumps are layering transitions and the final one, (d) to (e), is the wetting transition. As η_p^r is decreased the adsorption jumps discontinuously as each layering transition is encountered. For $\eta_p^r \lesssim 0.596$ the wall is completely wet by the colloid-rich phase.

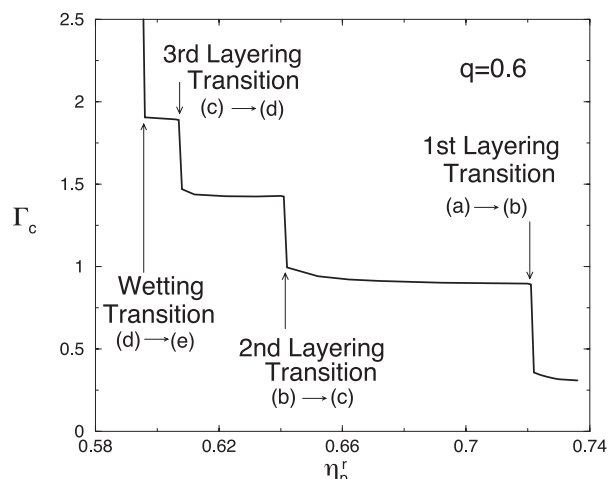


Figure 11. The Gibbs adsorption of the colloids Γ_c along the bulk coexistence curve corresponding to the profiles shown in figure 10, and the phase diagram of figure 9. At each of the layering transitions the adsorption changes discontinuously by a finite amount. At the wetting transition the adsorption diverges discontinuously as the wall is wet completely by the colloid-rich phase.

at which the first layering transition line intersects the phase boundary. Near this point the solution of the Euler–Lagrange equation becomes unstable; this instability is reflected in the number of iterations required to obtain a converged solution. At $\eta_p^r = 0.722$ the adsorption jumps discontinuously and a new layer is adsorbed, see figure 11.

Moving further down the coexistence curve, region (b), the adsorption increases smoothly until a second layering transition occurs at $\eta_p^r = 0.642$, where there is again a discontinuous jump in adsorption as a third layer is adsorbed at the wall. Again the new layer corresponds to a density lower than the coexisting bulk liquid density but it is still liquid-like in character. As the third layer appears the local density in the second layer also jumps significantly, to a value which appears to correspond more closely to that of the coexisting liquid density, i.e. the jump in adsorption at the second transition is only partially due to the appearance of the third layer. Similarly, for $\eta_p^r = 0.608$, we find a third layering transition, (c) to (d), whereby a fourth adsorbed layer develops, with an accompanying increase in density of layer three, giving rise to another jump in Γ_c . As η_p^r is reduced further Γ_c remains finite at bulk coexistence until $\eta_p^r = 0.596$, where the transition to complete wetting occurs. Having located the transition points on the phase boundary, we then take slices at fixed values of η_p^r to determine whether the layering transitions extend into the single phase region. As remarked earlier, the first layering transition extends away from the phase boundary and ends

at a surface critical point near $\eta_p^r = 0.62$. In determining the transition line we simply mark the locus of points where the adsorption jumps discontinuously. Such an approach will always be subject to some hysteresis effects, i.e. the actual transition line may be closer to the phase boundary as, for a given η_p^r , we may have to increase η_c above its value at the equilibrium transition in order to move to the next minimum in the free energy. In order to assess the extent of this effect we reversed some of the paths across the phase diagram, starting with a converged solution at coexistence and decreasing η_c until the transition is located. Although hysteresis effects do exist, these are small, and are not visible on the scale of the line in figure 9. Unlike the first transition, the second and third transition lines are extremely short in η_p^r . As it is very difficult to determine these accurately we have simply represented the transitions as large circles in figure 9. The wetting transition appears to be of first order, i.e. Γ_c appears to diverge discontinuously, see figure 11. However, it is difficult to determine any prewetting line, which should emerge tangentially from the coexistence curve at the wetting transition [49]. We can say with certainty that any prewetting line is extremely short. We repeated the calculations for $q = 0.7$ and we find the same pattern of three layering transitions and a wetting transition as was found for $q = 0.6$. The transitions occur at different values of η_p^r , see figure 12. Both the layering transitions and the wetting transition move to larger values of η_p^r on the phase boundary but the distance, in η_p^r , between the first layering transition and the wetting transition remains roughly the same. The first layering transition line is shorter in η_p^r for $q = 0.7$ than for $q = 0.6$ and lies closer to the phase boundary. Figure 13 shows the colloid profiles calculated at bulk coexistence in different regions of the phase diagram, and the corresponding adsorption is shown in figure 14.

For $q = 1$ the distance, in η_p^r , along the bulk phase boundary between the first layering transition and the wetting transition increases and a fourth layering transition appears above the wetting transition—see figure 15. The sequence of colloid density profiles is shown in figure 16. It is interesting to note from figure 17 that at subsequent layering transitions the jump in adsorption is slightly less than that at the preceding one. Since the profiles shown in figure 16 would indicate that the amount adsorbed in each new layer is roughly the same, the difference in adsorption at each transition is due chiefly to the contribution of jumps in the local density at the preceding layer. At the first layering transition the first peak in the colloid profile shows a clear jump, whereas at the fourth transition the local density in the third layer shows little change. We find

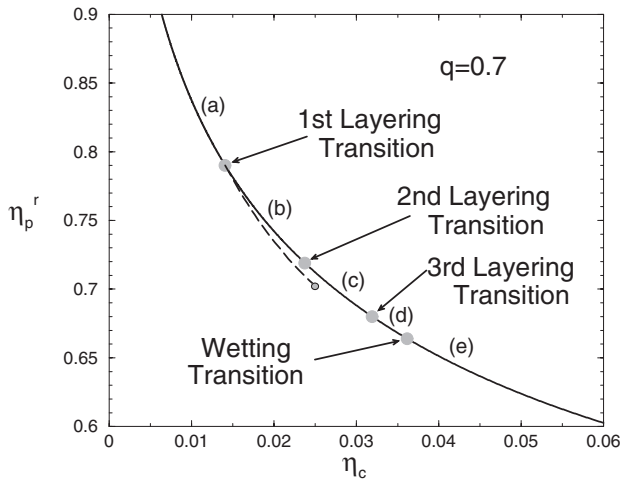


Figure 12. As in figure 9 but for size ratio $q = 0.7$. As for $q = 0.6$, we find three layering transitions but the first layering transition line is slightly shorter in η_p^r and lies closer to the bulk coexistence curve. The wetting transition occurs at $\eta_{p,\text{wet}}^r = 0.664$.

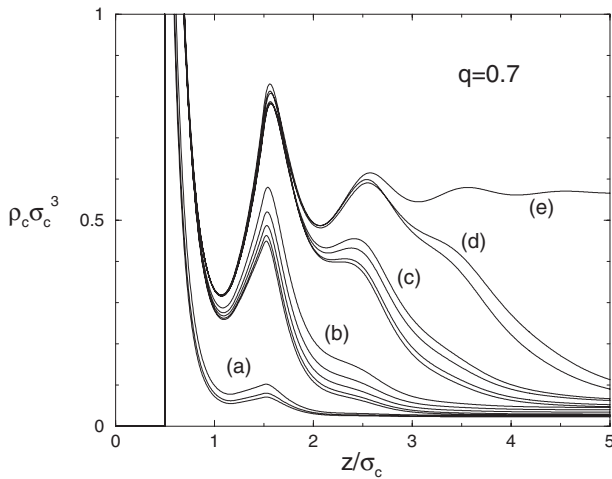


Figure 13. The colloid density profiles at bulk coexistence on decreasing η_p^r (bottom to top) for $q = 0.7$. The labels (a)–(e) indicate groups of profiles calculated on different sections of the coexistence curve, see figure 12.

that the first layering transition line is very short for $q = 1$ and lies extremely close to the coexistence curve so we simply represent this as a circle in figure 15.

4.3. A simulation study for $q = 1$

All the results we have described so far for wetting and layering were based on the DFT for the binary AO mixture. It is important to enquire how much of the rich behaviour predicted by DFT for this model can be found in simulation studies. After the completion of our DFT calculations [25, 26, 46], Dijkstra and van Roij [19] developed a novel Monte Carlo scheme for tackling the equilibrium statistical mechanics of

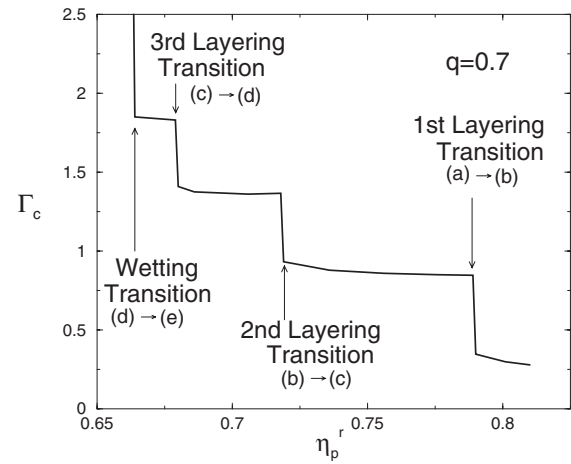


Figure 14. The Gibbs adsorption of the colloids Γ_c along the bulk coexistence curve corresponding to the profiles shown in figure 13 and the phase diagram in figure 12.

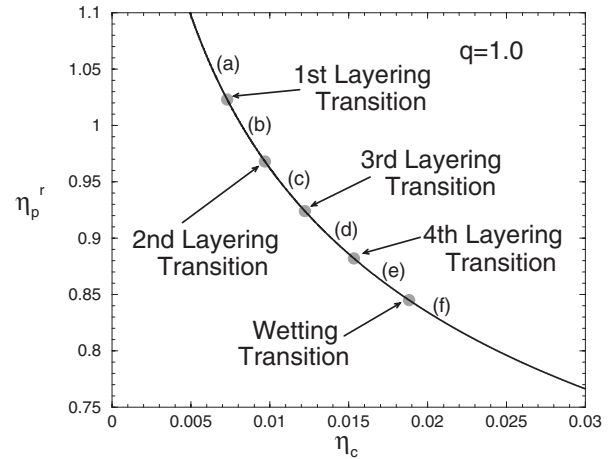


Figure 15. As in figure 9 but for size ratio $q = 1.0$. We find four layering transitions but now all the transition lines, including the first, lie extremely close to the bulk coexistence curve (solid line). The wetting transition occurs near $\eta_{p,\text{wet}}^r = 0.845$.

both homogeneous and inhomogeneous model colloid-polymer (AO) mixtures for arbitrary size ratios q , including those where effective many-body interactions between the colloids play an important role. Their approach is based on the exact effective one-component Hamiltonian entering equation (4). Because of the ideality of polymers, $\phi_{pp} = 0$, the grand potential of polymer in the external potential V_p^{ext} and in the static configuration $\{\mathbf{R}^{N_c}\}$ of the N_c colloidal hard spheres is given exactly by $\Omega = -\beta^{-1} z_p V_f$, where

$$V_f = \int d\mathbf{r} \exp(-\beta V_p^{\text{ext}}(\mathbf{r})) \prod_{i=1}^{N_c} [1 + f_{cp}(|\mathbf{r} - \mathbf{R}_i|)] \quad (23)$$

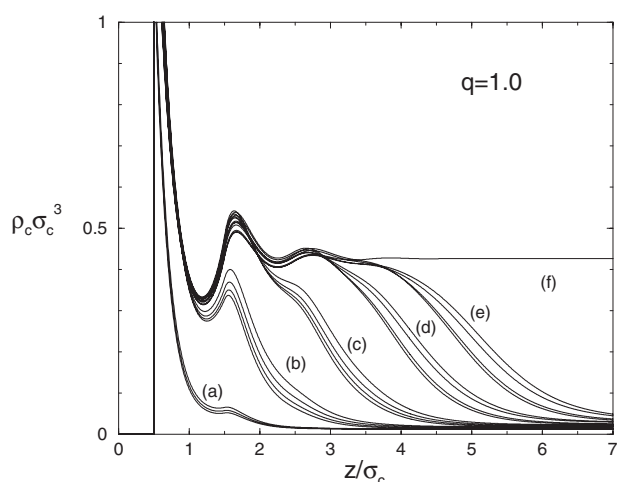


Figure 16. The colloid density profiles at bulk coexistence on decreasing η_p^r (bottom to top) for a size ratio $q = 1.0$. The labels (a)–(f) indicate groups of profiles calculated in different sections of the coexistence curve, see figure 15.

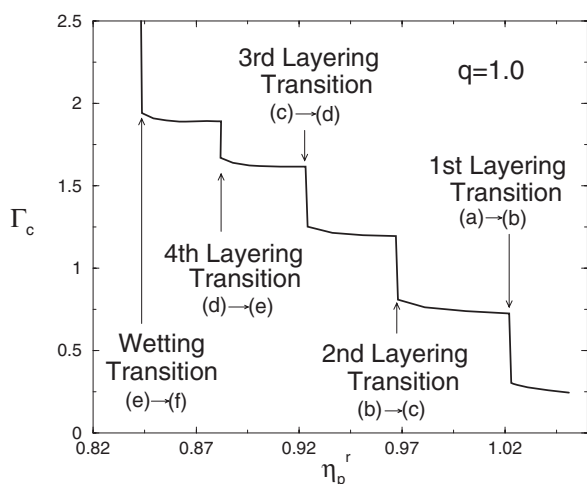


Figure 17. The Gibbs adsorption of the colloids Γ_c along the coexistence curve corresponding to the profiles shown in figure 16 and the phase diagram of figure 15.

is the *free volume*. The integral in equation (23) is over the total volume V of the system and $f_{cp}(r)$ is the colloid–polymer Mayer bond: $f_{cp} = -1$ for $0 < r < R_c + R_p$ and zero otherwise. Of course, the shape of the free volume is, generally, irregular and non-connected but computationally efficient methods were developed to calculate this [19]. Bulk simulations were performed for the case $q = 1$ where effective many-body interactions are expected to be crucially important. The semi-grand free energy was obtained using thermodynamic integration, at fixed colloid packing fraction η_c , with respect to the polymer fugacity z_p (see also [28]).

Phase coexistence was then determined by standard common tangent constructions at fixed z_p . The inset

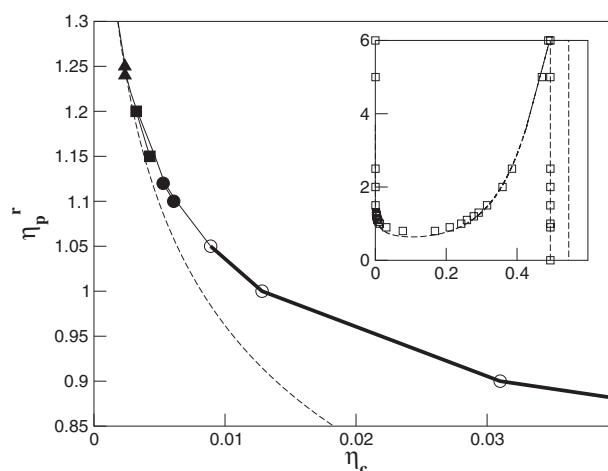


Figure 18. Simulation results (adapted from [19]) for bulk and surface phase diagram of the AO model (size ratio $q = 1$) as a function of the colloid packing fraction η_c and the polymer reservoir packing fraction η_p^r . The main figure is a blow-up of the saturated bulk gas branch, separated into a regime of complete wetting (thick curve, open circles), and partial wetting by colloidal liquid (thin curve) at a planar hard wall. The first (filled triangles), second (filled squares), and third (filled circles) layering transition lines extend from bulk coexistence into the single phase (gas) region. The inset shows the gas–liquid and fluid–solid bulk coexistence (open squares) to full scale. The dashed curves denote the bulk binodals obtained from free-volume theory.

to figure 18 shows the resulting phase diagram in the reservoir, η_p^r versus η_c , representation. Three phases are present; there is colloidal gas–liquid separation, with a critical point $\eta_{p,\text{crit}}^r \sim 0.70$, and a liquid–solid transition which is almost independent of η_p^r . The triple point is at $\eta_{p,t}^r \sim 6.0$, i.e. there is a very large stable gas–liquid coexistence region, much larger than the corresponding (inverse) temperature region for simple atomic fluids. Also plotted in this figure is the phase diagram obtained from the free-volume theory of [4]. Note that the latter can be viewed as a first-order perturbation theory that approximates V_f by its average in the pure hard-sphere fluid [10, 11]; it sets $V_f = \alpha(\rho_c)V$, where $\alpha(\rho_c)$ is the free-volume fraction in equation (16). On the scale of the inset, the free-volume theory, and therefore our DFT approach which yields the same free energy, provides an accurate description of the simulation data. There *are* significant deviations, as indicated on the expanded scale of the main figure where the gas branch of the coexistence curve is plotted, but the overall agreement is quite remarkable. As emphasized by Dijkstra and van Roij [19], it is important to compare the ‘exact’ simulation phase diagram for $q = 1$ with that obtained in [10] from simulations in which solely the pairwise effective potential $\phi^{\text{eff}}(R; z_p)$, equation (6), was employed.

For the latter, $\eta_{p,\text{crit}}^r \sim 0.5$ and $\eta_{p,t}^r \sim 0.8$. In other words, the effective many-body interactions extend greatly the region in η_p^r over which stable gas–liquid coexistence can occur. Moreover, these many-body contributions appear to be incorporated into the free-volume/DFT approximation. For completeness we should also note that Bolhuis *et al.* [15] have investigated the bulk phase behaviour of the AO binary mixture using Gibbs ensemble Monte Carlo simulations for size ratios $q = 0.34, 0.67$ and 1.05 . They find that for $q = 0.34$ the fluid–fluid binodal is (weakly) metastable, consistent with the prediction of the free-volume theory. For $q = 0.67$ and 1.05 their simulation results for the gas–liquid coexistence curves are in good overall agreement with those of the free-volume theory. These authors also performed simulations which incorporate excluded-volume interactions between polymers but we shall return to this aspect later.

The main part of figure 18 displays the surface phase diagram obtained in [19] for the $q = 1$ AO mixture adsorbed at a planar hard wall. Once again V_f (now given by equation (23) with V_p^{ext} corresponding to the hard-wall potential) is calculated within the simulation so that all many-body interactions are incorporated, including the modification of pair and higher-body interactions that occurs when two colloids are close to the wall—see section 2.1 and [11].

For small polymer reservoir packings $\eta_{p,\text{crit}}^r < \eta_p^r < 1.05$ there is strong evidence for complete wetting, i.e. formation of a thick film of colloidal liquid at the hard wall–colloidal gas interface with the adsorption Γ_c increasing continuously (logarithmically) as bulk coexistence is approached. In this regime the colloid density profiles (see figure 2(a) of [19]) are reminiscent of the DFT results in figure 7. By contrast, for about $\eta_p^r > 1.1$, there is partial wetting, i.e. Γ_c remains finite at bulk coexistence. The authors conclude that there is a wetting transition at some value of $\eta_{p,\text{wet}}^r$ in the range $1.05 < \eta_{p,\text{wet}}^r < 1.1$. They find no evidence for an accompanying prewetting transition out of bulk coexistence, i.e. there appears to be no thin–thick transition in the same range of values of η_p^r . For about $\eta_p^r > 1.1$, however, they find jumps in the adsorption which they attribute to layering transitions of the type we found in the DFT calculations described in section 4.2. Indeed the colloid density profiles near the layering transitions (see figure 2(b) of [19]) are very similar in form to those shown in figures 10, 13 and 16. Note that the latter refer to transitions encountered on reducing η_p^r at bulk coexistence, whereas the simulation data is for a path at fixed η_p^r , increasing η_c towards bulk coexistence. Figure 18 describes three separate layering transition lines, each of them rather short, lying close to bulk coexistence and very far from the bulk triple point. A reasonable

person would conclude that the wetting and layering phenomena found in the simulations for $q = 1$ mimic those found in the DFT calculations. There is not perfect agreement. The sequence of layering transitions gleaned from the simulations for $q = 1$, is arguably closer to that observed in DFT for $q = 0.6$ and 0.7 than for $q = 1$; the layering transitions extend very little out of bulk coexistence in the last case (see figure 15). But one should not expect an approximate DFT to provide a completely accurate account of what are very subtle interfacial phase transitions, resulting from a complicated competition between wall–fluid and fluid–fluid interactions. Given that the bulk gas–liquid coexistence curves obtained from DFT and simulation differ significantly on the scale relevant to the surface phase diagram it is not surprising that there are differences in the surface phase behaviour. What is more important is to establish that it is the many-body interactions entering the effective interfacial Hamiltonian for the colloids which give rise to the pattern of interfacial transitions that is observed. We shall return to this issue later.

5. Treating polymer–polymer interactions within a geometry-based DFT

So far in this paper we have treated the polymers as mutually non-interacting: $\phi_{pp}(r) = 0$. Real polymers, when dissolved in a good solvent, experience repulsive monomer–monomer interactions. As described in the introduction, when averaged over polymer conformations this repulsion at the polymer segment level gives rise to a soft, penetrable and repulsive interaction between polymer centres of mass. The range of this effective pair potential is \gtrsim the polymer radius of gyration and its strength (at zero separation between the two centres of mass) is of the order of the thermal energy, $k_B T$. Within this ‘soft colloid’ picture the effective polymer–polymer potential can be well represented by a Gaussian pair potential [52]. In the following we do not attempt to model this interaction realistically, rather we summarize the approach of [20] where a minimal model was considered that displays the essential features of polymer–polymer repulsion. With a simple geometric picture in mind, the interactions between polymers are represented by a repulsive step-function pair potential

$$\phi_{pp}(r) = \begin{cases} \epsilon, & \text{for } r < 2R_p, \\ 0, & \text{otherwise,} \end{cases} \quad (24)$$

whilst the colloid–colloid and colloid–polymer potentials remain hard-sphere-like. Note that in the limit $\epsilon/k_B T \rightarrow 0$ we recover the AO model with non-interacting polymers, equation (1) with $\sigma_p \equiv 2R_p$,

whereas for $\epsilon/k_B T \rightarrow \infty$ the model reduces to that of an additive binary hard-sphere mixture. A similar treatment of polymer interactions was introduced by Warren *et al.* [53], although in that work $\phi_{pp}(r)$ was assumed to have a range of R_p , the polymer radius of gyration. Our current (longer-ranged) choice is more consistent with the effective (Gaussian) potentials of Louis *et al.* [52], which extend even beyond $2R_p$. Our aim is to develop a DFT which retains most of the features of the DFT for the original AO model but which incorporates, albeit crudely, polymer–polymer interactions. We briefly review how the DFT of section 2.2 can be extended to the current case, following [20], and then describe the bulk fluid–fluid phase separation which arises in this theory.

5.1. Construction of the functional

In constructing functionals for hard-sphere fluids it has been shown [54, 55] that requiring an approximate functional to recover the properties of the system in the zero-dimensional (0d) limit, where the partition sum can be calculated exactly, is a powerful constraint which has guided the development of DFTs for other models, such as the AO model. Thus we first consider the current model in the 0d limit, in which particle centres are confined to a volume v_{0d} whose dimensions are smaller than all relevant length scales in the system. The microstates accessible are then completely specified by the occupation numbers of particles of both species and each microstate is assigned a statistical weight according to the grand ensemble. The grand partition sum for an arbitrary binary mixture in this limit is

$$\Xi = \sum_{N_p=0}^{\infty} \frac{z_p^{N_p}}{N_p!} \sum_{N_c=0}^{\infty} \frac{z_c^{N_c}}{N_c!} \exp(-\beta\phi_{\text{total}}), \quad (25)$$

where the (reduced) fugacities are $z_i = (v_{0d}/\Lambda_i^3) \times \exp(\beta\mu_i)$, Λ_i is the thermal wavelength, μ_i is the chemical potential of species i and ϕ_{total} is the total potential energy in the situation where all particles have vanishing separation. Note that for hard-core interactions, the Boltzmann factor vanishes for forbidden configurations, which then limits the upper bounds in the summations in equation (25). For the present case, where ϕ_{cc} and ϕ_{cp} are hard-body interactions, we obtain

$$\Xi = z_c + \sum_{N_p=0}^{\infty} \frac{z_p^{N_p}}{N_p!} \exp(-\beta\epsilon N_p(N_p - 1)/2), \quad (26)$$

where the N_p dependence in the Boltzmann factor stems from the counting of pairs of polymers. There are two important limiting cases. For $z_c = 0$ (no colloids),

the limit of one-component penetrable spheres [56] is recovered, whereas for $\beta\epsilon = 0$, equation (26) reduces to the AO result [16, 17], $\Xi = z_c + \exp(z_p)$. In order to obtain the Helmholtz free energy, a Legendre transform must be performed, and the dependence on the fugacities replaced with the dependence on the mean (occupation) numbers of particles, $\eta_i = z_i \partial \ln \Xi / \partial z_i$, $i = c, p$. Taking the particle volume of species i as the reference volume, η_i is also the 0d packing fraction of species i . Subtracting the ideal contribution, one calculates the excess Helmholtz free energy, $\beta F_{0d} = -\ln \Xi + \sum_{i=c,p} \eta_i \ln(z_i) - \sum_{i=c,p} \eta_i [\ln(\eta_i) - 1]$. In the present case (as for pure penetrable spheres [56]), this cannot be expressed analytically. As we are interested in the case of small ϵ (small deviations from the AO model), we perform an expansion in powers of $\beta\epsilon$, and obtain

$$\beta F_{0d}^{(1)} = (1 - \eta_c - \eta_p) \ln(1 - \eta_c) + \eta_c + \frac{\beta\epsilon}{2} \frac{\eta_p^2}{1 - \eta_c}, \quad (27)$$

which is exact up to lowest (linear) order in $\beta\epsilon$. In the limit $\beta\epsilon \rightarrow 0$, equation (27) reduces to the AO result [16, 17], which is $\beta F_{0d, \text{AO}} = (1 - \eta_c - \eta_p) \ln(1 - \eta_c) + \eta_c$. In the absence of colloids, $\eta_c \rightarrow 0$, we obtain a mean-field-like expression, $F_{0d, \text{MF}} = \epsilon \eta_p^2 / 2$.

Since some terms of higher than first order can be obtained analytically, we write the free energy as $F_{0d}^{(1)} + \Delta F_{0d}$, and we find that up to cubic order in $\beta\epsilon$

$$\beta \Delta F_{0d} = -\frac{\eta_p^2 (\beta\epsilon)^2}{4(1 - \eta_c)} + \left[\frac{\eta_p^2}{1 - \eta_c} + \frac{2\eta_p^3}{(1 - \eta_c)^2} \right] \frac{(\beta\epsilon)^3}{12}. \quad (28)$$

For large $\beta\epsilon$, the 0d free energy must be calculated numerically. This is straightforward [20].

Returning to three dimensions, we write the excess Helmholtz free energy functional of an inhomogeneous system as

$$\beta \mathcal{F}_{\text{ex}}[\rho_c(\mathbf{r}), \rho_p(\mathbf{r})] = \int d\mathbf{r} \Phi(\{n_v^c\}, \{n_v^p\}), \quad (29)$$

which is the same as in the ideal polymer case, equation (11). The weighted densities $\{n_v^i\}$ are defined as convolutions with the bare density profiles through equation (13). In addition to the weights (14) we also introduce Tarazona's [57] tensor weight function $\hat{\mathbf{w}}_{m2}^i(\mathbf{r}) = w_2^i(\mathbf{r})[\mathbf{r}\mathbf{r}/r^2 - \hat{\mathbf{1}}/3]$, where $\hat{\mathbf{1}}$ is the identity matrix.

The free energy density is composed of three parts

$$\Phi = \Phi_1 + \Phi_2 + \Phi_3, \quad (30)$$

which are defined as

$$\Phi_1 = \sum_{i=c,p} n_i^0 \varphi_i(n_3^c, n_3^p), \quad (31)$$

$$\Phi_2 = \sum_{i,j=c,p} (n_1^i n_2^j - \mathbf{n}_{v1}^i \cdot \mathbf{n}_{v2}^j) \varphi_{ij}(n_3^c, n_3^p), \quad (32)$$

$$\begin{aligned} \Phi_3 = & \frac{1}{8\pi} \sum_{i,j,k=c,p} \left(\frac{1}{3} n_2^i n_2^j n_2^k - n_2^i \mathbf{n}_{v2}^j \cdot \mathbf{n}_{v2}^k \right. \\ & \left. + \frac{3}{2} [\mathbf{n}_{v2}^i \mathbf{n}_{m2}^j \mathbf{n}_{v2}^k - \text{tr}(\mathbf{n}_{m2}^i \mathbf{n}_{m2}^j \mathbf{n}_{m2}^k)] \right) \varphi_{ijk}(n_3^c, n_3^p), \end{aligned} \quad (33)$$

where tr denotes the trace. The quantities φ_i, φ_{ij} etc. are derivatives of the 0d excess free energy

$$\varphi_{i\dots k}(\eta_c, \eta_p) \equiv \frac{\partial^m}{\partial \eta_i \dots \partial \eta_k} \beta F_{0d}(\eta_c, \eta_p). \quad (34)$$

In the absence of polymer, Φ_1 and Φ_2 are equivalent to the free energy densities for hard spheres introduced in [18] and Φ_3 is equivalent to the tensor treatment for pure hard spheres in [57]. Equations (31)–(33) are generalizations of these earlier treatments that include summations over species. If we set $\beta\epsilon = 0$, ideal polymer, and take the derivatives of $\beta F_{0d, AO}$ we recover the explicit expressions given in equation (12) for the AO model.

5.2. Fluid–fluid phase separation

In bulk, the one-body densities of both species are spatially uniform: $\rho_i(\mathbf{r}) = \text{const}$. This leads to simple analytic expressions for the weighted densities. The excess free energy density, equations (30)–(33), is easily evaluated provided the analytic approximations (27), (28) are employed for F_{0d} . If we retain only the linear term in $\beta\epsilon$, i.e. employ equation (27), then

$$\begin{aligned} \beta f_{\text{ex}}(\rho_c, \rho_p) = & \frac{\beta \mathcal{F}_{\text{ex}}(\rho_c, \rho_p)}{V} = \beta f_{\text{ex}}^{\text{HS}}(\rho_c) - \rho_p \ln \alpha_1(\rho_c) \\ & + \frac{\beta \tilde{\phi}_{\text{pp}}(0)}{2} \rho_p^2 [1 - \ln \alpha_2(\rho_c)], \end{aligned} \quad (35)$$

where the integrated potential is $\tilde{\phi}_{\text{pp}}(0) = 4\pi \int dr r^2 \phi_{\text{pp}}(r) = 4\pi\epsilon\sigma_p^3/3$. $f_{\text{ex}}^{\text{HS}}$ is the scaled-particle (Percus–Yeveick compressibility) approximation, and is given by

$$\beta f_{\text{ex}}^{\text{HS}} = \frac{3\eta_c[3\eta_c(2 - \eta_c) - 2(1 - \eta_c)^2 \ln(1 - \eta_c)]}{8\pi R_\zeta^3(1 - \eta_c)^2}, \quad (36)$$

and is the same quantity that enters equation (15). The quantities α_1 and α_2 , which depend solely on η_c and the size ratio $q = \sigma_p/\sigma_c$, are given by

$$\ln \alpha_1 = \ln(1 - \eta_c) - \sum_{m=1}^3 C_m^{(1)} \gamma^m, \quad (37)$$

$$\ln \alpha_2 = -\frac{1}{8} \sum_{m=1}^4 C_m^{(2)} \gamma^m, \quad (38)$$

where the dependence on colloid density is through $\gamma = \eta_c/(1 - \eta_c)$, and the coefficients are polynomials in the size ratio, given as $C_1^{(1)} = 3q + 3q^2 + q^3$, $C_2^{(1)} = (9q^2/2) + 3q^3$, $C_3^{(1)} = 3q^3$ and $C_1^{(2)} = 8 + 15q + 6q^2 + q^3$, $C_2^{(2)} = 15q + 24q^2 + 7q^3$, $C_3^{(2)} = 18q^2 + 15q^3$ and $C_4^{(2)} = 9q^3$.

For $\beta\epsilon = 0$, ideal polymer, our result is identical to that of free-volume theory for the AO model—see equations (15) and (16). The quantity α_1 in equation (37) is identical to α , the free-volume fraction of a single polymer sphere in the AO model. α_2 can be interpreted [20] as the free-volume ratio for pairs of overlapping polymers. α_1 and α_2 both decrease monotonically with increasing η_c due to the increasing excluded volume. However, $\alpha_2 > \alpha_1$ over the whole density range, which may be due to correlations between polymer pairs [20]. At fixed η_c , both α_1 and α_2 decrease monotonically with increasing size ratio.

The total canonical free energy is given by $F/V = f_{\text{ex}} + k_B T \sum_{i=c,p} \rho_i [\ln(\rho_i A_i^3) - 1]$. It is convenient to transform to the semi-grand ensemble, where the polymer chemical potential μ_p is prescribed instead of the system density ρ_p . The appropriate thermodynamic potential is the semi-grand free energy Ω_{semi} , related to F via a Legendre transform: $\Omega_{\text{semi}}/V = F/V - \mu_p \rho_p$, where μ_p is given as

$$\begin{aligned} \beta \mu_p = & \partial(\beta F/V)/\partial \rho_p \\ = & \ln(\rho_p A_p^3) - \ln \alpha_1(\rho_c) - \beta \tilde{\phi}_{\text{pp}}(0) \rho_p [1 - \ln \alpha_2(\rho_c)], \end{aligned} \quad (39)$$

which is a transcendental equation to be solved for ρ_p once μ_p is prescribed. This result is a generalization of the standard free-volume expression $\beta \mu_p = \ln(A_p^3 \rho_p / \alpha)$ pertaining to the original AO model [4].

As usual, phase coexistence is determined by requiring equality of the total pressure, of the chemical potentials μ_i , and of the temperatures in the coexisting phases. This can be carried out in the system representation (η_c, η_p) [20] or, using common tangent constructions on Ω_{semi} , in the polymer reservoir representation (η_c, μ_p).

Stable fluid–fluid phase separation (with respect to the fluid–solid transition) is observed in experiments

3372

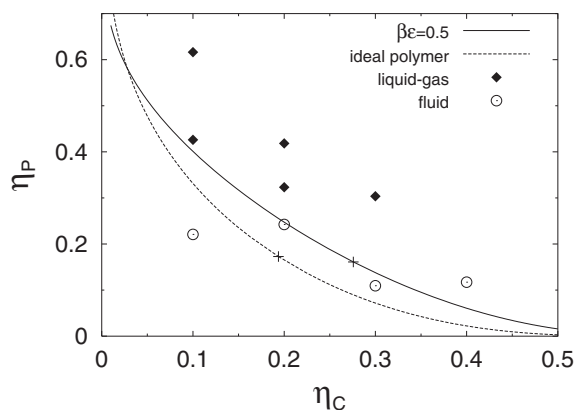
J. M. Brader *et al.*

Figure 19. Fluid demixing binodals in the system representation, i.e. as a function of the colloid (η_c) and polymer (η_p) packing fractions for size ratio $q = 0.57$. Results are shown for the case of non-interacting polymer (dashed line) and for interacting polymer (solid line) with strength $\beta\epsilon = 0.5$. The crosses denote the critical points. The symbols refer to the experimental state points taken from [5]. The open circles denote single-phase (fluid) states and the filled rhombuses two-phase (liquid-gas) states.

on colloid-polymer mixtures only at sufficiently large polymer-to-colloid size ratios. We consider the size ratio $q = 0.57$, for which experimental data are available for PMMA colloid and polystyrene (PS) in *cis*-decalin [5]. Figure 19 shows the calculated phase diagrams with and without polymer interactions. For non-interacting polymers ($\beta\epsilon = 0$), our result is identical to that from free volume theory for the AO model. In order to apply our theory to the experimental situation, we have prescribed the potential energy barrier to be $\beta\epsilon = 0.5$. This is based on considerations of the second virial coefficient of a pure polymer solution [20]. In order to achieve higher accuracy than is provided by the linear expansion of the 0d free energy, equation (27), we use the cubic order expression, equation (28), to determine the excess free energy. Figure 19 shows a comparison of the calculated theoretical binodal with the experimental data of [5] in the system representation.

Although the measured single-phase (fluid) state point at high colloid packing fraction lies inside the theoretical two-phase region, it is clear that our theory predicts a shift in the correct direction compared with the non-interacting (ideal) binodal. The theory also predicts that the coexisting colloidal gas phase is more strongly dilute in colloids, as compared with the non-interacting case.

In figure 20 the phase diagram is shown in polymer reservoir representation: a reservoir of *interacting* pure polymer is considered that is in chemical (osmotic) equilibrium with the system with respect to exchange of polymers. The tie lines are horizontal in this representation. Away from the critical point a gas,

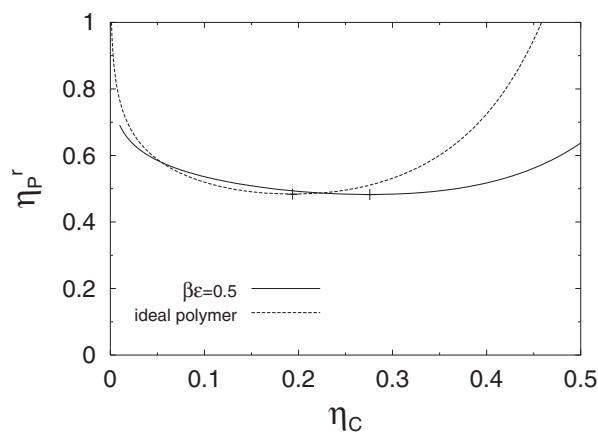


Figure 20. Same as figure 19 ($q = 0.57$), but in the reservoir representation, i.e. as a function of η_c and the packing fraction of polymer (η_p^r) in a reservoir of pure polymer in osmotic equilibrium with the system.

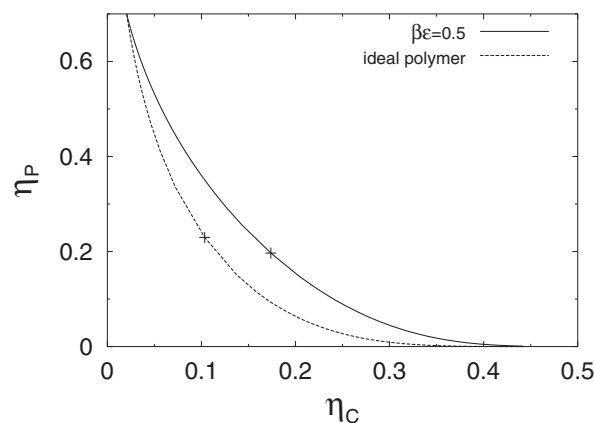


Figure 21. Same as figure 19, but for size ratio $q = 1$.

dilute in colloids, coexists with a liquid that has very high packing fraction of colloids, much higher than in the ideal case. We consider next the case of equally-sized species, $q = 1$. Phase diagrams are shown in the system representation (figure 21) and in the reservoir representation (figure 22). Again a marked shift of the critical point towards higher η_c is found and the single phase region is larger (in the system representation) compared to the case of ideal polymer. Figure 22 shows that the packing fraction of coexisting liquid increases quite rapidly with increasing η_p^r , which has repercussions for the location of the triple point. All these results can be understood in terms of a free energy penalty arising from polymer-polymer interactions. These manifest themselves primarily in the colloidal gas phase as only a small penalty arises in the colloidal liquid phase, where polymers are strongly diluted.

It is instructive to make some comparisons between the present results and the recent extensive Monte Carlo simulation results of Bolhuis *et al.* [15] mentioned in

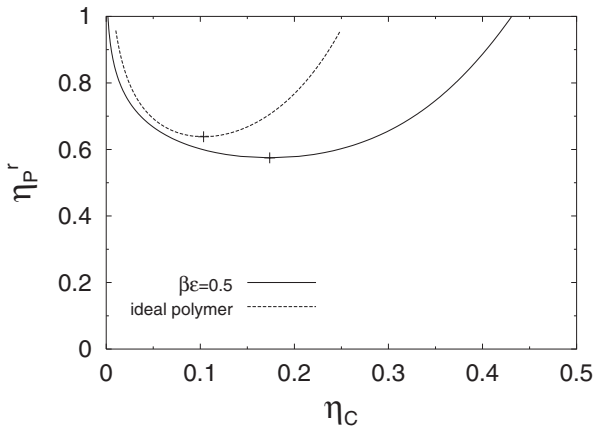


Figure 22. Same as figure 20, but for size ratio $q = 1$.

section 4.3. These authors consider hard-sphere colloids but obtain effective potentials for the polymer–polymer interaction from simulations of a bulk system of self-avoiding walks (SAW) at various concentrations—a procedure known to be reliable for polymers in a good solvent. The effective pair potentials ϕ_{pp} correspond to tracing out the monomer degrees of freedom and treating the polymer as ‘soft colloid’; ϕ_{pp} depends on the volume fraction of the polymer and is calculated by inversion of the centre-of-mass radial distribution function $g_{pp}(r)$. The colloid–polymer effective potential also depends on the volume fraction of polymer. It is obtained from simulations of a single hard sphere in a solution of SAW polymers by inverting the centre-of-mass concentration profile using the HNC equation—details are given in [15]. Phase diagrams are determined by Gibbs ensemble simulations of the binary mixture described by these effective pair potentials and results are presented for $q = 0.34, 0.67$ and 1.05 . We focus here on size ratios $q = 0.67$ and 1.05 where gas–liquid (fluid–fluid) phase separation is stable with respect to fluid–solid.

In the (η_c, η_p^r) representation including polymer–polymer interactions increases the critical point value of the packing fraction of colloids very slightly but increases the critical polymer reservoir fraction $\eta_{p,crit}^r$ by about 0.25 for $q = 0.67$. More significantly, the gas–liquid two-phase region is broadened significantly in η_c and the triple point $\eta_{p,t}^r$ is lowered considerably from what is found in the ideal polymer (AO) case—see figure 1 of [15]. The upshot is that there is a very narrow, in η_p^r , region of stable fluid–fluid phase coexistence when interactions are included. This is not totally different from what we find in figure 20, for $q = 0.57$, from the DFT; as freezing is expected to occur when $\eta_c \sim 0.5$, this permits only a small separation between $\eta_{p,t}^r$ and $\eta_{p,crit}^r$ when interactions are incorporated. However, our DFT does not predict the substantial increase in $\eta_{p,crit}^r$ which

is found in simulations when interactions are included. This is reflected clearly in the (η_c, η_p) representation where the binodal calculated with interactions appears to be more separated from the non-interacting case (see figure 2 of [15]) giving a larger single-phase region than in the corresponding DFT results, although the latter are for a smaller value of q . The situation is exaggerated for $q = 1.05$. Now the critical point is shifted from $\eta_{c,crit} \sim 0.11, \eta_{p,crit}^r \sim 0.75$ to $\eta_{c,crit} \sim 0.18, \eta_{p,crit}^r \sim 1.12$ and the triple point is lowered from what is a very high number $\eta_{p,t}^r \sim 6$ to $\eta_{p,t}^r \sim 1.65$ when interactions are included. Again the range in η_p^r over which stable fluid–fluid phase coexistence occurs is narrowed considerably. A similar trend is found in the DFT results of figure 22 for $q = 1$ but the latter predict a small *decrease* in $\eta_{p,crit}^r$ rather than the substantial increase found in simulation. Moreover, the DFT does not predict the very strong shift of the binodal in the (η_c, η_p) representation found in simulations (figure 3 of [15]) which results in a much larger single-phase region when interactions are included.

In summary, the DFT introduced in [20] and described above captures several, but not all, of the effects of polymer–polymer excluded volume interactions that are found in the computer simulations of bulk phase behaviour. (Note, however, that the freezing transition was not considered explicitly in the DFT calculations.) This should encourage applications of the theory to *inhomogeneous* situations—the primary purpose of DFT. Such problems are not easily tackled by simulations.

Of course, this model of polymer–polymer interactions is highly idealized and a detailed critique is given in [20]. The main limitations are: (i) $\phi_{pp}(r)$ is assumed to be a step function rather than a Gaussian-type function, (ii) the range of the step function is set equal to $2R_p$, twice the polymer radius of gyration, in order to derive a geometry-based DFT meeting ‘additive’ restrictions and (iii) the strength ϵ and range of ϕ_{pp} are assumed to be independent of the concentrations of polymer and colloids, whereas simulation studies of SAW [15, 52] indicate that the effective polymer–polymer potential should depend on the volume fraction of polymer.

We conclude this section by emphasizing [20] that the present DFT approach is *not* a perturbative treatment of polymer–polymer interactions. One might attempt to construct a DFT which starts with the AO functional for the AO reference model and then simply adds a (perturbative) contribution to account for polymer–polymer interactions. The latter could be the type of mean-field functional used recently to describe a pure polymer system [21], namely

$$\mathcal{F}_{MF}[\rho_p(\mathbf{r})] = \frac{1}{2} \int d\mathbf{r} \int d\mathbf{r}' \rho_p(\mathbf{r}) \rho_p(\mathbf{r}') \phi_{pp}(|\mathbf{r} - \mathbf{r}'|). \quad (40)$$

This functional generates the pair direct correlation function which corresponds to the random phase approximation: $c_{pp}^{(2)}(\mathbf{r}, \mathbf{r}') = c_{pp}^{(2)}(|\mathbf{r} - \mathbf{r}'|) = -\beta\phi_{pp}(|\mathbf{r} - \mathbf{r}'|)$, known to be a good approximation at high densities for penetrable potentials [21]. It has been used to good effect in investigations of repulsive Gaussian core particles adsorbed at a hard wall [58]. The generalization of equation (40) to binary Gaussian core mixtures was used in studies of fluid–fluid interfaces [41] and of wetting phenomena [48]. At first sight the functional $\mathcal{F}_{ex}^{AO} + \mathcal{F}_{MF}$ would appear to provide a reasonable description of the excess free energy of the AO mixture; note that the hard-body interactions between colloids and polymers are already included in \mathcal{F}_{ex}^{AO} . However, as shown in [20], this is *not* the case for the model described above. The perturbative contribution \mathcal{F}_{MF} depends solely on the polymer density $\rho_p(\mathbf{r})$ and therefore neglects exclusion of polymer from the volume occupied by the colloids. By contrast the geometry-based DFT builds in excluded volume effects. One can understand this by returning to the 0d free energy, equation (27). The final (polymer) contribution is enhanced over the corresponding mean-field expression $\beta\epsilon\eta_p^2/2$ by a factor $(1 - \eta_c)^{-1}$. The perturbative DFT exhibits some severe failings when applied to the calculation of phase behaviour and similar failings are to be expected [20] if the same approach, i.e. simply adding \mathcal{F}_{MF} to \mathcal{F}_{ex}^{AO} , were adopted for other models, e.g. mixtures of hard-core and Gaussian particles. Note that the approach of Warren *et al.* [53] for the bulk free energy can be viewed as a perturbative treatment in which $\phi_{pp}(r)$ is regarded as a perturbation about the AO reference system. Schmidt *et al.* [20] rederive the theory of [53] in a framework that allows them to understand relationships between the various approaches. They argue that the geometry-based DFT provides a more realistic account of the binodal than does the theory of [53].

6. Further developments

During the last two years several applications and extensions of the DFT for the AO model have been reported. We summarize some of them in this section. An overview of geometry-based DFT, which lists a wider range of developments, is given by Schmidt [59].

We mention first two direct applications of the DFT for the AO mixture described in section 2.2. As a planar hard wall prefers the colloid-rich (liquid) phase to the colloid-poor (gas) phase, the hard wall–liquid surface tension is lower than the hard wall–gas tension. General arguments [60] then imply that for the colloid–polymer mixture confined between two, parallel, planar hard walls, capillary condensation of the liquid phase should occur when the reservoir fluid is in the gas phase, i.e. for a given η_p^r the value of μ_c is lower than the bulk

coexistence value. Brader observed this phenomenon in his PhD studies [25] using the DFT. Systematic investigations were carried out recently [61] using both DFT and computer simulation. Lines of capillary condensation were determined for size ratio $q = 1$. These are most easily represented in the (μ_c, η_p^r) plane, where μ_c is the colloid chemical potential. Upon decreasing the (scaled) wall separation distance H/σ_c from ten to two a pronounced shift of the capillary binodal towards smaller values of μ_c occurs. The critical point shifts to larger η_p^r , corresponding to lower temperature in the case of a simple atomic fluid, *and* to larger μ_c upon reducing H . This latter trend seems to be much more pronounced in the simulation results than in those from DFT. Preliminary investigations demonstrated that the shift of the binodal could be described reasonably well using the generalized (to binary mixtures) Kelvin equation for capillary condensation [62]. The practical importance of this investigation lies in possible experimental realizations by strongly confining (between glass substrates) real colloid–polymer mixtures [63]. From a theoretical viewpoint one sees that since all the bare interactions in this system are either hard or ideal, this is an important example of shifting a bulk phase transition, via confinement, by means of purely entropic (depletion) forces.

The second application refers to the AO model colloid–polymer mixture exposed to a standing laser field that is modelled as an external potential acting on the colloids. This has a sinusoidal variation as a function of the space coordinate in the direction of the beam [64]. DFT results indicate that the external potential may stabilize a ‘stacked’ fluid phase which is a periodic succession of liquid and gas slabs. The regions of large laser intensity (where the external potential is small) are filled with colloidal liquid whereas the regions with small laser intensity are gas-like.

Several extensions of the AO model have been made and the bulk phase behaviour compared with the original. In order to take into account the effect of poor solvent quality on colloid–polymer mixtures, the solvent was modelled as a distinct component. Specifically it was taken to be a binary mixture of a primary solvent that is treated (as usual) as a homogeneous, inert background and a secondary cosolvent that is treated as an ideal gas of point particles [65]. These cosolvent particles are assumed to penetrate neither the polymers nor the colloids. In the absence of colloids, the polymer–cosolvent subsystem is the Widom–Rowlinson model [66] of a binary mixture in which particles of like species are non-interacting while unlike species interact with hard cores. Thus the cosolvent induces an effective many-body attraction between the polymers, reminiscent of that caused by poor solvent.

It was found that worsening the solvent quality, by increasing the cosolvent concentration, increases greatly the tendency to demix, i.e. this shifts the corresponding binodal to smaller colloid and polymer packing fractions [65].

The shape and size of real polymers will be affected by confinement effects, generated by the presence of the colloidal particles in a colloid–polymer mixture. In order to model the effect on the polymer size distribution, an AO model with polydisperse polymer spheres was considered [67]. The polymer spheres are mutually non-interacting but are excluded from the colloids; their radii are free to adjust to allow for colloid-induced compression. The size (radius of gyration) probability distribution in the polymer reservoir was taken to be that of ideal chains. It was found that the presence of the colloids reduces considerably the average polymer size. As a consequence, the bulk demixing binodal is shifted towards higher polymer densities, stabilizing the single, mixed phase as compared with the incompressible AO case.

For very large polymer-to-colloid size ratios the assumption that colloids cannot penetrate polymers is no longer valid. A small colloidal sphere may well penetrate the open coil structure of a big polymer. In order to incorporate this effect on the level of an effective sphere model a penetrable AO model was introduced [68]. The colloid–polymer interaction is assumed to be a step-function of *finite* height, in contrast to the hard-core repulsion of the conventional AO case. The range of this interaction is still taken to be $R_c + R_p$, and the strength is taken from the known immersion free energy of a single sphere in a dilute solution of polymer coils or in a theta solvent. The colloid–colloid interaction remains hard-sphere-like and $\phi_{pp} = 0$. For large size ratios, $q \gtrsim 3$, there is a significant increase in the extent of the mixed region in the phase diagram compared to the free-volume result for impenetrable polymer, i.e. for the AO model [68]. These findings are in keeping with results from more microscopic approaches which treat excluded volume at the segment level [14].

A system that is closely related to the AO model is a mixture of spherical hard-sphere colloids and hard, needle-like particles. The latter may represent either stretched polymers or stiff colloidal rods. In the simplest model [69] the thickness of the rods is set to zero such that rod–rod interactions can be ignored but there remains an excluded volume interaction between a rod and a hard sphere. For this model there is no liquid crystalline order, because of the absence of rod–rod interactions. However, simulation studies found isotropic gas and liquid phases as well as a solid phase [69]. The rods act as a depletant, in a similar fashion to the non-interacting polymer spheres in the AO

model, and give rise to an effective attraction between the hard-sphere colloids. Bolhuis and Frenkel [69] also determined the phase behaviour using a free-volume approximation for the free energy, similar to that of Lekkerkerker *et al.* [4] for the AO model, i.e. a first-order perturbation theory that sets the free-volume fraction for the needles equal to its average value in the pure hard-sphere fluid. A DFT was constructed [22] for this model and applied subsequently [23] to the planar (free) interface between demixed fluid phases, one of which, the liquid, is rich in spheres (and poor in needles) and the other, the gas, is dilute in spheres (and rich in needles). Note that in constructing the DFT it was necessary to introduce a weight function $w_2^{\text{SN}}(\mathbf{r}, \mathbf{\Omega})$, where $\mathbf{\Omega}$ refers to the orientation of the needles, which contains information about both species, the spheres and the needles, in order to generate the sphere-needle Mayer bond. The corresponding sphere-needle weighted density, $n_2^{\text{SN}}(\mathbf{r}, \mathbf{\Omega})$, is a convolution of the sphere density $\rho_s(\mathbf{r})$ and $w_2^{\text{SN}}(\mathbf{r}, \mathbf{\Omega})$, whereas all the remaining weighted densities involve only variables of an individual species. For uniform fluids the DFT yields the following expression for the excess free energy density:

$$\beta f_{\text{ex}}(\rho_S, \rho_N) = \beta f_{\text{ex}}^{\text{HS}}(\rho_S) - \rho_N \ln \alpha(\rho_S), \quad (41)$$

where ρ_S and ρ_N refer to the number densities of spheres and needles, respectively. $f_{\text{ex}}^{\text{HS}}$ is, as usual, the excess free energy density of pure hard spheres (36) and $\alpha(\rho_S)$ is the free-volume fraction for a single, test needle of length L in the hard-sphere fluid:

$$\alpha(\rho_S) = (1 - \eta) \exp[-(3/2)(L/\sigma)\eta/(1 - \eta)], \quad (42)$$

with $\eta = \pi\rho_S\sigma^3/6$, the packing fraction of spheres of diameter σ . Equation (41) is identical to the free-volume result [69] and can also be obtained by applying scaled-particle theory for non-spherical bodies [70] to the current model. It has the same form as the excess free energy for the AO model—see equation (15). The fluid–fluid binodal resulting from equation (41) was found to be rather close to that obtained by simulations for the case $L/\sigma = 1$ [69]. Brader *et al.* [23] chose the same size ratio for their DFT studies of the planar fluid–fluid interface. The bulk phase diagram, plotted in the reservoir representation, i.e. $\rho_*^r = \rho_N^r L^2 \sigma$ versus η , has a similar form to figure 2 with $\eta = \eta_c$ and ρ_*^r , the reduced needle density in the reservoir, replacing the polymer reservoir packing fraction η_p^r . The critical point is located at $\eta_{\text{crit}} = 0.158$ and $\rho_{*,\text{crit}}^r = 14.64$ whilst the triple point, estimated from first-order perturbation theory [69], is at $\rho_{*,t}^r = 24$. As in figure 2, there is a Fisher–Widom (FW) line intersecting the liquid branch of the binodal near $\rho_{*,\text{FW}}^r = 17$, see figure 2 of [23]. For coexisting states with higher values of ρ_*^r , on the

oscillatory side of the FW line, Brader *et al.* find sphere density profiles $\rho_S(z)$ that are oscillatory on the sphere-rich (liquid) side of the planar interface. However, the amplitude of the oscillations is considerably smaller than what was described in section 3 for the AO model. As expected, on the needle-rich (gas) side the density profile of the spheres decays monotonically into bulk for all states. The important new feature which arises in this study concerns the nature of the needle density profiles. Within DFT one can determine the one-body density $\rho_N(z, \theta)$, where z is the perpendicular distance from the interface and θ is the angle between the needle orientation and the interface normal, and hence both the orientation averaged needle density profile, $\bar{\rho}_N(z)$, and the orientational order parameter profile $\langle P_2(\cos \theta) \rangle$. For states above the FW line, $\bar{\rho}_N(z)$ displays very weak oscillations on the liquid side of the interface arising from the influence of the packing of the spheres on the distribution of the needles. From the result for $\langle P_2(\cos \theta) \rangle$, Brader *et al.* conclude that needles order parallel to the interface on the needle-rich side. This appears to be similar to the biaxial ordering of needles that occurs at a planar hard wall; in the present case the densely packed hard-sphere fluid acts as a ‘wall’ for the needles. On the sphere-rich side the needles prefer to orient themselves perpendicular to the interface and this is interpreted as the needles protruding through the voids in the first layers of the hard-sphere fluid. These general features of the orientational order are independent of the size ratio L/σ . As an optimal compromise between manageable needle particle numbers and simulation box size, Bolhuis *et al.* [71] chose to perform Monte Carlo simulations with ratio $L/\sigma = 3$. The different preferential alignment of needles on either side of the interface is confirmed by the simulation results. Moreover, there is remarkable quantitative agreement between simulation and DFT results for the density profiles $\rho_S(z)$, $\bar{\rho}_N(z)$ and the orientational order parameter profile [71]. Brader *et al.* [23] also describe results for the liquid–gas surface tension and discuss what might be appropriate scaling factors to bring about data collapse for different size ratios L/σ .

In a related study Roth *et al.* [24] considered the same sphere–needle mixture, with $L/\sigma = 1$, adsorbed at a planar hard wall—the same type of situation as that described in section 4. Density profiles calculated from the DFT for the binary mixture of spheres and needles show that complete wetting of the hard wall–gas interface by the sphere-rich, liquid phase occurs upon approaching the binodal on a path at fixed $\rho_*^r = 16$; the profiles are reminiscent of those in figure 7. There appears to be complete wetting for all the values of ρ_*^r considered. An effective one-component description of the same system was also investigated in [24]. This

follows the approach of section 2.1 in that a sphere–sphere and a wall–sphere depletion potential can be obtained by integrating out the degrees of freedom of the needles (rods) [72]. Since the needles are mutually non-interacting the depletion potentials depend linearly on ρ_N^r . Geometrical arguments, similar to those for the AO model, show that the effective one-component Hamiltonian corresponding to equation (9) should be exact for $L/\sigma < 1 - (2(3^{1/2}) - 3)^{1/2} = 0.31875$, which should be compared with the corresponding size ratio $q = \sigma_p/\sigma_c = 0.1547$ for the AO model. Thus, for the system under consideration, with $L/\sigma = 1$, there are many-body effective interactions which are not included in the analogue of equation (9). Ignoring these, Roth *et al.* [24] employed a one-component DFT, equivalent to that used in [11] for adsorption studies of the AO model with $q = 0.1$; this treats the hard-sphere contribution by the Rosenfeld FMT and the depletion attraction between pairs of spheres by means of a mean-field approximation. The resulting fluid–fluid binodal is in fair agreement with that from the free-volume theory, equivalent to the result of the binary mixture DFT. The effective one-component treatment also predicts complete wetting. However, there is also a partial wetting regime, at high ρ_*^r , followed by a sequence of five layering transitions and then a transition to the completely wet state as ρ_*^r is reduced following the gas branch of the binodal. The pattern of surface phase transitions (see figure 5 of [24]) is very similar to that seen in figures 9 and 12 for the AO model, i.e. the first layering transition is quite extended in ρ_*^r and the layering critical point, near $\rho_*^r = 20$, is well removed from the binodal. Subsequent transition lines are reduced in extent and lie close to the binodal. Thus, it is tempting to argue that this effective one-component treatment of the adsorbed sphere–needle mixture mimics what we found for the AO model. But there we argued that it was the incorporation of effective many-body interactions between the colloids that was responsible for the rich layering behaviour; our effective one-component treatment did not yield layering transitions in the case of the AO model. A full understanding of the results for the sphere–needle model is yet to emerge. The precise location of the triple point is important. Indeed a preliminary simulation study of the bulk system [73], using the same effective sphere–sphere potential as in [24], finds that $\rho_{*,\text{crit}}^r \approx 17.5$ and $\rho_{*,\text{t}}^r \approx 22.7$, i.e. gas–liquid coexistence is stable over a rather narrow region of ρ_*^r . More significantly, the triple point lies below the onset of the first layering transition found in [24], suggesting that the layering could be occurring in a region where the gas–liquid transition is metastable with respect to gas–solid. This is not the case in the AO model where in both the DFT calculations of

section 4.2 and in the simulation studies of section 4.3, the onset of layering occurs well below the triple point.

A further study [74] was devoted to developing a geometry-based DFT for a ternary mixture of hard-sphere colloids, ideal polymer spheres and vanishingly thin hard needles. The model combines those of AO and of Bolhuis–Frenkel. Both the mutually non-interacting polymers and mutually non-interacting needles act as depletion agents so that rich fluid phase separation can arise. As usual, colloid–colloid, colloid–polymer and colloid–needle interactions are hard. Schmidt and Denton [74] consider two cases: (i) the polymer–needle interaction $\phi_{PN}(r)$ vanishes for all distances r and (ii) it is hard, i.e. $\phi_{PN} = \infty$ if polymer and needle overlap, and zero otherwise. Constructing the DFT for the second case requires a generalization to needles of an earlier DFT treatment [75] of the Widom–Rowlinson model [66] since in the absence of colloids the polymer–needle mixture is of the Widom–Rowlinson type: interactions between like species vanish while unlike particles interact via hard-core repulsion. For case (i), two-phase coexistence between colloid-rich and colloid-poor fluid phases is found. For case (ii), there is the possibility of de-mixing between the polymers and the needles. Moreover, there can be a competition between the depleting effects of (interacting) polymers and needles; the two species compete to generate the attraction between the colloid spheres. Striking demixing fluid phase behaviour is found, with various critical points and a three-phase coexistence region [74]. It would be of considerable interest to investigate structural correlations in the various bulk fluid phases and to consider inhomogeneous situations, such as fluid–fluid or wall–fluid interfaces, in this model system.

A very different kind of confinement from that considered so far is present for fluids adsorbed in porous media. Rather than the well-defined geometries which occur at a planar wall or at fluid–fluid interfaces, irregular and random confinement acts on the adsorbed fluid. In order to model porous media one introduces the so-called quenched–annealed fluid, where the quenched components represent the porous medium in terms of immobilized fluid configurations. Since the quenched components act as an external potential on the annealed (equilibrated) components constituting the adsorbate, the one-body density distribution of the latter can be obtained using standard DFT methods. However, such an approach is computationally demanding since the spatial distribution of the adsorbate is extremely complicated. An alternative approach, termed quenched–annealed DFT, was proposed recently. This treats the quenched components on the level of their one-body density distributions [76]. The minimization condition differs from that of equilibrium (fully annealed)

mixtures, as the quenched components are treated as fixed input quantities in the grand potential functional. For the AO model adsorbed in different types of matrices the results of this DFT approach were compared to those from liquid integral equation theory (replica OZ using the optimized random-phase approximation) for the corresponding effective one-component model, where the polymers are integrated out and only the pairwise contributions to the effective Hamiltonian of section 2.1 are taken into account [77]. Thus, the effective interaction between colloids is given by $\phi_{AO}^{\text{eff}}(R)$ while the colloid and matrix particles interact via either a hard-sphere potential or $\phi_{AO}^{\text{eff}}(R)$. Both approaches predict, consistently, capillary condensation or evaporation, depending on the nature of the matrix–polymer interaction. If a matrix particle excludes both colloid and polymer, condensation occurs, whereas if the matrix excludes only colloid (there is vanishing matrix–polymer interaction) capillary evaporation occurs. The latter refers to the situation where phase separation occurs in the fluid adsorbed in the matrix at chemical potentials for which the reservoir would remain in a single, colloid-rich, liquid phase. The bulk pair correlation functions from DFT are in good agreement with computer simulation results [77]. A very recent study is devoted to demixing and the planar fluid–fluid interface of the AO mixture adsorbed in a matrix of homogeneously distributed hard-sphere particles [78]. Two cases are considered: (i) colloid-sized matrix particles at low packing fractions and (ii) large matrix particles at high packing fractions. The two cases exhibit very different behaviour; for details see [78].

7. Discussion

We have outlined two strategies for tackling the statistical mechanics of *inhomogeneous* colloid–polymer mixtures described by the simplest model that captures the effects of depletion attraction, namely the Asakura–Oosawa–Vrij (AO) model. The first of these, based on the well-trodden ‘integrating out’ route of McMillan–Mayer theory, is most useful for highly asymmetric mixtures with small size ratio $q < 0.1547$, where there are no three- or higher-body contributions to the effective one-component Hamiltonian for the colloids. The second employs a geometry-based DFT for the mixture that treats the two species on equal footing. Since there is no explicit integrating out of the polymer degrees of freedom, depletion effects are generated internally by the geometrical structure of the functional. This DFT approach has the advantage that it applies to arbitrary size ratios, including those where many-body contributions are known to be important. The main results of our investigations of interfacial properties are presented in sections 3 and 4 where we describe the

density profiles and surface tensions for the free fluid–fluid interface and the properties of the AO mixture adsorbed at a hard wall calculated using the functional derived in [16, 17]. For the free interface we find oscillatory structure in the density profiles on the colloid-rich (liquid) side of the interface for state points where the coexisting liquid density lies on the oscillatory side of the Fisher–Widom line and surface tensions which are in reasonable agreement with experiment. We find that for a highly asymmetric mixture, $q = 0.1$, at state points away from any phase boundary, the AO functional gives a good account of the simulation data for density profiles at a hard wall. For larger size ratios, where fluid–fluid coexistence occurs, the DFT predicts very rich interfacial phase diagrams which display both a wetting transition and several novel layering transitions. The interfacial phase diagram was determined for size ratios $q = 0.6, 0.7$ and 1.0 and we find the topology changes significantly with q . We make a comparison with recent Monte Carlo simulation results for the interfacial phase diagram for size ratio $q = 1$.

Here we discuss further some features of our results. The oscillations we observe in the free interface colloid density profiles are dramatic. They appear to have an amplitude larger than oscillations which have been calculated for simple liquids at state points near the triple point. We argue in section 3 that despite the very low interfacial tension of the colloid–polymer system, the capillary wave fluctuation erosion of the oscillations should not be greater than for a simple liquid. This suggests that colloid–polymer mixtures might provide an excellent opportunity to investigate oscillatory structure at fluid–fluid interfaces, as the large size of colloidal particles makes them well suited to ellipsometric measurements [39, 79]. Oscillations at a free fluid–fluid interface arise when that interface is ‘stiff’, i.e. for high values of the appropriate reduced surface tension γ^* , and when the density difference between the two coexisting bulk phases is large. Under these conditions the free interface (treated at mean-field level) behaves as a ‘wall’ and layered structure can develop due to packing effects. These effects are most pronounced near the triple point where both the reduced surface tension and the density difference are largest. Considering the phase diagram for $q = 0.6$, shown in figure 2, and identifying η_p^r with T^{-1} , it is clear that the separation between the critical and triple points is much larger in the present case than for a simple fluid such as argon. It is primarily for this reason that we can obtain such pronounced oscillations in the colloidal density profiles for states near the triple point. By contrast, as the temperature is reduced in simple liquids the oscillations can only grow slightly before the liquid–vapour coexistence region runs out and the triple point,

i.e. the crystalline phase, intervenes. One could argue that oscillatory liquid–gas interfaces would be a common feature in simple fluids at sufficiently low temperatures were it not for the onset of crystallization. The AO model can generate oscillations of even larger amplitude than those shown in figure 3. As the size ratio is increased the separation in η_p^r between the critical and triple points grows, e.g. for $q = 1$, $\eta_{p,t}^r/\eta_{p,crit}^r \sim 8$, see figure 18, and γ^* can become rather large—see figure 3. A similar scenario arises for binary mixtures of repulsive Gaussian core particles. There liquid–liquid coexistence can occur over a very large range of total density, since there is no crystalline phase present, and the resulting interfaces can be very ‘stiff’ leading to predictions of very weak erosion of the oscillations: the exponent in equation (20) is calculated to be about -0.1 [41]. Pronounced oscillatory structure is also well known in the study of liquid metals where there is a large separation between the triple and critical points and the reduced liquid–gas surface tensions are very large. Simulations of the liquid–gas interface of alkali metals [80] and of Ga [81] and X-ray reflectivity experiments on both Ga [82] and Hg [83, 84] all indicate stratification of the ion-density profile, with a spacing of about one atomic diameter, on the liquid side of the interface.

The recent Monte Carlo studies of Chacón and co-workers [43, 44] are significant in this context. These authors constructed classical pair potential (no explicit treatment of the electrons) models of a metal so that the melting temperature T_m was deliberately suppressed relative to the critical temperature T_c , typically $T_m/T_c \lesssim 0.2$. At low temperatures they find high surface tensions and thus a ‘stiff’ interface which seems to be the origin of the strongly stratified density profiles which they observe. Chacón and co-workers [44] also make the important point that for models of the type they consider, strong stratification can occur over a few atomic layers in the interface even when the bulk liquid is on the monotonic side of the FW line. However, we know the ultimate asymptotic decay into bulk of the density profile must be governed by the behaviour of the bulk pair correlation functions. At very low temperatures $T \sim T_m$, they estimate the erosion of the oscillations to be weak, with the exponent in equation (20) about -0.4 . The calculated exponent increases with T to a value of about -1 , near the FW line. Monte Carlo results for the density profiles calculated for increasing interfacial area are consistent with the power-law prediction of equation (20) [44]. There are, of course, important differences between the liquid metal models, where the large ratio T_c/T_m arises from the inclusion, albeit empirically, of electronic effects into the pair potential, and the AO model, where the large value of $\eta_{p,t}^r/\eta_{p,crit}^r$ arises from the presence of effective many-

body interactions between the colloids—recall that the latter are responsible for separating the triple and critical points at large size ratios—see the discussion of figure 18.

We turn now to the layering transitions we find in section 4.2. These are a very specific prediction of the AO functional and since they are found in simulation, appear to be a genuine feature of the AO model, rather than an artefact of the DFT.

Although the pattern of the layering transitions observed for $q = 1$ in the simulations of [19] is not identical to that from DFT, the shapes of the density profiles near the transitions are very close to those found in the theory so the layering *phenomena* are certainly the same. We argued in section 4.3 that the occurrence of such transitions, far from $\eta_{p,t}^r$, requires the effective many-body interactions that are incorporated into the DFT and into the simulations. Without these contributions the triple and critical points lie much closer together and there is less scope for the layering (and wetting) transitions to manifest themselves at the (stable) gas–hard wall interface. We emphasize, once again, that simulations employing only the effective pair potential $\phi^{\text{eff}}(R; z_p)$ yield a very narrow range, in η_p^r , of stable liquid–gas coexistence. The form of the wall-induced effective interactions must also be important for the occurrence of layering transitions. The effective pair interaction between colloids $\phi^{\text{eff}}(\mathbf{R}_i; \mathbf{R}_j; z_p)$ is a complicated function of the coordinates \mathbf{R}_i and \mathbf{R}_j when the colloids are close to the wall [11]; the strength of the attraction is lowered compared with that of $\phi_{AO}^{\text{eff}}(R_{ij}; z_p)$, which pertains to the homogeneous fluid. It is possible that this reduction in pairwise attraction, caused by the wall reducing the overlap volume of the depletion zones around each colloid, competes with the attractive one-body potential $\phi_{AO}^{\text{wall}}(z; z_p)$ and that this situation favours layering [19, 25]. However, it is fair to say that we do not, as yet, have a full understanding of what gives rise to these curious transitions[†]. The issues are compounded by the fact that layering transitions were found in an effective one-component DFT calculation for the analogous case of the sphere–needle mixture [24]. Although in this case, see section 6, there remain

questions as to how well the one-component theory accounts for the extent of stable liquid–gas coexistence.

Whether the layering transitions remain in models which treat the wall and/or the polymer more realistically remains to be seen. It would be of considerable interest to investigate adsorption at a hard wall for the simple model described in section 5. Incorporating polymer–polymer interactions is expected to reduce substantially the separation between $\eta_{p,t}^r$ and $\eta_{p,\text{crit}}^r$ (this is also what is found in the simulation studies for SAW models of the polymer [15]) which might make it difficult to observe any layering transitions and indeed the pronounced oscillations found in the colloid density profiles at the free interface for the AO model. Direct simulation studies for colloids and interacting polymers near a wall would be valuable, but extremely demanding! It seems unlikely that such layering transitions could be observed in adsorption experiments as the transition lines lie so close to the bulk coexistence curve that remarkable experimental accuracy would be required to resolve these. Moreover, polydispersity in both colloid and polymer sizes, roughness of the substrate etc. would tend to eliminate what are probably rather subtle and specific features of the AO mixture adsorbed at a hard wall.

We conclude this discussion of layering transitions by returning to the difference between the type of transitions found in the AO model and those found in DFT [51] and in simulation [87] studies of the adsorption of simple gases at strongly attractive substrates. In the latter case the transitions always occur close to the triple point where the density profiles are more highly structured than those shown in section 4.2, i.e. the individual layers are much sharper. When a transition occurs (at fixed T , increasing μ) the jump in the Gibbs adsorption corresponds to the addition of (roughly) one dense ‘liquid’ layer. As the sequence of transitions progresses the magnitude of the jump in adsorption increases, reflecting the broadening of the outer peaks in the profile and the fact that the local density in one or two of the previous layers also increases at the transition. There can be a very large number of transitions—nine or ten could be discerned in DFT calculations [51]—but their critical points all lie quite close to the triple point T_t . Indeed, within a mean-field treatment the number of transitions can be infinite, i.e. complete wetting of the gas–substrate interface by liquid, which is expected to occur for all $T > T_t$ for strongly attractive substrates, can occur by an infinite sequence of layering transitions out of coexistence. When capillary wave fluctuations in the wetting film are included the number of transitions must be finite, since the liquid–gas interface is always rough (in the statistical mechanics sense). By contrast, for the AO mixture

[†]It is well known that wetting transitions can depend sensitively on the details of the wall–fluid interactions. For example, in a Landau treatment which includes a surface term of third order in the surface magnetization m_1 , which is of opposite sign to the usual linear $-h_1 m_1$ term, Indekeu [85] found a *single* thin–thick transition, followed by a continuous wetting transition on increasing T along the bulk coexistence curve. An equivalent scenario was found by Piasecki and Hauge [86] in a simple DFT treatment of a Yukawa fluid adsorbed at a wall exerting both an attractive exponential and a square-well wall–fluid potential.

adsorbed at a hard wall the onset of layering transitions occurs far below $\eta_{p,t}^r$, where the density profiles of the colloid are not as highly structured (see figure 8) and the jump in the adsorption, Γ_c , does not necessarily increase as the sequence increases (but note that the results in section 4.2 refer to a path following the bulk coexistence curve rather than following paths at fixed η_p^r , equivalent to fixed T .) It is feasible, nevertheless, that within our DFT treatment of the AO mixture there could be an infinite sequence of layering transitions leading to complete wetting of the ‘gas’–hard wall interface. Our numerical results do not rule out this scenario. Given that the layering transition lines get shorter and shorter as this sequence progresses it is difficult to ascertain the precise sequence. If this is the correct interpretation, then, as observed, we would not expect to find a substantial pre-wetting line emerging from the wetting point. The simulation results [19] cannot shed much light on this issue; there one expects a finite but large number of transitions before the onset of complete wetting if the attractive one-body wall–fluid potential $\phi_{AO}^{wall}(z; z_p)$ is driving the wetting transition. Note that layering transitions at temperatures above the bulk triple point have been found recently in Gibbs ensemble Monte Carlo simulations of TIP4P water in cylindrical pores [88].

We complete this discussion of layering transitions between distinct adsorbed fluid phases by pointing out that there is much experimental evidence for such interfacial behaviour in *molecular* fluids adsorbed on a graphite substrate under near triple point conditions—see references in [51]. Ellipsometric studies of various liquids adsorbed on Pyrex glass [89] and on mica [90] at low temperatures also provide evidence for layering, i.e. steps in the adsorption isotherms. Steps in the relative adsorption of 2,5-dimethylpyridine in the liquid mixture with water, in contact with solid silica have also been identified as layering transitions [91]. Bonn *et al.* [92, 93] have argued on the basis of ellipsometric measurements, that a series of first-order layering transitions occurs at a *fluid* substrate, i.e. at the liquid–gas interface in a binary methanol–cyclohexane mixture at high temperatures.

The wetting transition in colloid–polymer mixtures is a much more promising candidate for experimental investigation and the basic phenomenon of wetting of a ‘hard’ substrate by the colloid-rich phase should, in principle, be experimentally observable. Although experiments with colloidal particles have an advantage over those using rare gases or fluids composed of small molecules in that they can be performed at room temperature, issues such as polydispersity obviously complicate matters. Nevertheless, systematic measurements of the contact angle for the liquid–gas meniscus of phase-separated colloid–polymer mixtures, at various

compositions and size ratios, in contact with glass walls would be most interesting. Indeed, there are already indications, from contact angle measurements [94, 95], of a transition from partial to complete wetting for a mixture of silica particles and PDMS, with size ratio ~ 0.93 , in a solvent of cyclohexane at a glass substrate coated with the same organophilic material as the silica particles (on which PDMS does not adsorb). The transition appears to take place further from the critical point, measured in terms of $\eta_c^l - \eta_c^g$, the difference in colloid packing fractions of the liquid and gas, than is found in simulations or in DFT for the AO model—see section 4. Measuring the contact angle for these systems is *not* straightforward, however. Although the static interfacial profile (shape of the meniscus) can be measured using an optical microscope and the capillary length extracted, thereby yielding the liquid–gas surface tension γ , the contact angle depends very sensitively on the precise location of the wall and studies by the Utrecht group [96] were unable to ascertain whether or not a wetting transition occurred for a silica–PDMS mixture. The values of γ which they obtained were close to those measured by the independent spinning drop technique [36, 79], given in figure 3. More recent results from confocal scanning laser microscopy demonstrate the presence of a thick colloidal liquid layer at the glass wall, consistent with complete wetting [63].

As mentioned in section 6, it should also be possible to design experiments which investigate, quantitatively, capillary condensation in simple confining geometries. Such experiments are difficult to perform for atomic fluids but for colloidal systems, where the particle sizes, and hence the confining length scales, are much larger, this is feasible and there are already some observations of the phenomenon in a colloid–polymer mixture [63]. One might also envisage studying some of the more subtle capillary phenomena, such as those associated with interfacial transitions in wedge geometry [97, 98].

Turning now to small size ratios, where the only equilibrium phase transition is the fluid–solid transition, we would encourage further theoretical and simulation studies of adsorption at a hard wall. As mentioned in section 4.1, we did not [11] make any effort to approach closely the fluid–solid phase boundary so we could not address the important issue of how crystalline layers develop prior to bulk crystallization. Various scenarios are possible [11], but given that the wall–colloid depletion potential $\phi_{AO}^{wall}(z; z_p)$ is strongly attractive, for say $q = 0.1$, this might favour an infinite sequence of (crystalline) layering transitions, culminating in complete wetting of the hard wall–fluid interface by a nearly close-packed crystal. However, it is not known how close to the phase boundary the bulk (reservoir) fluid must be before the first adsorbed layer becomes

crystalline. Of course, understanding wall-induced crystallization is not an easy problem. For pure hard spheres at a planar hard wall it is not fully established whether or not there is complete wetting by hard-sphere crystal—although recent simulation studies [73, 99] suggest that this is the case. The nature of the wetting behaviour has important repercussions for heterogeneous nucleation of the crystal [99].

In sections 5 and 6 we considered several extensions of the basic AO model that were designed to incorporate additional physical features pertaining to a real colloid–polymer mixture or to introduce entirely new ingredients, such as orientational degrees of freedom in the case of the sphere–needle mixture. All of these extensions make use of geometry-based DFT; indeed they were constructed with this purpose. Just how accurate the DFT proves to be for the various models remains to be seen for the most part. Where the DFT has been tested in detail for an inhomogeneous situation, it performs very well [71]. We envisage many applications of these extensions to various types of inhomogeneity.

We began this article by praising the virtues of simple models so it is appropriate to ask what other physical problems might be tackled within the context of the basic AO model. In particular, are there situations where depletion attraction is expected to play an important role and where our DFT might prove effective? Recall once more that entropic depletion effects are generated internally—unlike the case of DFT for simple fluids where van der Waals attraction is treated explicitly, usually in a perturbative or mean-field fashion [31]—in our geometry-based approach the attraction between colloids, or between a colloid and a hard wall, arises solely from the geometrical structure of the functional. The solvation of a single (big) hard sphere in a binary AO mixture is of particular interest. Since the planar hard wall can be wet completely by the colloid-rich liquid phase it follows that a liquid film will develop around a big hard sphere immersed in a colloid-poor gas that is very close to bulk coexistence. This circumstance leads to pronounced effects in the solvation free energy or excess chemical potential, measured as a function of the radius of the big sphere, R_b , and of the packing fraction of colloid, say. Indeed the situation mimics that of a simple *liquid* (solvent) adsorbed at a big solvophobic particle (hard sphere), except there drying always occurs, so that a film of gas develops on the sphere when the solvent is close to coexistence [100]. A new feature arising in the AO case is the presence of the layering and the wetting transitions. For sufficiently large R_b , these transitions are still present at the sphere, albeit rounded by finite-size effects, and lead to very striking features in the adsorption, density profiles at

contact with the sphere and in the solvation free energy of the sphere [101]. A single hard sphere in the AO mixture serves as an excellent model for investigating subtle effects of curvature on interfacial properties, especially when complete wetting occurs.

One can easily construct the DFT for a ternary mixture consisting of (big) hard spheres, colloidal hard spheres plus mutually non-interacting polymer spheres, i.e. a solution of big hard spheres in the AO solvent. For such a mixture one can determine the solvent-mediated potential between two big spheres or between a big sphere and a wall using a general DFT particle insertion approach [102]. Since the solvent exhibits fluid–fluid phase separation one can investigate the effects of layering, wetting and solvent criticality on the solvent-mediated potentials [101]. In order to implement the DFT particle insertion procedure one requires a density functional that can describe reliably a mixture of the solvent and the big particles in the limit of vanishing density of the big particles [102]. Such functionals are hard to come by (perturbative approaches are generally not appropriate) but the geometry-based DFT for this particular ternary mixture fits the bill†.

Finally we should mention briefly some of the topics that we have *not* covered in this article. There is a rapidly expanding body of work on glass transitions in colloid–polymer mixtures. Strong evidence is emerging for two types of glass; one is repulsion dominated (as in pure hard spheres) and the other is attraction dominated (as occurs when the addition of polymers gives rise to very deep depletion potentials). For an ‘Edinburgh model mixture’, i.e. PMMA and PS with $q = 0.08$, adding a little polymer (PS) to the hard-sphere colloidal glass, at fixed $\eta_c \sim 0.6$, disrupts the caging structure and brings about crystallization. Adding more polymer results in non-crystallization, there appears to be a re-entrant glass transition [13]. Simulations and mode coupling theory, based on an effective one-component depletion potential, have been used to investigate this behaviour [104, 105]. We have not considered in any detail the situation where $q \gg 1$, i.e. the so-called ‘protein limit’, where small particles such as proteins or micelles replace the colloids. There is much interesting physics in this limit but it is quite different from the depletion-driven phenomena we have described in this article. Interested readers should consult the recent articles [14, 106, 107] to obtain some overview of this regime. During the course of completing our paper

†Solvent-mediated potentials in the presence of wetting have also been investigated for big Gaussian core particles immersed in a binary mixture of smaller Gaussian particles using the mixture generalization of the mean-field functional (40). See [103].

we were alerted to the work of Forsman *et al.* [108] who extended a DFT developed for polymer solutions to the situation where solvent and monomer particles have different diameters. These authors consider capillary-induced phase transitions when the confining planar surfaces are hard.

The Urbana group [109] have investigated phase diagrams and osmotic compressibilities for silica particles and polystyrene in decalin comparing their results with the PRISM integral equation theory developed by Fuchs and Schweizer [14] and with the free-volume theory of [4]. These authors argue that PRISM accounts for all experimental trends whereas the free-volume approach appears to miss certain aspects of the experimental behaviour, even for theta solvent conditions. Chen *et al.* [110] also present a critique of the AO model for treating real colloid-polymer mixtures. We were also made aware of the work of Paricaud *et al.* [111] who consider bulk fluid-fluid phase separation in a model in which the polymer-polymer and polymer-colloid excluded volume interactions are treated at the same level of the monomeric segments making up the polymer chain, using the Wertheim thermodynamic perturbation theory. Once again we direct interested readers to these papers.

Much of the work described in this article would not have come to fruition without the substantial input of our co-workers, A. R. Denton, A. Esztermann, A. Fortini, M. Fuchs, I. O. Götze, G. Kahl, J. Köfinger, R. Roth, E. Schöll-Paschinger and P. P. F. Wessels. H. Löwen was instrumental in bringing the Bristol and Düsseldorf groups together and provided much stimulus for the research. We are grateful to our experimental colleagues in Utrecht, D. G. A. L. Aarts, E. H. A. de Hoog and, especially, H. N. W. Lekkerkerker, who shared with us their love and knowledge of real colloid-polymer mixtures (and free-volume theory!†). We thank R. Roth for many inspiring discussions about depletion forces, barmaids and nurses and for valuable comments on the manuscript. P. G. Bolhuis, J.-P. Hansen and A. A. Louis kept us busy with a steady supply of pre-prints; we admire their industry and regret that we cannot do more justice to their work in the present article. R. van Roij provided much illuminating insight into matters of integrating out and constructing effective Hamiltonians. We would not have embarked upon the research described here were it not for Marjolein Dijkstra. She introduced us to the subject, explained why it was interesting, carried out the key simulation studies and motivated many of the DFT studies. Marjolein

also provided healthy criticism of most of the results. She must share some of the responsibility for the length of this article! The early stages of this research were supported by the British-German ARC Programme (Project 104b) and by EPSRC. RE is grateful to S. Dietrich and his colleagues for their kind hospitality and to the Alexander von Humboldt Foundation for their support under GRO/1072637 during his stay at the MPI in Stuttgart. He also wishes to thank the editors of *Molecular Physics* for their patience in waiting for the article to be delivered.

References

- [1] PUSEY, P. N., 1991, *Liquids, Freezing and Glass Transition*, edited by J. P. Hansen, D. Levesque and J. Zinn-Justin (Amsterdam: Elsevier Science), Chap. 10.
- [2] RUTGERS, M. A., DUNSMUIR, J. H., XUE, J. H., RUSSEL, W. B., and CHAIKIN, P. M., 1996, *Phys. Rev. B*, **53**, 5043.
- [3] MEIJER, E. J., and FRENKEL, D., 1994, *J. chem. Phys.*, **100**, 6873.
- [4] LEKKERKERKER, H. N. W., POON, W. C. K., PUSEY, P. N., STROOBANTS, A., and WARREN, P. B., 1992, *Europhys. Lett.*, **20**, 559.
- [5] ILETT, S. M., ORROCK, A., POON, W. C. K., and PUSEY, P. N., 1995, *Phys. Rev. E*, **51**, 1344.
- [6] ASAKURA, S., and OOSAWA, F., 1954, *J. chem. Phys.*, **22**, 1255.
- [7] ASAKURA, S., and OOSAWA, F., 1958, *J. Polym. Sci.*, **33**, 183.
- [8] VRIJ, A., 1976, *Pure appl. Chem.*, **48**, 471.
- [9] GAST, A. P., HALL, C. K., and RUSSELL, W. B., 1983, *J. Coll. Int. Sci.*, **96**, 251.
- [10] DIJKSTRA, M., BRADER, J. M., and EVANS, R., 1999, *J. Phys.: condens. Matter*, **11**, 10079.
- [11] BRADER, J. M., DIJKSTRA, M., and EVANS, R., 2001, *Phys. Rev. E*, **63**, 041405.
- [12] LEAL CALDERON, F., BIBETTE, J., and BIASIS, J., 1993, *Europhys. Lett.*, **23**, 653.
- [13] POON, W. C. K., 2002, *J. Phys.: condens. Matter*, **14**, R859.
- [14] FUCHS, M., and SCHWEIZER, K. S., 2002, *J. Phys.: condens. Matter*, **14**, R239.
- [15] BOLHUIS, P. G., LOUIS, A. A., and HANSEN, J. P., 2002, *Phys. Rev. Lett.*, **89**, 128302.
- [16] SCHMIDT, M., LÖWEN, H., BRADER, J. M., and EVANS, R., 2000, *Phys. Rev. Lett.*, **85**, 1934.
- [17] SCHMIDT, M., LÖWEN, H., BRADER, J. M., and EVANS, R., 2002, *J. Phys.: condens. Matter*, **14**, 9353.
- [18] ROSENFELD, Y., 1989, *Phys. Rev. Lett.*, **63**, 980.
- [19] DIJKSTRA, M., and VAN ROIJ, R., 2002, *Phys. Rev. Lett.*, **89**, 208303.
- [20] SCHMIDT, M., DENTON, A. R., and BRADER, J. M., 2003, *J. chem. Phys.*, **118**, 1541.
- [21] See the review of LIKOS, C. N., 2001, *Phys. Rep.*, **348**, 267.
- [22] SCHMIDT, M., 2001, *Phys. Rev. E*, **63**, 050201(R).
- [23] BRADER, J. M., ESZTERMANN, A., and SCHMIDT, M., 2002, *Phys. Rev. E*, **66**, 031401.
- [24] ROTH, R., BRADER, J. M., and SCHMIDT, M., 2003, *Europhys. Lett.*, **63**, 549.
- [25] BRADER, J. M., 2001, PhD Thesis, University of Bristol, Bristol, UK.

†There is a special t-shirt describing the virtues of this theory available at a small cost from the Van't Hoff laboratory.

- [26] EVANS, R., BRADER, J. M., ROTH, R., DIJKSTRA, M., SCHMIDT, M., and LÖWEN, H., 2001, *Phil. Trans. Roy. Soc. (London) A*, **359**, 961.
- [27] McMILLAN, W. G., and MAYER, J. E., 1945, *J. chem. Phys.*, **13**, 276.
- [28] DIJKSTRA, M., VAN ROIJ, R., and EVANS, R., 1999, *Phys. Rev. E*, **59**, 5744.
- [29] DIJKSTRA, M., VAN ROIJ, R., and EVANS, R., 2000, *J. chem. Phys.*, **113**, 4799.
- [30] BRADER, J. M., and EVANS, R., 2002, *Physica A*, **306**, 287.
- [31] See for example EVANS, R., 1992, *Fundamentals of Inhomogeneous Fluids*, edited by D. Henderson (New York: Dekker), Chap. 3, p. 85.
- [32] FISHER, M. E., and WIDOM, B., 1969, *J. chem. Phys.*, **50**, 3756.
- [33] EVANS, R., HENDERSON, J. R., HOYLE, D. C., PARRY, A. O., and SABEUR, Z. A., 1993, *Molec. Phys.*, **80**, 755.
- [34] EVANS, R., LEOTE DE CARVALHO, R. J. F., HENDERSON, J. R., and HOYLE, D. C., 1994, *J. chem. Phys.*, **100**, 591.
- [35] DIJKSTRA, M., and EVANS, R., 2000, *J. chem. Phys.*, **112**, 1449.
- [36] DE HOOG, E. H. A., and LEKKERKERKER, H. N. W., 1999, *J. phys. Chem. B*, **103**, 5274.
- [37] VliegENTHART, G. A., and LEKKERKERKER, H. N. W., 1997, *Prog. colloid polym. Sci.*, **105**, 27.
- [38] BRADER, J. M., and EVANS, R., 2000, *Europhys. Lett.*, **49**, 678.
- [39] DE HOOG, E. H. A., LEKKERKERKER, H. N. W., SCHULZ, J., and FINDENEGG, G. H., 1999, *J. phys. Chem. B*, **103**, 10657.
- [40] TOXVAERD, S., and STECKI, J., 1995, *J. chem. Phys.*, **102**, 7163.
- [41] ARCHER, A. J., and EVANS, R., 2001, *Phys. Rev. E*, **64**, 041501.
- [42] MIKHEEV, L. V., and CHERNOV, A. A., 1987, *Sov. Phys. JETP*, **65**, 971.
- [43] CHACÓN, E., REINALDO-FALAGÁN, M., VELASCO, E., and TARAZONA, P., 2001, *Phys. Rev. Lett.*, **87**, 166101.
- [44] TARAZONA, P., CHACÓN, E., REINALDO-FALAGÁN, M., and VELASCO, E., 2002, *J. chem. Phys.*, **117**, 3941.
- [45] VRIJ, A., 1997, *Physica A*, **235**, 120.
- [46] BRADER, J. M., EVANS, R., SCHMIDT, M., and LÖWEN, H., 2002, *J. Phys.: condens. Matter*, **14**, L1.
- [47] CHEN, B., PAYANDEH, B., and ROBERT, M., 2000, *Phys. Rev. E*, **62**, 2369.
- [48] ARCHER, A. J., and EVANS, R., 2002, *J. Phys.: condens. Matter*, **14**, 1131.
- [49] See for example SCHICK, M., 1990, *Liquids at Interfaces*, edited by J. Charvolin, J. F. Joanny and J. Zinn-Justin (Amsterdam: North-Holland), chap. 9, p. 415.
- [50] HENDERSON, J. R., 1994, *Phys. Rev. E*, **50**, 4836.
- [51] BALL, P. C., and EVANS, R., 1988, *J. chem. Phys.*, **89**, 4412.
- [52] LOUIS, A. A., BOLHUIS, P. G., HANSEN, J. P., and MEIJER, E. J., 2000, *Phys. Rev. Lett.*, **85**, 2522.
- [53] WARREN, P. B., ILETT, S. M., and POON, W. C. K., 1995, *Phys. Rev. E*, **52**, 5205.
- [54] ROSENFELD, Y., SCHMIDT, M., LÖWEN, H., and TARAZONA, P., 1997, *Phys. Rev. E*, **55**, 4245.
- [55] TARAZONA, P., and ROSENFELD, Y., 1997, *Phys. Rev. E*, **55**, R4873.
- [56] SCHMIDT, M., 1999, *J. Phys.: condens. Matter*, **11**, 10163.
- [57] TARAZONA, P., 2000, *Phys. Rev. Lett.*, **84**, 694.
- [58] LOUIS, A. A., BOLHUIS, P. G., and HANSEN, J. P., 2000, *Phys. Rev. E*, **62**, 7961.
- [59] SCHMIDT, M., 2003, *J. Phys.: condens. Matter*, **15**, S101.
- [60] EVANS, R., 1990, *J. Phys.: condens. Matter*, **2**, 8989.
- [61] SCHMIDT, M., FORTINI, A., and DIJKSTRA, M., 2003, *J. Phys.: condens. Matter*, **15**, S3411.
- [62] EVANS, R., and MARINI BETTOLO MARCONI, U., 1987, *J. chem. Phys.*, **86**, 7138.
- [63] AARTS, D. G. A. L., and LEKKERKERKER, H. N. W., private communication (unpublished), Utrecht University.
- [64] GÖTZE, I. O., BRADER, J. M., SCHMIDT, M., and LÖWEN, H., 2003, *Molec. Phys.*, **101**, 1651.
- [65] SCHMIDT, M., and DENTON, A. R., 2002, *Phys. Rev. E*, **65**, 061410.
- [66] WIDOM, B., and ROWLINSON, J. S., 1970, *J. chem. Phys.*, **52**, 1670.
- [67] DENTON, A. R., and SCHMIDT, M., 2002, *J. Phys.: condens. Matter*, **14**, 12051.
- [68] SCHMIDT, M., and FUCHS, M., 2002, *J. chem. Phys.*, **117**, 6308.
- [69] BOLHUIS, P., and FRENKEL, D., 1994, *J. chem. Phys.*, **101**, 9869.
- [70] BARKER, J. A., and HENDERSON, D., 1976, *Rev. mod. Phys.*, **48**, 587.
- [71] BOLHUIS, P. G., BRADER, J. M., and SCHMIDT, M., 2003, *J. Phys.: condens. Matter*, **15**, S3421.
- [72] ROTH, R., 2003, *J. Phys.: condens. Matter*, **15**, S277.
- [73] DIJKSTRA, M., private communication (unpublished), Utrecht University.
- [74] SCHMIDT, M., and DENTON, A. R., 2002, *Phys. Rev. E*, **65**, 021508.
- [75] SCHMIDT, M., 2001, *Phys. Rev. E*, **63**, 010101(R).
- [76] SCHMIDT, M., 2002, *Phys. Rev. E*, **66**, 041108.
- [77] SCHMIDT, M., SCHÖLL-PASCHINGER, E., KÖFINGER, J., and KAHL, G., 2002, *J. Phys.: condens. Matter*, **14**, 12099.
- [78] WESSELS, P. P. F., SCHMIDT, M., and LÖWEN, H., 2003, *Phys. Rev. E*, **68**, 061404.
- [79] DE HOOG, E. H. A., 2001, Dissertation, Utrecht University, The Netherlands.
- [80] HARRIS, J. G., GRYKO, J., and RICE, S. A., 1987, *J. chem. Phys.*, **87**, 3069.
- [81] ZHAO, M., CHEKMAREV, D. S., CAI, Z. H., and RICE, S. A., 1999, *Phys. Rev. E*, **56**, 7033.
- [82] REGAN, M. J., KAWAMOTO, E. H., LEE, S., PERSHAN, P. S., MASKIL, N., DEUTSCH, M., MAGNUSSEN, O. M., OCKO, B. M., and BERMAN, L. E., 1995, *Phys. Rev. Lett.*, **75**, 2498.
- [83] MAGNUSSEN, O. M., OCKO, B. M., REGAN, M. J., PENANEN, K., PERSHAN, P. S., and DEUTSCH, M., 1995, *Phys. Rev. Lett.*, **74**, 4444.
- [84] DiMASI, E., TOSTMANN, H., OCKO, B. M., PERSHAN, P. S., and DEUTSCH, M., 1998, *Phys. Rev. B*, **58**, R13419.
- [85] INDEKEU, J. O., 1989, *Europhys. Lett.*, **10**, 165.
- [86] PIASECKI, J., and HAUGE, E. H., 1987, *Physica A*, **143**, 87.
- [87] FAN, Y., and MONSON, P. A., 1993, *J. chem. Phys.*, **99**, 6897.
- [88] BROVCHENKO, I., GEIGER, A., and OLENIKOVA, A., 2001, *Phys. Chem. chem. Phys.*, **3**, 1567.
- [89] LAW, B. M., 1990, *J. Colloid Interface Sci.*, **134**, 1.
- [90] BEAGLEHOLE, D., and CHRISTENSON, H. K., 1992, *J. phys. Chem.*, **96**, 3395.
- [91] SELLAMI, H., HAMRAOUI, A., PRIVAT, M., and OLIER, R., 1998, *Langmuir*, **14**, 2402.
- [92] BONN, D., WEGDAM, G. H., KELLAY, H., and NIEUWENHUIZEN, T. M., 1992, *Europhys. Lett.*, **20**, 235.

3384

J. M. Brader *et al.*

- [93] BONN, D., KELLAY, H., and WEGDAM, G. H., 1993, *J. chem. Phys.*, **99**, 7115.
- [94] WIJTING, W. K., BESSELING, N. A. M., and COHEN STUART, M. A., 2003, *Phys. Rev. Lett.*, **90**, 196101.
- [95] WIJTING, W. K., BESSELING, N. A. M., and COHEN STUART, M. A., 2003, *J. phys. Chem. B*, **107**, 10565.
- [96] AARTS, D. G. A. L., VAN DER WIEL, J. H., and LEKKERKERKER, H. N. W., 2003, *J. Phys.: condens. Matter*, **15**, S245.
- [97] RASCÓN, C., and PARRY, A. O., 2000, *Nature (London)*, **407**, 986.
- [98] BRUSCHI, L., CARLIN, A., and MISTURA, G., 2002, *Phys. Rev. Lett.*, **89**, 166101.
- [99] AUER, S., and FRENKEL, D., 2003, *Phys. Rev. Lett.*, **91**, 015703.
- [100] EVANS, R., ROTH, R., and BRYK, P., 2003, *Europhys. Lett.*, **62**, 5360.
- [101] ROTH, R., and EVANS, R., unpublished.
- [102] ROTH, R., EVANS, R., and DIETRICH, S., 2000, *Phys. Rev. E*, **62**, 5360.
- [103] ARCHER, A. J., and EVANS, R., 2003, *J. chem. Phys.*, **118**, 9726.
- [104] PHAM, K. N., PUERTAS, A. M., BERGENHOLTZ, J., EGELHAAF, S. U., MOUSSAID, A., PUSEY, P. N., SCHOFIELD, A. B., CATES, M. E., FUCHS, M., and POON, W. C. K., 2002, *Science*, **296**, 104, and references therein.
- [105] DAWSON, K., FOFFI, G., FUCHS, M., GÖTZE, W., SCIORTINO, F., SPERL, M., TARTAGLIA, P., VOIGTMANN, T., and ZACCARELLI, E., 2001, *Phys. Rev. E*, **63**, 011401.
- [106] SEAR, R., 2001, *Phys. Rev. Lett.*, **86**, 4696.
- [107] BOLHUIS, P. G., MEIJER, E. J., and LOUIS, A. A., 2003, *Phys. Rev. Lett.*, **90**, 068304.
- [108] FORSMAN, J., WOODWARD, C. E., and FREASIER, B. C., 2002, *J. chem. Phys.*, **117**, 1915.
- [109] SHAH, S. A., CHEN, Y. L., SCHWEIZER, K. S., and ZUKOSKI, C. F., 2003, *J. chem. Phys.*, **118**, 3350.
- [110] CHEN, Y. L., SCHWEIZER, K. S., and FUCHS, M., 2003, *J. chem. Phys.*, **118**, 3880.
- [111] PARICAUD, P., VARGA, S., and JACKSON, G., 2003, *J. chem. Phys.*, **118**, 8525.

LETTER TO THE EDITOR

Wall tensions of model colloid–polymer mixtures**Paul P F Wessels¹, Matthias Schmidt^{2,3} and Hartmut Löwen¹**¹ Institut für Theoretische Physik II, Heinrich-Heine-Universität Düsseldorf, Universitätsstraße 1, 40225 Düsseldorf, Germany² Debye Institute, Utrecht University, Princetonplein 5, 3584 CC Utrecht, The Netherlands

Received 5 November 2003

Published 15 December 2003

Online at stacks.iop.org/JPhysCM/16/L1 (DOI: 10.1088/0953-8984/16/1/L01)**Abstract**

Using the Asakura–Oosawa–Vrij model for mixtures of hard sphere colloids and non-adsorbing polymer coils, an analytic formula for the interfacial free energy of the fluid mixture in contact with a hard wall is obtained within a scaled-particle treatment. The results compare well with explicit density functional calculations for the binary mixture. We also give expressions for the wall tension of the mixture when polymers interact via a simple stepfunction pair potential, and for the case of contact with a polymer-coated wall, which we take to be hard for the colloids but penetrable for the polymers. On the gas side of the fluid–fluid demixing binodal we confirm the wetting transition at the hard wall and predict complete drying of the polymer-coated wall on the liquid side of the binodal.

Mixtures of sterically-stabilized colloidal particles and non-adsorbing globular polymers suspended in an organic solvent are valuable soft matter systems to study demixing phase transitions and wetting phenomena at walls; for a recent review see [1]. Controlling the wetting behaviour is mandatory for tailoring wall coatings with intriguing applications like self-cleaning surfaces [2]. Experimental investigations of well-characterized model systems have provided direct insight into the bulk phase diagram [1], the fluid–fluid surface tension (i.e. the interfacial free energy between colloidal liquid and colloidal gas phases) [3–6], and the wetting behaviour of walls [6–9]. In order to capture the key features of the microscopic interactions, the Asakura–Oosawa–Vrij (AO) model [10, 11] of hard sphere colloids and ideal polymer spheres has become a widely-used reference system. Recently, studies based on density functional theory (DFT) [12–16] and computer simulations [17–19] have been performed in order to explore the bulk phase diagram [13, 17, 18] (validating the accuracy of the celebrated free-volume theory [20]), the wetting and layering behaviour at a hard wall [14, 15, 17, 21], the surface tension between colloidal liquid and gas phases [12, 14, 15, 19, 21, 22], and capillary condensation in a slit pore [16]. The basic features are in agreement with experimental results

³ On leave from: Institut für Theoretische Physik II, Heinrich-Heine-Universität Düsseldorf, Universitätsstraße 1, 40225 Düsseldorf, Germany.

and some deviations in the fluid demixing binodal can be improved by approximating realistic polymer–polymer interactions [18] in a simple way [23]. The physical key quantities dictating wetting and drying behaviour at walls, when the bulk is at or near fluid–fluid coexistence, are the interface tensions between wall and liquid, γ_{wl} , and between wall and gas, γ_{wg} , as well as the surface tension of the (free) liquid–gas interface, γ_{lg} . Those enter directly into Young’s equation for the contact angle θ at which the gas–liquid interface hits the wall [24], $\gamma_{lg} \cos \theta = \gamma_{wg} - \gamma_{wl}$. Despite the rapidly growing number of experimental [6–9] and theoretical [14, 15, 17, 21] papers on wetting phenomena of colloid–polymer mixtures, investigations of the tension of polymers at surfaces of colloidal particles [25], and geometrical analysis of depletion near walls [21], neither γ_{wg} and γ_{wl} nor the wall–fluid tension away from coexistence, γ_{wf} , have been addressed directly.

In this letter, we present an analytical expression for γ_{wf} of the AO model at a hard wall using ideas from scaled particle theory (SPT) originally developed in [26–30] and successfully tested [31, 32] for hard sphere mixtures. The key idea is to consider a *ternary* system of colloids, polymers and a dummy component of large size and vanishing concentration that is equivalent to a planar wall. The bulk free energy F of the ternary mixture is required as an input, and a systematic expansion allows us to determine γ_{wf} . Evaluating γ_{wf} at the gas (liquid) branch of the binodal yields an estimate for γ_{wg} (γ_{wl}). We take F from (straightforward generalizations) of free-volume theory [20], and DFT [23], the latter including polymer–polymer interactions in a simple way. We find that polymer non-ideality significantly increases γ_{wf} compared to the case of ideal polymers at the same statepoint. We also consider the effect of polymer chains that are grafted to a substrate [9], and take this composite to exert a hard core repulsion on the colloids, but to be fully penetrable for the polymers. In all cases, analytical expressions for γ_{wf} are presented and found to compare well with the results from explicit DFT calculations for the binary AO model. Comparing $\gamma_{wl} - \gamma_{wg}$ to DFT results for γ_{lg} allows us to confirm the wetting transition at the hard wall on the gas branch [14, 15], and to predict complete drying of the polymer-coated wall everywhere on the liquid branch of the fluid demixing binodal. Our results for γ_{wf} can be tested against those from computer simulations (see, for example, [19] for an investigation of γ_{lg} and comparison to DFT results). The wall tension that we are concerned with is that which solely arises due to the presence of the mesoscopic particles and the suspended polymer chains. In a real mixture, there will also be a strong contribution to the tension due to the molecular solvent; we guess that this makes measuring the osmotic contribution a challenge. To the best of our knowledge interfacial tensions of non-additive mixtures have not been considered before with SPT [33].

The theoretical model [10, 11, 23] consists of hard sphere colloids (species c) and polymer spheres (species p) with diameters σ_c and σ_p and particle numbers N_c and N_p , respectively, within a volume V . The particles interact via pairwise potentials given as a function of the centre–centre distance r as $u_{cc}(r) = \infty$ if $r < \sigma_c$ and zero otherwise, $u_{cp}(r) = \infty$ if $r < (\sigma_c + \sigma_p)/2$ and zero otherwise, $u_{pp}(r) = \epsilon$ if $r < \sigma_p$ and zero otherwise. Control parameters are the size ratio $q = \sigma_p/\sigma_c$, and a scaled energy, $\beta\epsilon$, where $\beta = 1/(k_B T)$, k_B is the Boltzmann constant and T is the temperature. For $\beta\epsilon = 0$ the polymers are ideal and we are dealing with the AO model; for $\beta\epsilon \rightarrow \infty$ the binary hard sphere mixture is recovered. Two different cases for the dummy component (species d) are considered. In the first case of the hard wall, the dummy is similar to a (large) colloid, hence its interaction with species $i = c, p$ is $u_{di} = \infty$ if $r < (\sigma_d + \sigma_i)/2$ and zero otherwise. In the second case of the polymer-coated wall the dummy behaves like a (large) polymer and hence interacts with colloids as $u_{dc}(r) = \infty$ if $r < (\sigma_d + \sigma_c)/2$ and zero otherwise; the interaction with polymers is $u_{dp}(r) = \epsilon$ if $r < (\sigma_d + \sigma_p)/2$ and zero otherwise, and we will restrict ourselves to $\beta\epsilon = 0$ below. Number densities for species $i = c, p, d$ are $\rho_i = N_i/V$; packing fractions are denoted by

$\eta_i = \pi \sigma_i^3 \rho_i / 6$. In general, $s = \sigma_d / \sigma_c$ is a further control parameter for the ternary mixture; for the present purpose we are interested only in $s \rightarrow \infty$, such that we can expand the (Helmholtz) free energy F for the ternary mixture to linear order in the surface of the dummy particles, $\pi \sigma_d^2 \rho_d V$, as

$$F/V = (1 - \eta_d) f(\eta_c, \eta_p, q) + \pi \sigma_d^2 \rho_d \gamma_{\text{wf}}(\eta_c, \eta_p, q), \quad (1)$$

where f is the free energy per volume of the binary colloid–polymer mixture, and the factor $1 - \eta_d$ corrects for the finite volume that the dummies occupy. Once F (and $f = \lim_{\rho_d \rightarrow 0} F/V$) is known, equation (1) provides a means to determine γ_{wf} .⁴

In our first case we use F as obtained from free volume theory [20], where the dummy is a hard sphere, to obtain the hard wall–fluid interface tension of the AO model ($\beta\epsilon = 0$),

$$\beta \gamma_{\text{wf}} = \beta \gamma_{\text{hs}} + \rho_p \frac{\sigma_p}{2} [1 + (1 + 3q + q^2)\tau + (3q + 4q^2)\tau^2 + 3q^2\tau^3], \quad (2)$$

where $\tau = \eta_c / (1 - \eta_c)$ and $\beta \sigma_c^2 \gamma_{\text{hs}} = 3\eta_c(2 + \eta_c) / [2\pi(1 - \eta_c)^2]$ is the interface tension of pure hard spheres and a hard wall according to scaled particle theory [27]. Clearly, our result for the AO model recovers γ_{hs} for $\eta_p = 0$. In the case $\eta_c = 0$, equation (2) yields $\beta \gamma_{\text{wf}} = \sigma_p \rho_p / 2$, which is exact for the ideal gas of polymers at the hard wall. Different conventions for γ_{wf} exist; including the work to displace the particle centres over a distance of one radius (as for example in [27]) yields the tension $\gamma_{\text{wf}} - \sum_{i=c,p} P \sigma_i / 2$, where the bulk pressure is $\beta P = \beta P_{\text{hs}} + \rho_p(1 - \rho_c \alpha' / \alpha)$, with the hard sphere contribution $\beta P_{\text{hs}} = 6\eta_c(1 + \eta_c + \eta_c^2) / [\pi \sigma_c^3(1 - \eta_c)^3]$, and the term involving the free volume fraction α [20] and $\alpha' = \partial \alpha / \partial \rho_c$ is $-\rho_c \alpha' / \alpha = (1 + 3q + 3q^2 + q^3)\tau + (3q + 12q^2 + 7q^3)\tau^2 + (9q^2 + 15q^3)\tau^3 + 9q^3\tau^4$. It is interesting to note that γ_{wf} given through (2) shares linearity in ρ_p with the bulk excess (over ideal) free energy, F_{exc} , for the AO model from free-volume theory [20]. Recall that F_{exc} is related to the SPT result for the excess free energy of binary hard spheres through linearization of the latter with respect to the density of one of the components (becoming the polymer); see [13] for further discussion and the relation to DFT. Remarkably, the same property holds for the tension. Linearizing the result of γ_{wf} for binary hard sphere mixtures (given in equation (3.9) of [29] and reformulated in Rosenfeld form in equation (26) of [32]) in one of the packing fractions yields equation (2). For the step-function interaction between polymers, a free energy for the ternary mixture (where the dummies act like colloids) is given using the framework of [23]. We obtain for the hard wall-tension $\gamma_{\text{wf}} + \Delta \gamma_{\text{wf}}$, where γ_{wf} is given in (2) and up to cubic order⁵ in $\beta\epsilon$:

$$\begin{aligned} \Delta \gamma_{\text{wf}} \sigma_c^2 = & \frac{3\eta_p^2}{2\pi q^2} \left[\beta\epsilon - \frac{(\beta\epsilon)^2}{2} \right] (1 + \tau)^2 (5 + 12q\tau + 2q^2\tau + 9q^2\tau^2) + \frac{\eta_p^2 (\beta\epsilon)^3}{4\pi q^2} (1 + \tau)^2 \\ & \times [5 + 12q\tau + 2q^2\tau + 9q^2\tau^2 + 12\eta_p(1 + \tau)(4 + 9q\tau + q^2\tau + 6q^2\tau^2)]. \end{aligned} \quad (3)$$

In the second case, we apply the same procedure as above to a ternary AO model with a dummy *polymer* species (with $\beta\epsilon = 0$), in order to obtain γ_{wf} of a wall that acts as a big polymer, i.e. it is penetrable to the polymers but impenetrable to the colloids. Carrying out the analysis reveals that in this case simply $\gamma_{\text{wf}} = \gamma_{\text{hs}}$, being *independent* of the polymer density.

As benchmarks we have carried out numerical DFT calculations using the theory of [13], which is specifically tailored for the AO model. The planar walls are described by external

⁴ Note that similar to the hard sphere case [32], the geometrical DFT for the binary colloid–polymer mixture [13, 23] yields $\gamma_{\text{wf}} = \partial \Phi / \partial n_2^{(i)}$ as the tension of a planar wall that behaves like species i , where Φ is the free energy density and $n_2^{(i)}$ is the surface weighted density of species i .

⁵ Nonperturbative results can be obtained numerically from constructing the bulk free energy from numerical solution of the Od problem; see [23].

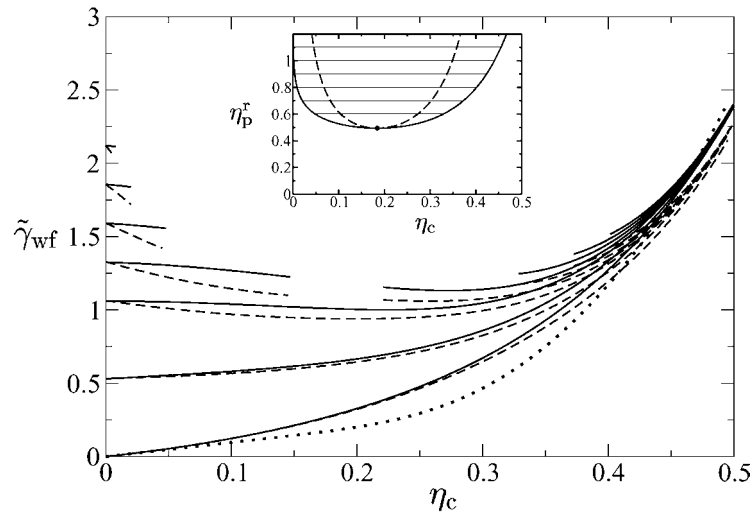


Figure 1. The hard wall–fluid interface tension $\tilde{\gamma}_{wf} = \beta\sigma_c^2\gamma_{wf}$ of the AO model for size ratio $q = \sigma_p/\sigma_c = 0.6$ as a function of the colloid packing fraction η_c and for increasing polymer reservoir packing fractions $\eta_p^r = 0, 0.2, 0.4, 0.5, 0.6, 0.7, 0.8$ (from bottom to top). The results from SPT (full curves) are compared to those of numerical DFT calculations (dashed curves). The gap in the top four curves corresponds to fluid phase coexistence. Also shown is the DFT result for the polymer-coated wall for $\eta_p^r = 0.4$ (dotted curve); the corresponding SPT result is equal to γ_{hs} (lowest full curve). The inset shows the fluid part of the phase diagram for $q = 0.6$ as a function of η_c and η_p^r ; indicated are the binodal (thick curve), spinodal (dotted curve), critical point and (horizontal) tielines connecting coexisting states.

potentials $u_i(z)$ acting on species $i = c, p$, where z is the distance from the wall, and $u_i(z) = \lim_{\sigma_d \rightarrow \infty} u_{di}(z - \sigma_d)$. Inhomogeneous colloid and polymer density profiles as a function of z are obtained through iteration. The wall tension γ_{wf} is calculated via evaluating the grand potential functional for these solutions and subtracting the bulk contribution $-PV$ where V is the volume with $z > 0$ and also subtracting $-\beta\rho_p V_-$ in the case of the polymer-coated wall, where V_- is the volume with $z < 0$; see for example [15] for more details.

We first consider the case of the hard wall; see figure 1 for γ_{wf} as a function of η_c for different values of η_p^r , being the packing fraction of polymers in a reservoir of pure polymer that is in chemical equilibrium with the system. In the pure hard sphere case, $\eta_p^r = 0$, the SPT result, (2), is equal to the accurate hard sphere result [27], whereas the DFT reduces to the also accurate Rosenfeld hard sphere functional. Both agree well [32], the DFT giving slightly smaller values for γ_{wf} for high η_c . Increasing η_p^r at constant η_c significantly increases γ_{wf} . Recall that for $\eta_c = 0$ equation (2) becomes exact, and indeed both approaches give this limiting value. The behaviour for small $\eta_c > 0$ is qualitatively correct in the SPT treatment, but quantitatively significantly stronger in DFT. The latter takes the depletion attraction between wall and colloid mediated by the polymer [34] correctly into account, which we expect not to be the case in the SPT. Increasing η_c at constant η_p^r reduces η_p in the system, and the hard sphere result is approached smoothly. γ_{wf} is non-monotonic and goes through a minimum located at an intermediate value of η_c , provided η_p^r is large enough, in the SPT $\eta_p^r > 1/(2+q)$ ($=0.384$ for $q = 0.6$). The gap for results above the critical point, $\eta_p^r > \eta_p^{r,crit} \approx 0.494$, indicates fluid–fluid phase coexistence. No apparent anomaly occurs in the analytic result either at the binodal or at the spinodal. Generally the agreement between results from SPT and DFT is good. In the case of the polymer-coated wall the SPT result for γ_{wf} is for all η_p^r identical to γ_{hs} , hence the polymers are predicted to have *no* effect on the interface tension. To test this

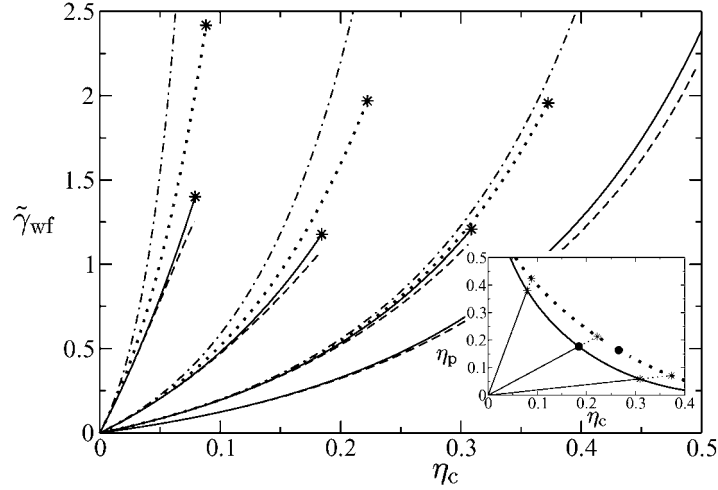


Figure 2. The hard wall–fluid interface tension $\tilde{\gamma}_{wf} = \beta\sigma_c^2\gamma_{wf}$ of the AO model for size ratio $q = 0.6$ as a function of η_c along dilution lines, $\eta_p = \kappa\eta_c$, for $\kappa/\kappa_{crit} = 0, 0.2, 1, 5$ (right to left), where $\kappa_{crit} = \eta_p^{crit}/\eta_c^{crit} = 0.9599$ is the slope of the dilution line through the critical point. Compared are results from SPT (full curves) and DFT calculations (dashed curves) for statepoints in the single-phase region and ending at the binodal (indicated by stars). Also shown are results from SPT for the case of interacting polymers for $\beta\epsilon = 0.5$ (dotted curves) and for binary hard spheres (chain curves) for the same densities and size ratio. The inset shows the phase diagram as a function of η_c and η_p with the binodals for the AO model (thick full curve) and for the interacting-polymer case ($q = 0.6; \beta\epsilon = 0.5$) (dotted curves), as well as the corresponding critical points (filled dots) and dilution lines (straight lines).

we compare for one fugacity, $\eta_p^f = 0.4$, with the DFT result for γ_{wf} , which takes the polymers explicitly into account. Indeed, it deviates little from the hard-sphere DFT result, mainly for intermediate values of η_c .

We next follow dilution lines, which are experimentally convenient paths in the phase diagram obtained by keeping the total colloid and polymer mass (inside a cuvette) constant; adding solvent then decreases both η_c and η_p while keeping the ratio $\kappa = \eta_p/\eta_c = \text{constant}$. In figure 2 γ_{wf} is plotted for different values of κ as a function of η_c in the one-phase region. The hard sphere result for $\kappa = 0$ serves as a reference. Following dilution lines at $\kappa > 0$ leads to a much stronger increase of γ_{wf} with η_c , clearly an effect of the added polymer. The increase becomes stronger for steeper dilution lines, i.e. upon increasing κ . The comparison between SPT and DFT results is somewhat better than in figure 1 (where more extreme statepoints were considered). It is interesting to compare these results with those for two other models. The first is the binary hard sphere mixture (obtained by replacing the polymers with hard spheres) of size ratio $q = 0.6$ and the same packing fractions; see figure 2 for the results. The SPT result for the binary hard sphere mixture [29], known to deviate only little from explicit DFT calculations [32], indicates significantly larger tension than the AO model at the same statepoint, clearly due to stronger packing effects. Secondly, we plot the result for polymers interacting with a stepfunction pair potential, equations (2) and (3). This model possesses an additional energy scale that governs the strength of the polymer–polymer interaction. Already for the very moderate value of $\beta\epsilon = 0.5$ (where we expect the cubic order expression given in (3) to be accurate) we find a significant increase of γ_{wf} over the ideal (AO) case. Moreover, along each dilution line larger values of η_c can be reached inside the one-phase region, as the binodal for the case of non-ideal polymers is shifted towards higher η_c and η_p , hence demixing is suppressed (see the inset in figure 2 and [23] for further background).

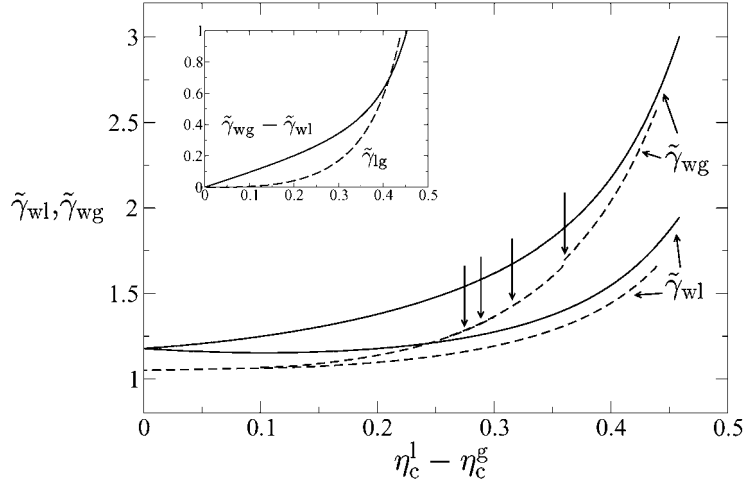


Figure 3. Hard wall–fluid interface tensions of the AO model for size ratio $q = 0.6$ at fluid–fluid coexistence as a function of the difference in coexisting colloid packing fractions, $\eta_c^l - \eta_c^g$. Shown are the results from SPT (full curves) and from numerical DFT calculations (dashed curves) for $\tilde{\gamma}_{wg} = \beta\sigma_c^2\gamma_{wg}$ and $\tilde{\gamma}_{wl} = \beta\sigma_c^2\gamma_{wl}$. Marked are the positions of the first, second and third layering transition and the wetting transition (vertical arrows, from right to left, taken from [14]) that appear on the gas branch of the binodal [14]. The DFT result for $\tilde{\gamma}_{wg}$ in the complete wetting regime (between the origin and the leftmost arrow) is obtained as $\tilde{\gamma}_{wl} + \tilde{\gamma}_{lg}$. Note the jump in the DFT result for $\tilde{\gamma}_{wg}$ at the first layering transition (rightmost arrow). The inset shows the analytic result for the difference $\tilde{\gamma}_{wg} - \tilde{\gamma}_{wl}$ and the DFT result for the interface tension of the free liquid–gas interface, $\tilde{\gamma}_{lg} = \beta\sigma_c^2\gamma_{lg}$ [14]; the crossing point indicates the result for the wetting transition within this treatment.

At bulk fluid–fluid coexistence a dense colloidal liquid with packing fractions η_c^l and η_p^l coexists with a dilute colloidal gas with packing fractions η_c^g and η_p^g . Evaluating the respective expressions for the wall fluid tension yields $\gamma_{wg} = \gamma_{wf}(\eta_c^g, \eta_p^g)$ and $\gamma_{wl} = \gamma_{wf}(\eta_c^l, \eta_p^l)$; see figure 3 for results for the AO model at a hard wall obtained from equation (2). The agreement with the results from DFT on the liquid side is again very good, but on the gas side deviations are larger due to crowding of colloids at the wall; any layering transitions [14] are not captured by the SPT. At the first layering transition [14, 15] we observe a kink in the DFT result for γ_{wg} . We expect the second and third layering transitions (with smaller jumps in the adsorption) to have similar anomalies, but have not been able to resolve them with the current numerical accuracy. Also the precise location of the transition from partial to complete wetting, where $\gamma_{lg} = \gamma_{wg} - \gamma_{wl}$, is not observable in this way. Comparing our SPT result for $\gamma_{wg} - \gamma_{wl}$ with the DFT result for γ_{lg} [14], we find that close to the critical point $\gamma_{wg} - \gamma_{wl} > \gamma_{lg}$, indicating complete wetting, and further away from the critical point $\gamma_{wg} - \gamma_{wl} < \gamma_{lg}$, indicating partial wetting. Despite the simplicity of the SPT, this is qualitatively in accordance with full DFT calculations (analysing the behaviour of the inhomogeneous colloid density profile at the wall) [14, 15]. The location of the wetting transition obtained by setting $\gamma_{lg} = \gamma_{wg} - \gamma_{wl}$, is $\eta_c^l - \eta_c^g = 0.41$, $\eta_p^r = 0.87$, whereas the DFT result is $\eta_c^l - \eta_c^g = 0.276$, $\eta_p^r = 0.596$ [14, 15].

Carrying out a similar analysis for the case of the polymer-coated wall (see figure 4) reveals a larger discrepancy between the SPT and DFT results, especially on the liquid side of the binodal. The SPT result for $\gamma_{wl} - \gamma_{wg}$ does *not* cross γ_{lg} from DFT, indicating complete drying everywhere on the liquid branch of the binodal. Indeed drying has been observed experimentally at a polymer-coated substrate [8]. It turns out that the DFT results for $\gamma_{wg} + \gamma_{lg}$ and γ_{wl} (not shown in figure 4) are practically equal on the scale of the plot. The colloid

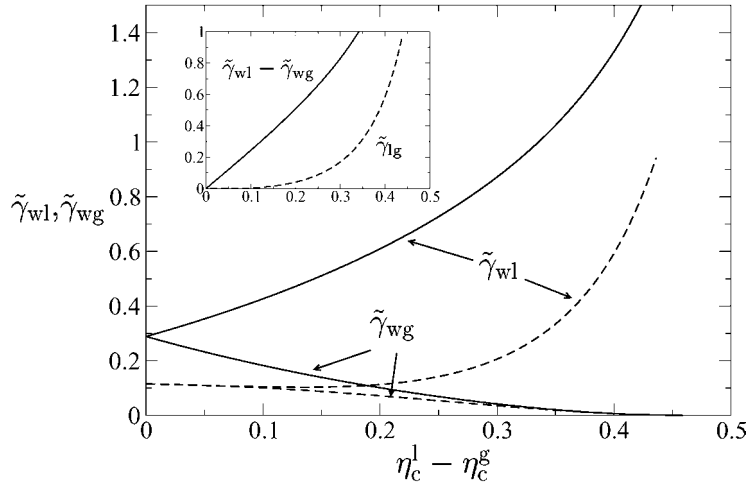


Figure 4. The same as figure 3 but for the polymer-coated wall. Note the different vertical scale compared to figure 3. Within the DFT we obtain $\tilde{\gamma}_{wl}$ as $\tilde{\gamma}_{wl} = \tilde{\gamma}_{wg} + \tilde{\gamma}_{lg}$. The inset shows that $\tilde{\gamma}_{wl} - \tilde{\gamma}_{wg} > \tilde{\gamma}_{lg}$, hence complete drying on the liquid branch of the binodal, compatible with results from full DFT calculations.

density profiles show a clear layer of gas density close to the wall (which is not treated within the SPT). For one statepoint, $\eta_p^r = 1$, far away from the critical point, we have checked within the DFT that the adsorption $\Gamma_c = \int_0^\infty dz (\rho_c(z) - \rho_c(\infty)) \propto \ln(\eta_c/\eta_c^l - 1)$ over more than two decades, $10^{-4} < \eta_c/\eta_c^l - 1 < 10^{-2}$, indicating complete drying. The current binary mixture adsorbed at a wall that does not generate an effective depletion interaction is closely related to simple fluids at a hard wall, where complete drying is found everywhere on the liquid branch of the binodal [35].

In conclusion, we have derived analytical expressions for the wall tension of a colloid–polymer mixture using a scaled particle approach. Both the Asakura–Oosawa model near a hard and a polymer-coated wall (the latter being penetrable for the polymers) as well as the case of interacting polymers at a hard wall are considered. Results are tested against explicit DFT calculations and good overall agreement is found. Applied to the fluid demixing binodal, our data confirm the wetting transition at the hard wall [14, 15]. Wetting at a hard wall was observed experimentally [7–9], and also a transition was claimed [8, 9]. The previously found layering transition [14, 15] manifests itself as a tiny kink in the interfacial tension. We predict complete drying near a polymer-coated wall; this was also reported in experiments [9]. Future work could be devoted to exploring the interfacial tensions by direct computer simulation via integrating the anisotropy of the pressure tensor [36], by thermodynamic integration [31] or, possibly, by using grand-canonical configurational-bias Monte Carlo [19] in order to test our predictions. It would also be interesting to study patterned surfaces [37] and structured walls which for example drastically influence the flow through microfluidic devices [38].

MS thanks M Dijkstra, A Fortini and D G A L Aarts for inspiring discussions and R Evans for very useful correspondence. A A Louis is thanked for informing us about his unpublished work. This work is financially supported by the SFB-TR6 ‘Physics of colloidal dispersions in external fields’ of the *Deutsche Forschungsgemeinschaft* (DFG). The work of MS is part of the research program of the *Stichting voor Fundamenteel Onderzoek der Materie* (FOM), that is financially supported by the *Nederlandse Organisatie voor Wetenschappelijk Onderzoek* (NWO).

References

- [1] Poon W C K 2002 *J. Phys.: Condens. Matter* **14** R859
- [2] Pospiech D *et al* 2003 *Surf. Coat. Int.* **B 86** 43
- [3] Vliegthart G A and Lekkerkerker H N W 1997 *Prog. Coll. Polym. Sci.* **105** 27
- [4] de Hoog E H A and Lekkerkerker H N W 1999 *J. Phys. Chem. B* **103** 5274
- [5] Chen B-H, Payandeh B and Robert M 2000 *Phys. Rev. E* **62** 2369
Chen B-H, Payandeh B and Robert M 2001 *Phys. Rev. E* **64** 042401
- [6] Aarts D G A L, van der Wiel J H and Lekkerkerker H N W 2003 *J. Phys.: Condens. Matter* **15** S245
- [7] Aarts D G A L and Lekkerkerker H N W 2003 private communication
- [8] Wijting W K, Besseling N A M and Cohen Stuart M A 2003 *Phys. Rev. Lett.* **90** 196101
- [9] Wijting W K, Besseling N A M and Cohen Stuart M A 2003 *J. Phys. Chem. B* **107** 10565
- [10] Asakura S and Oosawa F 1954 *J. Chem. Phys.* **22** 1255
Asakura S and Oosawa F 1958 *J. Polym. Sci.* **33** 183
- [11] Vrij A 1976 *Pure Appl. Chem.* **48** 471
- [12] Brader J M and Evans R 2000 *Europhys. Lett.* **49** 678
- [13] Schmidt M, Löwen H, Brader J M and Evans R 2000 *Phys. Rev. Lett.* **85** 1934
Schmidt M, Löwen H, Brader J M and Evans R 2002 *J. Phys.: Condens. Matter* **14** 9353
- [14] Brader J M, Evans R, Schmidt M and Löwen H 2002 *J. Phys.: Condens. Matter* **14** L1
- [15] Brader J M, Evans R and Schmidt M 2003 *Mol. Phys.* at press
- [16] Schmidt M, Fortini A and Dijkstra M 2003 *J. Phys.: Condens. Matter* **15** 53411
- [17] Dijkstra M and van Roij R 2002 *Phys. Rev. Lett.* **89** 208303
- [18] Bolhuis P G, Louis A A and Hansen J-P 2002 *Phys. Rev. Lett.* **89** 128302
- [19] Vink R L C and Horbach J 2003 *Preprint cond-mat/0310404*
- [20] Lekkerkerker H N W, Poon W C K, Pusey P N, Stroobants A and Warren P B 1992 *Europhys. Lett.* **20** 559
- [21] Aarts D G A L, Dullens R P A, Lekkerkerker H N W, Bonn D and van Roij R 2003 *J. Chem. Phys.* at press
- [22] Moncho-Jordá A, Rotenberg B and Louis A A 2003 *Preprint cond-mat/0309248*
- [23] Schmidt M, Denton A R and Brader J M 2003 *J. Chem. Phys.* **118** 1541
- [24] Dietrich S 1988 Wetting phenomena *Phase Transitions and Critical Phenomena* ed C Domb and J L Lebowitz (London: Academic) p 1
- [25] Louis A A, Bolhuis P G, Meijer E J and Hansen J-P 2002 *J. Chem. Phys.* **116** 10547
- [26] Reiss H, Frisch H L and Lebowitz J L 1959 *J. Chem. Phys.* **31** 369
- [27] Reiss H, Frisch H L, Helfand E and Lebowitz J L 1960 *J. Chem. Phys.* **32** 119
- [28] Lebowitz J L and Rowlinson J S 1964 *J. Chem. Phys.* **41** 133
- [29] Lebowitz J L, Helfand E and Praestgaard E 1965 *J. Chem. Phys.* **43** 774
- [30] Henderson J R 2002 *J. Chem. Phys.* **116** 5039
- [31] Heni M and Löwen H 1999 *Phys. Rev. E* **60** 7057
- [32] Roth R and Dietrich S 2000 *Phys. Rev. E* **62** 6926
- [33] Tenne R and Bergmann E 1978 *Phys. Rev. A* **17** 2036
- [34] Brader J M, Dijkstra M and Evans R 2001 *Phys. Rev. E* **63** 041405
- [35] Parry A O and Evans R 1988 *Mol. Phys.* **65** 45
Parry A O and Evans R 1993 *Mol. Phys.* **78** 1527
- [36] Walton J P R B, Tildesley D J, Rowlinson J S and Henderson J R 1983 *Mol. Phys.* **48** 1357
- [37] Henderson J R 2003 *Mol. Phys.* **101** 397
- [38] Drazer G, Koplik J, Acrivos A and Khusid B 2002 *Phys. Rev. Lett.* **89** 244501

The contact angle of the colloidal liquid–gas interface and a hard wall

Paul P F Wessels¹, Matthias Schmidt^{2,3} and Hartmut Löwen¹

¹ Institut für Theoretische Physik II, Heinrich-Heine-Universität Düsseldorf, Universitätsstraße 1, 40225 Düsseldorf, Germany

² Debye Institute, Soft Condensed Matter Group, Utrecht University, Princetonplein 5, 3584 CC Utrecht, The Netherlands

E-mail: wessels@thphy.uni-duesseldorf.de

Received 6 May 2004

Published 10 September 2004

Online at stacks.iop.org/JPhysCM/16/S4169

doi:10.1088/0953-8984/16/38/030

Abstract

We consider the Asakura–Oosawa–Vrij model of hard sphere colloids and ideal polymer coils in contact with a planar hard wall at (colloidal) liquid–gas coexistence. Using extensive numerical density functional calculations, the liquid–gas, wall–liquid and wall–gas interfacial free energies are calculated. The results are inserted into Young’s equation to obtain the contact angle between the liquid–gas interface and the wall. As a function of polymer fugacity this angle exhibits discontinuities of slope (‘kinks’) upon crossing first-order surface phase transitions located on the gas branch of the bulk binodal. Each kink corresponds to a transition from $n - 1$ to n colloid layers adsorbed at the wall, referred to as the n th layering transition. The corresponding adsorption spinodal points from $n - 1$ to n layers upon reducing the polymer fugacity along the bulk binodal were found in a previous study (Brader *et al* 2002 *J. Phys.: Condens. Matter.* **14** L1; Brader *et al* 2003 *Mol. Phys.* **101** 3349). Remarkably, we find desorption spinodal points from n to $n - 1$ layers to be absent upon increasing polymer fugacity at bulk coexistence, and many branches (containing up to seven colloid layers) remain metastable. Results for the first layering binodal and both spinodal branches off bulk coexistence hint at a topology of the surface phase diagram consistent with these findings. Both the order of the transition to complete wetting and whether it is preceded by a finite or an infinite number of layering transitions remain open questions. We compare the locations of the first layering binodal line and of the second layering binodal point at bulk coexistence with recent computer simulation results by Dijkstra and van Roij (2002 *Phys. Rev. Lett.* **89** 208303) and discuss our results for the contact angle in the light of recent experiments.

³ On leave from: Institut für Theoretische Physik II, Heinrich-Heine-Universität Düsseldorf, Universitätsstraße 1, 40225 Düsseldorf, Germany.

1. Introduction

In suspensions of sterically stabilized colloidal particles mixed with non-adsorbing globular polymers, the latter induce an effective attraction between the colloids due to the depletion effect [1]. Such mixtures can phase separate into two fluid phases, one being a colloidal liquid that is rich in colloids and poor in polymers and the other being a colloidal gas that is poor in colloids and rich in polymers. Colloid-polymer mixtures serve as excellent model systems in which to study many phenomena associated with liquid-gas phase separation as the scales of time and length are much larger than in atomic and molecular systems [1, 2]. Recent experiments have focused on the bulk phase behaviour (see [1] and references therein), (colloidal) liquid-gas interface tension [3–7], capillary wave fluctuations observed in real space [8], droplet coalescence [8] and further non-equilibrium phenomena [1, 7, 9]. The behaviour at non-adsorbing walls has been studied by measuring the contact angle between the free liquid-gas interface and a substrate acting as a hard wall. Complete wetting of the wall by the colloidal liquid has been observed for a wide variety of state points [9]. However, there are also reports of a transition from partial to complete wetting [10, 11]; hence this remains an interesting topic.

Most of the essential physics of colloid-polymer mixtures is captured by the Asakura-Oosawa-Vrij (AO) model of hard sphere colloids and ideal polymers [12–14], which has become a widely used reference system. Theoretical approaches [15, 16] and computer simulations [17–23] have given insight into its bulk phase behaviour, and some recent work [20, 24] aims at including more realistic colloid-polymer and polymer-polymer interactions. Studies based on a one-component description of colloids interacting with an effective depletion potential (obtained by integrating out the polymer degrees of freedom and truncating at the pairwise level) were devoted to inhomogeneous situations, such as the free fluid-fluid interface [25, 26] and adsorption at a hard wall [27]. Following the development of an accurate density functional theory (DFT) specific to the binary AO model [28, 29], further research was stimulated in inhomogeneous situations such as liquid-gas [30, 31] and wall-fluid interfaces [30–32] and results were compared to those from simulations [21–23, 33]. In particular, in [30, 31] the AO model was considered for contact with a planar hard wall. A sequence of first-order layering transitions was found on the gas branch of the (liquid-gas) binodal upon reducing the polymer fugacity. Further reducing the polymer fugacity leads to a transition to complete wetting of the wall by colloidal liquid. This scenario was corroborated by a simulation study [21]. The relation of the results from these different approaches will be re-examined in the light of the findings of the present study in more detail below. The adsorption properties at a wall are intimately related to the wall-fluid interfacial free energies (or ‘wall tensions’), for which an analytical expression was obtained from a scaled-particle treatment and which was found to compare well with results from full numerical DFT calculations [32]. However, despite its experimental accessibility [7, 9–11], the contact angle of the free liquid-gas interface and a hard planar wall has not been considered either via theory or simulations, in contrast to wetting behaviour [21, 30, 31, 34]. The aim of the present study is to obtain a quantitative understanding of the contact angle and elucidate its relation to the surface phase behaviour on the basis of the AO model.

We obtain the (macroscopic) contact angle, θ , from the liquid-gas (lg), the wall-gas (wg) and the wall-liquid (wl) interface tensions, γ_{lg} , γ_{wg} and γ_{wl} , respectively, via Young’s equation [35],

$$\cos\theta = \frac{\gamma_{wg} - \gamma_{wl}}{\gamma_{lg}}. \quad (1)$$

A depletion attraction similar to that acting between two colloids acts between one colloid and a hard wall [27]; the latter therefore favours the colloidal liquid. As a consequence, we expect

$\gamma_{\text{wg}} > \gamma_{\text{wl}}$ everywhere at coexistence, and $\theta < \pi/2$. For state points where $\gamma_{\text{wg}} < \gamma_{\text{wl}} + \gamma_{\text{lg}}$, the contact angle $\theta > 0$ and the surface is partially wetted by the liquid. However, as soon as $\gamma_{\text{wg}} = \gamma_{\text{wl}} + \gamma_{\text{lg}}$ a macroscopic liquid layer will intrude between the gas and the wall and the latter is completely wetted by the liquid. The transition from partial to complete wetting induced by changing an appropriate thermodynamic variable is referred to as the wetting transition [36, 37]. A study of θ can supply a link between theoretical predictions of surface phase behaviour and experiments and we display our central result in figure 6.

The paper is organized as follows. In section 2 we define the model and discuss in section 3 the density functional theory used to calculate the interface tensions. In section 4 we present results and we conclude in section 5.

2. Model

We consider the Asakura–Oosawa–Vrij (AO) model of N_c hard sphere colloids and N_p ideal polymers in a volume V . The colloids (species c) and polymers (species p) have diameters σ_i , bulk packing fractions $\eta_i = N_i V_i / V$ and particle volumes $V_i = (\pi/6)\sigma_i^3$ for $i = c, p$, respectively. The colloid–colloid as well as the colloid–polymer interaction potentials are those of hard spheres, so $u_{ij}(r) = \infty$ when $r < (\sigma_i + \sigma_j)/2$ and $u_{ij}(r) = 0$ otherwise, with $ij = cc, cp$. The polymers do not interact with each other, i.e. $u_{pp}(r) = 0$ for all r . Due to the non-additive ranges of these interaction potentials, the polymers induce an effective attraction between the colloids, which for sufficiently large size ratios σ_p/σ_c ($\gtrsim 0.35$) drives a thermodynamically stable phase separation into a colloid-rich (liquid) and a colloid-poor (gas) phase [15, 16]. All bare interactions are of an entropic nature, and therefore the temperature T does not play a role. The only relevant model parameter is the size ratio $q = \sigma_p/\sigma_c$. We often use the so-called polymer reservoir representation where the mixture is in contact with a polymer reservoir, which determines the polymer chemical potential. In this situation, the thermodynamic state parameters are η_c and η_p^r , the latter being the polymer packing fraction in the reservoir which is proportional to the polymer fugacity as these particles are ideal.

3. Density functional theory

We use the fundamental measure density functional for the AO model [28, 29] to calculate colloid and polymer density profiles from which the interface tensions can then be obtained. In density functional theory (DFT), the grand-canonical free energy is expressed as a functional, $\Omega[\rho_c(\mathbf{r}), \rho_p(\mathbf{r})]$, of the one-particle distribution functions $\rho_i(\mathbf{r})$ (with $i = c, p$), given by [38]

$$\begin{aligned} \Omega[\rho_c(\mathbf{r}), \rho_p(\mathbf{r})] = & F_{\text{exc}}[\rho_c(\mathbf{r}), \rho_p(\mathbf{r})] + k_B T \sum_{i=c,p} \int d\mathbf{r} \rho_i(\mathbf{r}) [\ln(\rho_i(\mathbf{r})\Delta_i) - 1] \\ & + \sum_{i=c,p} \int d\mathbf{r} \rho_i(\mathbf{r}) [u_{\text{ext},i}(\mathbf{r}) - \mu_i], \end{aligned} \quad (2)$$

where k_B is Boltzmann's constant, Δ_i is the ‘thermal volume’ of species i , i.e. the third power of the de Broglie wavelength, and $u_{\text{ext},i}(\mathbf{r})$ and μ_i are the external potential and the chemical potential for species i , respectively. The excess Helmholtz free energy functional, $F_{\text{exc}} = \int d\mathbf{r} \Phi(\mathbf{r})$, with Φ the excess free energy density, is given in [28, 29] and is not reproduced here⁴.

⁴ We do not include the tensorial weight function in the present calculations.

In thermodynamic equilibrium, the functional is stationary, $\delta\Omega/\delta\rho_i(\mathbf{r}) = 0$ (with $i = c, p$), and the resulting equations yield the stable distributions, i.e.

$$\rho_i(\mathbf{r}) = z_i \exp\left[-\beta u_{\text{ext},i}(\mathbf{r}) - \beta \frac{\delta F_{\text{exc}}[\{\rho_j(\mathbf{r})\}]}{\delta\rho_i(\mathbf{r})}\right], \quad (3)$$

with $z_i = \Delta_i^{-1} \exp[\beta\mu_i]$ the fugacity of component i and $\beta = 1/k_B T$. The equilibrium distribution functions are normalized, $\int d\mathbf{r} \rho_i(\mathbf{r}) = N_i$. We note that the polymer fugacity is proportional to the polymer packing fraction in the polymer reservoir, $\eta_p^r = z_p V_p$, and we usually refer to η_p^r as the polymer fugacity. We have solved these equations numerically for $\rho_i(z)$ in one spatial dimension z for the free liquid–gas interface (where $u_{\text{ext},i}(z) = 0$ everywhere) as well as both for the liquid and the gas at bulk coexistence in the presence of the external hard wall potential, i.e. for $u_{\text{ext},i}(z) = \infty$ for $z < \sigma_i/2$ and $u_{\text{ext},i}(z) = 0$ otherwise, for both species $i = c, p$, where z is the space coordinate perpendicular to the wall. The numerical routine we have used is a Picard iteration procedure with a Broydes mixing scheme [39]. The ‘mixing parameter’ is continuously adapted to obtain optimal convergence. Additionally, it is important to realize that in situations with several metastable minima, as we find to occur for the coexisting gas in contact with the hard wall, the initial guess for the profiles in the iteration procedure determines to which minimum the routine converges.

Once the density profiles are known, the interface tension is given by $\gamma = (\Omega_{\text{inh}} + PV)/A$, where $\Omega_{\text{inh}} = \Omega[\rho_c(\mathbf{r}), \rho_p(\mathbf{r})]$ (i.e. the functional, equation (2), evaluated at the solutions of equation (3)) is the grand-canonical free energy of the inhomogeneous system, P is the bulk pressure and A is the lateral (perpendicular to the z -direction) system area. In terms of density profiles this quantity can be written as

$$\gamma = \int dz [\omega(z) + P], \quad (4)$$

where

$$\omega(z) = k_B T \sum_{i=c,p} \rho_i(z) [\ln(\rho_i(z)\Delta_i) - 1] - \sum_{i=c,p} \mu_i \rho_i(z) + k_B T \Phi(z) \quad (5)$$

can be viewed as a local grand potential density (evaluated with the minimized density profiles). In case of the liquid–gas interface, the integral in equation (4) is over all space, i.e. z runs from $-\infty$ (bulk gas) to ∞ (bulk liquid). In the case of the fluid in contact with a hard wall, the integral runs from $z = 0$ (at the actual location of the hard wall) to ∞ (bulk). In the numerical routine, we compute the interface tensions for each state point for different system sizes and refined termination criteria for the iteration. This gives an estimate of the numerical error in the result for the interface tensions, which is important as the resulting contact angle can be very sensitive to these errors. Often the dividing surface [35] is chosen at $z = \sigma_c/2$; then subtraction of $\sum_{i=c,p} P\sigma_i$ from the present definition of the wall–fluid tension, equation (4), is required. For our present goal this is irrelevant as this term does not affect θ , as it drops out of the numerator in equation (1).

4. Results

4.1. Layered states at the hard wall

We have calculated colloid and polymer density profiles of the free liquid–gas interface, as well as the wall–gas and the wall–liquid interfacial profiles at bulk coexistence. For a given state point the liquid–gas and the wall–liquid profiles are both unique (disregarding trivial translations of the liquid–gas interface); such results have been presented elsewhere [30, 31].

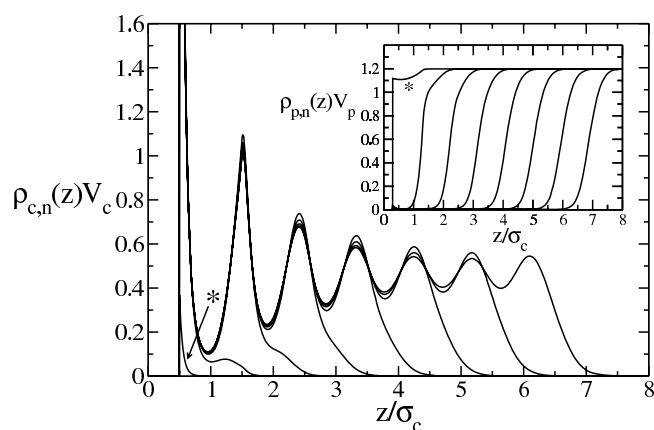


Figure 1. Colloid density profiles, $\rho_{c,n}(z)V_c$, at a hard wall as a function of the scaled distance, z/σ_c , from the wall at the gas branch of the liquid–gas binodal for $q = 0.6$ and $\eta_p^t = 1.2$. Shown are results for n -layer states with $n = 0, 1, 2, \dots, 7$ (left to right). All states are metastable except for the globally stable $n = 0$ -layer state (see the small peak at contact with the wall, marked with an asterisk). The inset shows the corresponding polymer profiles (also from left to right, with an asterisk the marking $n = 0$ -layer state), $\rho_{p,n}(z)V_p$, as a function of z/σ_c . The normalizations of the density profiles are such that in bulk they reduce to the packing fractions, $\lim_{z \rightarrow \infty} \rho_{i,n}(z)V_i = \eta_i$.

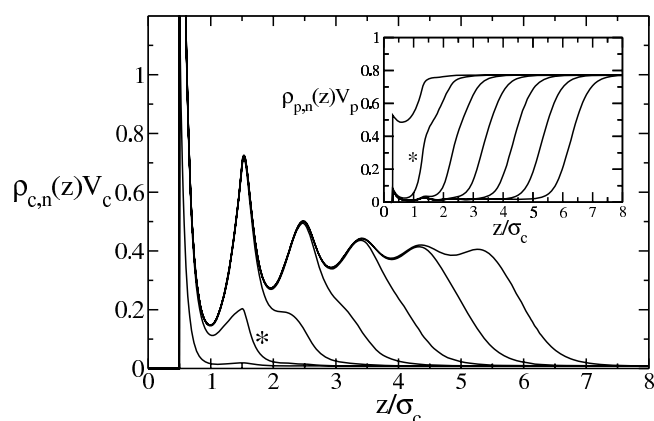


Figure 2. The same as figure 1, but for $\eta_p^t = 0.8$ and $n = 0, 1, 2, \dots, 6$ (left to right). All profiles are metastable except for the globally stable $n = 1$ state (marked with asterisks).

However, in the case of the coexisting gas in contact with the hard wall, we have found many metastable states, each corresponding to an integer number of layers, n , of colloids adsorbed at the wall. In figures 1 and 2, we have plotted a number of such profiles, denoted by $\rho_{c,n}(z)$, for size ratio $q = 0.6$ and fugacities $\eta_p^t = 1.2$ and 0.8 , respectively, along with the corresponding polymer profiles, $\rho_{p,n}(z)$, given in the respective insets (for reference, the bulk phase diagram for $q = 0.6$ is given in the inset of figure 9). For $\eta_p^t = 1.2$ the zero-layer state (marked with an asterisk in figure 1) exhibits practically no excess colloid adsorption and is the globally stable state. The grand potential, and hence the interface tension, increases with the number of layers, i.e. $\gamma_{wg,0} < \gamma_{wg,1} < \gamma_{wg,2} < \dots < \gamma_{wg,7}$, where $\gamma_{wg,n}$ is the wall–gas tension corresponding to n colloid layers (as given in equation (4) and evaluated with $\rho_{i,n}(z)$, $i = c, p$).

S4174

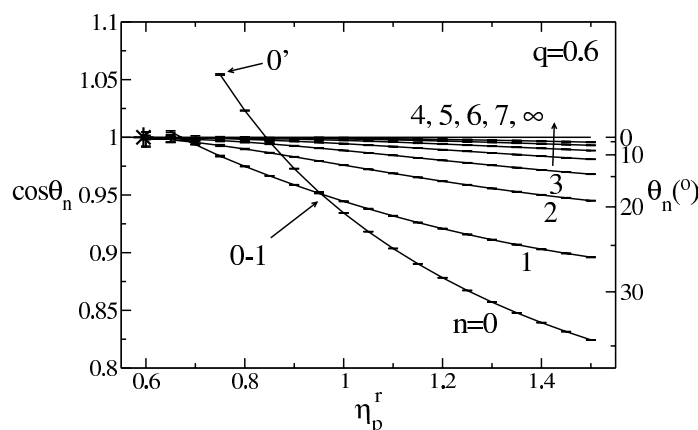
P P F Wessels *et al*

Figure 3. Cosines of the contact angle, $\cos \theta_n$ as defined via Young's equation as $(\gamma_{wg} - \gamma_{wl})/\gamma_g$, as a function of the polymer reservoir packing fraction, η_p^r , for size ratio $q = 0.6$. A scale of the bare angle (in degrees, $^\circ$) is given on the right vertical axis. Shown are branches, θ_n , corresponding to n colloid layers adsorbed at the wall–gas interface at liquid–gas coexistence (with $n = 0, 1, 2, \dots, 7$, increasing in the direction of the arrow). The constant $\cos \theta_n = 1$ ($\theta_n = 0^\circ$) is marked ∞ and corresponds to two macroscopically separated wall–liquid and liquid–gas interfaces. For every value of η_p^r , the branch corresponding to the lowest $\cos \theta_n$ (i.e. the largest contact angle θ_n) yields the thermodynamically stable state; all other branches are metastable. The crossing point of θ_0 and θ_1 (marked 0–1) denotes the first layering transition and the spinodal point of the zero-layer branch is marked 0'. Also indicated is the location of the wetting transition (star) according to Brader *et al* [30, 31].

For $\eta_p^r = 0.8$ the equilibrium profile is given by $\rho_{i,1}(z)$ (marked with an asterisk in figure 2). Remarkably, in this case, the solution $\rho_{i,0}(z)$ corresponds to a higher tension than all others, i.e. $\gamma_{wg,1} < \gamma_{wg,2} < \dots < \gamma_{wg,6} < \gamma_{wg,0}$. The two state points considered ($\eta_p^r = 0.8, 1.2$) are at polymer fugacities larger than that at which the Fisher–Widom line [40, 41] hits the bulk binodal (at $\eta_p^r \approx 0.533$ for $q = 0.6$ [29]), which implies that correlations decay asymptotically in an oscillatory fashion in the liquid phase. Apparently, this oscillatory nature also appears in the effective interface potential between the wall and the liquid–gas interface, yielding many metastable minima [31], see [42].

4.2. The wall contact angle of the liquid–gas interface

We have calculated the liquid–gas interface tension, γ_g , the wall–liquid tension, γ_{wl} , and the wall–gas tensions for all n -layer states identified, $\gamma_{wg,n}$, for the full range of polymer fugacities at bulk liquid–gas coexistence. The results have been inserted into Young's equation, equation (1), yielding a contact angle curve, θ_n , for each n -layer state. The results for $q = 0.6$ are plotted in figure 3 and a magnification of the region close to $\cos \theta_n = 1$ is displayed in figure 4. From the definition of the contact angle, equation (1), and the fact that γ_g and γ_{wl} are unique for each state point, η_p^r , the state n with the lowest free energy also possesses the lowest value of $\cos \theta_n$. Hence, for high η_p^r the equilibrium contact angle is given by θ_0 (corresponding to the zero-layer state); see figure 3. Decreasing η_p^r leads to an increase in $\cos \theta_0$, until it crosses the $\cos \theta_1$ branch and becomes metastable. The crossing point, where $\theta_0 = \theta_1$, denotes the 0–1 layering transition and is also referred to as the *first* layering transition. (Consistent with [30, 31], the surface phase transition from $n - 1$ to n adsorbed colloid layers at the wall–gas interface is referred to as the n th layering transition.) Upon further decreasing η_p^r (see figure 4),

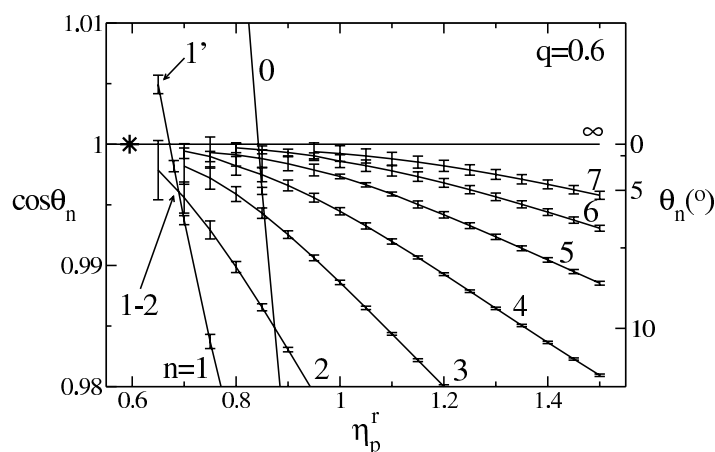


Figure 4. As figure 3, but magnified close to $\cos \theta_n = 1$. For the sake of clarity, some of the points of the three-, four- and five-layer branches close to the wetting transition are omitted. Indicated is the location of the second layering transition (marked 1-2) and the one-layer spinodal point (1').

$\cos \theta_1$ is in turn crossed by $\cos \theta_2$ and the crossing point, where $\theta_1 = \theta_2$, is the 1-2 (second) layering transition. This scheme suggests that there could well be further layering transitions upon reducing η_p^r , and this impression is strengthened by the fact that the (metastable) states $\cos \theta_n$ (with n from 3 to 7; see figure 4) all seem to converge to around the location of the wetting transition. However, we have not been able to resolve the third [30, 31] and (possible) higher layering transitions and we note that any of these should be located in the small region of $\cos \theta$ between 0.995 and 1 with η_p^r between 0.6 and 0.65; see figure 4. Consequently, we can also not obtain insight into the nature of the transition to complete wetting, i.e. whether this is second order and occurs via an infinite sequence of layering transitions or is first order and is preceded by only a finite number of layering transitions. For a more extensive discussion of these two possible scenarios, we refer the reader to [31].

Upon reducing η_p^r , metastable zero-layer states can be tracked into a region where the contact angle takes unphysical values, $\cos \theta_0 > 1$ (figure 3). The same happens for one-layer states as can be seen in figure 4. Inserting equilibrium values of the interface tensions obtained from DFT into equation (1) ensures that $\cos \theta \leq 1$, but this does not need to be the case when using interface tensions of metastable states. Reducing η_p^r even further, the metastable zero-layer state eventually becomes unstable at an adsorption spinodal point; see figure 3. Beyond this point (for even lower η_p^r), no zero-layer state can be stabilized and the numerical iteration rather converges to the one-layer state. Similar adsorption spinodal points were found for higher n and we have located those with a (moderate) resolution of 0.05 in η_p^r . From the present data the adsorption spinodal fugacities for n -layer states, $\eta_{p,n}^r$, are $\eta_{p,0}^r = 0.75$, $\eta_{p,1}^r = \eta_{p,2}^r = 0.65$ and $\eta_{p,3}^r = \eta_{p,4}^r = \eta_{p,5}^r = 0.6$. For states with an even thicker colloid film ($n = 6$ and 7), the profiles no longer converged properly at low η_p^r , and we have not been able to obtain precise values for $\eta_{p,6}^r$ and $\eta_{p,7}^r$. The evolution for surface states upon *increasing* η_p^r is in striking contrast. No spinodal points were found and each n -layer state remains metastable up to $\eta_p^r = 1.5$, a value close to the liquid–gas–crystal triple point according to free volume theory for the AO model [16]. Moreover, for large values of η_p^r the numerical routine converges very rapidly, which hints at deep (nevertheless metastable) free energy minima for these layered surface states.

S4176

P P F Wessels *et al*

As the layering transitions are thermodynamic surface phase transitions, they manifest themselves as discontinuous jumps in the Gibbs adsorption [30, 31],

$$\Gamma_i = \int_0^\infty dz (\rho_i(z) - \rho_i(\infty)), \quad (6)$$

for both components $i = c, p$, and these can be obtained from equation (5) and

$$\Gamma_c = -\left. \frac{\partial \gamma_{wf}}{\partial \mu_c} \right|_{\mu_p}, \quad \Gamma_p = -\left. \frac{\partial \gamma_{wf}}{\partial \mu_p} \right|_{\mu_c}, \quad (7)$$

where γ_{wf} is the wall tension of the fluid. Moving along the gas branch of the liquid–gas bulk binodal ties together changes in both chemical potentials:

$$\left. \frac{d\gamma_{wg}}{d\mu_p} \right|_{\text{coex}} = \left. \frac{\partial \gamma_{wg}}{\partial \mu_p} \right|_{\mu_c} + \left. \frac{\partial \gamma_{wg}}{\partial \mu_c} \right|_{\mu_p} \left. \frac{d\mu_c}{d\mu_p} \right|_{\text{coex}}, \quad (8)$$

where the slope of the bulk binodal fulfils a Clapeyron-type equation,

$$\left. \frac{d\mu_c}{d\mu_p} \right|_{\text{coex}} = -\frac{\Delta\rho_p}{\Delta\rho_c}, \quad (9)$$

which can be deduced from the Gibbs–Duhem equation in a straightforward fashion [43]. Here, $\Delta\rho_i = \rho_i^l - \rho_i^g$ is the difference between the densities of species $i = c, p$ in the liquid and gas phases (note that $\Delta\rho_p < 0$). Hence, we obtain

$$\left. \frac{d\gamma_{wg}}{d\mu_p} \right|_{\text{coex}} = -\Gamma_p + \Gamma_c \frac{\Delta\rho_p}{\Delta\rho_c}, \quad (10)$$

where the adsorptions Γ_c and Γ_p refer to those of the gas at bulk coexistence. Hence, crossing a layering transition (again at bulk coexistence) is necessarily accompanied by a jump in the adsorptions Γ_i ; consequently via equation (10) this leads to a discontinuity of slope of the wall–gas interface tension. From Young’s equation (1), it follows that this also leads to a jump in the slope of the contact angle, $d \cos \theta / d\eta_p^r$. This is consistent with our findings above of crossing of different branches, θ_{n-1} and θ_n .⁵

Note that all quantities in equation (10) can be independently obtained from our DFT results, namely the adsorption Γ_i from the integral over the respective density profile, equation (6), the differences $\Delta\rho_i$ from the bulk phase diagram and the left-hand side of equation (10) from a numerical derivative of the results for γ_{wg} , as obtained through equation (4). As a check for internal consistency of our calculations we have chosen the state point with $\eta_p^r = 1.1$ for $q = 1$ at bulk coexistence, which is very close to the binodal of the first layering transition (which is at $\eta_p^r \approx 1.104$, as discussed below). We find equation (10) to be fulfilled to three significant digits; for the zero-layer (one-layer) state both sides evaluate to $1.264/\sigma_c^2$ ($1.352/\sigma_c^2$). Together, these two estimates yield a jump in $d \cos \theta / d\eta_p^r$ of 0.247, which is consistent with our data for the contact angle for $q = 1$ (which gives 0.238) and which is discussed below.

We will now consider the case of larger polymer–colloid size ratios, $q = 1$; see figure 5 for more detail. The zero-layer branch is calculated for a number of fugacities from high values, $\eta_p^r = 3$, to the spinodal point close to $\eta_p^r = 1$. The higher- n branches are only calculated between 0.95 and 1.5 ($n = 1$) and between the wetting transition [31] and the crossing point of the zero-layer and the one-layer branch ($n = 2$ –6, which practically fall on top of each other). It is found that for this size ratio the zero-layer branch is stable everywhere except

⁵ The reported jump in γ_{wg} as a function of the difference of colloid packing fractions of the liquid and gas phases at the first layering transition [32] arises from crossing the adsorption spinodal rather than the binodal. The equilibrium curve for γ_{wg} is continuous.

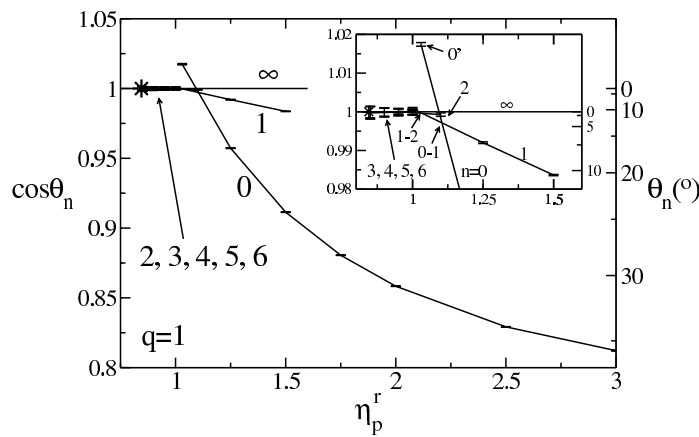


Figure 5. As figure 3, but for $q = 1$. The inset displays a magnification of the area close to the wetting transition. The points marked 0–1 and 1–2 are the first layering and second layering transitions, respectively, and the spinodal point of the zero-layer branch is denoted as 0'.

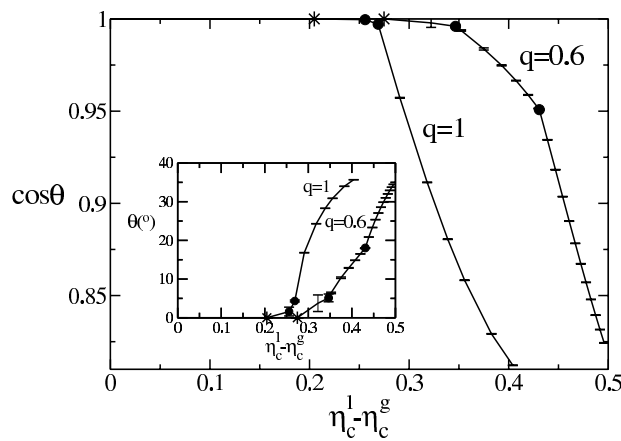


Figure 6. The equilibrium contact angle, $\cos \theta$ (main figure) and θ (in degrees, displayed in the inset), as a function of the difference in colloid packing fractions, $\eta_c^l - \eta_c^g$, of the coexisting bulk liquid and gas phases for two size ratios, $q = 0.6$ and 1 . The locations of the equilibrium layering transitions are marked by filled circles. The stars mark the transitions from partial to complete wetting according to Brader *et al* [30, 31].

in a small regime of η_p^r between 0.85 and 1.1 (where $\cos \theta_n$ is close to 1) and where layering transitions are located. We have been able to identify the locations of the first and second layering transitions; higher transitions are eroded by the numerical noise.

Figure 6 shows the resulting equilibrium values of $\cos \theta$ (see the inset for the bare angle θ) as a function of the difference in colloid packing fractions of the coexisting liquid and gas phases, $\eta_c^l - \eta_c^g$, for both size ratios considered, $q = 0.6$ and 1 . This representation enables one to make direct contact with experiments, where density differences of coexisting phases are rather directly accessible [7, 9–11]. For both size ratios the contact angle is of the same order of magnitude, i.e. $\cos \theta = 0.8$ – 1 , but for $q = 1$ the wetting transition lies closer (in this representation) to the bulk critical point. Only the first layering transition for $q = 0.6$ occurs at a considerably larger contact angle of $\cos \theta_{0-1} \approx 0.95$ or $\theta_{0-1} \approx 18^\circ$. A remarkable fact is that

for both size ratios, there is a substantial region in the partial wetting regime close to the wetting transition where the contact angle remains very small, i.e. the range $(\eta_c^l - \eta_c^g) \approx 0.28\text{--}0.35$ for $q = 0.6$ and $(\eta_c^l - \eta_c^g) \approx 0.2\text{--}0.27$ for $q = 1$.

4.3. Surface phase behaviour

Layering transitions of the AO model at a hard wall were reported earlier by Brader *et al* [30, 31] as obtained within the same DFT approximation [28, 29] and using numerical routines similar to those employed in the present work. However, in contrast to the present study, that of Brader *et al* determined (implicitly) spinodal points along two paths: first, by reducing η_p^r at bulk (liquid–gas) coexistence and following the evolution of the zero-layer state, observing jumps to one-layer and subsequently higher-layer states, and second, by keeping η_p^r fixed and approaching the gas branch of the binodal by increasing η_c , starting from very small values. Results along reversed paths for the second case, i.e. decreasing μ_c at constant η_p^r , were taken to ascertain that hysteresis effects are small, and it was concluded that the spinodal points give reasonable indications of the locations of the equilibrium layering transitions [31, 44]. We will discuss in the following the relation of these findings to those of the present work. For this purpose, we have chosen a reference case, i.e. the first layering transition for $q = 1$, and mapped out its surface phase behaviour completely, i.e. including binodal and spinodal lines off bulk coexistence. The result is plotted in figure 7.

The layering transition binodal is obtained by determining, for each value of η_p^r , the value of η_c at which the zero-layer and one-layer states have equal interface tensions and are thus in thermodynamic coexistence. The resulting binodal line extends below the first layering transition at bulk coexistence, at $\eta_{p,0-1}^r \approx 1.1$, to lower values of η_p^r into the bulk gas phase region. As this is a transition between two (surface) phases of the same symmetry, a van der Waals loop in the free energy and a critical point are mandatory. In order to find the location of the critical point, we fit our data for the colloid adsorption $\Gamma_c(\eta_p^r)$ of the coexisting zero-layer and one-layer states with a fourth-order polynomial, $\eta_p^r = a_0 + a_2(\Gamma_c - a_1)^2 + a_3(\Gamma_c - a_1)^3 + a_4(\Gamma_c - a_1)^4$, where the a_i are free fitting parameters; see figure 7. The value of a_0 is an estimate of the critical value of η_p^r , and the functional form is chosen to yield the mean-field critical exponent of $1/2$, i.e. $(\Gamma_c - a_1) \sim (\eta_p^r - a_0)^{1/2}$, as the DFT is a mean-field theory in the sense that it does not capture fluctuation effects. The accuracy of the colloid packing fraction η_c of points on the layering binodal is high; errors are typically smaller than 0.1% of η_c . However, the critical point is an extrapolation and is therefore much more sensitive to errors, i.e. these may be as large as 3% in η_p^r and 1% in η_c . We have also located the zero-layer spinodal by taking paths at constant η_p^r and increasing values of η_c , monitoring the stability of the solution under the iteration procedure. The values of η_c where the zero-layer state becomes unstable and converges to the one-layer state define the ‘adsorption spinodal’, located at *larger* values of η_c compared to the layering binodal. (The precise location of spinodal points is governed by the numerical resolution of the step size in η_c , i.e. typically 1% in η_c .) Similarly, we have investigated the stability of the one-layer states upon reducing η_c at constant η_p^r . This defines the ‘desorption spinodal’, where the one-layer solutions converge to the zero-layer states and which is located at *smaller* values of η_c as compared to the layering binodal. Upon decreasing η_p^r , both spinodals and the layering binodal end at the surface critical point. Indeed even for values of η_p^r quite far above the layering critical point the adsorption and desorption spinodals are very close and we can confirm the finding of Brader *et al* that hysteresis effects at constant η_p^r are small.

Next, we discuss the various aspects of this surface phase transition in relation to bulk liquid–gas coexistence. We first note that no intrinsic difference is observed between the

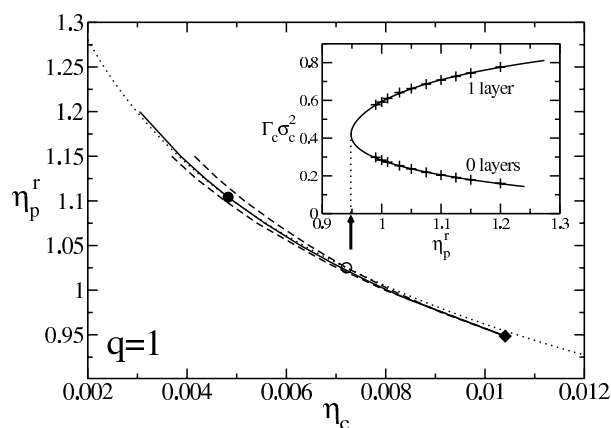


Figure 7. The full surface phase diagram of the first layering transition (from the zero-layer to the one-layer state) for $q = 1$ as a function of (bulk) colloid packing fraction, η_c , and polymer reservoir packing fraction, η_p^r . Shown is the layering binodal (full curve), the one-layer desorption spinodal (dashed curve, left), the zero-layer adsorption spinodal (dashed curve, right) and the gas branch of the bulk liquid–gas binodal (dotted curve). The point where the layering binodal crosses the bulk liquid–gas binodal is the first layering transition at bulk coexistence (filled circle). The point where the zero-layer adsorption spinodal line hits the bulk binodal is the zero-layer spinodal point at bulk coexistence (open circle), according to Brader *et al* [31]. Both spinodals and the binodal terminate at the layering critical point (filled diamond) located off bulk coexistence in the one-phase gas region. Note that the one-layer desorption spinodal runs entirely in the one-phase gas region and hence does not cross the bulk binodal. The inset shows the colloid adsorption, $\Gamma_c \sigma_c^2$, of the coexisting zero-layer and one-layer states (along the layering binodal) as a function of the polymer reservoir packing fraction, η_p^r ; the dividing surface is chosen at $z = \sigma_c/2$ (the lower bound of the integral in equation (6)). The symbols are obtained from DFT, the full curve is the fit (see the text) and the arrow at the horizontal axis denotes the estimated value of η_p^r at the layering critical point.

layering phase transition in the stable gas region and that in the two-phase region where the gas is metastable. In the following, we consider the three different surface phase transition lines, i.e. the adsorption spinodal, layering binodal and desorption spinodal, and their relation to the bulk binodal. First, the crossing point of the adsorption spinodal and the bulk liquid–gas binodal denotes the spinodal point terminating the metastability region of the zero-layer state upon reducing η_p^r at bulk coexistence. This corresponds to the adsorption spinodal point of the contact angle (see figure 5), as located previously by Brader *et al* (as well as other adsorption spinodal points at bulk coexistence for different size ratios, $q = 0.6, 0.7, 1$). Our numerical value of η_p^r agrees well with that of [31]. Second, the point of crossing between the layering binodal and bulk binodal is the layering transition at bulk coexistence (accompanied by a kink in the contact angle, as outlined above). This state point can be seen as a triple point between the bulk liquid and two different surface states of the bulk gas. The location of this triple point is quite different from the adsorption spinodal point at bulk coexistence. Although hysteresis for a path at constant η_p^r is small, this is not the case for the path along bulk coexistence, due to the fact that the gas branch of the bulk binodal and the layering (spinodal and binodal) lines have very similar slopes. Hence the location of any crossing point is very sensitive to the precise location of the individual lines. Third, in striking contrast to the previous two cases, the desorption spinodal *does not* cross the bulk binodal, but remains in the one-phase gas region for increasing values of η_p^r . We have checked this for one additional path at $\eta_p^r = 2$, starting with a one-layer profile at bulk coexistence and decreasing η_c and indeed found the

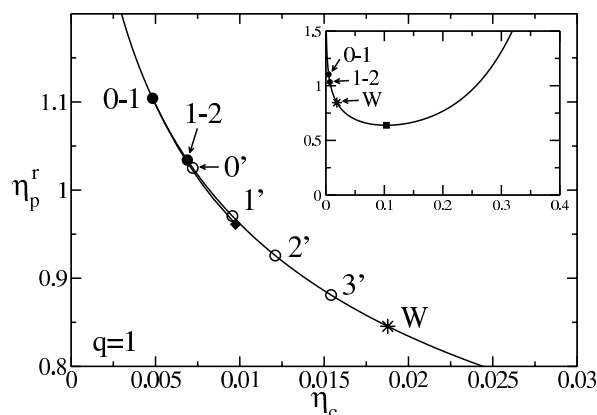


Figure 8. A summary of the known features of the surface phase diagram of the AO model at a hard wall for size ratio $q = 1$ as a function of the colloid packing fraction, η_c , and polymer reservoir packing fraction, η_p^r . Shown are the gas branch of the bulk binodal (full curve) and equilibrium first (filled circle, marked 0–1) and second (filled circle, marked 1–2) layering transitions at bulk coexistence, as obtained from the present work. The first layering critical point (diamond) is connected via the layering binodal line (full curve) to the first layering transition at bulk coexistence. The spinodal lines are omitted for clarity. The zero-, one-, two-, three-layer adsorption spinodal points at bulk coexistence (open circles, marked 0', 1', 2' and 3' respectively) and the wetting transition (star, marked W) are taken from [31]. The inset shows some of the data together with the bulk critical point (large filled square) on a larger scale.

desorption spinodal point in the one-phase gas region. This behaviour is consistent with the behaviour of the contact angle, which we discussed above for $q = 0.6$ and 1, and where adsorption spinodal points were found upon decreasing η_p^r , but no desorption spinodal points were found upon increasing η_p^r . Although we have determined this scenario only extensively for the first layering transition for $q = 1$, we believe it to hold more generally for higher layering transitions and other size ratios.

In order to summarize our present results and those of [31] for the layering transitions of the AO model at a hard wall, we draw the surface phase diagram for $q = 1$ in figure 8. The results for the n -layer adsorption spinodal points for $n = 0, 1, 2, 3$ at bulk coexistence are taken from [31]. At bulk coexistence, the first and the second layering binodal points are located at higher fugacities compared to the corresponding zero-layer and one-layer adsorption spinodal points, respectively. Higher layering transitions, corresponding to two- and three-layer spinodal points of Brader *et al* do not emerge from our present data. On the other hand, Brader *et al* have not found layering lines extending into the bulk gas phase for $q = 1$, which we have located for the first layering transition. We have not searched for a similar layering line in the case of the second layering transition. However, from the topology of the first layering transition, which we established above, and taking into account the considerable separation of the second layering binodal and the one-layer adsorption spinodal points at bulk coexistence, it seems plausible that such a layering binodal line also exists for the second layering transition.

Next, we compare our results to those from simulations by Dijkstra and van Roij for $q = 1$ [21]. They find different regimes of complete and partial wetting, and first, second and third layering transitions located off bulk coexistence. Our results for the first layering binodal line extending into the one-phase gas region are in qualitative agreement with their findings. Previous comparisons with DFT results [31] left a puzzle, because a layering line was found for $q = 0.6$, but not for $q = 1$. The length of this first layering binodal line obtained from

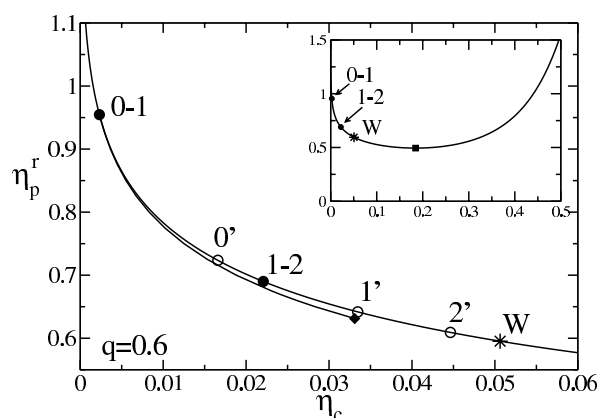


Figure 9. As figure 8, but for $q = 0.6$. The zero-layer adsorption spinodal [30, 31] connecting state point $0'$ with the surface critical point (diamond) is omitted for clarity.

DFT is considerably larger (in the range of η_p^r) than that found in simulations [21]. With hindsight, this deviation seems consistent with that in other situations, as too small values for the critical polymer fugacities compared to simulations are also found in bulk (see e.g. [23]) or in confinement in planar capillaries [45, 46]. We have not obtained results for the higher- n layering binodal lines, so we cannot compare the DFT for $n > 1$ efficiently with simulations. Nevertheless, the overall agreement is good and the DFT seems to capture all relevant effects: i.e. the layering transitions at bulk coexistence, a layering line extending into the one-phase region and a wetting transition [31]. Given the approximate nature of the free energy functional and the fact that the surface phase transitions are governed by tiny free energy differences, this is quite remarkable.

Coming back to $q = 0.6$, we summarize our results and that of Brader *et al* [30, 31] in figure 9. Similar to the case for $q = 1$, the first and second layering transitions at bulk coexistence are located at higher fugacities than the corresponding zero-layer and one-layer adsorption spinodal points, respectively. The effect, however, is more dramatic than for $q = 1$; see figure 8. Brader *et al* have also found a two-layer adsorption spinodal point, indicating the existence of a third layering transition, whose binodal we have not been able to locate. We have also determined the first layering line extending into the bulk gas phase and find it to be remarkably long. The location of the critical point is determined with the same fitting procedure as described above for the first layering transition for $q = 1$. The large separation along the bulk binodal of the second layering transition and the one-layer adsorption spinodal point suggests again the presence of a second layering line.

5. Conclusion

In conclusion, we have investigated the contact angle, θ , of the (colloidal) liquid–gas interface and a hard wall using the AO model colloid–polymer mixture and considering two different polymer-to-colloid size ratios, $q = 0.6$ and 1. Our results for θ are obtained via Young’s equation from independent numerical DFT calculations of the liquid–gas, the wall–gas and the wall–liquid interfacial free energies at bulk coexistence. At the planar wall–gas interface at bulk coexistence, we identify a range of different metastable states each corresponding to a number of adsorbed colloid layers at the wall. We argue that the globally stable state

corresponds to the lowest wall–gas interface tension, and therefore possesses the largest value of θ . For small density differences of the coexisting liquid and gas, i.e. close to the bulk critical point, the wall is completely wetted by colloidal liquid [30, 31] and, hence, $\theta = 0$. Moving along bulk coexistence, away from the critical point, the wetting transition [30, 31] is crossed, and θ becomes non-zero. However, typical values of θ remain very small over a considerable range of state points in the partial wetting regime. Mediated by a sequence of first-order layering transitions at the wall–gas interface, the contact angle grows upon moving further from the critical point and reaches typical values up to $\sim 35^\circ$. These layering transitions of the coexisting colloidal gas in contact with the wall appear as discontinuities in the slope of θ as a function of a thermodynamic control parameter, e.g. the polymer reservoir packing fraction or the colloid packing fraction difference between the two coexisting bulk phases.

Previous difficulties in measuring the contact angle accurately [7] have been overcome by Aarts and Lekkerkerker with the use of confocal scanning laser microscopy [9] in a system with $q = 0.56$. The authors conclude that $\theta = 0$ for all state points considered, consistent with their direct observation of a prominent colloid wetting film at the interface of the bulk gas with the wall. They point out that actual values of θ are very sensitive to the precise determination of the location of the wall. Large values of contact angles as well as the observation of the transition to complete wetting have been reported by Wijting *et al* [10, 11], using extrapolation of dynamical measurements (i.e. moving the wall) to zero velocity. However, some reservations have been voiced with respect to the latter results [9]. The magnitude of the contact angle results from subtle differences between the interface tensions and we do not expect our present results to resolve experimental issues. The contact angles which we have calculated for the highly idealized AO model in contact with a hard wall can therefore only serve as a reference case. Important effects due to more realistic polymer–polymer interactions [34], polydispersity and gravity are not captured in our present model (see [31] for a discussion).

We have also reconsidered the surface phase behaviour of the AO model colloid–polymer mixture at a hard wall. This system is known to exhibit a sequence of first-order layering transitions upon following the gas branch of the liquid–gas bulk binodal towards the bulk critical point (i.e. reducing η_p^r). In addition, layering lines extending off bulk coexistence into the one-phase gas region have been located. Such a layering transition is characterized by a jump in the colloid adsorption at the wall and can be identified as the growth of an additional colloid layer at the wall–gas interface [21, 30, 31]. For one specific case, the first layering transition for size ratio $q = 1$, we have determined the layering binodal, which gives the equilibrium location of the transition, to high accuracy. In addition, we have located the zero-layer adsorption spinodal line, beyond which (for higher η_c at constant η_p^r) the zero-layer state is unstable and the one-layer desorption spinodal line, marking the end of stability of the one-layer state (i.e. for lower η_c at constant η_p^r). The layering binodal and the adsorption and desorption spinodal lines end at a critical point, located in the single-phase gas region of the bulk phase diagram. The crossing point of the layering binodal and the bulk binodal represents a triple point between the bulk liquid and the two layered states (0 and 1 layers) of the bulk gas which have different values of adsorption of the two components. We find the location of this triple point to differ substantially from the (previously identified [30, 31]) crossing point of the adsorption spinodal and the bulk binodal. Remarkably, we could not find a crossing point of the desorption spinodal and the bulk binodal and its absence gives rise to continued (meta)stability of the one-layer state upon increasing η_p^r at coexistence. We believe that this scenario holds for higher layering transitions and other size ratios. We have presented further results for the second layering transition for $q = 1$ as well as for first and second layering transitions for $q = 0.6$. The order of the wetting transition and whether it occurs via an infinite or a finite sequence of layering transitions remain open questions. Whether

the occurrence of layering transitions is specific to the AO model (see also [31] for a more extensive discussion) or would be present in more realistic descriptions of colloid–polymer mixtures is another interesting question. However, any experimental attempt to reveal such (layering) phase behaviour would require exceptional accuracy for determining θ or resolution on the particle level for direct observation.

Acknowledgments

D G A L Aarts is thanked for pointing out the relevance of the wall contact angle of the colloidal liquid–gas interface to us. We acknowledge useful discussions and correspondence with R Evans, J M Brader, R Roth and M Dijkstra. R Evans is also thanked for critically reading what turned out to be a preliminary version of our manuscript and R Roth for an independent check of numerical results. This work is financially supported by the SFB-TR6 programme ‘Physics of colloidal dispersions in external fields’ of the *Deutsche Forschungsgemeinschaft* (DFG). The work of MS is part of the research programme of the *Stichting voor Fundamenteel Onderzoek der Materie* (FOM), which is financially supported by the *Nederlandse Organisatie voor Wetenschappelijk Onderzoek* (NWO).

References

- [1] Poon W C K 2002 *J. Phys.: Condens. Matter* **14** R859
- [2] Tuinier R, Rieger J and de Kruif C G 2003 *Adv. Colloid Interface Sci.* **103** 1
- [3] Löwen H 2001 *J. Phys.: Condens. Matter* **13** R415
- [4] de Hoog E H A and Lekkerkerker H N W 1999 *J. Phys. Chem. B* **103** 5274
- [5] de Hoog E H A, Lekkerkerker H N W, Schulz J and Findenegg G H 1999 *J. Phys. Chem. B* **103** 10657
- [6] Chen B-H, Payandeh B and Robert M 2000 *Phys. Rev. E* **62** 2369
- [7] Chen B-H, Payandeh B and Robert M 2001 *Phys. Rev. E* **64** 042401
- [8] Aarts D G A L, van der Wiel J H and Lekkerkerker H N W 2003 *J. Phys.: Condens. Matter* **15** S245
- [9] Aarts D G A L, Schmidt M and Lekkerkerker H N W 2004 *Science* **304** 847
- [10] Aarts D G A L and Lekkerkerker H N W 2004 *Proc. CODEF Conf.; J. Phys.: Condens. Matter* **16** S4231
- [11] Wijting W K, Besseling N A M and Cohen Stuart M A 2003 *Phys. Rev. Lett.* **90** 196101
- [12] Wijting W K, Besseling N A M and Cohen Stuart M A 2003 *J. Phys. Chem. B* **107** 10565
- [13] Asakura S and Oosawa F 1954 *J. Chem. Phys.* **22** 1255
- [14] Asakura S and Oosawa F 1958 *J. Polym. Sci.* **33** 183
- [15] Vrij A 1976 *Pure Appl. Chem.* **48** 471
- [16] Gast A P, Hall C K and Russell W B 1983 *J. Colloid Interface Sci.* **96** 251
- [17] Lekkerkerker H N W, Poon W C K, Pusey P N, Stroobants A and Warren P B 1992 *Europhys. Lett.* **20** 559
- [18] Meijer E J and Frenkel D 1991 *Phys. Rev. Lett.* **67** 1110
- [19] Meijer E J and Frenkel D 1994 *J. Chem. Phys.* **100** 6873
- [20] Dijkstra M, Brader J M and Evans R 1999 *J. Phys.: Condens. Matter* **11** 10079
- [21] Bolhuis P G, Louis A A and Hansen J-P 2002 *Phys. Rev. Lett.* **89** 128302
- [22] Dijkstra M and van Roij R 2002 *Phys. Rev. Lett.* **89** 208303
- [23] Vink R L C and Horbach J 2004 *Preprint cond-mat/0310404*
- [24] Vink R L C and Horbach J 2004 *Proc. CODEF Conf.; J. Phys.: Condens. Matter* **16** S3807
- [25] Dzubiella J, Jusufi A, Likos C N, von Ferber C, Löwen H, Stellbrink J, Allgaier J, Richter D, Schofeld A B, Smith P A, Poon W C K and Pusey P N 2001 *Phys. Rev. E* **64** 010401
- [26] Vrij A 1997 *Physica A* **235** 120
- [27] Brader J M and Evans R 2000 *Europhys. Lett.* **49** 678
- [28] Brader J M, Dijkstra M and Evans R 2001 *Phys. Rev. E* **63** 041405
- [29] Schmidt M, Löwen H, Brader J M and Evans R 2000 *Phys. Rev. Lett.* **85** 1934
- [30] Schmidt M, Löwen H, Brader J M and Evans R 2002 *J. Phys.: Condens. Matter* **14** 9353
- [31] Brader J M, Evans R, Schmidt M and Löwen H 2002 *J. Phys.: Condens. Matter* **14** L1
- [32] Brader J M, Evans R and Schmidt M 2003 *Mol. Phys.* **101** 3349
- [33] Wessels P P F, Schmidt M and Löwen H 2004 *J. Phys.: Condens. Matter* **16** L1

S4184

P P F Wessels *et al*

-
- [33] Fortini A *et al* 2004 in preparation
- [34] Aarts D G A L, Dullens R P A, Lekkerkerker H N W, Bonn D and van Roij R 2004 *J. Chem. Phys.* **120** 1973
- [35] Rowlinson J S and Widom B 2002 *Molecular Theory of Capillarity* 1st edn (New York: Dover)
- [36] Sullivan D E and Telo da Gama M M 1986 Wetting transitions and multilayer adsorption at fluid interfaces *Fluid Interfacial Phenomena* ed C A Croxton (New York: Wiley) p 45
- [37] Dietrich S 1988 Wetting phenomena *Phase Transitions and Critical Phenomena* vol 12, ed C Domb and J L Lebowitz (London: Academic) p 1
- [38] Evans R 1992 *Fundamentals of Inhomogeneous Fluids* ed D Henderson (New York: Dekker) chapter 3 (Density Functionals in the Theory of Nonuniform Fluids) p 85
- [39] Broyles A A 1960 *J. Chem. Phys.* **33** 456
- [40] Evans R, Henderson J R, Hoyle D C, Parry A O and Sabeur Z A 1993 *Mol. Phys.* **80** 755
- [41] Evans R, Leote de Carvalho R J F, Henderson J R and Hoyle D C 1994 *J. Chem. Phys.* **100** 591
- [42] Henderson J R 1994 *Phys. Rev. E* **50** 4836
- [43] Schmidt M, Dijkstra M and Hansen J P 2004 unpublished
- [44] Brader J M and Evans R 2004 private communication
- [45] Schmidt M, Fortini A and Dijkstra M 2003 *J. Phys.: Condens. Matter* **48** S3411
- [46] Schmidt M, Dijkstra M and Hansen J P 2004 *Proc. CODEF Conf.; J. Phys.: Condens. Matter* **16** S4185

Direct Visual Observation of Thermal Capillary Waves

Dirk G. A. L. Aarts,^{1*} Matthias Schmidt,^{2†}
Henk N. W. Lekkerkerker¹

We studied the free fluid-fluid interface in a phase-separated colloid-polymer dispersion with laser scanning confocal microscopy and directly observed thermally induced capillary waves at the interface in real space. Experimental results for static and dynamic correlation functions validate the capillary wave model down to almost the particle level. The ultralow interfacial tension, the capillary length, and the capillary time are found to be in agreement with independent measurements. Furthermore, we show that capillary waves induce the spontaneous breakup of thin liquid films and thus are of key importance in the process of droplet coalescence.

At rest, the free interface between any two fluids, like that between a liquid and its vapor, appears to be smooth. Yet thermal motion inevitably gives rise to statistical fluctuations of the local interface position, leading to a rough interface. This phenomenon was first predicted by von Smoluchowski in 1908 (*1*); 5 years later, Mandelstam quantitatively described the interface roughness in terms of thermally excited capillary waves (*2*). These capillary waves have been studied with light (*3*) and x-ray scattering (*4–8*). They play an important role in modern theories of interfaces (*9–11*) and have been argued to be essential in the rupture of thin liquid films (*12, 13*), as occurs in droplet coalescence. We show how to tune length and time scales with the use of colloidal suspensions, such that the fluctuating fluid-fluid interfaces can be seen directly in real space with a resolution comparable to the particle size. Moreover, the droplet coalescence event can be observed down to the scale of capillary fluctuations in quasi slow motion.

In the capillary wave spectrum, each Fourier component $h_{\mathbf{k}}$ of the interface displacement contributes according to the equipartition theorem

$$\langle |h_{\mathbf{k}}|^2 \rangle = \frac{k_B T}{\gamma L^2} \frac{1}{k^2 + \xi^{-2}} \quad (1)$$

¹Van't Hoff Laboratory, Debye Institute, Utrecht University, Padualaan 8, 3584 CH Utrecht, Netherlands.
²Soft Condensed Matter, Debye Institute, Utrecht University, Princetonplein 5, 3584 CC Utrecht, Netherlands.

*To whom correspondence should be addressed. E-mail: d.g.a.l.aarts@chem.uu.nl

†On leave from Institut für Theoretische Physik II, Heinrich-Heine-Universität Düsseldorf, Universitätsstraße 1, D-40225 Düsseldorf, Germany.

leading to an interface roughness proportional to $\sqrt{k_B T/\gamma}$. Here, γ is the interfacial tension between the two fluids, k_B is the Boltzmann constant, T is absolute temperature, L is the lateral system size, k is the absolute value of the wave vector \mathbf{k} , the angle brackets denote a thermal average, and ξ is the lateral correlation length (capillary length), defined as

$$\xi = \sqrt{\gamma/(g\Delta\rho)} \quad (2)$$

where g is Earth's acceleration and $\Delta\rho$ is the mass density difference between the two phases. In molecular fluids, γ is on the order of 10 to 100 mN/m and $\Delta\rho$ is about 10^2 to 10^3 kg/m³. Therefore, the interface roughness is ~ 0.3 nm, whereas the correlation length is ~ 3 mm, resulting in extreme roughness–correlation length ratios of 10^{-7} ; such ratios are only accessible through scattering techniques. Here we exploit the scaling up of lengths when going from molecules to mesoscopic colloidal particles (diameter ~ 100 nm) to directly observe capillary waves in real space.

Adding polymer to a colloidal suspension may induce a fluid-fluid demixing transition that is widely accepted to be the mesoscopic analog of the liquid-gas phase transition in atomic substances (*14*). The coexisting phases are a colloidal liquid (rich in colloid and poor in polymer) and a colloidal gas (poor in colloid and rich in polymer). The origin of the phase separation lies in the entropy-driven attraction between the colloids, which is mediated by the polymers (*15, 16*). It is known from experiment (*17–19*) and theory (*20–22*) that in such systems the interfacial tension scales as $\gamma \sim k_B T/d^2$, where d is the particle size, leading to ultralow values for γ (~ 1 μ N/m and below). This in turn implies that using colloidal suspensions scales up the interface roughness and simultaneously

scales down the correlation length. With the current system (see below), we successfully bring both into the μ m regime. In addition, the interplay between ultralow interfacial tension and relatively large viscosity, η , sets the capillary velocity γ/η [see, e.g., (*23*)] in the range of μ m/s, as opposed to typical velocities on the order of 10 m/s in molecular fluids. The associated characteristic time for the decay of interfacial fluctuations, which we refer to as the capillary time

$$\tau = \xi\eta/\gamma \quad (3)$$

becomes on the order of seconds in the case of colloids. The capillary velocity also sets the time in droplet coalescence (*24*). Thus, through the appropriate choice of the colloid diameter, we can trace both the statics and dynamics of the capillary waves at a free interface and fully explore the coalescence events with optical microscopy.

We used fluorescently labeled poly(methylmethacrylate) (PMMA) colloidal spheres (*25*) with radius $R_c = 71$ nm (obtained from static light scattering) and size polydispersity of less than 10%. The polymer was commercially available polystyrene (Fluka) with molecular weight $M_w = 2 \times 10^6$ g mol⁻¹ ($M_w/M_n < 1.2$, where M_n is number-average molecular weight) and radius of gyration $R_g \sim 44$ nm [estimated from data in the literature (*26*)]. Thus, the size ratio, $R_g/R_c = 0.6$, was sufficiently large to obtain stable fluid-fluid demixing (*27*). Both species were dispersed in cis/trans-decalin, and because all densities were known, mass fractions could be directly converted to packing fractions of colloids, $\phi_c = 4/3\pi R_c^3 n_c$, and polymers, $\phi_p = 4/3\pi R_g^3 n_p$, where n_c and n_p are the number densities of colloids and polymers, respectively. Samples were prepared by mixing colloid and polymer stock dispersions and diluting with decalin to control the overall packing fractions ϕ_c and ϕ_p . Large glass cuvettes (volume ~ 1 cm³) with very thin cover glass walls (0.17 mm) were used. A confocal scanning laser head (Nikon C1) was mounted on a horizontally placed light microscope (Nikon Eclipse E400). Each measurement was done after 1 day of equilibration. We checked that the system was well equilibrated by following the recovery of intensity after bleaching a space region in the gas and/or liquid phase. The recovery appeared to be governed solely through diffusion of particles without any indications of drift (e.g., through convection). Data sets were acquired at many different state points following several dilution lines. The underlying phase diagram is shown in Fig. 1.

REPORTS

Pictures such as those in Fig. 2 represent an intensity distribution of fluorescent light, $I(x, z, t)$ at a certain time t , with x the horizontal (along the interface) and z the vertical (opposite to gravity) components of the space vector. The microscope records the fluorescence of excited dye within the colloids, hence the colloid-rich (liquid) phase appears bright and the colloid-poor (gas) phase appears dark. $I(x, z, t)$ is a direct measure of the local and instantaneous distribution of colloidal particles and provides the starting point for a statistical analysis. Because of the finite resolution (2δ), we can access length scales of $\sim 2R_c$; we neglect effects induced by the finite time needed to scan each frame, and we take I as an instantaneous snapshot (justified by comparing the colloid self-diffusion time with the scanning time). Thus, the real-space pictures in Fig. 2 show the structure of a gas-liquid interface practically at the particle scale. We rely on the concept of a local interface between both phases. In the spirit of a Gibbs dividing surface, we define an interface position $h(x, t)$ such that in one column of vertical length L_z the total intensity can be written as

$$\int_0^{L_z} dz I(x, z, t) = I_{\text{liq}}(x)h(x, t) + I_{\text{gas}}(x)[L_z - h(x, t)] \quad (4)$$

where $I_{\text{gas}}(x)$ and $I_{\text{liq}}(x)$ are the average bulk intensities in the gas and liquid phase, respectively, and are taken to be functions of x to account for the microscope objective properties. In practice, integrals in the notation are sums over pixels, and we have checked that the results of the subsequent analysis do not depend sensitively on the precise definitions of I_{gas} and I_{liq} . The resulting "height" function $h(x)$ (yellow line in Fig. 2) describes the interface position quite accurately. From top to bottom in Fig. 2 we approach the critical point, and both the capillary waves and density fluctuations increase while the density (intensity) difference between the two phases decreases.

For each frame the average interface position is $\bar{h}(t) \equiv \langle h(x', t) \rangle$, in which the angle brackets denote averages over primed quantities. The time-dependent height-height correlation function is constructed as

$$g_h(x, t) = \langle [h(x', t') - \bar{h}(t')][h(x' + x, t' + t) - \bar{h}(t' + t)] \rangle \quad (5)$$

The corresponding static correlation function, $g_h(x) \equiv g_h(x, t = 0)$, is obtained (5) by Fourier-transforming Eq. 1 as

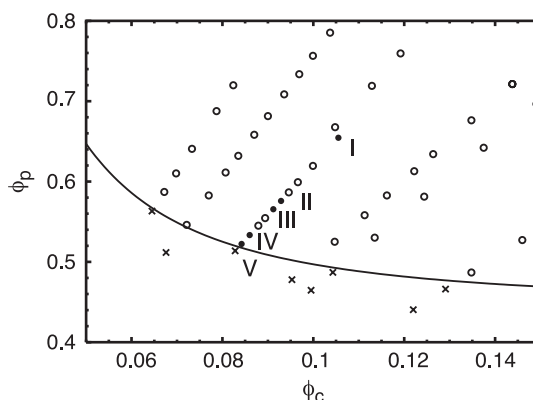


Fig. 1. Phase diagram in (ϕ_p, ϕ_c) representation. Indicated are state points where gas-liquid phase separation occurs (open and solid circles) and state points in the one-phase region (crosses). The line is an estimate of the binodal and is drawn to guide the eye. State points I to V (solid circles) are indicated.

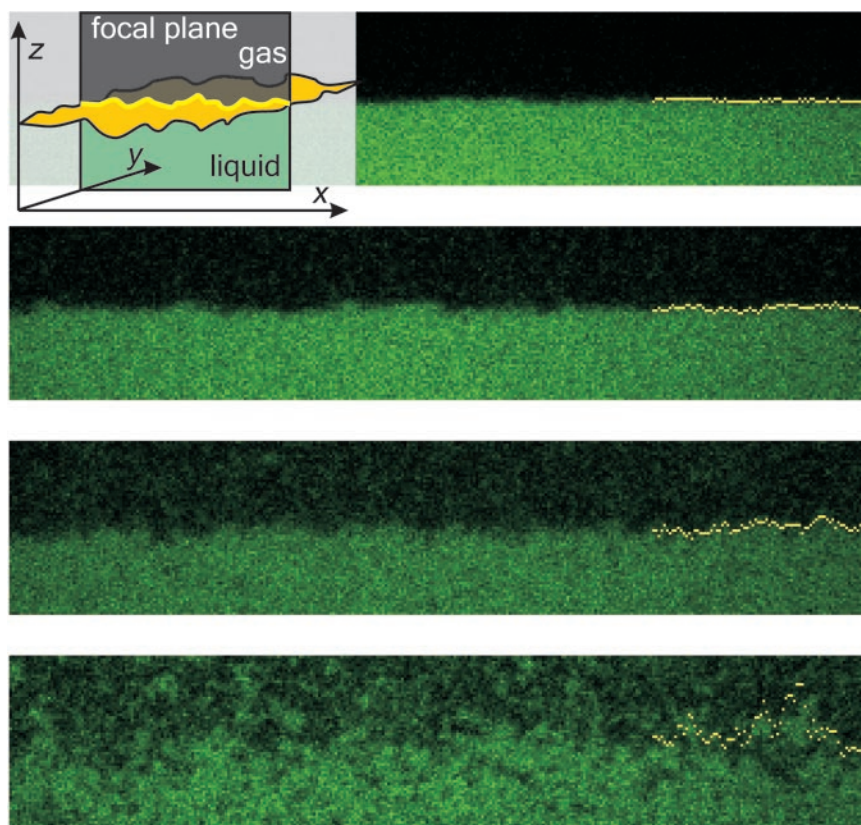


Fig. 2. Capillary waves at the free liquid-gas interface in a phase-separated colloid-polymer mixture imaged with laser scanning confocal microscopy (LSCM) at four different state points approaching the critical point (from top to bottom: state points I, III, IV, and V; see Fig. 1). The focal (viewing) plane is perpendicular to the interface, and only a very thin slice (thickness $\sim 0.6 \mu\text{m}$) is imaged (see inset). Gravity points downward; each image is $17.5 \mu\text{m}$ by $85 \mu\text{m}$. Thermally excited capillary waves corrugate the interface and their amplitude increases upon approaching the critical point. The yellow lines indicate the surface location $h(x)$ obtained with our method. See also movies S1 and S2 of the rough interfaces of state points III and IV.

$$g_h(x) = \frac{k_B T}{2\pi\gamma} K_0(x/\xi) \quad (6)$$

where K_0 is the modified Bessel function of the second kind as a function of x/ξ . Equation 6 holds for distances x larger than a small-distance cutoff on the order of the particle size. Capillary wave theory in the overdamped regime (29, 30) predicts modes with wave vector \mathbf{k} to decay according to $\exp[-t(\gamma k + g\Delta\rho/k)/\eta]$. Introducing $\bar{k} = \xi k$, the dynamical cor-

relation function at fixed position, $g_h(t) \equiv g_h(x = 0, t)$, can be expressed as

$$g_h(t) = \frac{k_B T}{2\pi\gamma} \int_0^\infty d\bar{k} \bar{k} \frac{\exp[-(\bar{k} + \bar{k}^{-1})t/\tau]}{1 + \bar{k}^2} \quad (7)$$

where τ is as given in Eq. 3 with $\eta = \eta_{\text{liq}} + \eta_{\text{gas}}$, the sum of the viscosities of the (colloidal) liquid and gas phase (29, 30).

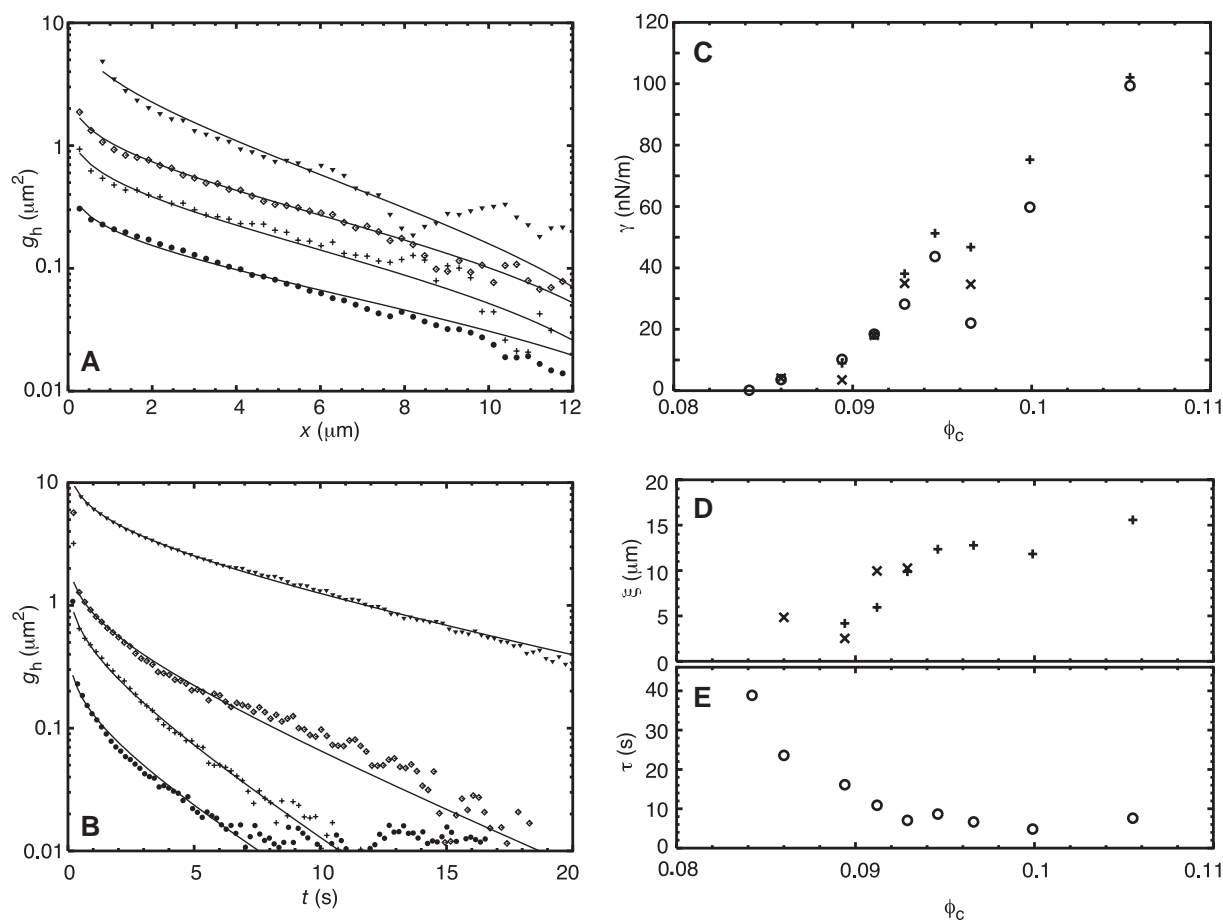
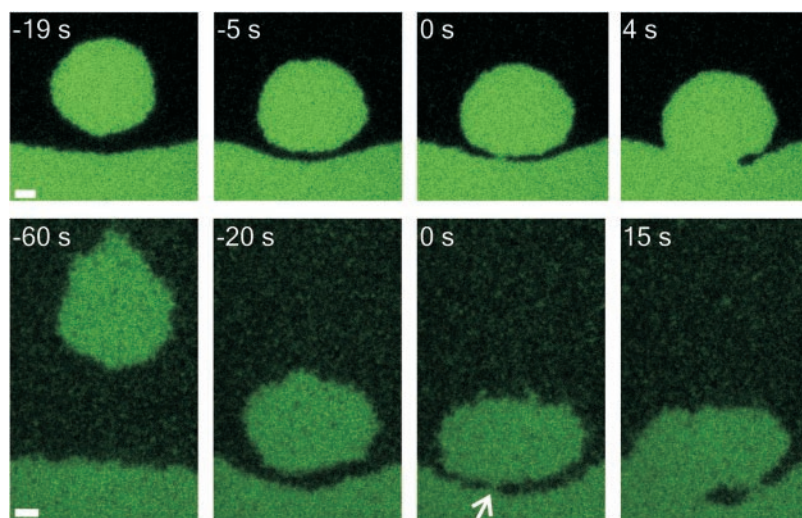


Fig. 3. Correlation functions characterizing the free (colloid) liquid-gas interface as obtained from quantitative analysis of LSCM pictures. **(A)** Static height-height correlation function $g_h(x)$ as a function of the (lateral) distance x for state points I, II, III, and IV (from bottom to top) approaching the critical point. Experimental results (symbols) are compared with predictions from the capillary wave model (lines). **(B)** Dynamical height-height correlation function at fixed position, $g_h(t)$, as a

function of time t again for state points I to IV (from bottom to top). **(C)** Interfacial tension γ as a function of the overall colloid packing fraction ϕ_c obtained from $g_h(x)$ (crosses, slow frame rate; pluses, fast frame rate) and $g_h(t)$ (circles). **(D)** Capillary length ξ as a function of ϕ_c obtained from $g_h(x)$. **(E)** Capillary time τ as a function of ϕ_c obtained from $g_h(t)$. Results displayed in (C) to (E) stem from state points on the same dilution line as state points I to V.

Fig. 4. Coalescence of colloidal liquid droplets with the bulk liquid phase. Occasionally, droplets that have condensed in the upper gas phase (during the final stages of phase separation) sediment toward the interface. The viewing setup is as shown in the inset of Fig. 2; scale bar, 5 μm . Top row, coalescence of a droplet of diameter $\sim 16.5 \mu\text{m}$ for state point I (far away from the critical point); bottom row, coalescence of a droplet of diameter $\sim 21.8 \mu\text{m}$ for state point IV (close to the critical point). The droplet surface is fluctuating and can be analyzed in a similar fashion as the planar interface. The three consecutive steps of the coalescence event can be followed in time (as indicated, where $t = 0$ corresponds to the instant of film breakup). Clearly, the capillary waves at both interfaces induce the breakup of the confined gas layer. In the series in the bottom row, the arrow denotes the place of film breakup. In this case, a second connection is made and the gas phase is being trapped in the liquid phase. See also movies S3 (corresponding to the top row) and S4 (corresponding to the bottom row) of these coalescence events.



Equations 6 and 7 describe the experimental data points very well, as can be clearly seen in Fig. 3, A and B, for various state points with only two physical parameters (γ , ξ in the static case and γ , τ in the

dynamic case). Results for the interfacial tension, capillary length, and capillary time are displayed in Fig. 3, C to E, respectively. The relation of these quantities through Eq. 3 allows for an independent check of the

consistency of our measurements. For example, for state point I, $\gamma = 100 \text{ nN/m}$, $\xi = 15 \mu\text{m}$, and $\eta_{\text{liq}} + \eta_{\text{gas}} = (30 + 12.6) \text{ mPa}\cdot\text{s}$, leading via Eq. 3 to a capillary time of 6 s. From the dynamical correlation function we find

REPORTS

$\tau = 7$ s. The quality of the fits and the internal agreement validate the capillary wave model down to the particle level.

The role of thermal capillary waves in droplet coalescence has long been a topic of speculation (12, 13). The coalescence event is known to follow three steps: (i) film drainage of the continuous phase between the droplet and the free interface, (ii) breakup of the film, and (iii) extrusion of the droplet material into its bulk phase. Figure 4 displays these steps on the time and length scale of capillary fluctuations. We show two cases: that of a droplet far away from the critical point (top row of Fig. 4) and that of a droplet close to the critical point (bottom row of Fig. 4). In each row, the first and second panels show the drainage step, the third panel the film breakup, and the fourth panel the growth of the neck of the liquid bridge. The well-known Reynolds equation (31) describes the rate of thinning of the film (step 1) and the film drainage becomes very slow at small film thicknesses. The actual breakup of the film (step 2) is elusive in molecular fluids; here it is evident that capillary waves induce the spontaneous breakup, which occurs when two opposite bulges at the two interfaces meet. The probability for such an event depends on the interface roughness and on the interface correlation length and time. Typically, the connection is made at film thicknesses of ~ 1 μm . A rough estimate shows that a fluctuation of 0.5 μm occurs in a couple of seconds. Hence, the breakup itself is a stochastic process dominated by capillary waves, but before and after the breakup, hydrodynamics apply. We observe that the neck of the liquid bridge (step 3) initially grows linearly with time. This initial regime is driven by the interfacial tension (24) and is extremely short in the case of molecular fluids because of the large capillary velocity, but in the present case the typical velocity is many orders of magnitude smaller. We thus see that the extremely low interfacial tension not only reveals the role of capillary waves in coalescence events, but also permits us to probe hydrodynamic regimes that were previously difficult to access in the laboratory.

References and Notes

- M. V. von Smoluchowski, *Ann. Phys.* **25**, 205 (1908).
- L. Mandelstam, *Ann. Phys.* **41**, 609 (1913).
- A. Vrij, *Adv. Colloid Interface Sci.* **2**, 39 (1968).
- M. K. Sanyal, S. K. Sinha, K. G. Huang, B. M. Ocko, *Phys. Rev. Lett.* **66**, 628 (1991).
- M. Tolan *et al.*, *Phys. Rev. Lett.* **81**, 2731 (1998).
- A. K. Doerr *et al.*, *Phys. Rev. Lett.* **83**, 3470 (1999).
- C. Fradin *et al.*, *Nature* **403**, 871 (2000).
- T. Seydel, A. Madsen, M. Tolan, G. Grübel, W. Press, *Phys. Rev. B* **63**, 073409 (2001).
- F. P. Buff, R. A. Lovett, F. H. Stillinger, *Phys. Rev. Lett.* **15**, 621 (1965).
- K. R. Mecke, S. Dietrich, *Phys. Rev. E* **59**, 6766 (1999).

- A. Milchev, K. Binder, *Europhys. Lett.* **59**, 81 (2002).
- A. Vrij, *Discuss. Faraday Soc.* **42**, 23 (1966).
- A. Scheludko, *Adv. Colloid Interface Sci.* **44**, 391 (1967).
- W. Poon, *J. Phys. Cond. Matter* **14**, R859 (2002).
- S. Asakura, F. Oosawa, *J. Chem. Phys.* **22**, 1255 (1954).
- A. Vrij, *Pure Appl. Chem.* **48**, 471 (1976).
- E. H. A. de Hoog, H. N. W. Lekkerkerker, *J. Phys. Chem. B* **103**, 5274 (1999).
- E. H. A. de Hoog, H. N. W. Lekkerkerker, *J. Phys. Chem. B* **105**, 11636 (2001).
- D. G. A. L. Aarts, J. H. van der Wiel, H. N. W. Lekkerkerker, *J. Phys. Cond. Matter* **15**, S245 (2003).
- A. Vrij, *Physica A* **235**, 120 (1997).
- J. M. Brader, R. Evans, *Europhys. Lett.* **49**, 678 (2000).
- J. M. Brader, R. Evans, M. Schmidt, H. Löwen, *J. Phys. Cond. Matter* **14**, L1 (2002).
- R. F. Probst, *Physicochemical Hydrodynamics* (Wiley, Hoboken, NJ, 2003), section 10.2.
- J. Eggers, J. R. Lister, H. A. Stone, *J. Fluid Mech.* **401**, 293 (1999).
- G. Bosma *et al.*, *J. Colloid Interface Sci.* **245**, 292 (2002).
- B. Vincent, *Colloids Surf.* **50**, 241 (1990).
- H. N. W. Lekkerkerker, W. C. K. Poon, P. N. Pusey, A. Stroobants, P. B. Warren, *Europhys. Lett.* **20**, 559 (1992).
- T. Wilson, *Confocal Microscopy* (Academic Press, London, 1990).
- J. Meunier, in *Liquids and Interfaces*, J. Charvolin, J. F. Joanny, J. Zinn-Justin, Eds. (North-Holland, New York, 1988), pp. 327–369.
- U. S. Jeng, L. Esibov, L. Crow, A. Steyerl, *J. Phys. Cond. Matter* **10**, 4955 (1998).
- O. Reynolds, *Philos. Trans. R. Soc. London* **177**, 157 (1886).
- We thank D. Bonn, A. Petukhov, W. Kegel, A. van Blaaderen, and R. Dullens for useful discussions, and M. Dijkstra for her support. This work is part of the research program of the Stichting voor Fundamenteel Onderzoek der Materie (FOM) supported by the Nederlandse Organisatie voor Wetenschappelijk Onderzoek (NWO). Also supported by Deutsche Forschungsgemeinschaft SFB TR6.

Supporting Online Material

www.sciencemag.org/cgi/content/full/304/5672/847/

DC1

Movies S1 to S4

23 February 2004; accepted 17 March 2004

RNA-Mediated Metal-Metal Bond Formation in the Synthesis of Hexagonal Palladium Nanoparticles

Lina A. Gugliotti, Daniel L. Feldheim,* Bruce E. Eaton*

RNA sequences have been discovered that mediate the growth of hexagonal palladium nanoparticles. In vitro selection techniques were used to evolve an initial library of $\sim 10^{14}$ unique RNA sequences through eight cycles of selection to yield several active sequence families. Of the five families, all representative members could form crystalline hexagonal palladium platelets. The palladium particle growth occurred in aqueous solution at ambient temperature, without any endogenous reducing agent, and at low concentrations of metal precursor (100 micromolar). Relative to metal precursor, the RNA concentration was significantly lower (1 micromolar), yet micrometer-size crystalline hexagonal palladium particles were formed rapidly (7.5 to 1 minutes).

Biomaterialization achieves exquisite control over crystal type and hierarchical materials self-assembly with protein biopolymer templates. RNA molecules are also highly structured biopolymers. Given the landmark discovery of in vitro selection (1, 2) and the use of these techniques to discover RNA catalysts that mediate a variety of organic reactions (3–10), we sought to determine whether RNA could serve as a template for inorganic-particle growth. Here we report examples of individual RNA sequences that mediate metal-metal bond formation to create novel inorganic materials.

Conventional methods for controlling metal-metal bond formation and crystal

growth primarily use synthetic polymers. Archetypical examples are the formation of cubic silver and palladium particles using poly(acrylate) (11) or poly(vinylpyrrolidone) templates (12). Smaller multidentate ligands such as trisodium citrate can be used to control crystal shape as well—for example, in the photoinduced conversion of silver nanospheres to triangular prisms (13).

In attempts to mimic natural biomaterialization, proteins and polypeptides have been studied extensively as templates for materials synthesis (14–17). Belcher *et al.* have used phage display techniques to mine for peptides that can bind selectively to various semiconductor crystal faces (18). Knowledge of peptide-surface binding affinity was then used to engineer a virus that could bind and organize semiconductor nanocrystals into well-ordered thin-film assemblies (19). Much less research has focused on the interactions between materials

Department of Chemistry, North Carolina State University, Raleigh, NC 27695, USA.

*To whom correspondence should be addressed. E-mail: bruce_eaton@ncsu.edu (B.E.E.), dan_feldheim@ncsu.edu (D.L.F.)

Laser-induced condensation in colloid–polymer mixtures

INGO O. GÖTZE¹, JOSEPH M. BRADER²†,
MATTHIAS SCHMIDT¹* and HARTMUT LÖWEN¹

¹Institut für Theoretische Physik II, Heinrich-Heine-Universität Düsseldorf,
D-40225 Düsseldorf, Germany

²The James Franck Institute, University of Chicago, South Ellis Ave 5640, Chicago,
IL 60637, USA

(Received 11 October 2002; accepted 22 November 2002)

We study a mixture of hard sphere colloidal particles and non-adsorbing polymers exposed to a plane wave external potential which represents a three-dimensional standing laser field. With computer simulations and density functional theory we investigate the structure and phase behaviour using the simple Asakura–Oosawa model. For varying laser wavelength λ we monitor the emergence of structure in response to the external field, as measured by the amplitude of the oscillations in the one-body density distribution. Between the ideal gas limit for small λ and the bulk limit of large λ there is a non-monotonic crossover that is governed by commensurability of λ and the colloid diameter. The theoretical curves are in good agreement with simulation results. Furthermore, the effect of the periodic field on the liquid–vapour transition is studied, a situation that we refer to as laser-induced condensation. Above a threshold value for λ the theoretical phase diagram indicates the stability of a ‘stacked’ fluid phase, which is a periodic succession (in the beam direction) of liquid and vapour slabs. This partially condensed phase causes a splitting of the liquid–vapour binodal leading to two critical and a triple point. All our predictions should be experimentally observable for colloid–polymer mixtures in an optical resonator.

1. Introduction

When a non-adsorbing polymer is added to a sterically-stabilized colloidal dispersion of spherical particles, an effective attraction between the colloids is generated via the depletion mechanism. This mechanism can be understood qualitatively as follows. Each colloidal particle is surrounded by a polymer depletion zone due to the repulsion between the colloidal surface and the polymer. Close to colloidal contact, two depletion zones overlap, such that the polymers have more accessible volume, i.e. their entropy increases. As a consequence, two colloidal particles effectively attract. The depletion attraction was first studied and explained in a simple model of non-interacting polymers by Asakura and Oosawa (AO) in 1958 [1], and later independently by Vrij [2]. In their model, the colloid–polymer interaction is hard-sphere like with a range $R_c + R_p$ larger than the colloidal radius R_c , where R_p is the radius of gyration of the polymer coils [3]. By inte-

grating out the polymeric degrees of freedom [4–6], an analytical form of the attraction is obtained. One lesson to be learned from this expression is that both the range and the depth of the attraction can be tuned by changing the molecular weight and the concentration of the polymers [7, 8].

The effective attraction causes fluid–fluid demixing of the colloids into a colloid-rich (liquid) and colloid-poor (vapour) phase above a critical polymer concentration. A full quantitative understanding of the demixing transition is meanwhile available and experimental data for fluid–fluid phase coexistence are well understood by theory and simulation. What is less clear in the bulk are kinetics from metastable states as well as the gel and glass transition (for a recent review see [9]).

If colloidal dispersions are exposed to an external field, a wealth of new phenomena occur both in equilibrium and non-equilibrium (for a recent review see [10]). One simple possibility for an external field is a hard planar system wall where the AO model of colloid–polymer mixtures was investigated recently. Building on Rosenfeld’s ideas [11] a density-functional theory (DFT) for the AO model [12, 13] was proposed and near fluid–fluid coexistence, a novel scenario of entropic wetting and a finite sequence of layering transitions was found [14, 15]. This scenario was recently con-

* Author for correspondence. e-mail: mschmidt@thphy.uni-duesseldorf.de. Present address: Soft Condensed Matter, Debye Institut, Utrecht University, Princetonpln 5, 3584 CC Utrecht, The Netherlands.

† Present address: Institute of Physiology, University of Bern, Buehlplatz 5, 3012 Bern, Switzerland.

firmed by computer simulations [16], and there exists also experimental indications [17, 18].

In this paper we study a different kind of external field which can be easily realized in experiments, namely a laser-optical field. This establishes a periodic external potential acting on the colloids of the form

$$U_{\text{ext}}(z) = U_0 \cos(2\pi z/\lambda), \quad (1)$$

where U_0 is the amplitude, λ is the wavelength and z is the spatial coordinate in the beam direction. Research is very active for the freezing transition in similar periodically modulated external potentials (so-called laser-induced freezing). Most of the studies have been done in two dimensions and with mutually repelling colloidal particles. Simultaneously, experiments [19–22], computer simulations [23–25] and theories such as density functional approaches of freezing [26–28] and phenomenological elastic theory [29, 30] have been developed recently. The most striking results are re-entrant melting transitions for increasing U_0 and novel hexatic-type intermediate phases.

However, to the best of our knowledge, a system with attractive interactions—such as the effective attraction generated in a colloid–polymer mixture—has not yet been studied in an external periodic field. This is the aim of the present paper, where we consider a fluid colloid–polymer mixture in an oscillatory potential. We investigate the density profiles caused by the external field, both far away and close to the bulk fluid–fluid phase separation and study them, in particular, as a function of the wavelength λ of the external field (equation (1)) for fixed average densities of both species. Since λ and the particle radii, R_c and R_p , are competing length scales of the problem, interesting behaviour can be expected as one of these variables is changed. For fixed size ratio R_p/R_c we find that there are marked oscillations of the density peak heights as a function of λ provided λ is smaller than about twice the colloid diameter σ_c . These oscillations reflect possible commensurability of λ and σ_c . For λ larger than about $2\sigma_c$, on the other hand, the colloidal density peak height *increases* monotonically with increasing λ . This is in contrast to a polymer-free colloidal system (hard spheres) where the density peak height *decreases* with increasing λ . As explained in detail below these results stem from computer simulations and a recent DFT. In general, we find good agreement between both approaches, hence we trust the theory to correctly describe the system.

Furthermore, we study the bulk liquid–vapour transition in the presence of the external potential (1). It is expected that the presence of the external field will change the phase diagram qualitatively, an effect that we anticipate as *laser-induced condensation*, in analogy

with laser-induced freezing in the case of the liquid–solid transition in a periodic field. The theoretical results for the phase diagram show a splitting of the colloid liquid–vapour binodal. In the colloid chemical potential versus polymer reservoir density representation, an unusual (for fluid states) shaped coexistence curve results, resembling an inverted letter *y*. It features two critical points, one between colloid vapour and a novel phase, the stacked fluid; the other is between stacked fluid and colloid liquid. Naturally, we find a triple point where colloid vapour, colloid liquid and the stacked fluid coexist. It is argued that upon decreasing λ the two critical points merge into a bicritical point. Below the corresponding *finite* value of λ the stacked phase ceases to exist and a single liquid–vapour binodal is recovered.

The paper is organized as follows: in §2 we describe the AO model in an external laser field. The simulation method and the density functional technique are described in §3 and §4, respectively. Results for the density profiles and the phase behaviour are presented and discussed in §5. We conclude in §6.

2. The model

The AO model is a simple idealized model for colloid–polymer mixtures, where the colloids are treated as hard spheres with a diameter $\sigma_c = 2R_c$, and the polymers as interpenetrating, non-interacting particles. The polymers are excluded by a centre-of-mass distance of $(\sigma_c + \sigma_p)/2$ from the colloids, where $\sigma_p = 2R_p$ with R_p the radius of gyration of the polymer. The number of colloids is denoted by N_c , the number of polymers by N_p and the total volume of the sample by V .

In detail, the pair interaction potentials $U_{ij}(r)$ between species $i, j = c, p$ as a function of the centre-to-centre distance r are given by

$$U_{cc}(r) = \begin{cases} \infty, & \text{for } r < \sigma_c, \\ 0, & \text{otherwise,} \end{cases} \quad (2)$$

$$U_{cp}(r) = \begin{cases} \infty, & \text{for } r < R_c + R_p, \\ 0 & \text{otherwise,} \end{cases} \quad (3)$$

$$U_{pp}(r) = 0. \quad (4)$$

Furthermore we consider the external potential $U_{\text{ext}}(z)$ given in equation (1) acting only on the colloids. No external potential is applied directly to the polymers.

Thermodynamic parameters are the packing fractions $\eta_i = \pi N_i \sigma_i^3 / (6V) = \pi \sigma_i^3 \rho_i / 6$ of species $i = c, p$, and we also use the packing fraction η_p^r in an ideal reservoir of polymers that is in chemical equilibrium with the system. The size ratios $q = \sigma_p / \sigma_c$ and λ / σ_c and the strength (relative to the thermal energy) of the external

potential βU_0 are control parameters, where $\beta = 1/(k_B T)$, k_B is the Boltzmann constant and T is absolute temperature.

By integrating out the polymer degrees of freedom the binary AO model can be mapped onto a one-component model with effective interactions [4]. Truncating at the two-body level one arrives at the familiar AO potential. If the distance r of two colloids is smaller than $\sigma_c + \sigma_p$, the polymers are excluded from a region between them, so that the osmotic pressure of the polymers on the opposite sides of the colloids is not compensated, and an effective depletion attraction between colloids is induced. The effective potential $U_{AO}(r)$ between colloids is proportional to the overlap-volume of the excluded volumes [1]:

$$U_{AO}(r) = \begin{cases} \infty, & \text{for } r \leq \sigma_c, \\ -\Pi_p V_{\text{overlap}}(r), & \text{for } \sigma_c < r \leq \sigma_c + \sigma_p, \\ 0, & \text{otherwise,} \end{cases} \quad (5)$$

where $\Pi_p = \rho_p^r k_B T$ is the osmotic pressure of the polymers, where ρ_p^r is the number density in the polymer reservoir. The pairwise overlap-volume V_{overlap} for $\sigma_c < r \leq \sigma_c + \sigma_p$ is given by

$$V_{\text{overlap}}(r) = \left(1 - \frac{3r}{2\sigma_c(1+q)} + \frac{1}{2} \left[\frac{r}{\sigma_c(1+q)} \right]^3 \right) \frac{\pi}{6} \sigma_c^3 (1+q)^3. \quad (6)$$

The effective potential (5) with (6) can be used to treat the mixture as a one-component system with pairwise interactions. This mapping is exact for $q < (2/3^{1/2} - 1) = 0.1547\dots$, where for geometrical reasons only pairwise overlaps occur. When q is above this threshold, there occur higher-body terms, and using only the pairwise contribution is an approximation.

3. Computer simulation method

In order to treat the full model we perform direct Monte Carlo (MC) simulations of the binary mixture, i.e. besides the colloids, we also simulate the polymers explicitly. This is potentially difficult due to the typically large number of polymers, but still possible as the polymers are non-interacting. Using N_c colloids and N_p polymers, the simulation time scales with N_c^2 and $N_c N_p$ (not with N_p^2 due to polymer ideality). Of course, an advantage of the hard interactions is that it is not necessary to calculate the energy; one only needs to check for overlap of particles. If the moved particles overlap with one other, the configuration is rejected, so the search for further overlaps can be aborted. As the colloid-colloid interaction and the colloid-polymer

interaction have different ranges, we employ two Verlet neighbour lists with different Verlet radii in order to optimize the number of particles in each list. We use straightforward canonical simulations, hence fix the numbers of colloids and polymers explicitly. This is easier than (semi-)grandcanonical methods, because inserting additional colloids is prohibited by the polymers, filling the space between the colloids. As we fix η_p in the system, η_p^r is not known *a priori*. This is determined during the simulation by the acceptance probability of inserting (homogeneously distributed) test polymers.

We also perform MC simulations of the effective one-component system of colloids employing only two-body interactions (equations (5) and (6)). These are much faster than the direct simulations of the binary system. As we are interested in $q > 0.1547$, where many-body terms arise in the effective potential, we can quantitatively assess the effect of the higher-order terms by comparing with the direct simulation. The strength of the attraction in the AO pair potential (equation (5)) is ruled by η_p^r . In order to compare with the results from the direct simulation we need to prescribe this value. We do this using the accurate free-volume expression [31].

In more detail, for a given state point we chose corresponding particle numbers of colloids and polymers, $N_c = 300$ and $N_p = 0, 1500, 3000$, respectively, as well as the system volume $V = 1500\sigma_c^3$. We match the box length L_z to be an integer multiple of the wavelength λ , and set the box volume to $V = L_x \times L_y \times L_z$, where L_γ are the box lengths in space direction γ , and $L_x = L_y$. Periodic boundary conditions are used in all three space directions. In the range $\sigma_c \leq \lambda \leq 7.5\sigma_c$ we use $L_z = 4\lambda$. For $0.25\sigma_c \leq \lambda \leq 1.25\sigma_c$ we set $L_z = 12\lambda$, in order to avoid finite size effects in the z direction for these smaller λ values.

In the direct simulation we use 5×10^6 MC cycles to equilibrate the system, and typically $2.5\text{--}5 \times 10^7$ cycles to gather statistics, where one MC cycle consists of one trial move per particle. In the simulation of the effective one-component system the maximum displacement per move can be chosen larger than in the direct simulation, so that less MC cycles are necessary. Here we use 10^6 MC cycles to equilibrate the system, and 10^7 cycles to gather statistics.

4. Density functional theory

In order to study the AO model in an external potential in the framework of DFT one considers the grand potential Ω as a functional of the one-particle density fields $\rho_c(\mathbf{r}), \rho_p(\mathbf{r})$. This is given as

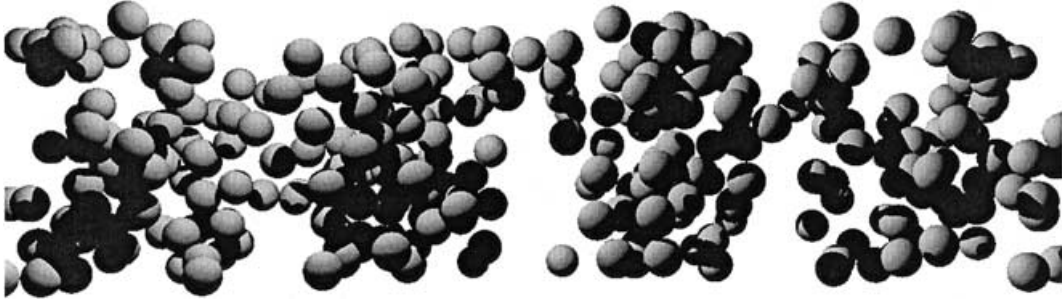


Figure 1. Snapshot of a colloid particle configuration from computer simulation. The polymers are not shown for clarity. The laser beam is along the horizontal direction in the paper plane. Four wavelengths λ are shown, corresponding to figure 2.

$$\begin{aligned} \beta\Omega[\rho_c(\mathbf{r}), \rho_p(\mathbf{r})] = & \sum_{i=c,p} \int d^3r \rho_i(\mathbf{r}) [\ln(\rho_i(\mathbf{r})\Lambda_i^3) - 1 - \beta\mu_i] \\ & + \beta F_{\text{exc}}[\rho_c(\mathbf{r}), \rho_p(\mathbf{r})] \\ & + \int d^3r \rho_c(\mathbf{r}) \beta U_{\text{ext}}(\mathbf{r}), \end{aligned} \quad (7)$$

where Λ_i is the (irrelevant) thermal wavelength and μ_i is the chemical potential of species i . The excess (over ideal gas) Helmholtz free energy F_{exc} arises from interactions between particles and is in general (and in the present case of the AO model) unknown. The crucial benefit of DFT is that F_{exc} is expressed as a functional only of the density profile(s), and that it does not explicitly depend on the external potential(s). This allows one to study different external potentials using the *same* prescription for the excess free energy functional.

Relying on an approximation, we use in the following the fundamental measure DFT for the binary AO model developed in [12, 13]. Here we do not report the details of the approximation; the interested reader is referred directly to [12, 13]. The theory was shown to give the same bulk fluid free energy and hence the same fluid demixing curve as free-volume theory [31], which was recently shown by computer simulations to be remarkably accurate for the AO model [32]. Concerning inhomogeneous situations, both fluid–fluid interfaces and wall adsorption have been considered [14, 15].[†]

5. Results

5.1. Structure

Fluid–fluid demixing is stable with respect to fluid–solid for size ratios of (about) $q \geq 0.35$ [33]. As we are interested primarily in fluid states we stay above this threshold and consider in the following $q = 0.6$. As a typical value for the strength of the external field we

chose $\beta U_0 = 1/2$, hence the difference between minima and maxima of the potential energy is $k_B T$.

The prominent effect of the plane wave external potential $U_{\text{ext}}(z)$ (equation (1)) on the structure is to generate wave-like (non-decaying) one-body distributions $\rho_i(z)$ of both species. To exemplify this (rather straightforward) effect, we show in figure 1 a snapshot and in figure 2 typical results from our computer simulations. The simulation box accommodates four wavelengths of the external potential $U_{\text{ext}}(z)$ (upper panel in figure 2). In response to this influence the colloid profile $\rho_c(z)$ exhibits an ‘out-of-phase’ behaviour, i.e. its maxima coincide with the minima of $U_{\text{ext}}(z)$ and vice versa (see the clustering of particles in figure 1). Of course, this effect occurs already without polymers, i.e. in the pure hard sphere case. The density distribution of added polymers, however, is again *in-phase* with $U_{\text{ext}}(z)$. This is expected as the external potential does

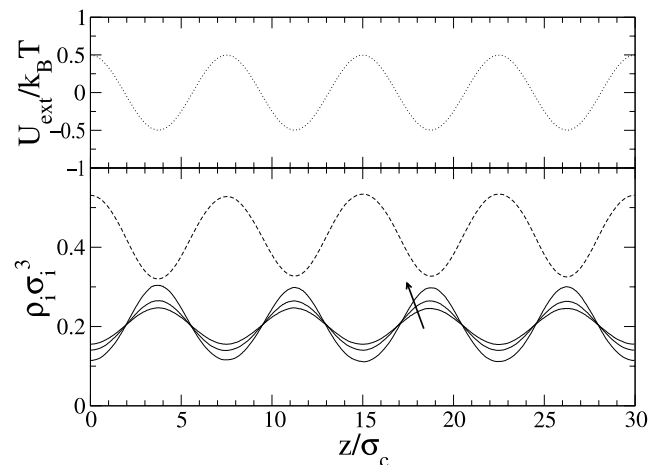


Figure 2. External potential $U_{\text{ext}}(z)$ as a function of z/σ_c (upper panel) and corresponding density profiles $\rho_i(z)$ (lower panel) of colloids (solid lines) and polymers (dashed line) for $\lambda = 7.5\sigma_c$. Average densities are $\rho_c \sigma_c^3 = 0.2$ and increasing $\rho_p \sigma_c^3 = 0, 1, 2$ (indicated by arrow); the polymer profile is only shown for $\rho_p \sigma_c^3 = 2$ for clarity.

[†] As we only deal with z -dependent fluid density profiles in the present study we follow [14, 15] and use the non-tensorial form of the DFT [12].

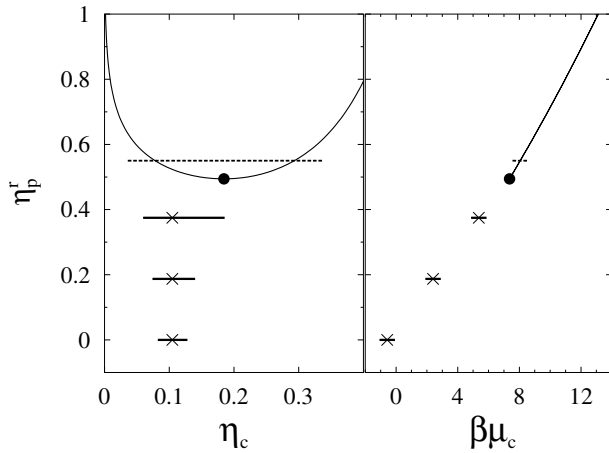


Figure 3. Bulk phase diagram of the AO model for size ratio $q = 0.6$ as a function of polymer reservoir packing fraction η_p^r and colloid packing fraction η_c (left panel) and colloid chemical potential $\beta\mu_c$ (right panel). The vapour–liquid binodal (thin line) and critical point (dot) is shown. Crosses denote the state points where we investigate density profiles. The horizontal bars centred at these state points indicate the variation of the chemical potential along one period of the external field. The dashed bar corresponds to the stacked fluid phase.

not affect directly the polymers, which merely pack in the free space between the colloids. Increasing the polymer concentration leads to an increase of the amplitude of the oscillation in $\rho_c(z)$. Clearly, the minimum and maximum values, defined as

$$\rho_c^{\min} = \min_z \rho_c(z), \quad \rho_c^{\max} = \max_z \rho_c(z), \quad (8)$$

are characteristic measures and we will monitor these below, in particular as a function of λ/σ_c .

Before doing so, we reconsider the bulk phase diagram. In figure 3 we plot the liquid–vapour binodal both as a function of η_c, η_p^r (left panel) and as a function of $\beta\mu_c, \eta_p^r$ (right panel). (In order to fix an arbitrary additive constant to μ_c we use the convention $A_c = \sigma_c$ in equation (7).) We also indicate the state points where we will carry out detailed structural analysis. In the limit of $\lambda/\sigma_c \rightarrow \infty$, a local density approximation is becoming asymptotically exact [34], and hence one can think of locally varying the (bulk) colloid chemical potential. The corresponding variations in μ_c are indicated in figure 3 as horizontal lines. We first examine the (three) cases that are completely inside the one-phase fluid region (hence do not cross the liquid–vapour binodal) and consider the variation with λ while all other parameters (amplitude of the potential, colloid and polymer density and diameters) are kept fixed.

First we consider a pure hard sphere system (i.e. $\eta_p = 0$) with colloid density $\rho_c \sigma_c^3 = 0.2$. In figure 4, results for ρ_c^{\min} and ρ_c^{\max} are plotted as a function of

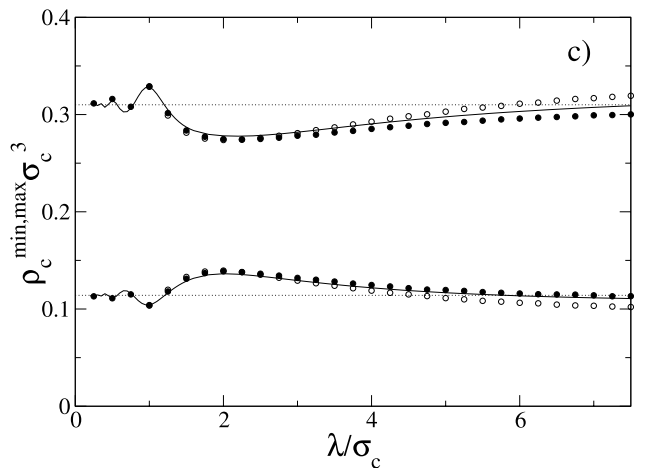
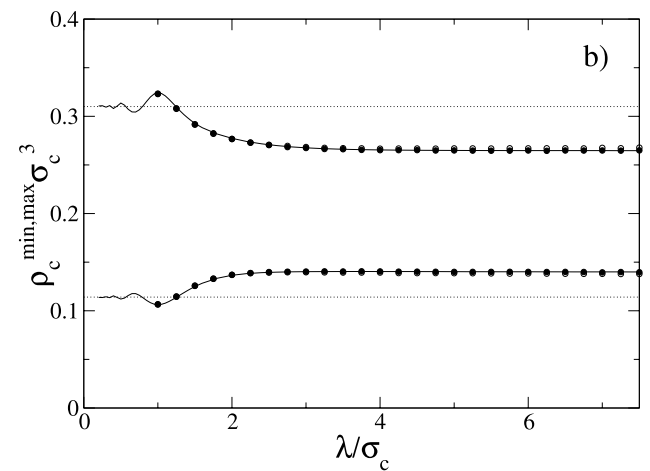
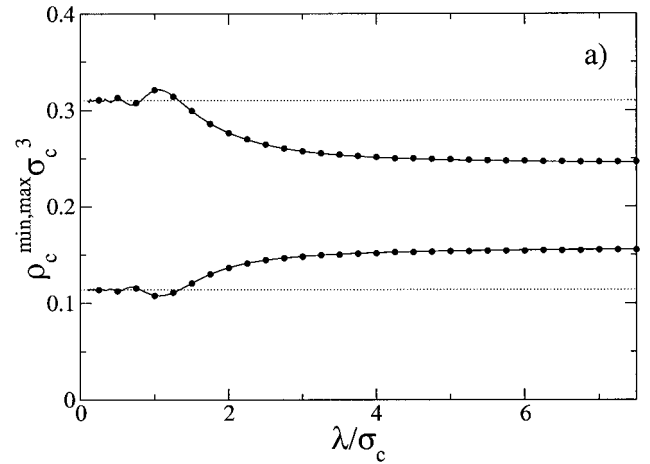


Figure 4. DFT (solid lines) and MC results for the full (filled circles) and effective model (open circles) for the minimum ($\rho_c^{\min} \sigma_c^3$) and maximum ($\rho_c^{\max} \sigma_c^3$) colloid density as a function of the wavelength λ of the external potential for $\rho_c \sigma_c^3 = 0.2$ and different values of ρ_p . The dotted lines represent the result for an ideal gas. (a) $\rho_p \sigma_c^3 = 0$ (i.e. pure hard spheres); (b) $\rho_p \sigma_c^3 = 1$; (c) $\rho_p \sigma_c^3 = 2$.

the (scaled) wavelength λ/σ_c . The DFT results match perfectly those from simulations demonstrating the excellent accuracy of the theory, which equals, in the absence of polymers, Rosenfeld's hard sphere functional.

For $\lambda \approx \sigma_c$ the amplitude of the density oscillation reaches a maximum. This is the case when two colloids *at contact* can be placed in neighbouring minima of the external potential. This leads to very efficient packing of the particles in the valleys of $U_{\text{ext}}(z)$. For $\lambda < \sigma_c$ oscillations appear that become smaller in amplitude and in wavelength as $\lambda \rightarrow 0$. We attribute this behaviour to the competition of the length scales σ_c and λ . In the limit of very small wavelength, i.e. $\lambda/\sigma_c \rightarrow 0$, an exactly solvable case is recovered. Since there are no hard sphere interactions when a particle moves over a length λ , mainly single-particle motion in an external field occurs. The corresponding density profile in this limit is

$$\rho_c(z) = A_c^{-3} \exp(-\beta[U_{\text{ext}}(z) - \mu_c]). \quad (9)$$

Hence $\rho_c^{\text{min}} = A_c^{-3} \exp(-\beta U_0 - \mu_c)$ and $\rho_c^{\text{max}} = A_c^{-3} \exp(\beta U_0 - \mu_c)$. This limit is shown in figure 4 as a dotted line.

For long wavelengths, on the other hand, the maximum density is lower than in the ideal gas case due to the repulsion of the hard spheres. It is decreasing, in general, with increasing λ . This can be understood intuitively as follows. A hard sphere system reacts with marked density oscillations to the presence of an external potential. The amplitude of the density response depends on the range of the external potential; if it is of the order of σ_c the density oscillations are most pronounced while for smooth and longer ranged external potentials the oscillations are weaker. For large λ/σ_c the above mentioned local density approximation holds, and ρ_c^{min} , ρ_c^{max} correspond to the end points of the paths indicated in figure 3.

In figure 4(b), the minimum and maximum colloid densities are plotted as a function of the wavelength for $\rho_p \sigma_c^3 = 1$. Adding polymers, the effective attraction causes a higher maximum density in the potential valleys. As the total density is constant, the minimum density decreases. We show results from the direct simulation of the binary mixture and from the simulation of the one-component model. From the binary simulation we determine $\eta_p^r = 0.18465$, which we use in equation (5). This value for η_p^r is slightly smaller than the free-volume bulk result $\eta_p^r = 0.187376$. We have also checked that η_p^r does not change significantly as λ/σ_c varies. From $\lambda/\sigma_c = 1-7.5$ only a small decrease $\eta_p^r = 0.185-0.1845$ is found, and we are confident that keeping η_p^r fixed is a good approximation. As is apparent in figure 4(b), the differences between the binary and

the effective models are very small, and we conclude that the higher-body terms neglected in the one-component model do not contribute significantly. Again the DFT gives a very good account of the observed behaviour.

In figure 4(c), the results for an even higher polymer concentration, $\rho_p \sigma_c^3 = 2$, are presented. At $\lambda \approx 2\sigma_c$, a minimum in the amplitude occurs and ρ_c^{max} increases with increasing λ in striking contrast to the pure hard sphere case. This can be understood in terms of the strong effective attraction which prefers locally higher density and acts oppositely to the correlation effect discussed above for pure hard spheres. Figure 4(b) is an intermediate case where the effective attraction is not strong enough to lead to increasing ρ_c^{max} with increasing λ .

For the simulation of the effective one-component system we use the simulated value $\eta_p^r = 0.365$. This was determined for small wavelengths (the free-volume result in bulk is $\eta_p^r = 0.374735$). In reality η_p^r decreases, but only very little with increasing λ/σ_c ; we estimate $\eta_p^r = 0.363$ for $\lambda/\sigma_c = 7.5$. From figure 4(c), one sees that in the effective model the effect of the polymers is overestimated. We attribute this mainly to the fact that the (repulsive) three-body forces are neglected. The DFT still describes the simulation results quite well, although the agreement is slightly inferior to the above cases.

Finally, we show results for $0.25 < \lambda/\sigma_c < 1.25$ on an expanded scale in figure 5. The damping and increasing of wavelength of oscillations as λ/σ_c decreases is apparent. The presence of the polymers shifts the absolute maximum (minimum) of ρ_c^{max} (ρ_c^{min}) to smaller λ_c/σ_c . Having gained confidence in the theory, in the

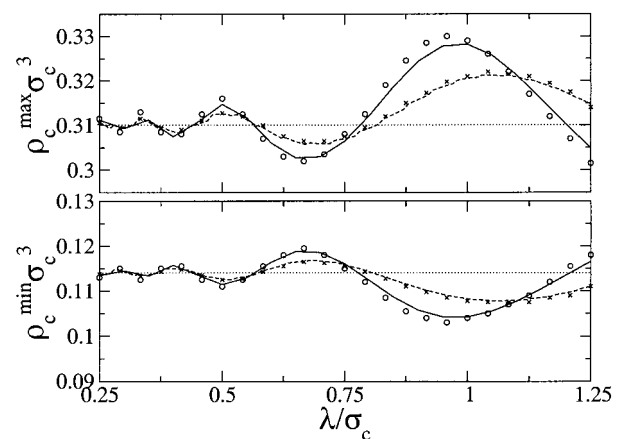


Figure 5. Same as figure 4, but for $0.25 < \lambda/\sigma_c < 1.25$. Lines are DFT results, symbols denote computer simulation results. The hard sphere case for $\rho_p = 0$ (dashed line and crosses) and $\rho_p \sigma_c^3 = 2$ (solid line and open circles) are shown; results for $\rho_c \sigma_p^3 = 1$ are omitted for clarity.

following we investigate the effect of increased polymer density so that demixing occurs.

5.2. Phase behaviour

In order to study the fluid demixing phase behaviour we use the same parameters as before, i.e. $q = 0.6$ and $\beta U_0 = 0.5$. We restrict ourselves to $\lambda = 8.192\sigma_c$, where we show detailed results, but we have also considered smaller λ to assess the principal scenario. In figure 6 the phase diagram as obtained from DFT is shown. For large η_p^r the presence of the plane wave potential shifts the bulk transition slightly to higher colloid chemical potentials $\beta\mu_c$. Strikingly however, at lower η_p^r values a bifurcation of the binodal occurs. It appears that the two bifurcated critical points lie at the same η_p^r value as the bulk critical point but numerically we could not determine whether they are exactly the same. Three state points are indicated where we plot the density profiles in figure 7, one in each region. The three state points are all at $\eta_p^r = 0.65$ and (i) modulated gas, $\beta\mu_c = 8.7$, (ii) stacked fluid, $\beta\mu_c = 9.2$ and (iii) modulated liquid, $\beta\mu_c = 9.7$. The stacked fluid phase is a novel phase which is absent in the bulk but is stabilized by the external field. It consists of periodic slabs of vapour centred around the maxima of the external potential and of slabs of liquid centred around the minima of the external potential. The relative width of the vapour and liquid portion do vary with the thermodynamic parameters. The occurrence of the stacked fluid phase is most directly understood in the limit $\lambda/\sigma_c \rightarrow \infty$ where

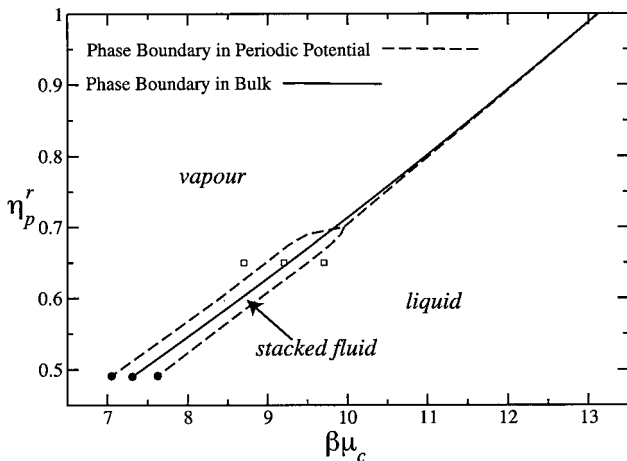


Figure 6. Fluid demixing phase diagram of the AO model as a function of colloid chemical potential $\beta\mu_c$ and polymer reservoir packing fraction η_p^r for size ratio $q = 0.6$ for the cases without external potential (solid line) and with external potential of strength $\beta U_0 = 0.5$ and wavelength $\lambda = 8.192\sigma_c$. In the latter case three phases (vapour, stacked fluid, liquid) are observed. Solid symbols denote critical points. Open symbols denote state points where we display density profiles in figure 6.

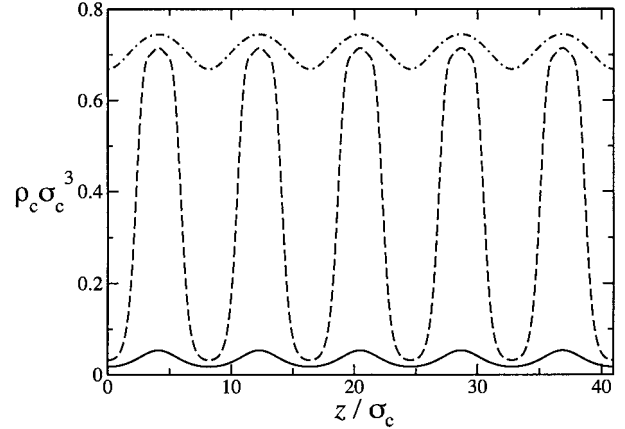


Figure 7. Colloid density profiles for $\beta U_0 = 0.5$, $\lambda = 8.192\sigma_c$, $q = 0.6$ and $\eta_p^r = 0.65$ in three different phases corresponding to different chemical potentials: modulated vapour for $\beta\mu_c = 8.7$ (solid line), stacked fluid for $\beta\mu_c = 9.2$ (dashed line) and modulated liquid for $\beta\mu_c = 9.7$ (dot-dashed line).

a local density approximation is valid. When the combination $\mu_c - U_{\text{ext}}(z)$ equals the chemical potential at liquid–vapour coexistence (see the dashed bar in the right panel of figure 3) a liquid–vapour interface is built up [34].

For smaller values of λ/σ_c we have confirmed that the stacked fluid ceases to exist and the usual type of vapour–liquid phase diagram is recovered. The disappearance is due to the increasing contribution of surface free energy between liquid and vapour slabs in the stacked phase as λ is decreased. We have checked that eventually, at a *finite* value of λ/σ_c , the stacked fluid is no longer stable. Upon decreasing λ/σ_c the triple point moves toward both critical points eventually merging in a bicritical point. We leave a more thorough study of the details of this scenario to possible future work.

6. Conclusions

We have considered a model colloid–polymer mixture exposed to a three-dimensional plane wave external potential representing an optical standing wave. By tuning the size and concentration of the polymers, one can influence the range and strength of an effective depletion attraction, and this can be adjusted so that stable colloid vapour–liquid coexistence is observed.

We have demonstrated that a recent DFT quantitatively predicts the inhomogeneous density profiles when compared to simulation results. As a function of the wavelength of the external potential we find interesting, non-monotonic behaviour of the amplitude of the oscillations in the one-body density distributions. Furthermore we demonstrate the stability of a stacked liquid phase. All our predictions can in principle be verified

in experiments of colloid-polymer mixtures. We believe that the trends and the appearance of the stacked fluid phase are very general phenomena which should also be present for more realistic polymer-polymer and colloid-polymer interactions [35].

Motivated by the experimental situation, in our study the external potential acts only on the colloids. It might, however, also be interesting to study external potentials that act solely or differently on the polymers. In the depletion picture this would lead to spatially varying pair potentials—an interesting issue.

In order to realize small λ/σ_c one needs to use core-shell colloidal particles, where the laser only couples to the particle core.

The principal physical mechanism that underlies the stability of the stacked fluid should also apply to two-dimensional systems; these might be easier to access experimentally.

Finally we note that an analogue of the stacked fluid phase was found before in parallel slit pores where the confining walls are periodically structured. The familiar capillary condensation from gas to liquid is enriched in this case by a phase that consists of liquid bridges between both walls [36, 37]. This phase was also obtained within a lattice model between decorated walls [38]. We emphasize, however, that our external potential is simpler as it has only two additional control parameters such that in our situation the occurrence of the intermediate fluid phase is more direct.

The work of JMB was supported by the National Science Foundation (through grant CHE9800074 and the NSF Materials Research Science and Engineering Center at the University of Chicago). MS and HL acknowledge support from the DFG through the SFB TR6.

References

- [1] ASAKURA, S., and OOSAWA, F., 1958, *J. polym. Sci.*, **33**, 183.
- [2] VRIJ, A., 1976, *Pure appl. Chem.*, **48**, 471.
- [3] PUSEY, P. N., 1991, *Liquids, Freezing and the Glass Transition*, edited by J. P. Hansen, J. Zinn-Justin, and D. Levesque (Amsterdam: North Holland).
- [4] DIJKSTRA, M., VAN ROIJ, R., and EVANS, R., 2000, *J. chem. Phys.*, **113**, 4799; BRADER, J. M., and EVANS, R., 2000, *Europhys. Lett.*, **49**, 678; BRADER, J. M., DIJKSTRA, M., and EVANS, R., 2001, *Phys. Rev. E*, **63**, 041405.
- [5] LIKOS, C. N., 2001, *Phys. Rep.*, **348**, 267.
- [6] HANSEN, J. P., and LÖWEN, H., 2003, *Effective Interactions for Large-scale Simulations of Complex Fluids*, Springer Series, edited by P. Nielaba, M. Mareschal, and G. Ciccotti (Berlin: Springer).
- [7] ANDERSON, V. J., and LEKKERKERKER, H. N. W., 2002, *Nature*, **416**, 811.
- [8] FUCHS, M., and SCHWEIZER, K. S., 2002, *J. Phys.: condens. Matter*, **14**, R239.
- [9] POON, W. C. K., 2002, *J. Phys.: condens. Matter*, **14**, R859.
- [10] LÖWEN, H., 2001, *J. Phys.: condens. Matter*, **13**, R415.
- [11] ROSENFELD, Y., 1989, *Phys. Rev. Lett.*, **63**, 980.
- [12] SCHMIDT, M., LÖWEN, H., BRADER, J. M., and EVANS, R., 2000, *Phys. Rev. Lett.*, **85**, 1934.
- [13] SCHMIDT, M., LÖWEN, H., BRADER, J. M., and EVANS, R., 2002, *J. Phys.: condens. Matter*, **14**, 9353.
- [14] EVANS, R., BRADER, J. M., ROTH, R., DIJKSTRA, M., SCHMIDT, M., and LÖWEN, H., 2001, *Phil. Trans. R. Soc. (London) A*, **359**, 961.
- [15] BRADER, J. M., EVANS, R., SCHMIDT, M., and LÖWEN, H., 2002, *J. Phys.: condens. Matter*, **14**, L1.
- [16] DIJKSTRA, M., and VAN ROIJ, R., 2002, *Phys. Rev. Lett.*, **89**, 208303.
- [17] AARTS, D. G. A. L., VAN DER WIEL, J. H., and LEKKERKERKER, H. N. W., 2003, *J. Phys.: condens. Matter*, **15**, S245.
- [18] WIJTING, W. K., BESSELING, N. A. M., and COHEN STUART, M. A., unpublished.
- [19] BECHINGER, C., WEI, Q. H., and LEIDERER, P., 2000, *J. Phys.: condens. Matter*, **12**, A425.
- [20] WEI, Q. H., BECHINGER, C., RUDHARDT, D., and LEIDERER, P., 1998, *Phys. Rev. Lett.*, **81**, 2606.
- [21] LOUDIYI, K., and ACKERSON, B. J., 1992, *Physica A*, **184**, 1.
- [22] CHOWDHURY, A., ACKERSON, B. J., and CLARK, N. A., 1985, *Phys. Rev. Lett.*, **55**, 833.
- [23] LOUDIYI, K., and ACKERSON, B. J., 1992, *Physica A*, **184**, 26.
- [24] CHAKRABARTI, J., KRISHNAMURTHY, H. R., SOOD, A. K., and SENGUPTA, S., 1995, *Phys. Rev. Lett.*, **75**, 2232.
- [25] STREPP, W., SENGUPTA, S., and NIELABA, P., 2001, *Phys. Rev. E*, **63**, 046106.
- [26] BARRAT, J. L., and XU, H., 1990, *J. Phys.: condens. Matter*, **2**, 9445.
- [27] CHAKRABARTI, J., KRISHNAMURTHY, H. R., and SOOD, A. K., 1994, *Phys. Rev. Lett.*, **73**, 2923.
- [28] RASMUSSEN, L. L., and OXTOBY, D. W., 2002, *J. Phys.: condens. Matter*, **14**, 12021.
- [29] FREY, E., NELSON, D. R., and RADZIHOVSKY, L., 1999, *Phys. Rev. Lett.*, **83**, 2977.
- [30] DAS, C., SOOD, A. K., and KRISHNAMURTHY, H. R., 1999, *Physica A*, **270**, 237.
- [31] LEKKERKERKER, H. N. W., POON, W. C. K., PUSEY, P. N., STROOBANTS, A., and WARREN, P. B., 1992, *Europhys. Lett.*, **20**, 559.
- [32] BOLHUIS, P. G., LOUIS, A. A., and HANSEN, J. P., 2002, *Phys. Rev. Lett.*, **89**, 128302.
- [33] DIJKSTRA, M., BRADER, J. M., and EVANS, R., 1999, *J. Phys.: condens. Matter*, **11**, 10079.
- [34] See e.g. DZUBIELLA, J., HARREIS, H. M., LIKOS, C. N., and LÖWEN, H. L., 2001, *Phys. Rev. E*, **64**, 011405.
- [35] JUSUFI, A., DZUBIELLA, J., LIKOS, C. N., VON FERBER, C., and LÖWEN, H., 2001, *J. Phys.: condens. Matter*, **13**, 6177.
- [36] SCHOEN, M., and DIESTLER, D. J., 1997, *Phys. Rev. E*, **56**, 4427.
- [37] RÖCKEN, P., SOMOZA, A., TARAZONA, P., and FINDENEGG, G., 1998, *J. chem. Phys.*, **108**, 8689.
- [38] BECK, H., DIESTLER, D. J., and SCHOEN, M., 2001, *J. Phys.: condens. Matter*, **13**, 4697.

Capillary condensation of colloid–polymer mixtures confined between parallel plates

Matthias Schmidt¹, Andrea Fortini and Marjolein Dijkstra

Soft Condensed Matter, Debye Institute, Utrecht University, Princetonplein 5,
3584 CC Utrecht, The Netherlands

Received 21 July 2003

Published 20 November 2003

Online at stacks.iop.org/JPhysCM/15/S3411

Abstract

We investigate the fluid–fluid demixing phase transition of the Asakura–Oosawa model colloid–polymer mixture confined between two smooth parallel hard walls using density functional theory and computer simulations. Comparing fluid density profiles for statepoints away from colloidal gas–liquid coexistence yields good agreement of the theoretical results with simulation data. Theoretical and simulation results predict consistently a shift of the demixing binodal and the critical point towards higher polymer reservoir packing fraction and towards higher colloid fugacities upon decreasing the plate separation distance. This implies capillary condensation of the colloid liquid phase, which should be experimentally observable inside slitlike micropores in contact with a bulk colloidal gas.

1. Introduction

Capillary condensation denotes the phenomenon that spatial confinement can stabilize a liquid phase coexisting with its vapour in bulk [1, 2]. In order for this to happen the attractive interaction between the confining walls and the fluid particles needs to be sufficiently strong. Although the main body of work on this subject has been done in the context of confined simple liquids, one might expect that capillary condensation is particularly well suited to be studied with colloidal dispersions. In these complex fluids length scales are on the micron rather than on the ångström scale which is typical for atomic substances. Attraction between colloidal particles can be generated and precisely tuned by adding non-adsorbing polymer. The presence of the polymers induces an effective attraction between the colloids that may lead to fluid–fluid phase separation reminiscent of the gas–liquid transition in atomic systems: the phase that is poor in colloids corresponds to the gas and the phase that is dense in colloids corresponds to the liquid [3].

¹ On leave from Institut für Theoretische Physik II, Heinrich-Heine-Universität Düsseldorf, Universitätsstraße 1, D-40225 Düsseldorf, Germany.

A particularly simple model to study colloid–polymer mixtures is that proposed by Asakura and Oosawa (AO) [4] and Vrij [5], where colloids are represented as hard spheres and polymers as effective, overlapping spheres that cannot penetrate the colloids. Indeed this model displays stable gas and liquid phases and also a crystalline solid [6–12].

The same mechanism that generates an effective attraction between two colloidal particles via depletion of polymers gives also rise to attraction between a single colloidal particle and a simple hard wall leading to strong adsorption of colloids at the wall [13]. Close to the gas branch of the demixing binodal the hard wall is wet by the colloidal liquid, purely driven by entropy, and an intriguing scenario of entropic wetting with a finite sequence of layering transitions in the partial wetting regime was found with density functional theory (DFT) [14, 15] and computer simulations [11], and recently also in a rod–sphere mixture [16]. In fact, there is also experimental evidence for wetting of a smooth hard substrate by the colloid-rich phase [17–19]. Less attention has been paid to the influence of strong confinement on colloid–polymer mixtures, exceptions being exposure to a standing laser field [20] and immersion into random sphere matrices acting as porous media [21, 22].

In this work we investigate the effect of contact with two narrowly spaced, parallel smooth hard walls. We use Monte Carlo (MC) computer simulation and DFT to investigate a range of wall separation distances from ten down to one colloid diameter—covering the dimensional crossover to two remaining space coordinates. Both theory and simulation treat the polymers explicitly, and hence include, in principle, all polymer-induced many-body interactions between colloids. Testing the theory for a case of strong confinement by comparing colloid and polymer density profiles away from coexistence with simulation data demonstrates good accuracy. From theory and simulation results for fluid–fluid coexistence we find that indeed confinement stabilizes the colloidal liquid inside the capillary, hence capillary condensation does occur. These findings should be experimentally observable in colloid–polymer mixtures prepared such that the colloidal bulk gas is in contact with a thin slit pore, and the adsorption inside the pore is measured.

The paper is organized as follows. In section 2 we define the AO model between parallel walls explicitly. In section 3 both the MC and DFT techniques are presented. Section 4 discusses results for one-body density profiles and the demixing phase diagram. We conclude in section 5.

2. Model

The AO model is a binary mixture of colloidal hard spheres (species *c*) of diameter σ_c and of spheres representing polymer coils (species *p*) with diameter σ_p [4, 5]. The pair interaction between colloids is that of hard spheres: $V_{cc}(r) = \infty$ if $r < \sigma_c$ and zero otherwise, where r is the separation distance between particle centres. The interaction between a colloid and a polymer is also that of hard spheres: $V_{cp}(r) = \infty$ if $r < (\sigma_c + \sigma_p)/2$ and zero otherwise. The polymers, however, are assumed to be ideal, hence the polymer–polymer interaction vanishes for all distances, $V_{pp}(r) = 0$. To model the confinement between smooth parallel hard walls we consider external potentials acting on species $i = c, p$, given by

$$V_{\text{ext},i}(z) = \begin{cases} 0 & \sigma_i/2 < z < H - (\sigma_i/2) \\ \infty & \text{otherwise,} \end{cases} \quad (1)$$

where z is the spatial coordinate normal to the walls, and H is the wall separation distance; see figure 1 for an illustration of the situation.

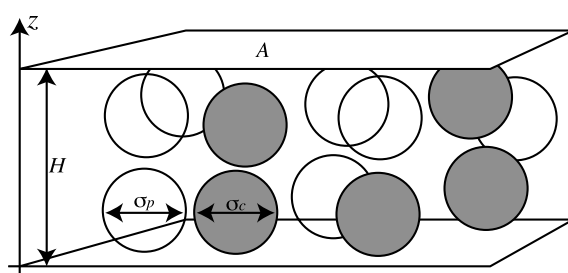


Figure 1. Illustration of the AO model of hard sphere colloids (grey circles) of diameter σ_c and ideal polymers (transparent circles) of diameter σ_p confined between parallel hard walls of area A and separation distance H . Colloids behave as hard spheres, polymers cannot penetrate colloids, and polymers may freely overlap. The walls are impenetrable to both components. The z -axis is perpendicular to the walls, and the origin is located at the lower wall.

The size ratio $q = \sigma_p/\sigma_c$ is a geometric control parameter; the ratio H/σ_c rules the strength of the confinement. We denote the packing fractions by $\eta_i = \pi\sigma_i^3 N_i/(6AH)$, where N_i is the number of particles of species i and A is the lateral (normal to the z -direction) area of the system. As alternative thermodynamic parameters, we use the packing fraction in a pure reservoir of polymers, η_p^r , and the fugacity of the colloids, z_c .

3. Methods

3.1. Computer simulations

We employ Gibbs ensemble MC simulations, where phase coexistence is directly accessible through the use of two simulation boxes, each representing one of the coexisting states [23, 24]. Both boxes contain the confining walls at fixed plate separation distance H . Let $N_{i,a}$ be the number of particles of species i in box $a = 1, 2$, and $A_a H$ be the volume of box a , where A_a is its lateral area. Then $A_1 H + A_2 H = \text{constant}$ and $N_{i,1} + N_{i,2} = \text{constant}$, while fluctuations of $N_{i,a}$ and A_a inside each individual box $a = 1, 2$ are allowed. Thus three different (randomly chosen) types of MC move are performed: single-particle moves of colloids and polymers inside each simulation box, moves that transfer particles from one box to the other to ensure equal chemical potential, and volume exchanges between both boxes to ensure equal wall–fluid interfacial tension via rescaling the lateral box dimensions (and the x - and y -components of particle positions) while keeping the plate separation distance H (and the z -components of all particle positions) constant. We start from a random, non-overlapping configuration, and use 10^8 MC moves for equilibration and typically 3×10^8 production moves for each pair of coexistence statepoints. Acceptance ratios for particle exchange depend strongly on statepoint and decrease, upon increasing η_p^r , from about 50% close to the critical point to about 5% for the highest values considered. The coexistence densities are obtained from the maxima of a histogram of the number of particles in each box. Fugacities are calculated via the test particle insertion method [25]. Typical total particle numbers are $N_{c,1} + N_{c,2} = 200\text{--}400$ for colloids and, dependent on the statepoint, $N_{p,1} + N_{p,2} = 600\text{--}2000$ for polymers. The total lateral area of both boxes, $A_1 + A_2$, is between $400\sigma_c^2$ and $2500\sigma_c^2$. Each run was divided into ten blocks and error bars were obtained from one standard deviation of the block averages.

3.2. Density functional theory

The grand potential of the binary mixture is written as a functional of the (inhomogeneous) one-body density distributions $\rho_i(\mathbf{r})$ as

$$\begin{aligned} \Omega[\rho_c, \rho_p] = & k_B T \sum_{i=c,p} \int d\mathbf{r} \rho_i [\ln(\rho_i(\mathbf{r})\Lambda_i^3) - 1] \\ & + F_{\text{exc}}[\rho_c, \rho_p] + \sum_{i=c,p} \int d\mathbf{r} \rho_i(\mathbf{r}) [V_{\text{ext},i}(\mathbf{r}) - \mu_i], \end{aligned} \quad (2)$$

where Λ_i is the thermal wavelength and μ_i is the chemical potential of species i , k_B is Boltzmann's constant and T is temperature. Although equation (2) is general, for the present application we take the external potentials, $V_{\text{ext},i}$, to be those modelling the slit pore, equation (1). The first term on the right-hand side of (2) is the free energy functional of a binary ideal gas; the unknown part in (2) is the (Helmholtz) excess free energy functional, F_{exc} , that describes the influence of interparticle interactions. Here we take the fundamental measures approximation [26] of [9, 10] that is specifically tailored for the AO model. This is a weighted density approximation where F_{exc} is expressed as a spatial integral over an excess free energy density, which depends on a set of weighted densities that are obtained through convolutions of the bare density profiles with geometrically inspired weight functions. Details can be found in [9, 10]. In order to obtain density profiles the minimization conditions,

$$\frac{\delta\Omega}{\delta\rho_i(\mathbf{r})} = 0, \quad i = c, p, \quad (3)$$

are solved by a standard iteration technique, and the value of the grand potential is obtained by inserting the solutions of (3) into (2). In order to have direct access to phase coexistence we minimize two systems simultaneously and adjust the chemical potentials of both species iteratively such that in the final state both systems possess the same grand potential. This procedure is inspired by the Gibbs ensemble MC method above.

4. Results

In the following we will restrict ourselves to the polymer-to-colloid size ratios $q = 1$. For this value considerable knowledge about bulk [11] and hard wall behaviour [11, 15] is available. Moreover, it is an experimentally readily accessible case.

4.1. Comparison

We start by comparing density profiles for statepoints where we expect the system to be in the one-phase mixed fluid state. As our DFT is known to be accurate in bulk [10], and at single hard planar walls [15], we focus on a case of strong confinement and hence consider $H/\sigma_c = 2$. Figure 2 displays colloid and polymer profiles as a function of the z -coordinate normal to the walls. Both colloid and polymer density profiles are largest at contact with the walls, $z/\sigma_c = 0.5, 1.5$.

The agreement of the theoretical curves with the simulation data is quantitatively good. We note, however, that for still larger values of η_p^* differences begin to emerge (results not shown). As such conditions get close to the demixing transition, we attribute this to the differences in the results for the demixing binodal.

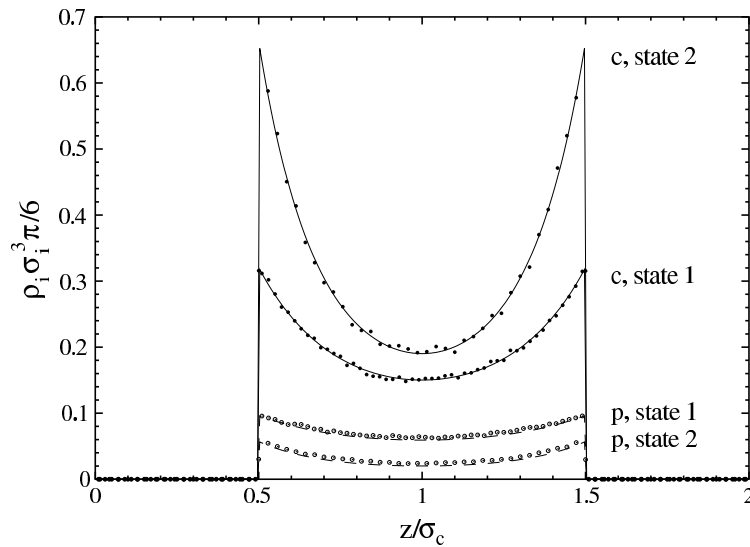


Figure 2. Density profiles $\rho_i(z)\sigma_c^3\pi/6$, $i = c, p$ as a function of the coordinate z/σ_c normal to the plates for plate separation distance $H/\sigma_c = 2$. Results from DFT (curves) and MC (symbols) are shown for $\eta_c = 0.0997$, $\eta_p^r = 0.266$ (statepoint 1) and $\eta_c = 0.157$, $\eta_p^r = 0.367$ (statepoint 2).

4.2. Phase diagram

For large enough concentration of polymer, phase separation into colloid-poor gas and colloid-rich liquid is expected to occur in our model capillary. As an illustration we display snapshots of a pair of coexisting states in figure 3 for large wall separation distance $H/\sigma_c = 10$. In the gas phase, there is a significant number of colloids located close to the wall, and density profiles (not shown) indicate strong adsorption of colloids at both walls in the capillary gas. This is due to the polymer-induced depletion attraction between colloid particle and wall. The capillary liquid is dense in colloids and polymers tend to build clusters of overlapping particles.

We have simulated many such coexisting states for varying densities and values of H/σ_c . The resulting set of phase diagrams is depicted in figure 4, where colloid packing fraction, η_c , and polymer reservoir packing fraction, η_p^r , are taken as independent parameters. The binodals possess a lower (in η_p^r) critical point, and a rapidly increasing density jump upon increasing η_p^r . The shape of the binodal is similar to that of the liquid–gas transition in simple fluids upon identifying η_p^r with inverse temperature.

Upon increasing confinement via decreasing H/σ_c , the critical point moves significantly upwards to higher η_p^r , again similar to the common trend of capillary-induced decrease of critical temperature. The theoretical binodals agree well with the simulation data, except for a slight overestimation of the coexisting liquid density, and a quite prominent underestimation of η_p^r at the critical point. The trend that the simulation result for the critical point is at higher η_p^r than in theory is already known in bulk [11], which we can confirm here. Decreasing H , the deviation gets stronger, and for $H/\sigma_c = 2$ quite strong deviations are found. As this is already close to a two-dimensional situation, this finding is in accordance with the expectation that the DFT becomes less accurate in the critical region.

Before discussing the ultimate crossover to two dimensions in more detail, we present the same phase diagram in a different representation, namely as a function of colloid chemical potential $\mu_c = \ln(z_c\sigma_c^3)$ and of η_p^r in figure 5. As a function of these variables, each pair of

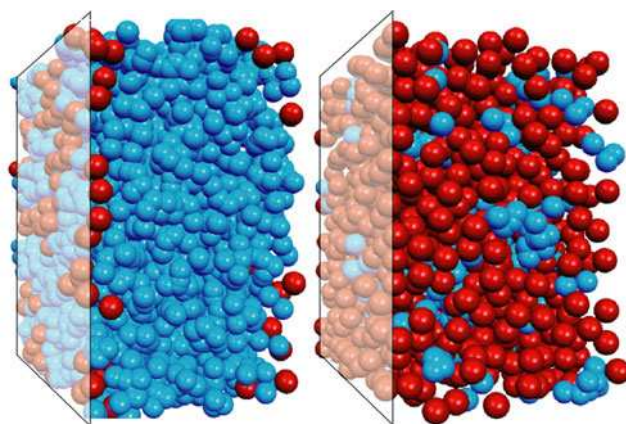


Figure 3. Snapshots from computer simulation of the confined colloidal gas (left) in coexistence with the confined colloidal liquid (right). Colloids (dark red) and polymers (light blue) are immersed between two parallel plates (transparent; only the left-hand wall is shown) with separation distance $H/\sigma_c = 10$ and orientation perpendicular to the horizontal axis. The polymer reservoir packing fraction is $\eta_p^r = 1.116$. Note that compared to figure 1 the system is rotated by 90° around the viewing direction.

(This figure is in colour only in the electronic version)

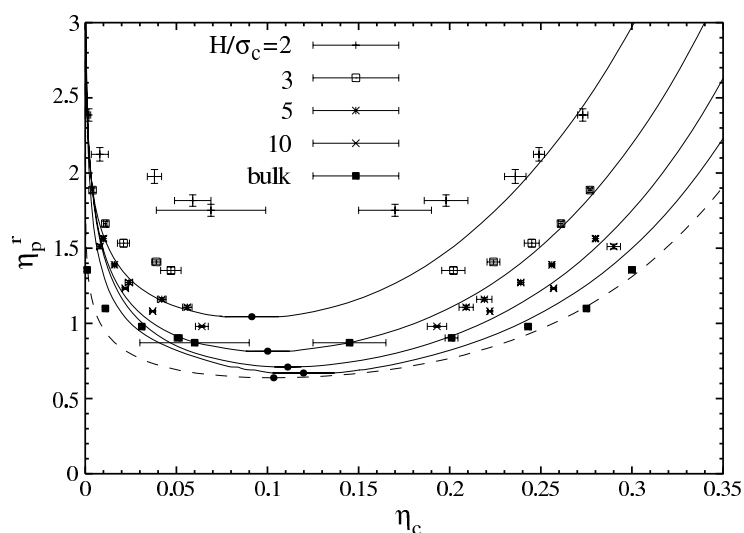


Figure 4. Phase diagram of the AO model between parallel hard walls with separation distance $H/\sigma_c = 2, 3, 5, 10, \infty$ (bulk) as a function of colloid packing fraction in the slit, η_c , and polymer reservoir packing fraction, η_p^r . DFT results for the binodal (curves; from top to bottom for increasing H); the dashed curve indicates the bulk result) and critical point (filled dots) are shown along with MC results for coexisting states (symbols). Coexistence is along horizontal tie lines (not shown).

coexisting phases (gas and liquid phases with different η_c) collapses to a single point as μ_c and η_p^r are equal for the coexisting phases. By reducing H , the critical point and the binodal shifts to larger z_c and larger η_p^r . Consider a statepoint on the gas side of the phase diagram. If this is chosen sufficiently close to the bulk binodal, it might well reside on the liquid side of

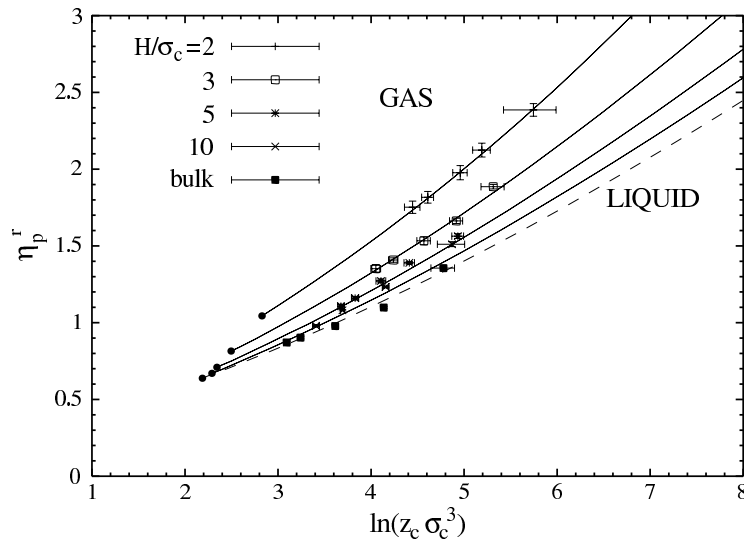


Figure 5. The same as figure 4, but as a function of colloid chemical potential $\ln(z_c \sigma_c^3)$ and of polymer reservoir packing fraction η_p^r . Shown are the results for $H/\sigma_c = 2, 3, 5, 10$ (solid lines and symbols as indicated from top to bottom) and bulk (dashed line and full squares).

the confined system, indicating a liquid phase in the capillary in equilibrium with a bulk gas. Hence this demonstrates the occurrence of capillary condensation in the slit pore. Except for the precise location of the critical point, the overall agreement between DFT and MC results is quite satisfactory.

We have compared these findings to those predicted by the Kelvin equation, generalized to binary mixtures [27]². Three statepoints were chosen: $\eta_p^r = 0.84$ in the complete wetting regime, $\eta_p^r = 1.1$ just above the first layering transition [15], and $\eta_p^r = 2$ deep in the partial wetting regime, see figure 6. For the intermediate case the shift in η_p^r and z_c is correctly predicted by the Kelvin equation, even for strong confinement. For high η_p^r there are differences emerging, especially for the cases $H/\sigma_c = 2, 3$. Close to the critical point, the performance is not very satisfactory, as the growth of wetting layers at the walls is not taken into account.

We have attempted to include results for H very close to σ_c . As can be guessed from the above results for larger H , we find that the values of η_p^r needed to induce phase separation become increasingly large and no longer fit on the same scale. In fact, close to $H/\sigma_c = 1$ this is a trivial effect of dimensional crossover, which we can remedy by using scaled variables. See figure 7 for the binodals in reservoir representation, but as a function of η_c and $\eta_p^r(H - \sigma_c)/H$. The simulation results for the quasi-two-dimensional system are obtained by choosing $H/\sigma_c = 1.01$ (and we have checked the independence from this precise value, by also considering $H/\sigma_c = 1.001$ at one statepoint and finding the same result within the error bars). Indeed, the two-dimensional result is now on the same scale as the results for larger slits. We also show the binodal obtained from the two-dimensional DFT [10], that is equivalent to free volume theory [28] in two dimensions. Again the theory overestimates the

² See equations (40) and (41) in [27]. Adapting those to the present case, we obtain the shifts in chemical potentials, $\Delta\mu_i$, of species $i = c, p$ from simultaneous solution of $2(\gamma_{wg} - \gamma_{wl})/(H - \sigma) = \Delta\mu_c \rho_c^l + \Delta\mu_p \rho_p^l$ and $\Delta\mu_p = -\Delta\mu_c \rho_c^g / \rho_p^g$, where ρ_i^l and ρ_i^g are the coexisting densities, γ_{wl} and γ_{wg} are the hard wall interface tensions of the liquid and the gas phase, respectively, and $\sigma \equiv \sigma_c = \sigma_p$ for the present size ratio, $q = 1$.

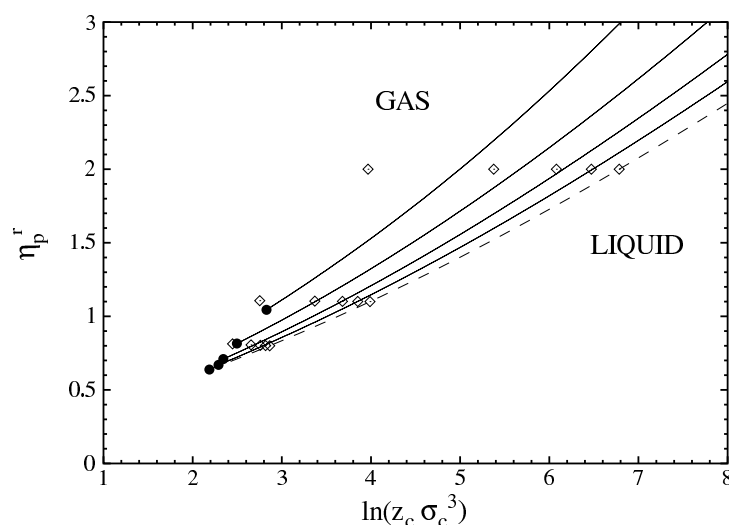


Figure 6. The same as figure 5; shown are the DFT results (curves) along with the predictions from applying the generalized Kelvin equation (open symbols) for statepoints $\eta_p^r = 0.84, 1.1, 2$ and $H/\sigma_c = \infty$ (bulk), 10, 5, 3, 2 (from right to left).

area of demixed states in the phase diagram, somewhat worse than in three dimensions. This probably reflects the difficulty of predicting critical points in two dimensions reliably.

More remarkably, however, is that the scaling leads to an almost complete data collapse of the MC results for *all* slit widths. This is an empirical finding, and we are not aware that such a scaling has been found previously in simple liquids, where one had to relate temperature to confinement in order to have a similar scaling. The binodals from DFT do not collapse as nicely as the MC results; the scaling somewhat overcompensates the shift in η_p^r with decreasing H . Finally, in figure 8 we show the phase diagram as a function of two rescaled variables, i.e. $\eta_p^r(H - \sigma_c)/H$ and $\ln(z_c(H - \sigma_c)/H)$ demonstrating that both fugacities need to be rescaled to obtain the data collapse. However, in this representation the collapse is not as perfect as in figure 7. Note also that the binodal for the 2D case lies on the opposite site of the bulk binodal, as compared to the cases of finite H . This indicates non-monotonic behaviour in the range $1 < \sigma_c/H < 2$. In fact the scaling overcompensates, as the binodals for $2 \leq H/\sigma_c \leq 10$ are in opposite order compared to figure 5.

5. Conclusions

In conclusion, we have considered a binary mixture of hard sphere colloidal particles and added non-adsorbing polymer modelled by effective spheres in contact with a slit pore of parallel hard walls. We find that this capillary induces stability of a (thin film) liquid phase that coexists with the bulk colloidal gas phase. This behaviour can be understood from the strong depletion attraction between (each) wall and the colloidal particles.

Both treatments, computer simulation and DFT, take into account all induced many-body terms in the polymer-mediated effective interaction between the colloidal spheres. We achieve this by treating, in both cases, the full binary mixture.

As an outlook on possible future work, we mention the interesting problem of freezing in confined systems, and in particular how the pure hard sphere behaviour [29, 30] is changed by adding polymer.

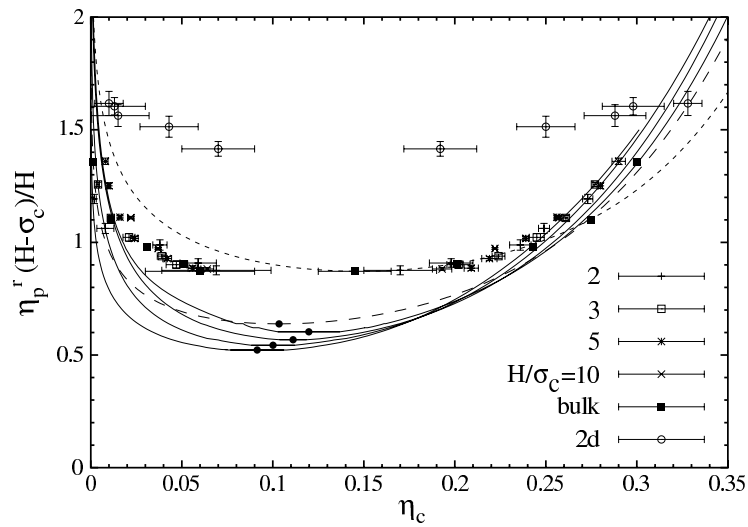


Figure 7. The same as figure 4, but as a function of η_c and the rescaled polymer packing fraction, $\eta_p^r(H - \sigma_c)/H$. Also shown are the results for the two-dimensional (2D) system obtained from simulations for $H/\sigma_c = 1.01$ and free volume theory (short dashed curve).

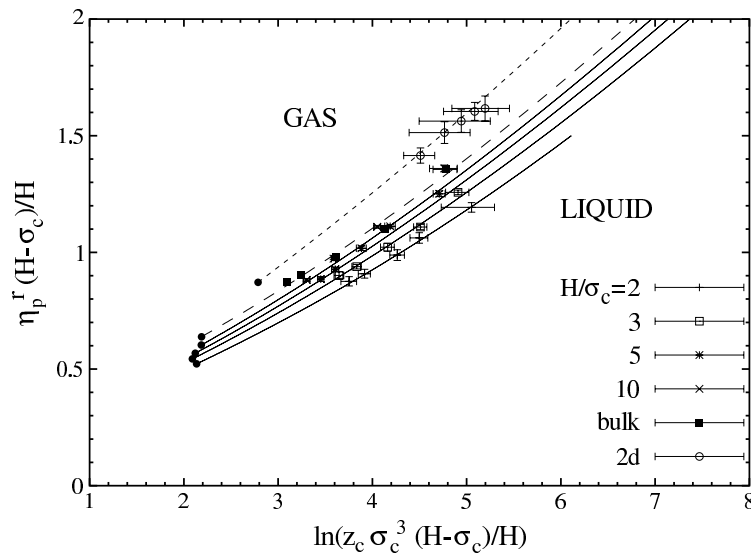


Figure 8. The same as figure 5, but as a function of the rescaled variables $\ln(z_c \sigma_c^3 (H - \sigma_c)/H)$ and $\eta_p^r(H - \sigma_c)/H$.

We emphasize that our predictions can, in principle, be experimentally tested with colloid-polymer mixtures confined between two glass walls. In particular, keeping this slit pore in contact with a bulk colloidal gas, very close to coexistence, and monitoring the amount of adsorbed colloid material in the slit should be fruitful.

Acknowledgments

We thank Dirk G A L Aarts, Henk N W Lekkerkerker, and Paul P F Wessels for many useful and inspiring discussions. J M Brader is acknowledged for sending us his surface tension data [15]. This work is part of the research program of the *Stichting voor Fundamenteel Onderzoek der Materie* (FOM), that is financially supported by the *Nederlandse Organisatie voor Wetenschappelijk Onderzoek* (NWO). Support by the DFG SFB TR6 ‘Physics of colloidal dispersions in external fields’ is acknowledged.

References

- [1] Evans R 1990 *J. Phys.: Condens. Matter* **2** 8989
- [2] Gelb L D, Gubbins K E, Radhakrishnan R and Sliwinski-Bartkowiak M 1999 *Rep. Prog. Phys.* **62** 1573
- [3] Poon W C K 2002 *J. Phys.: Condens. Matter* **14** R859
- [4] Asakura S and Oosawa F 1954 *J. Chem. Phys.* **22** 1255
- [5] Vrij A 1976 *Pure Appl. Chem.* **48** 471
- [6] Gast A P, Hall C K and Russell W B 1983 *J. Colloid Int. Sci.* **96** 251
- [7] Lekkerkerker H N W, Poon W C K, Pusey P N, Stroobants A and Warren P B 1992 *Europhys. Lett.* **20** 559
- [8] Dijkstra M, Brader J M and Evans R 1999 *J. Phys.: Condens. Matter* **11** 10079
- [9] Schmidt M, Löwen H, Brader J M and Evans R 2000 *Phys. Rev. Lett.* **85** 1934
- [10] Schmidt M, Löwen H, Brader J M and Evans R 2002 *J. Phys.: Condens. Matter* **14** 9353
- [11] Dijkstra M and van Roij R 2002 *Phys. Rev. Lett.* **89** 208303
- [12] Bolhuis P G, Louis A A and Hansen J P 2002 *Phys. Rev. Lett.* **89** 128302
- [13] Brader J M, Dijkstra M and Evans R 2001 *Phys. Rev. E* **63** 041405
- [14] Brader J M, Evans R, Schmidt M and Löwen H 2002 *J. Phys.: Condens. Matter* **14** L1
- [15] Brader J M 2001 *PhD Thesis* University of Bristol
- [16] Roth R, Brader J M and Schmidt M 2003 *Europhys. Lett.* **63** 549
- [17] Aarts D G A L, van der Wiel J H and Lekkerkerker H N W 2003 *J. Phys.: Condens. Matter* **15** S245
- [18] Aarts D G A L and Lekkerkerker H N W 2003 private communication
- [19] Wijting W K, Besseling N A M and Cohen Stuart M A 2003 *Phys. Rev. Lett.* **90** 196101
- [20] Götze I O, Brader J M, Schmidt M and Löwen H 2003 *Mol. Phys.* **101** 1651
- [21] Schmidt M, Schöll-Paschinger E, Köfinger J and Kahl G 2002 *J. Phys.: Condens. Matter* **14** 12099
- [22] Wessels P P F, Schmidt M and Löwen H 2003 unpublished
- [23] Panagiotopoulos A Z 1987 *Mol. Phys.* **61** 813
- [24] Panagiotopoulos A Z 1987 *Mol. Phys.* **62** 701
- [25] Smit B and Frenkel D 1989 *Mol. Phys.* **68** 951
- [26] Rosenfeld Y 1989 *Phys. Rev. Lett.* **63** 980
- [27] Evans R and Marini Bettolo Marconi U 1987 *J. Chem. Phys.* **86** 7138
- [28] Lee J-T and Robert M R 1999 *Phys. Rev. E* **60** 7198
- [29] Schmidt M and Löwen H 1996 *Phys. Rev. Lett.* **76** 4552
- [30] Schmidt M and Löwen H 1997 *Phys. Rev. E* **55** 7228

Capillary evaporation in colloid–polymer mixtures selectively confined to a planar slit

Matthias Schmidt¹, Andrea Fortini and Marjolein Dijkstra

Soft Condensed Matter, Debye Institute, Utrecht University, Princetonplein 5,
3584 CC Utrecht, The Netherlands

Received 26 April 2004

Published 10 September 2004

Online at stacks.iop.org/JPhysCM/16/S4159

doi:10.1088/0953-8984/16/38/029

Abstract

Using density functional theory and Monte Carlo simulations we investigate the Asakura–Oosawa–Vrij mixture of hard sphere colloids and non-adsorbing ideal polymers under selective confinement of the colloids to a planar slab geometry. This is a model for confinement of colloid–polymer mixtures by either two parallel walls with a semi-permeable polymer coating or through the use of laser tweezers. We find that such a pore favours the colloidal gas over the colloidal liquid phase and induces capillary evaporation. A treatment based on the Kelvin equation gives a good account of the location of the capillary binodal for large slit widths. The colloid density profile is found to exhibit a minimum (maximum) at contact with the wall for large (small) slit widths.

1. Introduction

Capillary evaporation denotes the situation where a confining pore is filled with a gas in equilibrium with its bulk liquid phase. The phenomenon is an antagonist of capillary condensation, where the pore instead stabilizes the liquid phase that in turn is in equilibrium with the bulk gas phase [1, 2]. Which of the two scenarios will occur for a given fluid depends on the nature of the confinement and in particular on the interaction between the fluid particles and the pore walls. Despite the fundamental analogy, capillary evaporation has only recently attracted more attention, in particular for the Lennard-Jones fluid, which was studied theoretically and with simulation, capillary evaporation being observed for purely repulsive walls (and capillary condensation for attractive walls) [3–5].

Colloid–polymer mixtures are mesoscopic model systems that enable one to study fundamental issues in condensed matter [6]. The Asakura–Oosawa–Vrij (AOV) model [7, 8] of hard sphere colloids and ideal polymers is a simple model that has been studied extensively using theory [9–13] and simulation [11, 14–18]. The presence of polymers induces an effective

¹ On leave from: Institut für Theoretische Physik II, Heinrich-Heine-Universität Düsseldorf, Universitätsstraße 1, D-40225 Düsseldorf, Germany.

attraction between colloids driving, for high enough polymer concentration and large enough colloid-to-polymer size ratio, a (colloidal) gas-liquid phase transition in bulk [7–10]. The same (depletion) effect leads to an attraction between a single colloidal particle and a planar hard wall (that is impenetrable to both colloids and polymers) [19]. Much attention has been devoted to the wetting of a (single) wall by the colloidal liquid as studied theoretically [20–24] and by means of simulations [14] and experiments [22, 25–27].

We have recently investigated capillary condensation of the AOV mixture confined between two parallel hard walls. Corresponding experimental set-ups can be well controlled due to their relatively large (as compared to molecular fluids) intrinsic length scales of the order of ~ 100 nm particle diameter [22, 27, 28]. Furthermore, surface corrugations of the confining walls are of minor importance as (glass) substrates are practically smooth on the colloidal length scale. Our results from Monte Carlo (MC) simulations and density functional theory (DFT) indicate that capillary condensation does occur. That purely repulsive walls lead to such behaviour might seem surprising at first glance. However, although the bare interaction between the wall and the two species is purely repulsive, the concept of integrating out degrees of freedom, in this case those of the polymers, permits us to relate the properties of the binary mixture to those of a corresponding one-component fluid (of colloids) interacting through an effective one-component Hamiltonian which consists of effective many-body interactions. The dominant term in this effective many-body Hamiltonian is the so-called depletion pair potential, which is known to be attractive. Via the same mechanism an effective attraction between the colloid and hard wall arises [19] as the dominant term for the effective polymer-mediated wall-colloid interaction. This gives a qualitative explanation of the occurrence of capillary condensation between parallel hard walls. However, care should be taken, as previous work [14, 20, 21, 24] showed that the effective higher-body interactions (repulsive and attractive) change the bulk phase behaviour and adsorption phenomena substantially from those found for pairwise simple fluids; e.g. an anomalously large bulk liquid regime is found and, far from the bulk triple point, several layering transitions in the partial wetting regime prior to a transition to complete wetting by colloidal liquid are found.

In this work, we consider two parallel semi-permeable walls that do not generate an effective wall-colloid attraction. The polymers are unconfined and can penetrate the walls which act solely on the colloids. Such situations have been investigated before for random sphere matrices [29] and for a single wall [23]. There are two possible experimental realizations for selective confinement between two planes:

- (i) A polymer-coated brush that is impenetrable to colloids but penetrable to polymers [26].
- (ii) Confinement of colloids via an appropriate set-up of laser tweezers to a thin sheet in space.

The paper is organized as follows. In section 2 we define the model explicitly and give an overview of the DFT and MC techniques used. In section 3 results are presented and concluding remarks are given in section 4.

2. Model and methods

The AOV model is a mixture of colloidal hard spheres (species *c*) of diameter σ_c and ideal polymers (species *p*) of diameter σ_p interacting with pair interactions $V_{ij}(r)$ between species $i, j = c, p$ as a function of the centre-centre distance. The colloid-colloid interaction is that of hard spheres: $V_{cc}(r) = \infty$ if $r < \sigma_c$ and zero otherwise. Polymers and colloids also behave as hard spheres: $V_{cp}(r) = \infty$ if $r < (\sigma_c + \sigma_p)/2$ and zero otherwise. The polymers are assumed to be non-interacting: $V_{pp}(r) = 0$ for all distances.

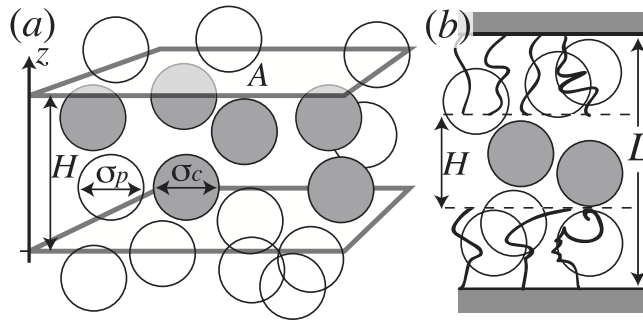


Figure 1. An illustration of the selectively confined AOV model of colloidal hard spheres (grey) and polymers (white). (a) The confinement is such that the volume accessible to the colloids is between two parallel planes at distance H . Polymers do not experience confinement. (b) The confinement between parallel substrates (grey) at distance L coated with a polymer brush (wiggles). The free distance between the two polymer brushes is H ; soluted polymers (open spheres) are able to penetrate the brush but not the substrate; the brush acts like a hard wall for colloids.

We consider a confining external potential acting solely on the colloids:

$$V_{\text{ext},c}(z) = \begin{cases} 0 & \sigma_c/2 < z < H - (\sigma_c/2), \\ \infty & \text{otherwise,} \end{cases} \quad (1)$$

where z is the space coordinate perpendicular to the confining walls. There is no external potential acting on the polymer, i.e. formally $V_{\text{ext},p} = 0$. See figure 1(a) for an illustration of the model. Note that any substrate that supports the polymer coating will be decoupled from the system due to the ideality of polymers provided that the separation distance between the two substrate walls is $L > H + 2\sigma_p$ (see figure 1(b) for an illustration).

As control parameters we use the packing fractions $\eta_i = \pi\sigma_i^3\rho_i/6$, where $\rho_i = N_i/(AH)$ is the number density of species $i = c, p$; N_i is the number of particles and A is the lateral area of the system (perpendicular to the z -direction). Furthermore, we use the packing fraction in a pure reservoir of polymers, η_p^r , that is in chemical equilibrium with the system.

The methods that we employ to study this model are very similar to those in a previous study of capillary condensation [30], hence we will give here only a brief overview. To obtain DFT results we use the excess free energy functional of [12, 13] that is an extension of Rosenfeld's fundamental measure theory for hard sphere mixtures [31] to the AOV model. Results for density profiles and phase behaviour are obtained by minimizing numerically the grand potential functional. Furthermore, we use the Gibbs ensemble Monte Carlo (MC) simulation method [32, 33], where both the structure and the phase behaviour are directly accessible. Fugacities are calculated via the test particle insertion procedure [34]. For more technical details of both approaches we refer the reader directly to [30].

3. Results

We first display results for the fluid demixing part of the bulk phase diagram in figure 2 as a function of the colloid packing fraction, η_c , and polymer reservoir packing fraction, η_p^r . In the unconfined (bulk) situation, which we recover formally for infinite plate separation distances $H/\sigma_c \rightarrow \infty$, the DFT result reduces to that of free volume theory which is known to be accurate far away from the critical point [14–16], but it underestimates the critical value of η_p^r . Our results confirm this finding. For decreasing values of H/σ_c the binodal shifts significantly to higher values of η_p^r . The shift of the critical point to higher η_p^r corresponds to the common

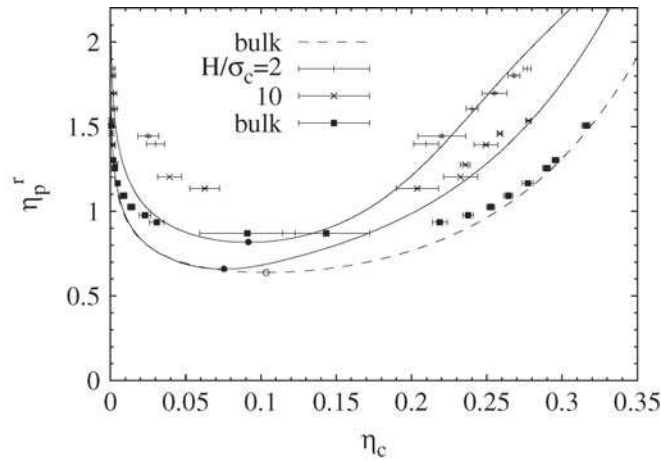


Figure 2. The phase diagram of the AOV model confined between depletionless walls as a function of the colloid packing fraction, η_c , and polymer reservoir packing fraction, η_p^r , for plate separation distances $H/\sigma_c = \infty$ (bulk), 10, 2 and size ratio $q = 1$. Shown are results from simulations (symbols) and DFT (solid curves). The bulk binodal from DFT is identical to that from free volume theory (dashed curve).

shift to smaller temperatures (i.e. larger inverse temperatures) in simple substances. As the attraction between the colloids is diminished due to the confinement, more polymer, yielding a stronger attractive depletion interaction between the colloids, is needed to drive the phase separation. For $L/\sigma_c = 10$ the liquid branch of the binodal shifts to considerably smaller values of η_c , similarly to the case of capillary condensation between parallel hard walls. As we will demonstrate below, when investigating structure in detail, this shift is accompanied with the growth of colloidal gas films on both walls. Close to the critical point the coexistence values of η_c in the capillary gas phase predicted by the two approaches deviate significantly from each other, i.e. the simulation results indicate larger values of η_c as compared to the theoretical calculation. This deviation is consistent with the (again) too high critical value of η_p^r from DFT as compared to the simulation results. Also the (estimated) critical value of η_c is higher in simulation than in theory.

We also plot the same phase diagram as a function of the scaled colloid chemical potential $\beta\mu_c = \ln(z_c\sigma_c^3)$, where z_c is the colloid fugacity, and the polymer reservoir packing fraction, η_p^r , in figure 3. It is apparent that the binodals for the confined system are shifted towards higher values of $\ln(z_c\sigma_c)$, the shift being small for $H/\sigma_c = 10$ but considerable for $H/\sigma_c = 2$. This trend implies that state points between the bulk binodal and the binodal of the confined system (and for values of η_p^r larger than either critical point) describe bulk liquid states in coexistence with gas states inside the capillary, clearly signalling capillary evaporation. The agreement between results from simulation and theory is quantitative except for the aforementioned difference in the location of the critical point.

As an alternative, simple treatment we use the Kelvin equation and restrict ourselves to the application of its one-component version, i.e. keeping the polymer reservoir packing fraction fixed. Previous density functional theory calculations showed complete drying everywhere along the liquid branch of the binodal [23] and, thus, $\gamma_{lg} = \gamma_{wl} - \gamma_{wg}$, where γ_{lg} , γ_{wl} and γ_{wg} are the interface tensions between liquid gas, wall liquid and wall gas, respectively. The shift in colloid chemical potential $\Delta\mu_c$ due to the confinement reads

$$\Delta\mu_c = \frac{2\gamma_g}{(\rho_c^l - \rho_c^g)(H - \sigma_c)}, \quad (2)$$

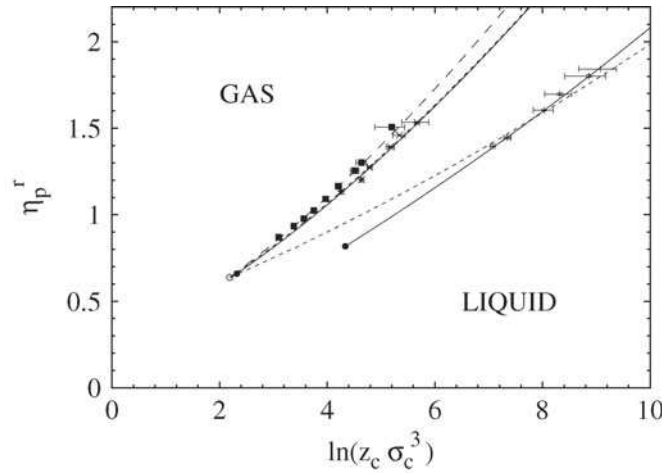


Figure 3. The same as figure 2, but as a function of the colloid chemical potential, $\ln(z_c \sigma_c^3)$, and polymer reservoir packing fraction, η_p^r . Also shown are the results from the Kelvin equation (short dashed curves) using the gas–liquid interface tension, γ_g , obtained from DFT as an input.

ρ_c^l (ρ_c^g) is the number density of the coexisting liquid (gas) bulk phase. $\Delta\mu_c = \mu_c^{\text{evap}} - \mu_c^{\text{coex}} > 0$ indicates capillary evaporation, where μ_c^{evap} denotes the chemical potential at the capillary binodal and μ_c^{coex} that at the bulk liquid binodal. We use DFT results for γ_g and display the corresponding binodals in figure 3. For $H/\sigma_c = 10$ the result is (except very close to the critical point) practically identical to the result from the full numerical DFT calculation. Even for the strongly confined system of $H/\sigma_c = 2$ the binodal is reproduced reasonably, albeit with a (typical) slope that is too small in the $(\ln(z_c \sigma_c^3), \eta_p^r)$ plane. We emphasize that we use a slab thickness reduced by one particle diameter, $H - \sigma_c$, in the Kelvin equation (2). Commonly, the bare value H is used, which we find to give far inferior results for the strongly confined system, $H/\sigma_c = 2$, i.e. a much too small magnitude of $\Delta\mu_c$. This behaviour is consistent with that found for capillary condensation of the AO model between parallel hard walls [30]. There it was argued that the dimensional crossover to the two remaining spatial dimensions upon approaching $H \rightarrow \sigma_c$ induces a divergence, which is correctly captured by a form similar to that of equation (2). The only prominent deficiency of the results from the Kelvin equation is the false prediction that the capillary critical point is identical to the bulk critical point.

We also display our results as a function of the colloid packing fraction of a bulk reservoir of the colloid–polymer mixture, η_c^{bulk} , which is in equilibrium with the confined system. As a second parameter we keep η_p^r . The topology of the resulting phase diagram, as displayed in figure 4, resembles closely that of a simple substance with capillary evaporation binodals running as lines along the liquid branch of the bulk binodal. The shift of the capillary evaporation binodals with respect to the bulk liquid binodal is larger for stronger confinement. The prediction from the Kelvin equation (not shown) is very close to the DFT result for $H/\sigma_c = 10$, but differs somewhat (similar to the difference in observed in figure 3) for $H/\sigma_c = 2$. As illustrations we display snapshots of coexisting states obtained from MC simulation in figure 5.

We also investigate density profiles of both species inside the slit pore; see figure 6 for MC and DFT results for $H/\sigma_c = 10$. In order to compare results from the two approaches, we take equal values of η_p^r at (capillary) coexistence. Sufficiently far away from the critical point, for $\eta_p^r = 1.39$ —see figure 6(a)—the gas phase is practically an ideal gas of polymers without any colloids. The colloid density profile in the liquid phase is flat in the middle of

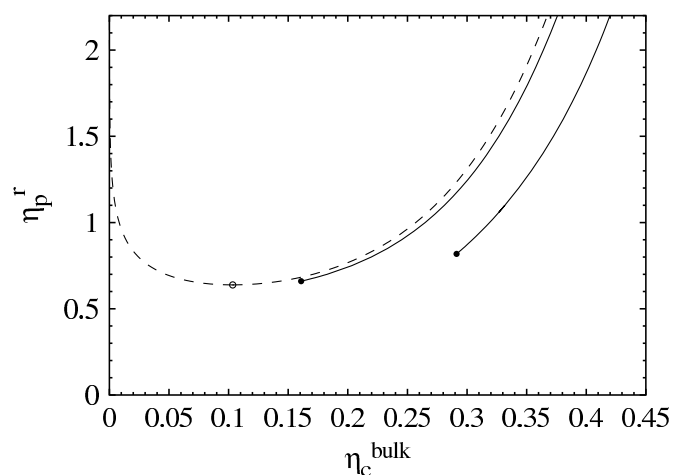


Figure 4. The same as figure 3, but as a function of the colloid packing fraction in the coexisting bulk mixture, η_c^{bulk} , and the polymer reservoir packing fraction, η_p^r . Shown are results from DFT.

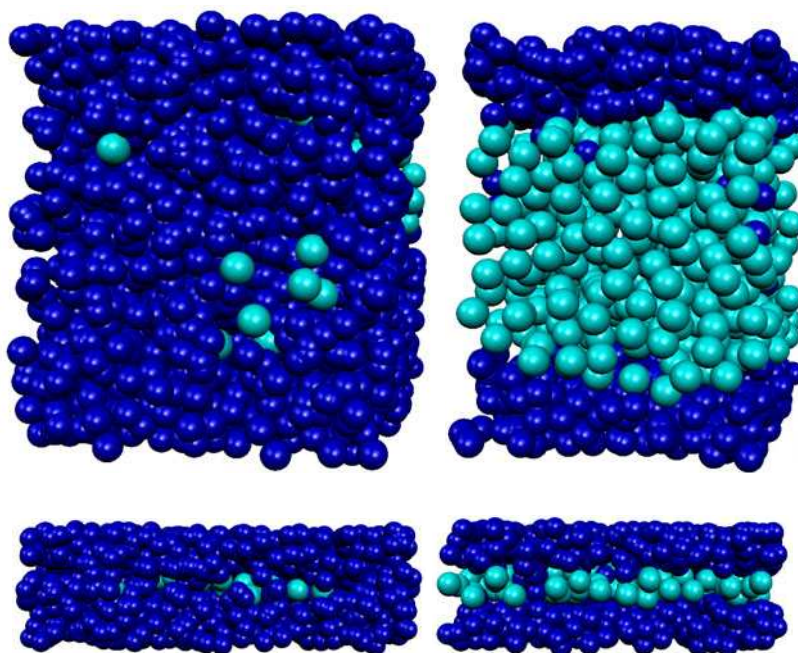


Figure 5. Snapshots of the coexisting capillary gas (left) and liquid (right) phases from MC simulations. Colloids (light) are confined to a slab; polymers (dark) are unconfined. The pore widths are $H/\sigma = 10$ (upper panels) and $H/\sigma = 2$ (lower panels).

(This figure is in colour only in the electronic version)

the capillary and decreases over a distance of $\sim\sigma_c$ to a significantly smaller contact value at the wall. The emergence of such ‘depletion layers’ at polymer-like walls is a single-wall phenomenon and it was found that there is indeed complete drying at a single polymer-coated wall as *bulk* gas–liquid coexistence is approached from the liquid side, i.e. the thickness of

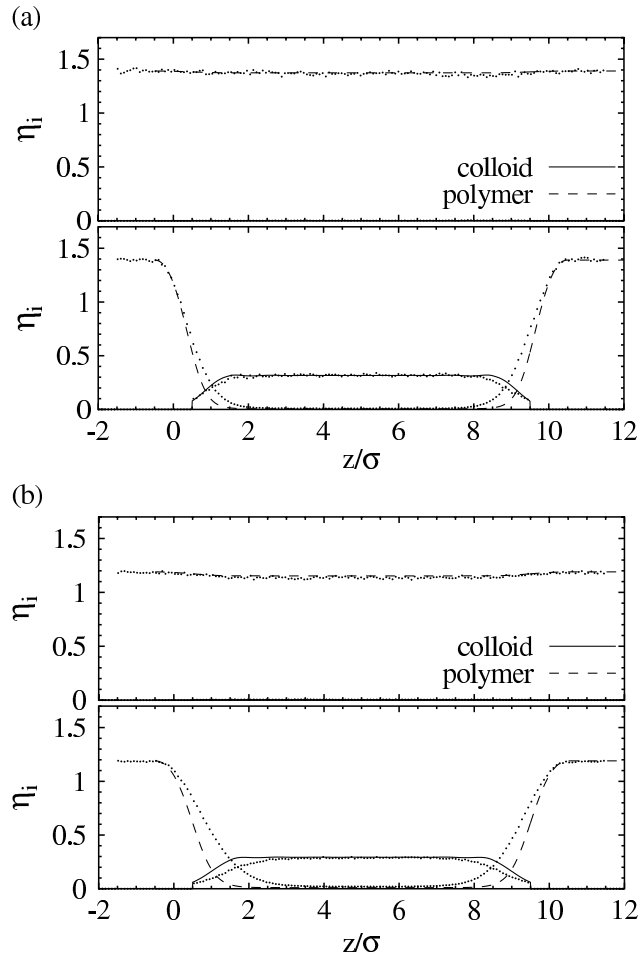


Figure 6. Scaled density profiles, $\eta_i(z) = \rho_i(z)\sigma_i^3\pi/6$, of colloids and polymers inside the slit pore as a function of the position between the walls, z/σ . Shown are results from MC simulations (symbols) and DFT (curves) in the coexisting colloidal gas (upper panel) and colloidal liquid (lower panel) phases for size ratio $q = 1$, wall separation distance $H/\sigma = 10$, and polymer reservoir packing fraction (a) $\eta_p^r = 1.39$ (with a statistical uncertainty of ± 0.01 in the MC case) and (b) $\eta_p^r = 1.19$ (with an uncertainty of ± 0.01 in the MC case).

the gas layer diverges [23]. In the present case of two walls at finite separation the capillary transition happens well inside the one-phase (liquid) region of the bulk phase diagram (see figure 3); hence any drying layer is expected to be of finite thickness, compatible with the shape of the profiles in figure 6. That the contact density $\rho_c^{\text{contact}} = \rho_c((\sigma_c/2)^+)$ is smaller than that in the middle of the capillary can be understood from the condition of hydrostatic equilibrium. For a single wall (one wall or the other) of our slab, it can be shown that

$$\rho_c^{\text{contact}} = \beta\Delta\Pi = \beta(P - \rho_p^r), \quad (3)$$

where $\Delta\Pi$ is the osmotic pressure difference across the wall; the pressure ‘outside’ the slab is just the (ideal gas) pressure of polymers, $k_B T \rho_p^r$, and P is the bulk pressure of the binary mixture. Using the free volume expression for $P(\rho_c, \rho_p^r)$, one finds that we indeed have $\rho_c^{\text{contact}} < \rho_c$ for typical state points.

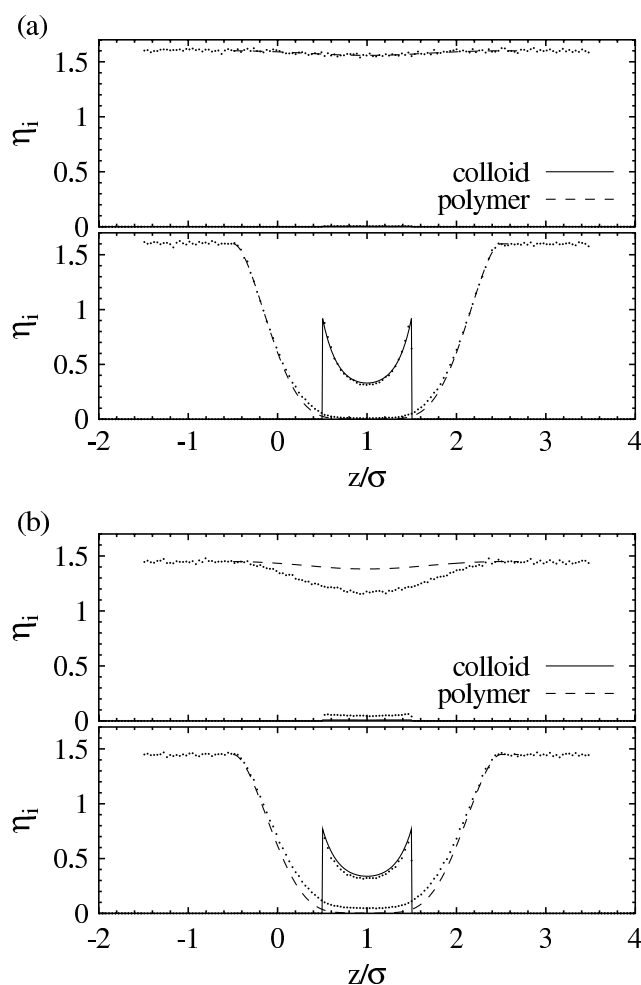


Figure 7. The same as figure 6, but for a plate separation distance of $H/\sigma = 2$, and polymer reservoir packing fractions (a) $\eta_p^r = 1.6$, (b) $\eta_p^r = 1.449$.

Closer to the critical point—see the density profiles for $\eta_p^r = 1.19$ in figure 6(b)—the density of colloids in the gas increases and the density of polymers decreases. The depletion layers in the liquid phase become slightly more extended. There is marked difference between DFT and MC results, which can be explained by the difference in location of the capillary critical point in the two approaches. For even lower values of η_p^r , the DFT profiles (not shown) resemble the simulation results displayed in figure 6(b) more closely. In the case of small slit widths we expect the behaviour not to be explicable using considerations for a single wall. Indeed results for $H/\sigma_c = 2$, as displayed in figure 7, indicate that in the liquid phase the density profile of colloids rises at each wall, and the contact value is a maximum of the density profile. This is consistent with findings for simple substance at a hard wall, where density profiles are known to either turn upward or downward depending on the state point (see e.g. [4]).

4. Conclusions

In conclusion, we have investigated a simple model for colloid–polymer mixtures confined between two semi-permeable parallel walls that are penetrable to polymers but exert a hard-core repulsion on colloids. We have argued that such a set-up does not generate an effective depletion interaction between colloids and the wall. Using DFT and MC simulation we find consistently that the capillary stabilizes the colloidal gas phase and that capillary evaporation does occur. As representative cases we have investigated (scaled) wall separations of $H/\sigma_c = 2, 10$. For $H/\sigma_c = 10$ we find excellent agreement with the prediction for the shift of the gas–liquid binodal from the one-component Kelvin equation (keeping the polymer reservoir density fixed). The density profiles indicate a depletion layer of colloids near each wall. For the small wall separation, $H/\sigma_c = 2$, the performance of the Kelvin equation becomes less good, but it still gives results in reasonable agreement with those from both DFT and MC simulation. Packing effects of colloids become more pronounced and we find the colloid density profiles to rise at the walls.

In our model the colloids cannot penetrate the walls; hence condensation of the liquid inside the wall, as found in references [35, 36] for one-component fluids exposed to penetrable walls, does not occur. The topology of the phase behaviour found in these studies, however, closely resembles that of an AOV model exposed to a standing laser field which exerts a plane-wave potential on the colloids only [37].

Acknowledgments

MS thanks Paweł Bryk for an interesting discussion and for pointing out the relevance of [35, 36]. This work is part of the research programme of the Stichting voor Fundamenteel Onderzoek der Materie (FOM), which is financially supported by the Nederlandse Organisatie voor Wetenschappelijk Onderzoek (NWO). We thank the Dutch National Computer Facilities foundation for access to the SGI Origin 3800 and SGI Altix 3700. Support by the DFG SFB TR6 ‘Physics of colloidal dispersions in external fields’ is acknowledged.

References

- [1] Evans R 1990 *J. Phys.: Condens. Matter* **2** 8989
- [2] Gelb L D, Gubbins K E, Radhakrishnan R and Sliwinski-Bartkowiak M 1999 *Rep. Prog. Phys.* **62** 1573
- [3] Dominguez H, Allen M P and Evans R 1999 *Mol. Phys.* **96** 209
- [4] Varga S, Boda D, Henderson D and Sokolowski S 2000 *J. Colloid Interface Sci.* **227** 223
- [5] Bryk P, Lajtar L, Pizio O, Sokolowska Z and Sokolowski S 2000 *J. Colloid Interface Sci.* **229** 526
- [6] Poon W C K 2002 *J. Phys.: Condens. Matter* **11** 10079
- [7] Tuinier R, Rieger J and de Kruif C G 2003 *Adv. Colloid Interface Sci.* **103** 1
- [8] Asakura S and Oosawa F 1954 *J. Chem. Phys.* **22** 1255
- [9] Vrij A 1976 *Pure Appl. Chem.* **48** 471
- [10] Gast A P, Hall C K and Russell W B 1983 *J. Colloid Interface Sci.* **96** 251
- [11] Lekkerkerker H N W, Poon W C K, Pusey P N, Stroobants A and Warren P B 1992 *Europhys. Lett.* **20** 559
- [12] Dijkstra M, Brader J M and Evans R 1999 *J. Phys.: Condens. Matter* **11** 10079
- [13] Schmidt M, Löwen H, Brader J M and Evans R 2000 *Phys. Rev. Lett.* **85** 1934
- [14] Schmidt M, Löwen H, Brader J M and Evans R 2002 *J. Phys.: Condens. Matter* **14** 9353
- [15] Dijkstra M and van Roij R 2002 *Phys. Rev. Lett.* **89** 208303
- [16] Bolhuis P G, Louis A A and Hansen J P 2002 *Phys. Rev. Lett.* **89** 128302
- [17] Vink R L C and Horbach J 2003 *J. Chem. Phys.* (Preprint cond-mat/0310404)
- [18] Vink R 2004 Entropy driven phase separation *Computer Simulation Studies in Condensed Matter Physics* vol 18, ed D P Landau, S P Lewis and H B Schuettler (Berlin: Springer)
- [19] Vink R L C and Horbach J 2004 *Proc. CODEF Conf.; J. Phys.: Condens. Matter* **16** S3807

-
- [19] Brader J M, Dijkstra M and Evans R 2001 *Phys. Rev. E* **63** 041405
- [20] Brader J M, Evans R, Schmidt M and Löwen H 2002 *J. Phys.: Condens. Matter* **14** L1
- [21] Brader J M, Evans R and Schmidt M 2003 *Mol. Phys.* **101** 3349
- [22] Aarts D G A L, van der Wiel J H and Lekkerkerker H N W 2003 *J. Phys.: Condens. Matter* **15** S245
- [23] Wessels P P F, Schmidt M and Löwen H 2004 *J. Phys.: Condens. Matter* **16** L1
- [24] Wessels P P F, Schmidt M and Löwen H 2004 *Proc. CODEF Conf. 2004; J. Phys.: Condens. Matter* **16** S4169
- [25] Wijting W K, Besseling N A M and Cohen Stuart M A 2003 *Phys. Rev. Lett.* **90** 196101
- [26] Wijting W K, Besseling N A M and Cohen Stuart M A 2003 *J. Phys. Chem. B* **107** 10565
- [27] Aarts D G A L and Lekkerkerker H N W 2004 *Proc. CODEF Conf. 2004; J. Phys.: Condens. Matter* **16** S4231
- [28] Lee T-C, Lee J-T, Pilaski D R and Robert M R 2003 *Physica A* **329** 411
- [29] Schmidt M, Schöll-Paschinger E, Köffinger J and Kahl G 2002 *J. Phys.: Condens. Matter* **14** 12099
- [30] Schmidt M, Fortini A and Dijkstra M 2003 *J. Phys.: Condens. Matter* **48** S3411
- [31] Rosenfeld Y 1989 *Phys. Rev. Lett.* **63** 980
- [32] Panagiotopoulos A Z 1987 *Mol. Phys.* **61** 813
- [33] Panagiotopoulos A Z 1987 *Mol. Phys.* **62** 701
- [34] Smit B and Frenkel D 1989 *Mol. Phys.* **68** 951
- [35] Bryk P, Patrykiewicz A, Reszko-Zygmunt J and Sokolowski S 1999 *Mol. Phys.* **96** 1509
- [36] Bryk P, Reszko-Zygmunt J, Rzysko W and Sokolowski S 2000 *Mol. Phys.* **98** 117
- [37] Götze I O, Brader J M, Schmidt M and Löwen H 2003 *Mol. Phys.* **101** 1651

Competition between sedimentation and phase coexistence of colloidal dispersions under gravity

Matthias Schmidt^{1,3}, Marjolein Dijkstra¹ and Jean-Pierre Hansen^{2,4}

¹ Soft Condensed Matter, Debye Institute, Utrecht University, Princetonplein 5, 3584 CC Utrecht, The Netherlands

² Dipartimento di Fisica, Università degli Studi di Roma 'La Sapienza', Piazzale Aldo Moro, 2, 00185 Roma, Italy

Received 17 April 2004, in final form 8 June 2004

Published 10 September 2004

Online at stacks.iop.org/JPhysCM/16/S4185

doi:10.1088/0953-8984/16/38/031

Abstract

After a brief review of the theory of sedimentation equilibria of colloidal systems, we consider the specific case of binary systems of hard sphere colloids and non-interacting polymer coils, the latter of vanishing buoyancy mass. The density profiles of the two components are calculated within density functional theory and using Monte Carlo simulations. Under appropriate conditions the profiles exhibit discontinuities or steeply varying regions associated with the interface separating colloid-rich and colloid-poor phases. The position of the interface is shown to be very sensitive to the strength of the gravitational field and, more surprisingly, to the total height L of the suspension. Phase coexistence in the absence of gravity is shown to be entirely suppressed beyond a critical ratio of the height L over the gravitational length of the colloids.

1. Introduction

Sedimentation profiles of macromolecules or colloidal dispersions subjected to gravity or centrifugal forces have been measured since the pioneering experiments of Jean Perrin in 1910 [1]. They contain a wealth of information about the osmotic equation of state [2] and phase behaviour [3] of interacting mesoscopic particles. Classical density functional theory (DFT) of inhomogeneous fluids [4] provides theoreticians with an ideal tool for the investigation of sedimentation equilibria. One of the open problems is understanding the influence of gravity, or more generally of external fields, on the phase diagram of colloidal systems, and in particular of binary systems, such as colloid–polymer mixtures, which will be the main focus of this paper. Phase equilibria of multi-component suspensions are examined under rather special

³ On leave from: Institut für Theoretische Physik II, Heinrich-Heine-Universität Düsseldorf, Universitätsstraße 1, D-40225 Düsseldorf, Germany.

⁴ On leave from: Department of Chemistry, University of Cambridge, Lensfield Road, Cambridge CB2 1EW, UK.

conditions in sedimentation experiments, since the total volume and overall composition of the system are fixed [5], rather than the chemical potentials and pressure, as is the case for bulk, open systems connected to reservoirs of particles of each species. We shall see that these circumstances can affect the very existences of phase coexistence under gravity upon varying the total height of the sediment.

After a brief summary of the DFT of sedimentation equilibria in colloidal suspensions (section 2), we review some earlier theoretical work on sedimenting spheres, rods and plates in section 3, before investigating in more detail the case of colloid–polymer mixtures in section 4, with special emphasis on the influence of colloidal sedimentation on the bulk phase separation of these binary systems. Some concluding remarks will be made in section 5.

2. Sedimentation profiles and the osmotic equation of state

Consider a dispersion of ν colloidal or macromolecular species in a suspending fluid, subjected to gravity. If m_α denotes the buoyant mass of species α ($1 \leq \alpha \leq \nu$), the effect of gravity may be characterized by the ν gravitational lengths $\xi_\alpha = k_B T / (m_\alpha g)$, where $k_B T$ is the thermal energy and g the gravitational acceleration. The external field induces a vertical inhomogeneity in the suspension, which is characterized by the density profiles $\rho_\alpha(z)$, where z is the vertical space coordinate. Under normal experimental conditions, the overall composition of the suspension is fixed, i.e.,

$$\frac{1}{L} \int_0^L \rho_\alpha(z) dz = n_\alpha; \quad 1 \leq \alpha \leq \nu, \quad (1)$$

where L is the vertical height of the container and n_α is the overall number density of species α . The profiles $\rho_\alpha(z)$ may be determined theoretically by minimizing the free energy functional (per unit area):

$$F[\{\rho_\alpha(z)\}] = k_B T \int_0^L dz \rho_\alpha(z) [\ln(\rho_\alpha(z) \Lambda_\alpha^3) - 1] + F_{\text{ex}}[\{\rho_\alpha\}] - \sum_\alpha \int_0^L dz \rho_\alpha(z) \Psi_\alpha(z). \quad (2)$$

The first term on the rhs of equation (2) is the familiar ideal contribution, F_{id} , to the free energy (Λ_α is an irrelevant length scale associated with species α), the second term is the non-trivial excess contribution arising from the interactions between the suspended particles, while the last term accounts for the constraint (1) and the coupling to the external field:

$$\Psi_\alpha(z) = \mu_\alpha - \phi_\alpha(z) = \mu_\alpha - m_\alpha g z, \quad (3)$$

where μ_α is the Lagrange multiplier associated with constraint (1) (in an open system μ_α would be the chemical potential of species α) and ϕ_α is the external potential acting on species α . The density profiles are formally determined by the ν coupled Euler–Lagrange equations associated with the extremum conditions

$$\frac{\delta F[\{\rho_\alpha\}]}{\delta \rho_\beta(z)} = k_B T \ln(\rho_\beta \Lambda_\beta^3) + \frac{\delta F_{\text{ex}}[\{\rho_\alpha\}]}{\delta \rho_\beta(z)} - (\mu_\beta - m_\beta g z) = 0. \quad (4)$$

Total neglect of particle interactions (i.e. $F_{\text{ex}} = 0$) leads back to the familiar barometric formula $\rho_\alpha(z) \propto \exp(-z/\xi_\alpha)$. If the gravitational lengths ξ_α are much larger than the particle sizes σ_α , the density profiles are expected to vary slowly over distances of the order of σ_α , so the local density approximation (LDA) is applicable, whereby

$$F_{\text{ex}}[\{\rho_\alpha\}] = \int_0^L f_{\text{ex}}(\{\rho_\alpha(z)\}) dz, \quad (5)$$

where $f_{\text{ex}}(\{\rho_\alpha\})$ is the excess free energy density of the homogeneous multi-component dispersion as a function of the local densities $\rho_\alpha(z)$. The Euler–Lagrange equations (4) now reduce to

$$\mu_\beta(\{\rho_\alpha(z)\}) = k_B T \ln(\rho_\beta(z)\Lambda_\beta^3) + \frac{\partial f_{\text{ex}}(\{\rho_\alpha(z)\})}{\partial \rho_\beta(z)} = \mu_\beta - m_\beta g z. \quad (6)$$

The ‘local’ chemical potential $\mu_\beta(\{\rho_\alpha(z)\})$ is the sum of ideal and excess contributions, and equation (6) expresses local chemical equilibrium in an external field. Taking the derivative of equations (6) with respect to z , one arrives at the following set of coupled first-order differential equations for the density profiles [6]:

$$\underline{\underline{M}} \begin{pmatrix} \frac{d\rho_1(z)}{dz} \\ \vdots \\ \frac{d\rho_\nu(z)}{dz} \end{pmatrix} = - \begin{pmatrix} 1/\xi_1 \\ \vdots \\ 1/\xi_\nu \end{pmatrix}, \quad (7)$$

where the matrix elements of the $\nu \times \nu$ matrix $\underline{\underline{M}}$ are $M_{\alpha\beta} = \partial(\mu_\alpha/(k_B T))/\partial \rho_\beta$, calculated for $\rho_\beta = \rho_\beta(z)$. In the one-component case ($\nu = 1$), equation (7) reduces to

$$\frac{d\rho(z)}{dz} = -\chi_T(\rho(z)) \frac{\rho(z)}{\xi}, \quad (8)$$

where $\chi_T(\rho)$ denotes the dimensionless osmotic compressibility $k_B T (\partial \Pi / \partial \rho)^{-1}$ and Π is the osmotic pressure of the suspension. The LDA equation (8) is equivalent to the macroscopic hydrostatic equilibrium condition:

$$\frac{d\Pi(\rho(z))}{dz} = -mg\rho(z). \quad (9)$$

Note that since $\chi_T \geq 0$, equation (8) can only yield monotonically decreasing density profiles $\rho(z)$, but this is no longer true of the multi-component generalization (7), which allows non-monotonic behaviour of the coupled profiles $\rho_\alpha(z)$, as will be illustrated abundantly in the following sections. Note also that the LDA cannot account for particle layering at the bottom of the container. In fact, it yields coarse grained profiles $\bar{\rho}(z)$, ‘smeared’ over distances of the order of the particle diameter σ_α [2]. Finally, LDA entails a remarkable scale invariance, i.e. the profiles $\rho_\alpha(z/\xi_\alpha)$ as functions of the reduced altitude z/ξ_α depend only on the ratios L/ξ_α , for any given overall composition $\{n_\alpha\}$. Integration of equation (9) gives

$$\Pi(z)/(k_B T) = \frac{1}{\xi} \int_0^L \rho(z') dz', \quad (10)$$

so a measurement of $\rho(z)$ and subsequent elimination of the parameter z between $\rho(z)$ and $\Pi(z)$ yields the osmotic equation of state $\Pi(\rho)$ of the *homogeneous* suspension [7].

3. Sedimenting spheres, rods and plates

The density profiles of suspensions of particles of various shapes can cross phase boundaries between phases of different bulk densities. Gravity-induced ordering is strikingly illustrated by the classic experiment of Pusey and van Megen [7] who were able to observe the coexistence of fluid and crystal phases of hard-sphere-like colloidal suspensions. The packing fractions of the coexisting phases agree perfectly with the predictions of computer simulations of bulk hard sphere systems. Complete density profiles can be measured by light scattering techniques [3] or using computer simulations [2].

Because of the finite resolution of the scattering experiments, profiles are naturally coarse grained (i.e. any rapid variation on the scale of the particle diameter is averaged out), so

the LDA-based inversion procedure described at the end of the previous section is directly applicable. Piazza *et al* [3] were thus able to measure the osmotic pressure of hard-sphere-like colloids over a wide range of packing fractions, and their data in the fluid phase agree well with the quasi-exact Carnahan–Starling equation of state [8].

Gravity-induced ordering has also been predicted and observed for highly anisometric particles, such as long rods or thin plates, which form isotropic as well as nematic and columnar phases [9]. Onsager’s celebrated theory of hard rod fluids [10] and its extensions are readily generalized to include sedimentation and for calculating density profiles of long hard rods under gravity [11]. The resulting profiles exhibit a sharp discontinuity as the isotropic-to-nematic boundary is crossed with decreasing altitude.

The ‘inverse problem’ was solved in Monte Carlo simulations of thin, disc-like platelets [12]: density profiles under gravity were inverted according to the prescription of equation (10) to extract the osmotic equation of state $\Pi(\rho)$. The results from a single simulation of the platelets subjected to gravity are in remarkable agreement with the classic data of Frenkel and Eppenga [13] from a series of simulations of the homogeneous system at various densities.

The remainder of this paper will deal with the sedimentation equilibrium of binary systems. The case of highly asymmetric binary mixtures of hard spheres was investigated in [6] within the LDA, i.e. by solving the coupled equations (7) (with $\nu = 2$), and using the accurate equation of state of homogeneous hard sphere mixtures due to Mansoori *et al* [14]. Although binary hard sphere mixtures do not undergo a thermodynamically stable fluid–fluid bulk phase separation (the latter is pre-empted by freezing [15]), the calculated sedimentation profiles exhibit a strong size segregation, signalled by highly localized density profiles of the larger spheres. A diffuse slab of predominantly large spheres appears to float at a given altitude within an inhomogeneous fluid of mainly small spheres. The exact vertical location of the slab may be tuned by varying the mass ratio [6]. This observation provided the motivation for the study of the related system of colloid–polymer mixtures which will be reported on in the next section.

4. Colloid sedimentation and phase coexistence of colloid–polymer mixtures

We consider now binary suspensions of hard sphere colloids and non-adsorbing polymer coils, which have been abundantly investigated in recent years, both experimentally and theoretically (see [16] for a review and [17, 18] for recent experimental work). Under θ -solvent conditions, the interactions between polymers may be neglected, and a popular model for describing mixtures of colloids and non-interacting polymers is that of Asakura and Oosawa [19] and Vrij [20] (AOV). This is a model of non-additive hard spheres with pair potentials:

$$v_{\alpha\beta}(r) = \begin{cases} \infty, & r < \sigma_{\alpha\beta}, \\ 0, & r > \sigma_{\alpha\beta}, \end{cases} \quad (11)$$

where the indices $\alpha, \beta = c$ (colloids) or p (polymers), $\sigma_{cc} = \sigma_c$ (colloid diameter), $\sigma_{pp} = 0$, $\sigma_{cp} = (\sigma_c + \sigma_p)/2$ and σ_p is twice the radius of gyration R_g of the polymer coils. Contrary to the case for additive hard spheres, the non-additive character of the model leads to phase separation into colloid-rich and colloid-poor fluid phases, for size ratios $q = \sigma_p/\sigma_c \gtrsim 0.4$. Complete phase diagrams have been established from theory [21, 22] and computer simulations [23, 24]. The phase separation survives when polymer interactions are included, although the full phase diagram and in particular the location of the critical point in the (η_c, η_p) plane are significantly modified [25]. Under most physical conditions, the ratio of buoyant masses $m_p/m_c \ll 1$ for comparable polymer and colloid sizes ($\sigma_p \sim \sigma_c$), because polymer coils are fractal objects. It is hence reasonable to consider the case of massless polymer such that the polymer gravitational

length $\xi_p \rightarrow \infty$, while ξ_c remains finite. In other words, in the absence of colloids the polymer solution would remain homogeneous under gravity. The corresponding external potentials are given by

$$v_c^{\text{ext}}(z) = \begin{cases} m_c g z, & \sigma_c/2 < z < L - (\sigma_c/2), \\ \infty, & \text{otherwise,} \end{cases} \quad (12)$$

$$v_p^{\text{ext}}(z) = \begin{cases} 0, & \sigma_p/2 < z < L - (\sigma_p/2), \\ \infty, & \text{otherwise.} \end{cases} \quad (13)$$

The overall composition of the suspension is fixed, i.e. conditions (1) (with $\alpha = c$ or p) are satisfied. For a given composition, the key control parameter of the problem is the ratio L/ξ_c . In the limit where L and $\xi_c \gg \sigma_c$ the LDA is applicable. The excess free energy of the bulk colloid–polymer mixture in equation (5) is conveniently taken from the accurate free volume theory [22], which yields an analytic expression for f_{exc} . Within the LDA the profiles $\rho_c(z)$ and $\rho_p(z)$ depend only on the control parameter L/ξ_c when plotted versus the rescaled altitude z/ξ_c or z/L . Results of LDA calculations for a size ratio $q = 1$ and overall packing fractions $\eta_c = \pi n_c \sigma_c^3/6 = 0.12$ and $\eta_p = \pi n_p \sigma_p^3/6 = 0.4$ are shown in figure 1 for several values of L/ξ_c . In the absence of gravity $L/\xi_c = 0$ and the profiles reduce to step functions separating the colloid-rich ‘liquid’ phase ($\eta_c \approx 0.23$) from the colloid-poor ‘gas’ phase ($\eta_p \approx 0.02$). Increasing the ratio L/ξ_c can be achieved by considering either higher recipients ($L \uparrow$) for a fixed gravitational length, or by reducing ξ_c (e.g. by changing the density of the suspending fluid) for fixed L . The latter situation is illustrated in figure 1(b).

Decreasing ξ_c amounts to increasing gravity so it is not surprising that the ‘liquid–gas’ interface shifts to lower altitudes. Note that the macroscopic LDA implies a discontinuous jump in the profile. The amplitude of the jump, i.e. the difference $\eta_c^l - \eta_c^g$ between the colloid packing fractions in the two coexisting phases, decreases with increasing L/ξ_c and shrinks to zero at about $L/\xi_c = 20.47$. In other words, for sufficiently strong gravity, phase coexistence is suppressed even well below critical conditions under field-free conditions. The same scenario for fixed ξ_c and increasing container height L is illustrated in figure 1(a): for given overall packing fractions of the two species, the interface moves to higher altitudes when the container height L increases, and vanishes beyond a critical height L , an observation which may appear intuitively less obvious. The polymer density profiles are shown in the two insets of figure 1: their partitioning between the two phases is complementary to that of the colloids, as expected.

The paths followed by the colloid–polymer mixture in the $\eta_c - \eta_p$ and $\eta_c - \eta_p^r$ planes (where η_p^r is the polymer packing fraction of a pure polymer reservoir that is in chemical equilibrium with the system) with increasing altitude are plotted relative to the phase separation binodals in figure 2, for increasing values of the ratio L/ξ_c . At the largest value of the latter, the path is seen to go through the critical point, so no phase separation will be observed for larger values of this ratio.

We consider next the case where no complete separation of length scales occurs, so that the macroscopic LDA is no longer exact. For a fixed container height $L = 100\sigma_c$, we have used a fundamental measure theory (FMT) free energy functional [26, 27], which accounts properly for non-local effects, and reduces to the free energy of the free volume theory [22] in the homogeneous (field-free) limit. We have also carried out Monte Carlo (MC) simulations of the AOV model under gravity. Density profiles for increasing gravity, $\sigma_c/\xi_c = 0.001, 0.04, 0.008$ and 0.2 (and hence $L/\sigma_c = 0.1, 4, 8, 20$) are plotted in figure 3: the FMT (MC) results are shown in figures 3(a), (b). The two sets of data are seen to be in quantitative agreement, and to reproduce the trends predicted by the LDA (see figure 1(b)). However, both FMT and MC results show clear indications of layering at the bottom of the recipient, a feature on the scale

S4190

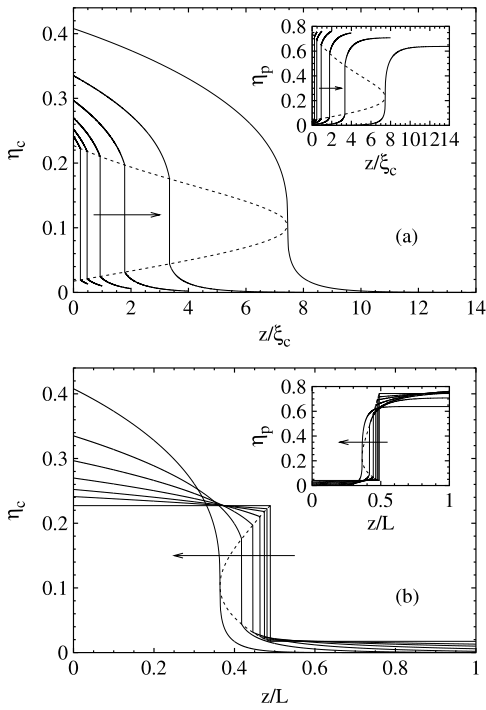
M Schmidt *et al*

Figure 1. Dimensionless density profiles, $\eta_c(z) = \pi\rho_c(z)\sigma_c^3/6$, as a function of the height variable scaled with the colloid gravitational length, z/ξ_c , for size ratio $q = 1$ and overall packing fractions $\eta_c = 0.12$, $\eta_p = 0.4$. (a) LDA results for different ratios of container height and gravitational length, $L/\xi_c = 0$ (on top of the vertical axes), 0.5, 1, 2, 4, 8, 20.47 (increasing as indicated by the arrow). The largest value corresponds to the case where the density jump (indicated by dashed curves) ends in a critical point. The inset shows the corresponding polymer profiles, $\eta_p(z) = \pi\sigma_p^3\rho_p(z)/6$. (b) Density profiles as a function of the height variable scaled with the height of the container, z/L .

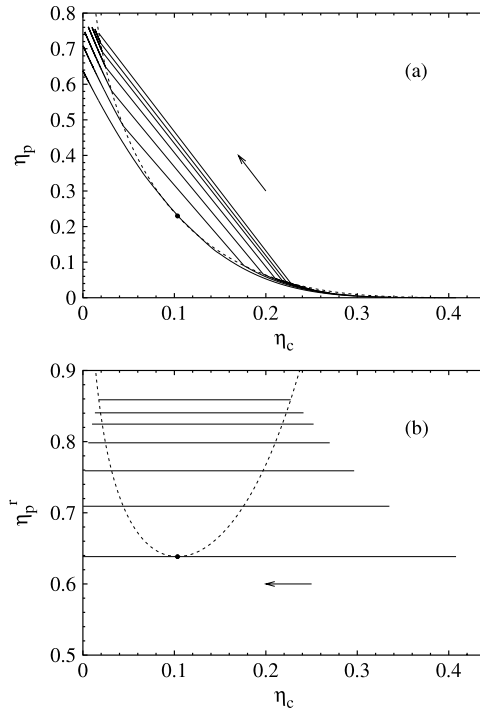


Figure 2. The bulk fluid–fluid demixing phase diagram of the AOV model as obtained from free volume theory for the size ratio $q = 1$. Shown are the binodal (dashed curve) and sedimentation paths (full curves) for increasing altitude (in the direction of the arrow) corresponding to the density profiles in figure 1. For each path the total packing fractions are $\eta_c = 0.12$, $\eta_p = 0.4$, while $L/\xi_c = 0, 0.5, 1, 2, 4, 8, 20.47$ (from top to bottom). (a) The representation in the η_c – η_p plane; (b) the representation in the η_c – η_p^r plane, where η_p^r is the packing fraction in the polymer reservoir.

of σ_c which cannot be accounted for by the LDA. Note also indications of wetting [28–32] of the upper wall of the recipient in the near homogeneous case $\sigma_c/\xi_c = 0.001$. Finally, the density profiles are seen to vary rapidly at the interface, but there is no discontinuous jump as was the case for the LDA profiles in figure 1. This reflects the finite interfacial width on the scale of a few σ_c . Since the calculations were carried out under conditions not far from the critical point of the bulk fluid–fluid demixing, the smoother variations of the MC profiles in the interfacial region compared to the FMT prediction reflect the differences in exact location of the critical point between the simulation results and the free volume theory [25, 30, 33, 34].

In order to highlight the qualitative differences between density profiles of fully miscible and phase-separating binary mixtures, we have carried out similar FMT [35] and MC calculations for a reference system, namely a binary system of additive hard spheres of identical diameters ($q = 1$), but with one of the species (playing the role of the polymer in the AOV model) being massless, i.e. not subject to gravitational effects. This system of course never phase separates, so the density profile is flat (except for layering oscillations near $z = 0$ and

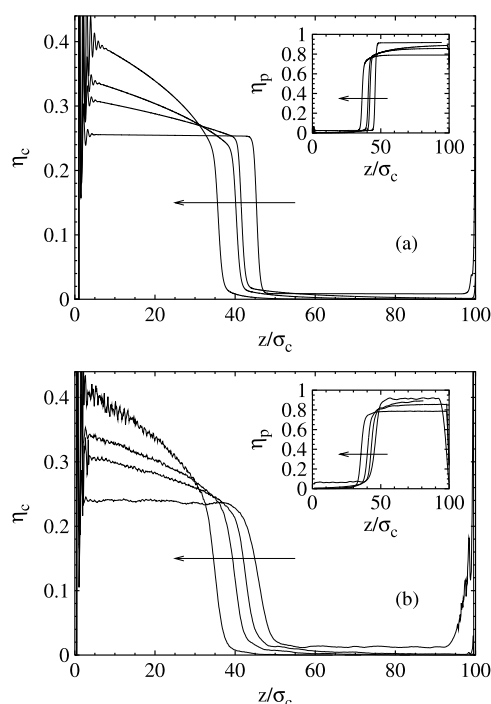


Figure 3. As figure 1, but for fixed container height $L = 100\sigma_c$ and inverse gravitational lengths $\sigma_c/\xi_c = 0.001, 0.04, 0.08, 0.2$ (along the direction of the arrows). Shown are results from FMT (a) and MC (b) studies for $\eta_c = 0.12$ and $\eta_p = 0.5$.

L) in the absence of gravity. Figure 4 shows the FMT (4(a)) and MC (4(b)) results under conditions similar to those of figure 3. The density profiles of the two species are seen to steepen as gravity increases, but there is no trace of an interface between two phases, contrary to the AOV model results in figure 3.

Returning to the AOV model, we investigated the influence of the container height on the density profiles for a fixed value of the inverse gravitational length, namely $\sigma_c/\xi_c = 0.08$. In figure 5 density profiles from FMT (5(a)) and MC (5(b)) are shown for increasing system size, $L/\sigma_c = 50, 100$ and 200 , versus altitude in units of σ_c (or equivalently ξ_c). The behaviour is seen to be similar to that predicted by the LDA for fixed ξ_c and increasing L (see figure 1(a)). The same data are shown in figure 6, with z now rescaled by L . These profiles may be compared to the LDA results shown in figure 1(b), since the latter may be reinterpreted as profiles for a given ξ_c and increasing L . Clearly the position of the interface moves to lower scaled altitudes z/L upon increasing the container height L .

The case where the polymer component is also subject to gravitational effects, i.e. ξ_p is finite, gives rise to interesting re-entrant behaviour over a restricted range of ratios ξ_c/ξ_p , for which the sedimenting mixture crosses the bulk phase coexistence line twice. The resulting ‘floating liquid’ phase has been investigated elsewhere by DFT and MC techniques similar to those used in the present study for the case $\xi_c/\xi_p = 0$ [36].

5. Conclusions

Sedimentation equilibria of colloidal systems allow phase coexistence lines to be crossed with varying altitude, i.e. an inhomogeneous suspension subjected to gravitational or centrifugal

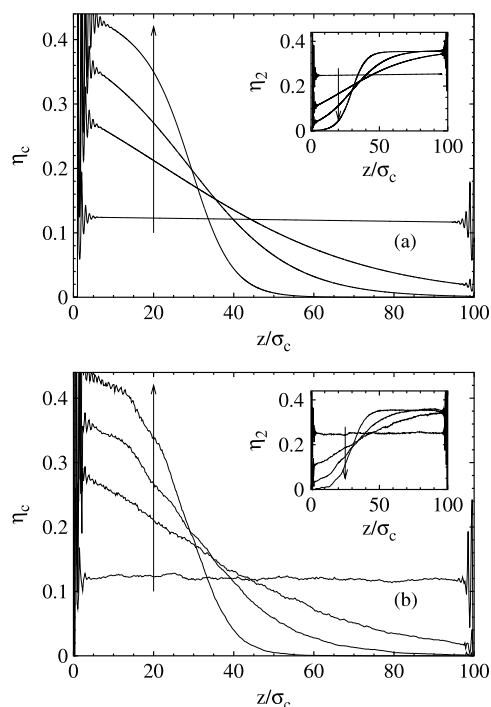


Figure 4. Density profiles of binary hard spheres obtained by formally replacing polymers of the AOV model with (additive) hard spheres of the same size (size ratio $q = 1$). Only the colloid component sediment, the secondary hard sphere species (species 2), is massless. The packing fractions are $\eta_c = 0.12$ and $\eta_2 = 0.25$, and the scaled inverse gravitational height is $\sigma_c/\xi_c = 0.001, 0.04, 0.08, 0.2$ (as indicated by the arrows). Results are shown from FMT (a) and MC simulation (b).

fields can exhibit coexisting phases of different symmetry or composition even if the homogeneous system of identical overall composition exists in a single phase. Gravity-induced density gradients have been exploited, both experimentally and theoretically, to determine the osmotic equation of state and the phase diagram of colloidal systems for many years, and some representative examples of this work have been briefly reviewed in sections 2 and 3. The main focus of this paper was on binary systems of hard sphere colloids and non-interacting, (buoyancy) massless polymers. We have investigated the influence of gravity on the coexistence between colloid-rich and colloid-poor phases. Except in the vicinity of the critical consolute point, phase coexistence in this system is characterized by large discontinuities in composition, and hence by steep variations of the density profiles in the interfacial region separating the two phases. The present LDA, FMT and MC calculations show that, for a given overall composition, the position of the interface is sensitive to the gravitational strength, and more specifically to the ratio of container height over gravitational length, L/ξ_c . In particular we find the somewhat surprising result that the position of the interface moves to lower rescaled altitudes z/L when the height L of the container increases. This sensitivity of the interface between coexisting phases to gravity and container height implies that some care has to be taken when information on phase coexistence of homogeneous (field-free) systems is to be extracted from experimental observations of phase separation under gravity. In particular, for sufficiently large ratios L/ξ_c , phase coexistence may be suppressed altogether in the sediment.

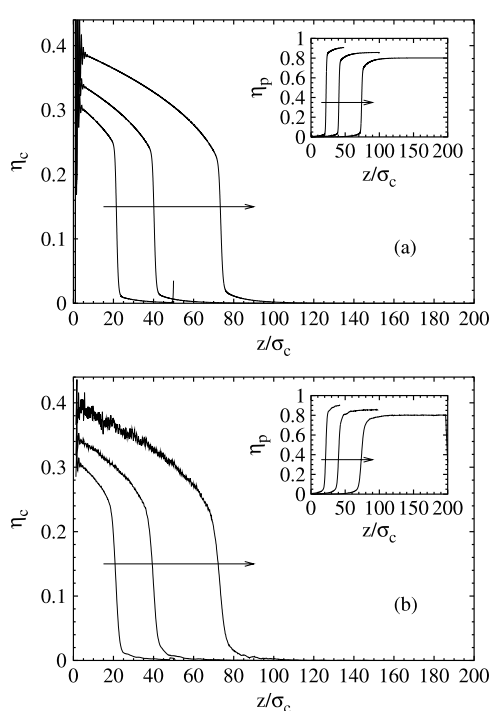


Figure 5. As figure 3, but for a fixed (inverse) gravitational length $\sigma_c/\xi_c = 0.08$ and increasing system size $L/\sigma_c = 50, 100, 200$ (as indicated by the arrows). Shown are results from FMT (a) and MC simulations (b).

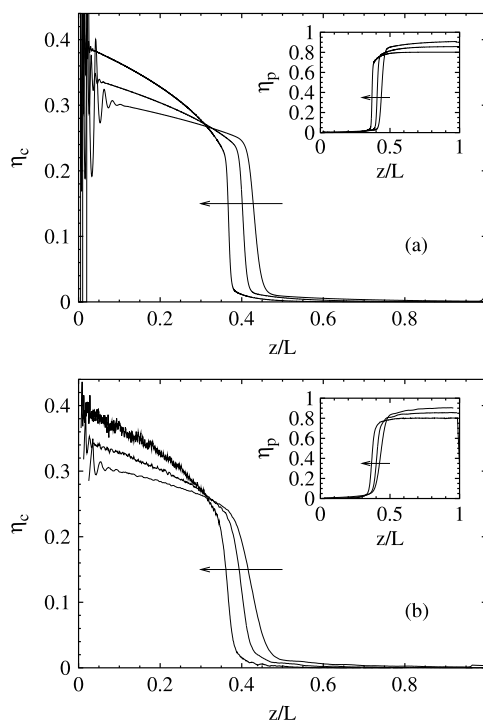


Figure 6. As figure 5, but as a function of the altitude scaled by the total container height, z/L . Clearly the position of the interface moves to smaller scaled altitudes upon increasing L .

All our considerations rely on equilibrium states; the timescale for reaching true equilibrium in an experimental colloid–polymer set-up may be considerable [37].

Acknowledgments

JPH is grateful to Giovanni Ciccotti, Giorgio Parisi and to INFM for their hospitality at La Sapienza University in Rome. MS thanks Dirk Aarts for many inspiring discussions. The work of MS is part of the research programme of the Stichting voor Fundamenteel Onderzoek der Materie (FOM), which is financially supported by the Nederlandse Organisatie voor Wetenschappelijk Onderzoek (NWO). We acknowledge support from the SFB-TR6 ‘Physics of colloidal dispersions in external fields’ of the Deutsche Forschungsgemeinschaft (DFG).

References

- [1] Perrin J 1910 *J. Physique* **9** 5
- [2] Biben T, Hansen J-P and Barrat J L 1993 *J. Chem. Phys.* **98** 7330
- [3] Piazza R, Bellini T and Degiorgio V 1993 *Phys. Rev. Lett.* **71** 4267
- [4] Evans R 1992 *Fundamentals of Inhomogeneous Fluids* ed D Henderson (New York: Dekker) chapter 3, p 85
- [5] Bodnár J and Oosterbaan W D 1997 *J. Chem. Phys.* **106** 7777
- [6] Biben T and Hansen J 1993 *Mol. Phys.* **80** 853
- [7] Pusey P N and van Meegen W 1984 *Nature* **320** 340

-
- [8] Carnahan N F and Starling K E 1969 *J. Chem. Phys.* **51** 635
[9] Wensink H H and Lekkerkerker H N W 2004 *Europhys. Lett.* **66** 125
[10] Onsager L 1949 *Ann. New York Acad. Sci.* **51** 627
[11] Allen R J, Goulding D and Hansen J-P 1999 *Phys. Chem. Commun.* **7**
[12] Dijkstra M, Hansen J-P and Madden P A 1995 *Phys. Rev. Lett.* **75** 2236
[13] Frenkel D and Eppenga R 1982 *Phys. Rev. Lett.* **49** 1089
[14] Mansoori G A, Carnahan N F, Starling K E and Leyland T W 1975 *J. Chem. Phys.* **54** 1523
[15] Dijkstra M, van Roij R and Evans R 1999 *Phys. Rev. E* **59** 5744
[16] Poon W C K 2002 *J. Phys.: Condens. Matter* **14** R859
[17] Aarts D G A L, van der Wiel J H and Lekkerkerker H N W 2003 *J. Phys.: Condens. Matter* **15** S245
[18] Aarts D G A L and Lekkerkerker H N W 2004 *Proc. CODEF Conf. (2004); J. Phys.: Condens. Matter* **16** S4231
[19] Asakura S and Oosawa F 1954 *J. Chem. Phys.* **22** 1255
[20] Vrij A 1976 *Pure Appl. Chem.* **48** 471
[21] Gast A P, Hall C K and Russell W B 1983 *J. Colloid Interface Sci.* **96** 251
[22] Lekkerkerker H N W, Poon W C K, Pusey P N, Stroobants A and Warren P B 1992 *Europhys. Lett.* **20** 559
[23] Meijer E J and Frenkel D 1994 *J. Chem. Phys.* **100** 6873
[24] Dijkstra M, Brader J M and Evans R 1999 *J. Phys.: Condens. Matter* **11** 10079
[25] Bolhuis P G, Louis A A and Hansen J P 2002 *Phys. Rev. Lett.* **89** 128302
[26] Schmidt M, Löwen H, Brader J M and Evans R 2000 *Phys. Rev. Lett.* **85** 1934
[27] Schmidt M, Löwen H, Brader J M and Evans R 2002 *J. Phys.: Condens. Matter* **14** 9353
[28] Brader J M, Evans R, Schmidt M and Löwen H 2002 *J. Phys.: Condens. Matter* **14** L1
[29] Brader J M, Evans R and Schmidt M 2003 *Mol. Phys.* **101** 3349
[30] Dijkstra M and van Roij R 2002 *Phys. Rev. Lett.* **89** 208303
[31] Aarts D G A L, Dullens R P A, Lekkerkerker H N W, Bonn D and van Roij R 2003 *J. Chem. Phys.* **120** 1973
[32] Wessels P P F, Schmidt M and Löwen H 2004 *Proc. CODEF Conf. (2004); J. Phys.: Condens. Matter* **16** S4169
[33] Vink R L C and Horbach J 2003 *Preprint cond-mat/0310404*
[34] Vink R L C and Horbach J 2004 *Proc. CODEF Conf.; J. Phys.: Condens. Matter* **16** S3807
[35] Rosenfeld Y 1989 *Phys. Rev. Lett.* **63** 980
[36] Schmidt M, Dijkstra M and Hansen J-P 2004 at press
[37] Aarts D G A L, private communication

Floating Liquid Phase in Sedimenting Colloid-Polymer Mixtures

Matthias Schmidt,^{1,*} Marjolein Dijkstra,¹ and Jean-Pierre Hansen^{2,†}

¹*Soft Condensed Matter, Debye Institute, Utrecht University, Princetonplein 5, 3584 CC Utrecht, The Netherlands*

²*Institute for Theoretical Physics, Utrecht University, Leuvenlaan 4, 3584 CE Utrecht, The Netherlands*

(Received 21 January 2004; published 20 August 2004)

Density functional theory and computer simulation are used to investigate sedimentation equilibria of colloid-polymer mixtures within the Asakura-Oosawa-Vrij model of hard sphere colloids and ideal polymers. When the ratio of buoyant masses of the two species is comparable to the ratio of differences in density of the coexisting bulk (colloid) gas and liquid phases, a stable “floating liquid” phase is found, i.e., a thin layer of liquid sandwiched between upper and lower gas phases. The full phase diagram of the mixture under gravity shows coexistence of this floating liquid phase with a single gas phase or a phase involving liquid-gas equilibrium; the phase coexistence lines meet at a triple point. This scenario remains valid for general asymmetric binary mixtures undergoing bulk phase separation.

DOI: 10.1103/PhysRevLett.93.088303

PACS numbers: 83.80.Hj, 64.70.Fx, 82.70.Dd

Equilibrium sedimentation profiles of colloidal dispersions or biomolecular solutions have been extensively measured since the pioneering experiments of Jean Perrin [1], and yield a wealth of information, in particular the osmotic equation of state of the suspension over a wide range of concentrations [2]. Sedimentation equilibria of suspensions involving two or more components often show highly nontrivial behavior, as in the case, e.g., of binary hard sphere colloid mixtures [3], of charged colloidal particles in the presence of a low ionic strength electrolyte [4–6] or of mixtures of colloidal platelets and nonadsorbing polymer [7]. Such multicomponent systems generally undergo a demixing transition in the bulk. Under gravity the density profiles may then cross phase boundaries at well-defined altitudes z , so that the suspension may be expected to segregate into horizontal slabs of different chemical compositions. In this Letter, we demonstrate that two-phase bulk coexistence of any asymmetric binary mixture can give rise to apparent three-phase coexistence in sedimentation equilibrium. A necessary condition is that the mass densities of both phases are equal for at least one statepoint at bulk coexistence, which can (in principle) be always fulfilled by choosing the mass ratio of both components appropriately. Before arguing that the phenomenon is general, we investigate in detail the particular case of binary mixtures of hard sphere colloids (of diameter σ_c), and of ideal polymer coils (of diameter σ_p). Within the familiar Asakura-Oosawa-Vrij (AOV) [8] model, the latter may freely interpenetrate while their centers are excluded from spheres of radius $(\sigma_c + \sigma_p)/2$ around each colloidal particle. Such highly nonadditive hard core interactions are known to drive a separation into a low colloid concentration “gas” phase and a high concentration colloidal “liquid” phase in the bulk, for size ratios σ_p/σ_c above a threshold value of the order of 1/3 [9,10].

We consider explicitly the case $\sigma_c = \sigma_p$. If m_i ($i = c$ or p) denotes the buoyant mass of particles of species i ,

the potential energy of the latter in the gravitational field is $V_i^{\text{ext}}(z) = m_i g z$ for $z > \sigma_i/2$ (the base of the vertical recipient of overall height L is taken to be $z = 0$), where g is the acceleration of gravity. The gravitational lengths associated with the two species are $\xi_i = k_B T / (m_i g)$, where k_B is Boltzmann’s constant and T is the absolute temperature. The equilibrium sedimentation profiles of the two species, $\rho_c(z)$ and $\rho_p(z)$, are determined, within density functional theory (DFT), by minimizing the grand potential $\Omega[\rho_c, \rho_p]$ of the inhomogeneous suspension with respect to the profiles $\rho_i(z)$. The functional Ω is conventionally split into ideal, excess and external parts:

$$\Omega[\rho_c, \rho_p] = F_{\text{id}}[\rho_c] + F_{\text{id}}[\rho_p] + F_{\text{exc}}[\rho_c, \rho_p] + \sum_{i=c,p} \int_0^L \rho_i(z) [V_i^{\text{ext}}(z) - \mu_i] dz, \quad (1)$$

where the ideal gas free energy functional is $F_{\text{id}}[\rho_i] = k_B T \int_0^L \rho_i(z) \{ \ln[\rho_i(z) \Lambda_i^3] - 1 \} dz$. Λ_i is an irrelevant length scale (which will be set equal to σ_i for convenience); μ_i is the chemical potential of species $i = c$ or p . The excess part, F_{exc} , arises from the interactions between the particles in the suspension. If the sedimentation lengths, ξ_i , are appreciably larger than the particle diameters σ_i , i.e., for slowly varying inhomogeneities, the local density approximation (LDA) for F_{exc} is expected to be accurate, except at the bottom of the suspension where layering occurs [11]. Within LDA: $F_{\text{exc}}[\rho_c, \rho_p] = \int_0^L \Phi[\rho_c(z), \rho_p(z)] dz$, where Φ is the bulk Helmholtz free energy density, which is accurately given by free-volume theory for the AOV model [9]. The LDA neglects nonlocal correlations, which are approximately included within the fundamental measure theory (FMT) [12], as adapted to the AOV model [13]. This theory leads back to the free-volume free energy in the homogeneous bulk limit, so that the two DFT treatments that we apply are consistent in this respect.

As a check of the predictions of the DFT calculations, we have also carried out extensive Monte Carlo (MC)

simulations of the same model under identical physical conditions. The simulation cell is of total height $L = 220\sigma_c$ and its square basis of edge length $l = 5\sigma_c$ is periodically repeated in the x and y directions; we checked system size dependence with simulations using $l = 25\sigma_c$ and we found that the sedimentation equilibria are similar within the statistical accuracy.

It is straightforward to show that the slope of the bulk liquid-gas binodal obeys

$$\left. \frac{d\mu_p}{d\mu_c} \right|_{\text{coex}} = - \frac{\Delta\rho_c}{\Delta\rho_p}, \quad (2)$$

where $\Delta\rho_i = \rho_i^l - \rho_i^g$, and ρ_i^g (ρ_i^l) is the density of species $i = c, p$ in the gas (liquid) phase. In the LDA spirit we define a “local” chemical potential $\mu_i(z) = \mu_i - m_i g z$ which describes a linear path, parametrized by z , in the (μ_c, μ_p) representation of the bulk phase diagram. The slope of the path is $d\mu_p/d\mu_c = m_p/m_c$, and one might hence anticipate interesting behavior when this ratio is of the order of the typical slope of the (generally curved [14]) binodal, which implies $m_c \Delta\rho_c \sim -m_p \Delta\rho_p$. Indeed for a size ratio $q = \sigma_p/\sigma_c = 1$, the DFT calculations predict a striking stacking of gas, liquid and gas phases within a limited window of (buoyant) mass ratios m_p/m_c . The density profiles calculated within the FMT version of DFT for $m_p/m_c = 0.235$ are shown in Fig. 1 for four values of the ratio σ_c/ξ_c , and keeping $\mu(z_0) = \text{const}$ at an (arbitrary) reference height, chosen as $z_0 = L/4 = 55\sigma_c$. For the largest value of σ_c/ξ_c , the system is in a colloidal gas phase. As the colloids are about 4 times heavier than the polymer, one would naively expect them to be at the bottom of the container; yet they rather accumulate at high altitudes. For decreasing values of σ_c/ξ_c , we find a novel layered structure of sedimentation profiles: a “floating” liquid slab, containing practically only colloidal particles, is seen to be sandwiched between two polymer rich slabs of gas. The lower slab is practically free of colloids, while the concentration of the latter remains significant in the upper slab. The absence of colloids in the lower slab is again counter intuitive. The interfaces between these three phases are very sharp, particularly at the lower liquid-gas interface, where the colloid density profiles are seen to exhibit some low-amplitude oscillations on the liquid side, representative of weak layering. The width of the floating liquid layer is of the order of 40 colloid diameters, so that it may be regarded as practically bulklike. The corresponding density profiles calculated within the LDA are very similar, but the lower liquid-gas interface is shifted to slightly lower altitudes and the small structure in the colloid profiles is of course suppressed. The inset in Fig. 1 shows that the thermodynamic path followed with increasing altitude indeed crosses the bulk liquid-gas coexistence curve twice, thus leading to the two observed interfaces. Upon increasing z , the sedimentation path crosses first the bulk binodal at large μ_p and μ_c , where

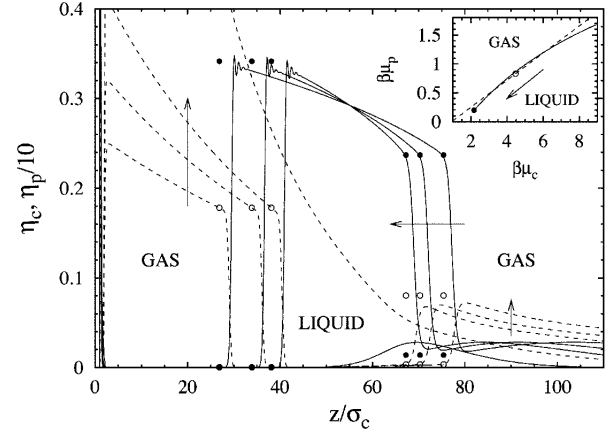


FIG. 1. Scaled density profiles of colloids $\eta_c(z)$ (solid lines) and polymers $\eta_p(z)/10$ (dashed lines) versus scaled height z/σ_c for size ratio $q = \sigma_p/\sigma_c = 1$ and mass ratio $m_p/m_c = 0.235$. Shown are DFT results for statepoint $\beta\mu_c = 4.4794 + \beta m_c g z_0$, $\beta\mu_p = 0.8294 + \beta m_p g z_0$, where $z_0 = 55\sigma_c$, and for increasing gravitational strength $\sigma_c/\xi_c = 0.06, 0.08, 0.1, 0.2$ (indicated by arrows). Also shown are the LDA predictions for the density jumps of colloids (filled circles) and polymers (open circles). The inset shows the fluid part of the bulk phase diagram as a function of the chemical potentials $\beta\mu_c$ and $\beta\mu_p$. The full line is the liquid-gas binodal terminating at a critical point (full circle). The sedimentation path (dashed line) for increasing z (indicated by the arrow) crosses the binodal twice. Also shown is the statepoint (open circle) corresponding to $z = z_0$.

a very dilute colloidal gas coexists with a rather dense colloidal liquid phase, and then crosses the bulk binodal closer to the critical point, where the colloid densities become comparable in the two coexisting phases. This explains why the lower slab is very dilute in colloids, while the upper slab contains more colloids, despite their larger mass. For significantly smaller or larger mass ratios m_p/m_c no, or only one intersection occurs corresponding to a single phase throughout the inhomogeneous colloid-polymer mixture, or to a single interface separating liquid and gas phases, as will be discussed in more detail below.

Three of the corresponding MC-generated profiles are shown in Fig. 2, together with snapshots of typical configurations of the equilibrated binary system. The agreement between DFT results shown in Fig. 1 and simulation results is seen to be quantitative. The mass density profiles (not shown) $\rho_m = m_c \rho_c + m_p \rho_p$ decrease monotonically, except for some oscillations at the lower liquid-gas interface and to a much lesser extent at the upper interface, with z . The rate of decrease is much smaller in the liquid slab, as expected from the lower osmotic compressibility of that phase.

In order to establish a tentative phase diagram for the observed stacked sedimentation, we carried out a semi-macroscopic, modified LDA calculation in the spirit of Kelvin’s theory of capillary condensation. Depending on

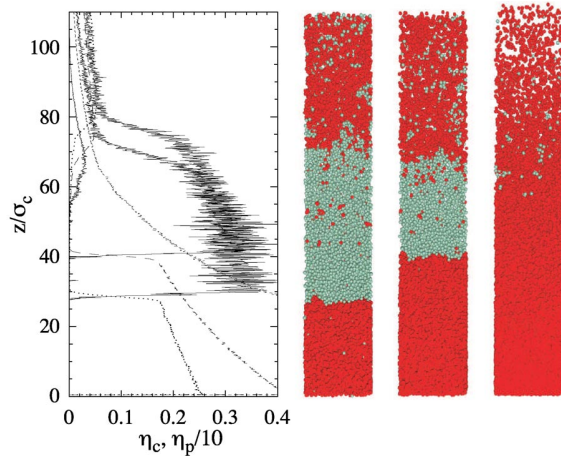


FIG. 2 (color online). Same as Fig. 1, but obtained from MC simulations, and interchanged axes. The (intermediate) case $\sigma_c/\xi_c = 0.08$ is omitted for clarity. Shown are colloid profile, $\eta_c(z)$ (solid lines), polymer profiles $\eta_p(z)$, ($\sigma_c/\xi_c = 0.06$, dotted line; 0.1, long dashed line; 0.2, short dashed line) as a function of height z/σ_c . The snapshots display particle configurations of colloids (light green) and polymers (dark red) for $\sigma_c/\xi_c = 0.06, 0.1, 0.2$ (from left to right).

the chemical potentials μ_c and μ_p , the three competing phases are a high μ_p gas phase (G), a phase containing a liquid slab at the bottom and a gas phase on top (LG), and finally the stacked gas-liquid-gas (GLG) phase. The grand potentials of these various phases have bulk contributions from the slabs, and different interfacial contributions involving the various interfacial tensions associated with the wall-fluid interface (γ_{wf}) at the bottom as well as with the liquid-gas interface(s) (γ_{lg}). In the GLG case let z_1 and z_2 denote the altitudes of the lower and upper liquid-gas interfaces; let $\Phi_\alpha(z) \equiv \Phi_\alpha[\rho_c(z), \rho_p(z)]$ denote the free energy per unit volume of the bulk liquid and gas phases ($\alpha = l$ or g), as calculated for each altitude from the LDA density profiles (these free energy densities contain now both F_{exc} and F_{id}). The grand potential per unit (horizontal) area is then written as the sum of bulk and surface contributions

$$\Omega = \int_0^{z_1} \Phi_g(z) dz + \int_{z_1}^{z_2} \phi_l(z) dz + \int_{z_2}^L \Phi_g(z) dz + \gamma_{wf}[\rho_c(0), \rho_p(0)] + \gamma_{lg}[\rho_c^l(z_1) - \rho_c^g(z_1)] + \gamma_{lg}[\rho_c^l(z_2) - \rho_c^g(z_2)]. \quad (3)$$

The three interfacial tensions appearing in Eq. (3) are calculated for the colloid and polymer densities at the three interfaces. The values of the interfacial tension for the liquid-gas interface are taken from the results of the nonlocal DFT [15], which have been shown to be very accurate for the AOV model [16]. For the wall-fluid interfacial tension γ_{wf} , we used the scaled-particle result [17]. The grand potential functional (3) was evaluated with the LDA solutions for ρ_c and ρ_p . Calculations, based on

expressions similar to (3), but involving only one or two interfaces, were carried out for the G and GL phases. The resulting grand potentials were then compared to determine the stable phase as a function of μ_c and μ_p . The resulting phase diagram for a mass ratio $m_p/m_c = 0.235$ is shown in Fig. 3. The floating liquid (GLG) phase is seen to be stable in a triangular region sandwiched between the G and LG phases. The three phases coexist at a triple point, below which the G and LG phases coexist along a line which terminates at a critical point. Compared to the bulk coexistence curve (i.e., in the absence of gravity) in the (μ_c, μ_p) plane, the phase diagram is seen to be shifted to larger values of μ_p , due to the action of gravity. The floating liquid phase arises from a delicate balance between gravity and interfacial tensions. The stability region of the GLG phase shrinks when the mass ratio decreases (in particular, it would be totally absent if polymer sedimentation were neglected altogether). In the limit of weak gravity, the interfacial contributions to the grand potential become negligible compared to the bulk contributions in Eq. (3). Yet the topology of the phase diagram remains unchanged, as illustrated by the inset in Fig. 3.

We have investigated the influence of polymer non-ideality using a stepfunction repulsion between polymers with range σ_p and height ϵ [18]. Already relatively small values of $\beta\epsilon$ (e.g., $= 0.25$) have a pronounced effect on

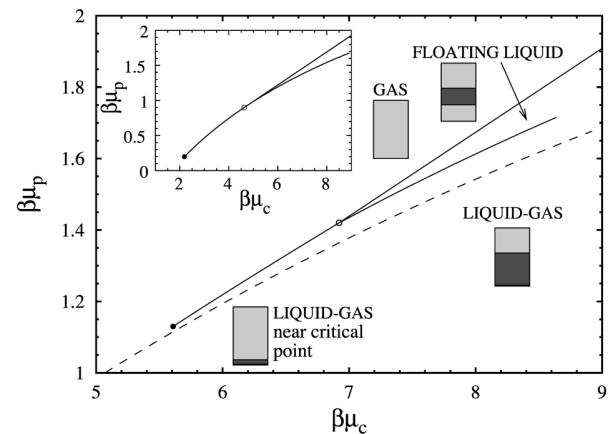


FIG. 3. The phase diagram of the AOV model under gravity as a function of the chemical potentials μ_c and μ_p , calculated within the LDA for $m_p/m_c = 0.235$, $q = 1$, and $\sigma_c/\xi_c = 0.06$. Three phases are stable: gas, floating liquid, and liquid-gas; these are sketched as cuvettes where liquid appears dark and gas appears light. Shown are the binodals (full lines), the triple point (open circle), and the liquid-gas critical point (full circle). Also shown is (part of) the bulk liquid-gas binodal (dashed line). Note that at phase coexistence the system will phase-separate *laterally*, i.e., build a vertical (curved) interface. The inset shows the result for the phase diagram for the same parameters, but in the limit of small gravity $\sigma_c/\xi_c \rightarrow 0$ and large container height $L/\sigma_c \rightarrow \infty$. The LG phase boundary is identical to the bulk binodal.

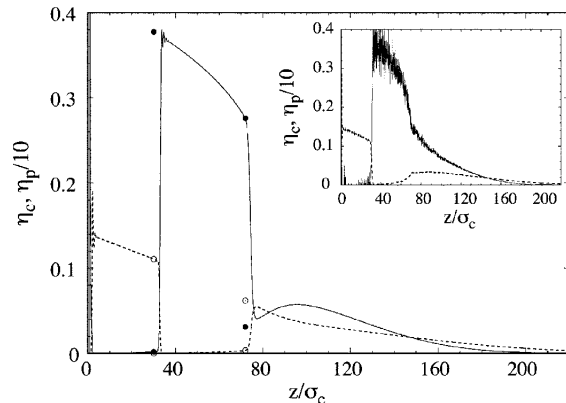


FIG. 4. Scaled density profiles of colloids (full line) $\eta_c(z)$ and polymers (dashed line) $\eta_p(z)$ versus altitude, z/σ_c , as obtained from FMT for hard spheres and nonideal polymers with $\beta\epsilon = 0.25$, mass ratio $m_p/m_c = 0.375$, size ratio $q = 1$, and inverse gravitational length $\sigma_c/\xi_c = 0.08$. Also indicated are the density jumps according to LDA for colloids (full symbols) and polymers (open symbols). The inset shows the corresponding results from MC simulation.

the location of the gas-liquid binodal [19]. Despite quantitative changes, we find the floating liquid phase to remain stable, as illustrated by the density profiles in Fig. 4. Using colloidal rods rather than polymer coils as depletant agents offers additional freedom to tune particle masses in experiments. We model such a system with colloidal hard spheres and stiff colloidal rods of length l_r and vanishing thickness [20]. Density profiles (not shown) obtained from LDA for the size ratio $l_r/\sigma_c = 1$ and a mass ratio of $m_r/m_c = 0.048$ point to the existence of the floating liquid phase.

In conclusion, DFT and MC simulations show the existence of a novel layered structure of sedimentation profiles in colloid-polymer and related mixtures. This structure demonstrates the existence, over a limited range of polymer-to-depletant mass ratios, of a floating liquid phase sandwiched between two gas slabs, the lower of which has almost vanishing colloid concentration, despite the fact that the colloidal particles are heavier than the (equal-sized) depletant particles. The required (buoyant) mass ratios might be achievable by density matching the colloidal particles to the solvent. In the case of polymer depletant, the required mass ratios are large, in view of the fact that the fractal polymer coils have a much lower bare mass than the compact colloidal particles. Using colloidal rods as depletants should render this problem less severe. The origin of the floating liquid is very different from that found in a one-component system with reentrant *bulk* phase behavior [21]. In the present case, the bulk phase diagram is fairly standard; nevertheless, there is the possibility that a sedimentation path crosses the binodal twice (see inset of Fig. 1). The stability region of the resulting floating liquid phase in the phase diagram is then determined by the balance between

bulk, gravitational, and interfacial contributions to the free energy. This scenario is generic for a wider range of binary mixtures undergoing phase separation in the bulk. Provided mass densities of both phases involved (not necessarily fluids) can be tuned to coincide at one statepoint, the phase towards which the binodal bends in the phase diagram spanned by both chemical potentials will float between slabs of the other phase.

This work was carried out during JPH's tenure of the Kramers Chair of the University of Utrecht. The work of MS is part of the research program of FOM, that is financially supported by the NWO. We acknowledge support by the SFB-TR6 of the DFG.

*On leave from Institut für Theoretische Physik II, HHUD, Universitätsstraße 1, D-40225 Düsseldorf, Germany.

†On leave from Department of Chemistry, University of Cambridge, Lensfield Road, Cambridge CB2 1EW, UK.

- [1] J. Perrin, *J. Phys.* **9**, 5 (1910).
- [2] R. Piazza, T. Bellini, and V. Degiorgio, *Phys. Rev. Lett.* **71**, 4267 (1993).
- [3] T. Biben and J. P. Hansen, *Mol. Phys.* **80**, 853 (1993).
- [4] T. Biben and J. P. Hansen, *J. Phys. Condens. Matter* **6**, A354 (1994).
- [5] A. P. Philipse and G. H. Koenderink, *Adv. Colloid Interface Sci.* **100**, 613 (2003).
- [6] R. van Roij, *J. Phys. Condens. Matter* **15**, S3569 (2003); A. P. Hynninen, R. van Roij, and M. Dijkstra, *Europhys. Lett.* **65**, 719 (2004).
- [7] H. H. Wensink and H. N. W. Lekkerkerker, *Europhys. Lett.* **66**, 125 (2004).
- [8] S. Asakura and F. Oosawa, *J. Chem. Phys.* **22**, 1255 (1954); A. Vrij, *Pure Appl. Chem.* **48**, 471 (1976).
- [9] H. N. W. Lekkerkerker *et al.*, *Europhys. Lett.* **20**, 559 (1992).
- [10] M. Dijkstra, J. M. Brader, and R. Evans, *J. Phys. Condens. Matter* **11**, 10079 (1999).
- [11] T. Biben, J. P. Hansen, and J. L. Barrat, *J. Chem. Phys.* **98**, 7330 (1993).
- [12] Y. Rosenfeld, *Phys. Rev. Lett.* **63**, 980 (1989).
- [13] M. Schmidt *et al.*, *Phys. Rev. Lett.* **85**, 1934 (2000).
- [14] See, e.g., I. Bodnár, W. D. Oosterbaan, *J. Chem. Phys.* **106**, 7777 (1997) for experimental results. The tielines in the (η_c, η_p) plane change slope as a function of statepoint implying a curved binodal in the (μ_c, μ_p) plane via (2).
- [15] J. M. Brader, *et al.*, *J. Phys. Condens. Matter* **14**, L1 (2002).
- [16] R. L. C. Fink and R. Horbach, *J. Chem. Phys.* **121**, 3253 (2004).
- [17] P. P. F. Wessels, M. Schmidt, and H. Löwen, *J. Phys. Condens. Matter* **16**, L1 (2004).
- [18] M. Schmidt, A. R. Denton, and J. M. Brader, *J. Chem. Phys.* **118**, 1541 (2003).
- [19] R. L. C. Vink (unpublished).
- [20] P. Bolhuis and D. Frenkel, *J. Chem. Phys.* **101**, 9869 (1994).
- [21] J. Dzubiella, H. M. Harreis, C. N. Likos, and H. Löwen, *Phys. Rev. E* **64**, 011405 (2001).

Fluid demixing in colloid–polymer mixtures: Influence of polymer interactions

Matthias Schmidt

*Institut für Theoretische Physik, Heinrich-Heine Universität Düsseldorf, Universitätsstraße 1,
D-40225 Düsseldorf, Germany*

Alan R. Denton

Department of Physics, North Dakota State University, Fargo, North Dakota 58105-5566

Joseph M. Brader

The James Franck Institute, University of Chicago, Chicago, Illinois 60637

(Received 29 July 2002; accepted 17 October 2002)

We consider a binary mixture of hard colloidal spheres and nonadsorbing polymer coils. The polymers are regarded as effective spheres that interact with one another via a repulsive step-function pair potential and with colloids solely via excluded volume. The system is treated with a geometry-based density functional theory based on the exact zero-dimensional limit of the model. For bulk fluid phases, we calculate demixing binodals and find that with increasing strength of polymer–polymer interaction the coexisting colloidal liquid (vapor) phase becomes more concentrated (dilute) in polymer. In contrast to a simple mean-fieldlike perturbative density functional, our approach yields good agreement with an experimental demixing phase diagram.

© 2003 American Institute of Physics. [DOI: 10.1063/1.1528191]

I. INTRODUCTION

Colloid–polymer mixtures are experimentally accessible, well-characterized systems, that serve as models for studying emergence of structure in condensed matter. In particular, phase transitions between colloidal vapor, liquid, and crystalline phases have attracted much experimental and theoretical interest. For mixtures of colloids and nonadsorbing polymer, the Asakura–Oosawa (AO) model^{1,2} treats the polymer chains as effective spheres that are mutually ideal (noninteracting) but that have excluded-volume interactions with the colloids. Within the AO model, perturbation theory³ and free-volume theory⁴ predict bulk fluid demixing, the latter theory qualitatively describing experimental trends of the phase behavior.^{5,6}

Recent work has been devoted to integrating out polymer degrees of freedom to obtain an effective (many-body) Hamiltonian for the colloids.⁷ A pairwise approximation to the effective Hamiltonian can then be input to standard bulk perturbation theory in order to calculate thermodynamic and structural properties.⁷ This principle approach was also used for investigation of interfacial properties^{8,9} in the framework of density-functional theory (DFT).¹⁰

An alternative approach is to explicitly treat the full binary mixture and hence effective many-body colloidal interactions. Following previous work on hard sphere mixtures,^{11–15} a DFT approach to the AO model was recently proposed.^{16,17} The bulk fluid free energy, and hence the fluid–fluid demixing phase diagram, that arise from this DFT are identical to the predictions of free volume theory.⁴ However, as the theory is constructed to deal with inhomogeneous systems, it also can be applied to (entropic) wetting at a hard wall and layering phenomena in the interface between demixed fluids.¹⁸

All of these approaches neglect direct polymer–polymer interactions, an assumption that is most valid at the theta temperature, where the second virial coefficient of the monomer–monomer interaction vanishes. In order to treat interactions between polymers, Warren *et al.*¹⁹ proposed a perturbation theory around the AO model as a reference system (which, again, is described with free-volume theory). A more microscopic picture that works on the segment level of the polymers is provided by the macromolecular approach of Fuchs and co-workers.^{20,21} In their theory, interactions between segments (and hence polymers) are intrinsically built in. However, both approaches seem to be limited primarily to *bulk* considerations.

Although a description on the segment level is desirable, we note that for pure polymer solutions, recent studies have suggested a “soft colloid” picture.²² In this picture, upon averaging over the monomer degrees of freedom, effective polymer interactions can be well represented by a Gaussian pair potential. Such penetrable potentials have been shown to be well described by a simple mean-fieldlike density functional, which in bulk is equivalent to the random phase approximation (RPA).²² In the same spirit, a recent study examined the *binary* Gaussian core mixture in inhomogeneous situations.^{23,24} In the context of colloid–polymer interactions, structural correlation functions were obtained from the Percus–Yevick theory applied to the AO model and also a (Gaussian) repulsion between polymers was taken into account.²⁵

In the present work, we aim at a DFT for a more realistic description of colloid–polymer mixtures than provided by the AO model, one that takes polymer–polymer interactions into account. Specifically, we consider a model in which the polymers, although still treated as effective spheres, interact

via a repulsive step-function pair potential. This model bridges recent studies by interpolating between the AO model for ideal polymers and the binary hard-sphere (HS) mixture. Note that while the AO model system displays stable fluid–fluid coexistence,^{3,4,7} binary HS mixtures do not, as freezing preempts fluid demixing.²⁶

In Sec. II, the model mixture of colloids and interacting polymers is defined. In Sec. III, we develop the nonperturbative geometry-based DFT. The explicit construction of the functional is guided by the exact solution of the model in the special zero-dimensional case. For comparison, we also discuss two mean-fieldlike perturbative theories. In Sec. IV, we derive the bulk free energy, which allows us to calculate phase behavior. We conclude in Sec. V.

II. THE MODEL

We consider a binary mixture of hard colloidal spheres (species C) of radius R_C and polymer coils (species P) with radius of gyration R_P . The colloid–colloid pair interaction potential as a function of the center–center interparticle distance, r , is $V(r) = \infty$, if $r < 2R_C$, and zero otherwise. We assume that the polymer–colloid interaction is also hard: $V_{CP}(r) = \infty$, if $r < R_C + R_P$, and zero otherwise. The interactions between polymers are represented by a step-function pair potential: $V_{PP}(r) = \epsilon$, if $r < 2R_P$, and zero otherwise. Apart from trivial kinetic energy terms and external potentials, the resulting Hamiltonian is

$$H(\{\mathbf{R}_i\}, \{\mathbf{r}_j\}) = \sum_{i < j}^{N_C} V_{CC}(|\mathbf{R}_i - \mathbf{R}_j|) + \sum_i^{N_C} \sum_j^{N_P} V_{CP}(|\mathbf{R}_i - \mathbf{r}_j|) + \sum_{i < j}^{N_P} V_{PP}(|\mathbf{r}_i - \mathbf{r}_j|), \quad (1)$$

where $\{\mathbf{R}_i\}$ denotes colloid and $\{\mathbf{r}_j\}$ polymer coordinates. Note that in the limit $\epsilon/k_B T \rightarrow 0$ we recover the AO model, and for $\epsilon/k_B T \rightarrow \infty$ binary hard spheres. Although in Ref. 19 $V_{PP}(r)$ is assumed to have a range of R_P , our (longer-ranged) choice is more consistent with the effective (Gaussian) potentials of Louis *et al.*,²² which extend out even beyond $2R_P$. We do not use the Gaussian potential as our aim is at a minimal model that displays the essential features.

As bulk thermodynamic parameters, we use the packing fractions $\eta_i = 4\pi R_i^3 \rho_i / 3$, $i = C, P$, where ρ_i is the number density of species i . The control parameters are the size ratio, $q = R_P / R_C$, of colloid and polymer radii and the reduced strength, $\epsilon / (k_B T)$, of polymer–polymer interactions, where k_B is the Boltzmann constant and T absolute temperature.

III. THEORY

A. Zero-dimensional limit

In the original context of hard spheres,¹⁴ it was shown that an idealized zero-dimensional (0D) limit can motivate the construction of density functionals for 3D systems. The benefit of zero dimensions is that the partition sum can be calculated exactly, as the configurational integral over the spatial degrees of freedom is trivial. Choosing an explicit (approximate) form for the free energy functional, one im-

poses that it correctly recovers the 0D properties, when applied to an appropriate (δ -functionlike) density profile. This constraint has guided the development of DFTs for models such as penetrable spheres²⁷ and the AO model.^{16,17}

Let us consider the current model in the 0D limit, in which particle centers are confined to a volume v_{0D} whose dimensions are smaller than all relevant length scales in the system. The microstates accessible in that limit are completely specified by the occupation numbers of particles of both species. Each microstate is assigned a statistical weight according to the grand ensemble. In general, the grand partition sum for a binary mixture is

$$\Xi = \sum_{N_P=0}^{\infty} \frac{z_P^{N_P}}{N_P!} \sum_{N_C=0}^{\infty} \frac{z_C^{N_C}}{N_C!} \exp(-\beta V_{\text{total}}), \quad (2)$$

where the (reduced) fugacities are $z_i = (v_{0D} / \Lambda_i^3) \exp(\beta \mu_i)$, Λ_i is the thermal wavelength, μ_i is the chemical potential of species i , $\beta = (k_B T)^{-1}$, and V_{total} is the total potential energy in the situation where all particles have vanishing separation. Note that for hard-core interactions, the Boltzmann factor vanishes for forbidden configurations, which practically limits the upper bounds in the summations in Eq. (2). For the present case, where V_{CC} and V_{CP} are hard-body interactions, we obtain

$$\Xi = z_C + \sum_{N_P=0}^{\infty} \frac{z_P^{N_P}}{N_P!} \exp[-\beta \epsilon N_P(N_P - 1)/2], \quad (3)$$

where the N_P dependence in the Boltzmann factor stems from combinatorial counting of pairs of polymers. Clearly, for $z_C = 0$, we recover the limit of one-component penetrable spheres;²⁷ for $\beta \epsilon = 0$, Eq. (3) reduces to the AO result,^{16,17} $\Xi = z_C + \exp(z_P)$. In order to obtain the Helmholtz free energy, a Legendre transform is to be performed, and the dependence on the fugacities is to be replaced with dependence on the mean numbers of particles, $\eta_i = z_i \partial \ln \Xi / \partial z_i$. Taking the particle volume of species i as the reference volume, η_i is also the 0D packing fraction of species i . Subtracting the ideal contribution, one calculates the excess free energy, $\beta F_{0D} = -\ln \Xi + \sum_{i=C,P} \eta_i \ln(z_i) - \sum_{i=C,P} \eta_i [\ln(\eta_i) - 1]$. In the present case (as for pure penetrable spheres), this cannot be achieved analytically. As we are interested in the case of small ϵ (close to the AO behavior), we perform an expansion in powers of $\beta \epsilon$, and obtain

$$\beta F_{0D} = (1 - \eta_C - \eta_P) \ln(1 - \eta_C) + \eta_C + \frac{\beta \epsilon}{2} \frac{\eta_P^2}{1 - \eta_C}, \quad (4)$$

which is exact up to lowest (linear) order in $\beta \epsilon$. In the limit $\beta \epsilon \rightarrow 0$, we recover the AO result,^{16,17} which is $\beta F_{0D, AO} = (1 - \eta_C - \eta_P) \ln(1 - \eta_C) + \eta_C$. In the absence of colloids, $\eta_C \rightarrow 0$, we obtain a mean-fieldlike expression, $F_{0D, MF} = \epsilon \eta_P^2 / 2$.

Some terms of higher than first order can be obtained analytically. We write the free energy as $F_{0D} + \Delta F_{0D}$, where F_{0D} is the linear contribution given by Eq. (4) and ΔF_{0D} up to cubic order in $\beta \epsilon$ is obtained as

$$\beta\Delta F_{0D} = -\frac{\eta_p^2(\beta\epsilon)^2}{4(1-\eta_C)} + \left[\frac{\eta_p^2}{1-\eta_C} + \frac{2\eta_p^3}{(1-\eta_C)^2} \right] \frac{(\beta\epsilon)^3}{12}. \quad (5)$$

In the case of large $\beta\epsilon$, the 0D free energy has to be calculated numerically, which is an easy task.

B. Geometry-based density functional

Returning to three dimensions, the total Helmholtz free energy of an inhomogeneous system may be written as $F = F_{id} + F_{exc}$, where $F_{id} = \sum_{i=C,P} \int d\mathbf{r} \rho_i(\mathbf{r}) \{ \ln[\rho_i(\mathbf{r}) \Lambda_i^3] - 1 \}$ is the ideal-gas free energy functional (for two species), and F_{exc} is the excess contribution arising from interactions between particles. Following previous work on mixtures,^{11–13,16,17} we express the Helmholtz excess free energy as a functional of colloid and polymer density fields as a spatial integral

$$F_{exc}[\rho_C(\mathbf{r}), \rho_P(\mathbf{r})] = k_B T \int d^3x \Phi(\{n_\nu^C(\mathbf{x})\}, \{n_\nu^P(\mathbf{x})\}), \quad (6)$$

where the weighted densities

$$n_\nu^i(\mathbf{x}) = \int d^3r \rho_i(\mathbf{r}) w_\nu^i(\mathbf{x}-\mathbf{r}), \quad i=C,P \quad (7)$$

are defined as convolutions of weight functions, w_ν^i , with the actual density profiles, and ν denotes the type of weight function.

In previous work on HS,¹¹ Φ is a function of species-independent weighted densities. Here we use the generalized form introduced in Ref. 16, where Φ is a function of species-dependent weighted densities. This form was shown to be necessary to capture the distinct properties of colloids and polymers. The weight functions w_ν^i are independent of the density profiles and are given by

$$w_3^i(\mathbf{r}) = \theta(R_i - r), \quad w_2^i(\mathbf{r}) = \delta(R_i - r), \quad (8)$$

$$\mathbf{w}_{v2}^i(\mathbf{r}) = w_2^i(\mathbf{r})\mathbf{r}/r, \quad \hat{\mathbf{w}}_{m2}^i(\mathbf{r}) = w_2^i(\mathbf{r})[\mathbf{r}\mathbf{r}/r^2 - \hat{\mathbf{1}}/3], \quad (9)$$

where $r = |\mathbf{r}|$, $\theta(r)$ is the step function, $\delta(r)$ is the Dirac distribution, and $\hat{\mathbf{1}}$ is the identity matrix. Further, linearly dependent, weights are $w_1^i(\mathbf{r}) = w_2^i(\mathbf{r})/(4\pi R_i)$, $\mathbf{w}_{v1}^i(\mathbf{r}) = \mathbf{w}_{v2}^i(\mathbf{r})/(4\pi R_i)$, $w_0^i(\mathbf{r}) = w_1^i(\mathbf{r})/R_i$. The weight functions are quantities with dimension (length) ^{$\nu-3$} . They differ in their tensorial rank: w_0^i , w_1^i , w_2^i , w_3^i are scalars; \mathbf{w}_{v1}^i , \mathbf{w}_{v2}^i are vectors (subscript v); and $\hat{\mathbf{w}}_{m2}^i$ is a (traceless) matrix (subscript m). The scalar and vectorial weights are borrowed from Ref. 11, whereas the tensor weight is equivalent to the formulation in Ref. 15.

The free energy density is composed of three parts,

$$\Phi = \Phi_1 + \Phi_2 + \Phi_3, \quad (10)$$

which are defined as

$$\Phi_1 = \sum_{i=C,P} n_0^i \varphi_i(n_3^C, n_3^P), \quad (11)$$

$$\Phi_2 = \sum_{i,j=C,P} (n_1^i n_2^j - \mathbf{n}_{v1}^i \cdot \mathbf{n}_{v2}^j) \varphi_{ij}(n_3^C, n_3^P), \quad (12)$$

$$\begin{aligned} \Phi_3 = & \frac{1}{8\pi} \sum_{i,j,k=C,P} \left(\frac{1}{3} n_2^i n_2^j n_2^k - n_2^i \mathbf{n}_{v2}^j \cdot \mathbf{n}_{v2}^k \right. \\ & \left. + \frac{3}{2} [\mathbf{n}_{v2}^i \hat{\mathbf{n}}_{m2}^j n_{v2}^k - \text{tr}(\hat{\mathbf{n}}_{m2}^i \hat{\mathbf{n}}_{m2}^j \hat{\mathbf{n}}_{m2}^k)] \right) \\ & \times \varphi_{ijk}(n_3^C, n_3^P), \end{aligned} \quad (13)$$

where tr denotes the trace, and derivatives of the 0D excess free energy [Eq. (4)] are

$$\varphi_{i\dots k}(\eta_C, \eta_P) \equiv \frac{\partial^m}{\partial \eta_i \dots \partial \eta_k} F_{0D}(\eta_C, \eta_P). \quad (14)$$

In the absence of polymer, Φ_1 and Φ_2 are treated as in Ref. 11 and Φ_3 as in Ref. 15. Equations (11)–(13) are generalizations of expressions in Refs. 11 and 15 that include summations over species.^{16,17}

C. Perturbative density functional

It is instructive to relate the above approach to a perturbative treatment, where the AO model is used as a reference system, and the polymer-polymer interactions are regarded as a perturbation. Apparently, perturbed and reference systems are very similar. Aside from sharing the same V_{CC} , the cross interactions V_{CP} are the same (namely hard-core interactions). Only the remaining polymer-polymer interaction differs (and vanishes in the reference system). The reference system may be well described by the AO functional,^{16,17} which is recovered by using $F_{0D} = (1 - \eta_C - \eta_P) \ln(1 - \eta_C) + \eta_C$ as a generator in the above geometrical recipe. What remains to be treated is the perturbative contribution to the free energy due to polymer-polymer interactions. To obtain that, a minimal requirement is that the pure polymer system (free of colloids) is described reasonably. As was recently discovered²⁸ for penetrable interactions, this is the case for a mean-field (excess) functional

$$F_{MF}[\rho_P(\mathbf{r})] = \frac{1}{2} \int d\mathbf{r} d\mathbf{r}' \rho_P(\mathbf{r}) V_{PP}(|\mathbf{r}-\mathbf{r}'|) \rho_P(\mathbf{r}'). \quad (15)$$

This DFT was utilized to investigate Gaussian core particles adsorbed at a hard wall.²⁸ The generalization of Eq. (15) to binary mixtures was used in Ref. 23 to study interfacial properties²³ and wetting²⁴ of the binary Gaussian core model. Note that in bulk Eq. (15) is equivalent to using the RPA, which is a reasonable approximation for penetrable interactions.^{29,30}

It might at first appear that $F' = F_{AO} + F_{MF}$ would give a good description of the excess free energy of the mixture, as the hard-body interactions between polymers and colloids are already accounted for in F_{AO} . Hence the perturbative contribution depends *solely on the polymer density profile*. This reasoning is independent of the precise model under consideration, and should hold also for soft repulsive interactions. For the present model, we can show, in contrast, that F' is (apart from trivial limits) never a good approximation to treat the mixture, and nonsensical trends in phase behavior

arise (see Sec. IV C). We expect similar failings when applying this approach to other models consisting of mixtures of hard-core and penetrable particles.

Within our framework, F' can be derived from $F_{0D} = F_{0D}^{AO} + \epsilon \eta_p^2/2$ and applying the recipe outlined in Sec. III B. By comparing with the exact linear-order result [Eq. (4)], $F_{0D} = F_{0D}^{AO} + \frac{1}{2} \epsilon \eta_p^2/(1 - \eta_c)$, one immediately observes that already the linear term in η_c differs. This discrepancy persists throughout the construction of the DFT, and hence F' displays a similar failing. The predictions of phase behavior from this approach are shown at the end of Sec. IV C below.

Evidently, the mean-field functional neglects exclusion of polymer from the volume occupied by the colloid. In contrast, the geometry-based functional naturally accounts for excluded volume: A given polymer interacts with polymer in the available volume whose density is higher than the density of polymer in the system.

D. Perturbative bulk theory

Warren *et al.*¹⁹ proposed a perturbative approach for the free energy of bulk colloid-polymer mixtures in which polymers interact with a penetrable repulsive interaction $V_{PP}(r)$. This can be viewed as a perturbative treatment where in the reference system $V_{PP}(r) = 0$, and $V_{PP}(r)$ is regarded as the perturbation. As input, the bulk void-void correlation function³¹ of the pure hard sphere system is required, and Ref. 19 proposes an empirical analytical form that interpolates between the known limits of vanishingly and infinitely separated polymers. In the following, we rederive this theory in a general framework. This will allow us to relate the approach of Warren *et al.* to the oversimplistic bulk theory that arises from the perturbative DFT. Moreover, we can quantitatively compare this approach against the bulk predictions of the geometry-based DFT.

We consider the fully interacting binary mixture with fixed colloid particle number N_C and polymer fugacity z_P . The semigrand partition function is given by

$$\Xi_{\text{semi}} = \text{Tr}_C e^{-\beta H_{CC}} \left[\sum_{N_P=0}^{\infty} \frac{z_P^{N_P}}{N_P!} \int d\mathbf{r}^{N_P} e^{-\beta(H_{CP} + \lambda H_{PP})} \right], \quad (16)$$

where λ is a charging parameter which is equal to unity in the fully interacting system, and the canonical trace over colloid coordinates is

$$\text{Tr}_C = \frac{1}{\Lambda_C^{3N_C N_C!}} \int d\mathbf{R}^{N_C}. \quad (17)$$

By expanding the integrand in Eq. (16) in a Taylor series about $\lambda = 0$, we obtain a perturbation theory

$$\begin{aligned} \beta\Omega_{\text{semi}} &= \beta\Omega_{\text{semi},0} + \int_0^1 d\lambda \left(\frac{\partial \beta\Omega_{\text{semi}}}{\partial \lambda} \right) \\ &\approx \beta\Omega_{\text{semi},0} + \left(\frac{\partial \beta\Omega_{\text{semi}}}{\partial \lambda} \right)_0, \end{aligned} \quad (18)$$

where $\beta\Omega_{\text{semi}} = -\ln \Xi_{\text{semi}}$. The first term on the right is the semigrand free energy of the AO model, given by

$$\beta\Omega_{\text{semi},0} = -\ln \left(\text{Tr}_C e^{-\beta H_{CC}} \sum_{N_P=0}^{\infty} \frac{z_P^{N_P}}{N_P!} \int d\mathbf{r}^{N_P} e^{-\beta H_{CP}} \right) \quad (19)$$

$$= -\ln \left(\text{Tr}_C e^{-\beta H_{CC}} \sum_{N_P=0}^{\infty} \frac{[z_P V \alpha(\{\mathbf{R}^{N_C}\})]^{N_P}}{N_P!} \right) \quad (20)$$

$$= -\ln \{ \text{Tr}_C e^{-\beta H_{CC}} \exp[z_P V \alpha(\{\mathbf{R}^{N_C}\})] \}, \quad (21)$$

where $\alpha(\{\mathbf{R}^{N_C}\})$ is the ratio of the free volume of a single polymer sphere, in the presence of the colloids, to the system volume, V . By replacing the exact $\alpha(\{\mathbf{R}^{N_C}\})$, which depends on all coordinates of the colloids, by its average for hard spheres, $\Omega_{\text{semi},0}$ becomes identical to the result from the free-volume theory of Lekkerkerker *et al.*⁴ The second term on the right side of Eq. (18) is given by

$$\left(\frac{\partial \beta\Omega_{\text{semi}}}{\partial \lambda} \right)_0 = \Xi_{\text{semi},0}^{-1} \text{Tr}_C e^{-\beta H_{CC}} \sum_{N_P=0}^{\infty} \frac{z_P^{N_P}}{N_P!} \int d\mathbf{r}^{N_P}$$

$$\times \sum_{i < j} \beta V_{PP}(|\mathbf{r} - \mathbf{r}'|) e^{-\beta H_{CP}} \quad (22)$$

$$= \Xi_{\text{semi},0}^{-1} \text{Tr}_C e^{-\beta H_{CC}} \sum_{N_P=0}^{\infty} \frac{z_P^{N_P}}{N_P!}$$

$$\times \int d\mathbf{r}^{N_P-2} \frac{N_P}{2} (N_P - 1) \alpha(\{\mathbf{R}^{N_C}\})^{N_P-2}$$

$$\times \int d\mathbf{r} \int d\mathbf{r}' \beta V_{PP}(|\mathbf{r} - \mathbf{r}'|) \alpha(\mathbf{r}; \{\mathbf{R}^{N_C}\}) \alpha(\mathbf{r}'; \{\mathbf{R}^{N_C}\}) \quad (23)$$

$$= \Xi_{\text{semi},0}^{-1} \text{Tr}_C e^{-\beta H_{CC}} \int d\mathbf{r} \int d\mathbf{r}' \beta V_{PP}$$

$$\times (|\mathbf{r} - \mathbf{r}'|) \alpha(\mathbf{r}; \{\mathbf{R}^{N_C}\}) \alpha(\mathbf{r}'; \{\mathbf{R}^{N_C}\}) \times \frac{z_P^2}{2} \sum_{N_P=0}^{\infty} \frac{[z_P V \alpha(\{\mathbf{R}^{N_C}\})]^{N_P-2}}{(N_P-2)!}, \quad (24)$$

where $\Xi_{\text{semi},0}$ is the term inside the logarithm in Eq. (21). The final result is thus

$$\begin{aligned} \left(\frac{\partial \beta\Omega_{\text{semi}}}{\partial \lambda} \right)_0 &= \Xi_{\text{semi},0}^{-1} \text{Tr}_C e^{-\beta H_{CC}} \exp[z_P V \alpha(\{\mathbf{R}^{N_C}\})] \\ &\times \frac{z_P^2}{2} \int d\mathbf{r} \int d\mathbf{r}' \beta V_{PP}(|\mathbf{r} - \mathbf{r}'|) \\ &\times \alpha(\mathbf{r}; \{\mathbf{R}^{N_C}\}) \alpha(\mathbf{r}'; \{\mathbf{R}^{N_C}\}). \end{aligned} \quad (25)$$

Equations (21) and (25) give the exact free energy to linear order in $\beta V_{PP}(r)$. We now proceed by making the mean-field approximations and replacing quantities by their average values in the unperturbed (AO) system

$$\alpha(\{\mathbf{R}^{Nc}\}) \rightarrow \alpha(\eta_C, z_P), \quad (26)$$

$$\alpha(\mathbf{r}; \{\mathbf{R}^{Nc}\}) \alpha(\mathbf{r}'; \{\mathbf{R}^{Nc}\}) \rightarrow g_{vv}(|\mathbf{r}-\mathbf{r}'|; \eta_C, z_P), \quad (27)$$

where $\alpha(\eta_C, z_P)$ is the exact free volume fraction for the AO model (noninteracting polymers) and $g_{vv}(|\mathbf{r}-\mathbf{r}'|; \eta_C, z_P) \equiv \langle \alpha(\mathbf{r}; \{\mathbf{R}^{Nc}\}) \alpha(\mathbf{r}'; \{\mathbf{R}^{Nc}\}) \rangle_{AO}$ is the void-void correlation function of the AO model. The voids are the spaces between the colloids that can be occupied by the polymer. Insertion of Eq. (26) into Eq. (21) clearly yields the exact AO free energy. The final result is thus

$$\beta\Omega_{\text{semi}} = \beta\Omega_{\text{semi},AO} + \frac{z_P^2}{2} V \int d\mathbf{r} \beta V_{PP}(r) \times g_{vv}(|\mathbf{r}-\mathbf{r}'|; \eta_C, z_P). \quad (28)$$

If we now further approximate the relevant quantities by their HS values, $\alpha(\eta_C, z_P) \rightarrow \alpha(\eta_C) \equiv \alpha(\eta_C, z_P=0)$ and $g_{vv}(|\mathbf{r}-\mathbf{r}'|; \eta_C, z_P) \rightarrow g_{vv}^{\text{HS}}(|\mathbf{r}-\mathbf{r}'|; \eta_C) \equiv g_{vv}(|\mathbf{r}-\mathbf{r}'|; \eta_C, z_P=0)$, then the first term reduces to the free-volume theory of Lekkerkerker *et al.* and we obtain

$$\beta\Omega_{\text{semi}} = \beta F_{\text{HS}} - z_P \alpha(\eta_C) V + \frac{z_P^2}{2} V \int d\mathbf{r} \beta V_{PP}(r) \times g_{vv}^{\text{HS}}(|\mathbf{r}-\mathbf{r}'|; \eta_C), \quad (29)$$

where F_{HS} is the Helmholtz free energy of pure HS. We give the explicit (approximative) expression for $\alpha(\eta_C)$ below in Sec. IV A. The original result of Warren *et al.* for the semi-grand free energy, Eq. (27) in Ref. 19, is identical to Eq. (29), if $\beta V_{PP}(r)$ in (29) is replaced by its corresponding Mayer function, $1 - \exp[-\beta V_{PP}(r)]$. The difference arises from the fact that in the original version a virial expansion in polymer density is performed, while we apply thermodynamic perturbation theory. However, for small $\beta\epsilon$ the differences are negligible.

An equivalent perturbation theory can be derived directly in the canonical ensemble. The result for the canonical excess free energy is

$$\frac{\beta F_{\text{exc}}^{\text{pert}}(\rho_C, \rho_P)}{V} = \beta \phi_{\text{HS}}(\rho_C) - \rho_P \ln \alpha(\rho_C) + \frac{\beta}{2} \left(\frac{\rho_P}{\alpha(\rho_C)} \right)^2 \int d\mathbf{r} V_{PP}(r) \times g_{vv}^{\text{HS}}(|\mathbf{r}-\mathbf{r}'|; \rho_C), \quad (30)$$

where $\phi_{\text{HS}}(\rho_C)$ is the excess free energy per unit volume of pure HS. While the same level of approximation is employed in both derivations, Eqs. (29) and (30) are inequivalent, in general, when related by a Legendre transform. They can be shown, however, to be equivalent to linear order in $V_{PP}(r)$.

IV. RESULTS

A. Bulk fluid phases

In bulk, the one-body densities of both species are spatially uniform: $\rho_i(\mathbf{r}) = \text{const}$. This leads to analytic expressions for the weighted densities, Eq. (7), and therefore for the

excess free energy density, Eqs. (10)–(13). The integration in Eq. (6) becomes trivial and gives a factor V . Explicitly, the result is

$$\frac{\beta F_{\text{exc}}(\rho_C, \rho_P)}{V} = \beta \phi_{\text{HS}}(\rho_C) - \rho_P \ln \alpha_1(\rho_C) + \frac{\beta \tilde{V}_{PP}(0)}{2} \rho_P^2 [1 - \ln \alpha_2(\rho_C)], \quad (31)$$

where the integrated potential is $\tilde{V}_{PP}(0) = 4\pi \int dr r^2 V_{PP}(r) = 4\pi \epsilon \sigma_P^3/3$ and ϕ_{HS} , in the scaled-particle (Percus–Yevick compressibility) approximation, is given by

$$\beta \phi_{\text{HS}} = \frac{3\eta_C [3\eta_C(2-\eta_C) - 2(1-\eta_C)^2 \ln(1-\eta_C)]}{8\pi R_C^3 (1-\eta_C)^2}. \quad (32)$$

In Eq. (31), the α_i , which depend solely on η_C and q , are given through

$$\ln \alpha_1 = \ln(1-\eta_C) - \sum_{m=1}^3 C_m^{(1)} \gamma^m, \quad (33)$$

$$\ln \alpha_2 = -\frac{1}{8} \sum_{m=1}^4 C_m^{(2)} \gamma^m, \quad (34)$$

where the dependence on density is through $\gamma = \eta_C/(1-\eta_C)$, and the coefficients are polynomials in the size ratio, given as $C_1^{(1)} = 3q + 3q^2 + q^3$, $C_2^{(1)} = (9q^2/2) + 3q^3$, $C_3^{(1)} = 3q^3$, and $C_1^{(2)} = 8 + 15q + 6q^2 + q^3$, $C_2^{(2)} = 15q + 24q^2 + 7q^3$, $C_3^{(2)} = 18q^2 + 15q^3$, $C_4^{(2)} = 9q^3$.

For $\beta\epsilon=0$, our result is identical to that of free-volume theory for the AO model.⁴ Central to that approach is the free volume ratio, α (defined in Sec. III D), which we find to be identical to α_1 . Hence the DFT recovers free-volume theory in bulk; a discussion of relations between the two approaches can be found in Ref. 17. According to the physical meaning of α_1 , we interpret α_2 as the ratio of two six-dimensional volumes, namely, the volume that is accessible to a pair of two overlapping polymer spheres and the same quantity in the absence of colloids, the latter being just $4\pi\sigma_P^3V/3$. In Fig. 1 we plot both free volume fractions as a function of η_C for size ratios $q=0.57$ and 1. Qualitatively, α_1 and α_2 both monotonically decrease with increasing η_C due to the excluded volume occupied by colloidal particles. Note, however, that $\alpha_2 > \alpha_1$ over the whole density range. This may be due to correlations between polymer pairs. At fixed η_C , both free-volume fractions decrease monotonically with increasing size ratio.

The total canonical free energy is given by $F/V = F_{\text{exc}}/V + k_B T \sum_{i=C,P} \rho_i [\ln(\rho_i \Lambda_i^3) - 1]$. It is convenient to transform to the semigrand ensemble, where the polymer chemical potential instead of the system density is prescribed. The appropriate thermodynamic potential is a semi-grand free energy Ω_{semi} , related to F via Legendre transform $\Omega_{\text{semi}}/V = F/V - \mu_P \rho_P$, where μ_P is the chemical potential of polymers, given as

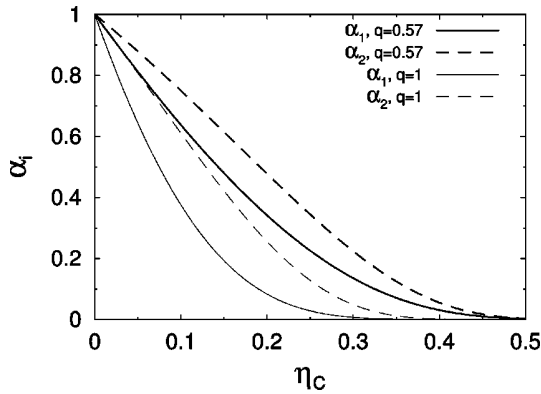


FIG. 1. Free-volume ratios of single polymers (α_1) and pairs of overlapping polymers (α_2) as a function of colloid packing fraction for polymer–colloid size ratios $q=0.57$ (top curves, thick) and $q=1$ (bottom curves, thin).

$$\begin{aligned} \beta\mu_p &= \partial(\beta F/V)/\partial\rho_p \\ &= \ln(\rho_p\Lambda_p^3) - \ln\alpha_1(\rho_C) - \beta\tilde{V}_{PP}(0)\rho_p[1 - \ln\alpha_2(\rho_C)]. \end{aligned} \quad (35)$$

Equation (35) is a transcendental equation to be solved for ρ_C once μ_p is prescribed, which is a trivial numerical task.

B. Comparison between DF and perturbative approaches

Comparing the density-functional and perturbative expressions for the bulk excess free energy [Eqs. (31) and (30), respectively], it is clear that they differ only in the interacting-polymer terms. Thus, focusing on these terms, we define the additional contribution $F_p \equiv F - F|_{\epsilon=0}$ to the free energy per volume due to polymer interactions, and find

$$\frac{F_p^{\text{DF}}}{V} \equiv \frac{\tilde{V}_{PP}(0)}{2} \rho_p^2 [1 - \ln\alpha_2(\rho_C)] \quad (36)$$

and

$$\frac{F_p^{\text{pert}}}{V} \equiv \frac{1}{2} \left(\frac{\rho_p}{\alpha_1(\rho_C)} \right)^2 \int \mathbf{dr} V_{PP}(r) g_{vv}(r; \rho_C). \quad (37)$$

As $r \rightarrow \infty$, two voids become uncorrelated and the void–void correlation function reduces to $g_{vv}(r) = \alpha_1^2$. Substituting this form for $g_{vv}(r)$ in Eq. (37) yields the mean-field (MF) result

$$\frac{F_p^{\text{MF}}}{V} = \frac{\tilde{V}_{PP}(0)}{2} \rho_p^2, \quad (38)$$

which is independent of colloid volume fraction. Similarly, as $r \rightarrow 0$, the two voids become perfectly correlated, $g_{vv}(r) = \alpha_1$. An approximate interpolation between these two extremes was proposed in Ref. 19:

$$g_{vv}(r) = \alpha_1^2 + \alpha_1(1 - \alpha_1)\exp(-r/R_C). \quad (39)$$

Substituting Eq. (39) into Eq. (37) and integrating over the step-function polymer–polymer pair potential, we obtain

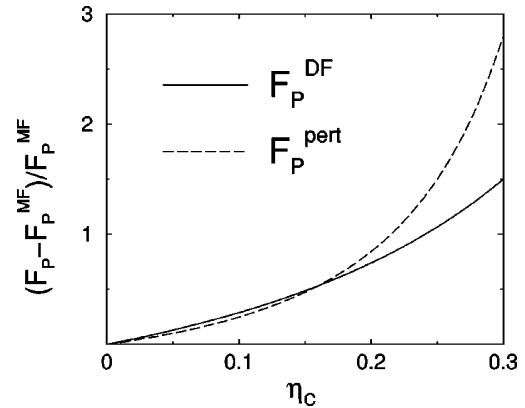


FIG. 2. Fractional excess over mean field (MF) of the free energy predicted by the density-functional (DF) and perturbative approaches [Eqs. (36) and (40)] vs colloid volume fraction η_C , for polymer–colloid size ratio $q=0.57$.

$$F_p^{\text{pert}} = F_p^{\text{MF}} \left[1 + \frac{3}{4} \left(\frac{1}{\alpha_1} - 1 \right) q^{-3} (1 - (2q^2 + 2q + 1)e^{-2q}) \right]. \quad (40)$$

We can now numerically compare the predictions of the different approximations for the interacting-polymer free energy. As the mean-field contribution is a constant (with respect to η_C), we take it as a reference and consider the fractional excess $(F_p - F_p^{\text{MF}})/F_p^{\text{MF}}$ as a function of η_C . Figure 2 compares the DF and perturbative results, computed from Eqs. (36) and (40). At lower colloid volume fractions ($\eta_C < 0.2$) both approaches give similar results. With increasing η_C , however, there is a crossover, beyond which the approaches deviate rapidly. In fact, beyond $\eta_C \approx 0.2$, the DF prediction increases much more gradually than the perturbative. The deviations in the free energy evident in Fig. 2 suggest a significant difference in the predicted phase behavior, which is confirmed upon explicit calculation of phase diagrams in the next section.

C. Phase diagrams

The general conditions for phase coexistence are equality of the total pressures p_{tot} , of the chemical potentials μ_i , and of the temperatures in the coexisting phases. For phase equilibrium between phases I and II,

$$p_{\text{tot}}^{\text{I}} = p_{\text{tot}}^{\text{II}}, \quad (41)$$

$$\mu_i^{\text{I}} = \mu_i^{\text{II}}, \quad i = C, P. \quad (42)$$

These are three equations for four unknowns (two state points each characterized by two densities). Hence two-phase coexistence regions depend parametrically on one free parameter. In our case $p_{\text{tot}}/k_B T = -\Phi_{\text{tot}} + \sum_{i=C,P} \rho_i \partial\Phi_{\text{tot}}/\partial\rho_i$, and $\mu_i = k_B T \partial\Phi_{\text{tot}}/\partial\rho_i$, where $\phi_{\text{tot}} = F/V$, yield analytical expressions. We solve the resulting sets of equations numerically, which is straightforward.

In order to compare the results from the different theoretical approaches, we consider the case of equal sizes, $q=1$, and moderately weak polymer–polymer interactions, namely $\beta\epsilon=0.25$. Our aim is to compare the fluid–fluid bin-

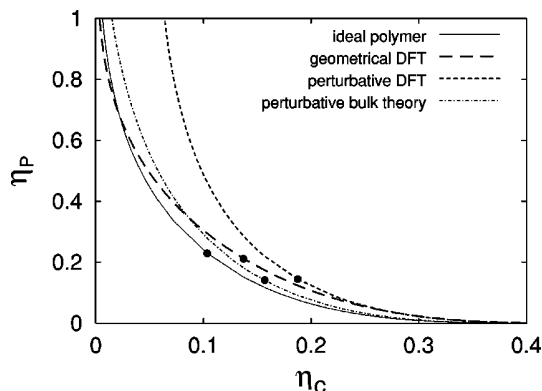


FIG. 3. Demixing phase diagram of a model colloid-polymer mixture for $q=1$ as a function of packing fractions of colloid and polymer, η_C and η_P . Shown are the theoretical binodals (lines) and critical points (dots) for ideal polymer ($\beta\epsilon=0$) as a reference case, along with the results for $\beta\epsilon=0.25$ from the geometry-based DFT, the perturbative DFT of Sec. III C, and the perturbative bulk theory of Sec. III D [Eq. (30)].

odals from the various approaches: the perturbative (Sec. III C) and geometry-based (Sec. III B) DFTs, and the perturbative bulk theory of Warren *et al.* (Sec. III D). We find that the semigrand version of the latter [Eq. (29)], when applied to our model, does not give fluid-fluid demixing for $\beta\epsilon=0.25$. Rather, the stability of demixing is restricted to a narrow range of interactions, where $\beta\epsilon$ is smaller than about 0.1. We believe that this is more a failure of the theory than of the model. As shown in Fig. 3, the binodals from the perturbative DFT and from the canonical version of the theory of Warren *et al.* [Eq. (30)] predict stabilization of the colloidal vapor phase when compared to the case of noninteracting polymers. This is at odds with the physical expectation that the polymer-polymer repulsion should *destabilize* the polymer-rich phase. In contrast, the binodal from our geometry-based DFT does capture this trend.

Stable fluid-fluid phase separation (with respect to freezing) in colloid-polymer mixtures is observed in experiments only at sufficiently large polymer-to-colloid size ratios. We consider the size ratio $q=0.57$, for which experimental data are available for poly(methyl methacrylate) (PMMA) colloid and polystyrene in *cis*-decalin.⁶ Figure 4 shows the predicted phase diagrams with and without polymer interactions. For noninteracting polymers [$\beta\epsilon=0$ in Fig. 4(a)], our result is identical to that from free-volume theory. Although the predicted phase diagram may appear to capture the main experimental trends, closer inspection reveals discrepancies. Experimentally, the colloidal liquid phase contains a significant concentration of polymer, whereas the theoretical binodal for ideal polymer suggests strong dilution in polymer. In order to apply our theory to this situation, we must first prescribe the potential energy barrier.

The potential energy barrier, ϵ , can be obtained by estimating the second virial coefficient, B_2 , of a pure polymer solution. For our repulsive step-function potential, B_2 is trivially related to ϵ via

$$B_2 = \frac{2\pi\sigma_P^3}{3}(1 - e^{-\beta\epsilon}). \quad (43)$$

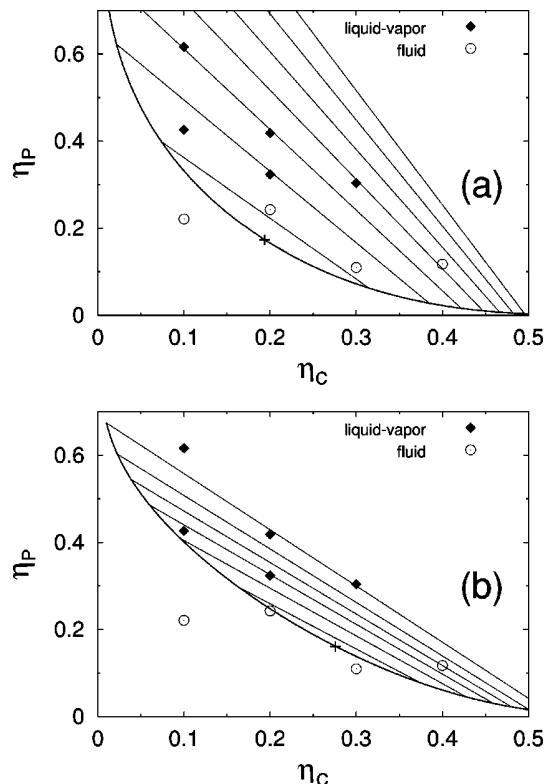


FIG. 4. Demixing phase diagram of a model colloid-polymer mixture for $q=0.57$ as a function of packing fractions of colloid and polymer, η_C and η_P . Shown are the theoretical binodal and critical point together with the experimental data of Ref. 6. (a) $\beta\epsilon=0$, equivalent to the result from free-volume theory (Ref. 4), (b) $\beta\epsilon=0.5$.

The second virial coefficient also can be expressed as^{19,32}

$$\frac{B_2}{4\pi^{3/2}R_P^3} = z - 4.8z^2 + O(z^3), \quad (44)$$

accurate up to $z \approx 0.1$, where z is the Fixman parameter. The Fixman parameter³² is a measure of polymer nonideality ($z=0$ corresponding to ideal polymers) that depends on temperature, radius of gyration, and molecular mass (M). An empirical relation for z was established by Berry³² for polystyrene in a range of hydrocarbon solvents:

$$z = 0.00975\sqrt{M} \left(1 - \frac{T_\theta}{T} \right), \quad (45)$$

valid over a wide range of temperatures around the theta temperature, T_θ .

Now, for the polymer-solvent system considered in Ref. 6, polystyrene in *cis*-decalin, $M=14.4 \times 10^6$ and $T_\theta=12.5^\circ\text{C}$, while the experimental phase diagrams were measured significantly above T_θ , at $T=23^\circ\text{C}$. From Eq. (45), this temperature corresponds to $z=1.3$, well beyond the range of validity of Eq. (44). However, Berry³² has measured B_2 over a considerable range of z , up to $z=5$. Thus, we can apply Eq. (44) to obtain B_2 for a small departure from ideality and then appeal to Berry's data. If we consider, for example, only a one-degree departure from T_θ , $T=13.5^\circ\text{C}$, then Eq. (45) gives $z=0.129$, for which Eqs. (43)

and (44) in turn yield $\beta\epsilon=0.068$. From Berry's measurements, as z increases from 0.13 to 1.3, B_2 increases by a factor of about 5, which, from Eq. (43), corresponds roughly to $\beta\epsilon\approx 0.5$ at $T=23^\circ\text{C}$.

A second, independent, estimate of ϵ can be drawn from simulations of interacting polymer coils (in the absence of colloids).²² At zero separation between two coils, the effective pair potential was determined to be about $(1-2)k_B T$. Hence, as a plausible value, we choose $\beta\epsilon=0.5$. To achieve higher accuracy than provided by the linear expansion of the OD free energy, Eq. (4), we use the cubic order expression, Eq. (5), in Eqs. (10)–(13). Figure 4 shows a comparison of the calculated theoretical binodal with the experimental data of Ref. 6.

Although the measured one-phase state point at high colloid packing fraction lies inside the theoretical two-phase region, it is obvious that our theory predicts a shift into the correct direction. We also predict that the coexisting colloidal vapor phase is more strongly diluted in colloids, as compared to the noninteracting case. All these results can be understood in terms of a free energy penalty due to polymer–polymer interactions. This primarily applies to the colloidal vapor phase. Only a small penalty arises in the colloidal liquid phase, where polymers are strongly diluted.

V. CONCLUSIONS

We have investigated a model of a colloid–polymer mixture in a good solvent, where excluded volume of monomers gives rise to a soft, penetrable repulsion between centers of masses of polymer coils. The model interpolates between the AO colloid–ideal-polymer model and binary hard spheres, through a repulsive step-function polymer–polymer interaction, whose height is a control parameter. We have derived a density-functional theory for the full crossover between both limits and have focused on the physically relevant case of weakly interacting polymers. Our theory predicts that with increasing strength of polymer–polymer interaction the coexisting colloidal liquid (vapor) phase becomes more concentrated (dilute) in polymer.

We stress that calculating bulk phase diagrams from the present theory is not more difficult than application of the original free volume theory.⁴ The only additional task is to convert from the polymer fugacity to the polymer density in the system. While this can be done analytically in the free-volume theory, here we need to solve Eq. (35) numerically. In order to compare to experiment, the strength of polymer–polymer interactions must be prescribed. This quantity and the polymer-to-colloid size ratio are adjustable parameters in our model.

We have shown that a simple perturbative DFT, in which the free energy is approximated by that of an AO reference system and an additive mean-field contribution is an inappropriate approach. We believe that this failure may hold also for other binary mixtures, where an additional interaction between particles of the same species is treated as a perturbation, neglecting the presence of the other component.

A recent assessment²¹ of the performance of free volume theory for the AO model in describing colloid–polymer mixtures in a good solvent (where polymers repel) found the AO

model to be seriously in error, particularly for long polymer chains with a radius of gyration greater than the radius of the colloids. Here we restrict ourselves to shorter chains, where we expect an effective sphere model to be reasonable.

We emphasize that our model of polymer–polymer interactions is idealized in (at least) four ways: (i) The shape of the pair interaction is assumed to be a step function rather than a more realistic smooth, Gaussian-type function. This has a prominent effect on the structural correlation (in particular on the polymer–polymer pair distribution function). We expect, however, that predictions of the phase behavior are reasonable provided appropriate values for both model parameters, step height and range are chosen. (ii) In order to be able to derive a geometrical DFT, we set the range of the step function equal to twice the polymer radius of gyration; the latter also sets the thickness of the depletion zones around colloids. This is an “additive” restriction, leading to well-defined particle shapes, that can be exploited to derive the theory. In general, however, a more realistic description would be provided by a freely adjustable range of polymer–polymer interaction. This would, however, include nonadditivity as an additional complication, which we have avoided in the present study. (iii) We assume that the strength and range of the interaction are independent of the concentrations of both colloids and polymers (in general, independent of the respective one-body profiles). It is, however, known²² that the effective polymer–polymer interaction (as obtained from simulations on the segment level) is density-dependent, although this effect appears to be quantitatively small. In principle, given some prescription of how the step height depends on the state point, this effect could be treated within the current approach. (iv) We neglect the effect of colloidal confinement on the polymer radius of gyration, and hence on the range of polymer–polymer interaction. Recently, we have modeled the influence of colloid-induced polymer compression, on demixing albeit only for the case of ideal polymer.³³ A similar model could, in principle, be applied to the case of interacting polymer.

Concerning future work, it is desirable to test our phase diagrams against simulation and more detailed experimental data for phase coexistence. It would be interesting to look at the depletion potential between colloids that is generated by the presence of nonideal polymer. The concept of integrating out degrees of freedom provides the necessary machinery, which already has been applied to limits of the present model, namely the AO⁷ and HS²⁶ cases. Of course, more realistic polymer–polymer interactions, such as a repulsive Gaussian pair potential, are worthy of investigation. Finally, we emphasize that because our theory is intrinsically constructed to deal with inhomogeneous situations, influence of polymer interactions on the properties of interfaces and behavior near walls, such as wetting and layering phenomena¹⁸ are problems open to investigation.

Note added. After completion of this work we became aware of a simulation study of colloid–polymer mixtures,³⁴ where similar phase behavior to that reported here was found.

ACKNOWLEDGMENTS

The work of one of the authors (J.M.B.) was supported by the National Science Foundation (through Grant No. CHE9800074 and the NSF Materials Research Science and Engineering Center at the University of Chicago).

- ¹S. Asakura and F. Oosawa, *J. Chem. Phys.* **22**, 1255 (1954).
- ²A. Vrij, *Pure Appl. Chem.* **48**, 471 (1976).
- ³A. P. Gast, C. K. Hall, and W. B. Russell, *J. Colloid Interface Sci.* **96**, 251 (1983).
- ⁴H. N. W. Lekkerkerker, W. C. K. Poon, P. N. Pusey, A. Stroobants, and P. B. Warren, *Europhys. Lett.* **20**, 559 (1992).
- ⁵W. C. K. Poon, J. S. Selfe, M. B. Robertson, S. M. Ilett, A. D. Pririe, and P. N. Pusey, *J. Phys. II* **3**, 1075 (1993).
- ⁶S. M. Ilett, A. Orrock, W. C. K. Poon, and P. N. Pusey, *Phys. Rev. E* **51**, 1344 (1995).
- ⁷M. Dijkstra, J. M. Brader, and R. Evans, *J. Phys.: Condens. Matter* **11**, 10079 (1999).
- ⁸J. M. Brader and R. Evans, *Europhys. Lett.* **49**, 678 (2000).
- ⁹J. M. Brader, M. Dijkstra, and R. Evans, *Phys. Rev. E* **63**, 041405 (2001).
- ¹⁰R. Evans, in *Fundamentals of Inhomogeneous Fluids*, edited by D. Henderson (Dekker, New York, 1992), p. 85.
- ¹¹Y. Rosenfeld, *Phys. Rev. Lett.* **63**, 980 (1989).
- ¹²Y. Rosenfeld, M. Schmidt, H. Löwen, and P. Tarazona, *J. Phys.: Condens. Matter* **8**, L577 (1996).
- ¹³Y. Rosenfeld, M. Schmidt, H. Löwen, and P. Tarazona, *Phys. Rev. E* **55**, 4245 (1997).
- ¹⁴P. Tarazona and Y. Rosenfeld, *Phys. Rev. E* **55**, R4873 (1997).
- ¹⁵P. Tarazona, *Phys. Rev. Lett.* **84**, 694 (2000).
- ¹⁶M. Schmidt, H. Löwen, J. M. Brader, and R. Evans, *Phys. Rev. Lett.* **85**, 1934 (2000).
- ¹⁷M. Schmidt, H. Löwen, J. M. Brader, and R. Evans, *J. Phys.: Condens. Matter* **14**, 9353 (2002).
- ¹⁸J. M. Brader, R. Evans, M. Schmidt, and H. Löwen, *J. Phys.: Condens. Matter* **14**, L1 (2002).
- ¹⁹P. B. Warren, S. M. Ilett, and W. C. K. Poon, *Phys. Rev. E* **52**, 5205 (1995).
- ²⁰M. Fuchs and K. S. Schweizer, *Europhys. Lett.* **51**, 621 (2000).
- ²¹S. Ramakrishnan, M. Fuchs, K. S. Schweizer, and C. F. Zukoski, *J. Chem. Phys.* **116**, 2201 (2002).
- ²²A. A. Louis, P. G. Bolhuis, J. P. Hansen, and E. J. Meijer, *Phys. Rev. Lett.* **85**, 2522 (2000).
- ²³A. J. Archer and R. Evans, *Phys. Rev. E* **64**, 041501 (2001).
- ²⁴A. J. Archer and R. Evans, *J. Phys.: Condens. Matter* **14**, 1131 (2002).
- ²⁵A. A. Louis, R. Finken, and J. Hansen, *Europhys. Lett.* **46**, 741 (1999).
- ²⁶M. Dijkstra, R. van Roij, and R. Evans, *Phys. Rev. Lett.* **81**, 2268 (1998).
- ²⁷M. Schmidt, *J. Phys.: Condens. Matter* **11**, 10163 (1999).
- ²⁸A. A. Louis, P. G. Bolhuis, and J. P. Hansen, *Phys. Rev. E* **62**, 7961 (2000).
- ²⁹A. Lang, C. N. Likos, M. Watzlawek, and H. Löwen, *J. Phys.: Condens. Matter* **12**, 5087 (2000).
- ³⁰C. N. Likos, A. Lang, M. Watzlawek, and H. Löwen, *Phys. Rev. E* **63**, 031206 (2001).
- ³¹H. Reiss, *J. Phys. Chem.* **96**, 4736 (1992).
- ³²G. C. Berry, *J. Chem. Phys.* **44**, 1550 (1966).
- ³³A. R. Denton and M. Schmidt, *J. Phys.: Condens. Matter* (special issue on density-functional theory) **14**, 12051 (2002).
- ³⁴P. G. Bolhuis, A. A. Louis, and J. P. Hansen, *Phys. Rev. Lett.* **89**, 128302 (2002).

Colloid-induced polymer compression

Alan R Denton¹ and Matthias Schmidt²

¹ Department of Physics, North Dakota State University, Fargo, ND 58105-5566, USA

² Institut für Theoretische Physik II, Heinrich-Heine-Universität Düsseldorf, Universitätsstraße 1, D-40225 Düsseldorf, Germany

E-mail: alan.denton@ndsu.nodak.edu and mschmidt@thphy.uni-duesseldorf.de

Received 10 June 2002, in final form 9 August 2002

Published 8 November 2002

Online at stacks.iop.org/JPhysCM/14/12051

Abstract

We consider a model mixture of hard colloidal spheres and nonadsorbing polymer chains in a theta solvent. The polymer component is modelled as a polydisperse mixture of effective spheres, mutually noninteracting but excluded from the colloids, with radii that are free to adjust to allow for colloid-induced compression. We investigate the bulk fluid demixing behaviour of this model system using a geometry-based density functional theory that includes the polymer size polydispersity and configurational free energy, obtained from the exact radius-of-gyration distribution for an ideal (random-walk) chain. Free energies are computed by minimizing the free energy functional with respect to the polymer size distribution. With increasing colloid concentration and polymer-to-colloid size ratio, colloidal confinement is found to increasingly compress the polymers. Correspondingly, the demixing fluid binodal shifts, compared to the incompressible-polymer binodal, to higher polymer densities on the colloid-rich branch, stabilizing the mixed phase.

1. Introduction

The physical properties of soft-matter systems are often influenced by size polydispersity on mesoscopic length scales [1, 2]. In colloidal suspensions, for example, variations in particle size can profoundly affect fluid–solid transitions [3]. In polymer solutions, chain length (degree of polymerization) often has a broad distribution. In practice, distributions in colloidal particle radius and polymer chain length often can be narrowed by physical selection or special synthesis methods. However, even monodisperse polymer chains have a radius of gyration that fluctuates in response to the surrounding environment. In this sense, polymers in solution are fundamentally polydisperse.

Polydispersity is especially relevant in mixtures of colloids and nonadsorbing (free) polymers, in which the polymer size sets the range of effective depletion-induced interactions between colloidal particles. A popular basis for modelling colloid–polymer (CP) mixtures is the Asakura–Oosawa (AO) model [4]. The AO model neglects fluctuations in chain

conformations by approximating the polymers as effective spheres of fixed radius that are excluded from the hard-sphere (HS) colloids. The model further ignores polymer–polymer interactions by treating the polymer spheres as freely interpenetrating, an approximation best justified in a theta solvent.

Despite its simplicity, the AO model qualitatively captures thermodynamic phase behaviour observed in real CP mixtures—in particular, bulk fluid demixing into colloid-rich and colloid-poor phases [5–8]. To address quantitative discrepancies with experiment, several recent studies have gone further to include polymer–polymer interactions—in both good solvents [9–11] and poor [12]—and polydispersity in polymer chain length [13–15]. In all of these studies, however, the polymers are modelled as effective spheres of fixed size (or fixed size distribution).

An issue that has not yet been widely explored is the influence of colloidal confinement on polymer conformations and implications for phase behaviour of CP mixtures. Polymers near surfaces and polymer-mediated interactions between surfaces have been examined by a variety of theoretical approaches, including scaling theory [16–18], integral equation theory [19, 20], classical density functional (DF) theory [21], and field-theoretic methods [22]. A far more challenging problem is the influence on polymers of confinement to a fluctuating random porous medium created by colloidal particles in suspension.

Numerical studies of colloids mixed with segmented polymer chains give some insight into polymer conformations in CP mixtures. Meijer and Frenkel [23] performed Monte Carlo simulations of hard spheres mixed with ideal (noninteracting) lattice-polymers. Dickman and Yethiraj [24] simulated mixtures of hard spheres and off-lattice polymer chains, modelled as freely jointed ‘pearl necklaces’ of hard spheres. Simulations such as these have revealed the potential importance of fluctuations in polymer size and shape in CP mixtures.

Here we consider an intermediate model in which the polymers maintain spherical shape but can adjust their radius-of-gyration distribution to the bulk colloid concentration. The constraint of fixed polymer size is thus relaxed by endowing the effective polymer spheres with an internal degree of freedom that can respond to colloidal confinement. We study the phase behaviour of a model mixture of HS colloids and compressible polymers by means of a geometry-based DF theory. Confinement-induced adjustments in polymer size are permitted by including in the free energy functional the free energy of ideal polymers, derived from the exact radius-of-gyration distribution of a random-walk chain.

The theory, when applied to bulk fluid phases, predicts both the demixing binodal and the polymer size distribution as a function of colloid and polymer concentrations. For sufficiently large polymer-to-colloid size ratio, the model displays bulk fluid demixing into colloid-rich and colloid-poor phases, qualitatively similar to the behaviour of the AO model. Upon demixing, however, the relatively unconfined polymers in the colloid-poor (vapour) phase coexist with compressed polymers in the colloid-rich (liquid) phase. We find that the polymer radius of gyration can be significantly reduced, by up to 20% or more, in the colloidal liquid phase. Correspondingly, the fluid demixing binodal shifts relative to the incompressible-polymer binodal.

Next, in section 2, we explicitly define the model system. In section 3, we construct an appropriate classical DF theory that incorporates the conformational free energy of the polymer chains. Results for demixing phase diagrams and polymer size distributions are presented in section 4. Finally, we conclude in section 5.

2. Model

The model we consider is a generalization of the AO model to the case of compressible polymers. Explicitly, we consider a mixture of hard colloidal spheres (species C), of

monodisperse radius R_C , and nonadsorbing, linear polymer chains (species P), monodisperse in length, but polydisperse in radius of gyration, R_P , in a volume V at a temperature T near the theta temperature. The restriction to a theta solvent allows the polymer chains to be reasonably approximated as noninteracting random walks. The colloids interact via a HS pair potential: $v_{CC}(r) = \infty$, if $r < 2R_C$, zero otherwise, where r is the centre–centre interparticle distance. When interacting with colloids, each polymer is assumed to behave as an effective hard sphere of radius equal to its radius of gyration: $v_{CP}(r) = \infty$, if $r < R_C + R_P$, zero otherwise. Finally, interactions between polymers vanish for all distances: $v_{PP}(r) = 0$.

To fix the polymer chemical potential, it is convenient to imagine a reservoir of pure polymer solution with which the system can freely exchange polymer (but not colloid) through a semi-permeable membrane. The reservoir also serves as a colloid-free reference state in which the polymer assumes an ideal radius-of-gyration distribution. Bulk fluid states are specified by the mean colloid and polymer (reservoir) number densities, ρ_C and ρ_P (ρ_P^r), respectively. As bulk thermodynamic parameters, we use the colloid packing fraction, $\eta_C = (4\pi/3)\rho_C R_C^3$, and effective polymer packing fractions, $\eta_P = (4\pi/3)\rho_P (R_g^r)^3$ and $\eta_P^r = (4\pi/3)\rho_P^r (R_g^r)^3$, where R_g^r denotes the root mean square (rms) radius of gyration in the reservoir, a quantity that is directly accessible in experiments. The reservoir polymer-to-colloid size ratio, R_g^r/R_C , provides a useful control parameter for tuning interparticle interactions, and thus thermodynamics.

3. Theory

3.1. Density functional theory

To investigate thermodynamic properties of the model system, we focus on the Helmholtz free energy as a functional of the inhomogeneous density profiles: the colloid density, $\rho_C(\mathbf{r})$, and a continuum of polymer densities, $\{\rho_P(\mathbf{r}; R_P)\}$, indexed by R_P and normalized to the mean polymer density via $V^{-1} \int d^3r \int_0^\infty dR_P \rho_P(\mathbf{r}; R_P) = \rho_P$. It is convenient to separate the total free energy functional into three terms:

$$F[\rho_C(\mathbf{r}), \{\rho_P(\mathbf{r}; R_P)\}] = F_{\text{id}}[\rho_C(\mathbf{r}), \{\rho_P(\mathbf{r}; R_P)\}] + F_{\text{ex}}[\rho_C(\mathbf{r}), \{\rho_P(\mathbf{r}; R_P)\}] + \int d^3r \int_0^\infty dR_P \rho_P(\mathbf{r}; R_P) f_{\text{chain}}(\mathbf{r}; R_P; [\rho_C(\mathbf{r})]), \quad (1)$$

where F_{id} is the ideal free energy, F_{ex} is the excess free energy in the AO model generalized to polydisperse (but incompressible) polymer, and $f_{\text{chain}}(\mathbf{r}; R_P; [\rho_C(\mathbf{r})])$ is the local free energy of a compressible polymer chain. The third term in equation (1) stems from the *internal* degrees of freedom of the chains and is formally equivalent to the contribution of an external potential acting on the polymers. The ideal free energy, associated with (centre-of-mass) translational and mixing entropy of the colloids and polymers, is given exactly by

$$\beta F_{\text{id}} = \int d^3r \rho_C(\mathbf{r}) [\ln(\rho_C(\mathbf{r}) \Lambda_C^3) - 1] + \int d^3r \int_0^\infty dR_P \rho_P(\mathbf{r}; R_P) [\ln(\rho_P(\mathbf{r}; R_P) \Lambda_P^3) - 1], \quad (2)$$

where $\beta \equiv 1/k_B T$, k_B is Boltzmann's constant, and Λ_C and Λ_P are the respective colloid and polymer thermal wavelengths.

The excess free energy, arising from interactions, must be approximated. For this purpose, we adopt a geometry-based DF approach, which is immediately applicable to multi-component systems. As a basis, we start from a recently proposed DF theory [27] for a binary CP mixture

in the AO model, the homogeneous limit of which is equivalent to the free volume theory of Lekkerkerker *et al* [7]. Here we generalize this theory [27] to mixtures of monodisperse colloids and polydisperse polymers. Following previous work [25, 27–29], the excess free energy is expressed in the form

$$\beta F_{\text{ex}} = \int d^3x \Phi(\{n_v^C(\mathbf{x})\}, \{n_v^P(\mathbf{x})\}), \quad (3)$$

where the excess free energy density, Φ , is a function of a set of weighted densities for colloid and polymer species. The weighted densities are defined as convolutions, with respect to geometric weight functions of the actual density profiles, and, in the case of polymers, integration over radius of gyration:

$$n_v^C(\mathbf{x}) = \int d^3r \rho_C(\mathbf{r}) w_v(\mathbf{x} - \mathbf{r}; R_C), \quad (4)$$

$$n_v^P(\mathbf{x}) = \int d^3r \int_0^\infty dR_P \rho_P(\mathbf{r}; R_P) w_v(\mathbf{x} - \mathbf{r}; R_P). \quad (5)$$

We use standard fundamental-measure weight functions [25, 26], $w_\nu(\mathbf{r}; R)$, $\nu = 0, 1, 2, 3, v1, v2, m2$, for spheres of radius R , given by

$$w_2(\mathbf{r}; R) = \delta(R - r), \quad w_3(\mathbf{r}; R) = \Theta(R - r), \quad (6)$$

$$w_{v2}(\mathbf{r}; R) = \delta(R - r) \frac{\mathbf{r}}{r}, \quad \hat{w}_{m2}(\mathbf{r}; R) = \delta(R - r) \left(\frac{\mathbf{r}\mathbf{r}}{r^2} - \frac{\hat{\mathbf{1}}}{3} \right), \quad (7)$$

where $r = |\mathbf{r}|$, $\delta(r)$ is the Dirac distribution, $\Theta(r)$ is the step function, and $\hat{\mathbf{1}}$ is the identity matrix. Further, linearly dependent weight functions are $w_1(\mathbf{r}; R) = w_2(\mathbf{r}; R)/(4\pi R)$, $w_0(\mathbf{r}; R) = w_1(\mathbf{r}; R)/R$, and $w_{v1}(\mathbf{r}; R) = w_{v2}(\mathbf{r}; R)/(4\pi R)$. The weight functions have dimensions (length) $^{\nu-3}$ and differ in tensorial rank: w_0, w_1, w_2 , and w_3 are scalars; w_{v1} and w_{v2} are vectors; and \hat{w}_{m2} is a (traceless) matrix.

The excess free energy density in equation (3) separates naturally into three parts:

$$\Phi = \Phi_1 + \Phi_2 + \Phi_3, \quad (8)$$

which are defined as

$$\Phi_1 = \sum_{i=C,P} n_0^i \varphi_i(n_3^C, n_3^P), \quad (9)$$

$$\Phi_2 = \sum_{i,j=C,P} (n_1^i n_2^j - \mathbf{n}_{v1}^i \cdot \mathbf{n}_{v2}^j) \varphi_{ij}(n_3^C, n_3^P), \quad (10)$$

$$\begin{aligned} \Phi_3 = \frac{1}{8\pi} \sum_{i,j,k=C,P} & \left(\frac{1}{3} n_2^i n_2^j n_2^k - n_2^i \mathbf{n}_{v2}^j \cdot \mathbf{n}_{v2}^k \right. \\ & \left. + \frac{3}{2} [\mathbf{n}_{v2}^i \hat{n}_{m2}^j \mathbf{n}_{v2}^k - \text{tr}(\hat{n}_{m2}^i \hat{n}_{m2}^j \hat{n}_{m2}^k)] \right) \varphi_{ijk}(n_3^C, n_3^P). \end{aligned} \quad (11)$$

Here tr denotes the trace operation and

$$\varphi_{i\dots k}(\eta_C, \eta_P) = \frac{\partial^m}{\partial \eta_i \dots \partial \eta_k} \beta F_{0d}(\eta_C, \eta_P) \quad (12)$$

are derivatives of the zero-dimensional (0d) excess free energy, with

$$\beta F_{0d}(\eta_C, \eta_P) = (1 - \eta_C - \eta_P) \ln(1 - \eta_C) + \eta_C. \quad (13)$$

Equations (3)–(13) completely specify the excess free energy in equation (1).

3.2. Application to bulk fluids

For bulk fluid states, the density profiles are spatially constant. In the homogeneous limit ($\rho_C(\mathbf{r}) \rightarrow \rho_C$ and $\rho_P(\mathbf{r}; R_P) \rightarrow \rho_P(R_P)$), equation (1) yields the bulk fluid free energy density:

$$\frac{\beta F}{V} = \rho_C [\ln(\rho_C \Lambda_C^3) - 1] + \int_0^\infty dR_P \rho_P(R_P) [\ln(\rho_P(R_P) \Lambda_P^3) - 1] + \phi_{\text{hs}}(\eta_C) - \int_0^\infty dR_P \rho_P(R_P) [\ln \alpha(R_P; \eta_C) - f_{\text{chain}}(R_P; \eta_C)], \quad (14)$$

which is still a functional of the polymer density distribution, $\rho_P(R_P)$. Here $\phi_{\text{hs}}(\eta_C)$ is the excess free energy density of the pure HS system, given by

$$\phi_{\text{hs}}(\eta_C) = \frac{3\eta_C [3\eta_C(2 - \eta_C) - 2(1 - \eta_C)^2 \ln(1 - \eta_C)]}{8\pi R_C^3 (1 - \eta_C)^2}, \quad (15)$$

the same result as in the scaled-particle and Percus–Yevick compressibility approximations [30], and $\alpha(R_P; \eta_C)$ is the free volume fraction, i.e., the fraction of the total volume not excluded to the polymer by the HS colloids, given implicitly by

$$\ln \alpha(R_P; \eta_C) = \ln(1 - \eta_C) - \sum_{m=1}^3 C_m \gamma^m, \quad (16)$$

where $\gamma = \eta_C/(1 - \eta_C)$ and the coefficients are polynomials in the polymer-to-colloid size ratio, $q = R_P/R_C$: $C_1 = 3q + 3q^2 + q^3$, $C_2 = 9q^2/2 + 3q^3$, and $C_3 = 3q^3$.

It is worth noting that the free volume fraction is related to the polymer one-particle direct correlation function,

$$c_P^{(1)}(\mathbf{r}; R_P; [\rho_C(\mathbf{r})]) = -\beta \frac{\delta F_{\text{ex}}}{\delta \rho_P(\mathbf{r}; R_P)}, \quad (17)$$

which has its physical origin in CP correlations. Substituting our DF approximation for F_{ex} into equation (17) and taking the homogeneous limit, we obtain

$$c_P^{(1)}(R_P; \eta_C) = - \sum_{\nu} \frac{\partial \Phi}{\partial n_{\nu}^P} * w_{\nu}(R_P) = \ln \alpha(R_P; \eta_C), \quad (18)$$

where $*$ denotes a convolution. Because our approximate excess free energy functional is linear in the polymer density, $c_P^{(1)}(R_P; \eta_C)$ is independent of $\rho_P(R_P)$, depending only on the colloid density.

In equilibrium, the polymer density distribution in equation (14) is fixed by the Euler–Lagrange equation for the polymers:

$$\frac{\delta(F/V)}{\delta \rho_P(R_P)} = \mu_P(R_P), \quad (19)$$

where $\mu_P(R_P)$ is the chemical potential of polymers with radius of gyration R_P . Substituting equation (14) into (19), we have

$$\ln(\rho_P(R_P; \eta_C) \Lambda_P^3) - \ln \alpha(R_P; \eta_C) + \beta f_{\text{chain}}(R_P) = \beta \mu_P(R_P), \quad (20)$$

where $\rho_P(R_P; \eta_C)$ is the *equilibrium* polymer density distribution at bulk colloid volume fraction η_C . Here we make the simplifying assumption that the chain free energy of a polymer with given R_P in the system is the same as that of an equal-sized polymer in the reservoir, and thus independent of colloid concentration. Because the system and reservoir must be in

equilibrium with respect to polymer exchange, the right side of equation (20) can be equated with the chemical potential of the corresponding polymer species in the reservoir:

$$\mu_P(R_P) = \mu_P^r(R_P) = \beta^{-1} \ln(\rho_P^r(R_P)\Lambda_P^3) + f_{\text{chain}}(R_P), \quad (21)$$

where $\rho_P^r(R_P)$ denotes the polymer density distribution in the reservoir. Further progress is facilitated by factoring the reservoir polymer density distribution, according to

$$\rho_P^r(R_P) = \rho_P^r P^r(R_P), \quad (22)$$

where ρ_P^r and $P^r(R_P)$ are the mean density and radius-of-gyration probability distribution, respectively, of polymers in the reservoir. The advantage of equation (22) is that the probability distribution is simply related to the chain free energy via [31, 32]

$$\beta f_{\text{chain}}(R_P) = -\ln P^r(R_P) + \text{constant independent of } R_P, \quad (23)$$

the arbitrary additive constant being chosen to normalize the distribution: $\int_0^\infty dR_P P^r(R_P) = 1$. Combining equations (20) and (21), and using (22) and (23), we obtain

$$\rho_P(R_P; \eta_C) = \rho_P^r \alpha(R_P; \eta_C) P^r(R_P) = \alpha(R_P; \eta_C) \rho_P^r(R_P). \quad (24)$$

The mean polymer densities in the system and reservoir are now seen to be related via

$$\rho_P(\eta_C) = \int_0^\infty dR_P \rho_P(R_P; \eta_C) = \rho_P^r \alpha_{\text{eff}}(\eta_C), \quad (25)$$

where

$$\alpha_{\text{eff}}(\eta_C) = \int_0^\infty dR_P \alpha(R_P; \eta_C) P^r(R_P) \quad (26)$$

is an *effective* free volume fraction. Equation (25) is a generalization of the incompressible-polymer relation, $\rho_P(\eta_C) = \rho_P^r \alpha(\eta_C)$, from free volume theory [7, 27]. Factoring $\rho_P(R_P; \eta_C)$ according to

$$\rho_P(R_P; \eta_C) = \rho_P(\eta_C) P(R_P; \eta_C), \quad (27)$$

serves to define

$$P(R_P; \eta_C) = \frac{\alpha(R_P; \eta_C)}{\alpha_{\text{eff}}(\eta_C)} P^r(R_P) \quad (28)$$

as the normalized radius-of-gyration probability distribution of polymers in the system. Equation (28) makes manifest that the radius-of-gyration distribution in the system depends on colloid concentration and differs from the distribution in the reservoir.

Finally, substituting equations (23) and (24) into (14) and rearranging, we obtain the equilibrium bulk fluid free energy density,

$$\frac{\beta F}{V} = \rho_C [\ln(\rho_C \Lambda_C^3) - 1] + \rho_P^r \alpha_{\text{eff}}(\eta_C) [\ln(\rho_P^r \Lambda_P^3) - 1] + \phi_{\text{hs}}(\eta_C). \quad (29)$$

Equations (28) and (29) are the main theoretical results of the paper and our basis for calculating polymer size distributions and phase behaviour in section 4. Practical implementation, however, first requires specification of $P^r(R_P)$.

3.3. Radius-of-gyration probability distribution

To approximate the radius-of-gyration probability distribution, we appeal to the statistical mechanics of a freely jointed chain. The configuration of a chain of N links, each link of

length a , can be specified by a set of position vectors, $\{\mathbf{R}_i\} = (\mathbf{R}_0 \dots \mathbf{R}_N)$, of the joints. For a given configuration, the radius of gyration, R_P , is defined by [31]

$$R_P^2 = \sum_{i=1}^N (\mathbf{R}_i - \mathbf{R}_{\text{cm}})^2, \quad (30)$$

where $\mathbf{R}_{\text{cm}} = N^{-1} \sum_{i=1}^N \mathbf{R}_i$ is the centre-of-mass position of the chain. Averaged over configurations, the radius of gyration follows the probability distribution, $P^r(R_P)$. Moments of the distribution are defined as

$$\langle R_P^n \rangle = \int_0^\infty dR_P R_P^n P^r(R_P), \quad (31)$$

the second ($n = 2$) moment being related to the rms radius of gyration of polymers in the reservoir [31, 32], $R_g^r = \sqrt{\langle R_P^2 \rangle} = a\sqrt{N/6}$. For polymers in the system, the rms radius of gyration is defined as

$$R_g(\eta_C) = \left(\int_0^\infty dR_P R_P^2 P(R_P; \eta_C) \right)^{1/2} = \left(\frac{1}{\alpha_{\text{eff}}(\eta_C)} \int_0^\infty dR_P R_P^2 \alpha(R_P; \eta_C) P^r(R_P) \right)^{1/2}, \quad (32)$$

which clearly varies with bulk colloid concentration. Note that $R_g(\eta_C = 0) = R_g^r$.

In general, the radius of gyration is a more appropriate measure of polymer size than the end-to-end displacement, which is not well defined for branched polymers. However, in contrast to the simple Gaussian distribution of the end-to-end displacement, the radius-of-gyration distribution is nontrivial, even for ideal chains. Flory and Fisk [33, 34] first proposed an empirical approximation for $P^r(R_P)$ based on the exact even moments calculated by Fixman [35]. Subsequently, Fujita and Norisuye [32, 36] calculated the distribution *exactly*, obtaining the analytical result

$$P^r(R_P) = \frac{1}{\sqrt{2\pi} R_g^r t^3} \sum_{k=0}^{\infty} \frac{(2k+1)!}{(2^k k!)^2} (4k+3)^{7/2} \exp(-t_k) \times \left[\left(1 - \frac{5}{8t_k}\right) K_{1/4}(t_k) + \left(1 - \frac{3}{8t_k}\right) K_{3/4}(t_k) \right], \quad (33)$$

where $t = (R_P/R_g^r)^2$, K_n are the modified Bessel functions of the second kind, and $t_k = (4k+3)^2/(8t)$. To confirm equation (33), we have carried out Monte Carlo simulations of an ideal chain for $N = 100$ and 1000 . Histograms of R_P , generated from 10^6 independent configurations, are in essentially perfect agreement with the analytical expression [37].

Equation (33) specifies the radius-of-gyration probability distribution and thus, together with equation (23), the chain free energy. We emphasize that in modelling the chains as freely jointed, and so applying the ideal-chain distribution (equation (33)) to polymers mixed with colloids, we implicitly neglect any effect of colloidal confinement on the basic shape of the distribution. In particular, confinement-induced nonspherical distributions are neglected, although variation in the polymer size is allowed.

4. Results: demixing phase behaviour and polymer size distribution

The general conditions for phase coexistence are equality of the total pressure,

$$p_{\text{tot}} = -\frac{F}{V} + \sum_{i=C,P} \rho_i \frac{\partial(F/V)}{\partial \rho_i}, \quad (34)$$

12058

A R Denton and M Schmidt

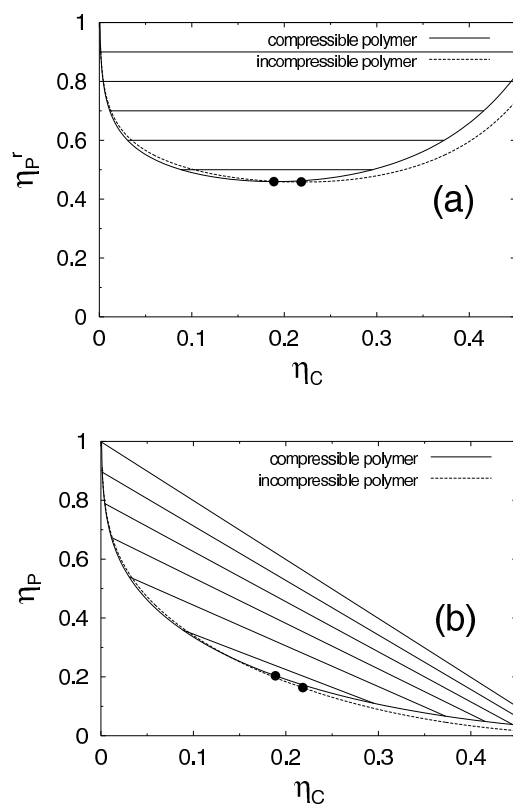


Figure 1. A fluid–fluid demixing phase diagram for rms reservoir polymer-to-colloid size ratio $R_g^r/R_C = 0.5$. Solid curve: the binodal from the present theory, taking into account polymer compressibility; dashed curve: the binodal from free volume theory for the AO model with incompressible polymer. Thin straight lines indicate tie lines between coexisting phases; dots indicate critical points. (a) The reservoir representation: polymer reservoir packing fraction η_P^r versus colloid packing fraction η_C ; (b) the system representation: system polymer packing fraction η_P versus η_C .

and of the chemical potentials for each species,

$$\mu_i = \frac{\partial(F/V)}{\partial\rho_i}, \quad i = C, P, \quad (35)$$

between the coexisting phases. Equilibrium between phases I and II requires $p_{\text{tot}}^I = p_{\text{tot}}^{\text{II}}$ and $\mu_C^I = \mu_C^{\text{II}}$, equality of the polymer chemical potentials being enforced by equation (19).

In practice, bulk fluid phase diagrams can be computed as follows. The effective free volume fraction, $\alpha_{\text{eff}}(\eta_C)$, is first determined by substituting equations (16) and (33) into (26). Then, for a given reservoir polymer density, ρ_p^r , equations (29), (34), and (35) ($i = C$) are solved numerically for the coexisting colloid packing fractions, η_C^I and η_C^{II} . Finally, equation (25) converts from reservoir to system representation, giving the corresponding system polymer packing fractions, η_P^I and η_P^{II} .

Figures 1 and 2 present bulk fluid phase diagrams for rms reservoir polymer-to-colloid size ratios $R_g^r/R_C = 0.5$ and 1, in both the system and reservoir representations. For comparison, we include demixing binodals both from the present theory, which takes into account polymer compressibility, and from the free volume theory of the AO model with incompressible polymer. For sufficiently high colloid and polymer packing fractions, the system demixes into colloid-

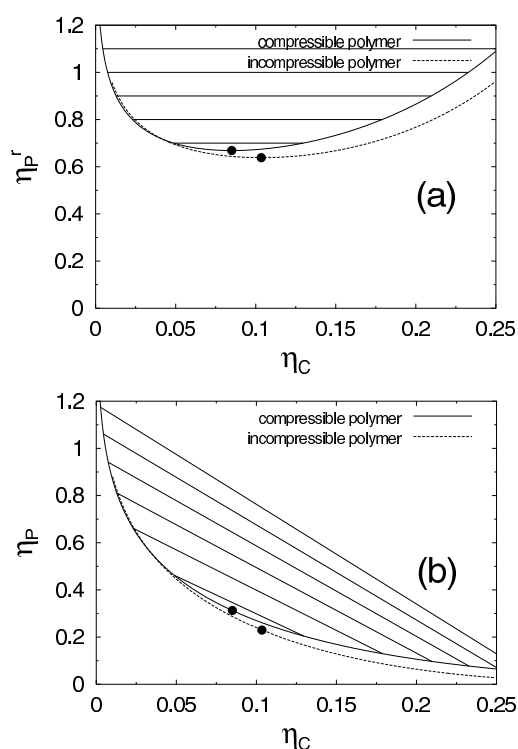


Figure 2. As figure 1, but for $R_g^r/R_C = 1$. Note the change in scale compared with figure 1.

rich (liquid) and colloid-poor (vapour) phases. We disregard here the liquid–solid branch of the phase diagram, since our size ratios are sufficiently high that fluid–fluid demixing can be assumed stable. The effect of polymer compressibility evidently is to shift the colloidal liquid branch of the binodal toward higher polymer density, stabilizing the system against demixing. Interpreted in terms of effective depletion-induced attraction between pairs of colloids, polymer compression shortens the range of attraction, tending to favour mixing. In passing, it may be anticipated that additional degrees of freedom allowing for nonspherical polymer conformations would tend to further stabilize the mixture if, as an alternative to bulk demixing, the polymer may simply distort its shape.

Figures 3 and 4 show the corresponding normalized polymer size distributions as a function of radius of gyration, scaled to the rms reservoir value. For given rms reservoir size ratio, with increasing colloid concentration, the distributions narrow and shift toward smaller radii, reflecting compression of the polymer by the confining colloids. In the case of $R_g^r/R_C = 0.5$, the polymer is compressed, relative to its rms size in the reservoir, to $R_g/R_g^r = 0.974, 0.938, 0.891$, and 0.829 at colloid packing fractions $\eta_C = 0.1, 0.2, 0.3$, and 0.4 , respectively. For $R_g^r/R_C = 1$, the polymer is even more strongly compressed to $R_g/R_g^r = 0.915, 0.826, 0.738$, and 0.653 at the same respective values of η_C . Note that, for given η_C , $P(R_P)$ does not depend on η_P (nor on η_P^r). Hence in the phase diagram, the polymer size distribution is constant along vertical lines (in both system and reservoir representations). What changes, of course, is the overall prefactor in $\rho_P(R_P)$. This invariance is an approximate feature of the theory resulting from the linearity of the excess free energy in polymer density. In reality, the presence of the polymers may alter the confining structure of the colloids, in turn modifying $P(R_P)$.

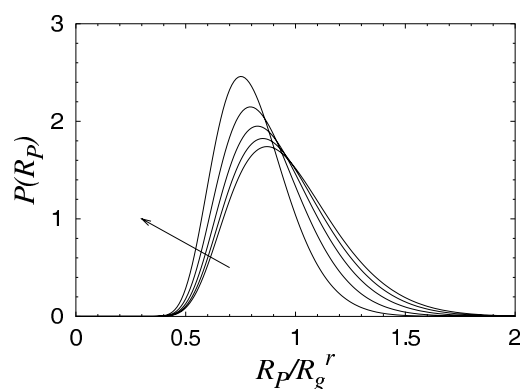


Figure 3. The normalized probability distribution, $P(R_P)$, of the scaled polymer radius of gyration, R_P/R_g^r for rms reservoir polymer-to-colloid size ratio $R_g^r/R_C = 0.5$ (corresponding to figure 1). The colloid packing fraction, η_C , increases in the direction of the arrow: $\eta_C = 0, 0.1, 0.2, 0.3$, and 0.4 . Corresponding rms polymer size ratios decrease: $R_g/R_g^r = 1, 0.974, 0.938, 0.891$, and 0.829 .

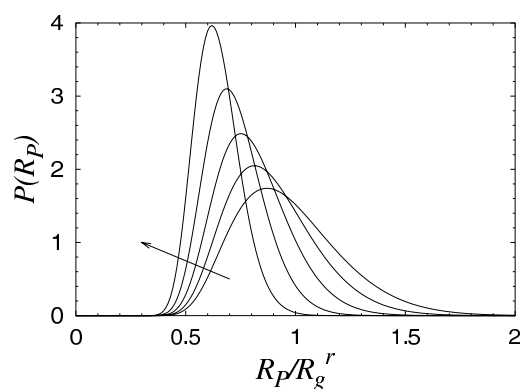


Figure 4. As figure 3, but for $R_g^r/R_C = 1$ (corresponding to figure 2). In the direction of the arrow, the rms polymer size ratios are $R_g/R_g^r = 1, 0.915, 0.826, 0.738$, and 0.653 . Note the change in scale compared with figure 3.

5. Conclusions

We have investigated the bulk fluid demixing behaviour of a model mixture of hard colloidal spheres and nonadsorbing polymer chains in a theta solvent. The polymer component is modelled, on a mesoscopic level, as a polydisperse mixture of effective spheres with radii free to adjust to allow for colloid-induced compression. The model goes beyond previous studies by treating the polymer radius of gyration as an internal degree of freedom that is polydisperse and varies between coexisting phases. Like all effective-sphere models, however, our approach ignores details of the polymers on the segment level and thereby neglects any effects of polymer shape anisotropy.

To describe the model system, we have developed a geometry-based DF theory that incorporates polymer configurational free energy from consideration of the statistical mechanics of an ideal (random-walk) chain. For simplicity, the polymer chain free energy is assumed to be insensitive to colloidal confinement. Minimization of an approximate free

energy functional with respect to the polymer size distribution yields both the equilibrium size distribution—modified by CP interactions—and the free energy, from which we compute bulk fluid phase diagrams. Polymer compression is found to increase with increasing colloid concentration and polymer-to-colloid size ratio. Correspondingly, the demixing fluid binodal shifts to higher polymer densities on the colloid-rich branch, favouring mixing.

Predictions of the theory may be tested by experiment and simulation. Although the predicted shift of the demixing binodal due to polymer compression would appear to improve agreement with limited experimental data near the theta point [8], more detailed measurements are certainly desirable. Polymer size distributions could be probed using either light scattering, by index matching the colloids (but not polymers) to the solvent, or neutron scattering by selectively deuterating the polymer (hydrocarbon) backbones. Detailed molecular simulations of segmented polymer chains mixed with hard spheres, along the lines of [23] and [24], could provide the clearest tests of our approximations and predictions.

Future applications to inhomogeneous CP mixtures under the influence of external potentials (due to walls, gravity, etc) and to liquid–solid transitions would be feasible and worthwhile. Extensions of the theory could explore the sensitivity of the polymer chain free energy to colloidal confinement, polydispersity in chain length, influences of anisotropic polymer conformations, distinctions between linear and branched polymers (as in colloid–star-polymer mixtures [38–40]), and effects of polymer nonideality in good and poor solvents.

Acknowledgment

A helpful discussion with Dr Michael Rubinstein is gratefully acknowledged.

References

- [1] Daoud M and Williams C E (ed) 1999 *Soft Matter Physics* (Berlin: Springer)
- [2] Sollich P 2002 *J. Phys.: Condens. Matter* **14** R79
- [3] Bolhuis P G and Kofke D A 1996 *Phys. Rev. E* **54** 634
Kofke D A and Bolhuis P G 1999 *Phys. Rev. E* **59** 618
- [4] Asakura S and Oosawa F 1954 *J. Chem. Phys.* **22** 1255
- [5] Gast A P, Russel W B and Hall C K 1986 *J. Colloid Interface Sci.* **109** 161
- [6] Pusey P N 1991 *Liquids, Freezing and Glass Transition* ed J-P Hansen, D Levesque and J Zinn-Justin (Amsterdam: North-Holland)
- [7] Lekkerkerker H N W, Poon W C K, Pusey P N, Stroobants A and Warren P B 1992 *Europhys. Lett.* **20** 559
- [8] Ilett S M, Orrock A, Poon W C K and Pusey P N 1995 *Phys. Rev. E* **51** 1344
- [9] Warren P B, Ilett S M and Poon W C K 1995 *Phys. Rev. E* **52** 5205
- [10] Schmidt M, Denton A R and Brader J M 2002 *Preprint*
- [11] Bolhuis P G, Louis A A and Hansen J-P 2002 *Preprint*
- [12] Schmidt M and Denton A R 2002 *Phys. Rev. E* **65** 061410
- [13] Sear R P and Frenkel D 1997 *Phys. Rev. E* **55** 1677
- [14] Warren P B 1997 *Langmuir* **13** 4588
- [15] Lee J-T and Robert M 1999 *Phys. Rev. E* **60** 7198
- [16] de Gennes P-G 1979 *Scaling Concepts in Polymer Physics* (Ithaca, NY: Cornell University Press)
- [17] Joanny J F, Leibler L and de Gennes P-G 1979 *J. Polym. Sci.* **17** 1073
- [18] de Gennes P-G 1981 *Macromolecules* **14** 1637
- [19] Yethiraj A, Hall C K and Dickman R 1992 *J. Colloid Interface Sci.* **151** 102
- [20] Chatterjee A P and Schweizer K S 1998 *J. Chem. Phys.* **109** 10 464
Chatterjee A P and Schweizer K S 1998 *J. Chem. Phys.* **109** 10 476
- [21] Bechinger C, Rudhardt D, Leiderer P, Roth R and Dietrich S 1999 *Phys. Rev. Lett.* **83** 3960
- [22] Eisenriegler E, Hanke A and Dietrich S 1996 *Phys. Rev. E* **54** 1134
Eisenriegler E 1997 *Phys. Rev. E* **55** 3116
Hanke A, Eisenriegler E and Dietrich S 1999 *Phys. Rev. E* **59** 6853

-
- [23] Meijer E J and Frenkel D 1991 *Phys. Rev. Lett.* **67** 1110
Meijer E J and Frenkel D 1994 *J. Chem. Phys.* **100** 6873
Meijer E J and Frenkel D 1995 *Physica A* **213** 130
- [24] Dickman R and Yethiraj A 1994 *J. Chem. Phys.* **100** 4683
- [25] Rosenfeld Y 1989 *Phys. Rev. Lett.* **63** 980
- [26] Tarazona P 2000 *Phys. Rev. Lett.* **84** 694
Cuesta J A, Martinez-Raton Y and Tarazona P 2002 *J. Phys.: Condens. Matter* **14** 11965
- [27] Schmidt M, Löwen H, Brader J M and Evans R 2000 *Phys. Rev. Lett.* **85** 1934
- [28] Rosenfeld Y, Schmidt M, Löwen L and Tarazona P 1996 *J. Phys.: Condens. Matter* **8** L577
- [29] Rosenfeld Y, Schmidt M, Löwen L and Tarazona P 1997 *Phys. Rev. E* **55** 4245
- [30] Hansen J P and McDonald I R 1986 *Theory of Simple Liquids* 2nd edn (London: Academic)
- [31] Doi M and Edwards S F 1986 *The Theory of Polymer Dynamics* (Oxford: Clarendon)
- [32] Yamakawa H 1970 *Modern Theory of Polymer Solutions* (New York: Harper & Row)
- [33] Flory P J and Fisk S 1966 *J. Chem. Phys.* **44** 2243
- [34] Flory P J 1969 *Statistical Mechanics of Chain Molecules* (New York: Wiley)
- [35] Fixman M 1962 *J. Chem. Phys.* **36** 306
- [36] Fujita H and Norisuye T 1970 *J. Chem. Phys.* **52** 1115
- [37] Schmidt M and Denton A R 2002 unpublished
- [38] Poon W C K, Egelhaaf S U, Stellbrink J, Allgaier J, Schofield A B and Pusey P N 2001 *Phil. Trans. R. Soc. A* **359** 897
- [39] Dzubiella J, Jusufi A, Likos C N, von Ferber C, Löwen H, Stellbrink J, Allgaier J, Richter D, Schofield A B, Smith P A, Poon W C K and Pusey P N 2001 *Phys. Rev. E* **64** 10401
- [40] Dzubiella J, Likos C N and Löwen H 2002 *J. Chem. Phys.* **116** 9518

Demixing of colloid-polymer mixtures in poor solvents

Matthias Schmidt* and Alan R. Denton

Department of Physics, North Dakota State University, Fargo, North Dakota 58105-5566

(Received 8 March 2002; published 26 June 2002)

The influence of poor solvent quality on fluid demixing of a model mixture of colloids and nonadsorbing polymers is investigated using density functional theory. The colloidal particles are modeled as hard spheres and the polymer coils as effective interpenetrating spheres that have hard interactions with the colloids. The solvent is modeled as a two-component mixture of a primary solvent, regarded as a background theta solvent for the polymer, and a cosolvent of point particles that are excluded from both colloids and polymers. Cosolvent exclusion favors overlap of polymers, mimicking the effect of a poor solvent by inducing an effective attraction between polymers. For this model, a geometry-based density functional theory is derived and applied to bulk fluid phase behavior. With increasing cosolvent concentration (worsening solvent quality), the predicted colloid-polymer demixing binodal shifts to lower colloid concentrations, promoting demixing. For sufficiently poor solvent, a reentrant demixing transition is predicted at low colloid concentrations.

DOI: 10.1103/PhysRevE.65.061410

PACS number(s): 82.70.Dd, 61.20.Gy, 64.10.+h, 64.60.Fr

I. INTRODUCTION

Solvents play a crucial role in the thermodynamic behavior of macromolecular solutions. Over the past half a century, effects of solvent quality on the physical properties of polymer solutions have been extensively studied [1,2]. Polymer-solvent and solvent-solvent interactions were first incorporated into the classic Flory-Huggins mean-field theory of polymer solutions [3]. Subsequently, excluded-volume interactions between polymer segments were identified as the key determinants of solvent quality. Polymer segments sterically repel one another in a good solvent, attract in a poor solvent, and behave as though nearly ideal (noninteracting) in a theta solvent. Interactions between polymer segments strongly influence chain conformations and, in turn, phase separation and other macroscopic phenomena.

Compared to solvent effects in pure polymer solutions, much less is known about the role of solvent quality in colloid-polymer mixtures. The simplest and most widely studied theoretical model of colloid-polymer mixtures is the Asakura-Oosawa (AO) model [4,5]. This treats the colloids as hard spheres and the polymers as effective spheres that are mutually noninteracting but have hard interactions with the colloids. The thermodynamic phase diagram of the AO model has been mapped out by thermodynamic perturbation theory [6], free volume theory [7], density functional (DF) theory [8], and Monte Carlo simulation [9]. By assuming ideal polymers, however, the AO model is implicitly limited to theta solvents. Recently, by incorporating polymer-polymer repulsion into the AO model, the influence of a good solvent on phase behavior has been explored via perturbation theory [10] and DF theory [11]. All of these studies assume an effective penetrable-sphere model for the polymer coils, which is supported by explicit Monte Carlo simulations of interacting segmented-chain polymers [12–14]. An

alternative, more microscopic, theoretical approach is the PRISM integral-equation theory [15], which models polymers on the segment level.

The purpose of the present paper is to investigate the effect of a *poor* solvent on the bulk phase behavior of colloid-polymer mixtures. To this end, we consider a variation of the AO model that explicitly includes the solvent as a distinct component. Specifically, the solvent is treated as a binary mixture of a primary solvent, which alone acts as a theta solvent for the polymer, and a cosolvent, which acts as a poor solvent for the polymer. The primary solvent is regarded as a homogeneous background that freely penetrates the polymer, but is excluded by the colloids. The cosolvent is modeled simply as an ideal gas of pointlike particles that penetrate neither colloids nor polymers.

In the absence of colloids, the polymer-cosolvent subsystem is the Widom-Rowlinson (WR) model of a binary mixture [16,17], in which particles of unlike species interact with hard cores and particles of like species are noninteracting. The WR model can be shown to be equivalent to a one-component system of penetrable spheres that interact via a many-body interaction potential, proportional to the cosolvent pressure and the volume covered by the spheres (with overlapping portions counted only once). Hence, in the polymer-cosolvent subsystem, the volume occupied by the polymer spheres costs interaction energy, inducing an effective attraction between polymers reminiscent of that caused by a poor solvent. By varying cosolvent concentration, the solvent quality can be tuned. Here we investigate whether and how added hard colloidal spheres mix with such effectively interacting polymers.

In Sec. II, we define more explicitly the model colloid-polymer-cosolvent mixture. In Sec. III, we develop a general geometry-based DF theory, which may be applied to both homogeneous and inhomogeneous states of the model system. The general theory provides the foundation for an application to bulk phase behavior in Sec. IV. Readers who are interested only in bulk properties may wish to skip Sec. III and turn directly to Sec. IV. We finish with concluding remarks in Sec. V.

*Permanent address: Institut für Theoretische Physik II, Heinrich-Heine-Universität Düsseldorf, Universitätsstraße 1, D-40225 Düsseldorf, Germany.

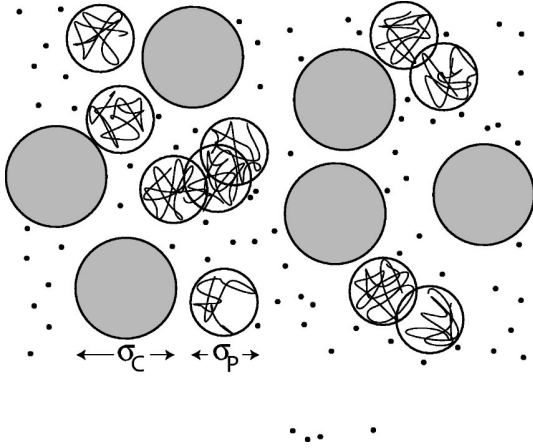


FIG. 1. Model ternary mixture of colloidal hard spheres of diameter σ_C , polymer effective spheres of diameter σ_P , and pointlike solvent particles.

II. THE MODEL

We consider a ternary mixture of colloidal hard spheres (species C) of radius R_C , globular polymers (species P) of radius R_P , and pointlike cosolvent particles (species S), as illustrated in Fig. 1. The respective number densities are $\rho_C(\mathbf{r})$, $\rho_P(\mathbf{r})$, and $\rho_S(\mathbf{r})$, where \mathbf{r} is the spatial coordinate. The primary solvent is regarded as a homogeneous background for the polymer and is not explicitly included. All particles experience only pairwise interactions, $V_{ij}(r)$, $i, j = C, P, S$, where r is the separation distance between particle centers. Colloids behave as hard spheres: $V_{CC}(r) = \infty$, if $r < 2R_C$, and zero otherwise. Colloids and polymers interact as hard bodies via $V_{CP}(r) = \infty$, if $r < R_C + R_P$, and zero otherwise, and both exclude cosolvent particles: $V_{CS}(r) = \infty$, if $r < R_C$, $V_{PS}(r) = \infty$, if $r < R_P$, and zero otherwise. The polymers and cosolvent particles behave as ideal gases: $V_{PP}(r) = 0$, $V_{SS}(r) = 0$, for all r . In essence, this is the AO model with additional point particles that cannot penetrate either colloids or polymers.

We denote the sphere diameters by $\sigma_C = 2R_C$ and $\sigma_P = 2R_P$, the bulk packing fractions by $\eta_C = 4\pi R_C^3 \rho_C / 3$ and $\eta_P = 4\pi R_P^3 \rho_P / 3$, and define a dimensionless solvent bulk density $\rho_S^* = \rho_S \sigma_P^3$. The polymer-colloid size ratio $q = \sigma_P / \sigma_C$ is regarded as a control parameter.

III. DENSITY FUNCTIONAL THEORY

We develop a geometry-based DF theory for the excess Helmholtz free energy of the model system, expressed as an integral over an excess free energy density,

$$F_{\text{exc}}[\rho_C, \rho_P, \rho_S] = k_B T \int d^3x \Phi(\{n_\nu^i\}), \quad (1)$$

where k_B is Boltzmann's constant, T is absolute temperature, and the (local) reduced excess free energy density Φ is a simple function (not a functional) of weighted densities n_ν^i . The weighted densities are smoothed averages of the possibly highly inhomogeneous density profiles $\rho_i(\mathbf{r})$ expressed as convolutions,

$$n_\nu^i(\mathbf{r}) = \rho_i(\mathbf{r}) * w_\nu^i(\mathbf{r}) = \int d\mathbf{r}' \rho_i(\mathbf{r}') w_\nu^i(\mathbf{r} - \mathbf{r}'), \quad (2)$$

with respect to weight functions $w_\nu^i(\mathbf{r})$ where $i = C, P, S$ and $\nu = 0, 1, 2, 3, v1, v2, m2$. The usual weight functions [18,19] are

$$w_2^i(\mathbf{r}) = \delta(R_i - r), \quad w_3^i(\mathbf{r}) = \Theta(R_i - r), \quad (3)$$

$$\mathbf{w}_{v2}^i(\mathbf{r}) = w_2^i(\mathbf{r}) \frac{\mathbf{r}}{r}, \quad \hat{\mathbf{w}}_{m2}^i(\mathbf{r}) = w_2^i(\mathbf{r}) \left(\frac{\mathbf{r}\mathbf{r}}{r^2} - \frac{\hat{\mathbf{1}}}{3} \right), \quad (4)$$

where $r = |\mathbf{r}|$, $\delta(r)$ is the Dirac distribution, $\Theta(r)$ is the step function, and $\hat{\mathbf{1}}$ is the identity matrix. Further linearly dependent weight functions are $w_1^i(\mathbf{r}) = w_2^i(\mathbf{r}) / (4\pi R)$, $\mathbf{w}_{v1}^i(\mathbf{r}) = \mathbf{w}_{v2}^i(\mathbf{r}) / (4\pi R)$, and $w_0^i(\mathbf{r}) = w_1^i(\mathbf{r}) / R$. The weight functions for $\nu = 3, 2, 1, 0$ represent geometrical measures of the particles in terms of volume, surface area, integral mean curvature, and Euler characteristic, respectively [18]. Note that the weight functions differ in tensorial rank: w_0^i , w_1^i , w_2^i , and w_3^i are scalars, \mathbf{w}_{v1}^i and \mathbf{w}_{v2}^i are vectors, and $\hat{\mathbf{w}}_{m2}^i$ is a (traceless) matrix.

The excess free energy density can be expressed in the general form

$$\Phi = \Phi_C + \Phi_{CP} + \Phi_{CS} + \Phi_{CPS}, \quad (5)$$

where the four contributions have forms motivated by consideration of the appropriate exact zero-dimensional limits. The colloid contribution Φ_C is the same as that for the pure hard-sphere (HS) system [18,19],

$$\Phi_C = -n_0^C \ln(1 - n_3^C) + \frac{n_1^C n_2^C - \mathbf{n}_{v1}^C \cdot \mathbf{n}_{v2}^C}{1 - n_3^C} + \left[\frac{1}{3} (n_2^C)^3 - n_2^C (\mathbf{n}_{v2}^C)^2 + \frac{3}{2} (\mathbf{n}_{v2}^C \cdot \hat{\mathbf{n}}_{m2}^C \cdot \mathbf{n}_{v2}^C - 3 \det \hat{\mathbf{n}}_{m2}^C) \right] / [8\pi(1 - n_3^C)^2]. \quad (6)$$

The colloid-polymer interaction contribution Φ_{CP} is the same as in the pure AO case [8],

$$\Phi_{CP} = \sum_\nu \frac{\partial \Phi_C}{\partial n_\nu^C} n_\nu^P, \quad (7)$$

while the colloid-solvent interaction contribution [20] is

$$\Phi_{CS} = -n_0^S \ln(1 - n_3^C). \quad (8)$$

Finally, in order to model the WR-type interaction between

polymers and cosolvent particles in the presence of the colloidal spheres, we assume

$$\Phi_{CPS} = \frac{n_0^S n_3^P}{1 - n_3^C}, \quad (9)$$

which takes into account the volume excluded to the polymer and cosolvent by the colloids.

It is instructive to compare the current theory to geometry-based DF theories previously formulated for two related ternary model systems. One starting point is a ternary AO model that combines a binary HS mixture and one polymer species [21]. Letting the radius of the smaller HS component go to zero, one obtains the cosolvent species. The other starting point is a recently introduced model [22] for a ternary mixture of colloids, polymers, and hard vanishingly thin needles of length L , where the needles are ideal amongst themselves but cannot penetrate the polymers (hard-core interaction). In the limit $L \rightarrow 0$, the needles become identical to the cosolvent particles. We have explicitly checked that the DF theories for both systems reduce to the theory described above, demonstrating the internal consistency of the geometry-based approach.

IV. RESULTS AND DISCUSSION

A. Bulk limit

For bulk fluid phases the density profiles are homogeneous: $\rho_i(\mathbf{r}) = \text{const}$. In this case, the integrations in Eq. (2) are trivial, and simple expressions for the weighted densities can be obtained. Inserting these expressions into the excess free energy density [Eqs. (6)–(9)] yields the bulk excess free energy in analytic form. The HS contribution, which is equal to the Percus-Yevick compressibility (and scaled-particle) result, is given as

$$\Phi_C = \frac{3\eta_C[3\eta_C(2-\eta_C) - 2(1-\eta_C)^2 \ln(1-\eta_C)]}{8\pi R_C^3(1-\eta_C)^2}. \quad (10)$$

The colloid-polymer contribution is equal to that predicted by free volume theory [7], and subsequently rederived by DFT [8],

$$\begin{aligned} \Phi_{CP} = & \frac{\eta_P/(8\pi R_P^3)}{(1-\eta_C)^3} \{3q\eta_C[6(1-\eta_C)^2 + 3q(2-\eta_C-\eta_C^2)] \\ & + 2q^2(1+\eta_C+\eta_C^2)] - 6(1-\eta_C)^3 \ln(1-\eta_C)\}. \end{aligned} \quad (11)$$

This contribution is linear in the polymer density and has a form that arises, as in the original free volume theory [7], from treating the polymers as an ideal gas occupying the free volume between the colloids. The colloid-cosolvent contribution is given by

$$\Phi_{CS} = -\rho_S \ln(1-\eta_C). \quad (12)$$

This contribution can be similarly interpreted as the free energy of an ideal gas in the free volume of the colloids. In this case, however, the ideal gas consists of pointlike cosolvent particles, considerably simplifying the analytical form of the free volume. In fact, by letting $q \rightarrow 0$ in Eq. (11), and identifying species P and S , Φ_{CP} reduces to Φ_{CS} . The remaining contribution couples the densities of all three species, and is given by

$$\Phi_{CPS} = \frac{\rho_S \eta_P}{1 - \eta_C}. \quad (13)$$

In the absence of colloids ($\eta_C = 0$), this is equivalent to the mean-field free energy of the WR model. Equation (13) is a nontrivial generalization thereof to the case of nonvanishing η_C . For completeness, the reduced ideal-gas free energy is

$$\Phi_{\text{id}} = \sum_{i=C,P,S} \rho_i [\ln(\rho_i \Lambda_i^3) - 1], \quad (14)$$

where the Λ_i are (irrelevant) thermal wavelengths of species i . This puts us in a position to obtain the reduced total free energy density $\Phi_{\text{tot}} = \Phi_{\text{id}} + \Phi$, of any given fluid state characterized by the bulk densities of the three components and the size ratio q .

B. Phase diagrams

The conditions for phase coexistence are equality of the total pressures p_{tot} and of the chemical potentials μ_i in the coexisting phases. For phase equilibrium between phases I and II, $p_{\text{tot}}^I = p_{\text{tot}}^{\text{II}}$ and $\mu_i^I = \mu_i^{\text{II}}$, $i = C, P, S$, yielding four equations for six unknowns (two state points, each characterized by three densities). In our case, a set of analytical expressions is obtained from

$$\frac{p_{\text{tot}}}{k_B T} = -\Phi_{\text{tot}} + \sum_{i=C,P,S} \rho_i \frac{\partial \Phi_{\text{tot}}}{\partial \rho_i} \quad (15)$$

and

$$\mu_i = k_B T \frac{\partial \Phi_{\text{tot}}}{\partial \rho_i}, \quad (16)$$

the numerical solution of which is straightforward.

In order to graphically represent the ternary phase diagrams, we choose the system reduced densities, η_C , η_P , and ρ_S^* as basic variables. For given q , these span a three-dimensional (3D) phase space. Each point in this space corresponds to a possible bulk state. Two-phase coexistence is indicated by a pair of points joined by a straight tie line. We imagine controlling the system directly with η_C and η_P , but indirectly via coupling to a cosolvent reservoir, whose chemical potential μ_S tunes the solvent quality. Note that, because the cosolvent is treated as an ideal gas, the reservoir's density is simply proportional to its activity. Thus, the reduced density $\rho_S^* = \exp(\mu_S/k_B T)$ may be equivalently taken as a control parameter, which is equal in coexisting phases. To make contact with Flory-Huggins theory, we are implicitly considering here the case in which the Flory inter-

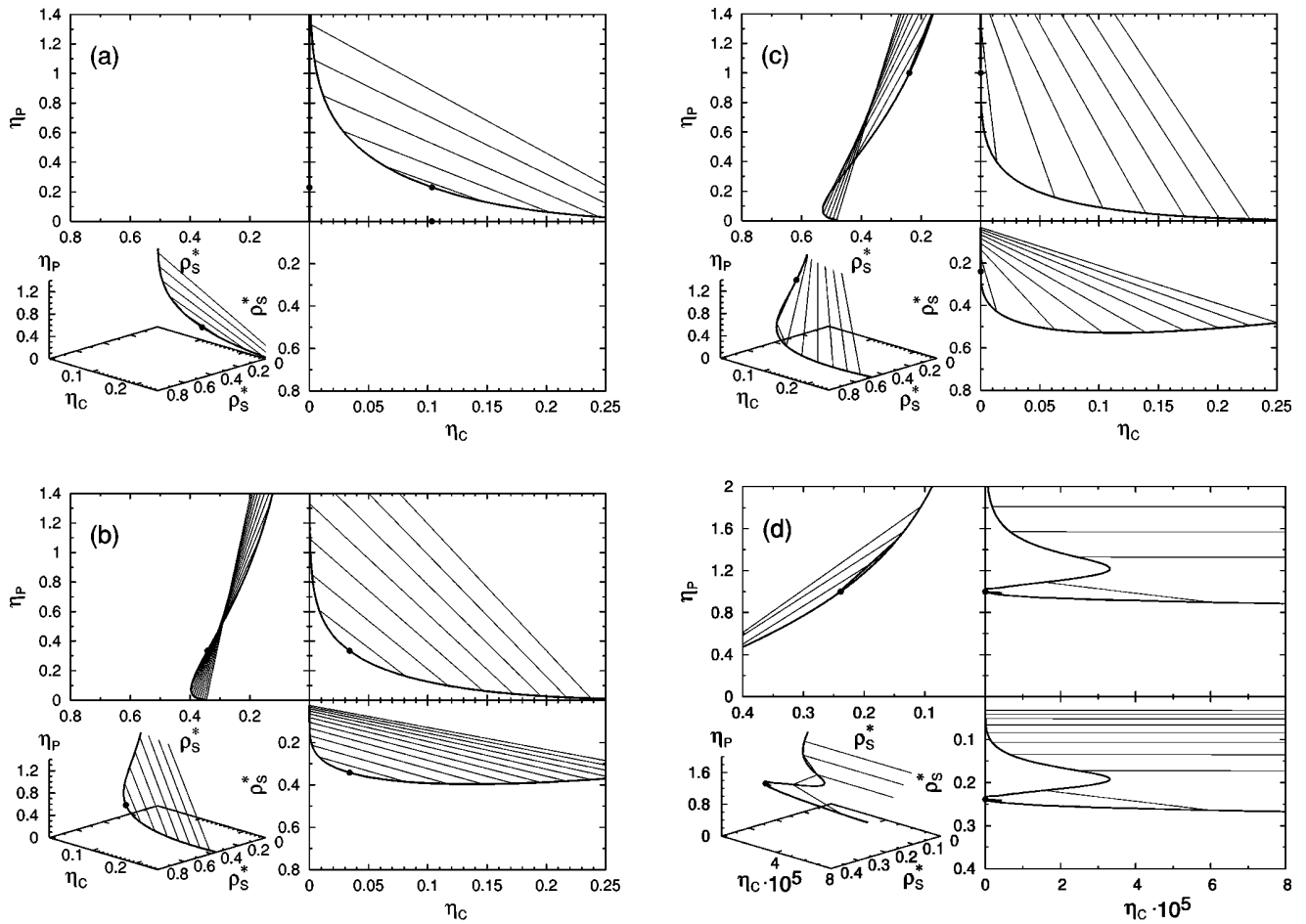


FIG. 2. Demixing phase diagram of the model ternary colloid-polymer-solvent mixture for $\sigma_C = \sigma_P$ and $\rho_S^{*r} = 0$ (a), 0.5 (b), and 0.64894 (c). The latter case is shown also on a finer scale (d).

action parameter χ falls in the range $0.5 < \chi < 1$, corresponding to a negative excluded-volume parameter, $v \propto (1 - 2\chi)$.

We initially consider colloids and polymers of equal size ($\sigma_C = \sigma_P$). For this case, Fig. 2 shows projections of constant- ρ_S^{*r} surfaces onto the three sides of the coordinate system, namely the η_C - ρ_S^* , η_C - η_P , and η_P - ρ_S^* planes, as well as a perspective 3D view. For reference, the phase diagram without cosolvent is shown in Fig. 2(a). This is identical to the common free volume demixing curve of the AO model [7,8]. For $\rho_S^{*r} = 0$, in which case $\rho_S^* = 0$, the η_C - ρ_S^* and η_P - ρ_S^* planes are inaccessible, i.e., all accessible states lie completely within the η_C - η_P plane. Upon increasing the cosolvent reservoir density to $\rho_S^{*r} = 0.5$, and thus worsening the solvent quality, the demixed region grows, as seen in Fig. 2(b). The critical point shifts towards lower η_C and higher η_P , the tie lines become steeper, and the area beneath the colloid-polymer binodal in the η_C - η_P plane (a measure of miscibility) decreases.

As a physical interpretation of the results, one can imagine the polymer spheres as tending to merge (overlap) to avoid contact with the solvent. The resulting polymer “dimers,” “trimers,” etc., act as larger depleting agents, increasing the range of the effective depletion potential be-

tween colloids. At the same time, the lower effective concentration of depletants reduces the osmotic pressure and thus the depth of the potential. Comparing the phase diagrams for different cosolvent reservoir densities, we can conclude that the net effect of merging polymers is to increase the integrated strength of the depletion potential and thus to promote demixing.

Eventually, at $\rho_S^{*r} = 0.64894$, the colloid-polymer critical point meets the η_P - ρ_S^* plane (where $\eta_C = 0$), as seen in Figs. 2(c) and (on a larger scale) 2(d). Polymers and cosolvent here begin to demix already in the absence of colloids (the critical point of the WR model). For still higher cosolvent reservoir densities (beyond the WR critical point), the critical point vanishes from the phase diagram and a polymer-cosolvent miscibility gap opens up at $\eta_C = 0$. It is tempting to interpret this demixing as aggregation of the polymer spheres, although it must be emphasized that the WR model can only crudely describe polymer aggregation.

Another intriguing prediction is the reentrant colloid-polymer mixing evident in Fig. 2(d). For sufficiently low colloid concentrations and high cosolvent reservoir densities (poor solvent), colloids and polymers initially demix with increasing η_P . Upon increasing η_P further, miscibility

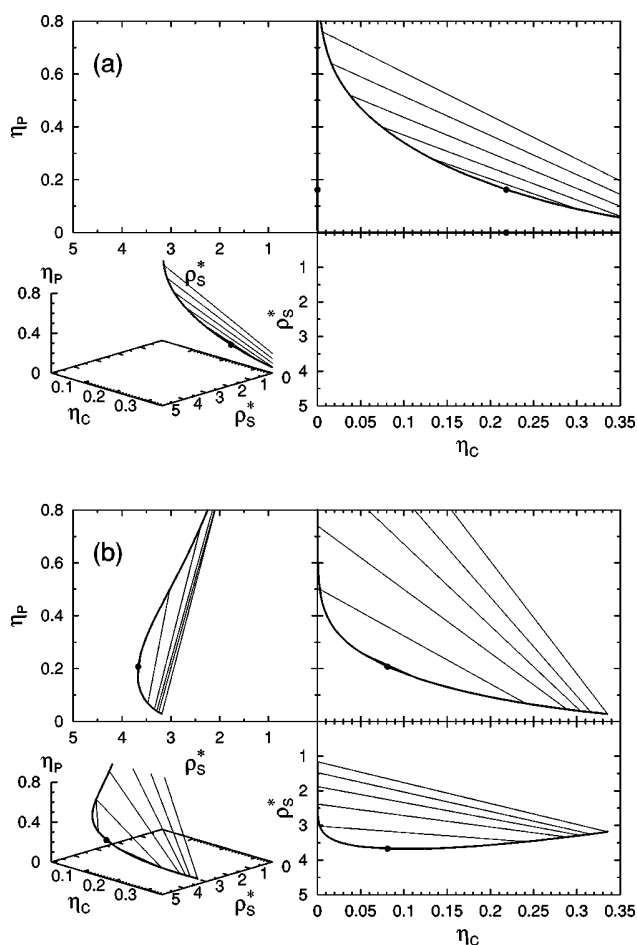


FIG. 3. Same as Fig. 2, but for $\sigma_C = 2\sigma_P$ and $\rho_S^{*r} = 0$ (a) and 0.5 (b).

returns over a small range before demixing again occurs at higher η_P . Such a phenomenon could conceivably result from the complex interplay between range and depth of the depletion potential arising from solvent-induced overlap of polymers.

For smaller polymer-to-colloid size ratios, the above scenario persists. Figure 3 shows qualitatively similar results for $q = 0.5$ and cosolvent reservoir densities $\rho_S^{*r} = 0$ [Fig. 3(a)] and 0.5 [Fig. 3(b)].

V. CONCLUSIONS

In summary, we have investigated the bulk fluid demixing behavior of model mixtures of colloids and nonadsorbing polymers in poor solvents. Our model combines the Asakura-Oosawa model of hard-sphere colloids plus ideal penetrable-sphere polymers with a binary solvent model. The solvent comprises a primary theta solvent and a cosolvent of point particles that are excluded from both colloids and polymers. Cosolvent exclusion energetically favors overlapping configurations of polymers. Although somewhat idealized, the model exhibits the essential feature of solvent-induced effective attraction between polymers, mimicking the effect of a poor solvent.

To study the equilibrium phase behavior of this model, we have derived a geometry-based density functional theory that combines elements of previous theories for the AO and Widom-Rowlinson models. Applying the theory to bulk fluid phases, we have calculated phase diagrams for cosolvent densities spanning a range from theta solvent to poor solvent. With increasing cosolvent concentration (worsening solvent quality), the predicted colloid-polymer binodal shifts to lower colloid concentrations, destabilizing the mixed phase. Beyond a threshold cosolvent concentration, a reentrant colloid-polymer demixing transition is predicted at low colloid concentrations.

Predictions of the theory could be tested by comparison with simulations of the model. Qualitative comparison with experiment also may be possible, but would require a relation between the cosolvent concentration (as a measure of solvent quality) and the Flory interaction parameter. In principle, such a relation could be established by calculating the effective second virial coefficient of the polymer in the polymer-cosolvent subsystem.

Although here we have approximated the polymers as mutually noninteracting, their effective attractions being driven only by cosolvent exclusion, future work should include non-ideality between polymers, arising fundamentally from excluded-volume repulsion between polymer segments. For this purpose, a reasonable model is an effective-sphere description based on a repulsive, penetrable pair interaction (finite at the origin), e.g., of step function or Gaussian shape [12]. The competition between such intrinsic repulsion and the solvent-induced attraction considered in this work is likely to produce rich phase behavior. As a further outlook, our approach also could be applied to effects of solvent quality on polymer brushes adsorbed onto surfaces of colloidal particles.

- [1] P. J. Flory, *Statistical Mechanics of Chain Molecules* (Interscience Publishers, New York, 1969).
- [2] P.-G. de Gennes, *Scaling Concepts in Polymer Physics* (Cornell University Press, Ithaca, NY, 1979).
- [3] P. J. Flory, *Principles of Polymer Chemistry* (Cornell University Press, Ithaca, NY, 1971).
- [4] S. Asakura and F. Oosawa, *J. Chem. Phys.* **22**, 1255 (1954).
- [5] A. Vrij, *Pure Appl. Chem.* **48**, 471 (1976).
- [6] A. P. Gast, C. K. Hall, and W. B. Russell, *J. Colloid Interface Sci.* **96**, 251 (1983).

- [7] H. N. W. Lekkerkerker, W. C. K. Poon, P. N. Pusey, A. Stroobants, and P. B. Warren, *Europhys. Lett.* **20**, 559 (1992).
- [8] M. Schmidt, H. Löwen, J. M. Brader, and R. Evans, *Phys. Rev. Lett.* **85**, 1934 (2000).
- [9] M. Dijkstra, J. M. Brader, and R. Evans, *J. Phys.: Condens. Matter* **11**, 10079 (1999).
- [10] P. B. Warren, S. M. Ilett, and W. C. K. Poon, *Phys. Rev. E* **52**, 5205 (1995).
- [11] M. Schmidt, A. R. Denton, and J. M. Brader (unpublished).
- [12] A. A. Louis, P. G. Bolhuis, J. P. Hansen, and E. J. Meijer, *Phys.*

MATTHIAS SCHMIDT AND ALAN R. DENTON

PHYSICAL REVIEW E **65** 061410

- Rev. Lett. **85**, 2522 (2000).
- [13] P. G. Bolhuis, A. A. Louis, J. P. Hansen, and E. J. Meijer, J. Chem. Phys. **114**, 4296 (2001).
- [14] P. G. Bolhuis, A. A. Louis, and J. P. Hansen, Phys. Rev. E **64**, 021801 (2001).
- [15] S. Ramakrishnan, M. Fuchs, K. S. Schweizer, and C. F. Zukowski, J. Chem. Phys. **116**, 2201 (2002).
- [16] B. Widom and J. S. Rowlinson, J. Chem. Phys. **52**, 1670 (1970).
- [17] J. S. Rowlinson and B. Widom, *Molecular Theory of Capillarity* (Clarendon Press, Oxford, 1982).
- [18] Y. Rosenfeld, Phys. Rev. Lett. **63**, 980 (1989).
- [19] P. Tarazona, Phys. Rev. Lett. **84**, 694 (2000).
- [20] M. Schmidt, Phys. Rev. E **63**, 050201(R) (2001).
- [21] M. Schmidt, H. Löwen, J. M. Brader, and R. Evans (unpublished).
- [22] M. Schmidt and A. R. Denton, Phys. Rev. E. **65**, 021508 (2002).

Penetrability in model colloid–polymer mixtures

Matthias Schmidt

Institut für Theoretische Physik, Heinrich-Heine Universität Düsseldorf, Universitätsstraße 1, D-40225 Düsseldorf, Germany

Matthias Fuchs^{a)}

Institut Charles Sadron, 6, rue Boussingault, 67083 Strasbourg Cedex, France

(Received 3 May 2002; accepted 5 July 2002)

In order to study the effects of penetrability in mixtures of dissimilar particles we consider hard (colloidal) spheres and penetrable spheres. The latter may be taken to represent ideal, noninteracting polymer coils. Polymers and colloids interact by means of a repulsive step-function pair potential, which allows for insertion of colloids into the polymer coil. The potential strength is obtained from scaling arguments for the cross virial coefficient of true colloid–polymer systems. For this model we construct a geometry-based density functional and apply it to bulk fluid demixing. We find that taking into account penetrability leads to a significant stabilization of the mixed phase for large polymer-to-colloid size ratio. © 2002 American Institute of Physics. [DOI: 10.1063/1.1503303]

I. INTRODUCTION

Different levels of description have been used to study the emergence of structure and phase behavior in colloid–polymer mixtures. Such systems are experimentally well characterized and the phase behavior typically displays (colloid) gas, liquid and crystalline phases. A coarse-grained level of description relies on effective spheres to model globular nonadsorbing polymers and goes back to Asakura and Oosawa (AO) (Ref. 1) and Vrij.² Perturbation theory,³ free volume theory,^{4,5} and simulations^{5,6} have been successfully employed to study the bulk properties of this model.

A deeper, more microscopic level of description is the basis for theories that operate on the blob⁷ or segment^{8–11} level of the polymers. It has also been the basis for computer simulations of colloidal spheres and lattice polymers.^{12–14} While these approaches consider translational *and* conformational (internal) contributions to the entropy, a reduction of the degrees of freedom to the center-of-mass translations of both species would among other advantages for example greatly speed up computer simulations of these complex mixtures. This aim has recently been pursued using soft sphere approaches to polymers^{15,16} and also motivates our study.

Density functional theory (DFT) (Ref. 17) is more powerful than the above bulk theories, as it is capable of dealing with *inhomogeneous* situations. In the context of effective sphere models previous hard sphere theories^{18,19} could be extended to a range of models, including the AO model without^{20,21} and with polymer–polymer interactions.²² Interesting inhomogeneous situations are realized in interfaces between demixed fluid states and near walls, where wetting and layering phenomena were found.²³

In this work we use effective polymer spheres and do one step towards a more realistic description by allowing

colloids to penetrate the polymer spheres. On the segment level (disregarded within our model), this leads to a restriction of allowed polymer configurations, hence a free energy penalty emerges. We calculate its strength from the cross virial coefficient and use this as an input for the effective sphere model, by setting the free energy penalty equal to an *internal* energy contribution to the Hamiltonian, both for a theta solvent and for a good solvent. As an approximation, we disregard polymer–polymer interactions, as would be justified for dilute polymers and at the theta temperature. We derive a DFT for the model and apply it to bulk fluid demixing. For small polymer-to-colloid size ratios the demixing binodal approaches the free volume result for impenetrable polymer.⁴ In the opposite regime of large polymer-to-colloid size ratios, our theory predicts a significant stabilization of the mixed fluid phase, the effect being stronger in the case of a good solvent.

We specify the model of hard colloids and penetrable polymer in Sec. II, and develop the theory in Sec. III. Bulk fluid–fluid demixing is calculated in Sec. IV and we finish with concluding remarks in Sec. V.

II. THE MODEL

We consider a mixture of colloidal particles (species *C*) and effective polymer spheres (species *P*) interacting by means of pair potentials $V_{ij}(r)$, where $i, j = C, P$, see Fig. 1 for a sketch of the model. The interactions between particles of the same species are

$$V_{CC}(r) = \begin{cases} \infty & \text{if } r < 2R_C \\ 0 & \text{else,} \end{cases} \quad (1)$$

$$V_{PP}(r) = 0. \quad (2)$$

The interaction between colloids and polymers is

$$V_{CP}(r) = \begin{cases} \epsilon_{CP} & \text{if } r < R_C + R_P \\ 0 & \text{else.} \end{cases} \quad (3)$$

^{a)}Permanent address: Physik Department, Technische Universität München, D-85747 Garching, Germany.

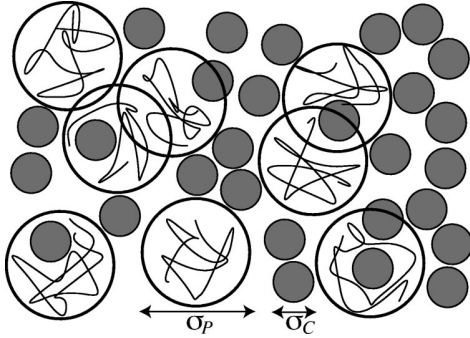


FIG. 1. Sketch of the model with hard colloidal spheres of diameter $\sigma_C = 2R_C$ and effective polymer spheres with diameter $\sigma_P = 2R_C$. Penetration of colloids into polymers is accompanied by an energy cost ϵ_{CP} .

In essence, this is the AO model where the colloid-polymer interaction is assumed to be penetrable rather than hard. Hence we refer to this model as the penetrable Asakura-Oosawa (PAO) model. The PAO model reduces in the limit $\beta\epsilon_{CP} \rightarrow \infty$ to the classic AO model,^{1,2} where $\beta = 1/k_B T$, k_B is the Boltzmann constant, and T is absolute temperature. Another (albeit trivial) limit is obtained for $\beta\epsilon_{CP} \rightarrow 0$ (and finite radii R_P , R_C), where the mixture decouples into a hard sphere colloid fluid and an ideal gas of polymers; these subsystems do not interact with each other.

As bulk thermodynamic parameters we use the packing fractions $\eta_C = 4\pi R_C^3 \rho_C / 3$, $\eta_P = 4\pi R_P^3 \rho_P / 3$, where ρ_C , ρ_P are the number densities of colloids and polymers, respectively. The system volume is denoted by V . The size ratio $q = R_P / R_C$ and the (reduced) strength $\beta\epsilon_{CP}$ act as control parameters.

III. THEORY

A. Zero-dimensional limit

In order to work out a density functional theory for the PAO model we follow the lines suggested in Refs. 18 and 19 for hard spheres and in Refs. 20–22, 24, and 25 for a broader class of models and determine the excess Helmholtz free energy from dimensional crossover starting with the zero-dimensional (0D) limit. The 0D limit corresponds to the problem of packing particles into cavities such that all particles overlap. This is an idealized situation and allows for an exact solution of the many-body problem. To obtain the 0D grand partition sum, Ξ , we count the possible states characterized by the particle numbers of colloids and polymers (which can be regarded as occupancy numbers of the 0D cavity). As we deal with a thermal system, where $\beta\epsilon_{CP}$ is a control parameter, we need to consider the appropriate statistical weight, given by the Boltzmann factor, in the grand ensemble. Summing-up the possible states, we have (i) all states with an arbitrary number of polymers but without colloids. This includes the empty state with vanishing particle numbers, and essentially constitutes the partition sum of an ideal gas of polymers. Furthermore, we need to consider (ii) a single colloidal particle and an arbitrary number of polymers. All remaining states are characterized by at least two colloidal particles. Due to the hard core potential between

colloids, these states carry vanishing statistical weight. Hence we obtain the 0D grand partition sum,

$$\Xi = \exp(z_P) + z_C \exp(z_P \exp(-\beta\epsilon_{CP})), \quad (4)$$

where the first (second) term corresponds to case i (ii) above, and z_i is the fugacity of species $i = C, P$. From the grand partition sum Ξ , Eq. (4), the (canonical) Helmholtz free energy can be obtained by a (double) Legendre transform from the fugacities z_i to the mean numbers of particles $\bar{\eta}_i = z_i \partial \ln \Xi / \partial z_i$. Hence the excess (over ideal gas) free energy F_{0D} is obtained from $\beta F_{0D} + \bar{\eta}_P [\ln(\bar{\eta}_P) - 1] + \bar{\eta}_C [\ln(\bar{\eta}_C) - 1] = -\Xi + \bar{\eta}_P \ln(z_P) + \bar{\eta}_C \ln(z_C)$. The straightforward calculation gives

$$\beta F_{0D} = (1 - \bar{\eta}_C) \ln(1 - \bar{\eta}_C) + \bar{\eta}_C - \bar{\eta}_P \ln(1 - \bar{\eta}_C [1 - \exp(-\beta\epsilon_{CP})]). \quad (5)$$

It is instructive to consider the limit of weak colloid-polymer interactions, $\beta\epsilon_{CP} \rightarrow 0$. By Taylor expanding Eq. (5) one obtains

$$\beta F_{0D} = (1 - \bar{\eta}_C) \ln(1 - \bar{\eta}_C) + \bar{\eta}_C - \beta\epsilon_{CP} \bar{\eta}_P \bar{\eta}_C + O(\beta^2 \epsilon_{CP}^2). \quad (6)$$

The sum of the first two terms in Eq. (6) equals the 0D free energy of hard spheres.^{26,27} The next term is bilinear in the densities involved—a typical mean-field contribution. This might be expected on physical grounds. We stress, however, that Eq. (6) is an *exact* expansion. We further note that in the limit of hard colloid-polymer interaction, $\beta\epsilon_{CP} \rightarrow \infty$, the 0D free energy is $\beta F_{0D} = (1 - \bar{\eta}_C - \bar{\eta}_P) \ln(1 - \bar{\eta}_C) + \bar{\eta}_C$, equal to the result for the AO model.^{20,21}

B. Density functional theory

The total Helmholtz free energy of an inhomogeneous system may be written as $F = F_{id} + F_{exc}$, where $F_{id} = \sum_{i=C,P} \int d\mathbf{r} \rho_i(\mathbf{r}) [\ln(\rho_i(\mathbf{r}) \Lambda_i^3) - 1]$ is the ideal-gas free energy functional (for two species), with Λ_i being the (irrelevant) thermal wavelength of species i , and F_{exc} is the excess contribution arising from interactions between particles. Following previous work on mixtures,^{18,20,21,26,27} we express the Helmholtz excess free energy as a functional of colloid and polymer density fields as a spatial integral

$$F_{exc}[\rho_C(\mathbf{r}), \rho_P(\mathbf{r})] = k_B T \int d^3x \Phi(\{n_\nu^C(\mathbf{x})\}, \{n_\nu^P(\mathbf{x})\}), \quad (7)$$

where the weighted densities

$$n_\nu^i(\mathbf{x}) = \int d^3r \rho_i(\mathbf{r}) w_\nu^i(\mathbf{x} - \mathbf{r}), \quad i = C, P \quad (8)$$

are defined as convolutions of weight functions, w_ν^i , with the actual density profiles, and $\nu = 0, 1, 2, 3, v1, v2, m2$ denotes the type of weight function.

The weight functions w_ν^i are independent of the density profiles and are given by

$$w_3^i(\mathbf{r}) = \Theta(R_i - r), \quad w_2^i(\mathbf{r}) = \delta(R_i - r), \quad (9)$$

$$w_{v2}^i(\mathbf{r}) = w_2^i(\mathbf{r}) \mathbf{r} / r, \quad \hat{w}_{m2}^i(\mathbf{r}) = w_2^i(\mathbf{r}) [\mathbf{r} \mathbf{r} / r^2 - \hat{\mathbf{1}} / 3], \quad (10)$$

where $r=|\mathbf{r}|$, $\Theta(r)$ is the step function, $\delta(r)$ is the Dirac distribution, and $\hat{\mathbf{1}}$ is the 3×3 identity matrix, and matrices are denoted by a hat. Further, linearly dependent, weights are $w_1^i(\mathbf{r})=w_2^i(\mathbf{r})/(4\pi R_i)$, $\mathbf{w}_{v1}^i(\mathbf{r})=\mathbf{w}_{v2}^i(\mathbf{r})/(4\pi R_i)$, $w_0^i(\mathbf{r})=w_1^i(\mathbf{r})/R_i$. The weight functions are quantities with dimension (length) $^{3-\nu}$. They differ in their tensorial rank: w_0^i , w_1^i , w_2^i , w_3^i are scalars; \mathbf{w}_{v1}^i , \mathbf{w}_{v2}^i are vectors; $\hat{\mathbf{w}}_{m2}^i$ is a (traceless) matrix.

The free energy density Φ is composed of three parts^{18,19} that arise from consideration of one, two and three cavities,²⁸

$$\Phi = \Phi_1 + \Phi_2 + \Phi_3. \quad (11)$$

They are defined as

$$\Phi_1 = \sum_{i=C,P} n_0^i \varphi_i(n_3^C, n_3^P), \quad (12)$$

$$\Phi_2 = \sum_{i,j=C,P} (n_1^i n_2^j - \mathbf{n}_{v1}^i \cdot \mathbf{n}_{v2}^j) \varphi_{ij}(n_3^C, n_3^P), \quad (13)$$

$$\begin{aligned} \Phi_3 = & \frac{1}{8\pi} \sum_{i,j,k=C,P} \left(\frac{1}{3} n_2^i n_2^j n_2^k - n_2^i \mathbf{n}_{v2}^j \cdot \mathbf{n}_{v2}^k \right. \\ & \left. + \frac{3}{2} [\mathbf{n}_{v2}^i \hat{\mathbf{n}}_{m2}^j \mathbf{n}_{v2}^k - \text{tr}(\hat{\mathbf{n}}_{m2}^i \hat{\mathbf{n}}_{m2}^j \hat{\mathbf{n}}_{m2}^k)] \right) \varphi_{ijk}(n_3^C, n_3^P), \end{aligned} \quad (14)$$

where tr denotes the trace, and m th order derivatives of the 0D excess free energy [Eq. (5)] are

$$\varphi_{i \dots k}(\bar{\eta}_C, \bar{\eta}_P) \equiv \frac{\partial^m}{\partial \bar{\eta}_i \dots \partial \bar{\eta}_k} F_{0D}(\bar{\eta}_C, \bar{\eta}_P). \quad (15)$$

This completes the prescription for the functional.

C. Penetrable colloid–polymer interactions

The theory we have presented so far is applicable to arbitrary (constant) colloid–polymer interaction strength ϵ_{CP} and polymer-to-colloid size ratios q . As our aim is a study of the effects of particle–coil penetration in real colloid–polymer mixtures, we seek to find a relation between ϵ_{CP} and q to match our effective sphere system with the behavior of true polymers. In the following this is carried out for the case of low density of polymer and a single sphere, where we consider the excess chemical potential or insertion free energy. In lowest order, it is determined by the cross virial coefficient between colloid and polymer. We consider two cases, namely a theta solvent and a poor solvent, in order to also learn about the effect of excluded volume swelling of the coil structure. The excess insertion free energies for adding $V\rho_C$ independent spheres to a dilute solution of polymers, or to a solution of noninteracting polymers at arbitrary density, are known from field-theoretic considerations and satisfy scaling limits for large q ,^{29,30}

$$\begin{aligned} & \beta \delta F_{\text{exc}}/(V\rho_C) \\ & \rightarrow \begin{cases} 4\pi\rho_P R_P^3/q & \text{for } \nu = \frac{1}{2} \text{ (theta solvent)} \\ 18.461\rho_P R_P^3 q^{1/\nu-d} & \text{for } \nu = 0.588 \text{ (good solvent),} \end{cases} \end{aligned} \quad (16)$$

where $d=3$ is the space dimension. Particle insertion into

the polymer coil is manifest in the decrease of $\beta \delta F_{\text{exc}}$ for large q where the open polymer structure becomes important. Using the potential given in Eq. (3), the virial expansion is in the limit of small interactions $\beta \epsilon_{CP}$ given by $\beta \delta F_{\text{exc}}/(V\rho_C) \rightarrow \frac{4}{3}\pi R_P^3 \rho_P \beta \epsilon_{CP}$. Requiring this to agree with Eq. (16) in the limit of large polymers, we find for the theta solvent,

$$\beta \epsilon_{CP}(q) = \frac{3}{q}, \quad (17)$$

and in a good solvent

$$\beta \epsilon_{CP}(q) = \frac{4.40724}{q^{3-1/\nu}} = \frac{4.40724}{q^{1.29932}}, \quad (18)$$

where $\nu=0.588$.

There is a crossover between both functional forms for $\epsilon_{CP}(q)$. For smaller (larger) values than $q=3.615$, the interaction strength ϵ_{CP} is weaker in the case of a theta (good) solvent.

IV. RESULTS

A. Thermodynamics

To obtain the thermodynamics of homogeneous fluid states, we apply the density functional described in Sec. III B to constant density fields, $\rho_C(\mathbf{r})=\text{const}$, $\rho_P(\mathbf{r})=\text{const}$. In this case the scalar weighted densities n_ν^i , $\nu=3,2,1,0$ become proportional to the bulk densities, $n_\nu^i = \xi_\nu^i \rho_i$, where the proportionality constants ξ_ν^i are so-called fundamental measures obtained as $\xi_\nu^i = \int d^3r w_\nu^i(\mathbf{r})$ [see Eq. (8)]. Explicitly the fundamental measures are given as $\xi_3^i = 4\pi R_i^3/3$, $\xi_2^i = 4\pi R_i^2$, $\xi_1^i = R_i$, $\xi_0^i = 1$, corresponding to the volume, surface, integral mean curvature, and Euler characteristic of the spheres of species i . The vectorial and tensorial weighted densities, \mathbf{n}_{v2}^i , \mathbf{n}_{v1}^i , $\hat{\mathbf{n}}_{m2}^i$ vanish for constant density fields, due to the symmetry of the corresponding weight functions [Eq. (10)]. Inserting the obtained expressions for the n_ν^i into Eqs. (12)–(14), and carrying out the derivatives in Eq. (15) yields the excess free energy density Φ [Eq. (11)]. As Φ is also constant in space, the integration in Eq. (7) becomes trivial, and the bulk excess Helmholtz free energy density is obtained as

$$\beta F_{\text{exc}}/V = \beta \phi_{\text{HS}}(\rho_C) - \rho_P \ln \alpha_{\text{PAO}}(\rho_C), \quad (19)$$

where $\phi_{\text{HS}}(\rho_C)$ is the excess free energy per unit volume of pure HS in the scaled-particle (and Percus–Yevick compressibility) approximation, given as

$$\beta \phi_{\text{HS}}(\rho_C) = \frac{3\eta_C [3\eta_C(2-\eta_C) - 2(1-\eta_C)^2 \ln(1-\eta_C)]}{8\pi R_C^3 (1-\eta_C)^2}, \quad (20)$$

and

$$\alpha_{\text{PAO}}(\rho_C) = (1-\eta_C') \exp(-A\gamma - B\gamma^2 - C\gamma^3), \quad (21)$$

where $\gamma = \eta_C'/(1-\eta_C')$, $\eta_C' = [1 - \exp(-\beta \epsilon_{CP})]\eta_C$, and the coefficients depend only on the size ratio and are given as $A = q^3 + 3q^2 + 3q$, $B = 3q^3 + 9q^2/2$, and $C = 3q^3$.

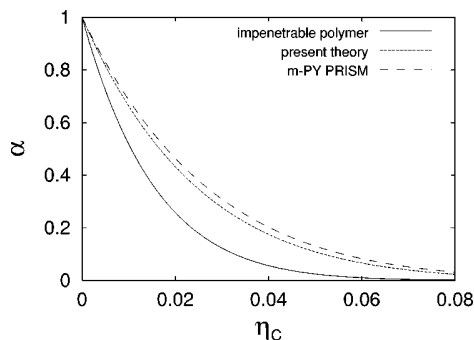


FIG. 2. Comparison of the free volume fraction α as a function of colloid packing fraction η_C and for size ratio $q=3$ for different models and approximations: Free volume theory for the AO model (solid line), present theory for the penetrable AO model (dotted line), m-PY PRISM approach (long-dashed line).

As pointed out in Sec. II, the PAO model reduces to the AO case for $\beta\epsilon_{CP} \rightarrow \infty$. In this limit, $\eta'_C = \eta_C$, and $\alpha_{PAO} = \alpha_{AO}$. As our DFT reduces to the corresponding functional for the AO model,^{20,21} we recover the same α_{AO} , which was strikingly shown to be equal to the expression for the free-volume fraction from the approach of Lekkerkerker *et al.*⁴ Hence our α_{PAO} generalizes the common free volume fraction to the case of penetrable colloid-polymer interactions.

Quantitatively, α_{PAO} significantly deviates from the free volume result, provided the size ratio q is large enough. We plot both quantities in Fig. 2 as a function of η_C for $q=3$, using the relation between size ratio and interaction strength in a theta solvent, $\beta\epsilon_{CP} = 3/q$. Except for the limiting value at $\eta_C=0$, significant deviations exist over the whole density range. These differences suggest significant deviations in the predicted phase behavior of both approaches—an issue that we will turn to in the next section.

In order to assess how well our α compares to the free volume fraction in real colloid-polymer mixtures, we consider the microscopic m-PY PRISM approach of Refs. 8–10. This theory was used to derive α from a description of polymers on the segment level [Eqs. (5) and (6) in Ref. 10]. We find that the free volume fractions from both approaches are similar, with α_{m-PY} being slightly larger. The deviations can be traced back to the fact that for large q and small η_C different expansions hold, namely $\alpha_{PAO} = 1 - 3\eta_C/q^2$ and $\alpha_{m-PY} = 1 - 2.42705\eta_C/q^2$.

B. Fluid demixing phase behavior

The conditions for phase equilibrium are equality of the chemical potentials of both species and of the total pressure in both phases. This is equivalent to performing a double tangent construction on the semigrand free energy where the polymer chemical potential is kept constant, see, e.g., Ref. 4 for further details.

We calculated binodals for the PAO model for size ratios $q=0.5, 1, 3, 10$ and display results in Fig. 3. For comparison we also show the binodals obtained from free volume theory for the AO model. Note that this predicts stable liquid-gas coexistence in the AO model for $q > 0.32$; for smaller values of q this transition becomes metastable with respect to the fluid-solid transition.^{4,5} Within our model both size ratio and colloid-polymer interaction strength are intimately coupled, hence by varying q , the interaction strength is $\beta\epsilon_{CP}$ varies. For the above sequence of q values, the colloid-polymer interaction strength in a theta solvent [given in Eq. (17)] takes on the values $\beta\epsilon_{CP} = 6, 3, 1, 0.3$, and the corresponding Boltzmann factor varies over a considerable range, namely $\exp(-\beta\epsilon_{CP}) = 0.00248, 0.0498, 0.368, 0.741$.

For $q=0.5$ [Fig. 3(a)] our binodals for both cases, theta solvent and good solvent, practically coincide (on the scale of the plot) with those for the AO model. This is due to the

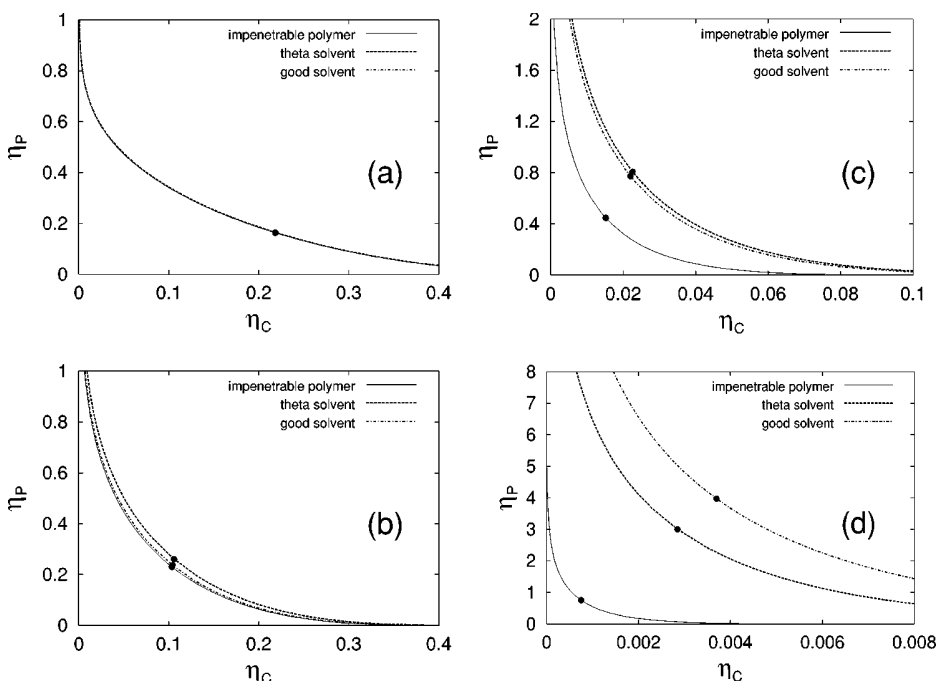


FIG. 3. Fluid-fluid demixing phase diagrams as a function of packing fractions η_C and η_P of colloids and polymers, respectively. Shown is the free volume result for the AO model with impenetrable polymer, along with the result of the present theory applied to the penetrable AO model for the cases of a theta solvent and a good solvent; the colloid-polymer interaction strength $\beta\epsilon_{CP}$ is prescribed by using Eq. (17) in the case of the theta solvent and by using Eq. (18) in the case of the good solvent. Dots represent the critical point. Different polymer-to-colloid size ratios q are shown: $q = 0.5$ (a), 1 (b), 3 (c), 10 (d).

fact that the Boltzmann factor for the cross interaction between colloids and polymers is tiny, hence penetrability is negligible. We conclude that both model and theory reduce to the correct limits. For $q=1$ [Fig. 3(b)] deviations begin to emerge. The binodal in the PAO cases is shifted upward to higher (polymer) fraction, leading to a stabilization of the mixed phase. Physically this is reasonable because the two different species repel each other weaker than in the AO case as the colloidal particles can now penetrate into the noncompact polymer coils. Stabilization of the mixed phase grows stronger upon increasing size ratio [see Figs. 3(c) and 3(d) for $q=3,10$]. For $q=10$ significant enhancement of the mixed phase is predicted. In the limit $q\rightarrow\infty$ for a theta solvent, we find that the critical point is at $\eta_C=1/(3q^2)-1/(2q^3)$, $\eta_P=q/3-1/2$ similarly as in Sear's recent blob-scaling extension of the free volume approximation of the AO model.⁷

V. CONCLUSIONS

Previous models of colloid-polymer mixtures employed interactions between polymer and colloid with a hard core, prohibiting overlap between colloids and polymers. This is a deficiency of these models, because in real systems, colloids may penetrate polymer coils, especially if the polymer radius of gyration is larger than the colloid size. In this work, we remedied this drawback by introducing a penetrable (finite for all distances) pair interaction between colloid and polymer. As a model, this was chosen to be a step-function and we have derived a geometry-based DFT and applied it to bulk fluid demixing. The free energy density is derived from the DFT by applying the functional to constant density profiles. The resulting analytical expression has a similar structure as the well-known free volume result.⁴ However, due to the penetrability, in the expression for the polymer free volume the bare colloid packing fraction η_C is replaced by a scaled packing fraction $\eta'_C=[1-\exp(-\beta\epsilon_{CP})]\eta_C$ [see Eq. (21)], where $\beta\epsilon_{CP}$ is the strength of colloid-polymer repulsion. We determine the latter via virial coefficient arguments for the cases of a theta and a good solvent. When the size ratio $q>1$, i.e., for long polymers $\beta\epsilon_{CP}\lesssim 1$, and hence η'_C differs markedly from η_C . As a consequence the free volume fraction is considerably larger than the classic result for impenetrable polymer⁴ and agrees reasonably well with the result from the microscopic m-PY PRISM approach.⁸⁻¹⁰ Our model is still effective in the sense that details on the segment level of the polymers are ignored *a priori*, and thus its phase boundaries become less reliable for large polymer-to-colloid size ratios where they shift deep into the semidilute polymer concentration range. Here, presumably our neglect of polymer-polymer interactions is not reliable anymore when applied to experimental systems. Nevertheless the

model's prediction that, for large polymers, particle penetration into the polymer coils becomes important compared to the classical AO picture should prove robust and agrees with more microscopic approaches^{8,11} where excluded volume is taken into account on the segment level. Our model also captures changes in miscibility resulting from excluded volume swelling of the polymer coils when varying the solvent quality, as has been seen experimentally,¹⁰ albeit for somewhat different parameters.

ACKNOWLEDGMENTS

Alan R. Denton, Joseph M. Brader, and Henk N. W. Lekkerkerker are gratefully acknowledged for useful discussions. M.F. was supported by the Deutsche Forschungsgemeinschaft under Grant No. Fu 309/3 and through the SFB 563.

¹S. Asakura and F. Oosawa, J. Chem. Phys. **22**, 1255 (1954).

²A. Vrij, Pure Appl. Chem. **48**, 471 (1976).

³A. P. Gast, C. K. Hall, and W. B. Russell, J. Colloid Interface Sci. **96**, 251 (1983).

⁴H. N. W. Lekkerkerker, W. C. K. Poon, P. N. Pusey, A. Stroobants, and P. B. Warren, Europhys. Lett. **20**, 559 (1992).

⁵M. Dijkstra, J. M. Brader, and R. Evans, J. Phys.: Condens. Matter **11**, 10079 (1999).

⁶P. G. Bolhuis, A. A. Louis, and J. P. Hansen (unpublished).

⁷R. Sear, Phys. Rev. Lett. **86**, 4696 (2001).

⁸M. Fuchs and K. S. Schweizer, Europhys. Lett. **51**, 621 (2000).

⁹M. Fuchs and K. S. Schweizer, Phys. Rev. E **64**, 021514 (2001).

¹⁰S. Ramakrishnan, M. Fuchs, K. S. Schweizer, and C. F. Zukoski, J. Chem. Phys. **116**, 2201 (2002).

¹¹M. Fuchs and K. S. Schweizer, J. Phys.: Condens. Matter **12**, R239 (2002).

¹²E. J. Meijer and D. Frenkel, Phys. Rev. Lett. **67**, 1110 (1991).

¹³E. J. Meijer and D. Frenkel, J. Chem. Phys. **100**, 6873 (1994).

¹⁴E. J. Meijer and D. Frenkel, Physica A **213**, 130 (1995).

¹⁵A. A. Louis, R. Finken, and J. Hansen, Europhys. Lett. **46**, 741 (1999).

¹⁶A. A. Louis, P. G. Bolhuis, J. P. Hansen, and E. J. Meijer, Phys. Rev. Lett. **85**, 2522 (2000).

¹⁷R. Evans, in *Fundamentals of Inhomogeneous Fluids*, edited by D. Henderson (Dekker, New York, 1992), p. 85.

¹⁸Y. Rosenfeld, Phys. Rev. Lett. **63**, 980 (1989).

¹⁹P. Tarazona, Phys. Rev. Lett. **84**, 694 (2000).

²⁰M. Schmidt, H. Löwen, J. M. Brader, and R. Evans, Phys. Rev. Lett. **85**, 1934 (2000).

²¹M. Schmidt, H. Löwen, J. M. Brader, and R. Evans, J. Phys.: Condens. Matter (issue in honor of J.-P. Hansen) (to be published).

²²M. Schmidt, A. R. Denton, and J. M. Brader, (unpublished).

²³J. M. Brader, R. Evans, M. Schmidt, and H. Löwen, J. Phys.: Condens. Matter **14**, L1 (2002).

²⁴M. Schmidt, J. Phys.: Condens. Matter **11**, 10163 (1999).

²⁵M. Schmidt, Phys. Rev. E **63**, 010101(R) (2001).

²⁶Y. Rosenfeld, M. Schmidt, H. Löwen, and P. Tarazona, J. Phys.: Condens. Matter **8**, L577 (1996).

²⁷Y. Rosenfeld, M. Schmidt, H. Löwen, and P. Tarazona, Phys. Rev. E **55**, 4245 (1997).

²⁸P. Tarazona and Y. Rosenfeld, Phys. Rev. E **55**, R4873 (1997).

²⁹E. Eisenriegler, A. Hanke, and S. Dietrich, Phys. Rev. E **54**, 1134 (1996).

³⁰A. Hanke, E. Eisenriegler, and S. Dietrich, Phys. Rev. E **59**, 6853 (1999).

Density functional theory for colloidal rod-sphere mixtures

Matthias Schmidt

Institut für Theoretische Physik II, Heinrich-Heine-Universität Düsseldorf, Universitätsstraße 1, D-40225 Düsseldorf, Germany

(Received 13 December 2000; published 11 April 2001)

We present a density functional theory for a model colloidal mixture of hard spheres and infinitely thin hard rods. For these freely rotating particles, we use a fundamental measures approach to obtain a functional that features the correct dimensional crossover and the exact low density limit. For isotropic bulk fluid mixtures, the free energy, and hence the demixing phase diagram, are identical to that obtained from free volume theory. Results for the partial pair correlation functions of the bulk mixture are in good agreement with those of our simulations.

DOI: 10.1103/PhysRevE.63.050201

PACS number(s): 61.20.Gy, 61.30.Cz, 64.70.Ja, 82.70.Dd

Colloidal mixtures of differently shaped or sized particles serve as well-defined model systems for the study of a wide range of phenomena in condensed matter. These include structural correlations, demixing phase transitions, and freezing. Such systems can be prepared so that they possess primarily hard body pair interactions; hence, entropy plays the dominant role. Creating binary mixtures by adding a second component to monodisperse colloidal hard spheres (HS) provides the work horse in the field. Among the various different second components are smaller-sized spherical particles, leading to binary hard sphere mixtures [1], globular nonadsorbing polymers [2], and rodlike colloids [3,4] or polymers. In these situations, the additive is often regarded as an agent that mediates an effective interaction between the spheres by means of the depletion mechanism. For rods considerable recent work was done to reveal the nature of the depletion [5,6]. The benefit of this approach is the analogy to simple substances possessing an attractive pair potential. However, the depletant's degrees of freedom are no longer accessible, and, in general, effective many-body interactions between the spheres occur, which are difficult to treat. Both drawbacks can be circumvented by treating the full binary mixture, without any explicit integrating-out procedure.

A simple rod-sphere model was introduced by Bolhuis and Frenkel (BF) [7]. It consists of a mixture of hard spheres and hard, infinitely thin rods (needles). The needle volume, and hence the interaction between needles, vanishes in this limit. Clearly, this is a gross simplification. However, rod aspect ratios can be as high as 25 in experiments with silica coated boehmite rods [4] mixed with silica spheres, and the rod densities are typically well below the Onsager nematic-isotropic transition [4]. BF's model can be thought of as the simplest in the present context, playing a role similar to the Asakura-Oosawa (AO) model [2] for the case of spherical colloids and added polymer. BF's computer simulations showed that the model undergoes a demixing transition into sphere-rich (rod-poor) and sphere-poor (rod-rich) phases. They also extended Lekkerkerker's free volume theory [8] for the AO model to their case. Comparing with simulation results for the binodals, they found that "... the accuracy of the theoretical curves is surprising" [7]. Subsequently, finite rod thickness could also be treated [3]. Little attention, however, has been paid to the model's bulk structural cor-

relations, to its behavior in inhomogeneous situations, as, for example, induced by walls, or to the free interface between demixed phases.

In this work, we present a density-functional theory (DFT) [9] for the binary needle-sphere mixture that allows us to study correlations in bulk as well as in arbitrary inhomogeneous situations. It is based on Rosenfeld's fundamental measures theory [10,11] and Tarazona's latest extension to this [12], ensuring that local packing effects are correctly included. The free energy of the homogeneous fluid, and hence, the demixing curve, are the same as in BF's free volume theory. Our DFT features the correct virial expansion. In the literature it has been stated by several authors [11,13,14], that an impossibility of deconvolution of the Mayer function for *arbitrary* convex bodies prohibits this sort of geometrically based DFT. Here we give an explicit counterexample; albeit dealing with a model where interactions between rods are absent, we present the first such theory for freely rotating anisotropic particles. Our functional has the correct dimensional crossover to situations of reduced spatial dimensionality, an important property that only recently was achieved for one-component hard spheres [12]. As an application, we reconsider the phase diagram and then focus on the bulk pair correlations in the sphere-needle mixture where we find good agreement between the DFT results and our computer simulations.

Let us first describe the needle-sphere model. We consider a mixture of hard spheres (species S) with radii R , and infinitely thin needles (species N) with length L , and number densities ρ_S and ρ_N , respectively. The pair interaction between spheres is $V_{SS} = \infty$ if the separation between sphere centers is less than $2R$, and zero otherwise; the pair interaction between a sphere and a needle is $V_{SN} = \infty$, if both overlap, and zero else; the interaction between needles vanishes for all separations, $V_{NN} = 0$. We denote the sphere diameter by $\sigma = 2R$, and the sphere packing fraction by $\eta = 4\pi R^3 \rho_S / 3$. In Fig. 1 a snapshot from computer simulation (described below) is shown to illustrate the model.

In order to construct the DFT, we start with a geometrical representation of the particles in terms of weight functions w_μ^i , where i labels the species, and $\mu = 3, 2, 1$, and 0 corresponds to the particles' volume, surface, integral mean curvature, and Euler characteristic, respectively [11]. The weight functions are determined to give the Mayer bonds

MATTHIAS SCHMIDT

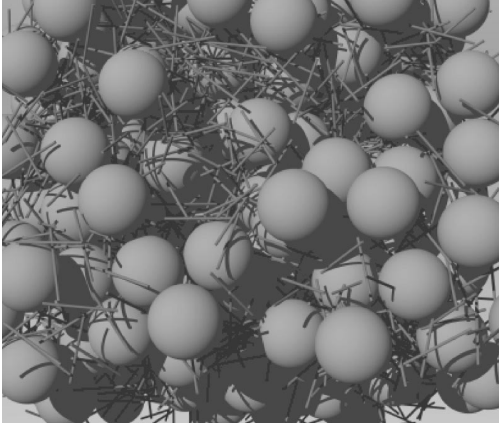
PHYSICAL REVIEW E **63** 050201(R)

FIG. 1. Snapshot from simulation of the rod-sphere mixture at $L = \sigma$, $\eta = 0.3$, $\rho_N = 8\rho_S$ (statepoint II in Fig. 2). The rods are rendered with a finite diameter of 0.02σ .

$f_{ij} = \exp(V_{ij}) - 1$ by a linear combination of terms $w_{\gamma}^i(\mathbf{r}') w_{3-\gamma}^j(\mathbf{r}'')$, where $g(\mathbf{r}') h(\mathbf{r}'') = \int d^3x g(\mathbf{x}) h(\mathbf{r} - \mathbf{x})$. For needles, we follow Ref. [11] to obtain

$$w_1^N(\mathbf{r}, \mathbf{\Omega}) = \frac{1}{4} \int_{-L/2}^{L/2} dl \delta(\mathbf{r} + \mathbf{\Omega}l), \quad (1)$$

$$w_0^N(\mathbf{r}, \mathbf{\Omega}) = \frac{1}{2} [\delta(\mathbf{r} + \mathbf{\Omega}L/2) + \delta(\mathbf{r} - \mathbf{\Omega}L/2)], \quad (2)$$

where $\delta(r)$ is the Dirac distribution, $\mathbf{\Omega}$ is a unit vector pointing along the needle axis, and \mathbf{r} is the spatial coordinate. The function w_1^N describes the linear extent of a needle [15], whereas w_0^N is characteristic of its endpoints. For infinitely thin needles, both surface and volume vanish, and so should the corresponding weights, $w_2^N = w_3^N = 0$. Indeed, as will be seen *a posteriori*, such terms are not needed to construct the DFT. For spheres, the usual weight functions [10,12] are

$$w_3^S(\mathbf{r}) = \theta(R - r), \quad w_2^S(\mathbf{r}) = \delta(R - r), \quad (3)$$

$$\mathbf{w}_{v2}^S(\mathbf{r}) = w_2^S(\mathbf{r})\mathbf{r}/r, \quad \hat{\mathbf{w}}_{m2}^S(\mathbf{r}) = w_2^S(\mathbf{r})[\mathbf{r}\mathbf{r}/r^2 - \hat{\mathbf{1}}/3], \quad (4)$$

where $r = |\mathbf{r}|$, $\theta(r)$ is the step function, and $\hat{\mathbf{1}}$ is the identity matrix. Further, linearly dependent, weights are $w_1^S(\mathbf{r}) = w_2^S(\mathbf{r})/(4\pi R)$, $\mathbf{w}_{v1}^S(\mathbf{r}) = \mathbf{w}_{v2}^S(\mathbf{r})/(4\pi R)$, $w_0^S(\mathbf{r}) = w_1^S(\mathbf{r})/R$. The weight functions for spheres have different tensorial rank: w_0^S , w_1^S , w_2^S , and w_3^S are scalars; \mathbf{w}_{v1}^S and \mathbf{w}_{v2}^S are vectors; and $\hat{\mathbf{w}}_{m2}^S$ is a (traceless) matrix. These functions give the Mayer bond between pairs of spheres [10] through $-f_{SS}/2 = w_3^S w_0^S + w_2^S Z w_1^S - \mathbf{w}_{v2}^S \mathbf{w}_{v1}^S$. However, they are not sufficient to recover the sphere-needle Mayer bond [11]. This is achieved through

$$w_2^{SN}(\mathbf{r}, \mathbf{\Omega}) = 2|\mathbf{w}_{v2}^S(\mathbf{r}) \cdot \mathbf{\Omega}|, \quad (5)$$

which contains information about *both* species: it is nonvanishing on the surface of a sphere with radius R , but this surface is ‘‘decorated’’ with an $\mathbf{\Omega}$ -dependence. Loosely

speaking, w_2^{SN} describes how a sphere looks from the viewpoint of a rod. Technically, it generates the Mayer bond through $-f_{SN}(\mathbf{r}, \mathbf{\Omega}) = w_3^S(\mathbf{r}') w_0^N(\mathbf{r}'', \mathbf{\Omega}) + w_2^{SN}(\mathbf{r}', \mathbf{\Omega}) w_1^N(\mathbf{r}'', \mathbf{\Omega})$, where \mathbf{r} is the difference vector between sphere and needle position. The weight functions are used to smooth the possibly highly inhomogeneous density profiles by convolutions,

$$n_v^N(\mathbf{r}, \mathbf{\Omega}) = \rho_N(\mathbf{r}', \mathbf{\Omega}) w_v^N(\mathbf{r}'', \mathbf{\Omega}), \quad (6)$$

$$n_v^S(\mathbf{r}) = \rho_S(\mathbf{r}') w_v^S(\mathbf{r}''), \quad (7)$$

$$n_2^{SN}(\mathbf{r}, \mathbf{\Omega}) = \rho_S(\mathbf{r}') w_2^{SN}(\mathbf{r}'', \mathbf{\Omega}), \quad (8)$$

where $\rho_S(\mathbf{r}')$, and $\rho_N(\mathbf{r}', \mathbf{\Omega})$ are the one-body density distributions of spheres and needles, respectively. Note that n_v^N and n_v^S are ‘‘pure’’ weighted densities, involving only variables of either species [10,11]. In contrast, our n_2^{SN} is a convolution of the sphere density with an orientation-dependent weight function; hence, it combines characteristics of both species.

Finally, the (Helmholtz) excess free energy is obtained by integrating over a free energy density,

$$F_{\text{exc}}[\rho_S, \rho_N] = k_B T \int d^3x \int \frac{d^2\mathbf{\Omega}}{4\pi} \Phi(\{n_{\gamma}^i\}), \quad (9)$$

where k_B is Boltzmann’s constant, T is temperature, and the (local) reduced free energy density Φ is a simple function (not a functional) of the weighted densities n_{γ}^i . The variable \mathbf{x} runs over space, as usual [10,11]. Here we allow Φ to depend on orientation, and hence integrate $\mathbf{\Omega}$ over the unit sphere. The functional form of Φ is obtained by consideration of the exact zero-dimensional (0D) excess free energy. For the present model this is identical to the AO case [17], namely, the statistics of η hard and η' ideal particles, and is given by $F_{0D}/k_B T = (1 - \eta - \eta') \ln(1 - \eta) + \eta$ [17]. Considering multicavity distributions [12], we obtain $\Phi = \Phi_S + \Phi_{SN}$ with

$$\begin{aligned} \Phi_S = & -n_0^S \ln(1 - n_3^S) + (n_1^S n_2^S - \mathbf{n}_{v1}^S \cdot \mathbf{n}_{v2}^S)/(1 - n_3^S) \\ & + [(n_2^S)^3/3 - n_2^S (\mathbf{n}_{v2}^S)^2 + 3(\mathbf{n}_{v2}^S \hat{\mathbf{n}}_{m2}^S \mathbf{n}_{v2}^S \\ & - 3 \det \hat{\mathbf{n}}_{m2}^S)/2]/[8\pi(1 - n_3^S)^2], \end{aligned} \quad (10)$$

which is equal to the pure HS case [10,12]. The contribution due to the presence of the needles is

$$\Phi_{SN} = -n_0^N \ln(1 - n_3^S) + \frac{n_1^N n_2^{SN}}{1 - n_3^S}, \quad (11)$$

where the arguments are suppressed in the notation; see Eqs. (6)–(8). This completes the prescription for the functional.

We investigate some of the properties of the homogeneous, isotropic bulk mixture. In this case the weighted densities become proportional to the respective bulk densities, $n_v^i = \xi_v^i \rho_i$, where the proportionality constants are fundamental measures given by $\xi_v^i = \int d^3x w_v^i$. For spheres ξ_3^S

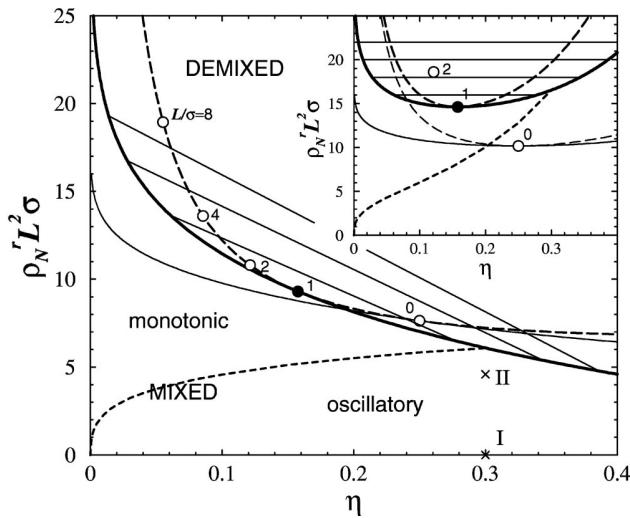


FIG. 2. Phase diagram of the rod-sphere mixture as a function of sphere density η and scaled needle density $\rho_N L^2 \sigma$. Shown is the universal spinodal (dashed line). For $L/\sigma=1$ the binodal (thick line), tie lines (thin straight lines), Fisher-Widom line (dotted line), and statepoints I and II (crosses) are indicated. Circles represent the critical points for $L/\sigma=0,1,2,4$, and 8. The thin line is the metastable binodal for $L/\sigma=0$. Inset shows corresponding plots as a function of needle reservoir density $\rho_N^r L^2 \sigma$. Note that there are now separate spinodals (dashed lines).

$=4\pi R^3/3, \xi_2^S = 4\pi R^2, \xi_1^S = R, \xi_0^S = 1$, whereas for needles $\xi_1^N = L/4, \xi_0^N = 1$, and, there is also a combined fundamental measure $\xi_2^{SN} = 4\pi R^2 (= \xi_2^S)$. Then the excess Helmholtz free energy per volume V is given by $F_{\text{exc}}(\rho_S, \rho_N)/V = f_{\text{HS}}(\rho_S) - \rho_N k_B T \ln \alpha(\rho_S)$, where $f_{\text{HS}}(\rho_S)$ is the excess free energy density of pure hard spheres in the scaled-particle [Percus-Yevick (PY) compressibility] approximation and $\alpha = (1 - \eta) \exp[-(3/2)(L/\sigma)\eta/(1 - \eta)]$, which is identical to that of Ref. [7], leading to (sphere) gas-liquid phase separation [7,18]. As an explanatory case, we choose $L/\sigma=1$, and display the gas-liquid portion of the phase diagram as a function of η and $\rho_N L^2 \sigma$ in Fig. 2. We find that in this representation the spinodals for all size ratios $s=L/\sigma$ collapse onto each other and are given analytically by $\rho_N^{\text{spin}} L^2 \sigma = 8(1 + 2\eta)^2/(3\pi\eta)$. The critical point moves along this curve as a function of s (see Fig. 2 for $s=0,1,2,4$, and 8) and is given by [7] $\eta_{\text{crit}} = (10 + 3s - 3\sqrt{4 + 12s + s^2})/(16 - 12s)$. The Fisher-Widom line [19] divides the phase diagram into regions of different asymptotic decay of the free bulk pair correlations. Here the decay is damped oscillatory for small needle densities, where the packing of spheres dominates. It becomes monotonic upon increasing needle density; the ideality between needles washes out the oscillations. In the inset of Fig. 2 the dependence on the actual needle density in the system is replaced by that in a needle reservoir, in chemical equilibrium with the system, which is given here by $\rho_N^r = \alpha \rho_N$. The reservoir density plays a role similar to that of inverse temperature in simple systems, and the topology of the phase diagram resembles that of a simple substance. Demixing is preempted by freezing for $s \leq 0.3$, as shown by BF. However, if we trace the critical point inside the metastable

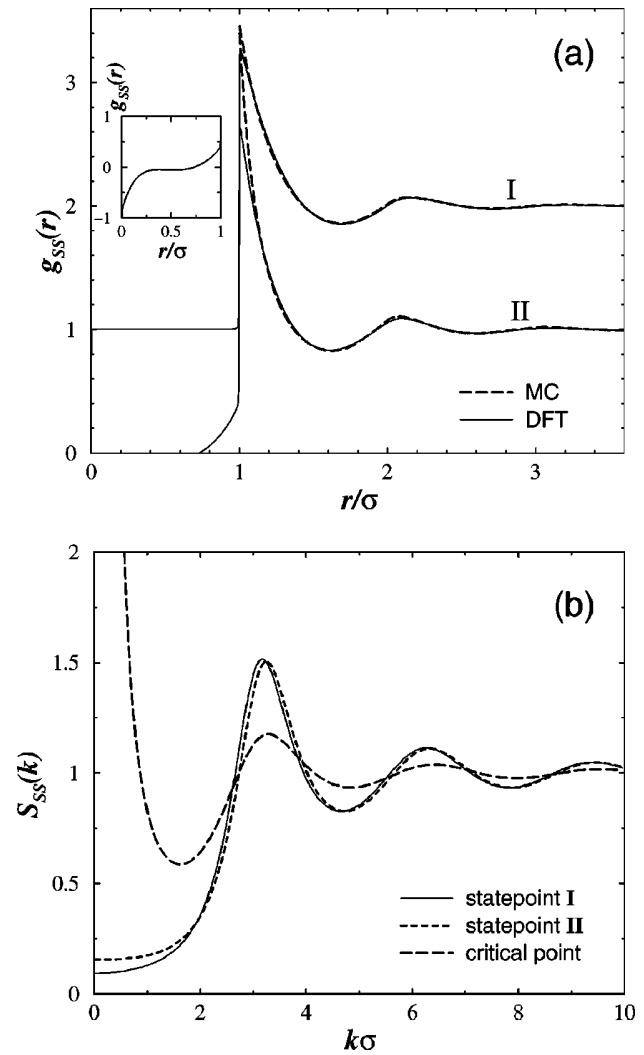


FIG. 3. Pair structure for spheres as obtained from DFT at $L/\sigma=1$, $\eta=0.3$, $\rho_N=0$ (statepoint I) and $\rho_N=4.58366/L^2\sigma$ (statepoint II). (a) Partial sphere-sphere pair correlation function compared to MC simulation. Results for statepoint I are shifted upwards by one unit for clarity. The inset shows the DFT result inside the core for statepoint II. (b) Corresponding partial structure factor at statepoints I and II, as well as at the gas-liquid critical point.

region, we find that it smoothly approaches $\eta=1/4$, $\rho_N L^2 \sigma = 24/\pi$, $\rho_N^r L^2 \sigma = 32/\pi$ for $s \rightarrow 0$. This is in contrast to free volume theory for the AO model, where demixing is preempted by freezing at a similar size ratio [16], but with the (metastable) critical point shifting to high density, thereby crossing hard sphere fluid-solid coexistence. Whether this difference has implications for the existence of an isostructural solid-solid transition in the present model constitutes an interesting aspect.

Next we investigate the bulk pair structure. The pair direct correlation functions are obtained as $c_{ij} = -(k_B T)^{-1} \delta^2 F_{\text{exc}} / \delta \rho_i \delta \rho_j$. Due to their geometric representation as convolutions of single particle functions, the c_{ij} vanish beyond the range of interaction, similar to what is found in PY. The Ornstein-Zernike (OZ) relations then yield partial structure factors and pair correlation functions. In or-

MATTHIAS SCHMIDT

PHYSICAL REVIEW E **63** 050201(R)

der to test the accuracy of the theoretical results, we have carried out canonical Monte Carlo (MC) computer simulations with 256 spheres and up to 2048 needles; for the pair correlations, 10^5 moves per particle were performed. Here we focus on the correlations $g_{SS}(r)$ between spheres. Figure 3(a) shows results for $L/\sigma=1$, $\eta=0.3$, and two different needle densities, $\rho_N=0$ (statepoint I, depicted in the phase diagram Fig. 2), and $\rho_N=8\rho_S=4.58366/L^2\sigma$ (statepoint II). In the absence of needles (statepoint I) the DFT result reproduces the rather accurate PY solution for hard spheres. Increasing the needle density (statepoint II, where the snapshot, Fig. 1, is taken) leads to an increase of the contact value; the period of oscillations becomes shorter, hence the spheres tend to be at smaller separation. The DFT provides a good description of the MC results, except for an underestimation of the contact value and nonzero values inside the core. This could be remedied by using the test-particle limit, i.e. minimizing the grand potential in the presence of a sphere fixed at the origin. The corresponding structure factors $S_{SS}(k)$ are shown in Fig. 3(b). Adding needles (statepoint II) leads to a small shift towards larger k -values, as well as to an increase in $S_{SS}(0)$. In addition, we plot $S_{SS}(k \rightarrow 0)$ diverges consistently.

Let us conclude with two remarks. First, in view of the successful treatment of the bulk, the present theory offers direct access to a wide range of interesting interfacial and confined situations, such as wetting, layering transitions, and capillary condensation, as well as the study of the free interface between demixed fluid phases. Especially appealing is the perspective to investigate the degree of universality of the entropic wetting scenario in the AO model [20], found recently by a similar DFT treatment [17]. For the current model, interesting orientational behavior of the rods may be anticipated: For example, at the free (gas-liquid) interface between demixed phases, the rod orientations will in general show a tendency to order, although the distributions are isotropic in both bulk phases. Second, the crucial extensions of geometry-based DFT done in this work are the integration over director space [Eq. (9)], and the introduction of double-indexed weight functions [Eq. (5)]. Whether these technical tools permit the treatment of other rotating hard bodies constitutes an important point for future investigations.

I thank Bob Evans and Holger Harreis for valuable remarks, and Gerrit Vliegthart and Arjun Yodh for stimulating discussions.

-
- [1] See e.g., M. Dijkstra, R. van Roij, and R. Evans, *Phys. Rev. Lett.* **81**, 2268 (1998); **82**, 117 (1999).
- [2] S. Asakura and F. Oosawa, *J. Chem. Phys.* **22**, 1255 (1954); see also A. Vrij, *Pure Appl. Chem.* **48**, 471 (1976).
- [3] G. A. Vliegthart and H. N. W. Lekkerkerker, *J. Chem. Phys.* **111**, 4153 (1999).
- [4] G. H. Koenderink *et al.*, *Langmuir* **15**, 4693 (1999).
- [5] Y. Mao, M. E. Cates, and H. N. W. Lekkerkerker, *Phys. Rev. Lett.* **75**, 4548 (1995); *J. Chem. Phys.* **106**, 3721 (1997).
- [6] K. Yaman, C. Jeppesen, and C. M. Marques, *Europhys. Lett.* **42**, 221 (1998).
- [7] P. Bolhuis and D. Frenkel, *J. Chem. Phys.* **101**, 9869 (1994).
- [8] H. N. W. Lekkerkerker *et al.*, *Europhys. Lett.* **20**, 559 (1992).
- [9] R. Evans, in *Fundamentals of Inhomogeneous Fluids*, edited by D. Henderson (Dekker, New York, 1992), p. 85.
- [10] Y. Rosenfeld, *Phys. Rev. Lett.* **63**, 980 (1989).
- [11] Y. Rosenfeld, *Phys. Rev. E* **50**, R3318 (1994).
- [12] P. Tarazona, *Phys. Rev. Lett.* **84**, 694 (2000).
- [13] J. A. Cuesta, *Phys. Rev. Lett.* **76**, 3742 (1996).
- [14] A. Chamoux and A. Perera, *J. Chem. Phys.* **104**, 1493 (1996).
- [15] Using $\mathbf{r}=(r_{\parallel}, r_{\perp 1}, r_{\perp 2})$, where r_{\parallel} is parallel, and $r_{\perp 1}, r_{\perp 2}$ are perpendicular to $\mathbf{\Omega}$, respectively, one obtains $w_1^N(\mathbf{r}, \mathbf{\Omega}) = \delta(r_{\perp 1})\delta(r_{\perp 2})$ if $|r_{\parallel}| < L/2$, and zero else.
- [16] J. M. Brader, M. Dijkstra, and R. Evans, *J. Phys.: Condens. Matter* **11**, 10 079 (1999).
- [17] M. Schmidt, H. Löwen, J. M. Brader, and R. Evans, *Phys. Rev. Lett.* **85**, 1934 (2000).
- [18] In Ref. [7] the Carnahan-Starling equation of state for hard spheres was used.
- [19] R. Evans *et al.*, *J. Chem. Phys.* **100**, 591 (1994).
- [20] J. M. Brader, R. Evans, M. Schmidt, and H. Löwen (unpublished).

Colloidal rod-sphere mixtures: Fluid-fluid interfaces and the Onsager limit

Joseph M. Brader

The James Franck Institute, University of Chicago, 5640 South Ellis Avenue, Chicago, Illinois 60637

Ansgar Esztermann and Matthias Schmidt

Institut für Theoretische Physik II, Heinrich-Heine-Universität Düsseldorf, Universitätsstraße 1, D-40225 Düsseldorf, Germany

(Received 3 May 2002; published 3 September 2002)

Using a geometry-based density functional theory we investigate the free interface between demixed bulk fluid phases of a colloidal mixture of hard spheres and vanishingly thin needles. Results are presented for the spatial and orientational density distributions of the particles, as well as for the interface tension. Density profiles display oscillations on the sphere-rich side of the interface provided the sphere liquid phase is on the oscillatory side of the Fisher-Widom line in the bulk phase diagram. Needles tend to align parallel (perpendicular) to the interface on the needle-rich (sphere-rich) side displaying biaxial (uniaxial) order. Furthermore, we generalize the theory to the Onsager limit for interacting rods, and give explicit expressions for the functional in simple geometries.

DOI: 10.1103/PhysRevE.66.031401

PACS number(s): 82.70.Dd, 61.20.Gy, 64.70.Ja, 61.30.Cz

I. INTRODUCTION

Mixtures of spherical and rodlike particles provide soft matter systems that display astonishingly rich phase behavior [1]. When a second component is added as a depletant agent to a suspension of colloidal spheres, the spheres may exhibit colloidal vapor, liquid, and crystalline phases. Rodlike depletants alone, however, already have rich liquid-crystalline phase behavior. The possible combinations of both types of ordering are vast. Experimental examples of rod-sphere mixtures are dispersions of silica spheres and silica coated bohemite rods [2,3], silica beads immersed in suspensions of rodlike *fd* bacteriophage virus [4], and, in the biological domain, microtubules inside vesicles modeling the eukaryotic cell [5,6]. Experimental work has also been devoted to self-diffusion and sedimentation of spheres in dispersions of rods [7]. Depletion-induced crystallization was found in mixtures of colloidal silica spheres and colloidal silica rods with light microscopy and confocal scanning laser microscopy [3]. Fluid-fluid phase separation was observed experimentally in a mixture of silica spheres and semiflexible polymeric rods [poly(γ -benzyl- α ,L-glutamate) (PBLG) with molecular weight 105 000] [8]. The free interface between demixed fluid phases is one topic that we address in the present work.

As a simple theoretical model of a rod-sphere mixture Bolhuis and Frenkel proposed a binary system of hard spheres and vanishingly thin hard needles [9]. Due to the vanishing needle thickness, and hence the absence of interactions between needles, this system does not display liquid crystalline order, but exhibits (sphere) vapor, liquid, and solid states, as was found in Ref. [9] with simulation and a perturbation theory. The theory is similar to the free volume treatment of the Asakura-Oosawa (AO) model [10,11] of colloidal spheres and noninteracting polymer spheres by Lekkerkerker *et al.* [12]. The depletion potential exerted on a pair of spheres due to the presence of the rods was studied theoretically [13], and experimentally using optical tweezers [4]. Considerable work was done to understand the nature of

the depletion force due to rod-like polymers in the Onsager limit [14], and the interactions between flat plates and between two large spheres via the Derjaguin approximation [15]. Theoretical phase behavior of mixtures of spheres and rods with finite diameter were studied in Ref. [2] and compared to experiment [3], and in a mixture of parallel hard spherocylinders and hard spheres layered phases were investigated [16].

Density-functional theory (DFT) [17,18] is a powerful tool to study equilibrium properties of inhomogeneous many-particle systems. For realistic systems, one usually has to rely on approximations for the central quantity of DFT, the excess free energy functional. One particularly successful example of such an approximation is Rosenfeld's density functional for hard sphere (HS) fluids [19], that also describes the HS solid [20–23]. An early extension of this theory to treat hard convex bodies was proposed [24], and used to derive bulk direct correlation functions for molecular fluids [25], two-dimensional anisotropic fluids [26], and hard sphere chain fluids [27]. The theory of Ref. [24] suffered from an incomplete deconvolution of the Mayer bond leading to an incorrect virial expansion, and an extension to remedy this deficiency was made for the model of hard spheres and hard, vanishingly thin needles [28]. Subsequently, this was also generalized to a hard body amphiphilic mixture [29] and to mixtures of colloidal spheres, rods and polymer spheres [30]. Recently, the entropic torque exerted on a single spherocylinder immersed in a hard sphere fluid at a hard wall was calculated with a similar approach [31].

In contrast to the case of simple fluids, interfaces in such complex systems are genuinely characterized by positional *and* orientational order. Interfaces between phases with different liquid crystalline ordering, like isotropic-nematic interfaces, have attracted considerable interest, see Ref. [32] for a recent study of the hard-rod fluid. In this work, we investigate the free interface between demixed (isotropic) fluid phases in a rod-sphere mixture, an issue that has not been addressed so far. We use the simplest nontrivial model in the context, namely, Bolhuis and Frenkel's mixture of hard

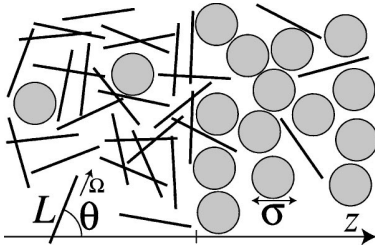


FIG. 1. Model of hard spheres with diameter $\sigma=2R$ and needles with length L . In planar geometry, the z direction is perpendicular to the interface between needle-rich ($z<0$) and sphere-rich ($z>0$) phases. The needle orientation is denoted by Ω , and the angle between Ω and the z axis is θ .

spheres and vanishingly thin needles, and investigate it by means of the geometry-based DFT proposed earlier [28]. As this theory reproduces the bulk fluid free energy and hence the accurate fluid demixing binodal of perturbation theory [9], and was also shown to yield bulk (sphere) pair correlation functions in good agreement with computer simulation results [28], we are confident to apply it to inhomogeneous situations. We find that, driven by packing effects of the spheres, orientational order of the needles occurs at the free fluid-fluid interface, and that the density profiles are oscillatory provided the sphere-rich fluid is on the oscillatory side of the Fisher-Widom line in the bulk phase diagram [33–36]. The interface tension is found to be of the order of the thermal energy per molecular area, and we investigate its scaling with needle length and sphere diameter in detail. Furthermore, we extend the DFT to the case of nonvanishing rod-rod interactions in the Onsager limit and give explicit expressions for the functional in simple geometries.

Similar interface studies using density-functional approaches were recently carried out [37,38] for the AO model [10,11] of colloid-polymer mixtures. Our present model, however, allows us to go beyond those studies through the investigation of orientational order at the interface. Clearly, such ordering is absent in the AO model of spherical bodies.

The paper is organized as follows. In Sec. II we define in more detail the hard sphere-needle mixture for vanishingly thin needles as well as for needles in the Onsager limit. Then we present our DFT approach in Sec. III, generalize it to the Onsager limit and give explicit expressions for the relevant quantities in simple geometries. In Sec. IV, after revisiting the bulk fluid phase behavior, we present results for density and order parameter profiles across the free interface between demixed phases, as well as for the interface tension. We finish with concluding remarks in Sec. V.

II. MODEL

We consider a mixture of hard spheres (species S) with radii R and straight hard needles (species N) with length L and diameter D , see Fig. 1 for a sketch. The spheres interact with a hard core potential $V_{SS}(r)$ as a function of their center separation distance r , which is given by $V_{SS}(r)=\infty$ if $r<2R$ and zero otherwise. Spheres and needles interact with a hard body interaction that depends, due to the particle

shapes, on the difference vector \mathbf{r} between sphere and needle center, as well as on the needle orientation given by a unit vector Ω pointing along the needle shape. (Hence the needles possess an inflection symmetry, $\Omega\rightarrow-\Omega$.) The sphere-needle interaction is given by $V_{SN}(\mathbf{r},\Omega)=\infty$ if both shapes overlap, and zero otherwise. In the following, we consider two cases of interactions between needles.

In the first, simpler, case we set $D=0$. Then the needles are noninteracting and $V_{NN}=0$, for all possible distances and orientations. Although these “line” particles would nontrivially collide in a dynamical description, their excluded volume vanishes due to the vanishing particle volume. Hence, configurations of overlapping needles carry vanishing statistical weight. As we are interested in static quantities only, the needles can be regarded as an ideal gas of rotators, solely due to their geometrical properties. As an aside, no such scaling holds in the somewhat similar AO model of hard sphere colloids and ideal (polymer) *spheres*. There the interactions between the particles of the second component are regarded as being ideal from the outset.

In our second case, the needles are treated in the Onsager limit [39], where for thin rods a residual excluded volume persists, leading to nontrivial interaction already in the pure needle system. Again, the pair potential is that of hard bodies and is given, for the difference vector \mathbf{r} between the centers of two needles with orientations Ω and Ω' , as $V_{NN}(\mathbf{r},\Omega,\Omega')=\infty$ if both rods overlap, and zero otherwise. Note that the Onsager limit is obtained by letting $L/D\rightarrow\infty$ while keeping the combination $\rho_N DL^2$ constant, where ρ_N is the number density of needles. Here we furthermore restrict ourselves to size ratios that fulfill $LD\ll R^2$, hence the sphere surface is assumed to be large compared to the needle surface. This additional restriction is similar in spirit to the Onsager limit for pure needles and constitutes the simplest scaling regime of the three lengths R,L,D . Note that due to the large aspect ratio, there is no need to specify the precise shape of the needle ends, whether, e.g., hemispherical or cylindrical.

We denote the number densities of spheres and needles by $\rho_S(\mathbf{r})$ and $\rho_N(\mathbf{r},\Omega)$, respectively. As bulk thermodynamic parameters, we use the packing fraction of spheres $\eta=4\pi R^3\rho_S/3$ and the scaled needle density $\rho_*=\rho_N L^2\sigma$, where $\sigma=2R$ denotes the sphere diameter. Furthermore, we denote the density in a reservoir of pure needles that is in chemical equilibrium with the system as ρ_N^r and use a scaled version $\rho_*^r=\rho_N^r L^2\sigma$. The ratio of needle length and sphere diameter, L/σ , and, in our second model, the ratio of needle diameter and length, D/L , are control parameters. As only hard core interactions are present, temperature T is an irrelevant variable that only sets the energy scale through $k_B T$, where k_B is Boltzmann’s constant.

III. DENSITY FUNCTIONAL THEORY

A. Spheres and vanishingly thin needles

In this section, we review briefly the DFT proposed in Ref. [28]. The starting point is a geometrical representation of the particles in terms of weight functions w_μ^i , where i

labels the species, and $\mu=3,2,1,0$ corresponds to the particles' volume, surface, integral mean curvature, and Euler characteristic, respectively [24]. The weight functions are determined to give the Mayer bonds $f_{ij} = \exp(-\beta V_{ij}) - 1$, where $\beta = 1/k_B T$, by a linear combination of terms $w_{\gamma}^i(\mathbf{r}) * w_{3-\gamma}^j(\mathbf{r})$, where the asterisk denotes the spatial convolution, $g(\mathbf{r}) * h(\mathbf{r}) = \int d^3x g(\mathbf{x}) h(\mathbf{r} - \mathbf{x})$. For needles, following Ref. [24] yields

$$w_1^N(\mathbf{r}, \mathbf{\Omega}) = \frac{1}{4} \int_{-L/2}^{L/2} dl \delta(\mathbf{r} + \mathbf{\Omega} l), \quad (1)$$

$$w_0^N(\mathbf{r}, \mathbf{\Omega}) = \frac{1}{2} [\delta(\mathbf{r} + \mathbf{\Omega} L/2) + \delta(\mathbf{r} - \mathbf{\Omega} L/2)], \quad (2)$$

where $\delta(x)$ is the Dirac distribution. The function w_1^N describes the linear shape of a needle, whereas w_0^N is only nonvanishing at the needle endpoints.

For spheres the weight functions [19,23] are

$$w_3^S(\mathbf{r}) = \Theta(R - r), \quad w_2^S(\mathbf{r}) = \delta(R - r), \quad (3)$$

$$\mathbf{w}_{v2}^S(\mathbf{r}) = w_2^S(\mathbf{r}) \mathbf{r}/r, \quad \hat{\mathbf{w}}_{m2}^S(\mathbf{r}) = w_2^S(\mathbf{r}) [\mathbf{r}\mathbf{r}/r^2 - \hat{\mathbf{1}}/3], \quad (4)$$

where $r = |\mathbf{r}|$, $\Theta(x)$ is the step function, $\hat{\mathbf{1}}$ is the 3×3 identity matrix, and $\mathbf{r}\mathbf{r}$ is a dyadic product. Further, linearly dependent, weights are $w_1^S(\mathbf{r}) = w_2^S(\mathbf{r})/(4\pi R)$, $\mathbf{w}_{v1}^S(\mathbf{r}) = \mathbf{w}_{v2}^S(\mathbf{r})/(4\pi R)$, $w_0^S(\mathbf{r}) = w_1^S(\mathbf{r})/R$. The weight functions for spheres have different tensorial rank: w_0^S , w_1^S , w_2^S , w_3^S are scalars; \mathbf{w}_{v1}^S , \mathbf{w}_{v2}^S are vectors; $\hat{\mathbf{w}}_{m2}^S$ is a (traceless) second-rank tensor. The Mayer bond between pairs of spheres is obtained through $-f_{SS}/2 = w_3^S * w_0^S + w_2^S * w_1^S - \mathbf{w}_{v2}^S * \mathbf{w}_{v1}^S$ [19]. In order to recover the sphere-needle Mayer bond one uses [28]

$$w_2^{SN}(\mathbf{r}, \mathbf{\Omega}) = 2 |\mathbf{w}_{v2}^S(\mathbf{r}) \cdot \mathbf{\Omega}|, \quad (5)$$

which contains information about both species: it is nonvanishing on the surface of a sphere with radius R , but also possesses (needle) orientation dependence. This function allows us to generate the Mayer bond through $-f_{SN}(\mathbf{r}, \mathbf{\Omega}) = w_3^S(\mathbf{r}) * w_0^N(\mathbf{r}, \mathbf{\Omega}) + w_2^{SN}(\mathbf{r}, \mathbf{\Omega}) * w_1^N(\mathbf{r}, \mathbf{\Omega})$, see Appendix A 1 for an explicit calculation. All weight functions are used to obtain weighted densities n_{ν}^i by smoothing the actual density profiles through spatial convolutions,

$$n_{\nu}^N(\mathbf{r}, \mathbf{\Omega}) = \rho_N(\mathbf{r}, \mathbf{\Omega}) * w_{\nu}^N(\mathbf{r}, \mathbf{\Omega}), \quad \nu = 1, 0, \quad (6)$$

$$n_{\nu}^S(\mathbf{r}) = \rho_S(\mathbf{r}) * w_{\nu}^S(\mathbf{r}), \quad \nu = 3, 2, 1, 0, v2, v1, m2, \quad (7)$$

$$n_2^{SN}(\mathbf{r}, \mathbf{\Omega}) = \rho_S(\mathbf{r}) * w_2^{SN}(\mathbf{r}, \mathbf{\Omega}). \quad (8)$$

Note that n_{ν}^N and n_{ν}^S are ‘‘pure’’ weighted densities, involving only variables of either species [19,23,24]. The function n_2^{SN} is obtained as a convolution of the sphere density with an orientation-dependent weight function; hence it combines characteristics of both species and couples the orientational degrees of freedom of the needles to the sphere distribution.

The (Helmholtz) excess free energy is obtained by integrating over a free energy density,

$$F_{\text{exc}}[\rho_S, \rho_N] = k_B T \int d^3r \int \frac{d^2\Omega}{4\pi} \Phi(\{n_{\nu}^i\}), \quad (9)$$

where the reduced free energy density Φ is a simple function (not a functional) of the weighted densities n_{ν}^i . The variable \mathbf{r} runs over space, and as Φ depends also on orientation, $\mathbf{\Omega}$ runs over the unit sphere. The functional form of Φ is obtained by consideration of the exact zero-dimensional excess free energy [28], and is given by

$$\Phi = \Phi_S + \Phi_{SN}, \quad (10)$$

$$\begin{aligned} \Phi_S = & -n_0^S \ln(1 - n_3^S) + (n_1^S n_2^S - \mathbf{n}_{v1}^S \cdot \mathbf{n}_{v2}^S)/(1 - n_3^S) \\ & + [(n_2^S)^3/3 - n_2^S (\mathbf{n}_{v2}^S)^2 + 3(\mathbf{n}_{v2}^S \hat{\mathbf{n}}_{m2}^S \mathbf{n}_{v2}^S \\ & - 3 \det \hat{\mathbf{n}}_{m2}^S)/2]/[8\pi(1 - n_3^S)^2], \end{aligned} \quad (11)$$

$$\Phi_{SN} = -n_0^N \ln(1 - n_3^S) + \frac{n_1^N n_2^{SN}}{1 - n_3^S}. \quad (12)$$

The contribution Φ_S is equal to the pure HS case [19,23], and Φ_{SN} arises from needle-sphere interactions [28]. The arguments of the weighted densities are suppressed in the notation in Eqs. (11, 12); see Eqs. (6–8) for the explicit dependence. This completes the prescription for the excess free energy functional for the case of vanishingly thin needles. For completeness, the ideal free energy is

$$\begin{aligned} F_{\text{id}}[\rho_S, \rho_N] = & \int d^3r \rho_S(\mathbf{r}) \{ \ln[\rho_S(\mathbf{r}) \Lambda_S^3] - 1 \} \\ & + \int d^3r \int \frac{d^2\Omega}{4\pi} \rho_N(\mathbf{r}, \mathbf{\Omega}) \\ & \times \{ \ln[\rho_N(\mathbf{r}, \mathbf{\Omega}) \Lambda_N^3] - 1 \}, \end{aligned} \quad (13)$$

where Λ_i is the (irrelevant) thermal wavelength of species $i = S, N$.

B. Spheres and rods in the Onsager limit

In order to deal with rod-rod interactions, we first express the Mayer bond between rods in the Onsager limit through $f_{NN}(\mathbf{r}, \mathbf{\Omega}, \mathbf{\Omega}')/2 = -w_2^{NN}(\mathbf{r}, \mathbf{\Omega}; \mathbf{\Omega}') * w_1^N(\mathbf{r}, \mathbf{\Omega}')$, where w_1^N is defined in Eq. (1), and we introduce

$$w_2^{NN}(\mathbf{r}, \mathbf{\Omega}; \mathbf{\Omega}') = 16D \sqrt{1 - (\mathbf{\Omega} \cdot \mathbf{\Omega}')^2} w_1^N(\mathbf{r}, \mathbf{\Omega}). \quad (14)$$

As a geometrical interpretation, the function w_2^{NN} describes the residual rod surface in the limit of large aspect ratio, see Appendix A 2 for details how the Mayer bond is obtained. We construct an associated weighted density

$$n_2^{NN}(\mathbf{r}, \mathbf{\Omega}') = \int \frac{d^2\Omega}{4\pi} \rho_N(\mathbf{r}, \mathbf{\Omega}) * w_2^{NN}(\mathbf{r}, \mathbf{\Omega}; \mathbf{\Omega}'), \quad (15)$$

BRADER, ESZTERMANN, AND SCHMIDT

PHYSICAL REVIEW E **66**, 031401 (2002)

where, besides the spatial convolution, an angular convolution is required. This turns out to be necessary for the present case of interacting anisotropic particles. As an aside, we can immediately reformulate the Onsager excess free energy functional for a pure system of rods, being precisely a second order virial expansion, by setting $\Phi = \Phi_{NN}$ in Eq. (9), with

$$\Phi_{NN} = n_1^N n_2^{NN}, \quad (16)$$

where the weighted density n_1^N is given through Eqs. (6) and (1).

For the case of the actual sphere-rod mixture, we insert $\Phi = \Phi_S + \Phi_{SN} + \Phi_{SNN}$ into Eq. (9), where the first two terms are equal to the case of vanishingly thin needles and are given by Eqs. (11) and (12), respectively. The additional contribution due to interactions between rods is found to be

$$\Phi_{SNN} = \frac{n_1^N n_2^{NN}}{1 - n_3^S}, \quad (17)$$

where (as before) the arguments of the weighted densities are suppressed in the notation. This completes the extension of the needle-sphere DFT to interacting rods.

C. Planar geometry

In order to facilitate the application of the theory to situations like the free interface considered below in Secs. IV B, IV C and to planar wall problems, we give explicit expressions for the weight functions in situations depending on a single spatial coordinate z and possessing translational invariance in the x and y directions, where $\mathbf{r} = (x, y, z)$ is a Cartesian coordinate system. Additionally, we assume invariance with respect to rotations around the z axis by an angle φ . The remaining relevant angle θ is that between an orientation $\mathbf{\Omega}$ and the z axis, see Fig. 1. Hence $\rho_S(\mathbf{r}) = \rho_S(z)$, and $\rho_N(\mathbf{r}, \mathbf{\Omega}) = \rho_N(z, \theta)$. Considering $\theta \in [0, \pi/2]$ is sufficient, due to the inflection symmetry of the needles. In this *planar geometry* the weighted densities, Eqs. (6)–(8) and (15), can be expressed as

$$n_v^N(z, \theta) = \int dz' \rho_N(z', \theta) w_v^N(z - z', \theta), \quad (18)$$

$$n_v^S(z) = \int dz' \rho_S(z') w_v^S(z - z'), \quad (19)$$

$$n_2^{SN}(z, \theta) = \int dz' \rho_S(z') w_2^{SN}(z - z', \theta), \quad (20)$$

$$n_2^{NN}(z, \theta) = \int dz' \int_0^\pi d\theta' \rho_N(z', \theta') w_2^{NN}(z - z', \theta'; \theta), \quad (21)$$

where the effective weight functions $w_v^N(z, \theta)$, $w_v^S(z)$, $w_2^{SN}(z, \theta)$ are obtained by carrying out the integrations in Eqs. (6)–(8) and (15) over coordinates x, y , see Appendix B for the details. Explicitly, for the needles one obtains

$$w_1^N(z, \theta) = (4 \cos \theta)^{-1} \Theta \left(\frac{L}{2} \cos \theta - |z| \right), \quad (22)$$

$$w_0^N(z, \theta) = \frac{1}{2} \delta \left(\frac{L}{2} \cos \theta - |z| \right). \quad (23)$$

For the spheres

$$w_3^S(z) = \pi(R^2 - z^2) \Theta(R - |z|), \quad (24)$$

$$w_2^S(z) = 2\pi R \Theta(R - |z|), \quad (25)$$

$$\mathbf{w}_{v2}^S(z) = 2\pi z \Theta(R - |z|) \mathbf{e}_z, \quad (26)$$

$$\hat{\mathbf{w}}_{m2}^S(z) = \pi \left(\frac{z^2}{R} - \frac{R}{3} \right) \Theta(R - |z|) \text{diag}(-1, -1, 2), \quad (27)$$

where \mathbf{e}_z is the unit vector pointing along the z axis and $\text{diag}(\cdot)$ denotes a 3×3 diagonal matrix. The linearly dependent weight functions are $w_1^S(z) = \Theta(R - |z|)/2$, $w_0^S(z) = \Theta(R - |z|)/(2R)$, $\mathbf{w}_{v1}^S(z) = z \Theta(R - |z|) \mathbf{e}_z/(2R)$. The mixed weight function is obtained as

$$w_2^{SN}(z, \theta) = \begin{cases} 8\sqrt{R^2 \sin^2 \theta - z^2} + 8z \cos \theta \\ \times \arcsin \left(\frac{z \cot(\theta)}{\sqrt{R^2 - z^2}} \right) & \text{if } |z| < R \sin \theta, \\ 4\pi |z| \cos \theta & \text{if } R \sin \theta \leq |z| \leq R, \\ 0 & \text{otherwise.} \end{cases} \quad (28)$$

For the case of nonvanishing rod-rod interactions (Sec. III B), the additional weight function can be obtained up to a quadrature as

$$w_2^{NN}(z, \theta; \theta') = \frac{D \tan \theta}{\pi} \Theta \left(\frac{L \cos \theta}{2} - |z| \right) \int_0^{2\pi} d\varphi \\ \times \sqrt{1 - (\sin \theta' \sin \theta \cos \varphi + \cos \theta' \cos \theta)^2}. \quad (29)$$

This fully specifies the DFT in planar geometry. We note that the tensorial weight function, Eq. (27), is included for reasons of completeness. Albeit being crucial for a reliable description of the solid [23], it is known to yield a small contribution to the free energy in planar geometry, and may be neglected to a good approximation. Below in Sec. IV we will adopt this strategy.

D. Spherical geometry

Here we focus on situations that only depend on the distance to the origin, r , and that remain invariant under rotations around the origin. This is realized, e.g., in the important test-particle limit that allows us to obtain pair distribution functions by minimizing the functional in the presence of a test sphere fixed at the origin. In spherical geometry, only the

angle θ between needle orientation $\mathbf{\Omega}$ and position \mathbf{r} remains relevant, and $\rho_S(\mathbf{r}) = \rho_S(r)$, and $\rho_N(\mathbf{r}, \mathbf{\Omega}) = \rho_N(r, \theta)$. Again, we can restrict to $0 \leq \theta \leq \pi/2$. The pure weighted densities, Eqs. (6)–(8) can be expressed as

$$n_v^N(r, \theta) = \int_0^\infty dr' \rho_N(r', \theta) w_v^N(r, r', \theta), \quad (30)$$

$$n_v^S(r) = \int_0^\infty dr' \rho_S(r') w_v^S(r, r'), \quad (31)$$

where the reduced weight functions are

$$w_1^N(r, r', \theta) = \frac{r'}{4\sqrt{r'^2 - r^2 \sin^2 \theta}} \times \sum_{\pm} \Theta\left(\frac{L}{2} - |r \cos \theta \pm \sqrt{r'^2 - r^2 \sin^2 \theta}|\right), \quad (32)$$

$$w_0^N(r, r', \theta) = \frac{1}{2} \sum_{\pm} \delta\left(r' - \sqrt{\left(r \pm \frac{L}{2} \cos \theta\right)^2 + \frac{L^2}{4} \sin^2 \theta}\right), \quad (33)$$

$$w_3^S(r, r') = \frac{\pi r'}{r} [R^2 - (r - r')^2] \Theta(R - |r - r'|), \quad (34)$$

$$w_2^S(r, r') = \frac{2\pi R r'}{r} [\Theta(R - |r - r'|) - \Theta(R - r - r')], \quad (35)$$

$$\mathbf{w}_{v2}^S(r, r') = \frac{R^2 + r^2 - r'^2}{2Rr} w_2^S(r, r') \frac{\mathbf{r}}{r}, \quad (36)$$

$$\hat{\mathbf{w}}_{m2}^S(r, r') = \frac{1}{2} \left[\left(\frac{R^2 + r^2 - r'^2}{2Rr} \right)^2 - \frac{1}{3} \right] w_2^S(r, r') \left(3 \frac{\mathbf{r}\mathbf{r}}{r^2} - \hat{\mathbf{1}} \right). \quad (37)$$

In Eqs. (36), (37) only the dependence on the scalar argument r is important; the dependence on \mathbf{r}/r is trivial due to the structure of Φ , Eq. (11). The linearly dependent weight functions are $w_1^S(r, r') = r'/(2r) [\Theta(R - |r - r'|) - \Theta(R - r - r')]$, $\mathbf{w}_{v1}^S(r, r') = (r^2 - r'^2 + R^2)/(2Rr) w_1^S(r, r')$, $w_0^S(r, r') = r'/(2Rr) [\Theta(R - |r - r'|) - \Theta(R - r - r')]$. The mixed weight function is

$$w_2^{SN}(r, r', \theta) = \begin{cases} \frac{8r'}{r} \left[\sqrt{r'^2(1-u^2) - R^2 \cos^2 \theta} + (r - r'u) \cos(\theta) \right. \\ \quad \left. \times \arcsin\left(\frac{(r - r'u) \cot \theta}{r' \sqrt{1-u^2}}\right) \right] & \text{if } |r - r'u| < r' \sqrt{1-u^2} \tan \theta, \\ 4\pi(r'/r) |r - r'u| \cos \theta & \text{if } |r - r'u| \geq r' \sqrt{1-u^2} \tan \theta, \\ 0 & \text{if } |u| \geq 1, \end{cases} \quad (38)$$

where $u = (r'^2 + r^2 - R^2)/(2rr')$. For the remaining needle weight w_2^{NN} we could not obtain simple analytic expressions; a full numerical calculation is required to obtain n_2^{NN} .

We note that for a test-particle limit calculation, where a hard sphere is fixed at the origin, the above expression can be simplified, as the density distributions vanish inside the test particle. This allows us to omit the second step function in Eq. (35) and rewrite the convolution kernels for spheres as a function of the difference $r - r'$ only. The expressions given above are completely general, hence apply also to cases of nonvanishing densities in the immediate vicinity of the origin.

IV. RESULTS

A. Bulk phase diagram

As a prerequisite for our interface study, we reconsider the bulk fluid demixing phase diagram of hard spheres and

vanishingly thin needles. Within our approach, this is obtained from the bulk Helmholtz free energy, which in turn is obtained by applying the density functional (outlined in Sec. III A) to constant density fields of spheres and needles. Then, the weighted densities become proportional to the respective bulk densities, $n_v^i = \xi_v^i \rho_i$, where the proportionality constants are fundamental measures given by $\xi_v^i = \int d^3x w_v^i$. For spheres $\xi_3^S = 4\pi R^3/3$, $\xi_2^S = \xi_2^{SN} = 4\pi R^2$, $\xi_1^S = R$, $\xi_0^S = 1$, whereas for needles $\xi_1^N = L/4$, $\xi_0^N = 1$. Then the excess Helmholtz free energy per volume V is given by $F_{\text{exc}}(\rho_S, \rho_N)/V = \phi_{\text{HS}}(\rho_S) - \rho_N k_B T \ln \alpha(\rho_S)$, where $\phi_{\text{HS}}(\rho_S)$ is the excess free energy density of pure hard spheres in the scaled-particle (and Percus-Yevick compressibility) approximation and $\alpha = (1 - \eta) \exp[-(3/2)(L/\sigma)\eta/(1 - \eta)]$. This expression for the free energy is identical to the result from the perturbation theory of Bolhuis and Frenkel [9]. We note that this is also equivalent to a straightforward application of scaled-particle theory for nonspherical bodies [40] to the current model.

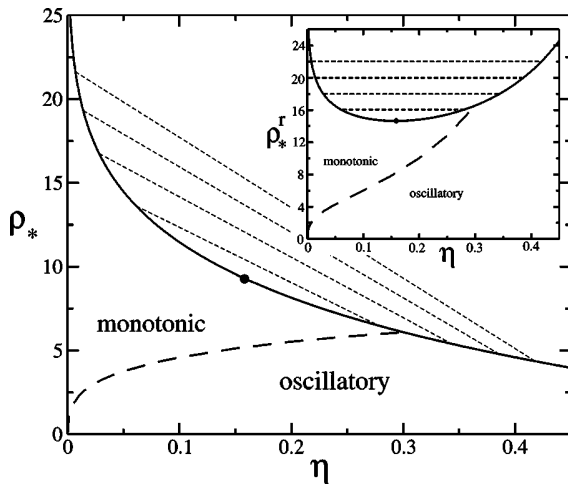


FIG. 2. Fluid-fluid demixing phase diagram of the mixture of hard spheres and vanishingly thin needles with size ratio $L/\sigma=1$ obtained from DFT. Shown are the binodal (solid line) and the Fisher-Widom line (dashed) dividing states where the ultimate decay of correlation functions is either monotonic or damped oscillatory. Tielines (short-dashed) between coexisting states are shown for $\rho_*^r = 16, 18, 20, 22$. The main plot uses system representation with η and ρ_* ; the inset is in reservoir representation with η and ρ_*^r .

From the free energy all thermodynamic quantities can be calculated, and equating the total pressure and the chemical potentials of both species in both phases yields the coexisting densities. The resulting binodal was found to be in remarkable agreement with simulation results [9].

Here we consider the case of equal sphere diameter and needle length, $\sigma=L$, where fluid-fluid phase separation is stable with respect to freezing [9] and display the phase diagram in system representation (as a function of η and ρ_*) in Fig. 2. Shown is the binodal for coexisting states, where a sphere-rich and needle-poor fluid (sphere liquid) coexists with a sphere-poor and needle-rich fluid (sphere gas). For low densities, the density discontinuity vanishes at a critical point. We also display the Fisher-Widom (FW) line, which separates regimes in the phase diagram where the ultimate decay of pair correlation functions (and inhomogeneous one-body density profiles) at large separation is either damped oscillatory or monotonic [33–36]. The FW line was calculated for the present model in Ref. [28] by considering the poles of the partial structure factors in the plane of complex wave vectors [34,35]. Furthermore, we display four tielines between coexisting fluid states. These belong to reservoir densities of needles $\rho_*^r = 16, 18, 20, 22$, and indicate the states where we will carry out detailed structural studies below. Tielines are horizontal in the phase diagram in needle reservoir representation (as a function of η and ρ_*^r), see the inset in Fig. 2. The smallest reservoir density, $\rho_*^r = 16$, is close to the critical point (which is located at $\eta=0.15767$, $\rho_* = 9.3141$, $\rho_*^r = 14.642$). For $\rho_*^r = 16$ the liquid density is located well on the monotonic side of the FW line, hence we expect one-body interface profiles to decay monotonically into both bulk phases. The set of the three higher reservoir densities ($\rho_*^r = 18, 20, 22$) covers the region up to the triple

point, which was located with perturbation theory at $\rho_*^r \approx 24$ [9]. For these states we expect damped oscillatory profiles on the sphere-rich side of the interface.

Before turning to the fluid-fluid interface, we summarize the bulk properties of spheres and rods in the Onsager limit in bulk given in Sec. III B. In an isotropic state, we find that $n_2^{NN} = \xi_v^{NN} \rho_N$, where $\xi_v^{NN} = \pi LD$ equals the leading contribution to the surface of a rod in the limit $L/D \rightarrow \infty$. It follows that the additional contribution to the free energy density due to rod-rod interactions is $(\pi/4) \rho_N^2 L^2 D / (1 - \eta)$, which is identical to the result from scaled-particle theory [40]. We leave a more detailed investigation of the phase behavior to possible future work.

B. Structure of the fluid-fluid interface

Here and in the following we restrict ourselves to the simple case of spheres mixed with vanishingly thin needles, and aim at an understanding of the free interface between demixed fluid states, see Fig. 1 for a schematic sketch of the following situation: Two demixed bulk fluids are in equilibrium in contact; the coordinate perpendicular to their (planar) interface is denoted by z , and the sphere-poor (-rich) phase is present for negative (positive) z values. The coordinate origin (in z) is set to the position of the Gibbs dividing surface, hence the z -coordinate fulfills $\int_{-\infty}^0 dz [\rho_S(z) - \rho_S(-\infty)] + \int_0^{\infty} dz [\rho_S(z) - \rho_S(\infty)] = 0$. Note that as we deal with isotropic states for $z \rightarrow \pm\infty$, the planar geometry considered in Sec. III C applies.

The numerical minimization of the density functional of Sec. III A is done by an iteration technique, see, e.g., [41]. We discretize $\rho_S(z)$ and $\rho_N(z, \theta)$ in z direction with a resolution of 0.01σ , and we find that angular discretization in 20–50 steps is sufficient to get reliable results for density profiles. For the calculation of interface tensions between demixed fluids (Sec. IV C), we use 120 steps. Note that when, say, 20 needle orientations are considered, we are dealing in effect (due to the additional sphere profile) with a 21 component mixture.

We chose the size ratio $\sigma/L=1$ for our interface study. This is of the same order as realized in the experiments [8] with silica spheres of 78 nm diameter and polymer rods (PBLG) with $L=70$ nm. However, we disregard effects arising from rod flexibility and finite rod thickness and hence consider only $D=0$ (note that $D=1.6$ nm for the polymer in [8]). We first turn to the sphere density profiles, $\rho_S(z)$, displayed in Fig. 3 as a function of the scaled distance z/σ for scaled needle reservoir densities $\rho_*^r = 16, 18, 20, 22$. These statepoints are indicated by tielines in Fig. 2. The asymptotic densities for $z \rightarrow \pm\infty$ in Fig. 3 correspond (up to the factor $\pi/6$) to the sphere packing fractions at both ends of the tielines. With increasing ρ_*^r , and hence increasing distance to the critical point, the interface becomes sharper, i.e., it crosses over from one to the other limiting (bulk) value over a shorter distance. For the highest needle reservoir density considered, $\rho_*^r = 22$, clear oscillations emerge on the liquid side of the interface, see the inset in Fig. 3. The amplitude of the oscillations, however, is considerably smaller than that typically found at interfaces in the AO model (where the

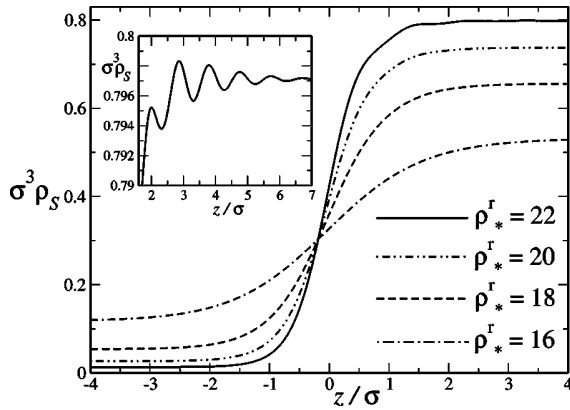


FIG. 3. Scaled sphere density profiles $\sigma^3 \rho_S(z)$ at the free interface between sphere-poor ($z < 0$) and sphere-rich ($z > 0$) phases as a function of the scaled distance z/σ perpendicular to the interface for $\rho_*^r = 16, 18, 20, 22$ corresponding to the tielines in the phase diagram, Fig. 2. The inset shows a magnified view of the (oscillatory) profile $\sigma^3 \rho_S(z)$ as a function of z/σ at the sphere-rich side for $\rho_*^r = 22$.

depletants are ideal spheres rather than needles) [37]. From the general theory of asymptotic decay of correlation functions [34,35], we expect that all statepoints where the liquid density is inside the oscillatory region of the phase diagram (separated by the FW line) will display similar behavior, and indeed we find oscillations on the liquid side of the interface also for $\rho_*^r = 18, 20$. The liquid state at density $\rho_*^r = 16$ is inside the monotonic region, and no oscillations emerge upon magnifying the corresponding density profile in Fig. 3.

In the present geometry, the needle density profile depends on two variables, namely, the perpendicular distance z from the interface and the angle θ of needle orientation and interface normal. The DFT yields $\rho_N(z, \theta)$ fully dependent on both variables. In order to demonstrate this, we chose $\rho_*^r = 22$ as an example and display in Fig. 4 $\rho_*(z, \theta) \sin \theta$ as

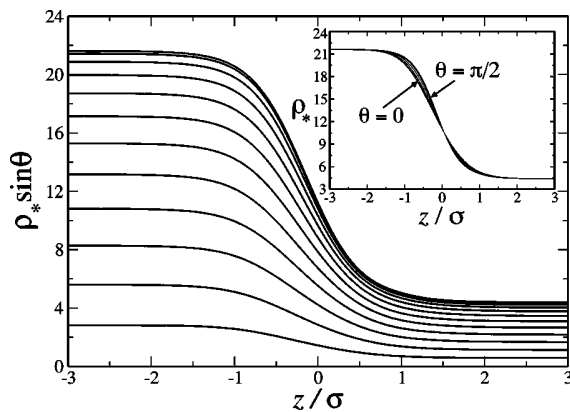


FIG. 4. Scaled needle density multiplied by the spherical volume element, $\rho_*(z, \theta) \sin \theta$, as a function of z/σ at the interface between sphere-poor ($z < 0$) and sphere-rich ($z > 0$) fluids for $\rho_*^r = 22$. Each curve is for fixed angle θ to the interface normal; from bottom to top θ increases from 0 (direction normal to the interface) to $\pi/2$ (direction parallel to the interface) in steps of $\pi/24$. The inset shows the bare $\rho_*(z, \theta)$ without the volume element $\sin \theta$.

a function of z/σ . The factor $\sin \theta$ is the spherical volume element, hence the density distribution at a given angle θ is weighted according to the actual probability that θ is attained. This weight is maximal for $\theta = \pi/2$ (parallel to the interface) and vanishes for $\theta = 0$ (perpendicular to the interface). In order to graphically represent the density profile, we display a set of curves parametrized by θ ; each curve then depends on the single variable z , see Fig. 4. As expected, the needles show a clear tendency to aggregate on the sphere-poor side of the interface. In order to assess the orientational distribution we also plot the bare $\rho_*(z, \theta)$ in the inset of Fig. 4. We observe that for fixed z on the needle-rich side of the profiles the density increases with increasing θ . This means that large angles are favored, hence the needles tend to arrange parallel to the surface, corresponding to biaxial order. On the needle rich side of the interface, however, the opposite trend is manifest. Upon increasing θ at fixed z the density decreases. Hence small angles are more favorable; needles arrange perpendicular to the interface displaying uniaxial order.

In order to investigate the needle behavior in more detail, we obtain two characteristic distributions from the full needle density profile $\rho_*(z, \theta)$. One is the orientation averaged needle density profile, defined as

$$\bar{\rho}_N(z) = \int \frac{d^2 \Omega}{4\pi} \rho_N(\mathbf{r}, \Omega), \quad (39)$$

$$= \frac{1}{2} \int_0^{\pi/2} d\theta \sin(\theta) \rho_N(z, \theta), \quad (40)$$

which measures the density of needle midpoints regardless of their orientation. The other is an orientational order parameter profile defined as

$$\langle P_2(\cos \theta) \rangle = \bar{\rho}_N(z)^{-1} \int \frac{d^2 \Omega}{4\pi} \rho_N(\mathbf{r}, \Omega) P_2(\cos \theta), \quad (41)$$

$$= [2\bar{\rho}_N(z)]^{-1} \int d\theta \sin(\theta) \rho_N(z, \theta) P_2(\cos \theta), \quad (42)$$

where $P_2(x) = (3x^2 - 1)/2$ is the second Legendre polynomial. Negative values of $\langle P_2(\cos \theta) \rangle$ indicate biaxial ordering, the extreme value being $-1/2$ for full parallel alignment to the interface (needles with $\theta = \pi/2$ lying in a plane). Positive values $\langle P_2(\cos \theta) \rangle$ indicate uniaxial ordering, the extreme value (unity) is attained for perpendicular alignment to the interface ($\theta = 0$). Finally, $\langle P_2(\cos \theta) \rangle = 0$ indicates isotropic states. Note that this order parameter has the same inflection symmetry as the needles.

In Fig. 5 we show $\bar{\rho}_N(z)$ for the four statepoints considered. A crossover from high values for negative z to low values for positive z is manifest; hence, as observed before, the needles are depleted in the space occupied by the colloids. The inset in Fig. 5 shows a magnified view of the profile for $\rho_*^r = 22$ on the sphere-rich side of the interface.

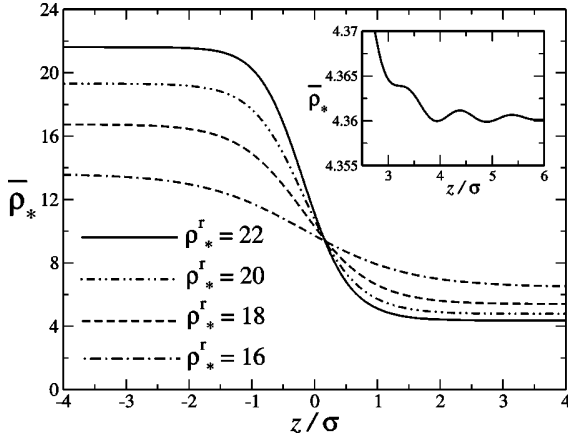


FIG. 5. Orientation averaged needle density profiles $\bar{\rho}_*(z)$ as a function of the scaled distance z/σ for $\rho_*^r = 16, 18, 20, 22$ corresponding to Fig. 3. The inset shows $\bar{\rho}_*(z)$ as a function of z/σ on the sphere-rich side ($z > 0$) of the interface for $\rho_*^r = 22$. Damped oscillations are visible.

Clear oscillations can be observed. These arise from the packing effects of the *spheres*, and are “imprinted” on the needle distribution.

We next turn to the order parameter profile $\langle P_2(\cos \theta) \rangle$, see Fig. 6. On the needle-rich side ($z < 0$) of the interface we find that $\langle P_2(\cos \theta) \rangle < 0$. This indicates needle ordering parallel to the interface, and can be understood in terms of packing effect, similar to those of rods near a hard wall. On the sphere-rich side ($z > 0$) we find that $\langle P_2(\cos \theta) \rangle > 0$, hence the needles are oriented preferentially perpendicular to the interface. We attribute the ordering to needles that stick through the voids in the first sphere layer.

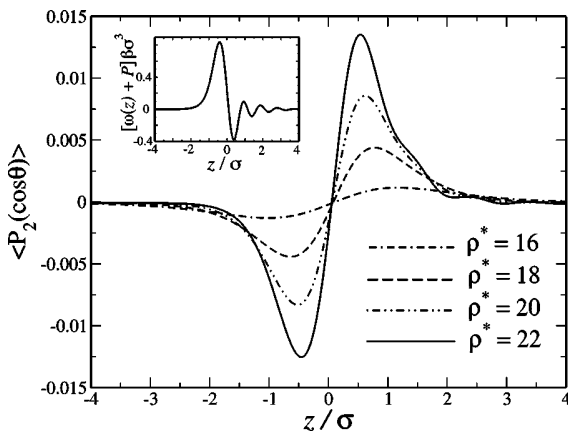


FIG. 6. Orientational order parameter profiles $\langle P_2(\cos \theta) \rangle$ as a function of the scaled distance z/σ for $\rho_*^r = 16, 18, 20, 22$ across the interface between sphere-poor ($z < 0$) and sphere-rich ($z > 0$) fluids. Negative values indicate parallel, positive values indicate normal alignment of needles relative to the interface. The inset shows the (scaled) integrand of the interface tension, $[\omega(z) + P]\beta\sigma^3$ as a function of z/σ for $\rho_*^r = 22$.

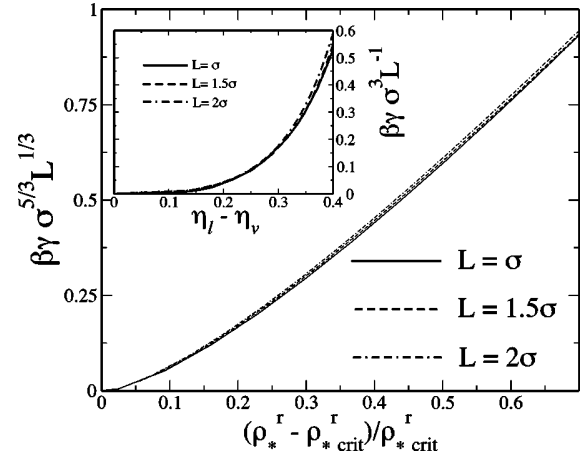


FIG. 7. Scaled interface tension $\beta\gamma\sigma^{5/3}L^{1/3}$ as a function of the scaled distance from the critical point $(\rho_*^r - \rho_{*crit}^r)/\rho_{*crit}^r$ for size ratios $L/\sigma = 1, 1.5, 2$. All curves practically collapse onto each other. The inset shows the scaled interface tension $\beta\gamma\sigma^3L^{-1}$ as a function of the difference between liquid and vapor sphere packing fractions, $\eta_l - \eta_v$, for the same size ratios $L/\sigma = 1, 1.5, 2$.

C. Interface tension

The interface tension γ between demixed fluids is defined as the difference per unit area in grand potentials in the inhomogeneous situation and in bulk. It is given by

$$\gamma A = \bar{\Omega} + PV, \quad (43)$$

where A is the interface area, $\bar{\Omega}$ is the grand potential in the inhomogeneous situation, and P is the total pressure. Within our DFT approach it is obtained from

$$\gamma = \int dz [\omega(z) + P], \quad (44)$$

$$\omega(z) = -\mu_S \rho_S(z) - \mu_N \bar{\rho}_N(z) + \beta \int \frac{d^2 \Omega}{4\pi} \Phi(\{n_v^i(z, \theta)\}), \quad (45)$$

where Φ is the excess free energy density [given through Eqs. (10–12)] dependent on the weighted densities n_v^i [Eqs. (18–20)], and μ_i is the chemical potential of species $i = S, N$. From dimensional analysis, it is clear that the typical scale of γ should be the thermal energy, $k_B T$, divided by an area that is related to molecular length scales. However, as we deal with a binary mixture it is not obvious which power b in $L^b \sigma^{2-b}$ gives the correct scaling with varying size ratio L/σ . We restrict ourselves to the cases $L/\sigma = 1, 1.5, 2$, where we find that $b = 1/3$ gives an almost complete data collapse, see Fig. 7 for a plot of $\beta\gamma\sigma^{5/3}L^{1/3}$ as a function of the scaled distance to the critical value of the needle reservoir density, $(\rho_*^r - \rho_{*crit}^r)/\rho_{*crit}^r$. For states close to the critical point, we find mean-field scaling of the surface tension, $\gamma \propto (\rho_*^r - \rho_{*crit}^r)^{3/2}$. For $(\rho_*^r - \rho_{*crit}^r)/\rho_{*crit}^r > 0.4$ a linear relation is found that extends up to the triple point, for $L = \sigma$ this is from the perturbation theory of Ref. [9] roughly at the right end of the horizontal axis in Fig. 7.

The magnitude of the interface tension is mainly governed by the difference in bulk densities of both phases. Hence a relevant variable is the difference $\eta_l - \eta_v$, where η_l (η_v) is the sphere packing fraction in the coexisting liquid (vapor) phase. In the same spirit as above, we seek a combination of length scales to scale $\beta\gamma$, in order to obtain data collapse for different L/σ . It turns out that this is the case for $\beta\gamma\sigma^3 L^{-1}$, see the inset in Fig. 7. Clearly, the different exponent to the case above arises from the relation between η and ρ_* given through the binodals for different L/σ . Although we only present results for $\sigma \leq L \leq 2\sigma$, we expect the scaling relations to hold beyond that range. However, for $L \gg \sigma$ there might well be a crossover to a different scaling regime, and preliminary results show deviations already for $L = 5\sigma$.

As a final issue, we seek to elucidate further the origin of the surface tension. A recent study by Archer and Evans addressed this issue in a binary mixture of Gaussian core particles [42] (see Figs. 11 and 12 therein). They consider two different regimes for their model: (a) where demixing is driven by nonadditivity and (b) where it is driven by energetics, and construct two new variables, namely the total density and a local concentration. In order to calculate the surface tension one must perform the integral Eq. (22) in Ref. [42] [corresponding to our Eq. (44)]. If the integrand is plotted they find that in regime (a) it closely resembles the local concentration and in regime (b) the total density. Their conclusion is that, in one regime, γ is dominated by concentration fluctuations and, in the other, by fluctuations in the total density.

Applying this analysis to our model, we find that neither local concentration nor total density resembles the integrand of the surface tension in Eq. (44). However, the integrand closely resembles the (negative) of the orientational order parameter, see the inset in Fig. 6 for a plot of $[w(z) + P]\beta\sigma^3$ as a function of z/σ for the largest reservoir density considered, $\rho_*^r = 22$. As interpretation of the similarity, negative values of $\langle P_2(\cos \theta) \rangle$ indicate a loss of rotational entropy, and hence a positive contribution to γ . Positive values of $\langle P_2(\cos \theta) \rangle$ indicate a relaxation of the needles sticking through the first sphere layer and hence lowering the tension. From this analysis, it is tempting to argue that in the present model the surface tension is determined by *orientation* fluctuations.

V. CONCLUSIONS

In conclusion, we have considered the free (planar) interface between demixed fluid phases in a model mixture of spherical and needle-shaped colloidal particles. We focused on the case of vanishingly thin needles, which constitutes a minimal model for orientational order at fluid interfaces. Both sphere and needle density profiles show either monotonic or damped oscillatory behavior on the sphere-rich (and needle-poor) side of the interface, depending on which side of the Fisher-Widom line in the bulk phase diagram the sphere liquid state resides. The amplitude of the oscillations, however, is considerably smaller than in the related AO model of spherical (polymer) depletants, and will be further reduced by capillary fluctuations that are not taken into ac-

count in the present treatment. It is tempting to interpret the smaller amplitude in the current model by a washing out of oscillations due to the depletants' rotator degrees of freedom, which are absent in the AO case. On the needle-rich (and sphere-poor) side of the interface both density profiles decay monotonically towards the respective bulk densities. Needles possess biaxial order on the needle-rich side, i.e., they lie preferentially parallel to the interface plane. This can be understood in terms of simple packing of needles against the dense hard sphere fluid. On the sphere-rich side uniaxial order of needles occurs, i.e., needles tend to be oriented normal to the interface. This is somewhat surprising, and we interpret this effect as being caused by the void structure of the hard sphere fluid, into which the needles stick to maximize their entropy.

We have furthermore shown that the geometry-based DFT can be consistently extended to the case of hard spheres mixed with interacting rods in the Onsager limit. The extensions of geometry-based DFT in Ref. [28] are the integration over director space [Eq. (9)], and the introduction of double-indexed weight functions [Eq. (5)] are supplemented in this work by the introduction of angular convolutions [Eq. (15)] to obtain weighted densities. The consistent treatment of nontrivial rod-rod interactions provides an important stepping stone towards the treatment of more general hard body systems. We have given explicit expressions for the present density functional for the important cases of planar and spherical symmetries, facilitating future studies.

We emphasize that testing our predictions for the fluid-fluid interface constitutes a demanding task for computer simulations due to the large numbers of needles involved at state points of interest, and due to the difficulty of stabilizing the free fluid-fluid interface in a finite simulation box. An alternative to circumvent the first problem could be to study an effective one-component system of spheres that interacts by means of the needle-depletion potential [13], although, such an approach would prevent study of the orientational distribution of the needles.

ACKNOWLEDGMENTS

We thank R. Evans, D. Oxtoby, H. Löwen, G. A. Vliegthart, and C. Bechinger for useful discussions. The work of J.M.B. was supported by the National Science Foundation (through Grant No. CHE9800074 and the NSF Materials Research Science and Engineering Center at the University of Chicago).

APPENDIX A: DECONVOLUTION OF MAYER BONDS

1. The sphere-needle Mayer bond

We take the difference vector between the centers of mass of needle and sphere to lie in the equatorial plane: $\mathbf{r} = (r \sin \varphi, r \cos \varphi, 0)$. Due to the rotational symmetry, we can choose the needle to be aligned parallel to the y axis: $\mathbf{\Omega} = (0, 1, 0)$. Then

$$w_3^S(\mathbf{r}) * w_0^N(\mathbf{r}, \mathbf{\Omega}) = \frac{1}{2} \int_0^\infty dr' \int_0^{2\pi} d\varphi' \int_0^\pi d\theta' r'^2 \sin \theta' \Theta(R-r') \sum_{\pm} \delta(r \sin \varphi - r' \sin \theta' \sin \varphi') \\ \times \delta\left(r \cos \varphi - r' \sin \theta' \cos \varphi' \pm \frac{L}{2}\right) \delta(-r' \cos \theta') \quad (\text{A1})$$

$$= \frac{1}{2} \sum_{\pm} \Theta\left(R^2 - r^2 - \frac{L^2}{4} \pm Lr \cos \varphi\right), \quad (\text{A2})$$

and

$$w_2^{SN}(\mathbf{r}, \mathbf{\Omega}) * w_1^N(\mathbf{r}, \mathbf{\Omega}) = \frac{1}{2} \int_0^\infty dr' \int_0^{2\pi} d\varphi' \int_0^\pi d\theta' r'^2 \sin \theta' \left| \begin{pmatrix} \sin \theta' \sin \varphi' \\ \sin \theta' \cos \varphi' \\ \cos \theta' \end{pmatrix} \cdot \begin{pmatrix} 0 \\ 1 \\ 0 \end{pmatrix} \right| \delta(R-r') \\ \times \int_{-L/2}^{L/2} dl \delta(r \sin \varphi - r' \sin \theta' \sin \varphi') \delta(r \cos \varphi - r' \sin \theta' \cos \varphi' + l) \delta(-r' \cos \theta') \quad (\text{A3})$$

$$= \frac{1}{2} \sum_{\pm} \Theta(R - |r \sin \varphi|) \Theta\left(\frac{L}{2} - \left| r \cos \varphi \pm \sqrt{R^2 - r^2 \sin^2 \varphi} \right|\right), \quad (\text{A4})$$

where the integrals over θ' , r' , and l in Eqs. (A1), (A3) are straightforward. The integral over φ is split into two domains: for $0 < \varphi < \pi$, $\sin \varphi$ is positive, while for $\pi < \varphi < 2\pi$ it is negative. The sum of Eqs. (A2), (A4) represents the (negative) Mayer bond between sphere and needle, hence $-f_{SN} = w_3^S * w_0^N + w_2^{SN} * w_1^N$. This can be seen by considering the cases where the above expressions are nonvanishing: In Eq. (A2), the step function counts the number of needle endpoints that lie in the sphere. In Eq. (A4) the first step function is nonzero only if the needle axis intersects the sphere. If it does, the second step function counts how often the needle intersects the surface of the sphere. This covers all cases of sphere-needle overlap.

2. The rod-rod Mayer bond in the Onsager limit

Since only the relative orientation of both rods is relevant, we take $\mathbf{\Omega}' = (0,0,1)$, $\mathbf{\Omega} = (0, \sin \theta, \cos \theta)$; the difference vector between both particle positions is (x, y, z) . We then perform the spatial convolution of the weight functions given in Eqs. (1), (14) as

$$-2w_2^{NN}(\mathbf{r}, \mathbf{\Omega}; \mathbf{\Omega}') * w_1^N(\mathbf{r}, \mathbf{\Omega}') \quad (\text{A5})$$

$$= -2D \int_{-\infty}^{\infty} dz' \int_{-\infty}^{\infty} dy' \int_{-\infty}^{\infty} dx' \sin \theta \int_{-L/2}^{L/2} dl \delta(x') \delta(y' + l \sin \theta) \delta(z' + l \cos \theta) \\ \times \int_{-L/2}^{L/2} dl' \delta(x - x') \delta(y - y') \delta(z - z' + l') \quad (\text{A6})$$

$$= -2D \int_{-\infty}^{\infty} dz' \int_{-\infty}^{\infty} dy' \int_{-\infty}^{\infty} dx' \tan \theta \delta(x') \Theta\left(\frac{L}{2} - \left| \frac{y'}{\sin \theta} \right|\right) \delta\left(z' - \frac{y'}{\tan \theta}\right) \\ \times \int_{-L/2}^{L/2} dl' \delta(x - x') \delta(y - y') \delta(z - z' + l') \quad (\text{A7})$$

$$= -2D \delta(x) \Theta\left(\frac{L}{2} - \left| \frac{y}{\tan \theta} + z \right|\right) \Theta\left(\frac{L}{2} - \left| \frac{y}{\sin \theta} \right|\right) \quad (\text{A8})$$

$$= f_{NN}(\mathbf{r}, \mathbf{\Omega}; \mathbf{\Omega}'). \quad (\text{A9})$$

From Eq. (A6) to (A7), we solve the integral over l as an explanatory case; the other integrals can be done analogously. In order to recognize that Eq. (A8) is indeed the rod-rod Mayer bond, we compare with the expressions given in Ref. [43], and observe that the step-functions in Eq. (A8) correspond to Eqs. (A1), (A2) in the Appendix of Ref. [43]. Since $\lim_{D \rightarrow 0} \Theta(D - |x|)/(2D) = \delta(x)$, the term $2D \delta(x)$ corresponds to Eq. (A3) in Ref. [43] in the limit of small values of D , hence Eq. (A9) constitutes a valid equality.

APPENDIX B: WEIGHT FUNCTIONS IN PLANAR GEOMETRY

The reduced weight functions in planar geometry appearing in Eqs. (18)–(20) are obtained as

$$w_\nu^N(z, \theta) = \int_{-\infty}^{\infty} dx \int_{-\infty}^{\infty} dy w_\nu^N(\mathbf{r}, \mathbf{\Omega}), \quad (\text{B1})$$

$$w_\nu^S(z) = \int_{-\infty}^{\infty} dx \int_{-\infty}^{\infty} dy w_\nu^S(\mathbf{r}), \quad (\text{B2})$$

$$w_2^{SN}(z, \theta) = \int_{-\infty}^{\infty} dx \int_{-\infty}^{\infty} dy w_2^{SN}(\mathbf{r}, \mathbf{\Omega}), \quad (\text{B3})$$

where $\mathbf{r} = (x, y, z)$, and in the following we employ cylindrical coordinates $\mathbf{r} = (r \cos \varphi, r \sin \varphi, z)$. For the scalar and vectorial sphere weight functions [Eqs. (3), (4)] as well as for the pure needle weight functions [Eqs. (1), (2)] the integrations in Eqs. (B1), (B2) are straightforward and yield the results given in Eqs. (22)–(26). The calculations for $\hat{\mathbf{w}}_{m2}^S(z)$ and $w_2^{SN}(z, \theta)$ [defined through Eqs. (4), (5), respectively] are slightly more involved, and are given explicitly in the following sections.

1. Tensor sphere weight function

We insert the definition of the tensor weight [Eq. (4)] into Eq. (B2),

$$\hat{\mathbf{w}}_{m2}^S(z) = \int_{-\infty}^{\infty} dx \int_{-\infty}^{\infty} dy \delta(R - |\mathbf{r}|) \left(\frac{\mathbf{r}\mathbf{r}}{r^2} - \frac{\hat{\mathbf{1}}}{3} \right) \quad (\text{B4})$$

$$= \int_0^{2\pi} d\varphi \int_0^\infty dr r \delta(R - \sqrt{r^2 + z^2}) \left[(r^2 + z^2)^{-1} \begin{pmatrix} r^2 \sin^2 \varphi & r^2 \sin \varphi \cos \varphi & r \sin \varphi z \\ r^2 \sin \varphi \cos \varphi & r^2 \cos^2 \varphi & r \cos \varphi z \\ r \sin \varphi z & r \cos \varphi z & z^2 \end{pmatrix} - \frac{\hat{\mathbf{1}}}{3} \right] \quad (\text{B5})$$

$$= \int_0^\infty dr r \delta(R - \sqrt{r^2 + z^2}) \left((r^2 + z^2)^{-1} \text{diag}(\pi r^2, \pi r^2, 2z^2) - \frac{2\pi}{3} \hat{\mathbf{1}} \right) \quad (\text{B6})$$

$$= \left(\frac{\pi}{R} \text{diag}(R^2 - z^2, R^2 - z^2, 2z^2) - \frac{2\pi R}{3} \hat{\mathbf{1}} \right) \Theta(R^2 - z^2), \quad (\text{B7})$$

from which Eq. (27) can be readily obtained. The off-diagonal elements in Eq. (B5) vanish due to the φ integration over a complete wavelength, and to obtain Eq. (B7) we have used $\delta[f(x)] = |f'(x_0)|^{-1} \delta(x - x_0)$, where x_0 is the zero of $f(x)$, hence $f(x_0) = 0$.

2. Mixed sphere-needle weight function

Due to the rotational symmetry around the z axis, we can take $\mathbf{\Omega} = (\sin \theta, 0, \cos \theta)$, and due to the inflection symmetry of the needles, we can restrict to $0 \leq \theta \leq \pi/2$. By inserting the definition of the mixed weight function [Eq. (5)] into Eq. (B3) we obtain

$$w_2^{SN}(z, \theta) = 2 \int dx \int dy \left| \delta(R - |\mathbf{r}|) \frac{1}{\sqrt{r^2 + z^2}} \begin{pmatrix} r \cos \varphi \\ r \sin \varphi \\ z \end{pmatrix} \cdot \begin{pmatrix} \sin \theta \\ 0 \\ \cos \theta \end{pmatrix} \right| \quad (\text{B8})$$

$$= 2 \int_0^{2\pi} d\varphi \int_0^\infty dr r \left| \delta(R - \sqrt{r^2 + z^2}) \frac{z \cos \theta + r \cos \varphi \sin \theta}{\sqrt{r^2 + z^2}} \right| \quad (\text{B9})$$

$$= \left\{ \left[8 \sqrt{(R^2 - z^2) \sin^2 \theta - z^2 \cos^2 \theta} + 4z \cos \theta \operatorname{sgn}(\sqrt{R^2 - z^2} \sin \theta) \right. \right. \\ \left. \left. \times \arcsin\left(\frac{z \cos \theta}{\sqrt{R^2 - z^2} \sin \theta}\right) \right] \Theta\left(1 - \left|\frac{z \cos \theta}{\sqrt{R^2 - z^2} \sin \theta}\right|\right) + 4\pi |z \cos \theta| \Theta\left(\left|\frac{z \cos \theta}{\sqrt{R^2 - z^2} \sin \theta}\right| - 1\right) \right\} \Theta(R - |z|) \quad (\text{B10})$$

$$= \begin{cases} 8 \sqrt{R^2 \sin^2 \theta - z^2} + 8z \cos \theta \arcsin\left(\frac{z \cot \theta}{\sqrt{R^2 - z^2}}\right) & \text{if } |z| < R \sin \theta, \\ 4\pi |z| \cos \theta & \text{if } R \sin \theta \leq |z| \leq R, \\ 0 & \text{otherwise.} \end{cases} \quad (\text{B11})$$

In Eq. (B9), we have used the same representation for the δ function as before. The nontrivial part is the integral over φ , which we discuss in the following. It is of the form

$$\int_0^{2\pi} |a + b \cos \varphi| d\varphi \quad (\text{B12})$$

with constants (with respect to φ) a, b . Due to the symmetry of the cosine function, the integration from 0 to π gives the same result as that from π to 2π . We consider two cases: The argument of $|\cdot|$ changes its sign once if $|a/b| < 1$, and we have

$$\int_0^\pi |a + b \cos \varphi| d\varphi \quad (\text{B13})$$

$$= \operatorname{sgn}(a + b) \left([a\varphi + b \sin \varphi]_0^\pi + [-a\varphi - b \sin \varphi]_x^\pi \right) \quad (\text{B14})$$

$$= \operatorname{sgn}(b)(2b \sin x + 2ax - a\pi) \quad (\text{B15})$$

$$= \operatorname{sgn}(b) \left(2b \sin \arccos \frac{-a}{b} + 2a \arccos \frac{-a}{b} - a\pi \right) \quad (\text{B16})$$

$$= 2\sqrt{b^2 - a^2} + 2a \operatorname{sgn}(b) \arcsin \frac{a}{b}, \quad (\text{B17})$$

where $x = \arccos(-a/b)$. If, on the other hand, $|a/b| > 1$, the argument does not change its sign. Then, $|a + b \cos \varphi| = (a + b \cos \varphi) \operatorname{sgn}(a)$,

$$\int_0^\pi |a + b \cos \varphi| d\varphi = |a| \pi. \quad (\text{B18})$$

Note that in Eq. (B10), $\operatorname{sgn}(\cdot) = +1$ holds, since $0 \leq \theta \leq \pi/2$.

-
- [1] M. Adams, Z. Dogic, S.L. Keller, and S. Fraden, *Nature (London)* **393**, 349 (1998).
 [2] G.A. Vliegthart and H.N.W. Lekkerkerker, *J. Chem. Phys.* **111**, 4153 (1999).
 [3] G.H. Koenderink, G.A. Vliegthart, S.G.J.M. Kluijtmans, A. van Blaaderen, A.P. Philipse, and H.N.W. Lekkerkerker, *Langmuir* **15**, 4693 (2000).
 [4] K. Lin, J.C. Crocker, A.C. Zeri, and A.G. Yodh, *Phys. Rev. Lett.* **87**, 088301 (2001).
 [5] M. Elbaum, D.K. Fyngenson, and A. Libchaber, *Phys. Rev. Lett.* **76**, 4078 (1996).
 [6] D.K. Fyngenson, M. Elbaum, B. Shraiman, and A. Libchaber, *Phys. Rev. E* **55**, 850 (1997).
 [7] S.G.J.M. Kluijtmans, G.H. Koenderink, and A.P. Philipse, *Phys. Rev. E* **61**, 626 (2000).
 [8] G. A. Vliegthart, Dissertation, Utrecht University, 1999.
 [9] P. Bolhuis and D. Frenkel, *J. Chem. Phys.* **101**, 9869 (1994).
 [10] S. Asakura and F. Oosawa, *J. Chem. Phys.* **22**, 1255 (1954).
 [11] A. Vrij, *Pure Appl. Chem.* **48**, 471 (1976).
 [12] H.N.W. Lekkerkerker, W.C.K. Poon, P.N. Pusey, A. Stroobants, and P.B. Warren, *Europhys. Lett.* **20**, 559 (1992).
 [13] K. Yaman, C. Jeppesen, and C.M. Marques, *Europhys. Lett.* **42**, 221 (1998).
 [14] Y. Mao, M.E. Cates, and H.N.W. Lekkerkerker, *Phys. Rev. Lett.* **75**, 4548 (1995).
 [15] Y. Mao, M.E. Cates, and H.N.W. Lekkerkerker, *J. Chem. Phys.* **106**, 3721 (1997).
 [16] Z. Dogic, D. Frenkel, and S. Fraden, *Phys. Rev. E* **62**, 3925 (2000).
 [17] R. Evans, in *Fundamentals of Inhomogeneous Fluids*, edited by D. Henderson (Dekker, New York, 1992), p. 85.
 [18] R. Evans, *Adv. Phys.* **28**, 143 (1979).
 [19] Y. Rosenfeld, *Phys. Rev. Lett.* **63**, 980 (1989).
 [20] Y. Rosenfeld, M. Schmidt, H. Löwen, and P. Tarazona, *J. Phys.: Condens. Matter* **8**, L577 (1996).
 [21] Y. Rosenfeld, M. Schmidt, H. Löwen, and P. Tarazona, *Phys. Rev. E* **55**, 4245 (1997).
 [22] P. Tarazona and Y. Rosenfeld, *Phys. Rev. E* **55**, R4873 (1997).
 [23] P. Tarazona, *Phys. Rev. Lett.* **84**, 694 (2000).
 [24] Y. Rosenfeld, *Phys. Rev. E* **50**, R3318 (1994).
 [25] A. Chamoux and A. Perera, *J. Chem. Phys.* **104**, 1493 (1996).
 [26] A. Chamoux and A. Perera, *Phys. Rev. E* **58**, 1933 (1998).

COLLOIDAL ROD-SPHERE MIXTURES: FLUID-FLUID . . .

PHYSICAL REVIEW E **66**, 031401 (2002)

- [27] A. Chamoux and A. Perera, *Mol. Phys.* **93**, 649 (1998).
[28] M. Schmidt, *Phys. Rev. E* **63**, 050201(R) (2001).
[29] M. Schmidt and C. von Ferber, *Phys. Rev. E* **64**, 051115 (2001).
[30] M. Schmidt and A.R. Denton, *Phys. Rev. E* **65**, 021508 (2002).
[31] R. Roth, R. van Roij, D. Andrienko, K. R. Mecke, and S. Dietrich, *Phys. Rev. Lett.* (in press), eprint cond-mat/0202443.
[32] K. Shundyak and R. van Roij, *J. Phys.: Condens. Matter* **13**, 4789 (2001), and references therein.
[33] M.E. Fisher and B. Widom, *J. Chem. Phys.* **50**, 3756 (1969).
[34] R. Evans, J.R. Henderson, D.C. Hoyle, A.O. Parry, and Z.A. Sabeur, *Mol. Phys.* **80**, 755 (1993).
[35] R. Evans, R.J.F. Leote de Carvalho, J.R. Henderson, and D.C. Hoyle, *J. Chem. Phys.* **100**, 591 (1994).
[36] M. Dijkstra and R. Evans, *J. Chem. Phys.* **112**, 1449 (2000).
[37] J.M. Brader, R. Evans, M. Schmidt, and H. Löwen, *J. Phys.: Condens. Matter* **14**, L1 (2002).
[38] J.M. Brader, M. Dijkstra, and R. Evans, *Phys. Rev. E* **63**, 041405 (2001).
[39] L. Onsager, *Ann. N.Y. Acad. Sci.* **51**, 627 (1949).
[40] J.A. Barker and D. Henderson, *Rev. Mod. Phys.* **48**, 587 (1976).
[41] R. van Roij, M. Dijkstra, and R. Evans, *Europhys. Lett.* **49**, 350 (2000).
[42] A.J. Archer and R. Evans, *Phys. Rev. E* **64**, 041501 (2001).
[43] H. Löwen, *Phys. Rev. E* **50**, 1232 (1994).

Simulation and theory of fluid–fluid interfaces in binary mixtures of hard spheres and hard rods

Peter G Bolhuis¹, Joseph M Brader² and Matthias Schmidt^{3,4}

¹ Department of Chemical Engineering, Faculty of Chemistry, University of Amsterdam, Nieuwe Achtergracht 166, 1018 WV Amsterdam, The Netherlands

² Institute of Physiology, University of Bern, Bülhplatz 5, 3012 Bern, Switzerland

³ Soft Condensed Matter, Debye Institute, Utrecht University, Princetonplein 5, 3584 CC Utrecht, The Netherlands

Received 21 July 2003

Published 20 November 2003

Online at stacks.iop.org/JPhysCM/15/S3421

Abstract

We consider the free interface between demixed fluid phases in a mixture of hard spheres and vanishingly thin hard rods using Monte Carlo simulations and density functional theory. Both approaches treat the full binary mixture and hence include all rod-induced many-body depletion interactions between spheres. The agreement between theoretical and simulation results for density and orientation order profiles across the interface is remarkable, even for states not far from the critical point. The simulation results confirm the previously predicted preferred vertical (parallel) alignment of rod orientation to the interface plane at the sphere-rich (sphere-poor) side. This ordering should be experimentally observable in phase-separated colloidal rod–sphere mixtures.

1. Introduction

The gas–liquid interface of a simple substance is characterized by the variation of the density of particles in the direction perpendicular to the interface. The number density is the only order parameter in this situation. Complex systems possess more than a single order parameter and hence may display richer interfacial structure, such as composition fluctuations in mixtures of different components and orientation fluctuations of anisotropic particles. Examples of complex model systems that display fluid–fluid phase separation and hence are suitable to study interfacial structure are mixtures of colloidal spheres and rods.

Much work has been devoted to understanding the bulk phase behaviour of rod–sphere mixtures [1–7]. Among the different techniques employed are computer simulations [1], free-volume [1, 2] and liquid integral equation [4, 5] theories, as well as experiments with silica spheres mixed with silica coated bohemite rods [2, 3] or polymeric rods [6, 7]. It can be concluded that the gas, fluid and solid phase are thermodynamically stable and that the rod

⁴ On leave from: Institut für Theoretische Physik II, Heinrich-Heine-Universität Düsseldorf, Universitätsstraße 1, D-40225 Düsseldorf, Germany.

fugacity plays a role similar to that of inverse temperature in simple fluids. The second control parameter is the ratio of rod length L to sphere diameter σ ; for large enough values, stable bulk fluid–fluid demixing occurs [1].

The simplest model in this context is the binary mixture of hard spheres and vanishingly thin hard rods proposed in [1]. Previous work on this model includes investigation of its phase behaviour with simulation and perturbation theory [1]. Recently, a density functional theory (DFT) [8], built upon Rosenfeld's ideas [9–11], was proposed [12]. Application to the free interface between demixed fluids predicts intriguing ordering behaviour at the interface [13]. By integrating out the rod degrees of freedom, effective pair depletion interactions between spheres and between sphere and a hard wall were derived [14, 15]. For small needle-to-sphere size ratios this was shown to be an accurate description and, using a theory for the effective one-component fluid of spheres, purely entropy-induced wetting of the hard wall was found [16]. Rod-induced depletion forces have been experimentally measured and were found to compare well with theoretical predictions [17–19]. Non-vanishing interactions between rods further enrich phase behaviour [20] and correlations between spheres [21].

Despite the existing applications of the rod–sphere DFT [12] to free interfaces [13] and wetting at a hard wall [16], results from the theory have so far been tested against simulation results only in bulk, namely those for the phase diagram and for partial pair distributions between spheres [12]. While theory has passed these (minimal) tests, a full simulation of wetting properties at a hard wall, for example, would be a very demanding task (see e.g. [22] for simulations of a related colloid–polymer mixture). In this work we consider the fluid–fluid interface between demixed fluid phases using Monte Carlo (MC) simulations to obtain density and orientation order parameter profiles which we compare to theoretical results. We find that the theory very accurately describes the simulation results for interface profiles. In particular the simulations confirm that on the needle-rich (sphere-rich) side of the interface the needles are aligned preferentially parallel (vertical) to the interface plane. This effect is present even for vanishing rod–rod interactions and hence is similar, but of different origin, to molecular ordering at the isotropic–nematic interface of hard rods [23].

The paper is organized as follows. In section 2 the theoretical model is defined and brief outlines of both simulation and theoretical methods are given. Section 3 presents results for the interfacial structure. We conclude in section 4.

2. Model and methods

2.1. Definition of the model

We consider a binary mixture of colloidal spheres with diameter σ (species S) and needle-like rods with length L and vanishing thickness (species N). The pair interaction between colloids as a function of centre-to-centre distance r is that of hard spheres: $V_{SS}(r) = \infty$ if $r < \sigma$ and zero otherwise. The pair interaction between a sphere and a needle depends on the distance vector from sphere centre to rod centre, \mathbf{r} , and on rod orientation Ω and is that of hard bodies: $V_{SN}(\mathbf{r}, \Omega) = \infty$ if both particles overlap and zero otherwise. Due to their vanishing thickness the rods can be regarded as non-interacting: $V_{NN} = 0$ for all distances and orientations. In figure 1 an illustration of the model is displayed.

As thermodynamic parameters we use the sphere packing fraction $\eta = \pi\sigma^3\rho_S/6$ and a reduced needle density $\rho_N\sigma^3$, where the number densities are defined as $\rho_i = M_i/V$, the numbers of particles are M_i and the system volume is V . The size ratio L/σ is a geometric control parameter. We restrict ourselves in the following to $L/\sigma = 3$, which is small enough to keep the size of the simulation box reasonably small, and large enough to keep the number of rods necessary to induce phase separation manageable.

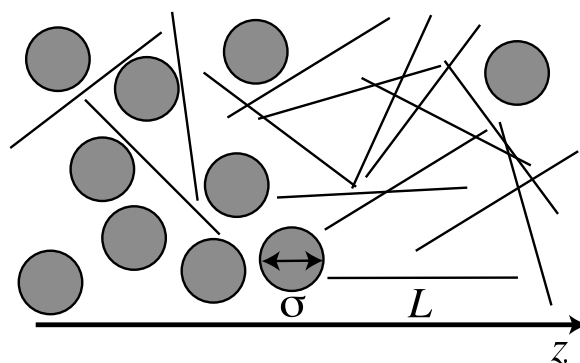


Figure 1. Illustration of the model of hard spheres of diameter σ (gray circles) and vanishingly thin needles of length L (lines). The z -coordinate is perpendicular to the free interface between sphere-rich (left) and sphere-poor (right) phases.

In the following we will seek to obtain the one-body density distributions of particles across planar fluid–fluid interfaces. For spheres, the dependence is only on the position coordinate, so we have $\rho_S(z)$. For needles, we have $\rho_N(z, \theta)$, where θ is the angle between rod orientation Ω and the z -direction normal to the interface. For simplification, we consider an angle-averaged needle density given by $\bar{\rho}_N(z) = \int d\Omega / (4\pi) \rho_N(z, \theta)$; this can be viewed as the density distribution of rod centres. Needle orientations are analysed by means of an orientation order parameter profile, defined as

$$P_2(z) = \bar{\rho}_N(z)^{-1} \int \frac{d\Omega}{4\pi} \rho_N(z, \theta) [3 \cos^2(\theta) - 1] / 2, \quad (1)$$

where the integrand is ρ_N weighted with the second Legendre polynomial in $\cos \theta$. This is the obvious local generalization with respect to the z -direction of the familiar bulk nematic order parameter.

2.2. Computer simulations

We perform canonical ensemble MC simulations using a simulation box with periodic boundary conditions, quadratic area in the xy -plane, and extended (compared to x and y) length in the z -direction in order to stabilize the interface. The movement of the whole system in the z -direction is suppressed by fixing the z -coordinate of the origin in the centre of mass of the spheres. The needle fugacity is obtained using Widom's particle insertion method [24].

Detailed parameters in the simulations are as follows. Statepoint A possesses particle numbers $M_S = 150$ and $M_N = 913$, the box length in the z -direction is 12σ , and the lateral box area is $32\sigma^2$. The resulting densities are $\eta = 0.2045$ and $\rho_N \sigma^3 = 2.3776$ ^{Note 5}. The sequence of statepoints B is for $M_S = 200$ and $M_N = 1000, 1200, 1400$ and 1600 , box length 24σ and box area $32\sigma^2$. The corresponding densities are $\rho_N \sigma^3 = 1.302, 1.563, 1.823$ and 2.083 , and $\eta = 0.1363$. An investigation of the effect of (lateral) finite size effects was done for the statepoint $\rho_N \sigma^3 = 1.823, \eta = 0.1363$, box length 12σ and two different (lateral) system sizes. The small system has $M_S = 200, M_N = 700$ and lateral box area $32\sigma^2$. The large system has $M_S = 800, M_N = 2800$ and lateral box area $128\sigma^2$.

⁵ In this work we consider only one fixed size ratio; when comparing results for different L/σ it is useful to scale the needle density as $\rho_N L^2 \sigma$ [12].

In all simulations the system was equilibrated for 5×10^4 MC cycles. In each cycle, every particle is moved and/or rotated once, on average. For production, we performed 4×10^5 cycles for each statepoint (except for the case of the largest system where 1×10^5 cycles were done).

2.3. Density functional theory

In our theoretical approach the grand potential is expressed as a functional of the one-body density distributions of spheres and needles, $\Omega[\rho_S, \rho_N]$, using the approximation of [12, 13]. The advantage over direct application of Rosenfeld's original approach [10, 11] for anisotropic particles is that the Mayer functions are correctly recovered in a low-density expansion of the free energy functional. The minimization conditions, $\delta\Omega/\delta\rho_S(z) = 0$ and $\delta\Omega/\delta\rho_N(z, \theta) = 0$, are solved numerically with a standard iteration procedure. The angular dependence is treated by discretizing θ ; our implementation follows closely that of [13], where many more technical details that also apply to the present work can be found.

In order to compare with the simulation results, we impose the same periodicity in the z -direction as given by the periodic simulation box. For each statepoint considered during the iteration, the total densities of both components are fixed to the corresponding values from the simulation.

3. Results

We plot in figure 2 the fluid–fluid demixing phase diagram as a function of total sphere packing fraction η and needle fugacity $\exp(\beta\mu_N)$, where β is the inverse temperature and μ_N is the needle chemical potential. For high enough values of $\exp(\beta\mu_N)$ phase separation into a dilute phase (sphere gas) and a dense phase (sphere liquid) occurs. As is known [12], the binodal obtained from DFT is equal to that from perturbation theory [1], and rather accurately describes the simulation results [1]. We also mark the deeply demixed statepoint A and the sequence of statepoints B at constant η , roughly the value at the critical point, and decreasing $\exp(\beta\mu_N)$.

As an illustration, in figure 3 we show a snapshot from the simulation of the deeply demixed state. This demonstrates that the fluid–fluid interface can indeed be stabilized in our simulation setup. Obviously, on this microscopic scale, the interface is not sharp, and we next turn to its detailed structure and consider the deeply demixed state at high $\exp(\beta\mu_N)$ (marked as statepoint A in figure 2).

As can be expected from the coexistence values of η for statepoint A, the sphere gas possesses nearly zero density, whereas all sphere particles reside in the liquid phase (see figure 4 for the density profile $\rho_S(z)$). A smooth crossover between both plateau values occurs in the interfacial region. The width of the interface is somewhat larger than one might expect for such a deeply demixed state, however, we attribute this to the relatively long needles considered, $L/\sigma = 3$. The (orientation-averaged) needle density distribution $\bar{\rho}_N(z)$ shows similar behaviour to $\rho_S(z)$ but is ‘out-of-phase’, as the dense sphere phase is dilute in needles and vice versa. Finally, the orientation order of the needles, as measured by $P_2(z)$, shows that indeed the needles align preferentially parallel to the interface plane on the needle-rich side ($P_2(z) < 0$), and align preferentially perpendicular to the interface plane on the sphere-rich side ($P_2(z) > 0$). Quantitatively, the effect is not very big; recall that the extreme values for perfectly aligned rods are $P_2 = -1/2, 1$. The overall agreement between simulation and theoretical results is very remarkable.

This gives us confidence to turn next to the sequence of statepoints approaching the critical point (marked as statepoint B in the phase diagram, figure 2). In this case, fluctuations are expected to be more important. In figure 5, results for $\rho_i(z)$, $i = S, N$ and $P_2(z)$ are shown.

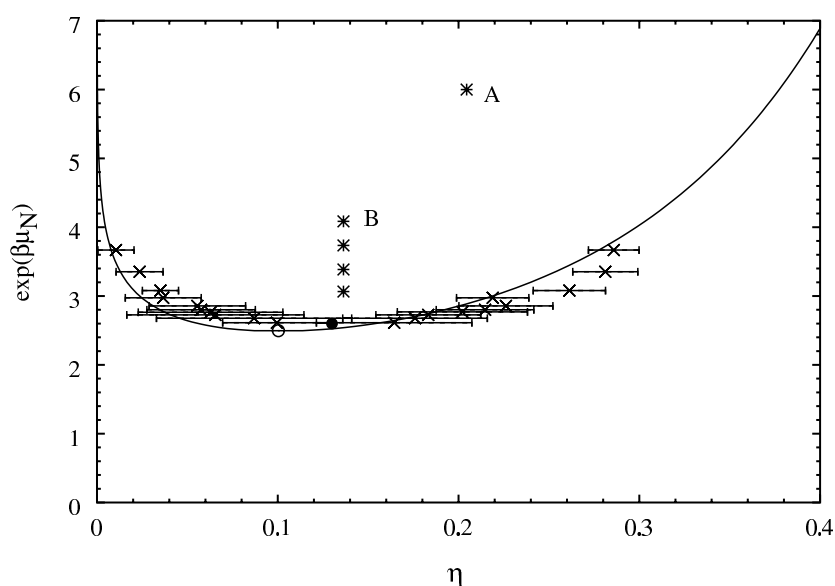


Figure 2. Phase diagram for sphere–needle size ratio $L/\sigma = 3$ as a function of sphere packing fraction η and needle fugacity $\exp(\beta\mu_N)$. The results for the binodal and critical point from DFT (line, open circle) and Gibbs ensemble MC simulations [1] (crosses, full circle) are shown. Coexistence is along horizontal tie lines (not shown). Statepoints (stars) where interface structure will be considered are indicated for deeply demixed conditions (A) and a sequence (B) approaching (approximately) the critical point.

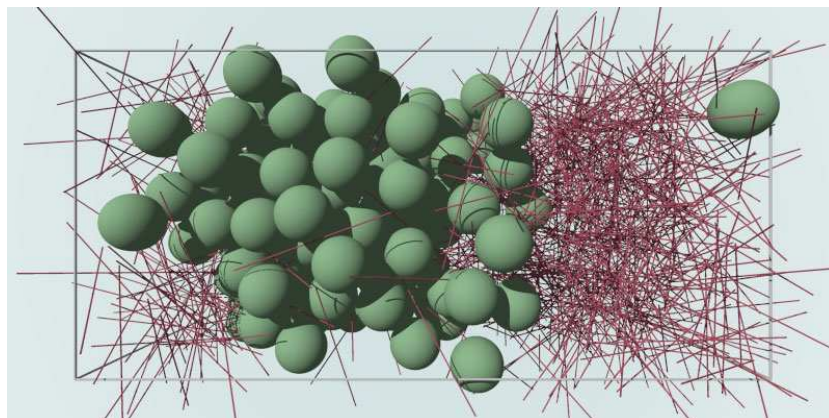


Figure 3. Snapshot from simulation of a phase-separated sphere–needle mixture for size ratio $L/\sigma = 3$ and statepoint A (marked in the phase diagram, figure 2). The simulation box is periodic in all three spatial directions.

(This figure is in colour only in the electronic version)

The qualitative behaviour is the same as for the deeply demixed state, however, the variations with z become much smoother as the critical point is approached and the amplitude of $P_2(z)$ becomes significantly smaller. The agreement between simulation and theoretical results stays remarkable. Except for a slight shift in z for $P_2(z)$ the theoretical curves appear almost as a fit to the MC data.

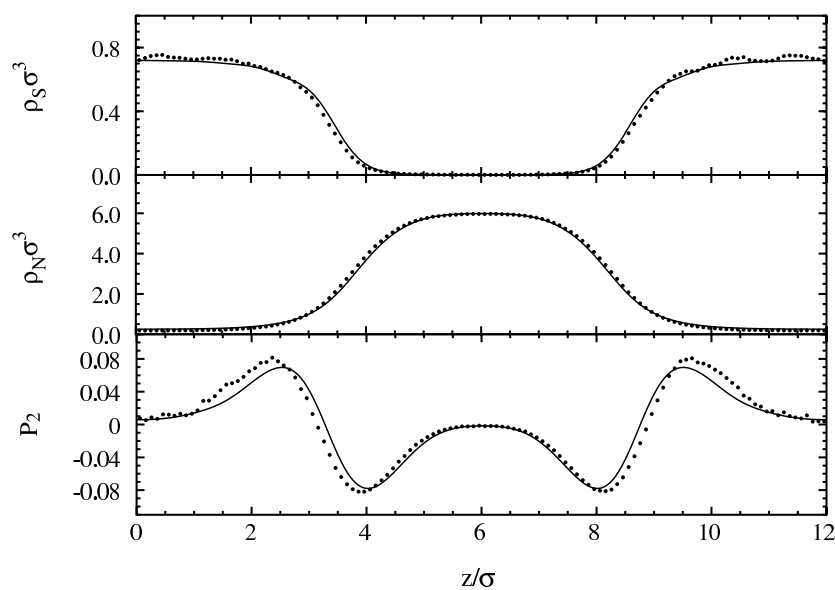


Figure 4. One-body distribution functions of the sphere–needle mixture as a function of the scaled coordinate z/σ normal to the free interface between deeply demixed fluid phases. The system is periodic in the z -direction with length 12σ ; the statepoint is in the deeply demixed regime, with $\eta = 0.2043$ and $\rho_N \sigma^3 = 2.3776$ (see statepoint A in figure 2). The size ratio is $L/\sigma = 3$. The results shown are from simulation (symbols) and theory (curves) for the sphere density profile $\rho_S(z)\sigma^3$ (upper panel), orientation-averaged needle density profiles $\rho_N(z)\sigma^3$ (middle panel) and orientation order parameter profile $P_2(z)$ (lower panel).

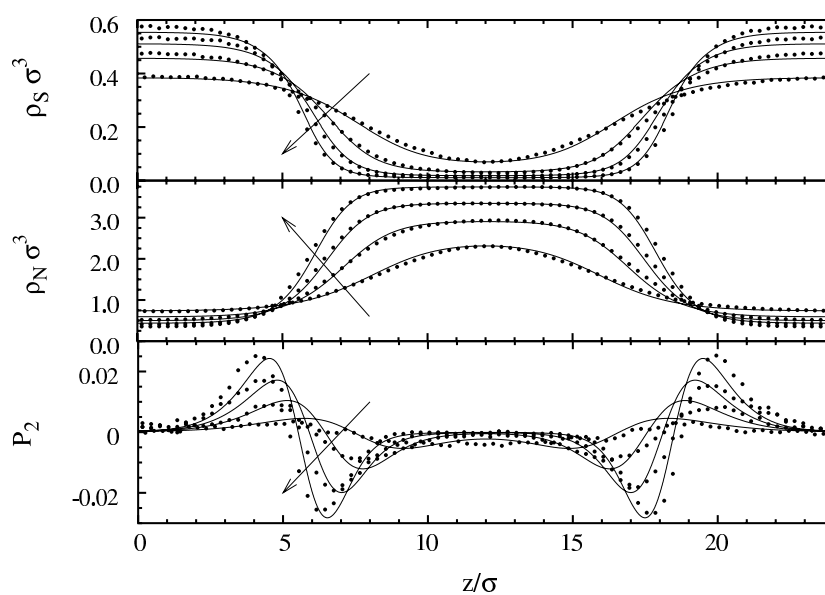


Figure 5. As figure 4, but for a sequence of statepoints with constant $\eta = 0.1363$ and increasing (in the direction of the arrow) needle density $\rho_N \sigma^3 = 1.3021, 1.5625, 1.8229$ and 2.083 (corresponding to the sequence of statepoints B in figure 2).

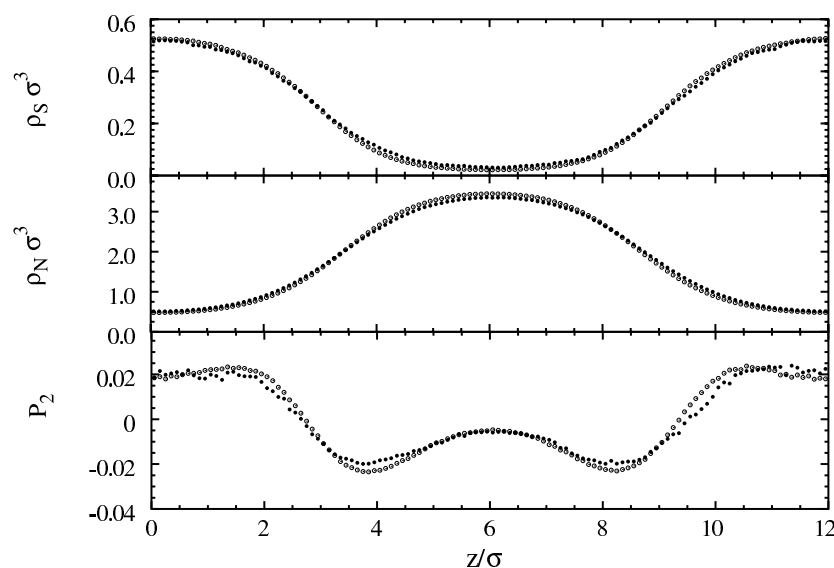


Figure 6. As figure 4 but for system length 12σ , $\eta = 0.1363$ and $\rho_N\sigma^3 = 1.8229$. Simulation results are shown for different lateral (perpendicular to the z -direction) system sizes: a small system with $M_S = 200$, $M_N = 700$ and lateral box area $32\sigma^2$ (open symbols), and a large system with $M_S = 800$, $M_N = 2800$ and lateral box area $128\sigma^2$ (filled symbols).

For completeness, we give the theoretical results for the surface tension γ . For the three high rod fugacities within sequence B, these are $\beta\gamma\sigma^2 = 0.500 \pm 0.003$, 0.343 ± 0.003 and 0.202 ± 0.006 , where the errors given are a conservative estimate and arise from the fact that the bulk values are not perfectly satisfied in the periodic geometry. For this reason no reliable value for γ at the statepoint closest to the critical point could be obtained.

As a final investigation, we compare simulation results for the same statepoint, but two different lateral (perpendicular to the z -direction) system sizes, differing by a factor of two in linear size (see figure 6). As expected, the larger system possesses slightly smoother profiles. However, the effect is small, and hence we trust that the simulation results do represent the ‘bare’ density profiles. We have not attempted a complete investigation of the influence of capillary waves, which would require much larger system sizes.

4. Conclusions

In conclusion, we have performed a detailed comparison between simulation and theoretical results for the free planar interface between demixed fluid states in a binary mixture of hard spheres and hard rods. The simulation results confirm the previously found ordering of the rods at the interface. While the alignment parallel to the interface on the needle-rich side can be understood in terms of packing against the sphere-rich phase, similar to packing of rods against a hard wall, the normal alignment inside the sphere-rich phase is more subtle. Consider a rod with fixed centre on the sphere-rich side close to the interface. Rotating this rod towards the surface normal will expose less of its shape to the spheres, and hence minimize collisions with spheres. This generates an entropic torque [25] that tends to align rods along the interface normal.

Very good quantitative agreement between results from simulation and theory for the density profiles of both species, as well as the orientation order parameter profile,

have been found. We have checked that the lateral system dimensions do not play a prominent role but have not attempted to do a systematic investigation of the influence of capillary waves on the interface structure.

We hope to stimulate experimental work on interfaces in rod–sphere mixtures. In particular, measuring the orientation order of rods either in real space or via the induced optical anisotropy would be a very interesting goal.

Acknowledgments

The work of MS is part of the research programme of the Stichting voor Fundamenteel Onderzoek der Materie (FOM), that is financially supported by the Nederlandse Organisatie voor Wetenschappelijk Onderzoek (NWO).

References

- [1] Bolhuis P and Frenkel D 1994 *J. Chem. Phys.* **101** 9869
- [2] Vliegthart G A and Lekkerkerker H N W 1999 *J. Chem. Phys.* **111** 4153
- [3] Koenderink G H, Vliegthart G A, Kluijtmans S G J M, van Blaaderen A, Philipse A P and Lekkerkerker H N W 1999 *Langmuir* **15** 4693
- [4] Chen Y L and Schweizer K S 2002 *J. Chem. Phys.* **117** 1351
- [5] Chen Y L and Schweizer K S 2002 *Langmuir* **18** 7354
- [6] Vliegthart G A 1999 *Dissertation* Utrecht University
- [7] Koenderink G H, Aarts D G A L, de Villeneuve V W A, Philipse A P, Tuinier R and Lekkerkerker H N W 2003 *Biomacromolecules* **4** 129
- [8] Evans R 1992 *Fundamentals of Inhomogeneous Fluids* ed D Henderson (New York: Dekker) p 85
- [9] Rosenfeld Y 1989 *Phys. Rev. Lett.* **63** 980
- [10] Rosenfeld Y 1994 *Phys. Rev. E* **50** R3318
- [11] Rosenfeld Y 1995 *Mol. Phys.* **86** 637
- [12] Schmidt M 2001 *Phys. Rev. E* **63** 050201(R)
- [13] Brader J M, Esztermann A and Schmidt M 2002 *Phys. Rev. E* **66** 031401
- [14] Yaman K, Jeppesen C and Marques C M 1998 *Europhys. Lett.* **42** 221
- [15] Roth R 2003 *J. Phys.: Condens. Matter* **15** S277
- [16] Roth R, Brader J M and Schmidt M 2003 *Europhys. Lett.* **63** 549
- [17] Lin K, Crocker J C, Zeri A C and Yodh A G 2001 *Phys. Rev. Lett.* **87** 088301
- [18] Lau A W C, Lin K H and Yodh A G 2002 *Phys. Rev. E* **66** 020401
- [19] Helden L, Roth R, Koenderink G H, Leiderer P and Bechinger C 2003 *Phys. Rev. Lett.* **90** 048301
- [20] Adams M, Dogic Z, Keller S L and Fraden S 1998 *Nature* **393** 349
- [21] van der Schoot P 2002 *J. Chem. Phys.* **117** 3537
- [22] Dijkstra M and van Roij R 2002 *Phys. Rev. Lett.* **89** 208303
- [23] Shundyak K and van Roij R 2001 *J. Phys.: Condens. Matter* **13** 4789
- [24] Frenkel D and Smit B 2002 *Understanding Molecular Simulations* 2nd edn (San Diego, CA: Academic)
- [25] Roth R, van Roij R, Andrienko D, Mecke K R and Dietrich S 2002 *Phys. Rev. Lett.* **89** 088301

Entropic wetting of a colloidal rod-sphere mixture

R. ROTH^{1,2}, J. M. BRADER³ and M. SCHMIDT^{4(*)}

¹ *Max-Planck-Institut für Metallforschung - Heisenbergstr. 3, 70569 Stuttgart, Germany*

² *ITAP, Universität Stuttgart - Pfaffenwaldring 57, 70569 Stuttgart, Germany*

³ *Institute of Physiology, University of Bern - Bühlplatz 5, 3012 Bern, Switzerland*

⁴ *Soft Condensed Matter, Debye Institute, Utrecht University
Princetonpln 5, 3584 CC Utrecht, The Netherlands*

(received 28 March 2003; accepted in final form 16 June 2003)

PACS. 68.08.Bc – Wetting.

PACS. 82.70.Dd – Colloids.

PACS. 64.70.Ja – Liquid-liquid transitions.

Abstract. – We investigate the behavior of a model colloidal mixture of hard spheres and rod-like particles near a planar hard wall using density functional theory. For small size ratios of rod length and sphere diameter we find that the colloidal liquid phase wets the wall completely upon approaching the fluid demixing binodal from the colloidal gas side, provided the density of the rods lies below the wetting point. Using an effective one-component description based on the pairwise depletion potential for higher density of rods, a finite sequence of layering phase transitions is found. For large rod-to-sphere size ratios, using a binary treatment, thick films are obtained even close to the triple point.

Purely repulsive interactions between the constituent mesoscopic particles may lead to surprisingly rich bulk phase behavior of multi-component colloidal suspensions. Such systems are often viewed as a primary system of colloids with added “depletant agents” that mediate an effective interaction between the particles of the primary component. Adding depletant agents to a colloidal hard-sphere dispersion may, under appropriate conditions, drive a fluid-fluid demixing phase transition, which is reminiscent of the gas-liquid transition in atomic and molecular fluids: The phase that is poor in colloids (and rich in depletants) corresponds to the gas and the phase that is rich in colloids (and poor in depletants) corresponds to the liquid phase. Among the broad range of depletant agents notable examples are smaller-sized spheres and globular non-adsorbing polymers. Another case of intriguing depletants are elongated particles, like colloidal rods or stretched polymers. One reason for such depletants being very interesting is the possibility of liquid-crystalline order, which will further enrich the bulk phase behavior [1] and the correlations between spheres [2].

For conditions where the density of rods is well below the onset of nematic order, much work has been devoted to understanding the bulk phase behavior of rod-sphere mixtures [3–8]. Among the different techniques employed are computer simulations [3], free-volume [3, 4] and liquid integral equation [5] theories, as well as experiments with silica spheres mixed with silica-coated bohemite rods [4, 6] or (semi-flexible) polymeric rods [7, 8]. It can be concluded

(*) On leave from Institut für Theoretische Physik II, Heinrich-Heine-Universität Düsseldorf - Universitätsstraße 1, D-40225 Düsseldorf, Germany.

that the gas, fluid, and solid phase are thermodynamically stable and that the density of rods (often one uses the density in a hypothetical reservoir of rods) plays a role similar to that of inverse temperature in simple fluids. The second control parameter is the ratio of rod length L and sphere diameter σ ; for large enough values stable bulk fluid-fluid demixing occurs.

One approach to describe such complex systems is based on the depletion picture where the depletants are regarded as mediating an effective interaction between the spheres [9–13]. Theoretically, one integrates out the depletant degrees of freedom in the partition sum [9, 13] to obtain the effective interactions, which have, in general, a many-body character. Under suitable conditions one may take into account only the one- and two-body contributions. Experimentally, one can measure the forces directly, *e.g.*, between two spheres [10] or between a sphere and a wall [12] immersed in a sea of rods.

Despite the considerable interest in the bulk properties of rod-sphere mixtures little is known about their behavior at interfaces. This is in contrast to the case of mixtures of colloidal spheres and globular non-adsorbing polymer, where recent results [14–16] indicate surprisingly rich behavior at a simple hard wall. Theoretical predictions of wetting and layering surface phase transitions [14] have been validated by computer simulations [15] and, partly, experimentally [16, 17], in particular by light microscopy in a mixture of silica spheres and poly(dimethyl siloxane) dispersed in cyclohexane [16]. The emerging picture is that the colloidal liquid wets the wall completely for sufficiently low polymer concentrations (on the gas-branch of the gas-liquid binodal). For higher polymer concentrations, partial wetting occurs via an unusual (finite) sequence of layering transitions, which has been attributed to the presence of many-body effective depletion interactions between the colloidal spheres [14, 15]. The layering behavior has not yet been experimentally confirmed.

In this letter we report on density functional [18] results for the interface behavior of a model rod-sphere mixture exposed to a hard wall. For equally sized species we find that the colloidal liquid wets the wall completely upon approaching the gas branch of the demixing binodal for low rod densities. There occurs a first-order wetting transition to the partial-wetting regime for higher rod densities. In the partial-wetting regime we can identify a finite number of distinct lines where a jump in the adsorption occurs. These results are obtained by a treatment that only includes the pair-wise contribution to the depletion interaction, and hence questions the above conjecture that many-body terms are a prerequisite for the occurrence of a finite sequence of layering transitions in the partial-wetting regime. We test the robustness of these results: Complete wetting remains upon including all higher body interactions, *i.e.* treating the full mixture. For longer rod-sphere size ratios, thick films result even for high rod densities, *i.e.* close to the triple point.

We use a model proposed in [3] and employed by others [5, 9, 13, 19, 20] that can be viewed as the most simplistic binary mixture that still captures the essentials: Hard spheres (species S) of diameter σ are mixed with hard needle-like rods (species N) of length L and vanishing thickness. The one-body density distributions are denoted by $\rho_S(\mathbf{r})$ and $\rho_N(\mathbf{r}, \hat{\omega})$, where \mathbf{r} is the space coordinate and the unit vector $\hat{\omega}$ is the (rod) orientation. This mixture is exposed to a planar smooth hard wall described by external hard-core potentials, $V_{\text{ext}}^S(\mathbf{r})$ and $V_{\text{ext}}^N(\mathbf{r}, \hat{\omega})$. Due to the symmetries of fluid states the only two relevant variables are the component of \mathbf{r} perpendicular to the wall, z , and the angle between $\hat{\omega}$ and the surface normal.

In the following a brief overview of the theory is given. In the *binary treatment* the grand potential is expressed as a functional of the density fields of both species,

$$\begin{aligned} \Omega_{\text{bin}}[\rho_S, \rho_N] = & F_{\text{id}}[\rho_S] + F_{\text{id}}[\rho_N] + F_{\text{exc}}^{\text{hs}}[\rho_S] + F_{\text{exc}}^{\text{SN}}[\rho_S, \rho_N] + \\ & + \int d\mathbf{r} \rho_S(\mathbf{r}) \left(V_{\text{ext}}^S(\mathbf{r}) - \mu_S \right) + \int d\mathbf{r} d\hat{\omega} \rho_N(\mathbf{r}, \hat{\omega}) \left(V_{\text{ext}}^N(\mathbf{r}, \hat{\omega}) - \mu_N \right), \quad (1) \end{aligned}$$

where the ideal-gas contribution is for spheres $F_{\text{id}}[\rho_{\text{S}}] = kT \int d\mathbf{r} \rho_{\text{S}}(\mathbf{r}) (\ln(\rho_{\text{S}}(\mathbf{r}) \Lambda_{\text{S}}^3) - 1)$ and for rods $F_{\text{id}}[\rho_{\text{N}}] = kT \int d\mathbf{r} d\hat{\omega} \rho_{\text{N}}(\mathbf{r}, \hat{\omega}) (\ln(\rho_{\text{N}}(\mathbf{r}, \hat{\omega}) \Lambda_{\text{N}}^3) - 1)$, where k is Boltzmann's constant, T is temperature, and Λ_i is the thermal wavelength of species $i = \text{S}, \text{N}$. The excess (over ideal gas) parts are Rosenfeld's functional [21] for hard spheres, $F_{\text{exc}}^{\text{hs}}[\rho_{\text{S}}]$, and the rod-sphere contribution, $F_{\text{exc}}^{\text{SN}}[\rho_{\text{S}}, \rho_{\text{N}}]$, of refs. [19, 20]. Clearly, the minimization of the grand potential needs to be performed with respect to both species, *i.e.* we solve simultaneously $\delta\Omega_{\text{bin}}/\delta\rho_{\text{S}}(\mathbf{r}) = 0$ and $\delta\Omega_{\text{bin}}/\delta\rho_{\text{N}}(\mathbf{r}, \hat{\omega}) = 0$. For practical reasons the angle between $\hat{\omega}$ and the surface normal of the wall is discretized in 60 steps, hence the latter condition is in fact a set of equations indexed by $\hat{\omega}$, see [20] for further details about the numerical strategy. This treatment takes into account all effective many-body terms, but is computationally demanding.

In the *effective one-component description* depletion potentials between spheres, W_{SS} , and between a sphere and the wall, W_{SW} , are obtained by integrating out the rod degrees of freedom [13]. Then the grand potential depends only on the sphere density distribution,

$$\begin{aligned} \Omega_{\text{eff}}[\rho_{\text{S}}] = & F_{\text{id}}[\rho_{\text{S}}] + F_{\text{exc}}^{\text{hs}}[\rho_{\text{S}}] + \frac{1}{2} \int d\mathbf{r} d\mathbf{r}' \rho_{\text{S}}(\mathbf{r}) K(|\mathbf{r} - \mathbf{r}'|) \rho_{\text{S}}(\mathbf{r}') + \\ & + \int d\mathbf{r} \rho_{\text{S}}(\mathbf{r}) \left(V_{\text{ext}}^{\text{S}}(\mathbf{r}) + W_{\text{SW}}(\mathbf{r}) - \mu_{\text{S}} \right), \end{aligned} \quad (2)$$

where the depletion attraction is treated in a mean-field-like manner [22]: The convolution kernel is $K(r) = W_{\text{SS}}(r)$ for $r \geq \sigma$, and $K(r) = W_{\text{SS}}(\sigma^+)$ for $r < \sigma$. Note that this is a particularly clean application of the framework: No mapping of a soft repulsion onto a hard-sphere reference system is to be performed; σ is the true physical particle size and $W_{\text{SS}}(\sigma^+)$ is the minimal value of the pair potential. The particular choice of $K(r < \sigma)$ to treat attractive interactions has been empirically found to improve the agreement between DFT and other theories. Due to the rod ideality, the depletion potentials W_{SW} and W_{SN} depend linearly on ρ_{N}^r , which is the density in an (ideal) reservoir of needles that is in chemical equilibrium with the system. ρ_{N}^r thus plays a role analogous to that of inverse temperature in simple fluids. Due to the particle geometries higher than two-body contributions vanish only for size ratios $L/\sigma < 1 - (2\sqrt{3} - 3)^{1/2} = 0.31875$. The crucial benefit of the one-component approach is that one has to deal with only one single minimization condition: $\delta\Omega_{\text{eff}}/\delta\rho_{\text{S}}(\mathbf{r}) = 0$.

From either approach the bulk free energy for fluid states is obtained by assuming the density field(s) to be constant. As thermodynamic variables we use the sphere packing fraction $\eta = \pi\rho_{\text{S}}\sigma^3/6$ and a scaled rod reservoir density, $\rho_{\text{N}}^r L^2\sigma$. The conditions of equal pressure and chemical potentials of both species yield the phase diagram as a function of η and ρ_{N}^r , as displayed in fig. 1 for $L/\sigma = 1$, which is large enough (> 0.3) so that a liquid phase exists [3]. For ρ_{N}^r above the critical point, phase separation occurs into a gas phase that is dilute in spheres and a liquid phase that is dense in spheres; phase coexistence is along horizontal tie lines at constant ρ_{N}^r . The free energy obtained from the binary treatment [19] is the same as that of [3], and was shown to give good account of the simulated coexistence curve [3]. The binodal from the effective treatment has the same qualitative behavior, the critical point, and accordingly the whole binodal, being shifted slightly toward lower densities. Comparing structure at two statepoints in the mixed region away from coexistence yields a further comparison of the consistency of both approaches; see fig. 2 for results for $\rho_{\text{S}}(z)$ at a hard wall. As a reference, corresponding profiles for the pure hard-sphere case (for the same values of η) are displayed. Clearly, the addition of rods leads to a strong increase near contact with the wall, $0.5 < z/\sigma < 0.7$, as well as an increase in the contact value, $\rho_{\text{S}}(\sigma^+/2)$, itself—the manifestation of the depletion effect. Remarkably, the results from both approaches are identical on the scale of the plot, except for a slightly higher contact value of the one-

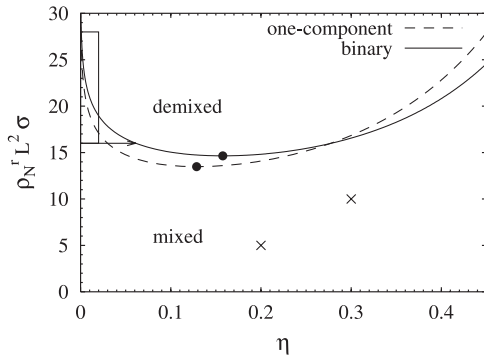


Fig. 1

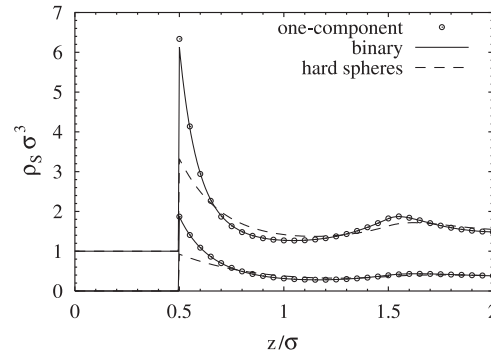


Fig. 2

Fig. 1 – Fluid-fluid demixing phase diagram for the rod-sphere mixture as a function of the sphere packing fraction, η , and scaled needle reservoir density, $\rho_N^r L^2 \sigma$, for size ratio $L/\sigma = 1$. The binodal (lines) and critical point (dots) from the binary and the effective one-component DFT are shown. Coexistence is along horizontal tie lines (not shown). The crosses mark statepoints where wall density profiles from both theories are compared in fig. 2. The arrow indicates a path along which wetting profiles are presented in fig. 3. The rectangle near the vertical axis indicates the region where the surface phase transitions near a hard wall are investigated in figs. 4 and 5.

Fig. 2 – Sphere density profiles, $\rho_S(z)\sigma^3$, at a hard wall as a function of the scaled distance, z/σ , from the wall for size ratio $L/\sigma = 1$ at two statepoints (marked by crosses in fig. 1): $\eta = 0.2$, $\rho_N^r L^2 \sigma = 5$ and $\eta = 0.3$, $\rho_N^r L^2 \sigma = 10$ (shifted upwards one unit for clarity). For comparison, the corresponding hard-sphere results (for the same values of η but $\rho_N^r = 0$) are displayed. Except for the region very near to contact with the wall ($z/\sigma \approx 0.5$) in the case of the higher packing fraction, the results from both theories are indistinguishable on the scale of the plot.

component treatment for the statepoint with higher densities. The good overall agreement for phase behavior and structure thus provides a solid basis for our subsequent interface study.

We first approach the gas branch of the fluid demixing binodal not too far from the critical point at $\rho_N^r \sigma L^2 = 16$ and increasing η , as indicated by the arrow in the phase diagram, fig. 1. A representative set of wall density profiles approaching coexistence is depicted in fig. 3 obtained from the one-component (upper panel) and binary (lower panel) treatments. Close to the wall, pronounced oscillations appear that can be attributed to packing effects of the spheres. For increasing z , the crossover to the low gas bulk density occurs via an intermediate plateau value of liquid-like density. The thickness of this region grows, and eventually diverges, upon approaching coexistence. The wall is wet completely by the colloidal liquid phase. The profiles from the one-component treatment possess a markedly thinner wetting film and a sharper interface of the liquid-gas part than those from the binary treatment. This is consistent with the difference in bulk phase diagrams. For the fixed value of ρ_N^r , the binary theory is relatively closer to its critical point, hence thicker films and broader liquid-gas interfaces are expected. We can, however, get similar wetting film thicknesses from the one-component treatment by going even closer to coexistence; an example of $\rho_S(z)$ is shown in fig. 3 (dashed line). Both theories consistently predict complete wetting, differences in the detailed structure can be fully understood from the differences in the respective bulk phase diagrams.

Having gained confidence into the one-component description, we use this computationally efficient approach to calculate the full surface phase diagram. As a first path we scan the phase diagram right at coexistence along the gas branch of the binodal by decreasing ρ_N^r (and

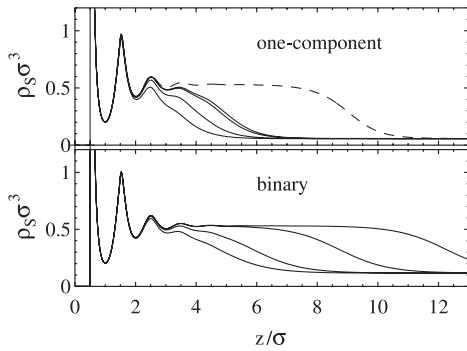


Fig. 3

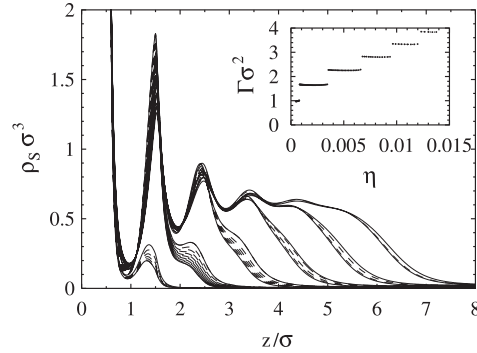


Fig. 4

Fig. 3 – Wetting density profiles, $\rho_S(z)\sigma^3$, as a function of the scaled distance from the wall, z/σ , for needle reservoir density $\rho_N^r L^2\sigma = 16$ following the path marked in fig. 1 and obtained from the one-component (upper panel) and the binary (lower panel) treatment. The profiles are for $(\eta_{\text{coex}} - \eta)/\eta_{\text{coex}} = 0.01305, 0.004894, 0.001631, 0.001305$ (from left to right); coexistence is at $\eta_{\text{coex}} = 0.06130$ (binary), 0.02994 (one-component). The dashed line in the upper panel indicates the one-component result even closer to coexistence, $(\eta_{\text{coex}} - \eta)/\eta_{\text{coex}} = 5.77 \cdot 10^{-6}$.

Fig. 4 – Sequence of sphere density profiles, $\rho_S(z)\sigma^3$, as a function of the scaled distance from the wall, z/σ , obtained from the one-component treatment for statepoints at coexistence moving down the gas-branch of the fluid demixing binodal. Density profiles from left to right correspond to increasing η and decreasing $\rho_N^r L^2\sigma$, spaced in steps of $\Delta\rho_N^r L^2\sigma = 0.04$ (dashed lines). Five pronounced jumps occur, the corresponding density profiles at these layering transitions are indicated by solid lines. The inset shows the corresponding adsorption $\Gamma\sigma^2$ as a function of η .

accordingly increasing η). Our aim is to stay below the triple point, which is obtained from perturbation theory at $\rho_N^r \approx 25$ [3]. For high ρ_N^r the excess adsorption, $\Gamma = \int dz(\rho_S(z) - \rho_S(\infty))$, is finite at coexistence, *i.e.* the liquid wets the wall partially. Decreasing ρ_N^r continuously leads to several (five) jumps in the density profiles and correspondingly in Γ , see fig. 4. The sixth jump is that to a bulk liquid, *i.e.* the wetting point. Along our chosen path all layering transitions and the wetting transition are first order.

To reveal the full surface phase diagram we have covered the region of stability of the gas phase in the phase diagram on a fine grid. From anomalies in the density profiles, *i.e.* from jumps in Γ , the full surface phase diagram is constructed, see fig. 5 for the result. Due to our method of locating the interfacial transitions, their exact location is subject to some hysteresis effects. By calculating the adsorption along the reverse path, *i.e.* along the binodal from low ρ_N^r to high ρ_N^r , we could confirm that these effects are very small. We find that the five layering transitions all extend into the bulk gas region. Moving away from coexistence along such a layering line the jump in the adsorption decreases in magnitude and eventually ends in a critical point. The first layering transition is very pronounced, the subsequent transition lines decrease in length. The transition point on the binodal closest to the critical point is the wetting point; for rod densities below the corresponding value (and above the critical point), complete wetting occurs. We could not find the corresponding prewetting line where a transition from a thin to a thick line appears, and conclude that it is too small to be identified within our current numerical accuracy.

The whole pattern of surface phase transitions found from this description using pair potentials is very similar to that recently found in a related model colloid-polymer mixture taking

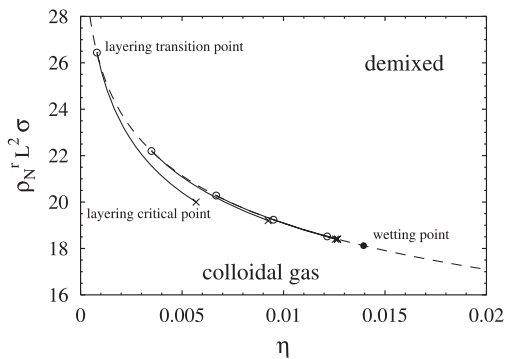


Fig. 5

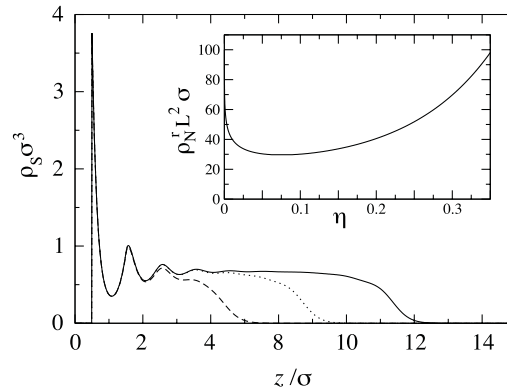


Fig. 6

Fig. 5 – Surface phase diagram of the rod-sphere mixture at a hard wall as a function of the sphere packing fraction, η , and scaled needle reservoir density, $\rho_N^r L^2 \sigma$, for size ratio $L/\sigma = 1$ obtained from the one-component theory. Shown are the bulk fluid demixing binodal (dashed line), layering transition points on the binodal (open circles), layering transition lines (solid lines), layering critical points (crosses), and wetting point (filled circle). The plot range corresponds to the rectangle in fig. 1.

Fig. 6 – Sphere density profiles $\rho_S(z)\sigma^3$ as a function of the distance z/σ from the wall for size ratio $L/\sigma = 5$, needle reservoir density $\rho_N^r = 100$ and increasing bulk colloid packing fraction $\eta = 1.04 \cdot 10^{-5}$ (dashed line), $1.06 \cdot 10^{-5}$ (dotted line) and $1.065 \cdot 10^{-5}$ (full line) obtained from the binary theory. Coexistence is at $\eta_{\text{coex}} = 1.077 \cdot 10^{-5}$. The inset shows the fluid demixing binodal as a function of η and needle reservoir density ρ_N^r for $L/\sigma = 5$.

into account all many-body interactions between colloids, *i.e.* treating the full binary mixture [14,15]. In that case, the inclusion of many-body terms is crucial; no layering transitions were found from a pair-wise treatment [14].

We believe that the occurrence of layering phase transitions is due to a subtle interplay between the relative strength of the particle-particle and the particle-wall attractions. Due to the particle geometries for the present case of rod depletants, the particle-wall attraction is relatively stronger than in the case of spherical (polymer) depletants. In that case a similar (relative) strengthening of the wall-particle attraction can happen due to the many-body terms. As a test for this hypothesis we have rescaled the wall-particle attraction, *i.e.* used $\lambda W_{\text{SW}}(z)$, $0 \leq \lambda \leq 1$, which artificially interpolates between the actual physical situation ($\lambda = 1$) and a (hypothetical) wall without depletion attraction ($\lambda = 0$). Indeed we find for $\lambda = 0.5$ complete wetting without any indications of layering transitions anywhere in the partial-wetting regime.

As a final investigation we consider a case of markedly longer rods: $L/\sigma = 5$. We expect many-body terms in the effective Hamiltonian to be important and that the effective one-component description with pair-wise interactions only will break down. In fact the phase diagram resulting from the one-component treatment is no longer comparable to the still rather accurate [3] binary treatment. From the binary DFT we find that thick films can be obtained even far away from the critical point, see fig. 6 for profiles close to the triple point at $\rho_N^r L^2 \sigma = 100$ [23]. Hence for observing thick films in experiment large L/σ are suitable.

In conclusion, we have investigated the adsorption properties of a colloidal mixture of rods and spheres at a hard wall. We find that for low rod densities the sphere liquid wets the wall completely upon approaching the fluid-fluid demixing binodal from the gas side. For high rod densities, above the wetting point, partial wetting occurs via a finite sequence of

layering phase transitions, where the adsorption jumps by finite increments. We argue that the crucial parameter for the occurrence of such layering transitions is the relative strength of wall-particle and particle-particle depletion interactions.

Colloidal mixtures of rods and spheres can be prepared so that they closely resemble the model system of hard spheres and needles [12] considered here. Therefore, our findings should be experimentally observable. In particular, it would be highly interesting to observe thick wetting films in the complete-wetting regime, *e.g.* with light [16] or confocal microscopy.

* * *

We thank R. EVANS for many inspiring discussions and R. VAN ROIJ and M. DIJKSTRA for valuable comments. The work of MS is part of the research program of FOM, that is financially supported by the Nederlandse Organisatie voor Wetenschappelijk Onderzoek (NWO).

REFERENCES

- [1] ADAMS M., DOGIC Z., KELLER S. L. and FRADEN S., *Nature (London)*, **393** (1998) 349.
- [2] VAN DER SCOOT P., *J. Chem. Phys.*, **117** (2002) 3537.
- [3] BOLHUIS P. and FRENKEL D., *J. Chem. Phys.*, **101** (1994) 9869.
- [4] Vliegenthart G. A. and Lekkerkerker H. N. W., *J. Chem. Phys.*, **111** (1999) 4153.
- [5] CHEN Y. L. and SCHWEIZER K. S., *J. Chem. Phys.*, **117** (2002) 1351; *Langmuir*, **18** (2002) 7354.
- [6] KOENDERINK G. H., Vliegenthart G. A., Kluijtmans S. G. J. M., van Blaaderen A., Philipse A. P. and Lekkerkerker H. N. W., *Langmuir*, **15** (1999) 4693.
- [7] Vliegenthart G. A., Dissertation, Utrecht University (1999).
- [8] KOENDERINK G. H., AARTS D. G. A. L., DE VILLENEUVE V. W. A., PHILIPSE A. P., TUINIER R. and Lekkerkerker H. N. W., *Biomacromolecules*, **4** (2003) 129.
- [9] YAMAN K., JEPPESEN C. and MARQUES C. M., *Europhys. Lett.*, **42** (1998) 221.
- [10] LIN K., CROCKER J. C., ZERI A. C. and YODH A. G., *Phys. Rev. Lett.*, **87** (2001) 088301.
- [11] LAU A. W. C., LIN K. H. and YODH A. G., *Phys. Rev. E*, **66** (2002) 020401.
- [12] HELDEN L., ROTH R., KOENDERINK G. H., LEIDERER P. and BECHINGER C., *Phys. Rev. Lett.*, **90** (2003) 048301.
- [13] ROTH R., *J. Phys. Condens. Matter*, **15** (2003) S277.
- [14] BRADER J. M., EVANS R., SCHMIDT M. and LÖWEN H., *J. Phys. Condens. Matter*, **14** (2002) L1.
- [15] DIJKSTRA M. and VAN ROIJ R., *Phys. Rev. Lett.*, **89** (2002) 208303.
- [16] AARTS D. G. A. L., VAN DER WIEL J. H. and Lekkerkerker H. N. W., *J. Phys. Condens. Matter*, **15** (2003) S245.
- [17] WIJTING W. K., BESSELING N. A. M. and COHEN STUART M. A., unpublished.
- [18] See, *e.g.*, EVANS R., in *Fundamentals of Inhomogeneous Fluids*, edited by HENDERSON D. (Marcel Dekker, New York) 1992, p. 85.
- [19] SCHMIDT M., *Phys. Rev. E*, **63** (2001) 050201(R).
- [20] BRADER J. M., ESZTERMANN A. and SCHMIDT M., *Phys. Rev. E*, **66** (2002) 031401.
- [21] ROSENFELD Y., *Phys. Rev. Lett.*, **63** (1989) 980.
- [22] WEEKS J. D., CHANDLER D. and ANDERSEN H. C., *J. Chem. Phys.*, **54** (1971) 5237.
- [23] We take η_{coex} determined by the numerical minimization of the DFT; the result from the analytic free energy is $\eta_{\text{coex}} = 1.0598 \cdot 10^{-4}$.

Density functional theory for sphere-needle mixtures: Toward finite rod thickness

Ansgar Esztermann

Institut für Theoretische Physik II, Heinrich-Heine-Universität Düsseldorf, Universitätsstraße 1, D-40225 Düsseldorf, Germany

Matthias Schmidt*

Soft Condensed Matter, Debye Institut, Utrecht University, Princetonplein 5, 3584 CC Utrecht, The Netherlands

(Received 23 April 2004; published 4 August 2004)

For mixtures of hard spheres and hard spherocylinders of large aspect ratio a recently proposed density functional theory is extended to incorporate effects due to nonvanishing rod thickness. This is accomplished by introducing several new geometric weight functions into the framework. We demonstrate explicitly how these weight functions recover the sphere-rod Mayer bond.

DOI: 10.1103/PhysRevE.70.022501

PACS number(s): 61.20.Gy, 82.70.Dd, 61.30.Cz, 64.70.Ja

Mixtures of colloidal spheres and mesoscopic rods, like colloidal rods or stiff polymer chains, suspended in a molecular solvent, are well-characterized model systems governed by steric (excluded volume) forces [1–6]. Interesting questions concern the bulk phase behavior and effective sphere–sphere and sphere–wall interactions mediated by the presence of the rods [3,6]. Based on Rosenfeld’s fundamental-measure theory for mixtures of nonconvex bodies [7,8], recently a density-functional theory (DFT) [9] for a minimal model of hard sphere colloids and infinitely thin needles [10] was proposed [11] and used to investigate the structure of the interface between sphere-rich and sphere-poor phases [12,13], and the wetting behavior of a hard wall [14]. This binary DFT proved to predict phase behavior accurately compared to the simulation results of [10], and to give high-quality results for (fluid) density profiles in inhomogeneous situations, when compared both to results from an effective one-component treatment [14] using the depletion potential between spheres [15,16], and to computer simulation results of the free fluid–fluid interface of the binary mixture [13]. By combining Yu and Wu’s functional for mixtures of polymeric fluids [17] and the theory of Ref. [11], Bryk arrived at a DFT for binary mixtures of hard rods and polymer chains [18].

In all these cases, the rods are assumed to have vanishing thickness. Due to the geometry, the statistical weight of configurations with overlapping rods vanishes, and hence the rods behave as though being ideal. (The rod–sphere interaction is unaffected by this argument and is governed by excluded volume.) Rosenfeld’s theory when applied to a mixture of hard spheres of finite (large) packing fraction and a second component of (thick) spherocylinders at vanishing density was shown to predict the entropic force and torque on the rod near a hard wall very accurately [19] and more general cases have also been considered [20].

In order to capture effects of finite rod thickness *and* finite rod density an extension to the theory for vanishingly thin

rods [11] was made in Ref. [12], incorporating the Onsager limit of the rods [21], hence recovering exactly the rod–rod Mayer bond in the limit of large aspect ratio. The Onsager model continues to be a valuable system to study the properties of anisometric particles, see, e.g., Refs. [22–24] for recent work. Cinacchi and Schmid proposed a DFT for general anisotropic particles interpolating between the Rosenfeld and the Onsager functional [25]. The theory of Ref. [12] is, however, restricted to the limit of $LD/\sigma^2 \ll 1$ where L and D are the rod length and thickness, respectively, and σ is the sphere diameter.

In the present contribution, we extend the framework, restricting ourselves still to the Onsager limit of $L/D \gg 1$. This is accomplished by introducing several new geometric weight functions. We demonstrate how these weight functions recover the leading order contribution (in D) to the rod–sphere Mayer bond. Our model is a binary mixture of hard spheres (species S) of diameter σ and hard needlelike spherocylinders (species N) with length L (of the cylindrical part) and diameter D . This is considered in the (Onsager) limit of large rod aspect ratio of length-to-thickness, $L/D \gg 1$. The one-body density distributions of spheres and needles are denoted by $\rho_S(\mathbf{r})$ and $\rho_N(\mathbf{r}, \mathbf{\Omega})$, respectively, where \mathbf{r} is the position coordinate (pointing to the center of the respective particle shape) and $\mathbf{\Omega}$ is a unit vector describing the needle orientation.

We start by defining the density functional. In order to not duplicate material, explicit expressions are given only for the new quantities. We refer the reader directly to Ref. [12] for a full account of the known terms. We do, however, discuss the relation to the sphere–rod Mayer bond in detail below. The Helmholtz excess (over ideal gas) free energy functional is expressed as

$$F_{\text{exc}}[\rho_S, \rho_N] = k_B T \int d^3r \int \frac{d^2\Omega}{4\pi} \Phi(\{n_i^\alpha\}), \quad (1)$$

where k_B is the Boltzmann constant and T is temperature, n_i^α are weighted densities that are obtained through convolutions of the bare density profiles with geometric weight functions w_i^α ; α refers to the particle species and i refers to the type of weighted density. The weight functions w_i^α are obtained by

*On leave from: Institut für Theoretische Physik II, Heinrich-Heine-Universität Düsseldorf, Universitätsstraße 1, D-40225 Düsseldorf, Germany.

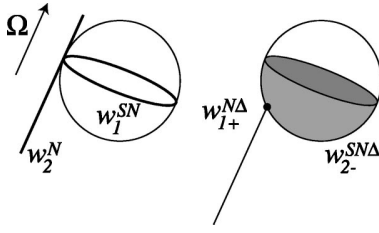


FIG. 1. Illustration of the geometry of the weight functions: w_2^N describes the residual rod surface (thick line), w_1^{SN} is nonvanishing on the equator of the sphere (bold circle), $w_{1\pm}^{N\Delta}$ corresponds to one rod endcap (dot), and $w_{2\pm}^{SN\Delta}$ describes a hemisphere (gray).

imposing the correct (second order) low-density behavior of (1); this is achieved by the so-called deconvolution of the Mayer bond, which we will turn to below. The functional form of Φ is obtained from consideration of the dimensional crossover [26,27] and scaled-particle ideas [28].

The weight functions necessary to recover the Mayer bond are found to be

$$w_1^{SN}(\mathbf{r}, \mathbf{\Omega}) = (2\pi)^{-1} \delta(\mathbf{r} \cdot \mathbf{\Omega}) \delta(R - r), \quad (2)$$

$$w_{2\pm}^{SN\Delta}(\mathbf{r}, \mathbf{\Omega}) = \delta(R - r) \Theta(\pm \mathbf{\Omega} \cdot \mathbf{r}), \quad (3)$$

$$w_{1\pm}^{N\Delta}(\mathbf{r}, \mathbf{\Omega}) = (D/2) \delta(\mathbf{r} \pm L\mathbf{\Omega}/2), \quad (4)$$

$$w_2^N(\mathbf{r}, \mathbf{\Omega}) = \pi D \int_{-L/2}^{L/2} dl \delta(\mathbf{r} + \mathbf{\Omega}l), \quad (5)$$

where $R = \sigma/2$ is the sphere radius, $\delta(\cdot)$ is the Dirac distribution, $\Theta(\cdot)$ is the stepfunction, and $r = |\mathbf{r}|$. We use “mixed” weight functions that depend on properties of both species (see Fig. 1 for illustrations). w_1^{SN} describes the “equator” of the sphere, where the polar axis is pointing into the direction given by the (needle) orientation $\mathbf{\Omega}$. $w_{2\pm}^{SN\Delta}$ describes the “northern” (subscript +) and “southern” (subscript -) hemisphere. Hence, $w_{2+}^{SN\Delta} + w_{2-}^{SN\Delta} = w_2^S$, where w_2^S is the usual sphere surface weight function [28]. The rod endcaps are described by $w_{1\pm}^{N\Delta}$, where $w_{1+}^{N\Delta} + w_{1-}^{N\Delta} = Dw_0^N$ (as defined in Ref. [11]). The weight function w_2^N makes the dimensional analysis consistent [7,8], and is proportional to a known weight, $w_2^N = 4\pi D w_1^N$, where w_1^N is given in [11] and obtained directly through [7,8].

Weighted densities are built using spatial convolution, but retaining the angular dependence:

$$n_1^{SN}(\mathbf{x}, \mathbf{\Omega}) = \int d^3r \rho_S(\mathbf{r}) w_1^{SN}(\mathbf{x} - \mathbf{r}, \mathbf{\Omega}), \quad (6)$$

$$n_{2\pm}^{SN\Delta}(\mathbf{x}, \mathbf{\Omega}) = \int d^3r \rho_S(\mathbf{r}) w_{2\pm}^{SN\Delta}(\mathbf{x} - \mathbf{r}, \mathbf{\Omega}), \quad (7)$$

$$n_{1\pm}^{N\Delta}(\mathbf{x}, \mathbf{\Omega}) = \int d^3r \rho_N(\mathbf{r}, \mathbf{\Omega}) w_{1\pm}^{N\Delta}(\mathbf{x} - \mathbf{r}, \mathbf{\Omega}), \quad (8)$$

$$n_2^N(\mathbf{x}, \mathbf{\Omega}) = \int d^3r \rho_N(\mathbf{r}, \mathbf{\Omega}) w_2^N(\mathbf{x} - \mathbf{r}, \mathbf{\Omega}). \quad (9)$$

Note that orientation-dependent *sphere* densities are built via (6) and (7).

Following Rosenfeld’s dimensional analysis [7,8,28], and in accordance with the scaled-particle theory for mixtures of non-spherical particles [29], the (reduced) free energy density is found to be $\Phi = \Phi_S + \Phi_{SN} + \Phi_{SNN} + \Delta\Phi$, where Φ_S is the hard sphere term [28], Φ_{SN} is the contribution in the case of infinitely thin needles [11], and Φ_{SNN} is the correction in the Onsager limit [12] with $LD/\sigma^2 \ll 1$; these terms are given explicitly in Eqs. (11), (12), and (17) of Ref. [12], respectively. The new contribution is

$$\Delta\Phi = \frac{n_1^{SN} n_2^N + n_{1+}^{N\Delta} n_{2-}^{SN\Delta} + n_{1-}^{N\Delta} n_{2+}^{SN\Delta}}{1 - n_3^S}, \quad (10)$$

where $n_3(\mathbf{r}) = \Theta(R - |\mathbf{r}|) \rho_S(\mathbf{r})$ is the usual local packing fraction for spheres. This completes the prescription of the functional.

The corresponding fundamental measures, ξ_{α}^i = $\int d^3r \int d^2\Omega w_{\alpha}^i / (4\pi)$, are

$$\xi_1^{SN} = R, \quad \xi_{2\pm}^{SN\Delta} = 2\pi R^2, \quad \xi_{1\pm}^{N\Delta} = D/2, \quad \xi_2^N = \pi LD, \quad (11)$$

equal to the integral mean curvature of the sphere, surface of a hemisphere of radius R , radius of a hemispherical endcap of the rod, and residual (for small D/L) rod surface, respectively.

The exact second virial coefficient between sphere and rod is

$$B_2^{SN} = \pi R^2 \left(L + \frac{4R}{3} \right) + \pi DR(L + 2R) + \pi D^2 \left(\frac{L}{4} + R \right) + \frac{\pi D^3}{6}, \quad (12)$$

where the theory of Ref. [12] obtains the first term (independent of D), and the present contribution recovers also the next term, linear in D .

Expanding (10) for small density leads to second (leading) order $\Delta\phi = n_1^{SN} n_2^N + n_{1+}^{N\Delta} n_{2-}^{SN\Delta} + n_{1-}^{N\Delta} n_{2+}^{SN\Delta} = \rho_S \rho_N (\xi_1^{SN} \xi_2^N + \xi_{1+}^{N\Delta} \xi_{2-}^{SN\Delta} + \xi_{1-}^{N\Delta} \xi_{2+}^{SN\Delta}) = \rho_S \rho_N \pi (LDR + 2DR^2)$. Hence, the additional contribution to the second virial coefficient is $B_2^{SN\Delta} = \Delta\phi / (\rho_S \rho_N) = \pi (LDR + 2DR^2)$, indeed equal to the second term of the exact result, given in (12).

In the following we demonstrate the relation to the sphere-rod Mayer bond f_{SN} being -1 if both particles overlap and zero otherwise. We split $f_{SN} = f_{SN}^{(D=0)} + \Delta f_{SN}$, where $f_{SN}^{(D=0)}$ is the Mayer bond for vanishingly thin needles, which can be deconvolved into one-body weight functions, see appendix A 1 of [12] (where this contribution is denoted by f_{SN}). We express the correction, valid for small D/L , as

$$\begin{aligned} -\Delta f_{SN}(\mathbf{r}, \mathbf{\Omega}) &= \frac{D}{2} (\Theta(|\mathbf{r} \cdot \mathbf{\Omega}| - L/2) \delta(|\mathbf{r} - (\mathbf{r} \cdot \mathbf{\Omega})\mathbf{\Omega}| - R) \\ &\quad + \delta(|\mathbf{r} + L\mathbf{\Omega}/2| - R) \Theta(-\mathbf{r} \cdot \mathbf{\Omega} - L/2) \\ &\quad + \delta(|\mathbf{r} - L\mathbf{\Omega}/2| - R) \Theta(\mathbf{r} \cdot \mathbf{\Omega} - L/2)), \end{aligned} \quad (13)$$

where \mathbf{r} is the difference vector between particle centers and $\mathbf{\Omega}$ is the rod orientation. Note that $D\delta(x)/2 = \Theta(D/4 - |x - D/4|)$ for $D \rightarrow 0$. Using the weight functions, (2)–(5), this can be expressed as

BRIEF REPORTS

PHYSICAL REVIEW E **70**, 022501 (2004)

$$-\Delta f_{SN} = w_1^{SN} w_2^N + w_{1+}^{N\Delta} w_{2-}^{SN\Delta} + w_{1-}^{N\Delta} w_{2+}^{SN\Delta}, \quad (14)$$

where $\bar{\varphi}$ denotes the spatial convolution.

We next chose a specific coordinate system, and demonstrate the validity of Eq. (14). We first consider the first term on the right-hand side of Eq. (14) and take the needle orientation $\mathbf{\Omega}$ to be parallel to the z axis and both needle and sphere to lie within the y - z plane, i.e., $\mathbf{\Omega} = (0, \bar{\varphi})$, $\mathbf{r} = (r, \vartheta, 0)$. Then,

$$w_1^{SN} w_2^N = \frac{D}{2} \int_0^\pi \int_0^{2\pi} \delta(R \cos \vartheta') \int_{-L/2}^{L/2} \delta \left(\begin{array}{c} -R \sin \vartheta' \sin \varphi' \\ r \sin \vartheta - R \sin \vartheta' \cos \varphi' \\ r \cos \vartheta - R \cos \vartheta' + l \end{array} \right) dl R^2 \sin \vartheta' d\varphi' d\vartheta' \quad (15)$$

$$= \frac{D}{2} \int_0^{2\pi} \int_{-L/2}^{L/2} \delta \left(\begin{array}{c} -R \sin \varphi' \\ r \sin \vartheta - R \cos \varphi' \\ r \cos \vartheta + l \end{array} \right) dl R d\varphi' \quad (16)$$

$$= \frac{D}{2} \Theta \left(\frac{L}{2} - |r \cos \vartheta| \right) \int_0^{2\pi} \delta(R \sin \varphi') \delta(r \sin \vartheta - R \cos \varphi') R d\varphi' \quad (17)$$

$$= \frac{D}{2} \Theta \left(\frac{L}{2} - |r \cos \vartheta| \right) \delta(r \sin \vartheta - R), \quad (18)$$

which recovers the first line of Eq. (13).

We next consider the term $w_{1+}^{N\Delta} w_{2-}^{SN\Delta}$ in Eq. (14); the calculation of $w_{1-}^{N\Delta} w_{2+}^{SN\Delta}$ can be performed analogously and is skipped here. We write the convolution in its most general form, i.e. using absolute coordinates,

$$\int w_{1+}^{N\Delta}(\mathbf{r} - \mathbf{r}', \mathbf{\Omega}) w_{2-}^{SN\Delta}(\mathbf{r}'' - \mathbf{r}') d^3 r' \quad (19)$$

$$= \int \frac{D}{2} \delta \left(\mathbf{r} - \mathbf{r}' + \mathbf{\Omega} \frac{L}{2} \right) \delta(R - |\mathbf{r}'' - \mathbf{r}'|) \Theta(-\mathbf{\Omega} \cdot (\mathbf{r}'' - \mathbf{r}')) d^3 r'. \quad (20)$$

Then we place everything in the x - y plane, $\vartheta = \bar{\vartheta} = \vartheta'' = \pi/2$; the sphere shall sit on the negative x axis: $\varphi' = -\pi/2$. Using the remaining translational symmetry, we put the tip of the needle in the origin: $r = L/2$, $\varphi = \pi + \bar{\varphi}$. To summarize, we have: $\mathbf{r} = (L/2, \pi/2, \pi + \bar{\varphi})$, $\mathbf{r}' = (r', \vartheta', \varphi')$, $\mathbf{r}'' = (r'', \pi/2, -\pi/2)$, $\mathbf{\Omega} = (\pi/2, \bar{\varphi})$. Using these coordinates, we can transform Eq. (20) and obtain:

$$w_{1+}^{N\Delta} w_{2-}^{SN\Delta} = \frac{D}{2} \int_0^\infty \int_0^{2\pi} \int_0^\pi \delta(r' \sin \vartheta' \sin \varphi') \times \delta(r' \sin \vartheta' \cos \varphi') \delta(r' \cos \vartheta') \times \delta(R - \sqrt{r''^2 + r'^2 + 2r'r'' \sin \vartheta' \sin \varphi'}) \times \Theta(r'' \sin \bar{\varphi} + r' \sin \vartheta' \sin \varphi' \sin \bar{\varphi} + r' \sin \vartheta' \cos \varphi' \cos \bar{\varphi}) r'^2 \sin \vartheta' d\vartheta' d\varphi' dr' \quad (21)$$

$$= \frac{D}{2} \int_0^\infty \int_0^{2\pi} \delta(r' \sin \varphi') \delta(r' \cos \varphi') \times \delta(R - \sqrt{r''^2 + r'^2 + 2r'r'' \sin \varphi'}) \Theta(r'' \sin \bar{\varphi} + r' \sin \varphi' \sin \bar{\varphi} + r' \cos \varphi' \cos \bar{\varphi}) r' d\varphi' dr' \quad (22)$$

$$= \frac{D}{2} \sum_{\pm} \int_0^\infty \delta(r') \delta(R - \sqrt{r''^2 + r'^2}) \Theta(r'' \sin \bar{\varphi} \pm r' \cos \bar{\varphi}) dr' \quad (23)$$

$$= \frac{D}{2} \delta(R - r'') \Theta(r'' \sin \bar{\varphi}) \quad (24)$$

which recovers the second line of Eq. (13).

We turn to a brief investigation of the prediction of the DFT for the bulk free energy. There the contribution of (10) to the free energy per volume is obtained by setting $\rho_i = \text{constant}$, and hence $n_i^\alpha = \xi_i^\alpha \rho_i$. With the sphere packing fraction $\eta = \pi \rho_s \sigma^3 / 6$, the resulting excess free energy is

$$\frac{\beta F_{\text{exc}}}{V} = \phi_{\text{hs}}(\eta) - \rho_N \ln(1 - \eta) + \frac{\pi L^2 D}{4} \frac{\rho_N^2}{1 - \eta} + \frac{3}{2} \left(\frac{L}{2R} + \frac{LD}{2R^2} + \frac{D}{R} \right) \frac{\rho_N \eta}{1 - \eta}, \quad (25)$$

where ϕ_{hs} is equal to the Percus–Yevick compressibility (scaled-particle) result for pure hard spheres, V is the system volume, and the second and third term inside the parentheses is the contribution due to (10).

In conclusion, we have extended the DFT of Refs. [11] and [12] to include effects of nonvanishing rod thickness. To that end, we have introduced two qualitatively new weight functions into the geometric framework. Our theory accounts for excluded volume effects caused by finite rod aspect ratios, D/L . We emphasize, however, that although we treat the statistical weight associated with finite D , the present theory will not resolve features of density variation on length scales comparable to D . We also have only dealt with contributions of the order of $1/(1-n_3^s)$ to the excess free energy. Rosenfeld's prescription [7,8] also involves terms proportional to $1/(1-n_3^s)^2$, which we have not treated here. Whether the weight functions introduced in the present work can be used to modify these terms is an interesting problem, that we leave for future research.

The proposed theory should lead to rich bulk phase behavior as one has, besides demixing into fluid phases with different chemical composition of species, also the possibility of nematic ordering of rods. In turn this clearly leads to a rich variety of interesting interfacial situations. It would also be interesting to see how the present theory performs against other theoretical approaches or computer simulations. From the practical point of view, the present functional causes only

a moderate increase of computational complexity as the new weighted densities are built with spatial convolutions only (the angular convolution of Ref. [12] is more involved).

The work of one of the authors (M.S.) is part of the research program of the *Stichting voor Fundamenteel Onderzoek der Materie* (FOM), that is financially supported by the *Nederlandse Organisatie voor Wetenschappelijk Onderzoek* (NWO).

-
- [1] G. A. Vliegenthart and H. N. W. Lekkerkerker, *J. Chem. Phys.* **111**, 4153 (1999).
- [2] G. H. Koenderink, G. A. Vliegenthart, S. G. J. M. Kluijtmans, A. van Blaaderen, A. P. Philipse, and H. N. W. Lekkerkerker, *Langmuir* **15**, 4693 (1999).
- [3] K. H. Lin, J. C. Crocker, A. C. Zeri, and A. G. Yodh, *Phys. Rev. Lett.* **87**, 088301 (2001).
- [4] G. A. Vliegenthart, Dissertation, Utrecht University, 1999.
- [5] G. H. Koenderink, D. G. A. L. Aarts, V. W. A. de Villeneuve, A. P. Philipse, R. Tuinier, and H. N. W. Lekkerkerker, *Biomacromolecules* **4**, 129 (2003).
- [6] L. Helden, R. Roth, G. H. Koenderink, P. Leiderer, and C. Bechinger, *Phys. Rev. Lett.* **90**, 048301 (2003).
- [7] Y. Rosenfeld, *Phys. Rev. E* **50**, R3318 (1994).
- [8] Y. Rosenfeld, *Mol. Phys.* **86**, 637 (1995).
- [9] R. Evans, in *Fundamentals of Inhomogeneous Fluids*, edited by D. Henderson (Marcel Dekker, New York 1992), Chap. 3, p. 85.
- [10] P. Bolhuis and D. Frenkel, *J. Chem. Phys.* **101**, 9869 (1994).
- [11] M. Schmidt, *Phys. Rev. E* **63**, 050201(R) (2001).
- [12] J. M. Brader, A. Esztermann, and M. Schmidt, *Phys. Rev. E* **66**, 031401 (2002).
- [13] P. G. Bolhuis, J. M. Brader, and M. Schmidt, *J. Phys.: Condens. Matter* **48**, S3421 (2003).
- [14] R. Roth, J. M. Brader, and M. Schmidt, *Europhys. Lett.* **63**, 549 (2003).
- [15] K. Yaman, C. Jeppesen, and C. M. Marques, *Europhys. Lett.* **42**, 221 (1998).
- [16] R. Roth, *J. Phys.: Condens. Matter* **15**, S277 (2003).
- [17] Y. X. Yu and J. Wu, *J. Chem. Phys.* **117**, 2368 (2002).
- [18] P. Bryk, *Phys. Rev. E* **68**, 062501 (2003).
- [19] R. Roth, R. van Roij, D. Andrienko, K. R. Mecke, and S. Dietrich, *Phys. Rev. Lett.* **89**, 088301 (2002).
- [20] K. R. Mecke (unpublished).
- [21] L. Onsager, *Ann. N.Y. Acad. Sci.* **51**, 627 (1949).
- [22] K. Shundyak and R. van Roij, *J. Phys.: Condens. Matter* **13**, 4789 (2001).
- [23] K. Shundyak and R. van Roij, *Phys. Rev. Lett.* **88**, 205501 (2002).
- [24] K. Shundyak and R. van Roij, *Phys. Rev. E* **68**, 061703 (2003).
- [25] G. Cinacchi and F. Schmid, *J. Phys.: Condens. Matter* **14**, 12 223 (2002).
- [26] P. Tarazona and Y. Rosenfeld, *Phys. Rev. E* **55**, R4873 (1997).
- [27] P. Tarazona, *Phys. Rev. Lett.* **84**, 694 (2000).
- [28] Y. Rosenfeld, *Phys. Rev. Lett.* **63**, 980 (1989).
- [29] J. A. Barker and D. Henderson, *Rev. Mod. Phys.* **48**, 587 (1976).

Colloids, polymers, and needles: Demixing phase behavior

Matthias Schmidt* and Alan R. Denton

Department of Physics, North Dakota State University, Fargo, North Dakota 58105-5566

(Received 3 October 2001; published 23 January 2002)

We consider a ternary mixture of hard colloidal spheres, ideal polymer spheres, and rigid vanishingly thin needles, which model stretched polymers or colloidal rods. For this model, we develop a geometry-based density functional theory, apply it to bulk fluid phases, and predict demixing phase behavior. In the case of no polymer-needle interactions, two-phase coexistence between colloid-rich and colloid-poor phases is found. For hard needle-polymer interactions, we predict rich phase diagrams, exhibiting three-phase coexistence, and reentrant demixing behavior.

DOI: 10.1103/PhysRevE.65.021508

PACS number(s): 83.80.Qr, 64.10.+h, 82.70.Dd, 61.25.Hq

I. INTRODUCTION

The richness of phase behavior of systems with purely repulsive interactions depends crucially on the number of components. For a one-component system like colloidal hard spheres, there occurs a freezing transition from a single fluid phase to a dense crystal. Adding a second component, such as nonadsorbing globular polymer coils [1] or rodlike particles [2,3] generates an effective depletion-induced attraction between colloidal spheres, leading to the possibility of demixing. This transition is an analog of the vapor-liquid transition in simple fluids: The phase that is concentrated in one of the components corresponds to a liquid, while the dilute phase corresponds to a vapor, and one frequently refers to such phases as colloidal liquid and colloidal vapor, although the “vapor” is concentrated in the added component.

Generic theoretical models for such systems are those introduced by Asakura and Oosawa (AO) and independently by Vrij [1,4], Bolhuis and Frenkel (BF) [5], and Widom and Rowlinson (WR) [6]. The AO model comprises hard colloidal spheres mixed with polymer spheres that are ideal amongst themselves but cannot penetrate the colloids. The BF model adds stiff vanishingly thin needles to a hard sphere system. Because of their vanishing thickness, the needles do not interact with one another. Clearly, both models are similar in spirit, as a noninteracting component is added to hard spheres. In the WR model this is different; two species of spheres interact symmetrically, such that hard core repulsion occurs only between particles of unlike species. Hence a pure system of either component is an ideal gas. All of these model binary mixtures exhibit liquid-vapor phase separation, well established by computer simulations and theories [7–12]. The WR model [6,13–15] has been studied with a range of approaches, including mean-field theory (MFT) [15], Percus-Yevick (PY) integral equation theory [14,16,17], scaled-particle theory (SPT) [18], as well as computer simulations [16,19,20]. The precise location of the liquid-vapor critical point was located by simulations about

50% higher than previously thought [16,19], still a challenge for theories (for a recent integral-equation closure, see Ref. [17]).

In the AO and BF cases a reservoir description has proven to be useful. The reservoir density of either polymers or needles rules the strength of effective attraction and hence plays a role similar to (inverse) temperature in simple substances. Although the WR model features an intrinsic symmetry that seems to preclude such a description, an effective model can also be formulated [15]. In the present paper we consider the phase behavior of a mixture of spheres, polymers, and needles, a natural combination of the above binary cases. We note that our ternary model may provide insight into certain real systems, such as paints, which contain colloidal latex and pigment particles, polymer thickeners and dispersants, as well as many other components [21].

Density functional theory (DFT) [22] is a powerful approach to equilibrium statistical systems, possibly under influence of an external potential. Building on Rosenfield’s work [23], a geometry-based approach was recently proposed that also predicts bulk properties, without the need of any input, allowing the AO [24], BF [25], and WR [26] models to be treated. Here we combine these tools to derive a DFT for ternary systems.

In Sec. II we define the model ternary mixtures of spheres, polymers, and needles. In Sec. III the DFT is developed. Application to bulk phases in Sec. IV yields the phase behavior. We finish with concluding remarks in Sec. V.

II. THE MODEL

We consider a mixture of colloidal hard spheres (species C) of radius R_C , globular polymers (species P) of radius R_P , and vanishingly thin needles (species N) of length L , with respective number densities $\rho_C(\mathbf{r})$, $\rho_P(\mathbf{r})$, and $\rho_N(\mathbf{r}, \mathbf{\Omega})$, where \mathbf{r} is the spatial coordinate and $\mathbf{\Omega}$ is a unit vector pointing along the needle axis (see Fig. 1). The pair interaction between colloids is $V_{CC} = \infty$ if the separation r between sphere centers is less than $2R_C$, and zero otherwise. The pair interactions between like particles of both other components vanish for all distances: $V_{PP} = V_{NN} = 0$. For polymers this is an assumption strictly valid only at the theta point; for needles it becomes exact in the present limit of large aspect ratio, where overlapping needles contribute a

*Permanent address: Institut für Theoretische Physik II, Heinrich-Heine-Universität Düsseldorf, Universitätsstraße 1, D-40225 Düsseldorf, Germany.

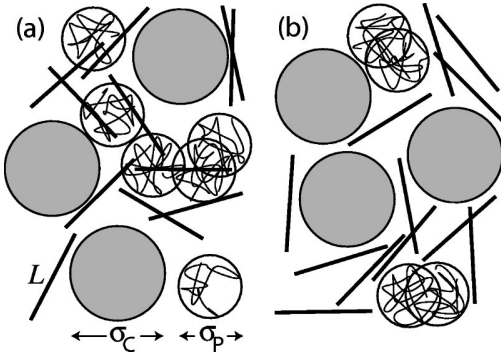


FIG. 1. Sketch of the ternary mixture of colloidal hard spheres with diameter σ_C , ideal polymer spheres of diameter σ_P and vanishingly thin needles of length L . Different cases for interactions between polymers and needles are depicted: (a) no interactions; (b) excluded volume interactions.

negligible fraction of configurations. The colloidal spheres interact with both other components via excluded volume: The pair interaction between colloids and polymers is $V_{CP} = \infty$ if $r < R_C + R_P$, and zero otherwise; the interaction between colloids and needles is $V_{CN} = \infty$, if both overlap, and zero otherwise. What remains to be prescribed is the interaction between needles and polymers. We consider two cases: (i) ideal interactions such that $V_{PN} = 0$ for all distances, and (ii) excluded volume interactions such that $V_{PN} = \infty$ if needle and polymer overlap, and zero otherwise. We denote the sphere diameters by $\sigma_C = 2R_C$, $\sigma_P = 2R_P$, the sphere packing fractions by $\eta_C = 4\pi R_C^3 \rho_C / 3$, $\eta_P = 4\pi R_P^3 \rho_P / 3$, and use a dimensionless needle density $\rho_N^* = \rho_N L^3$.

III. DENSITY FUNCTIONAL THEORY

A. Weight functions

We start with a geometrical representation of the particles in terms of weight functions w_μ^i , where $\mu = 3, 2, 1, 0$ corresponds to the particles' volume, surface, integral mean curvature, and Euler characteristic, respectively [27], and $i = C, P, N$ labels the species. We will use S as a unifying symbol for the spherical species C and P , and denote the radius as R , where $R = R_C$, R_P for $S = C, P$, respectively. The weight functions are determined to give the hard core Mayer bonds $f_{ij} = \exp(V_{ij}) - 1$ by a linear combination of terms $w_\gamma^i(\mathbf{r}) * w_{3-\gamma}^j(\mathbf{r})$, where the asterisk denotes the convolution, $g(\mathbf{r}) * h(\mathbf{r}) = \int d^3x g(\mathbf{x}) h(\mathbf{r} - \mathbf{x})$.

For spheres, the usual weight functions [23,28] are

$$w_3^S(\mathbf{r}) = \theta(R - r), \quad w_2^S(\mathbf{r}) = \delta(R - r), \quad (1)$$

$$w_{v2}^S(\mathbf{r}) = w_2^S(\mathbf{r}) \mathbf{r} / \tau, \quad \hat{\mathbf{w}}_{m2}^S(\mathbf{r}) = w_2^S(\mathbf{r}) [\mathbf{r} \mathbf{r} / r^2 - \hat{\mathbf{1}} / 3], \quad (2)$$

where $r = |\mathbf{r}|$, $\delta(r)$ is the Dirac distribution, $\theta(r)$ is the step function, and $\hat{\mathbf{1}}$ is the identity matrix. Further linearly dependent weights are $w_1^S(\mathbf{r}) = w_2^S(\mathbf{r}) / (4\pi R)$, $\mathbf{w}_{v1}^S(\mathbf{r}) = \mathbf{w}_{v2}^S(\mathbf{r}) / (4\pi R)$, $w_0^S(\mathbf{r}) = w_1^S(\mathbf{r}) / R$. Note that these weights have different tensorial rank: w_0^S , w_1^S , w_2^S , w_3^S are scalars;

\mathbf{w}_{v1}^S , \mathbf{w}_{v2}^S are vectors; $\hat{\mathbf{w}}_{m2}^S$ is a (traceless) matrix. These functions give the Mayer bond between pairs of spheres [23] through $-f_{SS}/2 = w_3^S * w_0^S + w_2^S * w_1^S - \mathbf{w}_{v2}^S * \mathbf{w}_{v1}^S$. However, they are not sufficient to recover the sphere-needle Mayer bond [27]. This is achieved through

$$w_2^{SN}(\mathbf{r}, \mathbf{\Omega}) = 2 |\mathbf{w}_{v2}^S(\mathbf{r}) \cdot \mathbf{\Omega}|, \quad (3)$$

which contains information about *both* species: it is nonvanishing on the surface of a sphere with radius R , but this surface is ‘‘decorated’’ with an $\hat{\mathbf{\Omega}}$ dependence. Furthermore, for needles, we follow Ref. [27] to obtain

$$w_1^N(\mathbf{r}, \mathbf{\Omega}) = \frac{1}{4} \int_{-L/2}^{L/2} dl \delta(\mathbf{r} + \hat{\mathbf{\Omega}} l), \quad (4)$$

$$w_0^N(\mathbf{r}, \mathbf{\Omega}) = \frac{1}{2} [\delta(\mathbf{r} + \hat{\mathbf{\Omega}} L/2) + \delta(\mathbf{r} - \hat{\mathbf{\Omega}} L/2)], \quad (5)$$

and \mathbf{r} is the needle center of mass. The function w_1^N describes the linear extent of a needle, whereas w_0^N is characteristic of its endpoints. For vanishingly thin needles, both surface and volume vanish, and so do the corresponding weights, $w_2^N = w_3^N = 0$. Technically, the Mayer bond is generated through $-f_{SN}(\mathbf{r}, \mathbf{\Omega}) = w_3^S(\mathbf{r}) * w_0^N(\mathbf{r}, \mathbf{\Omega}) + w_2^{SN}(\mathbf{r}, \mathbf{\Omega}) * w_1^N(\mathbf{r}, \mathbf{\Omega})$, where \mathbf{r} is the difference vector between sphere and needle position.

B. Weighted densities

The weight functions are used to smooth the possibly highly inhomogeneous density profiles by convolutions,

$$n_\nu^C(\mathbf{r}) = \rho_C(\mathbf{r}) * w_\nu^C(\mathbf{r}), \quad (6)$$

$$n_\nu^P(\mathbf{r}) = \rho_P(\mathbf{r}) * w_\nu^P(\mathbf{r}), \quad (7)$$

$$n_2^{CN}(\mathbf{r}, \mathbf{\Omega}) = \rho_C(\mathbf{r}) * w_2^{CN}(\mathbf{r}, \mathbf{\Omega}), \quad (8)$$

$$n_2^{PN}(\mathbf{r}, \mathbf{\Omega}) = \rho_P(\mathbf{r}) * w_2^{PN}(\mathbf{r}, \mathbf{\Omega}), \quad (9)$$

$$n_\tau^N(\mathbf{r}, \mathbf{\Omega}) = \rho_N(\mathbf{r}, \mathbf{\Omega}) * w_\tau^N(\mathbf{r}, \mathbf{\Omega}), \quad (10)$$

where $\nu = 0, 1, 2, 3, v1, v2, m2$, and $\tau = 0, 1$; $\rho_C(\mathbf{r})$, $\rho_P(\mathbf{r})$, and $\rho_N(\mathbf{r}, \mathbf{\Omega})$ are the one-body density distributions of spheres, polymers, and needles, respectively. Note that n_ν^C , n_ν^P , n_ν^N are ‘‘pure’’ weighted densities, involving only variables of either species [23,27]. In contrast, n_2^{CN} and n_2^{PN} are a convolution of the sphere densities with orientation-dependent weight function, combining characteristics of both species [25].

C. Free energy density

The Helmholtz excess free energy is obtained by integrating over a free energy density,

$$F_{\text{exc}}[\rho_C, \rho_P, \rho_N] = k_B T \int d^3x \int \frac{d^2\Omega}{4\pi} \Phi(\{n_\gamma^i\}), \quad (11)$$

where k_B is Boltzmann's constant, T is temperature, and the (local) reduced excess free energy density Φ is a simple function (not a functional) of the weighted densities n_γ^i . This leads to a dependence of Φ on orientation and position. The variable \mathbf{x} runs over space [23,27], and Ω over the unit sphere [25].

The functional form of Φ is obtained by consideration of the exact zero-dimensional excess free energy. We obtain

$$\Phi = \Phi_{CC} + \Phi_{CP} + \Phi_{CN} + \lambda \Phi_{PN}, \quad (12)$$

where in the case of ideal polymer-needle interaction $\lambda = 0$, and for hard polymer-needle interaction $\lambda = 1$. In the following, the arguments of the weighted densities are suppressed in the notation; see Eqs. (6)–(10) for the explicit dependence on \mathbf{r} and Ω . The hard sphere contribution, being equal to the pure HS case [23,28], is

$$\begin{aligned} \Phi_{CC} = & -n_0^C \ln(1 - n_3^C) + (n_1^C n_2^C - \mathbf{n}_{v1}^C \cdot \mathbf{n}_{v2}^C) / (1 - n_3^C) \\ & + [(n_2^C)^3 / 3 - n_2^C (\mathbf{n}_{v2}^C)^2 + 3(\mathbf{n}_{v2}^C \cdot \hat{\mathbf{n}}_{m2}^C \cdot \mathbf{n}_{v2}^C \\ & - 3 \det \hat{\mathbf{n}}_{m2}^C) / 2] / [8\pi(1 - n_3^C)^2]. \end{aligned} \quad (13)$$

The contribution due to interactions between colloids and polymers is the same as in the pure AO case [24] and is given by

$$\Phi_{CP} = \sum_v \frac{\partial \Phi_{CC}}{\partial n_v^C} n_v^P. \quad (14)$$

The contribution due to interactions between colloids and needles [25] is

$$\Phi_{CN} = -n_0^N \ln(1 - n_3^C) + \frac{n_1^N n_2^{CN}}{1 - n_3^C}. \quad (15)$$

Note that the simultaneous presence of Φ_{CP} and Φ_{CN} in Φ does not generate artificial interactions between P and N . For vanishing PN pair potential one can derive these terms from consideration of multicavity distributions like in the binary CP [24,12] and CN cases [25]. In order to model the WR-type interaction between polymers and needles in the presence of the colloidal spheres we use

$$\Phi_{PN} = \frac{n_0^N n_3^P + n_1^N n_2^{PN}}{1 - n_3^C}. \quad (16)$$

This can be derived as follows. The starting point is a functional for binary hard spheres with added needles. Linearization in one of the sphere densities (which becomes the polymer species) is performed in the same way as linearization of binary hard spheres leads to the CP functional [12]. In the absence of colloids, we obtain $\Phi = \Phi_{PN} = n_0^N n_3^P + n_1^N n_2^{PN}$. Then the density functional can be rewritten as $F_{\text{exc}} = -\int d^3r \int d^3r' \int d^2\Omega \rho_P(\mathbf{r}) f_{PN}(\mathbf{r}; \mathbf{r}', \Omega) \rho_N(\mathbf{r}, \Omega) / (4\pi)$. This is precisely (a generalization to needles of) the mean-field DFT for the WR model [15]. Although this does

not feature the exact zero-dimensional (0d) limit, as the geometry-based DFT [26] for WR *spheres* does, we expect differences to be small.

IV. RESULTS

A. Bulk fluid phases

For homogeneous density profiles, $\rho_i = \text{const}$, the integrations in Eqs. (6)–(10) can be carried out explicitly. The hard sphere contribution is equal to the Percus-Yevick compressibility (and scaled-particle) result, which is

$$\Phi_{CC} = \frac{3\eta_C [3\eta_C(2 - \eta_C) - 2(1 - \eta_C)^2 \ln(1 - \eta_C)]}{8\pi R_C^3 (1 - \eta_C)^2}. \quad (17)$$

The colloid-polymer contribution is equal to that predicted by free volume theory [8], and rederived by DFT [24] as

$$\begin{aligned} \Phi_{CP} = & \frac{\eta_P / (8\pi R_P^3)}{(1 - \eta_C)^3} \{3q\eta_C [6(1 - \eta_C)^2 + 3q(2 - \eta_C - \eta_C^2) \\ & + 2q^2(1 + \eta_C + \eta_C^2)] - 6(1 - \eta_C)^3 \ln(1 - \eta_C)\}, \end{aligned} \quad (18)$$

where $q = \sigma_P / \sigma_C$. The colloid-needle contribution equals the perturbative (around a pure hard sphere fluid) treatment of Ref. [5], which can be shown to equal the result from application of scaled-particle theory [29], and DFT [25], and is given by

$$\Phi_{CN} = \rho_N \left[-\ln(1 - \eta_C) + \frac{3L}{4R_C} \frac{\eta_C}{1 - \eta_C} \right]. \quad (19)$$

The WR-type polymer-needle contribution is

$$\Phi_{PN} = \left(1 + \frac{3L}{4R_P} \right) \frac{\rho_N \eta_P}{1 - \eta_C}. \quad (20)$$

For completeness, the ideal free energy contribution is

$$\phi_{\text{id}} = \sum_{i=C,P,N} \rho_i [\ln(\rho_i \Lambda_i^3) - 1], \quad (21)$$

where the Λ_i are (irrelevant) thermal wavelengths of species i . This puts us into a position to obtain the reduced total free energy per volume $\Phi_{\text{tot}} = \Phi_{\text{id}} + \Phi$ of any given fluid state characterized by the bulk densities and relative sizes of the three components.

B. Phase diagram

The general conditions for phase coexistence are equality of the total pressures p_{tot} , and of the chemical potentials μ_i in the coexisting phases. Equality of temperature is trivial in hard-body systems. For phase equilibrium between phases I and II,

$$p_{\text{tot}}^I = p_{\text{tot}}^{\text{II}}, \quad (22)$$

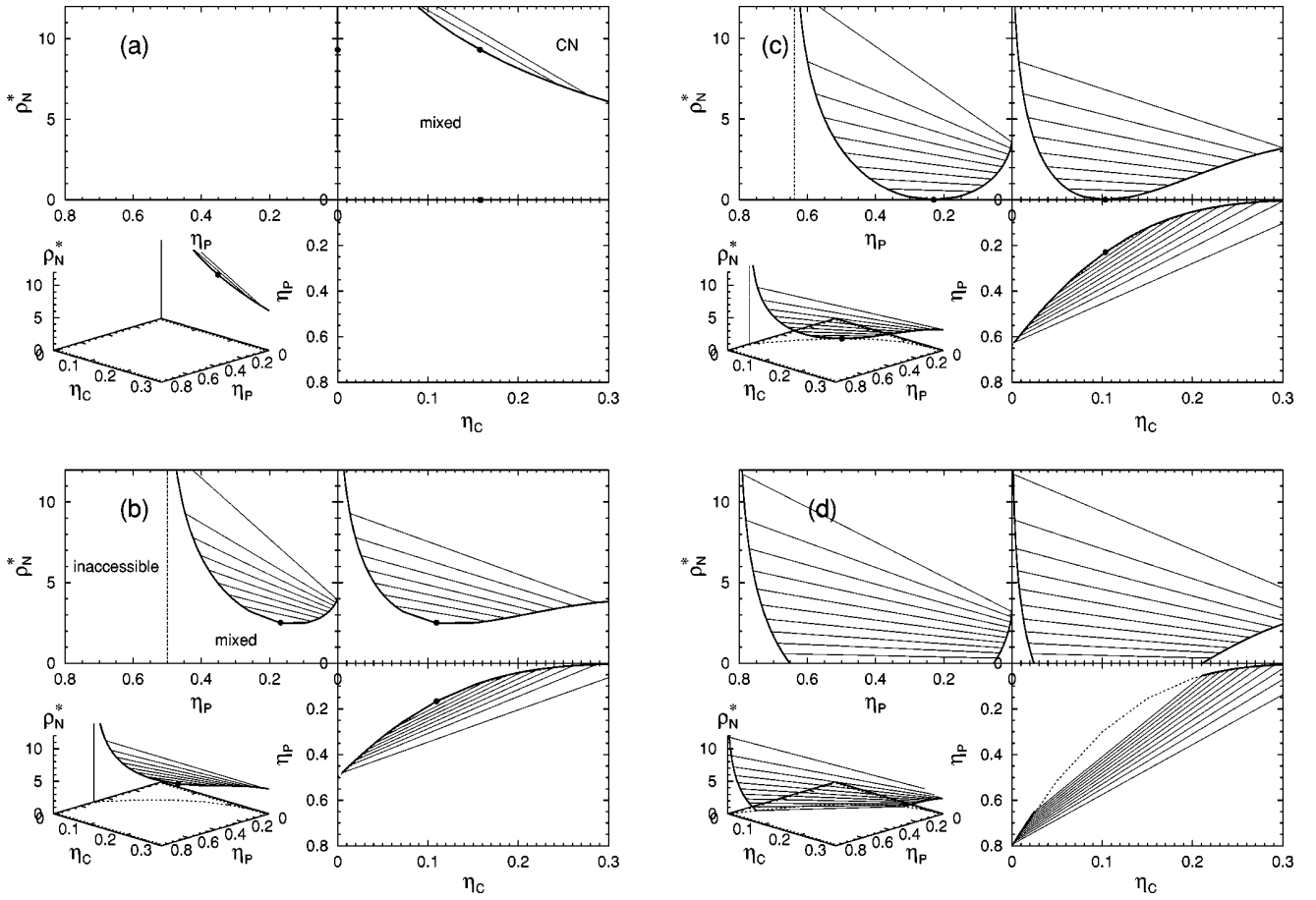


FIG. 2. Demixing phase diagram of a ternary colloid-polymer-needle mixture with ideal polymer-needle interactions for $\sigma_C = \sigma_P = L$, and $\eta_P^r = 0$ (a), 0.5 (b), 0.638 31 (c), 0.8 (d). Shown are binodals (lines), tielines between coexisting phases (thin lines), and critical points (dots).

$$\mu_i^I = \mu_i^{II}, \quad i = C, P, N. \quad (23)$$

These are four equations for six unknowns (two statepoints each characterized by three densities). Hence two-phase coexistence regions depend parametrically on two free parameters. For three-phase equilibrium between phases I, II, and III,

$$p_{\text{tot}}^I = p_{\text{tot}}^{II} = p_{\text{tot}}^{III}, \quad (24)$$

$$\mu_i^I = \mu_i^{II} = \mu_i^{III}, \quad i = C, P, N. \quad (25)$$

Eight equations for nine variables leave one free parameter.

In our case $p_{\text{tot}}/k_B T = -\Phi_{\text{tot}} + \sum_{i=C,P,N} \rho_i \partial \Phi_{\text{tot}} / \partial \rho_i$, and $\mu_i = k_B T \partial \Phi_{\text{tot}} / \partial \rho_i$ yield analytical expressions. We solve the resulting sets of equations numerically, which is straightforward.

1. Ideal polymer-needle interaction

Let us first explain our representation of the ternary phase diagrams. We take the system densities η_C, η_P, ρ_N^* as basic variables. For given particle sizes, these span a three-dimensional (3D) phase space. Each point in this space corresponds to a possible bulk state, at some pressure p_{tot} . Two-phase coexistence is indicated by a pair of points that are

joined by a straight tie line. Accordingly, three-phase coexistence is a triplet of points, defining a triangle. In order to graphically represent the phase diagram, we show surfaces defined by one thermodynamic parameter being constant. Such surfaces are conveniently taken such that coexistence lines (and triangles) lie completely within the surface. Clearly, this can be accommodated by imposing a constant value of p_{tot} or any of μ_C, μ_P , and μ_N . Here we choose $\mu_P = \text{const}$, and hence imagine controlling the system directly with η_C and ρ_N^* , but indirectly via coupling to a polymer reservoir of packing fraction $\eta_P^r = (4\pi/3)(R_P/\Lambda_P)^3 \exp(\mu_P/k_B T)$. A constant- η_P^r surface is nontrivially embedded in the 3D phase diagram. To depict it graphically, we show projections onto the three sides of the coordinate system, namely, the $\eta_C - \rho_N^*$, $\eta_C - \eta_P$, and $\eta_P - \rho_N^*$ planes, as well as a perspective 3D view. Furthermore, we indicate the accessible regions that are compatible with the constraint of fixed η_P^r . Their boundaries are implicitly defined through $\eta_P^r(\eta_C = 0, \eta_P, \rho_N^*) = \text{const}$ and $\eta_P^r(\eta_C, \eta_P, \rho_N^* = 0) = \text{const}$. Note that tielines are allowed to cross inaccessible regions.

For simplicity, and to establish a reference case, we initially ignore polymer-needle interactions and consider equal particle sizes, $\sigma_C = \sigma_P = L$. In the absence of polymer (η_P^r

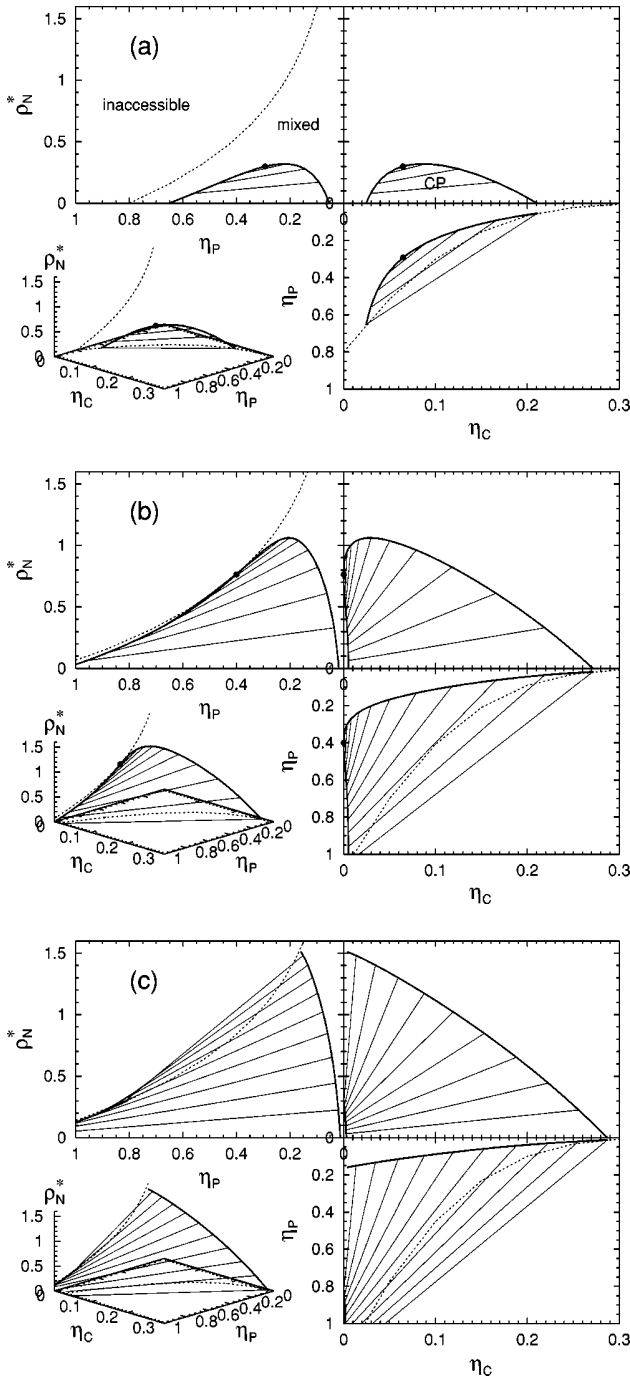


FIG. 3. Demixing phase diagram of a ternary colloid-polymer-needle mixture with hard polymer-needle interactions for $\sigma_C = \sigma_P = L$, and $\eta_P^r = 0.8$ (a), 1.087 31 (b), 1.2 (c).

$= 0$), colloids and needles demix, as shown in Fig. 2(a). Increasing the packing fraction of polymers in the reservoir causes the demixed region to grow and to shift to smaller η_C and ρ_N^* [see Fig. 2(b) for $\eta_P = 0.5$]. This behavior can be understood if addition of a second depleting species simply enhances the depletion-induced attraction between colloids. Increasing η_P^r further causes the critical point to hit the $\rho_N^* = 0$ axis. This is precisely the demixing critical point of the

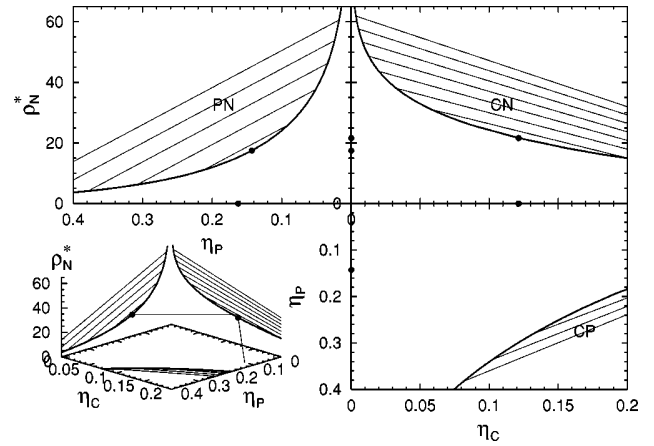


FIG. 4. Demixing phase diagrams in the binary subsystems with hard polymer-needle interactions for $\sigma_C = 2\sigma_P = L/2$.

binary CP (AO) model, which is located at $\eta_P^r = 0.638\ 31$ [see Fig. 2(c)]. Computer simulations are currently being carried out to test the accuracy of this value [30]. For still larger η_P^r , the mixed states become disconnected, hence there is no path between colloid-rich and colloid-poor phases that does not pass through a first-order phase transition [see Fig. 2(d) for $\eta_P^r = 0.8$].

2. Hard polymer-needle interaction

Turning on the excluded-volume interaction between polymers and needles allows the possibility of demixing between these components. In the absence of colloids, the PN mixture is of WR type: Interactions between particles of like species vanish, while unlike particles interact with a hard core repulsion. Our case is a generalization to nonspherical particle shapes. In the mean-field treatment this does not affect the phase diagram, as only the net excluded volume enters into the theory. This robustness is also present in our approach.

We first consider equal particle sizes, $\sigma_C = \sigma_P = L$. It turns out that interesting behavior is observed only for small $\rho_N^* < 0.2$. The colloid-needle demixing curve lies well above this region, and is only weakly affected by $\eta_P^r > 0$. In the absence of needles ($\rho_N^* = 0$) and for large enough polymer density, colloids and polymers demix, indicated by a miscibility gap along the $\rho_N^* = 0$ axis [see Fig. 3(a) for $\eta_P^r = 0.8$]. Increasing needle density $\rho_N^* > 0$ causes the gap to shrink and eventually to disappear in a critical point. Quite surprisingly, and in contrast to the former case of absent PN interactions, the addition of needles *favours* mixing. This behavior may reflect a competition between the depleting effects of interacting polymers and needles. By analogy with the CP subsystem it is clear that at sufficiently high polymer density, a PN miscibility gap will open for $\eta_C = 0$. However, this happens not by growing a small bump as in the CP case. Instead the CP demixing curve bends over to smaller η_C and touches (with its critical point) the $\eta_C = 0$ axis (see Fig. 3(b) for $\eta_P^r = 1.087\ 31$). For larger η_P^r , the critical point disappears [see Fig. 3(c) for $\eta_P^r = 1.2$].

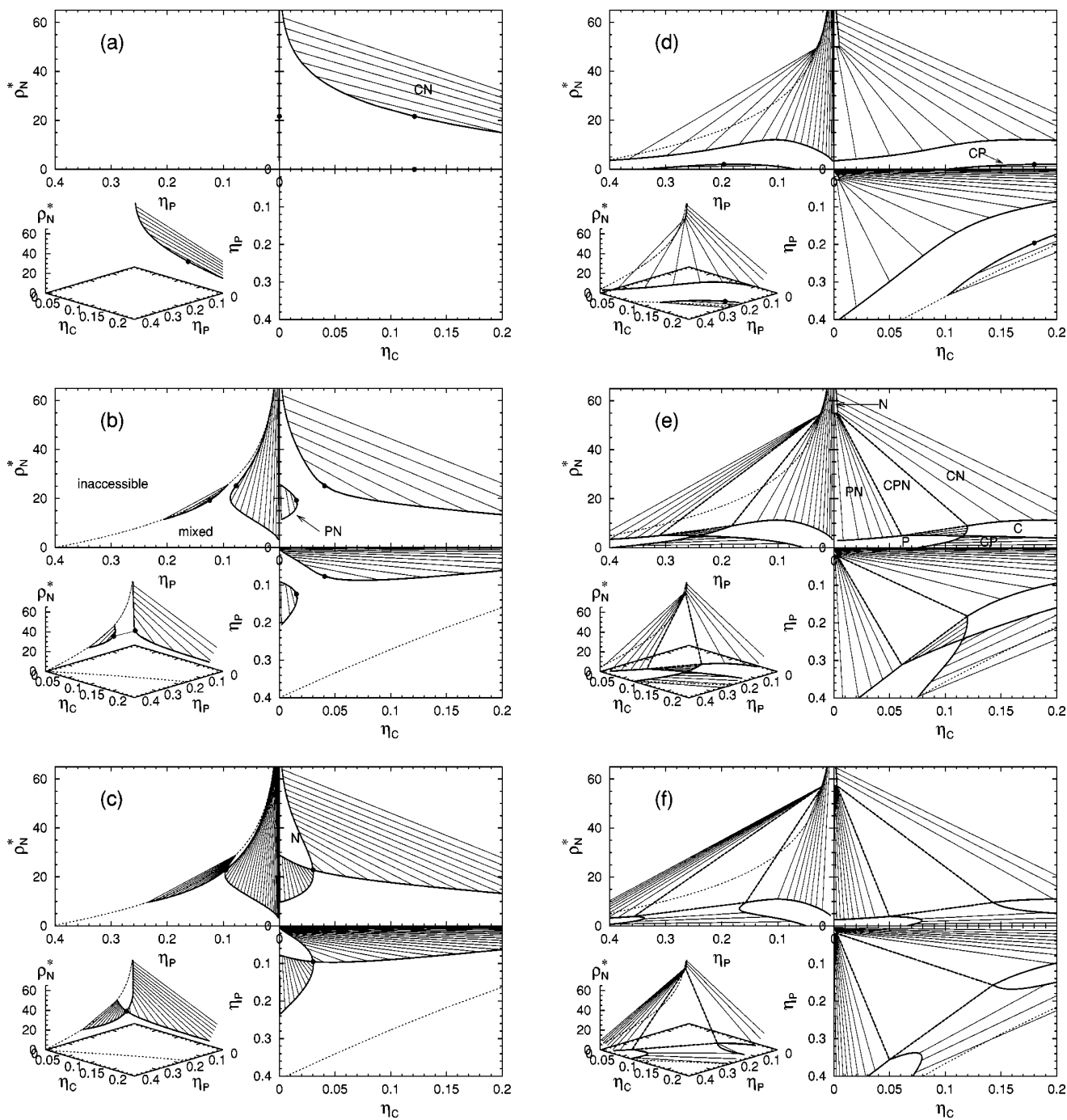


FIG. 5. Same as Fig. 3, but for $\sigma_C=2\sigma_P=L/2$, and $\eta_P^r=0$ (a), 0.4 (b), 0.408 107 (c), 0.5 (d), 0.526 26 (e), 0.54 (f).

In order to bring *CP* and *CN* demixing closer together, we consider a reduced polymer size $\sigma_P=\sigma_C/2$, generating a weaker depletion attraction between colloids (at the same number density of polymers), and longer needles, $L=2\sigma_C$ generating stronger depletion between colloids, and hence lower ρ_N^* at the critical point in the binary *CN* case. Figure 4 shows the binodals in the (three) binary subsystems. For the ternary mixture, we follow a path of increasing η_P^r , starting with $\eta_P^r=0$, for which the phase diagram is displayed in Fig. 5(a). There is no polymer present in the system, and phase

separation into colloid-rich and needle-rich phases occurs at high enough densities of these components. Both $\eta_P-\rho_N^*$ and $\eta_C-\eta_P$ planes are inaccessible as $\eta_P=0$. Increasing polymer density [$\eta_P^r=0.4$ in Fig. 5(b)] shifts the *CN* critical point to lower η_C , distorting the formerly rounded shape of the binodal. For $\eta_C=0$, polymers and needles demix, as η_P^r is above the critical value for the Widom-Rowlinson type demixing of these species. The presence of colloids ($\eta_C>0$) disturbs the *PN* transition; the miscibility gap narrows, eventually disappearing in a critical point, with subsequent mis-

cibility. At $\eta_p^r = 0.408\,107$ [Fig. 5(c)] the *CN* and *PN* critical points merge into a single one, and a needle-rich phase (*N*) becomes isolated. This coexists with a phase that consists (primarily) of colloids and polymers at varying composition. For growing η_p^r , the “double” critical point broadens into a line and results in a thin neck joining both transitions.

With increasing η_p^r the coexistence region broadens further [see Fig. 5(d) for $\eta_p^r = 0.5$]. Colloids and polymers also demix. For $\rho_N^* = 0$, the system is above the critical point for the pure AO model, and hence coexistence between colloid-rich and polymer-rich phases occurs. Again, the presence of the third component, in this case *N*, causes the density gap to shrink and eventually disappear with a critical point. As all binary subsystems are by now demixed, it is evident that the system will ultimately display coexistence between three phases, each one enriched by one of the components, and represented by a triangle in system representation. Each corner of the triangle corresponds to one of the three coexisting phases. The Gibbs phase rule dictates that one degree of freedom remains, which is p_{tot} or, equivalently, η_p^r (note that for hard-body systems, temperature is trivially related to pressure). It is striking, however, how this triangle develops. One might expect this to occur by the joining of existing binary coexistence regions. This is not the case. The ternary region instead grows solely out of the *N*-rich-poor coexistence, whereby *CP* coexistence is only a spectator, separated by mixed states. The initial three-phase triangle is extremely elongated (being a line as a boundary case). One corner corresponds to a needle-rich phase; both others differ only slightly in densities, one phase favoring colloids, the other polymers. Moving away from this CP edge of the triangle (by reducing ρ_N^*) leads to binary coexistence between *C* and *P*. This phase separation is reminiscent of the behavior of the pure AO model. However this reentrant coexistence is triggered by the presence of the needles, and it is separated (by mixed states) from the pure AO transition (and its region of stability in the presence of needles). In Fig. 5(e) we show results for $\eta_p^r = 0.526\,26$, where the critical points of both CP transitions have already merged, and again a neck is reminis-

cent of the formerly distinct transitions. For still larger η_p^r , the three-phase triangle grows further [see Fig. 5(f) for $\eta_p^r = 0.54$]. Ultimately, at sufficient concentration the colloids must freeze, but we disregard the solid phase in the present work. We finally note that the whole scenario is covered over a relatively small density interval $\eta_p^r = 0.4 - 0.54$, and that the packing fractions of colloids and polymers are only moderate. However, needle densities can be quite high.

V. DISCUSSION

In conclusion, we have considered a simple hard-body model for a mixture of spherical colloidal particles, globular polymer coils, and needle-shaped objects, which may represent either colloidal needles, stretched polymers or polyelectrolytes. We have extended a recent DFT approach to this model and applied it to bulk fluid phases. The resulting phase behavior is very rich, ensuing from competition of demixing in the binary subsystems.

The present paper has interesting implications for the techniques of integrating out degrees of freedom (see e.g., [31,32]). Note that by integrating out, e.g., the needles, effective interactions between pairs of colloids, pairs of polymers, as well as colloids and polymers arise. Hence one arrives at a binary mixture with (soft) depletion interactions. To what extent the ultimate mapping onto a one-component (colloid) system, by further integrating out the polymers, can be achieved is an interesting question. As a further outlook, the inclusion of freezing of colloids, disregarded in the present work, would further enrich the phase behavior. Computer simulations are desirable to test the theoretical phase diagrams. Furthermore it is interesting to elucidate the structural correlations present in the various fluid phases. Inhomogeneous situations, such as induced by walls or present at interfaces between demixed states, constitute further exciting directions of research.

ACKNOWLEDGMENT

We acknowledge useful discussions with Stuart G. Croll.

-
- [1] S. Asakura and F. Oosawa, *J. Chem. Phys.* **22**, 1255 (1954).
 - [2] G. A. Vliegenthart and H. N. W. Lekkerkerker, *J. Chem. Phys.* **111**, 4153 (1999).
 - [3] S. G. J. M. Kluijtmans, G. H. Koenderink, and A. P. Philipse, *Phys. Rev. E* **61**, 626 (2000).
 - [4] A. Vrij, *Pure Appl. Chem.* **48**, 471 (1976).
 - [5] P. Bolhuis and D. Frenkel, *J. Chem. Phys.* **101**, 9869 (1994).
 - [6] B. Widom and J. S. Rowlinson, *J. Chem. Phys.* **52**, 1670 (1970).
 - [7] A. P. Gast, C. K. Hall, and W. B. Russell, *J. Colloid Interface Sci.* **96**, 251 (1983).
 - [8] H. N. W. Lekkerkerker, W. C. K. Poon, P. N. Pusey, A. Stroobants, and P. B. Warren, *Europhys. Lett.* **20**, 559 (1992).
 - [9] M. Dijkstra, J. M. Brader, and R. Evans, *J. Phys.: Condens. Matter* **11**, 10 079 (1999).
 - [10] A. A. Louis, R. Finken, and J. Hansen, *Europhys. Lett.* **46**, 741 (1999).
 - [11] M. Dijkstra, R. van Roij, and R. Evans, *J. Chem. Phys.* **113**, 4799 (2000).
 - [12] J. M. Brader, Ph.D. thesis, University of Bristol, 2001.
 - [13] M. I. Guerrero, J. S. Rowlinson, and G. Morrison, *J. Chem. Soc., Faraday Trans. 2* **72**, 1970 (1976).
 - [14] J. S. Rowlinson, *Adv. Chem. Phys.* **41**, 1 (1980).
 - [15] J. S. Rowlinson and B. Widom, *Molecular Theory of Capillarity* (Clarendon, Oxford, 1982).
 - [16] C. Y. Shew and A. Yethiraj, *J. Chem. Phys.* **104**, 7665 (1996).
 - [17] A. Yethiraj and G. Stell, *J. Stat. Phys.* **100**, 39 (2000).
 - [18] E. Bergmann, *Mol. Phys.* **32**, 237 (1976).
 - [19] G. Johnson, H. Gould, J. Machta, and L. K. Chayes, *Phys. Rev. Lett.* **79**, 2612 (1997).

MATTHIAS SCHMIDT AND ALAN R. DENTON

PHYSICAL REVIEW E **65** 021508

- [20] P. Borgelt, C. Hoheisel, and G. Stell, *J. Chem. Phys.* **92**, 6161 (1990).
- [21] *Coatings Technology Handbook*, edited by D. Satas (Dekker, New York, 1991).
- [22] R. Evans, in *Fundamentals of Inhomogeneous Fluids*, edited by D. Henderson (Dekker, New York, 1992), p. 85.
- [23] Y. Rosenfeld, *Phys. Rev. Lett.* **63**, 980 (1989).
- [24] M. Schmidt, H. Löwen, J. M. Brader, and R. Evans, *Phys. Rev. Lett.* **85**, 1934 (2000).
- [25] M. Schmidt, *Phys. Rev. E* **63**, R05201 (2001).
- [26] M. Schmidt, *Phys. Rev. E* **63**, R01101 (2001).
- [27] Y. Rosenfeld, *Phys. Rev. E* **50**, R3318 (1994).
- [28] P. Tarazona, *Phys. Rev. Lett.* **84**, 694 (2000).
- [29] J. A. Barker and D. Henderson, *Rev. Mod. Phys.* **48**, 587 (1976).
- [30] M. Dijkstra (unpublished).
- [31] J. M. Brader and R. Evans, *Europhys. Lett.* **49**, 678 (2000).
- [32] J. M. Brader, M. Dijkstra, and R. Evans, *Phys. Rev. E* **63**, 041405 (2001).

PHYSICAL REVIEW E, VOLUME 64, 051115

Amphiphilic hard body mixtures

Matthias Schmidt and Christian von Ferber

Institut für Theoretische Physik II, Heinrich-Heine-Universität Düsseldorf, Universitätsstraße 1, D-40225 Düsseldorf, Germany

(Received 16 June 2001; published 29 October 2001)

In order to study ternary amphiphilic mixtures, we introduce a simplistic model of hard spheres corresponding to water and hard needles corresponding to oil and amphiphilic particles, where the hydrophilic head is modeled as a hard sphere and the hydrophobic tail as an infinitely thin needle attached radially to the sphere. For this system, we construct a geometry-based density functional and perform Monte Carlo computer simulations. The equation of state derived from the theory is found to be in remarkable agreement with our simulation results. We investigate the theoretical demixing phase diagram, and find that the predicted trends strongly support the amphiphilic character of the model.

DOI: 10.1103/PhysRevE.64.051115

PACS number(s): 82.70.Uv, 61.20.Gy, 64.70.Ja

I. INTRODUCTION

Adding amphiphiles to a system of oil and water considerably enhances the miscibility of these substances. Amphiphilic molecules consist of a hydrophilic head group and a hydrophobic tail, which prefer being dissolved in water and oil, respectively. The physics of amphiphilic systems is important in many areas, including industrial and domestic applications like washing, cleaning, emulsification, and many more. Due to the different preferences of their constituents, amphiphiles adsorb at oil-water interfaces and facilitate the creation of such interfaces. Depending on the thermodynamical variables, these interfaces arrange in a rich variety of structures [1–4], and much theoretical work has been devoted to understanding the underlying basic mechanisms. Microscopic approaches have often used a lattice fluid model [5–8], while coarse grained continuum descriptions are provided by Ginzburg-Landau [9] or integral geometrical [10] models.

Density functional theory (DFT) [11] is a powerful approach to inhomogeneous statistical systems, and has been applied to study amphiphilic behavior on different levels from microscopic to macroscopic. A model for membranes, vesicles, and micelles [12] based on a description for effective amphiphile interactions arising from the presence of solvent molecules has been studied. The phase behavior of a symmetrical ternary mixture was found to exhibit three-(isotropic)-liquid-phase coexistence [13]. This approach was generalized to asymmetric interactions between amphiphiles and water and oil, and lamellar and micellar phases were found [14]. The structure of droplet microemulsions was also treated [15]. The problem of separation of length scales into those of the microscopic domain (relevant for building up interfaces) and those of the mesoscopic regime (to capture the degrees of freedom of supramolecular aggregates) was addressed within a one-dimensional model of molecular aggregation [16], and later on generalized to the three-dimensional case [17]. The phase behavior [18] and gas-liquid nucleation [19] of amphiphilic binary mixtures consisting of Lennard-Jones monomers and bonded dimers has been investigated. Furthermore, a DFT approach has been applied to nucleation in micellar solutions [20].

In this work we propose a simple atomistic model in order

to investigate amphiphilic mixtures. The particles possess continuous (off-lattice) positions and orientations, and we prescribe the microscopic interparticle interactions. In our model, only hard core pair interactions are present; hence the behavior is solely driven by entropy. Using hard core systems has proved to be fruitful for important phenomena like freezing [21] and liquid crystalline ordering, and we believe that this could also be the case for amphiphiles. To study the model, we construct a geometry-based DFT. This approach originates from Rosenfeld's fundamental measure theory for hard sphere mixtures [22–25], which was also formulated for convex bodies [26] and parallel hard cubes [27,28]. Recently, within geometry-based DFT, a range of models has been treated successfully, including the Asakura-Oosawa colloid-ideal-polymer mixture [29], the Widom-Rowlinson model [30], and a model due to Bolhuis and Frenkel [31], where hard spheres are mixed with infinitely thin needles [32]. This needle-sphere mixture displays a demixing phase transition crudely reminiscent of that of water and oil. Here, we use this as a starting point, and supplement it with a third species of particle that consists of a sphere to which a needle is attached rigidly. The spherical part is a caricature of the hydrophilic head and the needle models the hydrophobic tail of an amphiphilic molecule. Hence we arrive at a simplistic model for a nonionic amphiphile ternary mixture, featuring explicit water-oil asymmetry. Hybrid shapes of spheres and (thin) rods are also realized in the colloidal domain by microtubules inside vesicles [33,34], and by rodlike fd bacteriophage viruses bound to silica beads [35].

As will be seen below, our hard body amphiphiles are nonconvex particles. In order to deal with nonconvexity, we carry over the recipes developed for convex particles [32], at the expense of a certain violation of the overlap condition within the theory. As we will show in detail, the violation is quantitatively small and does not hinder the development of a powerful theory.

Our final aim is to elucidate the phase behavior of the system. To have benchmark results to test the theory against, we have carried out Monte Carlo (MC) computer simulations, and have obtained results for the equation of state for typical compositions of species and over a broad range of densities in regions where the system remains in a fluid state. Comparing with the theoretical results, we find nice agree-

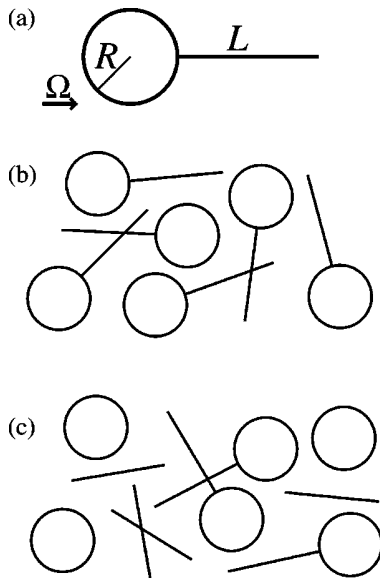


FIG. 1. Sketch of the model amphiphilic mixture. (a) Amphiphilic molecules consisting of a hard, infinitely thin needle of length L , which is attached radially to a hard sphere of radius R . The orientation of the particle is described by the unit vector Ω . (b) Pure amphiphile system. (c) Ternary system consisting of amphiphiles, hard spheres (water), and hard, infinitely thin needles (oil).

ment, and hence are confident in trusting the theoretical results for the phase diagram, without further checking against simulations. We find that amphiphiles mix better with either spheres or needles than do spheres with needles. The ratio of tail length to head radius acts as a control parameter governing the relative affinity of amphiphiles for either spheres or needles.

The paper is organized as follows. In Sec. II we define the ternary hard body mixture of amphiphiles, spheres, and needles, as well as a multicomponent generalization thereof. In Sec. III we develop the DFT first for this general system, and then specialize to the actual ternary mixture as well as to a pure system of amphiphiles. We also discuss the problem arising from the nonconvexity of the particles. Our computer simulation technique is presented in Sec. IV. In Sec. V we investigate demixing phase behavior for homogeneous fluid states. Discussion and an outlook are given in the concluding Sec. VI.

II. THE MODEL

Let us introduce amphiphilic hard core particles, which consist of a hard sphere of radius R and an infinitely thin needle of length L . The needle (tail) is attached radially to the sphere (head); see Fig. 1(a) for a sketch of the resulting geometrical shape. The direction of the needle is denoted by Ω . A single-component system of amphiphiles [see Fig. 1(b) for an illustration] is ruled by the number density ρ_A . We refer to this system in the following as *pure amphiphiles*; see Fig. 2(a) for a snapshot from a computer simulation (de-

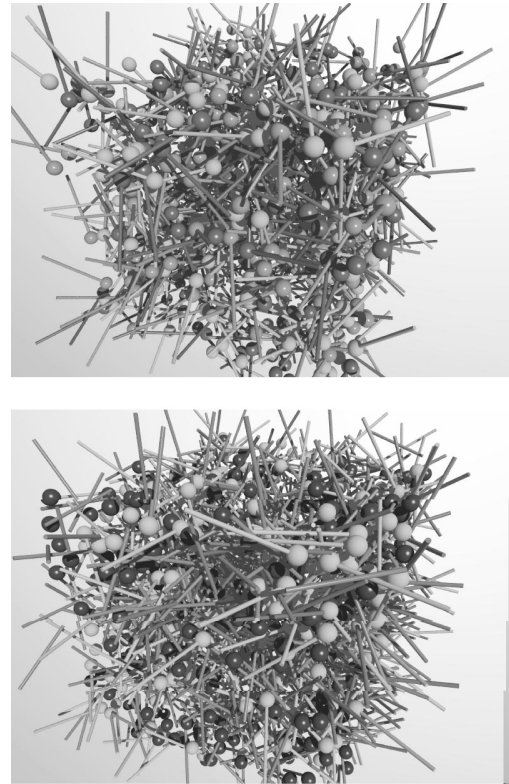


FIG. 2. Snapshots from computer simulation. (a) Pure amphiphile system; the particles possess different gray levels. (b) Ternary mixture of spheres (black), needles (gray), and amphiphiles (white).

scribed below) of this model.

We also consider a three-component mixture of (i) particles with amphiphilic character, (ii) particles corresponding to water, and (iii) particles corresponding to oil molecules. For our amphiphiles (species A), adding two further species for which their shape possesses an amphiphilic character is straightforward. We use hard spheres (species S) with radius R as a caricature of water. The role of oil is played by hard, infinitely thin needles (species N) of length L . Hence we arrive at a model that we refer to as the *ternary mixture*; see Fig. 1(c) for a sketch. The number densities are denoted by $\rho_i, i=A, N, S$, the sphere diameter by $\sigma=2R$, and the size ratio by $q=L/R$. The packing fraction of spheres is $\eta_S=4\pi R^3\rho_S/3$, and that of amphiphilic heads is $\eta_A=4\pi R^3\rho_A/3$. We show a typical particle configuration in Fig. 2(b) as an illustration.

Additionally, we generalize to a multicomponent mixture where the species are labeled by i (adopting a discrete picture of mixtures); the spherical head groups of species i possess radii R_i and the needle tails have lengths L_i . This *multicomponent mixture* will be used below to formulate the DFT. Clearly, it includes the case of monodisperse amphiphiles, if only a single species A is present. Also the ternary mixture is obtained as a special case. For $i=A, N, S$, we simply set $L_A=L_N, L_S=0, R_A=R_S$, and $R_N=0$.

III. THEORY

A. Density functional

The DFT we propose is a weighted density approximation. By convolutions of the position- and orientation-dependent density profiles $\rho_i(\mathbf{r}, \mathbf{\Omega})$, weighted densities are obtained. These weighted densities are converted by a simple function into an excess free energy density. This is a local quantity, depending on space point and orientation. The global excess free energy is obtained by integration over space and rotator degree of freedom. The weight functions with which the $\rho_i(\mathbf{r}, \mathbf{\Omega})$ are convoluted are obtained by geometric considerations and describe the geometrical shapes of the particles. We first formulate the theory for the general multicomponent mixture, and then specialize to pure amphiphiles as well as to the ternary mixture.

1. Multicomponent amphiphiles

We start by giving the weight functions. Those that are characteristic functions of the needle part of the particles are defined as

$$\bar{w}_q^{(i)}(\mathbf{r}, \mathbf{\Omega}) = \frac{1}{4} \int_{R_4}^{R_i+L_i} dl \delta(\mathbf{r} + l\mathbf{\Omega}), \quad (1)$$

$$\bar{w}_0^{(i)}(\mathbf{r}, \mathbf{\Omega}) = \frac{1}{2} [\delta(\mathbf{r} + (R_i + L_i)\mathbf{\Omega}) - \delta(\mathbf{r} + R_i\mathbf{\Omega})]. \quad (2)$$

Here and in the following, the overbar indicates needle (tail) quantities. The weight functions that describe the sphere part of the particles are equal to those for pure hard spheres (HS's) [22,25] and are defined as

$$w_3^{(i)}(\mathbf{r}) = \theta(R_i - r), \quad w_2^{(i)}(\mathbf{r}) = \delta(R_i - r), \quad (3)$$

$$\mathbf{w}_{v2}^{(i)}(\mathbf{r}) = w_2^{(i)}(\mathbf{r}) \cdot \mathbf{r}/r, \quad \hat{\mathbf{w}}_{m2}^{(i)}(\mathbf{r}) = w_2^{(i)}(\mathbf{r}) [\mathbf{r}\mathbf{r}/r^2 - \hat{\mathbf{1}}/3], \quad (4)$$

$$\bar{w}_2^{(i)}(\mathbf{r}, \mathbf{\Omega}) = 2|\mathbf{w}_{v2}^{(i)}(\mathbf{r}) \cdot \mathbf{\Omega}|, \quad (5)$$

where $r = |\mathbf{r}|$, $\theta(r)$ is the step function, and $\hat{\mathbf{1}}$ is the identity matrix. Further, linearly dependent, weights are $w_1^{(i)}(\mathbf{r}) = w_2^{(i)}(\mathbf{r})/(4\pi R_i)$, $\mathbf{w}_{v1}^{(i)}(\mathbf{r}) = \mathbf{w}_{v2}^{(i)}(\mathbf{r})/(4\pi R_i)$, and $w_0^{(i)}(\mathbf{r}) = w_1^{(i)}(\mathbf{r})/R_i$. The weight functions possess different tensorial rank: $w_0^{(i)}$, $w_1^{(i)}$, $w_2^{(i)}$, and $w_3^{(i)}$ are scalars; $\mathbf{w}_{v1}^{(i)}$ and $\mathbf{w}_{v2}^{(i)}$ are vectors; $\hat{\mathbf{w}}_{m2}^{(i)}$ is a (traceless) matrix. The weighted densities are

$$n_\nu(\mathbf{r}) = \sum_i \int \frac{d^2\Omega'}{4\pi} \rho_i(\mathbf{r}', \mathbf{\Omega}') * w_\nu^{(i)}(\mathbf{r}''), \quad (6)$$

$$\bar{n}_\nu(\mathbf{r}, \mathbf{\Omega}) = \sum_i \rho_i(\mathbf{r}', \mathbf{\Omega}') * \bar{w}_\nu^{(i)}(\mathbf{r}'', \mathbf{\Omega}), \quad \nu = 0, 1, \quad (7)$$

$$\bar{n}_2(\mathbf{r}, \mathbf{\Omega}) = \sum_i \int \frac{d^2\Omega'}{4\pi} \rho_i(\mathbf{r}', \mathbf{\Omega}') * \bar{w}_2^{(i)}(\mathbf{r}'', \mathbf{\Omega}), \quad (8)$$

where the star denotes convolution, $g(\mathbf{r}') * h(\mathbf{r}'') = \int d^3x g(\mathbf{x}) h(\mathbf{r} - \mathbf{x})$. The Helmholtz free energy is $F = F^{\text{id}} + F^{\text{exc}}$, where F^{exc} arises from interactions and the ideal gas contribution is

$$F^{\text{id}}[\rho_i(\mathbf{r}, \mathbf{\Omega})] = \sum_i \int d^3x \int \frac{d^2\Omega}{4\pi} \rho_i(\mathbf{r}, \mathbf{\Omega}) \times \{\ln[\rho_i(\mathbf{r}, \mathbf{\Omega}) \Lambda_i^3] - 1\}, \quad (9)$$

where Λ_i is the thermal wavelength of species i . [Note that the normalization is such that $\rho(\mathbf{r}, \mathbf{\Omega}) = \rho(\mathbf{r})$ for isotropic orientation distributions.] The excess free energy is

$$F^{\text{exc}}[\{\rho_i(\mathbf{r}, \mathbf{\Omega})\}] = k_B T \int d^3r \int \frac{d^2\Omega}{4\pi} \Phi(\{n_\gamma\}, \{\bar{n}_\gamma\}), \quad (10)$$

where k_B is Boltzmann's constant and T the temperature, and the (local) free energy density Φ is a simple function (not a functional) of the weighted densities n_γ . Considering multicavity distributions [25], we obtain $\Phi = \Phi_{\text{HS}} + \bar{\Phi}$ with

$$\begin{aligned} \Phi_{\text{HS}} = & -n_0 \ln(1 - n_3) + (n_1 n_2 - \mathbf{n}_{v1} \cdot \mathbf{n}_{v2}) / (1 - n_3) \\ & + [(n_2)^3 / 3 - n_2 (\mathbf{n}_{v2})^2 + 3 (\mathbf{n}_{v2} \cdot \hat{\mathbf{n}}_{m2} \cdot \mathbf{n}_{v2} \\ & - 3 \det \hat{\mathbf{n}}_{m2}) / 2] / [8\pi(1 - n_3)^2], \end{aligned} \quad (11)$$

which is equal to the pure HS case [22,25]. The contribution due to the presence of the needles is

$$\bar{\Phi} = -\bar{n}_0 \ln(1 - n_3) + \frac{\bar{n}_1 \bar{n}_2}{1 - n_3}. \quad (12)$$

This completes the prescription for the functional for multicomponent amphiphiles.

2. Pure amphiphiles

For a one-component system of amphiphile particles with radius R and needle length L , the general functional can easily be reduced. The summations over species i in Eqs. (6)–(8) vanish, and a density functional of a single density field $\rho_A(\mathbf{r}, \mathbf{\Omega})$ is obtained.

3. Ternary mixture

We consider a mixture of spheres (species S) with radii R , needles (species N) with length L , and amphiphiles (species A) with the same dimensions, namely, radius R and length L . The weight functions for spheres ($L_S = 0$) simplify, such that $\bar{w}_0^{(S)} = \bar{w}_1^{(S)} = 0$, and $\bar{w}_2^{(S)}$ is identical to the corresponding weight function in the case of the needle-sphere functional [32]. All $w_\nu^{(S)}$ are identical to those of the pure hard sphere case [22,25]. For needles, all densities with $\nu > 1$ vanish, $w_\nu^{(N)} = 0$. This is expected from dimensional arguments, because an infinitely thin needle does not possess surface area ($\nu = 2$), nor volume ($\nu = 3$). The remaining weight function $w_1^{(N)}$ is identical to that in the case of the needle-sphere functional. The weight function for $\nu = 0$ is also identical to that

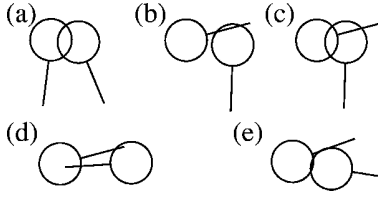


FIG. 3. Configurations of overlapping amphiphiles. Cases where the Mayer function is correct within the DFT, $f = -1$: (a) sphere-sphere; (b) sphere-needle; (c) sphere overlapping simultaneously with the needle and the sphere of a second particle. Problem cases, where $f = -2$ within the DFT: (d) simultaneous sphere-needle overlap; (e) sphere overlapping with the needle and the sphere of the second particle, so that the inner needle end point is outside the first sphere.

in this case, and is obtained as the sum $w_0^{(N)} + \bar{w}_0^{(N)}$. Note that in the present description the position coordinate of the needle is one of its end points, whereas using the needle midpoint might be more intuitive (see Ref. [32]). Both descriptions are of course equivalent, and are related by a simple coordinate transformation.

B. Mayer bonds

The Mayer f_{ij} bond between species i and j is $f_{ij} = -1$, if the two particles overlap, and zero otherwise. Within geometry-based DFT, the f_{ij} are represented as the (negative) Euler characteristics of the overlap region of the two bodies i and j . For convex bodies, the overlap region is also convex, and hence carries Euler characteristic of unity. For nonconvex bodies the situation is more complicated. The overlap region may consist of several disconnected portions, and its Euler characteristic equals the number of these portions.

For our model, the two-particle Mayer bonds are correct within the DFT, if no amphiphile is involved, i.e., f_{SS} and f_{SN} . Furthermore, f_{AN} is also correct. Problems arise between two amphiphiles, f_{AA} , as well as between an amphiphile and a sphere, f_{AS} . In Figs. 3(a–c) we display the cases where the Mayer bond is correct, and Figs. 3(d,e) show the cases where the Mayer bond is incorrect, namely, $f_{ij} = -2$. It might be physically expected that the statistical weight of such problem configurations is only small, because for a given position and orientation of the first particle the second particle's position *and* orientation are restricted.

C. Second virial coefficients

In order to measure quantitatively the degree of violation of the overlap condition, we evaluate the second virial coefficient for amphiphiles from the DFT and compare it to the exact result, which we can obtain analytically. Note that this is precisely a test of the accuracy of the present approach in the low-density limit. For simplicity, we perform the calculation for pure amphiphiles. The second virial coefficient is defined as

$$B_{2,ij} = -\frac{1}{2V} \int d^3r d^2\Omega d^3r' d^2\Omega' f_{ij}(\mathbf{r}, \mathbf{\Omega}; \mathbf{r}', \mathbf{\Omega}'), \quad (13)$$

TABLE I. Overview of simulated systems. Particle numbers (#) for needles (N), amphiphiles (A), and spheres (S) are given. η_{tot} denotes the total packing fraction of *spherical* entities.

	Species	# N	# A	# S	η_{tot}
Pure	A		1000		η_A
	S			1000	η_S
Binary	AN	1000	1000		η_A
	SN	1000		1000	η_S
	AS		500	500	$\eta_A + \eta_S$
Ternary	ASN	1000	500	500	$\eta_A + \eta_S$
		1000	500	1000	
		1000	1000	500	

where V is the system volume. We find the exact result for pure amphiphiles as

$$B_{2,AA}^{\text{exact}} = \frac{16\pi^3}{15(L+R)^2} \{ -2L^5 - 10L^4R + 5L^3R^2 + 5(25+6\sqrt{3}) \times L^2R^3 + 5(41+12\sqrt{3})LR^4 + (91+30\sqrt{3})R^5 + 2[R^2 + (L+R)^2]^{5/2} \}, \quad (14)$$

which holds for the case $L > (\sqrt{3}-1)R$. For $L \gg R$, the expansion is

$$B_{2,AA}^{\text{exact}} = 16\pi^3 \left[2LR^2 + \left(\frac{20}{3} + 2\sqrt{3} \right) R^3 + O\left(\frac{R^4}{L} \right) \right], \quad (15)$$

where $20/3 + 2\sqrt{3} = 10.1308$. The result from DFT is

$$B_{2,AA}^{\text{DFT}} = 16\pi^3 \left(2LR^2 + \frac{32}{3} R^3 \right), \quad (16)$$

which is free of terms of order R^4/L and higher. Note that the term of order LR^2 is the dominant contribution from sphere-needle overlap. This is exact in the DFT. The term of order R^3 stems from the hard core between spheres, and is overestimated by about 5% in the DFT. All higher-order corrections are not reproduced in the DFT result. We conclude that for $L \gg R$ the DFT result is an excellent approximation to $B_{2,AA}^{\text{exact}}$. Even for $L/R = 10$, the relative deviation is only $B_{2,AA}^{\text{DFT}}/B_{2,AA}^{\text{exact}} = 1.017$. For shorter needles, $L = R$, the deviation grows somewhat to $B_{2,AA}^{\text{DFT}}/B_{2,AA}^{\text{exact}} = 1.036$.

IV. COMPUTER SIMULATION

We use the canonical ensemble to carry out Monte Carlo simulations. Our method of obtaining the pressure is based on the probability density of a successful small change in system volume. In order to perform such a compression, we enlarge the dimensions of each particle by a factor $1 + \alpha$, where $\alpha = 0.00125 - 0.005$, and test for overlap. The statistics of this test yields the pressure p .

We have carried out simulations at 48 state points with different densities and compositions of species. At each state point 10^4 Monte Carlo cycles were done. Particle numbers range from 1000 to 2500 particles; see Table I for details. As

a compromise between considerable needle length and manageable simulation box size, we pick the size ratio $q=L/R=10$ for all runs. The simulation box is chosen to be larger than twice the particle length in order to avoid problems with multiple overlap of periodic images. In terms of the total packing fraction $\eta_{\text{tot}}=\eta_A+\eta_S$, we simulate in the range $\eta=0.05-0.3$ by varying the simulation box size.

V. FLUID PHASES

We proceed from simple to complex, and hence start with a discussion of one-component fluid phases, in particular, of the pure amphiphile system. We then turn to the (three) binary systems that are obtained by selecting pairs out of the three species. Formally, these are obtained from the ternary sphere-amphiphile-needle system by setting the density of one of the species to zero. Finally, we investigate the full ternary mixture.

In the following we restrict ourselves to homogeneous, isotropic fluid states, which are characterized by spatially and rotationally invariant density distributions, $\rho_i(\mathbf{r}, \mathbf{\Omega})=\text{const}$. Any mesophases, like lamellar or micellar ones, as well as liquid crystalline ordering, are explicitly excluded from our investigation. However, such density distributions allow for phase separation into macroscopically demixed phases. The strategy is to apply the DFT to the homogeneous densities and hence to derive the bulk free energy and the equation of state. This task can be performed analytically within the present theory. We then check the numerical accuracy of the equation of state obtained via differentiation of the free energy against computer simulation results. Finally, we calculate the theoretical demixing phase diagrams including binodal, spinodal, and critical point for the binary mixtures. In the final case of the ternary mixture, we restrict ourselves to the spinodal.

In detail, our calculations are as follows. For homogeneous, isotropic states, the weighted densities become proportional to the bulk density $n_\nu=\sum_i \xi_\nu^{(i)} \rho_i$. The proportionality constants are given as fundamental measures $\xi_\nu^{(i)}=\int d^3r w_\nu^{(i)}(\mathbf{r})$. For the ternary case, the fundamental measures are for spheres $\xi_3^S=4\pi R^3$, $\xi_2^S=4\pi R^2$, $\xi_1^S=R$, $\xi_0^S=1$, for amphiphiles $\xi_3^A=4\pi R^3$, $\xi_2^A=4\pi R^2$, $\xi_1^A=R+L/4$, $\xi_0^A=1$, and for needles $\xi_1^N=L/4$, $\xi_0^N=1$. Note that, although an amphiphile consist of a sphere and a needle, $\xi_\nu^A=\xi_\nu^S+\xi_\nu^N$ does not hold for all ν . This is because $\xi_0^{(i)}=1$ for all species, because each particle consists of a single body and hence possesses Euler characteristic unity. Hence the weighted densities in isotropic bulk fluids become $n_3=4\pi R^3(\rho_S+\rho_A)/3(=\eta_{\text{tot}})$, $n_2=4\pi R^2(\rho_S+\rho_A)(=3\eta_{\text{tot}}/R)$, $n_1=R(\rho_S+\rho_A)[=3\eta_{\text{tot}}/(4\pi R^2)]$, $n_0=\rho_S+\rho_A[=3\eta_{\text{tot}}/(4\pi R^3)]$, and $\bar{n}_1=(\rho_N+\rho_A)L/4$, $\bar{n}_0=\rho_N$.

We obtain the spinodal for demixing from the bulk free energy by solution of $\det \partial^2(F/V)/\partial \rho_i \partial \rho_j=0$, which indicates the boundary of stability. This was carried out previously for the case of the binary needle-sphere mixture ($\rho_A=0$) [32], and a *universal* (q -independent) spinodal was found. Here we follow the same recipe for the remaining two binary mixtures, namely, (i) adding needles to pure amphiphiles and (ii)

adding spheres to pure amphiphiles. For the full ternary mixture, we can also, somewhat surprisingly, find an analytical expression for the spinodal depending on all three densities.

In the case of one-component hard spheres our theory reduces to the Rosenfeld functional [22] in Tarazona's latest tensorial version [25]. The excess free energy density per volume for pure hard spheres with packing fraction η and radius R derived from the DFT is identical to the result of the Percus-Yevick compressibility (scaled-particle) approximation, and is given as $\beta F^{\text{exc}}(\eta_S)/V=\Phi_{\text{HS}}$, where $\beta=1/k_B T$ and

$$\Phi_{\text{HS}}(\eta)=\frac{3\eta[3\eta(2-\eta)-2(1-\eta)^2\ln(1-\eta)]}{8\pi R^3(1-\eta)^2}. \quad (17)$$

The pure system of needles constitutes an ideal gas of (non-interacting) rotators. Hence the excess free energy vanishes exactly, and indeed we recover this (trivial) result, $\Phi=0$. This is merely a check of the above method (Sec III A) for generating DFTs from the zero-dimensional limit, and demonstrates that this does not lead to artificial interactions.

A. Pure amphiphiles

The system of one-component amphiphiles provides a first nontrivial test case. For the homogeneous, isotropic bulk phase $\rho_A(\mathbf{r}, \mathbf{\Omega})=\text{const}$, we obtain the excess Helmholtz free energy per volume $\beta F^{\text{exc}}/V=\Phi_A$, with

$$\Phi_A=\Phi_{\text{HS}}(\eta_A)+\frac{9q\eta_A^2}{16\pi R^3(1-\eta_A)}. \quad (18)$$

In this additive expression, Φ_{HS} is the residual contribution for $q=0$, stemming only from the presence of the spherical heads. The contribution due to the presence of the needle tails scales *linearly* with size ratio q . The dependence on η_A is a rational expression typical of geometry-based DFT, with a (formal) divergence $\eta_A\rightarrow 1$. Clearly, for large q this second term dominates over Φ_{HS} .

In order to check the quality of this result, we compare the compressibility factor $Z=\beta p/\rho$, where the pressure is $p=-\partial F/\partial V$ and the total density ρ in this case $\rho=\rho_A$, against simulation results for $q=10$ in Fig. 4(a). Also shown are results for the pure hard sphere case. The compressibility factor is considerably larger for amphiphiles than for spheres. This is to be expected, as we compare states with equal packing fractions of spheres, but with (amphiphiles) and without (spheres) tails. The interactions of the tails with the sphere lead to the observed increase by more than a factor of 2. The shapes of both curves, however, are similar. The theoretical results are slightly smaller than the MC data, but the general agreement is remarkable. Finally, we note that Z is a quite sensitive quantity. Recall that our approximation is on the level of F^{exc} , and Z is obtained by differentiation and division by density, operations which in general will enhance any deviations. We also plot the low-density behavior governed by the second virial coefficient both from DFT and from the exact calculation. They essentially coincide on the resolution of the plot.

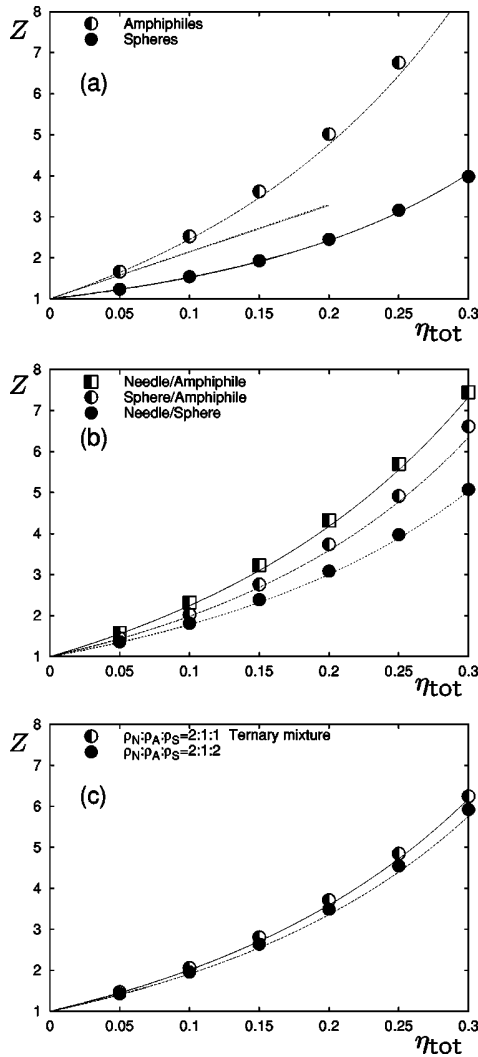


FIG. 4. Compressibility factor Z as a function of total packing fraction η_{tot} . Simulation results (symbols) are compared against theoretical predictions (lines). Straight lines indicate the low-density limit governed by the second virial coefficient. (a) Pure systems; (b) binary mixtures; (c) ternary mixtures.

B. Binary mixtures

Once a system possess two distinguishable components, it may undergo a demixing phase transition into two macroscopically distinct phases with different compositions of particles. In our case, binary mixtures are obtained by setting the density of one of the species of the ternary mixture to zero. For these systems, we shall investigate how the size ratio q plays the role of a control parameter for demixing behavior, and especially enlighten the limits $q \rightarrow 0, \infty$. Then we focus on the interesting question of how amphiphiles mix with either needles or spheres, compared to the mixing behavior of needles and spheres.

1. Needles and spheres

According to computer simulation results by Bolhuis and Frenkel [31], a mixture of spheres and infinitely thin needles displays a demixing phase transition into a sphere-rich

(needle-poor) phase and a sphere-poor (needle-rich) phase. The mechanism for this phase separation is, crudely speaking, the gain in configurational entropy in both demixed phases. In the needle-rich phase, interactions are considerably reduced, because the needles do not interact among themselves, and the presence of spheres is only a perturbing ‘‘impurity’’ effect to essentially an ideal gas of needles. The sphere-rich phase, however, is only weakly disturbed by the presence of the needles [32]. Bolhuis and Frenkel developed a first order perturbation theory that is similar to Lekkerkerker’s free volume approach for the Asakura-Oosawa colloid-ideal-polymer mixture. The present DFT approach recovers their result [32]; the excess free energy per volume is

$$\frac{\beta F^{\text{exc}}}{V} = \Phi_{\text{HS}}(\eta_S) + \rho_N \left[\frac{3q\eta_S}{4(1-\eta_S)} - \ln(1-\eta_S) \right]. \quad (19)$$

It is interesting to compare this result with that of the above case of pure amphiphiles, Eq. (18). To do so, we naively set $\rho_S = \rho_N$, and compare with Φ_A for a single component. The results are not identical (which should not be expected), but differ by a logarithmic expression. Its origin can be traced back to the fact that the needles in the binary mixture are individual particles with an Euler characteristic of unity. In the case of amphiphiles, the needle tails alone have vanishing Euler characteristic, and the corresponding term in the free energy functional vanishes (in bulk). Note also that this term is independent of q (as is the Euler characteristic). In summary, we stress that Φ_A cannot be obtained by the trivial restriction of equal densities in the free energy of the binary sphere-needle mixture. The naive calculation yields an additional term in the compressibility, which is q independent and given by $\eta_A/(1-\eta_A)$. This is a small contribution for large q , but destroys the hard sphere limit for $q \rightarrow 0$, which is correct in the proper DFT result.

As was already found in Ref. [31], a comparison with the simulation results demonstrates the excellent quality of the equation of state obtained from the theory. We repeat this comparison in Fig. 4(b), using the compressibility factor from both simulation and theory. Indeed, both results are in good agreement.

In the case of the needle-sphere binary mixture the analytic expression for the spinodal was found to be [32]

$$\rho_N \pi q^2 R^3 = \frac{4(1+2\eta_S)^2}{3\eta_S}. \quad (20)$$

This is universal (q independent) in the ‘‘natural’’ variables η_S and $\rho_N q^2 R^3$. Note that $\rho_N q^2 R^3$ is exactly the proper scaling in the Onsager limit. The critical point in the limit $q \rightarrow \infty$ is $q \rho_N R^3 = \pi [1 + (44/3)q^{-1} + O(q^{-2})]$ and $q \eta_S = (4/3) [1 - (28/3)q^{-1} + O(q^{-2})]$. We display the demixing phase diagram in Fig. 5 for $q = 10, 20, 50$, as well as the metastable (with respect to freezing) [31] case $q = 0$. For small densities the system is in a mixed state; increasing density leads to demixing. The critical point moves toward smaller η_S as q grows.

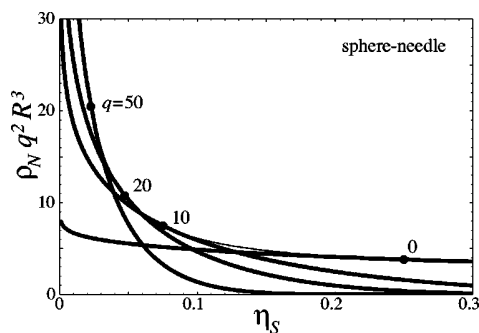


FIG. 5. Phase diagram for the sphere-needle mixture for $q = 10, 20, 50$ as a function of sphere packing fraction η_S and scaled needle density $\rho_N q^2 R^3$. The binodals (thick lines), q -independent spinodal (thin line), and critical points (dots) are shown.

2. Amphiphiles and needles

Adding needles to a fluid phase of amphiphiles should be easier than adding needles to a hard sphere fluid of the same density: The amphiphile tails are expected to create free volume for the needles, an effect that is absent in the case of hard spheres as a host fluid. The excess free energy for the amphiphile-needle mixture is

$$\frac{\beta F^{\text{exc}}}{V} = \Phi_A(\eta_A) + \rho_N \left[\frac{3q\eta_A}{4(1-\eta_A)} - \ln(1-\eta_A) \right]. \quad (21)$$

This result is the same as in the case of the sphere-needle mixture, but with Φ_{HS} replaced by Φ_A . Hence the contribution due to the presence of the free needles is the same in both cases. In other words, the free needles interact only with the heads of the amphiphiles. Clearly, this is true for the interaction potentials. On the level of the free energy, it represents an approximation and will not hold in general for the exact free energy. See Fig. 4(b) for comparison with the simulation results.

The demixing spinodal of the amphiphile-needle binary mixture is

$$\rho_N \pi L^2 R = \frac{4(1+2\eta_A)^2}{3\eta_A} + 2q(1-\eta_A). \quad (22)$$

We next investigate the limit of short needles, $q \rightarrow 0$. At fixed scaled density $\rho_N \pi L^2 R$, the model reduces to the sphere-needle mixture. This is physically reasonable, because the amphiphile shape reduces essentially to a sphere to which only a very short needle is attached. The latter should not matter. The free needles still play a role, because their density ρ_N grows large as $\rho_N \pi L^2 R$ is kept constant. See Fig. 6 for the demixing phase diagram as a function of η_A and $q^2 \rho_N$ for $q = 0, 10, 20$. As q increases, the spinodals shift to higher densities, and the critical point moves to smaller η_A . In the case of long rods, $q \rightarrow \infty$, the location of the critical point is $q \rho_N R^3 = (4/\pi)[1 + 2q^{-1} + O(q^{-2})]$ and $q \eta_A = (2/3)[1 - 2q^{-1} + O(q^{-2})]$.

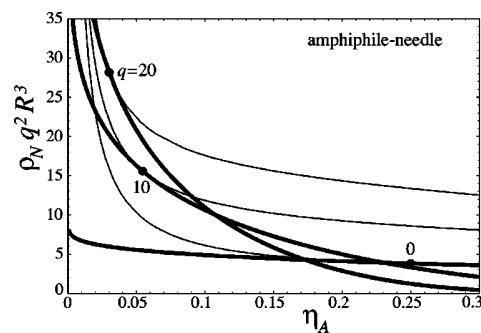


FIG. 6. Phase diagram for amphiphile-needle mixture for $q = 0, 10, 20$. The dots mark the critical points. The case $q = 0$ is equal to the sphere-needle binary mixture.

3. Amphiphiles and spheres

The excess free energy is

$$\frac{\beta F^{\text{exc}}}{V} = \Phi_{\text{HS}}(\eta_{\text{tot}}) + \frac{9q\eta_A\eta_{\text{tot}}}{16\pi R^3(1-\eta_{\text{tot}})}, \quad (23)$$

where $\eta_{\text{tot}} = \eta_S + \eta_A$. Here both densities are intimately coupled, through Φ_{HS} as a function of the total packing fraction. The additional contribution is again linear in q , and has a similar but not identical dependency on the densities as in the other cases. See Fig. 4(b) for comparison with the simulation results:

The spinodal for the amphiphile-sphere binary mixture is obtained as

$$\begin{aligned} \rho_A 8\pi(q'-1)R^3/3 \\ = 1 + q' - \eta_S(q'-1)(q'+2) \\ + \sqrt{3q'(1+q'/3)[1 + \eta_S(q'-1)(q'\eta_S-2)]}, \quad (24) \end{aligned}$$

where $q' = 3q/8$.

We next discuss the limiting cases. Clearly, for needles with vanishing length $q=0$, the amphiphiles reduce to spheres, and the system reduces to pure hard spheres. A particularly interesting case is the crossover between short and long needle tails. For amphiphiles with large q , the system demixes. For small q the phase transition is clearly absent, as both species become identical. The interesting question is how the crossover between the two cases happens. We find that demixing is absent for $q < q^* = 8/3$. If q^* is approached from above, the spinodal shifts to large amphiphile densities, and diverges formally. However, this scenario is likely to be preempted by freezing. For long needles $q \rightarrow \infty$, the effect of the attached head groups vanishes, and the amphiphiles behave like effective needles. Hence the model reduces to the needle-sphere mixture. As regards the spinodal, the limit is attained at quite large size ratios q .

In Fig. 7(a) we display the demixing phase diagram as a function of both packing fractions η_S and η_A . In order to have packing fractions inside the assumed fluid region, we use the rough criterion $\eta_S + \eta_A < 0.5$, which is about the value at freezing of pure hard spheres. Rather long needle tails with $q > 20$ are needed to access this region. The limit

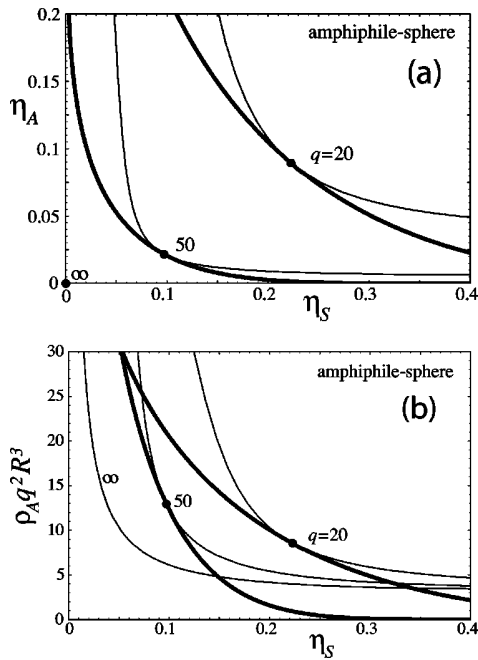


FIG. 7. Phase diagram for the amphiphile-sphere mixture for $q=20, 50, \infty$: (a) as a function of η_S and η_A ; (b) as a function of η_S and $\rho_A q^2$. The case $q=\infty$ is equal to the (universal) result for the sphere-needle binary mixture.

$q \rightarrow \infty$ can be traced by using the scaled density $\rho_A q^2 R^3$ instead of the packing fraction; see Fig. 7(b). In this representation, a well-defined limiting curve is obtained, which again coincides with the universal needle-sphere spinodal.

Let us discuss the disappearance of the demixing transition in both binary systems that contain amphiphiles. This crucially depends on the size ratio q . In the case of the amphiphile-needle mixture, increasing q leads to a suppression of demixing, i.e., to a shift toward higher densities. In contrast, for amphiphile-sphere mixtures, decreasing q is necessary to suppress demixing. In conclusion, q tunes the character of the amphiphiles, whether spherophile (small q) or needle loving (large q).

4. Comparison of binary mixtures

The sphere-needle mixture will constitute our reference system, with which we compare both other binary subsystems possessing amphiphiles. The amphiphile-needle system can be regarded as a derivative of the needle-sphere system that is obtained by replacing each sphere particle in the needle-sphere system with an amphiphile particle. It is interesting to investigate the differences of these two similar systems, namely, to monitor the effect of the attached needles. In Fig. 8(a) we show the demixing phase behavior as a function of packing fraction and scaled needle density. In order to compare with the needle-sphere mixture, we use η_A and η_S as variables for the respective systems. Hence we compare states with the same packing fraction of spheres, whether these are part of amphiphiles (in the amphiphile-needle case) or free (in the sphere-needle case). We observe that the amphiphile-needle system demixes for considerably

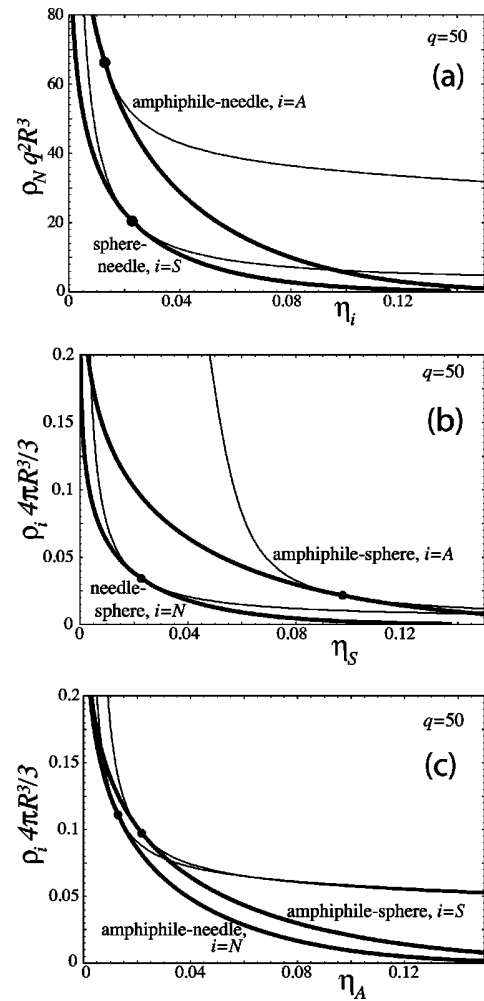


FIG. 8. Comparison of phase diagrams for different binary mixtures at $q=50$. Thick lines are binodals, thin lines spinodals, and the dots mark the critical points. (a) Sphere-needle and amphiphile-needle; (b) sphere-needle and amphiphile-sphere; (c) amphiphile-needle and amphiphile-sphere.

higher densities than the sphere-needle system, i.e., it still remains in a mixed state after the sphere-needle system has already undergone the demixing transition. Note that this happens even though the amount of particle “material” is larger in the amphiphile-needle case due to the additional presence of the amphiphile tails. However, this is precisely what is expected for amphiphilic behavior: The amphiphiles mix better with the needle phase than do pure spheres.

Next we seek to investigate how the behavior of the amphiphile-sphere system changes, if we replace the amphiphiles with needles. In Fig. 8(b) we compare both phase diagrams for $q=50$ as a function of sphere packing fraction η_S and the respective densities ρ_A and ρ_N , which we scale with the volume of a sphere $4\pi R^3/3$. The amphiphile-needle demixing curve is shifted toward larger densities compared to the sphere-needle case. This means that amphiphiles mix better with spheres than pure needles do. Again, this behavior is precisely the expected one for particles with amphiphilic character.

The final comparison aims at the question of which species, needles or spheres, mixes better with amphiphiles. In Fig. 8(c) the amphiphile-needle phase diagram is compared with the amphiphile-sphere phase diagram. As variables, we use the packing fraction of spheres and the number densities of either spheres or needles (again scaled by the volume of a sphere). The amphiphile-sphere spinodal is at slightly higher densities. The difference decreases upon increasing q . So the tendencies of spheres and needles to mix with amphiphiles are roughly equal (and become identical for $q \rightarrow \infty$.)

In summary, we observe a strong shift of the coexistence lines toward higher densities in those systems where particles are replaced by amphiphiles. Note that all our comparisons are done at equal densities. This also means that in the case with amphiphiles space is more density filled with particles, because amphiphiles are larger than either spheres or needles. In spite of this, the system favors the mixed state. All these findings strongly support the initial assumption, that our model particles indeed possess amphiphilic character.

C. Ternary mixture

For the three-component system of spheres, needles, and amphiphiles, the Helmholtz excess free energy per volume for homogeneous, isotropic states is

$$\frac{\beta F^{\text{exc}}}{V} = \Phi_{\text{HS}}(\eta_{\text{tot}}) + \rho_N \left[\frac{3q\eta_{\text{tot}}}{4(1-\eta_{\text{tot}})} - \ln(1-\eta_{\text{tot}}) \right] + \frac{9q\eta_A\eta_{\text{tot}}}{16\pi R^3(1-\eta_{\text{tot}})} \quad (25)$$

$$= -[\rho_N + 3\eta_{\text{tot}}/(4\pi R^3)] \ln(1-\eta_{\text{tot}}) + \frac{3\eta_{\text{tot}}}{16\pi R^3(1-\eta_{\text{tot}})^2} [6\eta_{\text{tot}}(2-\eta_{\text{tot}}) + 3q(1-\eta_{\text{tot}})] \times (\eta_{\text{tot}} - \eta_S) + 4\pi q R^3 \rho_N (1-\eta_{\text{tot}}). \quad (26)$$

From the excess pressure $p_{\text{exc}} = -\partial F^{\text{exc}}/\partial V = -\Phi + \sum_i \rho_i \partial \Phi / \partial \rho_i$, we obtain the (excess) compressibility factor as

$$\frac{\beta p_{\text{exc}}}{\rho} = \frac{\eta_{\text{tot}}}{4(1-\eta_{\text{tot}})^3} \left\{ (1-\eta_{\text{tot}})[3q+4(1-\eta_{\text{tot}})] + 9 \frac{4\eta_{\text{tot}} - q\eta_S(1-\eta_{\text{tot}})}{3\eta_{\text{tot}} + 4\pi R^3 \rho_N} \right\}, \quad (27)$$

where $\rho = \rho_A + \rho_N + \rho_S$ is the total density. We compare this expression with results from computer simulations in Fig. 4(c) for two different compositions of species, and find good agreement over the entire density range considered.

The density ρ_N^r in a reservoir of needles that is in equilibrium with the system is related to the system density via $\rho_N = \rho_N^r \exp(-\beta \mu_N)$, where the (reduced) excess chemical potential for the needles is $\beta \mu_N = \partial \Phi / \partial \rho_N$. Here the result is

$$\rho_N = \rho_N^r (1 - \eta_{\text{tot}}) \exp\left(-\frac{3q\eta_{\text{tot}}}{4(1-\eta_{\text{tot}})}\right), \quad (28)$$

which has the same structure as in the sphere-needle binary case, except that the *total* number of spheres contributes through η_{tot} , not only the free ones through η_S . It is the total packing fraction of spheres, whether pure or the heads of amphiphiles, that interacts with the needles.

A complete investigation of the demixing phase diagram of the ternary mixture is beyond the scope of the present work, and we restrict ourselves to a study of the spinodal. The spinodal for the full three-component system can be obtained as

$$\rho_N \pi R^3 q^2 = \frac{1}{\eta_{\text{tot}}} \left[\frac{4}{3} (2\eta_{\text{tot}} + 1)^2 + 2q\eta_A(1-\eta_{\text{tot}}) - \frac{3}{4} q^2 \eta_A (\eta_{\text{tot}} - \eta_A) \right], \quad (29)$$

where $\eta_{\text{tot}} = \eta_A + \eta_S$. This is an explicit expression for the needle density ρ_N as a function of the densities of spheres and amphiphiles. It can easily be converted into reservoir representation using Eq. (28). Given the complexity of the model containing three species, two of them possessing anisotropic shapes, we find it quite remarkable that a simple expression can be obtained for an (approximate) spinodal. Note that for fixed size ratio q the ternary mixture has three thermodynamic variables, namely, the densities of the three species. The spinodal is a two-dimensional manifold, which is embedded in the three-dimensional phase space.

VI. CONCLUSIONS AND OUTLOOK

We have proposed a hard body model for a ternary amphiphilic mixture. Water molecules are represented by hard spheres, oil molecules by infinitely thin hard needles, and amphiphiles are a hybrid of both. Clearly, this can at best mimic the complex molecular interactions in a real system. Nevertheless, our model features *continuous* degrees of freedom, in contrast to widely used lattice models. Our aim was to demonstrate that this model carries various characteristics of real amphiphilic mixtures. Using a specifically designed density functional theory, we have investigated the bulk fluid demixing phase diagram, and have discussed its rich behavior, demonstrating that phase boundaries are qualitatively in accordance with physical expectation. We expect that our theory accounts also for inhomogeneities on small length scales similar to the particle dimensions. As its hard sphere counterpart (Rosenfeld's functional) yields excellent results when compared to simulations, we expect a similar quality of results for our system. Such applications to inhomogeneous situations have been left out of the current work. The next step is to show whether the model exhibits lamellar and micellar phases. Their existence is crucial to the ability of the hard body amphiphile mixture to describe real systems.

As possible further directions of research, we mention the question of how freezing of hard spheres is affected by the presence of amphiphiles, as well as the nature of the solid phases built by the amphiphiles, which poses a challenging

packing problem. Furthermore, the study of the interfaces between demixed phases will be especially intriguing due to the number and nature of the different phases in the bulk phase diagram. This touches on the very relevant question of how the amphiphiles are arranged at the oil-water interface.

Concerning the general status of the theory, we are faced with an important example where geometry-based DFT yields previously unknown bulk thermodynamics. This is in contrast to the cases of hard spheres, the Asakury-Oosawa model, and Bolhuis-Frenkel's needle-sphere mixture, where expressions from scaled-particle or free volume theory were previously known, and where these results were rederived by

DFT. Geometry-based DFT is a systematic way to treat such hard core systems, whereas the scaled-particle or free volume approaches require considerable physical insight to be formulated. This is an advantage in terms of comprehensibility; however, it becomes increasingly difficult to apply these approaches to more complex systems like the one considered in this work.

ACKNOWLEDGMENT

One of us (M.S.) would like to thank B. Mulder for an inspiring discussion.

-
- [1] S. H. Chen, J. S. Huang, and P. Tartaglia, *Structure and Dynamics of Strongly Interacting Colloids and Supramolecular Aggregates in Solution* (Kluwer Academic Publishers, Dordrecht, 1992).
- [2] W. M. Gelbart, D. Roux, and A. Ben-Shaul, in *Micelles, Membranes, Microemulsions and Monolayers*, edited by S. H. Chen, J. S. Huang, and P. Tartaglia (Springer, Berlin, 1994).
- [3] J. Meunier, D. Langevin, and N. Boccaro, *Physics of Amphiphilic Layers* (Springer, Berlin, 1987).
- [4] R. Lipowsky, D. Richter, and K. Kremer, *The Structure and Conformation of Amphiphilic Membranes* (Springer, Berlin, 1992).
- [5] B. Widom, *J. Chem. Phys.* **84**, 6943 (1986).
- [6] A. Ciach and J. S. Hoye, *J. Chem. Phys.* **95**, 5300 (1991).
- [7] K. A. Dawson, M. P. Lipkin, and B. Widom, *J. Chem. Phys.* **88**, 5149 (1988).
- [8] G. Gompper and M. Schick, in *Micelles, Membranes, Microemulsions and Monolayers* (Ref. [2]).
- [9] G. Gompper and M. Schick, *Self-Assembling Amphiphilic Systems* (Academic Press, London, 1994).
- [10] C. N. Likos, K. R. Mecke, and H. Wagner, *J. Chem. Phys.* **102**, 9350 (1995).
- [11] R. Evans, in *Fundamentals of Inhomogeneous Fluids*, edited by D. Henderson (Dekker, New York, 1992), p. 85.
- [12] A. M. Somoza, E. Chacón, L. Mederos, and P. Tarazona, *J. Phys.: Condens. Matter* **7**, 5753 (1995).
- [13] S. de Miguel and M. M. T. da Gama, *J. Chem. Phys.* **107**, 6366 (1997).
- [14] C. Guerra, A. M. Somoza, and M. M. T. da Gama, *J. Chem. Phys.* **109**, 1152 (1998).
- [15] C. Guerra, A. M. Somoza, and M. M. T. da Gama, *J. Chem. Phys.* **111**, 7646 (1999).
- [16] D. Duque and P. Tarazona, *J. Chem. Phys.* **107**, 10 207 (1997).
- [17] P. Tarazona, D. Duque, and E. Chacon, *Phys. Rev. E* **62**, 7147 (2000).
- [18] I. Napari, A. Laaksonen, and R. Strey, *J. Chem. Phys.* **113**, 4476 (2000).
- [19] I. Napari, A. Laaksonen, and R. Strey, *J. Chem. Phys.* **113**, 4480 (2000).
- [20] V. Talanquer and D. W. Oxtoby, *J. Chem. Phys.* **113**, 7013 (2000).
- [21] H. Löwen, in *Spatial Statistics and Statistical Physics*, edited by K. R. Mecke and D. Stoyan, *Lecture Notes in Physics*, Vol. 554 (Springer, Berlin, 2000).
- [22] Y. Rosenfeld, *Phys. Rev. Lett.* **63**, 980 (1989).
- [23] Y. Rosenfeld, M. Schmidt, H. Löwen, and P. Tarazona, *J. Phys.: Condens. Matter* **8**, L577 (1996).
- [24] Y. Rosenfeld, M. Schmidt, H. Löwen, and P. Tarazona, *Phys. Rev. E* **55**, 4245 (1997).
- [25] P. Tarazona, *Phys. Rev. Lett.* **84**, 694 (2000).
- [26] Y. Rosenfeld, *Phys. Rev. E* **50**, R3318 (1994).
- [27] J. A. Cuesta, *Phys. Rev. Lett.* **76**, 3742 (1996).
- [28] J. A. Cuesta and Y. Martinez-Raton, *Phys. Rev. Lett.* **78**, 3681 (1997).
- [29] M. Schmidt, H. Löwen, J. M. Brader, and R. Evans, *Phys. Rev. Lett.* **85**, 1934 (2000).
- [30] M. Schmidt, *Phys. Rev. E* **63**, 010101(R) (2001).
- [31] P. Bolhuis and D. Frenkel, *J. Chem. Phys.* **101**, 9869 (1994).
- [32] M. Schmidt, *Phys. Rev. E* **63**, 050201(R) (2001).
- [33] M. Elbaum, D. K. Fygenson, and A. Libchaber, *Phys. Rev. Lett.* **76**, 4078 (1996).
- [34] D. K. Fygenson, M. Elbaum, B. Shraiman, and A. Libchaber, *Phys. Rev. E* **55**, 850 (1997).
- [35] K. Lin, J. C. Crocker, A. C. Zeri, and A. G. Yodh, *Phys. Rev. Lett.* **87**, 088301 (2001).

Hard body amphiphiles at a hard wall

JOSEPH M. BRADER^{1†}, CHRISTIAN VON FERBER² and MATTHIAS SCHMIDT^{3*}

¹The James Franck Institute, University of Chicago, 5640 South Ellis Avenue, Chicago, IL 60637, USA

²Theoretical Polymer Physics, Freiburg University, Herman-Herder-Straße 3, 79104 Freiburg, Germany,

³Institut für Theoretische Physik II, Heinrich-Heine-Universität Düsseldorf, Universitätsstraße 1, D-40225 Düsseldorf, Germany

(Received 18 December 2002; revised version accepted 17 January 2003)

We investigate the structure of amphiphilic molecules exposed to a substrate that is modelled by a hard wall. Our simple model amphiphiles consist of a hard sphere head group to which a vanishingly thin needle tail is radially attached, resulting in a lollipop shape. Such particles act as amphiphiles when added to a binary fluid of hard spheres and needles. Focusing on the pure amphiphile system we compare the results for the positional and orientational order profiles obtained from a recent density functional approximation to those of our computer simulations and find good agreement. For low densities the structure is ruled by the loss of orientational free volume near the wall, while for higher densities packing of the spherical heads dominates. Furthermore, we test the wall sum rule explicitly for this model fluid and find rich structure of the contact distribution which can be interpreted in terms of typical particle configurations.

1. Introduction

In order to understand the behaviour of ternary water–oil–surfactant mixtures on a microscopic level, different model systems have been utilized, ranging from very simplified phenomenological theories to more realistic simulation studies. The principal objective of such research is to start from model interactions between individual molecules and to predict macroscopic properties such as phase behaviour and structural correlations [1–6]. Often the attractive parts of the pair potentials are specifically tailored to generate the required amphiphilic properties. However, it was shown by computer simulations that hard body interactions alone are sufficient to generate mesoscopic micellar structures [7], using a model of amphiphilic molecules immersed in a hard sphere fluid. As a model for mesogens, van Duijneveldt *et al.* investigated the phase behaviour of hard spherocylinders with a flexible tail attached to either endcap [8] and to only one of the endcaps [9]. They found that the presence of the tails enhances the stability of the smectic-A phase and suppresses the nematic phase.

Recently, a similar simple model that features hard body interactions only was proposed [10]. To a binary mixture of hard spheres and vanishingly thin needles [11], a third component is added that consists of a sphere and a radially joined needle. Besides being the ‘natural’ amphiphile for the sphere–needle mixture, this mimics the shape of the hydrophilic headgroup and hydrocarbon tail of real amphiphile molecules. The appeal of the model stems from the absence of an energy scale, hence its behaviour is governed solely by the (three) densities of the species and the ratio of needle length and sphere diameter as an additional geometric parameter that determines the amphiphile strength. In the framework of density functional theory (DFT) [12, 13] extending Rosenfeld’s work [14–16] and following the treatment of a binary sphere–needle mixture [17], a geometry-based DFT for this model was proposed [10]. The bulk fluid equation of state derived from the theory was found to be in good agreement with that obtained from computer simulations. Theoretical results for the fluid demixing phase behaviour of the binary subsystems (obtained by setting the density of one of the components to zero) supported the amphiphilic character of the model. In particular it was found that compared to the demixing binodal in the sphere–needle mixture, the mixed region grows (demixing is suppressed) if either component is replaced with amphiphiles. Besides the ternary bulk phase behaviour (which has not been considered so far), the crucial test to prove the validity of the model is

*Author for correspondence. e-mail: mschmidt@thphy.uni-duesseldorf.de. Present address: Debye Institute, Utrecht University, Princetonpln 5, 3584 CC Utrecht, The Netherlands.

†Present address: Institute of Physiology, University of Bern, Buehlplatz 5, 3012 Bern, Switzerland.

whether the interfacial properties are in accordance with those of real ternary surfactant mixtures. Clearly, this is a potentially demanding project, and as a prerequisite, in the present study we seek to understand the nature of correlations that emerge from the shape (and hence the interactions) of the model amphiphiles.

We choose a generic situation, the hard, impenetrable wall, to study the packing effects caused by the hybrid shape of the particles. Besides the intrinsic interest in amphiphiles at surfaces, our aim is also to assess the accuracy of the theory in inhomogeneous situations. In contrast to fluid–fluid interface studies, the behaviour near walls can be obtained more easily from computer simulations, and hence we have carried out Monte Carlo (MC) simulations for the pure system of amphiphiles against a hard wall.

We find that for low densities the behaviour is driven by the (trivial) loss in rotational free volume (accessible particle orientations) that arises from the overlap of the particle tail with the wall. Increasing the bulk density leads to a crossover to behaviour that is governed by the packing of the heads, and thus resembles that of the hard sphere fluid. Theoretical and simulation results agree well, given the complexity of the situation, also very close to the wall. The peculiar shape of the second peak is captured correctly but its height is slightly overestimated. Our theoretical results for the wall–particle contact distribution show rich structure, which we can relate to special geometric particle arrangements at the wall.

The paper is organized as follows. In Section 2 we define the model explicitly. Section 3 is devoted to the density functional and computer simulation methods. In Section 4 we present results and we conclude in Section 5.

2. Model

We consider amphiphilic hard core particles which consist of a hard sphere of diameter σ and a vanishingly thin needle of length L . The needle (tail) is attached radially to the sphere (head). We take the centre of the sphere as the position of the particle (denoted by \mathbf{r}) and denote the direction of the tail by a unit vector $\mathbf{\Omega}$, see figure 1(a). The interparticle interactions are such that both sphere–sphere and sphere–needle overlaps are forbidden. The excluded volume between two needles is zero owing to their vanishing thickness. Hence configurations with overlapping needles carry vanishing statistical weight, and the needle–needle interactions can be assumed as being ideal. The wall (see figure 1(b)) is impenetrable to both the head and tail. Let θ be the angle between $\mathbf{\Omega}$ and the surface normal *towards* the wall (see again figure 1(b)), and let z be the component of \mathbf{r} perpendicular to the wall. Then we can describe the

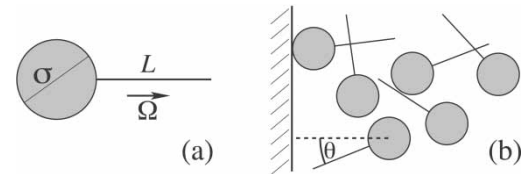


Figure 1. Sketch of the model amphiphilic system. (a) Each amphiphilic molecule consists of a hard sphere of diameter σ to which a vanishingly thin needle of length L is radially attached. The particle orientation is described by the unit vector $\mathbf{\Omega}$. (b) Typical configuration of amphiphiles against a hard wall. The needle tails may overlap with each other owing to their vanishing excluded volume, but they can penetrate neither the spheres nor the wall.

wall as an external potential

$$V_{\text{wall}}(z) = \begin{cases} \infty & z < z^+(\theta) \\ 0 & \text{otherwise,} \end{cases} \quad (1)$$

where $z^+(\theta)$ is the distance of closest allowed approach between the sphere centre and the wall, given by

$$z^+(\theta) = \begin{cases} (L + \sigma/2) \cos \theta & \theta < \arccos[1/(1 + 2L/\sigma)] \\ \sigma/2 & \text{otherwise.} \end{cases} \quad (2)$$

The system is governed by only one thermodynamic parameter, which we take to be the packing fraction of the spherical heads, $\eta_A = \rho_A \pi \sigma^3 / 6$, where ρ_A is the amphiphile number density. The size ratio of needle length and sphere diameter, L/σ , is a further geometric control parameter.

3. Methods

3.1. Density functional theory

As a theoretical approach to the study of the interfacial properties of our model fluid we use the DFT of [10] which extends Rosenfeld's fundamental measures theory [14–16] to an example of non-convex particles with orientational degrees of freedom. The only inputs to the theory are a geometrical description of the particle shape and exactly known limits for situations of extreme confinement. The theory in [10] is formulated for a multicomponent mixture. Here we apply it to a one-component system (monodisperse in sphere diameter and tail length). As an essential feature, this DFT describes the many-body behaviour of the system in terms of geometrically determined weight functions that correspond to the particle shape. The weight functions are used to obtain weighted densities by building convolutions with the actual density profile. The excess (over ideal gas) free energy density is expressed as a function of these weighted densities and integration over space and orientational degrees of freedom yields the excess free energy. For the full definition of the weight functions, that of the free energy density, and all further technical details we refer the reader directly to [10].

The numerical minimization of the density functional in the presence of the external potential, equation (1), is done via a standard iteration technique, and follows closely that of a related investigation in a binary sphere–needle mixture [18].

3.2. Computer simulations

In order to obtain benchmark results, we performed canonical Monte Carlo simulations with 500 particles. Periodic boundary conditions are used in both directions parallel to the walls. The two walls have square shapes. The distance between both walls is taken to be twice their lateral length, in order to reduce finite-size effects. For the simulated total densities $\eta_A = 0.05, 0.10, 0.15, 0.20, 0.25, 0.30$ we performed 2.1, 2.7, 3.6, 4.4, 4.7, 7.0 million MC moves per particle, respectively. The maximal spatial and orientational displacements were adjusted to obtain acceptance ratios of about 0.85. As we fix the volume V and the total particle number N , the mean density in the simulation box is prescribed, but not the bulk density. We determine this *a posteriori* from the (plateau) value of the density profile away from the wall, that is in the middle of the simulation box.

For the size ratio $L/\sigma = 1.5$ we obtained reliable results for the density and order parameter profiles; those are presented below. Increasing the needle length (we checked $L/\sigma = 5$) leads to significant slowing down of the equilibration of the system, and hence prohibited the obtaining of high-quality data.

3.3. Order parameters and the wall sum rule

In order to analyse the behaviour of the non-spherical particles we consider two characteristic distributions obtained from the full profile $\rho_A(\mathbf{r}, \mathbf{\Omega})$. The first is the orientation averaged profile which describes the distribution of the centres of the spheres, regardless of their tail orientation, given by

$$\bar{\rho}_A(\mathbf{r}) = \int \frac{d^2\Omega}{4\pi} \rho_A(\mathbf{r}, \mathbf{\Omega}). \quad (3)$$

The second is an orientational order parameter

$$\langle \cos\theta \rangle = \bar{\rho}_A(\mathbf{r})^{-1} \int \frac{d^2\Omega}{4\pi} \rho_A(\mathbf{r}, \mathbf{\Omega}) \cos\theta, \quad (4)$$

that varies between -1 for particles with tails pointing away from the wall and $+1$ for particles with tails pointing towards the wall. It vanishes in the (isotropic) bulk fluid. As we restrict ourselves to the study of states with planar symmetry, $\bar{\rho}_A$ and $\langle \cos\theta \rangle$ depend only on z .

For hard spheres, that is $L = 0$, the density profiles against a hard wall satisfy the well-known sum rule $\beta P = \rho(R^+)$, where $\beta = 1/k_B T$, k_B is the Boltzmann constant, T is absolute temperature, P is the bulk

pressure and $R^+ = (\sigma/2)^+$ is the distance of the closest approach between the sphere centre and the wall surface [19] (the upper plus indicates a limit from above). This sum rule was subsequently generalized to systems of hard anisotropic particles against a hard wall [20] which, for a one-component system of amphiphiles, is given by

$$\beta P = \int \frac{d^2\Omega}{4\pi} \rho_A(z^+(\theta), \theta), \quad (5)$$

where $z^+(\theta)$ is the distance of the closest approach between the particle centre and the surface of the wall for a particle with orientation θ , see equation (2).

4. Results

4.1. Density and order parameter profiles: comparison with simulations

To assess the performance of the amphiphile functional we compare positional and orientational order parameter profiles (equations (3) and (4)) from DFT and MC simulation for $L/\sigma = 1.5$. Owing to the complicated shape of the amphiphilic particles it is not obvious to what extent our approximate functional will capture the subtle packing effects which determine the interfacial structure in this system. Figure 2 shows the angle averaged density profiles $\bar{\rho}_A(z)$. At low densities ($\eta_A = 0.05212$ in figure 2(a) and $\eta_A = 0.10437$ in figure 2(b)) the amphiphile tails strongly perturb the density profiles from those of pure hard spheres at the same packing fraction. At these low densities the contact value is reduced compared to pure hard spheres owing to wall–amphiphile tail collisions which tend to move the sphere centres away from the wall. Note that the lowering of the contact value of the averaged density profile does not imply lowering of the bulk pressure (via relation through the wall sum rule), as collisions of the tails with the wall also need to be taken into account. We shall discuss this issue in the next subsection. The kink in the profile at $z = 2\sigma$ corresponds to a distance where an amphiphile with $\theta = 0$ makes contact with the wall. For these low densities we find good agreement between simulation and theory.

As η_A is increased the packing of the amphiphile heads begins to dominate and the structure becomes closer to that of hard spheres ($\eta_A = 0.15585$ in figure 2(c) and $\eta_A = 0.20728$ in figure 2(d)). For high densities ($\eta_A = 0.25810$ in figure 2(e) and $\eta_A = 0.30751$ in figure 2(f)) the profile is very close to that of hard spheres and the presence of the amphiphile tails acts only as a weak perturbation. The effect of the tails is overwhelmed by the sphere packing.

Figure 3 shows the orientational order parameter profile $\langle \cos\theta \rangle$ for two typical densities, namely $\eta_A = 0.05$ and 0.25 . Despite the markedly differing values the

2228

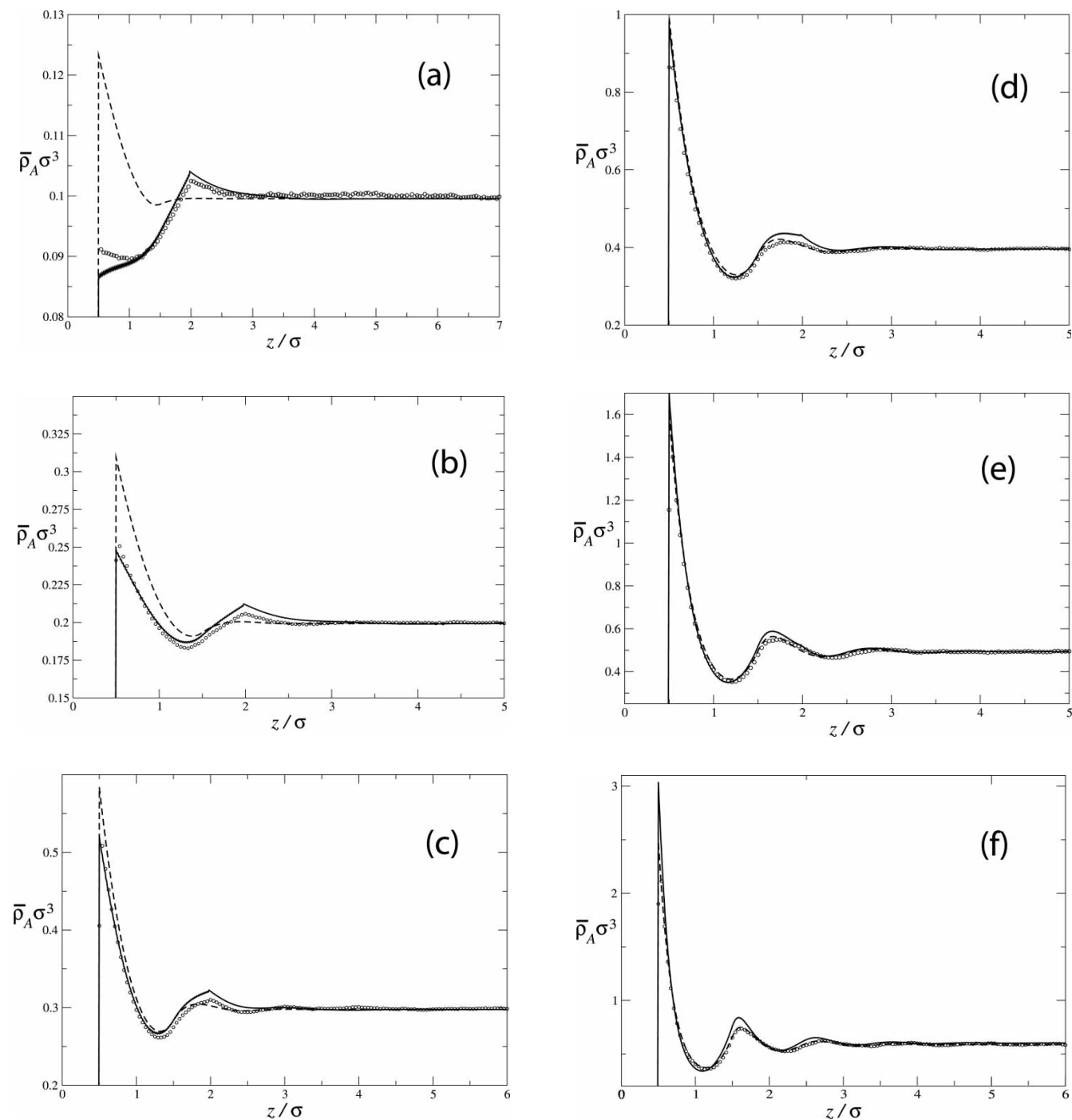
J. M. Brader *et al.*

Figure 2. Angle averaged amphiphile density profiles $\bar{\rho}_A$ as a function of the scaled distance from the wall z/σ for $L/\sigma = 1.5$ obtained from simulations (symbols) and DFT (solid curve). For comparison we also plot the DFT results for the pure hard sphere case ($L = 0$) for the same densities (dashed curve). Packing fractions are (a) $\eta_A = 0.05212$; (b) $\eta_A = 0.10437$; (c) $\eta_A = 0.15585$; (d) $\eta_A = 0.20728$; (e) $\eta_A = 0.25810$; (f) $\eta_A = 0.30751$.

simulation yields two very similar profiles, the only significant difference being the weak oscillations for $\eta_A = 0.25$ induced by sphere packing. The ‘triangle’ structure for $z < 2\sigma$ is almost completely determined by the reduction in solid angle available to each amphiphile

tail when close to the wall; interactions between the amphiphiles appear to have little effect. In fact the profile for $\eta = 0.05$ already lies very close to the low density limit with a small positive enhancement at $z = 2\sigma$. While the functional gives a good account of the

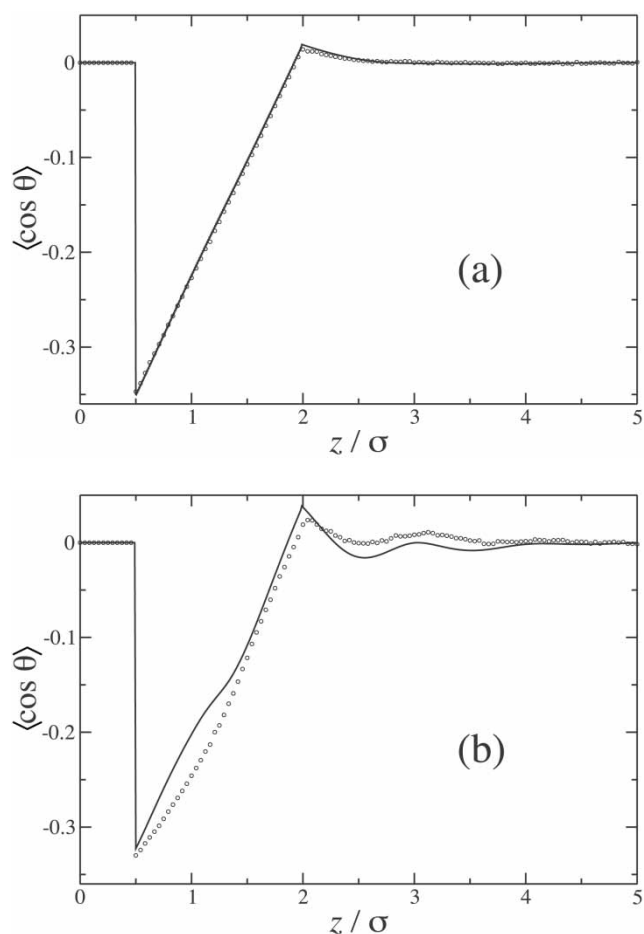


Figure 3. The orientational order parameter profiles $\langle \cos \theta \rangle$ as a function of the scaled distance z/σ from the wall obtained from simulation (circles) and DFT (curves). Packing fractions are (a) $\eta_A = 0.05$ and (b) $\eta_A = 0.25$.

low density behaviour of $\langle \cos \theta \rangle$ when compared to simulation, for higher densities the agreement is poor. As η is increased the simulation results show that (i) the contact value increases (becomes less negative), (ii) there is a deviation from linearity between contact and $z = 2$, (iii) there is enhancement at $z/\sigma = 2$ and, (iv) oscillations develop. All of these features are captured by the DFT, but are grossly overestimated. A possible explanation could lie in our assumption that there is no ordering parallel to the wall. This is implicit in our calculation of one-dimensional (z -dependent) density profiles but is still accounted for within the simulation. While this presents an interesting possibility, the numerical minimization of the amphiphile functional [10] allowing for such ordering presents a formidable numerical challenge and is beyond the scope of the present work.

Preliminary simulation results for longer tails, $L/\sigma = 5$, and $\eta_A = 0.2$ indicate deviations from the theoretical profiles. In particular we observe a dip in $\rho_A(z)$ ranging

from about $z = 2\sigma$ to $z = 5\sigma$, which is about 15% lower than the bulk density. This feature is absent in the starting configuration and develops over simulation time, albeit no equilibrated state could be reached. Our current DFT implementation is limited to planar symmetry, and does not reproduce this feature. Thus it is interesting to speculate that this could be an indication of lateral ordering at the wall, for example wall-induced micelle formation or freezing. We leave this issue for future work.

4.2. Wall contact distribution

The hard wall sum rule, equation (5), is an exact theorem. When used in an approximative DFT treatment it is expected, from general considerations, that the equality holds provided both sides of the equation are obtained from the *same* theory, that is the pressure (left-hand side of equation (5)) is obtained from the bulk equation of state while the right-hand side is obtained from the density profile which minimizes the functional. The sum rule should be satisfied by any non-local functional and thus provides a useful check of our numerical procedure. For each η_A value we find the sum rule (equation (5)) to be satisfied. The present study introduces two non-trivial complications over existing studies of hard particles at a hard wall: (i) the amphiphile particles are non-convex and (ii) the functional contains only an approximate Mayer function. To the best of our knowledge the sum rule has never been explicitly tested for either of these cases. Satisfaction of the sum rule for amphiphiles proves to be considerably more demanding than for pure hard spheres or the sphere–needle binary mixture [18]. A rather fine numerical mesh is required to achieve good accuracy; we use 200 spatial grid points per σ in z and 150 angular steps in the range $0 \leq \theta \leq \pi$. To provide good resolution in rapidly varying regions we employ a non-uniform grid in θ .

In addition to providing a numerical check, the investigation of the sum rule also yields insight into the liquid structure at the wall. Using $\langle \cos \theta \rangle$ as a measure of orientational order does demonstrate the *average* tendency of the amphiphile tails to point away from the wall. However, much detail is washed out in the averaging process. Figure 4 shows the contact distribution $\rho_A^+(\theta) \equiv \rho_A(z^+(\theta), \theta) \sin \theta$ (the integrand of equation (5)), for several values of η_A . For low η_A values the function is smooth (in θ) but as η_A increases it becomes sharply peaked at the point labelled a. A careful numerical integration is thus required to evaluate the right hand side of equation (5). For the size ratio considered ($L/\sigma = 1.5$) the peak is located at an angle $\theta_a = 1.318$, identifying the most common geometrical arrangement of a particle at the wall. This a-type

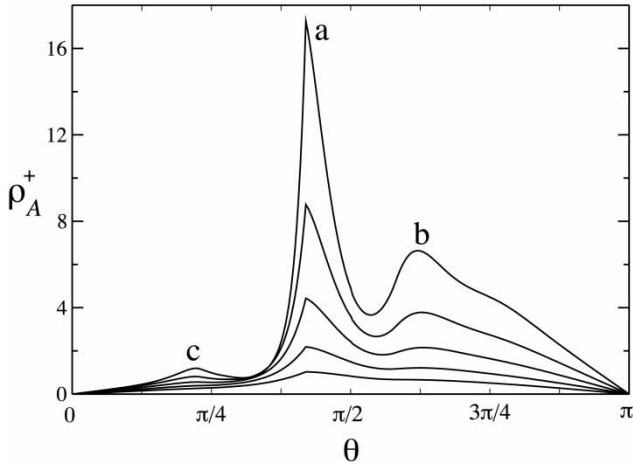


Figure 4. Amphiphile contact distribution $\rho_A^+ \equiv \rho_A(z_A^+(\theta), \theta) \sin \theta$ for packing fraction $\eta_A = 0.15\text{--}0.35$ in intervals of 0.05 (from bottom to top). θ is the angle between the amphiphile tail and the wall surface normal. The features labelled a, b, c correspond to the configurations shown in figure 5.

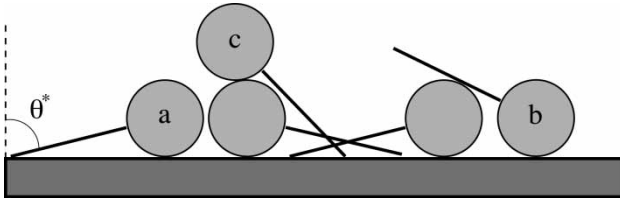


Figure 5. Typical configurations of model amphiphiles at contact with the hard wall, shown here for $L/\sigma = 1.5$. The configurations labelled a, b, c correspond to the peaks in the contact distribution, see figure 4.

configuration is shown in figure 5. It consists of an amphiphile with both the spherical surface and tail end simultaneously touching the wall. As η_A increases this configuration becomes more dominant and particles thus arranged play the largest role in balancing the bulk pressure via equation 5. We have checked that for longer tail lengths ($L/\sigma = 5$) the peak develops at lower η_A values as it becomes easier to ‘flatten’ the amphiphiles against the wall. Hence in general we expect $\theta_a = \arccos[1/(1 + 2L/\sigma)]$.

For $\eta_A > 0.3$ two more peaks become apparent at angles b and c in figure 4, each corresponding to a favoured amphiphile configuration at the wall. The interpretation of these higher order peaks is more subtle as they represent configurations involving pairs of amphiphile particles against the wall, see figure 5. Configuration b occurs when the amphiphile sphere surface touches the wall while the tail rests on top of a neighbouring sphere. If the needle touches the neighbouring surface such that it assumes the largest θ value possible for a given sphere–sphere separation, then for $L/\sigma = 1.5$, $1.824 < \theta_b < 2.094$ for sphere separations

where the needle is tangent to the neighbouring sphere surface. This is in excellent agreement with the location of peak b in figure 4. It should be noted that peak a is sharp because amphiphiles with angles close to θ_a all rapidly fall into a-type configurations; type-b configurations are more varied and include those where the needle has ‘slid off’ its neighbouring sphere to some extent. This accounts for the rounding of the peak. Also, the peak height of b is lower than that of a because b configurations are unstable and can easily fall into type a. The peak c is small, even for $\eta_A = 0.35$, and is the most unstable of the three identified configurations. If the head of amphiphile c in figure 5 is positioned directly on top of the second amphiphile head, that is the line joining the sphere centres is normal to the wall and the tail touches the wall, an angle of $\theta_c = \arccos[3/(1 + 2L/\sigma)]$ is achieved. For $L/\sigma = 1.5$ this yields $\theta_c = 0.723$, in excellent agreement with the peak location.

It is likely that the smooth background in the contact distribution (figure 4) also contains numerous other geometrically significant arrangements involving three- and higher-body structures but these are so weak that they cannot be resolved. The dominance of a-type configurations at large η_A values also provides an explanation for the increase in $\langle \cos \theta \rangle$ at contact with increasing η_A (see figure 3). As η_A is increased a-type configurations become more common, as $\theta_a < \pi/2$. Such configurations tend to make $\langle \cos \theta \rangle$ more positive.

5. Conclusions

In summary, we have investigated the structural correlations that arise near a hard wall in a hard body amphiphile fluid. In our simple model the amphiphile headgroup is taken to be a hard sphere and the tail is modelled as a rigid, vanishingly thin hard needle attached radially to the sphere. A fluid of such joined hard particles, when supplemented by species corresponding to water and oil (hard spheres and hard needles in this case) gives a simplistic representation of a ternary amphiphilic mixture. The simplicity stems from the absence of temperature as a relevant variable and hence the behaviour is solely governed by entropy.

Previous results for the fluid demixing phase behaviour indicated that the model indeed displays some of the features found in real systems [10]. Those results were obtained using a density functional approach that utilizes the fundamental measure concept to approximate the excess free energy. In this paper we presented the first application of the theory to an inhomogeneous situation. We chose a simple, albeit non-trivial test case, namely the pure amphiphile fluid against a hard wall, where non-trivial positional and orientational packing of particles is found. We have focused on the case of one-component amphiphiles in order to assess the

accuracy of the DFT and have carried out Monte Carlo computer simulations to provide benchmark results.

We find good agreement between results from the theory and the simulations for the total (integrated over orientations) density, and reasonable agreement for the angular order parameter profile. We conclude that the theory gives a good account of the structural correlations that arise from the packing effects in this model. Owing to the particle shape, interesting behaviour at contact with the wall is found. The (orientation-dependent) density at contact with the wall displays a highly irregular, peaked structure, and we could qualitatively interpret the results in terms of typical particle configurations. In particular the most probable configuration is where head and tail touch the wall simultaneously.

As concerns future work, we mention the problem of how adding amphiphiles changes the free interface between demixed fluids in the sphere–needle mixture [18]. Furthermore whether the model leads to mesoscopic structures such as micelles is interesting. A particular challenge is to reveal the nature of the crystalline state(s).

We gratefully acknowledge inspiring discussions with D. W. Oxtoby, R. Evans, and H. Löwen. P. Bolhuis and D. Frenkel are thanked for pointing out reference [7] to us. The work of JMB was supported by the National Science Foundation (through grant CHE9800074 and the National Science Foundation Materials Research Science and Engineering Center at the University of Chicago).

References

- [1] SOMOZA, A. M., CHACÓN, E., MEDEROS, L., and TARAZONA, P., 1995, *J. Phys.: condens. Matter*, **7**, 5753.
- [2] TALANQUER, V., and OXTOBY, D. W., 2000, *J. chem. Phys.*, **113**, 7013.
- [3] NAPARI, I., LAAKSONEN, A., and STREY, R., 2000, *J. chem. Phys.*, **113**, 4476.
- [4] NAPARI, I., LAAKSONEN, A., and STREY, R., 2000, *J. chem. Phys.*, **113**, 4480.
- [5] DUQUE, D., and TARAZONA, P., 1997, *J. chem. Phys.*, **107**, 10207.
- [6] GUERRA, C., SOMOZA, A. M., and TELO DA GAMA, M. M., 1998, *J. chem. Phys.*, **109**, 1152.
- [7] BOLHUIS, P. G., and FRENKEL, D., 1997, *Physica A*, **244**, 45.
- [8] VAN DUJNEVELDT, J. S., and ALLEN, M. P., *Molec. Phys.*, **92**, 855.
- [9] VAN DUJNEVELDT, J. S., GIL-VILLEGAS, A., JACKSON, G., and ALLEN, M. P., 2000, *J. chem. Phys.*, **112**, 9092.
- [10] SCHMIDT, M., and VON FERBER, C., 2001, *Phys. Rev. E*, **64**, 051115.
- [11] BOLHUIS, P., and FRENKEL, D., 1994, *J. chem. Phys.*, **101**, 9869.
- [12] EVANS, R., 1979, *Adv. Phys.*, **28**, 143.
- [13] EVANS, R., 1992, *Fundamentals of Inhomogeneous Fluids*, edited by HENDERSON, D., (New York: Dekker), p. 85.
- [14] ROSENFELD, Y., 1984, *Phys. Rev. Lett.*, **63**, 980.
- [15] ROSENFELD, Y., 1994, *Phys. Rev. E*, **50**, R3318.
- [16] ROSENFELD, Y., 1995, *Molec. Phys.*, **86**, 637.
- [17] SCHMIDT, M., 2001, *Phys. Rev. E*, **63**, 050201(R).
- [18] BRADER, J. M., ESZTERMANN, A., and SCHMIDT, M., 2002, *Phys. Rev. E*, **66**, 031401.
- [19] HENDERSON, J. R., and VAN SWOL, F., 1985, *Molec. Phys.*, **56**, 1313.
- [20] HOLYST, R., 1989, *Molec. Phys.*, **68**, 391.

Density-functional theory for fluids in porous media

Matthias Schmidt

Institut für Theoretische Physik II, Heinrich-Heine-Universität Düsseldorf, Universitätsstraße 1, 40225 Düsseldorf, Germany
(Received 2 August 2001; revised manuscript received 6 May 2002; published 17 October 2002)

As models for substances adsorbed within amorphous solid matrices, we consider mixtures of spheres with either hard or ideal interactions where several (matrix) components are quenched and the remaining (adsorbate) components are equilibrated. We propose a density-functional theory, based on the exact zero-dimensional limit, which treats both matrix and adsorbate components on the level of the respective one-body density profiles. As a test, we calculate pair correlation functions for hard spheres adsorbed in either a hard sphere or an ideal sphere matrix, and find good agreement with our computer simulation results.

DOI: 10.1103/PhysRevE.66.041108

PACS number(s): 64.10.+h, 31.15.Ew, 61.20.-p, 61.43.-j

I. INTRODUCTION

The behavior of atomic, molecular, and complex fluids, e.g., colloidal suspensions, adsorbed in porous media, is of considerable practical as well as fundamental interest. Disordered substrates that are permeable to a substance are encountered in environmental, biological, and industrial fields. From a fundamental point of view, one is interested how condensed matter phenomena (like phase transitions) are altered by confinement [1] and the presence of disorder [2]. The details of the porous medium are often disregarded and to model such amorphous substances one relies on equilibrium fluid configurations of model systems. The advantages are twofold: (i) The statistics of such model matrices are well studied and understood, e.g., in the case of the hard sphere (HS) systems. (ii) A direct link to the statistical mechanics of equilibrated fluids is provided. The primary tool in the description of adsorbates to such a matrix are quenched-annealed (QA) averages [3,4]. There the adsorbate free energy (rather than the partition sum) is averaged over (many) representations of disorder. Hence the matrix is quenched, while the adsorbate is annealed (allowed to equilibrate) in the presence of the disordered background. Typically, one assumes that there is no back feeding toward the matrix: The porous medium is unaffected by the presence of the adsorbate. Besides computer simulations, theoretical work is mainly based on the replica trick, which relates the QA system to a special limit of a corresponding fully equilibrated extended (replicated) system, which is tackled with integral equation theory and replica Ornstein-Zernike equations [3,4].

Density-functional theory (DFT) [5] is a powerful approach to equilibrium (fully annealed) fluids [6] and solids [7]. It models the influence of an external potential energy V^{ext} acting on the system. Commonly, DFT is applied to well defined, idealized pores (see e.g., Ref. [8]). In principle, a disordered matrix may be represented by an appropriate V^{ext} acting on the adsorbate. To treat amorphous pore structures within this approach requires solution (minimization of the grand potential) for a given V^{ext} , and subsequent explicit averaging “by hand” over many realizations of V^{ext} . This was recently carried out with a mean-field DFT for a lattice fluid model [9], and formidable insight into adsorption, metastability, and hysteresis was gained. However, the principle approach seems to be limited to simple models and is

cumbersome, if not inapplicable, in the case of more sophisticated DFTs and continuum models.

In this work, we argue that a more general DFT is feasible, where the matrix is described on the level of the (one-body) density distribution of its constituent particles, and where the functional is the average free energy (averaged over matrix realizations), depending on matrix and adsorbate density profiles. We expect this to be very powerful, as matrix details (of single representations) are disregarded, and only relevant statistical properties enter. Here, we present explicit approximations for (a restricted set of) common adsorbate-matrix models. Our approach is an extension of a theory for fully annealed mixtures [6], which is considered to be “for multicomponent HS fluids, the most accurate and successful approximate functional” [8]. The theory captures local packing effects, and correlation functions are predicted in a nonperturbative fashion, without need of external input. We demonstrate the good accuracy of the approach by comparing calculated pair distribution functions to computer simulation data.

II. MODELS

To model adsorbates in porous media, we restrict ourselves to mixtures with spherical symmetric pair interactions, where each species i consists of spheres with radii R_i . Two kinds of pair interactions $V_{ij}(r)$ between species i and j as a function of the separation distance r are considered: (i) ideal interactions such that $V_{ij}(r)=0$ for all distances r ; (ii) hard core interactions such that $V_{ij}(r)=V_{\text{HC}}(r)=\infty$, if $r < R_i + R_j$, and zero otherwise. This covers additive hard sphere mixtures, mixtures of hard and ideal spheres like realized in the Asakura-Oosawa (AO) colloid-ideal polymer model [10], as well as the Widom-Rowlison (WR) model [11], where only particles of unlike species experience hard core repulsion. We further discriminate between quenched ($i \equiv 0a$) and annealed ($i \equiv 1b$) species, where i is a composite index, such that the first digit 0,1 correspond to quenched and annealed species, respectively, and a, b are integers that label the different (sub)species.

Below we will consider two simple binary mixtures of one quenched (index 0) and one annealed (index 1) component. The first case is constituted by hard spheres in a hard sphere matrix, where all interactions are hard core, V_{ij}

MATTHIAS SCHMIDT

 PHYSICAL REVIEW E **66**, 041108 (2002)

$=V_{\text{HC}}$, for $i,j=0,1$. In the second case we treat the hard sphere adsorbate in an ideal sphere matrix, where $V_{00}=0, V_{01}=V_{\text{HC}}, V_{11}=V_{\text{HC}}$. (This is formally equivalent to an AO model where the polymer species is quenched and colloids are annealed.) In both of these binary cases the interactions between matrix and adsorbate are hard core interactions.

III. THEORY

A. Zero-dimensional limit

Let us start by considering a situation of extreme confinement, where all particles are forced to sit on top of each other, a situation which allows for an exact solution of the many-body problem. Although the detailed shape of the confining external potential V^{ext} will not affect the excess free energy, for clarity we explicitly choose $V^{\text{ext}}(r)=0$ if $r<\epsilon$, and ∞ otherwise. This corresponds to a hard cavity of (i dependent) radius $R_i+\epsilon$. Hence each particle's center is allowed to move inside a sphere of volume $4\pi\epsilon^3/3$. In the limit $\epsilon\rightarrow 0$, a zero-dimensional ($0d$) situation is encountered, and it is assured that all particles present in the cavity overlap.

In the following, we first give a detailed derivation of the $0d$ free energy for two simple QA models. Then, in Sec. III A 3, we proceed to the case of general mixtures, where an arbitrary number of components is treated. Readers primarily interested in the hard sphere examples (and subsequent results) may wish to skip Sec. III A 3.

1. Hard spheres in a hard sphere matrix

In order to illustrate the general procedure, we start with an example where both calculations and notation are simple. We consider a binary system of hard spheres, where species 0 is quenched (hence represents the matrix), and species 1 is annealed (hence represents the adsorbate). The first step is to calculate the grand partition sum Ξ_0 for the matrix particles in the $0d$ situation. This problem is equivalent to calculating the grand partition sum for pure hard spheres in $0d$ [12,13]. To obtain Ξ_0 we need to consider all states that are allowed (are compatible with the hard core exclusion). Those are (i) the empty state, and (ii) the state with exactly one hard sphere. Hence one obtains

$$\Xi_0 = 1 + z_0, \quad (1)$$

where the (scaled) fugacity is $z_i = \exp(\beta\mu_i)(4\pi\epsilon^3/3)\Lambda_i^{-3}$, and $\beta=1/k_B T$, where k_B is the Boltzmann constant and T being the absolute temperature, and Λ_i is the (irrelevant) thermal wavelength of species $i=0,1$. The first (second) term on the right hand side of Eq. (1) corresponds to case i (ii) above. The grand potential is then given as $\Omega_0 = -k_B T \ln \Xi_0$, and the mean particle number $\bar{\eta}_0$ can be obtained using the thermodynamic relation $\bar{\eta}_0 = z_0 \partial \ln \Xi_0 / \partial z_0$. The Helmholtz free energy is obtained by Legendre transform as $\beta A_0^{\text{tot}}(\bar{\eta}_0) = \beta \Omega_0 + \bar{\eta}_0 \ln(z_0)$. Its excess (over ideal gas) part is $\beta A_0 = \beta A_0^{\text{tot}} - \bar{\eta}_0 [\ln(\bar{\eta}_0) - 1]$. Carrying out the calculations yields

$$\beta A_0(\bar{\eta}_0) = (1 - \bar{\eta}_0) \ln(1 - \bar{\eta}_0) + \bar{\eta}_0, \quad (2)$$

the result for (fully annealed) hard spheres [12,13]

To obtain the $0d$ excess free energy of the annealed component A_1 we proceed in a similar fashion than above, but with the important distinction of using QA averages instead of fully annealed ones. We consider each matrix configuration as being fixed (in effect exerting an external potential on the adsorbate), and sum over all allowed adsorbate states with the correct statistical weight in the grand ensemble of the adsorbate. As in $0d$ the matrix has only two configurations (either the cavity is empty or a single matrix particle is present), this is an easy task and yields

$$\Xi_1 = \begin{cases} 1 + z_1 & \text{no matrix particle} \\ 1 & \text{else.} \end{cases} \quad (3)$$

The case of no matrix particles is the sum of the contributions from the state empty of adsorbate particles and the state with a single adsorbate particle. [This is again similar to the structure of Ξ_0 , Eq. (1).] In the case of one single matrix particle the matrix-adsorbate hard core repulsion prohibits all states except precisely that one where no adsorbate particles are present. Clearly, all terms proportional to higher than linear powers in z_1 vanish due to the hard core repulsion between adsorbate particles.

To obtain the QA free energy we need to average the logarithm of Ξ_1 over all matrix configurations. As $\ln 1=0$, only the first line in Eq. (3) contributes, and its statistical weight in the grand ensemble of matrix configurations is $1/\Xi_0$ (the factor unity stems from the fact that matrix particles are absent). Hence the $0d$ grand potential for the adsorbate Ω_1 is simply given by

$$-\beta \Omega_1 = \frac{\ln(1 + z_1)}{1 + z_0}. \quad (4)$$

To obtain the corresponding $0d$ excess free energy A_1 , essentially the same steps as those above in the case A_0 are required: The average particle number of adsorbates is given as $\eta_1 = -\partial \beta \Omega_1 / \partial z_1$, and the Helmholtz free energy is obtained as $\beta A_1^{\text{tot}} = \beta \Omega_1 + \bar{\eta}_1 \ln(z_1)$. Its excess part is obtained by subtracting the (adsorbate) ideal gas contribution, $\beta A_1 = \beta A_1^{\text{tot}} - \bar{\eta}_1 [\ln(\bar{\eta}_1) - 1]$. As final result, we find

$$\beta A_1(\bar{\eta}_0, \bar{\eta}_1) = (1 - \bar{\eta}_0 - \bar{\eta}_1) \ln(1 - \bar{\eta}_0 - \bar{\eta}_1) + \bar{\eta}_1 - (1 - \bar{\eta}_0) \ln(1 - \bar{\eta}_0). \quad (5)$$

As an aside it is interesting to note that in the present case the sum $A_0 + A_1$ equals the $0d$ excess free energy of binary annealed hard spheres. However, this constitutes a special case. In general, we do not find a simple relation between the QA and the corresponding fully annealed free energies. (The relation to the *replicated* fully annealed system is discussed below in Sec. III A 4.)

2. Hard spheres in an ideal sphere matrix

If the matrix particles are noninteracting, their grand partition sum is that of an ideal gas

$$\Xi_0 = \exp(z_0), \quad (6)$$

where we use the same notation as in the preceding subsection. Carrying out the same steps as above yields the (expected) result that the $0d$ excess free energy vanishes,

$$A_0(\bar{\eta}_0) = 0. \quad (7)$$

The grand partition sum for the matrix is equal to the above result, Eq. (3), in the case of the hard sphere matrix. In order to obtain the $0d$ QA grand potential for the adsorbate, Ω_1 , we again have to average the logarithm of the adsorbate partition sum over all matrix configurations. This yields

$$-\beta\Omega_1 = \frac{\ln(1+z_1)}{\exp(z_0)}, \quad (8)$$

from which the adsorbate free energy is obtained as

$$\beta A_1(\bar{\eta}_0, \bar{\eta}_1) = [\exp(-\bar{\eta}_0) - \bar{\eta}_1] \ln[\exp(-\bar{\eta}_0) - \bar{\eta}_1] + \bar{\eta}_1 + \bar{\eta}_0 \exp(-\bar{\eta}_0). \quad (9)$$

Note that in the fully annealed case, the present model is equal to the AO model where species 0 (1) is identified as polymer (colloid), where the (exact) $0d$ free energy is $\beta A_{AO}(\bar{\eta}_0, \bar{\eta}_1) = (1 - \bar{\eta}_1 - \bar{\eta}_0) \ln(1 - \bar{\eta}_1) + \bar{\eta}_1$ [14,15], clearly different from the above QA result.

3. Multicomponent mixtures

Here we give a formal derivation for general mixtures with more than two components. Let N_i particles of type i be in the cavity, and $\{N_i\}$ denote the set of occupation numbers. Irrespective of the precise particle coordinates, the (reduced) potential energy due to interactions between like particles of type i is $U(N_i) = (N_i/2)(N_i - 1)\beta V_{ii}(r=0)$. The contribution from interactions between unlike particles (of types i and j) is $U(N_i, N_j) = N_i N_j \beta V_{ij}(r=0)$. The total potential energy may be expressed as $U(\{N_i\}) = \sum_i U(N_i) + \sum_{i < j} U(N_i, N_j)$, where the summations run over all species. Due to the nature of interactions, $U(\{N_i\})$ takes on values $0, \infty$. Let us further decompose the occupation numbers into (disjunct) subsets of quenched and annealed species, $\{N_{0a}\} \cup \{N_{1b}\} = \{N_i\}$. The potential energy may be arranged similarly, such that $U(\{N_i\}) = U_{00}(\{N_{0a}\}) + U_{01}(\{N_{0a}\}, \{N_{1b}\}) + U_{11}(\{N_{1b}\})$, where U_{00} stems from matrix-matrix, interactions U_{01} from matrix-adsorbate interactions, and U_{11} from adsorbate-adsorbate interactions.

The grand partition sum for the matrix in the $0d$ situation is

$$\Xi_0 = \sum_{\{N_{0a}\}} \left[\prod_a \frac{(z_{0a})^{N_{0a}}}{N_{0a}!} \right] e^{-U_{00}(\{N_{0a}\})}, \quad (10)$$

where (for $i=0a$) the reduced fugacity is $z_i = \exp(\beta\mu_i) 4\pi\epsilon^3 / (3\Lambda_i^3)$, μ_i is the chemical potential, and Λ_i is the thermal wavelength of species i ; notation is such (for $t=0$) that $\sum_{\{N_{1a}\}} \equiv \sum_{N_{11}=0}^{\infty} \sum_{N_{12}=0}^{\infty} \dots$, and the product runs over all quenched species a . The grand potential is $\Omega_0 = -k_B T \ln \Xi_0$. In the context of fully equilibrated systems, it was demonstrated that imposing the exact crossover on an approximate functional may be exploited to derive systematically DFTs for systems including hard spheres [7], the AO model [14], and the WR mixture [16]. Here we add adsorbate particles. For a given matrix realization $\{N_{0a}\}$, the matrix particles are inert, and act as an external potential on the adsorbate. Its grand partition sum is

$$\Xi_1(\{N_{0a}\}) = \sum_{\{N_{1b}\}} \left[\prod_b \frac{(z_{1b})^{N_{1b}}}{N_{1b}!} \right] \times e^{-U_{11}(\{N_{1b}\})} e^{-U_{01}(\{N_{0a}\}, \{N_{1b}\})}. \quad (11)$$

To obtain the QA adsorbate grand potential Ω_1 , we need to average over all matrix realizations as

$$-\beta\Omega_1 = \frac{1}{\Xi_0} \sum_{\{N_{0a}\}} \left[\prod_a \frac{(z_{0a})^{N_{0a}}}{N_{0a}!} \right] \times e^{-U_{00}(\{N_{0a}\})} \ln \Xi_1(\{N_{0a}\}). \quad (12)$$

From Ω_0 and Ω_1 , standard relations yield the mean numbers of particles $\bar{\eta}_{0a}$, $\bar{\eta}_{1b}$ through $\bar{\eta}_{tc} = -z_{tc} \partial \beta \Omega_t / \partial z_{tc}$ (for $tc=0a, 1b$). The Helmholtz free energy is obtained via Legendre transform as $\beta A_t^{\text{tot}} = \beta \Omega_t - \sum_c \mu_{tc} \partial \beta \Omega_t / \partial \mu_{tc} \equiv \beta \Omega_t + \sum_c \ln(z_{tc}) \bar{\eta}_{tc}$. Its excess (over ideal gas) part is $\beta A_t = \beta A_t^{\text{tot}} - \sum_c \bar{\eta}_{tc} [\ln(\bar{\eta}_{tc}) - 1]$. Explicit dependence on the natural variables is $A_0(\{\bar{\eta}_{0a}\})$, and $A_1(\{\bar{\eta}_{0a}\}, \{\bar{\eta}_{1b}\})$.

4. Relation to the replica trick

Before proceeding with the construction of the DFT, let us elucidate the relation of the present analysis to the replica trick. Using the replica trick one starts from a fully equilibrated system, in which the adsorbate species are replicated s times. The replicas do not interact among each other (their interactions are ideal), but interact with the matrix particles in the same fashion. Such replicated models still fall into our class of models (provided the QA system aimed at does), hence the above formalism (for A_0) may be applied, and the $0d$ excess free energy, A_2 , of the replicated system obtained. The $0d$ QA free energy is obtainable in the limit $\beta A_1 = \lim_{s \rightarrow 0} [\partial \exp(-\beta A_2) / \partial s] \exp(\beta A_2)$. One can show that $A_2 = A_0(\{\bar{\eta}_{0a}\}) + s A_1(\{\bar{\eta}_{0a}\}, \{\bar{\eta}_{1b}\})$ for small s (where the absence of replica symmetry breaking is assumed).

B. Density-functional theory

1. Geometry-based free energy functional

Returning to three dimensions, we apply well-tried geometrical recipes to derive approximate DFTs [6,7,14,16]. The formalism requires as input the $0d$ excess free energy A of the model under consideration, and hence can be applied to

MATTHIAS SCHMIDT

PHYSICAL REVIEW E **66**, 041108 (2002)

either the pure matrix, where $A=A_0$, to the adsorbate, $A=A_1$, or even to the replicated system, $A=A_2$. Within the framework, the excess Helmholtz free energy is expressed as

$$F^{\text{exc}}[\{\rho_i(\mathbf{r})\}] = k_B T \int d^3x \Phi(\{n_\alpha^{(i)}(\mathbf{x})\}), \quad (13)$$

where $\{\rho_i(\mathbf{r})\}$ is the set of all density profiles. The reduced free energy density Φ is a function of a set of weighted densities $\{n_\alpha^{(i)}(\mathbf{x})\}$, where i labels the species and α the type of weighted density. The weighted densities are obtained by convolutions with the actual density profiles, $n_\alpha^{(i)}(\mathbf{x}) = \int d^3r \rho_i(\mathbf{r}) w_\alpha^{(i)}(\mathbf{x}-\mathbf{r})$. As all nonvanishing interactions are hard core, it is sufficient to take the usual fundamental measure weight functions [6,7], which recover (upon convolution) the Mayer bonds $\exp(-\beta V_{\text{HC}}(r)) - 1$. They are defined as

$$w_3^{(i)}(\mathbf{r}) = \theta(R_i - r), w_2^{(i)}(\mathbf{r}) = \delta(R_i - r), \quad (14)$$

$$\mathbf{w}_{v2}^{(i)}(\mathbf{r}) = w_2^{(i)}(\mathbf{r}) \mathbf{r}/r, \hat{\mathbf{w}}_{m2}^{(i)}(\mathbf{r}) = w_2^{(i)}(\mathbf{r}) \left[\frac{\mathbf{r}\mathbf{r}}{r^2} - 1/3 \right], \quad (15)$$

where $r=|\mathbf{r}|$, $\theta(r)$ is the Heaviside step function, $\delta(r)$ is the Dirac distribution, and 1 is the identity matrix. Further, linearly dependent, weights are $w_1^{(i)}(\mathbf{r}) = w_2^{(i)}(\mathbf{r})/(4\pi R_i)$, $\mathbf{w}_{v1}^{(i)}(\mathbf{r}) = \mathbf{w}_{v2}^{(i)}(\mathbf{r})/(4\pi R_i)$, $w_0^{(i)}(\mathbf{r}) = w_1^{(i)}(\mathbf{r})/R_i$. The weight functions $w_\alpha^{(i)}$ have dimension of $\text{length}^{3-\alpha}$. They differ in their tensorial rank: $w_0^{(i)}, w_1^{(i)}, w_2^{(i)}, w_3^{(i)}$ are scalars; $\mathbf{w}_{v1}^{(i)}, \mathbf{w}_{v2}^{(i)}$ are vectors; $\hat{\mathbf{w}}_{m2}^{(i)}$ is a matrix; the subscript letters identify the rank.

We determine the functional dependence of Φ on the weighted densities by imposing the exact crossover to $0d$, where $\rho_i(\mathbf{r}) = \bar{\eta}_i \delta(\mathbf{r})$, and follow recent treatments of fundamental measure theory [7] by considering multi-cavity limits to obtain $\Phi = \Phi_1 + \Phi_2 + \Phi_3$, with contributions

$$\Phi_1 = n_0^{(i)} \varphi_i(\{n_3^{(l)}\}), \quad (16)$$

$$\Phi_2 = (n_1^{(i)} n_2^{(j)} - \mathbf{n}_{v1}^{(i)} \cdot \mathbf{n}_{v2}^{(j)}) \varphi_{ij}(\{n_3^{(l)}\}), \quad (17)$$

$$\Phi_3 = \frac{1}{8\pi} \left(n_2^{(i)} n_2^{(j)} n_2^{(k)} / 3 - n_2^{(i)} \mathbf{n}_{v2}^{(j)} \cdot \mathbf{n}_{v2}^{(k)} + \frac{3}{2} [\mathbf{n}_{v2}^{(i)} \hat{\mathbf{n}}_{m2}^{(j)} \mathbf{n}_{v2}^{(k)} - \text{tr}(\hat{\mathbf{n}}_{m2}^{(i)} \hat{\mathbf{n}}_{m2}^{(j)} \hat{\mathbf{n}}_{m2}^{(k)})] \right) \varphi_{ijk}(\{n_3^{(l)}\}), \quad (18)$$

where repeated-index summation convention is used, and m th order derivatives of the $0d$ excess free energy are $\varphi_{i\dots k}(\{\bar{\eta}_l\}) \equiv \partial^m \beta A_t(\{\bar{\eta}_l\}) / \partial \bar{\eta}_i \dots \partial \bar{\eta}_k$. For $t=0,1,2$, functionals F_t^{exc} for matrix, adsorbate, and replicated system are obtained, respectively. Two routes to the QA free energy functional are possible: either directly through A_1 , giving F_1^{exc} , or via application of the replica trick to F_2^{exc} . The results from the two routes can be shown to be equal, which is a sign of internal consistency of the current approach.

2. Minimization principle

In order to apply the theory to an actual problem, the principal way is as follows. We first need to obtain the matrix density profiles from minimization (with respect to all matrix density fields $\rho_{0a}(\mathbf{x})$) of the grand potential functional

$$\begin{aligned} \tilde{\Omega}_0[\{\rho_{0a}(\mathbf{x})\}] &= F_0^{\text{exc}}[\{\rho_{0a}(\mathbf{x})\}] + k_B T \int d^3x \sum_a \rho_{0a}(\mathbf{x}) \\ &\quad \times [\ln(\rho_{0a}(\mathbf{x}) \Lambda_{0a}^3) - 1] \\ &\quad + \int d^3x \sum_a (V_{0a}^{\text{ext}}(\mathbf{x}) - \mu_{0a}) \rho_{0a}(\mathbf{x}), \quad (19) \end{aligned}$$

where V_{0a}^{ext} is an external potential acting on $0a$, generating matrix inhomogeneities. At the minimum

$$\frac{\delta \tilde{\Omega}_0}{\delta \rho_{0a}(\mathbf{r})} = 0. \quad (20)$$

Once the ρ_{0a} are known, the adsorbate densities are obtained from minimization [only with respect to the adsorbate density distributions $\rho_{1b}(\mathbf{x})$] of the grand potential

$$\begin{aligned} \tilde{\Omega}_1[\{\rho_{0a}(\mathbf{x})\}; \{\rho_{1b}(\mathbf{x})\}] &= F_1^{\text{exc}}[\{\rho_{0a}(\mathbf{x})\}; \{\rho_{1b}(\mathbf{x})\}] + k_B T \int d^3x \sum_b \rho_{1b}(\mathbf{x}) \\ &\quad \times [\ln(\rho_{1b}(\mathbf{x}) \Lambda_{1b}^3) - 1] + \int d^3x \sum_b (V_{1b}^{\text{ext}}(\mathbf{x}) \\ &\quad - \mu_{1b}) \rho_{1b}(\mathbf{x}), \quad (21) \end{aligned}$$

where V_{1b}^{ext} acts on adsorbate $1b$, and the $\rho_{0a}(\mathbf{x})$ are treated as *fixed input quantities*. Again, at the minimum

$$\frac{\delta \Omega_1}{\delta \rho_{1b}(\mathbf{r})} = 0. \quad (22)$$

Note that the (bulk) Gibbs adsorption equation is intrinsically fulfilled: $(\rho_{1b} - \rho_{1b}^{\text{free}}) \mathcal{V} = -\partial[\tilde{\Omega}_1 - \tilde{\Omega}_1(\{\rho_{0a} \equiv 0\})] / \partial \mu_{1b}$, where \mathcal{V} is the system volume, and ρ_{1b}^{free} is the density in equilibrium without matrix.

IV. RESULTS

A. Structural correlations

As an application, we consider the structural correlations of hard spheres adsorbed in sphere matrices. We consider the two types of matrices summarized in Sec. II, where the matrix is either a hard sphere fluid, or a fluid of noninteracting (hence freely overlapping) spheres.

Madden and Glandt [3] derived a set of replica Ornstein-Zernike (ROZ) equations for one quenched (index 0) and one annealed (index 1) species, given as

$$h_{00} = c_{00} + c_{00} \rho_0 h_{00}, \quad (23)$$

$$h_{01} = c_{01} + c_{01} \rho_0 h_{00} + c_{11} \rho_1 h_{01}, \quad (24)$$

$$h_{11} = c_{11} + c_{01} \rho_0 h_{01} + c_{11} \rho_1 h_{11}, \quad (25)$$

where \int denotes the spatial convolution, $h_{ij} = g_{ij} - 1$ are the total correlation functions, g_{ij} are the partial pair correlation functions, and c_{ij} are the direct correlation functions. Given and Stell [4] have shown that Eqs. (23)–(25) are approximations; the exact ROZ equations contain contributions from nonvanishing direct correlation functions between different replicas.

In liquid integral equation theories, Eqs. (23)–(25) are supplemented by (approximate) closures, and the resulting set of equations is solved numerically, see e.g., Ref. [17,18]. Here we proceed in a different fashion, and *derive* the direct correlation functions c_{ij} from our density functional. Then we use Eqs. (23)–(25) to obtain the h_{ij} and hence the $g_{ij}(r)$, which will be compared to computer simulation data below. This procedure constitutes a demanding test for the present theory, as the $c_{ij}(r)$ are obtained by second functional derivatives as

$$c_{00}(|\mathbf{r}-\mathbf{r}'|) = \left. \frac{\delta^2 F_0^{\text{exc}}[\rho_0]}{\delta \rho_0(\mathbf{r}) \delta \rho_0(\mathbf{r}')} \right|_{\rho_0 = \text{const}}, \quad (26)$$

$$c_{01}(|\mathbf{r}-\mathbf{r}'|) = \left. \frac{\delta^2 F_1^{\text{exc}}[\rho_0; \rho_1]}{\delta \rho_0(\mathbf{r}) \delta \rho_1(\mathbf{r}')} \right|_{\rho_0, \rho_1 = \text{const}}, \quad (27)$$

$$c_{11}(|\mathbf{r}-\mathbf{r}'|) = \left. \frac{\delta^2 F_1^{\text{exc}}[\rho_0; \rho_1]}{\delta \rho_1(\mathbf{r}) \delta \rho_1(\mathbf{r}')} \right|_{\rho_0, \rho_1 = \text{const}}. \quad (28)$$

Clearly, as the approximation is done on the level of F_i^{exc} , any inaccuracies will be enhanced by taking two derivatives to obtain the c_{ij} . We find that the approximate ROZ equations, Eqs. (23)–(25), are sufficient within the present approximations, i.e., the direct correlation functions between species from different replicas vanish identically.

In order to compare the DFT results, we have carried out Monte Carlo (MC) computer simulations with 1024 particles, and 2×10^6 MC moves per particles. Averages were taken over 20 different representations of the matrix, which we find to be sufficient to obtain reliable data.

We first turn to the case of hard spheres in a hard sphere matrix. For simplicity, we consider the case of equal sphere sizes $\sigma_0 = \sigma_1 (= \sigma)$, and equal packing fractions $\eta_0 = \eta_1 = 0.15$. (The total packing fraction is hence $\eta_0 + \eta_1 = 0.3$, a moderately large value.) To obtain the matrix pair correlation function $g_{00}(r)$, we need to solve Eq. (23), which is completely decoupled from Eqs. (24) and (25) containing also adsorbate distribution functions. Hence as input only c_{00} is required. We obtain it from Eq. (26), where F_0^{exc} is the density functional obtained from applying the procedure outlined in Sec. III B 1 to the HS $0d$ excess free energy for hard spheres, A_0 , which is given in Eq. (2). F_0^{exc} derived in this way is equal to Rosenfeld's functional [6] in Tarazona's tensorial formulation [7]. This reproduces the direct correlation function for pure hard spheres in the Percus-Yevick approxi-

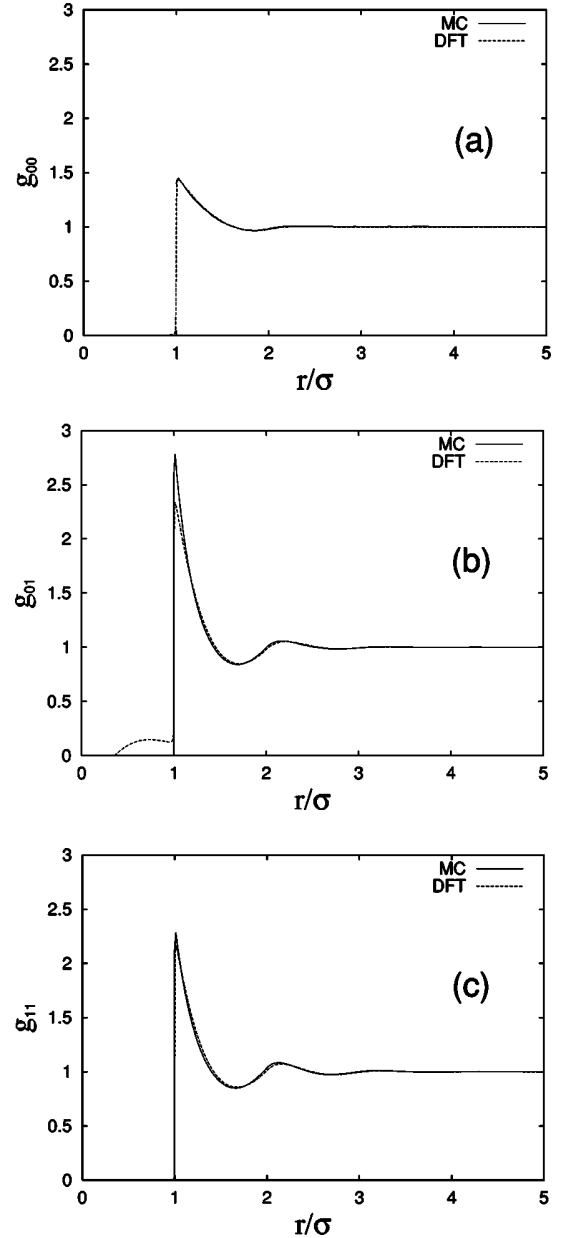


FIG. 1. Partial pair distribution functions $g_{ij}(r)$ as a function of the scaled distance r/σ for hard spheres of diameter σ and packing fraction $\eta_1=0.15$ adsorbed in a hard sphere matrix with the same diameter σ and packing fraction $\eta_0=0.15$. Solid lines denote Monte Carlo results, dashed lines denote DFT results. Different cases are shown: (a) g_{00} matrix-matrix pair correlations; (b) g_{01} matrix-adsorbate pair correlations; (c) g_{11} adsorbate-adsorbate pair correlations.

mation [6,7]. For $\eta_0=0.15$ this is known to be very accurate, as can be seen in Fig. 1(a), where we plot $g_{00}(r)$ along with the corresponding result from computer simulation. Both curves practically lie on top of each other.

In order to obtain the partial pair correlation functions involving the adsorbate species, $g_{01}(r)$ and $g_{11}(r)$, we solve Eqs. (24) and (25), where the direct correlation functions c_{01} and c_{11} are obtained through Eqs. (27) and (28), with F_1^{exc} obtained from the prescription in Sec. III B 1 applied to the

MATTHIAS SCHMIDT

PHYSICAL REVIEW E **66**, 041108 (2002)

$0d$ free energy of hard spheres in a hard sphere matrix, A_1 , given in Eq. (5). We display $g_{01}(r)$ and $g_{11}(r)$ in Figs. 1(b), 1(c), respectively. Both functions display considerably stronger oscillations than g_{00} . For g_{01} the agreement with MC data is very good for $r/\sigma \gtrsim 1.1$. In the immediate vicinity of contact, $r/\sigma \lesssim 1.1$, and at contact, $r \rightarrow \sigma^+$, the DFT result underestimates the simulation result. Inside the core region, $r/\sigma < 1$, due to the overlap restriction, $g_{ij}(r) = 0$ is an exact condition. Our theory fails to reproduce this and yields non-zero values [the extreme value being $g_{01}(r=0) = -0.46$]. This deficiency is known from other geometry-based density functionals for fully annealed systems [14,15], and could be remedied with a test-particle limit calculation, i.e., minimizing the density profiles (see Sec. III B 2) in the presence of an external potential V^{ext} that describes a particle fixed at the origin. We expect such results to also improve the behavior for $r/\sigma \lesssim 1.1$, albeit at the expense of more numerical work. Note further that the core condition is fulfilled in the low density (virial) expansion, i.e., we recover the correct limiting behavior $g_{ij} \rightarrow \exp[-\beta V_{ij}(r)]$. Finally, $g_{11}(r)$, displayed in Fig. 1(c), fares again better. The DFT result is very good even near contact, and the violation of the core condition is smaller [$g_{11}(r=0) = -0.09$].

To exemplify that the good quality of the DFT result is not accidental, we change the matrix properties by switching off the interactions between matrix particles. Hence the matrix is constituted by freely overlapping spheres that are homogeneously distributed. Clearly, such configurations act differently on the adsorbate than in the previous case of the hard sphere matrix. Again we restrict ourselves to $\sigma_0 = \sigma_1 (= \sigma)$, and consider slightly higher packing fractions $\eta_0 = \eta_1 = 0.2$. In order to calculate the $g_{ij}(r)$, we proceed as in the previous case, but instead of using Eqs. (2) and (5) for the $0d$ free energies A_0 and A_1 , we take the appropriate expressions for the current model, given in Eqs. (7) and (9), respectively. DFT and simulation results are displayed in Fig. 2. As the matrix is an ideal gas, $g_{00}(r) = 1$ for all distances, and the DFT trivially fulfills this relation, as $F_0^{\text{exc}} = 0$. The core condition is again violated [the extreme cases are $g_{01}(r=0) = -0.84, g_{11}(r=0) = -0.96$]. Apart from that, the accuracy of $g_{01}(r)$ and $g_{11}(r)$ is generally quite good and comparable to that found in the previous case. We conclude that the DFT correctly describes the structural correlations of bulk fluid states in homogeneously distributed random matrices.

V. CONCLUSIONS

In summary, we have presented the first DFT, to the best of our knowledge, for QA systems that treats the quenched species (which model a porous material) on the level of their one-body density profiles. This provides an enormous simplification over a treatment where the matrix particles are described by an external potential (which is a highly non-trivial three-dimensional field for a single matrix realization) and averaging over matrix realization has to be done explicitly. We have presented evidence for the potential of our approach, through the investigation of pair correlation functions of hard spheres adsorbed in two different types of ma-

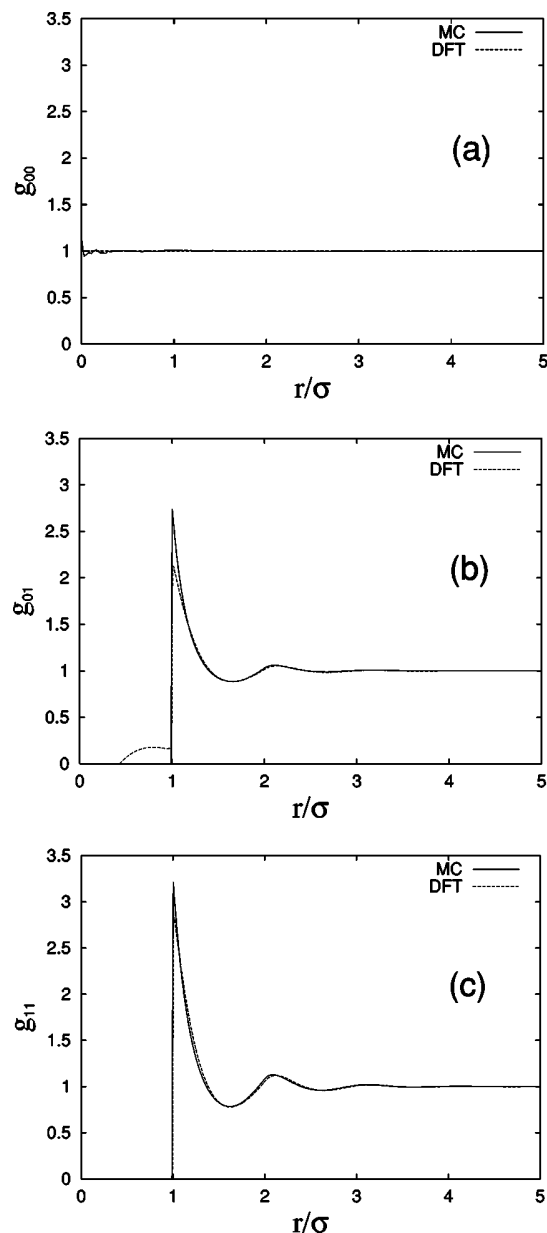


FIG. 2. Same as Fig. 1, but for a matrix of freely overlapping spheres of diameter σ and packing fractions $\eta_0 = \eta_1 = 0.2$.

trices, where we find good agreement with computer simulation results. Possible future applications may focus on freezing in porous media; note that the bulk (no matrix) HS transition is described very accurately [7]. Furthermore, the effects caused by inhomogeneous matrices should be interesting. Wetting of (macroscopic) surfaces of the porous material, confinement within slits, pores, or cavities that are filled with porous material, as well as behavior near rough walls would be further interesting applications. Results for fluid demixing will be presented elsewhere [19].

ACKNOWLEDGMENTS

I thank G. Kahl, R. Evans, H. Löwen, and A. R. Denton for inspiring discussions.

DENSITY-FUNCTIONAL THEORY FOR FLUIDS IN . . .

PHYSICAL REVIEW E **66**, 041108 (2002)

- [1] R. Evans, *J. Phys.: Condens. Matter* **2**, 8989 (1990).
- [2] L.D. Gelb, K.E. Gubbins, R. Radhakrishnan, and M. Sliwinski-Bartkowiak, *Rep. Prog. Phys.* **62**, 1573 (1999).
- [3] W.G. Madden and E.D. Glandt, *J. Stat. Phys.* **51**, 537 (1988).
- [4] J.A. Given and G. Stell, *J. Chem. Phys.* **97**, 4573 (1992).
- [5] R. Evans, in *Fundamentals of Inhomogeneous Fluids*, edited by D. Henderson (Dekker, New York, 1992), p. 85.
- [6] Y. Rosenfeld, *Phys. Rev. Lett.* **63**, 980 (1989).
- [7] P. Tarazona, *Phys. Rev. Lett.* **84**, 694 (2000).
- [8] D. Goulding, J.-P. Hansen, and S. Melchionna, *Phys. Rev. Lett.* **85**, 1132 (2000).
- [9] E. Kierlik, P.A. Monson, M.L. Rosinberg, L. Sarkisov, and G. Tarjus, *Phys. Rev. Lett.* **87**, 055701 (2001).
- [10] S. Asakura and F. Oosawa, *J. Chem. Phys.* **22**, 1255 (1954).
- [11] B. Widom and J.S. Rowlinson, *J. Chem. Phys.* **52**, 1670 (1970).
- [12] Y. Rosenfeld, M. Schmidt, H. Löwen, and P. Tarazona, *J. Phys.: Condens. Matter* **8**, L577 (1996).
- [13] Y. Rosenfeld, M. Schmidt, H. Löwen, and P. Tarazona, *Phys. Rev. E* **55**, 4245 (1997).
- [14] M. Schmidt, H. Löwen, J.M. Brader, and R. Evans, *Phys. Rev. Lett.* **85**, 1934 (2000).
- [15] M. Schmidt, H. Löwen, J.M. Brader, and R. Evans, *J. Phys.: Condens. Matter* (to be published).
- [16] M. Schmidt, *Phys. Rev. E* **63**, 010101(R) (2001).
- [17] E. Paschinger and G. Kahl, *Phys. Rev. E* **61**, 5330 (2000).
- [18] E. Paschinger, D. Levesque, G. Kahl, and J.J. Weis, *Europhys. Lett.* **55**, 178 (2001).
- [19] M. Schmidt, E. Schöll-Paschinger, J. Köfinger, and G. Kahl, *J. Phys.: Condens. Matter* (to be published).

Journal of Statistical Physics, Vol. 116, Nos. 5/6, September 2004 (© 2004)

Replica Density Functional Study of One-Dimensional Hard Core Fluids in Porous Media

Hendrik Reich¹ and Matthias Schmidt^{2,3}

Received November 23, 2003; accepted March 4, 2004

A binary quenched-annealed hard core mixture is considered in one dimension in order to model fluid adsorbates in narrow channels filled with a random matrix. Two different density functional approaches are employed to calculate adsorbate bulk properties and interface structure at matrix surfaces. The first approach uses Percus' functional for the annealed component and an explicit averaging over matrix configurations; this provides numerically exact results for the bulk partition coefficient and for inhomogeneous density profiles. The second approach is based on a quenched-annealed density functional whose results we find to approximate very well those of the former over the full range of possible densities. Furthermore we give a derivation of the underlying replica density functional theory.

KEY WORDS: Density functional theory; quenched-annealed fluid mixtures; hard core models in one dimension; random porous media.

1. INTRODUCTION

The one-dimensional hard rod model⁽¹⁾ continues to be an invaluable test bed for theoretical work as it provides the possibility to compare approximations to exact results. Recent examples of this strategy include investigations of depletion interactions in binary mixtures where one of the components is viewed as an agent that mediates an effective

¹Institut für Theoretische Physik II, Heinrich-Heine-Universität Düsseldorf, Universitätsstraße 1, D-40225 Düsseldorf, Germany.

²Soft Condensed Matter, Debye Institute, Utrecht University, Princetonplein 5, 3584 CC Utrecht, The Netherlands.

³On leave from: Institut für Theoretische Physik II, Heinrich-Heine-Universität Düsseldorf, Universitätsstraße 1, D-40225 Düsseldorf, Germany; e-mail: mschmidt@thphy.uni-duesseldorf.de

interaction between particles of the other component,^(2,3) a model colloid-polymer mixture⁽⁴⁾ where particles representing polymers can freely penetrate, dynamical density functional theory^(5,6) concerned with time-dependent transport phenomena, as well as a model porous medium⁽⁷⁾ of lines of random length accessible to the fluid particles. As concerns equilibrium statistical mechanics, Percus' exact free energy functional for pure systems⁽⁸⁾ and (additive) mixtures of particles with different sizes,⁽⁹⁾ provides a framework to compute thermodynamics, density distributions, and correlation functions in arbitrary inhomogeneous situations.

Fluids adsorbed in disordered matrices are often described in the context of so-called quenched-annealed (QA) fluid mixtures, where particles of the quenched component act as randomly distributed obstacles exerting an external potential on particles of the annealed component.^(10,11) The matrix particles are distributed according to the Hamiltonian of the quenched component, and hence can be treated with liquid state theory. The crucial difference to an equilibrium system of two annealed components is that the distribution of matrix particles is unaffected by the presence of the annealed component. As one is interested in the typical behavior of the system, a double average over the annealed degrees of freedom and over the quenched disorder is required. A short overview of this theoretical framework is given below. One standard approach to tackle fluid structure and phase behavior of QA models is via the replica Ornstein-Zernike relations^(10,11) supplemented with appropriate closure relations. Many standard liquid integral equation theories have been carried over to the QA case. The basic quantities in terms of which these theories are formulated are two-body (and possibly higher) correlation functions.

Recently it was proposed to rather work directly on the level of the free energy functional, pre-averaged over the disorder.⁽¹²⁾ Correlation functions can be obtained subsequently, in particular the hierarchy of direct correlation functions is obtained through functional differentiation with respect to the density fields. The advantage of formulating the theory on the one-body level of the density fields is that inhomogeneous situations, e.g. at free interfaces or caused by external fields like e.g. gravity, are straightforward to treat. Hence all advantages of equilibrium DFT^(13,14) apply to this QA or replica DFT. Also the disadvantage applies; in general the density functional is unknown. Moreover, whether one can learn anything about the important out-of-equilibrium behavior of QA systems, like hysteresis in sorption isotherms, is questionable. Based on Rosenfeld's fundamental-measure theory (FMT) for hard sphere mixtures,⁽¹⁵⁾ and the subsequent discovery that one can construct density functionals by imposing the correct behavior upon dimensional reduction (i.e. in situations of extreme confinement in one or more spatial directions through

Functional Study of One-Dimensional Hard Core Fluids

1685

suitably chosen external potentials),^(16,17) this DFT treats QA mixtures with either hard or ideal interactions.

Previous tests of QA DFT include the comparison with results from Monte Carlo (MC) simulations for the partial pair correlation functions in hard sphere systems⁽¹²⁾ and for density profiles across the surface of a porous medium, modeled as a step-like density distribution of (freely overlapping) matrix spheres.⁽¹⁸⁾ Such an interface was also investigated in a model of a random fiber network, being represented by quenched configurations of infinitely thin needle-like particles. Again comparison with simulation results shows satisfactory agreement with DFT results.⁽¹⁹⁾ Much work has been devoted to a model colloid-polymer mixture where the colloids are represented as hard spheres and the polymers as freely overlapping spheres. The crucial step beyond hard sphere systems is the occurrence of a fluid-fluid phase transition, and the questions how capillary condensation occurs inside a porous medium⁽²⁰⁾ and what the structure of the interface between demixed fluid phases is like⁽²¹⁾ were treated. A further, very promising, line of research is the application of the approach to lattice models. Note that using lattice models insight into hysteresis behavior and the relation to the appearance of a complex free energy landscape was gained.^(22,23) Combining the QA-DFT approach with the very powerful lattice DFT by Lafuente and Cuesta,^(24,25) freezing in a two-dimensional lattice model was investigated.⁽²⁶⁾

In this work we consider the one-dimensional hard rod model adsorbed in a quenched matrix of rods. Two cases of interactions between the quenched particles are considered. In the first case the rods interact with a hard core potential, hence we deal with a binary QA hard rod mixture. In the second case the matrix particles are ideal (non-interacting) amongst each other, but interact with a hard-core potential with particles of the annealed component; this model is the QA analog of the model colloid-polymer mixture of Ref. 4, obtained by quenching the polymers. We use two different density functional approaches to tackle the properties of these models in both homogeneous and inhomogeneous (on average over disorder) situations. In the first approach the matrix is treated explicitly on the level of particle coordinates distributed according to the matrix Hamiltonian, and practically generated with a Monte Carlo procedure. For each matrix configuration we use Percus' functional⁽⁸⁾ to obtain adsorbate properties, and the disorder-average over matrix configuration is carried out numerically by brute force generation of many (of the order of 1000) matrix realizations. The second approach is the QA DFT working directly on the level of the disorder-averaged adsorbate density profile, which is obtained via minimizing the disorder-averaged grand potential of the adsorbate, using the matrix density profiles as a fixed input. As the

1686

Reich and Schmidt

average over disorder is taken a priori, the corresponding Euler-Lagrange equation yields directly the averaged density profile. We compare results from both theories in bulk via calculation of the partition coefficient, which is the ratio of adsorbate density inside the matrix and the density in a bulk reservoir that is in chemical equilibrium. The results from the explicit matrix averaging procedure, which we also check against an independent elementary calculation, agree well with those from the QA DFT over the full range of accessible densities. Deviations appear at high densities, which we can trace back to an incorrect behavior of the QA-DFT near close-packing. As a generic inhomogeneous situation we consider a surface of the model porous matrix, that is generated by a hard wall acting on the matrix particles (before the quench). The wall is then removed and leaves a halfspace of bulk (free of matrix particles). The adsorbate is found to exhibit density oscillations on both sides of the interface, with significantly smaller amplitude than at a hard wall.

The paper is organized as follows. In Section 2 we define the model and give an overview of its statistical mechanics and the replica trick (which can be safely skipped by an expert reader). Section 3 is devoted to both density functional methods. In Section 4 results are presented and we conclude in Sec. 5.

2. THE MODEL

2.1. Definition of the Interactions

We consider a quenched-annealed fluid mixture of a quenched species 0 with N_0 particles with one-dimensional (1d) position coordinates x_1, x_2, \dots, x_{N_0} and an annealed species 1 with N_1 particles with 1d position coordinates X_1, X_2, \dots, X_{N_1} . The particles interact with pairwise potentials (for pairs $\alpha\gamma = 00, 01, 11$) given by

$$\phi_{\alpha\gamma}(x) = \begin{cases} \infty & x < (\sigma_\alpha + \sigma_\gamma)/2 \\ 0 & \text{otherwise,} \end{cases} \quad (1)$$

where x is the center-center distance between two particles; σ_α is the diameter (length) of particles of species $\alpha = 0, 1$, see Fig. 1a for an illustration. This describes our first case of the hard core matrix. The total potential energy due to particle-particle interactions is $V_{00} + V_{01} + V_{11}$, with contributions

$$V_{00} = \sum_{i=1}^{N_0} \sum_{j=i+1}^{N_0} \phi_{00}(|x_i - x_j|), \quad (2)$$

Functional Study of One-Dimensional Hard Core Fluids

1687

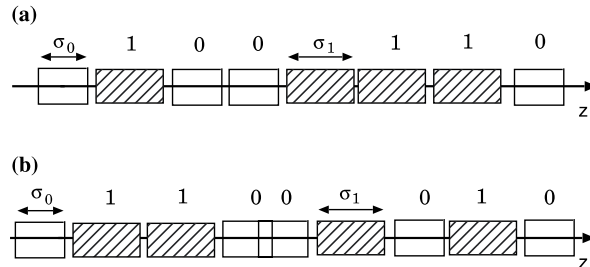


Fig. 1. Model of annealed hard rods in a matrix of quenched rods in one dimension. The quenched rods interact with a) a hard core potential, and b) are ideal.

$$V_{01} = \sum_{i=1}^{N_0} \sum_{j=1}^{N_1} \phi_{01}(|x_i - X_j|), \tag{3}$$

$$V_{11} = \sum_{i=1}^{N_1} \sum_{j=i+1}^{N_1} \phi_{11}(|X_i - X_j|). \tag{4}$$

We furthermore consider the influence of external potentials, $\phi_\alpha^{\text{ext}}(x)$, acting on species $\alpha=0, 1$, respectively. In particular $\phi_0^{\text{ext}}(x)$ acts on particles of species 0 *before* they are quenched, i.e. their density distribution is that generated in response to $\phi_0^{\text{ext}}(x)$. The resulting total external potential energy is $V_0^{\text{ext}} + V_1^{\text{ext}}$, with contributions

$$V_0^{\text{ext}} = \sum_{i=1}^{N_0} \phi_0^{\text{ext}}(x_i), \quad V_1^{\text{ext}} = \sum_{i=1}^{N_1} \phi_1^{\text{ext}}(X_i). \tag{5}$$

In our second case we consider ideal (non-interacting) matrix particles, i.e.

$$\phi_{00}(x) = 0, \tag{6}$$

valid for all distances x ; the two remaining interactions are unchanged, i.e. $\phi_{01}(x)$ and $\phi_{11}(x)$ are hard core potentials given through (1); see Fig. 1b for an illustration. The size ratio $s = \sigma_1/\sigma_0$ is a geometric control parameter. In the numerical results presented below we will restrict ourselves to equally sized particles, $s = 1$, and furthermore to situations where $\phi_1^{\text{ext}}(x) = 0$.

2.2. Partition Sum, Grand Potential and Replica Trick

We first make the statistical mechanics of the quenched-annealed mixture explicit. For notational convenience the grand canonical trace

1688

Reich and Schmidt

over matrix coordinates is denoted by $\int d0 \equiv \sum_{N_0=0}^{\infty} (N_0! \Lambda_0^{N_0})^{-1} \int dx_1 \dots \int dx_{N_0}$ and that over adsorbate coordinates by $\int d1 \equiv \sum_{N_1=0}^{\infty} (N_1! \Lambda_1^{N_1})^{-1} \int dX_1 \dots \int dX_{N_1}$, where Λ_α is the (irrelevant) thermal wavelength of species $\alpha=0, 1$, and the position integrals run over the total system volume V . The (equilibrium) grand partition of the matrix particles under the influence of the external potential $\phi_0^{\text{ext}}(x)$ is

$$\Xi_0(\mu_0, T, V) = \int d0 e^{-\beta(V_{00} + V_0^{\text{ext}} - \mu_0 N_0)}, \quad (7)$$

where $\beta = 1/(k_B T)$, k_B is the Boltzmann constant, T is absolute temperature and μ_i is the chemical potential of species $i=0, 1$. The grand potential for the matrix is then

$$\Omega_0(\mu_0, T, V) = -\beta^{-1} \ln \Xi_0(\mu_0, T, V). \quad (8)$$

For fixed matrix configuration $\{x_i\}$ the grand potential of the adsorbate is

$$\Omega_1(\{x_i\}, \mu_1, T, V) = -\beta^{-1} \ln \int d1 e^{-\beta(V_{11} + V_{01} + V_1^{\text{ext}} - \mu_1 N_1)}, \quad (9)$$

depending explicitly on $\{x_i\}$ through V_{01} , see (3). Note that from the viewpoint of the 1-particles, $V_{01} + V_1^{\text{ext}}$ is the *total* external potential energy. A (grand canonical) average over matrix configurations yields the disorder-averaged grand potential of the adsorbate,

$$\begin{aligned} \Omega_1(\mu_0, \mu_1, T, V) \\ = \Xi_0^{-1}(\mu_0, T, V) \int d0 e^{-\beta(V_{00} + V_0^{\text{ext}} - \mu_0 N_0)} \Omega_1(\{x_i\}, \mu_1, T, V). \end{aligned} \quad (10)$$

Note that (10) has a different structure than that of the partition sum of an equilibrium mixture due to the appearance of the logarithm, upon inserting (9) into (10), *inside* the trace over the 0-particles. However, a relation to a multi-component mixture can be established using the replica trick: One introduces replicas as s copies of species 1: $\phi_{\alpha\alpha}(x) = \phi_{11}(x)$, for $1 < \alpha \leq s$, where s is an integer. Particles from different replicas are non-interacting, $\phi_{\alpha\gamma}(x) = 0$ for all x and $\alpha \neq \gamma$, but they interact with matrix particles in the same fashion, $\phi_{0\alpha}(x) = \phi_{01}(x)$, for $1 < \alpha \leq s$. Then the (equilibrium) partition sum for this $(s+1)$ -component mixture can be written as

$$\Xi = \int d0 e^{-\beta(V_{00} + V_0^{\text{ext}} - \mu_0 N_0)} \left(\int d1 e^{-\beta(V_{11} + V_{01} + V_1^{\text{ext}} - \mu_1 N_1)} \right)^s, \quad (11)$$

Functional Study of One-Dimensional Hard Core Fluids

1689

and the grand potential is

$$\Omega(\mu_0, \mu_1, T, V; s) = -\beta^{-1} \ln \Xi. \tag{12}$$

Via analytical continuation in s , and noting that $\lim_{s \rightarrow 0} dx^s/ds = \ln x$, the disorder-averaged grand potential, (10), is obtained from the equilibrium grand potential of the replicated system as

$$\Omega_1(\mu_0, \mu_1, T, V) = \lim_{s \rightarrow 0} \frac{d}{ds} \Omega(\mu_0, \mu_1, T, V; s), \tag{13}$$

establishing a practical route to tackle the QA system via the replicated equilibrium system.

3. DENSITY FUNCTIONAL APPROACHES

The following subsections 3.1, 3.2 are valid in arbitrary space dimension d upon trivial alterations: spatial integrations become d -dimensional integrals, hence $\int dx$ is to be replaced with $\int d^d x$ and factors Λ_α are to be replaced with Λ_α^d . Although in our subsequent study we only deal with hard core interactions, where the dependence on temperature is trivial, the formalism also applies to thermal systems. Hence we consider a general binary QA mixture with arbitrary pair potentials $\phi_{\alpha\gamma}(x)$, $\alpha, \gamma = 0, 1$, not necessarily given through (1), at temperature T inside a volume V .

3.1. Equilibrium Case

In the equilibrium DFT formalism, applied to the present case, where both an explicit external potential, $\phi_1(x)$, and the (random) influence of the matrix particles at positions $\{x_i\}$ acts on the fluid, the grand potential of the adsorbate component is expressed as a functional of its one-body density distribution,

$$\begin{aligned} \tilde{\Omega}_1(\{x_i\}, [\rho_1], \mu_1, T, V) = & \mathcal{F}^{\text{id}}[\rho_1] + \mathcal{F}^{\text{exc}}[\rho_1] + \int dx \rho_1(x) \\ & \times \left[\left(\phi_1^{\text{ext}}(x) + \sum_{i=1}^{N_0} \phi_{01}(x-x_i) \right) - \mu_1 \right], \end{aligned} \tag{14}$$

where $\mathcal{F}^{\text{id}}[\rho_1] = \beta^{-1} \int dx \rho_1(x) [\ln(\rho_1(x)\Lambda_1) - 1]$ is the (Helmholtz) free energy functional of the ideal gas, $\mathcal{F}^{\text{exc}}[\rho_1]$ is the excess (over ideal) contribution that arises from interactions between (adsorbate) particles, and the

1690

Reich and Schmidt

term in round brackets is the *total* external potential acting on the adsorbate stemming from the explicit (non-random) external potential, $\phi_1^{\text{ext}}(x)$, and the sum over interactions with (randomly distributed) matrix particles. The latter contribution is parameterized by the set of matrix coordinates $\{x_i\}$, and hence $\tilde{\Omega}_1$ depends explicitly on $\{x_i\}$, which we stress in the notation of the l.h.s. of (14). The free energy functionals \mathcal{F}^{id} and \mathcal{F}^{exc} depend on T and V ; this is suppressed in the notation in (14) and in the following. The minimization condition is

$$\left. \frac{\delta \tilde{\Omega}(\{x_i\}, [\rho_1], \mu_1, T, V)}{\delta \rho_1} \right|_{\rho_1 = \rho_1(\{x_i\}, x)} = 0, \quad (15)$$

where $\rho_1(\{x_i\}, x)$ is the adsorbate density distribution that solves (15). The value of the grand potential is then obtained by reinserting the solution into the grand potential functional,

$$\Omega(\{x_i\}, \mu_1, T, V) = \tilde{\Omega}(\{x_i\}, [\rho_1(x, \{x_i\})], \mu_1, T, V), \quad (16)$$

from which the average over the disorder, $\Omega(\mu_0, \mu_1, T, V)$, can be obtained via (10). In a similar way as for the grand potential, the matrix-averaged adsorbate density profile is given as

$$\rho_1(x) = \Xi_0^{-1}(\mu_0, T, V) \int d0 e^{-\beta(V_{00} + V_0^{\text{ext}} - \mu_0 N_0)} \rho_1(x, \{x_i\}). \quad (17)$$

Note that *explicit* averages over the matrix configurations are to be performed in (10) and (17). In the numerical procedure described below, we will carry this out numerically via a Monte Carlo procedure.

3.2. Quenched-Annealed Case

Here we first formulate the equilibrium DFT of the replicated model from which we obtain, in the appropriate limit of vanishing number of components, the minimization condition of DFT for one quenched and one annealed component. Explicitly assuming absence of replica symmetry breaking, hence $\rho_1(x) = \rho_\alpha(x)$, $1 < \alpha \leq s$, the grand potential functional for the replicated *equilibrium* mixture reduces to

$$\tilde{\Omega}([\rho_0, \rho_1], \mu_0, \mu_1, T, V; s) \equiv \tilde{\Omega}([\{\rho_\alpha\}], \{\mu_\alpha\}, T, V) \quad (18)$$

Functional Study of One-Dimensional Hard Core Fluids

1691

The minimization conditions are

$$\frac{\delta \tilde{\Omega}([\rho_0, \rho_1], \mu_0, \mu_1, T, V; s)}{\delta \rho_\alpha(x)} = 0, \quad \alpha = 0, 1, \quad (19)$$

which are two *coupled* equations for the two unknown functions $\rho_0(x)$ and $\rho_1(x)$. At the minimum the value of the functional is the true grand potential

$$\Omega(\mu_0, \mu_1, V, T; s) = \tilde{\Omega}([\rho_0, \rho_1], \mu_0, \mu_1, T, V; s). \quad (20)$$

Via analytic continuation, and Taylor expanding in s around $s=0$, one obtains

$$\begin{aligned} \tilde{\Omega}([\rho_0, \rho_1], \mu_0, \mu_1, T, V; s) = & \tilde{\Omega}_0([\rho_0], \mu_0, T, V) \\ & + s \tilde{\Omega}_1([\rho_0, \rho_1], \mu_1, T, V) + O(s^2), \end{aligned} \quad (21)$$

where $\tilde{\Omega}_0$ is the grand potential of the pure system of 0-particles, that may formally be written as $\tilde{\Omega}_0([\rho_0], \mu_0, T, V) = \tilde{\Omega}([\rho_0, 0], \mu_0, \mu_1 \rightarrow -\infty, T, V)$, furthermore $\tilde{\Omega}_1[\rho_0, \rho_1] = \lim_{s \rightarrow 0} d\tilde{\Omega}([\rho_0, \rho_1], \mu_0, \mu_1, T, V; s)/ds$. Note that via this definition $\tilde{\Omega}_1$ is also the disorder-averaged grand potential, given in (13).

We decompose both contributions in the standard way:

$$\tilde{\Omega}_0([\rho_0], \mu_0, T, V) = \mathcal{F}^{\text{id}}[\rho_0] + \mathcal{F}_0^{\text{exc}}[\rho_0] + \int dx \rho_0(x) (\phi_0^{\text{ext}}(x) - \mu_0), \quad (22)$$

$$\tilde{\Omega}_1([\rho_0, \rho_1], \mu_1, T, V) = \mathcal{F}^{\text{id}}[\rho_1] + \mathcal{F}_1^{\text{exc}}[\rho_0, \rho_1] + \int dx \rho_1(x) (\phi_1^{\text{ext}}(x) - \mu_1), \quad (23)$$

which can be viewed as definitions for the excess (over ideal gas) free energy functionals, $\mathcal{F}_0^{\text{exc}}[\rho_0]$ and $\mathcal{F}_1^{\text{exc}}[\rho_0, \rho_1]$, that arise from interactions between particles. Note, however, that neither $\mathcal{F}^{\text{id}}[\rho_0]$ nor a contribution involving $\phi_0^{\text{ext}}(x)$ appear on the r.h.s. of (23), in contrast to the binary equilibrium case.

We insert the small- s -expansion of the grand potential functional, (21), into the equilibrium minimization condition, (19). Performing the limit $s \rightarrow 0$, the minimization conditions for the QA mixture result as

$$\frac{\delta \tilde{\Omega}_0([\rho_0], \mu_0, T, V)}{\delta \rho_0(x)} = 0, \quad (24)$$

$$\frac{\delta \tilde{\Omega}_1([\rho_0, \rho_1], \mu_1, T, V)}{\delta \rho_1(x)} = 0. \quad (25)$$

The derivation of (24) is straightforward. To obtain (25) one sets $\alpha=1$ in (19) i.e. differentiates w.r.t. to $\rho_1(x)$ and divides the resulting equation by s , assuming $s > 0$, before taking the limit $s \rightarrow 0$. Note that (24) is decoupled from (25), hence in particular $\rho_0(x)$ is solely determined through (24). The result then serves as an input to (25), which is solely to be solved for $\rho_1(x)$.

3.3. Excess Free Energy Functionals

The theoretical approaches described so far incorporate the complexity of the problem i) in the excess free energy functionals for the adsorbate, $\mathcal{F}^{\text{exc}}[\rho_1]$, and an explicit average over matrix configurations, and ii) in excess free energy functionals for the matrix component, $\mathcal{F}_0^{\text{exc}}[\rho_0]$, and for the adsorbate in the presence of the matrix, $\mathcal{F}_1^{\text{exc}}[\rho_0, \rho_1]$. For the present 1d model, the situation is fortunate, as an exact result for $\mathcal{F}^{\text{exc}}[\rho_1]$ and $\mathcal{F}_0^{\text{exc}}[\rho_0]$ is available, namely Percus' free energy functional for 1d hard rods.^(8,9) For a one-component system of hard rods of species α one writes (using Rosenfeld's terminology)

$$\mathcal{F}^{\text{exc}}[\rho_\alpha] = \int dx n_\alpha^{(0)}(x) \Phi'_{\text{hc}}(n_\alpha^{(1)}(x)), \quad (26)$$

where the weighted densities, $n_\alpha^{(0)}(x)$ and $n_\alpha^{(1)}(x)$, are obtained from the bare density profile (of species α) via

$$n_\alpha^{(0)}(x) = [\rho_\alpha(x - R_\alpha) + \rho_\alpha(x + R_\alpha)]/2, \quad (27)$$

$$n_\alpha^{(1)}(x) = \int_{x-R_\alpha}^{x+R_\alpha} dx' \rho_\alpha(x'), \quad (28)$$

where $R_\alpha = \sigma_\alpha/2$ is the particle "radius" of species $\alpha=0, 1$, and the upper index $\nu=0, 1$ of the weighted density is related to its dimension, which is $(\text{length})^{\nu-d}$, where $d=1$ is the space dimension. The prime in (26) denotes differentiation w.r.t. the argument, and $\Phi_{\text{hc}}(\eta)$ is the zero-dimensional free energy of hard core particles,⁽¹⁶⁾ given by

$$\Phi_{\text{hc}}(\eta) = (1 - \eta) \ln(1 - \eta) + \eta. \quad (29)$$

Our (approximate) QA functional has very similar structure.⁽¹²⁾ We start from the generalization of (26) to binary mixtures, which is

$$\mathcal{F}_1^{\text{exc}}[\rho_0, \rho_1] = \int dx \sum_{\alpha=0,1} n_\alpha^{(0)}(x) \Phi_\alpha(n_0^{(1)}(x), n_1^{(1)}(x)), \quad (30)$$

Functional Study of One-Dimensional Hard Core Fluids

1693

where the weighted densities are still given through (27) and (28), and derivatives of the zero-dimensional free energy, Φ , are defined as $\Phi_\alpha(\eta_0, \eta_1) = \partial\Phi(\eta_0, \eta_1)/\partial\eta_\alpha$. The particular form (30) ensures that the exact result for Φ is recovered if the functional is applied to a zero-dimensional density distribution, defined as $\rho_i(x) = \eta_i\delta(x)$ for $i=0, 1$. Hence it can be shown via elementary calculation that $\Phi(\eta_0, \eta_1) = \mathcal{F}_1^{\text{exc}}[\eta_0\delta(x), \eta_1\delta(x)]$. The exact result for $\Phi(\eta_0, \eta_1)$ is obtained by solving the zero-dimensional limit (where all particles present in the system overlap); a detailed calculation can be found in Ref. 12. Such a situation can be enforced by appropriate external potentials $\phi_\alpha^{\text{ext}}(x) = \infty$ if $|x| > L$ and zero otherwise, and represents a “cavity” of size L , where $L \ll \min(\sigma_0, \sigma_1)/2$. Hence any two particles (of species α and γ) present in the system will overlap, i.e. $x < \sigma_{\alpha\gamma}$, where x is the center-center distance between both particles. (As a consequence the density profiles vanish outside the cavity, $\rho_\alpha(|x| > L/2) = 0$.) This constitutes the crucial simplification that allows to calculate the free energy; its excess contribution is independent of L .⁽¹²⁾ In the case of the hard core matrix the result is

$$\Phi(\eta_0, \eta_1) = (1 - \eta_0 - \eta_1) \ln(1 - \eta_0 - \eta_1) + \eta_1 - (1 - \eta_0) \ln(1 - \eta_0). \quad (31)$$

It is interesting to note that in this special case there is a simple relation to the corresponding fully annealed binary hard core mixture: $\Phi(\eta_0, \eta_1) = \Phi_{\text{hc}}(\eta_0 + \eta_1) - \Phi_{\text{hc}}(\eta_0)$. In the case of the ideal matrix the result for the excess free energy is

$$\Phi(\eta_0, \eta_1) = (e^{-\eta_0} - \eta_1) \ln(e^{-\eta_0} - \eta_1) + \eta_1 + \eta_0 e^{-\eta_0}. \quad (32)$$

This does not have a similar relation as above to the corresponding fully annealed binary mixture (the colloid-polymer mixture of Ref. 4). As a further aside, we note that setting $\Phi(\eta_0, \eta_1) = \Phi_{\text{hc}}(\eta_0 + \eta_1)$ in (30) gives the exact excess free energy functional for equilibrium (where both species are annealed) binary hard rods.^(8,9)

The density functional thus defined is exact on the second virial level, which can be seen by Taylor expanding $\Phi(\eta_0, \eta_1)$ in both arguments to second order, and exploiting the property of the weight functions to recover the Mayer bond upon convolution.

3.4. Numerical Procedure

In order to calculate density profiles, the minimization is done with a standard iteration technique. We chose a very fine grid with spacing

1694

Reich and Schmidt

0.0002σ to discretize the space coordinate. The system is assumed to be periodic in x with length 20σ . To generate the matrix configurations $\{x_i\}$, a Monte Carlo scheme is used. We start from an initial configuration where the (matrix) particles have equally-spaced positions. Then particle displacements are performed according to the Metropolis algorithm, i.e. a new position is only accepted if no overlap with any other (matrix) particle or with the wall (introduced below) occurs. 1000 MC moves per particle are performed for equilibration, and 100 MC moves per particle are performed between configurations that are used for data production. For given matrix configuration $\{x_i\}$ the density profile for the adsorbate component, $\rho_1(x, \{x_i\})$, is then obtained from solution of the minimization condition of the equilibrium DFT, (15). Results from 1000 independent matrix realizations for each N_0 in the range $N_1=0-20$ are then used to carry out the average over the disorder and obtain $\rho_1(x)$ via (17).

4. RESULTS

4.1. Bulk

The bulk case constitutes the basis of the subsequent interface study, and is considered for the following three reasons: i) to assess the accuracy of the QA-DFT, ii) to demonstrate the correctness of the matrix-averaging procedure via comparing with an independent elementary calculation, and iii) to study the (exact) partition coefficient, which we find to possess (very unusual) non-monotonic behavior.

The matrix particles are distributed homogeneously on average, and hence are characterized by a one-body density distribution $\rho_0(x)=\eta_0/\sigma_0=\text{const}$. As a consequence, the adsorbate density distribution is on average $\rho_1(x)=\eta_1/\sigma_1=\text{const}$. We imagine the system to be in chemical equilibrium with a reservoir of hard rods of species 1 of packing fraction $\eta_1^r=\rho_1^r\sigma_1$, where ρ_1^r is the number density in the reservoir; there are no quenched matrix particles in the reservoir. The reservoir density sets the chemical potential of 1-particles via the (well-known) hard rod equation of state,

$$\beta\mu_1 = \ln(\eta_1^r \Lambda_1 / \sigma_1) - \ln(1 - \eta_1^r) + \frac{\eta_1^r}{1 - \eta_1^r}. \quad (33)$$

The central quantity that we use to characterize the coupled systems is the partition coefficient $K = \eta_1 / \eta_1^r = \rho_1 / \rho_1^r$, which we will study as a function of the reservoir packing fraction η_1^r .

Functional Study of One-Dimensional Hard Core Fluids

1695

Before applying both DFT methods to this case, we first seek to obtain a benchmark result for $K(\eta_1^r)$ from an independent, elementary calculation; see ref. 27 for more mathematical background and ref. 7 for an alternative application. We start from the probability $W(x)dx$ that the nearest-neighbor distance for 0-particles (measured between their centers) is between x and $x+dx$ (we call this a gap of size x), given by

$$W(x)\sigma_0 = \begin{cases} \frac{\eta_0}{1-\eta_0} \exp\left(\frac{\eta_0}{1-\eta_0}(1-x/\sigma_0)\right) & x > \sigma_0 \\ 0 & \text{otherwise,} \end{cases} \quad (34)$$

from which the average nearest-neighbor distance between matrix particles follows as $\bar{x} = \int dx x W(x) = \sigma_0/\eta_0$, which is an expected result. To derive (34), note that the occurrence of a gap of size x is proportional to the Boltzmann weight of the reversible mechanical work to create it, hence $W(x) \propto \exp(-P_0x)$, where P_0 is the pressure of the bulk (matrix) system, given for one-dimensional hard rods by $\sigma_0\beta P_0 = \eta_0/(1-\eta_0)$. One obtains the precise form of (34) by taking into account the correct normalization, $\int_0^\infty dx W(x) = 1$.

The average number of 1-particles in a gap of (fixed) size x between two 0-particles is $\bar{N}_1(x, \mu_1) = \beta^{-1} \partial \ln \Xi_1 / \partial \mu_1$, where the partition sum of 1-particles in the gap of volume $x - \sigma_0 - \sigma_1$ (being accessible to the centers of 1-particles) is

$$\begin{aligned} \Xi_1(x, \mu_1) &= \int d1 \exp(-\beta(V_{11} - \mu_1 N_1)) \\ &= \sum_{N_1=0}^\infty \frac{\exp(\beta\mu_1 N_1)}{\Lambda_1^{N_1} N_1!} (x - \sigma_0 - N_1\sigma_1)^{N_1}. \end{aligned} \quad (35)$$

The mean number of 1-particles in the gap between two neighboring 0-particles, averaged over all sizes of the gap, is $\bar{N}_1(\mu_1) = \int dx W(x) \bar{N}_1(x, \mu_1)$. Then the average density of 1-particles is $\rho_1 = \bar{N}_1(\mu_1)/\bar{x} = \bar{N}_1(\mu_1)\eta_0/\sigma_0$, from which the partition coefficient results as $K = \rho_1/\rho_1^r = \bar{N}_1\sigma_1/(\bar{x}\eta_1^r)$. Putting things together,

$$K = \frac{\eta_0\sigma_1}{\eta_1^r\sigma_0} \int_0^\infty dx W(x) \frac{\partial \ln \Xi_1(x, \mu_1)}{\partial \beta\mu_1}, \quad (36)$$

where the equation of state in the reservoir of 1-particles, (33), can be used to obtain μ_1 in terms of η_1^r in (36), hence K is solely a function of the packing fractions η_0, η_1^r and of the size ratio σ_1/σ_0 . In general, we solve

(36) numerically; we can, however, obtain analytic results in both (extreme) cases of high and low reservoir density,

$$K(\eta_1^r \rightarrow 0) = (1 - \eta_0) \exp(-s\eta_0/(1 - \eta_0)), \tag{37}$$

$$K(\eta_1^r \rightarrow 1) = \frac{s\eta_0}{\exp(s\eta_0/(1 - \eta_0)) - 1}, \tag{38}$$

where $s = \sigma_1/\sigma_0$. (38) is obtained by noting that for $\mu_1 \rightarrow \infty$ the mean number of 1-particles equals the maximal possible number, i.e. $\bar{N}_1(x, \mu_1 \rightarrow \infty) = \text{floor}((x - \sigma_0)/\sigma_1)$, where $\text{floor}(x)$ gives the next integer smaller than x .

In the case of the of the non-interacting matrix, the equation of state of the 0-particles is that of an ideal gas, $\sigma_0\beta P = \eta_0$. The gap size distribution is

$$W(x) = (\eta_0/\sigma_0) \exp(-\eta_0 x/\sigma_0), \quad x > 0, \tag{39}$$

from which K can be derived following the same steps as above. Again in the two limiting cases of either high or low reservoir packing fraction analytic expression can be obtained for the partition coefficient,

$$K(\eta_1^r \rightarrow 0) = \exp(-(1 + s)\eta_0), \tag{40}$$

$$K(\eta_1^r \rightarrow 1) = \frac{s\eta_0 \exp(-\eta_0)}{\exp(s\eta_0) - 1}. \tag{41}$$

In order to obtain K from the QA DFT, we use the predicted equation of state, which is in the case of the hard core matrix

$$\beta\mu_1 = \ln(\eta_1 \Lambda_1/\sigma_1) - \ln(1 - \eta_0 - \eta_1) + \frac{\eta_1 + s\eta_0}{1 - \eta_0 - \eta_1}, \tag{42}$$

which we set equal to the chemical potential in the reservoir, (33). For small η_1^r this gives the exact result, (37). In the high density limit, however, we do not recover (38), but obtain $K(\eta_1^r \rightarrow 1) = 1 - \eta_0$. Note that the small η_0 -expansion of the exact result, (38), is $K(\eta_1 = 1) = 1 - (1 + s/2)\eta_0 + O(\eta_0^2)$, differing already in linear order. For intermediate values of η_1^r we obtain numerical solutions.

Results for K as a function of reservoir packing fraction, η_1^r , are displayed in Fig.2a for three different matrix packing fractions, $\eta_0 = 0.1, 0.5, 0.7$. For the lowest value considered, $\eta_0 = 0.1$, K slightly increases as a function of η_1^r . Remarkably a maximum is reached at $\eta_1^r \sim$

Functional Study of One-Dimensional Hard Core Fluids

1697

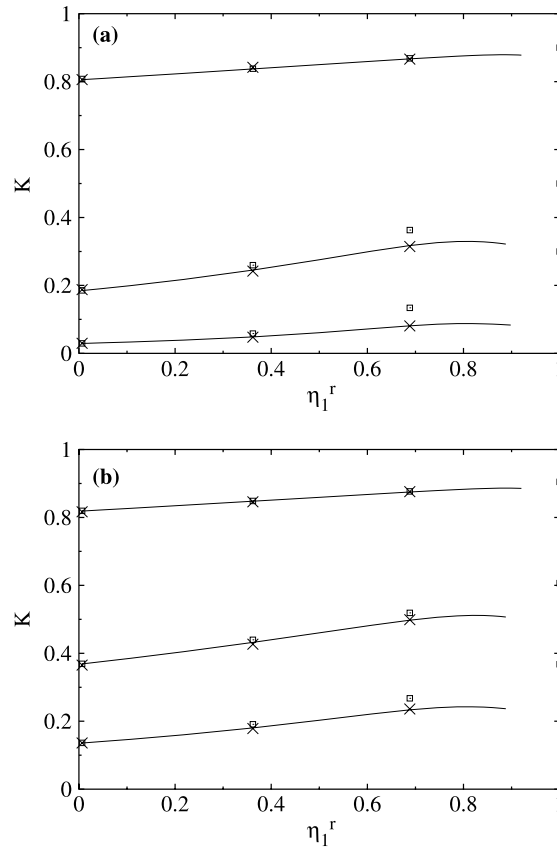


Fig. 2. Partition coefficient $K = \eta_1/\eta_1^r$ for 1d hard rods immersed in a 1d matrix of quenched rods as a function of the packing fraction in a reservoir of rods, η_1^r . Shown are results from the elementary calculation, (36), (lines and full squares), DFT with explicit matrix averaging (crosses) and QA DFT (open squares). a) Matrix particles are interacting with a hard core potential and possess packing fraction $\eta_0 = 0.1, 0.5, 0.7$ (from top to bottom). b) Matrix particles are ideal and possess packing fraction $\eta_0 = 0.1, 0.5, 1$ (from top to bottom).

0.9, significantly smaller than the close-packing limit, $\eta_1^r = 1$. We could not obtain numerical results for $0.9 < \eta_1^r < 1$, but the available data clearly tend towards the limiting value, obtained through (38). For the intermediate value $\eta_0 = 0.5$ the variation of K with η_1^r is stronger and the maximum is more pronounced. For $\eta_1^r = 0.7$ hardly any adsorbate particles can enter the matrix and the resulting values are $K \lesssim 0.1$, the variation with η_1^r being similar to the above cases. The exact results plotted in Fig. 2 are obtained from the elementary calculation above (lines) and from the

1698

Reich and Schmidt

DFT with explicit matrix averaging described in Sec. 3.1. Both agree with high numerical accuracy. The result from the QA DFT is exact in the low-density limit and stays accurate for intermediate η_1^r . At $\eta_1^r \sim 0.7$ deviations emerge, overestimating the values of K . Moreover, the maximum is absent, and monotonic increase with η_1^r is found. We hence conclude that the overall performance of the QA DFT is very satisfactory, but that the intriguing non-monotonic behavior near close-packing is missed.

The situation in the case of the ideal matrix is similar. The equation of state from QA DFT is

$$\beta\mu_1 = \ln(\eta_1 \Lambda_1 / \sigma_1) - \ln(e^{-\eta_0} - \eta_1) + \frac{s\eta_0 e^{-\eta_0} + \eta_1}{e^{-\eta_0} - \eta_1}. \quad (43)$$

Again the result from QA DFT for $\eta_1^r \rightarrow 0$ equals the exact result, (41). In the limit $\eta_1^r \rightarrow 1$ the result from QA DFT is $K(\eta_1^r \rightarrow 1) = \exp(-\eta_0)$, which overestimates the exact expression, (41). See Fig. 2b) for numerical results for K as a function of η_1^r for matrix packing fractions $\eta_0 = 0.1, 0.5, 1$. Compared to the case of the hard core matrix, at equal densities K is larger, clearly due to the more open void structure of the ideal matrix particles. Again K displays a maximum near $\eta_1^r \sim 0.8$, which is not captured within the QA DFT. Nevertheless, the overall agreement is again very reasonable, and gives us confidence to turn to inhomogeneous situations.

4.2. Behavior at the Matrix Surface

We consider matrix distributions that are generated by a hard wall, described by the external potential

$$\phi_0^{\text{ext}}(x) = \begin{cases} 0 & x > 0 \\ \infty & \text{otherwise,} \end{cases} \quad (44)$$

acting before the quench. In order to obtain $\rho_0(x)$, we solve the minimization condition, (24), using Percus' functional, given through (26)–(29), as $\mathcal{F}_0^{\text{exc}}$ in (22). This provides an exact (numerical) solution, see (Fig. 3a) for matrix density profiles for three different matrix packing fractions $\eta_0 = 0.1, 0.5, 0.7$. As η_0 increases the contact value at the wall increases and the layering near the wall becomes more pronounced, i.e. the amplitude of the density oscillations grows.

The density profile of the adsorbate being exposed to such an inhomogeneous matrix (note that the hard wall, (44), only acts on the matrix particles) are obtained using either the explicit matrix-averaging procedure

Functional Study of One-Dimensional Hard Core Fluids

1699

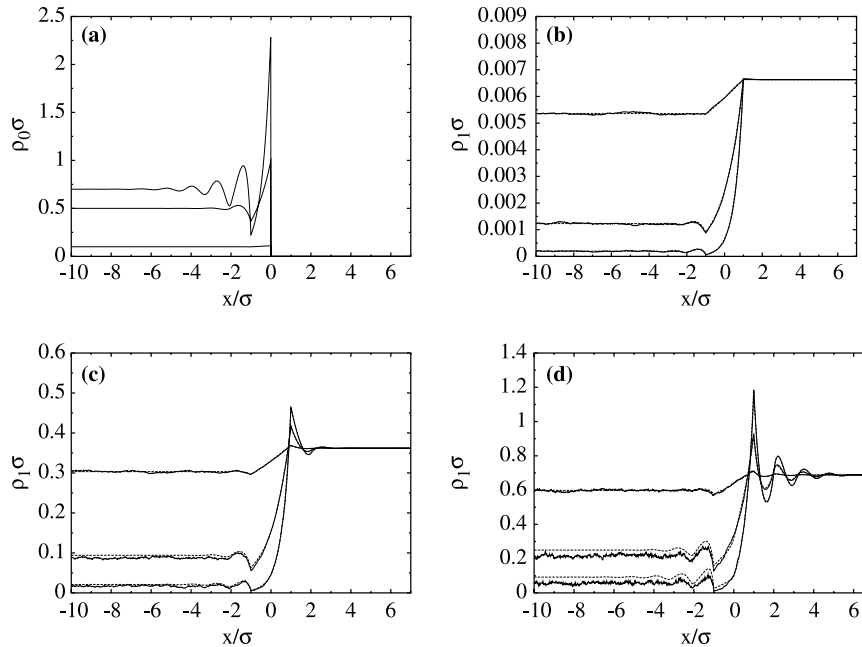


Fig. 3. Behavior of adsorbate particles near the surface of a matrix of quenched rods immersed in a hard core matrix. a) Density profile of the matrix particles, $\sigma\rho_0(x)$, as a function of the scaled distance x/σ for packing fractions $\eta_0=0.1, 0.5, 0.7$ (from bottom to top). Adsorbate density profiles $\sigma\rho_1(x)$ are shown for η_0 (from top to bottom) for $\beta\mu_1=-5$ (b), 0 (c), and 3 (d). Results from the QA DFT (dashed lines) are compared with those of the exact treatment (full lines).

of Sec. 3.1 or the QA DFT of Sec. 3.2. In Fig. 3b-d we display results for $\rho_1(x)$ for $\eta_0=0.1, 0.5, 0.7$. For $x > 0$ far away from the surface, the reservoir value is reached, $\rho_1(x \rightarrow \infty) = \rho_1^r$; for $x < 0$ deep inside the matrix, the asymptotic value is $\rho_1(x \rightarrow -\infty) = K\rho_1^r$, as studied above. For the lowest adsorbate density considered, result for $\beta\mu_1 = -5$ are displayed in Fig. 3, the crossover between the limiting cases happens in a narrow interval $-\sigma < x < \sigma$. Already for $x > \sigma$ the profile is flat. Inside the matrix, however, for $x < \sigma$ there are small oscillations with wavelength of the order of σ that decay rapidly with increasing distance from the surface. These oscillations are not due to the correlations between adsorbate particles, but are merely “imprinted” by the inhomogeneous *matrix* profiles as shown in Fig. 3a. Increasing the adsorbate chemical potential, see Fig. 3c for $\beta\mu_1 = 0$, leads to stronger structuring outside the matrix, $x > \sigma$. This layering is similar to that at a hard wall, but with significantly smaller amplitude. Clearly, this “washing out” is due to the average over the disorder. Note that for a given matrix configuration $\{x_i\}$ the matrix particle closest

1700

Reich and Schmidt

to the surface, say x_{N_0} , exerts a hard interaction on the fluid particles with $X_j > x_{N_0}$, and indeed the resulting $\rho_1(x)$ is that of a hard wall. The disorder-average then leads to the “washing out”. For $\beta\mu_1=3$, shown in Fig. 3d, even stronger layering is observed. As expected from the bulk analysis above, the QA DFT overestimates K and hence the adsorbate density inside the matrix, which is clearly visible for $x < -\sigma$. The shape of the curves, however, is predicted very accurately. Moreover, for $x > -\sigma$, the QA DFT lies practically on top of the exact result.

In the case of the ideal matrix particles exposed to the hard wall, Eq. 44, leads to step function density profiles, see Fig. 4a, hence is very different from highly structured profile of the hard core matrix, Fig. 3. The general trends upon varying the matrix density and the adsorbate chemical potential, see Fig. 4b-d for results for the same values of $\beta\mu_1$ as above, is similar. The ideal matrix allows to consider higher matrix packing fractions, and we have gone up to $\eta_0=1$. It is to be noted that oscillations do appear for $x < \sigma$, although the matrix profile is uniform. These oscillations clearly arise from packing effects between adsorbate particles. Again the results from the QA DFT agree very well with those of the exact calculation.

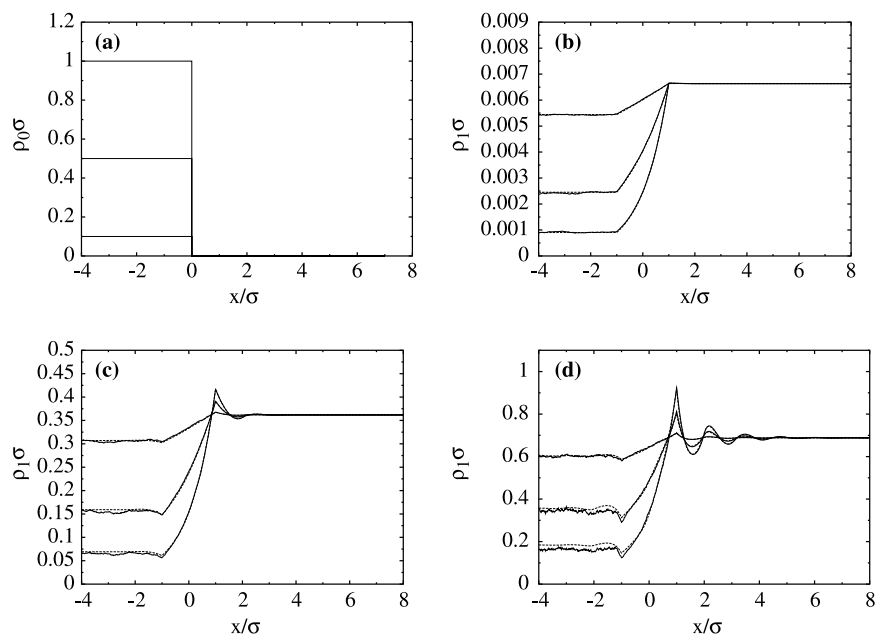


Fig. 4. Same as Fig. 3, but for ideal matrix particles of packing fraction $\eta_0=0.1, 0.5, 1$.

5. CONCLUSIONS

In conclusion we have applied a recent DFT for adsorbate fluids in random matrices to the one-dimensional hard core model. Comparing with analytic and numerical exact solutions in bulk and at matrix interfaces we have tested the accuracy of the QA DFT. The general performance is remarkable, both for the bulk partition coefficient and for the inhomogeneous density profiles. Subtleties like non-monotonic variation of the partition coefficient upon increasing adsorbate density are not captured by the QA DFT.

We note that by confining mesoscopic colloidal particles in narrow channels⁽²⁸⁾ one-dimensional model fluids are experimentally accessible. In principle we could imagine modifying setups of confining grooves as described in ref. 28 in order to prepare model systems that resemble the model described in the current work. Possible future work could be devoted to the impact of quenched disorder on three-dimensional narrow channels.^(29,30) Furthermore, it would be interesting to study the asymptotic decay of correlation functions^(31,32) of fluids with quenched disorder more systematically. Finally, whether non-monotonic variation of the partition coefficient appears in 3d hard core models is an intriguing question.

6. ACKNOWLEDGMENTS

We thank Hartmut Löwen, José A. Cuesta, René van Roij, and Martin-Luc Rosinberg for very useful comments. This research is supported by the SFB TR6 “Physics of colloidal dispersions in external fields” of the DFG. The work of MS is part of the research program of the *Stichting voor Fundamenteel Onderzoek der Materie* (FOM), that is financially supported by the *Nederlandse Organisatie voor Wetenschappelijk Onderzoek* (NWO).

REFERENCES

1. L. Tonks, *Phys. Rev.* **50**:955 (1936).
2. H. N. W. Lekkerkerker and B. Widom, *Physica A* **285**:483 (2000).
3. S. M. Oversteegen and H. N. W. Lekkerkerker, *Physica A* **310**:181 (2002).
4. J. M. Brader and R. Evans, *Physica A* **306**:287 (2002).
5. U. Marini Bettolo Marconi, and P. Tarazona, *J. Chem. Phys.* **110**:8032 (1999).
6. F. Penna and P. Tarazona, *J. Chem. Phys.* **119**:1766 (2003).
7. R. D. Kaminsky and P. A. Monson, *Langmuir* **9**:561 (1993).
8. J. K. Percus, *J. Stat. Phys.* **15**:505 (1976).
9. J. K. Percus, *J. Stat. Phys.* **28**:67 (1982).
10. W. G. Madden and E. D. Glandt, *J. Stat. Phys.* **51**:537 (1988).
11. J. A. Given and G. Stell, *J. Chem. Phys.* **97**:4573 (1992).

1702

Reich and Schmidt

12. M. Schmidt, *Phys. Rev. E* **66**:041108 (2002).
13. R. Evans, *Adv. Phys.* **28**:143 (1979).
14. R. Evans, in *Fundamentals of Inhomogeneous Fluids*, D. Henderson, ed. (Dekker, New York, 1992), Chap. 3, p. 85.
15. Y. Rosenfeld, *Phys. Rev. Lett.* **63**:980 (1989).
16. Y. Rosenfeld, M. Schmidt, H. Löwen, and P. Tarazona, *Phys. Rev. E* **55**:4245 (1997).
17. P. Tarazona and Y. Rosenfeld, *Phys. Rev. E* **55**, R4873 (1997).
18. M. Schmidt, *Phys. Rev. E* **68**:021106 (2003).
19. M. Schmidt and J. M. Brader, *J. Chem. Phys.* **119**:3495 (2003).
20. M. Schmidt, E. Schöll-Paschinger, J. Köfinger, and G. Kahl, *J. Phys. Condens. Matter* **14**:12099 (2002).
21. P. P. F. Wessels, M. Schmidt, and H. Löwen, *Phys. Rev. E* **68**:061404 (2003).
22. E. Kierlik, P. A. Monson, M. L. Rosinberg, L. Sarkisov, and G. Tarjus, *Phys. Rev. Lett.* **87**:055701 (2001).
23. E. Kierlik, P. A. Monson, M. L. Rosinberg, and G. Tarjus, *J. Phys. Condens. Matter* **14**:9295 (2002).
24. L. Lafuente and J. A. Cuesta, *Phys. Rev. Lett.* **89**:145701 (2002).
25. L. Lafuente and J. A. Cuesta, *J. Phys. Condens. Matter* **14**:12079 (2002).
26. M. Schmidt, L. Lafuente, and J. A. Cuesta, *J. Phys. Condens. Matter* **15**:4695 (2003).
27. S. Torquato, B. Lu, and J. Rubinstein, *Phys. Rev. A* **41**:2059 (1990).
28. Q.-H. Wei, C. Bechinger, and P. Leiderer, *Science* **287**:625 (2000).
29. D. Goulding, J. P. Hansen, and S. Melchionna, *Phys. Rev. Lett.* **85**:1132 (2000).
30. D. Goulding, S. Melchionna, and J. P. Hansen, *Phys. Chem. Chem. Phys.* **3**:1644 (2001).
31. R. Evans, J. R. Henderson, D. C. Hoyle, A. O. Parry, and Z. A. Sabeur, *Mol. Phys.* **80**:755 (1993).
32. R. Evans, R. J. F. Leote de Carvalho, J. R. Henderson, and D. C. Hoyle, *J. Chem. Phys.* **100**:591 (1994).

Hard sphere fluids at surfaces of porous media

Matthias Schmidt

Institut für Theoretische Physik II, Heinrich-Heine-Universität Düsseldorf, Universitätsstraße 1, D-40225 Düsseldorf, Germany

(Received 12 December 2002; published 18 August 2003)

An adsorbate fluid of hard spheres is brought into contact with a semi-infinite porous matrix modeled by immobilized configurations of freely overlapping spheres with a sharp kink one-body density distribution. Comparison of results from a recent density-functional approach to those of our computer simulations yields good agreement for the adsorbate density profile across the matrix surface. We show how the matrix can be replaced by a fictitious external potential that only depends on the distance from the interface, and that leads to the same adsorbate density profile. This potential is found to be a smooth function of distance, due to the geometry of the matrix particles. For high matrix densities, the porous medium becomes practically impenetrable, and its surface behaves like a rough hard wall whose roughness decreases with increasing matrix density.

DOI: 10.1103/PhysRevE.68.021106

PACS number(s): 64.10.+h, 61.20.-p, 61.43.-j, 78.55.Mb

I. INTRODUCTION

Fluids in porous media have considerable technical as well as fundamental importance [1]. Such systems are intrinsically inhomogeneous through the presence of a disordered medium that can be regarded as a random external potential acting on the adsorbed fluid. The behavior of such a confined fluid may be drastically different from that of the same substance in bulk [1,2]. As a theoretical model to study such systems, one often relies on so-called quenched-annealed (QA) fluid mixtures, where the immobilized particles of the quenched species constitute the matrix and the particles of the annealed species represent the adsorbate. Various approaches to such systems exist.

Within the framework of a lattice model the important problem of hysteresis in sorption isotherms was recently considered using a mean-field density-functional approach [3,4]. It was found that hysteresis can occur both with and without an underlying equilibrium phase transition. Subsequently, a pronounced change in the desorption behavior was found if a surface of the matrix is explicitly taken into account [5], and hence, direct contact with the gas reservoir is considered.

For continuum fluids similar inhomogeneous situations have been considered using integral equation theory and computer simulations. Dong, Kierlik, and Rosinberg derived the inhomogeneous replica Ornstein-Zernike equations to treat problems such as the adsorption near a plane boundary of a disordered matrix [6]. Pizio and Sokolowski [7] used a similar approach to investigate an annealed fluid in a slitlike pore filled with quenched hard spheres. They found that the matrix lowers the amount of adsorbed fluid at low chemical potentials and that layering occurs for high chemical potentials. Subsequently, Kovalenko *et al.* [8] extended upon this work and compared results from different integral equation closure relations to those from their computer simulations finding good agreement.

For such inhomogeneous situations density-functional theory (DFT) [9] seems to be a natural tool of investigation. Recently, a DFT, based on Rosenfeld's fundamental-measure theory [10], was proposed that is specially tailored for adsor-

bates in porous media [11]. An explicit approximation for mixtures of particles interacting with either hard core or (vanishing) interactions was given. The particular feature of this QA-DFT approach is that the matrix is described on the level of its one-body density distribution and the free-energy functional is directly the (over all matrix realizations) averaged free energy. This offers great advantages: First, one gains immediate access to matrices that are nonuniform *on average*; second, matrices that are uniform (on average) are described particularly simple, namely, by a *constant* one-body density distribution of quenched particles. This is in contrast to (computationally more involved) approaches that treat the matrix as an external potential [12]. However, the practical usefulness clearly depends on the quality of results. In the original work [11], the structural correlations in (on average) homogeneous matrices were considered and compared to computer simulation results. For both hard sphere and freely overlapping sphere matrices, it was found that the pair correlation functions obtained from the theory are in very good agreement with simulation results. The differing matrix-matrix correlations in these models have an effect on the detailed structure of the adsorbate, and the theory was shown to describe either case well. Subsequently, the problem of phase separation in porous media was treated using a simple model for a colloid-polymer mixture [13]. Besides the practical importance of mesoscopic particles in porous media, this is a convenient model as it displays a (colloid) liquid-vapor phase transition. The DFT results were compared with those from an integral-equation approach based on the replica Ornstein-Zernike relations together with the optimized random phase approximation (ORPA) [13]. All major trends found in the ORPA could be reproduced by the DFT. In particular, it was found that by tuning the matrix-adsorbate interactions either capillary condensation or evaporation is induced. Although these results seem promising, so far the theory has not yet been tested in inhomogeneous situations. This is the aim of the present work.

We use freely overlapping spheres to represent a porous medium and prescribe their density distribution to be a step function as a simple model for the surface of a porous medium. A hard sphere fluid is brought into contact with this model solid, and we obtain its density profile both from the DFT and, as a benchmark, from Monte Carlo computer

MATTHIAS SCHMIDT

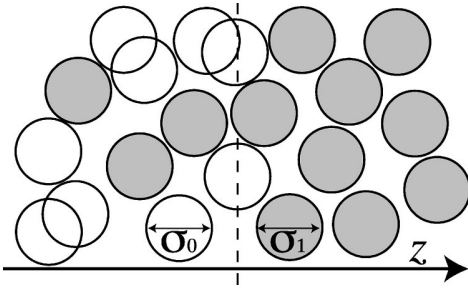
PHYSICAL REVIEW E **68**, 021106 (2003)

FIG. 1. Model of an adsorbate hard sphere fluid of diameter σ_1 (dark circles) inside a matrix of freely overlapping spheres of diameter σ_0 (white circles). There is hard core interaction between adsorbate and matrix particles. The matrix particles are homogeneously distributed in the half space $z < 0$ generating a planar surface of the porous medium perpendicular to the z direction and located at $z = 0$ (dashed line).

simulations. As expected from the above mentioned bulk results, the plateau density inside the matrix is reproduced well by the theory. Moreover, the interfacial structure is also described very satisfactorily, both on the outside and on the inside of the matrix surface. As a further investigation, we replace the matrix by a fictitious external potential that generates the same adsorbate density profile. This can be naturally done in the DFT framework by requiring the corresponding density profiles to be equal and solving the Euler-Lagrange equation for the fictitious external potential. We find that although the matrix density distribution is a step function, the fictitious external potential is a smoothly varying, slightly oscillating function.

The paper is organized as follows. In Sec. II, we define the model of hard spheres in a matrix of freely overlapping spheres more explicitly. In Sec. III, a brief overview of the theory is given. Section IV is devoted to the simulation method. Results are presented in Sec. V and we conclude in Sec. VI.

II. THE MODEL

We consider an annealed adsorbate of hard spheres (species 1) with diameter σ_1 immersed in a matrix of quenched ideal spheres (species 0) of diameter σ_0 . The interaction between matrix particles and adsorbate particles is again that of hard spheres. Explicitly, there are three pair interactions as a function of the center-to-center distance r between two particles given by

$$V_{00}(r) = 0, \quad (1)$$

$$V_{01}(r) = \begin{cases} \infty & \text{if } r < (\sigma_0 + \sigma_1)/2 \\ 0 & \text{otherwise,} \end{cases} \quad (2)$$

$$V_{11}(r) = \begin{cases} \infty & \text{if } r < \sigma_1 \\ 0 & \text{otherwise,} \end{cases} \quad (3)$$

see Fig. 1 for an illustration of the model. In order to achieve an (on average) inhomogeneous matrix, we consider an external potential acting on the matrix particles given by

$$V_0^{\text{ext}}(z) = \begin{cases} \infty, & z > 0 \\ 0 & \text{otherwise,} \end{cases} \quad (4)$$

where z is the space coordinate perpendicular to the matrix surface. As the matrix alone is a (quenched) ideal gas [Eq. (1)], its density distribution under the influence of Eq. (4) is simply a step function

$$\rho_0(z) = \rho_0^{\text{in}} \Theta(-z), \quad (5)$$

where ρ_0^{in} is the mean density “inside” the matrix and we denote one-body density distribution of species $i=0,1$ by $\rho_i(\mathbf{r})$, where \mathbf{r} is the spatial coordinate.

Packing fractions η_i , $i=0,1$ are used as thermodynamic variables: For the matrix $\eta_0 = \pi \rho_0^{\text{in}} \sigma_0^3 / 6$, where ρ_0^{in} is the number density inside the matrix [see Eq. (5)]. For the adsorbate, we use the overall packing fraction $\eta_1 = \pi \sigma_1^3 N_1 / (6V)$, where N_1 is the number of adsorbate spheres and V is the system volume. In general, the size ratio σ_1 / σ_0 is a further control parameter. We will, however, present results below only for the case of equal sizes, $\sigma_1 = \sigma_0 \equiv \sigma$.

III. THEORY

Let us start with a description of the matrix alone. For general matrix-matrix interactions, the grand potential of the matrix as a functional of its one-body distribution is given as

$$\begin{aligned} \beta \Omega_0[\rho_0] = & \int d\mathbf{r} \rho_0 [\ln\{\rho_0(\mathbf{r}) \Lambda_0^3\} - 1] + \beta F_0^{\text{exc}}[\rho_0] \\ & + \beta \int d\mathbf{r} \rho_0(\mathbf{r}) [V_0^{\text{ext}}(\mathbf{r}) - \mu_0], \end{aligned} \quad (6)$$

where $\beta = 1/(k_B T)$, k_B is the Boltzmann constant, T is the absolute temperature, Λ_i is the thermal wavelength, and μ_i is the chemical potential of species i . The first term on the right-hand side of Eq. (6) is the free energy of an ideal gas; the second term is the excess Helmholtz free energy F^{exc} that is due to interparticle interactions. In the present case of vanishing interactions between matrix particles [Eq. (1)], $F_0^{\text{exc}} = 0$. Once $V_0^{\text{ext}}(\mathbf{r})$ is prescribed, the corresponding density profiles is obtained from minimization of the grand functional

$$\frac{\delta \Omega_0[\rho_0]}{\delta \rho_0(\mathbf{r})} = 0. \quad (7)$$

In the present case [Eq. (4)], this is trivial and leads to the above step function for the matrix profile, Eq. (5).

Following Ref. [11] also, the (over all matrix realizations) averaged grand potential of the QA system is expressed as a functional, dependent on both the density distribution of the annealed component and that of the quenched component. Explicitly,

$$\beta\Omega_1[\rho_0;\rho_1]=\int d\mathbf{r}\rho_1(\mathbf{r})[\ln\{\rho_1(\mathbf{r})\Lambda_1^3\}-1]+\beta F_{\text{exc}}[\rho_0;\rho_1]+ \beta \int d\mathbf{r}\rho_1(\mathbf{r})[V_1^{\text{ext}}(\mathbf{r})-\mu_1]. \quad (8)$$

Again there is a minimization principle, but, in contrast to the case of a fully annealed binary mixture, this applies only to the adsorbate component

$$\left. \frac{\delta\Omega_1[\rho_0;\rho_1]}{\delta\rho_1(\mathbf{r})} \right|_{\rho_0(\mathbf{r})} = 0. \quad (9)$$

The matrix density field $\rho_0(\mathbf{r})$ is treated as a fixed input quantity in Eq. (9). Once the external potential acting on the adsorbate, $V_1^{\text{ext}}(\mathbf{r})$ in Eq. (8), is prescribed, solving Eq. (9) yields the adsorbate one-body density $\rho_1(\mathbf{r})$. This holds for the general case, in the present surface investigation we do not consider such an influence, and hence, restrict ourselves to $V_1^{\text{ext}}(\mathbf{r})=0$.

In general, unknown part in the grand potential, Eq. (8), is the Helmholtz excess free energy functional F_1^{exc} . Here, we rely on the geometrical DFT proposed in Ref. [11]. This is based on both the exact zero-dimensional limit of the QA model under consideration and on Rosenfeld's fundamental measure theory [10]. For technical details, we refer the reader directly to Ref. [11]. To obtain numerical solutions of Eq. (9), we employ a standard iteration procedure [14]. For the special case of constant density fields of both matrix and adsorbate the excess free energy per volume as obtained by applying the density functional to constant density fields is given by

$$\begin{aligned} & \frac{\beta F_{\text{exc}}(\rho_0;\rho_1)}{V} \\ &= \frac{3}{\pi\sigma_1^3} \left\{ \frac{3\eta_1(\eta_0+s)^3}{e^{2\eta_0}(e^{-\eta_0}-\eta_1)^2s^3} \right. \\ & \quad - \frac{3\eta_1\eta_0(\eta_0+s)(-2+2\eta_0+s)}{e^{\eta_0}(e^{-\eta_0}-\eta_1)s^3} \\ & \quad - \left. \frac{\eta_0(2+3(-2+\eta_0)\eta_0)(\eta_0+\ln(e^{-\eta_0}-\eta_1))}{e^{\eta_0}s^3} \right\} \\ & \quad - \eta_1[3+2\ln(e^{-\eta_0}-\eta_1)], \quad (10) \end{aligned}$$

where $s=\sigma_0/\sigma_1$.

In order to understand the inhomogeneities caused by the random matrix better, we find it useful to consider an equilibrium pure system under the influence of a fictitious deterministic (nonrandom) external potential V_1^{fict} that possesses the same symmetry as the one-body matrix density distribution; here, $\rho_0(z)$ and hence, $V_1^{\text{fict}}(z)$. The benefit is that $V_1^{\text{fict}}(z)$ is a much simpler function than the external potential corresponding to a given matrix realization that is fully de-

pendent on \mathbf{r} . To relate $V_1^{\text{fict}}(z)$ to the QA system, we impose that the corresponding adsorbate density profiles, $\rho_1(z)$, are the same. In the case of the QA system, this is the average density profile caused by the random medium. In the fictitious potential description, the density profile is the response of the system to $V_1^{\text{fict}}(z)$. Obtaining $V_1^{\text{fict}}(z)$ from $\rho_1(z)$ is straightforward in the DFT, as within this framework the one-to-one correspondence between the external potential and the one-body density distribution is explicit. In the common case, the external potential is known and one solves for the one-body density. Here, the situation is reversed. The one-body density distribution is known [as an output of treating the matrix on the level of its density field, Eq. (9)], and one seeks to obtain the corresponding (fictitious) external potential. Explicitly, the grand potential and minimization condition for this situation are given (upon replacing species index 0 by 1, and setting $V_0^{\text{ext}}=V_1^{\text{fict}}$) through Eqs. (6) and (7), respectively. Solving for the external potential yields (up to an irrelevant additive constant)

$$\beta V_1^{\text{fict}}(\mathbf{r}) = -\ln[\rho_1(\mathbf{r})\Lambda_1^3] - \frac{\delta\beta F^{\text{exc}}}{\delta\rho_1(\mathbf{r})}, \quad (11)$$

where the second term on the right-hand side is the one-body direct correlation functional, for which we take Rosenfeld's approximation [10].

IV. COMPUTER SIMULATIONS

In order to assess the accuracy of the theoretical results we have carried out canonical Monte Carlo (MC) computer simulations. The matrix was realized by placing N_0 matrix spheres randomly in one-half of the (cubic and periodic) simulation box. Hence, we consider a periodic system such that Eqs. (4) and (5) describing the matrix distribution are valid within the simulation box $-L/2 \leq z < L/2$, where L is the box length. This introduces (as usual) a second matrix surface located at $z=L/2$ (and identified with $z=-L/2$). Strictly speaking, the simulated system is a periodic succession of slit pores and layers of porous material.

The initial configuration for the adsorbate (species 1) is such that all particles are in the empty (of matrix particles) half space. We allow equilibration for half a million MC steps per adsorbate particle and then perform the same number of steps for data production. For each state point considered, we used 30 matrix realizations to perform the average over the disorder. Particle numbers are fixed to $N_0=N_1=512$ and then the system volume $V=L^3$ is adjusted to obtain the prescribed packing fractions. As an illustration, we display a snapshot of a configuration in Fig. 2.

V. RESULTS

For simplicity, we restrict ourselves to cases $\eta_0=2\eta_1$ and $\sigma_0=\sigma_1$. We consider a range of matrix packing fractions $\eta_0=2\eta_1=0.2, 0.3, 0.4$. To obtain theoretical results at these state points, we adjust μ_1 in Eq. (8) to obtain the prescribed η_1 . In Fig. 3, results for the adsorbate density profiles across

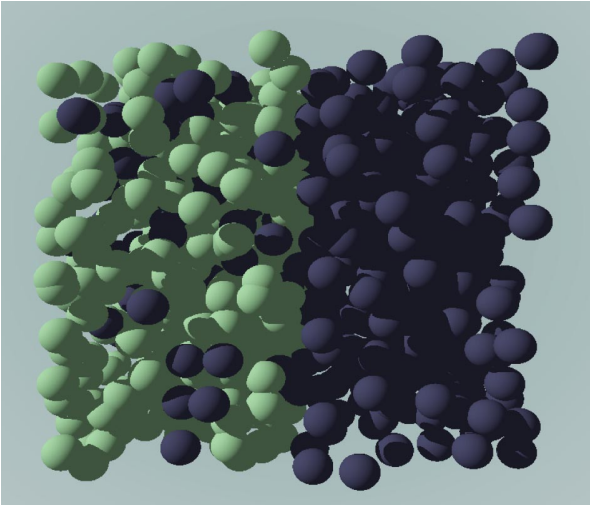


FIG. 2. Snapshot from computer simulation of the hard sphere fluid (dark spheres) adsorbed in a random matrix of freely overlapping spheres (light spheres) of the same size. The matrix particles are distributed homogeneously in the left half of the simulation box and possess packing fraction $\eta_0=0.3$. The overall adsorbate packing fraction is $\eta_1=\eta_0/2=0.15$.

the matrix surface are presented. As mentioned above, we consider a periodic system with periodicity length L . This length is different for the three state points considered, and hence, we display also parts of the periodic images in Fig. 3. These serve also as a guide to assess the actual size of the simulated system.

As the overall packing fraction of the adsorbate η_1 is prescribed, the partitioning between adsorbed fluid inside the matrix and bulk fluid outside the matrix is an output both of the computer simulation and of the theory. For the lowest packing fraction considered, $\eta_0=2\eta_1=0.2$, there is almost

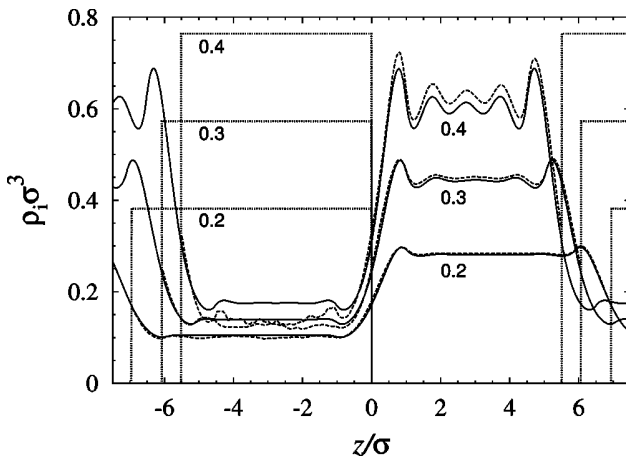


FIG. 3. Density profiles $\rho_1(z)\sigma^3$ of hard spheres at the surface of a porous medium as a function of the (scaled) coordinate z/σ perpendicular to the matrix surface. The matrix density distribution $\rho_0(z)\sigma^3$ is a step function (dotted line) and the system is periodic in the z direction. Results from the DFT (solid lines) and MC simulation (dashed lines) are shown for packing fractions $\eta_0=2\eta_1=0.2, 0.3, 0.4$ (as indicated).

perfect agreement between simulation and theoretical results. Both plateau values, inside and outside the matrix, are reproduced very well. Also the smooth crossover at the interface and the damped oscillations outside are reproduced accurately.

Increasing the packing fraction to $\eta_0=2\eta_1=0.3$, both plateau values also increase, hence, the higher density outside presses more adsorbate particles inside. The general agreement is again quite good, however, there are some differences inside the matrix, where the simulation profile is smaller than the theoretical one and displays irregular oscillations (a precursor of this behavior can be already observed for the above case $\eta_0=2\eta_1=0.2$). This behavior may be partially due to insufficient equilibration of the simulation. As we start from a situation where all adsorbate particles are outside the matrix, the MC dynamics needs to migrate the particles inside the matrix. Using simple single moves as we do, this can be a slow process at high matrix densities. This effect then may lead to a slightly higher density outside the matrix than that in true equilibrium. Moreover, in general, the matrix can have cavities that are kinetically inaccessible by the MC dynamics. As the DF is grand-canonical it will fill such cavities by coupling to the particle reservoir. This constitutes a principle difference between both approaches. For $\eta_0=2\eta_1=0.4$, the discrepancy grows worse, but still the agreement is reasonable. Here, pronounced oscillations develop outside, and the situation is more that of a slit pore than that of decoupled surfaces. Also inside the matrix some layering is predicted by the theory, which can, however, only be guessed from the simulation data.

That the theory works well outside the matrix is to be expected, as our theory reduces in the absence of matrix particles to the very accurate Rosenfeld hard sphere functional. However, in the present case the inhomogeneity is caused by the matrix surface and that this is described so accurately can be rated as a success of the current approach.

We display results for the fictitious external potential in Fig. 4. Normalization is such that $V_1^{\text{fict}}(z)=0$ outside the matrix (i.e., $z=3\sigma$). The plateau value inside the matrix (i.e., $z=-3\sigma$), when reinterpreted in the binary QA system, is the chemical potential change required to move a particle from outside to inside. In the binary model, this is solely due to a reduction of entropy for the particle in the confining matrix. In contrast to the sharp kink matrix density profile $V_1^{\text{fict}}(z)$ has a smooth, slowly varying shape. Considering the interface located at $z=0$, one observes deviations from the plateau values inside and outside the matrix in the range of about $-\sigma < z < \sigma$, consistent with a geometrical picture of the surface.

As the density is increased not only the vertical scale of $V_1^{\text{fict}}(z)$ changes, but also its shape. To demonstrate this, we show in Fig. 4 the result for $\eta_0=2\eta_1=0.2$, but multiplied by a factor of 2.78 to get agreement of the potential strength inside the matrix for the case $\eta_0=2\eta_1=0.4$. It can be clearly seen that the actual $V_1^{\text{fict}}(z)$ is a steeper function than would be expected from the simple rescaling. However, these differences are still small taking into account the considerable change in densities. In principle, this opens possi-

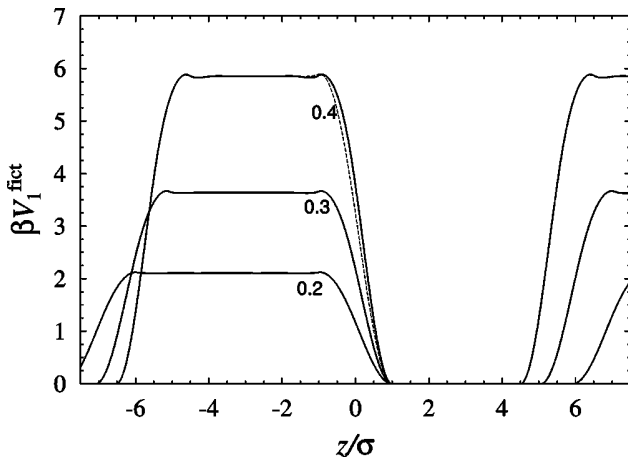


FIG. 4. Fictitious external potentials $\beta V_1^{\text{fict}}(z)$ as a function of the (scaled) coordinate z/σ for the same state points as in Fig. 3. $V_1^{\text{fict}}(z)$ is constructed to generate the same adsorbate density distribution $\rho_1(z)$ as the inhomogeneous porous matrix with density field $\rho_0(z)$ (see Fig. 3). The dashed line is the result for $\eta_0 = 2\eta_1 = 0.2$, but multiplied by a factor of 2.78; compare with the case $\eta_0 = 2\eta_1 = 0.4$.

bilities to a simplified description of such systems.

To conclude this section, we present theoretical results for two further paths along varying density. We will consider a single surface (without periodic images). To control the adsorbate, we prescribe its packing fraction in the half space without matrix, $\eta_1 = (\pi\sigma_1^3/6)\rho_1(z \rightarrow \infty)$. Practically, this acts as an adsorbate reservoir that is in direct contact with the porous medium. As a first case, we fix the matrix density at the highest packing fraction considered above, $\eta_0 = 0.4$, and increase the bulk packing fraction outside over a range $\eta_1 = 0.1, 0.2, 0.3, 0.4$, see Fig. 5 for results. Increasing the density outside increases the plateau density inside the matrix monotonically. For $\eta_1 = 0.1$, the profile is very smooth across the surface. Upon increasing η_1 pronounced oscillations outside develop and also somewhat smaller (in amplitude) oscillations are apparent for $z < 0$. The wavelength is of the order of the particle size, hence, as expected, these oscillations are due to packing effects of the particles. Figure 5 also shows results for the fictitious external potential. It is remarkable that the plateau value inside the matrix increases as a function of the *adsorbate* density. Hence, an adsorbate fluid at a higher density experiences a higher energy penalty, although the matrix density is unchanged.

The second path that we investigate is at constant bulk density outside, $\eta_1 = 0.4$, and increasing $\eta_0 = 0.1, 0.2, 0.4, 0.8, 1.5, 3$, see Fig. 6. For small matrix density, $\eta_0 = 0.1$, the adsorbate density remains almost constant, only a slight decrease is observed for $z < 0$. Increasing η_0 lowers ρ_1 inside the matrix considerably. For $\eta_0 = 1$, it is vanishing on the scale of the plot. Note that as the matrix consists of freely overlapping spheres, $\eta_1 = 1$ does not correspond to space filling, rather there remain occasional free voids inside the matrix. The surface of the matrix at such high densities is hardly penetrable and practically constitutes a rough hard wall with a random surface structure. Increasing further to

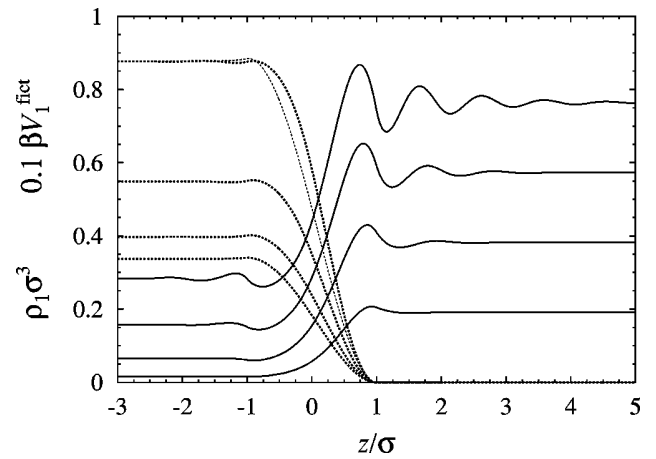


FIG. 5. Adsorbate density profiles $\rho_1(z)\sigma^3$ (solid lines) and fictitious external potentials $\beta V_1^{\text{fict}}(z)$ (dotted lines, scaled by a factor of 0.1) as a function of the distance from the matrix surface z/σ for matrix packing fraction $\eta_0 = 0.4$ and different reservoir adsorbate packing fractions $\eta_1 = 0.1, 0.2, 0.3, 0.4$ (from bottom to top). The matrix particles are homogeneously distributed in the half space $z < 0$. The fictitious external potentials generate the same $\rho_1(z)$ in a pure hard sphere fluid as the porous matrix. The thin dotted line is the fictitious external potential for $\eta_1 = 0.1$, but multiplied by a factor of 2.6; compare with the case $\eta_1 = 0.4$.

$\eta_0 = 3$ leads to more compact roughness. In the limit $\eta_0 \rightarrow \infty$, the matrix becomes a *smooth* hard wall located at $z = \sigma/2$. In Fig. 6, the density profile at a hard smooth wall is shown, and one can verify, from the structure of the DFT, that this is indeed the correct asymptotic behavior. As an illustration, we show in Fig. 7 views in the direction perpendicular towards the matrix surface. The matrices shown in Figs. 7(a,b) possess packing fractions $\eta_0 = 1, 3$, respectively, corresponding to the two densest matrices where results are shown in Fig. 6. It is clear that even in the case $\eta_0 = 3$, there

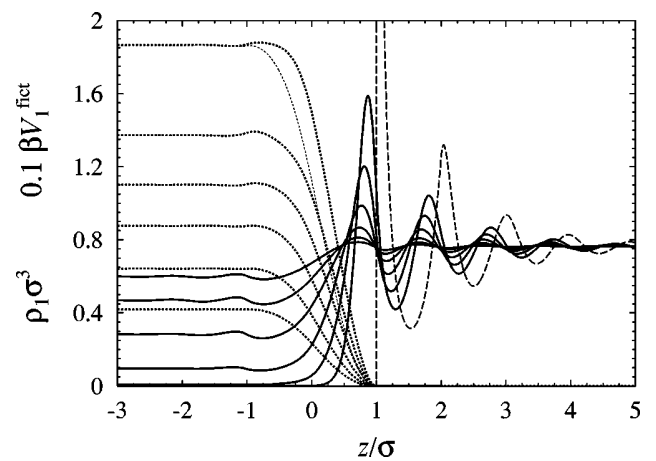


FIG. 6. Same as Fig. 5, but for fixed reservoir packing fraction $\eta_1 = 0.4$ and different matrix packing fractions $\eta_0 = 0.1, 0.2, 0.4, 0.8, 1.5, 3$ (from bottom to top). The dashed line indicates the hard wall result for $\rho_1(z)$; this is approached as $\eta_0 \rightarrow \infty$. The thin dotted line is the fictitious external potential for $\eta_0 = 0.2$, but multiplied by a factor of 2.9; compare with the case $\eta_0 = 3$.

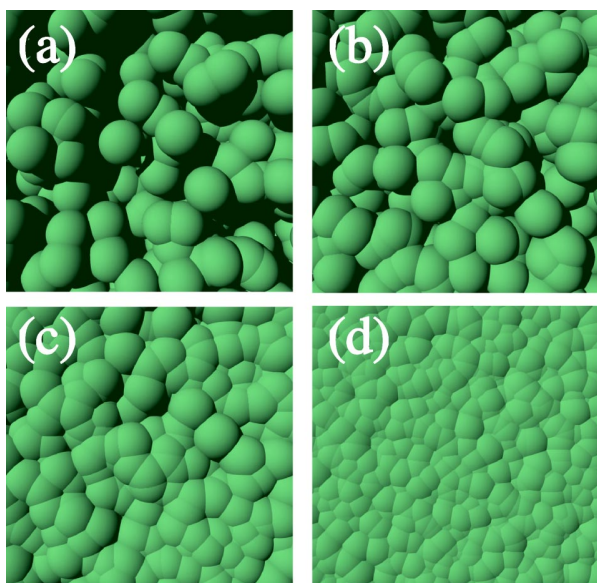


FIG. 7. Surface structure of randomly overlapping spheres with packing fractions $\eta_0=1$ (a), $\eta_0=3$ (b), $\eta_0=10$ (c), $\eta_0=100$ (d).

are considerable voids in the surface. The matrix packing fraction needs to be increased further in order to level out these voids, see Figs. 7(c,d) for $\eta=10,100$, respectively. Even for $\eta_0=100$, there remains residual surface roughness, although clearly the smooth wall is almost obtained.

VI. CONCLUSIONS

In conclusion, we have considered the behavior of an adsorbate hard sphere fluid at the surface of a porous matrix. The matrix is modeled by freely overlapping spheres with a

step function density distribution that models the surface (towards an adsorbate reservoir) of a porous medium. We have applied for the first time a recent DFT approach to such an inhomogeneous situation and have performed computer simulations in order to provide benchmark results. The theoretical results for the adsorbate one-body density distribution across the matrix interface are found to be in good agreement with simulation results up to considerably high matrix packing fractions, i.e., low porosities. The benefit of the theoretical approach is that the required double average over the equilibrated fluid configurations and the quenched disorder is already taken [11]; no subsequent averaging “by hand” is necessary. Within the DFT framework, we relate the QA model to a pure system exposed to a fictitious external potential that only depends on the perpendicular distance from the interface. Although the matrix surface has a sharp kink shape, the fictitious potential is found to be a smooth function that crosses over from its plateau values inside and outside the matrix over about two sphere diameters.

As an outlook to possible future work, we mention the possibility of a further explicit external potential, such as a gravitational field or confinement by walls. Furthermore, as we have shown, the important problem of surface roughness can be treated. Also the behavior for more asymmetric sizes and hence, the effect of size selectivity in porous media is an interesting topic.

ACKNOWLEDGMENTS

Very useful discussions with M.-L. Rosinberg, G. Tarjus, G. Kahl, R. Evans, H. Löwen, and P. Wessels are gratefully acknowledged. A. R. Denton is thanked for providing computer time at NDSU and P. Wessels is thanked for a critical reading of the manuscript. This work was supported by the DFG within the SFB TR6.

-
- [1] L.D. Gelb, K.E. Gubbins, R. Radhakrishnan, and M. Sliwinski-Bartkowiak, Rep. Prog. Phys. **62**, 1573 (1999).
 - [2] R. Evans, J. Phys.: Condens. Matter **2**, 8989 (1990).
 - [3] E. Kierlik, P.A. Monson, M.L. Rosinberg, L. Sarkisov, and G. Tarjus, Phys. Rev. Lett. **87**, 055701 (2001).
 - [4] E. Kierlik, P.A. Monson, M.L. Rosinberg, and G. Tarjus, J. Phys.: Condens. Matter **14**, 9295 (2002).
 - [5] M.L. Rosinberg, E. Kierlik, and G. Tarjus, Europhys. Lett. **62**, 377 (2003).
 - [6] W. Dong, E. Kierlik, and M.L. Rosinberg, Phys. Rev. E **50**, 4750 (1994).
 - [7] O. Pizio and S. Sokolowski, Phys. Rev. E **56**, R63 (1997).
 - [8] A. Kovalenko, S. Sokolowski, D. Henderson, and O. Pizio, Phys. Rev. E **57**, 1824 (1998).
 - [9] R. Evans, in *Fundamentals of Inhomogeneous Fluids*, edited by D. Henderson (Dekker, New York, 1992), p. 85.
 - [10] Y. Rosenfeld, Phys. Rev. Lett. **63**, 980 (1989).
 - [11] M. Schmidt, Phys. Rev. E **66**, 041108 (2002).
 - [12] L.J. Frink, A.G. Salinger, M.P. Sears, J.D. Weinhold, and A.L. Frischknecht, J. Phys.: Condens. Matter **14**, 12 167 (2002).
 - [13] M. Schmidt, E. Schöll-Paschinger, J. Köfinger, and G. Kahl, J. Phys.: Condens. Matter **14**, 12 099 (2002).
 - [14] The tensorial weight functions of Ref. [11] [see also P. Tarazona, Phys. Rev. Lett. **84**, 694 (2000)] are neglected in the numerical treatment. This is a good approximation in the present planar symmetry.

Hard sphere fluids in random fiber networks

Matthias Schmidt^{a)}

Soft Condensed Matter, Debye Institute, Utrecht University, Princetonpln 5, 3584 CC Utrecht, The Netherlands

Joseph M. Brader

Institute of Physiology, University of Bern, Buehlplatz 5, 3012 Bern, Switzerland

(Received 11 March 2003; accepted 12 May 2003)

We investigate an annealed hard sphere fluid in contact with a rigid, random fiber network modeled by quenched, vanishingly thin hard needles. For this model a quenched-annealed density functional theory is presented that treats arbitrary spatially inhomogeneous situations, in particular anisotropic and spatially varying needle distributions. As a test case we consider the structure of the hard sphere fluid at the surface of an isotropic fiber network and find good agreement of the theoretical density profiles with our computer simulation results. For high needle densities the surface acts like a rough impenetrable wall. In the limit of infinite needle density the behavior near a smooth hard wall is recovered. Results for the partition coefficient agree well with existing data. © 2003 American Institute of Physics. [DOI: 10.1063/1.1588993]

I. INTRODUCTION

The properties of fluids adsorbed in porous media can be drastically different from those of the same substance in bulk.¹ Among the wide range of disordered adsorbents one particular class are aggregates of mesoscopic fibers, such as those present in paper and in colloidal suspensions.^{2,3} Due to their geometrical properties the solid volume fraction of fiber networks can be remarkably low. Experimentally, suspensions of rods can be prepared such that the particles are practically immobilized (e.g., by sedimentation or coagulation) producing a random network of fibers. The resulting gels or clusters of colloidal rods or fibers were found to exhibit both homogeneous and heterogeneous (i.e., fractal) structures.⁴ One prominent material where the structure of the rod gel has been investigated is aqueous dispersions of colloidal boehmite.⁵ Other examples of gels of fairly well-defined colloidal rods are iron hydroxide rods, clay particles, and imogolite rods (see Ref. 4). Further very promising particles are etched silicon rods.⁶

Fiber networks provide genuine model porous media that can be used to address various relevant physical questions like the self-diffusion and sedimentation of (tracer) spheres.⁷ Particularly striking is the efficiency of randomly distributed thin rods to cage a test sphere.⁸ Sphere caging is relevant for the random dense sphere packing.⁹ Dense rod packing has been investigated and a random contact equation was found to be relevant,¹⁰ and packings of spherocylinders were simulated recently by mechanical contraction.¹¹ Furthermore, the spatial statistics of pore sizes in stochastic fiber networks was investigated.^{12,13}

Experimental rod aspect ratios (of length-to-thickness) can be as high as 25 for silica coated boehmite rods, and the

rod densities are typically well below the Onsager nematic-isotropic transition.³ Under equilibrium conditions (i.e., such that rods are mobile) also mixtures have been considered, e.g., silica spheres³ were added and also immersed in suspensions of rod-like fd bacteriophage viruses.¹⁴ For a simple theoretical model of hard spheres and vanishingly thin needles the phase behavior was obtained with computer simulations and perturbation theory.¹⁵ Fluids in contact with a single^{16,17} and several strictly aligned¹⁸ rod-like obstacles were treated theoretically finding intriguing adsorption behavior.¹⁸ A molecular model of adsorption in a semiflexible porous network was simulated¹⁹ taking into account structural response of the adsorbent.

The pore size distribution in a random fiber network was derived by Ogston in his classical work²⁰ (see Ref. 21 for brief personal recollections). This solution rules the adsorption probability of an infinitely diluted hard sphere fluid in a bulk fiber network. In the present work we are interested in the adsorption of a dense fluid in a random network of rods. We treat an annealed hard sphere fluid immersed in a quenched network of vanishingly thin hard needles. This model can be viewed as the quenched-annealed (QA) analog of the above equilibrium sphere-needle mixture.¹⁵ In particular we address the question how the geometry of the quenched particles affects the properties of such a network to act as an adsorbent.

We use density-functional theory (DFT),^{22,23} which is a powerful tool to study inhomogeneous fluids. In particular, Rosenfeld's fundamental measure theory (FMT) for hard sphere mixtures²⁴ is known for its high accuracy (for very recent work see, e.g., Refs. 25 and 26). Rosenfeld generalized his approach to nonspherical particles,^{27,28} albeit without incorporating the exact low-density (second virial) limit. Introducing angular convolutions into the theory enabled this exact limit to be recovered in binary mixtures of hard sphere and hard rods with either ideal (vanishing)²⁹ or residual excluded volume interactions (Onsager limit).³⁰ Using this

^{a)}On leave from: Institut für Theoretische Physik II, Heinrich-Heine-Universität Düsseldorf, Universitätsstraße 1, D-40225 Düsseldorf, Germany; Electronic mail: mschmidt@thphy.uni-duesseldorf.de

theory interesting orientational order at the free fluid–fluid interface between demixed phases was found,³⁰ and later supported by computer simulation results.³¹

To investigate the response of fluids to external confinement there are two main theoretical routes: First, one relies on idealized pore geometries, i.e., slit-like, cylindrical, or spherical pores with smooth walls.³² The insights gained here are then related to the behavior in random media by identifying typical pore sizes that are characteristic of the amorphous void structure. An example of this strategy is Fanti and Glandt’s investigation of the partitioning of spherical particles into fibrous matrices¹⁶ where the problem of a single fiber is solved explicitly and then related to a network of fibers via a superposition approximation. The second approach is to model the porous medium by immobilized configurations of model fluids. Then an adsorbate component is equilibrated (i.e., annealed) in the presence of the model porous medium, that acts like an external potential on the adsorbate. One refers to such models as quenched-annealed (QA) mixtures. While the first approach can be viewed as a *raison-d’être* of DFT, the second route was primarily followed by use of integral equation theory and application of the replica trick, e.g., Dong *et al.* derived the inhomogeneous replica Ornstein–Zernike equations to treat problems like the adsorption near a plane boundary of a disordered matrix.³³

For QA mixtures a DFT framework was proposed recently.³⁴ The benefit of this QA DFT is that the disorder is treated on the level of the one-body density distribution of the quenched species, rather than as a complicated external field (like, e.g., in Ref. 18). The one-body density has (in typical situations) a much simpler spatial dependence than the corresponding external potential that is exerted by the matrix particles on the adsorbate. As an illustration we remark that in a (bulk) matrix that is uniform on average over the disorder, the matrix one-body density is just a constant.

In this work we propose a QA DFT for the mixture of annealed spheres and quenched needles and test it against our computer simulation results. As a generic inhomogeneous situation we consider the surface of an isotropic needle network. We bring a dense hard sphere fluid in contact with this surface and investigate the structure that is built up as a response to the quenched needles. Comparing theoretical and simulated results we find that the plateau values away from the matrix surface deviate somewhat, but the detailed oscillatory structure at the interface is captured very well by the DFT. For high needle densities the network becomes practically impenetrable for the spheres, and the surface acts as a rough wall. Within the QA DFT the surface roughness is treated very easily, in particular it is not necessary to treat the lateral structure of the surface explicitly. Hence the computational effort is similar to that for treating a smooth wall. We find that the surface roughness decreases with increasing needle density and effectively a hard smooth wall is obtained in the limit of infinite needle density. Furthermore we check that our results for the partition coefficient compare reasonably to previous Monte Carlo results.¹⁷

The remainder of the paper is organized as follows: In Sec. II we define the model of hard spheres in a random fiber network more explicitly. Section III is devoted to an outline

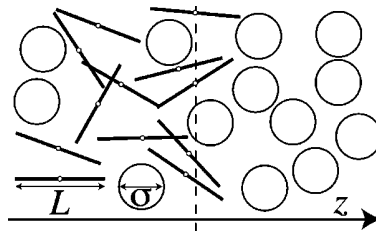


FIG. 1. Model of an adsorbate fluid of hard spheres with diameter σ in a porous matrix of quenched, vanishingly thin hard needles of length L . The needle orientations are assumed to be isotropically distributed and their midpoints to be confined to the halfspace $z < 0$. This generates a semi-infinite porous matrix with surface perpendicular to the z axis and located at $z = 0$; the model considered is three-dimensional.

of the density functional theory. Section IV gives details of the computer simulations. Results are presented in Sec. V and we conclude in Sec. VI.

II. THE MODEL

We consider annealed hard spheres (species S) of diameter σ immersed in a quenched matrix of vanishingly thin needles (species N) of length L . The model is characterized by the (three) pair interactions V_{ij} between species $i, j = S, N$. Due to their vanishing thickness (and hence vanishing pair excluded volume) the needles behave as if being ideal, hence interactions between needles vanish for all separation distances and orientations, $V_{NN} = 0$. The interaction between spheres is $V_{SS}(r) = \infty$ if the separation r between sphere centers is less than σ , and zero otherwise. The pair interaction between a sphere and a needle is $V_{SN} = \infty$, if both overlap, and zero otherwise.

As thermodynamic variables we use the sphere packing fraction $\eta = \pi\sigma^3\rho_S/6$, and a dimensionless needle density $\rho_N\sigma^3$, where $\rho_i, i = S, N$ is the number density of species i . The size ratio L/σ is a further (geometric) control parameter. In general the one-body density distributions will be inhomogeneous. In the case of spheres, dependence is on space point \mathbf{r} , hence $\rho_S(\mathbf{r})$. For needles the dependence is also on orientation $\mathbf{\Omega}$ (a unit vector), hence $\rho(\mathbf{r}, \mathbf{\Omega})$.

As a generic inhomogeneity we will consider the surface of a needle matrix modeled as a step-function density distribution,

$$\rho_N(\mathbf{r}, \mathbf{\Omega}) = \rho_N^{\text{in}} \Theta(-z), \quad (1)$$

where z is the spatial coordinate perpendicular to the matrix surface, ρ_N^{in} is the needle density “inside” the matrix, and we consider the (simplest) case where the needles are isotropically distributed. See Fig. 1 for an illustration of the situation.

III. DENSITY FUNCTIONAL THEORY

We seek a theory to determine the adsorbate (sphere) density distribution $\rho_S(\mathbf{r})$ (as well as associated thermodynamic quantities and correlation functions) for given one-body density distribution of needles, $\rho_N(\mathbf{r}, \mathbf{\Omega})$. As the needles are treated as being ideal, $\rho_N(\mathbf{r}, \mathbf{\Omega})$ can be trivially obtained from a corresponding external potential acting on

needles (before quenching). Within a DFT framework and following Ref. 34 we write the grand potential of the present QA mixture as

$$\begin{aligned} \Omega[\rho_S; \rho_N] = & k_B T \int d\mathbf{r} \rho_S(\mathbf{r}) [\ln(\rho_S(\mathbf{r}) \Lambda_S^3) - 1] \\ & + F_{\text{exc}}[\rho_S(\mathbf{r}); \rho_N(\mathbf{r}, \mathbf{\Omega})] \\ & + \int d\mathbf{r} \rho_S(\mathbf{r}) [V_S^{\text{ext}}(\mathbf{r}) - \mu_S], \end{aligned} \quad (2)$$

where k_B is the Boltzmann constant, T is absolute temperature, Λ_S is the thermal wavelength, μ_S is the chemical potential of spheres, and $V_S^{\text{ext}}(\mathbf{r})$ is a deterministic (nonrandom) external potential acting on the spheres. The first term on the right-hand side of Eq. (2) is the ideal gas free energy functional for spheres; the second term, F_{exc} , is the excess free energy describing the contributions from interparticle interactions. In the present QA case it contains the interactions between adsorbate particles (spheres and spheres), as well as contributions from interactions between adsorbate and matrix particles (spheres and needles).

To obtain the adsorbate density distribution, $\rho_S(\mathbf{r})$, in a given needle matrix, $\rho_N(\mathbf{r}', \mathbf{\Omega})$, the minimization condition is

$$\left. \frac{\delta \Omega}{\delta \rho_S(\mathbf{r})} \right|_{\rho_N(\mathbf{r}', \mathbf{\Omega})} = 0, \quad (3)$$

where $\rho_N(\mathbf{r}', \mathbf{\Omega})$ is treated as a fixed input quantity. Note that, in contrast to the case of an equilibrium (fully annealed) binary mixture, the minimization is to be performed only with respect to the annealed component.

In order to obtain a working theory an approximation for the unknown quantity in Eq. (2), the Helmholtz excess free energy functional F_{exc} , is required. Recently, this was accomplished for spherical particles in a geometrical framework. This provides a means to generate a three-dimensional excess free energy functional from an idealized strongly confined situation, the zero-dimensional (0D) limit. The 0D limit can be envisaged as a cavity situation that leads to strongly localized particle positions. The simplification that is due to the localization enables one to solve the many-body problem exactly and to obtain the corresponding 0D free energy. For the present case, it was shown that for a binary system of hard spheres (one annealed and one quenched species), F_{exc} is (practically) equal to the fully equilibrated case with only annealed species. The only difference is a shift by a trivial constant, $F_{\text{exc}}^{\text{QA}}[\rho_0, \rho_1] = F_{\text{exc}}^{\text{EQ}}[\rho_0, \rho_1] - F_{\text{exc}}^{\text{EQ}}[\rho_0]$, where the subscript 0 (1) refers to the quenched (annealed) component. Note that the presence of $-F_{\text{exc}}^{\text{EQ}}[\rho_0]$ on the right-hand side is necessary to fulfill $F_{\text{exc}}^{\text{QA}}[\rho_0, \rho_1 \rightarrow 0] = 0$, i.e., the (over disorder averaged) free energy vanishes in the absence of adsorbate particles. However, this does not change the minimization condition, as the functional derivative is only performed with respect to the *annealed* component, cf. Eq. (3).

For the present case of quenched needles and annealed spheres an additional simplification arises, because the needles behave as ideal particles due to their geometry. The excess free energy of an ideal gas of rotators vanishes, hence

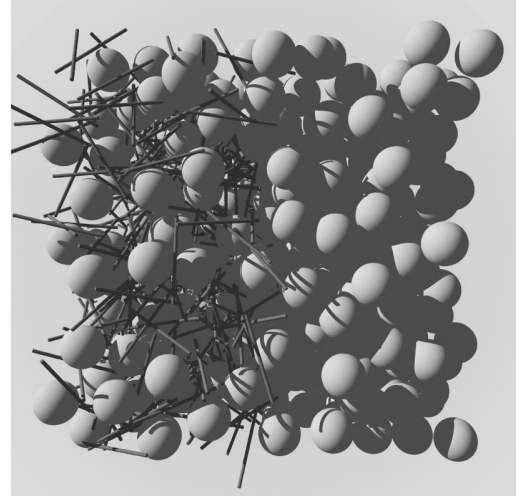


FIG. 2. Snapshot from computer simulation of the adsorbate hard sphere fluid in contact with a random fiber network. The fiber network is modeled as randomly and isotropically distributed vanishingly thin hard needles. Only the left part of the (periodic) simulation box is filled with needles; this acts as a model for the surface of a porous medium. The size ratio of needle length L and sphere diameter σ is $L/\sigma=2$; particle numbers are $M_S=M_N=512$.

we find that the FMT approximation for F_{exc} is *equal* to the excess free energy of the fully annealed sphere-needle mixture given in Ref. 29. The main features of this theory are density-independent, geometrically motivated weight functions that are used to build weighted densities by convolutions with the bare one-body densities. The excess free energy is then obtained as an integral that runs over space and orientation, the integrand being an excess free energy density that is a function of the weighted densities. For explicit expressions we refer the reader directly to the (compact) presentation in Ref. 29; many more technical details and explicit calculations in simple geometries can be found in Ref. 30.

IV. COMPUTER SIMULATIONS

In order to assess the quality of the DFT results we have carried out canonical Monte Carlo (MC) simulations. We used particle numbers $M_S=M_N=128, 512$, and a cubic simulation box with length L and periodic boundary conditions. The size ratio was fixed to $L/\sigma=2$. Needle configurations were generated by randomly and isotropically placing needles in the left ($-L/2 < z < 0$) half of the simulation box. Due to the periodic boundary conditions *two* matrix surfaces are generated. As an illustration we display in Fig. 2 a ray-traced snapshot from the simulation. For the state points considered the two surfaces are not completely decoupled, hence we merely deal with a periodic succession of slabs filled with needles and slabs free of needles. Hence the “free slab” has thickness $L/2$ and the “matrix slab” has also thickness $L/2$. For $M_S=128$ and $\eta=0.15, 0.3$, the box lengths are $L/\sigma=7.64491, 6.06777$, respectively. For $M_S=512$, and $\eta=0.15, 0.3$ the box lengths are $L/\sigma=12.1355, 9.63198$, respectively. As we consider equal numbers of particles, $M_S=M_N$, the relation between densities is ρ_N^{in}

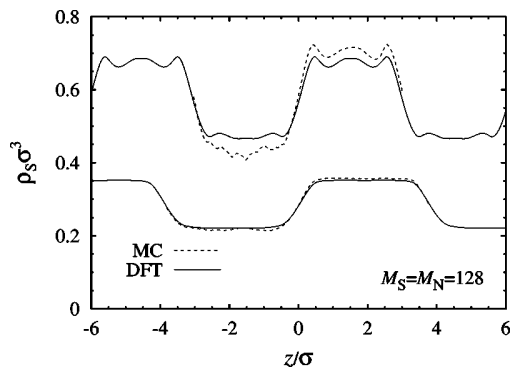


FIG. 3. One-body density distribution of spheres, $\rho_S(z)\sigma^3$, as a function of the (scaled) distance from the matrix surface, z/σ . Results from DFT (solid lines) and MC simulations (dashed lines) are shown for $\eta=0.15, 0.3$ (from bottom to top). The particle numbers in the simulated system are $M_S=M_N=128$.

$= 2\eta_S/(\sigma^3\pi/6)$, where the factor 2 comes from the fact that only one half of the box is occupied by needles; hence $\rho_N\sigma^3=0.572\,958$, and $\rho_N\sigma^3=1.145\,92$.

In the starting configuration all spheres are placed in the half-space $z>0$, then half of the total number of particle moves are discarded for equilibration and subsequently data are collected for the sphere density profile. Typical run lengths are 10^6 MC moves per particle and averages over the disorder are taken by using about 100 matrix realizations. In the case of $\eta=0.3$, $M_S=128$ we performed 10^7 MC moves for 100 independent needle configurations totaling in 10^9 MC moves per particle.

V. RESULTS

To obtain the same situation as in the simulation we imposed the same periodicity L on the DFT profiles. The sphere packing fraction was matched to that in the simulation by adjusting the sphere chemical potential, μ_S in Eq. (2), such that the integrated sphere density corresponds to the simulated packing fraction, i.e., $\eta=(\pi\sigma^3/6)L^{-1}\int_{-L/2}^{L/2}dz\rho_S(z)$, where $\eta=0.15,0.3$.

In Fig. 3 we show results for the smaller system with $M_S=M_N=128$ particles. For $\eta=0.15$ there occurs a smooth crossover from the plateau value inside ($z<0$) to the plateau value outside ($z>0$) the matrix. There is almost perfect agreement between the simulated and the theoretical density profiles. For $\eta=0.3$ there occur oscillations both outside and also inside the matrix, albeit smaller in amplitude inside. The wavelength of oscillations is of the order of σ , hence caused by sphere packing effects. The shape of the theoretical results outside is very similar to the simulation result, however, it is shifted toward lower density. The opposite behavior is found inside the matrix, where the theoretical profile lies above the simulation result. Part of this may be due to still insufficient equilibration in the simulations, despite the considerably large number of MC moves performed.

In Fig. 4 we show results at the same state points, but for a larger system with $M_S=M_N=512$ particles. For $\eta=0.15$ again the agreement between simulation and theory is very good. For $\eta=0.3$ there is an increased number of layers

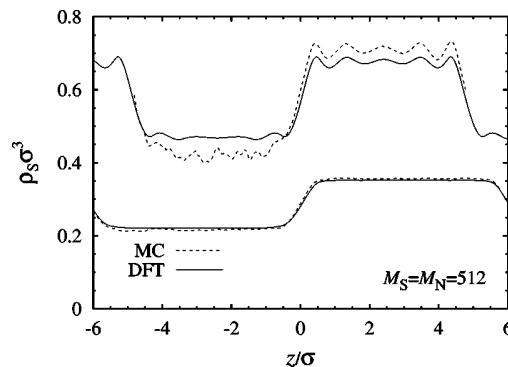


FIG. 4. Same as Fig. 3, but for larger systems with $M_S=M_N=512$ particles.

outside. The theory predicts weak oscillations inside the matrix, those cannot be identified from the simulation profiles—the statistical uncertainties being too large.

Having gained confidence in the theory, we consider a single surface of the fiber network, hence consider the case where the needles are distributed homogeneously and isotropically in the halfspace $z<0$. We bring this surface into contact with a hard sphere fluid of bulk packing fraction $\eta=0.4$ at $z\rightarrow\infty$. The size ratio is, as before, fixed to $L/\sigma=2$. For needle density $\rho_N\sigma^3=10$ practically no spheres can enter inside the matrix, and $\rho_S(z<0)$ vanishes on the scale of the plot, Fig. 5. The behavior of $\rho_S(z)$ near the surface, $0<z<\sigma/2$, is reminiscent of that of the hard sphere fluid at a soft repulsive wall. For larger z typical oscillations that decay with z are observed. Those possess a small amplitude, given the relatively high sphere packing fraction. Increasing the needle density (results for $\rho_N\sigma^3=100, 1000, 10\,000$ are shown in Fig. 5) gradually shifts $\rho_S(z)$ to larger z and increases the amplitude of the oscillations. These effects can be attributed to the denser, more “hairy” needle structure at the surface. It is evident that in the limit $\rho_N\rightarrow\infty$ the situation of an effective hard wall is encountered. The position of this effective hard wall is such that $\rho_S(z)$ drops to zero at $z=(L+\sigma)/2$ (for the present size ratio $z=1.5\sigma$), which is the limiting distance where spheres touch needles (those with orientation strictly perpendicular to the surface).

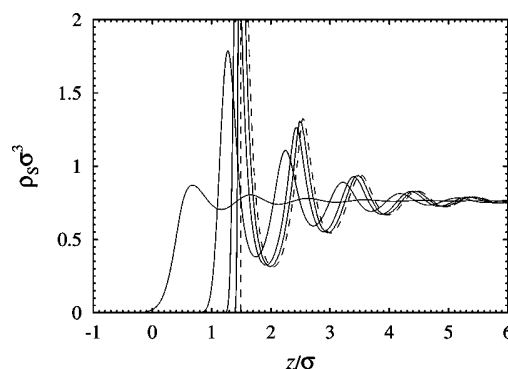


FIG. 5. Theoretical results for the density profiles $\rho_S\sigma^3$ as a function of z/σ from DFT for $\eta=0.4$, $L/\sigma=2$, and $\rho_N\sigma^3=10, 100, 1000, 10\,000$ (from left to right). Also shown is the result at a hard smooth wall (dashed line).

J. Chem. Phys., Vol. 119, No. 6, 8 August 2003

We emphasize that the high needle densities considered here are somewhat artificial and only allowed by the present idealization of vanishing particle thickness. Networks of more realistic fibers with small, but *finite* thickness possess an upper bound in density for random isotropic packings.^{10,11} This upper bound was estimated as $\rho_N L^2 D \pi/4 \approx 5.4$, where D is the rod thickness.¹⁰ In experimental realizations aspect ratios are typically limited¹¹ to $L/D < 100$. If we assume this boundary (and $L/\sigma = 2$) then realistically (about) $\rho_N \sigma^3 < 100$. So the higher densities should be seen merely as an idealized crossover to the smooth hard wall behavior providing a convenient check for the theory.

We finish with a discussion of the adsorption of the hard sphere fluid deep inside the fiber network, i.e., away from the surface. The hard sphere fluid outside the matrix acts as a reservoir, and we denote its packing fraction by η^r . We seek to obtain the corresponding equilibrium sphere packing fraction η inside the matrix. Applying the DFT to constant density fields we find that the free energy per system volume is

$$\beta\Phi = \rho_S(\ln(\rho_S \Lambda_S^3) - 1) + \beta\Phi_{\text{HS}}(\eta) + \rho_N \left(-\ln(1-\eta) + \frac{3L\eta}{2\sigma(1-\eta)} \right), \quad (4)$$

where $\beta = 1/k_B T$, and Φ_{HS} is the excess free energy density in the Percus–Yevick compressibility (and scaled-particle theory) approximation, given by

$$\beta\Phi_{\text{HS}} = \frac{9\eta^2(2-\eta)}{\pi\sigma^3(1-\eta)^2} - \frac{6\eta}{\pi\sigma^3} \ln(1-\eta). \quad (5)$$

Then the sphere chemical potential is obtained by $\mu_S = \partial\Phi/\partial\rho_S$. Clearly, the situation is determined by chemical equilibrium of spheres outside and inside the matrix, hence we solve $\mu_S(\eta, \rho_N) = \mu_S(\eta^r, \rho_N = 0)$ for η once η^r and ρ_N are prescribed. This is an easy numerical task. Before presenting results for high packing fractions we investigate the behavior for $\eta \rightarrow 0$. It is straightforward to show that the leading order in this limit is $\beta\mu_S = \ln(\rho_S \Lambda_S^3) + \pi\rho_N \sigma^3 (2 + 3L/\sigma)/12$. This is equivalent to Ogston's exact result,²⁰ i.e., the free volume fraction of a sphere in the needle matrix is obtained as the ratio of fugacities $\rho_S \Lambda_S^3 / \exp(\beta\mu_S) = \exp(\rho_N \mathcal{E}_{SN})$, where \mathcal{E}_{SN} is the pair-excluded volume between sphere and needle, given as $\mathcal{E}_{SN} = \pi\sigma^3/6 + \pi L\sigma^2/4$. (In Ref. 20 the derivative with respect to σ is given.) We next turn to the case of a dense adsorbate.

A common measure is the partition coefficient, that is defined as the ratio of adsorbed density and that in bulk, $K = \eta/\eta^r$. We first consider the case of infinitely long needles, $L/\sigma \rightarrow 0$, where benchmark results exist in the literature.^{16,17} In Fig. 6 we plot K as a function of η^r for scaled needle densities $\rho_N L \sigma^2 = 0.1, 0.5, 1, 2, 3$. For all densities considered K is a monotonically increasing function of η^r , hence the partitioning decreases (i.e., the densities in the network and in bulk become more similar) with increasing adsorbate density. Clearly the partitioning increases for denser matrices, i.e., with increasing $\rho_N \sigma^3$. Also shown in Fig. 6 are the MC simulation results of Fanti and Glandt.¹⁶ Reasonable agreement with the current theoretical curves can be observed. Deviations exist for high η^r , where the theoretical

Hard sphere fluids in random fiber networks 3499

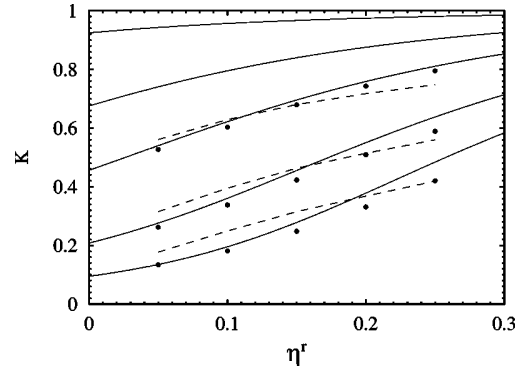


FIG. 6. Partition coefficient $K = \eta/\eta^r$ of spheres of packing fraction η in the random fiber network in chemical equilibrium with a pure hard sphere reservoir of packing fraction η^r for size ratio $L/\sigma = \infty$ and scaled needle densities $\rho_N \sigma^2 L = 0.1, 0.5, 1, 23$ (from top to bottom). Results from the current theory (solid lines) are compared to MC simulation data of Ref. 17 (symbols) and the single-fiber superposition approximation of Ref. 16 (dashed lines).

curves overestimate the MC results for K . This effect, that the DFT gives slightly too weak partitioning, was also apparent in the plateau values of the inhomogeneous density profiles above. The agreement of our results with the MC data of Ref. 17 and that of the results from single-fiber superposition approximation of Ref. 16 is comparable, although the current approach fares somewhat better in predicting the curvature correctly, especially at high matrix densities.

We return to the case of fibers with finite length and display results in Fig. 7 for K as a function of η^r for size ratio $L/\sigma = 2$ and over a broad range of densities, $\rho_N \sigma^3 = 0.1, 0.2, 0.5, 1, 2, 5, 10$. For high needle densities remarkable crossover behavior is observed. Consider $\rho_N \sigma^3 = 5$, where for small packing fractions ($\eta < 0.1$) practically no spheres will enter, but for $\eta > 0.2$ a pronounced increase with η^r occurs. Using such a porous medium as an efficient filter for the hard sphere fluid would require one to keep the reservoir fraction below this crossover region.

It turns out that a natural measure for the needle density is $\rho_N \mathcal{E}_{SN}$. For the needle densities above corresponding nu-

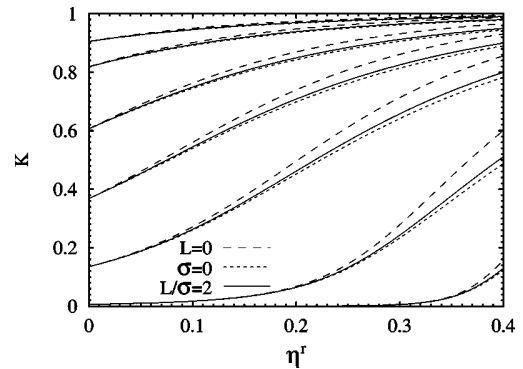


FIG. 7. Same as Fig. 6 but for size ratio $L/\sigma = 2$ and needle densities $\rho_N \sigma^3 = 0.1, 0.2, 0.5, 1, 2, 5, 10$ (solid lines, from top to bottom). For comparison also the corresponding results for $L/\sigma = 0$ and $L/\sigma = \infty$ are shown; densities are such that the needle density times the sphere-needle pair excluded volume, $\rho_N \mathcal{E}_{SN}$, is the same as for the curves for $L/\sigma = 2$.

merical values are $\rho_N \mathcal{E}_{SN} = 0.20944, 0.418879, 1.0472, 2.0944, 4.18879, 10.472, 20.944$. We now change the size ratio L/σ while keeping $\rho_N \mathcal{E}_{SN}$ constant. An almost complete data collapse is obtained, see Fig. 7 for results for the extreme cases $L/\sigma = 0, \infty$. The size ratio $L/\sigma = 0$ corresponds to a matrix of randomly distributed hard point particles. Interestingly, the corresponding adsorption, η , is only slightly larger than that for $L/\sigma = 2$ over the entire η^r range considered. The curves for infinitely long needles, $L/\sigma = \infty$, lie slightly below the corresponding results for $L/\sigma = 2$, but this is also only a small effect. We conclude that the adsorption behavior of the hard sphere fluid inside a random fiber network is ruled by the needle density, ρ_N , scaled with the sphere-needle pair excluded volume, \mathcal{E}_{SN} .

VI. CONCLUSIONS

In conclusion, we have developed and tested a DFT for the hard sphere fluid adsorbed in a quenched matrix of vanishingly thin needles. We find that theoretical density profiles near the surface of a needle matrix agree well with results from our computer simulations. This demonstrates that within the geometrically based DFT different extensions (orientational degrees of freedom^{29,30} and treating quenched-annealed mixtures³⁴) can be systematically combined.

We have dealt with the most simplistic model in the context using randomly placed needles and disregarding their explicit connectivity. In a real fiber network, contacts between neighboring fibers lead to mechanical stability, whereas in the present model, the needles are somewhat artificially frozen in space. Nevertheless, we expect this simple model to capture the main effects. Note that the excluded volume that is not accessible to a test sphere will have a connected pore structure due to overlapping sphere-needle excluded volumes from different needles. Furthermore we have also ignored correlations between rods that stem from finite rod diameter and hence finite rod-rod excluded volume. This is a common assumption. One could however, treat rod-rod interactions on the Onsager (second virial) level using the techniques developed in Ref. 30, i.e., angular convolutions to build weighted densities.

Our theory can treat nonisotropic fiber distributions. By assuming a needle one-body distribution that explicitly depends on orientation one could model, e.g., brush-like structures. Also mixtures of needles with different lengths should be readily accessible. Further very interesting questions concern phase transitions like the demixing phase behavior of a binary fluid confined in random fiber networks. We expect this to be accessible within the current DFT framework (see Ref. 35). Another interesting question concerns the size selectivity that should occur when immersing two (or more) differently sized hard sphere fluids in the random fiber net-

work. This opens further possibilities to study fiber networks acting as mesoscopic filters.

ACKNOWLEDGMENTS

M.S. thanks Albert Philipse, Patrick Johnson, Bob Evans, and Andy Archer for inspiring discussions and acknowledges support from the DFG through the Transregio SFB TR6. The work of M.S. is part of the Research Program of the *Stichting voor Fundamenteel Onderzoek der Materie* (FOM), which is financially supported by the *Nederlandse Organisatie voor Wetenschappelijk Onderzoek* (NWO).

- ¹L. D. Gelb, K. E. Gubbins, R. Radhakrishnan, and M. Sliwinski-Bartkowiak, *Rep. Prog. Phys.* **62**, 1573 (1999).
- ²G. A. Vliegenthart and H. N. W. Lekkerkerker, *J. Chem. Phys.* **111**, 4153 (1999).
- ³G. H. Koenderink, G. A. Vliegenthart, S. G. J. M. Kluijtmans, A. van Blaaderen, A. P. Philipse, and H. N. W. Lekkerkerker, *Langmuir* **15**, 4693 (1999).
- ⁴A. P. Philipse and A. M. Wierenga, *Langmuir* **14**, 49 (1998).
- ⁵A. Wierenga, A. P. Philipse, H. N. W. Lekkerkerker, and D. V. Bogner, *Langmuir* **14**, 55 (1998).
- ⁶P. M. Johnson and C. M. van Kats (private communication).
- ⁷S. G. J. M. Kluijtmans, G. H. Koenderink, and A. P. Philipse, *Phys. Rev. E* **61**, 626 (2000).
- ⁸A. P. Philipse and S. G. J. M. Kluijtmans, *Physica A* **274**, 516 (1999).
- ⁹E. A. J. F. Peters, M. Kollmann, T. A. O. M. Barenbrug, and A. P. Philipse, *Phys. Rev. E* **63**, 021404 (2001).
- ¹⁰A. P. Philipse, *Langmuir* **12**, 1127 (1996), **12**, 5971 (1996).
- ¹¹S. Williams and A. P. Philipse, *Phys. Rev. E* **67**, 051301 (2003).
- ¹²C. T. J. Dodson and W. W. Sampson, *Appl. Math. Lett.* **10**, 87 (1997).
- ¹³C. T. J. Dodson and W. W. Sampson, *J. Stat. Phys.* **96**, 447 (1999).
- ¹⁴K. Lin, J. C. Crocker, A. C. Zeri, and A. G. Yodh, *Phys. Rev. Lett.* **87**, 088301 (2001).
- ¹⁵P. Bolhuis and D. Frenkel, *J. Chem. Phys.* **101**, 9869 (1994).
- ¹⁶L. A. Fanti and E. D. Glandt, *J. Colloid Interface Sci.* **135**, 385 (1990).
- ¹⁷L. A. Fanti and E. D. Glandt, *J. Colloid Interface Sci.* **135**, 397 (1990).
- ¹⁸L. J. Frink, A. G. Salinger, M. P. Sears, J. D. Weinhold, and A. L. Frischknecht, *J. Phys.: Condens. Matter* **14**, 12167 (2002).
- ¹⁹J. Shen and P. A. Monson, *Mol. Phys.* **100**, 2031 (2002).
- ²⁰A. G. Ogston, *Trans. Faraday Soc.* **54**, 1754 (1958).
- ²¹A. G. Ogston, *Biophys. Chem.* **57**, 3 (1995).
- ²²R. Evans, *Adv. Phys.* **28**, 143 (1979).
- ²³R. Evans, in *Fundamentals of Inhomogeneous Fluids*, edited by D. Henderson (Dekker, New York, 1992), p. 85.
- ²⁴Y. Rosenfeld, *Phys. Rev. Lett.* **63**, 980 (1989).
- ²⁵R. Roth, R. Evans, A. Lang, and G. Kahl, *J. Phys.: Condens. Matter* **14**, 12063 (2002).
- ²⁶J. A. Cuesta, Y. Martinez-Raton, and P. Tarazona, *J. Phys.: Condens. Matter* **14**, 11965 (2002).
- ²⁷Y. Rosenfeld, *Phys. Rev. E* **50**, R3318 (1994).
- ²⁸Y. Rosenfeld, *Mol. Phys.* **86**, 637 (1995).
- ²⁹M. Schmidt, *Phys. Rev. E* **63**, 050201(R) (2001).
- ³⁰J. M. Brader, A. Esztermann, and M. Schmidt, *Phys. Rev. E* **66**, 031401 (2002).
- ³¹P. G. Bolhuis (private communication).
- ³²R. Evans, *J. Phys.: Condens. Matter* **2**, 8989 (1990).
- ³³W. Dong, E. Kierlik, and M. L. Rosinberg, *Phys. Rev. E* **50**, 4750 (1994).
- ³⁴M. Schmidt, *Phys. Rev. E* **66**, 041108 (2002).
- ³⁵M. Schmidt, E. Schöll-Paschinger, J. Köfinger, and G. Kahl, *J. Phys.: Condens. Matter* **14**, 12099 (2002).

Model colloid–polymer mixtures in porous matrices: density functional versus integral equations

Matthias Schmidt¹, Elisabeth Schöll-Paschinger², Jürgen Köfinger² and Gerhard Kahl²

¹ Institut für Theoretische Physik II, Heinrich-Heine-Universität Düsseldorf, Universitätsstraße 1, D-40225 Düsseldorf, Germany

² Center for Computational Materials Science and Institut für Theoretische Physik, TU Wien, Wiedner Hauptstraße 8-10, A-1040 Wien, Austria

Received 21 June 2002, in final form 22 August 2002

Published 8 November 2002

Online at stacks.iop.org/JPhysCM/14/12099

Abstract

We test the accuracy of a recently proposed density functional (DF) for a fluid in contact with a porous matrix. The DF was constructed in the spirit of Rosenfeld's fundamental measure concept and was derived for general mixtures of hard core and ideal particles. The required double average over fluid and matrix configurations is performed explicitly. As an application we consider a model mixture where colloids and matrix particles are represented by hard spheres and polymers by ideal spheres. Integrating over the degrees of freedom of the polymers leads to a binary colloid–matrix system with effective Asakura–Oosawa pair potentials, which we treat with an integral-equation theory. We find that partial pair correlation functions from both theories are in good agreement with our computer simulation results, and that the theoretical results for the demixing binodals compare well, provided the polymer-to-colloid size ratio, and hence the effect of many-body interactions neglected in the effective model, is not too large. Consistently, we find that hard (ideal) matrix–polymer interactions induce capillary condensation (evaporation) of the colloidal liquid phase.

1. Introduction

Considerable effort has been dedicated during the past years to developing theoretical tools that allow the determination of the structural and thermodynamic properties of a (continuum) fluid that is in contact with a porous matrix. Such situations are studied using ‘partly quenched’ or ‘quenched–annealed’ (QA) systems. Motivation for these activities can be traced back both to academic as well as to more practical reasons (for an overview see [1]).

- (i) In experimental and theoretical studies it was found that already a minute volume fraction of matrix material can modify the phase behaviour of the fluid substantially; current investigations are dedicated to gaining a deeper insight into this phenomenon.

- (ii) Fluids in contact with a porous matrix are of technological interest, with application in catalysis, gas separation and purification.

From the theoretical point of view one frequently models porous materials by frozen configurations of model fluids. The main problem in the description of such systems lies in the double average required for the calculation of thermodynamic and structural properties: one average is taken over the configurations of the liquid, keeping the matrix particles in fixed positions; the second average is then taken over different matrix configurations. This problem was solved successfully for microscopic approaches that are based on integral-equation and thermodynamic perturbation theories: introducing the replica trick (developed originally for the theory of spin glasses [2]), Given and Stell proposed a method which indeed could cope with this problem [3–5]. This approach has become meanwhile a powerful tool on which many of the present day microscopic approaches in the field are based. The replica trick exploits a mathematical isomorphism between a partly quenched system and a limiting case of a corresponding equilibrium (‘replicated’) system which consists of the now mobile matrix particles and of s non-interacting identical copies of the liquid. The properties of the quenched system are obtained by considering the limit $s \rightarrow 0$ of the properties of the equilibrium system, which, in turn, can be treated by standard liquid state theories. In the replica method, the so-called replica Ornstein–Zernike (ROZ) equations are introduced as the counterpart of the Ornstein–Zernike equations in standard liquid state theory, relating the liquid–liquid, the liquid–matrix and the matrix–matrix correlation functions. Thermodynamic relations for such systems that can be used to determine phase diagrams have been presented by Rosinberg, Stell and co-workers [7, 8].

Another approach that has not been treated yet is to tackle the problem with classical density functional theory (DFT). In particular during the past two or three decades, DFT has become a very powerful and attractive tool to study the structural and thermodynamic properties both of homogeneous and inhomogeneous fluid systems (for an overview see, for instance, [9]). The widespread use of DFT-based methods is to a considerable amount due to the fact that several concepts have been proposed for a constructive determination of a density functional (DF) for a given system. Restricting ourselves in this contribution to (partially penetrable) hard sphere (HS) particles and their mixtures, fundamental measure theory (FMT) is undoubtedly at present *the* approach of choice. The concept of FMT was originally introduced by Rosenfeld [10] and was alternatively formulated [11] and refined [12, 13] in subsequent work; its central idea is that the functional is derived from the geometric measures of the components of the mixture (denoted by the index i), i.e. the volume V_i , the surface S_i and the radius R_i . One of the main improvements with respect to the original idea was to include self-consistency of the functional with respect to the zero-dimensional limit which was lacking in the original FMT-DFT [10]. Nowadays, this consistency is often imposed right from the beginning by starting with the concept of the zero-dimensional limit, where the excess free energy can be calculated exactly. Then, well defined prescriptions allow the generalization to three dimensions. Successful applications of this approach include penetrable spheres that interact with a repulsive step function [14], the Asakura–Oosawa (AO) model [15] discussed below [16], the Widom–Rowlinson mixture, where particles of like species are non-interacting, while particles of unlike species experience HS repulsion [17], and also parallel [18] and rotating [19] non-spherical particles.

Recently, one of us [20] has provided a formalism of how to construct an FMT-based DF for a QA mixture of particles with ideal (vanishing) and HS interactions. Taking properly into account the double average (see above) that is required in the presence of an (ideal or HS) matrix this concept is able to provide functionals for a fluid in contact with a porous matrix.

It was found that the form of the functional is consistent with the special limiting case taken in the replica framework: the functional found for the fluid in contact with a matrix turns out to be the same as that obtained in the $s \rightarrow 0$ limit of the replicated system.

Up to now, only the formalism was presented in [20] and applied to HS mixtures; comparisons with other theories have not been performed yet. This will be done in the present contribution by comparing to results from integral-equation theory. The system we study is a model colloid–polymer mixture in contact with a porous matrix. As in the AO model the colloid particles are described by HS and globular non-adsorbing polymer coils as ideal effective spheres with a hard core cross interaction of range $R_c + R_p$, where R_c and R_p are the radii of the colloids and polymers, respectively. The AO model has been studied extensively in bulk [21–24] and recently also at walls by Brader *et al* [25]. However, confinement induced by complex pore geometries has not been considered yet and is the aim of the present work. We bring the binary AO mixture in contact with a porous matrix that is also represented by HS. Two different cases of polymer–matrix interaction are considered: first we assume HS repulsion between matrix and both colloids and polymers, hence we call this the *cp*-repelling matrix, or for short *cp*-matrix. Introducing the *cp*-matrix is a straightforward extension of the AO model, with *two* HS species where one of them is quenched and constitutes the matrix and the other is annealed and constitutes the mobile colloid component. In the second case, we envisage that due to their flexibility polymers may penetrate a porous medium easier than solid colloidal particles are able to. Hence, within our framework of effective polymer spheres, the matrix–polymer interaction should be weaker than the matrix–colloid interaction. As an extreme case, we assume ideal (vanishing) matrix–polymer interaction. The matrix only repels colloids, hence we use the term *c*-repelling matrix, or for short *c*-matrix. In both cases we deal with a ternary system which we construct following the description given earlier [20].

Starting from a description of the colloid–polymer mixture [15], by integrating out the degrees of freedom of the polymer particles [23], the fully equilibrated system can be mapped onto a one-component fluid of colloids, interacting (under certain conditions) via effective pair potentials, known in the literature as AO potentials [15]. The fluid that is in contact with a matrix becomes a two-component system with effective pair potentials: in both matrices studied here the effective interaction between colloidal particles is an AO potential; in the first case (*cp*-matrix) the colloid and matrix particles interact via an effective AO potential, while in the second case (*c*-matrix) the colloid–matrix interaction is a HS potential. For these binary systems with corresponding effective interactions we have solved the ROZ equations along with the optimized random phase approximation (ORPA) [27] as closure relation.

We have compared data for the structure functions and the phase diagram obtained from DFT and from ORPA. We find that both theories give good account of the pair correlation functions, when compared to data from our computer simulations. For moderate polymer-to-colloid size ratio $q = R_p/R_c$, where the ternary mixture can be reasonably well approximated by an effective binary model, we find that fluid–fluid demixing binodals from both theories are in good agreement. The two types of matrix considered have a qualitatively different effect on the phase behaviour. The *cp*-matrix induces capillary condensation, while the *c*-matrix leads to capillary evaporation.

The paper is organized as follows: in section 2 we introduce our model colloid–polymer–matrix mixture. The DF is constructed in section 3, where we also briefly outline the ROZ-based integral-equation approach. In section 4 we present data starting with a comparison of pair distribution functions obtained via DFT, integral-equation theory and computer simulations. We then present comparisons of phase diagrams obtained via DFT and integral-equation theory and study in particular the effects generated by varying the size ratio q . The paper is closed with a discussion and concluding remarks in section 5.

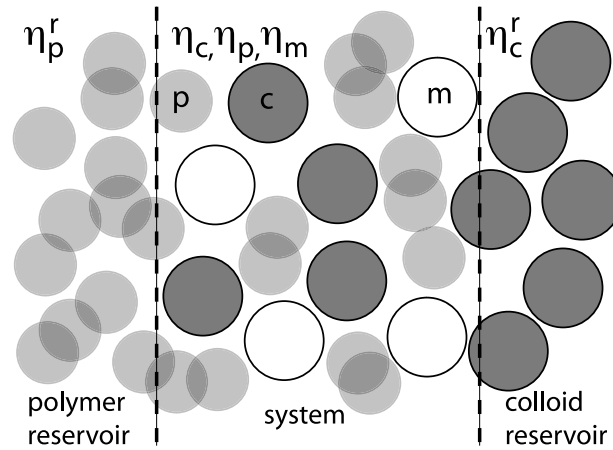


Figure 1. Illustration of the mixture of colloids (dark grey) and polymers (light grey) adsorbed in a HS matrix (white). The system (middle) is coupled to both a reservoir of polymers with packing fraction η_p^r (left), and a reservoir of colloids with packing fraction η_c^r (right). The dashed lines represent semi-permeable walls that can be penetrated solely by the corresponding reservoir species.

2. The model

In our model of a colloid–polymer mixture in contact with a porous matrix we use the following notation: the particles are characterized by radii R_i , where $i = m, c, p$ for matrix, colloid and polymer particles, and we also use the diameters $\sigma_i = 2R_i$. The interactions between the three different species are given via pair potentials $V_{ij}(r)$. In the DFT approach we will consider the full ternary system, while in the integral-equation approach we shall treat binary systems (matrix and colloid particles) with effective pair interactions $V_{ij}^{\text{eff}}(r)$ obtained via integrating out the polymer degrees of freedom and truncating at the two-body level [23]. As bulk thermodynamic parameters we use the packing fractions $\eta_i = 4\pi\sigma_i^3\rho_i/3$, where ρ_i is the number density of species i . We imagine the system being in chemical equilibrium with a reservoir of pure polymers of packing fraction η_p^r , and a reservoir of pure colloids of packing fraction η_c^r , see figure 1 for an illustration. Control parameters are the two size ratios $q = R_p/R_c$ and R_m/R_c .

We shall consider three cases.

- (i) In the equilibrated colloid–polymer mixture, the matrix is absent and the three pair potentials that specify the AO model are given by

$$V_{cc}(r) = \begin{cases} \infty & r \leq \sigma_c \\ 0 & \text{otherwise,} \end{cases} \quad (1)$$

$$V_{pp}(r) = 0, \quad (2)$$

$$V_{cp}(r) = \begin{cases} \infty & r \leq R_c + R_p \\ 0 & \text{otherwise.} \end{cases} \quad (3)$$

Integrating over the degrees of freedom of the polymer particles in the partition function leads to an effective interparticle potential, $V_{cc}^{\text{eff}}(r)$, between the colloid particles, that features an attractive depletion attraction, $V_{\text{AO}}(r)$, known in the literature as the AO potential [15]. The effective interaction in the resulting one-component system of colloids is found to be

$$\begin{aligned} \beta V_{cc}^{\text{eff}}(r) &= \beta V_{cc}(r) + \beta V_{\text{AO}}(r) \\ &= \begin{cases} \infty & r \leq \sigma_c \\ -\eta_p^r \frac{(1+q)^3}{q^3} \left[1 - \frac{3r}{2(1+q)\sigma_c} + \frac{r^3}{2(1+q)^3\sigma_c^3} \right] & \sigma_c < r < \sigma_c + \sigma_p \\ 0 & \sigma_c + \sigma_p < r, \end{cases} \end{aligned} \quad (4)$$

where $\beta = 1/k_B T$, k_B is Boltzmann's constant and T is absolute temperature. It should be pointed out that this mapping is only exact for size ratios $q < 2/\sqrt{3} - 1 \approx 0.1547$. For larger q -values many-body effective potentials are non-vanishing, and using solely the pairwise contribution, equation (4), is an approximation.

- (ii) The colloid–polymer mixture is in contact with an HS matrix that repels both colloids and polymers (cp -matrix). The matrix–matrix interaction is that of HS:

$$V_{mm}(r) = \begin{cases} \infty & r \leq \sigma_m \\ 0 & \text{otherwise.} \end{cases} \quad (5)$$

The interactions between c and p are given in (1)–(3), while the interaction between matrix and both adsorbate components is

$$V_{cm}(r) = \begin{cases} \infty & r \leq R_c + R_m \\ 0 & \text{otherwise,} \end{cases} \quad (6)$$

$$V_{pm}(r) = \begin{cases} \infty & r \leq R_p + R_m \\ 0 & \text{otherwise.} \end{cases} \quad (7)$$

The situation is depicted in the upper panel in figure 2(a). Integration over the degrees of freedom of the polymer particles leads to a binary system (lower panel in figure 2(a)); the effective interactions between colloidal particles and between colloid and matrix particles are $V_{cm}^{\text{eff}}(r) = V_{cc}^{\text{eff}}(r)$ as given in (4) where we have restricted ourselves to $R_c = R_m$ for simplicity.

- (iii) Finally, we consider the colloid–polymer mixture in contact with a colloid-repelling matrix (c -matrix), see figure 2(b). The HS potential between matrix particles is again given via (5), while the interaction between the polymer and the matrix particles is ideal

$$V_{pm}(r) = 0. \quad (8)$$

As the polymers do not interact with the matrix no depletion attraction is generated in the binary cm -mixture and hence $V_{cm}^{\text{eff}}(r) = V_{cm}(r)$ as given in (6). The effective potential between colloid particles remains an AO interaction, $V_{cc}^{\text{eff}}(r)$ given in (4).

3. Theory

3.1. Free energy in the zero-dimensional limit

We first consider an idealized situation, where all particles are forced to sit on top of each other. This zero-dimensional limit can be envisaged as extreme confinement of the system inside a small cavity of particle size. The advantage is that it allows us an exact solution of the many-body problem, as the configurational integral (over all particle coordinates) becomes trivial. What remains to be considered is the statistical problem of counting the allowed particle configurations of the model under consideration. Although the detailed shape of the cavity is irrelevant, for clarity we explicitly choose a spherical pore, such that only space points

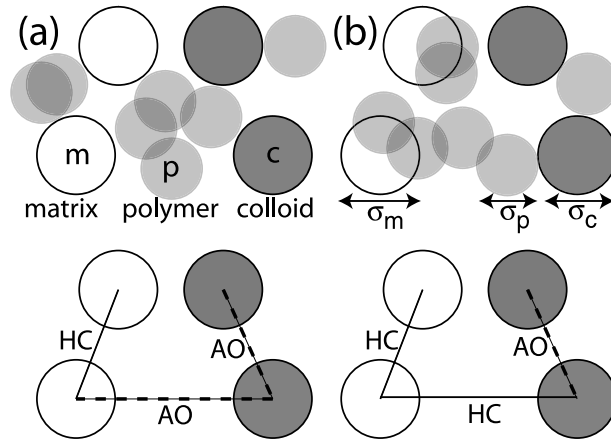


Figure 2. Sketch of the AO model of colloids (dark grey) and polymers (light grey) adsorbed in different HS matrices (white). The upper panels show the ternary mixtures with explicit polymers; the lower panels show the binary mixtures where colloid–colloid effective interactions are given by the AO potential (dashed line). The matrix particles behave as HS (solid line) without depletion attraction because they are quenched before having been brought into contact with polymers. (a) *cp*-matrix: in the ternary system all interactions are hard core except for the ideal polymer–polymer interaction. In the binary model, this leads to an effective AO potential between colloids and matrix particles. (b) *c*-matrix: in the ternary system the interactions between polymers and matrix particles are ideal; in the binary mixture the effective matrix–colloid interaction is hard core.

r with $|r| < \epsilon$ are accessible to the particle centres, and $\epsilon \ll R_i$. This corresponds to a hard spherical pore of (i -dependent) radius $R_i + \epsilon$. Hence each particle's centre is allowed to move inside a sphere of volume $v_{0d} = 4\pi\epsilon^3/3$. In the following we review the zero-dimensional free energy of the AO model without matrix, and calculate this quantity for both ternary mixtures considered in this contribution. We use the symbol A to indicate zero-dimensional Helmholtz free energies, and F for the three-dimensional case.

3.1.1. Equilibrated AO model. For the (fully equilibrated) binary AO mixture it was shown [16] that the zero-dimensional partition sum is given by

$$\Xi = z_c + \exp(z_p), \quad (9)$$

where $z_i = v_{0d}\Lambda_i^{-3} \exp(\beta\mu_i)$ is the scaled fugacity, Λ_i is the (irrelevant) thermal wavelength and μ_i is the chemical potential of species $i = c, p$. The first term on the rhs of equation (9) corresponds to the state where the cavity is occupied by one colloidal particle. All states with more than one colloid are forbidden due to the HS repulsion between colloids, and therefore carry vanishing statistical weight. Hence terms of higher than linear order in z_c are absent in equation (9). The second term on the rhs of equation (9) is simply the partition sum of an ideal gas of polymers, reflecting the absence of interactions between these particles in the AO model.

From the grand potential Ω given through $\beta\Omega = -\ln \Xi$ the mean particle numbers are obtained as $\bar{\eta}_i = -z_i \partial \beta\Omega / \partial z_i$, $i = c, p$. The Helmholtz free energy is $\beta A^{\text{tot}} = \beta\Omega + \sum_{i=c,p} \bar{\eta}_i \ln(z_i)$. The excess (over ideal) part is obtained by subtracting the ideal gas contribution, $\beta A = \beta A^{\text{tot}} - \sum_{i=c,p} \bar{\eta}_i [\ln(\bar{\eta}_i) - 1]$. Explicitly, this leads to the zero-dimensional excess free energy,

$$\beta A(\bar{\eta}_c, \bar{\eta}_p) = (1 - \bar{\eta}_c - \bar{\eta}_p) \ln(1 - \bar{\eta}_c) + \bar{\eta}_c, \quad (10)$$

which was used in [16] as an input to derive a three-dimensional DF for the AO model.

3.1.2. AO model in a colloid- and polymer-repelling matrix. In order to calculate the zero-dimensional excess free energy for the AO model in the presence of the *cp*-matrix, we follow the same steps as above, with the important distinction of using a double QA average instead of a single one for the fully annealed system [20]. We first consider the matrix alone. Either the cavity is empty, or it carries a single matrix particle. Summing up these states in the grand ensemble yields the matrix grand partition sum,

$$\Xi_0 = 1 + z_m, \quad (11)$$

which equals the result for (fully annealed) HS, first considered (via a different route) in [12]. The grand potential is given through $\beta\Omega_0 = -\ln \Xi_0$. The average number of matrix particles is $\bar{\eta}_m = -z_m \partial \beta\Omega_0 / \partial z_m$. We Legendre transform to the Helmholtz free energy, $\beta A_0^{\text{tot}}(\bar{\eta}_0) = \beta\Omega_0 + \bar{\eta}_m \ln(z_m)$. Its excess part is obtained from $\beta A_0 = \beta A_0^{\text{tot}} - \bar{\eta}_m [\ln(\bar{\eta}_m) - 1]$, and is explicitly given by

$$\beta A_0(\bar{\eta}_m) = (1 - \bar{\eta}_m) \ln(1 - \bar{\eta}_m) + \bar{\eta}_m. \quad (12)$$

In order to obtain the QA zero-dimensional free energy of the AO mixture, we need to average the free energy of the adsorbate over all configurations of the matrix. If the matrix is empty, the adsorbate grand partition sum is equal to the case of the fully annealed AO model (given in equation (9)). If the cavity is non-empty, i.e. is occupied by one single matrix particle, the HS potentials between matrix and colloid and between matrix and polymers prohibit the presence of any adsorbate particles, and hence the only allowed state is free of colloids and polymers. Summarizing, the adsorbate grand partition sum is given by

$$\Xi_1 = \begin{cases} z_c + \exp(z_p) & \text{no matrix particle} \\ 1 & \text{otherwise.} \end{cases} \quad (13)$$

The adsorbate free energy is then obtained as the average over all matrix realizations of $-k_B T \ln \Xi_1$, with the appropriate statistical weight according to the matrix partition sum, equation (11); note that Ξ_1 still depends on the matrix configuration. The weight is given by $1/\Xi_0$ for the first, and by z_m/Ξ_0 for the second line in equation (13). Hence the (scaled) zero-dimensional adsorbate grand potential is

$$\beta\Omega_1 = -\frac{\ln(z_c + \exp(z_p))}{1 + z_m}. \quad (14)$$

Albeit a standard Legendre transformation, we again briefly sketch the necessary steps to obtain the corresponding Helmholtz free energy, A_1 . The average particle numbers of adsorbate particles are given as $\bar{\eta}_i = -z_i \partial \beta\Omega_1 / \partial z_i$, $i = c, p$, and the Helmholtz free energy is obtained as $\beta A_1^{\text{tot}} = \beta\Omega_1 + \sum_{i=c,p} \bar{\eta}_i \ln(z_i)$. The excess part is found by subtracting the (adsorbate) ideal gas contribution, $\beta A_1 = \beta A_1^{\text{tot}} - \sum_{i=c,p} \bar{\eta}_i [\ln(\bar{\eta}_i) - 1]$. The final result is

$$\beta A_1(\bar{\eta}_m; \bar{\eta}_c, \bar{\eta}_p) = (1 - \bar{\eta}_m - \bar{\eta}_p - \bar{\eta}_c) \ln(1 - \bar{\eta}_m - \bar{\eta}_c) + \bar{\eta}_c - (1 - \bar{\eta}_m) \ln(1 - \bar{\eta}_m). \quad (15)$$

3.1.3. AO model in a colloid-repelling matrix. In the case of the *c*-matrix, the matrix is a HS fluid that repels only colloids but is penetrable to the polymers. $A_0(\bar{\eta}_m)$ is again given by equation (12). The allowed adsorbate states are the following: if the cavity is empty, the situation is the same as above (first line on the rhs of equation (13)). If the cavity is occupied by a single colloid, however, an arbitrary number of polymers may be present, as the interaction between matrix particles and polymers is ideal. We obtain

$$\Xi_1 = \begin{cases} z_c + \exp(z_p) & \text{no matrix particle} \\ \exp(z_p) & \text{otherwise.} \end{cases} \quad (16)$$

Following the same steps as above yields the Helmholtz excess free energy for the adsorbate,

$$\beta A_1(\bar{\eta}_m; \bar{\eta}_c, \bar{\eta}_p) = (1 - \bar{\eta}_m - \bar{\eta}_c) \ln(1 - \bar{\eta}_m - \bar{\eta}_c) - \bar{\eta}_p \ln(1 - \bar{\eta}_c) + \bar{\eta}_c - (1 - \bar{\eta}_m) \ln(1 - \bar{\eta}_m). \quad (17)$$

3.1.4. Relation to the replica trick. Using the replica trick one starts from a fully equilibrated system, in which the adsorbate species are replicated s times. Particles of different replicas do not interact among each other (their interactions are ideal), but interact with the matrix particles in the same fashion. For such replicated models the above formalism (section 3.1.1) may be applied, and the zero-dimensional excess free energy, A_2 , of the replicated system is obtained. The zero-dimensional QA free energy is the limit $A_1 = \lim_{s \rightarrow 0} [\partial \exp(-A_2)/\partial s] \exp(A_2)$. One can show that for the models considered here $A_2 = A_0(\bar{\eta}_m) + s A_1(\bar{\eta}_m; \bar{\eta}_c, \bar{\eta}_p)$. Hence the free energy obtained from the replica trick is equal to the result from the explicit double average, $A_1 = A_2$.

3.2. Density functional theory

3.2.1. Geometry-based free energy functional. Returning to three dimensions, we apply well tried geometrical recipes to derive approximative DFTs [10, 12–14, 16, 17]. The formalism requires as input the zero-dimensional excess free energy A of the model under consideration and yields as an output (an approximation for) the three-dimensional excess free energy functional, F^{exc} . It can be applied to either the pure matrix, where $A = A_0$, to the adsorbate, $A = A_1$, or even to the replicated system, $A = A_2$. Within the framework, the excess Helmholtz free energy is expressed as

$$F^{\text{exc}}[\{\rho_i(\mathbf{r})\}] = k_B T \int d^3x \Phi(\{n_\alpha^{(i)}(\mathbf{x})\}), \quad (18)$$

where $\{\rho_i(\mathbf{r})\}$ is the set of all density profiles. The reduced free energy density Φ is a function of a set of weighted densities $\{n_\alpha^{(i)}(\mathbf{x})\}$, where i labels the species and α the type of weighted density. The weighted densities are obtained by convolutions of the actual density profiles with weight functions $w_\alpha^{(i)}$, explicitly given as

$$n_\alpha^{(i)}(\mathbf{x}) = \int d^3r \rho_i(\mathbf{r}) w_\alpha^{(i)}(\mathbf{x} - \mathbf{r}). \quad (19)$$

As all non-vanishing interactions are HS interactions, it is sufficient to take the usual fundamental measure weight functions [10, 13], which recover (upon convolution) the Mayer bonds $\exp(-\beta V_{ij}(r)) - 1$. The weight functions are defined as

$$w_3^{(i)}(\mathbf{r}) = \Theta(R_i - r), \quad w_2^{(i)}(\mathbf{r}) = \delta(R_i - r), \quad (20)$$

$$w_{\sqrt{2}}^{(i)}(\mathbf{r}) = w_2^{(i)}(\mathbf{r}) \mathbf{r}/r, \quad \hat{w}_{12}^{(i)}(\mathbf{r}) = w_2^{(i)}(\mathbf{r}) \left[\frac{\mathbf{r}\mathbf{r}}{r^2} - \hat{\mathbf{1}}/3 \right], \quad (21)$$

where $r = |\mathbf{r}|$, $\Theta(r)$ is the Heaviside step function, $\delta(r)$ is the Dirac distribution, $\mathbf{r}\mathbf{r}$ is a dyadic product and $\hat{\mathbf{1}}$ is the rank-two unit tensor. Further, linearly dependent, weights are $w_1^{(i)}(\mathbf{r}) = w_2^{(i)}(\mathbf{r})/(4\pi R_i)$, $w_{v1}^{(i)}(\mathbf{r}) = w_{\sqrt{2}}^{(i)}(\mathbf{r})/(4\pi R_i)$, $w_0^{(i)}(\mathbf{r}) = w_1^{(i)}(\mathbf{r})/R_i$. The weight functions $w_\alpha^{(i)}$ have dimension of length $^{3-\alpha}$. They differ in their tensorial rank: $w_0^{(i)}$, $w_1^{(i)}$, $w_2^{(i)}$, $w_3^{(i)}$ are scalars; $w_{v1}^{(i)}$, $w_{\sqrt{2}}^{(i)}$ are vectors (subscript v); $\hat{w}_{12}^{(i)}$ is a rank-two tensor (subscript t). This formulation is equivalent to the tensorial formalism in [26], see equations (1.16), (1.17) therein. In principle, the rank-three tensorial form introduced in [26] could be used for problems where the dimensional crossover is delicate.

We determine the functional dependence of Φ on the weighted densities by imposing the exact crossover to zero dimensions, where $\rho_i(\mathbf{r}) = \bar{\eta}_i \delta(\mathbf{r})$, and follow recent treatments of FMT [13, 26] by considering multi-cavity limits to obtain $\Phi = \Phi_1 + \Phi_2 + \Phi_3$, with contributions

$$\Phi_1 = n_0^{(i)} \varphi_i(\{n_3^{(l)}\}), \quad (22)$$

$$\Phi_2 = (n_1^{(i)} n_2^{(j)} - \mathbf{n}_{v1}^{(i)} \cdot \mathbf{n}_{v2}^{(j)}) \varphi_{ij}(\{n_3^{(l)}\}), \quad (23)$$

$$\Phi_3 = \frac{1}{8\pi} (n_2^{(i)} n_2^{(j)} n_2^{(k)} / 3 - n_2^{(i)} \mathbf{n}_{v2}^{(j)} \cdot \mathbf{n}_{v2}^{(k)} + \frac{3}{2} [n_{v2}^{(i)} \hat{\mathbf{n}}_{v2}^{(j)} \mathbf{n}_{v2}^{(k)} - \text{tr}(\hat{\mathbf{n}}_{v2}^{(i)} \hat{\mathbf{n}}_{v2}^{(j)} \hat{\mathbf{n}}_{v2}^{(k)})]) \varphi_{ijk}(\{n_3^{(l)}\}), \quad (24)$$

where the repeated-index summation convention is used, derivatives of the zero-dimensional excess free energy are $\varphi_{i\dots k}(\{\bar{\eta}_l\}) \equiv \partial^m \beta A_\tau(\{\bar{\eta}_l\}) / \partial \bar{\eta}_i \dots \partial \bar{\eta}_k$ and tr denotes the trace. For $\tau = 0, 1, 2$, functionals F_τ^{exc} for matrix, adsorbate and replicated system are obtained, respectively. Two routes to the QA free energy functional are possible: either directly through A_1 , giving F_1^{exc} , or via application of the replica trick to F_2^{exc} . The results from the two routes can be shown to be equal, $F_1^{\text{exc}} = F_2^{\text{exc}}$, which is a sign of internal consistency of the current approach.

3.2.2. Minimization principle. For reasons of completeness, we give the general strategy for how to apply the theory to an inhomogeneous problem. One first needs to obtain the matrix density profiles from minimization (with respect to the matrix density field $\rho_m(\mathbf{r})$) of the grand potential functional

$$\begin{aligned} \tilde{\Omega}_0[\rho_m(\mathbf{r})] &= F_0^{\text{exc}}[\rho_m(\mathbf{r})] + k_B T \int d^3r \rho_m(\mathbf{r}) [\ln(\rho_m(\mathbf{r}) \Lambda_m^3) - 1] \\ &\quad + \int d^3r [V_m^{\text{ext}}(\mathbf{r}) - \mu_m] \rho_m(\mathbf{r}), \end{aligned} \quad (25)$$

where V_m^{ext} is an external potential acting on m , generating matrix inhomogeneities. (In our subsequent study, section 4, we only consider matrices that are spatially uniform on average, hence $V_m^{\text{ext}}(\mathbf{r}) = 0$.) At the minimum

$$\frac{\delta \tilde{\Omega}_0}{\delta \rho_m(\mathbf{r})} = 0. \quad (26)$$

Once $\rho_m(\mathbf{r})$ is known, the adsorbate densities are obtained from minimization (only with respect to the adsorbate density distributions $\rho_c(\mathbf{r})$ and $\rho_p(\mathbf{r})$) of the grand potential

$$\begin{aligned} \tilde{\Omega}_1[\rho_m(\mathbf{r}); \rho_c(\mathbf{r}), \rho_p(\mathbf{r})] &= F_1^{\text{exc}}[\rho_m(\mathbf{r}); \rho_c(\mathbf{r}), \rho_p(\mathbf{r})] \\ &\quad + k_B T \int d^3r \sum_{i=c,p} \rho_i(\mathbf{r}) [\ln(\rho_i(\mathbf{r}) \Lambda_i^3) - 1] + \int d^3r \sum_i [V_i^{\text{ext}}(\mathbf{r}) - \mu_i] \rho_i(\mathbf{r}), \end{aligned} \quad (27)$$

where V_i^{ext} act on species $i = c, p$, and $\rho_m(\mathbf{r})$ is treated as a *fixed input quantity*. Again, at the minimum

$$\frac{\delta \tilde{\Omega}_1}{\delta \rho_c(\mathbf{r})} = 0, \quad \frac{\delta \tilde{\Omega}_1}{\delta \rho_p(\mathbf{r})} = 0. \quad (28)$$

3.2.3. Direct correlation functions. From the excess free energy functionals F_0^{exc} and F_1^{exc} given in section 3.2.1 one obtains direct correlation functions $c_{ij}(\mathbf{r})$ by calculating functional

derivatives and setting the density profiles to constant values. Explicitly for matrix and fluid species:

$$c_{mm}(r) = \left. \frac{\partial^2 \beta F_0^{\text{exc}}}{\partial \rho_m(\mathbf{r}) \partial \rho_m(\mathbf{r}')} \right|_{\rho_m = \text{const}}, \quad (29)$$

$$c_{ij}(r) = \left. \frac{\partial^2 \beta F_1^{\text{exc}}}{\partial \rho_i(\mathbf{r}) \partial \rho_j(\mathbf{r}')} \right|_{\rho_i, \rho_j, \rho_m = \text{const}}, \quad ij \neq mm, \quad (30)$$

where $r = |\mathbf{r} - \mathbf{r}'|$. Performing these calculations yields analytical expressions for the $c_{ij}(r)$, which are similar to the bulk AO case discussed in [16]. We will use these results below in our study of the liquid structure.

3.3. Integral-equation approach

Integral-equation approaches to calculate the structural and thermodynamic behaviour of fluids in contact with a porous matrix have been derived in the framework of the replica formalism. As shown by Given and Stell [3–5] one can relate the properties of the QA mixture to those of a fully equilibrated $(s + 1)$ -component mixture: the latter consists of the now mobile matrix particles and of s non-interacting identical copies of the liquid. Using standard liquid state methods [6] for the equilibrated mixture and taking appropriately the limit $s \rightarrow 0$ one obtains expressions that allow the determination of the structural and thermodynamic properties of the QA system.

The structure functions (i.e. total and direct correlation functions $h_{ij}(r)$ and $c_{ij}(r)$ between the different particle species involved) are obtained from a numerical solution of the ROZ equations, the counterpart of the Ornstein–Zernike equations of equilibrium fluids; they read

$$h_{mm}(r) = c_{mm}(r) + \rho_m [c_{mm} \otimes h_{mm}](r), \quad (31)$$

$$h_{mc}(r) = c_{mc}(r) + \rho_0 [c_{mm} \otimes h_{mc}](r) + \rho_c [c_{mc} \otimes h_{cc}](r) - \rho_c [c_{mc} \otimes h_{cc'}](r), \quad (32)$$

$$h_{cc}(r) = c_{cc}(r) + \rho_0 [c_{mc} \otimes h_{mc}](r) + \rho_c [c_{cc} \otimes h_{cc}](r) - \rho_c [c_{cc'} \otimes h_{cc'}](r), \quad (33)$$

$$h_{cc'}(r) = c_{cc'}(r) + \rho_m [c_{mc} \otimes h_{mc}](r) + \rho_c [c_{cc} \otimes h_{cc'}](r) + \rho_c [c_{cc'} \otimes h_{cc}](r) - 2\rho_c [c_{cc'} \otimes h_{cc'}](r), \quad (34)$$

where \otimes denotes convolution, and index c' denotes a colloidal particle from a different replica. Once the correlation functions are known one can calculate the thermodynamic properties. In our case we have solved the ROZ equations along with the ORPA closure relation [27] which allows us to determine explicit expressions for the thermodynamic properties; they are summarized along with the details of the numerical solutions in [28]. Coexistence curves are obtained from solution of the phase coexistence conditions.

4. Results

4.1. Structural correlations

As a first quantitative test of the accuracy of both theoretical approaches, we investigate the partial pair correlation functions $g_{ij}(r) = 1 + h_{ij}(r)$. To provide benchmark results, we have carried out Monte Carlo (MC) computer simulations in the canonical ensemble with 1026 particles. Statistics for the $g_{ij}(r)$ were obtained by averaging over 20 independent matrix realizations obtained from equilibrium MC simulation. For each matrix realization 10^5 MC moves per particle were performed.

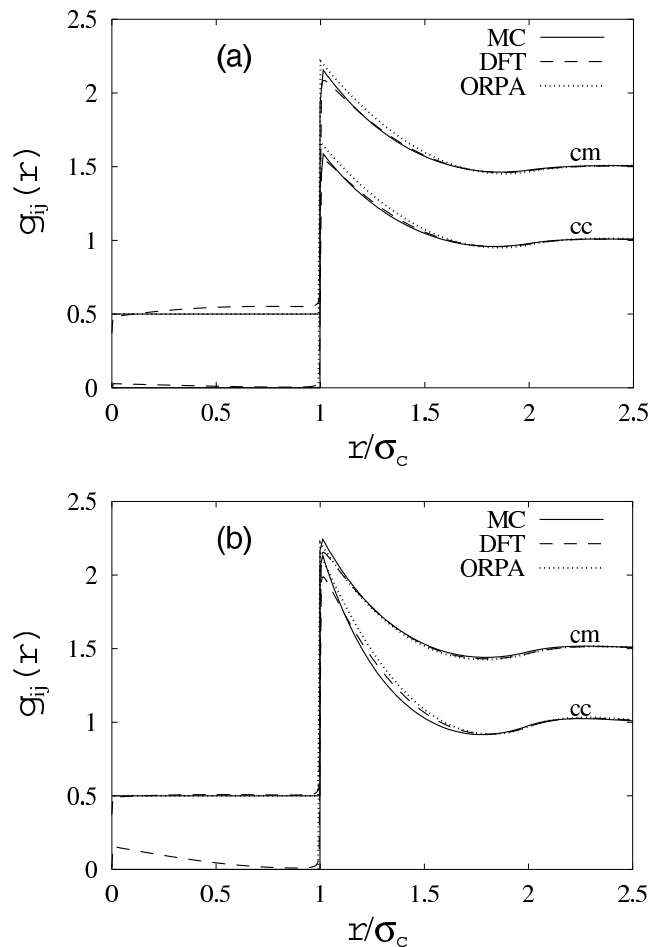


Figure 3. Partial pair correlation functions $g_{cc}(r)$ and $g_{cm}(r)$ for the AO model adsorbed in a HS matrix as a function of r/σ_c for equal sizes $\sigma_m = \sigma_c = \sigma_p$ obtained from DFT, ORPA and MC computer simulations. (a) cp -matrix for $\eta_m = \eta_c = \eta_p = 0.06$. (b) c -matrix for $\eta_m = \eta_c = \eta_p = 0.1$. The cm -curves are shifted upward by 0.5 for clarity.

In order to obtain the $g_{ij}(r)$ from DFT, we use the analytical approximations for the $c_{ij}(r)$ (see section 3.2.3) in conjunction with the ROZ equations (the generalization of equations (31)–(34) to ternary systems [29]). Within our approximate DF, direct correlation functions for particles of different replicas vanish identically, $c_{cc'} = 0$, etc. This ROZ route constitutes a severe test of the DF, as the approximation is performed on the level of F^{exc} and two (functional) derivatives will in general enhance any inaccuracies.

Figure 3 shows the partial pair correlations that concern no polymer species, i.e. $g_{cc}(r)$ and $g_{cm}(r)$, as functions of the scaled distance r/σ_c . We do not display the $g_{mm}(r)$ which are simply the HS pair correlation functions. For simplicity we restrict ourselves to equal sizes ($\sigma_m = \sigma_c = \sigma_p$, i.e. $q = 1$) and consider the two matrices introduced above: in figure 3(a) we show results for the cp -matrix for packing fractions $\eta_m = \eta_c = \eta_p = 0.06$. In figure 3(b) we consider the c -matrix; due to the polymer penetrability we can choose somewhat higher packing fractions, $\eta_m = \eta_c = \eta_p = 0.1$, while still staying away safely from any (demixing)

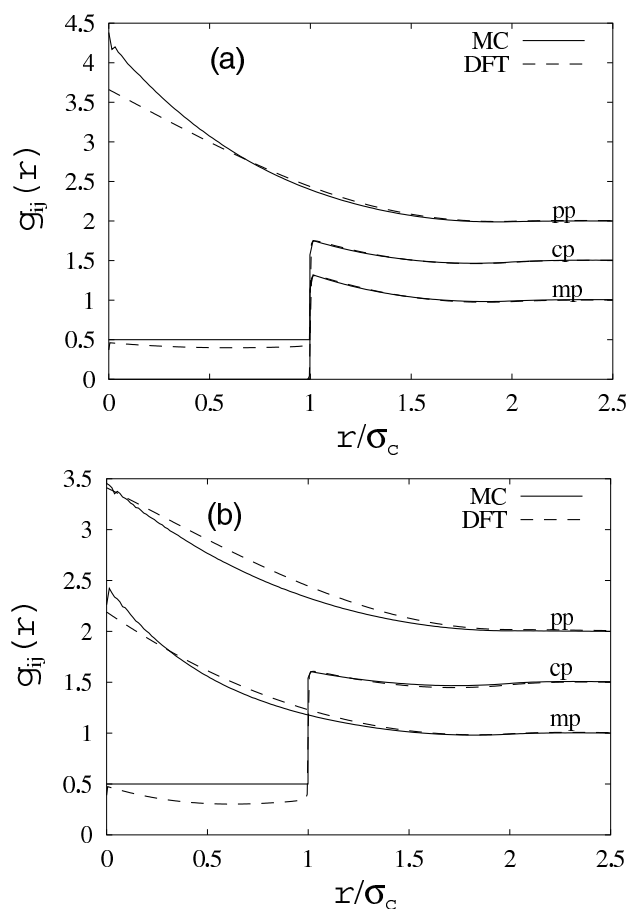


Figure 4. Partial pair correlation functions $g_{ij}(r)$ for the AO model adsorbed in an HS matrix as a function of r/σ_c for equal sizes $\sigma_m = \sigma_c = \sigma_p$ obtained from DFT and MC computer simulations. (a) *cp*-matrix for $\eta_m = \eta_c = \eta_p = 0.06$. (b) *c*-matrix for $\eta_m = \eta_c = \eta_p = 0.1$. The curves are shifted upward by 0.5 for clarity, as labelled.

phase boundary. We emphasize that the matrix packing fractions considered in this part of our study are relatively large compared to experimental studies. The densities we investigate are moderate, i.e. overall densities are $\eta_c + \eta_p + \eta_m = 0.18$ in case of the *cp*-matrix and 0.3 in case of the *c*-matrix. We believe that such densities constitute non-trivial tests of the theories. A stronger test would be provided by approaching the demixing phase boundary by increasing colloid and polymer densities, an issue that we leave for possible future work.

The general agreement of the results from DFT and ORPA with MC data is in both cases very good. The DFT result slightly violates the core conditions, $g_{cc}(r < 2R_c) = 0$ and $g_{cm}(r < R_c + R_m) = 0$. It is even closer to the MC result than the ORPA outside the core. Undoubtedly a certain amount of the differences can be attributed to the fact that the MC and DFT results are obtained for the full ternary system, while ORPA data are calculated for a binary system with effective forces, neglecting three- and higher-body forces for $q > 0.1547$. In particular for the large q -value chosen here ($q = 1$), this truncation has non-negligible effects. Summarizing we can conclude that DFT and ORPA are capable of describing the fluid correlations correctly.

The other pair correlation functions concern correlations with polymer particles, namely, $g_{mp}(r)$, $g_{cp}(r)$ and $g_{pp}(r)$. These functions can be obtained if the full ternary system is treated (as this is the case in the DFT approach); in the ORPA, where we consider only the binary system with effective pair interactions, information about these correlation functions is lost. In figure 4 the DFT results are shown and again compared to MC data. We observe pronounced differences between the results for the cp -matrix and the c -matrix in the behaviour of $g_{mp}(r)$ for $r < R_m + R_p$, demonstrating the tendency for polymers to sit on the top of the matrix particles in the case of the c -matrix. Again agreement between MC and DFT results is satisfactory.

4.2. Fluid demixing

We next investigate the fluid demixing phase diagram of the model colloid–polymer mixture in contact with the matrix. The parameter q plays here an important role. While for $q < 0.1547$ the above mentioned mapping of the ternary system onto a binary system with effective pair potentials is exact, we did not choose q -values that are that small, since only for $q \gtrsim 0.35$ does the fluid–fluid transition become stable with respect to the freezing transition [22, 23]. As a compromise we have therefore chosen as the lowest value $q = 0.3$, and compare how the (possibly metastable) demixing binodals from ORPA and DFT are affected by the presence of the matrix. Here and in the following we have chosen equal sizes for the matrix and the colloid particles, $\sigma_m = \sigma_c$. The matrix packing fraction is $\eta_m = 0.05$; here we know [29] that for matrix packing fractions larger than ~ 0.1 discrepancies between computer simulation data and ORPA results are observed.

We display the binodal in two different representations (see figure 5): first, in the (η_c, η_p^r) -plane (left panels in figure 5), corresponding to the density versus inverse temperature representation for a simple fluid; second, in the (η_c^r, η_p^r) -plane (right panels in figure 5), where η_c^r is the packing fraction of colloids in a reservoir of pure colloids. η_c^r is obtained by equating the colloid chemical potential of the system and of the colloid reservoir (within the DFT the expression for the reservoir chemical potential is identical to the Percus–Yevick compressibility result). As the relation between η_c^r and the colloid chemical potential is monotonic, the second representation corresponds to a chemical potential versus inverse temperature phase diagram. Note that if we consider the binary model with effective pair interactions (as done in the ORPA treatment), we need to take into account the one-body polymer contribution that emerges in the partition sum. This generates an *additive* constant $k_B T \eta_p^r (1 + q)^3 / q^3$ to the colloid chemical potential, which does not affect phase equilibria, but needs to be taken into account when assuming equilibrium with a *pure* system of colloids with fraction η_c^r .

In figure 5 we show the phase diagrams obtained from DFT and ORPA for the bulk (no matrix) colloid–polymer mixture and for the case where this mixture is in contact with the cp -matrix or c -matrix. Comparing the bulk case with the computer simulation results by Bolhuis *et al* [24] for a similar size ratio ($q = 0.34$) we find that the ORPA fares better, indicating that the accuracy of the free volume free energy worsens for strongly asymmetric size ratios. (Note that ORPA results in figure 5(b) are displayed only in a smaller η_p^r -interval, as the solution of the integral equations becomes involved as we proceed to higher polymer densities.) The effect of both matrices is to shift the critical point and hence the binodal toward larger η_p^r , corresponding to the common shift of the critical point to smaller temperatures in simple fluids. In the cp -matrix case, we observe only a rather small effect. This is understandable as matrix and colloid particles interact in a similar way with the polymer particles (HS interactions with polymers in the ternary model, AO attraction in the binary model with effective interactions), and the critical colloid packing fraction is large compared to the η_m . Hence in this case where a small portion of identical particles is quenched the effect of the matrix is only a minor one. For

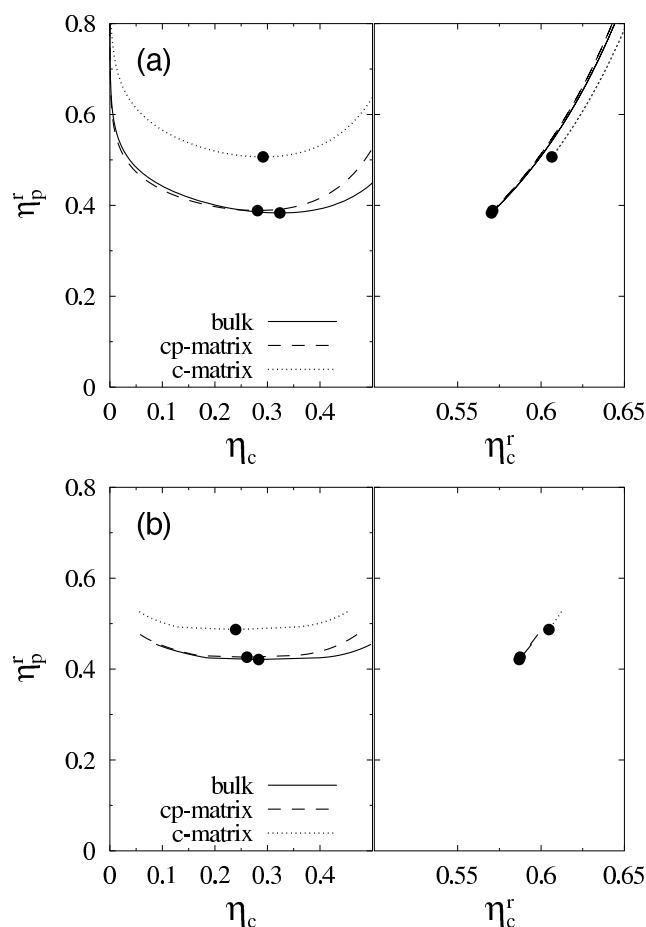


Figure 5. Demixing phase diagram for the model colloid–polymer mixture in contact with different HS matrices as a function of η_c, η_p^r (left panels) and η_c^r, η_p^r (right panels) for $\eta_m = 0.05$ and size ratios $q = 0.3, \sigma_m/\sigma_c = 1$. Tielines between coexisting phases are horizontal in the left panels. (a) DFT result, (b) ORPA result.

the *c*-matrix we observe a considerably larger effect: the presence of matrix particles that can be penetrated by polymers (and which consequently do not feature depletion attraction in the effective system) shifts the critical point and the binodal toward larger η_c^r , reflecting capillary evaporation. The ORPA results in figure 5(b) show the same tendencies for the shift of the critical point as observed in DFT, however the effects are quantitatively smaller.

Increasing the size ratio to $q = 0.6$ we expect the fluid demixing phase transition to be stable with respect to the freezing transition [23]; results for this case are depicted in figure 6. Again comparing the bulk case to the simulations for $q = 0.67$ [24] we find that both theories predict the binodal and the location of the critical point reasonably well. It is manifest that in the case of the *cp*-matrix the critical point and the binodal shift to *smaller* η_c^r , reflecting capillary condensation of the colloidal liquid phase. In contrast, we observe that the *c*-matrix shifts the critical point and the binodal to *larger* η_c^r which is the indication of capillary evaporation of the colloid liquid. The qualitatively different behaviour is predicted consistently in DFT and ORPA.

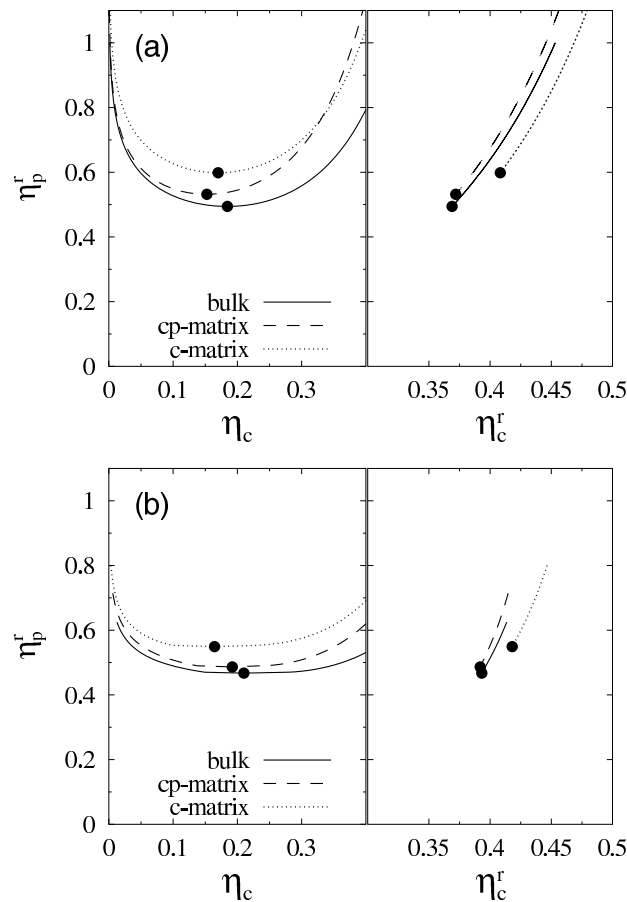


Figure 6. The same as figure 5, but for size ratio $q = 0.6$.

Finally, we display results for size ratio $q = 1$ in figure 7. This is a rather large q -value, where many-body contributions to the effective interactions of the binary system must be considered as important, hence the mapping from the ternary to the binary system with effective pair potentials is certainly questionable. Certainly as a consequence of this fact, marked differences in the binodals between both theories are observed.

- (i) Within the ORPA the bulk critical point (and hence the binodal) is shifted toward larger η_c and smaller η_p^r compared to the treatment of the full mixture (DFT). A similar trend was found before in a comparison of free-volume theory and perturbation theory for the AO potential [23] (see the results for $q = 0.8$ therein). Note also that the free volume result is quite accurate for large size ratios compared to simulation results ($q = 1.05$ in [24]).
- (ii) In the DFT a crossover has occurred, namely the c -matrix shifts the binodal to *higher* values of η_p^r than the cp -matrix, while this now reversed succession is not predicted by the ORPA. In addition, the binodals in the (η_c^r, η_p^r) -representation have different slopes in ORPA and DFT.

We attribute these differences rather to the above mentioned differences in the models considered, than to the respective theoretical treatments.

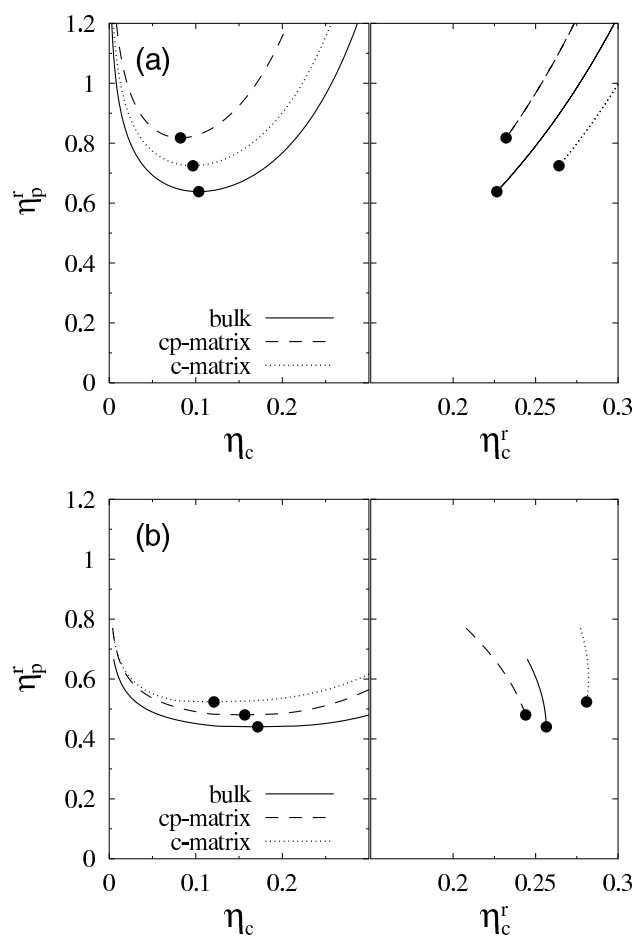


Figure 7. The same as figure 5, but for size ratio $q = 1$.

As our DFT treatment operates on the level of the full ternary system, the system polymer packing fraction, η_p , is easily accessible. In figure 8 we display the demixing binodal in the (η_c, η_p) -plane (left panel). Qualitatively different behaviour emerges for the two types of matrix: the *cp*-matrix promotes demixing, while the *c*-matrix suppresses demixing. Finally, in the (η_c^r, η_p) -representation again we observe the binodal shift toward higher η_c^r . The same trend is observed for the larger size ratios $q = 0.6$ (figure 9) and $q = 1$ (figure 10).

5. Conclusions

In this paper we have compared results for the structure and the phase behaviour of a model colloid–polymer mixture that is in contact with a porous matrix. All interparticle interactions encountered in this ternary system are either HS-like or ideal. We have first considered the pure bulk mixture (colloids—HS—and polymers—ideal particles) and have then brought this fluid into contact with a porous matrix, represented by HSs.

We have studied two cases, the *cp*-matrix where the matrix and the polymer particles interact as HSs and the *c*-matrix where the polymer particles are allowed to overlap the matrix

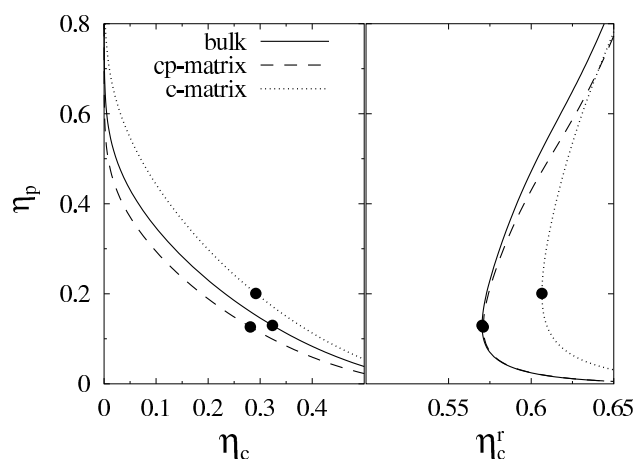


Figure 8. DFT result for the demixing phase diagram for the model colloid–polymer mixture in contact with different HS matrices as a function of the system fractions η_c, η_p (left panel) and of η_c^r, η_p (right panel) for packing fraction $\eta_m = 0.05$ and size ratios $q = 0.3, \sigma_m/\sigma_c = 1$ (corresponding to figure 5). Tielines between coexisting phases have negative slopes in the left panel and are vertical in the right panel.

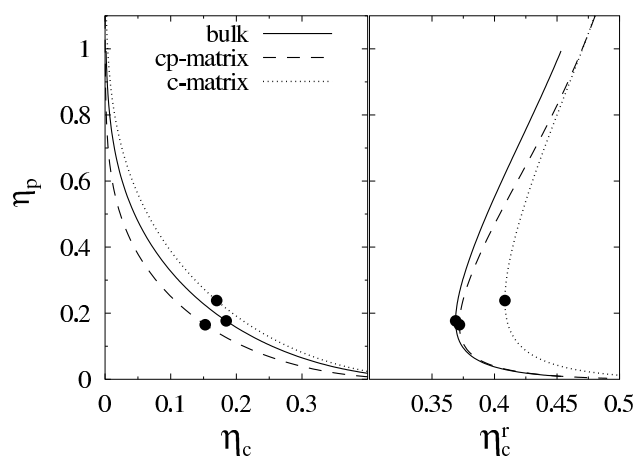


Figure 9. The same as figure 8, but for $q = 0.6$ corresponding to figure 6.

particles. The phase diagram has been calculated on one hand from an FMT-based DF for the full ternary system. On the other hand, we have used an integral-equation approach for the two-component system with effective pair potentials which is obtained by averaging over the polymer degrees of freedom. We have found excellent agreement for the matrix–colloid and the colloid–colloid pair distribution functions obtained via the two theoretical approaches for a system with a rather large matrix packing fraction and not too close to a phase boundary; additional MC results confirm the reliability of the results. We have then calculated the phase diagram for the bulk colloid–polymer mixture and for the situation where this binary mixture is in contact with a matrix that repels colloids and polymers (*cp*-matrix) or repels solely colloids (*c*-matrix). We have considered three values of the size ratio q of colloid and polymer particles (0.3, 0.6 and 1). For the two smaller q -values the *c*-matrix leads—consistently in the ORPA

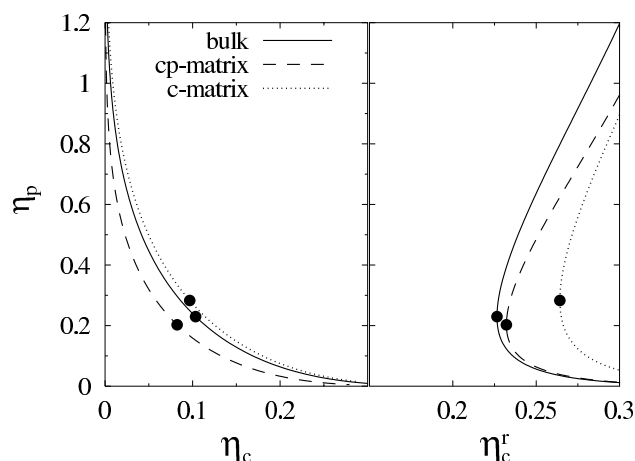


Figure 10. The same as figure 8, but for $q = 1$ corresponding to figure 7.

and DFT—to a considerable shift of the critical point (and consequently of the entire binodal) toward higher polymer packing fractions. For the *cp*-matrix we observe a similar but less pronounced effect. For $q = 1$, inconsistent predictions are observed from the two theories; this can undoubtedly be attributed to a considerable degree to the fact that the mapping of the ternary system onto the binary system with effective pair potentials neglects substantial contributions due to three- and many-body forces. Both approaches predict that the *cp*-matrix and *c*-matrix induce capillary condensation and evaporation, respectively.

Acknowledgments

MS thanks H Löwen for useful discussions and acknowledges support from the DFG within the SFB TR6 ‘Physics of colloidal dispersions in external fields’. ESP and GK acknowledge financial support by the Österreichische Forschungsfond under project nos P13062-TPH, P15857-TPH and W004.

References

- [1] Rosinberg M-L 1999 *New Approaches to Problems in Liquid State Theory (NATO Science Series)* ed C Caccamo, J-P Hansen and G Stell (Dordrecht: Kluwer)
- [2] Edwards S F and Anderson P W 1975 *J. Phys. F: Met. Phys.* **5** 965
Edwards S F and Jones C 1976 *J. Phys. A: Math. Gen.* **9** 1595
- [3] Given J A 1992 *Phys. Rev. A* **45** 816
- [4] Given J A 1992 *J. Chem. Phys.* **96** 2287
- [5] Given J A and Stell G 1994 *Physica A* **209** 495
- [6] Hansen J-P and McDonald I R 1986 *Theory of Simple Liquids* 2nd edn (New York: Academic)
- [7] Rosinberg M-L, Tarjus G and Stell G 1994 *J. Chem. Phys.* **100** 5172
- [8] Kierlik E, Rosinberg M-L, Tarjus G and Monson P 1995 *J. Chem. Phys.* **103** 4256
- [9] Evans R 1979 *Adv. Phys.* **28** 143
Evans R 1992 *Fundamentals of Inhomogeneous Fluids* ed D Henderson (New York: Dekker) ch 3
- [10] Rosenfeld Y 1989 *Phys. Rev. Lett.* **63** 980
- [11] Kierlik E and Rosinberg M L 1990 *Phys. Rev. A* **42** 3382
Kierlik E and Rosinberg M L 1991 *Phys. Rev. A* **44** 5025
Phan S, Kierlik E, Rosinberg M L, Bildstein B and Kahl G 1993 *Phys. Rev. E* **48** 618

- [12] Rosenfeld Y, Schmidt M, Löwen H and Tarazona P 1996 *J. Phys.: Condens. Matter* **8** L577
Rosenfeld Y, Schmidt M, Löwen H and Tarazona P 1997 *Phys. Rev. E* **55** 4245
- [13] Tarazona P and Rosenfeld Y 1997 *Phys. Rev. E* **55** R4873
Tarazona P 2000 *Phys. Rev. Lett.* **84** 694
- [14] Schmidt M 1999 *J. Phys.: Condens. Matter* **11** 10 163
- [15] Asakura S and Oosawa F 1954 *J. Chem. Phys.* **22** 1255
Vrij A 1976 *Pure Appl. Chem.* **48** 471
- [16] Schmidt M, Löwen H, Brader J M and Evans R 2000 *Phys. Rev. Lett.* **85** 1934
Schmidt M, Löwen H, Brader J M and Evans R 2002 *J. Phys.: Condens. Matter* **14** 9353–82
- [17] Schmidt M 2001 *Phys. Rev. E* **63** 010101(R)
- [18] Cuesta J A 1996 *Phys. Rev. Lett.* **76** 3742
Cuesta J A and Martinez-Raton Y 1997 *Phys. Rev. Lett.* **78** 3681
- [19] Rosenfeld Y 1994 *Phys. Rev. E* **50** R3318
Rosenfeld Y 1995 *Mol. Phys.* **86** 637
Schmidt M 2001 *Phys. Rev. E* **63** 050201(R)
von Ferber C and Schmidt M 2001 *Phys. Rev. E* **64** 051115
Brader J M, Esztermann A and Schmidt M 2002 *Phys. Rev. E* **66** 031401
Roth R, van Roij R, Andrienko D, Mecke K R and Dietrich S 2002 *Phys. Rev. Lett.* **89** 088301
- [20] Schmidt M 2002 *Phys. Rev. E* at press
- [21] Gast A P, Hall C K and Russell W B 1983 *J. Colloid Interface Sci.* **96** 251
- [22] Lekkerkerker H N W, Poon W C K, Pusey P N, Stroobants A and Warren P B 1992 *Europhys. Lett.* **20** 559
- [23] Dijkstra M, Brader J M and Evans R 1999 *J. Phys.: Condens. Matter* **11** 10 079
- [24] Bolhuis P G, Louis A A and Hansen J-P 2002 *Phys. Rev. Lett.* **89** 128302
- [25] Brader J M, Dijkstra M and Evans R 2001 *Phys. Rev. E* **63** 041405
Evans R, Brader J M, Roth R, Dijkstra M, Schmidt M and Löwen H 2001 *Phil. Trans. R. Soc. A* **359** 961
Brader J M 2001 *Statistical Mechanics of a Model Colloid-Polymer Mixture* (Bristol: University of Bristol)
Brader J M, Evans R, Schmidt M and Löwen H 2002 *J. Phys.: Condens. Matter* **14** L1
- [26] Cuesta J A, Martinez-Raton Y and Tarazona P 2002 *J. Phys.: Condens. Matter* **14** 11965–80
- [27] Andersen H C, Chandler D and Weeks J D 1972 *J. Chem. Phys.* **56** 3812
Andersen H C and Chandler D 1972 *J. Chem. Phys.* **57** 1918
- [28] Kierlik E, Rosinberg M-L, Tarjus G and Monson P A 1997 *J. Chem. Phys.* **106** 264
- [29] Paschinger E, Levesque D, Weis J-J and Kahl G 2001 *Phys. Rev. E* **64** 011502

PHYSICAL REVIEW E **68**, 061404 (2003)

Capillary condensation and interface structure of a model colloid-polymer mixture in a porous medium

Paul P. F. Wessels*

Institut für Theoretische Physik II, Heinrich-Heine-Universität Düsseldorf, Universitätsstraße 1, 40225 Düsseldorf, Germany

Matthias Schmidt†

Debye Institute, Utrecht University, Princetonplein 5, 3584 CC Utrecht, The Netherlands

Hartmut Löwen

Institut für Theoretische Physik II, Heinrich-Heine-Universität Düsseldorf, Universitätsstraße 1, 40225 Düsseldorf, Germany

(Received 29 July 2003; published 17 December 2003)

We consider the Asakura-Oosawa model of hard sphere colloids and ideal polymers in contact with a porous matrix modeled by immobilized configurations of hard spheres. For this ternary mixture a fundamental measure density functional theory is employed, where the matrix particles are quenched and the colloids and polymers are annealed, i.e., allowed to equilibrate. We study capillary condensation of the mixture in a small sample of matrix as well as demixing and the fluid-fluid interface inside a bulk matrix. Density profiles normal to the interface and surface tensions are calculated and compared to the case without matrix. Two kinds of matrices are considered: (i) colloid-sized matrix particles at low packing fractions and (ii) large matrix particles at high packing fractions. These two cases show fundamentally different behavior and should both be experimentally realizable. Furthermore, we argue that capillary condensation of a colloidal suspension could be experimentally accessible. We find that in case (ii), even at high packing fractions, the main effect of the matrix is to exclude volume and, to high accuracy, the results can be mapped onto those of the same system without matrix via a simple rescaling.

DOI: 10.1103/PhysRevE.68.061404

PACS number(s): 82.70.Dd, 61.20.Gy, 68.05.-n, 81.05.Rm

I. INTRODUCTION

Bringing a fluid in contact with a porous medium has a profound influence on its characteristics and phase behavior [1,2]. Due to abundance of surfaces and their necessary proximity, surface-fluid interactions as well as capillarity effects play a prominent role. Moreover, the system may be trapped in locally stable states, and its behavior governed by hysteresis. Apart from the above fundamental questions, the study of adsorbates in porous media is also of great interest in applied fields ranging from industrial and geophysical to biomedical and pharmaceutical systems [2,3].

Many natural porous materials are tremendously complex on a microscopic scale: irregularly shaped pores build a connected void space that percolates throughout the sample [4,5]. In contrast, to facilitate systematic studies, one often relies on model pores like slitlike, cylindrical or spherical pores (see Refs. [1,2] and references therein). The pore is then described conveniently in terms of a single parameter—its size. A different class of idealized system makes use of immobilized arrangements of fluid particles (i.e., a quenched hard sphere fluid) to model a porous medium (see Ref. [2] and references therein). In turn, this is characterized through its density and the size of the spheres. However, the relevant difference to idealized pores is the presence of *random* confinement.

The study of porous media has been focused so far mainly on atomic liquids. In a colloidal fluid, length and time scales are much larger, facilitating, e.g., studies in real space and time [6]. We believe that the use of colloidal suspensions as model systems to study the behavior of adsorbates in porous media can be as beneficial as their use to study many other phenomena in condensed matter. However, the experimental challenge lies in constructing three-dimensional porous media suitable for colloidal suspensions.

Colloidal two-dimensional (2D) porous media have been prepared by Cruz de León and co-workers [7,8] by confining a suspension of large colloids between parallel glass plates. Then, these served as a porous matrix to a fluid of smaller particles which remained mobile and of which they measured the structure and effective potentials. To our knowledge, no experiment similar in spirit has been performed in three dimensions to date. On the other hand, Kluijtmans and co-workers constructed 3D porous glasses of silica spheres [9,10] and silica rods [11], but studied the dynamics of isolated tracer colloids in these media. Weroński *et al.* studied transport properties in porous media of glass beads [12]. Still, such glassy arrangements of spherical colloids are a direct candidate for porous media suitable for colloidal suspensions. Sediments of large and heavy colloids as used in Refs. [9,10,12] could be brought in contact with a suspension of smaller density-matched (to the solvent) colloids of which the local structure could be determined [7,8]. However, the size ratio of the two species is a crucial control parameter: It has to be large enough (≥ 10) such that the small particles can penetrate the void space, but should still be small enough such that no complete separation of length scales occurs.

*Electronic address: wessels@thphy.uni-duesseldorf.de

†On leave from Institut für Theoretische Physik II, Heinrich-Heine-Universität Düsseldorf, Universitätsstraße 1, 40225 Düsseldorf, Germany.

Another way to realize such porous media would be to use laser tweezers. In a binary colloid mixture of which one of the species possesses the same index of refraction as the solvent (via index matching) and the other type has a higher index of refraction, the second species could be trapped while the first would still remain mobile. Using multiple traps at random positions in space (mimicking a fluid) one could then realize a model porous matrix [13]. The advantages of this method are the accessibility of very low matrix packing fractions and the full control of the confinement. However, the number of trapped colloids in such setups is typically limited to the order of 100—probably too little to approach real macroscopic porous media, but in the right regime to be able to compare to computer simulations, where similar numbers are accessible. The crucial advantage of these setups over the use of “natural” porous media is their model character arising from the use of well-defined monodisperse matrix spheres, while these still possess the essential features of random confinement and a highly interconnected void structure.

One prominent phenomenon that is induced by confinement is capillary condensation: A liquid inside the porous medium is in equilibrium with its vapor outside the medium. In order for a substance to phase separate into a dense liquid and a dilute gas phase, a sufficiently long-ranged and sufficiently strong attraction between the constituting particles is necessary. It is well known that the addition of nonadsorbing polymers to colloidal dispersions induces an effective attraction between the colloids. The polymer coils are depleted from a shell around each colloid and overlap of these (depletion) shells generates more available volume to the polymers, yielding an effective attraction between the colloids. Consequently, these colloid-polymer mixtures may separate into a colloid-poor (gas) phase and a colloid-rich (liquid) fluid [14].

The most simplistic theoretical model that has been applied for the study of such colloid-polymer mixture is the Asakura-Oosawa (AO) model [15–17] that takes the colloids to be hard spheres and the polymers to be ideal spheres that are excluded from the colloids. The bulk phase behavior of this model was studied with a variety of techniques, such as effective potentials [18,19], free volume theory [20], density functional theory (DFT) [21,22], and simulations [19,23,24]. Recent work has also been devoted to inhomogeneous situations, i.e., the free interface between demixed fluid phases [25–28] and the adsorption behavior at a hard wall, where in particular a novel type of entropic wetting was found [24,27,28] and the behavior in spatially periodic external potentials [29]. The surface tension between demixed colloid-polymer systems has been measured experimentally and established to be much lower than for atomic systems [30–33]. Further, recent experiments confirm wetting of the colloid-rich liquid at a hard wall [34,35].

DFT [36] can be used in two ways to treat adsorbates in porous media. The first is the (conceptually) straightforward approach via treating the porous medium as an external potential (see, e.g., Refs. [37–39]) and to solve for the one-body density distributions of the fluid species. Those can be complicated spatial distributions, hence this approach is computationally demanding, but also yields information on

out-of-equilibrium behavior, such as hysteresis in adsorption and desorption curves [40–42].

A recently proposed alternative is to describe the quenched component on the level of its one-body density distribution [43]. Following the fundamental measure theory (FMT) of hard spheres [44–46], an explicit scheme was obtained to generate an approximate excess free energy for (not necessarily additive) hard-sphere mixtures in contact with hard-sphere matrices [43]. Applied to the AO model, the results were compared with those from solving the so-called replica-Ornstein-Zernike (ROZ) equations [47–50] and found to be in good agreement [51]. Meanwhile, this quenched-annealed (QA) DFT has been compared to computer simulations [52] and extended to hard-rod matrices [53] and lattice fluids [54,55]. FMT in combination with mean field theory has also been applied to fluids inside model pores [56,57].

In this paper, we revisit the AO model in contact with a hard-sphere matrix using the QA DFT of Refs. [43,51]. We study capillary condensation in a small sample of matrix as well as the fluid-fluid interface inside a bulk matrix. For both these phenomena, we distinguish two cases of matrices: (i) matrix particles having the same size as the colloids and (ii) where they are much larger. These correspond to the two possible experimental realizations we discussed earlier in the Introduction, but also serve as representative cases because their behavior is fundamentally different. Concerning capillary condensation, we focus on the possible experimental realization and consider a bulk mixture in contact with a small sample of matrix. Furthermore, we elaborate if and how capillary condensation could be observable in such experiments. Concerning the fluid-fluid interface, we study the interfacial profiles as well as the surface tensions inside the matrix. For the case of small matrix particles (i), we determine the nature of decay (monotonic or periodic) of the interfaces which we compare with the bulk pair correlations. For the case of large matrix particles (ii), we observe a simple rescaling of the bulk as well as the interface results with respect to the case without matrix. Inhomogeneous situations such as the fluid-fluid interface are treated within QA DFT in a direct fashion, in contrast to, e.g., the ROZ equations. Fluid-fluid interfaces have been studied before in Lennard-Jones systems in contact with porous media using the Born-Green-Yvon equation as well as computer simulations [58,59] and we briefly compare to results of our profiles.

The paper is organized as follows. In Sec. II we define our theoretical model explicitly. The QA DFT approach is reviewed in Sec. III, and the results are presented in Sec. IV. We first consider capillary condensation in a small sample and then demixing the interfacial profiles and tensions inside a matrix. We conclude with a discussion in Sec. V.

II. MODEL

We consider a three-component mixture of colloids (denoted by c), polymers (p), and immobile matrix particles (m). Each of these particles are spherical objects with radii R_i and $i=c,p,m$ and corresponding number densities ρ_i

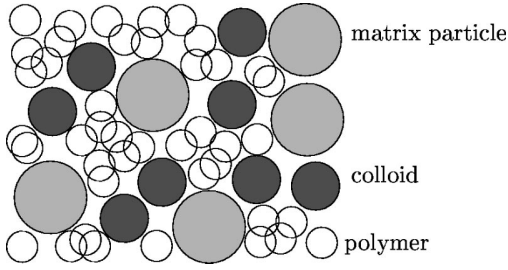


FIG. 1. Sketch of the ternary mixture of mobile colloids (dark), mobile polymers (transparent), and immobile matrix particles (gray). The polymer coils can freely overlap. There are three model parameters, i.e., the packing fraction of matrix particles (η_m), and two size ratios $q=R_p/R_c$ and $s=R_m/R_c$, where R_i is the radius of particles of species i . The packing fractions of colloids and polymers, η_c and η_p , respectively, are the thermodynamic parameters.

$=N_i/V$, where N_i is the total number of molecules of species i and V is the system volume. All of these components are modeled as hard bodies, meaning that they cannot overlap but otherwise do not interact with each other, except for the polymer-polymer interaction, which is taken to be ideal, see Fig. 1. Consequently, when r is the mutual distance, the pair potentials become

$$u_{ij}(r) = \begin{cases} \infty & \text{if } r < R_i + R_j \\ 0 & \text{if } r \geq R_i + R_j \end{cases} \quad (1)$$

for $i, j = c, p, m$ except for $i = j = p$,

and concerning the polymer-polymer interaction, this simply becomes

$$u_{pp}(r) = 0 \quad \text{for all } r. \quad (2)$$

As all interactions are either hard core or ideal, the (phase) behavior is governed by entropic (packing) effects and the temperature T does not play a role. The only thermodynamic parameters are the colloid and polymer packing fractions $\eta_c = 4\pi R_c^3 \rho_c / 3$ and $\eta_p = 4\pi R_p^3 \rho_p / 3$, respectively. The remaining model parameters are two size ratios $q = R_p/R_c$ and $s = R_m/R_c$ and the packing fraction of matrix particles ($\eta_m = 4\pi R_m^3 \rho_m / 3$). It has to be mentioned that due to the fact that the polymers can freely overlap, the ‘‘polymer packing fraction’’ can easily be larger than one (Fig. 1). The mixture of hard spheres with these last-mentioned ideal polymers (i.e., without the matrix particles) is called the AO mixture [15,16].

III. DENSITY FUNCTIONAL THEORY

A. Zero-dimensional limit

In this section we derive the zero-dimensional (0D) Helmholtz free energy for the three-component system of the AO colloid-polymer mixture in contact with quenched hard spheres. This 0D free energy is used as an input to construct the fundamental measure theory in the following section. Here, we give only a brief derivation, a more extensive version with more comments is given in Refs. [43,51]. The es-

sential ingredient is that we need to perform the so-called ‘‘double average’’ which refers to the statistical average over all fluid configurations and subsequently over all matrix realizations. To that end we consider a 0D cavity which either does or does not contain a matrix particle. Hence, the 0D partition sum is that of a simple hard-sphere fluid,

$$\bar{\Xi}_m = 1 + \bar{z}_m, \quad (3)$$

where $\bar{z}_m = \zeta \exp(\beta \bar{\mu}_m)$ is the fugacity of the hard spheres. Further, $\beta = 1/k_B T$ with k_B Boltzmann’s constant and $\bar{\mu}_m$ the chemical potential. The irrelevant prefactor ζ scales with the vanishing volume of the cavity but has no effect to the final free energy and will not be discussed further. In general, we use an overbar to refer to quantities of 0D systems. With the grand potential, $\beta \bar{\Omega}_m = -\ln \bar{\Xi}_m$, the average number of matrix particles is $\bar{\eta}_m = -\bar{z}_m \partial \beta \bar{\Omega}_m / \partial \bar{z}_m = \bar{z}_m / (1 + \bar{z}_m)$.

Next, we consider the colloid-polymer mixture in contact with the matrix in zero dimensions. If the cavity is occupied by a matrix particle, no colloid, or polymer can be present. On the other hand, if there is no matrix particle, it can either be empty, occupied by a single colloid, or an arbitrary number of polymers. Hence,

$$\bar{\Xi} = \begin{cases} 1 & \text{(matrix particle in cavity)} \\ \bar{z}_c + \exp(\bar{z}_p) & \text{(no matrix particle in cavity),} \end{cases} \quad (4)$$

where \bar{z}_c and \bar{z}_p are the colloid and polymer fugacities, respectively. Then, the contribution $-\ln \bar{\Xi}$ to the grand potential should contain the appropriate statistical weight for each of the cases, i.e., $\bar{z}_m / \bar{\Xi}_m$ for the first and $1 / \bar{\Xi}_m$ for the second,

$$\beta \bar{\Omega} = -\frac{\ln[\bar{z}_c + \exp(\bar{z}_p)]}{1 + \bar{z}_m}. \quad (5)$$

Average particle numbers are again readily obtained via $\bar{\eta}_i = -\bar{z}_i \partial \beta \bar{\Omega} / \partial \bar{z}_i$ for $i = c, p$ (not for m). The Helmholtz free energy can then be calculated using a standard Legendre transformation $\beta \bar{F} = \beta \bar{\Omega} + \sum_{i=c,p} \bar{\eta}_i \ln(\bar{z}_i)$, and we obtain for the excess part, $\beta \bar{F}_{\text{exc}} = \beta \bar{F} - \sum_{i=c,p} \bar{\eta}_i [\ln(\bar{\eta}_i) - 1]$,

$$\beta \bar{F}_{\text{exc}}(\bar{\eta}_c, \bar{\eta}_p; \bar{\eta}_m) = (1 - \bar{\eta}_c - \bar{\eta}_p - \bar{\eta}_m) \ln(1 - \bar{\eta}_c - \bar{\eta}_m) + \bar{\eta}_c - (1 - \bar{\eta}_m) \ln(1 - \bar{\eta}_m). \quad (6)$$

This result can be shown to be equal from that which would be obtained using the so-called ‘‘replica trick’’ [50].

B. Fundamental measure theory

FMT is a nonlocal density functional theory, in which the excess part of the *three-dimensional* free energy F_{exc} is expressed as a spatial integral over the free energy density Φ ,

$$\beta F_{\text{exc}}[\{\rho_i(\mathbf{r})\}] = \int d\mathbf{r} \Phi(\{n_i^i(\mathbf{r})\}). \quad (7)$$

WESSELS, SCHMIDT, AND LÖWEN

 PHYSICAL REVIEW E **68**, 061404 (2003)

This free energy density in turn is assumed to depend on the full set of weighted densities $\{n_v^i(\mathbf{r})\}$,

$$\begin{aligned} n_v^i(\mathbf{r}) &= \int d\mathbf{r}' w_v^i(\mathbf{r}-\mathbf{r}') \rho_i(\mathbf{r}'), \\ &= (w_v^i \rho_i)(\mathbf{r}), \end{aligned} \quad (8)$$

which are convolutions (denoted with \cdot) with the single-particle distribution functions $\rho_i(\mathbf{r})$ for species $i=c,p,m$. The weight functions are obtained from the low-density limit where the virial series has to be recovered,

$$\begin{aligned} w_3^i(\mathbf{r}) &= \theta(R_i - r), \\ w_2^i(\mathbf{r}) &= \delta(R_i - r), & \mathbf{w}_{v2}^i(\mathbf{r}) &= \delta(R_i - r) \mathbf{r}/r, \\ w_1^i(\mathbf{r}) &= \delta(R_i - r)/(4\pi r), & \mathbf{w}_{v1}^i(\mathbf{r}) &= \delta(R_i - r) \mathbf{r}/(4\pi r^2), \\ w_0^i(\mathbf{r}) &= \delta(R_i - r)/(4\pi r^2), \end{aligned} \quad (9)$$

with again $i=c,p,m$ being one of the three components, θ the Heaviside function, and δ the Dirac delta function. There are four scalar weight functions, with 3 to 0, corresponding to the volume of the particles, the surface area, the mean curvature, and the Euler characteristic, respectively, and these are the so-called ‘‘fundamental measures’’ of the sphere. The two weights on the right-hand side of Eq. (9) are vector quantities. Often a seventh tensorial weight is used in the context of freezing but this will not be used here [21,22,46]. The dimensions of the weight functions w_v^i are (length) $^{v-3}$.

Then, the sole approximation made is that Φ is taken to be a *function* of the weighted densities $n_v^i(\mathbf{r})$ whereas most generally one would expect this to be a *functional* dependence. This approximation totally sets the form of Φ and following Refs. [22,43,51] we give the expression for $\Phi = \Phi_1 + \Phi_2 + \Phi_3$ in terms of the zero-dimensional free energy derived in the preceding section,

$$\Phi_1 = \sum_{i=c,p,m} n_0^i \varphi_i(\{n_3^l\}), \quad (10)$$

$$\Phi_2 = \sum_{i,j=c,p,m} (n_1^i n_2^j - \mathbf{n}_{v1}^i \cdot \mathbf{n}_{v2}^j) \varphi_{ij}(\{n_3^l\}), \quad (11)$$

$$\Phi_3 = \frac{1}{8\pi} \sum_{i,j,k=c,p,m} \left(\frac{1}{3} n_2^i n_2^j n_2^k - n_2^i \mathbf{n}_{v2}^j \cdot \mathbf{n}_{v2}^k \right) \varphi_{ijk}(\{n_3^l\}), \quad (12)$$

with

$$\varphi_{i_1, \dots, i_t}(\{\bar{\eta}_j\}) = \partial^t \beta \bar{F}_{\text{exc}}(\{\bar{\eta}_j\}) / \partial \bar{\eta}_{i_1} \cdots \partial \bar{\eta}_{i_t}. \quad (13)$$

All $\varphi_{i_1, \dots, i_t}$ of which more than one indices equal p are zero due to the form of $\beta \bar{F}_{\text{exc}}$. Together, Eqs. (6) to (13) constitute the excess free energy functional for this QA system.

C. Minimization

Having constructed the excess free energy, we can now immediately move on to the grand-canonical free energy functional of the colloid-polymer mixture in contact with a matrix,

$$\begin{aligned} \Omega[\rho_c(\mathbf{r}), \rho_p(\mathbf{r}); \rho_m(\mathbf{r})] \\ = F_{\text{exc}}[\rho_c(\mathbf{r}), \rho_p(\mathbf{r}); \rho_m(\mathbf{r})] + k_B T \sum_{i=c,p} \int d\mathbf{r} \rho_i(\mathbf{r}) \\ \times [\ln(\rho_i(\mathbf{r}) \Delta_i) - 1] + \sum_{i=c,p} \int d\mathbf{r} \rho_i(\mathbf{r}) [V_i(\mathbf{r}) - \mu_i]. \end{aligned} \quad (14)$$

Here, Δ_i is the ‘‘thermal volume’’ which is the product of the relevant de Broglie wavelengths of the particles of species i . Further, μ_i is the chemical potential and V_i is the (external) potential acting on component i . In this paper, we study bulk phase behavior and the free fluid-fluid interfaces, so we use $V_i=0$. The equilibrium profiles are the ones that minimize the functional,

$$\frac{\delta \Omega}{\delta \rho_c(\mathbf{r})} = 0 \quad \text{and} \quad \frac{\delta \Omega}{\delta \rho_p(\mathbf{r})} = 0. \quad (15)$$

This yields the Euler-Lagrange or stationarity equations ($i=c,p$),

$$\rho_i(\mathbf{r}) = z_i \exp[c_i^{(1)}(\{\rho_j(\mathbf{r})\})], \quad (16)$$

with $z_i = \Delta_i^{-1} \exp[\beta \mu_i]$ the fugacity of component i and the one-particle direct correlation functions given by

$$c_i^{(1)}(\mathbf{r}) = -\beta \frac{\delta F_{\text{exc}}[\{\rho_j(\mathbf{r})\}]}{\delta \rho_i(\mathbf{r})} = -\sum_v \left(\frac{\partial \Phi}{\partial n_v^i} w_v^i \right)(\mathbf{r}). \quad (17)$$

Obviously, the functional is not minimized with respect to the matrix distribution $\rho_m(\mathbf{r})$ as this serves as an *input* profile. In principle, as we are dealing with a quenched-annealed system in which the matrix is initially (before quenching) a hard-sphere fluid, $\rho_m(\mathbf{r})$ should still minimize the hard-sphere functional [43,51]. However, as density functional theory allows us to generate any distribution $\rho_m(\mathbf{r})$ by applying any suited external potential (which we can then remove after quenching), we do not need to go into the scheme of generating matrix profiles. Moreover, in the present paper we use fluid distributions of the matrix particles which minimize (at least locally) the hard-sphere functional without external potential for any packing fraction. This restricts the matrix distribution to be homogeneous, i.e., constant in space, $\rho_m(\mathbf{r}) = \text{const}$.

IV. RESULTS

In this section, we show results of the effect of the hard-sphere matrix on the AO colloid-polymer mixture concerning capillary condensation in a small sample of matrix, and

phase behavior and free fluid-fluid interfaces inside a bulk matrix. Throughout this section, we distinguish between the colloid-sized matrix particles ($s=1$) and the large matrix particles (we use $s=50$). In the first case, as we will see, one is limited to small matrix packing fractions (up to η_m of the order of 0.2) as for high packing fractions the pores become too small for the colloids and the polymers to constitute a real fluid in the matrix. For the large matrix particles, higher matrix packing fractions are accessible (up to $\eta_m=0.5$). Finally, in all cases we use $q=0.6$, for which size ratio the AO model has a stable fluid-fluid demixing area (with respect to freezing, which we do not consider).

A. Bulk fluid free energy

In the fluid phase, the densities are spatially homogeneous, and the constant distributions $\rho_i(\mathbf{r})=\rho_i$ solve the stationarity Eqs. (16) and (17). Therefore, we only have to integrate the weights over space, $\int d\mathbf{r} w_v^i$, and the weighted densities become

$$\begin{aligned} n_3^i &= \eta_i, \\ n_2^i &= 3 \eta_i / R_i, \\ n_1^i &= 3 \eta_i / (4 \pi R_i^2), \\ n_0^i &= 3 \eta_i / (4 \pi R_i^3), \\ \mathbf{n}_{v2}^i &= \mathbf{n}_{v1}^i = 0, \end{aligned} \quad (18)$$

with $i=c,p,m$. Substituting these expressions in the free energy density, Eqs. (10)–(12), we obtain an analytical expression for the bulk excess free energy. Defining the dimensionless bulk free energy density, $f=\beta F V_c/V$, with $V_c=4\pi R_c^3/3$ the volume of a colloid, this becomes

$$\begin{aligned} f(\eta_c, \eta_p; \eta_m) &= \eta_c (\ln \eta_c - 1) + \frac{\eta_p}{q^3} (\ln \eta_p - 1) + f_0(\eta_c, \eta_m) \\ &\quad - \frac{\eta_p}{q^3} \ln \alpha(\eta_c, \eta_m), \end{aligned} \quad (19)$$

with the last two terms being the excess free energy. We have separated the excess free energy in two terms where f_0 is the excess free energy density of a fluid of hard spheres in contact with a hard-sphere matrix and α is the fraction of free volume for the polymers in the presence the hard sphere colloidal fluid *and* the hard sphere matrix [20,22]. The expressions for f_0 and α are quite extensive and given in the Appendix. In going from Eq. (7) to (19) we have discarded two terms, $\eta_c \ln(\Delta_c/V_c)$ and $(\eta_p/q^3) \ln(\Delta_p/V_p)$, linear in the colloid and polymer packing fractions. These have no effect on the phase behavior. Due to the ideal interactions of the polymers, the excess free energy density is only linear in η_p and the polymer fugacity becomes simply

$$z_p V_p = \eta_p / \alpha(\eta_c, \eta_m). \quad (20)$$

This relation is trivially invertible, so switching from system representation [using $f(\eta_c, \eta_p; \eta_m)$] to the polymer reservoir representation [in terms of $\tilde{\omega}(\eta_c, z_p; \eta_m) = f - \mu_p \eta_p / q^3$] is straightforwardly done. Moreover, for zero packing fractions of colloids and matrix particles, the polymer free volume fraction is trivial, $\alpha(0,0)=1$. Consequently, the fugacity equals the packing fraction of polymers in the polymer reservoir, $z_p V_p = \eta_{p,r}$ (where there are no colloids and matrix particles), and often, we use $\eta_{p,r}$ when referring to the fugacity. Finally, we mention that in the absence of matrix particles, $\eta_m=0$, this theory is equivalent to the free-volume theory for the AO model [20–22].

Concerning the fluid-fluid demixing, the spinodals are calculated in the canonical representation, by solving $\det[\partial^2 f / \partial \eta_i \partial \eta_j] = 0$ with $i, j = c, p$, which can be done analytically. Binodals are determined by constructing the common tangents of the semigrand potential $\tilde{\omega}(\eta_c, \eta_{p,r}; \eta_m)$ at fixed fugacity $\eta_{p,r}$.

When the matrix particles are very large, it is expected that the excluded volume effects dominate over other (surface or capillary) effects. In particular, if one considers only one infinitely large particle, still corresponding to a nonzero matrix packing fraction, one would expect normal bulk behavior of the mixture as most of the mixture is “far” away from the matrix particle. Equivalently, for very large matrix particles, the total volume of the surrounding depletion layers that are responsible for the surface effects, compared to the actual volume occupied by the matrix particles, scales with $[4\pi(R_m+R_c)^3 \rho_m / 3 - \eta_m] / \eta_m \propto 3/s$ for the colloids and $[4\pi(R_m+R_p)^3 \rho_m / 3 - \eta_m] / \eta_m \propto 3q/s$ for the polymers, and these both go to zero for $s \rightarrow \infty$. However, in this limit, we still need to correct for the volume as this is partly occupied by infinitely large matrix particles, i.e., $V \rightarrow (1 - \eta_m)V$. Indeed, applying $s \rightarrow \infty$ to the bulk free energy of Eq. (19), we reobtain the bulk behavior of the plain AO colloid-polymer mixture *without* matrix, i.e., it can be shown that

$$\lim_{s \rightarrow \infty} f(\eta_c, \eta_p; \eta_m) = (1 - \eta_m) f\left(\frac{\eta_c}{1 - \eta_m}, \frac{\eta_p}{1 - \eta_m}; 0\right), \quad (21)$$

where the free energy density has to be rescaled as well. This term can be considered to be the zeroth in a $1/s$ expansion of the free energy of which higher order terms should correspond to effects due to surfaces, capillarity, curvature, etc. However, because of the formidable form of the free energy it is a daunting task to connect every term to a certain phenomenon and we leave this to future investigation. It is worth mentioning that a power series in $1/s$ is only a simple model dependence. In general, there can be nonanalyticities, e.g., arising from wetting phenomena around curved surfaces [60] of matrix particles.

B. Capillary condensation in a small sample of porous matrix

A porous matrix of quenched hard-spheres stabilizes the colloid-rich phase with respect to the colloidal gas phase [51]. This is called capillary condensation and it is due to the attractive depletion potential between the colloids, which

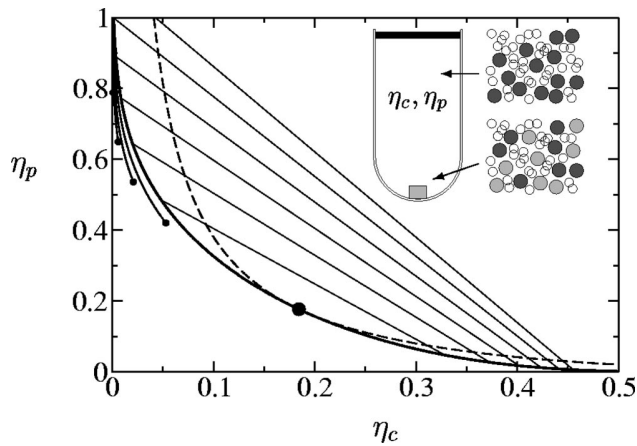


FIG. 2. Phase diagram of a bulk AO colloid-polymer mixture ($q=0.6$) in chemical contact with a small sample of porous material ($s=1$). Concerning the bulk mixture: the thick full curve is the binodal, the dashed is the spinodal, the large filled circle (where they meet) is the critical point, and the straight (thin) lines are the tie lines connecting coexisting state points. The capillary lines (full curves) appear in the upper left (colloid-poor) part of the phase diagram and each terminates in a capillary critical point (small filled circles). From lower right to upper left, the curves correspond to an increasing packing fraction of the matrix, $\eta_m=0.05,0.1,0.15,0.2$ (the last one is practically on the vertical axis near $\eta_p=0.8$). The inset shows a sketch of the setup: a test tube is sealed at the top and filled with the colloid-polymer mixture (densities η_c and η_p) and at the bottom lies the small sample of porous matrix.

also acts between colloids and matrix particles. In this section we present capillary condensation in a representation which is appropriate to compare with experiments. In an experimental setup one typically has a canonical ensemble, i.e., a test tube, of colloid-polymer mixture. By adding a small sample of porous material, the bulk mixture in the test tube acts as a colloid-polymer reservoir to the sample, but vice versa, if the sample is small enough, its state will not have any effect on that of the bulk mixture [see Fig. 2 (inset)]. In the colloid-poor (and polymer-rich) part of the phase diagram, on approaching bulk coexistence, the conditions for coexistence in the porous sample are reached before those in bulk, i.e., capillary condensation in the sample occurs. Hence, capillary condensation appears as a line in the system representation terminating in a capillary critical point. This is shown in Figs. 2 and 3 for the case of $s=1$ and $s=50$, respectively, and various densities of the matrix. The coexistence of the bulk colloid-polymer mixture appears in the usual system representation, where tie lines connect coexisting states. For each of the matrix densities, a capillary line runs along the bulk binodal in the colloid-poor part of the phase diagram.

First, we determine the conditions for coexistence inside the matrix, i.e., we compute the combinations of chemical potentials $\mu_{c,\text{coex}}^{\text{porous}}$ and $\mu_{p,\text{coex}}^{\text{porous}}$, for which demixing occurs within the porous sample. These are fixed by the chemical potentials of the bulk colloid-polymer mixture, μ_c^{bulk} and μ_p^{bulk} , so solving

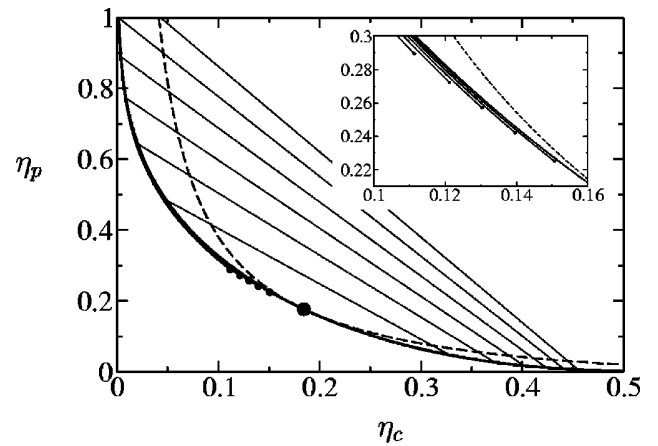


FIG. 3. Same as in Fig. 2, but now for a sample of porous matrix with $s=50$. Here the matrix packing fractions increase as follows: $\eta_m=0.1,0.2,0.3,0.4,0.5$ (again from lower right to upper left). The inset is the magnification of the area with the capillary critical points.

$$\begin{aligned}\mu_c^{\text{bulk}}(\eta_c, \eta_p) &= \mu_{c,\text{coex}}^{\text{porous}}, \\ \mu_p^{\text{bulk}}(\eta_c, \eta_p) &= \mu_{p,\text{coex}}^{\text{porous}}\end{aligned}\quad (22)$$

for η_c and η_p , we obtain the capillary lines in the phase diagram in system representation. The trend can be spotted from Figs. 2 and 3, increasing the matrix packing fraction in the sample, the capillary line moves away from the bulk binodal but at the same time the capillary critical point shifts away from the bulk critical point. Qualitatively, this applies to both the $s=1$ and $s=50$ cases. However, in the $s=50$ case the capillary lines extend to much closer to the bulk critical point, but they are hardly distinguishable from the bulk binodal. Concerning the colloid-sized matrix particles, $s=1$, these capillary lines are well separated from the bulk binodal, but the capillary critical points are located much deeper into the colloidal gas regime.

Next, we briefly discuss the implications this has for possible experiments. Focusing on the case of the large matrix particles, $s=50$, we take as an example $\eta_m=0.5$. In this case the difference in chemical potential at coexistence of the mixture in bulk and inside the porous sample at constant polymer fugacity is of the order, $\beta\Delta\mu_c^{\text{coex}}\sim 0.1$, and it scales roughly with $1/s$. This difference is very small and brings up the question if this (i.e., capillary condensation) is observable in experiments. Typically, the effect of gravity is reduced by density matching the colloids with the solvent, i.e., canceling gravity by means of buoyancy. However, this density matching is never perfect, and the length scale $(\beta m_c g)^{-1}$ is a measure for its success (at infinity it is perfect). Here g is the gravitational acceleration and $m_c=(\rho_{\text{colloid}}-\rho_{\text{solvent}})V_c$ the effective mass of the colloid in solution, with ρ_{colloid} and ρ_{solvent} the mass densities inside the colloid and of the solvent, respectively. Therefore this length scale is strongly dependent on the colloid size, $(\beta m_c g)^{-1}\propto R_c^{-3}$, and can range from micrometers (large colloids) to meters (small colloids) in experiments [32]. Typically, polymers are much less sen-

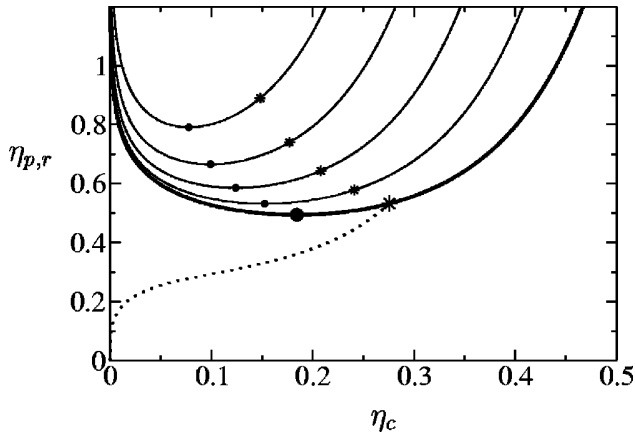


FIG. 4. Fluid-fluid binodals of an AO colloid-polymer mixture ($q=0.6$) inside a bulk porous matrix ($s=1$). Tie lines connecting coexisting state point are not drawn but run horizontal. The lower (thicker) curve is the result in the absence of any matrix, $\eta_m=0$. For the other curves, the matrix packing fraction increases from bottom to top, $\eta_m=0,0.05,0.1,0.15,0.2$. The filled circles are the critical points (large, $\eta_m=0$). The dotted line is the Fisher-Widom line for $\eta_m=0$, below which the decay of correlations in the fluid is oscillatory and above which these are monotonic. The point where the FW line hits the binodal is marked by a (large) star. The FW lines for the other matrix packing fractions are not shown, only their crossings with the binodals (small stars).

sitive to gravity as long as the solvent is good. When there is coexistence inside a test tube, there is only real coexistence at the liquid-gas interface, whereas below and above, the colloids have slightly different chemical potentials due to their gravitational energy. Consequently, moving upward from the interface, say Δz , the colloid chemical potential is $(\beta m_c g)\Delta z$ lower than at coexistence. By placing the porous sample within $\Delta z^* = \beta \Delta \mu_c^{\text{coex}} / (\beta m_c g)$ of the interface, capillary condensation should take place. Taking as an example, $\beta \Delta \mu_c^{\text{coex}} \sim 0.1$ and $(\beta m_c g)^{-1} \sim 1$ m, it becomes clear that, within the context of this (idealized) model, values of $\Delta z^* \sim 0.1$ m should be accessible in experiments, meaning that capillary condensation could in principle be observed. Using smaller matrix particles, with size similar to the size of the colloids (our case $s=1$), the effect of capillary condensation becomes much more pronounced and it should therefore be observable in a similar way as for large matrix particles. From an experimental point of view, however, we think that it is a much larger effort to produce such matrices with low enough packing fractions (see Fig. 4, where we discuss $\eta_m \lesssim 0.2$) in order to be penetrable to the mobile colloids and polymers. We recall the possible realization given in Sec. I using laser tweezers.

C. Phase behavior inside a bulk porous matrix

We now return to the full ternary mixture in bulk, i.e., where in the preceding section, the matrix was only a small sample immersed in a large system of colloid-polymer mixture, in this and the following sections we consider the colloid-polymer mixture in a system-wide matrix. In this sec-

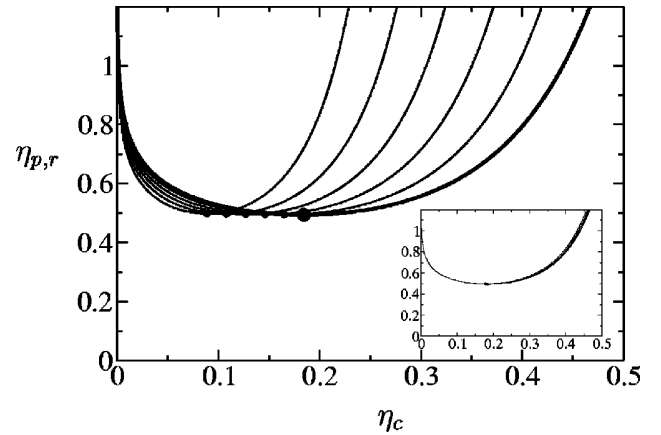


FIG. 5. Same as in Fig. 4, but now for $s=50$. Matrix packing fractions increase from right to left, $\eta_m=0,0.1,0.2,0.3,0.4,0.5$. Inset: same curves now rescaled, i.e., $\eta_{p,r}$ vs $\eta_c/(1-\eta_m)$.

tion, we revisit the demixing phase behavior which we need in the following sections where we study the fluid-fluid interface inside a matrix. Figure 4 is the phase diagram in the polymer-reservoir representation for colloid-sized matrix particles, $s=1$, for various matrix densities. Increasing the matrix packing fraction, there is less volume available to the colloids and the critical point shifts to smaller colloid packing fractions. At the same time, the porous matrix acts to keep the mixture “mixed” and therefore, the critical point shifts to higher polymer fugacities. For the case of $s=1$, we cannot go to much higher packing fractions than $\eta_m \sim 0.2$ as then the critical fugacity shoots up dramatically to unphysically large values. This may be partly due to the relatively large depletion shells around the matrix particles which cause the pore sizes to become too small for the colloids and polymers to enter the matrix. In case of large matrix particles ($s=50$, see Fig. 5), the latter effect is negligible and the pore sizes are always large enough. Consequently, only the excluded volume remains and rescaling the binodals with $(1-\eta_m)$ is very effective practically mapping the binodals onto each other, Fig. 5 (inset). This rescaling is unsuccessful for $s=1$ as can be directly seen from the fact that the critical fugacities in Fig. 4 are different for each of the matrix densities.

In addition, we have determined the nature of the asymptotic decay of pair correlations of the fluid inside the matrix [61]. These can either be monotonic or periodic and the corresponding regions in the phase diagram are separated by the Fisher-Widom (FW) line, at which both types of decay are equally long range. This line can be determined by studying the pole structure of the total correlation functions h_{ij} in Fourier space [61]. In the present case of QA systems, rather than using the usual Ornstein-Zernike equations, one has to use the replica-Ornstein-Zernike (ROZ) equations [50]. Neglecting correlations between the replicas, these are

$$h_{mm}(\mathbf{r}) = c_{mm}(\mathbf{r}) + \rho_m(c_{mm} h_{mm})(\mathbf{r}),$$

$$h_{ij}(\mathbf{r}) = c_{ij}(\mathbf{r}) + \sum_{t=c,p,m} \rho_t(c_{it} h_{tj})(\mathbf{r}), \quad (23)$$

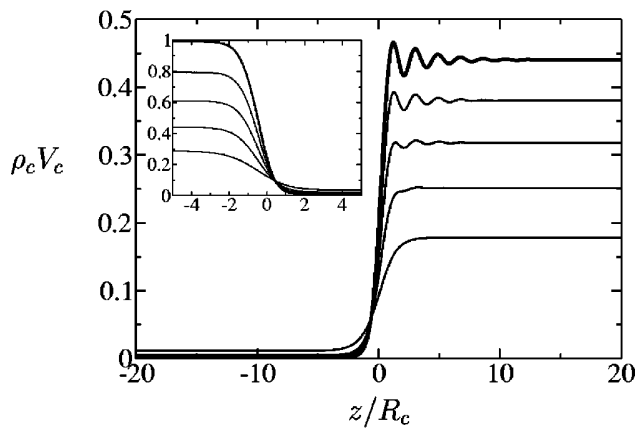


FIG. 6. Colloid density profiles ($V_c = \frac{4}{3}\pi R_c^3$) normal to the free fluid-fluid interface for increasing matrix packing fractions at fixed polymer fugacity. Parameters are $q=0.6$, $s=1$, and $\eta_{p,r}=1$ (see Fig. 4). The matrix packing fraction increases from top (thick profile, $\eta_m=0$) to bottom: $\eta_m=0, 0.05, 0.1, 0.15, 0.2$. Inset: corresponding polymer profiles ($\rho_p V_p$ vs z/R_c , with $V_p = \frac{4}{3}\pi R_p^3$) for the same values of the matrix packing fractions (also increasing from top to bottom).

with $i, j = c, p, m$ except $i = j = m$. Here, for $ij \neq mm$, the $c_{ij}(\mathbf{r}) = -\delta^2 F_{\text{exc}} / \delta \rho_i(\mathbf{r}) \delta \rho_j(\mathbf{r})$ are the direct correlation functions for which we obtain analytic expressions by differentiating Eq. (7). The matrix structure is determined before the quench, so c_{mm} and h_{mm} are those of the normal hard-sphere fluid at density ρ_m (Percus-Yevick-compressibility closure, see Refs. [43,51]). This analysis follows closely that of Ref. [22] in which more details are given. In view of our subsequent interface study, we focus on the point where the FW line meets the binodal. In Fig. 4 ($s=1$), these are denoted by stars, and we observe that the shifts due to the matrices follow the same trend as the critical points. In case of $s=50$, we have not determined the FW lines, but there is no reason to expect the simple rescaling of the case without matrix to fail in this case. Furthermore, concerning the density profiles (in the following section, $s=50$), we stay well within the oscillatory regime.

D. Fluid-fluid profiles inside a bulk porous matrix

We have calculated density profiles at coexistence normal to the colloidal gas-liquid interface. In this case of planar interfaces, the density distribution is only a function of one spatial coordinate z ; i.e., $\rho_i(\mathbf{r}) = \rho_i(z)$. The only dependence on the other two degrees of freedom is in the weights and this can be integrated out, to obtain projected weights, $\tilde{w}_v^i(z) = \int dx dy w_v^i(\mathbf{r})$ (see, e.g., Ref. [62]). The profiles are discretized and calculated via an iteration procedure, i.e., we insert profiles on the right hand side of Eq. (16) and then obtain new profiles on the left hand side, which are then reinserted on the right. Using step functions as iteration seeds, this procedure converges in the (local) direction of the lowest free energy. We normalize the densities as in bulk, i.e., we plot $\rho_i(z) V_i$ so that $\rho_i(\pm\infty) V_i = \eta_i^{(I,II)}$, with I and II referring to the coexisting phases. The zero of z is set at the

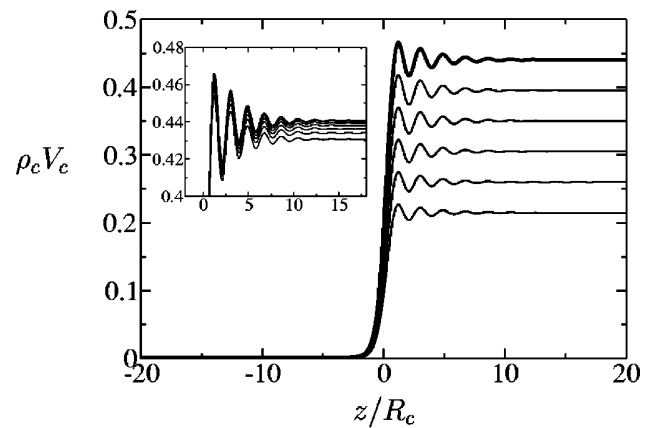


FIG. 7. Same as in Fig. 6 but now for $s=50$. Other parameters are $q=0.6$ and $\eta_{p,r}=1$ (see Fig. 5). The matrix packing fractions increase from top (thick profile, $\eta_m=0$) to bottom: $\eta_m=0, 0.1, 0.2, 0.3, 0.4, 0.5$. Inset: magnification of the rescaled profiles for the same curves, i.e., $\rho_c V_c / (1 - \eta_m)$ vs z/R_c (where again, matrix packing fractions increase from top to bottom).

location of the interface, defined through the Gibbs dividing surface of the colloids: $\int_{-\infty}^0 dz [\rho_c(z) - \rho_c(-\infty)] + \int_0^{\infty} dz [\rho_c(z) - \rho_c(\infty)] = 0$.

In Figs. 6 and 7, we have plotted the colloid profiles normal to the interface for $s=1$ and $s=50$, respectively. Colloid profiles are shown for increasing densities of the matrix at fixed fugacity, $\eta_{p,r}=1$, corresponding to the bulk binodals in Figs. 4 and 5. For the case of $s=1$, this means that, as the critical point shifts to higher fugacities, the profiles are effectively taken at fugacities closer to the critical value. We observe this well-known behavior in Fig. 6; close to the critical point the profiles are smoother and modulations less pronounced. Away from the critical point, the interface is sharp but the periodic modulations due to the surface extend far in the bulk fluid. The inset of Fig. 6 shows the corresponding polymer profiles. In Ref. [58], the main result is that the interface widens due to the porous medium. The same happens here and is due to fact that one is effectively closer to the critical point.

In Fig. 7, as we saw for the bulk phase diagram, there is a simple rescaling at work and the profiles merely differ by a factor $(1 - \eta_m)$. The inset in Fig. 7 shows the same colloid profiles but now rescaled, and we have zoomed in on the region close to the interface. Clearly, even the modulations follow the case without matrix with the same accuracy as the bulk coexistence values in the inset of Fig. 5.

We have also studied the asymptotic decay of correlations with the interface via the density profiles. These must be of the same nature as the decay of the direct correlations in bulk (determined via the ROZ equations, see the preceding section), i.e., either monotonic or periodic [61]. However, determining the crossing points of the FW line with the binodals using the interfacial profiles yields a systematic shift away from the critical point, compared to the bulk calculation ($\sim 5\%$). Probably, this is due to numerical limits. Close to this crossing point both (the periodic and the monotonic) modes of decay are equally strong, so only far away from the

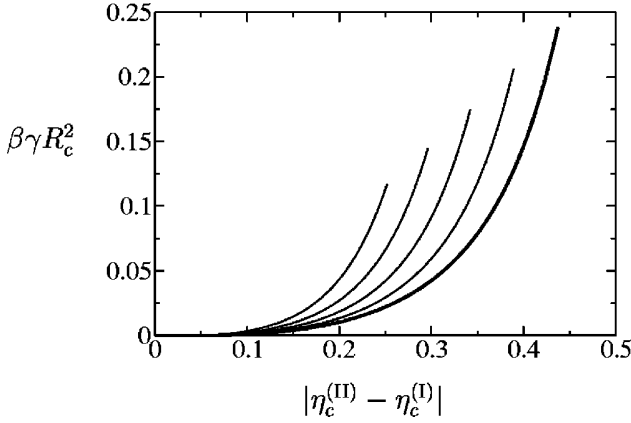


FIG. 8. Fluid-fluid surface tensions vs the difference in colloid packing fractions of the two fluid phases for $q=0.6$, $s=1$, and various values of the matrix packing fraction. The matrix packing fractions increase from right ($\eta_m=0$, thick curve) to left, $\eta_m=0,0.05,0.1,0.15,0.2$. Each curve is computed from the critical point, $\eta_{p,r}=\eta_{p,r}^{(\text{crit})}$ (where $\gamma=0$) until twice the critical fugacity, $\eta_{p,r}=2\eta_{p,r}^{(\text{crit})}$.

interface truly asymptotic behavior may be observed. However, there, the periodic modulations may have become too small to be observable. Furthermore, our numerical routine has no real incentive to minimize the tails of the profiles as the gain in free energy is very low.

E. Fluid-fluid surface tension inside a bulk porous matrix

The presence of the matrix also affects the surface tension between the colloidal liquid and gas phases. The interfacial or surface tension γ of planar interfaces in the grand canonical ensemble is defined through

$$\gamma A = \Omega_{\text{inh}} + PV, \quad (24)$$

where A is the amount of surface area, Ω_{inh} is the grand potential for the inhomogeneous system, and P the pressure (i.e., $-PV$ is the grand potential for the homogeneous bulk system). With our numerical scheme we calculate density profiles in z direction so it makes sense to write the surface tension as an integral,

$$\gamma = \int dz [\omega(z) + P], \quad (25)$$

with

$$\omega(z) = k_B T \sum_{i=c,p} \rho_i(z) [\ln(\rho_i(z)\Delta_i) - 1] - \sum_{i=c,p} \mu_i \rho_i(z) + k_B T \Phi(\{n_v^i(z)\}). \quad (26)$$

The quantity $\omega(z)$ is a “local” grand potential density whose average over space yields the actual grand potential per unit

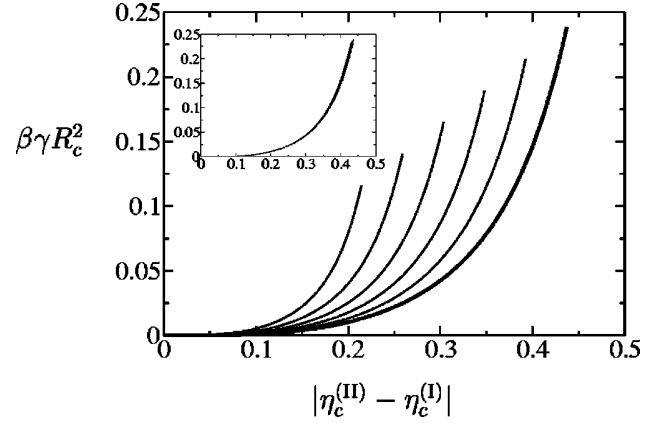


FIG. 9. Same as in Fig. 8 but now for $s=50$. Again, matrix packing fractions increase from right ($\eta_m=0$, thick curve) to left, $\eta_m=0,0.1,0.2,0.3,0.4,0.5$. Each curve is computed from the critical point, $\eta_{p,r}=\eta_{p,r}^{(\text{crit})}$ (where $\gamma=0$) until twice the critical fugacity, $\eta_{p,r}=2\eta_{p,r}^{(\text{crit})}$. Inset: the same (but rescaled) curves are shown, i.e., $\beta\gamma R_c^2/(1-\eta_m)$ vs $|\eta_c^{(\text{II})}-\eta_c^{(\text{I})}|/(1-\eta_m)$.

of volume Ω_{inh}/V . In Figs. 8 and 9 we have plotted the surface tension versus the colloidal density difference in the two phases for $s=1$ and $s=50$, respectively. In both cases the effect of the matrix is that the surface tensions increase faster with the difference $|\eta_c^{(\text{II})}-\eta_c^{(\text{I})}|$ which is of course due to the fact that the coexistence area becomes less wide as the coexisting packing fractions themselves become smaller. In the inset of Fig. 9, we show the same curves rescaled with $(1-\eta_m)$, and the rescaled graphs fall almost on top of the original one without any matrix. Here, we note that also the surface tension has been rescaled with $(1-\eta_m)$; this is needed from Eq. (21) as the free energy density $\omega(z)$ needs to be rescaled as well. Again, this rescaling procedure is not successful for $s=1$.

Often, the surface tension is plotted against the relative distance to the critical point, $(\eta_{p,r}/\eta_{p,r}^{(\text{crit})}-1)$ [27]. However, this does not improve the rescaling for $s=1$ and this can be seen from the fact that the end points of the curves in Figs. 8 and 9 are all at twice the critical fugacity, $\eta_{p,r}=2\eta_{p,r}^{(\text{crit})}$, and the surface tensions (rescaled or not) are at quite different values at the end points.

V. CONCLUSION

We have considered the full ternary system of hard spheres and ideal polymers (represented by the AO model) in contact with a quenched hard-sphere fluid acting as a porous matrix. Using a QA DFT in the spirit of Rosenfeld’s fundamental measure approach, we studied capillary condensation in a small sample of matrix as well as the fluid-fluid interface inside a bulk matrix. The results have been presented in terms of two types of matrices: (i) colloid-sized matrix particles (size ratio $s=1$) being a reference system and (ii) matrix particles which are much larger than the colloids (size ratio $s=50$). The case of small matrix particles is limited to relatively low packing fractions ($\eta_m \sim 0.2$), whereas in the second case, much higher matrix packing fractions are acces-

sible ($\eta_m \sim 0.5$), the pores of the matrix being much larger. Additionally, we have suggested that case (i) as well as (ii) could in principle be realized experimentally in 3D, i.e., using laser tweezers and colloidal sediments, respectively, to serve as a model porous medium for colloidal suspensions.

We have shown that in the limit of infinitely large matrix particles, the standard AO results (without matrix) are recovered via a simple rescaling. In case of $s=50$ our bulk but also the interface results can be mapped onto the case without matrix with high accuracy. However, in the case of small matrix particles ($s=1$) this mapping fails, which is due to the more complex (and smaller) pore geometry on the colloidal scale.

Assuming a more “experimental” point of view, we have considered a small sample of porous matrix immersed in a large system of colloid-polymer mixture. When the fluid-fluid binodal is approached in the colloid-poor region of the phase diagram, capillary condensation occurs in the sample. This transition appears as a capillary line in the phase diagram (in system representation) extending along the binodal and ending in a capillary critical point. In case of small matrix particles, the capillary lines (for various densities of the matrix) are well separated from the bulk binodal but the capillary critical points lie deep into the colloidal gas regime. Concerning the large matrix particles, these capillary critical points are located closer to the bulk critical point, however, the capillary lines are also very close to the binodal. Still, using density-matched colloidal suspensions, we argue that capillary condensation may be observable in experiments.

We have computed fluid-fluid profiles inside the porous matrix as well as the corresponding surface tensions. For $s=50$, these can be mapped onto the case without matrix but for $s=1$ the critical point shifts to higher polymer fugacities. Therefore, increasing the density of the matrix, profiles become smoother due to effective approach of the critical point. Solving the ROZ equations, we have also determined the crossover between monotonic and periodic decay of pair correlations of the mixture inside the matrix for $s=1$. Comparing these with the decay of the interfacial correlations we find a small discrepancy which is probably due to numerical limits.

It should be noted that we do not expect our current approach to satisfactorily describe the (subtle) phenomena associated with wetting of the curved surfaces of the matrix particles by the colloidal liquid [60,63]. Especially for $s=50$ close to the critical point in the complete wetting regime, we can well imagine that the growths of thick films of colloidal liquid on the matrix spheres have a profound influence on the occurrence and precise location of the capillary condensation transition and on the structure of the fluid-fluid interface inside the matrix. We do not expect this effect to be included in our current treatment. Note that in order to obtain the wetting transition at a hard wall [27,28] and at a curved surface [63] inhomogeneous density profiles need to be calculated, which we do not do in our present method of investigation of the bulk phase behavior.

We also note that the attraction between colloids, as well as that between colloids and matrix particles (which is generated by the polymers), arises naturally from our DFT treat-

ment. This depletion attraction, however, has a many-body character for the size ratio considered ($q=0.6$) as multiple overlap between one polymer and three or more colloids can occur; for a discussion of how to obtain an effective Hamiltonian for the colloids by integrating out the polymer degrees of freedom in the equilibrium binary AO model, see Ref. [64]. The presence of many-body effective interactions has a profound influence on phase behavior inside a porous matrix. For a detailed comparison of the bulk phase behavior obtained via the present treatment including all polymer-induced many-body interactions, and one, based on the ROZ equations, that only retains the pairwise contribution to the effective Hamiltonian, see Ref. [51]. A more detailed study of the present approach compared to findings for simple fluids interacting with pairwise attractive forces would be very interesting, but is beyond the scope of the present work.

Concerning the fluid profiles, we have only considered a homogeneous background of matrix particles in this paper. It would be interesting to use inhomogeneous matrix realizations, as, e.g., a step function of zero and nonzero matrix packing fraction (i.e., the interface of empty space and matrix) or a constant matrix background in contact with a hard wall. Both types could give rise to interesting and substantially modified wetting behavior. Additionally, one could also consider other types of matrices, e.g., quenched polymers or combinations of quenched colloids with quenched polymers [43,51]. These are maybe less realistic from an experimental point of view but still interesting due to the competition of capillary condensation with evaporation.

As we have mentioned in the Introduction, there are no experiments concerning phase behavior of colloidal suspensions in contact with 3D porous media to our knowledge. We hope that the accumulating results [7–12,43,51], including those in this paper, may encourage more experimental efforts in that direction. It is important to keep in mind that a suitable porous matrix is a compromise between length scales: large enough to allow penetration of the colloids into the void space, but small enough to retain significant surface and capillary effects. In colloidal fluids in general, these last-mentioned effects are known to be much smaller than in atomic systems, thus providing a formidable challenge to experimentalists aiming to observe, e.g., capillary condensation of a colloidal suspension in a porous matrix.

ACKNOWLEDGMENTS

The authors would like to thank D. G. A. L. Aarts for useful discussions and R. Blaak for a critical reading of the manuscript. M.S. thanks D. L. J. Vossen for detailed explanations of the laser-tweezer setup, T. Gisler for pointing out Refs. [7,8], and R. Evans for valuable remarks. This work was financially supported by the SFB-TR6 program “Physics of colloidal dispersions in external fields” of the *Deutsche Forschungsgemeinschaft* (DFG). The work of M.S. was part of the research program of the *Stichting voor Fun-*

damenteel Onderzoek der Materie (FOM), which is financially supported by the *Nederlandse Organisatie voor Wetenschappelijk Onderzoek* (NWO).

APPENDIX: BULK FLUID FREE ENERGY

The bulk free energy of the colloid-polymer mixture in contact with a homogeneous hard-sphere porous matrix as given in Eq. (19) is

$$f(\eta_c, \eta_p, \eta_m) = \eta_c(\ln \eta_c - 1) + \frac{\eta_p}{q^3}(\ln \eta_p - 1) + f_0(\eta_c, \eta_m) - \frac{\eta_p}{q^3} \ln \alpha(\eta_c, \eta_m). \quad (\text{A1})$$

We note the occurrence of only third and lower powers of $1/s$ in both f_0 and α , which are given by

$$f_0(\eta_c, \eta_m) = \frac{\eta_m}{s^3} \ln(1 - \eta_m) - \left(\frac{\eta_m}{s^3} + \eta_c \right) \ln(1 - \eta_c - \eta_m) + \frac{3\eta_c \eta_m^2 [2 + \eta_c(\eta_m - 2) - 2\eta_m]}{2s^3(1 - \eta_m)^2(1 - \eta_c - \eta_m)^2} + \frac{3\eta_c}{2s^3(1 - \eta_c - \eta_m)^2} \{ \eta_m(2 - 2\eta_c + \eta_m)s + \eta_m(2 + \eta_c - 2\eta_m)s^2 + \eta_c(2 - \eta_c - 2\eta_m)s^3 \} \quad (\text{A2})$$

and

$$\ln \alpha(\eta_c, \eta_m) = \ln(1 - \eta_c - \eta_m) - \frac{q}{2s^3(1 - \eta_c - \eta_m)^3} \{ 2\eta_m [1 + \eta_c^2 + \eta_m + \eta_m^2 - \eta_c(2 + \eta_m)] q^2 - 3\eta_m q [-2 + \eta_m + \eta_m^2 + 2\eta_c^2(-1 + q) - \eta_c(-4 + \eta_m + 2q + 4\eta_m q)] s + 6\eta_m [(1 - \eta_c - \eta_m)^2 + 3\eta_c(1 - \eta_c - \eta_m)q + \eta_c(1 + 2\eta_c - \eta_m)q^2] s^2 + \eta_c \{ -\eta_c(1 - \eta_m)[12 + (3 - 2q)q] + 2(1 - \eta_m)^2[3 + q(3 + q)] + \eta_c^2[6 + q(-3 + 2q)] \} s^3 \}. \quad (\text{A3})$$

-
- [1] R. Evans, *J. Phys.: Condens. Matter* **2**, 8989 (1990).
 [2] L.D. Gelb, K.E. Gubbins, R. Radhakrishnan, and M. Sliwinski-Bartkowiak, *Rep. Prog. Phys.* **62**, 1573 (1999).
 [3] R.G. Smith and G.C. Maitland, *Trans. IChemE, Part A* **76**, 539 (1998).
 [4] R. Hilfer, in *Statistical Physics and Spatial Statistics*, edited by K.R. Mecke and D. Stoyan, Springer Lecture Notes in Physics Vol. 554 (Springer, Berlin, 2000), p. 203.
 [5] K.R. Mecke, *Physica A* **314**, 655 (2002).
 [6] H. Löwen, *J. Phys.: Condens. Matter* **13**, R415 (2001).
 [7] G. Cruz de León, J.M. Saucedo-Solorio, and J.L. Arauz-Lara, *Phys. Rev. Lett.* **81**, 1122 (1998).
 [8] G. Cruz de León and J.L. Arauz-Lara, *Phys. Rev. E* **59**, 4203 (1999).
 [9] S.G.J.M. Kluijtmans, J.K.G. Dhont, and A.P. Philipse, *Langmuir* **13**, 4982 (1997).
 [10] S.G.J.M. Kluijtmans and A.P. Philipse, *Langmuir* **15**, 1896 (1999).
 [11] S.G.J.M. Kluijtmans, G.H. Koenderink, and A.P. Philipse, *Phys. Rev. E* **61**, 626 (2000).
 [12] P. Weroński, J.Y. Walz, and M. Elimelech, *J. Colloid Interface Sci.* **262**, 372 (2003).
 [13] J.P. Hoogenboom, D.L.J. Vossen, C. Faivre-Moskalenko, M. Dogterom, and A. van Blaaderen, *Appl. Phys. Lett.* **80**, 4828 (2002).
 [14] W.C.K. Poon, *J. Phys.: Condens. Matter* **14**, R859 (2002).
 [15] S. Asakura and F. Oosawa, *J. Chem. Phys.* **22**, 1255 (1954).
 [16] S. Asakura and F. Oosawa, *J. Polym. Sci.* **33**, 183 (1958).
 [17] A. Vrij, *Pure Appl. Chem.* **48**, 471 (1976).
 [18] A.P. Gast, C.K. Hall, and W.B. Russell, *J. Colloid Interface Sci.* **96**, 251 (1983).
 [19] M. Dijkstra, J.M. Brader, and R. Evans, *J. Phys.: Condens. Matter* **11**, 10079 (1999).
 [20] H.N.W. Lekkerkerker, W.C.K. Poon, P.N. Pusey, A. Stroobants, and P.B. Warren, *Europhys. Lett.* **20**, 559 (1992).
 [21] M. Schmidt, H. Löwen, J.M. Brader, and R. Evans, *Phys. Rev. Lett.* **85**, 1934 (2000).
 [22] M. Schmidt, H. Löwen, J.M. Brader, and R. Evans, *J. Phys.: Condens. Matter* **14**, 9353 (2002).
 [23] P.G. Bolhuis, A.A. Louis, and J.P. Hansen, *Phys. Rev. Lett.* **89**, 128302 (2002).
 [24] M. Dijkstra and R. van Roij, *Phys. Rev. Lett.* **89**, 208303 (2002).
 [25] A. Vrij, *Physica A* **235**, 120 (1997).
 [26] J.M. Brader and R. Evans, *Europhys. Lett.* **49**, 678 (2000).
 [27] J.M. Brader, R. Evans, M. Schmidt, and H. Löwen, *J. Phys.: Condens. Matter* **14**, L1 (2002).
 [28] J.M. Brader, Ph.D. thesis, University of Bristol, 2001.
 [29] I.O. Götze, J.M. Brader, M. Schmidt, and H. Löwen, *Mol. Phys.* **101**, 1651 (2003).
 [30] E.H.A. de Hoog and H.N.W. Lekkerkerker, *J. Phys. Chem. B* **103**, 5274 (1999).
 [31] E.H.A. de Hoog, H.N.W. Lekkerkerker, J. Schulz, and G.H. Findenegg, *J. Phys. Chem. B* **103**, 10657 (1999).

WESSELS, SCHMIDT, AND LÖWEN

PHYSICAL REVIEW E **68**, 061404 (2003)

- [32] E.H.A. de Hoog, Dissertation, Utrecht University, 2001.
- [33] D.G.A.L. Aarts, J.H. van der Wiel, and H.N.W. Lekkerkerker, *J. Phys.: Condens. Matter* **15**, S245 (2003).
- [34] D.G.A.L. Aarts and H.N.W. Lekkerkerker (private communication).
- [35] W.K. Wijting, N.A.M. Besseling, and M.A. Cohen Stuart, *Phys. Rev. Lett.* **90**, 196101 (2003).
- [36] R. Evans, in *Fundamentals of Inhomogeneous Fluids*, edited by D. Henderson (Dekker, New York, 1992), p. 85.
- [37] L.J.D. Frink, A.G. Salinger, M.P. Sears, J.D. Weinhold, and A.L. Frischknecht, *J. Phys.: Condens. Matter* **14**, 12167 (2002).
- [38] A.G. Salinger and L.J.D. Frink, *J. Chem. Phys.* **118**, 7457 (2003).
- [39] L.J.D. Frink and A.G. Salinger, *J. Chem. Phys.* **118**, 7466 (2003).
- [40] E. Kierlik, P.A. Monson, M.L. Rosinberg, L. Sarkisov, and G. Tarjus, *Phys. Rev. Lett.* **87**, 055701 (2001).
- [41] E. Kierlik, P.A. Monson, M.L. Rosinberg, and G. Tarjus, *J. Phys.: Condens. Matter* **14**, 9295 (2002).
- [42] M.L. Rosinberg, E. Kierlik, and G. Tarjus, *Europhys. Lett.* **62**, 377 (2003).
- [43] M. Schmidt, *Phys. Rev. E* **66**, 041108 (2002).
- [44] Y. Rosenfeld, *Phys. Rev. Lett.* **63**, 980 (1989).
- [45] Y. Rosenfeld, M. Schmidt, H. Löwen, and P. Tarazona, *Phys. Rev. E* **55**, 4245 (1997).
- [46] P. Tarazona, *Phys. Rev. Lett.* **84**, 694 (2000).
- [47] W.G. Madden and E.D. Glandt, *J. Stat. Phys.* **51**, 537 (1988).
- [48] W.G. Madden, *J. Chem. Phys.* **96**, 5422 (1992).
- [49] J.A. Given and G. Stell, *J. Chem. Phys.* **97**, 4573 (1992).
- [50] J.A. Given and G.R. Stell, *Physica A* **209**, 495 (1994).
- [51] M. Schmidt, E. Schöll-Paschinger, J. Köfinger, and G. Kahl, *J. Phys.: Condens. Matter* **14**, 12099 (2002).
- [52] M. Schmidt, *Phys. Rev. E* (to be published).
- [53] M. Schmidt and J.M. Brader, *J. Chem. Phys.* (to be published).
- [54] L. Lafuente and J.A. Cuesta, *Phys. Rev. Lett.* **89**, 145701 (2002).
- [55] M. Schmidt, L. Lafuente, and J.A. Cuesta, *J. Phys.: Condens. Matter* (to be published).
- [56] P.I. Ravikovitch, A. Vishnyakov, and A.V. Neimark, *Phys. Rev. E* **64**, 011602 (2001).
- [57] S. Figueroa-Gerstenmaier, F.J. Blas, J.B. Avalos, and L.F. Vega, *J. Chem. Phys.* **118**, 830 (2003).
- [58] A. Trokhymchuk and S. Sokolowski, *J. Chem. Phys.* **109**, 5044 (1998).
- [59] J. Reszko-Zygmunt, A. Patrykiewicz, S. Sokolowski, and Z. Sokolowska, *Mol. Phys.* **100**, 1905 (2002).
- [60] R. Evans, R. Roth, and P. Bryk, *Europhys. Lett.* **62**, 815 (2003).
- [61] R. Evans, R.J.F. Leote de Carvalho, J.R. Henderson, and D.C. Hoyle, *J. Chem. Phys.* **100**, 591 (1994).
- [62] J.M. Brader, A. Esztermann, and M. Schmidt, *Phys. Rev. E* **66**, 031401 (2002).
- [63] R. Roth and R. Evans (private communication).
- [64] J.M. Brader, M. Dijkstra, and R. Evans, *Phys. Rev. E* **63**, 041405 (2001).

Freezing in the presence of disorder: a lattice study

Matthias Schmidt^{1,3}, Luis Lafuente² and José A Cuesta²

¹ Soft Condensed Matter, Debye Institut, Utrecht University, Princetonpln 5, 3584 CC Utrecht, The Netherlands

² Grupo Interdisciplinar de Sistemas Complejos (GISC), Departamento de Matemáticas, Universidad Carlos III de Madrid, Avenida de la Universidad 30, 28911 Leganés, Madrid, Spain

E-mail: mschmidt@thphy.uni-duesseldorf.de

Received 22 January 2003

Published 27 June 2003

Online at stacks.iop.org/JPhysCM/15/4695

Abstract

We investigate the freezing transition in a two-dimensional lattice model of annealed hard squares that are subject to the influence of randomly placed quenched particles of the same size. The latter model is a porous medium. By combining two recent density functional approaches we arrive at a theory for quenched–annealed lattice fluids that treats the quenched particles on the level of their one-body density distribution. We show that this approach yields thermodynamics that compare well with results from treating matrix realizations explicitly and performing subsequent averaging over the disorder. The freezing transition from a fluid to a columnar phase is found to be continuous. On increasing matrix density it shifts towards close packing and vanishes beyond a threshold matrix density.

1. Introduction

Ordering phenomena, like the freezing transition, in the presence of disorder [1] and confinement [2] are genuinely interesting, as self-organization competes with external constraints. Much work has been devoted to understand liquid condensation in porous media—for recent work see e.g. [3–5], where insight was gained into hysteresis in sorption curves and its relation to the occurrence of a complex free-energy landscape. However, generally speaking the freezing transition under confinement is not as well understood as in the bulk. Thalmann *et al* [6] have investigated a hard sphere fluid in a random pinning potential, finding that the first-order crystallization transition of the pure fluid changes to a continuous glass transition as the strength of the disorder is increased above a critical value. For the same system, Dasgupta and Valls [7] have mapped out regions in the phase diagram corresponding to liquid, glassy and crystalline states. As a theoretical toy one often models disordered, amorphous matrices

³ On leave from: Institut für Theoretische Physik II, Heinrich-Heine-Universität Düsseldorf, Universitätsstraße 1, D-40225 Düsseldorf, Germany.

by quenched (immobilized) configurations of a (model) fluid. Then the adsorbate is annealed (allowed to equilibrate) in the presence of the matrix particles that act as an external potential.

In this work we study freezing in porous media by combining two recent density functional techniques [8], both of which originate from Rosenfeld's fundamental measure theory (FMT) [9], and construct the functional from the zero-dimensional (0D) limit [10]. The first technique is lattice fundamental measure theory (LFMT), which is the generalization of continuum FMT to lattice models [11, 12]. The second technique is a formulation of density functional theory (DFT) where the functional gives directly the free energy averaged over matrix realizations [13]; we refer to this approach as a quenched–annealed (QA) DFT, as the free-energy functional operates on density profiles of both quenched and annealed species. These approaches have been tested before in some situations. In particular, the latter produces results for fluid demixing and liquid structure that compare well with those from integral equation approaches [14]. The comprehensible structure of FMT allows us to derive a DFT for QA lattice fluids. The main motivation for considering such an approach is the computational simplicity of the lattice model over the continuum model. On the lattice it is practical (as will be shown below) to also consider the matrix explicitly as an external potential and minimize the inhomogeneous adsorbate density profile. In the continuum case this would be a daunting task (although some progress has been reported [15]). In essence we follow the same strategy as that in [3–5], albeit not for liquid condensation but for an ordering phase transition. Despite the fact that our main concern is the study of equilibrium properties, we have also checked for the presence of out-of-equilibrium hysteresis in the sorption isotherms.

Hard-body systems provide a paradigm in the study of freezing within statistical mechanics. The simplicity introduced by lattice models, compared to continuum models, led many authors to use them to investigate the liquid–solid transition [16]. Since hard-body systems have no interaction energy in any admissible configuration, the driving force of phase transitions is entropy alone. Thus, calculating the partition function of such systems amounts to counting the number of allowed microscopic configurations compatible with a certain macroscopic state (in a one-component system determined by the density or the fugacity). This task can only be performed in an exact manner for a few models, thus approximate schemes are needed in order to deal with a broad range of models. The most successful theories in this respect are based on combinatorial facts, however this makes the calculation of an approximate entropy a daunting task [17]. The theory we use in this work (LFMT) [12] has the advantage of circumventing the counting task and producing a closed-form density functional from which the thermodynamics and structure can be extracted through the standard routes of DFT. Furthermore, the results obtained are of the same level of accuracy as those produced by the classical approaches [11].

As a simple model for both the adsorbate and the matrix species we use two-dimensional hard square particles. This is just the lattice gas with nearest- and second-nearest-neighbour exclusion on the simple square lattice. This system has been studied before [18–21] but no definitive conclusion has been reached about its phase behaviour. Some authors have claimed it to have a second-order transition [18, 20], others a weaker (third-order) transition [18, 21] and others even no transition at all [18–20]. The only thing that seems clear is the structure near close packing: periodic along one coordinate axis while uniform along the other (i.e. columnar). The period of the density oscillation equals the particle size. The FMT also predicts the columnar phase to be stable and a continuous fluid–columnar transition [12].

We add freely overlapping matrix particles and describe their influence via two different routes. First, we model the matrix as an external potential and minimize the functional explicitly. This is a straightforward application of the equilibrium LFMT; we refer to this as the external potential method. Second, we use the QA DFT and compare results for

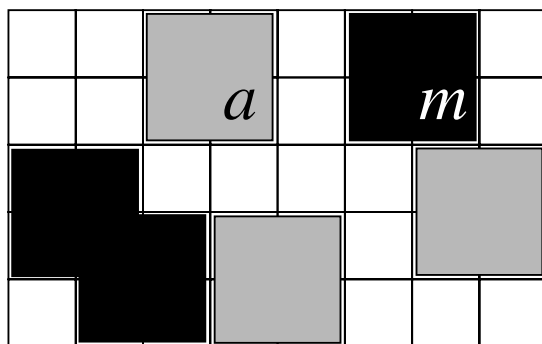


Figure 1. Illustration of the lattice model of adsorbate square particles (grey, species a) and matrix square particles (black, species m) on a two-dimensional cubic lattice. The adsorbate–adsorbate and adsorbate–matrix interactions are hard core; the matrix–matrix interaction is ideal.

thermodynamic quantities, where we find reasonably good agreement over a broad range of densities in the fluid phase. Hence we trust the results for the phase diagram of the QA DFT. This indicates that the fluid–columnar transition remains continuous in the presence of disorder. On increasing the matrix density, the critical density shifts towards close packing and the ordered phase ceases to exist beyond a certain threshold value (very close to the percolation threshold of the matrix).

We do not find any signs for the occurrence of hysteresis in sorption curves, i.e. the same results for the adsorption are obtained whether increasing or decreasing the adsorbate fugacity. We speculate that this is due to the fact that the underlying equilibrium phase transition is continuous.

This paper is organized as follows. We define the lattice hard-body model in section 2. In section 3 we describe both density functional approaches (the details of the derivation of the QA DFT are given in the appendix). Section 4 is devoted to the thermodynamics and phase behaviour, and we conclude in section 5.

2. Model

As an adsorbate we consider square hard-core particles (species a) on a two-dimensional square lattice (with unit-length lattice spacing) that interact by means of a pair potential as a function of the relative distance vector \mathbf{s} of particle centres given by

$$V_{aa}(\mathbf{s}) = \begin{cases} \infty & \text{if } |s_x| < 2 \text{ and } |s_y| < 2, \\ 0 & \text{otherwise.} \end{cases} \quad (1)$$

The adsorbate is subject to the influence of a porous matrix that is modelled by freely overlapping particles (species m) of the same shape as the adsorbate particles. Then the interaction between matrix and adsorbate particles is also $V_{am}(\mathbf{s}) = V_{aa}(\mathbf{s})$. As the matrix consists of freely overlapping particles, it is just an ideal gas, hence $V_{mm}(\mathbf{s}) = 0$. Figure 1 shows a sketch of the model. Notice that ideality of the matrix implies the possibility of multiple occupancy of lattice sites.

We denote the one-body distributions of adsorbate and matrix particles by $\rho_a(\mathbf{s})$ and $\rho_m(\mathbf{s})$, respectively, and the fugacity of the adsorbate particles by z_a .

3. Theory

3.1. Matrix as an external potential

The grand potential functional (in fact a function of the density at the lattice sites) for the system is expressed as

$$\Omega[\rho_a] = F_{id}[\rho_a] + F_{exc}[\rho_a] + \sum_{s \in \mathbb{Z}^2} \rho_a(s) [V_{ext}^{rand}(s) + V_{ext}^{misc}(s) - \mu_a], \quad (2)$$

where $\mu_a = k_B T \ln z_a$ is the adsorbate chemical potential, $k_B T$ being the Boltzmann constant multiplied by the absolute temperature. We have split the external potential into two parts: $V_{ext}^{rand}(s)$ models the presence of the matrix particles; $V_{ext}^{misc}(s)$ is a possible additional contribution such as a gravitational field. (In the following we will restrict ourselves to situations where $V_{ext}^{misc} = 0$.) The ideal free-energy functional in equation (2) is given by

$$F_{id}[\rho_a] = k_B T \sum_{s \in \mathbb{Z}^2} \rho_a(s) \ln[\rho_a(s) - 1]. \quad (3)$$

Following the recent extension of FMT to lattices [11, 12], the excess free-energy functional is approximated as

$$F_{exc}[\rho_a] = k_B T \sum_{s \in \mathbb{Z}^2} [\Phi_0(\text{⊖}_a) - \Phi_0(\text{⊙}_a) - \Phi_0(\text{⊖-⊙}_a) + \Phi_0(\text{⊙}_a)], \quad (4)$$

where the exact 0D excess free energy as a function of the mean number of adsorbate particles, η_a , is

$$\Phi_0(\eta_a) = (1 - \eta_a) \ln(1 - \eta_a) + \eta_a. \quad (5)$$

The arguments in equation (4) are weighted densities, for which we use a diagrammatic notation [22]: each circle corresponds to the density at a lattice point and lines indicate lattice spacings; the subscript i indicates the species (here only a). More explicitly, the weighted densities for species i are given as

$$\text{⊖}_i = \rho_i(s_x, s_y) + \rho_i(s_x + 1, s_y) + \rho_i(s_x, s_y + 1) + \rho_i(s_x + 1, s_y + 1), \quad (6)$$

$$\text{⊙}_i = \rho_i(s_x, s_y) + \rho_i(s_x, s_y + 1), \quad (7)$$

$$\text{⊖-⊙}_i = \rho_i(s_x, s_y) + \rho_i(s_x + 1, s_y), \quad (8)$$

$$\text{⊙}_i = \rho_i(s_x, s_y). \quad (9)$$

As usual in DFT for one-component systems, the equilibrium condition is

$$\frac{\delta \Omega[\rho_a]}{\delta \rho_a(s)} = 0, \quad (10)$$

from which the equilibrium density profile and grand potential are obtained once a matrix realization V_{ext}^{rand} is prescribed.

The average over different matrix realizations is performed subsequently. In practice we use a two-dimensional lattice of 64×64 sites with periodic boundary conditions. A realization of the external potential is generated by randomly placing matrix particles on the lattice:

$$V_{ext}^{rand}(s) = \sum_{s' \in M} V_{am}(s - s'), \quad (11)$$

where M is a set of random lattice sites. Clearly, this yields a discrimination into forbidden and allowed lattice sites. Then, for a given adsorbate fugacity z_a , the Euler–Lagrange equation (10) is solved by a simple iteration procedure. From the converged solution both the grand potential, $\beta \Omega$, where $\beta = 1/(k_B T)$, and the density of the adsorbate, ρ_a , are obtained. This procedure is carried out multiple times and a subsequent average over the disorder is taken. We use 50 independent matrix realizations, which we find to be sufficient.

3.2. Quenched–annealed density functional theory

Here we express the grand potential of the adsorbate in the presence of the quenched matrix particles as

$$\Omega[\rho_m; \rho_a] = F_{id}[\rho_a] + F_{exc}[\rho_m; \rho_a] + \sum_{s \in \mathbb{Z}^2} \rho_a(s) [V_{ext}^{misc}(s) - \mu_a]. \quad (12)$$

This functional is to be minimized only with respect to the adsorbate component,

$$\left. \frac{\delta \Omega[\rho_m; \rho_a]}{\delta \rho_a(s)} \right|_{\rho_m} = 0, \quad (13)$$

while the matrix density field, $\rho_m(s)$, is kept fixed. We remark that the structure of equations (12) and (13) is different from that of DFT for fully annealed systems, whether pure or binary. Although the first and third term on the right-hand side of equation (12) also appear in a one-component theory for ρ_a , the dependence of the excess free energy (second term on the right-hand side of equation (12)) on ρ_m is absent in such a treatment (see equation (2)). In the theory for a fully annealed (equilibrium) binary system, minimization would be required not only with respect to ρ_a but also with respect to ρ_m .

Furthermore, the excess free energy in the current treatment has a fundamentally different meaning to that of the equilibrium case. It includes not only the adsorbate–adsorbate interactions but also the interactions between (annealed) adsorbate and (quenched) matrix particles. It is an approximation for the free energy *averaged* over matrix realizations. As an aside, it differs (in general, but not necessarily) from the free energy of a corresponding equilibrium system, where the matrix is annealed rather than quenched.

Since (12) is a disorder-averaged grand potential, the meaning of the $\rho_a(s)$ resulting from equation (13) differs from that of the solution of equation (10): the latter represents the equilibrium density profile for a given realization of the matrix and will be non-uniform even in fluid phases; the former is an average density profile over matrix realizations and will be uniform in fluid phases.

In [13] the functional $F_{exc}[\rho_m; \rho_a]$ was obtained by first computing the exact excess free energy of a continuum system in a 0D cavity (i.e. one that is so small that all particles inside overlap) and then applying a general procedure to obtain a fundamental measure functional in three dimensions. As equation (4) reflects, a similar procedure to pass from 0D to higher dimensions exists for lattice models [12], which involves evaluating the 0D functional, Φ_0 , for a certain set of 0D cavities (the diagrams (6)–(9)). The derivation of Φ_0 for those cavities in the presence of matrix particles and the subsequent construction of the functional is deferred to the appendix. We quote here that the final functional for an ideal matrix has the form

$$F_{exc}[\rho_m; \rho_a] = k_B T \sum_{s \in \mathbb{Z}^2} [\Phi_0(\text{⊖}_{\circ_m}; \text{⊖}_{\circ_a}) - \Phi_0(\text{⊖}_m; \text{⊖}_a) - \Phi_0(\text{⊖}_{\circ_m}; \text{⊖}_{\circ_a}) + \Phi_0(\text{⊖}_m; \text{⊖}_a)], \quad (14)$$

where the weighted densities are defined in equations (6)–(9) and Φ_0 is a function of the mean numbers of matrix particles, η_m , and adsorbate particles, η_a , given by

$$\Phi_0(\eta_m; \eta_a) = (e^{-\eta_m} - \eta_a) \ln(e^{-\eta_m} - \eta_a) + \eta_a + \eta_m e^{-\eta_m}. \quad (15)$$

In what follows we will be concerned with homogeneous matrices, i.e. those for which $\rho_m(s) = \text{constant}$. This allows us to evaluate the functional (12) and obtain analytical results. Hence, as could already be anticipated from the overall structure, this approach is computationally much simpler than that of the external potential method in section 3.1.

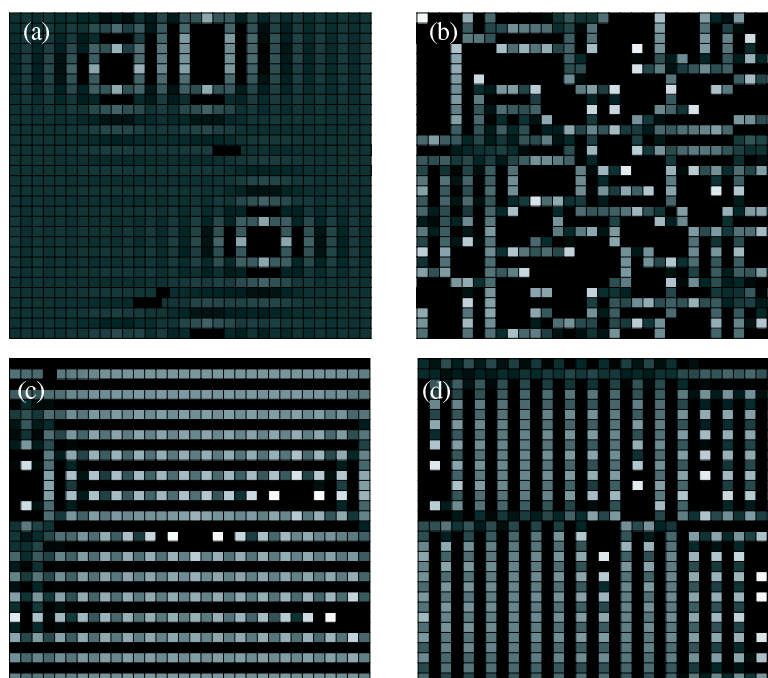


Figure 2. The density profile of the hard square adsorbate in a porous medium. Bright (dark) colours correspond to high (low) values of adsorbate density, ρ_a ; black squares indicate lattice sites that are forbidden due to matrix particles. Fluid (a), (b) and columnar (c), (d) configurations are shown. Adsorbate fugacities and matrix densities are: (a) $z_a = 4$, $\rho_m = 0.00391$; (b) $z_a = 4$, $\rho_m = 0.05078$; (c) $z_a = 16$, $\rho_m = 0.00391$; and (d) $z_a = 16$, $\rho_m = 0.00782$. These snapshots are from lattices with 32×32 sites; the results presented are obtained with 64×64 sites.

4. Results

4.1. Thermodynamics

We start by comparing, over a broad range of densities of both adsorbate and matrix particles, the results from the QA DFT (section 3.2) with those from treating the matrix as an external potential (section 3.1). This serves as a benchmark to assess the accuracy of the QA DFT.

As an illustration, we plot the adsorbate density profiles, $\rho_a(\mathbf{s})$, in figure 2. For clarity we used a smaller system with 32×32 sites. Fluid configurations for low (a) and moderate (b) matrix densities are shown. As expected, the matrix causes inhomogeneities in the adsorbate density profile. For small ρ_m this is only a weak perturbation, but for larger ρ_m a highly irregular distribution results.

We first consider the change in grand potential due to the presence of the matrix. In particular, we consider the change in grand potential per matrix particle, $\beta[\Omega(\rho_m) - \Omega(\rho_m = 0)]/N_m$, where N_m is the number of matrix particles, along a path of increasing ρ_m and fixed fugacity of the adsorbate, z_a . In figure 3 results are shown for $z_a = 0.2, 1, 4, 10, 20, 60$ and for matrix densities in the range $\rho_m = 0-0.25$. Were the interaction between matrix particles that of hard bodies, $\rho_m = 0.25$ would correspond to close packing; the ideality, however, causes a void structure with non-zero free volume. The agreement is remarkably good up to $z_a = 10$ (corresponding to moderate adsorbate densities) in the entire range of ρ_m . At and above this

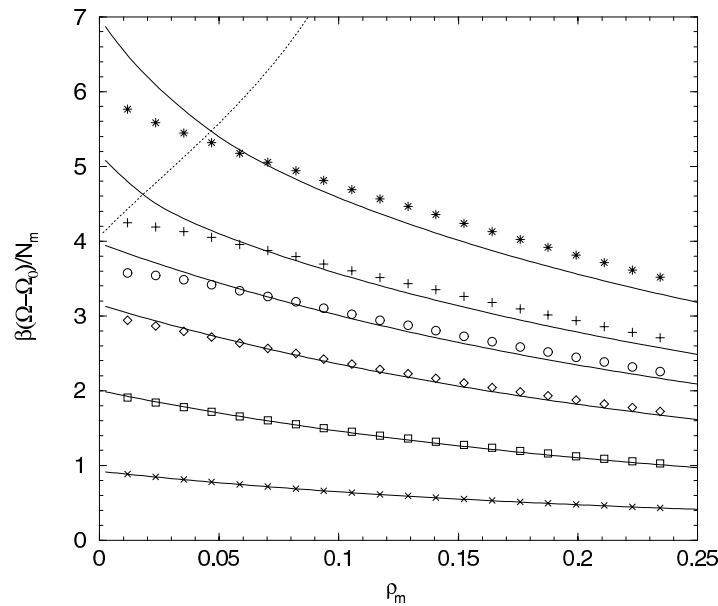


Figure 3. The change in grand potential, $\beta[\Omega - \Omega(\rho_m = 0)]/N_m$, due to the presence of matrix particles as a function of matrix density ρ_m for prescribed adsorbate fugacities $z_a = 0.2, 1, 4, 10, 20, 60$. Solid curves are from the QA DFT; the symbols are from treating the matrix as an external potential and averaging over explicit matrix configurations. Dashed curves depict the over-imposed phase diagram of figure 5 (adapted to represent the change in grand potential versus ρ_m).

value, deviations become more and more pronounced. Those occurring at low ρ_m are very significant: they may reveal the inherent inaccuracy of the external potential method due to the small system size.

Next we investigate the adsorbate density, ρ_a , for prescribed z_a and increasing ρ_m ; results are shown in figure 4. The agreement is also good for z_a up to 10; above that value there are deviations for high matrix densities, $\rho_m > 0.1$, where the QA DFT over-estimates ρ_a .

Despite the discrepancies between the two approaches, we should acknowledge that the overall agreement is sufficiently good to take the QA functional seriously. Besides, we want to stress that it is not clear *a priori* which of the two methods is more accurate. It will be shown below by considering order parameters (figure 6) that considerable finite-size effects are present in the external potential method. Those may partly account for the discrepancy. It would be interesting to compare our results with those from computer simulations that would serve as a benchmark.

4.2. Phase diagram

Having thus gained confidence in the QA DFT, we will use it to calculate phase behaviour, which would be a challenging task with the external potential method. In the absence of the matrix, the LFMT predicts a second-order transition from a fluid phase to a columnar phase [12]. For small but non-zero ρ_m this continuous phase transition persists. In figure 5 the phase diagram is plotted as a function of ρ_a and ρ_m . For $\rho_m = 0$ the critical density and fugacity are $\rho_a^{crit} = (3 - \sqrt{5})/4 = 0.19098$ and $z_a^{crit} = (11 + 5\sqrt{5})/2 = 11.0902$ [12]. This result is compatible with that obtained by Bellemans and Nigam [18] using Rushbrooke

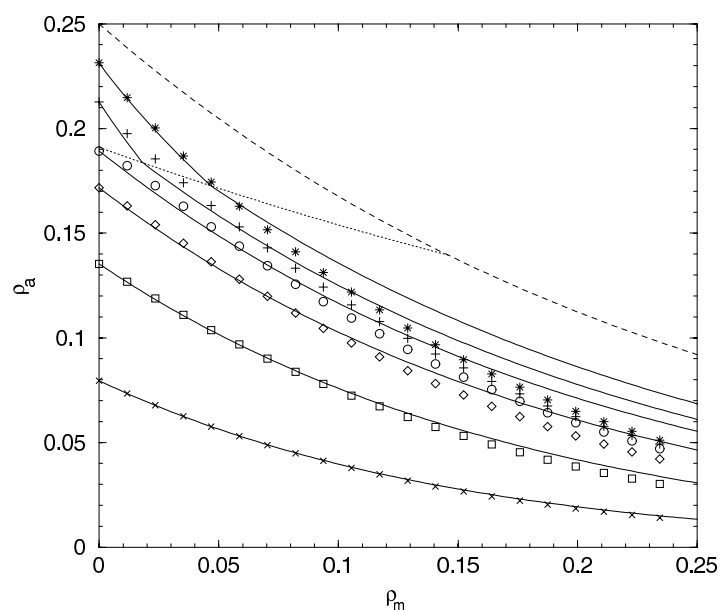


Figure 4. The adsorbate density ρ_a inside a porous matrix of density ρ_m for different adsorbate fugacities $z_a = 0.2, 1, 4, 10, 20, 60$. Solid curves indicate results from the QA DFT; symbols are from treating the matrix as an external potential. Dashed curves depict the over-imposed phase diagram of figure 5.

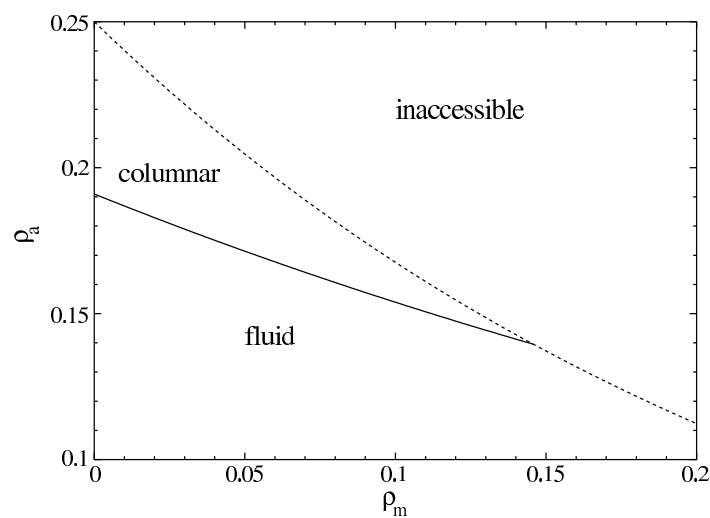


Figure 5. The phase diagram of hard squares of density ρ_a in a matrix of freely overlapping squares of density ρ_m . The solid curve indicates a continuous phase transition from fluid to columnar; the transition density ρ_a^{crit} is given by equation (18). The dashed curve indicates close packing, given by equation (20). Both curves meet at $\rho_m^* = 0.14580$, $\rho_a^* = 0.13953$; for larger ρ_m the fluid is the only stable phase.

and Scoins' method [23]. They also found a second-order transition but at slightly different parameters, namely $\rho_a^{crit} = 0.20175$ and $z_a^{crit} = 17.2878$.

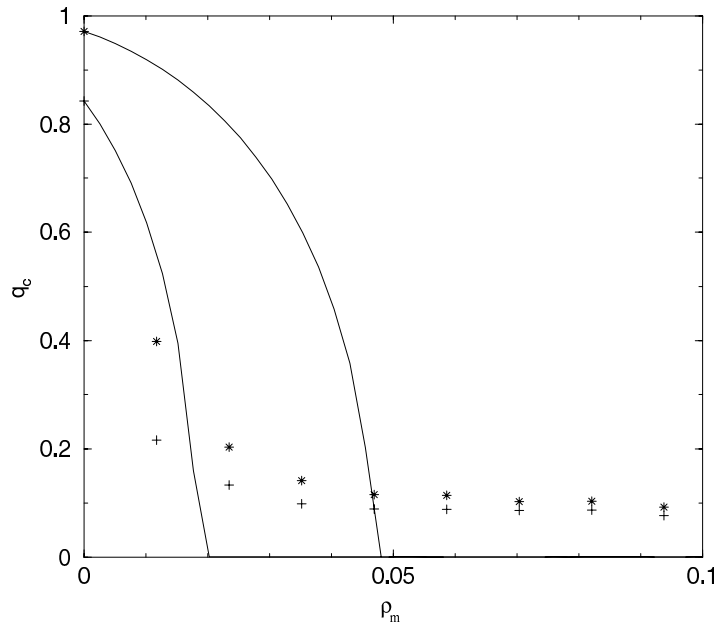


Figure 6. The columnar order parameter q_c of equation (21) computed for varying matrix density ρ_m and at constant adsorbate fugacity ($z_a = 20$ and 60). Curves are obtained from the QA density functional (top $z_a = 60$; bottom $z_a = 20$) and stars ($z_a = 60$) and pluses ($z_a = 20$) are the values computed with the random matrix approach averaged over 50 matrix realizations. Notice the strong finite-size effect in the fluid regions (where q_c should vanish).

The transition to a columnar phase can be studied by particularizing the functional (14) to a density profile which is uniform along columns that alternately take values ρ_1 and $2\rho_a - \rho_1$. The fluid phase corresponds to $\rho_1 = \rho_a$. The result is the free-energy density

$$\begin{aligned} \beta F V^{-1} = & \frac{\rho_1}{2} \ln \rho_1 + \left(\rho_a - \frac{\rho_1}{2} \right) \ln(2\rho_a - \rho_1) - \rho_a + \Phi_0(4\rho_m; 4\rho_a) \\ & - \Phi_0(2\rho_m; 2\rho_a) - \frac{1}{2} \Phi_0(2\rho_m; 2\rho_1) - \frac{1}{2} \Phi_0(2\rho_m; 4\rho_a - 2\rho_1) \\ & + \frac{1}{2} \Phi_0(\rho_m; \rho_1) + \frac{1}{2} \Phi_0(\rho_m; 2\rho_a - \rho_1), \end{aligned} \tag{16}$$

where V is the number of lattice sites (i.e. the system ‘volume’). Minimizing with respect to ρ_1 leads to a third-degree polynomial in ρ_1 , one of whose roots is ρ_a (corresponding to the fluid phase); of the other two, one is

$$\rho_1 = \rho_a + \sqrt{\frac{(e^{-2\rho_m} - 2\rho_a)(\rho_a - \rho_a^{crit})(\frac{3}{2}e^{-\rho_m} - \rho_a^{crit} - \rho_a)}{2\rho_a + (1 - e^{-\rho_m})e^{-\rho_m}}} \tag{17}$$

and the other one $2\rho_a - \rho_1$, where

$$\rho_a^{crit} = \frac{3}{4}e^{-\rho_m}(1 - \sqrt{1 - (4/9)e^{-\rho_m}}). \tag{18}$$

These two roots are real whenever $\rho_a^{crit} \leq \rho_a \leq e^{-2\rho_m}/2$ (the upper bound is never reached because it is higher than the close-packed density; cf equation (20) below); this means that alternating columns have different densities, thus ρ_a^{crit} is the critical density of the continuous fluid–columnar transition.

Isofugacity curves are obtained as

$$z_a = \frac{(e^{-2\rho_m} - 2\rho_a)^2 (e^{-2\rho_m} - 2\rho_1)^2 \rho_1}{(e^{-4\rho_m} - 4\rho_a)^4 (e^{-\rho_m} - \rho_1)} \tag{19}$$

where $\rho_1 = \rho_a$ for $\rho_a < \rho_a^{crit}$ and ρ_1 is given by (17) for $\rho_a \geq \rho_a^{crit}$; thus z_a^{crit} results from substituting $\rho_1 = \rho_a = \rho_a^{crit}$ in this expression. As $\rho_a \leq \rho_1 < 2\rho_a$ and $e^{-\rho_m} \geq e^{-4\rho_m}$, on increasing ρ_a the fugacity z_a diverges at

$$\rho_a^{cp} = \exp(-4\rho_m)/4, \tag{20}$$

the close-packed density. This result has a very clear physical meaning: $4\rho_a$ is the packing fraction of the adsorbate particles and $\exp(-4\rho_m)$ is the free volume left by the matrix particles; according to (20), close packing is reached when both are equal. This result is expected if the surface is negligible with respect to volume, so the true close-packed density must deviate from this prediction whenever the matrix consists of an ensemble of relatively small cavities.

The two curves $\rho_a^{crit}(\rho_m)$ and $\rho_a^{cp}(\rho_m)$ meet at $\rho_m^* = 0.14580$. This means that, for $\rho_m > \rho_m^*$, the columnar phase ceases to exist and only the fluid phase is stable. In order to understand the meaning of this special value of ρ_m we can relate it to the percolation threshold of the matrix. We do not know the precise value for this threshold, but we can check that of similar models: for 2×2 hard squares the estimated site percolation threshold is $\rho = 0.155$ [24], while a quarter of that of an ordinary lattice gas (squares occupy four sites) is $\rho = 0.148$ [25]. Both values are very close to ρ_m^* . This suggests that the disappearance of the fluid–columnar transition at this matrix density is associated with the splitting of the free volume left by the matrix into a disconnected ensemble of meso- and microscopic cavities within which the adsorbate is confined. Further investigations of the true percolation threshold for this particular matrix would be needed to settle this point.

Although we have not attempted to calculate the phase diagram using the external potential method, we have been able to check the phase that the system exhibits with the help of two order parameters. If we divide the lattice into four sublattices—such that sublattice 1 is formed by all sites, s , with even s_x and even s_y ; sublattice 2 by those with even s_x and odd s_y ; sublattice 3 by those with odd s_x and odd s_y , and sublattice 4 by those with odd s_x and even s_y —and compute the average of the density in every sublattice, q_i ($i = 1, 2, 3, 4$), then the order parameters are defined as

$$q_c = \frac{1}{2\rho_a} \sqrt{|q_1 - q_3||q_2 - q_4|}, \tag{21}$$

$$q_s = \frac{1}{4\rho_a} |q_1 + q_3 - q_2 - q_4|. \tag{22}$$

Clearly, q_c is non-zero only in a columnar phase while it vanishes in the fluid and solid phases, and q_s is non-zero only in a solid phase while it vanishes in the fluid and columnar phases. Normalization is chosen so that $0 \leq q_{c,s} \leq 1$. These order parameters are also averaged over matrix realizations.

The first observation to be made is that both order parameters are affected by strong finite-size effects, so that they fluctuate around 0.1 when they should vanish. Apart from that, q_s is never found to increase anywhere in the phase diagram, while q_c rises rather close to the points where the fluid–columnar transition is predicted (see figure 6). The precise values of q_c in the columnar phase deviates from the analytical curves derived from the QA functional, but the region where this occurs is such a narrow gap in ρ_m and contains so few points that it is hard to tell how much of this deviation is due to the strong finite-size effect.

To give an illustration of what an ordered phase in a random matrix looks like, we present density profiles for the columnar phase in figures 2(c) and (d). In figure 2(c) the columns are

horizontal. Matrix particles generate a disturbance, mainly along the columns, which decays with distance.

We have confirmed the prediction of the external potential method that the solid phase is less stable than the columnar phase. To this purpose we have carried out an analysis similar to that performed for the columnar phase, but for a solid-like density profile. We have found that, for any $0 \leq \rho_m \leq \rho_m^*$, the solid—like the columnar—is more stable than the fluid for densities $\rho_a > \rho_a^{crit}$, but its free energy is larger than that of the columnar all the way up to close packing.

The location of the columnar phase with the help of the order parameters has allowed us to check for the existence of hysteresis. As in [3–5], for a given matrix density in the range $0 < \rho_m < \rho_m^*$ we have started off from a converged density profile at a low fugacity z_a and used it as the initial configuration to converge the density profile at a slightly higher z_a . We have iterated this procedure, making sure to be well in the columnar phase, and then repeated the whole process by decreasing z_a . For the convergence criterion from iteration step n to $n + 1$ we used $\max_i |\rho_i^{(n+1)} - \rho_i^{(n)}| < 10^{-5}$. (Notice that Kierlik *et al* used $(1/N) \sum_i (\rho_i^{(n+1)} - \rho_i^{(n)})^2 < 10^{-8}$, which is milder than ours: the square root of this is less than 10^{-4} and there is an average over lattice sites; we take the worst case instead.) We performed this analysis at a single value of $\rho_m = 0.03$ where we are certain that, by increasing sufficiently the fugacity, the columnar phase is stable. We find that the two curves $\rho_a(z_a)$ thus obtained coincide, showing no sign of hysteresis. In the light of the study carried out in [3–5], this may be justified by the continuous character of the fluid–columnar transition of this model.

One final remark concerns the close packing. In figures 3 and 4 we have over-imposed the phase diagram obtained from the QA functional. Although the higher fugacity considered is $z_a = 60$, it is very clear that the close packing predicted by equation (20) strongly over-estimates that obtained from the external potential approach (for a few large values of ρ_m we have increased z_a up to 1000; the resulting values are very close to those obtained for $z_a = 60$ —still very far from the close packing). It is not difficult to understand what happens. For (20) to hold, it is necessary that surface contributions are negligible compared to bulk contributions. But for large ρ_m the fluid is confined in an ensemble of (relatively small) cavities, so both contributions are comparable and (20) becomes a bad estimate for the close-packed density. The percolation threshold of the matrix is then an upper bound for the limit of validity of the QA functional, at least for high adsorbate densities.

5. Conclusions

In conclusion, we have considered the freezing of a hard-body lattice model in a porous medium. The latter is modelled as immobilized configurations of freely overlapping particles (or others—see appendix) which have the same size as the adsorbate particles. We have combined two recent density functional approaches to obtain the thermodynamics of the system via two routes. First, we treat the matrix as an external potential and minimize the free energy explicitly for many such matrix realizations. Subsequently, an explicit average over the different matrix realization is performed. The second route is direct via a DFT for mixtures of quenched and annealed species and gives the *average* free energy directly. The functional is constructed using the FMT recipe to generate a higher-dimensional theory from the 0D limit—an idealized situation where the many-body problem can be solved exactly. The second approach is computationally much simpler. We compare results for the free energy and the equation of state from both approaches and find reasonable agreement over a large density regime. Some deviations are apparent at high densities, but the overall agreement is quite good.

We note that the present combination of the lattice theory with the QA DFT indicates that the FMT is a flexible toolbox, where different components can be combined systematically.

For the present model we have not found any indications for the occurrence of hysteresis in sorption curves. We believe this is related to the fact that the model undergoes a continuous phase transition. The principal route that we followed in this work is applicable to other (also three-dimensional) lattice models [11, 12] that display first-order phase transitions. It would be interesting to address questions like hysteresis and the relation with the occurrence of metastable states in future work.

Acknowledgments

MS thanks Martin-Luc Rosinberg, Gilles Tarjus and Hartmut Löwen for useful discussions and acknowledges support from the Deutsche Forschungsgemeinschaft within the SFB TR6. The work of MS is part of the research program of the Stichting voor Fundamenteel Onderzoek der Materie (FOM), which is supported financially by the Nederlandse Organisatie voor Wetenschappelijk Onderzoek (NWO). LL's and JAC's work is part of the project BFM2000-0004 of the Ministerio de Ciencia y Tecnología (Spain).

Appendix. Construction of the quenched–annealed fundamental measure functional

The present lattice case allows us to make the construction of a QA fundamental measure functional more explicit than in the continuum case [13]. In the latter, one uses idealized 0D cavities, represented by delta-spike density distributions. On the lattice, however, one is able to treat cavities with varying shapes extending over several lattice sites (not just a single lattice site). Such cavities are still 0D, in the sense that placing two particles at arbitrary sites within the cavity induces pair overlap. We are led to consider such cavities due to the particular structure of the lattice fundamental measure functional (4): weighted densities are nothing but the probability of finding a fluid particle in the cavity defined by the diagrams, given that the density profile of the fluid is $\rho_a(s)$. In the following we make this fully explicit. This will allow us to also treat other pair interactions representing, alternatively to the ideal case, point and hard square matrix particles.

So let us start by considering a particular 0D cavity for the adsorbate, \mathcal{C} . As in [13], we must determine $p(\mathcal{C}) = \Xi_m(\mathcal{C})^{-1}$, the probability that the cavity is devoid of matrix particles, where $\Xi_m(\mathcal{C})$ is the grand partition function of the matrix particles in the cavity \mathcal{C} . A 0D cavity for the adsorbate does not mean a 0D cavity for the matrix particles: due to the different interaction potential, \mathcal{C} may allocate more than one matrix particle at the same time. Once $p(\mathcal{C})$ is determined, the grand potential of the adsorbate in the cavity will be given by

$$\beta\Omega^{0d} = -p(\mathcal{C}) \ln[1 + z_a(\mathcal{C})], \tag{A.1}$$

where $z_a(\mathcal{C}) \equiv \sum_{s \in \mathcal{C}} z_a(s)$, with $z_a(s) = z_a e^{-\beta V_{ext}(s)}$ the ‘local’ fugacity of the adsorbate. From this,

$$\rho_a(s) = -z_a(s) \frac{\delta\beta\Omega^{0d}}{\delta z_a(s)} = p(\mathcal{C}) \frac{z_a(s)}{1 + z_a(\mathcal{C})}, \tag{A.2}$$

thus

$$z_a(\mathcal{C}) = \frac{\rho_a(\mathcal{C})}{p(\mathcal{C}) - \rho_a(\mathcal{C})} \tag{A.3}$$

where $\rho_a(\mathcal{C}) \equiv \sum_{s \in \mathcal{C}} \rho_a(s)$, and

$$\beta\Omega^{0d} = -p(\mathcal{C}) \ln p(\mathcal{C}) + p(\mathcal{C}) \ln[p(\mathcal{C}) - \rho_a(\mathcal{C})]. \tag{A.4}$$

Therefore the excess free energy of the OD cavity will be given by

$$\beta F_{exc}^{0d} = \beta \Omega^{0d} + \sum_{s \in \mathcal{C}} [\rho_a(s) \ln z_a(s) - \rho_a(s) \ln \rho_a(s) + \rho_a(s)] \tag{A.5}$$

$$= \Phi_0(p(\mathcal{C}); \rho_a(\mathcal{C})), \tag{A.6}$$

where

$$\Phi_0(p(\mathcal{C}); \eta) \equiv \eta + [p(\mathcal{C}) - \eta] \ln [p(\mathcal{C}) - \eta] - p(\mathcal{C}) \ln p(\mathcal{C}). \tag{A.7}$$

As in equation (4), the functional will be given by

$$F_{exc}[\rho_m; \rho_a] = \sum_{s \in \mathbb{Z}^2} [\Phi_0(p(\text{circ}); \text{circ}_a) - \Phi_0(p(\text{circ}); \text{circ}_a) - \Phi_0(p(\text{circ}); \text{circ}_a) + \Phi_0(p(\text{circ}); \text{circ}_a)]. \tag{A.8}$$

The diagrams used as arguments of p are meant to denote the OD cavities formed by the lattice nodes defining the corresponding weighted densities, cf equations (6)–(9).

It only remains to determine $p(\mathcal{C})$ in terms of $\rho_m(s)$ to complete the description. For that purpose we must compute $\Xi_m(\mathcal{C})$ for the three types of interaction potentials between matrix particles:

$$(a) \text{ ideal: } V_{mm}(s) = 0, \tag{A.9}$$

$$(b) \text{ points: } V_{mm}(s) = \begin{cases} \infty & \text{if } s_x = s_y = 0, \\ 0 & \text{otherwise,} \end{cases} \tag{A.10}$$

$$(c) \text{ squares: } V_{mm}(s) = \begin{cases} \infty & \text{if } |s_x| < 2 \text{ and } |s_y| < 2, \\ 0 & \text{otherwise.} \end{cases} \tag{A.11}$$

In the ideal case (a),

$$\Xi_m(\mathcal{C}) = e^{z_m(\mathcal{C})}, \quad \rho_m(s) = z_m(s), \tag{A.12}$$

and therefore

$$p(\mathcal{C}) = e^{-\rho_m(\mathcal{C})}. \tag{A.13}$$

In the points case (b),

$$\Xi_m(\mathcal{C}) = \sum_{N=0}^{|\mathcal{C}|} z_m^N Z_N(\mathcal{C}), \tag{A.14}$$

where $Z_N(\mathcal{C})$ is the partition function of N matrix particles in the cavity \mathcal{C} made of $|\mathcal{C}|$ lattice sites. If we order these sites from 1 to $|\mathcal{C}|$, then this partition function is easily expressed as

$$z_m^N Z_N(\mathcal{C}) = \sum_{s_1 < s_2 < \dots < s_N} z_m(s_1) z_m(s_2) \dots z_m(s_N), \tag{A.15}$$

hence

$$\Xi_m(\mathcal{C}) = \prod_{s \in \mathcal{C}} [1 + z_m(s)]. \tag{A.16}$$

Now, from this grand partition function,

$$\rho_m(s) = \frac{z_m(s)}{1 + z_m(s)}, \quad z_m(s) = \frac{\rho_m(s)}{1 - \rho_m(s)}; \tag{A.17}$$

therefore

$$p(\mathcal{C}) = \prod_{s \in \mathcal{C}} [1 - \rho_m(s)] = e^{-\rho_m^*(\mathcal{C})}, \tag{A.18}$$

where we have made clear that $p(C)$ has the same expression as in the ideal case in terms of the new densities $\rho_m^*(s) \equiv -\ln[1 - \rho_m(s)]$. This makes sense if we take into account that the configuration of the ideal case corresponds to the configuration of this case with multiple occupancy of the sites. So, despite its higher complexity, this case maps trivially to the ideal case.

Finally, for the squares case (c), matrix and adsorbate particles have the same interaction potential, so

$$\Xi_m(C) = 1 + z_m(C), \quad \rho_m(s) = \frac{z_m(s)}{1 + z_m(C)}, \quad z_m(C) = \frac{\rho_m(C)}{1 - \rho_m(C)}, \quad (\text{A.19})$$

and therefore

$$p(C) = 1 - \rho_m(C). \quad (\text{A.20})$$

Substituting in (A.8) the expressions of $p(C)$ obtained for the two nontrivial cases (a) and (c), we end up with the expression (14), where $\Phi_0(\eta_m; \eta_a)$ is given by (15) for the ideal case (a) and by $\Phi_0(\eta_m; \eta_a) = (1 - \eta_m - \eta_a) \ln(1 - \eta_m - \eta_a) + \eta_a + \eta_m - (1 - \eta_m) \ln(1 - \eta_m)$ for the squares case (c).

References

- [1] Gelb L D, Gubbins K E, Radhakrishnan R and Sliwinski-Bartkowiak M 1999 *Rep. Prog. Phys.* **62** 1573
- [2] Evans R 1990 *J. Phys.: Condens. Matter* **2** 8989
- [3] Kierlik E, Monson P A, Rosinberg M L, Sarkisov L and Tarjus G 2001 *Phys. Rev. Lett.* **87** 055701
- [4] Kierlik E, Monson P A, Rosinberg M L and Tarjus G 2002 *J. Phys.: Condens. Matter* **14** 9295
- [5] Rosinberg M L, Kierlik E and Tarjus G 2003 *Europhys. Lett.* **62** 377 (*Preprint cond-mat/0206108*)
- [6] Thalmann F, Dasgupta C and Feinberg D 2000 *Europhys. Lett.* **50** 54
- [7] Dasgupta C and Valls O T 2000 *Phys. Rev. E* **62** 3648
- [8] Evans R 1992 *Fundamentals of Inhomogeneous Fluids* ed D Henderson (New York: Dekker) p 85
- [9] Rosenfeld Y 1989 *Phys. Rev. Lett.* **63** 980
- [10] Tarazona P and Rosenfeld Y 1997 *Phys. Rev. E* **55** R4873
- [11] Lafuente L and Cuesta J A 2002 *Phys. Rev. Lett.* **89** 145701
- [12] Lafuente L and Cuesta J A 2002 *J. Phys.: Condens. Matter* **14** 12079
- [13] Schmidt M 2002 *Phys. Rev. E* **66** 041108
- [14] Schmidt M, Schöll-Paschinger E, Köfinger J and Kahl G 2002 *J. Phys.: Condens. Matter* **14** 12099
- [15] Frink L J, Salinger A G, Sears M P, Weinhold J D and Frischknecht A L 2002 *J. Phys.: Condens. Matter* **14** 12167
- [16] Runnels L K 1972 *Phase Transitions and Critical Phenomena* vol 2, ed C Domb and M S Green (London: Academic) ch 8 p 305
- [17] Burley D M 1972 *Phase Transitions and Critical Phenomena* vol 2, ed C Domb and M S Green (London: Academic) ch 9 p 329
- [18] Bellemans A and Nigam R K 1967 *J. Chem. Phys.* **46** 2922
- [19] Nisbet R M and Farquhar I E 1974 *Physica* **73** 351
- [20] Slotte P A 1983 *J. Phys. C: Solid State Phys.* **16** 2935
- [21] Ree F H and Chesnut D A 1967 *Phys. Rev. Lett.* **18** 5
- [22] Lafuente L and Cuesta J A 2003 *Preprint cond-mat/0306221*
- [23] Rushbrooke G S and Scoins H I 1955 *Proc. R. Soc. A* **230** 74
- [24] Binder K and Landau D P 1980 *Phys. Rev. B* **21** 1941
- [25] Stauffer D and Aharony A 1994 *Introduction to Percolation Theory* revised 2nd edn (London: Taylor and Francis)

Density-functional theory for soft interactions by dimensional crossover

Matthias Schmidt

Institut für Theoretische Physik II, Heinrich-Heine-Universität Düsseldorf, Universitätsstraße 1, D-40225 Düsseldorf, Germany

(Received 22 June 1999)

A density-functional theory for spherical particles interacting via an arbitrary soft pair potential is presented. The derivation is solely based on limits, where the behavior is exactly known, namely, a zero-dimensional cavity and the low-density virial expansion. The approach generalizes the fundamental-measure theory for hard bodies and yields the structure and thermodynamics of the homogeneous fluid as an output. We apply the theory to an ultrasoft logarithmic potential that mimics star polymers in a good solvent. The theory, when supplemented by a rescaling procedure, reproduces the peculiar features of the pair correlations in this system that we also find in computer simulations. [S1063-651X(99)50712-5]

PACS number(s): 61.20.Gy, 64.10.+h, 61.25.Hq, 05.20.Jj

Particles interacting via soft pair potentials build up a general class of statistical systems ranging from the Coulomb interaction of charged bodies, the screened Coulomb or Yukawa potential present in suspensions of charged colloidal particles to inverse-power potentials [1]. Another important example is the Lennard-Jones potential that describes the noble gases accurately. In the context of soft matter one is faced with a zoo of potentials acting on a mesoscopic length scale. Two examples are the depletion potential that acts between large spheres immersed in a suspension of small spheres [2] and the ultrasoft repulsive logarithmic potential between star polymers [3]. These examples clarify that a soft potential is a pairwise interaction that is finite everywhere except for a possible singularity at the origin. The counterpart of soft potentials are hard-body interactions, as in the famous hard sphere system. The interaction in these systems is infinite once two particles overlap. There are elaborate theories dealing with these purely entropic forces.

We propose a generalization of a successful density-functional theory (DFT) for hard bodies, the so-called fundamental-measure theory (FMT), to soft potentials. The FMT approach has proven to describe accurately the structure and thermodynamics of hard bodies, as hard spheres [4,5], or aligned hard cubes [6,7]. It is able to yield the structure of the homogeneous fluid, namely, the pair correlation function as an output rather than needing it as an input as other DFTs do [8]. In the case of hard spheres the resulting fluid structure is the same as the solution of the Percus-Yevick closure relation. Also the freezing transition into a face-centered cubic crystal is captured correctly [4,5].

The FMT has also been used to deal with soft potentials. In these approaches it is used to describe the hard spheres as a reference system for a perturbation theory, e.g., via the assumption of universality of the bridge functional [9]. Concerning non-FMT approaches for soft potentials there is a large literature of successful applications; see the reviews by Singh [10], Evans [8], and Löwen [1]. Recently, Kol and Laird studied the inverse-power potentials [11].

We attempt to find a generalization of the FMT to soft potentials. Let us therefore first outline the major features of the FMT. The FMT is a weighted density approximation (WDA). In this approach a smoothing of the density profile

is used to cope with highly inhomogeneous situations, like the density peaks representing the lattice sites in a crystal. In a WDA this smoothing is implemented by a convolution of the one-particle density distribution with appropriate weight functions yielding weighted densities. To construct a WDA one has to define the weight functions. It is worth noting that the FMT uses a set of several weight functions. Another important feature of the FMT opposed to other WDAs is the range of the weight functions. While to our knowledge all other WDAs for hard spheres use weight functions with a range of the particle diameter σ , the FMT weight functions have a range of half the particle diameter, or particle radius $R = \sigma/2$. In this way the non-overlap criterion for hard spheres can be fulfilled exactly. The small range of the weights is not a drawback in cases where a range of non-locality of the sphere diameter σ is needed, e.g., for the pair correlation function. In this case the arising convolutions of two weights render the functional non-local with range σ .

One essential ingredient of the FMT is a geometrical view of hard particles. The basic statistical objects such as the Mayer function are either zero or unity for hard particles. In the geometrical picture a function value of unity means "inside the geometrical shape," while a function value of zero means "outside of the geometrical shape." Using this correspondence one can exploit powerful results from integral geometry like the Gauss-Bonnet theorem [12]. In the case of soft cores the statistically relevant functions take on non-trivial values different from zero and unity.

The main modification of the FMT we present here is a generalization of the weight functions to handle soft cores while keeping their short range. The emerging new weights are built to

- (i) deconvolve the Mayer function,
- (ii) yield the exact zero-dimensional single cavity limit.
- (iii) give a reasonable, albeit not exact, multi-cavity limit.

It turns out that the "thermodynamic ingredients," namely, the free energy density depending on the weighted densities remain unaffected and keep their hard body form.

Let us start by introducing a generic form of a DF. The excess free energy is expressed as

$$F^{\text{exc}}(T, [\rho(\mathbf{r})]) = k_B T \int d\mathbf{x} \Phi(T, \{n_\alpha(T, \mathbf{x})\}), \quad (1)$$

where T is the temperature, and k_B is Boltzmann's constant. The integrand is a reduced free energy density Φ depending on T and on a set of weighted densities $\{n_\alpha\}$ indexed by α . Each weighted density is given by a convolution of its temperature-dependent weight function w_α with the density profile

$$n_\alpha(T, \mathbf{x}) = \int d\mathbf{r} \rho(\mathbf{r}) w_\alpha(T, \mathbf{x} - \mathbf{r}). \quad (2)$$

To summarize, the DF has the following properties:

1. There is a *set* of weighted densities.
2. The free energy density is a function of the weighted densities.
3. The weighted densities are obtained by convolutions of the density profile with appropriate weight functions.
4. The weight functions are explicitly known, i.e., do not implicitly depend on the density distribution.

The task is to give explicit expressions for Φ and $\{n_\alpha\}$ to model the DF for a given pair potential. Let us discuss the range of non-locality of the present functional by considering the direct correlation function which can be obtained by functional differentiation

$$c_2([\rho], \mathbf{r}_1, \mathbf{r}_2) = -(k_B T)^{-1} \left. \frac{\delta^2 F^{\text{exc}}}{\delta \rho(\mathbf{r}_1) \delta \rho(\mathbf{r}_2)} \right|_{\rho=\rho_0}, \quad (3)$$

where ρ_0 is the equilibrium density. In the framework of the FMT, the differentiation of the generic functional results in

$$c_2([\rho], \mathbf{r}_1, \mathbf{r}_2) = \sum_{\alpha, \gamma} \psi_{\alpha\gamma} n_\alpha * n_\gamma, \quad (4)$$

where $\psi_{\alpha\gamma} = \partial^2 \Phi / (\partial n_\alpha \partial n_\gamma)$ are numerical coefficients not depending on any spatial coordinate and the convolution of two weights is defined as

$$n_\alpha * n_\gamma = \int d^3x n_\alpha(\mathbf{r}_1 - \mathbf{x}) n_\gamma(\mathbf{r}_2 - \mathbf{x}). \quad (5)$$

The crucial point is that c_2 has the double range compared to that of the weight functions w_α . The direct correlation function is only known in the low-density limit $c_2 \rightarrow f = \exp(-\beta V) - 1$, as $\rho \rightarrow 0$, where f is the Mayer function, and $\beta = 1/k_B T$. The requirement to fulfill this limit will be used to find the explicit form of the weight functions.

The second requirement is to reproduce the exact free energy in the zero-dimensional (0D) limit. The 0D limit is defined through the density distribution $\rho_{0d} = \eta \delta(\vec{r})$. Physically, it describes a small cavity that can hold only one single particle. The 0D limit has proven to be a useful construct for hard spheres [4,5,13]. In this case it can be realized by a spherical cavity with diameter σ with hard walls. It has only two states: Either it is empty, or it holds a single particle. However, the idea is not restricted to hard bodies. We use it to model a cavity for a soft particle. As we assume a divergence to infinity of the soft potential under consideration, it

would cost infinite energy to insert a second particle. Hence, the 0D limit for soft cores is the same as for hard bodies! It was shown [13] that a functional that fulfills the 0D limit is given by

$$\Phi_1 = -n_0 \ln(1 - n_3), \quad (6)$$

if the weight functions have the property

$$w_0(r) = -(4\pi r^2)^{-1} \frac{\partial}{\partial r} w_3(r), \quad (7)$$

with boundary conditions $w_3(0) = 1$, and $w_3(\infty) = 0$. The index $\alpha = 0, 3$ is related to the dimension of the weighted densities, which is $(\text{length})^{\alpha-3}$. The emerging integral can be solved and yields the exact 0d free energy $F^{\text{exc}} = \eta + (1 - \eta) \ln(1 - \eta)$ [4,5], no matter what the functional dependence of n_3 on r is. The freedom can be used to tune the weight functions to fit a prescribed interaction potential.

We assume that the set of weight functions is related to the ‘‘generating’’ weight function w_3 through

$$w_2(r) = -\frac{\partial w_3(r)}{\partial r} = -w_3'(r), \quad (8)$$

$$\mathbf{w}_{v2}(\mathbf{r}) = w_2(r) \mathbf{r}/r, \quad (9)$$

$$w_1(r) = w_2(r)/(4\pi r), \quad (10)$$

$$\mathbf{w}_{v1}(\mathbf{r}) = w_1(r) \mathbf{r}/r, \quad (11)$$

$$w_0(r) = w_1(r)/r, \quad (12)$$

where w_2 , w_1 , and w_0 are scalar quantities and $\mathbf{w}_{v1}, \mathbf{w}_{v2}$ are vectors. What remains is to find an explicit expression for the generalized local packing fraction weight $w_3(r)$. Therefore, we consider the low-density limit of the true density functional,

$$F^{\text{exc}} \rightarrow -\frac{k_B T}{2} \int d\mathbf{r}_1 d\mathbf{r}_2 f(|\mathbf{r}_1 - \mathbf{r}_2|) \rho(\mathbf{r}_1) \rho(\mathbf{r}_2), \quad (13)$$

and impose that we recover the Mayer-bond, $f(r) = \exp[-\beta V(r)] - 1$, by a sum of convolutions of weight functions

$$-\frac{1}{2} f(r) = w_0 * w_3 + w_1 * w_2 - \mathbf{w}_{v1} * \mathbf{w}_{v2}, \quad (14)$$

where the convolution product, denoted by $*$, also implies scalar products between vectors. Inserting the hierarchical relations yields

$$1 - \exp[-\beta V(r)] = \frac{2}{4\pi} \left(-\frac{w_3'(r)}{r^2} * w_3(r) + \frac{w_3'(r)}{r} * w_3'(r) - \frac{w_3'(r)}{r^2} \mathbf{r} * \mathbf{r} \frac{w_3'(r)}{r} \right), \quad (15)$$

which is an equation for the determination of the generating weight w_3 , once a pair potential $V(r)$ is specified. The de-

pendence of w_3 on temperature has been suppressed in the notation, and the prime denotes differentiation with respect to the argument r .

For the free energy density we take over the hard sphere expression $\Phi = \Phi_1 + \Phi_2 + \Phi_3$, with the contributions $\Phi_1 = -n_0 \ln(1-n_3)$, $\Phi_2 = (n_1 n_2 - \mathbf{n}_{v1} \cdot \mathbf{n}_{v2}) / (1-n_3)$, $\Phi_3 = n_2^3 [1 - (\mathbf{n}_{v2}/n_2)^2]^3 / [24\pi(1-n_3)^2]$. As discussed above, Φ_1 yields the exact single-cavity limit. The additional terms Φ_2 and Φ_3 correctly vanish in this limit. The two-cavity case is not reproduced exactly, but a numerical evaluation shows satisfactory agreement [14].

We want to apply the theory to star polymer solutions that are characterized by an ultra-soft repulsive interaction [15]. This system has two parameters, the functionality or arm number of the stars f and a length scale σ^* , which are used to build a dimensionless density $\eta^* = (\pi/6)\sigma^{*3}N/V$, where N is the particle number inside a volume V . The pair potential [16] consists of a logarithmic potential for small distances and an exponentially decaying Yukawa potential for large distances. In order to keep the present analysis simple we use a modified form for large distances,

$$\beta V(r) = \begin{cases} -2q \ln(r/R) + \ln\left(\frac{2q}{q}\right) & 0 \leq r < R \\ \phi_q(r) + \ln\left(\frac{2q}{q}\right) & R \leq r < 2R \\ 0 & 2R \leq r, \end{cases} \quad (16)$$

where $\binom{2q}{q}$ is the binomial coefficient. The crossover function between small and large distances is given by

$$\phi_q(r) = -\ln[(1+\xi)^{2q} - \xi^{q+1} B_{q,2} F_1(1, 1-q; 2+q; -\xi)], \quad (17)$$

where $\xi = (r/R) - 1$, $B_{q,2} = 2\Gamma(1+2q)\Gamma^{-1}(q)\Gamma^{-1}(2+q)$, and ${}_2F_1$ is the hypergeometric function. The parameters are related to Ref. [16] via $q = (5/36)f^{3/2}$, and $R/\sigma^* = \exp[(1 + \sqrt{f}/2)^{-1} - (2q)^{-1} \ln\binom{2q}{q}]$. It is natural to define a dimensionless density $\eta = (4\pi/3)R^3 N/V = 8\eta^*(R/\sigma^*)^3$. The potential $V(r)$ given by Eq. (16) is shorter ranged than the original one. It is slightly smoother as it is q times differentiable at $r=R$ and one time differentiable at $r=2R$.

The specific form of the crossover function $\phi_q(r)$ allows us to deconvolve the Mayer function [Eq. (14)] and construct the weight functions analytically. The solution is

$$w_3(r) = \begin{cases} 1 - (r/R)^q & \text{if } 0 \leq r \leq R \\ 0 & \text{else.} \end{cases} \quad (18)$$

In the limit $q \rightarrow \infty$ we recover hard spheres: The weight function approaches a step-function, $w_3(r) \rightarrow \Theta(R-r)$ and the potential becomes hard core with range $2R$.

The weighted densities, Eq. (2), when evaluated for the homogeneous fluid are constant in space,

$$n_\alpha = 4\pi\rho \int_0^a dr r^2 w_\alpha(r), \quad (19)$$

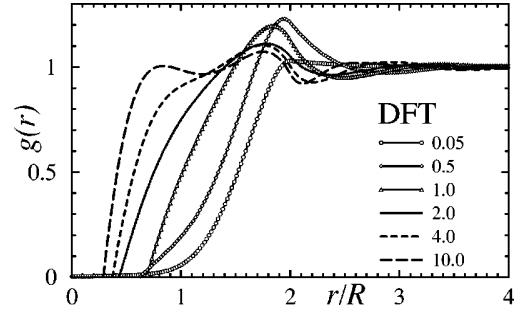


FIG. 1. Pair correlation functions $g(r)$ as a function of the scaled distance r/R obtained from density-functional theory for a solution of star polymers [Eq. (16)]. The variation with density η is shown.

with $a \rightarrow \infty$. In particular, n_3 is proportional to ρ . The free energy density Φ , however, is only defined for $n_3 < 1$, thus implying an unphysical upper limit of densities. To circumvent this problem, we propose to reduce the upper limit of integration in Eq. (19) to the Wigner-Seitz (WS) radius $a = R\eta^{-1/3}$, so that only the density field within a WS cell contributes to the weighted density. As usually $w_3 \leq 1$ holds, it can be seen that the cutoff ensures $n_3 \leq 1$. When applied to the hard sphere case no harm is done, as only unphysical states are affected: All $\eta > 1$ are mapped onto $\eta = 1$. The validity of the procedure will be checked by comparison with simulations.

To test the theory, we calculate pair distribution functions $g(r)$ in the fluid phase. We choose the extremely soft case $q=3$, that corresponds to a (noninteger) arm number of roughly 7.75. To perform a severe test, no use of the test-particle limit is made, i.e., no minimizing of the functional with an external field given by the pair potential itself is done. Instead, we use the direct correlation function given by the second functional derivative of the excess free energy functional, Eq. (3). The Ornstein-Zernike relation yields the pair correlation function $g(r)$. In Fig. 1 we show results for a large range of densities, $\eta = 0.05-10$, corresponding to $\eta^* = 0.00797-1.595$. For comparison, Monte Carlo simulation data are shown in Fig. 2. The reasonable agreement is, however, achieved by an empirical modification. We rescale heuristically the direct correlation function, $\lambda * c_2$, where λ is roughly proportional to η^{-1} . The particular values are (η given in parentheses) $\lambda = 1$ (0.05), 0.7 (0.5), 0.2 (1.0), 0.05 (2.0), 0.04 (4.0), and 0.02 (10.0). The main effect is a res-

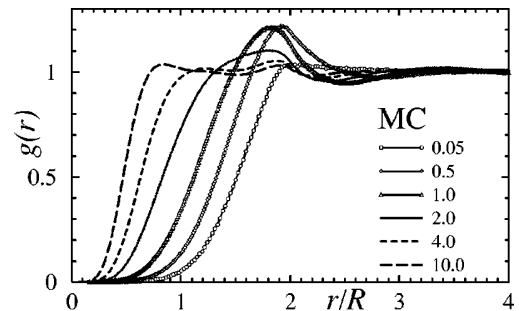


FIG. 2. Same as Fig. 1, but obtained from Monte Carlo computer simulation.

caling of the amplitude of the oscillations in $g(r)$. From a strict point of view, we have introduced one fit parameter per curve. We note, that this is only necessary for the extremely soft case $q=3$. For $q>12$ and $\eta=0.5$ good agreement is found without rescaling (i.e., $\lambda=1$).

The results are fairly good. Wavelength and phase of the oscillations are correct. The peculiar shrinking of the first peak and growing of the second peak upon decreasing the density is reproduced. For small distances, the theory yields unphysical negative values of $g(r)$ (not shown in Fig. 1). The worst case is $g(0)=-1.11$ for $\eta=10$. Apart from this, we find a remarkable agreement between theory and simulation.

In conclusion, we have proposed a systematic way to generalize the fundamental-measure density-functional theory for hard bodies to soft interactions. This “soft FMT” is based on the exactly solvable dimensional crossover to a set of zero-dimensional cavities and on the virial expansion. As

a test case, we studied the ultrasoft logarithmic potential that mimics the effective interaction between star polymers in solution. Prominent features such as the anomalous pair correlation function are captured qualitatively correct. An empirical modification leads to good quantitative agreement with computer simulation results. Concerning future work, it is highly desirable to apply the soft FMT to the recently found freezing transitions for star polymers [17] and to inhomogeneous liquid situations. Furthermore, the performance for other soft repulsive interactions like the Yukawa or inverse-power potentials should be investigated. It would also be highly interesting to test the current approach for attractive interactions like the Lennard-Jones potential, where preliminary investigations have shown that the numerical deconvolution of the Mayer function is possible.

It is a pleasure to thank Hartmut Löwen, Benito Groh, and Christian von Ferber.

-
- [1] H. Löwen, *Phys. Rep.* **237**, 249 (1994).
 [2] M. Dijkstra, R. van Roij, and R. Evans, *Phys. Rev. Lett.* **81**, 2268 (1998).
 [3] A. Jusufi, M. Watzlawek, and H. Löwen, *Macromolecules* **32**, 4470 (1999).
 [4] Y. Rosenfeld, M. Schmidt, H. Löwen, and P. Tarazona, *J. Phys.: Condens. Matter* **8**, L577 (1996).
 [5] Y. Rosenfeld, M. Schmidt, H. Löwen, and P. Tarazona, *Phys. Rev. E* **55**, 4245 (1997).
 [6] J. A. Cuesta, *Phys. Rev. Lett.* **76**, 3742 (1996).
 [7] J. A. Cuesta and Y. Martinez-Raton, *Phys. Rev. Lett.* **78**, 3681 (1997).
 [8] R. Evans, in *Fundamentals of Inhomogeneous Fluids*, edited by D. Henderson (Wiley, New York, 1992), p. 85.
 [9] Y. Rosenfeld, *Phys. Rev. E* **54**, 2827 (1996).
 [10] Y. Singh, *Phys. Rep.* **207**, 351 (1991).
 [11] A. Kol and B. B. Laird, *Mol. Phys.* **90**, 951 (1997).
 [12] Y. Rosenfeld, *Phys. Rev. E* **50**, R3318 (1994).
 [13] P. Tarazona and Y. Rosenfeld, *Phys. Rev. E* **55**, R4873 (1997).
 [14] M. Schmidt (unpublished).
 [15] M. Watzlawek, H. Löwen, and C. N. Likos, *J. Phys.: Condens. Matter* **10**, 8189 (1998).
 [16] C. N. Likos, H. Löwen, M. Watzlawek, B. Abbas, O. Jucknischke, J. Allgaier, and D. Richter, *Phys. Rev. Lett.* **80**, 4450 (1998).
 [17] M. Watzlawek, H. Löwen, and C. N. Likos, *Phys. Rev. Lett.* **82**, 5289 (1999).

Density functional for additive mixtures

Matthias Schmidt

Institut für Theoretische Physik II, Heinrich-Heine-Universität Düsseldorf, Universitätsstrasse 1, D-40225 Düsseldorf, Germany
(Received 30 March 2000)

We present a density functional theory for mixtures of particles interacting with a radially symmetric pair potential. The approach is suitable for systems with soft or hard interactions between like species. The cross interactions between unlike species are restricted to obey an additivity constraint. The functional is a generalization of the soft fundamental measure theory (SFMT) for one-component systems and reduces to Rosenfeld's functional in the case of hard sphere mixtures. It respects both, the zero-dimensional limit and the virial expansion. The structure of the homogeneous fluid phase is an output. As an application, we calculate the pair distributions of colloidal hard spheres mixed with star polymers and find good agreement with computer simulation results.

PACS number(s): 64.10.+h, 61.20.Gy, 61.25.Hq, 05.20.Jj

I. INTRODUCTION

One way of proceeding from simple to complex fluids is by increasing the number of different components in a system. Many new physical phenomena arise, like mixing and demixing, depletion effects or freezing into complicated crystalline structures. Hence it is fair to say that mixtures are intriguing systems.

One theoretical tool for studying mixtures is density-functional theory (DFT) [1]. In particular for hard body mixtures powerful approaches are known [2–5]. Recently, a density functional theory for soft interactions was proposed [6]. This soft fundamental measure theory (SFMT) is based on the dimensional crossover from zero to three dimensions, and does not require input from the bulk liquid. Instead, the correlation functions in the homogeneous fluid are an output of the theory. SFMT was applied successfully to structure and freezing of star polymer solutions [7].

Here we demonstrate that the theory can be generalized to mixtures in a straightforward way. The generalization keeps the simplicity of the approach, as well as its desirable features, namely an exact zero-dimensional limit, exact virial expansion up to second order in density and *prediction* of the correlations and thermodynamics of the bulk liquid.

There is, however, an additivity constraint. This means that only the pair interactions between like species can be prescribed. The cross interactions between unlike species are not at our disposal. Nevertheless, these interactions turn out to have a physically reasonable form. For example, for mixtures of hard and soft spheres, a hard core is preserved. As an application we calculate pair distribution functions for a mixture of star polymers and colloids. When compared to simulation results, we find nice agreement.

In Sec. II the SFMT density functional is described; we give its definition Sec. (II A), explain the additivity constraint Sec. (II B), summarize the properties of the functional Sec. (II C), and treat mixtures of hard spheres and soft spheres Sec. (II D) as one special case. As an application we consider star polymers mixed with colloidal particles in Sec. III. We define the theoretical model (Sec. III A), set up the density functional (Sec. III B), and show results for the fluid

structure (Sec. III C). We finish with concluding remarks in Sec. IV.

II. DENSITY FUNCTIONAL THEORY

A. Definition

Consider a system with m components that interact with pair potentials $V^{(ij)}(r)$, and possess density fields $\rho^{(i)}(\mathbf{r})$, $i, j = 1, \dots, m$. The discrete picture of mixtures is adopted; all consideration equally apply to polydisperse systems. The excess free energy functional is expressed as

$$F_{\text{excl}}[\{\rho^{(i)}(\mathbf{r})\}] = k_B T \int d^3x \Phi(\{n_\alpha(\mathbf{x})\}). \quad (1)$$

The density profiles are convolved with weight functions; summation over all species yields weighted densities as

$$n_\alpha(\mathbf{x}) = \sum_{i=1}^m \int d^3r \rho^{(i)}(\mathbf{r}) w_\alpha^{(i)}(\mathbf{x} - \mathbf{r}). \quad (2)$$

Within the set of weight functions, the following relations hold:

$$w_2^{(i)}(r) = -\frac{\partial}{\partial r} w_3^{(i)}(r), \quad (3)$$

$$\mathbf{w}_{v2}^{(i)}(\mathbf{r}) = w_2^{(i)}(r) \mathbf{r}/r, \quad (4)$$

$$w_1^{(i)}(r) = w_2^{(i)}(r)/(4\pi r), \quad (5)$$

$$\mathbf{w}_{v1}^{(i)}(\mathbf{r}) = w_1^{(i)}(r) \mathbf{r}/r, \quad (6)$$

$$w_0^{(i)}(r) = w_1^{(i)}(r)/r, \quad (7)$$

where $w_\alpha^{(i)}(r)$, $\alpha = 0, 1, 2, 3$ are scalar quantities and $\mathbf{w}_{v1}^{(i)}(r)$, $\mathbf{w}_{v2}^{(i)}(r)$ are vectors. The weight functions are quantities with dimension of length scale to the power of $\alpha - 3$.

The weight functions for species i are determined so that the Mayer bond $f^{(ii)}(r) = \exp(-V^{ii}(r)) - 1$ between particles of the same species is obtained. This intraspecies deconvolution is

$$-\frac{1}{2}f^{(ii)}(r) = w_0^{(i)*}w_3^{(i)} + w_1^{(i)*}w_2^{(i)} - \mathbf{w}_{v1}^{(i)*}\mathbf{w}_{v2}^{(i)}, \quad (8)$$

where the convolution product, denoted by $*$, also implies scalar products between vectors.

The free energy density is $\Phi = \Phi_1 + \Phi_2 + \Phi_3$, with the contributions

$$\Phi_1 = -n_0 \ln(1 - n_3), \quad (9)$$

$$\Phi_2 = \frac{n_1 n_2 - \mathbf{n}_{v1} \cdot \mathbf{n}_{v2}}{1 - n_3}, \quad (10)$$

$$\Phi_3 = \frac{(n_2)^3 (1 - (\mathbf{n}_{v2}/n_2)^2)^3}{24\pi(1 - n_3)^2}. \quad (11)$$

We note that recently, more sophisticated versions of Φ_3 using tensorial weights have been successfully used [7,8].

B. Cross interactions

Once the weight functions $w_\alpha^{(i)}$ are calculated by solving the deconvolution equation (8), the interactions between unlike species are restricted to obey

$$-f^{(ij)}(r) = w_0^{(i)*}w_3^{(j)} + w_1^{(i)*}w_2^{(j)} - \mathbf{w}_{v1}^{(i)*}\mathbf{w}_{v2}^{(j)} + w_0^{(j)*}w_3^{(i)} + w_1^{(j)*}w_2^{(i)} - \mathbf{w}_{v1}^{(j)*}\mathbf{w}_{v2}^{(i)}. \quad (12)$$

Loosely speaking, the cross interactions are a combination of the intraspecies interactions. This behavior is also present in the hard sphere FMT [2], that is primarily a theory for additive mixtures of hard spheres.

C. Properties

We show that the functional is exact in the zero-dimensional limit and gives the virial expansion up to second order correctly.

The zero-dimensional limit for a mixture is defined by density distributions $\rho^{(i)}(\mathbf{r}) = \eta^{(i)}\delta(\mathbf{r})$, where $\eta^{(i)}$ is the average occupation number of species i . We assume that all pair interactions diverge at the origin. Then the delta-spike can be occupied by at most one single particle. The excess free energy is $F_{0d} = (1 - \eta)\ln(1 - \eta) + \eta$, where $\eta = \sum_{i=1}^m \eta^{(i)}$ is the total number of particles. In the following we show that the functional gives F_{0d} exactly. We observe that Φ_2 and Φ_3 vanish, because $|\mathbf{n}_{v2}| = n_2$, and $|\mathbf{n}_{v1}| = n_1$, and the antisymmetry upon exchanging scalar and vectorial densities.

We still have to evaluate the remaining Φ_1 contribution

$$F[\{\eta^{(i)}\delta(\mathbf{r})\}] = - \int_0^\infty dr 4\pi r^2 n_0(r) \ln[1 - n_3(r)], \quad (13)$$

$$n_\alpha(r) = \sum_{i=1}^m \eta^{(i)} w_\alpha^{(i)}(r). \quad (14)$$

From the hierarchy of weight functions, Eqs. (3)–(7), we obtain the relation

$$w_0^{(i)}(r) = -(4\pi r^2)^{-1} \partial w_3^{(i)}(r) / \partial r. \quad (15)$$

Integrating and using the boundary conditions $w_3^{(i)}(0) = 1$, $w_3^{(i)}(\infty) = 0$ yields the 0d excess free energy F_{0d} .

The correct virial expansion can be checked by Taylor expanding for low densities $\Phi \rightarrow n_0 n_3 + n_1 n_2 - \mathbf{n}_{v1} \cdot \mathbf{n}_{v2}$, and using the deconvolution equations (8) and (12).

We finally note that in the case of hard spheres, Rosenfeld's functional is recovered.

D. Hard and soft spheres

As an important case we consider the cross interaction between a hard sphere i with radius $R^{(i)}$ and a soft sphere j for which the functional is valid. Deconvolution of the step function yields the well-known hard sphere weights [2] (also given in Sec. III B)

From Eq. (12) we obtain the cross-Mayer function with the particularly simple form

$$-f^{(ij)} = \begin{cases} 1 & \text{if } r < R^{(i)} \\ w_3^{(j)}(r - R^{(i)}) & \text{else.} \end{cases} \quad (16)$$

We observe that the hard core with radius R is preserved, and that the interaction outside the core is given by a shifted $w_3^{(j)}(r)$ function.

III. STAR POLYMERS AND COLLOIDS

The star polymer system has attracted considerable recent interest [9–16]. In this work we investigate a mixture of star polymers and colloidal hard spheres.

A. The model

We consider N^c colloids with radii R^c and N^s star polymers with radii R^s within a volume V . The interaction potential between colloids is hard,

$$V^{(cc)}(r) = \begin{cases} \infty & \text{if } r \leq 2R^c \\ 0 & \text{else.} \end{cases} \quad (17)$$

The interaction between the star polymers is logarithmic

$$\beta V^{(ss)}(r) = \begin{cases} -2q \ln(r/R^s) + \ln\left(\frac{2q}{q}\right) & 0 \leq r < R^s \\ \phi_q(r) + \ln\left(\frac{2q}{q}\right) & R^s \leq r < 2R^s \\ 0 & 2R^s \leq r, \end{cases} \quad (18)$$

where $\frac{2q}{q}$ is the binomial coefficient. The crossover function between small and large distances is given by $\phi_q(r) = -\ln[(1 + \xi)^{2q} - \xi^{q+1} B_q F_1(1, 1 - q; 2 + q; -\xi)]$, where $\xi = (r/R^s) - 1$, $B_q = 2\Gamma(1 + 2q)\Gamma^{-1}(q)\Gamma^{-1}(2 + q)$, and ${}_2F_1$ is the hypergeometric function (see Ref. [7] for a discussion).

The interaction between colloids and polymers is assumed to have a hard core due to the excluded volume induced by a colloid and an additional logarithmic repulsion

$$V^{(cs)}(r) = \begin{cases} \infty & \text{if } r \leq R^c \\ -q \ln\left(\frac{r-R^c}{R^s}\right) & \text{if } R^c < r \leq R^c + R^s \\ 0 & \text{else.} \end{cases} \quad (19)$$

This form is similar to the result from a microscopic analysis of the interactions between star polymers and hard spheres [17].

The system is governed by the packing fractions of colloids, $\eta^c = 4\pi N^c (R^c)^3 / (3V)$, and of polymers $\eta^s = 4\pi N^s (R^s)^3 / (3V)$, and the size ratio $a = R^s / R^c$.

B. The weights functions

The set of weight functions for the colloids is identical to the pure hard sphere case and is given by

$$w_3^{(c)}(\mathbf{r}) = \theta(R^c - r), \quad (20)$$

$$w_2^{(c)}(\mathbf{r}) = \delta(R^c - r), \quad (21)$$

$$w_1^{(c)}(\mathbf{r}) = \delta(R^c - r) / (4\pi r), \quad (22)$$

$$w_0^{(c)}(\mathbf{r}) = \delta(R^c - r) / (4\pi r^2), \quad (23)$$

$$\mathbf{w}_{v2}^{(c)}(\mathbf{r}) = \delta(R^c - r) \mathbf{r} / r, \quad (24)$$

$$\mathbf{w}_{v1}^{(c)}(\mathbf{r}) = \delta(R^c - r) \mathbf{r} / (4\pi r^2), \quad (25)$$

where $r = |\mathbf{r}|$, and $\Theta(r)$ is the Heaviside step function, $\delta(r)$ denotes the Dirac delta function.

The weight functions for the star polymers are

$$w_3^{(s)}(\mathbf{r}) = [1 - (r/R^s)^q] \theta(R^s - r), \quad (26)$$

$$w_2^{(s)}(\mathbf{r}) = q r^{q-1} (R^s)^{-q} \theta(R^s - r), \quad (27)$$

$$w_1^{(s)}(\mathbf{r}) = q r^{q-2} (R^s)^{-q} (4\pi)^{-1} \theta(R^s - r), \quad (28)$$

$$w_0^{(s)}(\mathbf{r}) = q r^{q-3} (R^s)^{-q} (4\pi)^{-1} \theta(R^s - r), \quad (29)$$

$$\mathbf{w}_{v2}^{(s)}(\mathbf{r}) = q r^{q-1} (R^s)^{-q} \theta(R^s - r) \mathbf{r} / r, \quad (30)$$

$$\mathbf{w}_{v1}^{(s)}(\mathbf{r}) = q r^{q-2} (R^s)^{-q} (4\pi)^{-1} \theta(R^s - r) \mathbf{r} / r. \quad (31)$$

These are the same as for the one-component case considered in Refs. [6,7].

C. Results

In order to calculate the partial pair correlation functions we do not make use of the test-particle limit. Instead, the partial direct correlation functions are calculated from the density functional via $c_{ij}(r) = -(k_B T)^{-1} \delta^2 F^{\text{exc}} / (\delta \rho^{(i)} \delta \rho^{(j)})$. Using the Ornstein-Zernike relation gives the partial structure factors in reciprocal space [18] and a Fourier transform yields the pair correlations. We adopt this method, because no density profile equation is solved. This is a severe test for the quality of the density functional. To compare the results, we have carried out standard canonical Monte Carlo computer simulations.

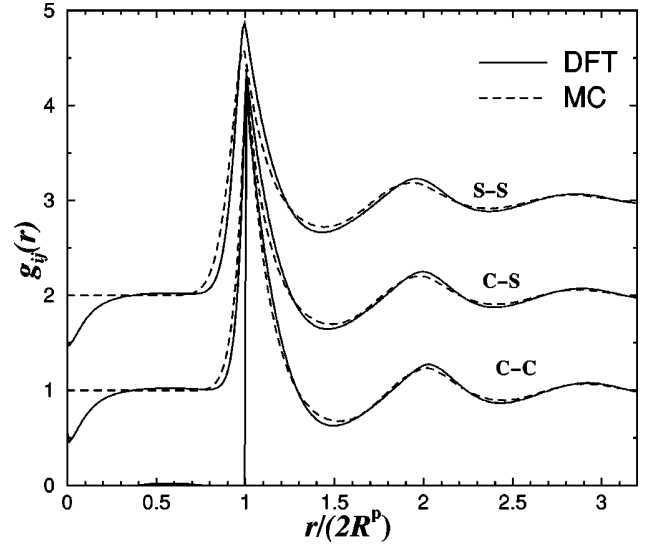


FIG. 1. Pair correlation functions $g^{cc}(r)$, $g^{cs}(r)$, and $g^{ss}(r)$ for a mixture of hard spheres and star polymers as a function of the scaled distance $r/(2R^p)$ at packing fractions $\eta^c = 0.25, \eta^s = 0.25$, and size ratio $a = 1$. Full lines are DFT, dashed lines are simulation results. The curves are shifted upwards one unit for reasons of clarity.

We investigate the partial pair distribution functions between pairs of colloids $g^{cc}(r)$, pairs of stars $g^{ss}(r)$ and between a colloid and a star polymer, $g^{cs}(r)$ for the intermediate softness $q = 12$, and for equal number densities of colloids and stars, hence $\eta^c a^3 / \eta^s = 1$. In Figs. 1, 2, and 3 results for the size ratios $a = 1, 0.5, 2$ are given, respectively. The general agreement is good. Phase and amplitude are correct. However, the DFT peaks are slightly too steep. The worst case is $g^{ss}(r)$, $a = 2$, Fig. 3. Also small spurious values inside the core appear, especially for the cross correlations $g^{cs}(r)$. Using the test-particle limit, one could get rid of these values.

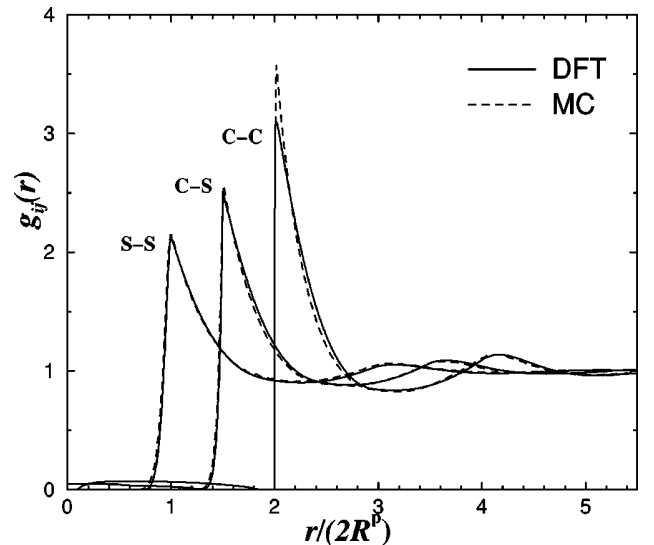


FIG. 2. Same as Fig. 1, but at densities $\eta^c = 0.35$, $\eta^s = 0.04375$, and size ratio $a = 0.5$, corresponding to small stars.

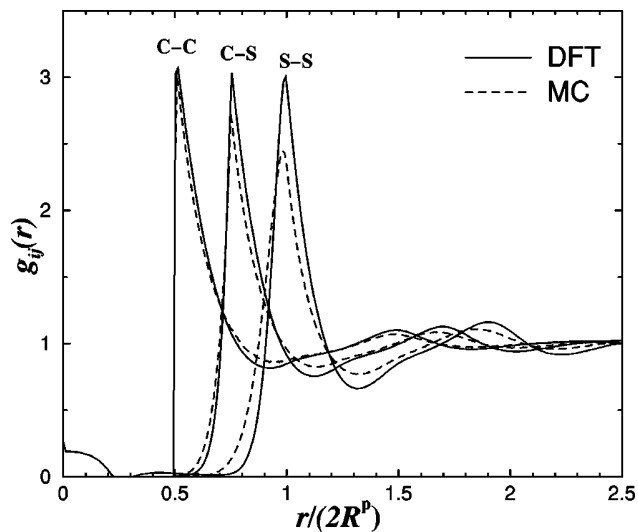


FIG. 3. Same as Fig. 1, but at densities $\eta^c=0.0625$, $\eta^s=0.5$, and size ratio $a=2$, corresponding to large stars.

IV. CONCLUSIONS

We have shown that the soft fundamental measure theory can be formulated for multi-component mixtures. The properties of the theory are preserved in comparison to the one-

component case. In particular, the virial expansion and the zero-dimensional limit for the mixture are exact.

The current theory can only be applied to a limited class of systems, that we call additive. This constraint enforces the cross interactions to be a combination of the interactions between the like species. However, for mixtures of soft and hard spheres the cross interaction was shown to be meaningful, because a hard core is preserved.

As an application, we have investigated the fluid structure of a mixture of colloidal hard spheres and star polymers. When compared to simulation results, we find a remarkable agreement.

It is intriguing that the fluid structure of a multicomponent system can be understood on the basis of two simple ingredients: First, particles cannot sit on top of each other. Second, the Mayer f -bond governs the behavior at low densities.

As possible future applications we mention the investigation of depletion potentials that has attracted considerable recent interest [19–22] in the context of hard sphere mixtures. The current functional offers the possibility to study the effects of soft interactions essentially with the same theoretical tools as developed in Ref. [19].

ACKNOWLEDGMENTS

The author thanks Joachim Dzubiella, Christos N. Likos, and Hartmut Löwen for useful discussions.

-
- [1] R. Evans, in *Fundamentals of Inhomogeneous Fluids*, edited by D. Henderson (Wiley, New York, 1992), p. 85.
- [2] Y. Rosenfeld, *Phys. Rev. Lett.* **63**, 980 (1989).
- [3] Y. Rosenfeld, M. Schmidt, H. Löwen, and P. Tarazona, *J. Phys.: Condens. Matter* **8**, L577 (1996); *Phys. Rev. E* **55**, 4245 (1997).
- [4] J. A. Cuesta, *Phys. Rev. Lett.* **76**, 3742 (1996); J. A. Cuesta and Y. Martinez-Raton, *ibid.* **78**, 3681 (1997).
- [5] P. Tarazona and Y. Rosenfeld, *Phys. Rev. E* **55**, R4873 (1997).
- [6] M. Schmidt, *Phys. Rev. E* **60**, R6291 (1999).
- [7] B. Groh and M. Schmidt (unpublished).
- [8] P. Tarazona, *Phys. Rev. Lett.* **84**, 694 (2000).
- [9] C. N. Likos, H. Löwen, M. Watzlawek, B. Abbas, O. Jucknischke, J. Allgaier, and D. Richter, *Phys. Rev. Lett.* **80**, 4450 (1998).
- [10] M. Watzlawek, H. Löwen, and C. N. Likos, *J. Phys.: Condens. Matter* **10**, 8189 (1998).
- [11] M. Watzlawek, H. Löwen, and C. N. Likos, *Phys. Rev. Lett.* **82**, 5289 (1999).
- [12] M. Watzlawek, *Phase Behavior of Star Polymers* (Shaker Verlag, Aachen, 1999).
- [13] A. Jusufi, M. Watzlawek, and H. Löwen, *Macromolecules* **32**, 4470 (1999).
- [14] C. von Ferber, A. Jusufi, C. N. Likos, H. Löwen, and M. Watzlawek, *Eur. Phys. J. E* (to be published).
- [15] J. Stellbrink, B. Abbas, J. Allgaier, M. Monkenbusch, D. Richter, C. N. Likos, H. Löwen, and M. Watzlawek, *Prog. Colloid Polym. Sci.* **110**, 25 (1998).
- [16] C. N. Likos, H. Löwen, A. Poppe, L. Willner, J. Roovers, B. Cubitt, and D. Richter, *Phys. Rev. E* **58**, 6299 (1998).
- [17] J. Dzubiella, C. N. Likos, and H. Löwen (private communication).
- [18] J. P. Hansen and I. R. McDonald, *Theory of Simple Liquids*, 2nd ed. (Academic, London, 1986).
- [19] B. Götzelmann, R. Roth, S. Dietrich, M. Dijkstra, and R. Evans, *Europhys. Lett.* **47**, 398 (1999).
- [20] R. Roth, Ph.D. thesis, Bergische Universität-Gesamthochschule Wuppertal, 1999.
- [21] R. Roth, B. Götzelmann, and S. Dietrich, *Phys. Rev. Lett.* **83**, 448 (1999).
- [22] C. Bechinger, D. Rudhardt, P. Leiderer, R. Roth, and S. Dietrich, *Phys. Rev. Lett.* **83**, 3960 (1999).

Fluid structure from density-functional theory

Matthias Schmidt

Institut für Theoretische Physik II, Heinrich-Heine-Universität Düsseldorf, Universitätsstraße 1, D-40225 Düsseldorf, Germany
(Received 11 May 2000)

We treat various common fluid models, like the inverse-power, Asakura-Oosawa, and Lennard-Jones potentials, within the soft fundamental measure theory (SFMT). We show that this recently proposed density-functional approach is able to predict the pair correlations in the fluid phase reliably compared to computer simulations. Explicit expressions for certain quantities of SFMT are given, namely, for the weight functions and the fundamental measures. These technical tools permit practical calculations for a large class of inhomogeneous systems.

PACS number(s): 64.10.+h, 61.20.Gy

I. INTRODUCTION

It is desirable that approximative density functionals [1] be simple. Simple theories are comprehensible and useful. Comprehensibility is desirable, because one can learn easily about the physics of the system. A theory is useful, of course, if it can be applied with small (or at least moderate) effort to an actual problem. The goal of theorists is to construct such simple theories, which despite their simplicity give excellent (or at least reasonable) results.

Among the many ways to construct density-functional theories (DFT's) the fundamental measure theory (FMT) is special, as it is able to predict the structure of the homogeneous bulk fluid state rather than needing it as an input. Following Rosenfeld's pioneering work for hard spheres [2], improved hard sphere functionals have been obtained [3–5] that are capable of describing inhomogeneous situations like, e.g., a solid [6,7,5] or depletion potentials in mixtures [8,9] excellently. For quite some time the FMT for hard sphere mixtures played a monolithic role, as its structure was (and still is) quite different from other DFTs. Heavily relying on insights in the analytic Percus-Yevick solution, scaled-particle theory, and integral geometry, it seemed, not only at first glance, that FMT works only for the special system of hard spheres. However, there have been numerous attempts to broaden the range of models covered by the theory, like the proposal of an extension to general hard convex bodies [10]. The FMT has been generalized to the more tractable system of hard parallel cubes [11–13].

It has turned out that the correct dimensional crossover [3,4] from three dimensions (3D) to lower ones, is an essential test for a DFT. One may even start from 0D situations of extreme confinement and construct 3D functionals systematically [14,5] using the idea of “functional interpolation” [5] between dimensions.

Surprisingly, the FMT machinery generates the thermodynamics, i.e., free energy, from the very basic situation of a cavity that has the size of one particle. For hard spheres the occupation number is zero or 1, and one can calculate the excess free energy exactly [3,4]. Applying this method to penetrable spheres, i.e., particles that may overlap at a finite energy cost, one obtains a reasonable approximation to the exact density functional of this system [15]. Concerning mixtures, recently a FMT for a nonadditive model colloid-

polymer mixture was found [16]. However, in all these systems, the interactions are still step functions. This is a great simplification, as integral geometry can be fully exploited, essentially unchanged to the hard sphere case.

Among the attempts to treat soft interactions [17–19], the so-called soft fundamental measure theory (SFMT) [18,19] is also built on well-defined limiting cases, where the behavior of the exact free energy functional is known. These cases are the virial expansion and the 0D limit. However, two or three cavities, which are exact in hard sphere FMT, are not exact in SFMT. Nevertheless the application to the effective logarithmic interaction in star polymer solutions yields excellent results for the structure and the phase diagram [20]. Concerning its ease of use, however, the SFMT has the drawback that its weight functions are related to the Mayer function in a nontrivial way. This relation, the so-called deconvolution equation, is an integro-differential equation of second order in the unknown function. As will be discussed below, straightforward attempts to solve the deconvolution numerically are cumbersome; one encounters an inverse problem.

The aim of the present work is to give an explicit solution to the deconvolution equation. The availability of this solution allows the application of SFMT to a large class of statistical systems. Here we calculate the pair distribution functions in the bulk liquid for a variety of common models and find good agreement with simulation results.

In Sec. II the SFMT density functional is presented. The solution of the deconvolution equation is given in Sec. III. Examples for fluid structure are considered in Sec. V. Remarks are summarized in Sec. VI.

II. A DENSITY FUNCTIONAL

Within SFMT the excess free energy is approximated as

$$F^{\text{exc}}(T, [\rho(\mathbf{r})]) = k_B T \int d\mathbf{x} \Phi(\{n_\alpha(T, \mathbf{x})\}), \quad (1)$$

where T is the temperature, and k_B is Boltzmann's constant. The weighted densities n_α are obtained by convolutions of the weight functions with the one-body density profile $\rho(\mathbf{r})$,

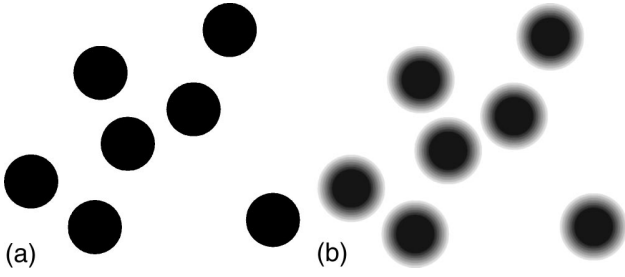


FIG. 1. Visualization of the weight functions describing single particles. (a) Hard spheres, (b) soft spheres.

$$n_\alpha(T, \mathbf{x}) = \int d\mathbf{r} \rho(\mathbf{r}) w_\alpha(T, \mathbf{x} - \mathbf{r}), \quad (2)$$

where α labels the type of the weight function. In the following we assume that the pair potential diverges at the origin. Then the free energy density is given by $\Phi = \Phi_1 + \Phi_2 + \Phi_3$, with the contributions

$$\Phi_1 = -n_0 \ln(1 - n_3), \quad (3)$$

$$\Phi_2 = (n_1 n_2 - \mathbf{n}_{v1} \cdot \mathbf{n}_{v2}) / (1 - n_3), \quad (4)$$

$$\Phi_3 = \frac{\frac{1}{3} n_2^3 - n_2 \mathbf{n}_{v2} \cdot \mathbf{n}_{v2} + \frac{3}{2} (\mathbf{n}_{v2} \hat{\mathbf{n}}_{m2} \mathbf{n}_{v2} - 3 \det \hat{\mathbf{n}}_{m2})}{8\pi(1 - n_3)^2}, \quad (5)$$

where the caret denotes a second-rank tensor, and \det is the determinant. The introduction of tensorial weighted densities, first done for hard spheres [5], leads to superior results in inhomogeneous situations [20] compared to the vectorial form [3,4,18]. The bulk fluid free energy and direct correlation function $c(r)$ are unaffected.

III. THE WEIGHT FUNCTIONS

The weight functions are given by the hierarchy

$$w_2(r) = -\frac{\partial w_3(r)}{\partial r}, \quad (6)$$

$$\mathbf{w}_{v2}(\mathbf{r}) = w_2(r) \mathbf{r}/r, \quad (7)$$

$$\mathbf{w}_{m2}(\mathbf{r}) = w_2(r) (\mathbf{r}\mathbf{r}/r^2 - \hat{\mathbf{1}}/3), \quad (8)$$

$$w_1(r) = w_2(r)/(4\pi r), \quad (9)$$

$$\mathbf{w}_{v1}(\mathbf{r}) = w_1(r) \mathbf{r}/r, \quad (10)$$

$$w_0(r) = w_1(r)/r, \quad (11)$$

where w_2, w_1, w_0 are scalar quantities; $\mathbf{w}_{v1}, \mathbf{w}_{v2}$ are vectors, and $\hat{\mathbf{w}}_{m2}$ is a traceless matrix (where $\mathbf{r}\mathbf{r}$ is a dyadic product and $\hat{\mathbf{1}}$ is the identity matrix). Dimensional analysis shows that the weight functions w_α carry the dimension of length to the power of $\alpha - d$, where $d = 3$ is the dimensionality of the physical space. The hierarchy of weights (6)–(11) is built to recover the FMT weight functions [2,5] in the hard sphere limit. See Fig. 1 for a sketch; hard spheres are represented by sharp objects, soft spheres are washed out.

The weight functions are related to the Mayer function $f = \exp[-V(r)/k_B T] - 1$, where $V(r)$ is the pair potential, by

$$-\frac{1}{2} f(r) = w_0 * w_3 + w_1 * w_2 - \mathbf{w}_{v1} * \mathbf{w}_{v2}, \quad (12)$$

where the three-dimensional convolution, denoted by $*$, also implies scalar products between vectors. More explicitly, using Eqs.(6)–(11), this can be written (in r space) as

$$1 - \exp[-\beta V(r)] = \frac{1}{2\pi} \left(-\frac{w_3'(r)}{r^2} * w_3(r) + \frac{w_3'(r)}{r} * w_3'(r) - \frac{w_3'(r)}{r^2} \mathbf{r} * \mathbf{r} \frac{w_3'(r)}{r} \right), \quad (13)$$

where the prime denotes differentiation with respect to the argument r , and $\beta = 1/k_B T$. This *deconvolution equation* has to be solved for the unknown function $w_3(r)$ once a pair potential $V(r)$ is prescribed. The boundary conditions are $w_3(0) = 1$ and $w_3(\infty) = 0$ (see Appendix D). However, a direct numerical solution turns out to be impractical. Any uncertainties in w_3 become completely washed out under the convolution operation. Hence, iterative solution algorithms are unstable.

However, we can construct an explicit solution. It turns out that the Mayer function and the weight function w_2 have the simple relation

$$\frac{\partial f(r)}{\partial r} = \int_{-\infty}^{\infty} dr' w_2(r') w_2(r - r'), \quad (14)$$

where we formally set $w_2(r < 0) = 0$ to simplify the limits of integration. See Appendix A for the derivation of Eq. (14). In reciprocal space, we can write

$$\tilde{w}_2(k) = \pm \sqrt{ik\tilde{f}(k)}, \quad (15)$$

where the tilde denotes a one-dimensional Fourier transform, $\tilde{f}(k) = \int_{-\infty}^{\infty} dr f(r) \exp(ikr)$. Care has to be taken with the sign in Eq. (15). It may change depending on the value of k . As a physically meaningful prescription, we chose a continuous and differentiable function in k space.

A simple numerical algorithm works as follows. We start from $k = 0$ and choose one of the signs, say the positive one. We proceed in small steps Δk . For each step, we check whether $ik\tilde{f}(k)$ attempts to cross the branch cut. If it does, we change the sign. Of course, more sophisticated root-finding algorithms can be used.

IV. FLUID FREE ENERGY

The free energy of the homogeneous fluid phase at a given density ρ and temperature T is

$$\frac{\beta F^{\text{exc}}}{V} = -n_0 \ln(1 - n_3) + \frac{n_1 n_2}{1 - n_3} + \frac{n_2^3}{24\pi(1 - n_3)^2} \quad (16)$$

The weighted densities become $n_\alpha = \xi_\alpha \rho$, where the fundamental measures ξ_α are defined as

$$\xi_\alpha = 4\pi \int_0^\infty dr r^2 w_\alpha(r). \quad (17)$$

The dimension of the fundamental measure ξ_α is the length scale to the power of α . For hard spheres, they are the volume $\xi_3 = 4\pi R^3/3$, surface area $\xi_2 = 4\pi R^2$, integral mean curvature $\xi_1 = R$, and Euler characteristic $\xi_0 = 1$. Using the soft weight functions one generalizes these quantities. The Euler characteristic is an integer, that is, roughly speaking, the number of connected portions minus the number of holes of a geometric shape. We find that the Euler characteristic is $\xi_0 = 1$, for any pair potential (see Appendixes B and D). This is consistent with the intuitive picture of soft spheres.

The ξ_α for $\alpha = 1, 2, 3$, however, need not be calculated directly from the weight functions. There is an easier way, as there are straightforward relations to moments of the Mayer function. We define

$$m_\alpha \equiv \int_0^\infty dr r^{\alpha-1} \{1 - \exp[-\beta V(r)]\} \quad (18)$$

as dimensional quantities. The index α gives the power of the length scale. Note that m_1 is the Barker-Henderson effective diameter [21]. Then the fundamental measures are related to the moments of the Mayer function via

$$\xi_0 = 1, \quad (19)$$

$$\xi_1 = m_1/2, \quad (20)$$

$$\xi_2 = 4\pi(m_2 - m_1^2/4), \quad (21)$$

$$\xi_3 = 2\pi(m_3 - m_2 m_1 + m_1^3/4). \quad (22)$$

This can be seen by a straightforward calculation (given in Appendix C).

V. APPLICATIONS

To test the theory we calculate pair distribution functions $g(r)$ for various fluid models. To this end we take the direct correlation function $c(r)$ given as a second functional derivative of the excess free energy, and use the Ornstein-Zernike relation in Fourier space to obtain the structure factor $S(k)$. A Fourier transform yields $g(r)$.

This procedure does not imply solving any equation numerically, except for the deconvolution Eq. (14). In particular, no density profile is calculated using the test-particle limit. Hence this is a severe test for the quality of the functional.

The results will be compared to simulations. We have carried out canonical Monte Carlo (MC) computer simulations with 512 particles and 10^5 MC moves per particle to collect data for $g(r)$. In all examples we have considered two reduced densities $\rho\sigma^3 = 0.1, 0.5$, where σ is the length scale appearing in the corresponding pair potential.

A. Error function model

We first consider a model potential that can be deconvolved analytically. It is a short-ranged potential with a steep repulsion given by the Mayer bond

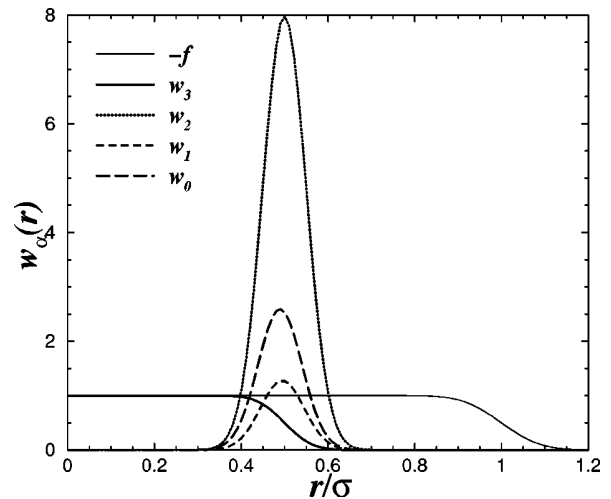


FIG. 2. Family of weight functions $w_\alpha(r)$ and the Mayer function $-f(r)$ for the erf model with $a/\sigma = 0.1$ as a function of the scaled distance r/σ .

$$f(r) = -\frac{1}{2} \left[1 - \operatorname{erf}\left(\frac{r-\sigma}{a}\right) \right], \quad (23)$$

where we use the convention $\operatorname{erf}(z) = (2/\sqrt{\pi}) \int_0^z dt \exp(-t^2)$. We will assume that the scaled width a/σ is small, so that we can approximate $f(r=0) \approx -1$, as $\operatorname{erf}(r \rightarrow -\infty) = -1$ holds. As the Mayer bond equals an error function, we call this the erf model.

The derivative in real space is $f'(r) = \exp[-(r-\sigma)^2/a^2]/(a\sqrt{\pi})$. Its Fourier transform is also a Gaussian. Taking the square root, Eq. (15), Fourier transforming back, and integrating yields

$$w_3(r) = \frac{1}{2} \left[1 - \operatorname{erf}\left(\frac{r-(\sigma/2)}{a/\sqrt{2}}\right) \right]. \quad (24)$$

As expected, the length scale has changed from σ to $\sigma/2$. This means going from a description in terms of particle diameters to one in terms of particle radii. The shape of the two functions, however, is different. The width decreases only from a to $a/\sqrt{2}$. See Fig. 2 for a plot of the weight functions. In Fig. 3 results for the pair correlations are plotted for $a/\sigma = 0.1$. We find good agreement with the simulation result. The core condition, however, is not fulfilled exactly; small negative values for $g(r)$ are found for small distances. One could get rid of those using the test-particle limit.

B. Inverse-power potentials

We write the pair potential for ‘‘soft spheres’’ [22] as

$$V(r) = k_B T (\sigma/r)^p. \quad (25)$$

The moments of the Mayer function, Eq. (18), can be obtained analytically as

$$m_\alpha = \frac{\sigma^\alpha}{\alpha} \Gamma\left(1 - \frac{\alpha}{p}\right). \quad (26)$$

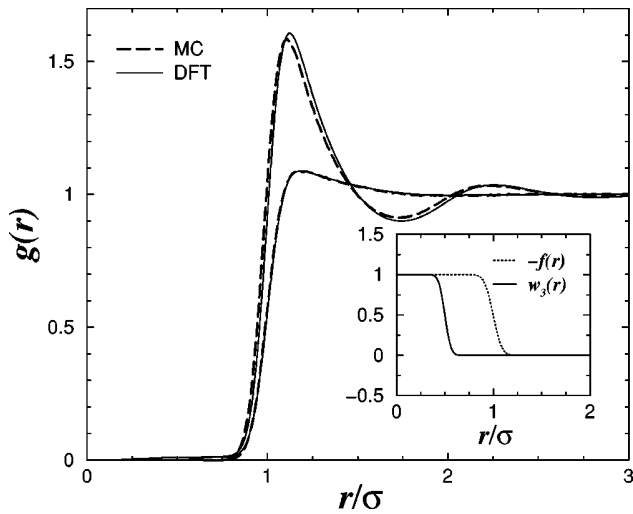


FIG. 3. Pair correlation function $g(r)$ obtained from density-functional theory (solid lines) compared to simulations (dashed) for the erf model with $a/\sigma=0.1$, $\rho\sigma^3=0.1,0.5$. The negative Mayer function $-f(r)$ and the weight function $w_3(r)$ are shown in the inset.

Using the relations between the m_α and the fundamental measures ξ_α , Eqs. (19) and (20)–(22), we get an analytical expression for the fluid free energy (16), similar, but not identical to the Barker-Henderson construction.

For small powers, $p \leq 3$, the fundamental measures diverge. Hence the theory cannot be applied as is. This reasoning is valid for any potential that has an inverse-power tail, i.e., decays as r^{-p} for $r \rightarrow \infty$. We will stay safely away from this problem and consider the exponent $p=12$. In Fig. 4 the pair correlations $g(r)$ are shown. The general agreement with MC data is good. For the moderate density $\rho\sigma^3=0.5$ the DFT result is shifted slightly to larger distances.

C. Asakura-Oosawa potential

The Asakura-Oosawa potential [23] is a prototype for depletion interactions. Considerable recent work is devoted to it; see, e.g., Refs. [24–26,16]. We write it as

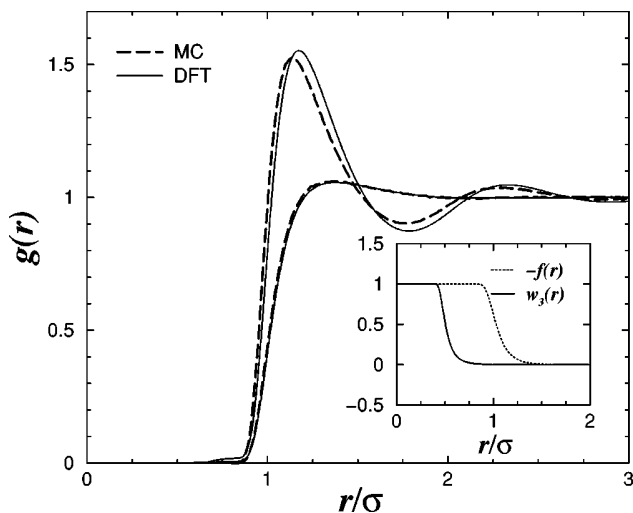


FIG. 4. Same as Fig. 3, but for the inverse-power potential with exponent $p=12$.

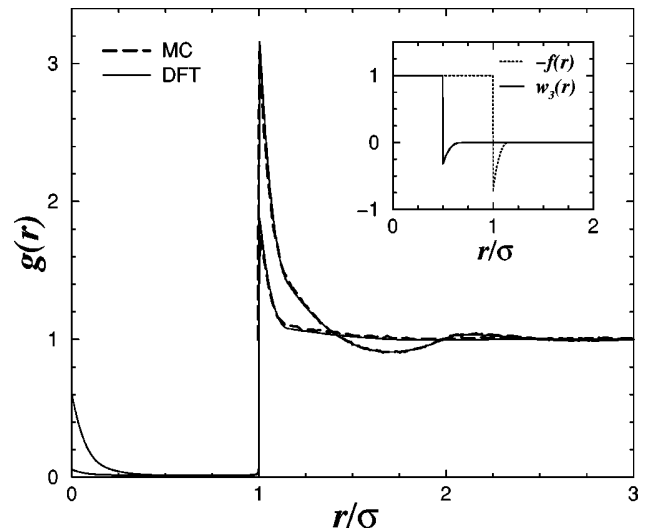


FIG. 5. Same as Fig. 3, but for the Asakura-Oosawa potential for $q=0.15, z=0.05$.

$$V(r) = \begin{cases} \infty, & r < \sigma \\ k_B T z \varphi(r), & \sigma < r < (1+q)\sigma \\ 0, & (1+q)\sigma < \infty, \end{cases} \quad (27)$$

$$\varphi(r) = -\left(\frac{1+q}{q}\right)^3 \left(1 - \frac{3r/\sigma}{2(1+q)} + \frac{(r/\sigma)^3}{2(1+q)^3}\right), \quad (28)$$

where the attraction is ruled by the (reduced) range q and the (reduced) strength z .

We show results for the state point $q=0.15, z=0.05$ in Fig. 5. The pair distributions $g(r)$ are remarkably good. The strong peak at contact as well as the second one are captured correctly. The core condition, however, is violated. A cusp near $r=0$ appears, where $g(r)$ has unphysical values that are forbidden by the hard core.

We emphasize that the deconvolution can be done for attractive potentials. The inset in Fig. 5 shows a comparison of $f(r)$ and the weight function $w_3(r)$. Apart from the halved length scale, both look similar, but $w_3(r)$ has a shallower negative well.

D. Lennard-Jones potential

The Lennard-Jones pair potential [22] is

$$V(r) = V_0[(\sigma/r)^{12} - (\sigma/r)^6]. \quad (29)$$

Again the deconvolution is possible for this attractive potential. The pair correlations shown in Fig. 6 are slightly worse than in the above examples. For $\rho\sigma^3=0.5$ the height of the first peak is underestimated. The core is not reproduced, but has positive values.

The dotted line is the result for $\rho\sigma^3=0.5$ using a cutoff in the integration of the fundamental measures, Eq. (17). The upper limit of integration is reduced from infinity to the Wigner-Seitz radius $a=(4\pi\rho/3)^{-1/3}$. This procedure improves the result, but is somewhat heuristic and requires a better theoretical foundation.

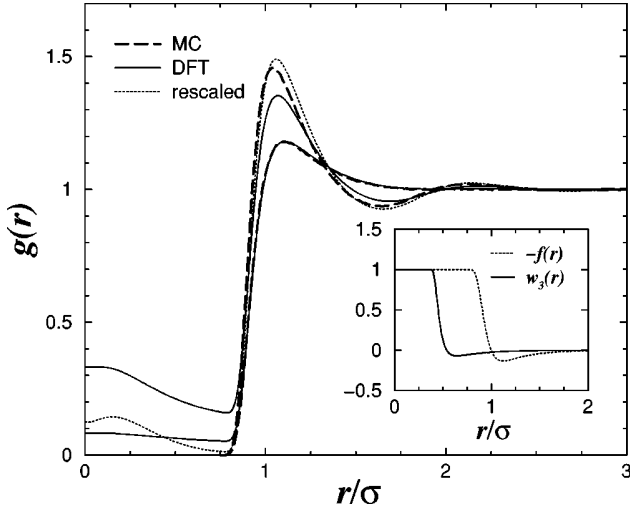


FIG. 6. Same as Fig. 3, but for the Lennard-Jones potential at $V_0/k_B T=0.5$.

VI. CONCLUSIONS

We have shown that soft fundamental measure theory is capable of predicting the fluid structure for repulsive as well as attractive interaction potentials. We have tested the pair correlations from the theory against computer simulation results at moderate density, moderate softness, and moderate attraction. We find good agreement, except for small artifacts inside the core.

We emphasize that the current approach is expected to work best for potentials that are still dominated by packing effects, i.e., are sufficiently short ranged. True long-ranged potentials like the Coulomb or inverse-power potential with small exponents cannot be tackled. Also, a possible attraction needs to be sufficiently weak and short ranged, as present in the example of the Asakura-Oosawa potential above, to be described correctly.

The utility of SFMT depends crucially on the accessibility of the functional form of the weight functions. In this work we give an explicit solution to the deconvolution equation that relates the Mayer bond to the weight functions. The solution requires only one-dimensional Fourier transforms and the handling of a root-finding problem in reciprocal space. Numerically, both operations are simple.

ACKNOWLEDGMENTS

I thank Roland Roth and Andreas Lang for useful comments.

APPENDIX A: DECONVOLUTION OF THE MAYER BOND

From the relation between the weights, Eq. (6), we obtain

$$w_3(r) = \int_r^\infty dr' w_2(r'), \quad (\text{A1})$$

which can be turned into a convolution

$$w_3(r) = \int_0^\infty dr' w_2(r') \Theta(r' - r). \quad (\text{A2})$$

Applying the hierarchy of weights Eqs. (6)–(11) to Eq. (A2) yields the relations

$$w_\alpha(r) = \int_0^\infty dr' w_2(r') h_{\alpha,r'}(r), \quad (\text{A3})$$

where the $h_{\alpha,r'}(r)$ equal the hard sphere weight functions with radius r' and are given by $h_{3,r'}(r) = \Theta(r' - r)$, $h_{2,r'}(r) = \delta(r' - r)$, $h_{1,r'}(r) = \delta(r' - r)/(4\pi r)$, $h_{0,r'}(r) = \delta(r' - r)/(4\pi r^2)$, $\mathbf{h}_{v2,r'}(r) = \delta(r' - r)\mathbf{r}/r$, $\mathbf{h}_{v1,r'}(r) = \delta(r' - r)\mathbf{r}/(4\pi r^2)$.

Next we insert Eq. (A3) into the deconvolution equation (12) to obtain

$$-\frac{1}{2}f(r) = \int_0^\infty dr' w_2(r') \int_0^\infty dr'' w_2(r'') K(r, r', r''), \quad (\text{A4})$$

$$K(r, r', r'') = h_{3,r'}(r) * h_{0,r''}(r) + h_{2,r'}(r) * h_{1,r''}(r) - \mathbf{h}_{v2,r'}(r) * \mathbf{h}_{v1,r''}(r). \quad (\text{A5})$$

We observe that the convolution kernel, Eq. (A5), is the well-known deconvolution of the hard sphere Mayer bond [2],

$$K(r, r', r'') = \frac{1}{2} \Theta(r' + r'' - r). \quad (\text{A6})$$

Inserting this into Eq. (A4) and differentiating gives

$$f'(r) = \int_0^\infty dr' w_2(r') \int_0^\infty dr'' w_2(r'') \delta(r' + r'' - r), \quad (\text{A7})$$

from which we obtain Eq. (14) by a straightforward integration over r'' .

APPENDIX B: FUNDAMENTAL MEASURES AND THE VOLUME WEIGHT

Integrating Eq. (17) by parts yields the useful relations

$$\xi_3 = 4\pi \int_0^\infty dr r^2 w_3(r), \quad (\text{B1})$$

$$\xi_2 = 8\pi \int_0^\infty dr r w_3(r), \quad (\text{B2})$$

$$\xi_1 = \int_0^\infty dr w_3(r), \quad (\text{B3})$$

$$\xi_0 = w_3(0) - w_3(\infty) = 1. \quad (\text{B4})$$

See Appendix D for the justification of the last equality sign.

APPENDIX C: FUNDAMENTAL MEASURES AND THE MAYER FUNCTION

Integrating the definition of the moments of the Mayer function, Eq. (18), by parts yields

$$m_\alpha = \alpha^{-1} \int_0^\infty dr r^\alpha f'(r), \quad (\text{C1})$$

where the boundary terms vanish, as we assume $f(0) = -1$, $f(\infty) = 0$. Expressing the derivative of the Mayer bond through the convolution of weights (14) gives

$$m_\alpha = \alpha^{-1} \int_0^\infty dr r^\alpha \int_0^\infty dr' w_2(r') w_2(r-r'). \quad (\text{C2})$$

Changing integration variables, $r'' = r - r'$, gives

$$\alpha m_\alpha = \int_0^\infty dr' \int_0^\infty dr'' (r' + r'')^\alpha w_2(r') w_2(r'') \quad (\text{C3})$$

$$= \sum_{i=0}^{\alpha} \binom{\alpha}{i} \int_0^\infty dr' (r')^i w_2(r') \int_0^\infty dr'' (r'')^{\alpha-i} w_2(r''). \quad (\text{C4})$$

Explicitly treating the cases $\alpha = 1, 2, 3$ yields Eqs. (20), (21), and (22), respectively.

APPENDIX D: BOUNDARY CONDITIONS OF THE VOLUME WEIGHT

The requirement that the DFT fulfils the 0D limit yields boundary conditions for the volume weight function w_3 . Consider a 0D density distribution $\rho(\mathbf{r}) = \eta \delta(\mathbf{r})$. The weighted densities are $n_\alpha(\mathbf{r}) = \eta w_\alpha(\mathbf{r})$. Symmetry between the weight functions leads to $\Phi_2 = \Phi_3 = 0$. The remaining term Φ_1 gives

$$\beta F^{\text{exc}}[\eta \delta(\mathbf{r})] = \int_0^\infty dr \eta w_3'(r) \ln[1 - \eta w_3(r)], \quad (\text{D1})$$

where we have used $w_0(r) = -(4\pi r^2)^{-1} \partial w_3(r) / \partial r$ [see Eqs. (6)–(11)]. We change integration variables to $u = \eta w_3$ and obtain

$$\beta F^{\text{exc}}[\eta \delta(\mathbf{r})] = \int_{u_0}^{u_\infty} du \ln(1 - u), \quad (\text{D2})$$

where the limits are $u_0 = \eta w_3(0)$ and $u_\infty = \eta w_3(\infty)$. If we assume that the boundary conditions are $w_3(0) = 1$ and $w_3(\infty) = 0$, then the integral gives the exact 0D excess free energy [3,4,18], which is $\beta F_{0D} = \eta + (1 - \eta) \ln(1 - \eta)$.

-
- [1] R. Evans, in *Fundamentals of Inhomogeneous Fluids*, edited by D. Henderson (Wiley, New York, 1992), p. 85.
- [2] Y. Rosenfeld, Phys. Rev. Lett. **63**, 980 (1989).
- [3] Y. Rosenfeld, M. Schmidt, H. Löwen, and P. Tarazona, J. Phys.: Condens. Matter **8**, L577 (1996).
- [4] Y. Rosenfeld, M. Schmidt, H. Löwen, and P. Tarazona, Phys. Rev. E **55**, 4245 (1997).
- [5] P. Tarazona, Phys. Rev. Lett. **84**, 694 (2000).
- [6] B. Groh and B. Mulder, Phys. Rev. E **61**, 3811 (2000).
- [7] B. Groh, Phys. Rev. E **61**, 5218 (2000).
- [8] R. Roth, B. Götzmann, and S. Dietrich, Phys. Rev. Lett. **83**, 448 (1999).
- [9] R. Roth, Ph.D. thesis, Bergische Universität-Gesamthochschule Wuppertal, 1999.
- [10] Y. Rosenfeld, Phys. Rev. E **50**, R3318 (1994).
- [11] J. A. Cuesta, Phys. Rev. Lett. **76**, 3742 (1996).
- [12] J. A. Cuesta and Y. Martinez-Raton, Phys. Rev. Lett. **78**, 3681 (1997).
- [13] J. A. Cuesta and Y. Martinez-Raton, J. Chem. Phys. **107**, 6379 (1997).
- [14] P. Tarazona and Y. Rosenfeld, Phys. Rev. E **55**, R4873 (1997).
- [15] M. Schmidt, J. Phys.: Condens. Matter **11**, 10163 (1999).
- [16] M. Schmidt, H. Löwen, J. M. Brader, and R. Evans, Phys. Rev. Lett. **85**, 1934 (2000).
- [17] M. B. Sweatman, Ph.D. thesis, University of Bristol, 1995.
- [18] M. Schmidt, Phys. Rev. E **60**, R6291 (1999).
- [19] M. Schmidt, Phys. Rev. E **62**, 3799 (2000).
- [20] B. Groh and M. Schmidt (unpublished).
- [21] J. A. Barker and D. Henderson, J. Chem. Phys. **47**, 4714 (1967).
- [22] J. P. Hansen and I. R. McDonald, *Theory of Simple Liquids*, 2nd ed. (Academic Press, London, 1986).
- [23] S. Asakura and F. Oosawa, J. Chem. Phys. **22**, 1255 (1954).
- [24] A. A. Louis, R. Finken, and J. Hansen, Europhys. Lett. **46**, 741 (1999).
- [25] M. Dijkstra, J. M. Brader, and R. Evans, J. Phys.: Condens. Matter **11**, 10079 (1999).
- [26] J. M. Brader and R. Evans, Europhys. Lett. **49**, 678 (2000).

Density-functional theory for structure and freezing of star polymer solutions

Benito Groh^{a)}

FOM Institute for Atomic and Molecular Physics, Kruislaan 407, 1098 SJ Amsterdam, The Netherlands

Matthias Schmidt

Institut für Theoretische Physik II, Heinrich-Heine-Universität Düsseldorf, Universitätsstraße 1, D-40225 Düsseldorf, Germany

(Received 10 October 2000; accepted 21 December 2000)

We use the soft fundamental measure theory (SFMT) to investigate a system of classical particles interacting with the pair potential of star polymers in solution. To that end we calculate liquid and solid structural properties, as well as freezing, solid-to-solid, and remelting phase transitions. Even subtle physical effects, like deviations from Gaussian crystal peaks and an anomalous peak broadening upon increasing density as well as a reasonable vacancy concentration are captured correctly. Good overall quantitative agreement with simulation data is found, however, with a tendency to overestimate the structural correlations. Furthermore, we demonstrate that all recent developments of its hard core counterpart can be incorporated systematically into SFMT. © 2001 American Institute of Physics. [DOI: 10.1063/1.1349092]

I. INTRODUCTION

The understanding of classical many-body systems has received a boost by the development of density functional theory (DFT).¹ The density functional of a given system is an extremely powerful object, from which a complete understanding of an equilibrium system can be gained. The thermodynamics and correlation functions up to an arbitrary order are accessible in principle. Moreover, this is not only true for the bulk but also for situations where an arbitrary influence that can be modeled by an external potential energy, is acting on the system. Apart from externally caused spatial inhomogeneities, DFT also accounts for self-sustained density-waves that are present in a crystal. Thus, it is able to describe the liquid and solid phases on an equal footing, and hence gives a physical explanation of the existence of the freezing phase transition.

As the free energy density functional (DF) is such a powerful object, it may become obvious that it is unknown for most realistic systems. To construct an approximation to the exact DF, the common strategy is to require that the approximative DF yields the correct behavior in situations where one can solve the system, at least approximatively. The more conventional approach uses the homogeneous liquid phase as this starting point, and requires that the approximative DF reproduces known results from liquid state theory, like the equation of state and correlation functions. These quantities can be considered as *input* to the theory.

A newer approach utilizes situations of reduced spatial dimensionality as limiting cases that are captured correctly. There one has the advantage that the system can be solved exactly in dimensions as low as one or even zero, so no approximations enter at that stage. The Rosenfeld hard-

sphere functional² can be derived in this way,³ and improved versions of it can be systematically obtained,^{4,5} as well as functionals for parallel hard cubes.^{6,7} The approximation one has to do is to construct a “functional interpolation”⁵ between spatial dimensions. The fundamental measure functionals yield the Percus–Yevick direct correlation function and equation of state for the bulk hard sphere liquid, give excellent results for the coexistence densities and describe the crystal structure up to close-packing excellently,⁸ as well as the vanishingly small vacancy concentration.⁹ We note that recently a similar approach was used to find a DFT for adhesive hard spheres.¹⁰

The idea that a three-dimensional functional can be constructed by imposing its correct dimensional crossover to lower dimensions is not limited to hard interactions. It can be applied to penetrable spheres,^{11,12} the Asakura–Oosawa colloid-ideal polymer mixture,¹³ and has been exploited to derive a DFT for arbitrary soft pair interactions^{14,15} and additive mixtures.¹⁶ This so-called soft fundamental measure theory (SFMT) was demonstrated to predict the properties of the homogeneous liquid phase. The fluid equation of state and pair correlation function are an *output* of the theory.

In this work we apply the SFMT to a system of star polymers in a good solvent, which has attracted a lot of recent interest.^{17–22,24,25} The logarithmic pair interaction¹⁷ present in this system leads to an anomalous liquid structure¹⁸ and to a rich phase diagram^{19,20} with various solid phases and reentrant melting upon increasing density. Pair²¹ and triplet²² interactions have been investigated. Besides computer simulations, liquid integral equations^{17,18} and Einstein-crystal perturbation theory^{19,20} have been employed. It is of great interest to investigate the system from the unifying viewpoint that DFT provides. In addition, because of the richness of physical phenomena, star polymers provide a severe test to any DFT.

^{a)}Current address: Fachbereich Physik, Bergische Universität Wuppertal, D-42097 Wuppertal, Germany.

Our results show that the SFMT stands this test. In particular, the predicted bulk pair correlations are in good agreement with simulations over the whole range from hard-sphere-like to ultrasoft behavior. The DFT yields thermodynamically stable face-centered cubic (fcc) and body-centered cubic (bcc) crystals and reentrant melting. We find that the lattice peaks have broader wings than Gaussians. A peculiar decreasing of the Lindemann parameter upon increasing the density is captured correctly.

In Sec. II the SFMT functional is described. We also give its refinements according to the latest developments in FMT for hard spheres, and discuss briefly its properties. Section III defines the theoretical model for star polymer solutions and gives explicit expressions for the quantities involved in SFMT. In Sec. IV we present results for the liquid and solid structure as well as the phase diagram. The present approach is discussed in the concluding Sec. V.

II. THE DENSITY FUNCTIONAL

A. Definition

The SFMT is a weighted density approximation. It employs a set of weight functions which are independent of the density profile. The free energy density is a function of the weighted densities and is analytically given.

The excess free energy is expressed as

$$F^{\text{exc}}(T, [\rho(\mathbf{r})]) = k_B T \int d\mathbf{x} \Phi(\{n_\alpha(T, \mathbf{x})\}), \quad (1)$$

where T is the temperature, and k_B is Boltzmann's constant. The integrand is a reduced free energy density Φ depending on a set of weighted densities $\{n_\alpha\}$ indexed by α . Each weighted density is given by a convolution of its temperature-dependent weight function w_α with the density profile,

$$n_\alpha(T, \mathbf{x}) = \int d\mathbf{r} \rho(\mathbf{r}) w_\alpha(T, \mathbf{x} - \mathbf{r}). \quad (2)$$

Within the set of weight functions there is a hierarchy,

$$w_2(r) = -\frac{\partial w_3(r)}{\partial r}, \quad (3)$$

$$\mathbf{w}_{v2}(r) = w_2(r) \mathbf{r}/r, \quad (4)$$

$$\hat{\mathbf{w}}_{t2}(r) = \mathbf{w}_{v2}(r) \mathbf{r}/r, \quad (5)$$

$$w_1(r) = w_2(r)/(4\pi r), \quad (6)$$

$$\mathbf{w}_{v1}(r) = w_1(r) \mathbf{r}/r, \quad (7)$$

$$w_0(r) = w_1(r)/r, \quad (8)$$

where w_2 , w_1 , w_0 are scalar quantities, \mathbf{w}_{v1} , \mathbf{w}_{v2} are vectors, and $\hat{\mathbf{w}}_{t2}$ is a second rank tensor given by a dyadic product of a vector density and a unit spatial vector. The introduction of the tensorial weight $\hat{\mathbf{w}}_{t2}$ is justified below. The ‘‘generating’’ weight function w_3 is determined so that a deconvolution of the Mayer bond $f(r) = \exp[-\beta V(r)] - 1$, where $\beta = 1/k_B T$, is generated,

$$-\frac{1}{2}f(r) = w_0 * w_3 + w_1 * w_2 - \mathbf{w}_{v1} * \mathbf{w}_{v2}, \quad (9)$$

where the convolution product, denoted by $*$, also implies scalar products between vectors.

The free energy density is given by $\Phi = \Phi_1 + \Phi_2 + \Phi_3$, with the contributions

$$\Phi_1 = -n_0 \ln(1 - n_3), \quad (10)$$

$$\Phi_2 = \frac{n_1 n_2 - \mathbf{n}_{v1} \cdot \mathbf{n}_{v2}}{1 - n_3}. \quad (11)$$

The third term exists in various refined forms,

$$\Phi_3^{\text{FMT1}} = \frac{1}{24\pi} \frac{n_2^3 (1 - (\mathbf{n}_{v2}/n_2)^2)^3}{(1 - n_3)^2}, \quad (12)$$

$$\Phi_3^{\text{FMT2}} = \frac{9}{8\pi} \frac{\det \hat{\mathbf{n}}_{t2}}{(1 - n_3)^2}, \quad (13)$$

$$\Phi_3^{\text{FMT3}} = \frac{\mathbf{n}_{v2} \cdot \hat{\mathbf{n}}_{t2} \cdot \mathbf{n}_{v2} - n_2 \mathbf{n}_{v2} \cdot \mathbf{n}_{v2} - \text{tr}(\hat{\mathbf{n}}_{t2}^3) + n_2 \text{tr}(\hat{\mathbf{n}}_{t2}^2)}{(16\pi/3)(1 - n_3)^2}, \quad (14)$$

where tr denotes the trace, and \det is the determinant of a second-rank tensor.

FMT1 (Ref. 3) is the form that first gave a freezing transition for hard spheres and was used in the proposal of SFMT¹⁴ FMT2 (Ref. 8, 4) produces a far better description of the hard sphere solid, but gives less accurate direct correlations for the liquid. FMT3 (Ref. 5) is the latest improvement combining the power of both ancestors. Each of these forms is taken over from the corresponding hard sphere functional. Our modification is the replacement of the hard sphere weight functions with those for the soft potential. This requires the introduction of a tensorial soft weight, done in Eq. (5). The form of $\hat{\mathbf{w}}_{t2}$ is unique in the current framework. This can be seen as follows. The numerator of Φ_3^{FMT2} and Φ_3^{FMT3} is of third order in weighted densities. Hence a single weighted density has to have the dimension of inverse length to give an overall inverse volume, which is the dimension of the free energy density. Hence the tensorial weight carries the index $t2$. The simplest way to construct such a weight function, so that the hard sphere case is respected, is by multiplying \mathbf{w}_{v2} by a spatial unit vector, and Eq. (5) is obtained.

B. Properties

The density functional defined above is exact in two extreme limiting cases, the zero-dimensional (0D) and the low-density limit. The 0D limit is an extremely confined situation, represented by $\rho(\mathbf{r}) = \eta \delta(\mathbf{r})$. We note that as the excess free energy functional does not depend on the external potential V_{ext} , there is no need to specify a V_{ext} that causes the 0D distribution. Nevertheless it might be useful to think of a small cavity that immobilizes a particle. There can be at most one particle, because the pair interaction diverges at the origin. The free energy can be calculated exactly.³ The SFMT reproduces this solution.¹⁴

In the low-density limit, the functional becomes exact up to second order in the virial expansion. The reason is that the weight functions restore the Mayer function upon convolution. Details of the calculation can be found in Ref. 14.

III. STAR POLYMERS

Star polymers are macromolecular entities consisting of a functional center to which f polymeric arms are attached. The arm-number or functionality f is an integer ranging from 2 to values as high as 256. When soluted in a good solvent, star polymers can be regarded as colloidal particles on a mesoscopic length scale, that is much larger than the microscopic scale of individual monomers building up the arms. The colloidal picture involves an effective pair²¹ or even triplet²² interaction between the stars, which arises from entropic effects due to reduction of the number of accessible states if the stars are very close to each other. The resulting interaction is repulsive with a logarithmic law. For large distances it decays faster and a hybrid between logarithmic and a Yukawa form was proposed¹⁷ and validated by simulations.²¹ The arm-number governs the softness ranging from ultra-soft for small f to practically hard spheres for large f .

A. The potential

As a model interaction between star polymers we use the modified potential of Ref. 14 given by

$$\beta V(r) = \begin{cases} -2q \ln(r/R) + \ln\left(\frac{2q}{q}\right) & 0 \leq r < R \\ \phi_q(r) + \ln\left(\frac{2q}{q}\right) & R \leq r < 2R \\ 0 & 2R \leq r \end{cases}, \quad (15)$$

where $\binom{2q}{q}$ is the binomial coefficient. The crossover function between small and large distances is given by

$$\phi_q(r) = -\ln[(1 + \xi)^{2q} - \xi^{q+1} B_{q,2} \times F_1(1, 1 - q; 2 + q; -\xi)], \quad (16)$$

where $\xi = (r/R) - 1$, $B_q = 2\Gamma(1 + 2q)\Gamma^{-1}(q)\Gamma^{-1}(2 + q)$, Γ is the Euler gamma function, and ${}_2F_1$ is the hypergeometric function. For integer q the crossover function can be simplified to a polynomial, $\phi_q(r) = -\ln[(1 + \xi)^{2q} - \sum_{j=0}^q \binom{2q}{j} \xi^j]$. The parameters q and R are related to the arm-number f and length scale σ of the log-Yukawa potential¹⁷ via $q = (5/36)f^{3/2}$, and $R/\sigma = \exp[(1 + \sqrt{f}/2)^{-1} - (2q)^{-1} \ln\binom{2q}{q}]$. We define a dimensionless density $\rho^* = (2R)^3 N/V$. The relation $\eta^* = (\pi/6)(2R/\sigma)^{-3} \rho^*$ holds, where η^* is the density of Ref. 17.

The log-hypergeometric form (15) for the potential is not chosen on physical grounds. It only simplifies the actual calculations, because the weight functions can be obtained analytically. This makes the numerical work easier, as no inaccuracies enter at that stage. We plot both interactions in Fig. 1. The force $F = -dV/dr$ as well as the potential itself are shown for both functional forms and are compared to the simulation data by Jusufi *et al.*^{21,26} Both functions are mathematically identical for $r/R < 1$. On the scale of the plot, however, both forces coincide for larger distances up to $r/R \approx 1.5$, where the cusp in the log-Yukawa force appears. The cusp is absent in the present case of the hypergeometric crossover. However, it falls off too quickly for larger distances and even vanishes for $r/R > 2$. There the simulations

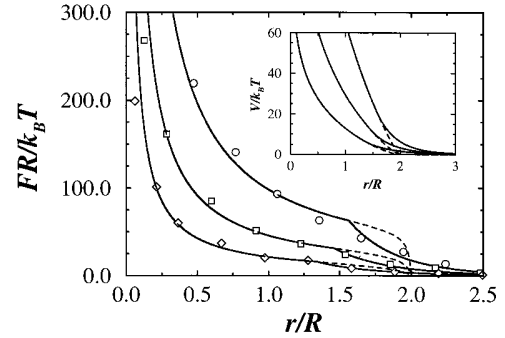


FIG. 1. Comparison of two functional forms for the star polymer pair interactions. The main plot shows the scaled force $FR/(k_B T)$, the inset indicates the scaled potential $V/(k_B T)$ itself. Both are plotted as a function of the scaled distance r/R . The solid lines represent the log-Yukawa potential by Likos *et al.* (Ref. 17), the dotted lines indicate where the log-hypergeometric potential used in this work differs. The symbols are the computer simulation results by Jusufi *et al.* (Ref. 21), Fig. 3(b) therein (Ref. 26). From top to bottom the arm number changes as $f = 50, 30, 18$, corresponding to $q = 49.1, 22.8, 10.6$.

indicate a finite force that is well described by the log-Yukawa potential. Nevertheless, we conclude that the gross features are the same for both models and the use of the log-hypergeometric potential is justified for our investigations.

B. Setting up the density functional

The weight functions for star polymers are obtained by solution of the deconvolution Eq. (9), and are explicitly given by

$$w_3(r) = \theta(R - r)[1 - (r/R)^q], \quad (17)$$

$$w_2(r) = \theta(R - r)qr^{q-1}/R^q, \quad (18)$$

$$w_{v2}(r) = \theta(R - r)[qr^{q-1}/R^q]\hat{\mathbf{r}}, \quad (19)$$

$$\hat{w}_{t2}(r) = \theta(R - r)[qr^{q-1}/R^q]\hat{\mathbf{r}}\hat{\mathbf{r}}, \quad (20)$$

$$w_1(r) = \theta(R - r)qr^{q-2}/(4\pi R^q), \quad (21)$$

$$w_{v1}(r) = \theta(R - r)[qr^{q-2}/(4\pi R^q)]\hat{\mathbf{r}}, \quad (22)$$

$$w_0(r) = \theta(R - r)qr^{q-3}/(4\pi R^q), \quad (23)$$

where $\hat{\mathbf{r}} = \mathbf{r}/r$ is a unit vector, and θ is the Heaviside step function. The weight functions do not depend on temperature, because the pair interaction, Eq. (15), is of entropic origin, hence $V(r)/k_B T$ is constant with respect to temperature. As a quasithermodynamic quantity the softness parameter q tunes the shape of the interaction and of the weight functions.

C. Computer simulation

To provide data for comparison with the DFT results, we have carried out Monte Carlo (MC) computer simulations of the log-hypergeometric pair potential, Eq. (15). Canonical simulations with 108–864 particles and 10^5 – 10^6 MC moves per particle were performed. We collect data for the pair correlation function in the fluid state and crystal density dis-

J. Chem. Phys., Vol. 114, No. 12, 22 March 2001

tributions. For the latter the usual subtraction of the center-of-mass movement was done. The actual data presented are from a system with 256 particles. We checked that the finite size dependence is negligible at one state point, $q=100$, $\rho^* = \sqrt{2}$.

IV. RESULTS

A. Liquid structure

The SFMT has the ability to *predict* the properties of the homogeneous liquid. The thermodynamics and correlation functions can be derived from the functional and are not put in by hand, say from liquid state theory. In the following, we calculate the bulk liquid free energy and pair distribution functions. The latter are compared to simulations.

For a liquid state with homogeneous density $\rho(\mathbf{r}) = \rho$, the weighted densities become $n_\alpha = \xi_\alpha \rho$, where the soft fundamental measures ξ_α are given by $\xi_\alpha = 4\pi \int_0^\infty dr r^2 w_\alpha(r)$. We obtain $\xi_\alpha = \xi_\alpha^{\text{HS}} / (q + \alpha)$, where the fundamental measures of a hard sphere of radius R are the Euler characteristic $\xi_0^{\text{HS}} = 1$, integral mean curvature $\xi_1^{\text{HS}} = R$, surface area $\xi_2^{\text{HS}} = 4\pi R^2$, and volume $\xi_3^{\text{HS}} = 4\pi R^3/3$. For the star polymers the Euler characteristic remains unity, $\xi_\alpha = 1$, the other fundamental measures are $\xi_1 = Rq/(q+1)$, $\xi_2 = 4\pi R^2 q/(q+2)$, $\xi_3 = (4\pi/3)R^3 q/(q+3)$. We emphasize that the flexibility contained in ξ_α , $\alpha=1,2,3$ cannot be obtained by a mapping onto a reference hard sphere system.

The vector densities vanish, $\mathbf{n}_{v1} = \mathbf{n}_{v2} = 0$, and $(\hat{\mathbf{n}}_{r2})_{ij} = \delta_{ij} n_2/3$. The excess free energy is

$$\frac{\beta F^{\text{exc}}}{V} = -n_0 \ln(1-n_3) + \frac{n_1 n_2}{1-n_3} + \frac{n_2^3}{24\pi(1-n_3)^2} \quad (24)$$

in all three approximations for Φ_3 . The liquid equation of state is easily derived by differentiation and reduces to the hard sphere Percus–Yevick compressibility result for $q \rightarrow \infty$.

To calculate pair correlations from a density functional there are various ways to go. They differ in the number of *test particles* that one inserts. A test particle corresponds to an external potential coinciding with the pair potential itself. For one test particle the pair correlations are proportional to the density profile itself. This is a widely used approach; the profile depends on the radial coordinate. Without a test particles, $g(r)$ can be computed via the direct correlation function given by the second functional derivative of the excess free energy using the Ornstein–Zernike relation. We employ this strategy because we consider it as the tougher test for the functional itself, as no oscillating density profile is minimized.

We will investigate the crossover behavior of the pair correlations from soft to hard sphere behavior for the density $\rho^* = 3/\pi = 0.955$. The ultrasoft case, $q=3$, was already considered in Ref. 14. In Fig. 2 the theoretical results are shown together with simulation data for different softness parameters $q=6,12,24$. We observe that the phase and amplitude of the oscillations are reproduced nicely by the DFT. The only deficiencies are an overshooting of the first peak for $q=6$ and negative values for small distances for all q . On physical grounds, these values may be disregarded, as $g(r)$

Structure and freezing of star polymer solutions 5453

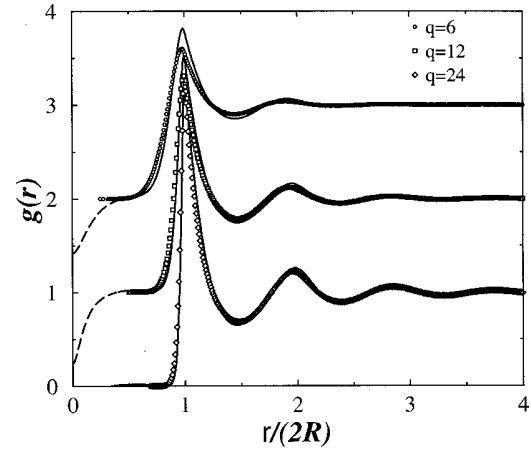


FIG. 2. Pair distribution function $g(r)$ as a function of the scaled distance $r/(2R)$. Results for various softness parameters are shown, $q=6, 12, 24$ (from top to bottom) and density $\rho^* = 3/\pi = 0.955$. The lines are the DFT results, the symbols are Monte Carlo data. The curves are shifted upwards one unit for reasons of clarity. For small distances the theoretical result becomes negative (indicated by a dashed line).

is a non-negative function. They present a shortcoming of the current approach, but incorporating the feature $g(r) \geq 0$ on the level of the density functional itself is not an easy task. Of course, one could get rid of the negative values using the test-particle method where the ideal gas free energy ensures non-negative results.

B. Solid structure

A general crystalline density has the form,

$$\rho(\mathbf{r}) = \sum_{\mathbf{R}} \rho_{\Delta}(\mathbf{r} - \mathbf{R}) \quad (25)$$

with identical lattice peaks $\rho_{\Delta}(\mathbf{r})$ centered at the lattice sites $\{\mathbf{R}\}$. A corresponding decomposition is induced for the weighted densities,

$$n_{\alpha}(\mathbf{r}) = \sum_{\mathbf{R}} n_{\Delta}^{(\alpha)}(\mathbf{r} - \mathbf{R}) \quad (26)$$

with

$$n_{\Delta}^{(\alpha)}(\mathbf{r}) = \int d^3 r' \rho_{\Delta}(\mathbf{r}') w_{\alpha}(\mathbf{r} - \mathbf{r}'). \quad (27)$$

In the following we assume spherical density peaks $\rho_{\Delta}(\mathbf{r}) = \rho_{\Delta}(r)$, but, for the time being, do not restrict their shape further, in contrast to the common approximation by Gaussians.¹ For the scalar weight functions this leads to

$$n_{\Delta}^{(\alpha)} = \frac{2\pi}{r} \int_0^\infty dr' r' \rho_{\Delta}(r') \int_{|r-r'|}^{r+r'} dr_{12} r_{12} w_{\alpha}(r_{12}). \quad (28)$$

Since the second integral can easily be performed for our polynomial weight functions only a one-dimensional numerical integration is necessary to compute the weighted densities. Similar, slightly more complex expressions result for the vector and tensor weighted densities.

Usually $\rho_{\Delta}(r)$ is zero (or negligible small) for distances r beyond a cutoff r_c , which implies an upper cutoff for

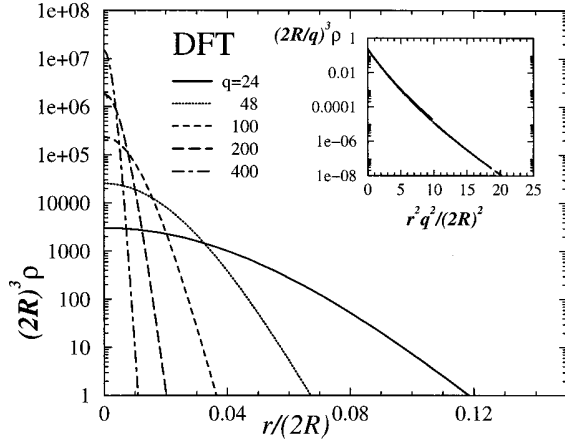


FIG. 3. Density functional results for the density peaks in an fcc crystal as a function of the distance r from the lattice site. Results for different softness are shown, $q=24, 48, 100, 200, 400$; at the density $\rho^*=\sqrt{2}$ corresponding to a close-packed hard-sphere ($q\rightarrow\infty$) crystal. Note the logarithmic ordinate extending over eight decades in density. The inset shows the same data scaled as $(2R/q)^3\rho$ as a function of the scaled and squared distance $r^2q^2/(2R)^2$.

$n_{\Delta}^{(\alpha)}(r)$ at $r=R+r_c$. (In contrast to the hard sphere case there is no lower cutoff.) Therefore only a few lattice sites \mathbf{R} contribute in Eq. (26) to the full weighted densities at any point. For the determination of the free energy we have employed two different numerical methods, depending on the width of the density profile. Method I applies to narrow profiles, for which only either one or two lattice sites contribute at every point. By taking advantage of the resulting symmetries the integration in Eq. (1) can be reduced to a one- and a two-dimensional numerical integral. Details can be found in Ref. 8. In method II we perform a full three-dimensional integration over an asymmetric unit, i.e., the smallest region with which space can be filled by applying the space group symmetries. For fcc and bcc crystals this corresponds to 1/48 of the Wigner–Seitz cell. For a given profile width we first make a list of the relevant lattice sites whose distance to the integration region is smaller than $R+r_c$. This approach fails for too narrow peaks because then the integration routine cannot reliably sample the integrand which takes on considerable values only in a narrow quasi-two-dimensional subset of the integration region.

The functional derivative $\delta F^{\text{exc}}/\delta\rho(r)$ is determined as demonstrated for hard spheres in Ref. 8, using analytical expressions for $\delta n_{\Delta}^{(\alpha)}(r')/\delta\rho_{\Delta}(r)$ and the same integration method as for the functional itself. In order to solve the stationarity equation

$$\rho_{\Delta}(r) = \frac{\exp\{-(1/4\pi r^2)\delta f^{\text{exc}}/\delta\rho_{\Delta}(r)\}}{4\pi \int dr' r'^2 \exp\{-(1/4\pi r'^2)\delta f^{\text{exc}}/\delta\rho_{\Delta}(r')\}} \quad (29)$$

with $f^{\text{exc}} = \beta F^{\text{exc}}/N$ the profile is discretized over a mesh in r . Then Eq. (29) is iterated starting from a reasonable initial guess until the maximum relative change of $\rho_{\Delta}(r)$ in one iteration is less than 10^{-5} .

In Fig. 3 we show the results for different softness parameters q at a fixed density $\rho^*=\sqrt{2}$, equal to the close

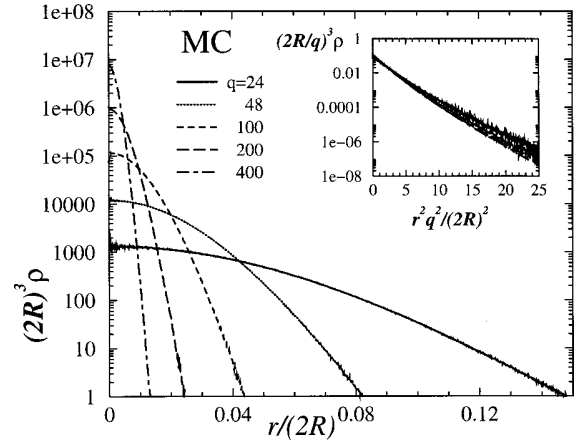


FIG. 4. Same as Fig. 3, but obtained from Monte Carlo computer simulations.

packing density for hard spheres. As expected the profiles become wider when the interaction potential softens. The *shape* remains essentially the same; if distance is scaled by q (and correspondingly density by q^{-3}) all curves practically coincide, as shown in the inset. Using a logarithmic plot of ρ vs r^2 moreover demonstrates that the peaks are almost Gaussian but have wider wings than a Gaussian fitted to the central part. In Fig. 4 we provide a direct comparison with computer simulations for the same parameters. They exhibit the same scaling behavior, but are slightly narrower (about 30%). Even the deviations from the Gaussian shape agree with the density-functional result. Note that strictly speaking, simulation and theoretical profiles differ in the following respect. The theoretical profiles minimize the DFT, if radially symmetric profiles are assumed. In principle, this is different from a spherical average of the minimizing profile with angular anisotropy. In the simulation, clearly, the equivalent of the latter is obtained. The difference, however, is expected to be small, because anisotropy of lattice sites is small (see, e.g., Ref. 23 for hard sphere results).

Here and in the following we always used the most advanced DFT version FMT3. We checked one state point ($\rho^*=1.4127, q=100$) for the older versions. The peak width is measured by

$$w = \left[\frac{8\pi}{3} \int_0^{\infty} dr r^4 \rho_{\Delta}(r) \right]^{1/2} \quad (30)$$

so that for Gaussian peaks

$$\rho_{\Delta}(r) = \frac{1}{\pi^{3/2} w^3} \exp[-(r/w)^2]. \quad (31)$$

It differs only by 5% between FMT3 and FMT2, whereas the FMT1 result is narrower by a factor 5. Also the shapes are very similar for the first two cases, but a peculiar long tail arises in FMT1.

In Fig. 5 we present the dependence of the profile width on the nearest neighbor distance $R_{nn}=2R(\sqrt{2}/\rho^*)^{1/3}$ in an fcc crystal with $q=100$. The lower and upper part of the solid line are obtained by methods I and II, respectively. There is no overlap range where both methods can be ap-

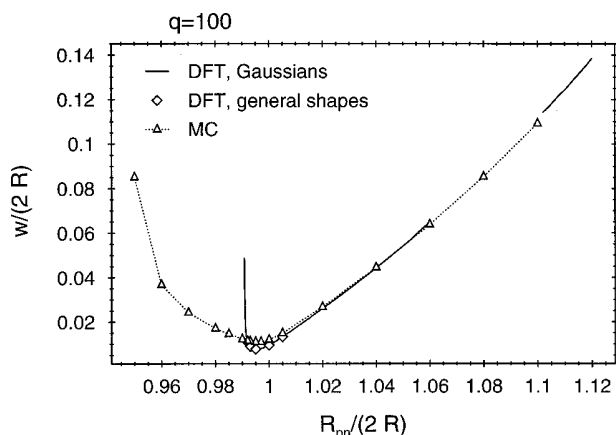


FIG. 5. Dependence of the width of the crystalline peaks [as defined in Eq. (30)] on the nearest neighbor distance in a fcc solid for $q=100$. The solid line is the DFT result assuming a Gaussian peak shape, obtained with methods I (lower part) and II (upper part) described in the text. The diamonds are obtained by the minimization with radially symmetric peaks. The triangles are Monte Carlo data.

plied, but the results connect nicely with each other. In both cases Gaussian profiles [Eq. (31)] were assumed. The widths from the radial minimization, indicated by diamonds, are not distinguishable from the Gaussians on the scale of the figure. Upon compression from the low density side the peaks first become narrower. However, just above $R_{nn}=2R$ surprisingly the width increases again. This increase is found both in simulation and theory, but is much steeper in DFT. The same behavior occurs for smaller q , even for the bcc crystal, but the minimum shifts towards higher R_{nn} and larger widths w .

The occurrence of vacancies can be taken into account within DFT by allowing non-normalized density peaks, i.e., less than one particle per lattice site on average, and treating the normalization constant as an additional minimization parameter. The FMT is the first DFT for which this procedure yields reasonably small vacancy concentrations⁹ for hard spheres.

Determining the average occupancy number in this way for star polymers, we find that SFMT also predicts almost normalized density peaks. There is a tiny negative vacancy concentration of the order of 10^{-5} near melting. This would mean that there are more double occupied sites than empty ones. Whether this is an artifact of the DFT or a feature of the peculiar logarithmic interaction of star polymers remains an open question.

C. The phase diagram

In order to compute the phase diagram of our star polymer model we determined the free energy in the Gaussian approximation for a large number of densities and softness parameters. Phase coexistence densities then follow by the usual common tangent construction. Our results are displayed in Fig. 6. For relatively hard interactions the fluid freezes into an fcc crystal, for soft interactions ($q \leq 4$) into a bcc crystal. Upon further compression both crystals eventually remelt. The broadening of the profile discussed in the

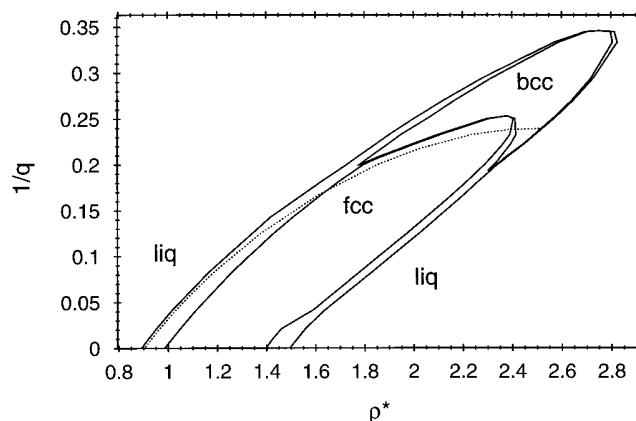


FIG. 6. Phase diagram of star polymers obtained by density functional theory as a function of the density ρ^* and the inverse softness parameter q^{-1} . All phase transitions are first order. The dotted line indicates the estimate of the freezing density by the Hansen-Verlet criterion.

previous section is a precursor of this remelting transition. Note that formally hard spheres ($q = \infty$) also remelt, because the solid but not the liquid free energy diverges at close packing. However, in this case the coexistence region extends into the unphysical density range beyond close packing. It must be stated that the present DFT has intrinsic limitations at high density. Any density distribution, where locally $n_3 > 1$ is punished by an infinite energy cost. In reality, such distributions will have large, but finite free energy.

In an intermediate softness range both fcc and bcc solids occur with the sequence liquid-fcc-bcc-fcc-liquid. The dotted line denotes the points where the main peak of the liquid structure factor reaches the value 2.8. This has been suggested as a general phenomenological freezing criterion by Hansen and Verlet²⁷ and lies close to the actual phase transition for not too small q . This demonstrates the internal consistency of the theory. For $q \lesssim 2.9$ the solid phase disappears completely.

Freezing and remelting of star polymers have been theoretically predicted before²⁸ and were observed experimentally in the closely related system of diblock copolymer micelles.^{29,30} In the latter work bcc was observed for softer interactions and fcc for harder interactions, in qualitative agreement with our findings. The same trend is known for simple liquids with inverse power potentials.³¹⁻³⁴ The most direct comparison is possible with the computer simulations of the log-Yukawa potential by Watzlawek *et al.*¹⁹ These authors obtained a phase diagram with exactly the same topology at low and intermediate densities. However, for large arm number the remelting is replaced by transitions to more “exotic” crystal structures at high densities: body-centered orthogonal (bco) and diamond lattices. A search for body-centered tetragonal (bct) and diamond crystals within the present theory produced no thermodynamically stable states. Especially the diamond lattice requires rather small nearest neighbor distances in the interesting density range, which is excluded by the following mechanism. When two neighboring sites come closer to each other the value of n_3 at their midpoint increases and eventually approaches unity, which

obviously induces a divergence of the functional. For high densities the differences between the log-hypergeometric and the log-Yukawa potential are expected to be small, as the logarithmic core dominates. We conclude that the absence of the exotic structures is a shortcoming of the theory. We did not attempt to determine the phase diagram by simulation since this would necessitate a large number of expensive free energy calculations. But the fcc crystal for $q=100$ is mechanically unstable for $\rho^* > 1.76$, slightly above the theoretical remelting transition.

V. DISCUSSION

The proposal of a new DFT has to be accompanied by examples of successful use. As a meaningful application, one could choose a well-studied model, e.g., the inverse-power potentials (see, e.g., Refs. 31–34), and let the new candidate compete with established theories. We have postponed this necessary work and have tackled the star polymer system, which has a quite young history. Besides the technical advantage that we can calculate certain quantities analytically, this system is of great actual interest.

The strategy of the SFMT is to assume a generic form of a density functional and to impose the correct behavior in well-defined limiting cases. In its present form, the theory captures the virial expansion up to second order correctly, as well as a density distribution given by a single delta peak times an average occupation number which is called zero-dimensional limit. The theory has deficiencies: Two delta functions which are separated within the range of the pair interaction are not described exactly. In this respect the SFMT is in a poorer state than the hard sphere FMT, which describes even three delta spikes exactly.⁵ Improving the SFMT along these lines is desirable; also Sweatman's work³⁵ and Percus' general rank two representation³⁶ should be useful.

We could show that the recent improvements in hard sphere FMT using tensorial weighted densities can (and need to) be done in SFMT to get a good description of the crystal. This situation is similar for hard spheres.^{8,9,5} No empirical rescaling like in Ref. 14 was used in the present work in order to highlight the power of the approach and its deficiencies. The deficiencies occur at high density, where the star polymers freeze into exotic bcc and diamond structures, that are not found to be stable within our approach. Nevertheless, intriguing high-density effects, like the broadening of density peaks upon increasing the density and remelting are described by SFMT. The sequence liquid–fcc–bcc–fcc upon increasing densities is correct. From the investigation of the star polymer model, we conclude that freezing, liquid and crystal properties of particles with soft interactions can be understood on the basis of a density functional that does not need input from the homogeneous fluid phase.

ACKNOWLEDGMENTS

Arben Jusufi is gratefully acknowledged for providing the simulation data in Fig. 1. We thank Bela Mulder for useful remarks. This work is part of the research program of

the Stichting voor Fundamenteel Onderzoek der Materie. B.G. acknowledges financial support from the EU and from the Nederlandse Organisatie voor Wetenschappelijk Onderzoek.

- ¹R. Evans, in *Fundamentals of Inhomogeneous Fluids*, edited by D. Henderson (Dekker, New York, 1992), p. 85.
- ²Y. Rosenfeld, *Phys. Rev. Lett.* **63**, 980 (1989).
- ³Y. Rosenfeld, M. Schmidt, H. Löwen, and P. Tarazona, *J. Phys.: Condens. Matter* **8**, L577 (1996); *Phys. Rev. E* **55**, 4245 (1997).
- ⁴P. Tarazona and Y. Rosenfeld, *Phys. Rev. E* **55**, R4873 (1997).
- ⁵P. Tarazona, *Phys. Rev. Lett.* **84**, 694 (2000).
- ⁶J. A. Cuesta, *Phys. Rev. Lett.* **76**, 3742 (1996).
- ⁷J. A. Cuesta and Y. Martinez-Raton, *Phys. Rev. Lett.* **78**, 3681 (1997).
- ⁸B. Groh and B. Mulder, *Phys. Rev. E* **61**, 3811 (2000).
- ⁹B. Groh, *Phys. Rev. E* **61**, 5218 (2000).
- ¹⁰C. Tutschka and G. Kahl, *Phys. Rev. E* **62**, 3640 (2000).
- ¹¹M. Schmidt, *J. Phys.: Condens. Matter* **11**, 10163 (1999).
- ¹²Y. Rosenfeld, M. Schmidt, M. Watzlawek, and H. Löwen, *Phys. Rev. E* **62**, 5006 (2000).
- ¹³M. Schmidt, H. Löwen, J. Brader, and R. Evans, *Phys. Rev. Lett.* **85**, 1934 (2000).
- ¹⁴M. Schmidt, *Phys. Rev. E* **60**, R6291 (1999).
- ¹⁵M. Schmidt, *Phys. Rev. E* **62**, 4976 (2000).
- ¹⁶M. Schmidt, *Phys. Rev. E* **62**, 3799 (2000).
- ¹⁷C. N. Likos, H. Löwen, M. Watzlawek, B. Abbas, O. Jucknischke, J. Allgaier, and D. Richter, *Phys. Rev. Lett.* **80**, 4450 (1998).
- ¹⁸M. Watzlawek, H. Löwen, and C. N. Likos, *J. Phys.: Condens. Matter* **10**, 8189 (1998).
- ¹⁹M. Watzlawek, H. Löwen, and C. N. Likos, *Phys. Rev. Lett.* **82**, 5289 (1999).
- ²⁰M. Watzlawek, "Phase behavior of star polymers," Ph.D. thesis, University of Düsseldorf, 1999, published by Shaker Verlag, Aachen.
- ²¹A. Jusufi, M. Watzlawek, and H. Löwen, *Macromolecules* **32**, 4470 (1999).
- ²²C. von Ferber, A. Jusufi, C. N. Likos, H. Löwen, and M. Watzlawek, *Eur. Phys. J. E* **2**, 311 (2000).
- ²³R. Ohnesorge, H. Löwen, and H. Wagner, *Europhys. Lett.* **22**, 245 (1993).
- ²⁴J. Stellbrink, B. Abbas, J. Allgaier, M. Monkenbusch, D. Richter, C. N. Likos, H. Löwen, and M. Watzlawek, *Prog. Colloid Interface Sci.* **110**, 25 (1998).
- ²⁵C. N. Likos, H. Löwen, A. Poppe, L. Willner, J. Roovers, B. Cubitt, and D. Richter, *Phys. Rev. E* **58**, 6299 (1998).
- ²⁶To convert the variables from Fig. 3(b) in Ref. 21 to the present ones, we divide the distances and multiply the forces by the same correction parameter, given as $2\lambda \exp((1+\sqrt{f}/2)^{-1} - (2q)^{-1} \ln(2q))$, where λ is the ratio between the corona diameter σ^* and twice the radius of gyration. The actual values are $\lambda=0.68, 0.66, 0.69$ for $f=18, 30, 50$, respectively, as given in Table I of Ref. 21.
- ²⁷J. Hansen and L. Verlet, *Phys. Rev.* **184**, 151 (1969).
- ²⁸T. A. Witten, P. A. Pincus, and M. E. Cates, *Europhys. Lett.* **2**, 137 (1986).
- ²⁹G. A. McConnell, A. P. Gast, J. S. Huang, and S. D. Smith, *Phys. Rev. Lett.* **71**, 2102 (1993).
- ³⁰G. A. McConnell and A. P. Gast, *Macromolecules* **30**, 435 (1997).
- ³¹R. Agrawal and D. A. Kofke, *Mol. Phys.* **85**, 23 (1995).
- ³²D. C. Wang and A. P. Gast, *J. Phys.: Condens. Matter* **11**, 10133 (1999).
- ³³D. C. Wang and A. P. Gast, *Phys. Rev. E* **59**, 3964 (1999).
- ³⁴D. C. Wang and A. P. Gast, *J. Chem. Phys.* **110**, 2522 (1999).
- ³⁵M. B. Sweatman, "Density functional theories of simple fluids and their mixtures," Ph.D. thesis, University of Bristol, 1995.
- ³⁶J. K. Percus, *J. Stat. Phys.* **52**, 1157 (1988).

Density functional theory for random sequential adsorption*

Matthias Schmidt

Institut für Theoretische Physik II, Heinrich-Heine Universität Düsseldorf, Universitätsstraße 1, D-40225 Düsseldorf, Germany

E-mail: mschmidt@thphy.uni-duesseldorf.de

Received 21 June 2002, in final form 29 August 2002

Published 8 November 2002

Online at stacks.iop.org/JPhysCM/14/12119

Abstract

We treat the non-equilibrium process of random sequential adsorption of hard particles onto a solid substrate by means of a geometry-based density functional theory. As a prerequisite we solve the zero-dimensional case exactly and use it to construct density functionals in higher dimensions, permitting the treatment of adsorption onto arbitrary spatially inhomogeneous substrates. As applications we study the influence of a hard boundary of the adsorption region in the one-dimensional car-parking problem and for colloidal deposition on a two-dimensional solid substrate. Comparing to our computer simulation results, we find that the respective density functionals correctly predict the oscillatory density profiles near the boundary, with amplitudes that are considerably smaller than in the corresponding equilibrium models.

1. Introduction

Random sequential adsorption (RSA) is one process that allows the systematic study of structure emerging in non-equilibrium situations (see [1] for a classic work and [2, 3] for reviews). In RSA a d -dimensional space (the substrate) is sequentially filled by particles. Each newly placed (deposited) particle is subject to the influence of the particles already present. In contrast, all deposited particles remain frozen at their positions and do not adjust to the presence of any newly deposited particles. Due to the intrinsic asymmetry of interactions, such a system is not characterized by an equilibrium distribution.

In the simplest case the particles are represented by hard spheres (HS), but generalizations exist; moreover RSA is often studied in low spatial dimensionality. In one dimension (1D) one refers to the (random) car-parking problem where exact results, e.g. for the pair correlation function [4], are known. In 2D, the RSA of HS is a common model for describing the adsorption of proteins [5, 6] or colloids [3] on solid surfaces.

* This work is dedicated to the memory of Yasha Rosenfeld.

Standard equilibrium liquid-state methods have been extended to treat such systems [7]; one particular example is the Percus–Yevick integral equation for RSA [8]. The principal derivation relies on the replica trick for studying quenched–annealed systems. In a binary quenched–annealed system the quenched species is commonly used to model a porous material and the annealed species an adsorbate fluid. Extending this framework to multi-component systems and *differentially* quenching single species allows one to treat the RSA process, where in a certain limit each particle in RSA corresponds to one species in the differentially quenched system.

Within the framework of density functional theory (DFT) [9] the equilibrium systems that correspond to the above-mentioned RSA models (hard rods in 1D, hard discs in 2D) are prototype examples where in 1D Percus derived the exact free energy functional [10], and in higher dimensions, via Rosenfeld’s fundamental-measure theory (FMT), excellent approximations are available [11–14].

Along a similar route to that above for integral equation theory, recently DFT was extended to quenched–annealed systems [15, 16]. The ‘trick’ for arriving at an approximation for the excess free energy is to solve the statistical mechanics in an idealized strongly confined situation called the 0D limit exactly, and input this knowledge into the geometric concept of FMT.

In the present contribution we propose, to the best of our knowledge, the first DFT for RSA. It is based on the exact solution for RSA in the 0D limit, and uses Rosenfeld’s concept to generalize to higher dimensions. As test cases, we consider particle deposition near a hard wall in 1D and 2D. Good agreement of the theoretical density profiles with our computer simulation data is found. The density profiles show considerably less pronounced structure when compared to the corresponding equilibrium systems. We can trace that back to the relatively smaller contribution of the excess part of the free energy compared to the ideal part in the RSA case, a feature that is already present in 0D.

The paper is organized as follows. In section 2 we define the process of RSA on an inhomogeneous substrate more explicitly. Section 3 is devoted to the exact solution for RSA in 0D and the subsequent DFT generalization to higher dimensions. In section 4 we use hard boundaries of the adsorption region in the 1D car-parking problem and for 2D colloidal deposition on a smooth wall as test cases to compare theoretical results to those from our computer simulations. We conclude in section 5.

2. The model

Inhomogeneous RSA is characterized by spheres with radius R that are placed sequentially onto a d -dimensional space characterized by an external potential $V_{\text{ext}}(\mathbf{r})$ where \mathbf{r} is the spatial coordinate. The placement is done according to repeated application of the following procedure.

- A trial sphere is placed at a random position \mathbf{r} .
- The trial sphere is removed with probability $1 - \exp(-\beta V_{\text{ext}}(\mathbf{r}))$, where β is the inverse temperature.
- The trial sphere is removed if it overlaps with any other sphere. Thereby overlap is characterized by a separation of sphere centres less than $2R$.

As a dimensionless density we use the coverage $\theta = v_d \rho$, where ρ is the number density of particles and v_d is the volume of a d -dimensional ‘sphere’, i.e. $v_1 = 2R$, $v_2 = \pi R^2$. The particle diameter is denoted by σR .

3. Theory

3.1. Overview

We seek to obtain the density distribution $\rho(\mathbf{r})$ for inhomogeneous RSA from a grand potential functional $\Omega[\rho(\mathbf{r})]$, which becomes minimal for the actual RSA profile. Hence the RSA profile fulfils the Euler–Lagrange equation $\delta\Omega/\delta\rho(\mathbf{r}) = 0$. We write the functional as a sum

$$\Omega[\rho(\mathbf{r})] = F_{\text{id}}[\rho(\mathbf{r})] + F_{\text{exc}}[\rho(\mathbf{r})] + \int d\mathbf{r} \rho(\mathbf{r}) [V_{\text{ext}}(\mathbf{r}) - \mu], \quad (1)$$

where \mathbf{r} is the d -dimensional space coordinate, μ is a Lagrange parameter used to adjust the overall density, F_{id} is the ideal-gas free energy functional, and F_{exc} is the contribution due to interactions with already adsorbed particles. The ideal-gas part is the same as in the equilibrium case and is given by

$$\beta F_{\text{id}}[\rho(\mathbf{r})] = \int d\mathbf{r} \rho(\mathbf{r}) [\ln(\Lambda^d \rho(\mathbf{r})) - 1], \quad (2)$$

where Λ is the (irrelevant) thermal wavelength. In the following we will obtain an approximation for F_{exc} using Rosenfeld’s fundamental-measure concept, starting from the exact solution for RSA in zero dimensions.

3.2. Zero dimensions

The 0D limit is represented by a hard cavity that confines the particle centres to a small volume $v_{0\text{D}}$. Explicitly, we may chose a spherical cavity of radius ϵ , such that $v_{0\text{D}} = 4\pi\epsilon^3/3$, and it is assumed that $\epsilon \ll R$. Due to the HS interaction, the cavity may either be empty or be occupied by a single particle. Canonically this is trivial, but in the grand ensemble a non-trivial relation between average number of particles and chemical potential results. This can be used (see below) to construct density functionals (DF) in higher dimensions. In the following we deal with multi-component HS where $i = 1, \dots, m$ is an index that labels the species. This labelling will later permit description of RSA in terms of differential quenching. We first lay out the general procedure by reviewing the equilibrium case.

For an equilibrium m -component mixture of HS in 0D, the mean number of particles of species i is given as

$$\bar{\eta}_i = \frac{z_i}{1 + \sum_{j=1}^m z_j}, \quad (3)$$

where, for species i , the scaled fugacity is defined as $z_i = \exp(\beta\mu_i)v_{0\text{D}}/\Lambda_i^3$. Summing the individual contributions yields the total number of particles

$$\bar{\eta} = \sum_{i=1}^m \bar{\eta}_i = \frac{z_{\text{tot}}}{1 + z_{\text{tot}}}, \quad (4)$$

where we have defined the total fugacity $z_{\text{tot}} = \sum_{i=1}^m z_i$. Hence, not surprisingly, we recover the solution for one-component HS (without distinction of species) by setting $m = i = 1$ in (3) and identifying z_1 in (3) with z_{tot} in (4). The total fugacity is related to the total chemical potential via $\beta\mu_{\text{tot}} = \ln(z_{\text{tot}})$, and the excess (over ideal gas) part is $\beta\mu_{\text{ex}} = \beta\mu_{\text{tot}} - \ln \bar{\eta}$, which is explicitly obtained from inversion of (4) as

$$\beta\mu_{\text{ex}} = -\ln(1 - \bar{\eta}). \quad (5)$$

The relation to the 0D excess free energy F_{0D} is via $\partial F_{0D}/\partial \bar{\eta} = \mu_{\text{ex}}$. Integration yields

$$\beta F_{0D} = (1 - \bar{\eta}) \ln(1 - \bar{\eta}) + \bar{\eta}. \quad (6)$$

From this result, DFs for equilibrium systems in higher dimensions can be derived (see sections 3.3, 3.4).

We next perform the same steps as above for RSA. Particles are inserted into the cavity with *increasing* species index i , such that species i is subject only to the influence of species $1, \dots, i - 1$. Later we will turn to the *differentially* quenched case by taking the proper limit of infinitely many components m each at vanishing fugacity z_i . The mean number of particles of species i is given by the relation

$$\bar{\eta}_i = \frac{z_i}{\prod_{j=1}^i (1 + z_j)}, \quad (7)$$

differing from the equilibrium result (3). The total number of particles is obtained as

$$\bar{\eta} = \sum_{i=1}^m \frac{z_i}{\prod_{j=1}^i (1 + z_j)}. \quad (8)$$

In the following we assume all fugacities to be equal, $z \equiv z_i = z_j$ for all i, j . This simplifies the subsequent calculations but is not mandatory; we have checked that other choices (where z_i is i -dependent) lead to the same final result after the RSA limit is taken. We can now simplify equation (8) and obtain

$$\bar{\eta} = \sum_{i=1}^m \frac{z}{(1+z)^i} = 1 - \frac{1}{(1+z)^m}. \quad (9)$$

In order to describe RSA a limiting procedure is required. We need to let $z \rightarrow 0$, to ensure that only a minute fraction of i -particles are present so that no interactions between particles of the same species i occur. However, to arrive at non-vanishing $\bar{\eta}$ we let the number of components diverge, $m \rightarrow \infty$. Both limits are taken while keeping the total fugacity $z_{\text{tot}} = \sum_{i=1}^m z_i = mz$ constant. Performing the limit in (9) yields $\bar{\eta} = 1 - \exp(-z_{\text{tot}})$, which can readily be inverted to $\beta \mu_{\text{tot}} = \ln(-\ln(1 - \bar{\eta}))$. The excess part is

$$\beta \mu_{\text{ex}} = \ln(-\ln(1 - \bar{\eta})) - \ln \bar{\eta}, \quad (10)$$

which can be integrated to give the 0D excess free energy for RSA:

$$F_{0D} = \text{li}(1 - \bar{\eta}) - \gamma - (1 - \bar{\eta}) \ln(-\ln(1 - \bar{\eta})) - \bar{\eta}[\ln(\bar{\eta}) - 1], \quad (11)$$

where $\gamma \approx 0.577216$ is Euler's constant, and $\text{li}(x) = \int_0^x dt/\ln t$ is the logarithmic integral function. Note that the limiting procedure, $z \rightarrow 0, m \rightarrow \infty, mz = \text{constant}$, can also be (trivially) applied in the equilibrium case (4) leading to an unchanged result (6).

It is interesting to compare (11) with the equilibrium result (6). Both free energies increase monotonically with $\bar{\eta}$, have positive curvature, and are defined for $0 \leq \bar{\eta} \leq 1$. We find, however, that the result for RSA is smaller by a factor of roughly 1/2 over almost the entire density range; hence as a rule of thumb $F_{0D}^{\text{RSA}} \approx F_{0D}^{\text{eq}}/2$. (Explicit numerical values, e.g. for $\bar{\eta} = 0.7$, are $\beta F_{0D}^{\text{RSA}} = 0.1594$, $\beta F_{0D}^{\text{eq}}/2 = 0.3388/2 = 0.1694$.) As a consequence the ideal free energy (which is the same in both cases) gives a stronger contribution in RSA than in the equilibrium system. This property will persist through the construction of the DFs for higher dimensions, which we next turn to.

3.3. One dimension

The excess (over ideal gas) free energy functional is expressed as

$$\beta F_{\text{exc}}[\rho(x)] = \int dx \Phi(\{n_\nu(x)\}), \quad (12)$$

where the weighted densities $n_\nu(x)$ are obtained by 1D convolutions of the actual density profile $\rho(x)$ with weight functions w_ν :

$$n_\nu(x) = \int dx' \rho(x') w_\nu(x - x'), \quad \nu = 0, 1. \quad (13)$$

The weight functions are defined as

$$w_1(x) = \Theta(R - |x|), \quad (14)$$

$$w_0(x) = \delta(R - |x|)/2, \quad (15)$$

where $\Theta(r)$ is the step function, and $\delta(r)$ is the Dirac distribution. The excess free energy density is given by

$$\Phi = n_0 \beta F'_{0D}(n_1). \quad (16)$$

where the prime denotes differentiation w.r.t. the argument. In the equilibrium case $\Phi = \Phi_{\text{eq}}$, where we use (6) to obtain

$$\Phi_{\text{eq}} = -n_0 \ln(1 - n_1). \quad (17)$$

Up to now this is a reformulation of Percus's *exact* hard-rod functional [10]. For RSA we set $\Phi = \Phi_{\text{RSA}}$ and usage of (11) gives

$$\Phi_{\text{RSA}} = n_0 [\ln(-\ln(1 - n_1)) - \ln n_1]. \quad (18)$$

We emphasize that although this procedure generates the exact functional for the case of equilibrated hard rods, this does not hold in general; e.g. in the case of a 1D model colloid-polymer mixture [17] it yields bulk free energies differing from (albeit approximating well) the exact result [18].

3.4. Two dimensions

Again the excess free energy is a spatial integral:

$$\beta F_{\text{exc}}[\rho(\mathbf{r})] = \int d\mathbf{x} \Phi(\{n_\nu(\mathbf{x})\}), \quad (19)$$

and the weighted densities are obtained by 2D convolutions:

$$n_\nu(\mathbf{x}) = \int d\mathbf{r} \rho(\mathbf{r}) w_\nu(\mathbf{x} - \mathbf{r}), \quad \nu = 0, 1, v1, 2 \quad (20)$$

of the four 2D weight functions

$$w_2(\mathbf{r}) = \Theta(R - r), \quad (21)$$

$$w_1(\mathbf{r}) = \delta(R - r), \quad (22)$$

$$\mathbf{w}_{v1}(\mathbf{r}) = \delta(R - r) \mathbf{r}/r, \quad (23)$$

$$w_0(\mathbf{r}) = \delta(R - r)/(2\pi R), \quad (24)$$

where \mathbf{r} in equations (21)–(24) denotes the 2D position vector; the subscript v is a reminder that \mathbf{w}_{v1} is a vector. The free energy density has the generic structure

$$\Phi = n_0 \beta F'_{0D}(n_1) + \frac{n_1 n_1 - \mathbf{n}_{v1} \cdot \mathbf{n}_{v1}}{4\pi} \beta F''_{0D}(n_1). \quad (25)$$

Inserting the equilibrium 0D excess free energy (6) yields the free energy density of Rosenfeld's functional in 2D:

$$\Phi_{\text{eq}} = -n_0 \ln(1 - n_2) + \frac{n_1 n_1 - n_{v1} \cdot n_{v1}}{4\pi(1 - n_2)}. \quad (26)$$

For RSA we use (11) to obtain

$$\Phi_{\text{RSA}} = n_0 [\ln(-\ln(1 - n_2)) - \ln n_2] - \frac{n_1 n_1 - n_{v1} \cdot n_{v1}}{4\pi} \left[\frac{1}{(1 - n_2) \ln(1 - n_2)} + \frac{1}{n_2} \right]. \quad (27)$$

This completes the prescription for the 2D case. The generalization to 3D is straightforward, and also higher $d > 3$ can be treated in principle [19].

4. Results

4.1. One dimension

Here and in the 2D case below, we study the influence of an external potential V_{ext} that describes the boundary of the adsorption region, given by

$$V_{\text{ext}}(x) = \begin{cases} \infty & x < R, \\ 0 & \text{otherwise.} \end{cases} \quad (28)$$

In order to provide benchmark results we have carried out computer simulations of the RSA process with fixed total number of insertion trials. We have stayed somewhat away from the jamming limit, where no further particles can be deposited due to hard-core overlap. In 1D this jamming coverage is $\theta = 0.7476$, and we have considered $\theta = 0.6883$, i.e. $\sim 92\%$ of the jamming value.

In the simulations a second wall is used in order to build up a finite system. The resulting external potential is $V_{\text{ext}}(x) + V_{\text{ext}}(L - x)$, where the wall distance L is chosen sufficiently large that the density profiles from both walls are well decoupled from each other; we use $L = 20\sigma$, which we find to be amply sufficient. The number of insertion trials is fixed to 100; hence the number of particles present in the system fluctuates from realization to realization. Averaging over 10^6 realizations yields the above-quoted value for the coverage. Histograms of the particle coordinates are used to obtain $\rho(x)$.

Within DFT we numerically minimize (via iteration of the corresponding Euler-Lagrange equation) the grand potential functional Ω , equation (1), where the excess part, F_{exc} , in the present 1D case is given in section 4.1. The Lagrange parameter μ is determined to yield the prescribed coverage.

Results from simulation and theory are displayed in figure 1. The density has a maximal value at contact with the wall, $x = R^+$. It decreases monotonically over a distance of one particle diameter ($\sigma/2 < x < 3\sigma/2$). At $x = 3\sigma/2$ a kink occurs, and for larger x the oscillations are rapidly damped as the bulk value is approached. The results from theory and simulation agree well, except that the DFT underestimates the behaviour near contact and the contact value itself. The behaviour of $\rho(x)$ away from the contact region is reproduced quite well, with the correct wavelength and decay length of the oscillations. We emphasize that the coverage considered is relatively large (the arrow in figure 1 indicates the jamming coverage).

In figure 1 we also show the density profiles of equilibrium hard rods against a hard wall (i.e. the external potential given in (28)) at the same density. This is obtained from numerical minimization of Percus's functional [10] given in section 3.3. As the hard wall exerts a similar effect to a fixed particle, in the equilibrium case the density profile at the hard wall is equal (up to the bulk density as a multiplicative constant) to the pair correlation function $g(x)$. We have

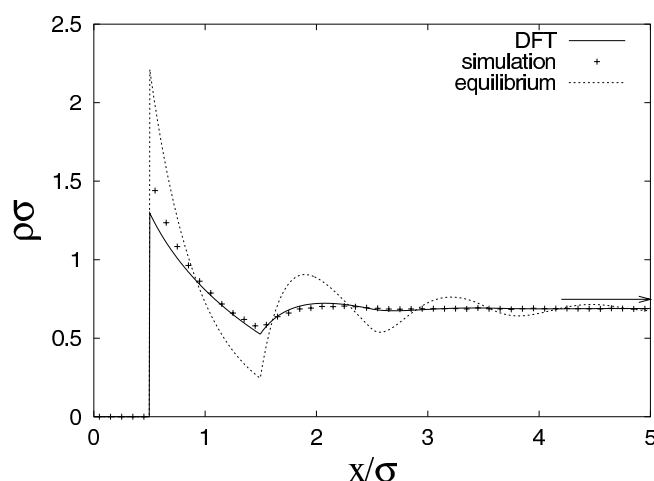


Figure 1. Density profile $\rho(x)\sigma$ as a function of the scaled distance x/σ for 1D RSA against a hard wall. The solid curve is the DFT result; the symbols indicate computer simulation data. For comparison, the equilibrium profile of hard rods against a hard wall is also shown (dashed curve). The arrow indicates the density at the jamming limit $\theta = 0.7476$.

checked that our result agrees (within reasonable numerical accuracy) with the exact analytic result for the pair distribution function for 1D hard rods [20].

It is striking that in the equilibrium system more structure is built up; the amplitude and decay length of the density profile are considerably larger than in the RSA case. Physically, this means that non-equilibrium in RSA hinders the emergence of structure. Technically, within the DFT approach the origin can be traced back to the fact that the RSA excess free energy functional is smaller (by about a factor 1/2) compared to the equilibrium functional. Hence the ideal free energy functional (2) plays a more dominant role than the excess part, which generates the structural correlations. (Note that in the case of adsorption of non-interacting particles, i.e. $F_{\text{exc}} = 0$, the density profile is constant for $x > \sigma/2$.)

As an aside, for RSA in 1D the pair distribution is also known exactly [4]. However, there is a slightly more subtle relation between $\rho(x)$ at the hard wall and $g(x)$. As the hard wall is present from the beginning of the RSA process, it exerts a similar effect to the *first* particle placed in the bulk case without a wall. To obtain $g(x)$, however, an average over *all* particle pairs is to be performed; hence this will in general differ from $\rho(x)$.

4.2. Two dimensions

Here we apply the 2D functional outlined in section 3.4 to the hard wall represented by the external potential (28), where x is the coordinate perpendicular to the wall. In 2D the jamming limit is known to be $\theta \approx 0.547$ from computer simulations [21]. We consider $\theta = 0.4712$ corresponding to $\sim 86\%$ of the jamming coverage. For the computer simulations we use a wall separation distance $L = 11\sigma$ and periodic boundary conditions in the y -direction (10σ perpendicular to the x -direction); the number of insertion trials is 1000. In figure 2 DFT and simulation results are shown. The qualitative behaviour is similar to the result in 1D; however, no kink at $x = 3\sigma/2$ is present.

Again the agreement of theory and simulation is satisfactory; the only significant deviation is near contact, where the DFT result again underestimates the simulation value. As above in the 1D investigation, we attribute these deviations to the relatively large coverage considered.

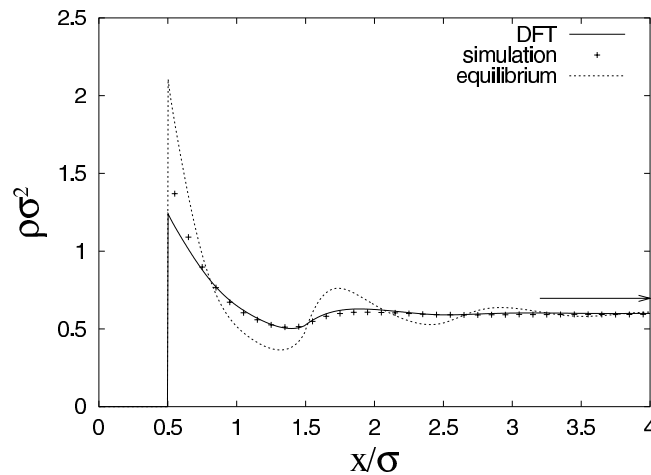


Figure 2. Density profile $\rho(x)\sigma^2$ as a function of the scaled distance x/σ for 2D RSA against a hard wall. The key is the same as in figure 1. The arrow indicates the density at the jamming limit $\theta = 0.547$.

We also present the profile for equilibrium hard discs against a hard wall obtained from numerical minimization of Rosenfeld's 2D functional (section 3.4). Again the equilibrium profile shows significantly stronger structure than the RSA profile.

5. Conclusions

In conclusion, we have derived a DFT for the non-equilibrium process of RSA of d -dimensional HS onto a d -dimensional substrate focusing on the resulting structure not on the adsorption kinetics. To the best of our knowledge, DFT has so far not been applied to RSA. We have explicitly treated in this contribution the space dimensions $d = 1, 2$; the extension to $d = 3$ is straightforward. As was done for other systems before, the exact solution of the 0D limit was used as an input into the powerful machinery of FMT to arrive at explicit approximations for the RSA free energy functional.

Our theory permits the study of spatially inhomogeneous substrates where the adsorption probability at space point r is governed by a Boltzmann weight according to a freely prescribed external potential $V_{\text{ext}}(r)$. Such applications include the study of deposition onto stripe-patterned substrates [22].

As test applications we focused on the 1D car-parking problem and on 2D colloidal deposition on a solid substrate, and have studied in both cases the effect of an impenetrable boundary region (hard wall) of the adsorption region. When compared to our computer simulation results, we find the theoretical results to correctly describe the oscillatory behaviour with a slight tendency to underestimate the contact value, but with very good agreement of wavelength and decay length of the oscillations into the bulk. The densities in both cases considered are close to the jamming limit; hence a severe test of the accuracy of the DFT is provided. We expect the accuracy of the theoretical curves to further improve upon lowering the density (i.e. moving further away from the jamming limit).

When compared to the corresponding equilibrium systems of hard rods and hard discs against a hard wall, significantly less structured density profiles result at equal bulk densities. We can trace that back to the fact that in RSA the ideal-gas free energy (that smooths out

structure) plays a more dominant role over the excess free energy (arising from interactions) than in the equilibrium case. This feature was found to be already present in OD. As a rule of thumb, we find the d -dimensional excess free energy functional for RSA to be roughly half that of the corresponding equilibrium system.

Hence in conjunction with the machinery of FMT, the OD limit is an, albeit seemingly trivial, useful seed for studying non-trivial behaviour in physically relevant dimensions, and permits one to broaden the scope of DFT to non-equilibrium situations.

References

- [1] Widom B 1966 *J. Chem. Phys.* **44** 3888
- [2] Evans J W 1993 *Rev. Mod. Phys.* **65** 1281
- [3] Schaaf P, Voegel J and Senger B 2000 *J. Phys. Chem. B* **104** 2204
- [4] Bonnier B, Boyer D and Viot P 1994 *J. Phys. A: Math. Gen.* **27** 3671
- [5] Feder J and Giaever J 1980 *J. Colloid Interface Sci.* **78** 144
- [6] Feder J 1980 *J. Theor. Biol.* **87** 237
- [7] Given J A 1992 *Phys. Rev. A* **45** 816
- [8] Boyer D, Tarjus G and Viot P 1995 *J. Chem. Phys.* **103** 1607
- [9] Evans R 1992 *Fundamentals of Inhomogeneous Fluids* ed D Henderson (New York: Dekker) p 85
- [10] Percus J K 1976 *J. Stat. Phys.* **15** 505
- [11] Rosenfeld Y 1989 *Phys. Rev. Lett.* **63** 980
- [12] Rosenfeld Y, Schmidt M, Löwen H and Tarazona P 1996 *J. Phys.: Condens. Matter* **8** L577
- [13] Rosenfeld Y, Schmidt M, Löwen H and Tarazona P 1997 *Phys. Rev. E* **55** 4245
- [14] Cuesta J A, Martínez-Raton Y and Tarazona P 2002 *J. Phys.: Condens. Matter* **14** 11965–80
- [15] Schmidt M 2002 *Phys. Rev. E* at press
- [16] Schmidt M, Schöll-Paschinger E, Köfinger J and Kahl G 2002 *J. Phys.: Condens. Matter* **14** 12099–12117
- [17] Schmidt M, Löwen H, Brader J M and Evans R 2002 *J. Phys.: Condens. Matter* **14** 9353–82
- [18] Brader J M and Evans R 2002 *Physica A* **306** 287
- [19] Finken R, Schmidt M and Löwen H 2002 *Phys. Rev. E* **65** 016108
- [20] Meeron E A and Siegert A J 1968 *J. Chem. Phys.* **48** 3139
- [21] Hinrichsen E L, Feder J and Jossang T 1986 *J. Stat. Phys.* **44** 793
- [22] Harreis H M, Schmidt M and Löwen H 2002 *Phys. Rev. E* **65** 041602

Freezing transition of hard hyperspheres

Reimar Finken,¹ Matthias Schmidt,² and Hartmut Löwen²

¹University Chemical Laboratory, Lensfield Road, Cambridge CB2 1EW, United Kingdom

²Institut für Theoretische Physik II, Heinrich-Heine-Universität Düsseldorf, Universitätsstraße 1, 40225 Düsseldorf, Germany

(Received 22 May 2001; published 14 December 2001)

We investigate the system of D -dimensional hard spheres in D -dimensional space, where $D > 3$. For the fluid phase of these hyperspheres, we generalize scaled-particle theory to arbitrary D and furthermore use the virial expansion and the Percus-Yevick integral equation. For the crystalline phase, we adopt cell theory based on elementary geometrical assumptions about close-packed lattices. Regardless of the approximation applied, and for dimensions as high as $D = 50$, we find a first-order freezing transition, which preempts the Kirkwood second-order instability of the fluid. The relative density jump increases with D , and a generalized Lindemann rule of melting holds. We have also used ideas from fundamental-measure theory to obtain a free energy density functional for hard hyperspheres. Finally, we have calculated the surface tension of a hypersphere fluid near a hard smooth (hyper-)wall within scaled-particle theory.

DOI: 10.1103/PhysRevE.65.016108

PACS number(s): 64.60.Cn, 64.70.Dv, 61.20.Gy

I. INTRODUCTION

In the last decades, our understanding of the freezing transition has greatly advanced [1,2]. Most of the success comes from the insight that the essential molecular mechanism that drives freezing can be understood in terms of different kinds of entropy [3]. This is demonstrated by ordering transitions that purely entropy-driven hard-core particles exhibit. The simple model of hard spheres, which has only the sphere packing fraction as thermodynamical parameter, has played a key role in a statistical description of freezing; for a recent review see [4]. Computer simulations [5,6] have shown that there is a first-order freezing transition from a fluid into a face-centered-cubic crystal at a packing fraction of around 0.5 with a relative density jump across freezing of about 10%. In two spatial dimensions (hard discs), the precise nature of freezing is still a matter of debate but there is recent evidence from computer simulations that the transition is in accordance with the Kosterlitz-Thouless scenario [7]. The thermodynamics of the one-dimensional model, namely, hard rods, can be calculated analytically [8] revealing that there is no freezing transition at packing fractions away from close packing.

From a more theoretical point of view, it is interesting to study systems in spatial dimension D higher than three. The motivation to do so is twofold. First, the limit of infinite dimension may lead to enormous simplifications allowing sometimes even for an analytical solution of the thermodynamics, fluid structure, and phase transformations. Recent examples include the hypercube [9] and hypersphere [10] fluid, the lattice plasma [11], the Gaussian potential [12,13] as well as systems with attractions [14,15]. The advantage in high dimensions is that the third and higher virial coefficients vanish asymptotically. Once the limit $D \rightarrow \infty$ is known, it may serve as a reference system in order to include finite dimensions in a perturbative analysis as a function of $1/D$, see e.g., Refs. [13,16] for such discussions. Second, the crossover between different spatial dimensions imposes physical consistency constraints on the theories. Understanding a fluid in different dimensions is important for constructing, e.g., density functionals explicitly. For hard spheres, ap-

proximate functionals can be obtained by imposing the correct crossover to reduced D . This idea was exploited particularly in the construction of fundamental-measure density functionals [17,18] in dimensions $D = 2, 3$ [19–21].

Systems composed of hard hyperspheres, being the natural extension of hard spheres to arbitrary spatial dimensions D , have, therefore, been considered quite extensively. The limit of infinite dimensions was studied in relation to the thermostatics [10,22,24,23,13] and dynamics [25]. Furthermore, the third and fourth virial coefficients have been calculated for arbitrary dimensions [26], and different fluid state theories for the thermodynamics and structure proposed based either on an overlap volume approach [27], the Percus-Yevick [28], mean spherical [29], or hypernetted chain [30] approximation. For $D = 4, 5$, a crystalline phase of hyperspheres has been studied with free-volume theory [31], the freezing transition has been examined by computer simulation [32], and density functional theory [33]. Furthermore, the demixing transition in a binary hypersphere mixture has been discussed [34,35] on the basis of a Carnahan-Starling-type equation of state [36,37].

In this paper we investigate the freezing transition of hyperspheres in *arbitrary* dimension, which has not been addressed until now. This aim requires a detailed description for the free energies of the fluid and solid state. For the fluid free energy, we use several methods such as the virial expansion, scaled-particle theory, fundamental-measure density functional, and the Percus-Yevick liquid-integral equation. All these approaches feature the exact second virial coefficient. For large dimensions, higher-order contributions are known to vanish, and consequently we obtain similar fluid free energies from all approaches. To access the free energy of the solid, we use the free-volume theory together with geometric results about the close-packed density and the structure of so-called laminated lattices in high dimension. In contrast to earlier approaches based on a fluid instability analysis [13,23], we obtain a first-order freezing transition even for high dimensions. We show that the freezing transition preempts this Kirkwood-type second-order spinodal instability of the fluid. The relative density jump across freezing even increases with rising dimension D . The Lindemann

parameter at melting is very robust with respect to a change of dimensionality such that the Lindemann rule of melting can be carried over to arbitrary dimensions. As a side product of scaled-particle theory, we derive an analytical expression for the surface tension between a smooth hard (hyper-)wall and a hard hypersphere fluid for any D . Furthermore, we develop a density functional for arbitrary spatial dimension in the spirit of Rosenfeld's fundamental-measure theory [17–21].

The paper is organized as follows. In Sec. II, we briefly summarize mathematical properties of close-packing densities. The solid free energy is outlined in Sec. III. In Sec. IV, we describe different approaches to the fluid free energy. Section V is devoted to the construction of a density functional for inhomogeneous hard hyperspheres. Results for freezing are presented in Sec. VI, and we finally conclude in Sec. VII.

II. HYPERSPHERES, LATTICES, AND CLOSE PACKING

The interaction between hard hyperspheres is pairwise and given by the potential

$$u(r) = \begin{cases} \infty, & r < 2R \\ 0, & r \geq 2R, \end{cases} \quad (1)$$

where r is the Euclidian center-to-center separation in D dimensions and R denotes the hypersphere radius. Thermodynamical and structural properties of the hard hypersphere system are independent of temperature T , which only sets the energy scale $k_B T \equiv 1/\beta$. The system's only relevant parameter is the number density ρ , measuring the number of particles per D -dimensional volume. A suitable dimensionless packing fraction is defined via $\eta = \rho V_D(R)$, where $V_D(R) = R^D \pi^{D/2} / \Gamma(1 + D/2)$ denotes the D -dimensional volume of the hypersphere of radius R and $\Gamma(x)$ is the gamma function. To simplify the notation, we denote the volume of the unit sphere of radius $R=1$ as $V_D \equiv V_D(1)$. We also define the $(D-1)$ -dimensional surface as $s_{D-1}(R) = DV_D R^{D-1}$.

Due to packing constraints, η has a D -dependent upper limit, which is the so-called close-packing fraction η_{cp} . The value of η_{cp} is known in a mathematically rigorous sense only in the cases $D=1,2,3$, see e.g., Ref. [4]. While obviously $\eta_{cp}=1$ for $D=1$, the close-packed configuration for $D=2$ is a triangular lattice with $\eta_{cp} = \pi/(2\sqrt{3}) = 0.91$ and a face-centered-cubic lattice for $D=3$ with $\eta_{cp} = \pi/(3\sqrt{2}) = 0.74$. The latter structure is degenerate with respect to the stacking sequence. For higher dimensions, there is Minkowski's lower bound and Blichfeldt's upper bound [38] for η_{cp} , such that

$$\frac{\zeta(D)}{2^{D-1}} \leq \eta_{cp} \leq \frac{D+2}{2} \left(\frac{1}{\sqrt{2}} \right)^D \quad \text{for } D > 1, \quad (2)$$

where $\zeta(x)$ denotes the Riemann zeta function. The class of *laminated lattices* [38] is defined inductively and gives in general high packing fractions. The numerical values of η_{cp} are shown in Fig. 1 as a function of D . In particular, for $D < 25$, their packing is close to the upper bound, Eq. (2).

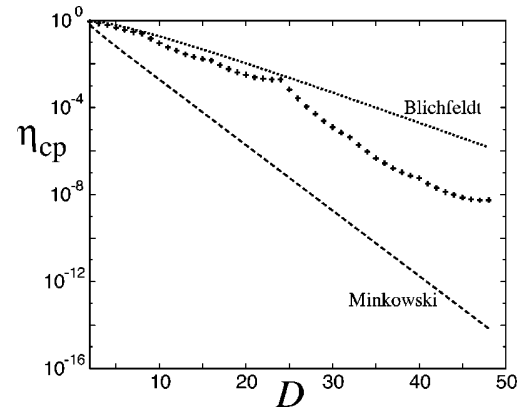


FIG. 1. Close-packing fraction η_{cp} as a function of dimensionality D . Blichfeldt's upper bound (dotted line), Minkowski's lower bound (dashed line), and the corresponding data for the laminated lattices (symbols) are shown. Note the logarithmic scale for η_{cp} .

Therefore, we restrict our investigation of the solid state to laminated lattices. However, as we shall show below, the general methodology can be applied to other crystals as well, provided their close-packing fraction is known.

III. FREE-VOLUME THEORY FOR THE SOLID STATE

We employ free-volume (or cell) theory in order to calculate free energies of the solid state. This approach, see e.g., [39], was also discussed for arbitrary D recently in Ref. [31]. Cell theory is based on the common partitioning of physical space into Wigner-Seitz cells (WSC) of the lattice structure under consideration. For hard spheres, no overlap between neighboring particles can occur, provided that each sphere stays completely within its WSC. Carrying out a partition sum where only this restricted set of configurations is taken into account strictly underestimates the full (exact) partition sum. In detail, let a denote the distance between nearest neighbors. The boundaries of the WSC are the distance $a/2$ apart from the lattice site. The spheres are supposed to stay completely within the WSC, such that each sphere center is allowed to move only a distance $a/2 - R$ from its lattice site towards a neighboring site. We assume that the shape of the accessible ("free") volume is the same as that of the WSC. Then the free volume of each sphere scales with the D th power of $(a - 2R)/a$, and we obtain

$$V_{\text{free}} = V_{\text{WS}} \left[\frac{a - 2R}{a} \right]^D. \quad (3)$$

If one relaxes the assumption of the same shape of free-volume cell and WSC, the real free volume is still larger than V_{free} . Let the free energy per particle be $f_s^{\text{exc}} + f^{\text{id}}$, where the ideal contribution is $f^{\text{id}} = \ln(\eta) - 1$. One obtains a strict upper bound for the excess free energy per particle of the solid state

$$\beta f_s^{\text{exc}} \leq 1 - D \ln \left[1 - \left(\frac{\eta}{\eta_{cp}} \right)^{1/D} \right]. \quad (4)$$

Note that if one inserts a lower bound for η_{cp} (as, e.g., for the laminated lattices considered in this paper) the resulting expression is still an upper bound for the free energy. An alternative for obtaining an estimate of the free energy is to calculate the free volume of each sphere with all the other spheres kept fixed. This allows each sphere to move twice as far from its lattice site as in the former approach. Of course, here one counts also forbidden configurations, so that the bounding property of the free energy is lost. However, in $D=3$ this gives a more accurate, albeit empirical estimate of the exact free energy. For general D , we obtain

$$\beta f_s^{\text{exc}} \approx 1 - D \ln \left[1 - \left(\frac{\eta}{\eta_{cp}} \right)^{1/D} \right] - D \ln 2. \quad (5)$$

IV. THEORIES FOR THE FLUID STATE

A. Virial expansion

Wyler, Rivier, and Frisch [24,10] have considered the Mayer series of the hard hypersphere fluid, and have shown that in the limit of infinite dimensionality, the virial expansion up to second order becomes asymptotically exact. The virial coefficients are defined by the expansion

$$\beta p = \rho + \sum_{n=2}^{\infty} B_n \rho^n, \quad (6)$$

where p is the pressure. The second virial coefficient is known analytically as $B_2 = 2^{D-1} V_D(R)$. The expansion of the excess free energy of the fluid state then reads

$$\beta f_f^{\text{exc}} = \frac{1}{2} \eta 2^D + \frac{1}{2} \frac{B_3}{[V_D(R)]^2} \eta^2 + O(\eta^3). \quad (7)$$

The third virial coefficient B_3 can be expressed by a quadrature [24] that can be solved analytically in even dimensions [26]. For odd dimensions we rely on a numerical solution. Our results for B_3 are shown versus D in Fig. 2. Although the numerical value of B_3 is quite large as $D \rightarrow \infty$, for small η its contribution to the free energy may become negligible. This is indeed the case for the densities relevant for freezing, as we will demonstrate below. We remark, however, that it is not proven that the virial expansion converges in the density region important for freezing [40]. There is thus still the possibility that the virial expansion does not describe the fluid state correctly. A similar situation exists in three dimensions, where the convergence of the virial expansion can only be proven rigorously up to $\eta \approx 0.02$ [40]. Numerical evaluation of the expansion to seventh order, however, show satisfactory results up to $\eta \approx 0.5$.

B. Percus-Yevick integral equation

Integral equations provide a very successful description of fluids. For hard spheres, the Percus-Yevick closure [41] is remarkably successful in three dimensions. One of its appealing properties is that it can be solved analytically for this system. Leuthesser generalized the solution to all odd dimensions $D=2k+1$, $k=0,1,2,\dots$ [28] and solved the

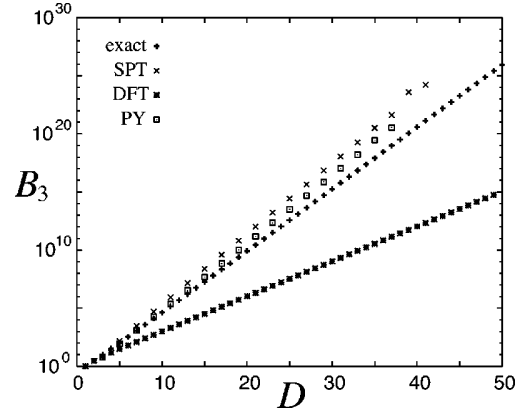


FIG. 2. Various approximations for the third virial coefficients B_3 as a function of dimension D . Shown is the exact result, as well as the results from scaled-particle theory (SPT), density-functional theory (DFT), and Percus-Yevick theory (PY).

equations explicitly for $D=1,3,5$. We follow his approach and treat the equations numerically for higher (odd) dimensions. We use the Wiener-Hopf factorization of the structure factor $S(q) = 1/[\tilde{Q}(q)\tilde{Q}(-q)]$, where q is the wave vector magnitude. Here $\tilde{Q}(q)$ is a regular function, which can be written as

$$\tilde{Q}(q) = 1 - (2\pi)^k \rho \int_0^{2R} Q(r) e^{ikr} dr. \quad (8)$$

It can be shown that $Q(r)$ is a polynomial of order $2k$ in r of the general form

$$Q(r) = (2R)^{2k} \sum_{n=0}^k Q_n \left(\frac{r}{2R} - 1 \right)^{n+k}, \quad 0 \leq r \leq 2R. \quad (9)$$

The system of integral equations can be reduced to a system of $k+1$ algebraic equations for the unknowns Q_0, \dots, Q_k . Two out of these equations are linear

$$(-1)^k = -k! 2^k Q_k + \rho (2\pi)^k (2R)^{2k+1} \times \sum_{n=0}^k (-1)^n \frac{Q_n}{(k+n+1)}, \quad k \geq 0, \quad (10)$$

$$(-1)^k = -(k-1)! 2^{k-1} Q_{k-1} + \rho (2\pi)^k (2R)^{2k+1} \times \sum_{n=0}^k (-1)^n \frac{Q_n}{(k+n+2)}, \quad k \geq 1, \quad (11)$$

and the remaining $k-1$ equations are nonlinear

$$Q^{(2n+1)}(0) = \frac{1}{2} \rho (2\pi)^k (-1)^{n+1} [Q^{(n)}(0)]^2 - \rho (2\pi)^k \times \sum_{\nu=0}^{n-1} (-1)^\nu Q^{(\nu)}(0) Q^{(2n-\nu)}(0), \quad 0 \leq n < k-1, \quad (12)$$

where $Q^{(k)}(0)$ denotes the k th derivative of $Q(r)$ at $r=0$. We solve Eqs. (10)–(12) numerically. As the effort quickly increases with rising dimension [we are faced with $(D+1)/2$ coupled equations], we restrict ourselves to $D \leq 33$. The function $Q(r)$ provides us with all the necessary information about the thermodynamics of the fluid state, as it is related to the contact value of the pair distribution function $g(r)$ of the hyperspheres via

$$g(2R^+) = (-1)^{k+1} Q^{(k)}(2R)/(2R)^{2k}, \quad (13)$$

which in turn determines the free energy via the virial route [28,41]

$$\beta p/\rho = 1 + 2^{D-1} \eta g(2R^+). \quad (14)$$

The second virial coefficient determined in this way is exact for any dimension. Formally expanding the solution into a power series with respect to η , we obtain the third virial coefficient numerically. As can be seen in Fig. 2, B_3 obtained in this way slightly overestimates the exact result.

C. Scaled-particle theory

The key idea of scaled-particle theory (SPT) [42] is to insert a spherical test particle of variable radius into a bulk fluid of hard spheres. The test particle is gradually expanded to the same size as the other spheres. One then obtains the free energy by thermodynamic integration of the virial equation. The key function by which all other properties can be expressed is $G(r)$, which is the contact value of the pair distribution function between test particle and the other spheres, if the radius of the test particle equals $r-R$.

In what follows, we generalize the SPT (which was originally developed for $D=3$) to arbitrary dimensions. The probability $p_0(r)$ of a spontaneous appearance of a cavity large enough to hold the test particle of radius r is directly connected to the work required in making it. This probability is equivalent to the probability of finding a spherical space with radius r unoccupied. By elementary statistical reasoning such as in $D=3$ [42], one obtains a relation between p_0 and $G(r)$, which is

$$\frac{1}{p_0(r)} \frac{dp_0(r)}{dr} = -\rho s_{D-1}(r) G(r). \quad (15)$$

If the cavity is so small that at most one sphere fits inside, i.e., $r \leq R$, the probability of finding this cavity unoccupied is clearly $p_0(r) = 1 - \rho V_D r^D$. Therefore,

$$G(r) = \frac{1}{1 - \rho V_D r^D} \quad \text{for } r \leq R. \quad (16)$$

Next we consider a cavity with radius $R < r < 2R/\sqrt{3}$. Then two, but not three spheres fit into the cavity. We have to correct for double-counting pairs, and obtain

$$p_0 = 1 - \rho V_D r^D + \int \int_{\text{cavity}} g(\mathbf{r}_1, \mathbf{r}_2) d\mathbf{r}_1 d\mathbf{r}_2 \quad (17)$$

$$= 1 - \rho V_D r^D + \frac{\rho^2}{2} \int_0^{2r} g(r') V_r(r') s_{D-1}(r') dr', \quad (18)$$

where $g(\mathbf{r}_1, \mathbf{r}_2)$ is the hypersphere pair distribution function and $r' = |\mathbf{r}_2 - \mathbf{r}_1|$; furthermore $V_r(r')$ denotes the overlap volume of two spheres with radius r at a distance r' . We will restrict ourselves in the following to odd dimensions $D = 2k+1$. From $g(r) = 0$ for $r < 2R$ it follows that p_0 is $k+1$ times continuously differentiable at $r=R$. Since $G(r)$ follows from $p_0(r)$ by differentiation [see Eq. (15)], $G(r)$ is k times continuously differentiable at $r=R$. Since we know the exact behavior of $G(r)$ for $r < R$, the first k derivatives of $G(r)$ at $r=R$ are also known.

A further constraint on $G(r)$ is obtained by noting that $G(\infty) = \beta p/\rho$ [42]. Equating with the virial expression for the pressure yields

$$1 + \frac{1}{2} 2^D \eta G(2R) = G(\infty). \quad (19)$$

Together with the $k+1$ values of the derivatives we have got $k+2$ constraints on $G(r)$. Next we expand $G(r)$ into a series in $1/r$,

$$G(r) = 1 + a_0 + \sum_{i=1}^{k+1} \frac{a_i}{(r/R)^i}. \quad (20)$$

This involves $k+2$ unknowns a_i , which must be chosen to fulfill

$$\frac{1}{1-\eta} = 1 + a_0 + \sum_{i=1}^{k+1} a_i, \quad (21)$$

$$\begin{aligned} \sum_{i=1}^{k+1} a_i (-1)^j \frac{(i+j-1)!}{(i-1)!} &= \eta (1+a_0) \frac{D!}{(D-j)!} \\ &+ \eta \sum_{i=1}^{k+1} a_i \frac{(D-i)!}{(D-i-j)!}, \end{aligned} \quad (22)$$

$$a_0 = \frac{1}{2} 2^D \eta \left(1 + a_0 + \sum_{i=1}^{k+1} a_i 2^{-i} \right). \quad (23)$$

The first two sets of equations (21) and (22) are linear and can be used to express the a_1, \dots, a_{k+1} in terms of η and a_0 . The last Eq. (23) can then be turned into a quadratic equation for a_0 , which can be solved analytically. The non-linear equation (23) has to be solved numerically. From $a_0 = -1 + 1/G(\infty)$ we obtain directly the pressure [see Eq. (19)] and the equation of state. Decomposing the equation of state into a power law expansion with respect to density, we get the second and third virial coefficients. The second virial coefficient is exact. The third virial coefficient is shown as a function of spatial dimension D in Fig. 2. As in Percus-Yevick theory it is larger than the exact value.

It is possible to obtain the surface tension γ between a hard hypersphere fluid and a hard (hyper) planar wall via

FREEZING TRANSITION OF HARD HYPERSPHERES

SPT. In order to access γ , we consider the work required to form a cavity with a very large radius R , which can be expressed as

$$W(r) = pV_D(r) + \tilde{\gamma}s_{D-1}(r). \tag{24}$$

The quantity $\tilde{\gamma}$ is connected to the physical surface tension γ via the relation $\gamma = \tilde{\gamma} + pR$, compare, e.g., [43]. The probability $p_0(r)$ of observing a fluctuation containing such a cavity is further given by [10]

$$p_0(r) = \exp[-\beta W(r)]. \tag{25}$$

Hence, one finally obtains γ as a function of D and η as

$$\gamma = \frac{k_B T D}{s_{D-1}(R)} \eta \left(1 + a_0 - \frac{a_1}{D-1} \right), \tag{26}$$

which we will discuss as a function of D in Sec. VI.

V. DENSITY-FUNCTIONAL THEORY

Density-functional theory (DFT) has been very successful in describing inhomogeneous fluids in three dimensions [2]. It provides in principle a concept unifying the fluid and solid state within a single approach. For hard spheres, one particular approximation, the Rosenfeld functional, has the remarkable property of describing both the fluid state and the solid state very well incorporating the limit of close-packing correctly [44]. Within the Rosenfeld functional, or fundamental-measure theory, the nonlocal dependency of the excess free energy \mathcal{F} of the density ρ is treated via averages of the density over the sphere volume, surface, and other fundamental geometric measures [18]. The Rosenfeld functional may be formulated in such a way that it gives the correct zero-dimensional crossover [19,20]. The thermodynamics of a hard sphere system inside a cavity so small, that at most one sphere fits into it can be solved exactly. One obtains the excess free energy [19,20]

$$\beta\mathcal{F}^{(D=0)}[\rho] = \varphi_0(N) = N + (1-N)\ln(1-N), \tag{27}$$

where $0 \leq N \leq 1$ denotes the average number of particles inside the cavity. The same free energy is obtained from the Rosenfeld functional, if an external potential corresponding to the walls of the cavity is introduced. This provides a systematic way of deriving a similar DFT in arbitrary dimensions [21]. In the sequel we will work this out explicitly.

The general functional $\mathcal{F}[\rho]$ is assumed to be a sum of terms of the form

$$\beta\mathcal{F}[\rho] = \Phi_1^{(D)}[\rho] + \Phi_2^{(D)}[\rho], \tag{28}$$

$$\Phi_1^{(D)}[\rho] = \int d\mathbf{r} \varphi_1[\eta(\mathbf{r})] \int d\mathbf{R}_1 w_D(\mathbf{R}_1 - \mathbf{r}) \rho(\mathbf{R}_1), \tag{29}$$

$$\begin{aligned} \Phi_2^{(D)}[\rho] = & \int d\mathbf{r} \varphi_2[\eta(\mathbf{r})] \int d\mathbf{R}_1 \int d\mathbf{R}_2 \\ & \times w_D(\mathbf{R}_1 - \mathbf{r}) w_D(\mathbf{R}_2 - \mathbf{r}) P_D(\mathbf{R}_1, \mathbf{R}_2). \end{aligned} \tag{30}$$

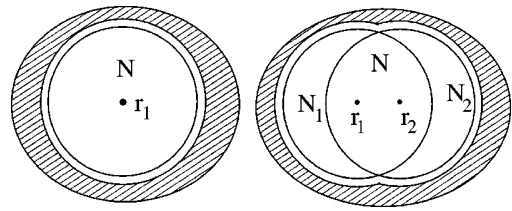


FIG. 3. Geometry of the two cavities used to derive the free energy functional $\mathcal{F}[\rho]$. Indicated are the possible positions of the sphere (r_1 or r_2) and the local packing fraction $\eta(r)$ within the respective region.

Here $\eta(\mathbf{r}) = \int d\mathbf{r}' \rho(\mathbf{r}') \Theta(R - |\mathbf{r}' - \mathbf{r}|)$ is the local packing density and $w_D(\mathbf{R}_1) = 1/s_{D-1}(R) \delta(R - |\mathbf{R}_1|)$ is a measure over the surface of the sphere. The integral kernel $P_D(\mathbf{R}_1, \mathbf{R}_2)$, therefore, couples densities averaged over the sphere surface. In order to make this functional unique we consider cavities of increasing complexity. These cavities are sketched in Fig. 3. A simple cavity capable of holding a sphere in just one place will uniquely determine $\varphi_1(\eta)$ and thus $\Phi_1^{(D)}[\rho]$. It turns out, however, that the exact free energy is not reproduced in a slightly more complicated cavity that can hold a sphere at either of two places. The requirement that the functional should give the analytically known value even in this case uniquely determines the functional form of $\varphi_2(\eta)$ and $P_D(\mathbf{R}_1, \mathbf{R}_2)$. This procedure has been invented (for $D=3$) in [21].

The simplest cavity is spherical, and just large enough to hold one sphere. The single particle density must then be $\rho(\mathbf{r}) = N\delta(\mathbf{r})$. The local packing density $\eta(\mathbf{r})$ equals N within a sphere of radius R and vanishes outside. Introducing the quantity $\eta_{R+\epsilon}(\mathbf{r}) = N\Theta(R + \epsilon - |\mathbf{r}|)$, we can write

$$\begin{aligned} \Phi_1^{(D)}[\rho] &= \int d\mathbf{r} \varphi_1[\eta(\mathbf{r})] \frac{1}{s_{D-1}(R)} \frac{\partial}{\partial \epsilon} \eta_{R+\epsilon}(\mathbf{r}) \Big|_{\epsilon=0} \\ &= \frac{1}{s_{D-1}(R)} \frac{\partial}{\partial \epsilon} \int d\mathbf{r} F[\eta_{R+\epsilon}(\mathbf{r})] \Big|_{\epsilon=0} \\ &= \frac{1}{s_{D-1}(R)} \frac{\partial}{\partial \epsilon} F(N) V_D(R + \epsilon) \Big|_{\epsilon=0} \\ &= F(N), \end{aligned} \tag{31}$$

with F denoting the integral of φ_1 . Comparing this with the correct zero dimensional limit, one gets

$$\Phi_1^{(D)}[\rho] = \int d\mathbf{r} \varphi_1[\eta(\mathbf{r})] \int d\mathbf{R}_1 w_D(\mathbf{R}_1 - \mathbf{r}) \rho(\mathbf{R}_1), \tag{32}$$

with $\varphi_1(\eta) \equiv \partial\varphi_0(\eta)/\partial\eta = -\ln(1-\eta)$.

Consider another cavity with $\rho(\mathbf{r}) = N_1\delta(\mathbf{r} - \mathbf{r}_1) + N_2\delta(\mathbf{r} - \mathbf{r}_2)$, $N = N_1 + N_2 \leq 1$, and $r_{12} = |\mathbf{r}_1 - \mathbf{r}_2| \leq 2R$. For this kind of cavity the first term $\Phi_1^{(D)}$ of the free energy functional derived above does not give the correct free energy $\varphi_0(N)$ but

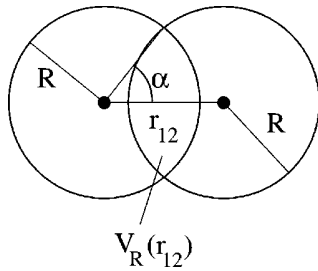


FIG. 4. Geometrical interpretation of $V_R(r_{12})$ as the overlap volume of two spheres of radius R with distance r_{12} .

$$\Phi_1^{(D)}[\rho] = \varphi_0(N) - \xi(r_{12})[\varphi_0(N) - \varphi_0(N_1) - \varphi_0(N_2)], \quad (33)$$

$$\begin{aligned} \xi(r_{12}) &= 1 - \frac{1}{s_{D-1}(R)} \frac{\partial}{\partial \epsilon} V_{R+\epsilon}(r_{12})|_{\epsilon=0} \\ &= 1 - \frac{V_{D-1}}{DV_D} (D-1) I_{D-2}(\alpha), \end{aligned} \quad (34)$$

$$I_D(\alpha) = \int_0^\alpha \sin^D(\varphi) d\varphi, \quad (35)$$

$$R \cos(\alpha) = r_{12}/2. \quad (36)$$

$V_{R+\epsilon}(r_{12})$ denotes the overlap volume of two spheres of radius $R+\epsilon$ at a distance r_{12} , see the sketch in Fig. 4.

We next determine the second contribution $\Phi_2^{(D)}[\rho]$ so that the deviation of the free energy from the exact zero-dimensional limit is corrected for. We obtain

$$\begin{aligned} \Phi_2^{(D)}[\rho] &= \int d\mathbf{r} \varphi_2[\eta(\mathbf{r})] \int d\mathbf{R}_1 w_D(\mathbf{R}_1 - \mathbf{r}) \rho(\mathbf{R}_1) \\ &\quad \times \int d\mathbf{R}_2 w_D(\mathbf{R}_2 - \mathbf{r}) \rho(\mathbf{R}_2) P(\mathbf{R}_1, \mathbf{R}_2), \end{aligned} \quad (37)$$

with

$$\xi(r_{12}) = 1 - \frac{V_{D-1}}{DV_D} (D-1) I_{D-2}(\alpha), \quad (38)$$

$$\begin{aligned} P_D(r_{12}) &= \frac{\xi(r_{12}) D^2 V_D^2 r_{12}^2}{V_{D-1} R^D (D-1) \sin^{D-3}(\alpha) \cos(\alpha)} \\ &\quad \text{for } r_{12} \leq 2R, \end{aligned} \quad (39)$$

$$\varphi_2(\eta) = \frac{\partial \varphi_1(\eta)}{\partial \eta} = \frac{1}{1-\eta}. \quad (40)$$

This completes the prescription of our functional. In principle, one could go further, and consider cavities that enforce δ density distributions composed of three or more δ spikes. Indeed in the case $D=3$ [21], up to *three* δ spikes were considered. One might speculate that up to D δ spikes should

be necessary in D dimensions. Due to the geometrical complexity, we have not followed this (albeit desirable) route in the present work.

For the homogeneous phase the integrals in Eq. (40) can be evaluated analytically. One obtains for the excess free energy per particle

$$f_f^{\text{exc}} = \varphi_1(\eta) + \frac{1}{2} \eta \varphi_2(\eta) (2^D - 2), \quad (41)$$

which we will also use as an estimate for the fluid free energy. Expanding into a power series with respect to η , one obtains

$$f_f^{\text{exc}} = \frac{1}{2} 2^D \eta + \frac{1}{2} (2^D - 1) \eta^2 + O(\eta^3), \quad (42)$$

hence, the correct second virial coefficient is reproduced by our density functional. The third virial coefficient is shown versus D in Fig. 2. It is significantly smaller than the exact result. We attribute this failure to the restricted set of cavities considered. (Note that in $D=3$ three δ spikes are needed to get B_3 correctly.) However, our functional has all terms that are important near close packing in $D=3$ [44], and we believe that this holds also for $D>3$. We further emphasize that this functional has much more predictive power than just giving the equation of state of the fluid. In principle, it could further be used to derive structural fluid correlations and inhomogeneous situations including freezing. We have not considered such applications here but leave them for future studies.

VI. RESULTS AND DISCUSSION

With the theories described above, we calculated freezing/melting coexistence densities using Maxwell's double tangent construction. We find a first-order freezing transition occurring at densities well below close packing. In Fig. 5, we plot the coexisting fluid (η_f) and solid (η_s) packing fractions obtained by using either third-order virial expansion or scaled-particle theory for the fluid and free-volume theory with unfixed neighbors [Eq. (4)] for the solid as a function of dimension D . Close-packing fractions η_{cp} are included for comparison. It might seem from this graph that the fluid and solid coexisting densities are not affected very much by the variation of the close-packed density with dimension but this is due to the logarithmic density scale.

We note that the coexistence densities do only depend weakly on the particular solid state theory for large D . If the virial expansion up to third order is used for the fluid free energy (Fig. 5), a freezing transition shows up for $D>11$. On the other hand, Percus-Yevick, scaled-particle and density-functional theory (all of which are more reliable for smaller dimensionalities) result in a freezing transition at any $D \geq 3$. We have compared our theoretical results to computer simulation data in the special cases $D=3,5$ [32], (see Table I). For $D=5$, we find reasonable agreement within the statistical error of the simulation.

The agreement between the different fluid state theories becomes better with increasing dimensionality. This is expected, since the virial expansion becomes exact for $D \rightarrow \infty$ and all our approaches reproduce the exact second virial co-

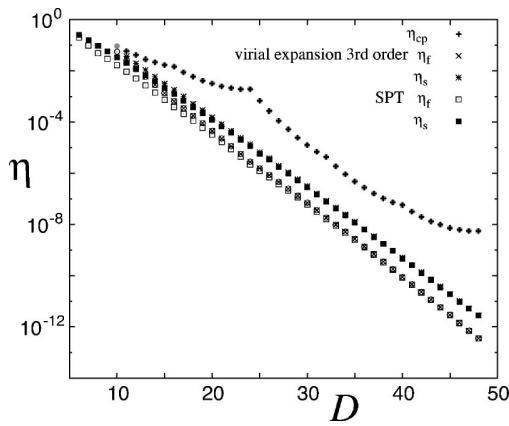


FIG. 5. Fluid (η_f) and solid (η_s) coexistence packing fractions and the close packing fraction η_{cp} of the corresponding laminated lattice versus dimension D .

efficient. The relative density jump in the coexistence densities, $(\eta_s - \eta_f)/\eta_s$, is plotted against dimension in Fig. 6. This quantity approaches its maximal value of unity for large D . That implies that the transition is strongly first order. On the basis of our data we conclude that $\eta_s/\eta_{cp} \rightarrow 0$ and $\eta_f/\eta_s \rightarrow 0$, for large D .

Let us discuss the relation of this theory to a perturbative analysis based on the Kirkwood spinodal instability of the fluid. A second-order freezing transition was predicted [23] in the case of first taking the limit $D \rightarrow \infty$ and then taking the thermodynamical limit. For finite D the instability density has been worked out explicitly by Frisch and Percus [23] as

$$\eta \approx 0.871(e/8)^{D/2} D^{1/6} e^{1.473D^{1/3}}. \quad (43)$$

Bagchi and Rice [13] found the same functional dependence on D , but a different prefactor such that

$$\eta \approx 0.239(e/8)^{D/2} D^{1/6} e^{1.473D^{1/3}}. \quad (44)$$

These densities are compared to our fluid coexisting densities based on the virial expansion and free-volume theory in Fig. 7. Our η_f are smaller than the instability densities. This implies that the fluid instability is preempted by first-order freezing at all high dimensions such that the Kirkwood in-

TABLE I. Results for the coexistence densities η_f, η_s for small dimensionality $D=3$ and 5 obtained from cell theory (CT) with fixed and unfixed neighbors compared to simulation results. We estimated the simulation values for $D=5$ from the results given in Ref. [32].

D	Method	η_f	η_s	η_{cp}
3	CT, unfixed			0.74048
	CT, fixed	0.562138	0.601772	
	simulation	0.494	0.545	
5	CT, unfixed	0.27353	0.348053	0.465258
	CT, fixed	0.202184	0.258753	
	simulation [32]	≈ 0.19	≈ 0.29	

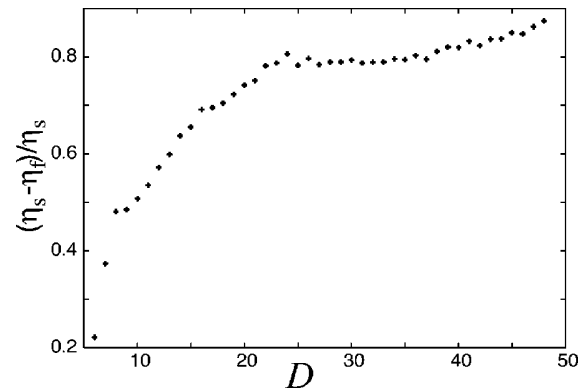


FIG. 6. Relative jump in coexistence densities $(\eta_s - \eta_f)/\eta_s$ versus dimension D .

stability only applies for a metastable fluid. This has indeed been suggested in a recent paper by Frisch and Percus [16], where relevant diagram resummations are carried out before taking the limit $D \rightarrow \infty$ resulting in a prior spinodal. The authors suggest that “at a density less than that of the Kirkwood, a first-order transition intervenes.” Provided the virial expansion approaches exactness (as assumed in the instability analysis of Refs. [13,24]) [45], our analysis indicates a first-order phase transitions for large dimensions, because the free-volume theory provides a strict upper bound for the solid free energy (see Sec. III), which means that the real coexisting fluid density can only be smaller than in our calculation. As an aside, we apply the same analysis to hard hypercubes and find a qualitatively different result. The instability densities as calculated analytically by Kirkpatrick [9] are smaller than the coexisting densities obtained from our analysis. This implies that for hard hypercubes the fluid instability can be real. Of course, this system is qualitatively different from hard hyperspheres. The close-packing fraction of hard hypercubes is unity, independent of dimension, and the fluid is anisotropically ordered due to the fixed orientations of the particles. Apparently, this makes it easier for the solid to step in via a second-order phase transition.

The Lindemann parameter is defined via L

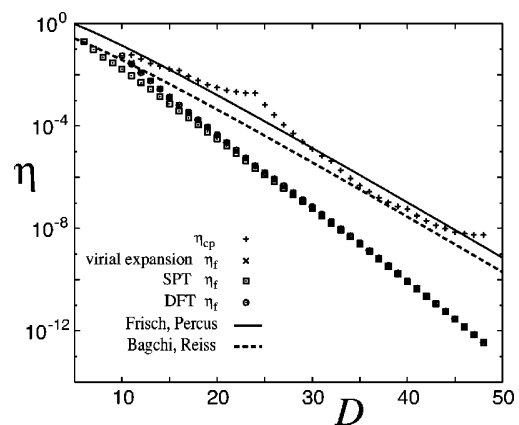


FIG. 7. Comparison of the freezing densities η_f from different theories against the Kirkwood instability density obtained by Frisch and Percus [Eq. (43)] and Bagchi and Reiss [Eq. (44)].

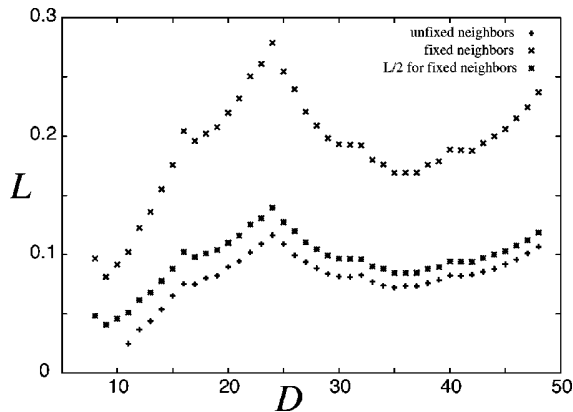


FIG. 8. Lindemann parameter L at melting as a function of dimension D .

$= \sqrt{\langle (\Delta \vec{r})^2 \rangle} / a$ as the ratio between the root-mean-square displacement of a particle in the solid and the lattice constant a . Three-dimensional crystal melting is accompanied by a Lindemann parameter of roughly 0.1. We test this rule [46] within our theory for arbitrary D in Fig. 8. Free-volume theory, where we assume a constant density profile within the free volume cell, can be used to estimate L . We have used approaches with both unfixed and fixed nearest neighbors. The main effect of using the fixed nearest neighbors approach is a doubling of the available space for the spheres in each direction. If the coexistence densities were the same, the difference in L between the fixed and unfixed approach would be a factor of 2. However, if the approach with the fixed nearest neighbors is used, the solid coexistence densities η_s change slightly, leading to a different a in L . Data for L at coexistence are presented in Fig. 8. For the fluid state we have used the virial expansion. The difference in L between the approaches using unfixed and fixed nearest neighbors are nearly a factor of 2. Within cell theory the Lindemann parameter at coexistence does not vary dramatically from its threshold value of 0.1, valid in three dimensions, and it is rather insensitive to the dimensionality. The data for L obtained within the fixed neighbor approach show that the result is stable (up to a trivial factor of 2) with respect to a different solid state theory. Thus the crude melting rule also holds in higher spatial dimensions. The Lindemann criterion is thus pretty robust. Note that it is also valid for $D=2$, provided the relative mean-square displacement [47] is used. Furthermore it holds in $D=3$ even for interfacial freezing [48] and freezing of polydisperse spheres both in equilibrium and nonequilibrium [49].

We finally show, as a side product, the wall-fluid tension γ of hard hyperspheres, as given by Eq. (26). In Fig. 9, we plot γ for a fixed scaled packing fraction $\eta = 2^{2-D}$ versus dimensionality D . This packing fraction is close to bulk freezing. For this choice of parameters, γ increases with D . Note that in three dimensions, the scaled-particle expression was found to be in very good agreement with computer simulations [43] and density-functional studies [50] for any packing fraction up to freezing.

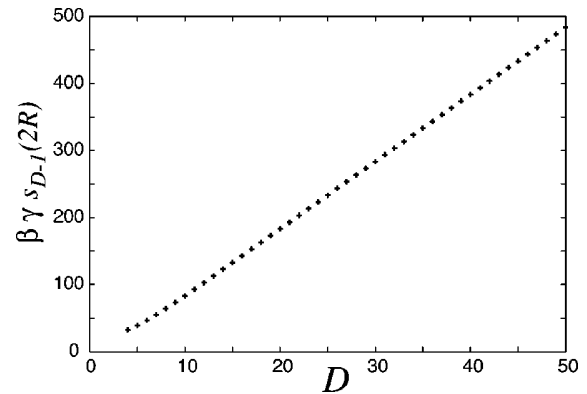


FIG. 9. Reduced surface tension $\beta \gamma s_{D-1}(2R)$ according to scaled-particle theory as a function of the dimension D at the respective density $\eta = 4/2^D$, which is close to freezing.

VII. CONCLUSIONS

In conclusion, we have studied the fluid and solid free energies for hard hyperspheres. We have generalized scaled-particle theory to arbitrary dimensions and solved the Percus-Yevick liquid integral equation theory numerically in odd dimensions up to $D=33$. We have further proposed a free energy density functional for an inhomogeneous hard hypersphere fluid for arbitrary dimension. Assuming laminated lattice structures for the solid, we have used free-volume theory for the solid that provides a strict upper bound to the free energy. As a result, we find a first-order freezing transition where the density jump approaches the solid coexistence density as D grows. We have shown that this first-order freezing transition preempts the second-order Kirkwood spinodal instability of the fluid.

We point out that computer simulations are needed for $D > 3$ in order to improve the statistics of the simulations done for $D=4,5$ [32] and to explore the fluid-solid phase boundaries for $D > 5$. The numerical effort for such simulations, however, increases rapidly with dimension, as the number of particles in a hypercubic box (with periodic boundaries) increases significantly with D .

It would also be interesting to access hypersphere freezing by the unifying concept of density functional theory. The fluid free energy was derived in this paper. To get the solid free energy, one could use an ansatz based on Gaussian density peaks centered on a (laminated or any other) lattice and minimize the free energy with respect to the width of the peaks and the lattice structure. One could further extract the wall-fluid and wall-solid surface tensions from DFT. We leave these problems for further studies.

ACKNOWLEDGMENTS

We thank Y. Rosenfeld and J.-P. Hansen for helpful remarks, and T. White for proofreading the manuscript.

- [1] D.W. Oxtoby, *Nature (London)* **347**, 725 (1990).
- [2] H. Löwen, *Phys. Rep.* **237**, 249 (1994).
- [3] D. Frenkel, *Physica A* **263**, 26 (1999).
- [4] For a review and related references, see H. Löwen, in *Spatial Statistics and Statistical Physics*, edited by K. Mecke and D. Stoyan, Springer Lecture Notes in Physics Vol. 554 (Springer, Berlin, 2000), p. 295.
- [5] P.G. Bolhuis, D. Frenkel, S.-C. Mau, and D.A. Huse, *Nature (London)* **388**, 235 (1997).
- [6] W.G. Hoover, and F.H. Ree, *J. Chem. Phys.* **49**, 3609 (1968).
- [7] A. Jaster, *Europhys. Lett.* **42**, 277 (1998); *Phys. Rev. E* **59**, 2594 (1999).
- [8] L. Tonks, *Phys. Rev.* **50**, 955 (1936).
- [9] T.R. Kirkpatrick, *J. Chem. Phys.* **85**, 3515 (1986).
- [10] H.L. Frisch, N. Rivier, and D. Wyler, *Phys. Rev. Lett.* **54**, 2061 (1985).
- [11] M. Schulz, and H.L. Frisch, *Phys. Rev. E* **52**, 442 (1995).
- [12] F.H. Stillinger *J. Chem. Phys.* **70**, 4067 (1979).
- [13] B. Bagchi and S.A. Rice, *J. Chem. Phys.* **88**, 1177 (1988).
- [14] R.P. Sear and B.M. Mulder, *Mol. Phys.* **93**, 181 (1998).
- [15] K.K. Mon and J.K. Percus, *J. Chem. Phys.* **11**, 2734 (1999).
- [16] H.L. Frisch and J.K. Percus, *Phys. Rev. E* **60**, 2942 (1999).
- [17] Y. Rosenfeld, *Phys. Rev. Lett.* **63**, 980 (1989).
- [18] For a review, see Y. Rosenfeld, *Mol. Phys.* **94**, 929 (1998).
- [19] Y. Rosenfeld, M. Schmidt, H. Löwen, and P. Tarazona, *J. Phys.: Condens. Matter* **8**, L577 (1996).
- [20] Y. Rosenfeld, M. Schmidt, H. Löwen, and P. Tarazona, *Phys. Rev. E* **55**, 4245 (1997).
- [21] P. Tarazona, Y. Rosenfeld, *Phys. Rev. E* **55**, R4873 (1997).
- [22] W. Klein, H.L. Frisch, *J. Chem. Phys.* **84**, 968 (1986).
- [23] H.L. Frisch, and J.K. Percus, *Phys. Rev. A* **35**, 4696 (1987).
- [24] D. Wyler, N. Rivier, and H.L. Frisch, *Phys. Rev. A* **36**, 2422 (1987).
- [25] Y. Elskens, and H.L. Frisch, *Phys. Rev. A* **37**, 4351 (1988).
- [26] M. Luban, and A. Baram, *J. Chem. Phys.* **76**, 3233 (1982).
- [27] L.E. González, D.J. González, and M. Silbert, *J. Chem. Phys.* **97**, 5132 (1992).
- [28] E. Leutheusser, *Physica A* **127**, 667 (1984).
- [29] E.S. Velazquez, L. Blum, H.L. Frisch, *J. Stat. Phys.* **89**, 203 (1997).
- [30] G. Parisi, and F. Slanina, *Phys. Rev. E* **62**, 6554 (2000).
- [31] E. Velasco, L. Mederos, and G. Navascues, *Mol. Phys.* **97**, 1273 (1999).
- [32] J.P.J. Michels, and N.J. Trappeniers, *Phys. Lett. A* **104**, 425 (1984).
- [33] J.L. Colot, and M. Baus, *Phys. Lett. A* **119**, 135 (1986).
- [34] A. Santos, S.B. Yuste, and M. López de Haro, *Mol. Phys.* **96**, 1 (1999).
- [35] S.B. Yuste, A. Santos, and M. López de Haro, *Europhys. Lett.* **52**, 158 (2000).
- [36] A. Santos, *J. Chem. Phys.* **112**, 10 680 (2000).
- [37] M. Bishop, A. Masters, and J.H.R. Clarke, *J. Chem. Phys.* **110**, 11 449 (1999).
- [38] C. A. Rogers, *Packing and Covering* (Cambridge University Press, Cambridge, 1964).
- [39] A. Münster, *Statistical Thermodynamics*, (Springer-Verlag, Berlin, 1974), Vol. II, pp. 337–346.
- [40] J. Groeneveld, *Phys. Lett.* **3**, 50 (1962).
- [41] J. -P. Hansen and I. R. McDonald, *Theory of Simple Liquids*, 2nd ed. (Academic Press, New York, 1986).
- [42] H. Reiss, H.L. Frisch, and J.L. Lebowitz, *J. Chem. Phys.* **31**, 369 (1959).
- [43] M. Heni, and H. Löwen, *Phys. Rev. E* **60**, 7057 (1999).
- [44] B. Groh, and B. Mulder, *Phys. Rev. E* **61**, 3811 (2000).
- [45] An even less severe assumption is that the second-order virial free energy is a lower bound to the exact free energy. Although this is physically plausible (and confirmed in $D=3$), we are not aware of a strict mathematical proof of this assumption and leave it as an open question.
- [46] F.A. Lindemann, *Phys. Z.* **11**, 609 (1910).
- [47] K. Zahn, and G. Maret, *Phys. Rev. Lett.* **85**, 3656 (2000).
- [48] M. Heni, and H. Löwen, *J. Phys.: Condens. Matter* **13**, 4675 (2001).
- [49] H. Löwen, and G.P. Hoffmann, *Phys. Rev. E* **60**, 3009 (1999).
- [50] B. Götzelmann, A. Haase, and S. Dietrich, *Phys. Rev. E* **53**, 3456 (1996).

Colloids confined to a flexible container

Lutz Maibaum, Matthias Schmidt, Hartmut Löwen

Institut für Theoretische Physik II, Heinrich-Heine-Universität Düsseldorf, Universitätsstraße 1, D-40225 Düsseldorf, Germany

(Received 9 November 2000; published 16 April 2001)

A model of hard spheres trapped inside a container of fluctuating shape is proposed to describe colloidal particles in a vesicle or in an emulsion droplet. The container is assumed to be the convex hull of the particles and is described by an integral geometric approach including volume and surface terms. In the limit of large volume coupling, the model reduces to the well-known geometric problem of natural bin packing. Using computer simulations and cell theory, we calculate equilibrium properties for various finite numbers of confined particles in conformations ranging from clusters to planar and linear structures and identify transitions between these different conformations.

DOI: 10.1103/PhysRevE.63.051401

PACS number(s): 82.70.Dd, 61.46.+w, 87.16.Dg, 64.70.Dv

I. INTRODUCTION

Clusters are present in a variety of systems, ranging from atomic systems [1] such as silicon [2] or noble gases [3] to aggregated colloidal suspensions. Clusters are built up by a finite number of particles that tend to be closely separated. The structural organization inside a cluster can be very rich and originates from the interactions between particles and the interaction with the surrounding. One simple mechanism to generate such structures is the packing of hard spheres (HS) under different boundary conditions.

The efficient packing of spheres is an old problem dating back to Kepler and Gauss [4]. One question concerns the densest packing of an infinite number of spheres. Only recently, a mathematical proof stating that no packing denser than a face-centered-cubic structure (fcc) is possible in three dimensions was announced and published in parts [5]. Related problems are optimal shapes of compact strings [6] and the efficient packing of a finite number of spheres inside a given container. A particular simple container is the *natural bin*. This is the smallest convex body that contains a given configuration of spheres. It is canonical to ask for the configuration of spheres that leads to the smallest natural bin. Contrary to intuition, this is not a spherelike cluster for a small number of spheres. Up to 56 spheres, a linear configuration in which the sphere centers lie on a straight line (“sausage”) is denser than any spherelike or platelike configuration. In four dimensions, the crossover from a sausage to a spherelike cluster happens at about 300 000 spheres. This effect has become known as the “sausage catastrophe” [4,7].

Hard spheres are widely used to model dense liquids and solids and they can be experimentally realized by suspensions of sterically stabilized *PMMA* particles [8,9]. Besides the bulk freezing transition into an fcc crystal, hard spheres have been considered in a variety of confining situations, such as confinement between parallel plates [10,11], inside a spherical cavity [12–14], or inside emulsion droplets [15]. In all these cases, there is rigid confinement: The pores do not change their shapes.

However, shape fluctuations do exist in nature. Examples are the deformations of liquid droplets in emulsions, where the surface tension between the continuous phase, say water,

and the dispersed phase, say oil, tends to keep the droplet shape spherical and thermal fluctuations tend to deform this ideal shape. Another system that exhibits many complicated shapes is vesicles [16,17], which are closed two-dimensional membranes [18] that are suspended in a molecular liquid. Besides the fluctuations of a spherical object, toroidal configurations with holes or even starlike shapes are possible. They originate from the highly nontrivial membrane structure itself, including curvature and elasticity contributions.

Colloidal particles can be trapped inside larger objects in quite a number of ways. Experimentally realized examples are magnetic beads inside biological cells [19], liquid droplets inside liquid droplets in double emulsions [20], small vesicles inside giant ones [21], and colloidal particles inside lipid bilayer vesicles [22]. Vesicles in contact with nanoparticles and colloids were studied also theoretically [23].

In the present work, we investigate which shape fluctuations can be driven not by the membrane itself but by colloidal particles that are imprisoned inside the object. The shape fluctuations are coupled to the positions of the colloidal particles resulting in new cluster structures as well as new vesicle shapes. One interesting question is whether the peculiar transition from a compact cluster to a linear configuration, the sausage catastrophe, is present in a system that not only describes close-packed structures, but also accounts for the entropy due to the positional degrees of freedom of the particles. We consider particles inside a container, which is modeled through a coarse-grained approach involving an integral geometric description. Integral geometry is a powerful tool that is becoming increasingly popular [24]. There are applications ranging from microemulsions [25] to complex fluids [26,27]. The basic ingredients of our model involve a surface tension and an external pressure acting on the container modeled as surface and volume couplings. As a result, we identify different types of conformations corresponding to rodlike, platelike, and spherelike vesicle shapes, and we determine their relative stability as a function of temperature by using cell theory and computer simulations.

The paper is organized as follows. In Sec. II, we define our theoretical model for colloids inside a fluctuating object. A cell theory is developed in Sec. III. Details of the Monte Carlo computer simulation are given in Sec. IV. Results

thereof are presented in Sec. V, and compared to cell theory. We finish with concluding remarks in Sec. VI.

II. MODEL OF COLLOIDS IN A CONTAINER

A. Definition of the model

We consider N hard spheres with diameter σ with position coordinates \mathbf{r}_i , $i=1,\dots,N$ in three spatial dimensions that interact with the pair potential,

$$\phi(r) = \begin{cases} \infty & \text{if } r < \sigma \\ 0 & \text{otherwise,} \end{cases}$$

where r is the separation distance between two particles. The number of particles we consider is finite and small, typically $N=2-55$.

The particles are wrapped into a closed membrane that is modeled as the convex hull of the set of spheres $\{\mathbf{r}_i\}$. Mathematically, the convex hull of one or more geometric bodies is the smallest convex body that encloses the basic objects. A body is called convex if for any two points inside the body all points that lie on a straight line between both points lie also inside the body. The convex hull is a uniquely defined object.

The physical motivation for using the convex hull is a situation in which the surface tension between the inside and the outside is large enough so that any free deformation of the membrane can be neglected. On the other side, the thermal energy $k_B T$ of the colloids is large enough, so that they can move and squeeze the membrane. To allow for volume growth, oil may diffuse into the inside of the vesicle.

Once we have established the membrane shape, it is straightforward to assign a potential energy ϕ_{Hull} to it by considering integral geometry,

$$\phi_{\text{Hull}} = J_V V + J_A A + J_M M + J_\chi \chi. \quad (1)$$

Here, the Minkowski functionals or Quermass integrals (see, e.g., Ref. [25]) are volume V , surface area A , integral of mean curvature M , and the Euler characteristic χ of the convex hull. For a convex body $\chi=4\pi$ holds, so J_χ is an irrelevant parameter for the current investigation and is set to zero without loss of generality. A nonzero value of J_χ may be of interest once fission processes of the container are taken into account, or, e.g., toroidal shapes are considered. Furthermore, we set the coupling to the mean curvature to zero, $J_M=0$. This ensures that the model does not favor spontaneous curvature. The remaining coupling constants are volume coupling, J_V , modeling an external pressure acting on the container, and a surface tension J_A . We define dimensionless parameters as $\lambda_V = J_V \sigma^3 / (k_B T)$ and $\lambda_A = J_A \sigma^2 / (k_B T)$. See Fig. 1 for a sketch of the model.

B. Computational details

Let us show how the container volume and surface area can be computed efficiently. We exploit the relation of the convex hull of a set of spheres and the convex hull of the corresponding sphere centers. In both cases the crucial point is to identify which points (or spheres) contribute to the hull,

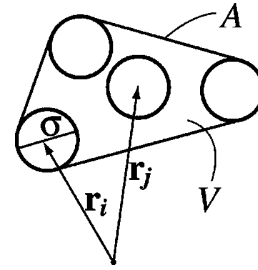


FIG. 1. Sketch of the model of colloids inside a container. The circles represent the particles with diameter σ ; \mathbf{r}_i and \mathbf{r}_j are position vectors. The solid line is the convex hull with surface S and volume V . The model considered in this work is three-dimensional.

i.e., lie at the boundary, and which of the points lie inside and do not contribute to the hull. For a collection of points this is a well-known problem in geometry and efficient numerical algorithms are available [28]. We start from the set \mathbf{r}_i and identify the boundary points, denoted by $\mathbf{r}_j^{(0)}$. The $\mathbf{r}_j^{(0)}$ define the corners of a polyhedron, which we call the *core* of the container. Elementary geometry is used to calculate the Minkowski functionals V_0, A_0, M_0 of the core. In particular, the core surface is obtained by summing up the surface areas of all its faces. The integral mean curvature is

$$M_0 = \frac{1}{2} \sum_k l_k \alpha_k, \quad (2)$$

where l_k is the length of ridge k and α_k is the angle between the normal vectors of the two faces adjacent to ridge k . As the actual container is the parallel body of radius R to the container core, we can use Steiner's theorem (see, e.g., Ref. [25]) to obtain

$$V = V_0 + A_0 R + M_0 R^2 + 4\pi R^3/3, \quad (3)$$

$$A = A_0 + 2M_0 R + 4\pi R^2, \quad (4)$$

$$M = M_0 + 4\pi R. \quad (5)$$

C. Relation to the Helfrich Hamiltonian

Concerning the status of the model ϕ_{Hull} introduced above, we note that the familiar Helfrich Hamiltonian [29,17] for membranes is recovered if the membrane conformations are restricted to convex hulls of spheres. To see this, consider

$$\phi_{\text{Helfrich}} = \oint dA \left[\frac{\kappa}{2} \left(\frac{1}{r_1} + \frac{1}{r_2} - \frac{1}{r_s} \right)^2 + \frac{\bar{\kappa}}{r_1 r_2} \right], \quad (6)$$

where r_s is the radius of spontaneous curvature, κ is the bending rigidity, $\bar{\kappa}$ is the elastic modulus of Gaussian curvature, and the local curvature radii on the surface are denoted by r_1 and r_2 . If the set of possible surface shapes is restricted to convex hulls of N spheres of radius R , we obtain

$$\phi_{\text{Helfrich}} = \frac{\kappa}{2r_s^2} A + \left(\frac{\kappa}{R} - \frac{2\kappa}{r_s} \right) \mathcal{M} + (\kappa + \bar{\kappa}) \chi, \quad (7)$$

which is a linear combination of Minkowski functionals, apart from the missing volume term precisely like the container energy ϕ_{Hull} . The parameters are related by $J_{\mathcal{A}} = \kappa/(2r_S^2)$, $J_{\mathcal{M}} = (\kappa/R) - (2\kappa/r_S)$, and $J_{\chi} = \kappa + \bar{\kappa}$.

D. Ensembles

The central quantity in the microcanonical ensemble is the density of states, defined as

$$\Omega(V', A') = \int d\mathbf{r}_1 \cdots \int d\mathbf{r}_N \times \delta[V' - V(\{\mathbf{r}_i\})] \delta[A' - A(\{\mathbf{r}_i\})], \quad (8)$$

where the integration only runs over allowed hard-sphere configurations. The (microcanonical) entropy is obtained as $S = k_B \ln \Omega$. The central quantity in the canonical ensemble is the partition sum

$$Z = \frac{1}{\Lambda^{3N} N!} \int d\mathbf{r}_1 \cdots \int d\mathbf{r}_N e^{-\beta \phi(\mathbf{r}_1, \dots, \mathbf{r}_N)}, \quad (9)$$

where Λ is the thermal wavelength of the colloids. The Helmholtz free energy is $F = -k_B T \ln Z$. Note that as we are dealing with a finite system, the canonical and the microcanonical ensembles are not equivalent.

III. CELL THEORY

The cell theory (CT) is a simple, yet accurate, approach to hard-sphere systems. Crystals are well-described in bulk [30,31] as well as in rigid confined geometries [10,11] and near walls [32]. Here we generalize the concept to flexible confinement. The striking feature of yielding an exact upper bound to the free energy is preserved.

A. General scheme

Our strategy consists of two steps. First, we constrain the colloids to fixed cells in space. Instead of integrating over all space, we require the center of each particle i to lie inside its cell C_i . Thus, the integration region in the partition sum [Eq. (9)] becomes smaller. Second, we construct a body K^* that is larger than any possible container K in this restricted system. Replacing the volume and the surface in the Boltzmann factor by those of K^* , the Boltzmann factor also becomes smaller and the approximate partition sum Z^* we obtain is a lower bound to the exact partition sum Z . From that naturally an upper bound to the free energy is obtained.

In detail we proceed as follows. Let us introduce the notion of cells C_i , $i = 1, \dots, N$, which are geometric objects that are constructed such that they have a distance of at least the particle diameter σ from each other. If each particle i is confined to its cell C_i , the particles of neighboring cells cannot overlap. We can then drop the hard-core term in the Boltzmann factor and obtain

$$Z \geq \frac{1}{\Lambda^{3N}} \int_{C^{(1)}} d\mathbf{r}_1 \cdots \int_{C^{(N)}} d\mathbf{r}_N \exp[-\beta \phi_{\text{Hull}}(\{\mathbf{r}_i\})] \quad (10)$$

$$= \frac{1}{\Lambda^{3N}} \int_{C^{(1)}} d\mathbf{r}_1 \cdots \int_{C^{(N)}} d\mathbf{r}_N \exp[-\lambda_V V(\{\mathbf{r}_i\}) - \lambda_A A(\{\mathbf{r}_i\})], \quad (11)$$

where the factor $1/N!$ in the definition of Z , Eq. (9), is canceled by the number of possibilities to distribute N particles on N cells.

In order to obtain a tractable integral, we construct an approximate container

$$K^* = \bigcup_{\mathbf{r}_i \in C_i} K(\{\mathbf{r}_i\}), \quad (12)$$

which is the union of all possible K that are realized if each particle moves freely inside its cell. The crucial point is that K^* is independent of the position coordinates \mathbf{r}_i . This will allow us to carry out the integrations over space, Eq. (11). K^* depends, however, on the shape and positions of the C_i . In particular, it can be computed as the parallel body of radius R of the convex hull (\mathcal{C} , see also Sec. II A) of the cells,

$$K^* = \Gamma_R, \quad (13)$$

$$\Gamma = \mathcal{C}(C_1, \dots, C_N), \quad (14)$$

where the subscript denotes the parallel body with radius R . If Γ is known, Steiner's theorem can be used to calculate the volume V^* and surface area A^* of K^* . Due to the definition of K^* and the fact that only convex bodies are involved,

$$V^* \geq V(\{\mathbf{r}_i \in C_i\}), \quad (15)$$

$$A^* \geq A(\{\mathbf{r}_i \in C_i\}) \quad (16)$$

hold. Finally, the lower bound $Z^* < Z$ for the partition function is obtained as

$$Z^* = \frac{1}{\Lambda^{3N}} \int_{C^{(1)}} d\mathbf{r}_1 \cdots \int_{C^{(N)}} d\mathbf{r}_N e^{-\lambda_V V^* - \lambda_A A^*} \quad (17)$$

$$= \exp(-\lambda_V V^* - \lambda_A A^*) \prod_{i=1}^N [v_{\text{free}}^{(i)} / \Lambda^3] \quad (18)$$

$$= \exp(-\lambda_V V^* - \lambda_A A^*) (v_{\text{free}} / \Lambda^3)^N, \quad (19)$$

where $v_{\text{free}}^{(i)}$ is the volume of cell C_i . The last equality holds if all cells have the same volume $v_{\text{free}} = v_{\text{free}}^{(i)}$. The free energy within CT is readily obtained as

$$F^* = -k_B T \ln Z^* \quad (20)$$

$$= -N k_B T \ln(v_{\text{free}} / \Lambda^3) + k_B T (\lambda_V V^* + \lambda_A A^*), \quad (21)$$

where the property of being an upper bound $F^* > F$ to the exact free energy is inherited from the bound to the partition

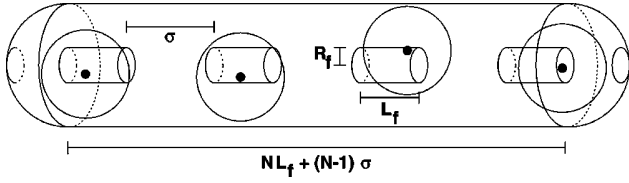


FIG. 2. Cell model for sausage configurations. Shown are particles (spheres), cells (cylinders), and the container K^* (enclosing cigarlike shape).

sum. The remaining task is to optimize with respect to the positions of the cells in space, their shape, and their size. Then V^* and A^* serve as estimates for average container volume and average surface area.

B. Application to different structures

The structure of the (crystalline) arrangement of particles is an input to the CT. We prescribe this by specifying the positions \mathbf{c}_i of the cell centers. All cells are chosen to have an identical shape C . Calculation of the body Γ [Eq. (14)] yields volume V^* and surface area A^* of the approximate container K^* . In the following, this recipe is carried out for the three types of conformations under consideration, see also Fig. 3.

1. Rodlike shapes (“sausages”)

We assume a one-dimensional arrangement of cells, $\mathbf{c}_i = i d \mathbf{e}$, where the cells are labeled by $i=1, \dots, N$, d is the distance between cell centers, and \mathbf{e} is some unit vector that we refer to as “sausage axis.” The free volume for each particle is assumed to be rotationally symmetric around \mathbf{e} , and to have different magnitudes along and perpendicular to \mathbf{e} . Hence the cell is a cylinder with radius r_f and height l_f , and is aligned along \mathbf{e} . The distance between the centers of two neighboring cells must be $d = \sigma + l_f$, so overlap of neighboring particles cannot occur. Obviously the convex hull Γ of the cells is a cylinder of length $N l_f + (N-1)\sigma$ and radius r_f . Its Minkowski functionals are

$$V_\Gamma = \pi r_f^2 [N l_f + (N-1)\sigma], \quad (22)$$

$$A_\Gamma = 2\pi r_f [N l_f + (N-1)\sigma] + 2\pi r_f^2, \quad (23)$$

$$M_\Gamma = \pi^2 r_f + \pi [N l_f + (N-1)\sigma]. \quad (24)$$

The volume V^* and surface area A^* of the approximate container K^* , see Fig. 2, are obtained through Steiner’s theorem as

$$V^* = \pi \left[N l_f r_f^2 + (N r_f^2 + N l_f r_f) \sigma + \left(N-1 + \frac{\pi}{4} \right) r_f \sigma^2 + \frac{N l_f \sigma^2}{4} + \left(\frac{N-1}{4} + \frac{\pi}{6} \right) \sigma^3 \right], \quad (25)$$

$$A^* = \pi [2 r_f^2 + 2 N l_f r_f + (2N-2 + \pi) r_f \sigma] \quad (26)$$

$$+ N l_f \sigma + (N-1 + \pi) \sigma^2]. \quad (27)$$

F^* can be easily minimized numerically with respect to l_f and r_f .

2. Platelike shapes (“Pizzas”)

The cell centers are assumed to build a portion of a two-dimensional (2D) hexagonal lattice with lattice spacing d . Hence $\mathbf{c}_i = j d \mathbf{e}_1 + (\sqrt{3}/2) k d \mathbf{e}_2$, where j, k are integers enumerating lattice sites, and the \mathbf{e}_i build the basis of the Cartesian coordinate system. The cells are assumed to be different in magnitude within the $\mathbf{e}_1 - \mathbf{e}_2$ “pizza plane” and perpendicular to it. For simplicity, we assume rotationally symmetric cells around \mathbf{e}_3 . Hexagonal shapes could be considered, but we expect the differences to be small [33]. Hence C again is a cylinder with radius r_f and height l_f , and is aligned along \mathbf{e}_3 . In order to avoid overlap, $d = \sigma + 2r_f$.

We obtain with straightforward calculus

$$V_\Gamma = A'' l_f, \quad (28)$$

$$A_\Gamma = 2A'' + U'' l_f, \quad (29)$$

$$M_\Gamma = \frac{\pi}{2} U'' + \pi l_f, \quad (30)$$

where

$$A'' = \gamma^2 A' + \gamma \mathcal{U}' r_f + 4\pi r_f^2, \quad (31)$$

$$\mathcal{U}'' = \gamma \mathcal{U}' + 2\pi r_f, \quad (32)$$

and A' and U' are the surface area and perimeter of the hull of the cell positions \mathbf{c}_i . The precise arrangement of cells only enters through A' and U' . This remarkable property is even true for arbitrary 2D cell arrangements other than portions of the hexagonal lattice.

3. Spherelike shapes (“clusters”)

In contrast to the above structures, clusters are (approximately) isotropic in all three spatial directions. Therefore, we choose spherical cells of radius r_f .

From V' , A' , M' of the hull of the \mathbf{c}_i , the body K^* can be computed as the parallel body with radius $R + r_f$. Volume V^* and surface A^* are directly obtained without the need to calculate Γ as

$$V^* = V' + A'(R + r_f) + M'(R + r_f)^2 + \frac{4\pi}{3} (R + r_f)^3, \quad (33)$$

$$A^* = A' + 2M'(R + r_f) + 4\pi (R + r_f)^2. \quad (34)$$

IV. COMPUTER SIMULATION

We have performed Monte Carlo (MC) simulations for particle numbers $N=4, 13, 55$. These were done in the canonical ensemble with prescribed (reduced) volume and surface coupling. Each MC consists of a check for possible overlap with other particles, as well as calculation of the change in the hull potential energy ϕ_{Hull} . For $N > 4$, the

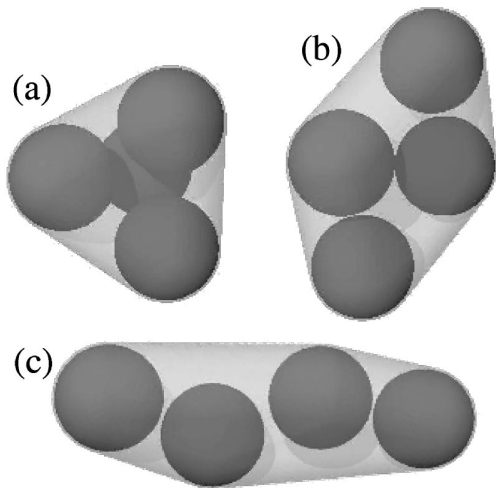


FIG. 3. Different conformations. (a) Spherelike (cluster), (b) platelike (pizza), (c) rodlike (sausage).

quick hull algorithm [28] is used to identify the convex hull of the position coordinates. Using umbrella sampling, we obtain the microcanonical entropy as a function of volume and surface. This is a delicate task that we only do for small $N=4$. Typically, between 10^7 ($N=4$) and 5×10^5 ($N=55$) MC moves per particle were done.

V. RESULTS

A. Entropy landscape

As an illustration, let us first show snapshots of typical configurations including cluster, sausage, and pizza in Fig. 3. For $N=4$, we have calculated the complete entropy landscape as a function of volume V and surface area A (see Fig. 4). There are three maxima in the entropy, which are indicated by the dark color. These are separated by “forbidden regions” (white), which do not contain any allowed configurations. The gap between the sausage and the pizza state is considerably bigger than the gap between the pizza and the

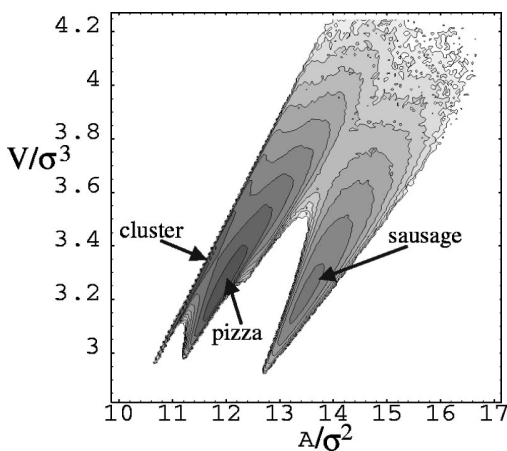


FIG. 4. Contour plot of the entropy $S(V,A) - \lambda_V V$ with $\lambda_V = 15$ as a function of the container volume V and surface area A for $N=4$.

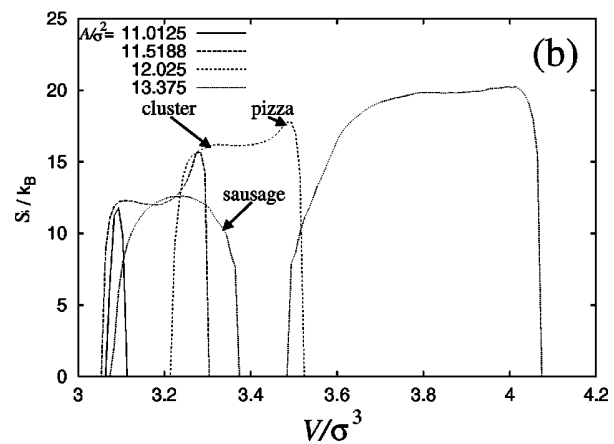
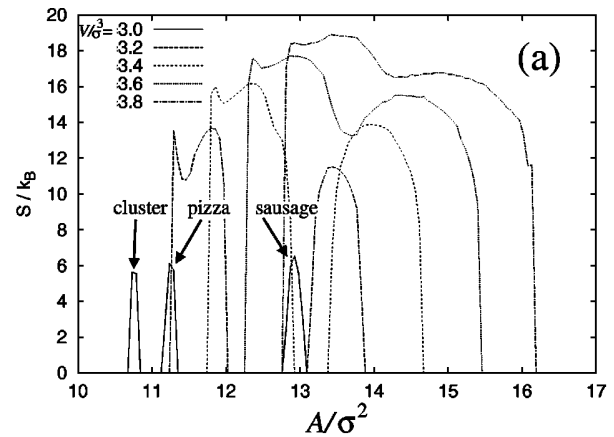


FIG. 5. One-dimensional cuts of the entropy landscape. (a) S/k_B at fixed values of volume V/σ^3 (as indicated) as a function of surface area A/σ^2 . (b) S/k_B at fixed values of A/σ^2 (as indicated) as a function of V/σ^3 .

cluster states. Figure 5(a) shows intersections of the entropy landscape with lines of constant volume. One observes that for V fixed to $3\sigma^3$, there are three separate regions of finite entropy, representing the three classes of configurations. For this fixed volume, it is thus not possible to switch continuously from one class to the other. For $V=3.2\sigma^3$, on the other hand, there is a connection between the cluster and the pizza region, while the sausage configurations still appear in a separate peak. Only for $V \geq 3.6\sigma^3$ is there a continuous connection between all these states. In Fig. 5(b), intersections with lines of constant surface area are shown. For $A=11.0125\sigma^2$, only the cluster state has a finite entropy. For intermediate values $A=11.5188\sigma^2, 12.025\sigma^2$ the pizza also appears and is separated by a pronounced minimum from the cluster. For $A=13.375\sigma^2$, this minimum becomes shallower and shifts towards larger V . An additional maximum appears for small V due to the sausage conformations.

B. Canonical averages

For large N , it becomes increasingly hard to perform a sampling of the complete configuration space using simulations. The computation of the container properties slows

down the speed of the simulation. In addition, for many particles the system has a large number of stable and metastable states, making the sampling with correct statistical weights much more difficult.

However, it is possible to study specific structures of the system. This is similar to the treatment in CT. We will compare results from CT and MC for systems with small ($N=4$), medium ($N=13$), and large ($N=55$) particle numbers. Remember that $N=55$ is a boundary case, where the sausage is still denser than any cluster.

We compute canonical averages $\langle V \rangle$ and $\langle A \rangle$, for volume and surface area, respectively, as a function of the coupling parameter λ_V . See Fig. 6(a) for a comparison of simulation and cell theory for $N=4$. The three structures occurring for this system—the sausage, the pizza, and the cluster—are studied separately.

First, note that the CT gives the correct succession of the structures. The volume of the sausage system is smaller than that of a cluster system, which in turn is less than the volume of pizza configurations. On the other hand, the surface area (see the inset) is largest for sausages, then comes the pizza, and finally the cluster configurations. Upon increasing λ_V , both volume and area decrease, as expected, and the conformations become more compressed.

Apparently the CT results give larger values for volume and surface area than the computer simulation. However, the general dependence of the volume coupling looks very similar, especially the limiting behavior for $\lambda_V \rightarrow 0$ and for $\lambda_V \rightarrow \infty$. The latter even gives the correct value, since the CT becomes exact for zero temperature.

Remember that the CT neglects configurations where particles are located outside their cells. These have larger containers than those taken into account in CT. Hence one might be misled to conclude that CT should give too small $\langle V \rangle$ and $\langle A \rangle$. The fact that both quantities are overestimated is merely due to the construction of the approximate container K^* . This object is a superset of all possible containers where particles are inside cells.

Next, we study the case of $N=13$ particles [Fig. 6(b)] as an example of a system with an intermediate number of particles. In order to apply CT to that system, we have to specify the configurations under examination. This is clear for the sausage, and we choose an exemplary pizza. For the cluster, we pick a regular icosahedron, with an extra particle at its center. We chose this configuration because it was found frequently during simulation runs. However, this structure has some special properties. First, it is not the densest possible cluster for $N=13$. One with smaller volume can be obtained by cutting a spherical region out of a close-packed fcc lattice. Second, in this configuration all particles in the outer shell have enough space to move around freely on the surface of the central sphere. Therefore, the assumption made in CT that all particles are confined to separate regions might be critical. The results are plotted in Fig. 6(b), which shows the same quantities as before. For the surface area (inset), we now see very good agreement between simulation and CT results. At first sight, the plot of the container volume shows the same tendencies as for $N=4$. The general behavior is correct, but the CT overestimates the volume.

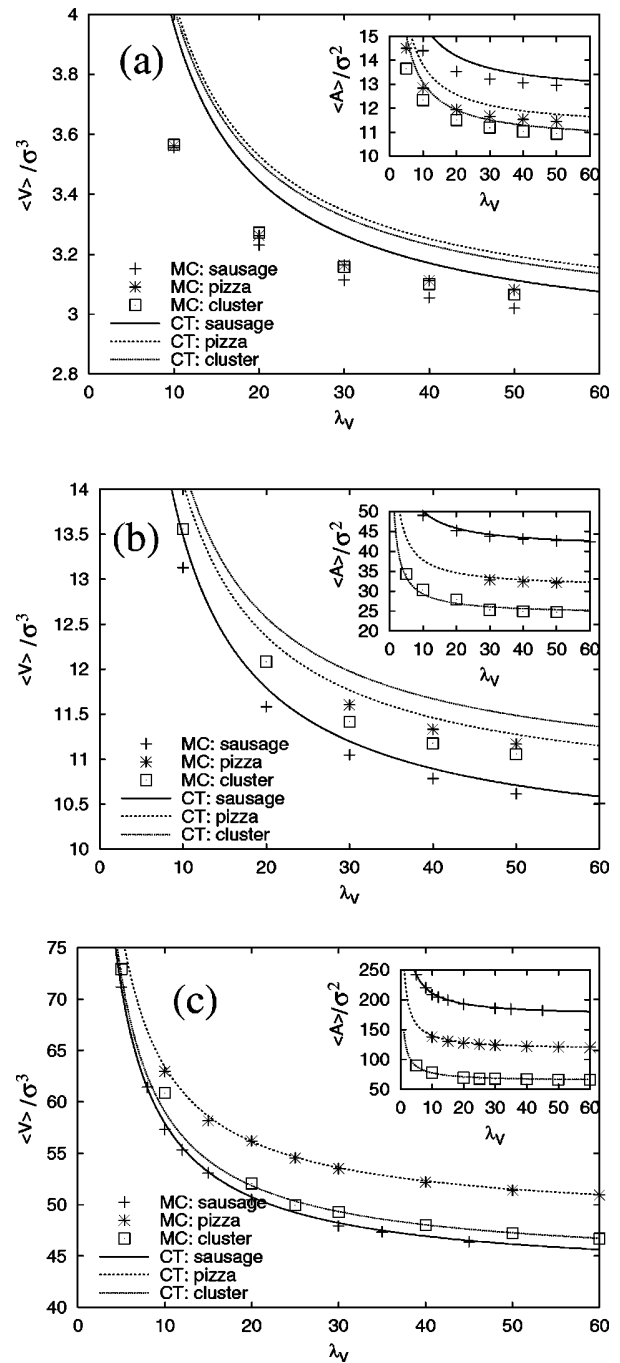


FIG. 6. Average volume $\langle V \rangle / \sigma^3$ as a function of volume coupling λ_V from simulation (MC) and cell theory (CT). Shown are the values for sausage, pizza, and cluster configurations. The inset shows the average surface area $\langle A \rangle / \sigma^2$ as a function of λ_V for different particle numbers N . (a) $N=4$; (b) $N=13$; (c) $N=55$.

Here the discrepancy is smaller for sausage and pizza structures. Note, however, that the order of the lines is shifted. Here, the CT gives a higher volume for the cluster than for the pizza configurations. We attribute this failure of CT to the special properties of the icosahedron cluster. The particles do not stay in the cells as assumed in the theory, so it cannot give accurate results.

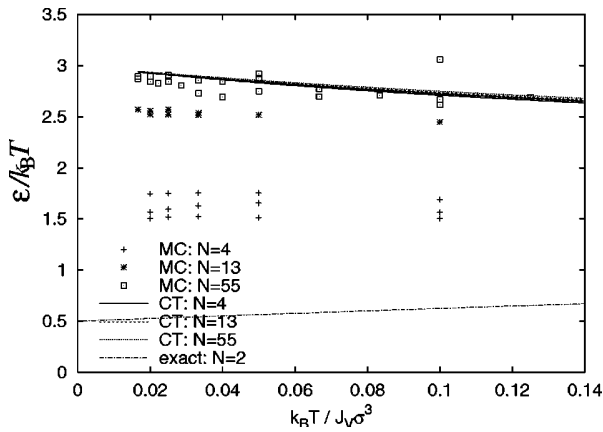


FIG. 7. Excess (over ground-state) internal energy ϵ (in units of $k_B T$) per particle as a function of temperature. Shown are the simulation (MC) and cell theory (CT) results for sausage, pizza, and cluster configurations for $N=4, 13, 55$, together with the exact solution for $N=2$.

For $N=55$, we cut out a portion of a hexagonal lattice for a representative pizza configuration. Similarly, we construct a cluster of 55 particles by cutting a spherical portion out of an fcc lattice. In Fig. 6(c), results for average volume and surface area are given. Excellent agreement between theory and simulation is found.

Summarizing these results, we find that CT gives the correct behavior of equilibrium properties of the system. It overestimates the mean volume, but this deviation decreases for larger particle numbers. One exception is the icosahedral structure of the $N=13$ cluster, which causes a special difficulty due to its geometric properties. As the complete packing problem is a complicated one, we expect that more such exceptional cases can be found by varying N . The fact that CT predicts more accurate results for higher particle numbers can be attributed to the relative decrease of the number particles at the boundary. We believe that the high accuracy for $N=55$ is preserved when N is increased, even far beyond this value. Remember that in the thermodynamical limit, $N \rightarrow \infty$, CT gives a fair description of the bulk crystal [30,31].

We next consider the question of how much each particle contributes to the total internal energy of the system. If the temperature of the system is increased, the container swells, which results in an excess volume compared to its close-packed volume V_{CP} at zero temperature. This increase in container volume leads to a gain in internal energy per particle, which is given as $\epsilon = J_V((V) - V_{CP})/N$. We plot $\epsilon/k_B T$ in Fig. 7 as a function of scaled temperature. Shown are the results from both simulation and CT for $N=4, 13, 55$ and for sausage, pizza, and cluster configurations. For comparison, the exact solution for $N=2$ is also shown. The dependence on the scaled temperature $k_B T / J_V \sigma^3$ is weak. The simulation data show a global shift to higher values as N increases, but only a minor dependence on the conformation. CT fails to describe the behavior for small N , but gives the correct results for $N=55$.

C. Transitions between different shapes

As the CT permits direct access to the free energy, we can calculate a “phase diagram” as a function of the coupling

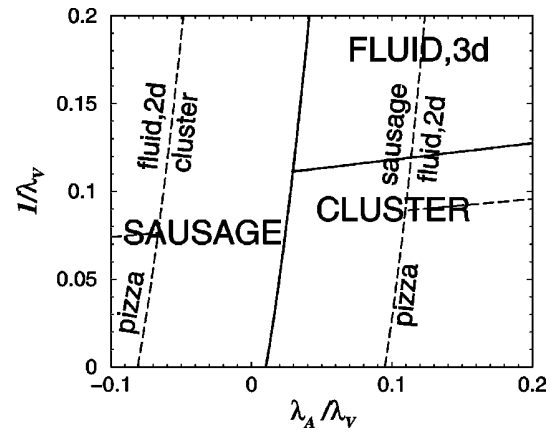


FIG. 8. Phase diagram for $N=55$ confined colloids as a function of the ratio between surface and volume coupling, λ_A / λ_V , and inverse volume coupling $1/\lambda_V$. The solid lines separate stable states (uppercase), the dashed lines separate metastable states (lowercase).

parameters. We define a stable phase as the structure with the smallest free energy, which has the largest statistical weight. However, as the system is not in the thermodynamical limit, the probability for conformation with larger free energy does not vanish. We find that either the sausage or the cluster is most stable, see Fig. 8. The horizontal axis is the ratio between volume and surface coupling, λ_A / λ_V . The vertical axis is the inverse volume coupling $1/\lambda_V$. Remember that $\lambda_V = J_V \sigma^3 / k_B T$, so that $1/\lambda_V$ can be regarded as a temperature, whereas $\lambda_A / \lambda_V = J_A / (J_V \sigma)$ is independent of temperature. For fixed temperature, we follow a horizontal path in the phase diagram by changing the ratio λ_A / λ_V . The container is in either the sausage or the cluster state. For small λ_A / λ_V the sausage is stable, as this is the most dense structure in terms of occupied volume. Increasing λ_A / λ_V leads to stabilization of the cluster, because this more compact object possesses smaller surface area. The location of the crossover (phase boundary) shifts towards large λ_A / λ_V upon increasing temperature. If λ_A / λ_V is sufficiently large, the cluster is the ground state at $T=0$ and remains stable for small T . Increasing T leads to a transition to the sausage. In both regions of the phase diagram, there are two metastable states. The free energies of those can also be compared in order to conclude which of both is relatively more stable. The resulting boundaries show that close to the sausage-cluster transition, the pizza is least stable, but at extreme λ_A / λ_V it will be more stable than the other metastable state. However, the pizza structure never has the lowest free energy of all three conformations. For high T , it is expected that the container does not exert enough pressure on the particles to confine them to well-defined lattice sites, and melting will occur. In infinite bulk systems, this phenomenon depends crucially on dimensionality. It is absent (for short-ranged interactions) in 1D, and the location and even the scenario are different in 2D and 3D. In order to estimate where melting occurs in the present system, we use the following rough criterion. The particles will be fluidlike if the nearest-neighbor distance exceeds the value in the corresponding bulk system, which is

$d=1.086$ in 2D and $d=1.11$ in 3D. Within CT, the nearest-neighbor distance is directly accessible and the corresponding state point can be obtained. The fluid regions obtained in this way are indicated in Fig. 8. As expected, the 2D and 3D fluid appear for large $1/\lambda_V$ (large temperature).

VI. CONCLUSIONS

We have investigated a system of spherical particles confined within a fluctuating container. Our model is a hybrid of colloidal cluster physics and membrane theory and couples the degrees of freedom of the particles and the membrane resulting in new vesicle shapes as rodlike, platelike, and spherelike forms. The container may be physically realized by a membrane that constitutes a vesicle or by an oil droplet in an emulsion. We allow this object to change its shape, and take into account an external pressure and a surface tension towards the surrounding. Our theoretical model uses a description of the droplet shape on a coarse-grained level based on integral geometrical methods. The particles are modeled as a finite number of hard spheres, ranging from 2 to 55.

For this system, we have demonstrated that a zoo of different particle conformations arises. These fall into different classes, namely three-dimensional (3D), planar (2D), and linear (1D) ones, called clusters, pizzas, and sausages, respectively.

The breaking of rotational symmetry is especially striking, as *a priori* the model does not contain any anisotropic interactions. The driving force of these transitions is merely the highly nontrivial close-packed structure of a finite number of spheres. Here, this purely geometric packing problem is cast into a physical one through the consideration of the entropy of the system. It allows us to investigate the behavior away from close-packing as a function of container volume and surface area.

As an outlook, we comment on possible future work.

Within the current model, there are still many open questions. One could investigate the effect of nonvanishing coupling to the integral mean curvature, i.e., $\lambda_M \neq 0$. This might be a way to stabilize pizza structures, which were found to be only metastable in the current investigation. Furthermore, one could consider insertion and escape of particle, i.e., use the grand-canonical ensemble with respect to N . A straightforward generalization is towards a collection of more than one container. The coupling to the Euler characteristic λ_χ plays the role of a chemical potential of the containers. As the simplest model, one could neglect the steric interaction between the container hulls themselves, and only take into account the hard cores of particles of different containers.

Furthermore, it would be interesting to model the container in more detail. Using Helfrich's Hamiltonian and a microscopic model for the membrane constitutes an interesting as well as demanding perspective. It is in principle possible to find a suitable experimental setup in which one is able to observe the predicted transitions. Then one could also investigate the dynamics of the rare events of the conformational changes, which is also interesting from a more theoretical point of view. We also mention the interesting problem of crystallization of many of these flexible objects filled with colloidal spheres. Furthermore, it would be interesting to investigate tangent hard spheres inside a flexible container in order to study a polymer chain confined to a vesicle. In this case, one would expect that the "pizza" conformation is much less stable. Whether our geometric approach can be used to study hydrophobicity[34] constitutes a further interesting point.

ACKNOWLEDGMENTS

We thank David Chandler, Pieter Rein ten Wolde, Mauro Merolle, Jörg M. Wills, Brad Barber, Bela Mulder, Daan Frenkel, Alice Gast, Gerhard Gompper, Christos N. Likos, and Joachim Dzubiella for valuable discussions.

-
- [1] P. K. Doye and D. J. Wales, *Science* **271**, 484 (1996).
 - [2] K. M. Ho, A. A. Shvartsburg, B. C. Pan, Z. Y. Lu, C. Z. Wang, J. G. Wacker, J. L. Fye, and M. F. Jarrold, *Nature (London)* **392**, 582 (1998).
 - [3] D. J. Wales and P. K. Doye, *J. Phys. Chem. A* **101**, 5111 (1997).
 - [4] J. M. Wills, *Mathematika* **43**, 229 (1996).
 - [5] T. C. Hales, *Discrete Comput. Geom.* **17**, 1 (1997); **18**, 135 (1997).
 - [6] A. Maritan, C. Micheletti, A. Trovato, and J. R. Banavar, *Nature (London)* **406**, 287 (2000).
 - [7] J. M. Wills, in *Spatial Statistics and Statistical Physics*, edited by K. Mecke and D. Stoyan, *Lecture Notes in Physics Vol. 332* (Springer, Berlin, 2000).
 - [8] H. Löwen, *Phys. Rep.* **237**, 249 (1994).
 - [9] H. Löwen, in *Spatial Statistics and Statistical Physics*, edited by K. R. Mecke and D. Stoyan, *Lecture Notes in Physics Vol. 554* (Springer, Berlin, 2000).
 - [10] M. Schmidt and H. Löwen, *Phys. Rev. Lett.* **76**, 4552 (1996).
 - [11] M. Schmidt and H. Löwen, *Phys. Rev. E* **55**, 7228 (1997).
 - [12] A. K. Macpherson, Y. P. Carignan, and T. Vladimiroff, *J. Chem. Phys.* **87**, 1768 (1987).
 - [13] A. González, J. A. White, F. L. Román, S. Velasco, and R. Evans, *Phys. Rev. Lett.* **79**, 2466 (1997).
 - [14] Z. T. Nemeth and H. Löwen, *J. Phys.: Condens. Matter* **10**, 6189 (1998).
 - [15] F. L. Roman, M. Schmidt, and H. Löwen, *Phys. Rev. E* **61**, 5445 (2000).
 - [16] U. Seifert, *Adv. Phys.* **46**, 13 (1997).
 - [17] R. Lipowsky, *Encyclopedia Appl. Phys.* **23**, 199 (1998).
 - [18] G. Gompper and D. M. Kroll, *Curr. Opin. Colloid Interface Sci.* **2**, 373 (1997).
 - [19] A. R. Bausch, F. Ziemann, A. A. Boulbitch, K. Jacobson, and E. Sackmann, *Biophys. J.* **75**, 2038 (1998).
 - [20] M. Ficheux, L. Bonakdar, F. Leal-Calderon, and J. Bibette, *Langmuir* **14**, 2702 (1998).
 - [21] R. Bar-Ziv, T. Frisch, and E. Moses, *Phys. Rev. Lett.* **75**, 3481 (1995).

COLLOIDS CONFINED TO A FLEXIBLE CONTAINER

PHYSICAL REVIEW E **63** 051401

- [22] A. D. Dinsmore, D. T. Wong, P. Nelson, and A. G. Yodh, *Phys. Rev. Lett.* **80**, 409 (1998).
- [23] R. Lipowsky and H. Döbereiner, *Europhys. Lett.* **43**, 219 (1998).
- [24] K. R. Mecke, in *Spatial Statistics and Statistical Physics*, edited by K. R. Mecke and D. Stoyan, *Lecture Notes in Physics* Vol. 111 (Springer, Berlin, 2000).
- [25] C. N. Likos, K. R. Mecke, and H. Wagner, *J. Chem. Phys.* **102**, 9350 (1995).
- [26] K. R. Mecke, *J. Phys.: Condens. Matter* **8**, 9663 (1996).
- [27] K. R. Mecke, *Int. J. Mod. Phys. B* **12**, 861 (1998).
- [28] C. B. Barber, D. P. Dobkin, and H. Huhdanpaa, *ACM Trans. Math. Softw.* **22**, 469 (1996).
- [29] W. Helfrich, *Z. Naturforsch. C* **28c**, 693 (1973).
- [30] J. G. Kirkwood, *J. Chem. Phys.* **18**, 380 (1950).
- [31] W. W. Wood, *J. Chem. Phys.* **20**, 1334 (1952).
- [32] M. Heni and H. Löwen, *Phys. Rev. E* **60**, 7057 (1999).
- [33] Different cell shapes primarily generate a constant factor in the partition sum, which does not affect expectation values.
- [34] K. Lum, D. Chandler, J. D. Weeks, *J. Phys. Chem. B* **103**, 4570 (1999).

Topological defects in nematic droplets of hard spherocylinders

Joachim Dzubiella, Matthias Schmidt, and Hartmut Löwen

Institut für Theoretische Physik II, Heinrich-Heine-Universität Düsseldorf, Universitätsstraße 1, D-40225 Düsseldorf, Germany

(Received 22 June 1999; revised manuscript received 17 May 2000)

Using computer simulations we investigate the microscopic structure of the singular director field within a nematic droplet. As a theoretical model for nematic liquid crystals we take hard spherocylinders. To induce an overall topological charge, the particles are either confined to a two-dimensional circular cavity with homeotropic boundary or to the surface of a three-dimensional sphere. Both systems exhibit half-integer topological point defects. The isotropic defect core has a radius of the order of one particle length and is surrounded by free-standing density oscillations. The effective interaction between two defects is investigated. All results should be experimentally observable in thin sheets of colloidal liquid crystals.

PACS number(s): 61.30.Jf, 83.70.Jr, 77.84.Nh

I. INTRODUCTION

Liquid crystals (LC) show behavior intermediate between liquid and solid. The coupling between orientational and positional degrees of freedom leads to a large variety of mesophases. The microscopic origin lies in anisotropic particle shapes and anisotropic interactions between the particles that constitute the material. The simplest, most liquidlike LC phase is the nematic phase where the particles are aligned along a preferred direction while their spatial positions are, like in an ordinary liquid, homogeneously distributed in space. The preferred direction, called the nematic director, can be macroscopically observed by illuminating a nematic sample between crossed polarizers.

There are many different systems that possess a nematic phase. Basically, one can distinguish between molecular LCs where the constituents are molecules and colloidal LCs containing mesoscopic particles, e.g., suspensions of tobacco mosaic viruses [1]. Furthermore, there is the possibility of self-assembling rodlike micelles [2], which can be studied with small-angle neutron scattering [3].

There are various theoretical approaches to deal with nematic liquid crystals. On a coarse-grained level one may use Ginzburg-Landau theories, including phenomenological elastic constants. The central idea is to minimize an appropriate Frank elastic energy with respect to the nematic director field [4]. Second, there are spin models, like the Lebwohl-Lasher model, see, e.g., Refs. [5–7]. There the basic degrees of freedom are rotators sitting on the sites of a lattice and interacting with their neighbors. The task is to sample appropriately the configuration space. The third class of models consists of particles with orientational and positional degrees of freedom. Usually, the interaction between particles is modeled by an anisotropic pair potential. Examples are Gay-Berne particles, e.g., [8,9], and hard bodies, e.g., hard spherocylinders (HSC) [10]. Beginning with the classical isotropic-nematic phase transition for the limit of thin, long needles due to Onsager [11], our knowledge has grown enormously for the system of hard spherocylinders. The bulk properties have recently been understood up to close packing. The phase diagram has been calculated by computer simulations [12], density-functional theory [13], and cell theory [14]. There are various stable crystal phases,

like an elongated face-centered-cubic lattice with an *ABC* stacking sequence, a plastic crystal, smectic-*A* phase, and nematic and isotropic fluid. Besides bulk properties, one has investigated various situations of external confinement, like nematics confined to a cylindrical cavity [15] or between parallel plates [16,17]. Also effects induced by a single wall have been studied, like depletion-driven adsorption [18], anchoring [19], wetting [20], and the influence of curvature [21]. Furthermore, solid bodies immersed in nematic phases experience nontrivial forces [22–24], and point defects experience an interaction [25].

Topological defects within ordered media are deviations from ideal order, loosely speaking, that can be felt at an arbitrary large separation distance from the defect position. Complicated examples are screw dislocations in crystalline lattices and inclusions in smectic films [26]. To deal with topological defects the mathematical tools of homotopy theory may be employed [27] to classify all possible structures. The basic ingredients are the topology of both the embedding physical space and the order parameter space. For the case of nematics, there are two kinds of stable topological defects in three dimensions (3D), namely point defects and line defects, whereas in two dimensions (2D) there are only point defects. These defects arise when the system is quenched from the isotropic to the nematic state [28]. Also the dynamics have been investigated [29] experimentally. On the theoretical side, there is the important work within the framework of Landau theory by Schopohl and Sluckin on the defect core structure of half-integer wedge disclinations [30] and on the hedgehog defect core [31] in nematic and magnetic systems. The latter predictions have been confirmed with computer simulations of lattice spin models [32]. The topological theory of defects has been used to prove that a uniaxial nematic either melts or exhibits a complex biaxial structure [33]. Sonnet, Kilian, and Hess [34] have considered droplet and capillary geometries using an alignment tensor description.

The investigation of equilibrium topological defects in nematics has received a boost through a striking possibility to stabilize defects by imprisoning the nematic phase within a spherical droplet. The droplet boundary induces a nontrivial effect on the global structure within the droplet. Moreover, it can be experimentally controlled in a variety of ways

to yield different well-defined boundary conditions, namely homeotropic or tangential ones. One famous experimental system is polymer-dispersed LCs. Concerning nematic droplets, there are various studies using the Lebwohl-Lasher model [5–7]. There are investigations of the droplet shape [35,36], the influence of an external field [37], chiral nematic droplets [38], structure factor [39], and ray propagation [40]. Also simulations of Gay-Berne droplets have been performed [41]. Other systems that exhibit topological defects are nematic emulsions [42–44] and defect gels in cholesteric LCs [45]. The formation of disclination lines near a free nematic interface was reported [46].

In this work we are concerned with the microscopic structure of topological defects in nematics. We use a model for rodlike particles with a pairwise hard core interaction, namely hard spherocylinders. It accounts for both the orientational degrees of freedom as well as the positional degrees of freedom of the particles constituting the nematic. Especially, it allows for mobility of the defect positions. This system is investigated with Monte Carlo computer simulations. There exist successful simulations of topological line defects using hard particles, namely integer [47] and half-integer line defects [48].

Here, we undertake a detailed study of the microscopic structure of the defect cores focusing on the behavior of the local nematic order and on the density field, an important quantity that has not been studied in the literature yet. As a theoretical prediction, we find that the arising half-integer point defects are surrounded by an oscillating density inhomogeneity. This can be verified in experiments. We also investigate the statistical properties of two defects interacting with each other extracting the distribution functions of the positions of the defect cores and their orientations. These are not accessible in mean-field calculations. We emphasize that both properties, the free-standing density wave which is due to microscopic *correlations* and the defect position distribution which is due to *fluctuations*, cannot be accessed by a coarse-grained mean-field-type calculation.

The paper is organized as follows: In Sec. II our theoretical model is defined, namely hard spherocylinders within a planar spherical cavity and on the surface of a sphere. For comparison, we also propose a simplified toy model of aligned rods. Section III is devoted to the analytical tools employed, such as order parameter and density profiles. Section IV gives details about the computer simulation techniques used. The results of our investigation are given in Sec. V and we finish with concluding remarks and a discussion of the experimental relevance of the present work in Sec. VI.

II. MODEL

A. Hard spherocylinders

We consider N identical particles with center-of-mass position coordinates $\mathbf{r}_i = (r_{xi}, r_{yi})$ and orientations \mathbf{n}_i , where the index $i = 1, \dots, N$ labels the particles. Each particle has a rodlike shape: It is composed of a cylinder of diameter σ and length $L - \sigma$ and two hemispheres with the same diameter capping the cylinder on its flat sides. In 3D this geometric shape is called a spherocylinder, see Fig. 1. The 2D analog is sometimes called discorectangle as it is made of a rectangle

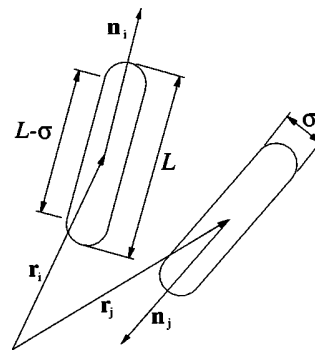


FIG. 1. Two hard spherocylinders with position coordinates \mathbf{r}_i and \mathbf{r}_j , and orientations \mathbf{n}_i and \mathbf{n}_j . The width of the particles is σ ; the total rod length is denoted by L .

and two half disks. We assume a hard core interaction between any two spherocylinders that forbids particle overlap. Formally, we may write

$$U(\mathbf{r}_i, \mathbf{n}_i; \mathbf{r}_j, \mathbf{n}_j) = \begin{cases} \infty & \text{if particles } i \text{ and } j \text{ overlap} \\ 0 & \text{else.} \end{cases} \quad (1)$$

The geometric overlap criterion involves a sequence of elementary algebraic tests. They are composed of scalar and vector products between the distance vector of both particles and both orientation vectors. The explicit form can be found, e.g., in Ref. [49]. The bulk system is governed by two dimensionless parameters, namely the packing fraction η , which is the ratio of the space filled by the particle ‘‘material’’ and the system volume V . In two dimensions it is given by $\eta = (N/V)[\sigma(L - \sigma) + \pi\sigma^2/4]$. The second parameter is the anisotropy $p = L/\sigma$ which sets the length-to-width ratio. The bulk phase diagram in 3D was recently mapped out by computer simulation [12] and density-functional theory [13]. The nematic phase is found to be stable for anisotropies $p > 5$. In 2D the phase diagram is not known completely but there is an isotropic to nematic phase transition for infinitely thin needles [50]. The nematic phase is also present in a system of hard ellipses [51,52] verified by computer simulations. In 2D the nematic-isotropic transition was investigated using density-functional theory [53] and scaled-particle theory [54]. There is work about equations of state [55], and direct correlation functions [56] within a geometrical framework.

B. Planar model

To align the particles near the system boundary homeotropically we apply a suitably chosen external potential. The particles are confined within a spherical cavity representing the droplet shape. The interaction of each HSC with the droplet boundary is such that the center of mass of each particle is not allowed to leave the droplet, see Fig. 2. The corresponding external potential is given by

$$U_{\text{ext}}(\mathbf{r}_i) = \begin{cases} 0 & \text{if } |\mathbf{r}_i| < R - L/2 \\ \infty & \text{else,} \end{cases} \quad (2)$$

where R is the radius of the droplet and we chose the origin of the coordinate system as the droplet center. The system

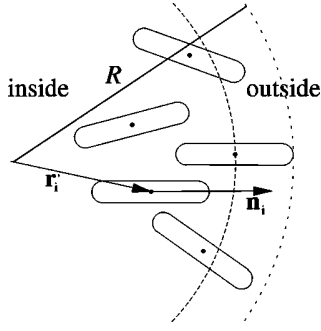


FIG. 2. Homeotropic boundary conditions for the planar droplet. The particle centers (points) are not allowed to cross a circle with diameter $R - L/2$ (dashed line). Then the shape of each particle lies inside a circle with radius R .

volume is $V = \pi R^2$. This boundary condition is found to induce a nematic order perpendicular to the droplet boundary as the particles try to stick one of their ends to the outside [57]. Hence the topological charge is one. In the limit, $p = 1$, we recover the confined hard sphere system recently investigated in 2D [58] and 3D [59–61].

C. Spherical model

A second possibility to induce an overall topological charge is to confine the particles to a non-planar, curved space, which we chose to be the surface of a sphere in three-dimensional space. The particles are forced to lie tangentially on the sphere with radius R , see Fig. 3. Mathematically, this is expressed as

$$|\mathbf{r}_i| = R, \quad (3)$$

$$\mathbf{r}_i \cdot \mathbf{n}_i = 0. \quad (4)$$

The director field on the surface of a sphere has to have defects. This is known as the ‘‘impossibility of combing a hedgehog.’’ The total topological charge [27] is two. The topological charge is a winding number that counts the number of times the nematic director turns along a closed path

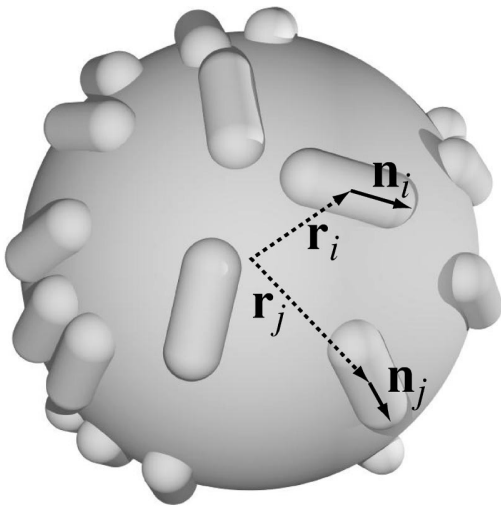


FIG. 3. Spherical system. Each particle with position \mathbf{r}_i and orientation \mathbf{n}_i is forced to lie tangentially on the surface of a sphere.

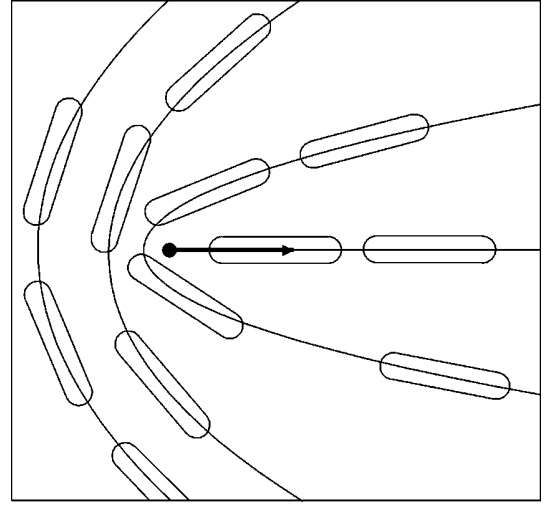


FIG. 4. Model of aligned rods. Each particle (discorectangles) has an orientation according to a prescribed director field (lines). The position of the arising $1/2$ defect is indicated by a filled circle, the orientation by an arrow.

around the defect. It may have positive and negative, integer, or half-integer values, namely $0, \pm 1/2, \pm 1, \dots$

D. Aligned rods

To investigate pure positional effects we study a further simplified model where the orientation of each rod is uniquely determined by its position. Therefore we consider an arbitrary unit vector field $\mathbf{n}(\mathbf{r})$ describing a given nematic order pattern. In reality, the particles fluctuate around this mean orientation. Here, however, we neglect these fluctuations by imposing $\mathbf{n}_i = \mathbf{n}(\mathbf{r}_i)$. In particular, we chose the director field to possess a singular defect with topological charge t , see Fig. 4. The precise definition of this director field $\mathbf{n}^{(t)}(\mathbf{r})$ is postponed to the next section [and given therein in Eq. (5)]. The case of parallel aligned rods, $\mathbf{n} = \text{const}$, has been used to study phase transitions to higher-ordered liquid crystals [62].

III. ANALYTICAL TOOLS

A. Order parameters

In order to analyze the fluctuating particle positions and orientations, we probe against a director field possessing a topological defect with charge t . It is given by

$$\mathbf{n}^{(t)}(\mathbf{q}, \mathbf{r}) = \underline{\mathbf{D}}^{(t)}(\mathbf{r}) \mathbf{q}, \quad (5)$$

where the rotation matrix is

$$\underline{\mathbf{D}}^{(t)}(\mathbf{a}) = \begin{pmatrix} \cos(t\phi) & -\sin(t\phi) \\ \sin(t\phi) & \cos(t\phi) \end{pmatrix}, \quad (6)$$

with $\phi = \arctan(a_y/a_x)$, and $\mathbf{a} = (a_x, a_y)$ being a 2D vector. The vector \mathbf{q} is the orientation of particles if one approaches the defect along the x direction.

As an order parameter, we probe the actual particle orientations \mathbf{n}_i against the ideal ones

$$S^{(t)}(\mathbf{c}, \mathbf{q}; r) = 2 \langle [\mathbf{n}_i \cdot \mathbf{n}^{(t)}(\mathbf{q}, \mathbf{r}_i - \mathbf{c})]^2 \rangle_r - 1, \quad (7)$$

where the radial average is defined as $\langle \dots \rangle_r = \langle \sum_{i=1}^N \delta(|\mathbf{r}'_i| - r) \dots \rangle / \langle \sum_{i=1}^N \delta(|\mathbf{r}'_i| - r) \rangle$, with $\mathbf{r}'_i = \mathbf{r}_i - \mathbf{c}$ and $\langle \dots \rangle$ is an ensemble average. Normalization in Eq. (7) is such that usually $0 \leq S^{(t)} \leq 1$, where unity corresponds to ideal alignment, and zero means complete dissimilarity with the defect of charge t at position \mathbf{c} and vector \mathbf{q} , Eq. (5). (In general, $-1 \leq S^{(t)} < 1$ is possible, where negative values indicate an anticorrelation.)

If \mathbf{c} and \mathbf{q} are not dictated by general symmetry considerations (e.g., $\mathbf{c} = 0$ because of the spherical droplet shape), we need to determine both quantities. To that end we measure the similarity of an actual particle configuration compared to a defect, Eq. (5). We probe this inside a spherical region around \mathbf{c} with radius R^* using

$$I^{(t)}(\mathbf{c}, \mathbf{q}) = \frac{2}{(R^*)^2} \int_0^{R^*} dr r S^{(t)}(\mathbf{c}, \mathbf{q}; r), \quad (8)$$

where R^* is a suitably chosen cutoff length. We maximize $I^{(t)}(\mathbf{c}, \mathbf{q})$ with respect to \mathbf{c} and \mathbf{q} . The value at the maximum is

$$\lambda^{(t)} = \max_{\mathbf{c}, \mathbf{q}} \{I^{(t)}(\mathbf{c}, \mathbf{q})\}, \quad (9)$$

and the argument at the maximum is $\mathbf{q}^{(t)}$.

Before summarizing the quantities we compute during the simulation, let us note that $\mathbf{q}^{(t)}$ and $\lambda^{(t)}$ are eigenvector and the corresponding (largest) eigenvalue of a suitable tensor. To see this, we attribute to each particle the general tensor

$$\underline{\underline{\mathbf{Q}}}_i^{(t)} = 2[\underline{\underline{\mathbf{D}}}_i^{(t)}(\mathbf{r}_i - \mathbf{c})\mathbf{n}_i \cdot \underline{\underline{\mathbf{D}}}_i^{(t)}(\mathbf{r}_i - \mathbf{c})\mathbf{n}_i] - \underline{\underline{\mathbf{1}}}, \quad (10)$$

where $\underline{\underline{\mathbf{D}}}_i^{(t)}$ denotes the dyadic product and $\underline{\underline{\mathbf{1}}}$ is the identity matrix. Summing over particles gives

$$\underline{\underline{\mathbf{Q}}}^{(t)} = \sum_i \underline{\underline{\mathbf{Q}}}_i^{(t)}. \quad (11)$$

Note that for $t=0$ the usual bulk nematic order parameter is recovered.¹ The order parameter profile, Eq. (7), is then obtained as

$$S^{(t)}(\mathbf{c}, \mathbf{q}, r) = \langle \mathbf{q} \cdot \underline{\underline{\mathbf{Q}}}^{(t)} \cdot \mathbf{q} \rangle_r, \quad (12)$$

and then the relation $\lambda^{(t)} \mathbf{q}^{(t)} = \underline{\underline{\mathbf{Q}}}^{(t)} \mathbf{q}^{(t)}$ holds, if the sum over i in Eq. (11) is restricted to particles located inside a spherical region of radius R^* around \mathbf{c} .

Let us next give three combinations of $t, \mathbf{c}, \mathbf{q}$ that apply to the current model. First, we investigate the (bulk) nematic order, $t=0$. We resolve this as a function of the distance from the droplet center, hence $\mathbf{c} = 0$. The nematic director $\mathbf{q}^{(0)}$ is obtained from Eq. (9) with $R^* = R$. The order parameter, defined in Eq. (7), then simplifies to

$$S^{(0)}(r) = 2 \langle (\mathbf{n}_i \cdot \mathbf{q}^{(0)})^2 \rangle_r - 1. \quad (13)$$

Second, we probe for starlike order, hence $t=1$, $\mathbf{c} = 0$. As we do not expect spiral arms of the star pattern to occur, we can set $\mathbf{q} = \mathbf{e}_x$, where \mathbf{e}_x is the unit vector in the x direction. We can rewrite Eq. (7) as

$$S^{(1)}(r) = 2 \langle (\mathbf{n}_i \cdot \hat{\mathbf{r}}_i)^2 \rangle_r - 1, \quad (14)$$

where $\hat{\mathbf{r}}_i = \mathbf{r}_i / |\mathbf{r}_i|$.

Third, we investigate $t=1/2$ defects. To that end, we need to search for \mathbf{c} and \mathbf{q} , as these are not dictated by the symmetry of the droplet. Hence we numerically solve Eq. (9) with $R^* = 2L$ (see Sec. IV B). We obtain

$$S^{(1/2)}(r) = 2 \langle [\mathbf{n}_i \cdot \mathbf{n}^{(1/2)}(\mathbf{q}^{(1/2)}, \mathbf{r}_i - \mathbf{c}^{(1/2)})]^2 \rangle_r - 1. \quad (15)$$

The distribution of the *positions* of the particles is analyzed conveniently using the density profile $\rho(r)$ around \mathbf{c} , which we define as

$$\rho(r) = \left\langle \left(2\pi r \right)^{-1} \frac{1}{N} \sum_{i=1}^N \delta(|\mathbf{r}_i - \mathbf{c}| - r) \right\rangle. \quad (16)$$

We consider two cases: the density profile around the center of the droplet, i.e., $\mathbf{c} = 0$, and around the position of a half-integer defect, $\mathbf{c} = \mathbf{c}_1, \mathbf{c}_2$.

It is convenient to introduce a further direction of a $t=1/2$ defect by

$$\mathbf{d} = \underline{\underline{\mathbf{D}}}^{(1/2)}(\mathbf{q}^{(1/2)})\mathbf{q}^{(1/2)}. \quad (17)$$

The vector \mathbf{d} is closely related to $\mathbf{q}^{(1/2)}$ by a rotation operation, where the rotation angle is the angle between $\mathbf{q}^{(1/2)}$ and the x axis. The direction \mathbf{d} is where the field lines are radial; see the arrow in Fig. 4.

B. Defect distributions

For a given configuration of particles the planar nematic droplet has a preferred direction given by the global nematic director $\mathbf{q}^{(0)}$. Each of the two topological defects has a position \mathbf{c}_i and an orientation \mathbf{d}_i , $i=1,2$. These quantities can be set in relation to each other to extract information about the average defect behavior and its fluctuations. In particular, we investigated the following probability distributions depending on a single distance or angle.

Concerning single defect properties, we investigate the separation distance from the droplet center,

$$P(r) = (2\pi r)^{-1} \frac{1}{2} \sum_{i=1,2} \langle \delta(|\mathbf{c}_i| - r) \rangle, \quad (18)$$

and the orientation relative to the nematic director,

$$P(\theta) = \frac{1}{2} \sum_{i=1,2} \langle \delta(\arccos(\mathbf{d}_i \cdot \mathbf{q}^{(0)}) - \theta) \rangle. \quad (19)$$

Between both defects there is a distance distribution,

$$P(c_{12}) = (2\pi c_{12})^{-1} \langle \delta(|\mathbf{c}_1 - \mathbf{c}_2| - c_{12}) \rangle, \quad (20)$$

and an angular distribution between defect orientations,

¹The constants in Eq. (10) depend on the dimensionality of the system and are different from 3D, where, e.g., $\underline{\underline{\mathbf{Q}}}^{(0)} = (3/2)\sum_i \mathbf{n}_i \mathbf{n}_i - \underline{\underline{\mathbf{1}}}/2$ holds.

$$P(\theta_{12}) = \langle \delta(\arccos(\mathbf{d}_1 \cdot \mathbf{d}_2) - \theta_{12}) \rangle, \quad (21)$$

which can equivalently be defined with $\mathbf{q}_1^{(1/2)}, \mathbf{q}_2^{(1/2)}$ by using the identity $\arccos(\mathbf{d}_1 \cdot \mathbf{d}_2) = 2 \arccos(\mathbf{q}_1^{(1/2)} \cdot \mathbf{q}_2^{(1/2)})$.

IV. COMPUTER SIMULATION

A. Monte Carlo

All our simulations were performed with the canonical Monte Carlo technique keeping particle number N , volume V , and temperature T constant; for details we refer to Ref. [63]. To simulate spherocylinders with only hard interactions, each Monte Carlo trial is exclusively accepted when there is no overlap of any particles. One trial always consists of a small variation of position and orientation of one HSC.

For the planar case the translation for the particle i is constructed by adding a small random displacement $\Delta \mathbf{r}_i$ to the vector \mathbf{r}_i , similarly the rotation consists of adding a small random vector $\Delta \mathbf{n}_i$ to the direction \mathbf{n}_i with $\Delta \mathbf{n}_i \cdot \mathbf{n}_i = 0$.

To achieve an isotropic trial on the surface of the sphere, the rotation matrix $\underline{\mathbf{M}}$ is applied simultaneously to the vectors \mathbf{r}_i and \mathbf{n}_i . It is defined as

$$\underline{\mathbf{M}} := \begin{pmatrix} 1 - c + \alpha^2 c & \gamma s + \alpha \beta c & -\beta s + \alpha \gamma c \\ -\gamma s + \beta \alpha c & 1 - c + \beta c & \alpha + \beta \gamma c \\ \beta s + \gamma \alpha c & -\alpha s + \gamma \beta c & 1 - c + \gamma^2 c \end{pmatrix} \quad (22)$$

with $s = \sin \Delta \theta$ and $c = 1 - \cos \Delta \theta$. α, β, γ are for every trial randomly chosen Cartesian coordinates of the unit vector specifying the rotation axis, $\Delta \theta$ is a small random angle. With this method a simultaneous translation and rotation is warranted by keeping the vectors \mathbf{r}_i and \mathbf{n}_i normalized and perpendicularly oriented.

The maximal variation in all cases is adjusted such that the probability of accepting a move is about 50%. The overlap criteria were checked by comparing the second virial coefficient of two- and three-dimensional HSC with simulation results, where the excluded volume of two HSC were calculated. Each of the runs I–VII was performed with 5×10^7 trials per particle. One-tenth of each run was discarded for equilibration. Especially the strongly fluctuating distance distribution between both defects, $P(c_{12})$, needs good statistics. All quantities were averaged over 25 partial runs, from which also error bars were calculated.

An overview of the simulated systems is given in Table I. The systems I–VII are planar. System I is the reference. To study finite-size effects, system II has half as many particles, and system III has twice as many particles as I. To investigate the dependence on the thermodynamic parameters, system IV has a lower packing fraction η , and system V has a higher one compared to system I. The other thermodynamic parameter is the anisotropy, which is smaller for system VI and higher for system VII compared to the system I. To keep the nematic phase stable for the short rods of system VI, the packing fraction η had to be increased. The packing fraction of the dense system V is $\eta = 0.4143$. The spherical system has the same number of particles N , packing fraction η , and anisotropy p as the reference (I). The radius of the sphere is

TABLE I. Overview of the simulated parameter range: number of particles N , anisotropy p , packing fraction η , scaled droplet diameter $2R/L$. Systems I–VII are planar; the system named ‘‘sphere’’ corresponds to spherical geometry.

System	N	p	η	$2R/L$
I	2008	21	0.3321	19.05
II	1004	21	0.3321	13.41
III	4016	21	0.3321	26.94
IV	1750	21	0.2894	19.05
V	2500	21	0.4143	19.05
VI	1855	16	0.4143	18.75
VII	3050	31	0.3321	19.35
Sphere	2008	21	0.3321	9.53
Aligned	2008	21	0.3321	19.05

half the radius of the planar droplet. The aligned rod model has the same parameters as the reference system (I).

B. Technical issues

We discuss briefly a projection method for the spherical problem and a search algorithm to find defect positions. In order to perform calculations for the spherical system all interesting vectors in three dimensions are projected to a two-dimensional plane. Imagine a given vector \mathbf{c} from the middle of the sphere pointing to an arbitrary point of the surface. We convert a position \mathbf{r}_i and orientation \mathbf{n}_i to the vectors \mathbf{r}_i^p and \mathbf{n}_i^p in a plane perpendicular to \mathbf{c} through

$$\mathbf{r}_i^p = \mathbf{r}_i - (\mathbf{c} \cdot \mathbf{r}_i) \mathbf{c}, \quad (23)$$

$$\mathbf{n}_i^p = \mathbf{n}_i - (\mathbf{c} \cdot \mathbf{n}_i) \mathbf{c}. \quad (24)$$

After obtaining a set $\{\mathbf{r}_i^p, \mathbf{n}_i^p\}$ of three-dimensional vectors this way, we transform them into a set of two-dimensional vectors by typical algebraic methods. As a reference the projection of the \mathbf{x} unit vector of the fixed three-dimensional coordinate system is always the x orientation of the ‘‘new’’ coordinate-system in two dimensions. The results show that curvature effects are small.

To investigate the radial structure and interactions of the disclinations it is necessary to localize the centers of the two point defects. As described in Sec. IV, the $\lambda^{(1/2)}$ parameter measures the degree of order of a half-integer defect in a chosen area, so the task is to find the two maxima of $\lambda^{(1/2)}$ in the droplet. In the planar case, we do this search with the following algorithm: A circular test-probe samples the droplet on a grid with a grid spacing of 5σ . At this point all the particles in the circle are taken to calculate $\lambda^{(1/2)}$ in the described way. After sampling the grid both maxima are stored and for every maximum a refining Monte Carlo search is performed. The surrounding of the size of the grid spacing is randomly sampled and the probe is only moved when $\lambda^{(1/2)}$ increases. The search is stopped when the probe does not move for 200 trials. In the spherical case the method is the same, but the grid is projected onto the sphere surface and the calculations of $\lambda^{(1/2)}$ were performed with projected two-dimensional vectors as described before.

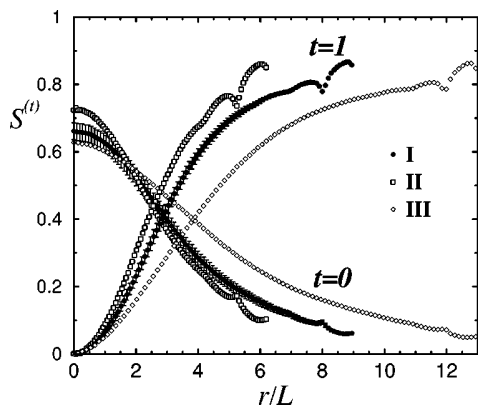


FIG. 5. Nematic order parameters $S^{(t)}$ as a function of the radial distance r from the droplet center, scaled by the rod length L . Star order $S^{(1)}$ and bulk order $S^{(0)}$ is shown. System I is reference, II has halved, and III has a doubled particle number. See Table I for a compilation of system parameters. Error bars are only given for I.

It is important to choose an adequate radius R^* for the probe. If R^* is too large, the probe overlaps both defects. As they have opposite orientations on the average, the located point of the maximum deviates from the point we are interested in. If the R^* is too small, an ill-defined position results, as fluctuations become more important. The simulation results show that a good choice is $R^* = 2L$. Although this definition contains some freedom, we find the defect position to be a robust quantity. A detailed discussion is given in the following section.

V. RESULTS

A. Order within the droplet

Let us discuss the order parameters $S^{(t)}$ as a function of the radial distance from the center of the droplet; see Fig. 5. $S^{(0)}$ is the usual bulk nematic order parameter, but radially resolved. It reaches values of 0.6–0.75 in the middle of the droplet, $r < 2L$, indicating a nematic portion that breaks the global rotational symmetry of the system. For $r > 3L$, $S^{(0)}$ decays to values slightly larger than the isotropic value of 0. The decrease, however, is not due to a microscopically isotropic fluid state, as can be seen from the behavior of $S^{(1)}$. This quantity indicates globally starlike alignment of particles for $r > 3L$. It vanishes in the nematic “street” in the center of the droplet. The distance where $S^{(0)}$ and $S^{(1)}$ intersect is an estimate for the defect positions. In Fig. 5 the finite-size behavior of $S^{(t)}$ is plotted for particle numbers $N = 1004, 2008, 4016$ corresponding to systems II, I, and III. There is a systematic shift of the intersection point of $S^{(0)}$ and $S^{(1)}$ to larger values as the system grows; the numerical values are $r/L = 2.54, 2.91, 3.87$. However, if r is scaled by the droplet radius R , a slight shift to smaller values is observed as the system size grows. Keeping the medium-sized system I as a reference, we have investigated the impact of changing the thermodynamic variables. For different packing fractions, $\eta = 0.2894$ (IV), 0.3321 (I), 0.4143 (V), we found that the intersection distances are $r/L = 3.90, 2.91, 1.43$. In the bulk, upon increasing the density the nematic order grows. Here, this happens for the star order $S^{(1)}$. But this increase happens on the cost of the nematic street (see $S^{(0)}$)

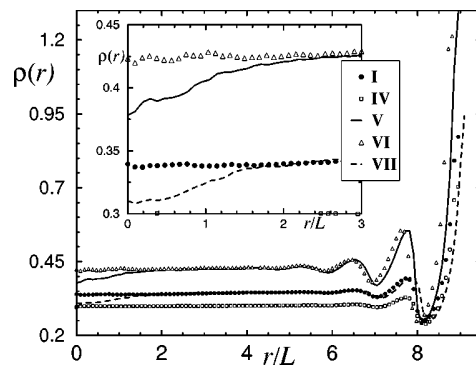


FIG. 6. Radially resolved density profiles $\rho(r)$ as a function of the distance from the droplet center r scaled by the particle length L . System I is reference, compared to the lower (IV) and higher (V) packing fractions and lower (VI) and higher (VII) anisotropies. The inset shows the behavior near the origin where a density decrease for V and VII appears for $r < 2L$.

at small r values. Increasing η leads to a compression of the inhomogeneous, interesting region in the center of the droplet. A similar effect can be observed upon changing the other thermodynamic variable, namely the anisotropy p . The nematic street is compressed for longer rods, $p = 31$ (VII), $r/L = 1.33$. Shorter rods, $p = 16$, need a higher density to form a nematic phase, so the values for systems (I), $r/L = 3.16$, and (VI), $r/L = 2.91$, are similar, as both effects cancel out.

The behavior of $S^{(1)}$ is similar to the findings for a three-dimensional droplet, where a quadratic behavior near $r = 0$ was predicted within Landau theory [31]. A simulation study using the Lebwohl-Lasher model [32] confirmed this finding and revealed that a ringlike structure that breaks the spherical symmetry is present. A comparison to the results for a 3D capillary by Andrienko and Allen [47] seems qualitatively possible as they find alignment of particles predominantly normal to the cylinder axis. Their findings are consistent with the behavior of $S^{(1)}$. Although our system is simpler as it only has two spatial dimensions, we could also establish the existence of a director field that breaks the spherical symmetry by considering the order parameter $S^{(0)}$.

Having demonstrated that the system exhibits a broken rotational symmetry, we have to assure that no freezing into a smectic or even crystalline state occurs. Therefore we plot radial density profiles $\rho(r)$, where r is the distance from the droplet center, in Fig. 6. The density shows pronounced oscillations for large r near the boundary of the system. They become damped upon increasing the separation distance from the droplet boundary and practically vanish after two rod lengths for intermediate density and four rod lengths for high density. Approaching the droplet center, $r = 0$, the density reaches a constant value for the weakly nematic systems I, IV, and V. For the strongly nematic systems, V with high density and VII with large anisotropy, a density decay at the center of the droplet occurs. This effect is not directly caused by the boundary as the density oscillations due to packing effects are damped. It is merely due to the topological defects present in the system. Quantitatively, the relative decrease is $[\rho(3L) - \rho(0)]/\rho(3L) = 0.11$ (V), 0.09 (VII). The finite-size corrections for systems II and III are negligible.

From both, the scissorlike behavior of the nematic order (Fig. 5) and from the homogeneity of the density profile

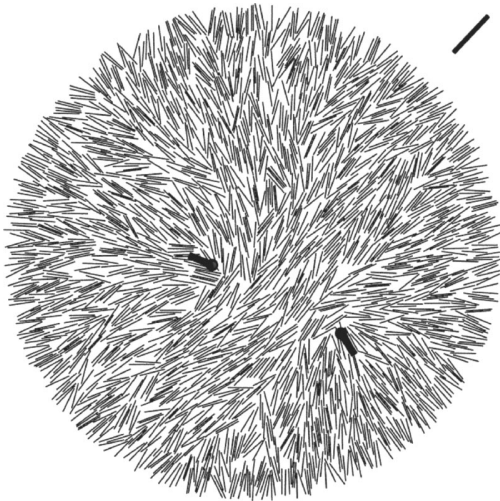


FIG. 7. Snapshot of a typical particle configuration for the planar system I. The particles are rendered dark. The two black symbols inside the droplet indicate positions and orientations of defects. The black bar outside the droplet indicates the global nematic director $\mathbf{q}^{(0)}$.

away from the system wall (Fig. 6), we conclude that the system is in a thermodynamically stable nematic phase, and seems to contain two topological defects with charge $1/2$.

In a 2D bulk phase, two half-integer ($1/2$) defects are more stable than a single integer (1) defect, as the free energy is proportional to the square of the charge. However, in the finite system of the computer simulation that is also affected by influence from the boundaries, it could also be possible that the defect pair merge into a single one [47,34].

Next we investigate the defect positions and their orientations. To illustrate both, a snapshot of a configuration of the planar system is shown in Fig. 7 (I). One can see the coupling of the nematic order from the first layer of particles near the wall to the inside of the droplet. The particles near the center of the droplet are aligned along a nematic director (indicated by the bar outside the droplet). The two emerging defects are depicted by symbols. See Fig. 8 for a snapshot of the spherical system. There the total topological charge is not induced by a system boundary but by the topology of the sphere itself.

B. Defect core

The positions of the defects are defined by maxima of the $\lambda^{(1/2)}$ order parameter; see Sec. III for its definition. In Fig. 9, $\lambda^{(1/2)}$ is plotted as a function of the spatial coordinates r_x and r_y for one given configuration. There are two pronounced maxima, indicated by bright areas, which are identified as the positions of the defect cores \mathbf{c}_1 and \mathbf{c}_2 . There are several more local maxima appearing as gray islands. These are identified as statistical fluctuations already present in the bulk nematic phase.

A drift of the positions of a defect core was also reported in [32]. Here we follow this motion, to investigate the surrounding of the defects. The order parameter $S^{(1/2)}$ is radially resolved around the defect position in Fig. 10. It has a pronounced maximum around $r=1.2L$. For smaller distances it decreases rapidly due to disorder in the core region. For

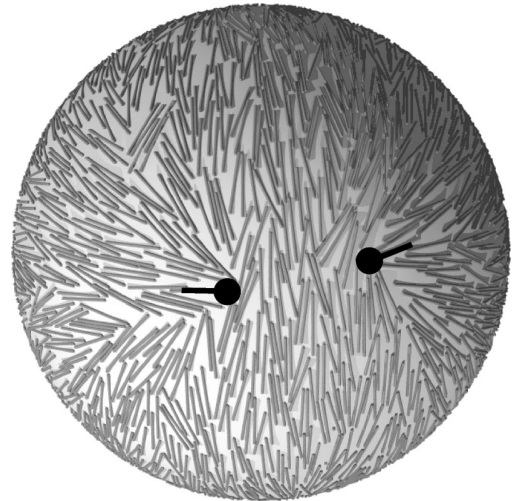


FIG. 8. Snapshot of a typical particle configuration for the spherical system. The particles are rendered dark. There is one $1/2$ defect on the left side and one on the right side. They point away from each other.

larger distances the influence from the second defect partner decreases the half-integer order $S^{(1/2)}$. Increasing the overall density and increasing the anisotropy leads to a more pronounced hump. The finite-size corrections, (II and III) and the boundary effects (sphere) are negligible. However, the curves show two artifacts: A rise near $r=0$ and a jump at the boundary of the search probe, $r=2L$. In the inset the profile around a bulk defect is shown. It has a plateau value inside the probe, $r<2L$, and vanishes outside. If we subtract this contribution from the pure data (I), continuous behavior at $r=2L$ can be enforced.

However, the model does not account for 3D effects like the ‘‘biaxial escape,’’ namely the sequence planar uniaxial-

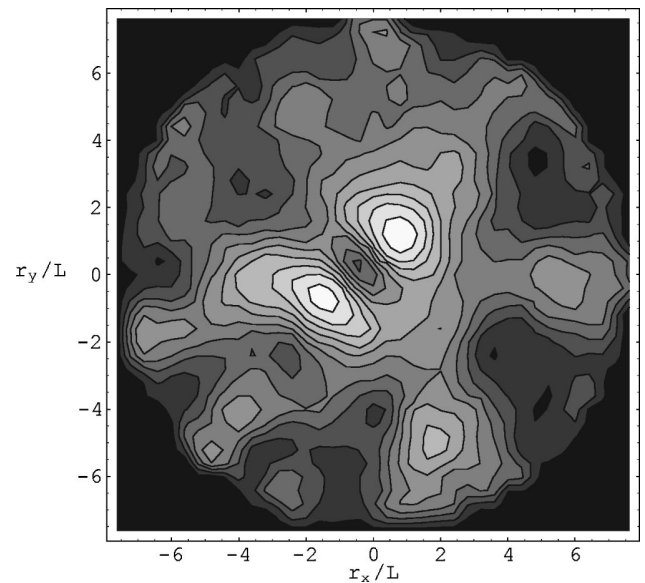


FIG. 9. Order parameter $\lambda^{(1/2)}$ as a function of spatial coordinates r_x, r_y . Bright areas correspond to large values; dark areas correspond to small values of $\lambda^{(1/2)}$. The two bright spots near the center are identified as topological defects, the gray islands as bulk defects.

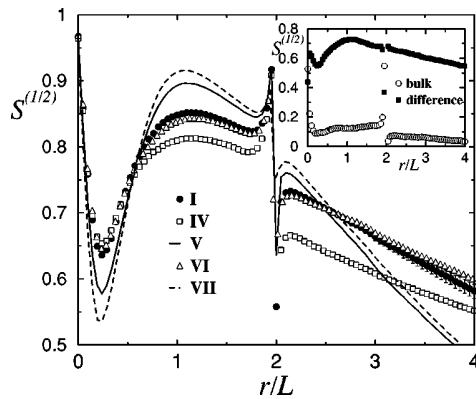


FIG. 10. Order parameter profiles $S^{(1/2)}$ around the defect center as a function of the scaled distance r/L from the defect center. The reference system I is to be compared with lower (IV) and higher (V) packing fractions and lower (VI) and higher (VII) anisotropies. The inset shows $S^{(1/2)}$ for bulk defects and for the difference between I and the bulk.

biaxial-uniaxial with increasing distance from the core center [34], as the particles are only 2D rotators. Schopohl and Sluckin [30] found an interfacelike behavior between the inner and outer parts of a disclination line in 3D. In our system we do not find a sign of an interface between the isotropic core and the surrounding nematic phase. This might be due to a small interface tension and a very weak bulk nematic-isotropic phase transition.

By radially resolving the probability of finding a particle around a defect center, we end up with density profiles depicted in Fig. 11. The defect is surrounded by density oscillations with a wavelength of the particle length. The finite-size dependence is small. To estimate the influence from the system wall, one may compare with the spherical system. It shows slightly weaker oscillations. This might be due to curvature effects, as the effective packing fraction is slightly smaller as the linear particles may escape the spherical system. The toy model of aligned rods also exhibits a nontrivial density profile, showing a decrease towards small distance and oscillations compared to rotating rods. In all cases the first peak has a separation distance of half a particle length from the defect center. The second peak appears at $r=3/2L$. Again the search probe induces an artificial structure near r

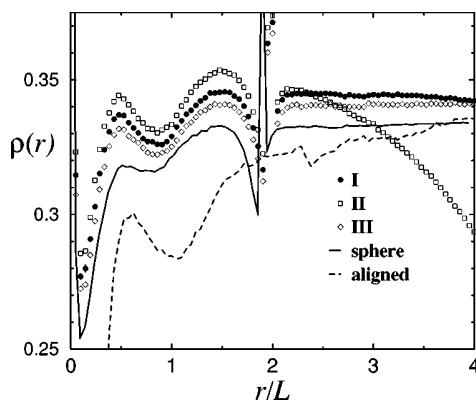


FIG. 11. Density profile as a function of the distance from the defect center. System I is reference, II has fewer particles, III has more. The spherical and aligned models are shown.

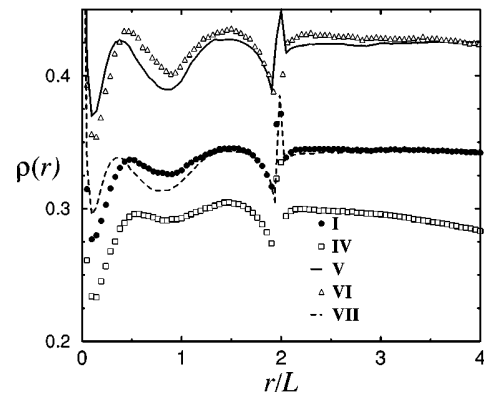


FIG. 12. Same as Fig. 11, but for lower (IV) and higher (V) packing fractions and shorter (VI) and longer particles (VII) compared to system I.

$=2L$. From this analysis, we can conclude that the oscillations are due to packing effects. The density oscillations become more pronounced at higher density, and for larger anisotropy, see Fig. 12.

C. Defect position

In the planar system, each defect is characterized by its radial distance r from the center, and the angle θ between its orientation and the global nematic director $\mathbf{q}^{(0)}$. We discuss the probability distributions of these quantities. In Fig. 13 the distribution for finding the defect at a distance r from the center is shown. Generally, the distributions are very broad. This indicates *large mobility* of the defects. Changing the thermodynamical variables has a large effect. For the stronger nematic systems V and VII, the distribution becomes sharper with a pronounced maximum at $r=1.5L$. Decreasing the anisotropy weakens the nematic phase, so system IV has a very broad distribution. The inset shows that the distribution becomes broader upon increasing system size.

D. Interactions between two defects

A complete probability distribution of both positions of the defect cores can be regarded as arising from an effective

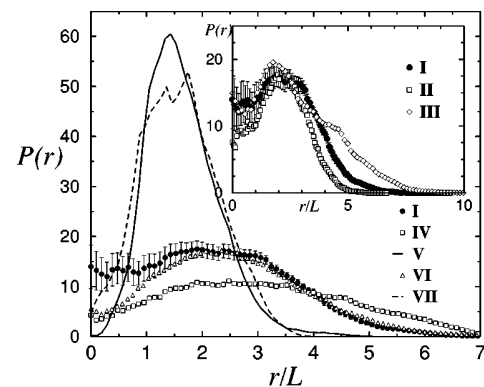


FIG. 13. Probability distribution $P(r)$ for the distance of a defect from the center of the droplet r/L for lower (IV) and higher (V) packing fractions and shorter (VI) and longer particles (VII) compared to system I. The inset shows the finite-size behavior for halved (II) and doubled (III) particle numbers.

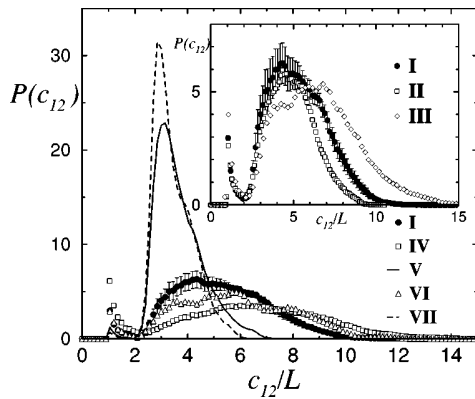


FIG. 14. Probability distribution $P(c_{12})$ for the separation distance between both defect positions scaled by the particle length for lower (IV) and higher (V) packing fractions and shorter (VI) and longer spherocylinders (VII) as compared to system I. The inset shows the finite-size behavior for halved (II) and doubled (III) particle numbers compared to I.

interaction potential $V_{\text{eff}}(\mathbf{c}_1, \mathbf{c}_2)$ between the defects. The latter play the role of quasiparticles. The effective interaction arises from averaging over the particle positions while keeping the defect positions constant. The effective interaction and the probability distribution are related via $P(\mathbf{c}_1, \mathbf{c}_2) \propto \exp[-\beta V_{\text{eff}}(\mathbf{c}_1, \mathbf{c}_2)]$.

Instead of the full probability distribution, we show its dependence on the separation distance between both defects and on their relative orientation. In Fig. 14 the probability distribution of finding two defects at a distance c_{12} is shown. It has small values for small as well as large c_{12} . Hence at small distances the defects repel each other. At large distances their effective interaction is attractive. Increasing the nematic order by increasing the density (V) or rod length (VII) causes the average defect separation distance to shrink. The rise near $r/L=1$ is an artifact: These are events where the search algorithm does not find two different defects, but merely finds the same defect two times. To avoid the problem a cutoff at $r=L$ was introduced. The finite-size behavior is strong; see the inset. The large system (III) allows the defects to move further away from each other, whereas in the smaller system (II) they are forced to be closer together. However, from the simulation data, it is hard to obtain the behavior in the limit $R/L \rightarrow \infty$.

This is somewhat in contrast to the phase diagram of a 3D capillary [34] containing isotropic, planar-radial, and planar-polar structures, if one is willing to identify the dependence on temperature with our athermal system. There it was found that the transition from the planar-polar to the planar-radial structure happens upon increasing the temperature (and hence decreasing the nematic order).

The difference angle θ_{12} between both defect orientations in the planar system, see Fig. 15, is most likely π , hence the defects point on average away from each other. However, the orientations are not very rigid. For the least ordered system IV there is still a finite probability of finding the defects with a relative orientation of 90° . Even for the strongly nematic systems V and VII the angular fluctuations are quite large. The inset in Fig. 15 shows the distribution of the angle θ

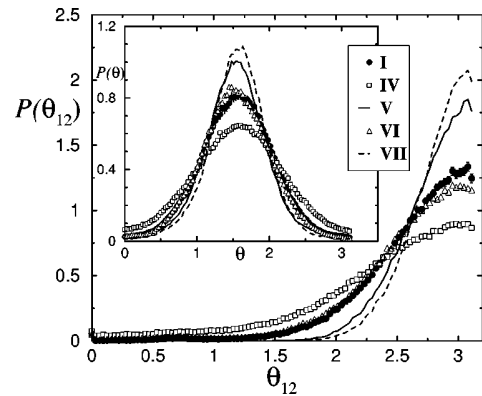


FIG. 15. Probability distribution $P(\theta_{12})$ for the difference angle between both defect orientations. The reference system I is to be compared with lower (IV) and higher (V) packing fractions, and lower (VI) and higher (VII) anisotropies. The inset shows the distribution $P(\theta)$ of the difference angle between the direction of one of the defects and the global nematic director for the same parameters.

between the defect orientation and the global nematic director. A clear maximum near $\pi/2$ occurs. Again, the distributions become sharper as density or anisotropy increase.

E. Outlook

Finally, it is worth mentioning that the spherical system still contains surprises. See Fig. 16 for an unexpected configuration, namely an assembly of three positive $1/2$ defects sitting at the corners of a triangle and a negative $-1/2$ defect in its center. This is remarkable, because the negative defect could annihilate with one of the outer positive defects.

In all cases, integer defects seem to dissociate into half-integer defects. The complete equilibrium defect distribution of hard spherocylinders lying tangentially on a sphere remains an open question.

VI. CONCLUSIONS

In conclusion, we have investigated the microscopic structure of topological defects of nematics in a spherical

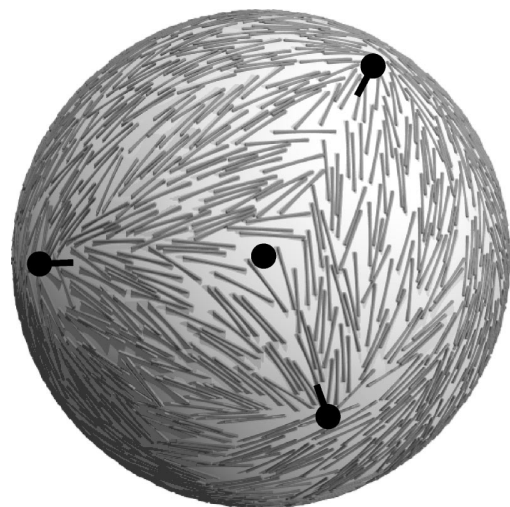


FIG. 16. Triangular configuration of three positive defects around a spontaneously formed negatively charged defect (central dot).

droplet with the appropriate homeotropic boundary and for particles lying on the surface of a sphere. We have used hard spherocylinders as a model system for a lyotropic nematic liquid crystal. This system allows us to study the statistical behavior of the microscopic rotational and positional degrees of freedom. For this system we find half-integer topological point defects in two dimensions to be stable. The defect core has a radius of the order of one particle length. As an important observation, the defect generates a free-standing density oscillation. It possesses a wavelength of one particle length. Considering the defects as fluctuating quasiparticles we have presented results for their effective interaction. The microscopic structure revealed by radially resolving density and order parameter profiles around the defect position is identical for the planar and the spherical system.

An experimental investigation using anisotropic colloidal particles [64,65] like tobacco mosaic viruses or carbon nanotubes is highly desirable to test our theoretical predictions. Then larger accessible system sizes can be exploited. Also of interest is the long-time dynamical behavior of the motion of topological defects. The advantage of colloidal systems over

molecular liquid crystals is the larger length scale that enables real-space techniques like digital video-microscopy to be used.

From a more theoretical point of view it would be interesting to describe the microstructure of topological defects within the framework of density-functional theory. Using phenomenological Ginzburg-Landau models, one could take the elastic constants of the HSC model as an input, and could calculate the defect positions and check against our simulations.

Finally we note that we currently investigate the three-dimensional droplets that are filled with spherocylinders. In this case more involved questions appear, as both point and line defects may appear.

ACKNOWLEDGMENTS

It is a pleasure to thank Jürgen Klaus, Karin Jacobs, Holger Stark, and Zsolt Németh for useful discussions, and Holger M. Harreis for a critical reading of the manuscript.

-
- [1] G. J. Vroege and H. N. W. Lekkerkerker, *Rep. Prog. Phys.* **55**, 1241 (1992).
- [2] L. Herbst, J. Kalus, and U. Schmelzer, *J. Phys. Chem.* **97**, 7774 (1993).
- [3] G. Fröba and J. Kalus, *J. Phys. Chem.* **99**, 14 450 (1995).
- [4] S. Chandrasekhar, *Liquid Crystals* (Cambridge University Press, London, 1977).
- [5] C. Chiccoli, P. Pasini, and F. Semeria, *Phys. Lett. A* **150**, 311 (1990).
- [6] E. Berggren, C. Zannoni, C. Chiccoli, P. Pasini, and F. Semeria, *Phys. Rev. E* **50**, 2929 (1994).
- [7] E. Berggren, C. Zannoni, C. Chiccoli, P. Pasini, and F. Semeria, *Phys. Rev. E* **49**, 614 (1994).
- [8] M. P. Allen, M. A. Warren, M. R. Wilson, A. Sauron, and W. Smith, *J. Chem. Phys.* **105**, 2850 (1996).
- [9] J. Stelzer, L. Longa, and H.-R. Trebin, *J. Chem. Phys.* **103**, 3098 (1995).
- [10] M. P. Allen, G. T. Evans, D. Frenkel, and B. M. Mulder, *Adv. Chem. Phys.* **LXXXVI**, 1 (1993).
- [11] L. Onsager, *Ann. (N.Y.) Acad. Sci.* **51**, 627 (1949).
- [12] P. Bolhuis and D. Frenkel, *J. Chem. Phys.* **106**, 666 (1997).
- [13] H. Graf and H. Löwen, *J. Phys.: Condens. Matter* **11**, 1435 (1999).
- [14] H. Graf, H. Löwen, and M. Schmidt, *Prog. Colloid Polym. Sci.* **107**, 177 (1997).
- [15] Z. Bradac, S. Kralj, and S. Zumer, *Phys. Rev. E* **58**, 7447 (1998).
- [16] A. Borstnik and S. Zumer, *Phys. Rev. E* **56**, 3021 (1997).
- [17] T. Gruhn and M. Schoen, *Phys. Rev. E* **55**, 2861 (1997).
- [18] R. Sear, *Phys. Rev. E* **57**, 1983 (1998).
- [19] P. C. Schuddeboom and B. Jérôme, *Phys. Rev. E* **56**, 4294 (1997).
- [20] R. van Roij, M. Dijkstra, and R. Evans, *Europhys. Lett.* **49**, 350 (2000).
- [21] B. Groh and S. Dietrich, *Phys. Rev. E* **59**, 4216 (1999).
- [22] S. Ramaswamy, R. Nityananda, V. A. Raghunathan, and J. Prost, *Mol. Cryst. Liq. Cryst. Sci. Technol., Sect. A* **288**, 175 (1996).
- [23] F. Alouges and B. D. Coleman, *J. Phys. A* **32**, 1177 (1999).
- [24] P. Poulin, N. Francés, and O. Mondain-Monval, *Phys. Rev. E* **59**, 4384 (1999).
- [25] A. N. Semenov, *Europhys. Lett.* **46**, 631 (1999).
- [26] D. Pettey, T. C. Lubensky, and D. Link, *Liq. Cryst.* **25**, 579 (1998).
- [27] N. D. Mermin, *Rev. Mod. Phys.* **51**, 591 (1979).
- [28] M. Hindmarsh, *Phys. Rev. Lett.* **75**, 2502 (1995).
- [29] W. Wang, T. Shiwaku, and T. Hashimoto, *J. Chem. Phys.* **108**, 1618 (1998).
- [30] N. Schopohl and T. J. Sluckin, *Phys. Rev. Lett.* **59**, 2582 (1987).
- [31] N. Schopohl and T. J. Sluckin, *J. Phys. (France)* **49**, 1097 (1988).
- [32] C. Chiccoli, P. Pasini, F. Semeria, T. J. Sluckin, and C. Zannoni, *J. Phys. II* **5**, 427 (1995).
- [33] P. Biscari, G. G. Peroli, and T. J. Sluckin, *Mol. Cryst. Liq. Cryst. Sci. Technol., Sect. A* **292**, 91 (1997).
- [34] A. Sonnet, A. Kilian, and S. Hess, *Phys. Rev. E* **52**, 718 (1995).
- [35] W. Huang and G. F. Tuthill, *Phys. Rev. E* **49**, 570 (1994).
- [36] M. Ambrožić, P. Formoso, A. Golemme, and S. Zumer, *Phys. Rev. E* **56**, 1825 (1997).
- [37] F. Xu, H.-S. Kitzerow, and P. P. Crooker, *Phys. Rev. E* **49**, 3061 (1994).
- [38] J. Bajc, J. Bezić, and S. Zumer, *Phys. Rev. E* **51**, 2176 (1995).
- [39] M. Zapotocky and P. Goldbart, e-print cond-mat/9812235.
- [40] J. A. Reyes, *Phys. Rev. E* **57**, 6700 (1998).
- [41] A. P. J. Emerson and C. Zannoni, *J. Chem. Soc., Faraday Trans.* **91**, 3441 (1995).
- [42] P. Poulin, H. Stark, T. C. Lubensky, and D. A. Weitz, *Science* **275**, 1770 (1997).
- [43] H. Stark, *Eur. Phys. J. B* **10**, 311 (1999).
- [44] T. C. Lubensky, D. Pettey, N. Currier, and H. Stark, *Phys. Rev. E* **57**, 610 (1998).

- [45] M. Zapotocky, L. Ramos, P. Poulin, T. C. Lubensky, and D. A. Weitz, *Science* **283**, 209 (1999).
- [46] J. Ignés-Mullol, J. Baudry, L. Lejcek, and P. Oswald, *Phys. Rev. E* **59**, 568 (1999).
- [47] D. Andrienko and M. P. Allen, *Phys. Rev. E* **61**, 504 (2000).
- [48] S. D. Hudson and R. G. Larson, *Phys. Rev. Lett.* **70**, 2916 (1993).
- [49] H. Löwen, *Phys. Rev. E* **50**, 1232 (1994).
- [50] D. Frenkel and R. Eppenga, *Phys. Rev. A* **31**, 1776 (1985).
- [51] J. Viellard-Baron, *J. Chem. Phys.* **56**, 4729 (1972).
- [52] J. A. Cuesta and D. Frenkel, *Phys. Rev. A* **42**, 2126 (1990).
- [53] P. van der Schoot, *J. Chem. Phys.* **106**, 2355 (1997).
- [54] H. Schlacken, H.-J. Mögel, and P. Schiller, *Mol. Phys.* **93**, 777 (1998).
- [55] M. J. Maeso and J. R. Solana, *J. Chem. Phys.* **102**, 8562 (1995).
- [56] A. Chamoux and A. Perrera, *Phys. Rev. E* **58**, 1933 (1998).
- [57] M. P. Allen, *Mol. Phys.* **96**, 1391 (1999).
- [58] Z. T. Németh and H. Löwen, *J. Phys.: Condens. Matter* **10**, 6189 (1998).
- [59] Z. T. Németh and H. Löwen, *Phys. Rev. E* **59**, 6824 (1999).
- [60] A. González, J. A. White, F. L. Román, S. Velasco, and R. Evans, *Phys. Rev. Lett.* **79**, 2466 (1997).
- [61] A. González, J. A. White, F. L. Román, and R. Evans, *J. Chem. Phys.* **109**, 3637 (1998).
- [62] A. M. Bohle, R. Holyst, and T. A. Vilgis, *Phys. Rev. Lett.* **76**, 1396 (1996).
- [63] M. P. Allen and D. J. Tildesley, *Computer Simulation of Liquids* (Oxford University Press, Oxford, 1987).
- [64] K. Zahn, R. Lenke, and G. Maret, *J. Phys. II* **4**, 555 (1994).
- [65] K. Zahn and G. Maret, *Curr. Opin. Colloid Interface Sci.* **4**, 60 (1999).

Colloidal particles in emulsions

Francisco L. Román,* Matthias Schmidt, and Hartmut Löwen

Institut für Theoretische Physik II, Heinrich-Heine-Universität Düsseldorf, Universitätsstrasse 1, D-40225 Düsseldorf, Germany
(Received 2 December 1999)

We propose a statistical mechanical model for colloidal particles suspended in an emulsion of liquid droplets. The particles are modeled as hard spheres. The interaction between droplets is also hard, but the particles are able to penetrate the droplets. A swelling of droplets is taken into account to ensure material conservation of the droplet liquid. Hence the presence of the colloids generates droplet polydispersity. Using computer simulation and liquid state theory, we find that the relative polydispersity exhibits nonmonotonic behavior as a function of the particle packing fraction and can be traced back to hard sphere bulk density fluctuations.

PACS number(s): 82.70.Kj, 61.20.Gy, 05.20.Jj

I. INTRODUCTION

Soft matter is divided into many subdisciplines dealing with membranes, polymers, colloidal suspensions, or emulsions. These systems have in common that they exhibit structure on a mesoscopic length scale and that they include many degrees of freedom, so one is usually interested in the average, statistical behavior. Nevertheless, the physical phenomena as well as the methods employed to understand them may differ substantially from, say, polymers to colloidal suspensions. Insight can be gained by investigating systems that bridge such areas. In the present work we investigate the interplay between colloidal suspensions and liquid emulsions.

Suspensions of colloidal particles are mixtures between a molecular solvent and mesoscopic solid particles [1]. The latter are often loosely called “colloids.” Apart from effects of gravity like sedimentation, the colloids float in their solvent liquid and interact with each other in similar ways to the interaction of atoms in “hard” condensed matter. The important and interesting difference is the large variety of interaction potentials present between colloidal particles. These interactions are effective in the sense that they arise from underlying microscopic mechanisms like van der Waals forces, Coulomb forces, or the Born repulsion. One simple theoretical model for the treatment of these systems is the hard sphere model, namely, a collection of spherical particles that cannot interpenetrate each other. It is the generic model to understand dense fluids and crystalline solids. Surprisingly, it is realized in nature in suspensions of sterically stabilized colloidal particles. By matching the refractive indices of the solvent with the colloid material, it is possible to turn down the van der Waals attraction. The particles are coated with short polymer brushes needed to stabilize the suspension against coagulation of particles. As the polymer brushes are tiny compared to the particle diameter, which is of the order of microns, a repulsive potential emerges that is almost hard-sphere-like. There is also considerable current activity in the field of computer simulations of colloids [2].

Hard spheres are also considered as a model for the second area we want to cover, namely, liquid emulsions. These

are mixtures of two (or more) liquid phases, one being the continuous phase that contains droplets of the dispersed phase(s). The droplets can be very well controlled to have unique sizes [3] so that even freezing occurs. Although both dispersed particles and dispersed droplets float in a surrounding liquid, the important difference is that the dispersed objects in emulsions are in the fluid rather than in the solid state.

In the present work, we investigate a mixture of colloidal particles and emulsion droplets; see Fig. 1 for a schematic sketch of the physical situation. Therefore we propose and study a model system. This system is simplified in many respects, but it keeps the freedom for the particles to choose between being dissolved in the continuous phase or within a dispersed droplet. In reality, the surface tensions between the colloid material and both solvents will determine whether the colloids tend to aggregate within or become depleted from the droplets. There is, however, an even more fundamental mechanism based on material conservation that we aim at. As we consider the emulsion on a small time scale, where no coalescence of droplets appears, we are faced with the fact that the amount of the dispersed phase (oil) and that of the continuous phase (water) are conserved quantities. These constraints lead to a nontrivial behavior of the droplet sizes. As particles penetrate inside an empty droplet, the droplet size (diameter) has to grow, in order to keep the oil volume constant. The present work aims at the study of the emerging droplet size distribution, its polydispersity, and the structural correlations present in the system.

There are important phenomena present in emulsions that are neglected within the current approach. Here, we deal only with perfect spherical droplets. Fluctuations of the drop-

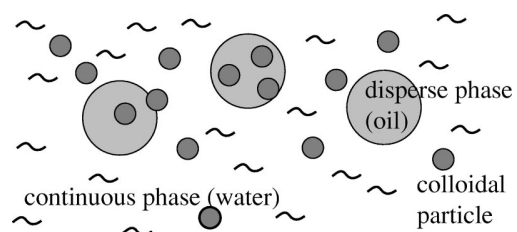


FIG. 1. Physical system of colloidal particles suspended in an emulsion. The different components are colloids (small spheres), emulsion droplets (big spheres), and solvent (wiggles). Particles can penetrate inside droplets.

*Present address: Departamento de Física Aplicada, Facultad de Ciencias, Universidad de Salamanca, E-37008 Salamanca, Spain.

let shape [4,5] are ignored. Denkov *et al.* [6] have considered colloidal particles pinned at the surface of emulsion droplets and have proposed that this coating may lead to stabilization of the emulsion against coalescence. Similar to our current study is the theoretical work on colloids suspended in a two-phase solvent [7,8] and measurements of the phase behavior of colloids in binary liquid mixtures [9]. In our system, however, both liquids are in a metastable emulsion state. This enables the preparation of spherical droplets of one phase within the other, which is not the case in the above mentioned bulk systems.

The study of polydisperse systems, especially polydisperse hard spheres, has attracted a lot of recent interest; see, e.g., [10–13]. In these studies, the distribution of sphere sizes is an input quantity, and the impacts on phenomena like freezing are investigated. In the present work, however, the polydispersity is generated through material conservation and hence is an output quantity.

Our system has two components with hard sphere interactions among like species. However, as our results will show, it is quite dissimilar from a binary additive hard sphere mixture, which has also attracted a lot of recent interest (see, e.g., [14]). We note that this system has been prepared experimentally using either colloids (see, e.g., [15]) or binary emulsions (see, e.g., [16]). Hence, it is conceivable that experimentalists will be able to prepare well-defined mixtures of droplets and colloids, which are the issue of interest of the present work.

In Sec. II the model for colloidal particles suspended in an emulsion is proposed. Then a theoretical approach linking density fluctuations to polydispersity is presented in Sec. III. Various limiting cases are discussed. Section IV explains the Monte Carlo simulation method, and results are given in Sec. V. We finish with concluding remarks in Sec. VI.

II. THE MODEL

We consider a mixture of two components. One component is made of N_C monodisperse hard spheres, called colloids, with diameters σ_C and position vectors $\mathbf{r}_{C,i}$, where $i = 1, \dots, N_C$. They interact with a pairwise hard core potential

$$\phi_{CC}(r_{C,ij}) = \begin{cases} \infty & \text{if } r_{C,ij} < \sigma_C \\ 0 & \text{otherwise,} \end{cases} \quad (1)$$

where $r_{C,ij} = |\mathbf{r}_{C,i} - \mathbf{r}_{C,j}|$ is the separation distance between colloids i and j .

The second component is constituted of N_D droplets with polydisperse diameters $\sigma_{D,k}$, $k = 1, \dots, N_D$, and position vectors $\mathbf{r}_{D,k}$. Again, the interaction between droplets is pairwise hard core,

$$\phi_{DD}(r_{D,kl}) = \begin{cases} \infty & \text{if } r_{D,kl} < \frac{1}{2}(\sigma_{D,k} + \sigma_{D,l}) \\ 0 & \text{otherwise,} \end{cases} \quad (2)$$

where $r_{D,kl} = |\mathbf{r}_{D,k} - \mathbf{r}_{D,l}|$ is the separation distance between droplets k and l . The total system volume is V_0 .

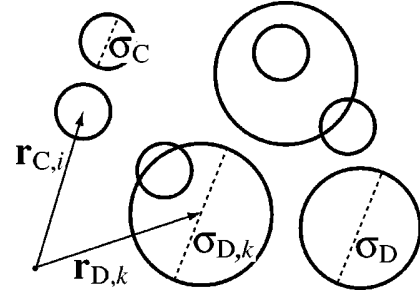


FIG. 2. Theoretical model of colloids in emulsions containing colloids (small circles) with positions $\mathbf{r}_{C,i}$ and diameters σ_C , and droplets (large circles) with positions $\mathbf{r}_{D,k}$. The diameter of an empty droplet is σ_D ; the actual diameter of the k th droplet is denoted by $\sigma_{D,k}$.

For each set of particle positions $\{\mathbf{r}_{C,i}\}$, the droplet radius of the k th droplet at position $\mathbf{r}_{D,k}$ is determined by material conservation, expressed as

$$\frac{\pi}{6} \sigma_{D,k}^3 = \frac{\pi}{6} \sigma_D^3 + \int d^3x \Theta\left(\frac{\sigma_{D,k}}{2} - |\mathbf{x} - \mathbf{r}_{D,k}|\right) \times \sum_{i=1}^{N_D} \Theta\left(\frac{\sigma_C}{2} - |\mathbf{x} - \mathbf{r}_{C,i}|\right), \quad (3)$$

where $\Theta(x)$ is the Heaviside step function. The diameter of an empty droplet is σ_D . Equation (3) expresses the fact that the volume of a swollen droplet equals the volume of an empty droplet plus the volume of particles inside the droplet. The latter is expressed as an integration over a function that is unity for space points \mathbf{x} that are both inside a particle and inside a droplet, and vanishes otherwise. The total potential energy is

$$\phi_{\text{total}} = \sum_{i < j = 1}^{N_C} \phi_{CC}(r_{C,ij}) + \sum_{k < l = 1}^{N_D} \phi_{DD}(r_{D,kl}). \quad (4)$$

In Fig. 2 the model is sketched.

Next we introduce dimensionless quantities that govern the system. The packing fractions of colloids and of droplets are defined as

$$\eta_C = \frac{N_C \pi}{6 V_0} \sigma_C^3, \quad (5)$$

$$\eta_D = \frac{N_D \pi}{6 V_0} \sigma_D^3. \quad (6)$$

The third reduced parameter is the size ratio σ_D/σ_C of the diameter of colloids and empty droplets.

III. THEORY

As the droplet size distribution is not prescribed *a priori* in our model, we have to find means to analyze it. Therefore we will develop a theory for the calculation of the polydispersity of the emulsion. The droplet size distribution is defined by

$$p(\sigma) = \left\langle \frac{1}{N_D} \sum_{k=1}^{N_D} \delta(\sigma - \sigma_{D,k}) \right\rangle, \quad (7)$$

where $\langle \dots \rangle$ denotes a canonical average with the total potential energy given in Eq. (4).

The polydispersity s is the standard deviation of the droplet size distribution divided by the mean (see, e.g., [17,18]),

$$s = \frac{\sqrt{(m_2 - m_1^2)}}{m_1}, \quad (8)$$

where m_i are moments of the droplet size distribution $p(\sigma)$,

$$m_i = \int_0^\infty d\sigma p(\sigma) \sigma^i. \quad (9)$$

The calculation of the polydispersity requires knowledge of the moments m_1 and m_2 of the distribution $p(\sigma)$. Since in our system the droplet diameter σ is related (via material conservation) to the number N of colloids inside the droplet, we shall use this relation to obtain approximate expressions for m_1 and m_2 . Explicitly, material conservation implies

$$N = \frac{\sigma^3 - \sigma_D^3}{\sigma_C^3} \quad (10)$$

and then

$$\langle N \rangle = \frac{m_3 - \sigma_D^3}{\sigma_C^3} \quad (11)$$

and

$$\langle N^2 \rangle - \langle N \rangle^2 = \frac{m_6 - m_3^2}{\sigma_C^6}, \quad (12)$$

where we have used the identity $m_k = \langle \sigma^k \rangle$. Expressions (11) and (12) are exact but difficult to handle since they involve the moments m_3 and m_6 . These moments can be related to m_1 and m_2 if we assume that $p(\sigma)$ can be approximated by a Gaussian of mean m_1 and standard deviation $\sqrt{m_2 - m_1^2} = m_1 s$. We obtain

$$\langle N \rangle = \frac{1}{\sigma_C^3} (m_1^3 + 3s^2 m_1^3 - \sigma_D^3), \quad (13)$$

$$\langle N^2 \rangle - \langle N \rangle^2 = \frac{1}{\sigma_C^6} 3s^2 m_1^6 (3 + 12s^2 + 5s^4), \quad (14)$$

which are our final expressions for linking the polydispersity s and the first moment m_1 to the average number of particles in a droplet and its fluctuations. In the following subsection we consider the case of low emulsion density where one can address suitable approximations for the relative fluctuation $(\langle N^2 \rangle - \langle N \rangle^2) / \langle N \rangle$ and the moment m_1 that will allow us to obtain the polydispersity of the droplets.

A. The limit of low droplet densities

For low droplet densities $\eta_D \rightarrow 0$, the interaction between emulsion droplets can be neglected. The interaction in our system is such that the colloidal particles are undisturbed by the presence of the droplet. Then the colloids form a simple bulk hard sphere system, which is, of course, monodisperse. We can therefore obtain the moment m_1 (the mean diameter of the droplets) from the following material conservation expression [see Eq. (3)]:

$$\frac{\pi}{6} m_1^3 (1 - \eta_C) = \frac{\pi}{6} \sigma_D^3. \quad (15)$$

Moreover, if we consider a droplet with volume $V = \pi \sigma^3 / 6$ then it is possible to write the fluctuation in the number of colloidal particles inside the droplet as

$$\frac{\langle N^2 \rangle - \langle N \rangle^2}{\langle N \rangle} = 1 + \frac{\rho_C}{V} \int_V \int_V d\mathbf{r} d\mathbf{r}' [g_{CC}(|\mathbf{r} - \mathbf{r}'|) - 1], \quad (16)$$

where $\rho_C = 6\eta_C / \pi \sigma_C^3$ is the number density of the colloid and g_{CC} is the uniform fluid pair distribution function of the colloid. When the size V of the droplets becomes very large, Eq. (16) can be written in terms of the isothermal compressibility of the colloid χ_T ,

$$\lim_{V \rightarrow \infty} \frac{\langle N^2 \rangle - \langle N \rangle^2}{\langle N \rangle} = \rho_C k_B T \chi_T, \quad (17)$$

where k_B is Boltzmann's constant and T is the temperature of the system. However, for small droplets finite size effects arise (see, e.g., Refs. [19], [20]) and one must take into account the limits of integration in Eq. (16).

The procedure for the calculation of Eq. (16) follows the same basic ideas of Refs. [21], [19], [20]. First we write Eq. (16) in Fourier space,

$$\frac{\langle N^2 \rangle - \langle N \rangle^2}{\langle N \rangle} = 1 + \frac{\rho_C}{(2\pi)^3 V} \int d\mathbf{k} \hat{G}^2(\mathbf{k}) \hat{h}(\mathbf{k}), \quad (18)$$

where $\hat{G}(\mathbf{k})$ is the Fourier transform of a geometry function that accounts for the limits of integration (it is 1 inside the droplet and zero otherwise), and $\hat{h}(\mathbf{k})$ is the Fourier transform of the total correlation function $h(\mathbf{r}) = g(\mathbf{r}) - 1$. Then, taking into account that $G(\mathbf{r})$ is a sphere of diameter σ , we get

$$\hat{G}(\mathbf{k}) = \hat{G}(k) = \frac{4\pi}{k^3} \left[\sin\left(\frac{k\sigma}{2}\right) - \frac{k\sigma}{2} \cos\left(\frac{k\sigma}{2}\right) \right]. \quad (19)$$

On the other hand, we use the Ornstein-Zernike relation for the total correlation function

$$\hat{h}(k) = \frac{\hat{c}(k)}{1 - \rho_C \hat{c}(k)}, \quad (20)$$

where $\hat{c}(k)$ is the Fourier transform of the direct correlation function. For simplicity, we use the Percus-Yevick solution for the direct correlation function since in this case we obtain analytical results for $\hat{h}(k)$ and the fluctuations (18). In our

system the diameter σ is not a constant but depends on the number of particles inside the droplet. As an approximation we consider the following effective diameter:

$$\bar{\sigma} = m_1 + \sigma_C, \quad (21)$$

where σ_C accounts for the size of the colloids. From Eq. (21) we obtain

$$V = \frac{\pi}{6} (m_1 + \sigma_C)^3. \quad (22)$$

In summary, the calculation of the polydispersity for the low density case is as follows. First we use Eq. (15) to obtain m_1 . Then, from Eqs. (22) and (18) we calculate the fluctuations $(\langle N^2 \rangle - \langle N \rangle^2) / \langle N \rangle$. Finally, making use of Eqs. (13) and (14) we solve

$$\frac{\langle N^2 \rangle - \langle N \rangle^2}{\langle N \rangle} = \frac{1}{\sigma_C^3} \frac{3s^2 m_1^6 (3 + 12s^2 + 5s^4)}{m_1^3 + 3s^2 m_1^3 - \sigma_D^3} \quad (23)$$

to obtain the polydispersity s .

B. Intermediate and high emulsion densities

For high or intermediate densities of the emulsion, the interaction between droplets cannot be neglected. This interaction has an impact on the colloidal fluid. Thus the effective volume of the droplet used in expression (18) cannot be calculated as in Eq. (15), since in this case it depends not only on the mean density of colloidal particles but also on the density of the emulsion droplets. Because of this inhomogeneous character of the density of the colloid, we have not derived theoretical results for the polydispersity.

However, on the basis of the behavior at low density, it is possible to argue about the behavior of the polydispersity at higher emulsion densities. On the one hand, the exclusion interaction between droplets does not allow for the possibility of growth, but, on the other hand, at intermediate and high densities the colloid particles do not allow for the shrinking of the droplets. As a consequence, we expect that the probability distribution $p(\sigma)$ should become narrow and then the polydispersity should decrease. As we shall see below, this will be confirmed from results of computer simulation. These simulation results indicate that, for a given fixed colloid density, the low emulsion density result provides an upper bound for the polydispersity of the emulsion.

IV. COMPUTER SIMULATION

A. Monte Carlo technique

From a general viewpoint, the simulation handles two coupled systems. One is the emulsion droplet system, which is a polydisperse system of hard spheres of variable diameters $\{\sigma_{D,i}\}_{i=1,\dots,N_D}$. The other is the colloid system, which consists of a standard monodisperse hard sphere system with particles of diameter σ_C . Both, the emulsion droplets and colloidal particles are coupled via the interaction potential (4).

The simulation runs with a fixed number of emulsion droplets N_D and a fixed number of colloidal particles N_C . In accordance with the standard Monte Carlo method, one pro-

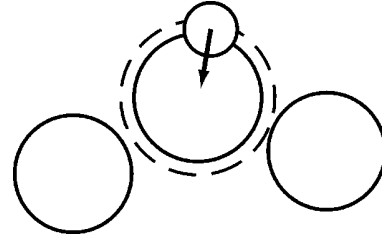


FIG. 3. Swelling of droplets. If a colloidal particle tries to move (arrow) inside a droplet, the swelling of the droplet happens against the pressure of the surrounding droplets.

ceeds as follows. First, one particle is randomly chosen (it can be either a droplet or a colloid particle) and a random displacement is proposed. The test for acceptance or rejection of the move depends on the energy change. As we are dealing with a hard potential, the energy change is either zero (if no overlapping situation is reached) or infinity (when there is an overlap). In the former case the state is accepted, in the latter it is rejected. The overlapping states can be reached because of both the simple movement of a particle or the growth of a droplet due to the inclusion of colloidal particles.

After proposing a new position for a droplet or colloid, it is necessary to calculate the new diameters for the droplets in order to test for possible overlapping situations. This is done by means of conservation of both the total amount of material in the droplets and the positions of the centers of the droplets. The growth for the droplets is isotropic with respect to the center of each droplet (see Fig. 3).

The algorithm for calculating the new proposed diameter of the droplet is as follows. Let us suppose that a trial move is proposed for the droplet j with diameter $\sigma_{D,j}$ and position $r_{D,j}$, and the proposed position for this droplet is $\mathbf{r}_{D,j}^*$. In order to calculate its new diameter $\sigma_{D,j}^*$, we solve the equation

$$\frac{\pi}{6} (\sigma_{D,j}^*)^3 - \sum_{i=1}^{N_C} I(|\mathbf{r}_{D,j}^* - \mathbf{r}_{C,i}|, \sigma_C, \sigma_{D,j}^*) - \frac{\pi}{6} \sigma_D^3 = 0, \quad (24)$$

where I is the intersection volume between particle i and the displaced droplet j . The geometrical function I is given for two intersecting spheres with center separation distance r and diameters σ_1, σ_2 ($\sigma_1 < \sigma_2$) by

$$I(r, \sigma_1, \sigma_2) = \begin{cases} \pi \sigma_1^3 / 6 & \text{if } r \leq (\sigma_2 - \sigma_1) / 2 \\ L(r, \sigma_1, \sigma_2) & \text{if } (\sigma_2 - \sigma_1) / 2 < r \leq (\sigma_2 + \sigma_1) / 2 \\ 0 & \text{otherwise,} \end{cases} \quad (25)$$

where the auxiliary function L is the volume of a lenslike shape and is given by

$$L(r, \sigma_1, \sigma_2) = \frac{\pi}{12r} \left(\frac{\sigma_2 + \sigma_1}{2} - r \right)^2 \times \left[r^2 - 3 \left(\frac{\sigma_2 - \sigma_1}{2} \right)^2 + 2r \left(\frac{\sigma_2 + \sigma_1}{2} \right) \right]. \quad (26)$$

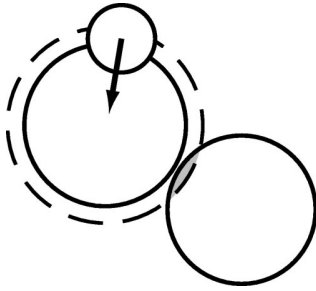


FIG. 4. Overlap due to swelling. A colloidal Monte Carlo move (indicated by an arrow) may be rejected, because the swollen droplet would overlap (shaded region) with another droplet.

In practice, the terms that actually contribute to the sum over i in Eq. (24) are selected through a neighbor list.

Once the new diameter is calculated, the next step is to verify whether an overlapping situation is reached. Fig. 4 shows that it is possible to reject a colloid particle displacement because of droplet growth. This is also possible if a droplet is displaced in such a way that its growth leads to an overlap with a neighboring droplet. Then the displacement has to be rejected. Of course, situations in which a colloidal particle can interact with two or even more droplets are possible, and it is necessary to calculate the final diameter of each droplet before testing for droplet overlaps.

B. Simulation details

Several simulations for different values of the parameters η_C and η_D have been performed to obtain the behavior of the polydispersity of the emulsion droplets. In all of the simulations the size ratio is $\sigma_D/\sigma_C=3$. A typical run starts from a face-centered cubic lattice of $N_D=32$ droplets and a given number of colloidal particles N_C ranging from 50 to 1000. The number of Monte Carlo steps (MCS) used to thermalize the system is 10^7 . After that the probability distribution function $p(\sigma)$ as well as the pair correlation functions are measured during 10^8 MCS. Finally, the polydispersity is calculated by using Eq. (8).

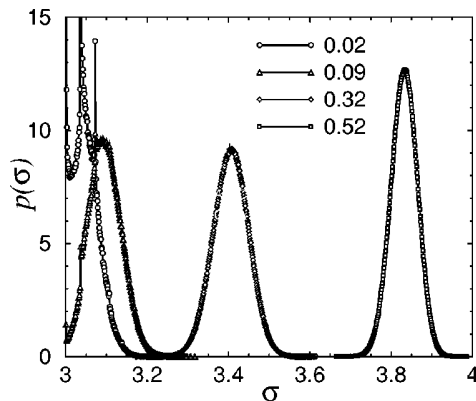


FIG. 5. The diameter probability distribution $p(\sigma)$ for a system with a single emulsion droplet and various packing fractions of the colloid $\eta_C=0.02, 0.09, 0.32, 0.52$, and size ratio $\sigma_D/\sigma_C=3$. As the packing fraction of colloid increases, the width of the distribution (polydispersity) decreases.

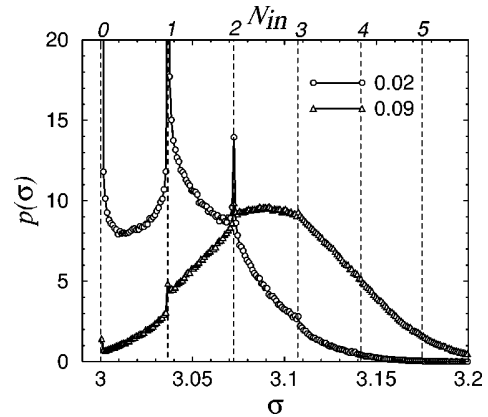


FIG. 6. Detail of Fig. 5. Note the probability spikes corresponding to integer numbers N_{in} of colloid particles inside the droplet.

V. RESULTS

A. Intrinsic polydispersity

The behavior of the probability distribution function $p(\sigma)$ for several colloid densities $\eta_C=0.02, 0.09, 0.32, 0.52$ is shown in Fig. 5. We consider the case of infinite dilution of droplets, namely, a system with a single droplet. For large colloid packing fractions, nearly Gaussian behavior for $p(\sigma)$ emerges. The mean value grows upon increasing η_C , reflecting the size of a typically swollen droplet. The width of the distribution, however, decreases upon increasing the colloid density from $\eta_C=0.32$ to 0.52 . The underlying mechanism is the reduction of bulk hard sphere density fluctuations for the dense colloidal fluid.

The Gaussian picture, however, breaks down for low densities of colloids, $\eta_C=0.02$ and 0.09 (see Fig. 6). A hump-like shape is still present, but there arise additional spikes. We find that these spikes appear in the distribution when an integer number of particles N_{in} is completely inside the droplet so that no particle intersects with the droplet surface. This happens at $\sigma/\sigma_C=[(\sigma_D/\sigma_C)^3+N_{in}]^{1/3}$, where N_{in} is an integer or zero. As an explanation for this droplet size distribution, we note that the number of states with one particle

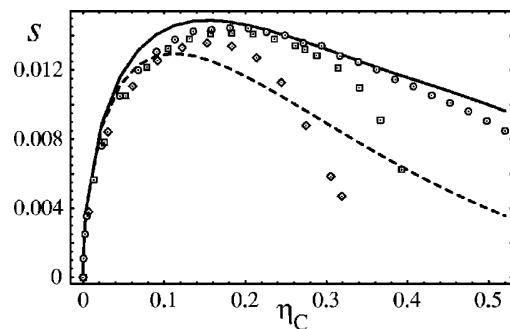


FIG. 7. Polydispersity s of the droplets versus the packing fraction of the colloid η_C . Circles, squares, and diamonds represent the simulation data obtained for systems of one droplet, $\eta_D=0.45$, and $\eta_D=0.53$, respectively. The solid line represents the theoretical results coming from Eq. (18). The dashed line represents Eq. (17) (when the size of the droplet is very large). Note that the very low density case (one droplet) is an upper bound for the polydispersity. The size ratio is $\sigma_D/\sigma_C=3$.

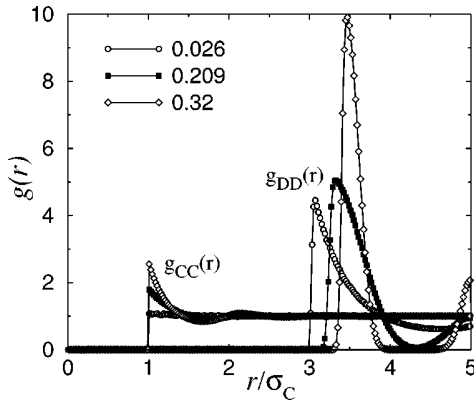


FIG. 8. Distribution functions of colloidal pairs $g_{CC}(r)$ and droplet pairs $g_{DD}(r)$. The droplet packing fraction is $\eta_D=0.452$. Three concentrations for colloids are shown, $\eta_C=0.026, 0.209, 0.314$. Lines are guides to the eye.

inside the droplet (proportional to the volume of one sphere of diameter $\sigma_D - \sigma_C/2$) will be greater than the number of states with one particle intersecting the surface of the droplet (proportional to the surface of the droplet). For higher densities of colloid, the presence of more particles located at the border of the droplet smooths the behavior of the probability distribution. This leads to a highly nontrivial size distribution that consists of finite probabilities at discrete diameter values with a superimposed continuous probability density that interpolates between the spikes.

In order to condense the information, we study the width of the distribution as a function of the thermodynamic parameters. Figure 7 shows the simulation results for the polydispersity versus the packing fraction of the colloid. Circles correspond to the case of one emulsion droplet in the system, squares and diamonds correspond, respectively, to packing fractions of the emulsion droplets $\eta_D=0.45$ and $\eta_D=0.53$. We observe that the case of low emulsion densities is an upper bound for the polydispersity. Its behavior is as follows. All points start from the value zero that corresponds to a monodisperse emulsion. As the density increases, more colloidal particles are added to the system and, as a consequence of that, the polydispersity increases up to a maximum

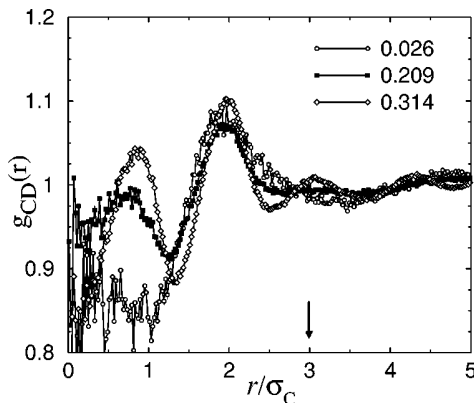


FIG. 9. Distribution function for colloid-droplet pairs $g_{CD}(r)$, for the same parameters as in Fig. 8. The arrow denotes the radius of an empty droplet. Note the different ordinate scale compared to Fig. 8.

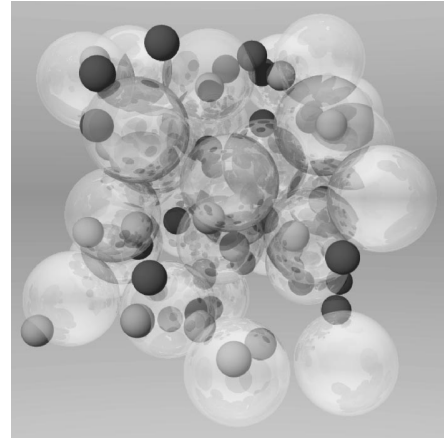


FIG. 10. Snapshot from computer simulation. The large transparent spheres are droplets, the smaller ones represent colloidal particles. A colloid is shaded dark if its center is not inside any droplet. The packing fractions are $\eta_C=0.026, \eta_D=0.452$. The droplet subsystem is in a fluid state.

value. When still more colloid particles are added, the polydispersity decreases since the colloid system approaches a dense liquid or even solid phase, and fluctuations in the number of particles inside a droplet decrease. We have found that, as the density of the emulsion increases, it is not possible to reach high colloid densities. This is due to the exclusion interaction for the droplets since the more colloid is added, the bigger the emulsion droplets become, and it is even possible to freeze the emulsion.

Solid and dashed lines in Fig. 7 represent the theoretical results obtained from Eqs. (18) and (17), respectively. Note that our incorporation of finite size effects improves on the result for the thermodynamic limit. We get good agreement for the case of low emulsion density. Differences between simulation results and results obtained by using Eqs. (18) and (23) have a different origin depending on the colloid density. For low colloid densities, our Gaussian approximation for $p(\sigma)$ breaks down (see Fig. 6.) For the high colloid density case, deviations arise partly because of the Percus-Yevick form of the total correlation function in Eq. (18) and

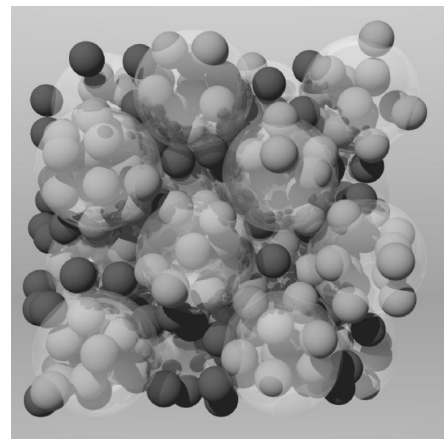


FIG. 11. Same as Fig. 10, but at a higher particle volume fraction $\eta_C=0.314$. The droplets are frozen on a face-centered cubic lattice, while the colloids remain liquid.

mainly because the volume V in Eq. (18) is approximated by that of a sphere of the mean diameter of the droplets.

B. Structural correlations

As the system has two components, one can investigate three different static pair distributions. First, we discuss the symmetric correlations $g_{CC}(r)$ between colloidal pairs and $g_{DD}(r)$ between droplet pairs (see Fig. 8). The packing fraction of the droplets is high, $\eta_D=0.452$, and there are three cases of particle packing fractions shown, namely, $\eta_C=0.026, 0.209, 0.314$. The behavior of the colloids is similar to that of monodisperse hard spheres, except for a slight shift of the second peak toward larger distances compared to the one-component system. The droplet behavior is also hard-sphere-like but the intrinsic polydispersity washes out the first peak. At the largest values of $\eta_C=0.314$, the droplet subsystem is found to be in a crystalline state.

A quite different behavior is found for the asymmetric correlations between pairs of one particle and one droplet, $g_{CD}(r)$, Fig. 9. This distribution function can be regarded as the density profile of particles inside (and around) a fixed droplet. Of course, it also has the meaning of the density profile of droplets around a fixed particle. There are weak oscillations inside one droplet radius, which become rapidly damped outside. The amplitude of the oscillations is tiny, even at the highest packing fraction considered. The behavior is dissimilar from that of a hard sphere fluid inside a hard cavity [22–25], where much stronger structure emerges.

To illustrate our findings we show snapshots generated from the simulation. In Fig. 10 the high density droplet liquid phase containing few particles is shown. By adding more particles, freezing of the droplet system occurs, Fig. 11. The bare droplet packing fraction of $\eta_D=0.452$ is well inside the fluid branch of the hard sphere phase diagram. The swollen droplets, however, build a nearly close-packed face-centered cubic crystal.

VI. CONCLUSIONS

A model for the behavior of emulsions in the presence of colloidal particles has been proposed. It describes colloids as monodisperse hard spheres and emulsion droplets as polydisperse hard spheres. Migration of colloids into and out of the droplets is allowed. The droplet size distribution is not assumed *a priori*, but evolves self-consistently. Therefore interactions between colloidal particles and emulsion droplets are taken into account so that conservation of the emulsion droplet material is fulfilled. Then the exclusion rule of hard spheres drives the droplet size distribution. We show that this distribution has quite a rich structure, ranging from multipike to Gaussian behavior. By means of the study of the size dependent fluctuations in the number of particles located inside the droplets, we found an upper bound for the polydispersity of the emulsion.

Concerning future work, we remark that the present model may be readily generalized to account for nonvanishing surface tensions. In general, there are three surface tensions between the three materials, colloid, oil, and water. Within the current approach, the surfaces themselves are given geometrically by intersections of spheres. Hence one can take into account the potential energy that comes from the presence of these interfaces. By tuning the surface tensions, one then has additional control over the colloidal tendency to aggregate inside droplets.

ACKNOWLEDGMENTS

We thank Lutz Maibaum, Holger M. Harreis, and Juan A. White for valuable contributions. F.L.R. acknowledges the financial support from the Dirección General de Investigación Científica y Técnica (DGICYT) of Spain under Grant Nos. PB 95-0934 and PB 98-0261 and from the Ministerio de Educación y Cultura.

-
- [1] H. Löwen, Phys. Rep. **237**, 249 (1994).
 - [2] M. Schmidt, in *Computational Methods in Colloid and Interface Science*, edited by M. Borówko (M. Dekker, New York, 1999), Chap. 15, p. 745.
 - [3] T. G. Mason and J. Bibette, Phys. Rev. Lett. **77**, 3481 (1996).
 - [4] Hu Gang, A. H. Krall, and D. A. Weitz, Phys. Rev. Lett. **73**, 3435 (1994).
 - [5] W. Cai, Phys. Rev. E **54**, 2780 (1996).
 - [6] N. D. Denkov, I. B. Ivanov, P. A. Kralchevsky, and D. T. Wasan, J. Colloid Interface Sci. **150**, 589 (1992).
 - [7] H. Löwen, Phys. Rev. Lett. **74**, 1028 (1995).
 - [8] H. Löwen, Z. Phys. B: Condens. Matter **97**, 269 (1995).
 - [9] Y. Jayalakshmi and E. W. Kaler, Phys. Rev. Lett. **78**, 1379 (1997).
 - [10] P. Bartlett, Mol. Phys. **97**, 685 (1999).
 - [11] D. A. Kofke and P. G. Bolhuis, Phys. Rev. E **59**, 618 (1999).
 - [12] R. P. Sear, Phys. Rev. Lett. **82**, 4244 (1999).
 - [13] J. F. Zhang, R. Blaak, E. Trizac, J. A. Cuesta, and D. Frenkel, J. Chem. Phys. **110**, 5318 (1999).
 - [14] M. Dijkstra, R. van Roij, and R. Evans, Phys. Rev. Lett. **81**, 2268 (1998).
 - [15] A. Imhof and J. K. G. Dhont, Phys. Rev. Lett. **75**, 1662 (1995).
 - [16] U. Steiner, A. Meller, and J. Stavans, Phys. Rev. Lett. **74**, 4750 (1995).
 - [17] H. Löwen, J.-N. Roux, and J.-P. Hansen, J. Phys.: Condens. Matter **3**, 997 (1991).
 - [18] P. N. Pusey, J. Phys. (France) **48**, 709 (1987).
 - [19] F. L. Román, J. A. White, and S. Velasco, J. Chem. Phys. **107**, 4635 (1997).
 - [20] F. L. Román, A. González, J. A. White, and S. Velasco, J. Chem. Phys. **110**, 9821 (1999).
 - [21] J. J. Salacuse, A. R. Denton, and P. A. Egelstaff, Phys. Rev. E **53**, 2382 (1996).
 - [22] A. González, J. A. White, F. L. Román, S. Velasco, and R. Evans, Phys. Rev. Lett. **79**, 2466 (1997).
 - [23] A. González, J. A. White, F. L. Román, and R. Evans, J. Chem. Phys. **109**, 3637 (1998).
 - [24] Z. T. Németh and H. Löwen, J. Phys.: Condens. Matter **10**, 6189 (1998).
 - [25] Z. T. Németh and H. Löwen, Phys. Rev. E **59**, 6824 (1999).

Do effective interactions depend on the choice of coordinates?

Matthias Schmidt

Institut für Theoretische Physik II, Heinrich-Heine-Universität Düsseldorf, Universitätsstraße 1, D-40225 Düsseldorf, Germany
(Received 2 August 2001; published 25 January 2002)

A common approach to complex systems such as colloidal suspensions or polymer solutions describes the mesoscopic behavior using effective interactions. These potentials act between the macromolecular entities and can be derived by integrating out the microscopic degrees of freedom. The remaining macroparticle coordinates need to be chosen *a priori*. Two obvious choices are (i) the centers of mass and (ii) distinct microscopic entities, such as special “tagged” monomers. Here we compare both in the framework of the Asakura-Oosawa colloid-ideal polymer mixture. Using computer simulations, we find that although the effective pair interaction between colloid and polymer differ markedly, correlation functions are in fair agreement.

DOI: 10.1103/PhysRevE.65.022801

PACS number(s): 61.25.Hq, 61.20.Gy, 61.20.Ja, 82.70.Dd

Choosing optimal coordinates is often the first step to solve a physical problem. Optimal coordinates are such that they exploit the simplifying physical properties, e.g., symmetries, of a system, and help to find the relevant degrees of freedom that are responsible for the physical effect under consideration. As concerns any exact treatment, changing coordinates is an exact mathematical transformation that preserves all properties of a model. Approximations, however, usually depend on the variables used. Different results may be obtained if the same approximation is done in different coordinates. Approximations are usually necessary if one is dealing with complex systems. In soft matter systems there is a hierarchy of relevant variables on different length scales. While basic microscopic degrees of freedom, namely, the positions of the atoms, are responsible for the behavior on all length scales, there exist variables that especially govern the interesting mesoscopic regime. Colloidal particles have the positions of their atoms as basic position coordinates; an obvious choice for the (mesoscopic) degree of freedom of the colloid is its center of mass. The concept, however, to derive effective interactions between mesoscopic objects from an averaging over the microscopic degrees of freedom extends far beyond colloids and has been applied to systems like star polymers [1] or linear polymers [2–6], and mixtures of colloids and star polymers [7]. The choice of meaningful position coordinates for such macromolecular entities is not in all cases as straightforward as it may seem at first glance. In the case of star polymers, the position of the central molecule to which the polymeric arms are attached was used to derive an effective interaction [8,9]. In the context of linear polymer coils, one can think of tagged monomers (segments) that are visible in a scattering experiment. Both are, in general, different from the position of the center of mass of the whole object. The question arises: what is the superior variable? Is it the center of mass or the position of the special microscopic object?

In this paper, we study this question in the context of the Asakura-Oosawa (AO) colloid-ideal polymer mixture [10,11] that consists of a hard-sphere model for the colloids, and a hard-core exclusion between a colloid and a spherical polymer coil. The polymers do not interact with themselves; they are assumed to be ideal. Recently the phase diagram and structure [12,13], and the interface between demixed phases

[14] were studied. An effective Hamiltonian was derived [15], and a density-functional theory [16] was proposed and entropic wetting investigated [17].

Here we supplement this model with a simple prescription for the behavior of a tagged monomer on each polymeric chain: The monomer is allowed to move freely inside the sphere that represents the polymer. It is, however, not allowed to leave the sphere, and hence is bound to its chain [18]. Although both the AO model and the tagged monomer prescription are highly approximative as concerns the real world, there is one feature that makes the model suitable for the present investigation: The position of the polymer center of mass differs strongly from that of the tagged monomer. Hence going from one to the other is not a small change, and we expect insight into the question raised above.

We treat this *full model* two ways: First by integrating out the positions of the tagged monomers. This leads to the usual AO model with colloid positions and polymer center of mass position, and constitutes our *reference* system. The second treatment is by integrating out the polymer centers. This is done exactly in the limit of vanishing colloid density and leads to an effective pair potential between a colloid and a tagged monomer. We neglect all higher-body interactions between colloids and tagged monomers, as is usually done. This constitutes the *effective model* with colloid and monomer position coordinates. The comparison of the reference model with the effective model is the purpose of this paper. As expected, the effective interactions between tagged monomer and colloid as well as polymer center and colloid are markedly different. Also, a comparison of the appropriate correlation functions shows differences. However, only small deviations exist, as we show by simulations. This leads to the conclusion that the choice of coordinates matters if high accuracy is reached for, but not if one aims at the gross physical features of the system.

The model we consider consists of N^c colloids with coordinates \mathbf{r}_i^c and N^p polymers with centers of mass \mathbf{r}_j^p and N^m tagged monomers (segments) with positions \mathbf{r}_j^m in a volume V_0 . The interaction between colloids is

$$V^{cc}(r) = \begin{cases} \infty & \text{if } r \leq 2R^c, \\ 0 & \text{else.} \end{cases} \quad (1)$$

BRIEF REPORTS

PHYSICAL REVIEW E 65 022801

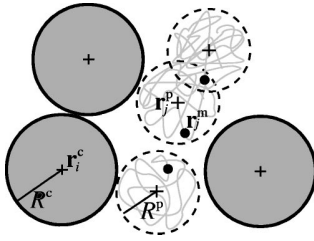


FIG. 1. Sketch of the Asakura-Oosawa model. Gray spheres are colloids with radii R^c and positions \mathbf{r}_i^c , dashed spheres are ideal polymers with radii R^p and centers of mass \mathbf{r}_j^p , dots are tagged monomers with positions \mathbf{r}_j^m .

The interaction between a colloid and a polymer center is

$$V^{cp}(r) = \begin{cases} \infty & \text{if } r \leq R^c + R^p, \\ 0 & \text{else,} \end{cases} \quad (2)$$

while a tagged monomer interacts with (its) polymer through

$$V^{mp}(r) = \begin{cases} 0 & \text{if } r \leq R^p, \\ \infty & \text{else.} \end{cases} \quad (3)$$

The total potential energy is given by

$$V^{\text{total}}(r) = \sum_{i < j} V^{cc}(|\mathbf{r}_i^c - \mathbf{r}_j^c|) + \sum_{i,j} V^{cp}(|\mathbf{r}_i^c - \mathbf{r}_j^p|) + \sum_i V^{mp}(|\mathbf{r}_i^p - \mathbf{r}_i^m|). \quad (4)$$

Note that the last summation only includes contributions from pairs of polymer centers and tagged monomers with *equal* indices. This ensures that each tagged monomer i is uniquely bound to its polymer i . See Fig. 1 for a sketch of the model. As thermodynamical variables, we use the packing fractions of colloids, $\eta^c = 4\pi N^c (R^c)^3 / (3V_0)$, and of polymers $\eta^p = 4\pi N^p (R^p)^3 / (3V_0)$, and the size ratio $q = R^p / R^c$. The diameters are denoted by $\sigma^c = 2R^c$ and $\sigma^p = 2R^p$.

To derive effective interactions, we keep the hard-core colloid-colloid interaction, and integrate out either the tagged monomers or the polymer centers. Effective binary models result that differ in the cross interaction between unlike species. In both cases, the polymeric degrees of freedom remain ideal. The first case, integrating out the monomer positions \mathbf{r}_i^m , is especially simple, as each monomer is homogeneously distributed inside its polymeric sphere. Note that no overlap between colloid and monomer can occur due to V^{cp} and V^{mp} . We end up with a model containing \mathbf{r}_i^p and \mathbf{r}_j^c . The “effective” interaction between a polymer center and a colloid is the same as the pure interaction $V^{cp}(r)$. In the second case, we intend to derive an effective interaction V_{eff}^{cm} between a tagged monomer and a colloid. This is done in the limit $\eta^c \rightarrow 0$, so that no colloid-colloid interactions need to be taken into account. Due to the ideality of the polymeric degrees of freedom, whether center or monomer, of *different* chains, only a single polymer needs to be considered. Naturally a *pair* potential $V_{\text{eff}}^{cm}(r)$ arises. It is given by

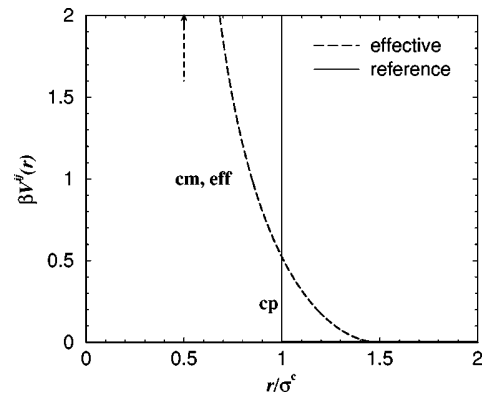


FIG. 2. Comparison of two cross potentials $V^{cp}(r)$ (reference) and $V_{\text{eff}}^{cm}(r)$ (effective) for size ratio $q=1$. The arrow denotes the hard core of $V_{\text{eff}}^{cm}(r)$.

$$V_{\text{eff}}^{cm}(r) = -k_B T \ln \Xi, \quad (5)$$

$$\Xi = \int d^3x \exp \left[-\frac{V^{mp}(|\mathbf{r} - \mathbf{x}|) + V^{cp}(\mathbf{x})}{k_B T} \right], \quad (6)$$

where $r = |\mathbf{r}|$. The integration variable \mathbf{x} is the polymer center of mass, \mathbf{r} is the position of the tagged monomer, and the colloid sits at the origin. For small distances $r < R^c$, all configurations are forbidden due to overlap of the colloid and the polymer, $V^{cp} = \infty$, hence $\Xi = 0$. For large distances, $r > R^c + 2R^p$ no overlap with the colloid occurs and we obtain $\Xi = 4\pi(R^p)^3/3$. The contribution for $R^c \leq r \leq R^c + 2R^p$ is given by the overlap volume of two spheres with radii $R^c + R^p$ and R^p , which is

$$I(r) = \frac{\pi}{12r} (R^c + 2R^p - r)^2 [r^2 - 3(R^c)^2 + 2r(R^c + 2R^p)], \quad (7)$$

and $\Xi = 4\pi(R^p)^3/3 - I(r)$ is obtained. In summary, the effective interaction potential is

$$V_{\text{eff}}^{cm}(r) = \begin{cases} \infty & \text{if } r \leq R^c, \\ -\ln \left[1 - \frac{3I(r)}{4\pi(R^p)^3} \right] & \text{if } R^c \leq r \leq R^c + 2R^p, \\ 0 & \text{else,} \end{cases} \quad (8)$$

where we have shifted the potential by an irrelevant constant of $\ln[4\pi(R^p)^3/3]$, so that it vanishes for large separations. This has no effect on observable quantities. In Fig. 2 we compare both cross potentials V^{cp} and V_{eff}^{cm} as a function of r . Both differ considerably.

The full model has three components: colloids, polymer centers, and tagged monomers; hence one can investigate six different pair correlation functions $g^{ij}(r)$. Both the effective as well as the reference model have two components, of which only the colloid-colloid pair distribution function $g^{cc}(r)$ can be compared directly. The other two involve polymeric degrees of freedom, whether the polymer center or the tagged monomer, and cannot be compared directly. However,

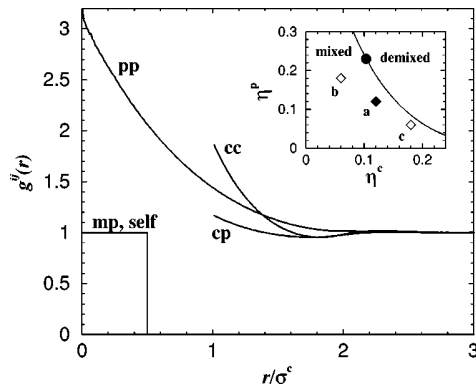


FIG. 3. Full model. Pair-distribution functions $g^{ij}(r)$ for pairs of colloids (cc), polymer centers (pp), colloids and polymer centers (cp), and monomers and polymer centers (mp , self-part) for $q=1$, $\eta^c = \eta^p = 0.12$ [statepoint (a)]. The inset shows the phase diagram from free volume theory [19] with a critical point (dot), and three statepoints [(a), (b), (c), see Table I] marked.

we can compare $g_{\text{self}}^{mp} * g^{cp}$ with g^{mc} , and $g_{\text{self}}^{mp} * g^{pp} * g_{\text{self}}^{mp}$ with g^{mm} , where the star denotes convolution. This is equivalent to multiplying the corresponding structure factors in Fourier space, where the Fourier transform of g_{self}^{mp} plays the role of the polymer form factor. In order to obtain the pair distribution functions, we have carried out Monte Carlo (MC) computer simulations with 512 particles and 10^6 Monte Carlo moves per particle. To obtain the correlation functions involving monomers for the reference system, instead of calculating the convolutions explicitly, a simulation of the full model was done. MC moves for the monomers are particularly simple. Any random vector \mathbf{r}_i^m within a sphere with radius R^p around \mathbf{r}_i^p is a valid monomer position.

As an illustration, we first show pair-correlation functions for the full model in Fig. 3 for equal sizes, $q=1$, and equal densities, $\eta^c = \eta^p = 0.12$. Both, $g^{cc}(r)$ and $g^{cp}(r)$ show hard-sphere-like behavior. They vanish inside the core, $r < \sigma^c$ and $r < R^c + R^p$, respectively, and have oscillations outside. The behavior of $g^{pp}(r)$ is different; polymers tend to form clusters, as can be seen from the rise for small separations. Also plotted is $g_{\text{self}}^{mp}(r)$, which is unity for $r < R^p$, and zero outside. The inset shows the phase diagram from free volume theory [19] for $q=1$. We pick three statepoints in the mixed phase, at equal total density $\eta^c + \eta^p = 0.24$. Statepoint (c) has higher colloid density, and statepoint (b) has lower colloid density compared to (a), see Table I. In Fig. 4 we compare results from the effective model to those from the reference model. See Fig. 4 for results at statepoint (a). The results for the reference model are obtained by appropriate

TABLE I. Summary of statepoints where pair distribution functions are considered.

Statepoint	η^c	η^p
(a)	0.12	0.12
(b)	0.06	0.18
(c)	0.18	0.06

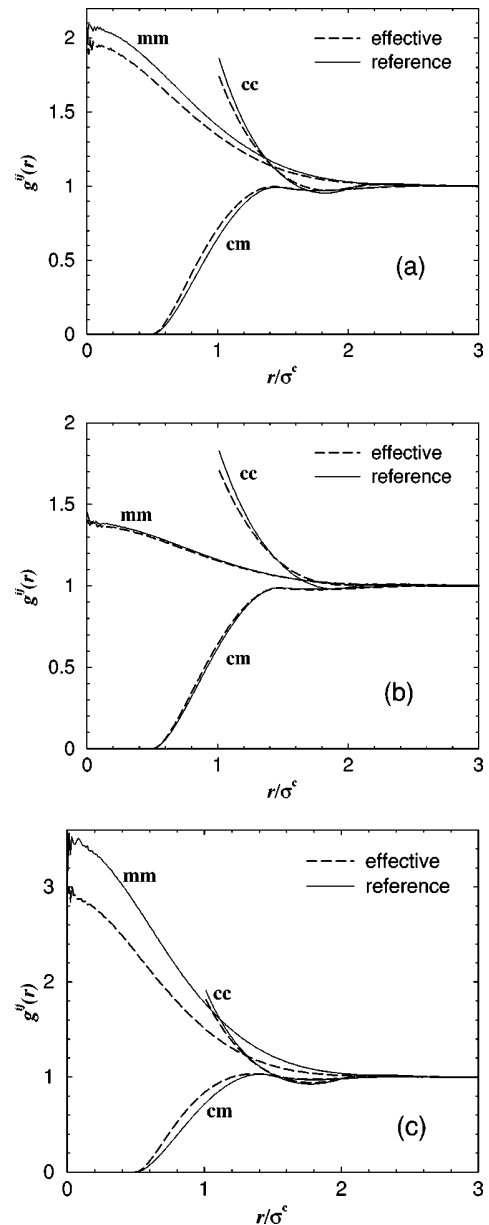


FIG. 4. Comparison of an effective and reference model. Pair-distribution functions $g^{ij}(r)$ for pairs of colloids (cc), tagged monomers (mm), as well as colloids and monomers (cm) for $q=1$ at statepoints $\eta^c = \eta^p = 0.12$ (a); $\eta^p = 0.18$, $\eta^c = 0.06$ (b); and $\eta^p = 0.06$, $\eta^c = 0.18$ (c).

convolutions with g_{self}^{mp} . This implies that g^{cc} is identical to Fig. 3. A single convolution turns the jump in g^{cp} to the gradual decrease to zero of g^{mp} . Via two convolutions the cusp at $r=0$ of g^{pp} becomes flat in g^{mm} . The corresponding results for the effective model are close to those for the reference model, except for slightly less structured behavior. Increasing the polymer concentration [statepoint (b)] reduces the overall structure and reduces the differences between results for the effective and reference model. As expected, as in the limit $\eta^c \rightarrow 0$, the effective model becomes exact by con-

BRIEF REPORTS

PHYSICAL REVIEW E **65** 022801

struction. If we increase η^c [statepoint (c)], stronger deviations occur. The strong clustering of g^{mm} is especially underestimated by the effective model. The colloid-colloid structure, however, is affected only a little.

Coming back to the question, whether effective interactions depend on the choice of coordinates, the answer is certainly yes. However, the more relevant question is: to what extent does the choice of coordinates affect the structural properties calculated from the effective interactions? There the answer is only a little. A few cautionary remarks are in

order. First, it is unclear whether the robustness of correlation functions is also present in more realistic models than the highly simplified AO colloid-ideal polymer mixture. In particular, long-ranged forces could lead to different behavior. Second, the present paper covers only bulk fluid states. In crystals or inhomogeneities caused by external influence, the situation may also be different.

The author thanks J. Dzubiella, A. Jusufi, C. N. Likos, C. von Ferber, and H. Löwen for stimulating discussions.

-
- [1] C. N. Likos, *Phys. Rep.* **348**, 267 (2001).
 [2] A. A. Louis, P. G. Bolhuis, J. P. Hansen, and E. J. Meijer, *Phys. Rev. Lett.* **85**, 2522 (2000).
 [3] P. G. Bolhuis, A. A. Louis, J. P. Hansen, and E. J. Meijer, *J. Chem. Phys.* **114**, 4296 (2001).
 [4] P. G. Bolhuis, A. A. Louis, and J. P. Hansen, *Phys. Rev. E* **64**, 021801 (2001).
 [5] A. A. Louis, *Philos. Trans. R. Soc. London, Ser. A* **359**, 939 (2001).
 [6] P. G. Bolhuis, A. A. Louis, and J. P. Hansen, *Phys. Rev. E* **64**, 021801 (2001).
 [7] J. Dzubiella, A. Jusufi, C. N. Likos, C. von Ferber, H. Löwen, J. Stellbrink, J. Allgaier, D. Richter, A. B. Schofield, P. A. Smith, W. C. K. Poon, and P. N. Pusey, *Phys. Rev. E* **64**, 010401(R) (2001).
 [8] C. N. Likos, H. Löwen, M. Watzlawek, B. Abbas, O. Jucknischke, J. Allgaier, and D. Richter, *Phys. Rev. Lett.* **80**, 4450 (1998).
 [9] A. Jusufi, M. Watzlawek, and H. Löwen, *Macromolecules* **32**, 4470 (1999).
 [10] S. Asakura and F. Oosawa, *J. Chem. Phys.* **22**, 1255 (1954).
 [11] A. Vrij, *Pure Appl. Chem.* **48**, 471 (1976).
 [12] M. Dijkstra, J. M. Brader, and R. Evans, *J. Phys.: Condens. Matter* **11**, 10079 (1999).
 [13] A. A. Louis, R. Finken, and J. Hansen, *Europhys. Lett.* **46**, 741 (1999).
 [14] J. M. Brader and R. Evans, *Europhys. Lett.* **49**, 678 (2000).
 [15] J. M. Brader, M. Dijkstra, and R. Evans, *Phys. Rev. E* **63**, 041405 (2001).
 [16] M. Schmidt, H. Löwen, J. M. Brader, and R. Evans, *Phys. Rev. Lett.* **85**, 1934 (2000).
 [17] J. M. Brader, R. Evans, M. Schmidt, and H. Löwen, *J. Phys. Condens. Matter*, **14**, L1 (2002).
 [18] For a macromolecular approach to colloid-polymer mixtures see M. Fuchs and K. S. Schweizer, *Europhys. Lett.* **51**, 621 (2000).
 [19] H. N. W. Lekkerkerker, W. C. K. Poon, P. N. Pusey, A. Stroobants, and P. B. Warren, *Europhys. Lett.* **20**, 559 (1992).

Decoration lattices of colloids adsorbed on stripe-patterned substrates

H. M. Harreis,* M. Schmidt, and H. Löwen

Institut für Theoretische Physik II, Heinrich-Heine-Universität Düsseldorf, Universitätsstraße 1, D-40225 Düsseldorf, Germany

(Received 27 November 2001; published 26 March 2002)

The equilibrium structure of decoration lattices composed of colloidal particles adsorbed on periodic stripe-patterned substrates is calculated as a function of the stripe width and separation and for different interparticle interactions. Due to a competition of length scales, a wealth of different stable decoration lattices occurs such as triangular, quadratic, rhombic, kitelike, and sheared honeycomb lattices, triangular slices as well as triangle superlattices. This is of relevance for constructing templates that enforce crystal growth of unusual solid structures.

DOI: 10.1103/PhysRevE.65.041602

PACS number(s): 67.70.+n, 82.70.Dd, 68.43.-h, 68.08.Bc

I. INTRODUCTION

Recent advances in microfabrication have allowed to prepare chemically or topographically patterned substrates in a controlled way by using e.g., lithographic printing or other etching techniques [1,2]. There is a profound influence of such a substrate pattern on wetting [3–10], on adsorption of soft matter [11,12] and biological macromolecules [13,14], on crystal nucleation [15], and on bulk phase transitions such as freezing [16,17] and fluid-fluid phase separation [18]. Patterned substrates have also been used in so-called microfluidics in order to control chemical reactions on a microscale or nanoscale [19,20]. For this purpose, one-dimensional channels are considered that carry the reacting material. These channels can either be attractive stripes or topographical grooves.

In this paper we study the adsorption of colloidal particles on a sticky periodic stripelike pattern. Our motivation to do so is first coming from experiments where decorations were obtained by adsorbing colloidal spheres on a patterned substrate mask [11,21–29], or in an external laser field [30], for a recent review see Ref. [31]. Such a decorated substrate may be offered as a template to other mobile colloidal particles in order to nucleate further colloidal crystalline sheets and to grow “exotic” colloidal bulk crystals [16,32,33]. The colloidal particles can both be sterically stabilized [34] or charge stabilized. In the former case, the pattern can be prepared by a different chemical coating while in the latter the surface pattern is dictated by the inhomogeneous surface charge density [13,35,36]. Another experimental system to observe structure formation near interfaces is magnetic bubble arrays with periodic line pinning [37]. While much experience has been accumulated in how to prepare the substrate in order to realize a prescribed mask, a more systematic theoretical understanding of possible decoration structures as induced by an underlying sticky periodic pattern is missing. In this paper we investigate this problem for a periodic stripe pattern within a simple model calculation including both attractive and repulsive effective interparticle interactions. In equilibrium, we discover a wealth of possible stable decoration lattices. Hence although the substrate pattern is relatively

simple, the decoration can be fascinatingly complex so that a wide range of decoration structures can be generated in a controlled and simple way. Even for a single stripe, periodic decoration structures as buckled alternating superlattices with a unit cell involving a large triangle of particles and finite slices of a triangular bulk lattice may become stable. For a periodic stripe pattern, there are even more stable decoration lattices, involving triangular, quadratic, rhombic, kite-like, and sheared honeycomb lattices.

The paper is organized as follows: We describe the model in Sec. II and outline our theory in Sec. III. Results are presented in Sec. IV, and we conclude in Sec. V.

II. THE MODEL

We consider a periodically stripe-patterned smooth surface, shown schematically in Fig. 1. The width of the sticky stripes is d , while the distance between neighboring stripes is b , so that the structure is periodic in a direction perpendicular to the stripes with periodicity length $b+d$. This patterned surface is exposed to a suspension of spherical colloidal particles with hard-core diameter σ aggregating onto the pattern. An aggregated sphere exhibits a point contact with the substrate gaining a potential energy $-\epsilon < 0$, provided the contact point is inside a sticky stripe. We assume strongly attractive substrates, such that ϵ is much larger than the ther-

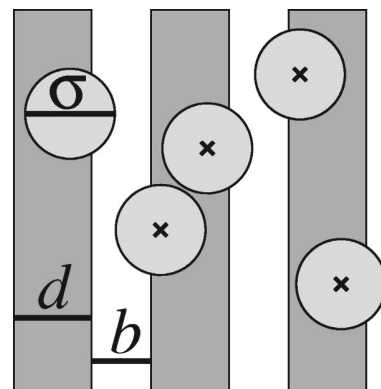


FIG. 1. Model of hard spheres of diameter σ on an attractive stripe pattern (dark gray) of width d and interstripe distance b . The sphere centers (crosses) are constrained to lie inside the stripes.

*Email address: harreis@thphys.uni-duesseldorf.de

H. M. HARREIS, M. SCHMIDT, AND H. LÖWEN

PHYSICAL REVIEW E **65** 041602

mal energy $k_B T$. Aggregation on the interstripe regions is neglected. Aggregation occurs from a dilute bulk solution of colloids. Here, we do not discuss the dynamics of aggregation or deposition [38], but rather focus on the equilibrium structure present after relaxation of the adsorption process. Typical pair potentials $V(r)$ as a function of separation distance r between colloids have an inner hard core and a short-ranged tail. By addition of nonadsorbing polymers or salt ions to the bulk solution, both attractive or repulsive tails can be realized [39]. For simplicity, we use a square-well/square-shoulder potential,

$$V(r) = \begin{cases} \infty & \text{for } r < \sigma, \\ v_0 & \text{for } \sigma \leq r < \sigma(1 + \delta), \\ 0 & \text{else,} \end{cases} \quad (1)$$

with a small positive (reduced) range δ . Depending on the sign of v_0 , the tail is either repulsive ($v_0 > 0$) or attractive ($v_0 < 0$). Thermodynamics of this system in bulk has been studied in detail, see e.g., Refs. [40–43] and references therein. Here, we expose the model to an inhomogeneous surface, and restrict ourselves to zero temperature, i.e., to the classical ground state [44]. Let A be the area of the surface, N be the number of adsorbed particles, $\rho = N/A$ denote the (two-dimensional) number density, and $\eta = \pi\rho\sigma^2/4$ the corresponding area fraction. The whole system is characterized by four reduced parameters, namely, the reduced width d/σ of the attractive stripe, the reduced interstripe width b/σ , the range of the potential δ , and the ratio v_0/ϵ of colloid-colloid to substrate-colloid interaction.

III. THEORY

For zero temperature the energetically most favorable configurations of the adsorbate will be attained. Technically, we need to minimize the total potential energy U per substrate area A . One may decompose $u \equiv U/A = u_1 + u_2$, where u_1 stems from substrate-particle attraction, and u_2 from particle-particle interactions. These contributions are

$$u_1 = -\epsilon\rho, \quad (2)$$

$$u_2 = A^{-1} \sum_{i=1}^N \sum_{j=i+1}^N V(|\vec{r}^{(i)} - \vec{r}^{(j)}|), \quad (3)$$

where $\vec{r}^{(i)}$ denote (two-dimensional) particle positions on the surface. It will prove useful to rewrite u_2 in terms of the *kissing numbers* $k^{(i)}$ (of particle i), that equal the number of touching spheres (i.e., $|\vec{r}^{(i)} - \vec{r}^{(j)}| = \sigma$) for particle i . If we assume absence of hard-core overlap, and all particle separations r being either at contact ($r = \sigma$), or outside the range of interaction [$r > \sigma(1 + \delta)$], we can write

$$u_2 = \frac{v_0}{2A} \sum_{i=1}^N k^{(i)} \equiv v_0 \rho k/2, \quad (4)$$

where $k = N^{-1} \sum_{i=1}^N k^{(i)}$ is the (over system) averaged kissing number. Note that u_1 favors optimal packing of spheres,

while u_2 couples to the number of sphere contacts. Decisive for phase behavior is the competition between optimization of packing and kissing, where the ratio v_0/ϵ is a control parameter. In practice, we start with different candidate lattices for the colloids, calculate u for each one in order to find the optimal lattice that minimizes u . The choice of candidates is motivated by mathematical packing and includes rhombic, square, triangular, kite, and other structures involving superlattices. We disregard the disordered fluid phase, as temperature is zero. We have not considered nonperiodic structures as quasicrystals [45], that are expected to be unfavorable for a one-component colloidal system, but could become relevant for binary and ternary mixtures. A similar zero-temperature calculation on structured substrates can be found in Ref. [44], for quadratic substrate patterns and Lennard-Jones interparticle interactions. We further remark that similar crystalline lattice structures were obtained in Ref. [46] for a different physical system, namely, flux lattices in layered superconductors. In contrast to the short-range interactions employed in the present paper, the interaction between flux lines is long ranged.

IV. RESULTS

A. Single stripe

For $b/\sigma > 1 + \delta$, the spheres adsorbed on neighboring stripes are decoupled and the problem reduces to that of adsorption onto a single stripe. For simplicity, we let $\delta \rightarrow 0$ and $v_0 \leq 0$, so that we deal with sticky hard spheres. Geometrical considerations as well as numerically checking other structures makes it possible for us to restrict the actually realized candidates to two n -layered crystals, namely (i) triangular lattices ($n\Delta$), and (ii) *supertriangle* structures (nS), see Fig. 2 for illustrations. $n\Delta$ is a portion of the triangular (bulk) lattice. The nS crystal consists of a buckled superlattice of alternating close-packed triangles.

The relevant properties of both candidates are the following. For n close-packed layers on a stripe of width d , we find

$$\rho_\Delta = \frac{n}{d\sigma}, \quad (5)$$

$$\rho_S = \frac{n(n+1)}{d\sigma[(n-1) + 2 \cos \alpha]}, \quad (6)$$

where $\alpha \in [0, \pi/3]$ is the mismatch angle between adjacent supertriangles, see Fig. 2. For close-packed states, α is related to d via

$$\alpha(d) = \arcsin[d - \sqrt{3}(n-1)/2]. \quad (7)$$

Note that for $\alpha = 0$ (no mismatch), $n\Delta$ coincides with nS , and trivially $\rho_\Delta = \rho_S$. These configurations define the close-packed area fraction η_{cp} plotted in Fig. 3(a) as a function of stripe width d . For the average kissing number, we obtain via counting of sphere contacts,

$$k_\Delta = 6 - \frac{4}{n}, \quad (8)$$

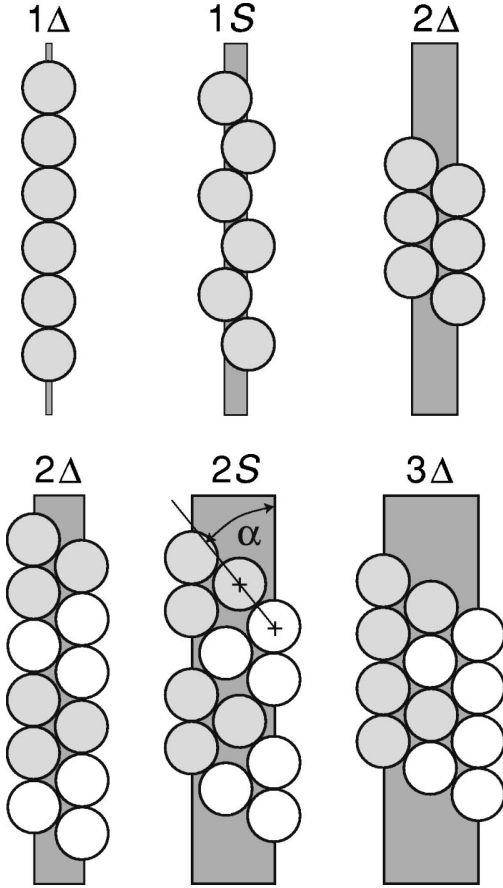


FIG. 2. Crystal structures $n\Delta$ and nS of hard spheres sticking to a single stripe of width d for $n=1,2,3$. The stripe width d increases from left to right. $\alpha \in [0, \pi/3]$ is the mismatch angle between adjacent supertriangles. Spheres building equilateral (super)triangles are shaded to guide the eye. For larger d the sequence continues in an analogous way.

$$k_S = 6 - \frac{8}{n+1}. \quad (9)$$

Although in the limit $\alpha \rightarrow 0$ the structures themselves become identical, k_S does not approach k_Δ smoothly, but jumps at $\alpha=0$. Relevant for the potential energy [Eq. (4)] is not the kissing number alone, but $\rho k/2$, that is plotted in Fig. 3(b) as a function of stripe width d .

In the limit $v_0 \rightarrow -\infty$, maximal kissing *per unit area* determines the equilibrium structure, as the dominant contribution $\rho k/2$ [Eq. (4)] to the energy u is to be maximized. Quite surprisingly, in each interval $n\sqrt{3}\sigma/2 < d < (n+1)\sqrt{3}\sigma/2$, a transition $n\Delta \rightarrow nS$ exists, that is located at $d/\sigma = (n-1)\sqrt{3}/2 + \sqrt{1 - [(2-n^{-1})/(3-2n^{-1})]^2}$, where large k and low ρ in $n\Delta$ are outperformed by low k and high ρ in nS . Note that as $n \rightarrow \infty$, the transition persists, and the relative phase transition point $d/\sigma - (n-1)\sqrt{3}/2$ approaches $\sqrt{5}/3 = 0.7454$.

Putting things together, we can turn to the full energetically driven phase diagram for arbitrary $|v_0/\epsilon|$. Asking first how additional layers $n \rightarrow n+1$ jump in, we find the simple

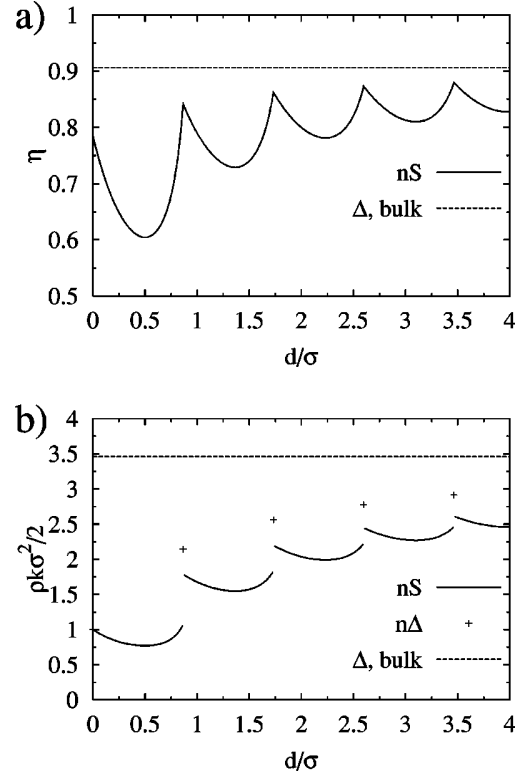


FIG. 3. Relevant densities for close-packed hard spheres of diameter σ on a stripe of width d as a function of d/σ for $n\Delta$ (symbols) and nS (lines) structures, as well as for the bulk triangular lattice (dashed lines). (a) Area packing fraction η . (b) Kissing number density per unit area, $\rho\sigma^2 k/2$.

answer: A transition $nS \rightarrow (n+1)\Delta$ is located at $d = n(\sqrt{3}/2)\sigma$, independent of v_0/ϵ . The $n\Delta \rightarrow nS$ transition is less trivial. We obtain

$$d = (n-1)(\sqrt{3}/2)\sigma + \sigma \sqrt{1 - \frac{[(\epsilon/v_0) - 2 + n^{-1}]^2}{[(\epsilon/v_0) - 3 + 2n^{-1}]^2}}. \quad (10)$$

In the limiting cases, for $v_0/\epsilon=0$, we recover the close-packing structure of discs between lines, and for $v_0/\epsilon \rightarrow -\infty$ the structure with maximal number of kisses. Equation (10) interpolates smoothly between these limits.

The resulting phase diagram is shown in Fig. 4 as a function of d and $\exp(v_0/\epsilon)$. We restrict ourselves to $n \leq 4$; the succession of nS and $n\Delta$ continues for larger d . In the limit of broad stripes ($d \rightarrow \infty$) and infinitely many layers ($n \rightarrow \infty$), we consider $d - (n-1)(\sqrt{3}/2)\sigma$, that maps d/σ onto the $[0,1]$ interval and obtain the universal (n -independent) result,

$$d - (n-1)(\sqrt{3}/2)\sigma \rightarrow \sigma \sqrt{\frac{5 - 2(\epsilon/v_0)}{[(\epsilon/v_0) - 3]^2}}. \quad (11)$$

Narrow stripes with $0 < d < (\sqrt{3}/2)\sigma$ constitute a special case, because of dominance of a single phase $1S$ (1Δ is

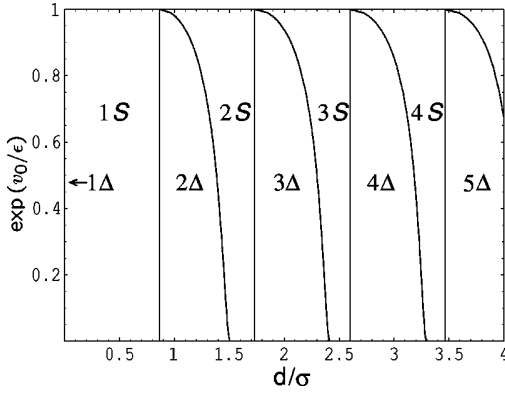


FIG. 4. Phase diagram for sticky hard spheres adsorbed on a single sticky stripe as a function of reduced stripe width d/σ , and the (exponentiated) ratio v_0/ϵ of interparticle versus substrate potential. Lines are phase boundaries between $n\Delta$ and nS structures. The 1Δ phase is a vertical line at $d/\sigma=0$.

squeezed to a vertical line at $d=0$.) The reason for this behavior is that 1Δ and $1S$ possess equal kissing numbers. This is in contrast to $n>1$, where $k_\Delta > k_S$.

Two remarks are in order: First, the supertriangular phases nS are the two-dimensional analog of three-dimensional prism phases [47] found for hard spheres confined between parallel hard plates. A similar cascade of phases has been found there, although this is interrupted by other additional phases such as a rhombic structure [48,49]. Second, in contrast to the bulk problem [50,51], we are not aware of a strict mathematical proof for close-packed configurations, nor of any other numerical investigation of the packing problem of discs between lines. Other confining geometries such as the square [52–54], triangles [55,56], and the circle [57–59] have been treated in a rigorous way.

B. Coupled stripes

For $b/\sigma < 1 + \delta$, particles on adjacent stripes interact. We limit ourselves to the hard sphere case, $\delta=0$, and hence deal with a packing problem. To break possible degeneracy of close-packed states, we consider $v_0/\epsilon \rightarrow 0^-$, favoring sphere contacts.

1. Triangular lattice

We focus on the close-packed triangular lattice, of which is known that there is no denser structure in bulk. If we succeed to identify patterns that are compatible (all lattice sites lie on sticky stripes) with the triangular lattice, we have then *proved* that there is no denser decoration lattice. The task is to determine the (b, d) regimes in which the triangular lattice is geometrically possible. Let the lattice sites of a triangular lattice be

$$\vec{A}(j, k) = j\vec{a}_1 + k\vec{a}_2, \quad j, k = 0, \pm 1, \pm 2, \dots, \quad (12)$$

where $\vec{a}_1 = (\sigma, 0)$, $\vec{a}_2 = (\sigma/2, \sqrt{3}\sigma/2)$ are basis vectors. In the following, we imagine the lattice to be fixed on the surface and attempt to determine those stripe patterns that are com-

patible with the particle lattice. For given b, d the pattern is determined by the orientation along the stripes. This orientation may be expressed as $\vec{A}(j, k)/|\vec{A}(j, k)|$, with suitably chosen values for j, k . In order to find stripe patterns that fit the lattice, we calculate the distance $\xi(j, k)$ between adjacent lattice lines (the analog to lattice *planes* in three dimensions), that are parallel to $\vec{A}(j, k)/|\vec{A}(j, k)|$. To this end, we introduce a vector $\vec{B}(j, k)$, that is orthogonal to $\vec{A}(j, k)/|\vec{A}(j, k)|$ as

$$\vec{B}(j, k) = -(j+2k)\vec{a}_1 + (2j+k)\vec{a}_2. \quad (13)$$

Projection of $(-1/k)\vec{a}_1$ onto \vec{B} gives the lattice line distance

$$\xi(j, k) = -\frac{\vec{a}_1 \cdot \vec{B}}{k|\vec{B}|} = \frac{\sqrt{3}\sigma/2}{\sqrt{j^2 + jk + k^2}}. \quad (14)$$

Upon varying j and k , the argument $j^2 + jk + k^2$ generates a (seemingly irregular when sorted) sequence of integer numbers, namely, 1, 3, 4, 7, 9, 12, 13, 16, 19, 21, 25, 27, 28, 31, 36, 37, 39, 43, 48, 49, Expression (14) gives the lattice line distance for an orientation of lattice lines (parallel to the stripes) defined by j, k . Assuming that $b+d$ and the lattice structure $\xi(j, k)$ have the same periodicity, a triangular lattice fits, whenever the stripe width d (with the stripe orientation given by $\vec{A}(j, k)/|\vec{A}(j, k)|$) and the interstripe distance b have periodicity $\xi(j, k)$, $j, k \in \mathbb{Z}$,

$$b + d = \xi(j, k). \quad (15)$$

This introduces a linear relationship between stripe width d and interstripe distance b . In the b - d plane, lines joining $(\xi, 0)$ and $(0, \xi)$ indicate regions where the triangular lattice fits the stripe pattern. For smaller values of ξ , these lines get increasingly dense and finally converge into the origin.

The assumption of $b+d$ periodicity is not mandatory. Rather, we could let the structure be periodic after m lattice spacings $\xi(j, k)$, and after l stripe spacings $(b+d)$. This relation reads

$$b + d = \frac{m}{l} \xi(j, k), \quad (16)$$

where m and l must be undivisible integers, in order to avoid redundances. The periodicity brings about a set of inequalities to be satisfied, expressing the condition that no sphere may lie outside a stripe,

$$i\xi(j, k) \leq j(b+d) \vee i\xi(j, k) \geq j(b+d) + b, \quad (17)$$

that is to be fulfilled for all i, j . Solving this leads to the relation

$$(m-1)b \leq d. \quad (18)$$

If we assume equality and use Eq. (16), we can solve for the minimal stripe width d_{\min} and simultaneous maximal interstripe distance b_{\max} . These are

$$b_{\max} = \frac{1}{l} \xi(j, k), \quad (19)$$

$$d_{\min} = \frac{(m-1)}{l} \xi(j, k), \quad (20)$$

and fulfill the relation

$$(m-1)b_{\max} = d_{\min}. \quad (21)$$

Hence the triangular regimes are lines from $(0, \xi)$ to (b_{\max}, d_{\min}) . The above case [lines from $(0, \xi)$ to $(\xi, 0)$] is recovered for $m=l=1$. For each combination of m and l we thus get a one-dimensional regime, where the triangular lattice fits. Variation of j and k , at fixed m and l , then gives additional lines, shifted on the d axis with their length being reduced. This is illustrated in Fig. 5(a), where j and k are varied with $m=1$ and $l=1$ fixed (solid lines) as well as $m=4$ and $l=1$ fixed (dashed lines). The shift of the lines is according to Eq. (21), their upper end points lying on a line defined by Eq. (19), whose slope changes with m . In Fig. 5(b), the lattice line distances $\xi(j, k)$ are fixed via $j=0, k=1$ (solid lines), $j=0, k=2$ (dotted lines); and $j=1, k=2$ (dash-dotted lines), while m and l are varied. Figure 5(b) illustrates that (j, k) for a given combination of (m, l) determine the height and position of one line, with other combinations of (m, l) producing replicas that are shifted on the d axis. Figure 5(c) covers the full range (relevant for the scale of the plot) of values j, k, m, l . Note how the lines get denser for $b \rightarrow 0$, and ultimately approach stripe-free bulk packing. Although we cannot prove that the triangular lattice does *not* fit any other parts in the phase diagram, we find that quite likely.

The geometrical features of the regimes are visually quite striking and may be unexpected from the outset. It is, however, known that competition of length scales may induce fractal structures [60]. One simple tool to analyze these is box counting [61]. In a two-dimensional situation, one covers the structure under consideration with a rectangular mesh with mesh width W , and counts the number of boxes, B , that touch (or are completely inside) the structure. This is performed successive times on smaller length scales W . For a fractal, a scaling law $B \propto W^{-\gamma}$ holds, where the dimension γ is not an integer. We have carried out such an analysis and could confirm quite well power law scaling with a noninteger exponent. A precise determination of γ , however, turned out to be subtle. We have restricted ourselves to a physically reasonable lower cutoff $W > 10^{-3} \sigma$. For $m=l=1$, we obtain a $\gamma=1.5$. Superimposing ‘‘fence’’ patterns by varying m, l over a broad range of values changes the dimension to $\gamma=1.6$. Such an increase seems reasonable, as apparently, the structure gets denser. We leave a more thorough investigation to possible future research.

2. More general cases

We will approach the general case by considering interacting stripes that are themselves densely packed. Results are known for $b/\sigma > 1$, periodic arrangement of the stripes will,

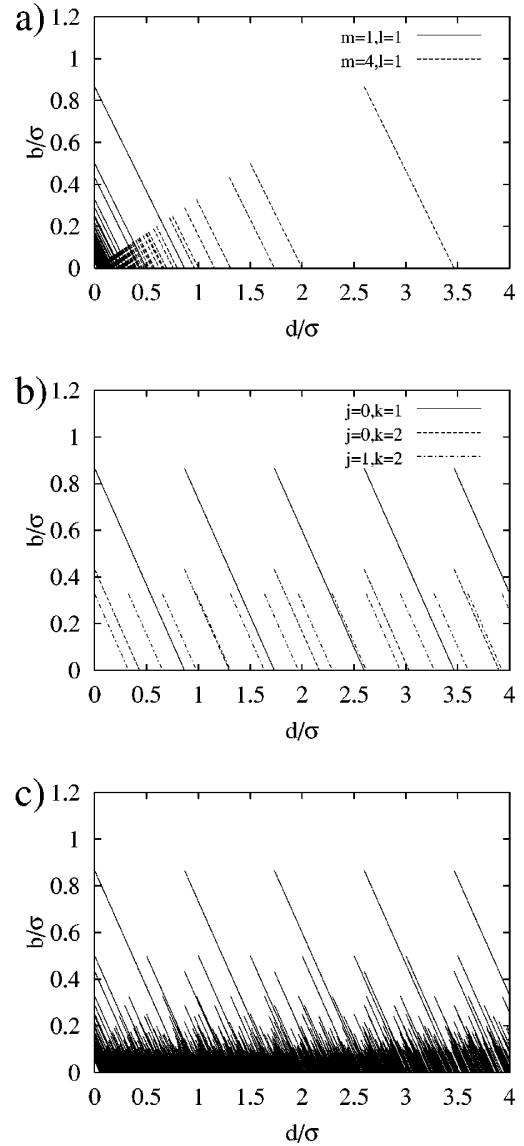


FIG. 5. Regions of stability of the triangular lattice (lines). (a) m, l kept constant (as indicated), and j, k varied. (b) j, k kept constant (as indicated), and m, l varied. (c) Full range of j, k, m, l (relevant for the scale of the plot).

however, give rise to special lattices. For $b/\sigma=1$, the spheres from different stripes can touch and the stable phase is determined by the equilibrium structure on the stripes, together with the degeneracy breaking condition $v_0/\epsilon \rightarrow 0^-$. We thus get *quadratic* ordering in the interstripe region. A pure quadratic lattice is stable only in one point: $b/\sigma=d$ and $d=0$. For lower b and $d=0$ it gets distorted to a lattice of alternating rhombi, as illustrated in Fig. 6(a). For $d < \sqrt{3}\sigma/2$ the situation is sketched in Figs. 6(b)–6(d) for decreasing values of b . Figure 6 (b) shows $1\mathcal{S}$ structures on decoupled stripes forming kite-structures in a periodic stripe arrangement. The kite structure of Fig. 6(b), however, is degenerated with respect to an arbitrary relative shift of two single stripe patterns. Upon approach and coupling of the stripes a honeycomb (HC) in Fig. 6(c), and eventually a

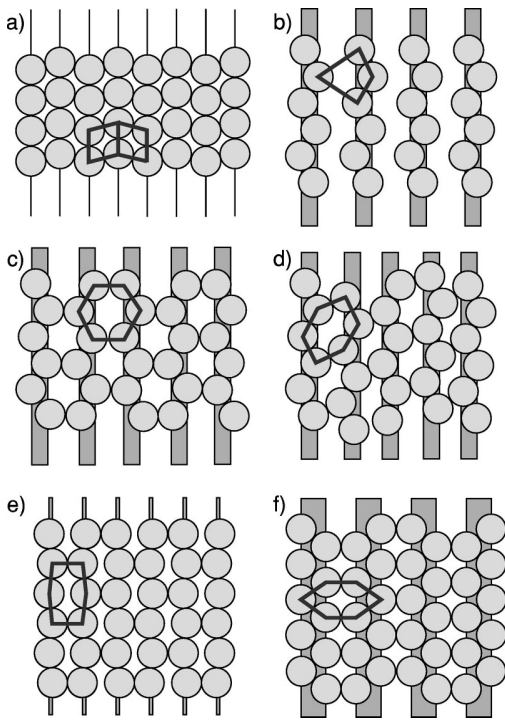


FIG. 6. Crystal structures for $d/\sigma < \sqrt{3}/2$. (a) Alternating rhombic for $d=0$ and $\sqrt{3}/2 < b/\sigma < 1$; in (b)–(d) the situation is shown for $0 < d/\sigma < \sqrt{3}/2$ for decreasing values of the interstripe width b/σ ; (b) 1S structures on decoupled stripes giving rise to kite structures in a periodic stripe arrangement; (c) honeycomb (1HC); (d) sheared honeycomb (sheared 1HC); (e) and (f): squeezed 1HC for $b/\sigma = 1$, with $d/\sigma < 0.5$ and $d/\sigma > 0.5$, respectively. Solid lines indicate unit cells.

sheared honeycomb, shown in Fig. 6(d), emerge. For still smaller b , we expect another alternating rhombic phase, as shown in Fig. 6(a), but with finite $d > 0$, to be stable.

For infinitely thin stripes, the situation for decreasing interstripe distances b is sketched in Fig. 7. A sequence of triangular lattices and centered rectangular lattices arises. Similar structures were observed in recent experiments [29,33].

For large $d > \sqrt{3}\sigma/2$, a squeezed honeycomb structure [Fig. 8(a)] that can also be sheared [Fig. 8(b)] appears. More complex crystal unit cells involving two supertriangular honeycomb structures, both sheared [Fig. 8(c)] and unsheared [Fig. 8(d)] occur for even larger d .

The resulting phase diagram of possible decoration lattices as a function of b/σ and d/σ is depicted in Fig. 9. While for $b/\sigma > 1$ supertriangles are stable (compare Fig. 4), a cascade of sheared honeycomb phases consisting of supertriangles occurs for $b/\sigma < 1$ and increasing d . Along coexistence lines (dashed lines in Fig. 9), these sheared supertriangle honeycomb phases degenerate into different special cases: square lattice ($d/\sigma = 0, b/\sigma = 0$), unsheared honeycomb, squeezed honeycomb [see Figs. 6(e) and 6(f)], and alternating rhombic.

We combine the main results of this investigation with the regions of stability of the undistorted triangular lattice (Sec. IV B 1) and display the whole phase diagram of possible

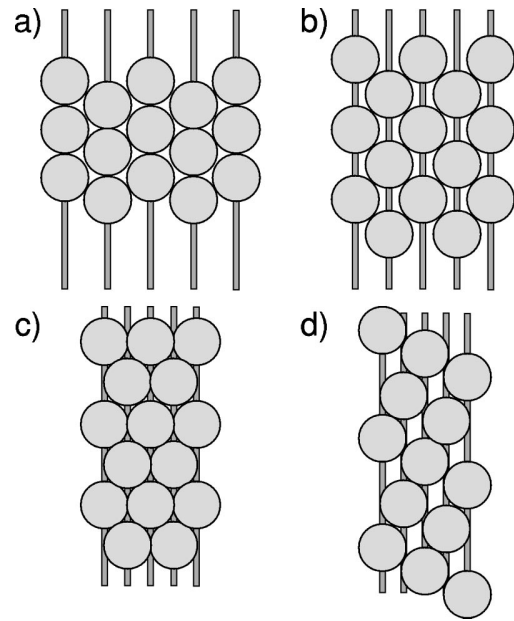


FIG. 7. Crystal structures for infinitely thin stripes $d/\sigma = 0$ and decreasing values of b/σ : (a) hexagonal lattice ($b/\sigma = \sqrt{3}/2$); (b) centered rectangular ($0.5 < b/\sigma < \sqrt{3}/2$); (c) hexagonal lattice ($b/\sigma = 0.5$); (d) centered rectangular ($b/\sigma < 0.5$).

decoration lattices as a function of b/σ and d/σ in Fig. 10. The states between the lines of stability of the triangular lattice are unexplored in our study. We leave those to future work.

Figures 9 and 10 prove that even though our model is relatively simple, competition of different length scales leads to quite different stable decoration lattice structures. On the basis of Figs. 9 and 10 one can tailor the attractive stripe pattern in order to produce a given decoration lattice. This is of direct importance for further crystal growth on top of the

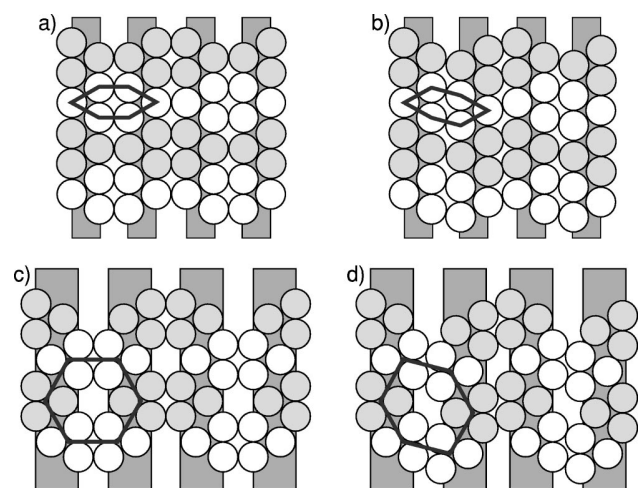


FIG. 8. Crystal structures for $\sqrt{3}/2 \leq d/\sigma < \sqrt{3}$ and $b/\sigma \leq 1$: (a) 2Δ -square hybrid; (b) sheared 2Δ -square hybrid; (c) two-honeycomb structure (2HC); (d) sheared two-honeycomb (sheared 2HC). Spheres building equilateral triangles are shaded to guide the eye. Solid lines indicate unit cells.

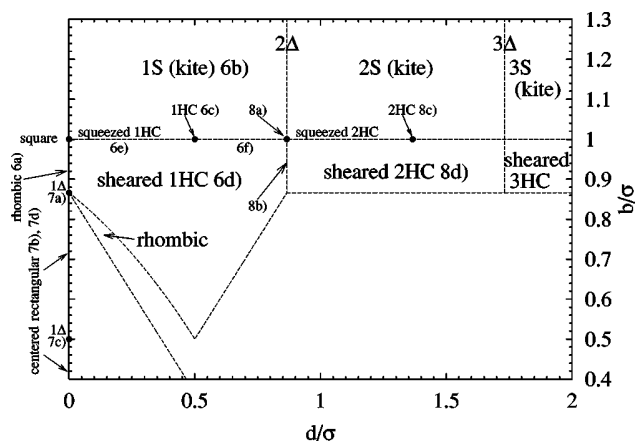


FIG. 9. Phase diagram of attractive hard spheres in a periodic arrangement of sticky stripes with stripe width d and interstripe separation b . Dashed lines indicate two-phase coexistence. Various crystals are stable, as displayed in Figs. 6–8.

decoration lattice used as a template. One can expect [16] that quite exotic bulk crystalline structures can be aggregated on top of such a template [32]. This is of relevance for the construction of optical band-gap materials such as photonic crystals [62].

V. CONCLUSION

In conclusion, we have systematically investigated and predicted decoration lattices composed of colloidal particles adsorbed on an attractive stripe-patterned substrate. Our results show, that due to a competition of various length scales, a wealth of different decoration lattices can be stable. This knowledge can be exploited to generate exotic lattice structures by a tailored surface pattern that could be of relevance for fabricating photonic crystals grown on such templates. Our work can be extended into several directions: First, other periodic patterns such as alternating triangular or chessboard patterns can be studied, where even more complicated deco-

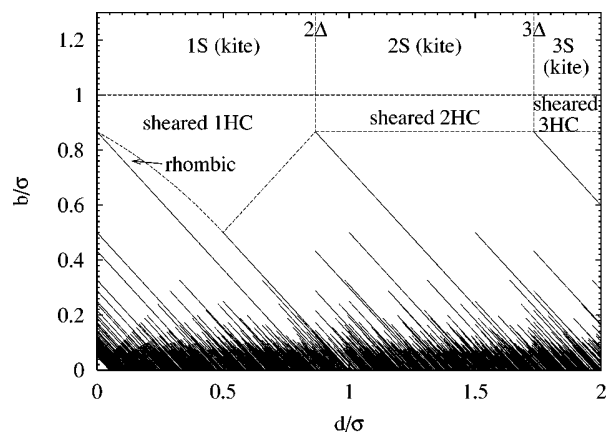


FIG. 10. Phase diagram of attractive hard spheres in a periodic arrangement of sticky stripes with stripe width d and interstripe separation b . Solid lines indicate triangular regimes, dashed lines indicate two-phase coexistence.

ration lattices are expected. Second, the effect of finite temperature and longer ranged and more realistic particle-particle and particle-wall interaction should be investigated. Still we think that the main possibility of decoration lattices will be very similar to the results obtained for the more simplistic interactions. Also, the nonequilibrium problem of particle deposition can produce even much richer nonequilibrium fractal and random closed-packing structures [63–66] that have not been considered in the present equilibrium study. Finally, proving rigorously the different structures to be close packed should be an interesting problem in mathematical geometry.

ACKNOWLEDGMENTS

We thank A. Esztermann, C. N. Likos, and C. von Ferber for helpful remarks. This work was supported by the DFG within the wetting priority program under Contract No. LO 418/5-3.

- [1] For a recent review see: Y. Xia, D. Qin, and Y. Yin, *Curr. Opin. Colloid Interface Sci.* **6**, 54 (2001).
- [2] S. Friebel, J. Aizenberg, S. Abad, and P. Wiltzius, *Appl. Phys. Lett.* **77**, 2406 (2000).
- [3] P. Lenz and R. Lipowsky, *Phys. Rev. Lett.* **80**, 1920 (1998).
- [4] P. Lenz and R. Lipowsky, *Eur. J. E* **1**, 249 (2000).
- [5] S. Herminghaus, A. Fery, S. Schlagowski, K. Jacobs, R. Seemann, H. Gau, W. Mönch, and T. Pompe, *J. Phys.: Condens. Matter* **12**, A57 (2000).
- [6] C. Bauer and S. Dietrich, *Phys. Rev. E* **60**, 6919 (1999).
- [7] L. J. Frink and A. G. Salingers, *J. Chem. Phys.* **110**, 5969 (1999).
- [8] H. Bock and M. Schoen, *Phys. Rev. E* **59**, 4122 (1999).
- [9] H. Bock and M. Schoen, *J. Phys. Condens. Matter* **12**, 1569 (2000).
- [10] R. Lipowsky, *Curr. Opin. Colloid Interface Sci.* **6**, 40 (2001).
- [11] J. Aizenberg, P. V. Braun, and P. Wiltzius, *Phys. Rev. Lett.* **84**, 2997 (2000).
- [12] T. R. Weigl and R. Lipowsky, *Langmuir* **16**, 9338 (2000).
- [13] H. Clausen-Schaumann and H. E. Gaub, *Langmuir* **15**, 8246 (1999).
- [14] A. Sanjoh and T. Tsukihara, *J. Cryst. Growth* **196**, 691 (1999).
- [15] J. Aizenberg, A. J. Black, and G. M. Whitesides, *Nature (London)* **398**, 495 (1998).
- [16] M. Heni and H. Löwen, *Phys. Rev. Lett.* **85**, 3668 (2000).
- [17] M. Heni and H. Löwen, *J. Phys.: Condens. Matter* **13**, 4675 (2001).
- [18] M. Böltau, S. Walheim, J. Mlynek, G. Krausch, and U. Steiner, *Nature (London)* **391**, 877 (1998).
- [19] B. H. Weigl and P. Yager, *Science* **283**, 346 (1999).
- [20] H. Gau, S. Herminghaus, P. Lenz, and R. Lipowsky, *Science* **283**, 46 (1999).

- [21] F. Burmeister, W. Badowsky, T. Braun, S. Wieprich, J. Boneberg, and P. Leiderer, *Appl. Surf. Sci.* **145**, 461 (1999).
- [22] F. Burmeister, C. Schäfle, B. Keilhofer, C. Bechinger, J. Boneberg, and P. Leiderer, *Chem. Eng. Technol.* **21**, 761 (1998).
- [23] C. Mio and D. W. M. Marr, *Langmuir* **15**, 8565 (1999).
- [24] K. M. Chen, X. Jiang, L. C. Kimerling, and P. T. Hammond, *Langmuir* **16**, 7825 (2000).
- [25] C. A. Murray, *Abstr. Pap.-Am. Chem. Soc.* **220**, 74 (2000).
- [26] K. Mangold, R. Bubeck, P. Leiderer, and C. Bechinger, *Prog. Colloid Polym. Sci.* **118**, 77 (2001).
- [27] Z. Adamczyk, B. Siwek, and E. Musial, *Langmuir* **17**, 4529 (2001).
- [28] Q. Guo, C. Arnoux, and R. E. Palmer, *Langmuir* **17**, 7150 (2001).
- [29] Y.-H. Ye, S. Badilescu, V.-V. Truong, P. Rochon, and A. Natansohn, *Appl. Phys. Lett.* **79**, 872 (2001).
- [30] A. Chowdhury, B. J. Ackerson, and N. A. Clark, *Phys. Rev. Lett.* **55**, 833 (1985).
- [31] A. K. Arora and R. Rajagopalan, *Curr. Opin. Colloid Interface Sci.* **2**, 391 (1997).
- [32] A. van Blaaderen, R. Ruel, and P. Wiltzius, *Nature (London)* **385**, 321 (1997).
- [33] K. hui Lin, J. C. Crocker, V. Passad, A. Schofield, D. A. Weitz, T. C. Lubensky, and A. G. Yodh, *Phys. Rev. Lett.* **85**, 1770 (2000).
- [34] F. Burmeister, C. Schäfle, T. Matthes, M. Bohmisch, J. Boneberg, and P. Leiderer, *Langmuir* **13**, 2983 (1997).
- [35] C. Rotsch and M. Radmacher, *Langmuir* **13**, 2825 (1997).
- [36] S. J. Miklavic, D. Y. C. Chan, L. R. White, and T. W. Healy, *J. Phys. Chem.* **98**, 9022 (1994).
- [37] J. Hu and R. M. Westervelt, *Phys. Rev. B* **55**, 771 (1997).
- [38] P. Meakin and R. Jullien, *Physica A* **175**, 211 (1991).
- [39] P. N. Pusey, in *Liquids, Freezing and the Glass Transition*, edited by J. P. Hansen, D. Levesque, and J. Zinn-Justin, *Les Houches Lectures*, Vol. 51 (North Holland, Amsterdam, 1991), p. 763.
- [40] P. Bolhuis, M. Hagen, and D. Frenkel, *Phys. Rev. E* **50**, 4880 (1994).
- [41] C. N. Likos, Z. T. Németh, and H. Löwen, *J. Phys.: Condens. Matter* **6**, 10 965 (1994).
- [42] A. R. Denton and H. Löwen, *J. Phys.: Condens. Matter* **9**, L1 (1997).
- [43] P. Bolhuis and D. Frenkel, *J. Phys.: Condens. Matter* **9**, 381 (1997).
- [44] A. Patrykiewicz, S. Sokolowski, and K. Binder, *J. Chem. Phys.* **115**, 983 (2001).
- [45] A. R. Denton and H. Löwen, *Phys. Rev. Lett.* **81**, 469 (1998).
- [46] L. Levitov, *Phys. Rev. Lett.* **66**, 224 (1991).
- [47] S. Nesper, C. Bechinger, P. Leiderer, and T. Palberg, *Phys. Rev. Lett.* **79**, 2348 (1997).
- [48] M. Schmidt and H. Löwen, *Phys. Rev. Lett.* **76**, 4552 (1996).
- [49] M. Schmidt and H. Löwen, *Phys. Rev. E* **55**, 7228 (1997).
- [50] M. Leppmeier, *Kugelpackungen: Von Kepler bis Heute* (Vieweg, Wiesbaden, 1997).
- [51] H. Löwen, in *Spatial Statistics and Statistical Physics*, edited by K. Mecke and D. Stoyan, *Lecture Notes in Physics* Vol. 554 (Springer, Berlin, 2000), p. 295.
- [52] R. Peikert, *El. Math.* **49**, 17 (1994).
- [53] H. Melissen, *El. Math.* **49**, 27 (1994).
- [54] R. K. Bowle and R. J. Speedy, *Physica A* **262**, 76 (1999).
- [55] H. Melissen, *Am. Math. Monthly* **100**, 916 (1993).
- [56] H. Melissen, *Acta Math. Hung.* **65**, 389 (1994).
- [57] H. Melissen, *Geometria Dedicata* **50**, 15 (1994).
- [58] B. D. Lubachevsky and R. L. Graham, *Discrete. Comput. Geom.* **18**, 179 (1997).
- [59] Z. T. Németh and H. Löwen, *J. Phys.: Condens. Matter* **10**, 6189 (1998).
- [60] P. M. Chaikin and T. C. Lubensky, *Principles of Condensed Matter Physics* (Cambridge University Press, Cambridge, U.K., 2000).
- [61] K. J. Falconer, *Fractal Geometry, Mathematical Foundations and Applications* (Wiley, New York, 1990).
- [62] C. E. Reese, C. D. Guerrero, J. M. Weissman, K. Lee, and S. A. Asher, *J. Colloid Interface Sci.* **232**, 76 (2000).
- [63] P. Meakin and R. Jullien, *Europhys. Lett.* **15**, 667 (1991).
- [64] P. Meakin and R. Jullien, *Europhys. Lett.* **15**, 851 (1991).
- [65] B. D. Lubachevsky, F. H. Stillinger, and E. N. Pinton, *J. Stat. Phys.* **64**, 501 (1991).
- [66] J. E. Socolar, *Europhys. Lett.* **18**, 39 (1992).

